

P-775

NASA Conference Publication 2437

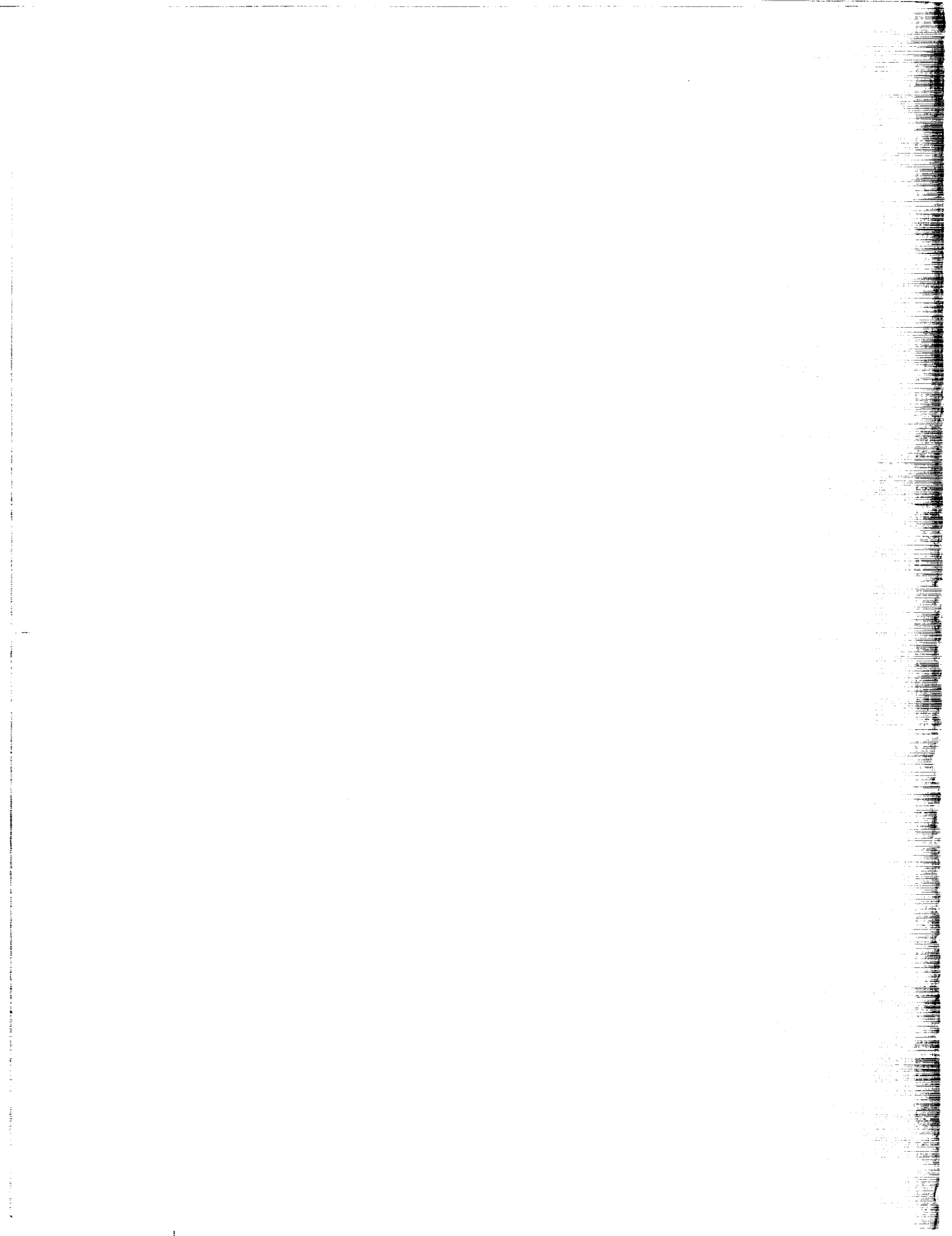
# Advanced Earth-to-Orbit Propulsion Technology 1986

*Volume II*

(NASA-CP-2437-Vol-2) ADVANCED  
EARTH-TO-ORBIT PROPULSION TECHNOLOGY 1986,  
VOLUME 2 (NASA) 775 F CSCL 21H

89-12626  
--1HRU--  
N89-12661  
Unclass  
0164946

H1/20





*NASA Conference Publication 2437*

# Advanced Earth-to-Orbit Propulsion Technology 1986

*Volume II*

*Edited by*  
R. J. Richmond  
*George C. Marshall Space Flight Center*  
*Huntsville, Alabama*

S. T. Wu  
*The University of Alabama in Huntsville*  
*Huntsville, Alabama*

Proceedings of a conference held at  
NASA George C. Marshall Space Flight Center  
Huntsville, Alabama  
May 13-15, 1986

**NASA**  
National Aeronautics  
and Space Administration  
**Scientific and Technical  
Information Branch**

1986



C O N F E R E N C E   C O - C H A I R M E N

S. F. Morea & R. J. Richmond  
Structures & Propulsion Laboratory  
NASA/Marshall Space Flight Center

S. T. Wu  
Department of Mechanical Engineering  
The University of Alabama in Huntsville

A R R A N G E M E N T S   C O - C H A I R M E N

Mr. Vance Houston, NASA/Marshall Space Flight Center

Ms. Sue Weir, The University of Alabama in Huntsville

S T E E R I N G   C O M M I T T E E

Biliyar Bhat, NASA/MSFC

Thomas Marshall, NASA/MSFC

Frederick Braam, NASA/MSFC

William Nieberding, NASA/LeRC

Christos Chamis, NASA/LeRC

Louis Povinelli, NASA/LeRC

Fred Dolan, NASA/MSFC

Donald Pryor, NASA/MSFC

Robert Dreshfield, NASA/LeRC

Richard Quentmeyer, NASA/LeRC

Sol Gorland, NASA/LeRC

Larry Salter, NASA/MSFC

Loren Gross, NASA/MSFC

Luke Schutzenhofer, NASA/MSFC

Gary Halford, NASA/LeRC

Heinrich Struck, NASA/MSFC

Albert Kascak, NASA/LeRC

John Wanhainen, NASA/LeRC

Larry Kiefling, NASA/MSFC

Erwin Zaretsky, NASA/LeRC

Brian McPherson, NASA/MSFC

A D M I N I S T R A T I V E   S T A F F

Mrs. Pat Corder

Ms. Amy Cain

The University of Alabama in Huntsville

## FOREWORD

During the next 15-20 years, the nation's need for easy access to space is expected to increase significantly. A highly efficient and versatile space transportation system will be needed to support a variety of activities in both low earth and higher orbits. The elements of this space transportation system will range from the current space shuttle with planned improvements to heavy lift launch vehicles using booster propulsion systems operating on oxygen/hydrocarbon propellants. These elements, although differing in size and configuration depending on the requirements, will be dependent on highly efficient and reliable propulsion systems.

For the past several years, the Marshall Space Flight Center has been managing and conducting NASA-wide research and technology programs dealing with advanced oxygen/hydrogen and oxygen/hydrocarbon earth-to-orbit rocket propulsion. These programs are under the aegis of the Office of Aeronautics and Space Technology at NASA Headquarters, and includes Lewis Research Center participation. The overall objective is to enhance the analysis and design capability for oxygen/hydrogen and oxygen/hydrocarbon propulsion to meet the continuing needs of earth-to-orbit space transportation. The accomplishment of this objective is expected to contribute to the nation's space program by providing the technological foundation necessary for the design and development of improved liquid rocket propulsion systems.

On June 27 - 29, 1984 the first conference to describe the initial products of the oxygen/hydrogen program was held at Marshall Space Flight Center, Huntsville, Alabama. Proceedings of the conference entitled "Advanced High Pressure O/H Technology" were published in NASA Conference Publication 2372. Since that first conference, NASA's separate research and technology programs dealing with oxygen/hydrogen and oxygen/hydrocarbon propulsion have been combined into one program entitled "Advanced Earth-to-Orbit Propulsion Technology". Accordingly the title of this, the second conference has been changed to reflect this increased scope. Results of the oxygen/hydrocarbon research effort are reported herein along with the oxygen/hydrogen results. The purpose of these conferences is to provide a forum for the timely dissemination to the propulsion community of the results emerging from this program with particular emphasis on the transfer of information from the scientist/researcher to the designer.

In addition to the regular conference sessions, a one-day workshop on Hydrogen Environment Embrittlement in Advanced Propulsion Systems was included in the program for this conference. Thus, the content of the proceedings is organized into twelve sessions plus a

workshop, which follows the structure of the NASA earth to orbit research and technology program. These sessions are:

- o STRUCTURAL DYNAMICS
- o INSTRUMENTATION
- o DYNAMIC CHARACTERISTICS OF TURBOMACHINERY
- o MATERIAL TECHNOLOGY
- o FLUID AND GAS DYNAMICS I
- o FLUID AND GAS DYNAMICS II
- o ROTORDYNAMICS
- o FATIGUE/FRACTURE AND LIFE
- o BEARINGS I
- o BEARINGS II
- o COMBUSTION AND COOLING PROCESSES I
- o COMBUSTION AND COOLING PROCESSES II
- o HYDROGEN ENVIRONMENT EMBRITTLEMENT IN ADVANCED PROPULSION SYSTEMS

There is a total of eighty-three papers in these proceedings; this large number required publishing in two volumes. Volume I contains manuscripts from the first six sessions and the remainder are included in Volume II. Volume I carries an "International Traffic in Arms Regulation" statement and Volume II carries a "Limited Distribution" statement. These documents are available only to organizations registered with the NASA Scientific and Information Facility.

We wish to thank the authors for their high quality contributions and for their timely submittal of manuscripts. We wish to thank the session co-chairmen for planning the program and conducting the sessions. We wish to acknowledge the arrangements co-chairpersons, Ms. Sue Weir and Mr. Vance Houston for the professional manner in which they supported the conference. Last, but not least we wish to thank the administrative staff, Mrs. Pat Corder and Ms. Amy Cain, and the Public Affairs Office at the Marshall Space Flight Center for their dedicated efforts in coordinating and supporting this meeting.

June 1986  
Huntsville, Alabama

R. J. Richmond, S. T. Wu and  
S. F. Morea, Conference Co-Chairmen

VOLUME TWO

TABLE OF CONTENTS

FOREWORD . . . . . ii

VII ROTORDYNAMICS

Damping Seal Tester Progress and Initial Test Results  
K. L. Cappel and G. L. von Pragenau . . . . . 2

High-Pressure Oxygen Turbopump Low-Speed Flexible Rotor  
Balancing for Smooth, High-Speed Operation,  
E. Zori, J. C. Giordano and G. von Pragenau . . . . . 9

The Effects of Internal Rotor Friction on Dynamic  
Characterisitcs of Turbopumps  
J. F. Walton II, A. Artiles, J. Lund and C. Lee . . . . . 33

Efficient Transient Analysis Methods for the Space  
Shuttle Main Engine (SSME) Turbopumps  
S. T. Noah, U. J. Fan, Y.-S. Choi and T. Fox . . . . . 62

Vibrations Induced by Nonlinearities in Rotordynamics  
William B. Day . . . . . 83

VIII FATIGUE/FRACTURE AND LIFE

Simplified Cyclic Structural Analyses of SSME Turbine  
Blades  
A. Kaufman and J. M. Manderscheid . . . . . 107

Effects of High Mean Stress on the High-Cycle Fatigue of  
PWA-1480 and DS MAR 246 + Hf at 1000°F  
S. Majumdar . . . . . 125

Constitutive Behavior of Single Crystal PWA 1480 and  
Directionally Solidified MAR-M 246 Under Monotonic and  
Cyclic Loads at High and Low Temperature  
Walter W. Milligan, Eric S. Huron, and Stephen D. Antolovich . . 134

High-Temperature LCF of Ni-201 and 304L S. S.  
G. R. Halford, L. R. Johnson, and J. A. Brown . . . . . 172

Fatigue Crack Retardation Following Overloads in Inconel  
718, Ti-5Al-2.5Sn and Haynes 188  
D. E. Matejczyk, R. P. Jewett, D. W. Schmidt and  
and G. C. Hresko III . . . . . 205

IX BEARINGS I

Thermo-mechanical Performance Evaluation of Cryogenic  
Turbopump Ball Bearings  
Robert A. Pallini . . . . . 221

Thermal Analysis of SSME Turbopump Bearings  
Joe C. Cody, David Marty and Bruce K. Tiller . . . . . 241

Lubrication Evaluation of SSME Turbopump Bearings  
K. F. Dufrane, J. W. Kannel and S. A. Barber . . . . . 266

Surface Characteristics of Liquid Oxygen Cooled Ball  
Bearings  
Myles Butner and Mary Shoemaker . . . . . 293

Powder Metallurgy Bearings for Advanced Rocket Engines  
B. N. Bhat, T. S. Humphries, R. L. Thom, G. I. Friedman  
and V. Moxson . . . . . 311

X BEARINGS II

Rolling Contact Fatigue Life of Zirconium and Molybdenum  
Nitride Sputter Plated AMS-5749 Bearing Steel  
R. L. Thom and F. J. Dolan . . . . . 327

Measurement of Rotordynamic Coefficients for a  
Hydrostatic Radial Bearing  
B. T. Murphy and M. N. Wagner . . . . . 341

Surface Modification for Wear Resistance in a Liquid  
Oxygen Turbopump Environment  
Lillian Ng and Yngve Naerheim . . . . . 366

SSME Bearing Health Monitoring Using a Fiberoptic  
Deflectometer  
Michael E. Hampson, J. J. Collins, M. R. Randall and  
Sarkis Barkhoudarian . . . . . 377

XI COMBUSTION AND COOLING PROCESSES I

Aerojet Techsystems Company Contribution to LOX/HC  
Combustion and Cooling Technology  
S. D. Mercer and D. C. Rousar . . . . . 393

Survey of LOX/Hydrocarbon Combustion and Cooling  
A. I. Masters, W. A. Visek and R. G. Carroll . . . . . 439

LOX/Hydrocarbon Combustion and Cooling Survey,  
R. T. Cook and F. M. Kirby . . . . . 461

Liquid Oxygen Cooling of High Pressure LOX/Hydrocarbon Rocket Thrust Chambers H. G. Price . . . . .	474
RP-1 and Methane Combustion and Cooling Experiments C. R. Bailey . . . . .	529
XII COMBUSTION AND COOLING PROCESSES II	
Results of Coaxial Injector Element Testing S. C. Fisher. . . . .	550
Combustion Modeling: Progress and Projections P. Y. Liang . . . . .	570
Effects of Oxygen/Hydrogen Combustion Chamber Environment on Copper Alloys M. Murphy, R. E. Anderson, D. C. Rousar and J. A. Van Kleeck . . . . .	580
HYDROGEN ENVIRONMENT EMBRITTLEMENT IN ADVANCED PROPULSION SYSTEMS WORKSHOP	
Hydrogen-Environment Embrittlement and Its Control in High Pressure Hydrogen/Oxygen Rocket Engines W. T. Chandler . . . . .	618
Multispecimen Test Facility for High-Pressure Hydrogen Creep Studies S. K. Verma . . . . .	635
Pratt & Whitney's Hydrogen Test Facilities R. L. Fowler, Jr. . . . .	660
A High Pressure, High Temperature Hydrogen Environment for Metals Properties Testing System Michael J. Rother . . . . .	661
Development of a Computer-Controlled Technique to Determine Crack Growth Rate Properties in Controlled Environments Using Crack Opening Displacement D. R. Moore, D. T. Drinan and J. D. Hodo . . . . .	672
Hydrogen Effects on the Fatigue and Tensile Behavior of CMSX-2 Nickel Base Superalloy Single Crystals I. M. Berstein, S. Walston, M. Dollar, A. Domnanovich and W. Kroump . . . . .	698
The Determination of Mobile Hydrogen in Aerospace Engine Alloys Merlin D. Danford . . . . .	715



LCF and Crack Growth Rate of Turbine Blade Alloys in Hydrogen and Hydrogen/Steam Environments B. A. Cowles, D. P. Deluca, J. R. Warren and F. K. Haake . . . .	729
Progress Report on the Development of a Hydrogen Resistant Alloy W. B. McPherson . . . . .	749
Hydrogen Effects on Crack Growth Resistance of an Iron Base Superalloy N. R. Moody, M. W. Perra and R. E. Staltz . . . . .	758
PARICIPANTS . . . . .	759
APPENDIX Table of Contents of Volume One . . . . .	763





## VII ROTORDYNAMICS

**DAMPING SEAL TESTER PROGRESS  
AND INITIAL TEST RESULTS**

K. L. Cappel, Wyle Laboratories  
and

G. L. von Pragenau, NASA/MSFC

**Introduction**

Two years ago, at this conference, we presented an experimental plan for investigating the effectiveness of so-called damping seals, i.e. bushing seals with a multiplicity of pockets, to dampen the asynchronous whirl which presently limits the performance of the high-pressure oxygen turbopump in the Space Shuttle Main Engine.

This paper summarizes the design of the test rig, including modifications made since the original concept, and presents initial test results.

**Test System Description**

The test device substitutes water, supplied by a 1500 gallon blowdown system, at flow rates up to 300 gpm and inlet pressures up to 2300 psi, for liquid oxygen while the test shaft is being driven by a steam turbine at speeds that will eventually reach 37000 rpm. Figure 1 shows the arrangement of the test rig and turbine on the test stand.

The test seals have a diameter of 3.6 in. and a length of 1.8 in. Triangular pockets are machined (EDM) into the inside surface of the seal. The pockets are almost equilateral triangles, with a side length of about 0.2 in. bordered by 0.02 in. wide lands. The first seal to be tested had a radial clearance of 0.020 in. and a pocket depth of 0.020 in.

As shown in Figure 2, the test seal is housed in a seal carrier which is suspended from a transverse shaft by a pair of ball-jointed links. The seal carrier is captured between two water-lubricated hydrostatic bearings whose supply lines are connected so as to form a hydraulic servo which centers the carrier axially under all conditions of pressure and flow. The seal carrier is free to translate in a plane transverse to the shaft axis without touching the shaft because the seal's fluid film forces center the carrier in the radial direction.

**Test Objectives and Conditions**

The linkages by which the seal is suspended are oscillated by an electrodynamic shaker along one transverse axis. Because of cross coupling through the fluid film, the seal is also excited along the other transverse axis. A major objective of the ongoing test program is the determination of the cross-coupling coefficients, as well as the stiffness and damping of the fluid film in the seal gap, as a function of exciting frequency and shaft rotation speed.

A lower limit to the maximum inlet pressure and resulting flow is set by the necessity for carrying away most of the heat generated in the upper, high-pressure

ORIGINAL PAGE IS  
OF POOR QUALITY

ORIGINAL PAGE IS  
OF POOR QUALITY

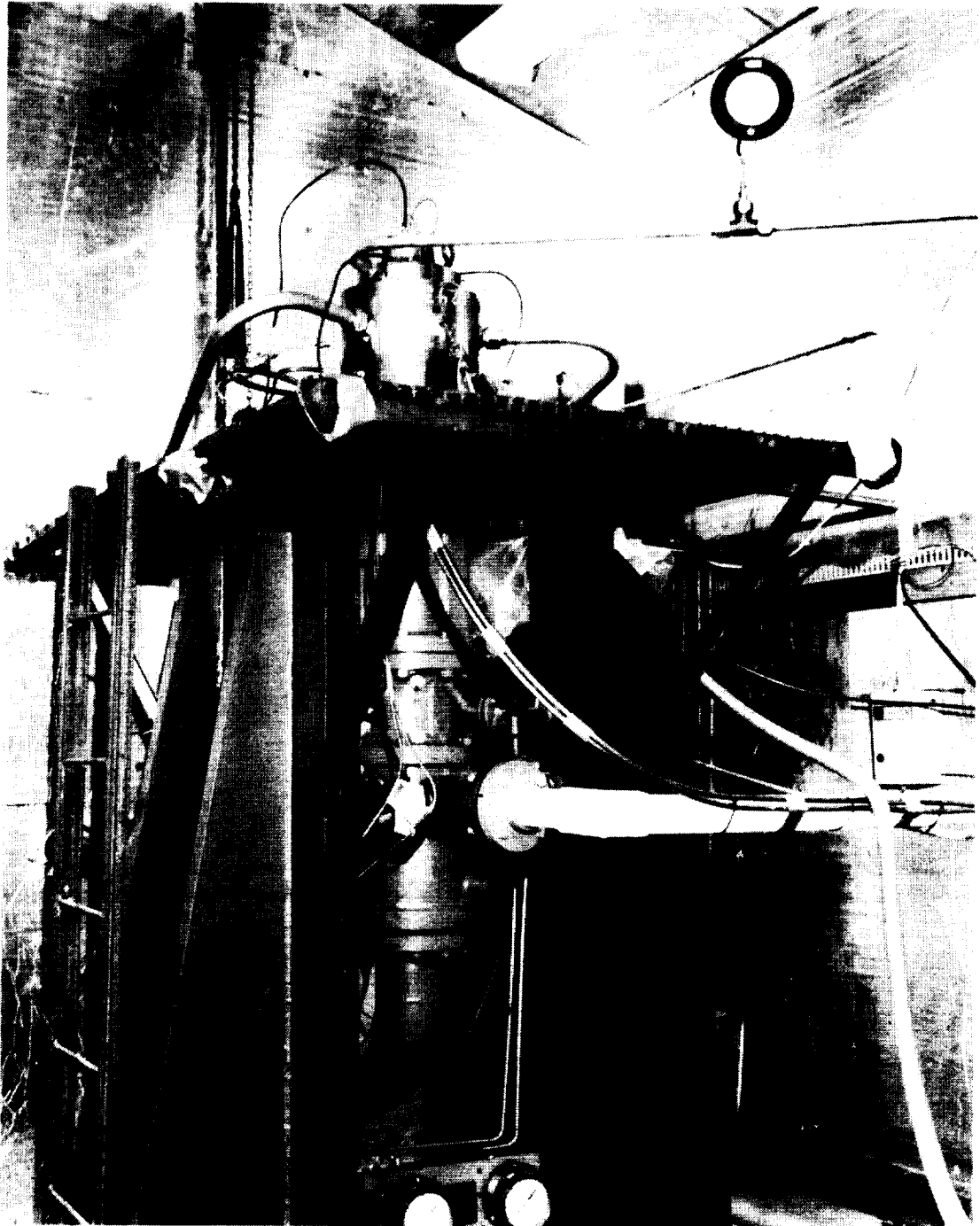


**Figure 1**

**Damping Seal Tester and Steam Turbine on Test Stand**

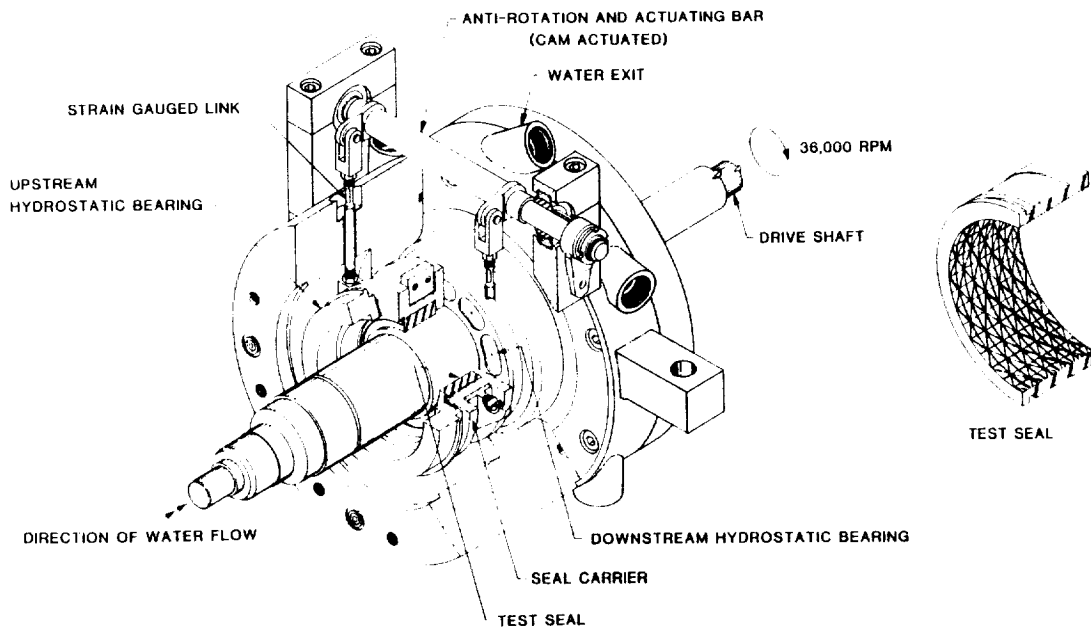


Figure 2

Internal Arrangement of Damping Seal Tester

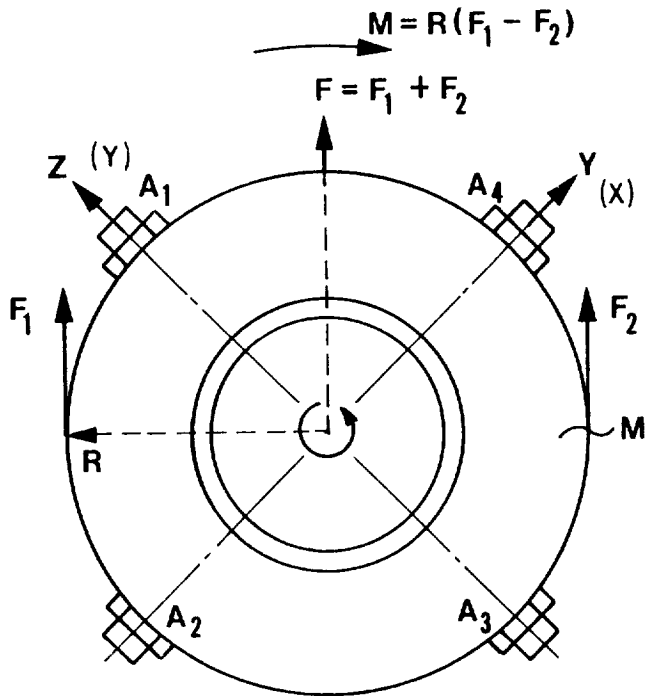


Figure 3

Seal Instrumentation and Coordinate System

bushing seal which incorporates orifice-compensated hydrostatic recesses to ensure centering. The shaft is mounted in angular contact ball bearings which are separated from the water environment by segmented carbon seals tightened by air pressure.

### **Instrumentation**

Water inlet and outlet pressures, flows and temperatures are monitored, as is the entrance loss in two diametrically opposed pockets. These measurements, as well as shaft speed, are recorded on a datalogger. The dynamic behavior of the seal is measured by strain gauges in the suspension links which give the applied force, and by four accelerometers on the seal carrier, mounted at 45 degrees with respect to the main axes. These data are recorded on FM tape. It had originally been intended to use two accelerometers, and two displacement sensors to measure the relative motion between the shaft and seal, i.e. the fluid gap. This proved to be unfeasible, but such displacement sensors will later be mounted just upstream of the seal. The error in the fluid film properties introduced by the compliance of the shaft and bearings is estimated to be of the order of 20 percent.

### **Data Reduction Scheme**

Since measurements are made of motions in two degrees of freedom, but four system constants are to be determined for each test condition, it is necessary to measure phase relations with great precision to supply the two additional measurements. Figure 3 shows the relations between forces, displacements and accelerations in the complex plane, normal to the shaft axis. Displacements are determined from the accelerations, divided by the square of the frequency, with the proper sign change. Figures 4 and 5 show the procedure for extracting the system constants from the LaPlace-transformed equations of motion by inversion of the response matrix.

By reinserting the values of stiffness, damping and cross-coupling coefficients into the equation of motion, it was found possible to reproduce the measured test conditions very accurately.

### **Test Data Comparison**

Initial test data and derived coefficients are shown in Tables 1 and 2, for test run number 10 (shaft not rotating) and run number 11 (13,254 rpm), respectively. The Reynolds numbers for these conditions were 68,200 and 101,000. Maximum Reynolds number with hot water should be 280,000.

Table 3 lists analytical predictions, except for the seal inlet losses. The losses are the average values determined from two pressure measurements: upstream of the seal inlet and inside the seal gap in the pocket next to the inlet edge. The inlet losses are 0.188 without rotation and 0.133 for rotation. The values are less than the common assumption of 0.25.

The measured leakage values for equal pressures are 20 lbs without and with rotation. The predicted leakage is 10 percent higher.

$$\begin{aligned}
 F_y &= F/(\sqrt{2}) - m\ddot{y} & \begin{bmatrix} F_y \\ F_z \end{bmatrix} &= \begin{bmatrix} K+SC & QS\ G \\ -Q-SG & K+SC \end{bmatrix} \begin{bmatrix} \Delta y \\ \Delta z \end{bmatrix} \\
 F_z &= F/(\sqrt{2}) - m\ddot{z} \\
 F_y &= A_y + j B_y & \Delta y &= y_a + j Y_b \quad j^2 = -1 \\
 F_z &= A_z + j B_z & \Delta z &= z_a + j Z_b \\
 y &= Y \sin (wt + a) & y_a &= Y \cos a \quad Y_b = Y \sin a \\
 z &= Z \sin (wt + b) & z_a &= Z \cos b \quad Z_b = Z \sin b
 \end{aligned}$$

$$\ddot{y} = \frac{-Y w^2}{\ddot{Y}} \sin (wt + a) \quad \ddot{z} = \frac{-Z w^2}{\ddot{Z}} \sin (wt + b)$$

$$\underline{\underline{Y}} = \frac{-\ddot{Y}}{w^2} \quad \underline{\underline{Z}} = \frac{-\ddot{Z}}{w^2}$$

$$\begin{aligned}
 A_y + j B_y &= K y_a - w C y_b + j (K y_b + w C y_a) - Q z_a + w G z_b - j (Q z_b + w G z_a) \\
 A_z + j B_z &= K z_a - w C z_b + j (K z_b + w C z_a) + Q y_a + w G y_b - j (Q y_b + w G y_a)
 \end{aligned}$$

**Figure 4**  
**Dynamic Equations**

$$\underbrace{\begin{bmatrix} A_y \\ B_y \\ A_z \\ B_z \end{bmatrix}}_S = \underbrace{\begin{bmatrix} Y_a & -W Y_b & Z_a & -W Z_b \\ Y_b & W Y_a & Z_b & W Z_a \\ Z_a & -W Z_b & -Y_a & W Y_b \\ Z_b & W Z_a & -Y_b & -W Y_a \end{bmatrix}}_R \underbrace{\begin{bmatrix} K \\ C \\ Q \\ G \end{bmatrix}}_D$$

S Side Force Vector

R Response Matrix

D Dynamic Parameter

$D = R^{-1}S$  Solution for each vibration frequency  $W$

**Figure 5**



**Table 1**  
**Results - Run No. 10 (Non-Rotating)**  
**Inlet Pressure: 1525 psi; Flow: 156 gpm**

Frequency Hz	Spring Rate K lb/in.	Damping C lb sec/in.	Cross Coupling	
			Q lb/in.	G lb sec/in.
40.800	37,700	94.76	1.07	-6.206
71.635	41,915	131.24	-6,573.6	-4.991
102.240	43,338	139.71	-12,036.5	-9.164
131.180	63,667	124.79	-3,014.1	-1.436
131.180	65,214	133.02	-3,079.7	-5.395

**Table 2**  
**Results - Run No. 11:13,254 rpm**  
**Inlet Pressure: 1577 psi; Flow: 142 gpm**

Frequency Hz	Spring Rate K lb/in.	Damping C lb sec/in.	Cross Coupling	
			Q lb/in.	G lb sec/in.
40.29	45,021	111.49	31,122	-11.187
69.95	45,487	53.25	559	-13.000
100.00	47,957	131.78	26,387	-13.350
128.86	-72,055	116.59	-9,406	24.430

**Table 3**  
**Seal Data Prediction**

Conditions rpm psi in-loss	Freq Hz	Stiffness K, lb/in.	Damping C, lb*s/in.	Cross Coupling		Leakage W, lb/s
				Q, lb/in.	G, lb*s/in.	
0 1525 0.188  Run 10, 156 gpm 126:11:32:07	0	99,000	129	0	0	22
	40	98,000 (81,000)				
	70	97,000 (80,000)				
	100	95,000 (79,000)				
	130	92,000 (77,000)				
13254 1577 0.133  Run 11, 142 gpm 132:16:27:55	0	98,000	127	35,000	8.3	22
	40	97,000 (81,000)				
	70	95,000 (80,000)				
	100	94,000 (78,000)				
	130	91,000 (76,000)				

**Note:** Only seal stiffness is frequency dependent. Parenthetical stiffnesses are corrected with 472,000 lb/in. for rotor bending and bearing stiffness in series. In-loss is an abbreviation for seal inlet loss.

The predicted stiffness (including the corrections) is 53 percent to 75 percent higher than measured averages. The predicted damping is 4 percent to 23 percent higher than measured averages. No cross coupling is predicted without rotation, and the predicted Q with rotation is 81 percent above the measured average. The predicted cross coupled damping G has the opposite sign from the measured values. The measured G value is 57 percent above the absolute value of the prediction. However, G is still so low in magnitude that it is dynamically insignificant.

### **Conclusion**

The comparison shows good agreement for damping and leakage. Stiffness seems to be less than the corrected prediction values. Future test will measure the rotor displacement and thus should increase the accuracy of the measurements. The cross coupling without rotation is rather small and should be due to unpredictable flow splitting when the stator oscillates transversely to the axis. The measured cross coupling Q under rotation is less than the prediction and will be more accurately measured in the future when rotor motion is determined.

### **Outlook**

The data comparison is encouraging. A bearing failure occurred owing to bearing misalignment. The rotational test data seem to reflect the failing bearing in the last line of Table 2 where the cross coupling sign changes. The tester is in repair and is being improved for obtaining better data soon. The initial data already have increased our confidence in our analytical predictions. Future tests are expected to contribute much to the damping seal development and the formulation of analytical predictions.

### **Acknowledgements**

The contributions of Wyle staff members Larry Millsaps, who acted as test project engineer, and Dr. Jen Jong, who performed the data analysis, are gratefully acknowledged.

High-Pressure Oxygen Turbopump

LOW-SPEED FLEXIBLE ROTOR BALANCING FOR SMOOTH,  
HIGH-SPEED OPERATION

E. Zorzi and J. Giordano  
Mechanical Technology Incorporated  
Latham, New York

and

G. von Pragenau  
NASA-Marshall Space Flight Center  
Huntsville, Alabama

**ABSTRACT**

A method for balancing flexible rotors at low speeds while ensuring smooth high-speed operation has been developed and demonstrated through proof-of-principle tests. A potential application of this method is for the Space Shuttle Main Engine (SSME) turbopump rotors. These rotors operate above one or more critical speeds and must be balanced to ensure smooth operation at those speeds. Conventional low-speed rigid balancing is inadequate. SSME hardware and geometry restrictions preclude the use of high-speed, flexible rotor, in-housing balancing. The use of a low-speed flexible rotor balancing method could substantially improve the state of balance of these rotors, because this technique eliminates the need for the high-speed runs during the balancing process that are required by classical flexible rotor balancing methods. This paper describes the analytic formulation of the low-speed flexible rotor balancing method and presents the results of proof-of-principle tests. These results indicate that low-speed flexible rotor balancing is not only a viable technology, but that it is a valuable method for ensuring smooth operation above more than one bending critical speed. Also, the High-Pressure Oxygen Turbopump (HPOTP) rotor is shown to be a candidate application for this method.

## INTRODUCTION

The need to develop a low-speed flexible rotor balancing method arises from the need to minimize shaft response amplitude and to reduce to a minimum the force transmitted through the bearings. Because rotor imbalance is a major cause of large amplitudes and high forces, it is necessary that the SSME pumps be well balanced throughout their operating speed range. In general, shaft response and transmitted force caused by imbalance are greatest at or near critical speeds. Both SSME turbopumps, the HPOTP and the High-Pressure Fuel Turbopump (HPFTP), operate above their first critical speeds and exhibit considerable rotor bending. The maximum operating speed for the HPFTP is above its second critical speed. As the power level of the HPOTP increases, its operating speed approaches its second critical speed. Thus, a method of balancing both rotors for two critical speeds is needed.

The two general approaches to balancing rotating equipment are low-speed rigid [1,2] and high-speed flexible methods [3,4,5]. Both of these methods are well documented. For the HPOTP and HPFTP, low-speed rigid balancing, by itself, is inadequate. In particular, correction weights applied during rigid body balancing may worsen the state of balance at operating speed. That is, increased rotor response and bearing forces may occur when operating at or above flexible critical speeds. Therefore, flexible balancing of the SSME turbopumps is recommended to ensure smooth, balanced operation at high speeds. The ideal situation would be to balance at critical and maximum operating speeds using a conventional multiplane, multispeed flexible rotor balancing method. Furthermore, balancing should be performed within the housing, but out-of-housing balancing at critical and maximum operating speeds could be a satisfactory alternative, if suspension characteristics are similar to those in the housing. However, these balancing approaches are impractical for the HPOTP for several reasons.

- Operating speeds are above one critical speed and approaching the second, yet only one plane is readily available for in-housing balancing of the assembled rotor
- Balancing speed is limited to 1500 rpm when performing in-housing balancing of the rotor since no coolant is available for the bearings during the balancing operation other than a liquid oxygen (LOX) compatible lubricant
- Bearing life is very short, precluding a significant number of high-speed balancing runs regardless of coolant/lubricant
- Bearing pairs are uniquely matched to each rotor, thereby effectively preventing approaches where sacrificial bearings might be used during an out-of-housing assembled rotor-balancing procedure
- Excessive bearing loads that limit the already short life must be minimized

- Only LOX-compatible substances can be used to cool and lubricate the bearings to avoid system contamination, if speeds higher than those currently used are anticipated
- Rotor vibration data are extremely difficult to record from in-housing operation, since only case-mounted accelerometers are used.

As a result of these hardware constraints, neither in-housing nor out-of-housing, high-speed, flexible balancing can currently be used on SSME turbopumps.

A method has been developed that shows promise in overcoming many of these limitations. This method establishes one or more "windows" for low-speed, out-of-housing balancing of flexible rotors. The windows are regions of speed and support flexibility where two conditions are simultaneously fulfilled. First, the rotor system behaves flexibly, providing separation among balance planes. Second, the response effected by balance weights is sufficiently large to measure reliably. The details of the work described are documented in Reference 6.

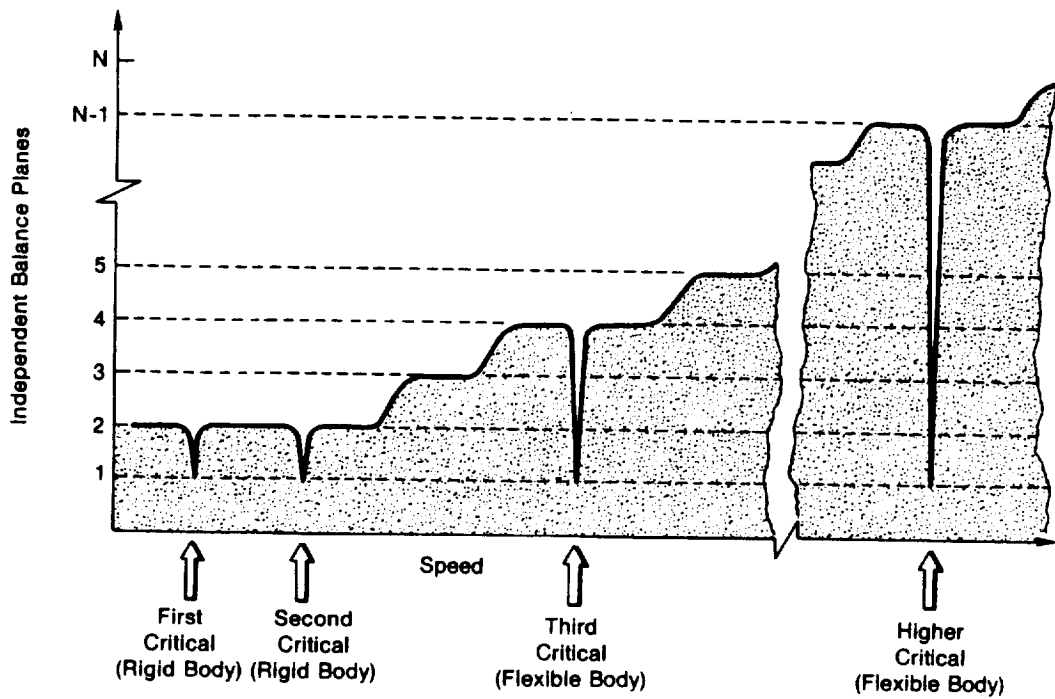
#### **METHOD FORMULATION**

Rotor balancing methods predict weights to be added or removed from a rotor-bearing system to minimize imbalance response. With the low-speed flexible rotor balancing method, weights are predicted at a low speed (or speeds) for balance planes located at the major sources of potential unbalance. Response is minimized at the balancing speed and at higher speeds, including the operating speed. The purpose of low-speed flexible balancing is to determine the lowest speed at which balancing can be performed where the rotor behaves "flexibly". The major steps in balancing a rotor using the low-speed flexible method are described in the following paragraphs.

**Select Balance Planes.** First, balance planes are chosen that represent actual hardware locations (i.e., axial planes where weight can be added or removed at any circumferential location). Next, active balance planes are selected, rather than nodes, at the speeds of interest and at maximum equipment operating speed.

**Determine Plane Separation and Expected Rotor Response.** The rotational speed of the shaft and the flexibility of the rotor supports (i.e., bearing supports to ground) are the chief determinants of plane separation. The following three cases, represented schematically in Figure 1, are possible.

- There is only one required balance plane at any critical speed, since (at any critical speed) the entire rotor vibration is controlled by any one active balance plane on the rotor.
- At off-critical speeds where the supports are flexible as compared to the rotor, the rotor behaves as a rigid body and two balance



86900

Fig. 1 Available Number of Balance Planes

planes are necessary. At these speeds, the rotor can be balanced by counteracting the forces and moments due to imbalance. Two balance planes provide the required two degrees of freedom.

- At off-critical speeds where the rotor is flexible, plane separation exists for all balance planes (except for those in close proximity to one another).

One approach to determine plane separation uses the influence coefficient matrix. With this approach, separation among selected balance planes can be assessed for different support flexibilities and speeds. Regions of expected plane separation are then mapped as functions of support flexibility and speed.

In addition to locating plane separation regimes, it is necessary to determine the expected levels of rotor response. Low-speed flexible rotor balancing is performed at off-critical speeds where response is usually small; therefore, "responsiveness" must be assessed so as to determine when the expected response is large enough to measure. In this way, vibration probes can be selected that have the desired sensitivity.

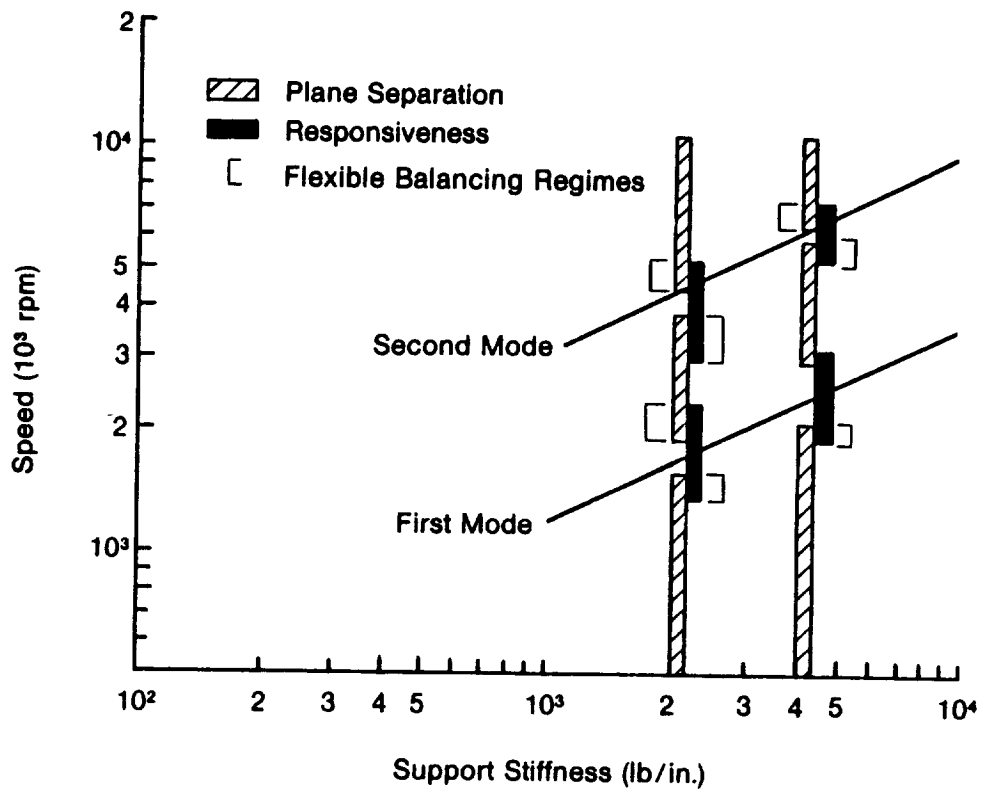
**Perform Influence Coefficient Balancing.** Actual balancing is performed in regimes where plane separation exists and response can be measured using a multiplane influence coefficient balance method. One way to establish specific low-speed flexible balancing regimes is to plot plane separation and rotor responsiveness on a critical speed map. An example of such a plot is shown in Figure 2. The solid lines on this figure show the predicted first and second critical speeds as a function of support stiffness. Speed ranges where plane separation and rotor responsiveness exist are shown by cross-hatched and solid vertical bars, respectively. For a given value of support stiffness, speeds where the cross-hatched and solid bars overlap are the predicted low-speed flexible balance regimes.

## TEST RIG DESCRIPTION

An empirical evaluation of the flexible rotor balancing method was conducted using a rotordynamic test rig. The objective of this proof-of-principle testing was to determine the effectiveness of low-speed, flexible rotor balancing in a controlled laboratory environment. Furthermore, test hardware and test conditions were selected based on the fact that a potential application of the method is for the HPOTP.

The test rig used for the empirical evaluation was originally designed to simulate the power turbine of a gas turbine engine and included:

- Flexible shaft with an integral drive turbine and overhung disk
- Maximum speed of 24,000 rpm
- Two pairs of duplex ball bearings for shaft support
- Bearing pedestals with interchangeable support cartridges.



85612-1

Fig. 2 Typical Low-Speed Flexible Rotor Balancing Map



A schematic of the test rig shaft assembly is shown in Figure 3. This assembly consists of a slender shaft with a disk attached to each end. Both of these disks were originally designed to simulate inertias on a power turbine. The smaller disk also serves as a drive turbine. Both of these disks were also used as balance planes. There are two additional balance planes along the slender shaft. These are integral rings with 12 flats, each flat having a radial hole for insertion of a balance weight. The maximum amount of weight which can be installed in each hole of these center balance planes is one gram.

The shaft assembly is supported on two duplex pairs of angular contact ball bearings; their locations are shown in Figure 3. A schematic of the bearing support pedestals is shown in Figure 4. The pedestals provide bearing lubrication and cooling oil and were designed to accept interchangeable support cartridges.

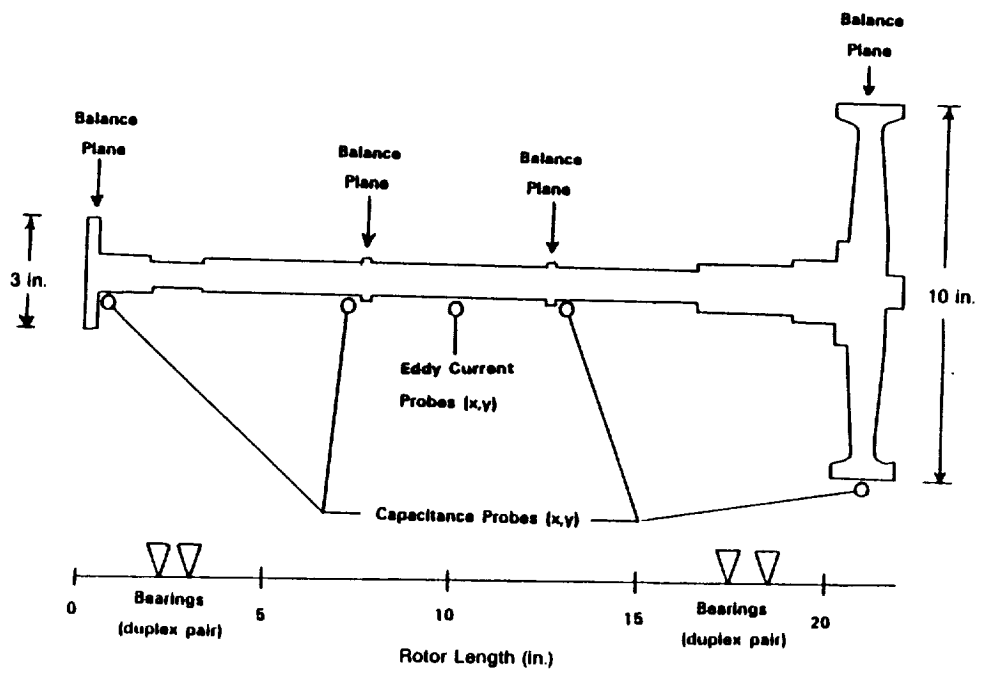
The support cartridges used for the balancing evaluation are shown schematically in Figure 5. As seen in this figure, the cartridges were designed to accept spring washers so that different sized washers (i.e., wavy or belleville) could be used to achieve different support flexibilities. The design values for support flexibility were selected using the results of the test rig analysis discussed below. In particular, pedestal support flexibilities of 2, 4, 20, and 100 thousand lb/in. were required.

To design for the desired support stiffness values, a method for predicting cartridge stiffness based on individual washer stiffness was established and the cartridge stiffnesses were calibrated. The calibration procedure consisted of applying a compressive load through the center of the cartridge assembly and measuring applied force and displacement. Table 1 is a summary of the measured cartridge displacement as compared to the predicted stiffness. These results show that the predicted and measured values of cartridge stiffness are in reasonable agreement.

The test rig was instrumented with a series of capacitance and eddy-current displacement probes. The probe locations are shown in Figure 3. The capacitance probes were used for balancing since they provide greater accuracy than the eddy-current probes. The eddy-current probes were used for initial debugging and for monitoring rig response during high-speed operation. They were installed with a larger probe/shaft gap than the capacitance probes so that there would be less risk of damage if large shaft orbits were encountered.

## TEST RIG ANALYSIS

The rig was analyzed to determine its critical speeds and to calculate the low-speed flexible balance speed and stiffness regimes. A computer-drawn plot of the analytical model is shown in Figure 6. One set of bearing supports was selected to match the HPOTP critical speed mode shapes. Figures 7 and 8 show that the predicted first and second critical speed mode shapes for the HPOTP and for the test rig are similar - the first mode being a "disk bounce" mode, and the second, a bending mode. In addition, measured test rig mode shape data points are added to the lower plot on



86901

Fig. 3 Power Turbine Simulator Test Rotor

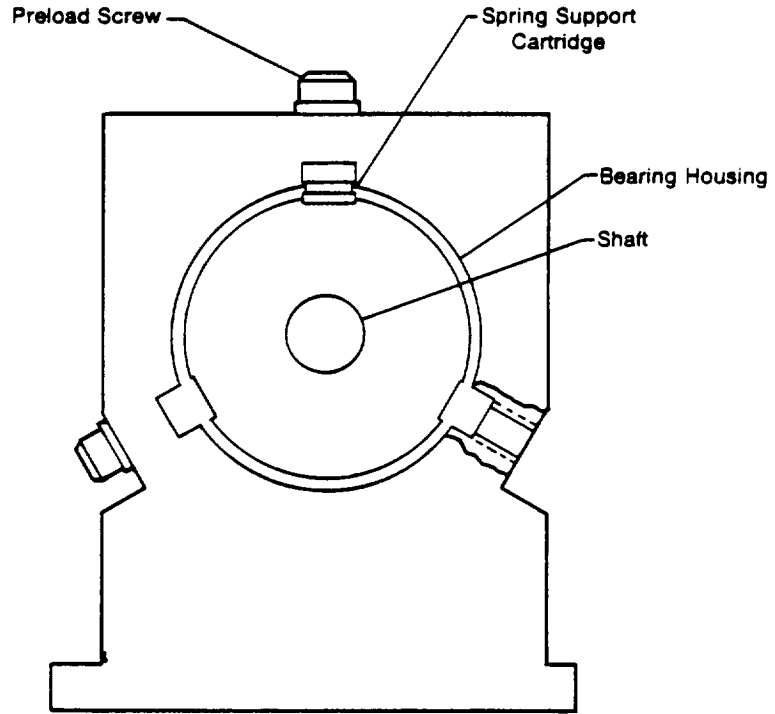


Fig. 4 Bearing Pedestal

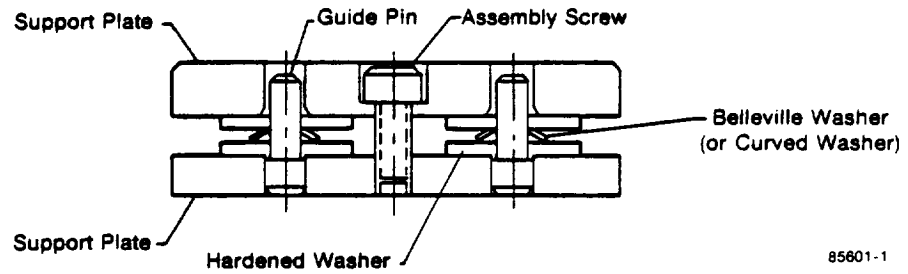


Fig. 5 Spring Support Cartridge

Table 1  
Measured Versus Predicted Cartridge Stiffness

<u>Spring Number</u>	<u>Predicted Stiffness (lb/in.)</u>	<u>Measured Stiffness (lb/in.)</u>
1	1200	1100
2	2333	2083
3	15466	13800
4	66876	85000

TEST RIG MODEL

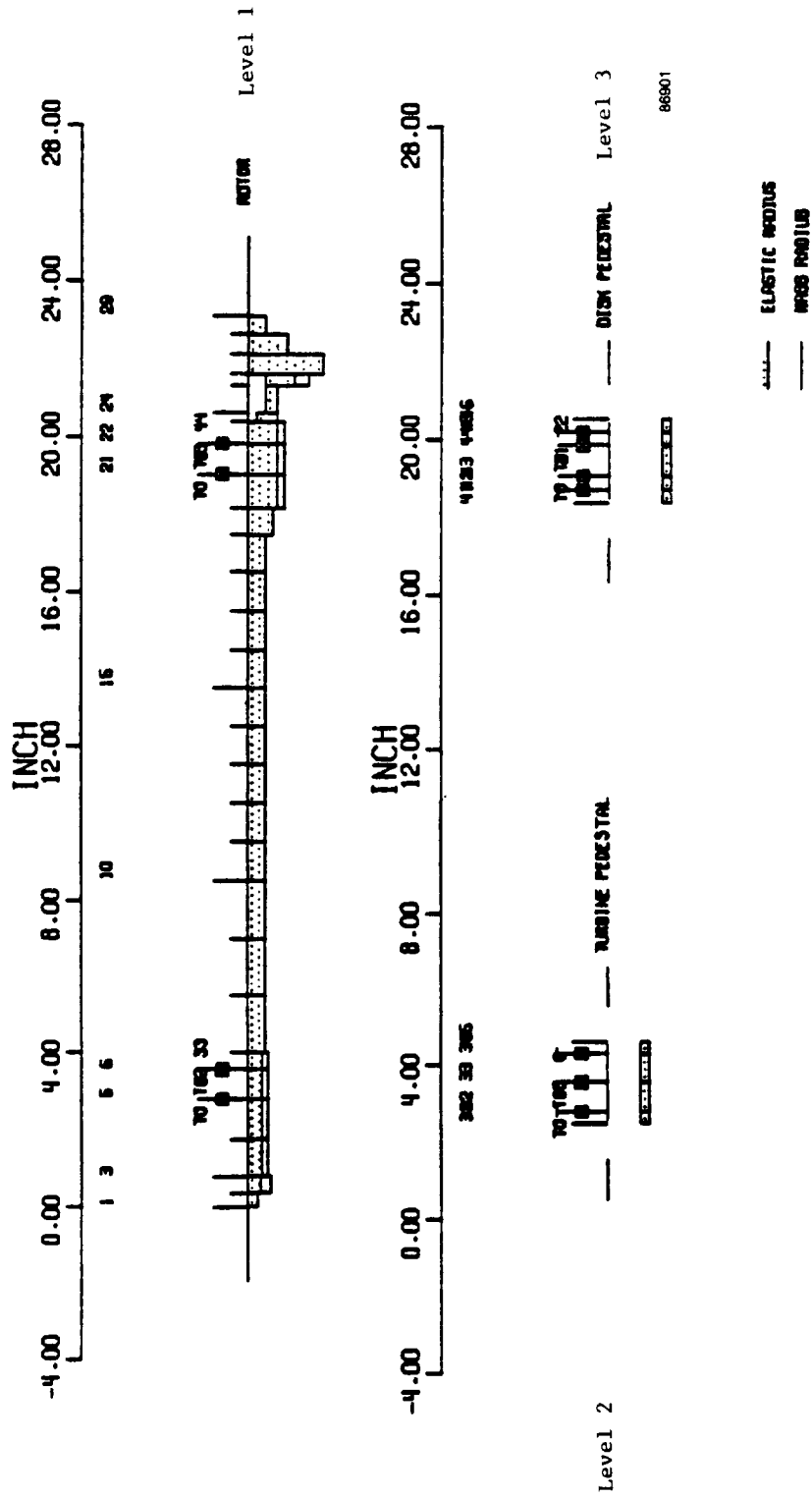
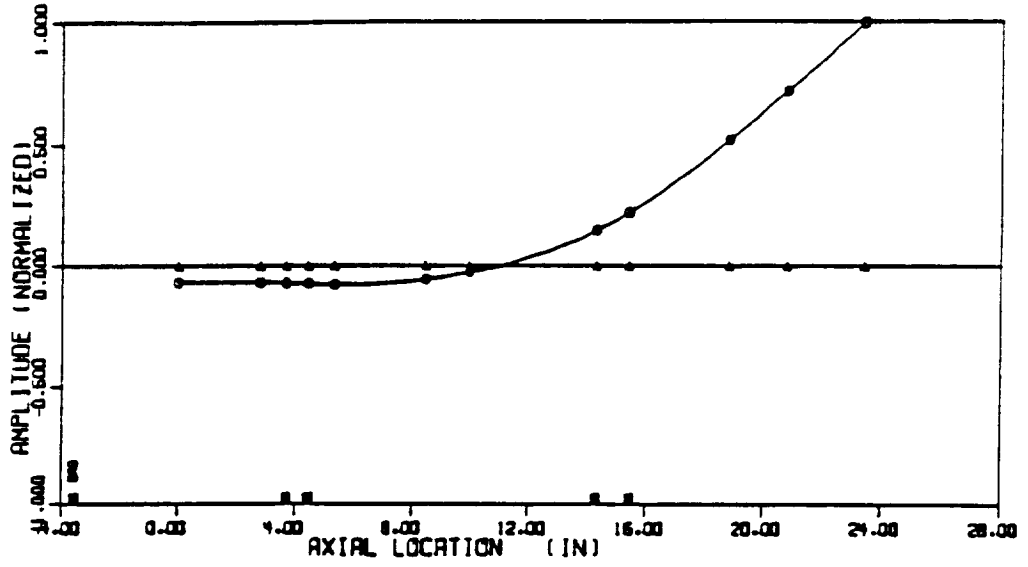


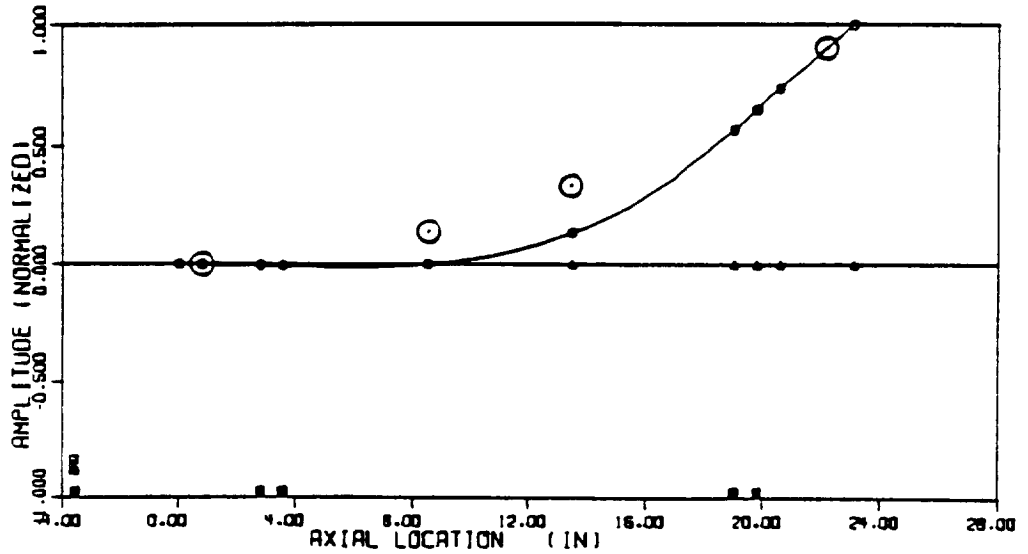
Fig. 6 Test Rig Rotordynamic Model

ORIGINAL PAGE IS  
OF POOR QUALITY

HPOTP ROTOR Mode Number 1: 11,537 rpm



TEST RIG ROTOR Mode Number 1: 4,967 rpm



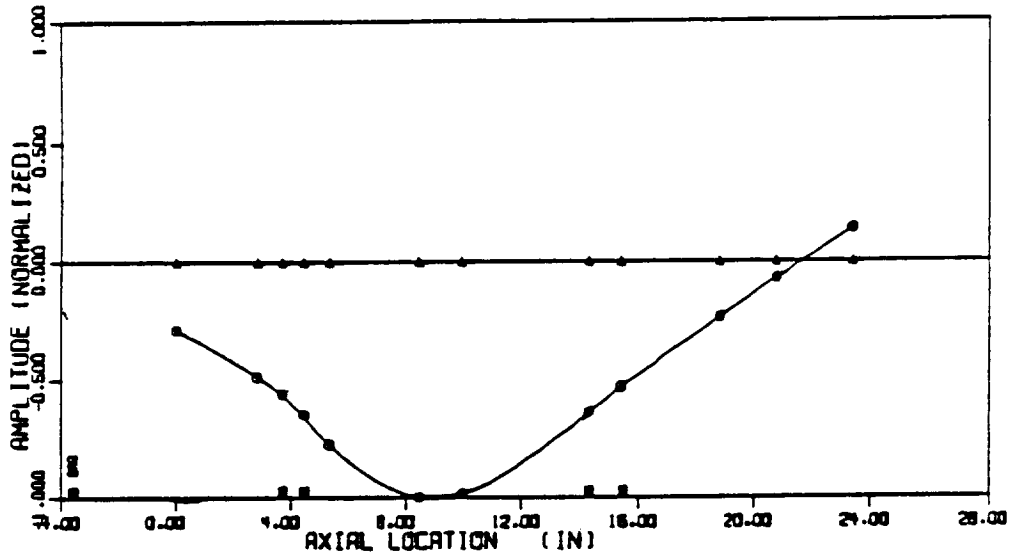
o Measured at 4,700 rpm

86532

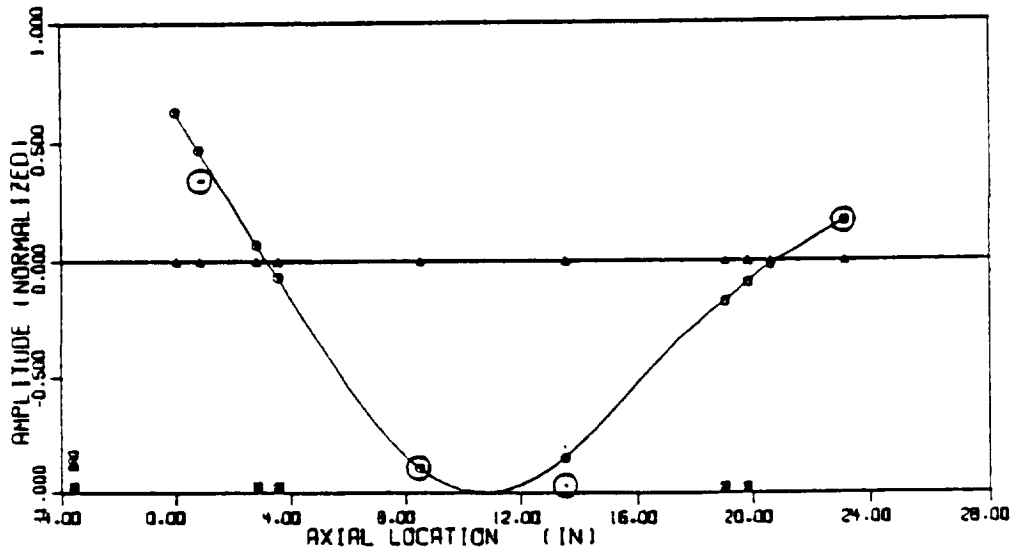
Fig. 7 HPOTP and Test Rig First Mode Comparison

ORIGINAL PAGE IS  
OF POOR QUALITY

HPOTP ROTOR Mode Number 2: 36,082 rpm



TEST RIG ROTOR Mode Number 2: 23,550 rpm



⊙ Measured at 21,500 rpm

85833

Fig. 8 HPOTP and Test Rig Second Mode Comparison

each figure. Mode shape measurements were made at the speeds indicated by using the capacitance displacement probes. The measured data were normalized and added to the predicted mode shape plots. There is good agreement between the measured and predicted shapes for the first mode and excellent agreement for the second mode.

The calibrated rotordynamic model of the test rig was used to analyze the rig for application of the low-speed flexible rotor method. That is, rotor responsiveness and plane separation of the rig were assessed for different speed and support flexibility ranges. Two support configurations which gave good potential low-speed balance "windows" were selected. One used the supports that simulated the HPOTP mode shapes. The other used supports that were more flexible on the disk end of the rig. The low-speed flexible balance assessment for these two configuration regions is shown in Figure 9.

The results presented in this figure were used to determine the actual balance test points. For example, with the HPOTP mode shape simulator supports, the low-speed flexible balancing window is predicted to begin at approximately 8,000 rpm, since this is the lowest speed at which the solid and cross-hatched vertical bars overlap for these support stiffnesses.

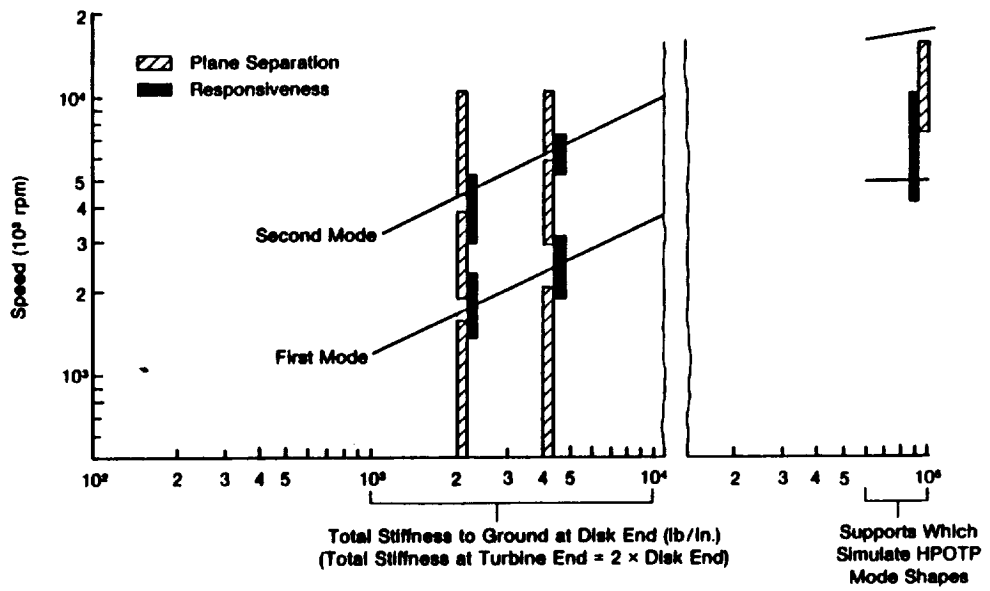
## TEST RESULTS

Table 2 lists the support stiffnesses and the predicted and measured critical speeds for each of the two rig configurations. For Test Configuration I, support stiffnesses simulated the HPOTP mode shapes. The objectives of the Configuration I tests were threefold --- to determine the acceptability of 8,000 rpm as a balance speed, to determine whether it is the lowest acceptable balance speed, and to compare low-speed flexible balancing results with conventional high-speed balancing. To meet the first two objectives, the rig was balanced at 8,000 rpm and at speeds below 8,000 rpm. High-speed flexible rotor balancing techniques were then used to balance the rotor to meet the third objective.

Figure 10 shows uncorrected rotor response (i.e., response before balancing) and response after balancing at 8,000 rpm. The post-balance response is lower than the uncorrected rotor response at all speeds. Furthermore, correction weights predicted with low-speed flexible balancing permitted operation up to the maximum rig speed of 24,000 rpm, which is above the first and second critical speeds.

To determine whether 8,000 rpm was the minimum speed at which successful balancing could be performed, correction weights were predicted at speeds of 2,500 rpm, 5,000 rpm and 7,500 rpm. When correction weights predicted at 2,500 rpm were installed, response at all speeds was greater than uncorrected rotor response, indicating a degradation in the state of balance. For correction weights predicted at 5,000 and 7,500 rpm, response was lower than uncorrected rotor response at low speeds, but the maximum achievable speed was limited by high responses at approximately 16,600 rpm and 19,800 rpm, respectively. For example, Figure 11 shows the results of balance weights predicted at 5,000 rpm. Thus, "correction"





85612-1

Fig. 9 Test Rig Low-Speed Flexible Rotor Balancing Map

Table 2  
Test Rig Configurations

<u>Configuration-I</u>				<u>Configuration II</u>			
Rig configured to simulate HPOTP mode shapes				Rig configured to simulate HPOTP first critical speed location			
<u>Total Radial Support Stiffness</u>				<u>Total Radial Support Stiffness</u>			
Turbine End Bearing = 100,000 lb/in. Disk End Bearing = 20,000 lb/in.				Turbine End Bearing = 100,000 lb/in. Disk End Bearing = 100,000 lb/in.			
<u>Critical Speeds (rpm)</u>				<u>Critical Speeds (rpm)</u>			
	<u>Predicted</u>	<u>Measured</u>	<u>Type</u>		<u>Predicted</u>	<u>Measured</u>	<u>Type</u>
1st	4,967	4,700	Flexible - Disk Bounce	1st	11,358	12,100	Bending - Disk Precession
2nd	23,550	23,400	Bending - Turbine Precession				

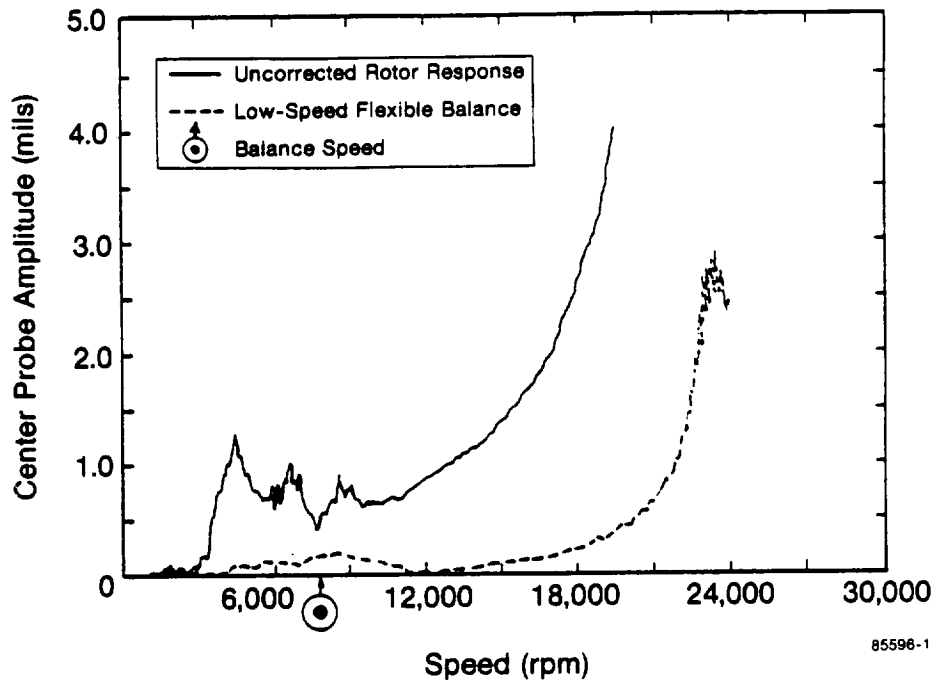


Fig. 10 Rig Configuration I: Balance at 8,000 rpm (4 planes)

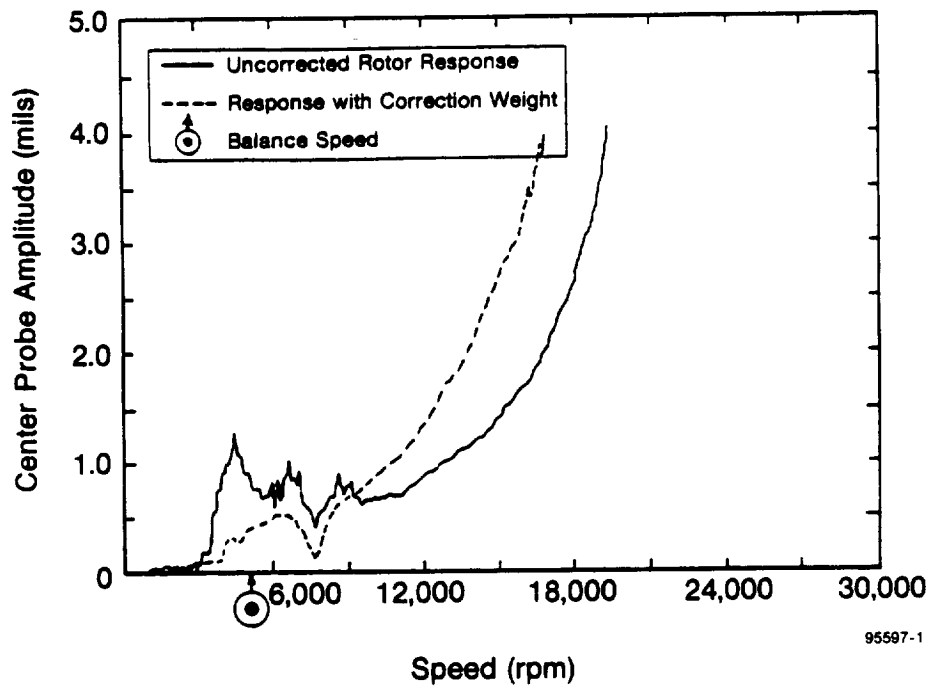


Fig. 11 Rig Configuration I: Balance at 5,000 rpm (4 planes)

weights predicted at speeds below 8,000 rpm did not permit operation above the second critical speed. These results show that the low-speed flexible balancing method predicted the minimum speed at which the rotor can be balanced to permit operation through two flexible critical speeds.

The rotor was also balanced using conventional high-speed balancing at two speeds. These speeds were 4,800 rpm and 16,000 rpm which correspond to the first critical and close to the maximum uncorrected rotor speeds, respectively. In this case (see Figure 12), it was possible to operate to the maximum rig speed of 24,000 rpm. The results in Figures 10 and 12 show that the quality of balance for the 8,000 rpm low-speed flexible balance method is nearly equivalent to the high-speed balancing method.

A two-plane, low-speed rigid body balance was then performed and the weights were installed in the rotor with Configuration I supports. These correction weights produced little change in the first mode maximum amplitude, and the maximum speed was limited to 20,000 rpm. Thus, for this hardware, rigid body balancing is not effective for high-speed operation.

Results for rigid body, low-speed flexible and high-speed flexible balancing are shown in Figure 13. The following conclusions can be drawn from the data in this figure.

1. Rigid body balancing showed virtually no improvement at or above the first critical.
2. High-speed flexible balancing results in the smallest residual response, but it required bringing the rotor to 16,000 rpm during the balancing process.
3. A satisfactory state of balance for operating above two flexible modes (to 24,000 rpm) can be achieved with low-speed flexible balancing. Also, the balancing speeds are significantly lower than required for high-speed balancing (8,000 rpm compared to 16,000 rpm).

These results demonstrate the payoff of low-speed flexible balancing when compared to rigid body and high-speed methods --- that is, a significant reduction in balancing speed for satisfactory high-speed operation.

For test Configuration II, support stiffnesses of 100,000 lb/in. were installed in each pedestal, and the correction weights predicted at 8,000 rpm from Configuration I were installed in the balance planes. The pedestal stiffnesses were changed to simulate the location of the HPOTP first bending critical speed. Installing weights predicted from Configuration I allowed Configuration II to assess the effectiveness of using out-of-housing, low-speed flexible balancing to minimize in-housing high-speed response.

The balance results for Configuration II, which are shown in Figure 14, indicate that before installing the correction weights, the maximum speed was limited to approximately 9,000 rpm. After installing the Configura-

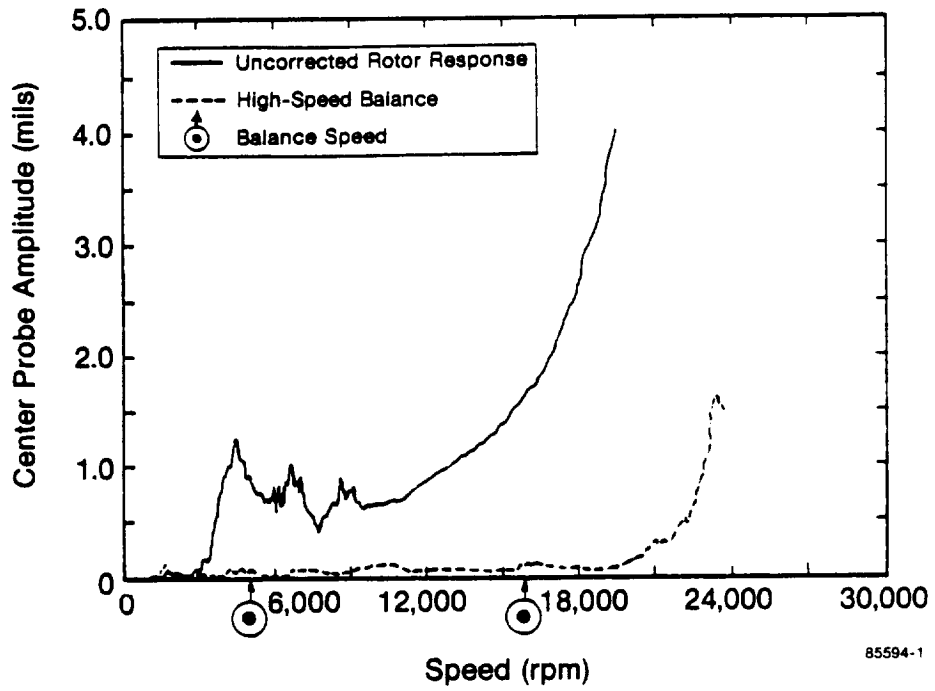


Fig. 12 High-Speed Balance (4 planes)

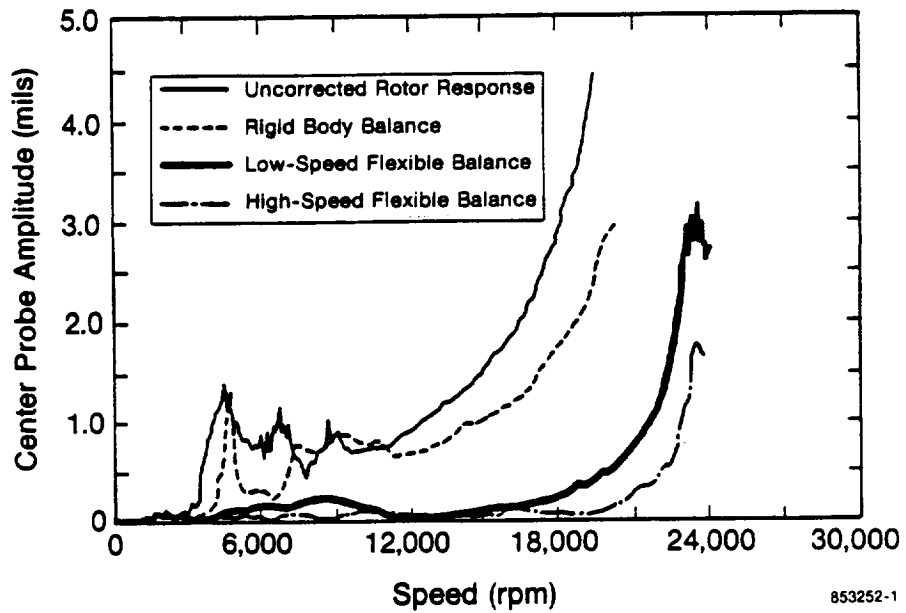
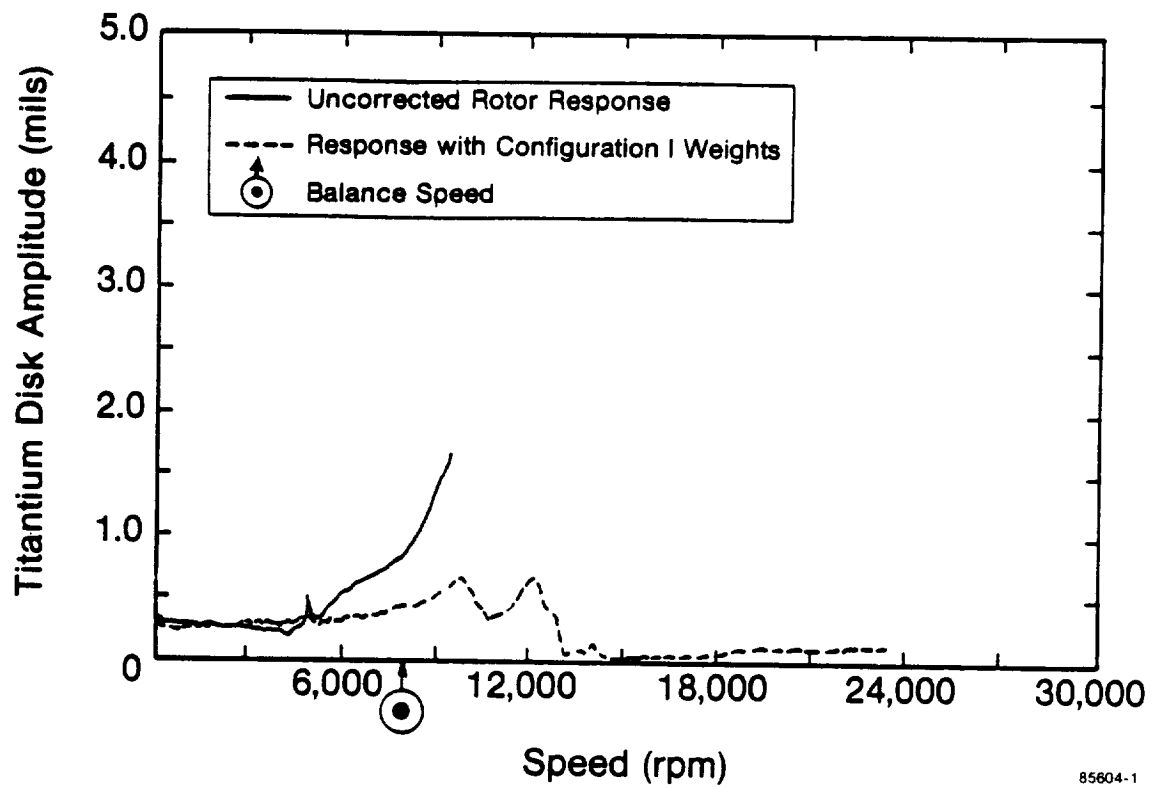


Fig. 13 Comparison of Rigid Body, Low-Speed and High-Speed Balance Results



85604-1

Fig. 14 Rig Configuration II with Low-Speed Flexible Balance Weights from Rig Configuration I

tion I weights (predicted at 8,000 rpm), it was possible to traverse the first mode and operate up to a maximum rig speed of 24,000 rpm. These data show that, for this system, the correction weights predicted using low-speed flexible rotor balancing supports are satisfactory for other supports. In terms of the HPOTP, this shows that out-of-housing low-speed flexible rotor balancing may significantly reduce in-housing high-speed response.

### **HPOTP LOW-SPEED FLEXIBLE BALANCING ASSESSMENT**

The low-speed flexible rotor balancing method was analytically applied to the HPOTP to determine the overall feasibility of using the method for this turbopump. The evaluation method consisted of selecting the balance planes, determining the plane separation, and determining responsiveness.

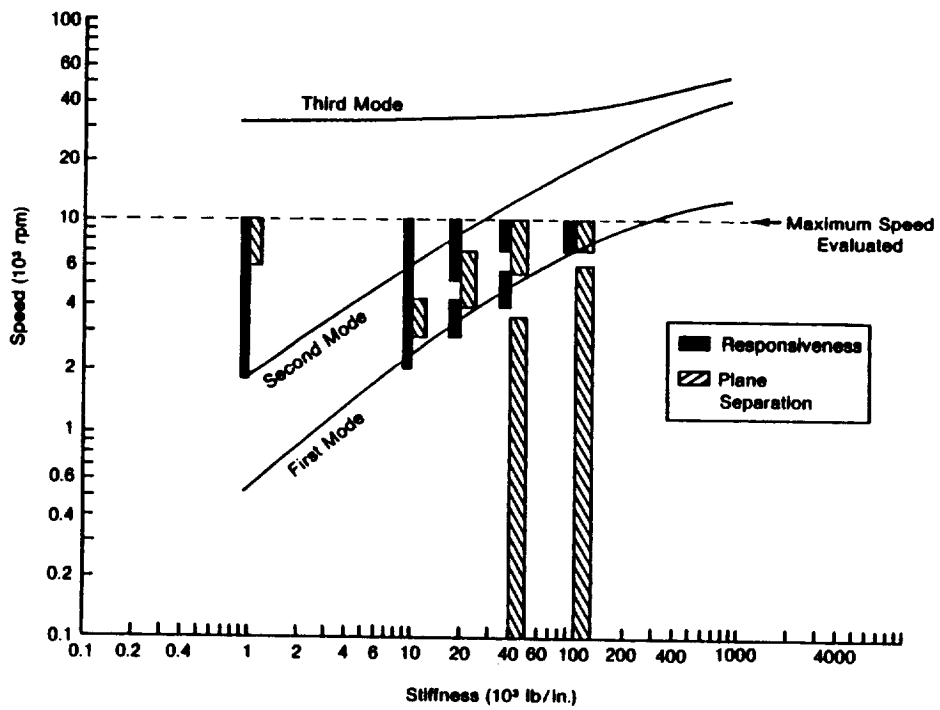
Balance plane selection was based on a review of HPOTP drawings and design information, mode shapes, and plane availability. The main impeller, the preburner impeller, and the first-stage turbine end were the three locations selected for determination of plane separation, based on the available planes and the critical speed mode shapes.

The low-speed flexible balancing method has been applied to the HPOTP rotor for these three planes. Figure 15 shows, for different values of speed and support flexibility, the regions where plane separation occurs and where the rotor is responsive. The regimes where these two conditions occur simultaneously are the low-speed flexible rotor balance regimes. As shown in the figure, for a support flexibility of 1,000 lb/in., balancing could be performed at a speed as low as 6,000 rpm. As flexibility decreases, the speed at which successful balancing is predicted decreases. In particular, for support stiffness values between 10,000 lb/in. and 100,000 lb/in., there are "windows" between the first and second mode where low-speed flexible balancing regimes are predicted. These occur where plane separation and rotor responsiveness coincide. The lowest predicted balance speed in these regions is approximately 3,000 rpm for a support stiffness of 10,000 lb/in.

In Figure 15, it is interesting to note that for support stiffnesses of 50,000 lb/in. and 100,000 lb/in., plane separation is predicted at very low speeds. However, this figure also shows that for these speeds, predicted response is below the measureable regimes. This demonstrates that instrumentation sensitivity may be a key parameter for the low-speed flexible balancing method. In particular, lower balance speeds will be predicted for instrumentation with greater sensitivity.

### **CONCLUSIONS**

A method for determining low-speed flexible balancing "windows" has been established and demonstrated in the laboratory using a flexible rotor rig. These "windows" are combinations of support stiffness, balancing speed, and probe and balance plane locations which, when combined with probes of sufficient sensitivity and a suitable existing balance weight computation



85609-1

Fig. 15 HPOTP Low-Speed Flexible Rotor Balancing Map



method, allow true flexible rotor balancing to be performed at low speeds. Major conclusions from the test data show that:

- Low-speed flexible rotor balancing is a viable technology.
- The quality of balance achieved with low-speed flexible rotor balancing is roughly equivalent to high-speed flexible balancing.
- For the test rig used, successful low-speed balancing required operation above the first mode.
- Balance speed/stiffness regimes predicted using the low-speed flexible rotor balancing approach are generally consistent with analytic predictions.
- Rigid body balance was found unacceptable for satisfactory high-speed operation.
- Correction weights predicted using the flexible supports required for low-speed flexible rotor balancing are acceptable for different support stiffnesses.

These test results show that the low-speed flexible method can be used for balancing at low speed to ensure smooth high-speed operation. Furthermore, by judicious implementation of this methodology, the range of balance speeds can be controlled and the state of balance achieved can be satisfactory for different flexibilities. Therefore, if applied to the HPOTP, the low-speed flexible rotor method may provide a means for low-speed, out-of-housing balancing, which results in smooth, high-speed operation.

## REFERENCES

1. McQuery, D. E. "Understanding Balancing Machines." American Machinist June 11, 1973.
2. Muster, D. and Stadelbauer, D. "Balancing of Rotating Machinery." Shock and Vibration Handbook Harris, C. and Crede, C., Eds., 2nd Edition, New York: McGraw-Hill (1976): Ch 39.
3. Tessarzik, J. M., et. al. "Flexible Rotor Balancing by the Exact Point-Speed Influence Coefficient Method." ASME Paper No. 71-Vibr.-91.
4. Goodman, T. P. "A Least-Squares Method for Computing Balance Corrections." Journal of Engineering for Industry Trans. ASME (Aug. 1964): 273-279.
5. Zorzi, E. S., Giordano, J. C. and Lee, C. C. "A Unified Approach to Balancing with Multiple Constraints." IFTOMM Conference on

Rotordynamic Problems in Power Plants, Rome: Italy, Sept.28 - Oct.2, 1982.

6. Giordano, J. C. and Zorzi, E. S. "HPOTP Low-Speed Flexible Rotor Balancing, Phase I Final Report." Mechanical Technology Incorporated, Jul. 1985, 85TR28.

#### **ACKNOWLEDGMENTS**

The authors express their appreciation to Mr. Chester Lee of Mechanical Technology Incorporated for his assistance in formulating the low-speed flexible rotor balancing method and to the NASA-Marshall Space Flight Center for funding the proof-of-principle tests described in this paper.

THE EFFECTS OF INTERNAL ROTOR FRICTION  
ON  
DYNAMIC CHARACTERISTICS OF TURBOPUMPS

By

J. Walton  
A. Artiles  
J. Lund  
C. Lee

Mechanical Technology Incorporated  
Latham, New York



## INTRODUCTION

Modern high speed turbomachinery designs are resulting in both higher power densities and rotating speeds. These trends are yielding a class of designs which operate above one or more bending critical speeds and may be made of complex, built-up assemblies. Therefore, there are many joints, fits, and areas for friction if slippage takes place. That internal friction forces can cause catastrophic failure of a rotor system has been known since the early 1920's based on the reported work of A. L. Kimball [1]. This and subsequent work has shown the possibility of internal friction-induced instability, but little work has been completed which attempts to quantify the magnitude of the destabilizing forces. It is important to understand the magnitude of the destabilizing mechanisms in order to either incorporate the appropriate external damping for control of the vibrations or to design to minimize their effect. In this paper, an analytical model developed to determine the stiffness and damping for an axial spline will be presented. Following the analytical development, a series of parametric evaluations showing the destabilizing effects of the axial spline on a supercritical rotor system will also be presented.

## THE STIFFNESS AND FRICTION OF A SPLINE COUPLING

To evaluate the forces and moments transmitted across a spline coupling, the lateral and angular stiffnesses without friction are first considered, to which the frictional contributions are added later.

### STIFFNESS

To evaluate the overall stiffness of a spline coupling, the stiffness of two

teeth in contact (shown in Figure 1), is first considered. The loading on a tooth is represented by the force,  $F$ , acting at the pitch circle under the pressure angle,  $\psi$ . This force has tangential and radial components given by:

$$F_t = F \cos\psi, \quad F_r = F \sin\psi \quad (1)$$

The resulting deflection has the components  $\delta_t$  and  $\delta_r$  such that the deflection in the load direction becomes:

$$\delta = \delta_t \cos\psi - \delta_r \sin\psi \quad (2)$$

Each tooth may be treated as a cantilever beam, mounted in a flexible base as shown in Figure 2. The tooth deflection is obtained as the sum of several contributions: a) Bending of the tooth; b) Rotation of the base; and c) Radial compression of the tooth.

First there is the bending of the tooth as a cantilever beam with a rigid base. The bending moment at the distance  $r$  from the base is equal to  $F_t(h-r) - F_r b$  where  $b$  is half the width of the tooth at the pitch circle and  $h$  is the tooth height at the pitch circle. With a cross-sectional area moment of inertia,  $I$ , a cross-sectional area,  $A$ , an elasticity modulus,  $E$ , and an effective shear modulus,  $G$ , the slope of the bent tooth is:

$$\frac{\partial \delta_t}{\partial r} = \int_0^r \frac{1}{EI} [F_t(h-r') - F_r b] dr' \quad (3)$$

and the deflection at the pitch circle ( $r = h$ ) becomes:

$$\delta_t = \int_0^h \int_0^r \frac{1}{EI} [F_t(h-r') - F_r b] dr' dr + \int_0^h \frac{F_t}{GA} dr \quad (4)$$

where the last integral is the contribution from shear deformation. The slope causes a radial displacement at the pitch circle, given by:

$$\delta_r = b \left( \frac{\partial \delta_t}{\partial r} \right)_{r=h} = b \int_0^h \frac{1}{EI} [F_t(h-r) - F_r b] dr \quad (5)$$

Eqs. (4) and (5) shall be written as:

$$\begin{aligned} \delta_t &= \delta_{1t} F_t - \delta_{3t} F_r \\ \delta_r &= \delta_{1r} F_t - \delta_{3r} F_r \end{aligned} \quad (6)$$

where:

$$\delta_{1t} = \int_0^h \frac{(h-r)^2}{EI} dr + \int_0^h \frac{1}{GA} dr \quad (7)$$

$$\delta_{3t} = \delta_{1r} = b \int_0^h \frac{(h-r)}{EI} dr \quad (8)$$

$$\delta_{3r} = b^2 \int_0^h \frac{1}{EI} dr \quad (9)$$

For a beam with constant cross-section,  $\delta_{1t} = (h^3/3EI + h/GA)$  and  $\delta_{3t} = \delta_{1r} = bh^2/2EI$  and  $\delta_{3r} = b^2 h/EI$ . For a tooth, however, the cross-section varies and integration is required to evaluate equations (7), (8) and (9). A numerical procedure can be found in Ref. 2.

Next, there is the bending of the base which will be represented by a moment stiffness,  $k_M$ . In Ref. 2, page 77, a suggested value is:

$$k_M = EA_0 B_0 / 5.3 \quad (10)$$

where  $A_0$  is the cross-sectional area at the base of the tooth,  $B_0$  is the width at the base ( $A_0 = B_0 L$  where  $L$  is the length of the tooth), and  $E$  is the modulus of elasticity.

The deflections at the pitch circle become:

$$\delta_t = \frac{h}{k_M} (F_t h - F_r b) \quad (11)$$

$$\delta_r = \frac{b}{k_M} (F_t h - F_r b)$$

These equations shall be written as:

$$\delta_t = \delta_{2t} F_t - \delta_{4t} F_r \quad (12)$$

$$\delta_r = \delta_{2r} F_t - \delta_{4r} F_r$$

where:

$$\delta_{2t} = h^2/k_M \quad (13)$$

$$\delta_{2r} = \delta_{4t} = hb/k_M \quad (14)$$

$$\delta_{4r} = b^2/k_M \quad (15)$$

Finally, there is a radial compression of the tooth:

$$\delta_r = \delta_{5r} F_r \quad (16)$$

where:

$$\delta_{5r} = \frac{1}{k_C} + \int_0^h \frac{h \, dr}{EA} \quad (17)$$

and  $k_C$  is the radial stiffness of the base. The total deflection is the sum of the separate contributions. By adding equations (6), (12), and (16), it is found that:

$$\begin{aligned} \delta_t &= (\delta_{1t} + \delta_{2t}) F_t - (\delta_{1r} + \delta_{2r}) F_r \\ \delta_r &= (\delta_{1r} + \delta_{2r}) F_t - (\delta_{3r} + \delta_{4r} + \delta_{5r}) F_r \end{aligned} \quad (18)$$

The flexibility coefficients  $\delta_{1t}$  to  $\delta_{5r}$  include the contributions from both of the teeth.

The deflection in the load direction is determined from equation (2) with substitution from equations (1) and (18):

$$\delta = [ (\delta_{1t} + \delta_{2t}) \cos^2 \psi + (\delta_{3r} + \delta_{4r} + \delta_{5r}) \sin^2 \psi - (\delta_{1r} + \delta_{2r}) \sin 2\psi ] F \quad (19)$$

Hence, the stiffness of two teeth in contact is:

$$K_\psi = F/\delta \quad (20)$$

$$= 1/[ (\delta_{1t} + \delta_{2t}) \cos^2 \psi + (\delta_{3r} + \delta_{4r} + \delta_{5r}) \sin^2 \psi - (\delta_{1r} + \delta_{2r}) \sin 2\psi ] \quad (20)$$

Let the number of teeth be  $n$  and introduce a  $\xi$ - $\eta$ - $\zeta$ -coordinate system with the  $\zeta$ -axis coinciding with the rotor axis, as shown in Figure 3a. Tooth No.  $j$  is located at the angle  $\gamma_j$  from the  $\xi$ -axis. If the relative lateral displacements between the two coupling parts are  $\Delta\xi$  and  $\Delta\eta$ , the displacement in the load direction becomes:

$$\delta_j = -\Delta\xi \sin(\gamma_j - \psi) + \Delta\eta \cos(\gamma_j - \psi) \quad (21)$$

The corresponding contact force is  $F_j = K_\psi \delta_j$ . When projected into the two axes and summed over all  $n$  teeth, the result is:

$$\begin{aligned} -F_\eta &= \sum_{j=1}^n -F_j \sin(\gamma_j - \psi) \\ &= K_\psi \sum_{j=1}^n [ \Delta\xi \sin^2(\gamma_j - \psi) - \Delta\eta \cos(\gamma_j - \psi) \sin(\gamma_j - \psi) ] \end{aligned} \quad (22)$$

$$\begin{aligned} -F_\xi &= \sum_{j=1}^n -F_j \cos(\gamma_j - \psi) \\ &= K_\psi \sum_{j=1}^n [ \Delta\eta \cos^2(\gamma_j - \psi) - \Delta\xi \cos(\gamma_j - \psi) \sin(\gamma_j - \psi) ] \end{aligned}$$

For evenly spaced teeth and  $n > 3$ , the following identities apply:

$$\sum_{j=1}^n \cos^2 \gamma_j = \sum_{j=1}^n \sin^2 \gamma_j = n/2 \quad (23)$$

$$\sum_{j=1}^n \cos^2 \gamma_j \sin^2 \gamma_j = 0$$



Thereby equation (22) can be written as:

$$F_{\xi} = -K_L \Delta\xi, \quad F_{\eta} = -K_L \Delta\eta \quad (24)$$

where the lateral stiffness is given by:

$$K_L = nK_{\psi}/2 \quad (25)$$

To determine the angular stiffness of the spline coupling, the tooth stiffness per unit length shall be set equal to  $K_{\psi}/L$  where  $L$  is the axial length of the teeth. The relative angular displacements between the two coupling parts are  $\Delta\alpha$  and  $\Delta\beta$ , assigned at the center plane of the coupling ( $\alpha$  and  $\beta$  represent the local slopes of the deformed rotor axis such that  $\alpha \sim d\xi/d\zeta$  and  $\beta \sim d\eta/d\zeta$ ). At the distance  $\zeta$  from the center plane, the displacement in the tooth load direction is:

$$\delta_j = \zeta [ -\Delta\alpha \sin(\gamma_j - \psi) + \Delta\beta \cos(\gamma_j - \psi) ] \quad (26)$$

The corresponding contact force, acting over an infinitesimal length  $d\zeta$ , is:

$$dF_j = \delta_j (K_{\psi}/L) d\zeta$$

The associated bending moment at the center plane is  $\zeta dF_j$  and integrated over the length of the tooth, the resulting bending moment becomes:

$$\int_{-L/2}^{L/2} \zeta dF_j = \frac{1}{12} L^2 K_{\psi} [ -\Delta\alpha \sin(\gamma_j - \psi) + \Delta\beta \cos(\gamma_j - \psi) ] \quad (27)$$

By summing over all teeth, the two components of the bending moment along the axes become:

$$\begin{aligned} -M_{\xi} &= \sum_{j=1}^n \frac{L^2 K_{\psi}}{12} [ \Delta\alpha \sin(\gamma_j - \psi) - \Delta\beta \cos(\gamma_j - \psi) ] \sin(\gamma_j - \psi) \\ -M_{\eta} &= \sum_{j=1}^n \frac{L^2 K_{\psi}}{12} [ -\Delta\alpha \sin(\gamma_j - \psi) + \Delta\beta \cos(\gamma_j - \psi) ] \cos(\gamma_j - \psi) \end{aligned} \quad (28)$$

By making use of equation (23), the equations reduce to:

$$\begin{aligned}
 M_{\xi} &= - K_A \Delta\alpha \\
 M_{\eta} &= - K_A \Delta\beta
 \end{aligned}
 \tag{29}$$

where the angular stiffness is given by:

$$K_A = L^2 n K_{\psi} / 24 = L^2 K_L / 12
 \tag{30}$$

It should be emphasized that this derivation, as also the one for the lateral stiffness, tacitly assumes that all teeth are in contact and stay in contact during the motion. The assumption implies that the prestress caused by the steady torque is never completely relieved by the dynamic stresses or, in other words, that the dynamic contact force,  $F_j$ , never exceeds the steady contact force. This is the equivalent of the assumption of no backlash in a torsional vibration analysis.

In practice, tolerance effects will prevent equal sharing of the load among the teeth even to the point where some teeth may not be engaged at all. For this reason, the number of teeth,  $n$ , which is used to compute the stiffnesses, should be replaced by some effective number, based on tests and experience.

### FRICTION

In addition to stiffness, the spline coupling will also have friction. In the preceding analysis, the tooth contact offers no resistance to motion tangent to the surface and here sliding may take place. Under idealized conditions, where the teeth share the load equally, the normal force equals  $T/nR\cos\psi$  where  $T$  is the steady transmitted torque,  $R$  is the radius of the pitch circle,  $n$  is the number of teeth, and  $\psi$  is the pressure angle. Hence, the friction force per unit length is  $\mu T/nRL\cos\psi$  where  $\mu$  is the coefficient of friction. It is directed opposite the local sliding velocity.

From Figure 3, the velocity tangent to the tooth profile is:

$$v_j = (\Delta\dot{\xi} + \zeta\Delta\dot{\alpha})\cos(\gamma_j - \psi) + (\Delta\dot{\eta} + \zeta\Delta\dot{\beta})\sin(\gamma_j - \psi) \quad (31)$$

The velocity in the axial direction at the pitch circle is:

$$w_j = R (\Delta\dot{\alpha} \cos\gamma_j + \Delta\dot{\beta} \sin\gamma_j) \quad (32)$$

where "dot" means time derivative. A side view of the tooth flank depicts the situation in Figure 3b. The friction force from the infinitesimal length  $d\zeta$  has radial and axial components given by:

$$\begin{aligned} dF_{v_j} &= \frac{\mu T}{nRL\cos\psi} \frac{v_j}{\sqrt{v_j^2 + w_j^2}} d\zeta \\ dF_{w_j} &= \frac{\mu T}{nRL\cos\psi} \frac{w_j}{\sqrt{v_j^2 + w_j^2}} d\zeta \end{aligned} \quad (33)$$

By integrating  $dF_{v_j}$  over the length, next projecting it onto the  $\xi$  and  $\eta$  axes and finally summing over all teeth gives the  $F_\xi$  and  $F_\eta$  components of the friction force. Similarly, by integrating  $\zeta dF_{v_j} + R dF_{w_j}$  over the length, projecting onto the axes and summing over all teeth gives the  $M_\xi$  and  $M_\eta$  components of the friction moment.

The procedure as such is straightforward and is readily implemented in a time step integration of the motion. It is, however, cumbersome and results in a non-linear coupling of the lateral and angular motions through the term  $\sqrt{(v_j^2 + w_j^2)}$ . This appears to be an unwarranted complication considering the uncertainties and approximations inherent in the idealized physical model. Instead, a simplified model shall be adopted in which  $v_j$  is ignored such that all the friction is taken up in the bending moment while the shear force is unaffected. The principal justification is that the bending moment plays a bigger role in the deformation of the rotor than the shear force.

Furthermore, in some spline coupling designs, the lateral motion may be restricted by pilots. With  $V_j$  equal to zero,  $dF_{wj}$  in equation (33) is readily integrated to give:

$$F_{wj} = \text{sgn}(w_j) \frac{\mu T}{2\pi R \cos \psi} \Delta \gamma \quad (34)$$

where  $\Delta \gamma = 2\pi/n$ . The corresponding components of the bending moment are:

$$\begin{aligned} -M_\xi &= \sum_j^n F_{wj} R \cos \gamma_j \\ -M_\eta &= \sum_j^n F_{wj} R \sin \gamma_j \end{aligned} \quad (35)$$

When the number of teeth,  $n$ , is sufficiently large,  $\Delta \gamma$  in equation (34) can be replaced by  $d\gamma$ , and the summations in equation (35) replaced by integrations over  $\gamma$ , such that:

$$\begin{aligned} -M_\xi &= \frac{\mu T}{2\pi \cos \psi} \int_0^{2\pi} \text{sgn}(w) \cos \gamma \, d\gamma \\ -M_\eta &= \frac{\mu T}{2\pi \cos \psi} \int_0^{2\pi} \text{sgn}(w) \sin \gamma \, d\gamma \end{aligned} \quad (36)$$

where:

$$\text{sgn}(w) = \begin{cases} +1 & \text{when } w > 0 \\ -1 & \text{when } w < 0 \end{cases} \quad (37)$$

$w$  is given by equation (32) as:

$$\begin{aligned} w &= R ( \dot{\Delta \alpha} \cos \gamma + \dot{\Delta \beta} \sin \gamma ) \\ &= R \sqrt{(\dot{\Delta \alpha}^2 + \dot{\Delta \beta}^2)} \cos(\gamma - \lambda) \end{aligned} \quad (38)$$

where:

$$\begin{aligned} \cos(\lambda) &= \dot{\Delta \alpha} / \sqrt{(\dot{\Delta \alpha}^2 + \dot{\Delta \beta}^2)} \\ \sin(\lambda) &= \dot{\Delta \beta} / \sqrt{(\dot{\Delta \alpha}^2 + \dot{\Delta \beta}^2)} \end{aligned} \quad (39)$$

Thereby it is seen that:

$$\text{sgn}(w) = \begin{cases} +1 & \text{when } \lambda - \pi/2 < \gamma < \lambda + \pi/2 \\ -1 & \text{when } \lambda + \pi/2 < \gamma < \lambda + 3\pi/2 \end{cases} \quad (40)$$

The integrals in equation (36) are then computed as:

$$\int_0^{2\pi} \text{sgn}(w) \cos(\gamma) d\gamma = 4\cos\lambda \quad (41)$$

$$\int_0^{2\pi} \text{sgn}(w) \sin(\gamma) d\gamma = 4\sin\lambda$$

Equation (36) reduces to:

$$-M_\xi = \frac{2\mu T}{\pi \cos\psi} \Delta\dot{\alpha} / \sqrt{(\Delta\dot{\alpha})^2 + (\Delta\dot{\beta})^2} \quad (42)$$

$$-M_\eta = \frac{2\mu T}{\pi \cos\psi} \Delta\dot{\beta} / \sqrt{(\Delta\dot{\alpha})^2 + (\Delta\dot{\beta})^2}$$

These should be added to equation (29) to obtain the total bending moment. They apply in a coordinate system which is fixed in the spline coupling and, therefore, is rotating with the angular speed,  $\Omega$ , of the rotor.

#### TRANSFORMATION TO A FIXED REFERENCE FRAME.

To convert into fixed coordinates, an x-y-z-coordinate system, fixed on the ground, is introduced, with the z-axis along the rotor axis (coinciding with the  $\zeta$ -axis). The relative lateral displacements between the two coupling parts are  $\Delta x$  and  $\Delta y$ , and the relative angular displacements are  $\Delta\theta$  and  $\Delta\phi$  (they give the slope of the deflected rotor axis such that  $\theta \approx dx/dz$  and  $\phi \approx dy/dz$ ). The corresponding shear forces are  $V_x$  and  $V_y$ , and the bending moments are  $M_x$  and  $M_y$ . The transformations between the two coordinate systems are (See Figure 4):

$$\begin{aligned}\Delta\theta &= \Delta\alpha \cos\Omega t - \Delta\beta \sin\Omega t \\ \Delta\phi &= \Delta\alpha \sin\Omega t + \Delta\beta \cos\Omega t\end{aligned}\quad (43)$$

$$\begin{aligned}\dot{\Delta\theta} + \Omega\Delta\phi &= \dot{\Delta\alpha} \cos\Omega t - \dot{\Delta\beta} \sin\Omega t \\ \dot{\Delta\phi} - \Omega\Delta\theta &= \dot{\Delta\alpha} \sin\Omega t + \dot{\Delta\beta} \cos\Omega t\end{aligned}\quad (44)$$

$$\begin{aligned}M_x &= M_\xi \cos\Omega t - M_\eta \sin\Omega t \\ M_y &= M_\xi \sin\Omega t + M_\eta \cos\Omega t\end{aligned}\quad (45)$$

By substituting equations (29) and equation (42) into equation (45) and by making use of equations (43) and (44), it is found that:

$$\begin{aligned}-M_x &= K_A \Delta\theta + \frac{2\mu T}{\pi \cos\psi} (\dot{\Delta\theta} + \Omega\Delta\phi) / \sqrt{(\dot{\Delta\alpha}^2 + \dot{\Delta\beta}^2)} \\ -M_y &= K_A \Delta\phi + \frac{2\mu T}{\pi \cos\psi} (\dot{\Delta\phi} - \Omega\Delta\theta) / \sqrt{(\dot{\Delta\alpha}^2 + \dot{\Delta\beta}^2)}\end{aligned}\quad (46)$$

where:

$$\dot{\Delta\alpha}^2 + \dot{\Delta\beta}^2 = (\dot{\Delta\theta} + \Omega\Delta\phi)^2 + (\dot{\Delta\phi} - \Omega\Delta\theta)^2 \quad (47)$$

Similarly, the shear forces become:

$$\begin{aligned}V_x &= -K_L \Delta x \\ V_y &= -K_L \Delta y\end{aligned}\quad (48)$$

The omission of a minus sign in both of equations (46) is due to the adopted sign convention as shown in Figure 4. In the rotor model, the two parts of the spline coupling are represented by two lumped mass stations, connected by the contacting teeth. The relative displacements across the coupling are:

$$\begin{aligned}\Delta x &= x_2 - x_1, & \Delta y &= y_2 - y_1 \\ \Delta\theta &= \theta_2 - \theta_1, & \Delta\phi &= \phi_2 - \phi_1\end{aligned}\quad (49)$$

With these definitions, equations (46) and (48) can be used directly in a rotor dynamics calculation. In the general case, numerical integration of the equations of motion is required.

In the special case of a rotor in isotropic bearings, the whirl orbit will be circular and equation (46) gives rise to a closed hysteresis loop depicted in Figure 6. The circular motion is given by:

$$\Delta\theta = r \cos \omega t \qquad \Delta\phi = r \sin \omega t \qquad (50)$$

where  $\omega$  is a resonant frequency of the rotor and  $r$  is the "radius" in the orbit. The energy dissipated over one cycle is:

$$U = \int_0^{2\pi/\omega} (M_x \dot{\Delta\theta} + M_y \dot{\Delta\phi}) dt = \operatorname{sgn}(\omega - \Omega) \frac{4\mu T}{\cos\psi} r \qquad (51)$$

When  $\Omega > \omega$ , the energy becomes negative and the dry friction acts destabilizing. The whirl motion given by equation (50) is forward whirl. For a backward whirl (change sign of  $\Delta\phi$ ) the dissipated energy will always be positive. In the general case, the whirl orbit is elliptical, containing both a forward and a backward whirl component, and the hysteresis loop will not necessarily close.

### ANALYTICAL RESULTS

Once the spline friction model was integrated into the rotorbearing nonlinear time transient dynamics code, a series of test cases were run to evaluate the effect of the spline coupling on rotor system stability. For the first of these test cases, a simple two-inch diameter shaft was used with a 24 inch bearing span and the spline centrally located (Figure 7). Table 1

lists the baseline case parameters all of which were then individually varied, with the exception of the imbalance ( $M_e$ ).

Table 1: Spline Coupling Parameters

---

$K_L$	= $5.10^5$ lb/in
$K_A$	= $5.10^5$ in-lb/rad
$M_e$	= 0.02 in-lb
Speed	= $3. \times 10^4$ r/min
Friction Torque	= $1. \times 10^5$ in-lb
$K_B$	= $5.10^5$ lb/in
$C_B$	= 0.0 lb-sec/in

---

The results of the parametric variations are shown in Figures 8 through 12. In Figure 8, it is seen that when running below the first bending critical speed of 26,550 r/min, the rotor system is stable. However, when the rotor is operated supercritically, a self excited instability results as expected. To control the instability demonstrated in Figure 8, two additional cases were run where damping was included. Figure 9 shows that a small increase in external bearing damping ( $C_B = 10.0$  lb-sec/in) only delayed the onset of instability. A large increase in the external damping, however, did demonstrate that the instability is indeed controllable. Returning to the baseline case, the next parameter varied was the external bearing stiffness ( $K_B$ ). As seen in Figure 10, increases in the bearing stiffness result in reduced stability. This is most likely due to the increased bending en-



ergy stored in the shaft as a result of the stiffer bearings. Another important parameter that was investigated was the product of the coefficient of friction and spline torque. As seen in Figure 11, increases in the friction torque product increase stability. This is most likely due to a locking up of the spline joint which would then limit the relative motion between the elements and thus reduce the internal friction effects. It should also be noted that the growth in vibration amplitudes with time appears linear, especially for the low friction torque value. This is to be expected since a coulomb friction model is used in the spline component analysis. In the final parameter test cases, both the lateral ( $K_L$ ) and angular ( $K_A$ ) spline joint stiffness were varied. Figure 12 presents the results of this variation. As with the other cases, Figure 12 shows that rotor system stability is affected by changes in the rotor system and particularly the spline joint.

Following the parametric variation test cases, a simplified rotor system model of the SSME LOX Turbopump (Figure 13) was established including the preburner spline. Table 2 presents the baseline parameters used.

Figure 14 shows the results obtained from the time transient analysis. As seen, regardless of the friction torque value no rotor system instability was observed for this model, even though the rotor was operated well above the first bending critical speed of approximately 10,000 r/min. When viewing the mode shape for the first critical speed, it becomes readily evident that relative motion between both sides of the spline are likely to be extremely small if not nonexistent. As a result, it would be highly unlikely that rotor system stability would be adversely affected in this model.

Table 2: SSME Turbopump Spline Coupling Parameters

---

$$K_L = 5 \times 10^6 \text{ lb/in}$$

$$K_A = 5 \times 10^5 \text{ in-lb/rad}$$

$$M_e = 0.02 \text{ in-lb}$$

$$\text{Speed} = 3 \times 10^4 \text{ r/min}$$

$$\text{Friction Torque} = 2 \times 10^4 \text{ in-lb}$$

$$K_B = 1 \times 10^6 \text{ lb/in}$$

$$C_B = 1.0 \text{ lb-sec/in}$$

---

Further work in this area is continuing with the development of internal friction models to represent both the interference fit and curvic coupling joints. With the completion of these additional models, a complete LOX Turbopump rotor system analysis will be performed. In addition, efforts are currently underway to characterize the coefficients of friction experienced under small amplitude oscillatory motion at a range of frequencies, temperatures, and normal loads. These tests will be followed by non rotating modal testing to assess the validity of the basic component models developed prior to the rotordynamic verification tests.

### ACKNOWLEDGEMENT

The authors would like to acknowledge Mr. George von Pragenau of NASA Marshall Space Flight Center for his active support. This work was performed under NASA contract NAS8-35601.

### REFERENCES

1. Kimball, A.L., "Internal Friction Theory of Shaft Whirling," General Electric Review, Vol. 27, 1924, p. 244.
2. Marmol, R.A., "Engine Rotor Dynamics, Synchronous and Nonsynchronous Whirl Control," U.S. Army Report: USARTL-TR-79-2, February 1979.

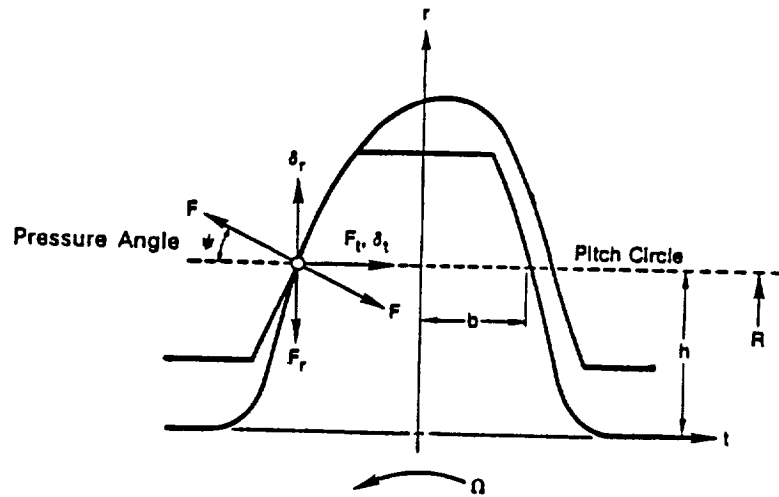


Figure 1. Axial Spline Teeth in Contact

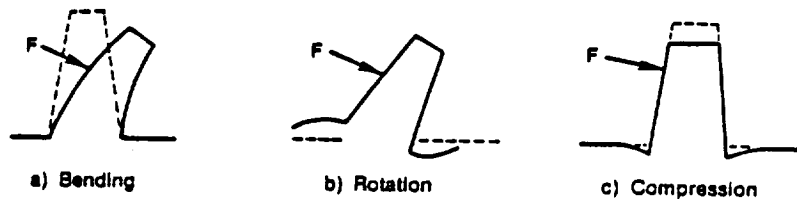
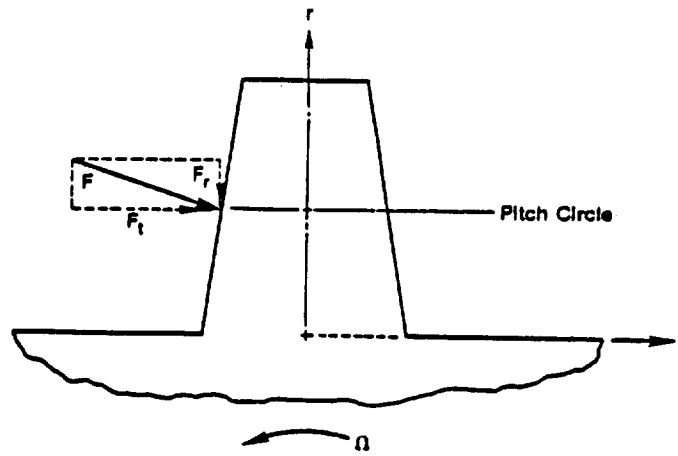


Figure 2  
Components of Tooth Flexibility

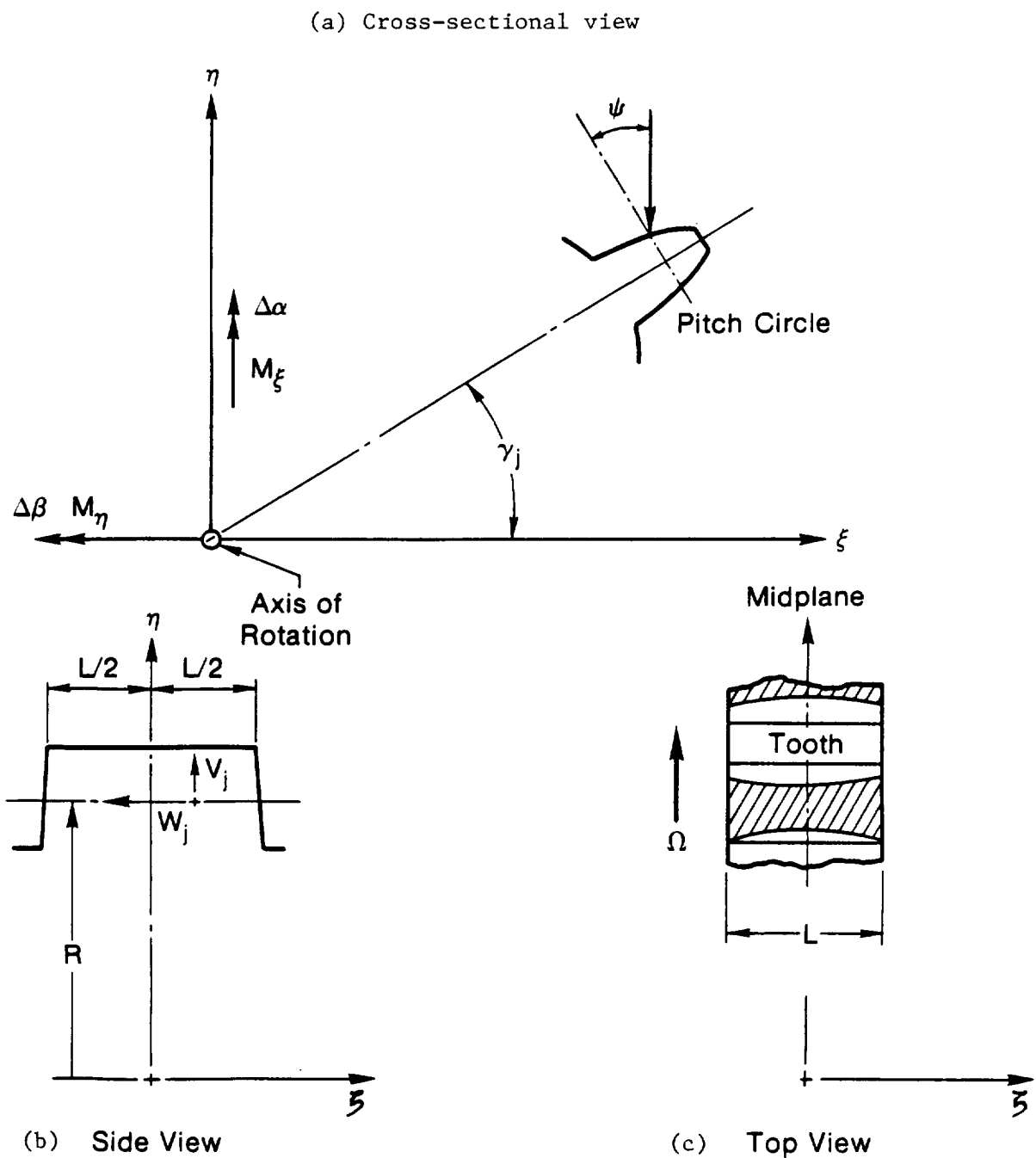


Figure 3  
Tooth Geometry and Coordinate System fixed on the Rotor

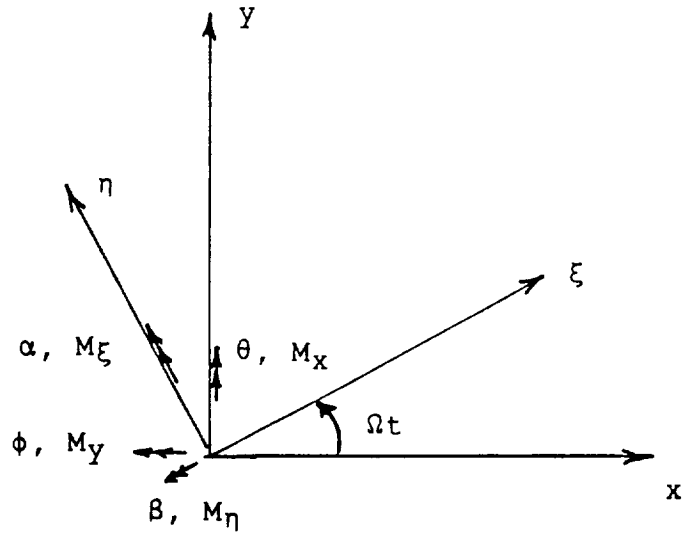


Figure 4

Transformation from Rotating to Fixed Coordinate Systems

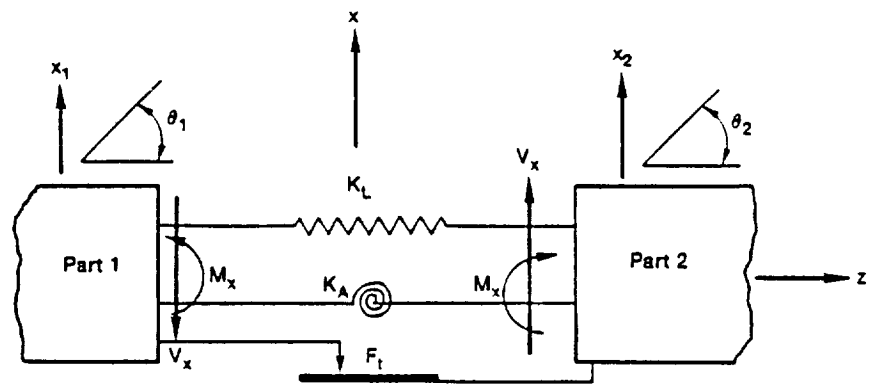


Figure 5

Schematic of the Parts of the Rotor Interconnected by the Spline Coupling Model.

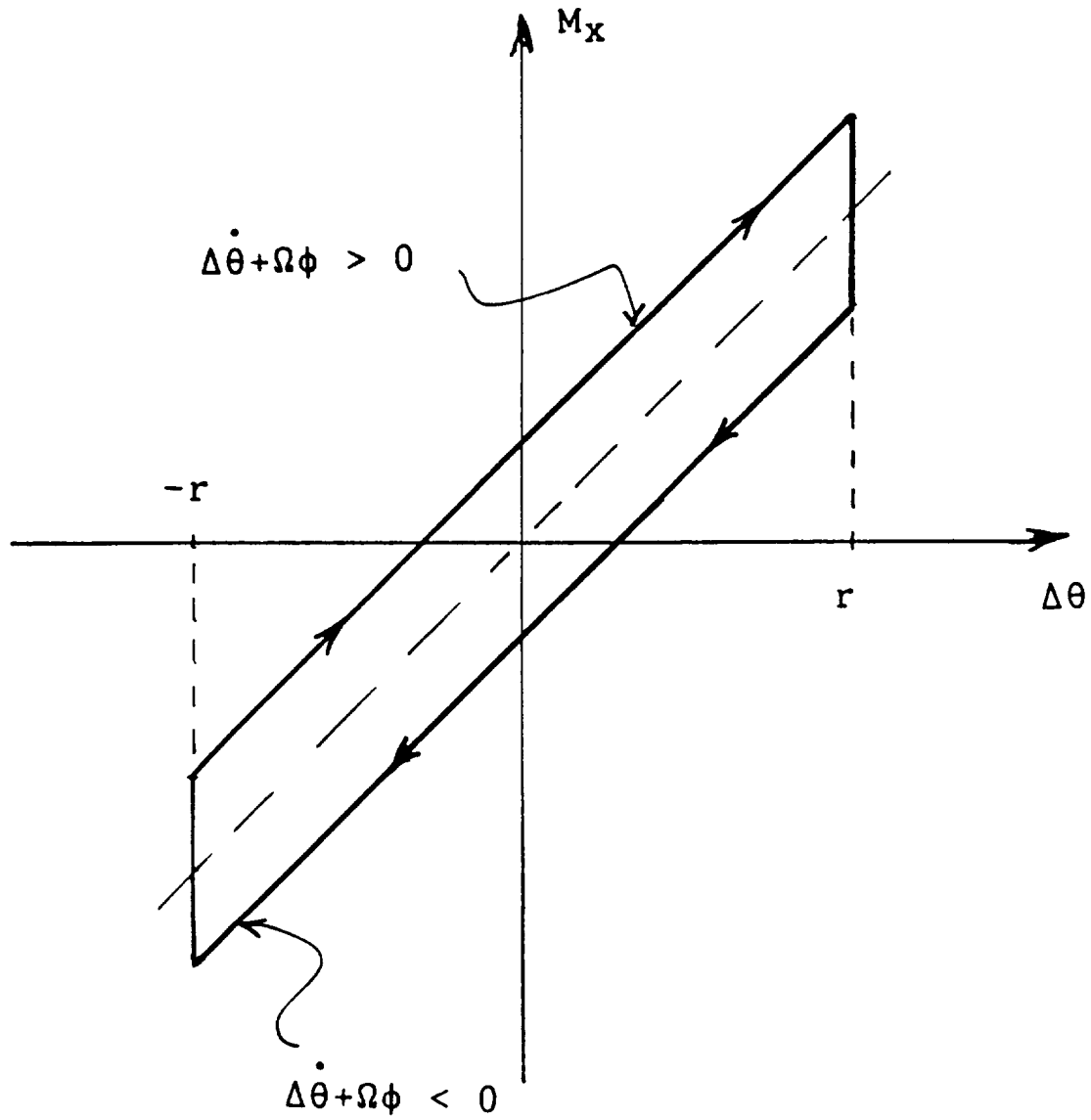


Figure 6

Hysteresis Loop in the Plane of Transmitted Moment Versus  
Relative Deflection Across the Spline for a Circular Orbit

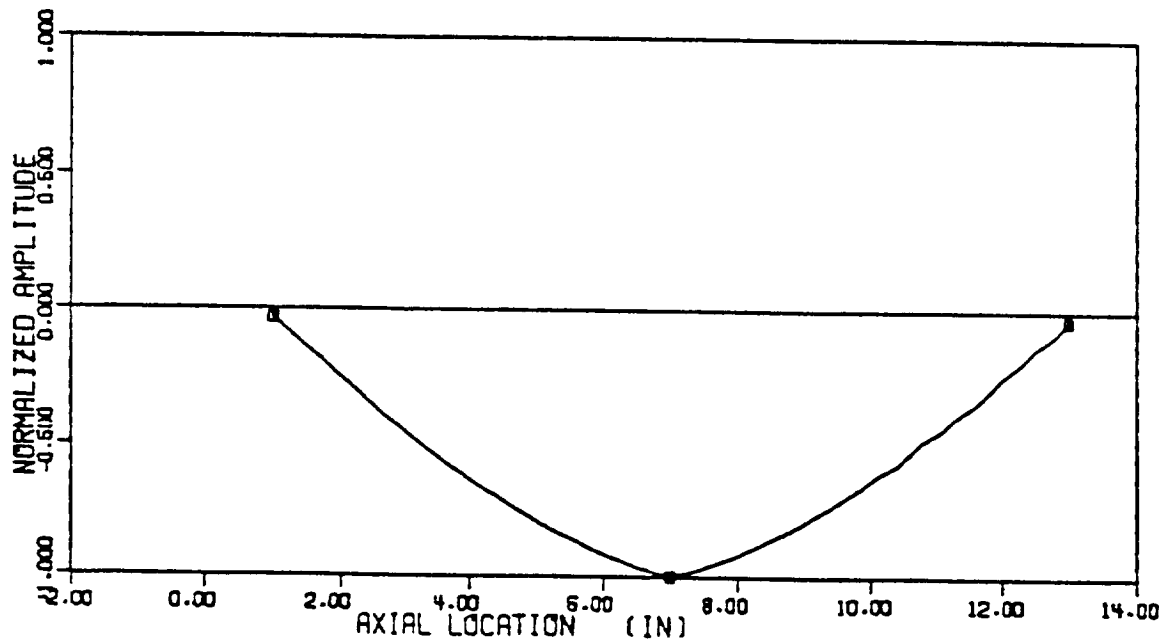
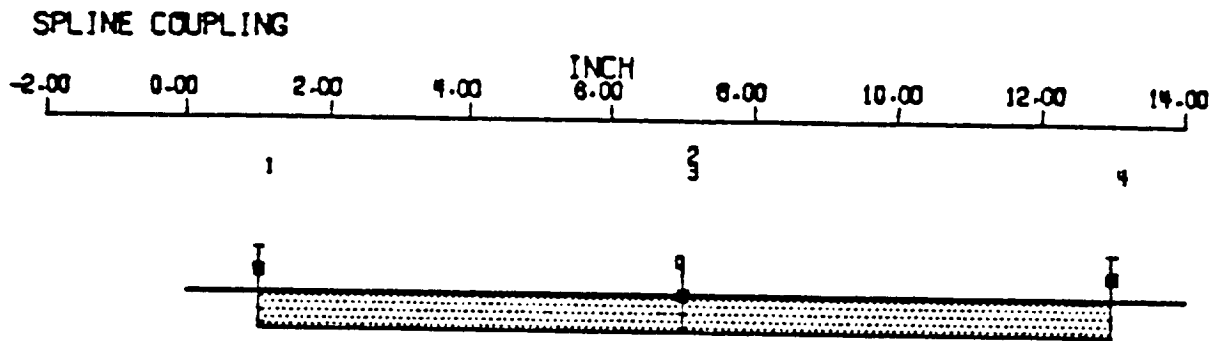
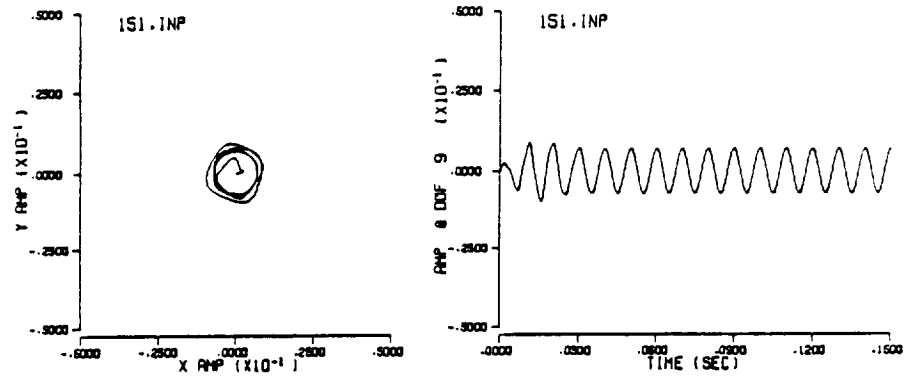


Figure 7

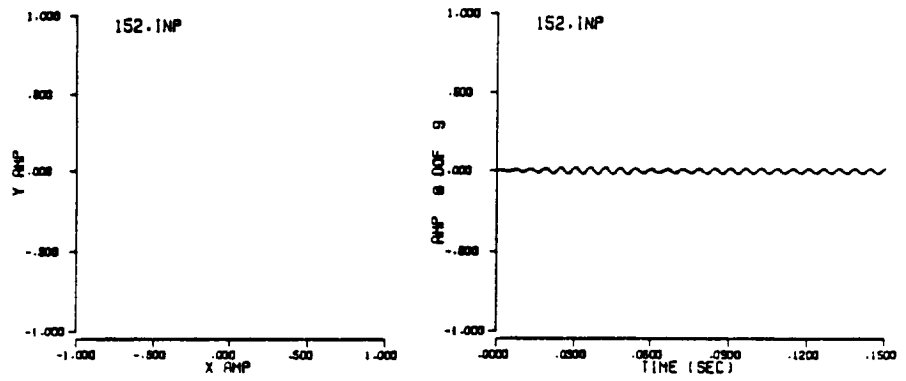
Geometry and Mode Shape Plot for Simple Rotor with Spline Coupling



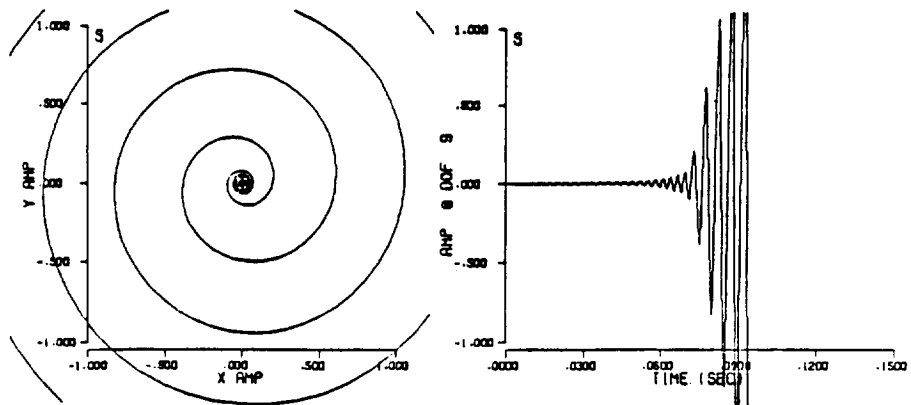
SPEED PARAMETER



6,000 RPM



10,000 RPM

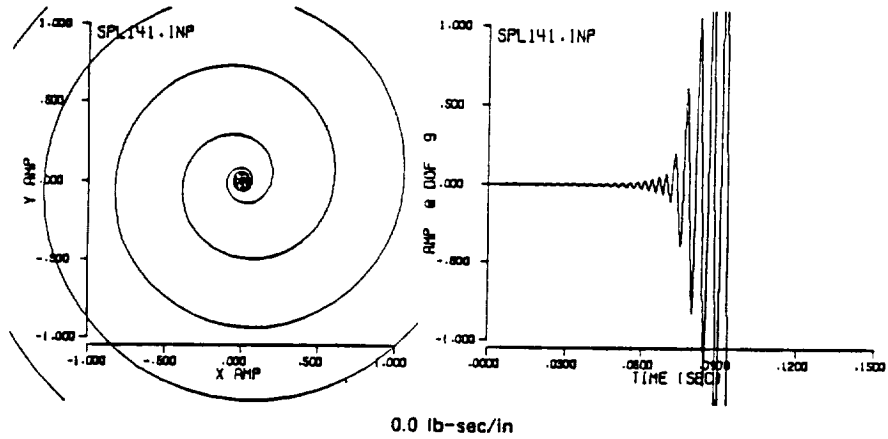


30,000 RPM

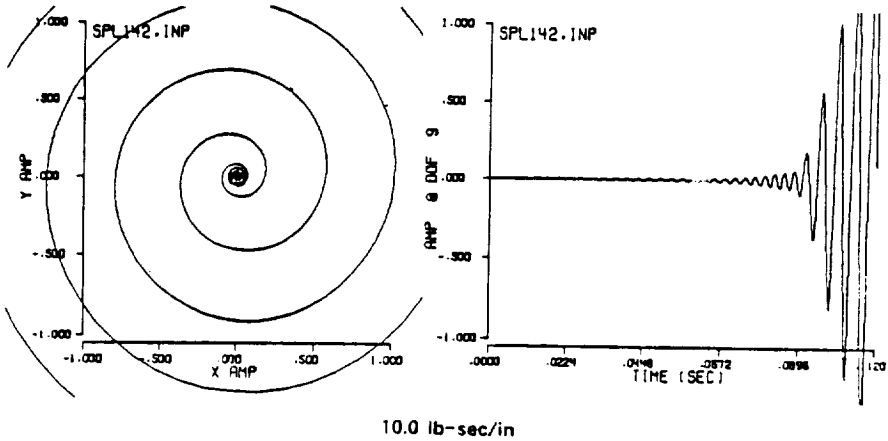
Figure 8

Time Transient Response as a Function of Speed

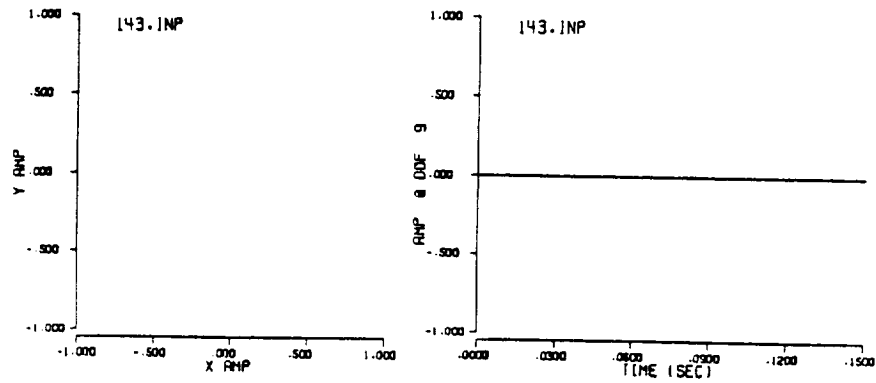
EXTERNAL DAMPING PARAMETER



0.0 lb-sec/in



10.0 lb-sec/in



100. lb-sec/in

Figure 9

The Effect of External Damping on Rotor Stability

BEARING STIFFNESS PARAMETER

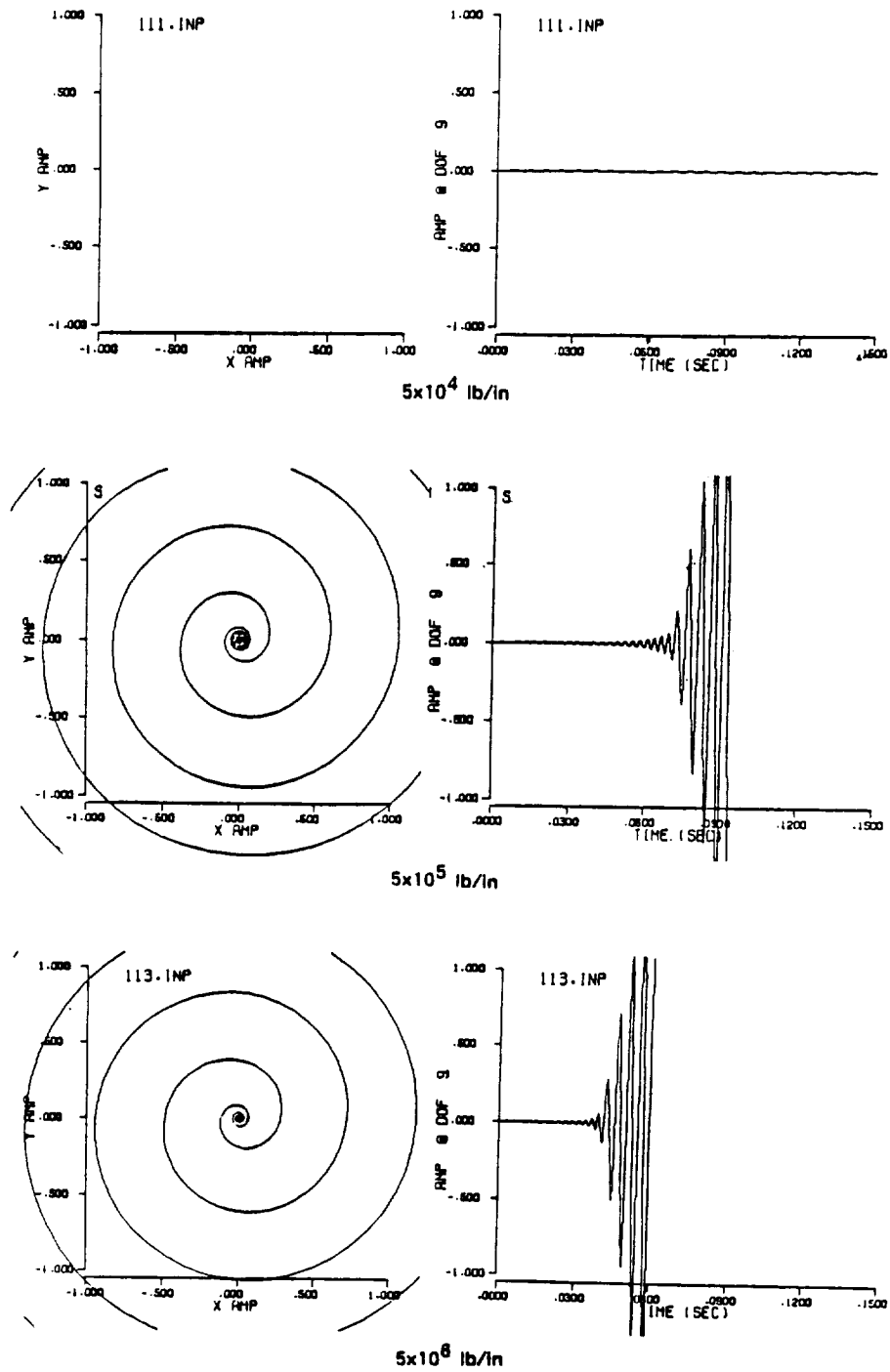


Figure 10

The Effect of External Bearing Stiffness on Rotor Stability

FRICITION TORQUE PARAMETER

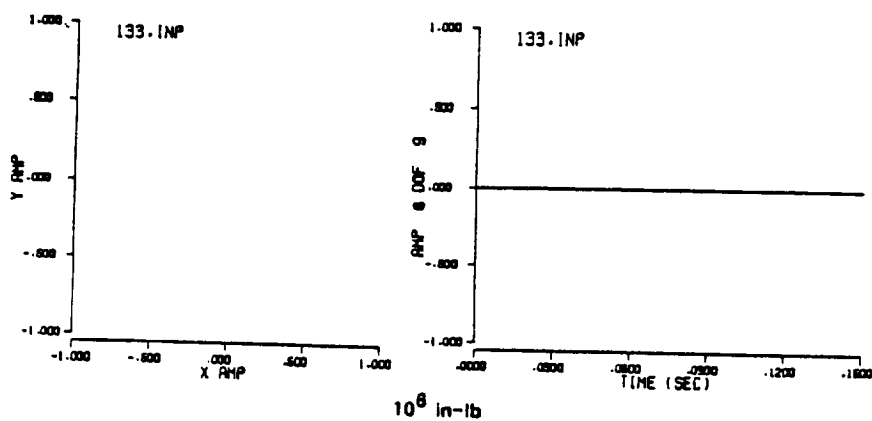
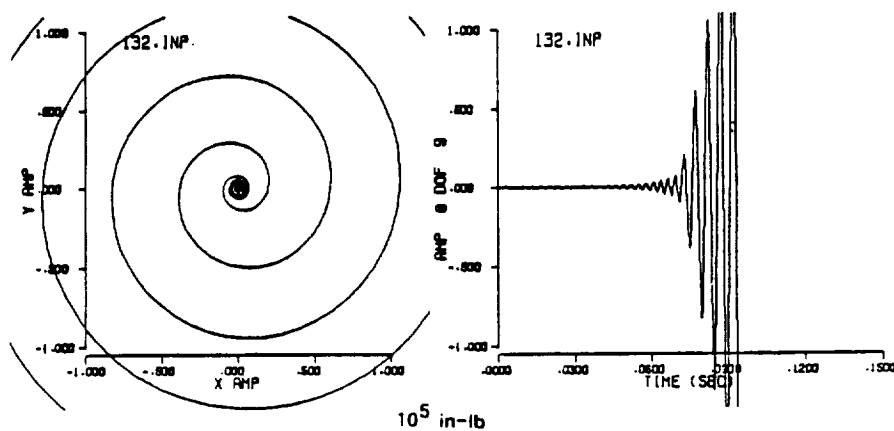
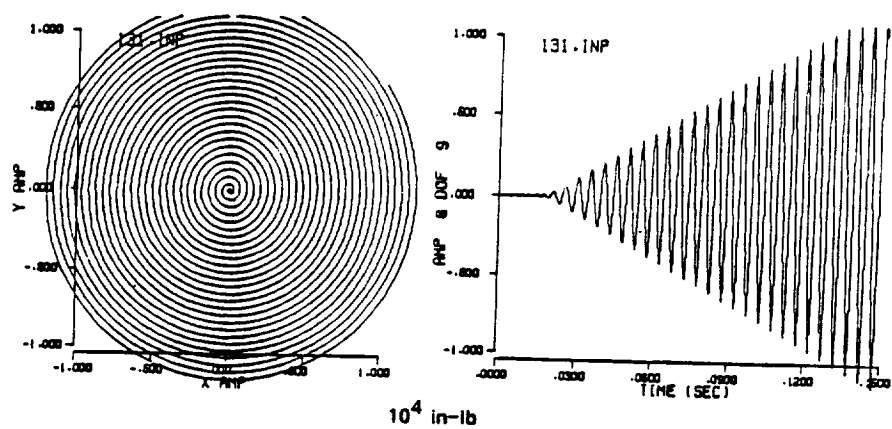
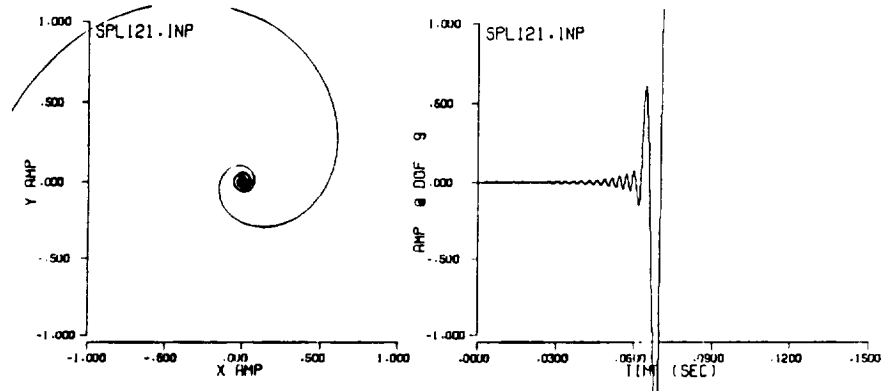


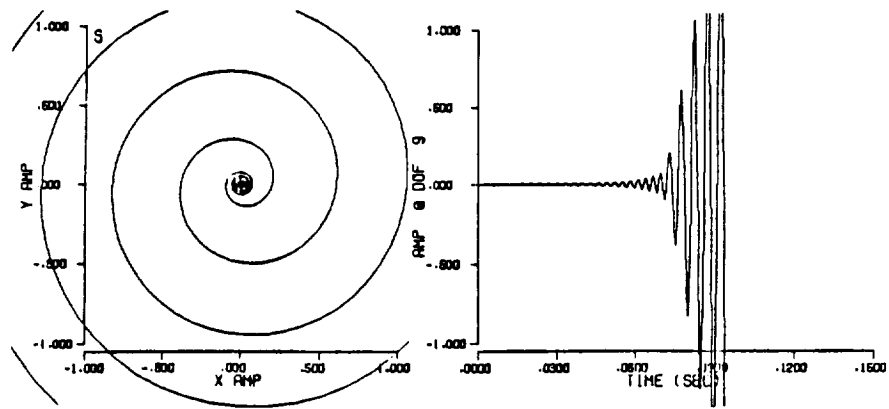
Figure 11

The Effect of Friction Torque on Rotor Stability

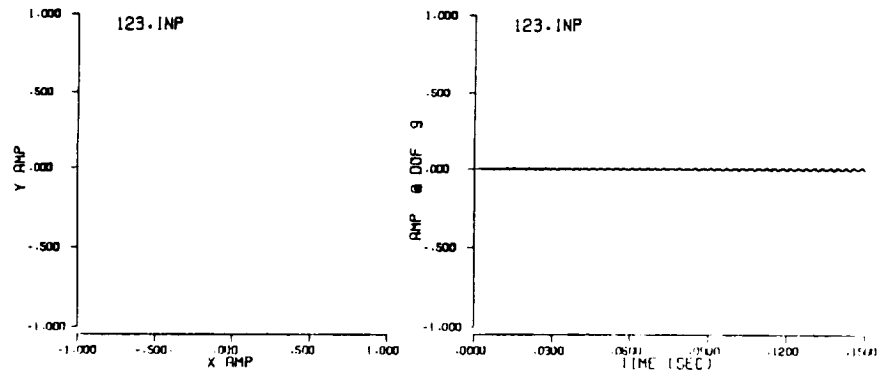
SPLINE STIFFNESS PARAMETER



$K_L = 5 \times 10^4$  lb/in       $K_A = 5 \times 10^4$  in-lb/rad



$K_L = 5 \times 10^5$  lb/in       $K_A = 5 \times 10^5$  in-lb/rad



$K_L = 5 \times 10^8$  lb/in       $K_A = 5 \times 10^8$  in-lb/rad

Figure 12  
The Effect of Spline Coupling Stiffness

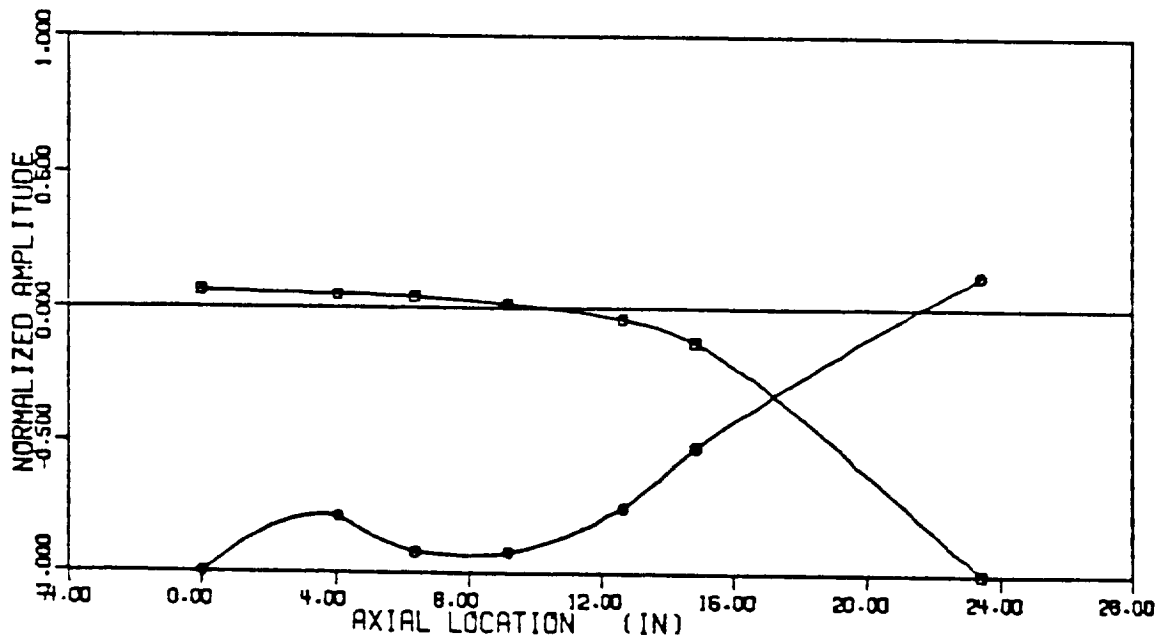
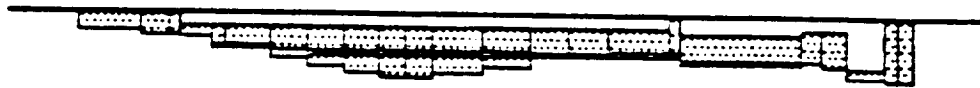
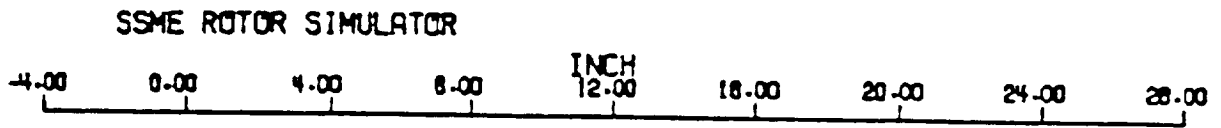


Figure 13

SSME Turbopump Rotor Model and Mode Shapes

FRICITION TORQUE PARAMETER FOR HPOTP

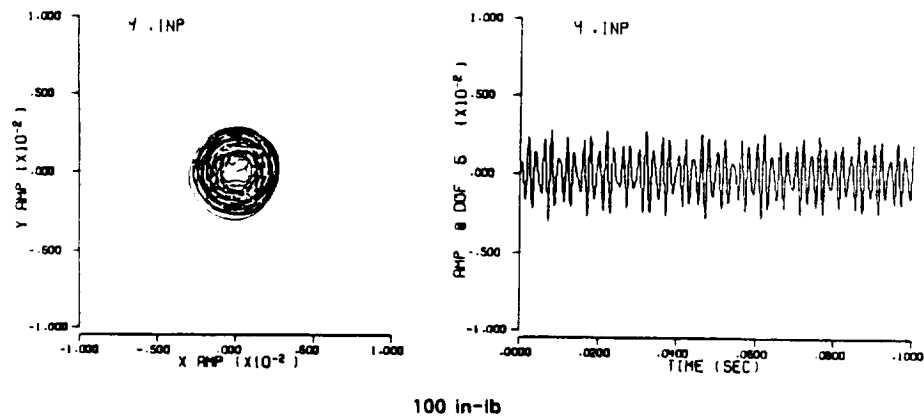
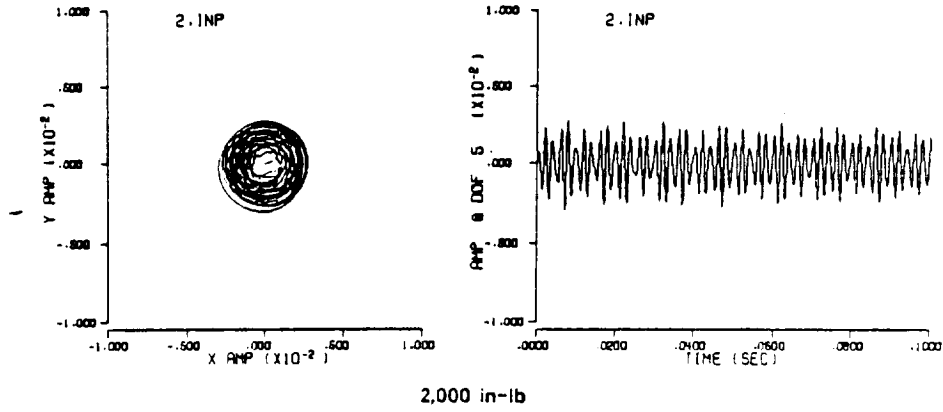
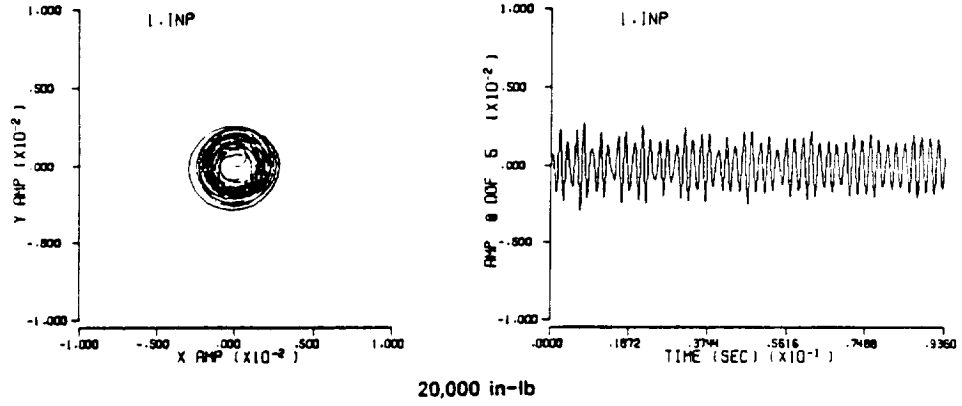


Figure 14

The Effect of Preburner Spline Friction Torque on SSME  
LOX Turbopump Response.

Efficient Transient Analysis Methods for the Space Shuttle  
Main Engine (SSME) Turbopumps

S.T. Noah\*, U.J. Fan\*, Y.-S. Choi\* and T. Fox\*\*

Abstract

Effective procedures are presented for the response analysis of the SSME turbopumps under transient loading conditions. Of particular concern is the determination of the nonlinear response of the systems to rotor imbalance in presence of bearing clearances. The proposed methods take advantage of the nonlinearities involved being localized at only few rotor/housing coupling points.

The methods include those based on alternative integral formulations for the incremental solutions involving the transition matrices of the rotor and housing. Alternatively, a convolutional representation of the housing displacements at the coupling points can be utilized to an advantage.

For purposes of assessing the numerical integration results for the nonlinear rotor/housing systems, an FFT-based harmonic balance procedure is being developed to enable determining all possible harmonic, subharmonic and nonperiodic solutions of the systems. A brief account of the Fourier approach is presented.

\*Mechanical Engineering Dept.  
Texas A&M University  
College Station, Texas 77840  
USA

\*\*NASA Marshall Space Flight Center  
Huntsville, Alabama 35812  
USA



## INTRODUCTION

The dynamic transient response analysis of the SSME turbopumps is essential for further development and prediction of the engine performance under various load levels and required maneuvers. Childs [1] conducted numerical analysis for critical speed-transitions of the HPOTP. A rubbing condition was predicted for that earlier configuration at the turbine floating-ring seals during shutdown. More recently, Childs [2] concluded a series of studies concerning the development of a reliable RPL engine and a description of new problems which are being encountered in developing FPL performance. The analysis was based on a model method developed earlier by the same author [3]. The method takes advantage of the modal representation in constructing reduced size models based on truncated set of rotor modes at zero running speed and of housing modes. Childs [2] demonstrated that although a linear transient analysis remains an efficient procedure for general characterization of the turbopump's rotor-dynamics, nonlinear analysis is essential. An important case considered by Childs is that of the effect of the radial clearances provided at the outer races of the bearings. The results of the nonlinear analysis showed a significant reduction in the subsynchronous rotor motion. More significantly, the bearing clearances can drop the peak-vibration running speed into the operating range where the synchronous whirling loads might pose a serious threat to bearing life.

For large complex rotor systems, such as the SSME turbopumps, various modeling and analysis techniques vary in their ability to accurately describe the systems' behavior. This ability mainly depends on the configuration of the systems analyzed and on the forcing conditions. In rotating components, this also involve whether the rotating speed is constant or varying with time. A hybrid representation by various types of coordinates and formulation for the various components of the systems may prove valuable.

Different procedures have been utilized by analysts to determine the transient response of large order rotor systems. The procedures can be recognized as falling under one of two basic approaches. Those using physical or modal coordinates of the complete system and those using the coordinates of the individual components of the system. The methods also differ in the numerical integration methods selected for the analysis.

Rouch and Kao [4] employed Guyan (static) reduction method to arrive at a reduced size model in terms of the remaining physical coordinates. Accuracy of the results could be expected to be acceptable since the rotor is basically a train of mass-stiffness subsystems. Nordmann [5] attempted to minimize the inaccuracy of static

condensation by applying the static reduction technique to an arbitrarily substructured rotor system and then assemble the reduced substructures to form a reduced system. The procedure is very laborious and no guarantees of accuracy are apparent.

Childs [5] utilized free-interface modes of the various system components to represent the assembled SSME turbopumps. The method, using fourth order Runge-Kutta integration, but does not provide for accommodating accurate modal representation of the large housing model while maintaining a small size for the model. Nelson *et al.* [7] on the other hand used fixed-interface complex component modes to assemble a reduced size model. For systems with large number of coupling points among the components, the approach suffers the problem of introducing higher frequencies resulting from excessive number of constraints imposed at the coupling (or boundary) points. In a transient analysis, this will necessarily result in much smaller time increments and consequently, will lead to excessive computational time and larger round-off errors.

For nonlinear large rotor systems, only a few analysts have presented techniques for the general transient analysis of such systems. Adams [8] used a normal mode representation for the rotor in terms of its undamped, free symmetric modes and treated gyroscopic and nonlinear terms as pseudo-external loads. The method presented by Childs [6] makes use of a similar procedure to couple the rotor to its flexible housing. Nelson *et al.* [7] developed a general computer code for the transient analysis of large rotor systems. The user may utilize time-step integration in the constrained-rotor (fixed-interface) modal space. Again, all connection points, including those at the nonlinearities must be constrained, leading to the same shortcomings described previously.

None of the above studies have adequately addressed the problems of attempting to use reduced size, accurate models and the associated efficiency of computation. A judicious selection of the system configurations and the numerical methods is essential for achieving the required efficiency while maintaining acceptable accuracy.

In this study, integration methods based on the transition matrices [9] of the separate rotor and housing are used to efficiently determine the nonlinear transient coupled system response under imbalance forces and in presence of bearing clearances. Pragenau [10] utilized the transition matrix for integration, stating that it offers the simplicity of the Euler method without requiring small steps. Pragenau maintained that for constant subsystems, the stability and accuracy of the method are acquired through the closed form solution of the transition matrix.

Alternatively, a discretized Duhamel [9] (convolution) integral method can be used to an advantage to represent the response at the housing coupling points to the rotor. Kubomura [11] used a convolution based method to achieve dynamic condensation of a substructure to its coupling points to other structures. Convolution was also used in [12,13] to reduce system coordinates to that of the nonlinearities.

Along with the response analysis in presence of bearing clearance under imbalance forces, a numerical harmonic balance method is developed toward verifying possible steady state synchronous and subsynchronous rotor response. This is essential to ensure that no possible potentially damaging solution is missed due to unfortunate selections of particular initial conditions. The harmonic method locates all possible periodic solutions. The method is briefly presented here as applied to a modified Jeffcott model.

## THE TURBOPUMP MODEL

### Housing

The modal equations of the housing in the X-Z, Y-Z planes in terms of a truncated set of its modal coordinates  $\{q_H\}$ , normalized with respect to the mass matrix, can be written as [14,15]

$$\{\ddot{q}_H\} + [2 \xi_H \Lambda_H^{1/2}] \{\dot{q}_H\} + [\Lambda_H] \{q_H\} = [A_{HC}]^T \{F_H\} \quad (1)$$

where  $\xi_H$  and  $\Lambda_H$  are the modal damping coefficients and natural frequencies, respectively,  $F_H$  is the vector of coupling forces to the rotor, including the balance piston axial force. The axial force is a function of the axial displacement and velocity as well as the spinning speed. The coupled physical displacements in the X and Y directions at the coupling points to the rotor are given by

$$\{W_H\} = \begin{Bmatrix} X \\ Y \end{Bmatrix} = [A_{HC}] \{q_H\} \quad (2)$$

where  $[A_{HC}]$  is the normalized modal vectors, with respect to the mass matrix, associated with the coupling points.

### Rotor

As in the case of housing, the symmetric-rotor equations of motion may be written in terms of a truncated set of modal coordinates  $\{q_R\}$  of the free-free nonspinning, undamped rotor as

$$\{\ddot{q}_R\} + [D_R] \{\dot{q}_R\} + [\Gamma_R] \{q_R\} = [A_{RC}]^T \{F'_R + P'_R\} \quad (3)$$

where  $D_R$  and  $\Gamma_R$  are nondiagonal matrices which are speed,  $\dot{\phi}$ , dependent, and  $P'_R$  is the imbalance forces which are, in general, functions of  $\dot{\phi}$  and  $\ddot{\phi}$ . The vector  $F'_R$  represents the interaction forces with the housing such as the bearing, seal, side loads (which are functions of  $\dot{\phi}$ ), etc. the physical displacements at these coupling points are given by

$$\{W_R\} = \begin{Bmatrix} X_R \\ Y_R \end{Bmatrix} = \begin{bmatrix} A'_{RC} & 0 \\ 0 & A'_{TC} \end{bmatrix} \{q_R\} = [A'_{RC}]^T \{q_R\} \quad (4)$$

### Interaction Forces

The coupling forces between the housing and rotor can be expressed as (see Fig. 1) [13]

$$- \{F_H\} = [C] \{\dot{W}_H\} + [K] \{W_H\} - [C] \{\dot{W}_R\} - [K] \{W_R\} \quad (5)$$

$$\text{and} \quad \{F_R\} = \{F_H\} \quad (6)$$

where  $[C]$  and  $[K]$  involve direct and cross coupled stiffness and damping forces as well as spinning velocity dependent coefficients. The coefficients of the bearing forces allow for presence of clearances (deadbands).

### TRANSITION MATRIX FORMULATIONS

The rotor's modal equations of motion are written in the first order form

$$\{\dot{U}_R\} = [\alpha_R] \{U_R\} + \{F_R\} \quad (7)$$

where

$$\{U_R\} = \begin{Bmatrix} q_R \\ \dot{q}_R \end{Bmatrix}, \quad [\alpha_R] = \begin{bmatrix} 0 & I \\ -\Gamma_R & -D_R \end{bmatrix} \quad (8)$$

and

$$\{F_R\} = \{A_{RC}\}^T \{F'_R + P'_R\} \quad (9)$$

Similar first order equations can be written for the housing.

The solution of equations (7) and the analogous ones for the housing in terms of the associated transition matrices of the rotor and housing takes the form [9]

$$\{U(t)\} = e^{[\alpha]t} \{U(0)\} + \int_0^t e^{[\alpha](t-\tau)} \{F(\tau)\} d\tau \quad (10)$$

This representation can be cast in discretized form as

$$\{U_{i+1}\} = e^{[\alpha]T} \{U_i\} + \int_{t_i}^{t_{i+1}} e^{[\alpha](t_{i+1}-t)} \{F(t)\} dt \quad (11)$$

where  $\{U_i\} \equiv \{U(t_i)\}$  and  $T = t_{i+1} - t_i$  (12)

The force vector in eq. (11) can be either treated as (i) constant within a small time increment  $T$  or (ii) a linear function of time. Clearly, the linear representation would result in more accuracy for a given increment  $T$ . An assumption of a step load (constant load within an increment) allows equation (11) to be written in the simple form

$$\{U_{i+1}\} = [\Phi(T)] \{U_i\} + ([\Phi(T)] - [I]) [\alpha]^{-1} \{F_i\} \quad (13)$$

where  $[\Phi(T)] = e^{[\alpha]T}$ ,  $\{F_i\} = \{F(t_i)\}$  (14)

$$e^{[\alpha]T} = \sum_{n=0}^{\infty} \frac{T^n}{n!} [\alpha]^n \quad (15)$$

so that  $([\Phi(T)] - I) [\alpha]^{-1} = T \left[ [I] + \sum_{n=1}^{\infty} \frac{T^n}{(n+1)!} [\alpha]^n \right]$  (16)

Both expressions in (15) and (16) converge very rapidly for small increment,  $T$ , and when used as above (constant  $[\alpha]$ ), need only be

calculated once for the entire time response history of the coupled rotor/housing system.

A more efficient algorithm can be constructed by representing the coupling forces as linear functions of time within each increment T, or

$$\{F(t)\} = \{F_i\} + \frac{t - t_i}{T} (\{F_{i+1}\} - \{F_i\}) \quad (17)$$

Using this representation, the solution (11) may take the form

$$\begin{aligned} \{U_{i+1}\} = & [\Phi]\{U_i\} + ([\Phi] - [I] [\alpha^{-1}]) \left\{ \{F_i\} + [\alpha^{-1}] \frac{\{F_{i+1}\} - \{F_i\}}{T} \right\} \\ & - [\alpha^{-1}] [\{F_{i+1}\} - \{F_i\}] \end{aligned} \quad (18)$$

An incremental solution using equation (18) for the Rotor and a similar matrix equation for the housing, along with equations (5) and (6) in first order form, can be employed to construct the response time history of the turbopump considered. The particular recurrence procedure used will depend on the type of transient response sought as well as on the accuracy versus computational time tradeoffs. Some discussion of the computational procedure is presented in a later section.

#### Use of the Convolution Integral

An efficient incremental representation of the housing displacements can be achieved using the convolution integral. As with the transition matrix formulation, the coupling forces are treated as external loads on the housing and may be assumed linear in time for every increment T. The response at any time t is given for zero initial conditions, using equation (1), as

$$\{W_H\} = [A_{HC}] \int_0^t \left[ \frac{1}{\omega_d} e^{-\xi_n \omega_n (t-\tau)} \sin \omega_d (t-\tau) \right] [A_{HC}]^T \{F_H(\tau)\} d\tau \quad (19)$$

where  $\omega_d$  is the damped natural frequency of the nth mode.

To enhance the accuracy of the modal representation of the housing, the deleted higher housing modes can be approximately accounted

for through the residual flexibility corresponding to these modes, or at any time  $t$ ,

$$\{W_H\} = [A_{HC}] \{q_H\} + [G_H] \{F_H\} , \quad (20)$$

where  $[G_H]$  is the residual flexibility matrix corresponding to the coupling points on the housing's  $n$ th mode of the uncoupled housing.

For the purpose of demonstrating the method in simpler terms, consider the generalized housing coordinate of the undamped  $n$ th mode

$$q_n(t) = \frac{1}{\omega_n} \int_0^t \sin \omega_n(t-\tau) P_n(\tau) d\tau \quad (21)$$

where  $P_n(\tau)$  is the unknown modal coupling force. If the force is assumed linear in time within each increment, the generalized displacement in equation (21) due to a coupling force applied between  $t_i$  and  $t_{i+1}$  is given by

$$q_n(t) = \frac{1}{\omega_n} \int_{t_i}^{t_{i+1}} \left( P_n(t_i) + \frac{\tau-t_i}{T} (P_n(t_{i+1}) - P_n(t_i)) \right) \sin \omega_n(t-\tau) d\tau \quad (22)$$

After some manipulation, the integration in equation (22) can be written in closed form in terms of the unknowns  $P_n$ 's as

$$\begin{aligned} q_n(t) = & \frac{1}{\omega_n} \left\{ \cos \omega_n t (P_n(t_{i+1}) \cos \omega_n t_{i+1} - P_n(t_i) \cos \omega_n t_i) \right. \\ & - \frac{P_n(t_{i+1}) - P_n(t_i)}{\omega_n} (\sin \omega_n t_{i+1} - \sin \omega_n t_i) \\ & + \sin \omega_n t (P_n(t_{i+1}) \sin \omega_n t_{i+1} - P_n(t_i) \sin \omega_n t_i) \\ & \left. + \frac{P_n(t_{i+1}) - P_n(t_i)}{\omega_n} (\cos \omega_n t_{i+1} - \cos \omega_n t_i) \right\} \quad (23) \end{aligned}$$

$$\text{or } q_n(t) = \frac{1}{\omega_n} \{A^{(i)} \cos \omega_n t + B^{(i)} \sin \omega_n t\} \quad (24)$$

The total response at time  $t$  due to the contribution of the coupling forces from zero to time  $t = N.T.$  is

$$q_n(t) = \frac{1}{\omega_n} \left[ \cos \omega_n NT \sum_{i=0}^N A_i^{(i)} + \sin \omega_n NT \sum_{i=0}^N B_i^{(i)} \right] \quad (25)$$

The generalized velocity can be expressed as

$$\dot{q}_n(t) = \frac{1}{\omega_n} \left[ \cos \omega_n N.T \sum_{i=0}^N B_i^{(i)} - \sin \omega_n N.T \sum_{i=0}^N A_i^{(i)} \right] \quad (26)$$

The generalized displacements and velocities of the rotor in incremental form are given previously in the form of equation (18). Equations (18), (26), (5) and (6) can be readily employed to calculate the response time history for the coupled rotor/housing system.

### Computational Procedures and Results

Various alternative procedures have been explored for the efficient implementation of the integral formulations based on the transition matrices and the convolution integral. Although studies are continuing to fully make use of the computational advantages offered by these formulations, the following appears to be the most attractive to date.

For both the transition and convolution methods, a linearized representation of the coupling forces (including those at the bearing deadband) are utilized. Equations of the form of (18), (25) and (26) are used along with the coupling forces relations given by (5) and (6). If the rotor system is linear, the forces are expressed in terms of the displacements at the coupling points. The system is then represented by a simultaneous system of equations involving the housing and rotor coupling coordinates so that at each increment of time

$$\{W_{t_{i+1}}\} = \{f(W_{t_i}, F_{t_i})\} \quad (27)$$



where  $f$  stands for a function.

Another alternative which proves to be very effective specially in presence of the bearing deadband nonlinearity is by again using a linear force within each time increment, but including an iterative procedure at each time step. The iteration work as follows:

The coupling forces at time  $t_{i+1}$  are predicted as follows:

Predict the response at the coupling point as

$$W_{t_{i+1}} = f (W_{t_i}, F_{t_i}) \quad (28)$$

Then predict the forces at  $t_{i+1}$  from

$$F_{t_{i+1}} = f' (W_{H_{i+1}}, W_{R_{i+1}}) \quad (29)$$

Finally, reiterate to get the displacement at  $t_{i+1}$  as

$$W_{t_{i+1}} = f'' (W_{H_i}, W_{R_i}, F_{t_{i+1}}) \quad (30)$$

Convergence to acceptable accuracy occurs rapidly.

The efficiency of the convolution formulation can be greatly enhanced by utilizing a Taylor series expansion for the displacements at time  $t_{i+1}$  in terms of the displacements and their derivatives at  $t_i$ , or

$$\begin{aligned} W_{t_{i+1}} = & W_{t_i} + \overset{\circ}{W}_{t_i} (t_{i+1} - t_i) \\ & + \frac{1}{2} \overset{\circ\circ}{W}_{t_i} (t_{i+1} - t_i)^2 \end{aligned} \quad (31)$$

For linearized coupling force representation involving both  $F_{t_i}$  and  $F_{t_{i+1}}$ , the force  $F_{t_{i+1}}$  is predicted using the above expression. The resulting value is entered in the right-hand side of the current convolution expression for  $W_{t_{i+1}}$ . This method is found to be very effective when applied to structural models. It is yet to be applied, along with a transition matrix representation to a rotor system.

Both the step force (eq. 16) and linear force (eq. 18) formulations using the transition matrices of the separate rotor and housing were applied to the HPOTP. the computational procedure represented by equations (28), (29) and (30) proved most effective.

### NUMERICAL HARMONIC BALANCE METHOD

A method is developed [16] in order to check all possible nonlinear responses of simple rotor systems under periodic imbalance load in presence of bearing clearances, rubbing, seal forces, side forces and others. The method requires the spinning speed of the rotor to be constant so that the model is represented by an autonomous system of nonlinear equations. The developed method is a modification of that due to Yamauchi [17]. The method is being extended to more general rotor systems with local nonlinearities.

The procedure developed in [16] is based on a numerical harmonic balance method using an FFT algorithm. The modified method presented here uses discrete Fourier transformation and its inverse. This transformation, rather than an FFT procedure was utilized in order to reduce computational time and errors. This is achieved by calculating the complex exponential values at the beginning of computation and then store them in active memory for subsequent calculations. A brief account of the method and some results obtained for the response of the modified Jeffcott rotor system selected for the analysis is outlined in what follows. The details of the method and the results are given in [16].

#### The Rotor Model

A horizontal Jeffcott rotor of constant spinning speed  $\omega$ , is whirling around its axis under an imbalance force. The rotor bearings have deadband clearance  $\delta$  with their support. The equations of motion of the rotor relative to the inertial frame Y-Z can be written as

$$\ddot{M}y + C_{sy} \dot{y} + K_{sy} y + Q_{sz} z + K_b \left( y - y \frac{\delta}{\sqrt{y^2 + z^2}} \right) \quad (32a)$$

$$- \mu K_b \left( z - z \frac{\delta}{\sqrt{y^2 + z^2}} \right) = M e \omega^2 \cos \omega t + Mg$$

$$\begin{aligned} \ddot{Mz} + C_s \dot{z} + K_s z - Q_s y + K_b \left( z - z \frac{\delta}{\sqrt{y^2 + z^2}} \right) , & \quad (32b) \\ + \mu K_b \left( y - y \frac{\delta}{\sqrt{y^2 + z^2}} \right) = M e \omega^2 \sin \omega t & \end{aligned}$$

where the bearing forces, associated with  $K_b$ , vanish whenever

$$\sqrt{y^2 + z^2} < \delta$$

in which  $M$  and  $K_b$  are the mass of the disk and the bearings' stiffness (including that of the shaft) respectively so that  $Mg$  is the weight of the rotor in the negative  $Y$  direction. The seal's direct and cross coupling stiffnesses are denoted by  $K_s$  and  $Q_s$ , respectively. The coefficient of friction due to rub at the bearing is  $\mu$  and the rotor mass eccentricity is  $e$ , as measured from the disk center.

The equations are cast in nondimensional form using the deadband  $\delta$  as the reference displacement and the natural frequency of the undamped system with " $\delta=0$ " as the reference frequency, so that

$$Y = \frac{y}{\delta} , \quad Z = \frac{z}{\delta} , \quad \Omega = \frac{\omega}{\omega_n} \quad (33)$$

The time is nondimensionalized by the scaling factor  $\nu$ , to read

$$\nu \theta = \omega t \quad (34)$$

so that  $\nu$  is the subharmonic order sought.

### The Steady State Solutions

The steady periodic solution of the nondimensional form of Eq. (32) (see ref. [16]), including any subharmonic, superharmonic and harmonic vibration can be written as the Fourier series

$$Y(\theta) = a_{y0} + 2 \sum_{n=1}^N (a_{yn} \cos n\theta - b_{yn} \sin n\theta) \quad (35a)$$

$$Z(\theta) = a_{z0} + 2 \sum_{n=1}^N (a_{zn} \cos n\theta - b_{zn} \sin n\theta) \quad (35b)$$

where  $N$  is the number of harmonics to be taken into account under the assumption of small frequency bandwidth in the final solution. In the same way, the time series representation of the nonlinear bearing force, which occurs only when the deadband is closed, can be expressed as Fourier series of the form.

$$G(\theta) = c_{y0} + 2 \sum_{n=1}^N (c_{yn} \cos n\theta - d_{yn} \sin n\theta) \quad (36a)$$

$$F(\theta) = c_{z0} + 2 \sum_{n=1}^N (c_{zn} \cos n\theta - d_{zn} \sin n\theta) \quad (36b)$$

Since these nonlinear bearing forces are consequence of the existence of a deadband in the system. The Fourier coefficients of nonlinear restoring forces are the function of the Fourier coefficients of steady periodic solution. Substituting Eq. (35), and Eq. (36) into the nondimensionalized equations corresponding to equation (32) and applying a harmonic balance procedure yields  $4N + 2$  nonlinear simultaneous equations, involving  $8N + 4$  unknowns.

Another set of  $4n + 2$  equations will have the relationship between the Fourier coefficients of nonlinear bearing forces and those of steady-state periodic solution. This relationship can be found by determining  $Y(\theta)$ ,  $Z(\theta)$  from the Fourier coefficients of steady state periodic solution using the discrete inverse Fourier transformation

$$x_r = \text{Real} \left( \sum_{k=0}^{N-1} X_k e^{i(2\pi kr/n)} \right) \quad (37)$$

Using the expression for the nonlinear bearing force, its discrete time series can be found. The inverse discrete Fourier transformation of the time series solution for the nonlinear bearing forces can yield their Fourier coefficients. The resulting nonlinear simultaneous equations can be handled using a Newton-Raphson iteration method by which an incremental procedure is used to determine the value of the next iteration as follows. Let

$$S = S^0 + \Delta S \quad , \quad (38)$$

where  $S$  represents all the Fourier coefficients of the steady state solution, and the superscript  $^o$  denotes current state and  $\Delta S$  stands for their increments during one step iteration. Similarly, the Fourier coefficients of the nonlinear restoring force terms are expressed as

$$B = B^o + \Delta B \quad (39)$$

so that

$$\Delta B = \sum_{n=1}^{4N+2} \frac{\partial B^o}{\partial S_n} \Delta S_n \quad (40)$$

in which the partial derivatives are to be calculated at the current state value. In order to account for the large nonlinearity in the system, the increments,  $\Delta S_n$ , must be chosen comparatively smaller than  $S_n$  whenever numerical differentiation is performed.

Plugging Eq. (38), Eq. (39), and Eq. (40) into the relationships obtained involving the coefficients  $a_n$ ,  $b_n$ ,  $c_n$  and  $a^o$ ,  $b^o$ ,  $c^o$  results in

$$[K] \{\Delta x\} = \{R\} \quad (41)$$

where  $[K]$  corresponds to the Jacobian matrix whose elements are calculated at every step. this iteration is continued until all the components of the correction vector  $\{R\}$  become sufficiently close to zero.

#### The Harmonic Balance Numerical Results

The frequency response results using the numerical harmonic balance procedure demonstrate good agreement with those of the direct numerical integration method [16]. As an example, a comparison between the subharmonic and harmonic motions in the Y-Z plane can be made from the results presented in Fig. 2. The radius of the shaft center traces circular paths in a harmonic response case or otherwise has the more complicated shapes and possibly a larger radius, a less desirable behavior in rotating machinery.

The existence of second-order subharmonic resonances are probed for various values of the nondimensionalized side force factor  $\phi = g/\omega_n^2 \delta$  (Fig. 3). The figure shows subharmonic vibration not to exist for  $n$  either zero or comparatively large  $\phi$  values. This is so since only symmetric motion is maintained in these cases. Fig. 3 also shows that a smaller  $\phi$  value results in subharmonic response within a broader frequency range. The choice of a smaller clearance or a

softer bearing stiffness can therefore reduce the possibility of a damaging resonance.

#### USE OF COMPONENT MODE METHODS

A modified fixed-interface component mode procedure of Glasgow and Nelson [18] was applied to a generic rotor system with flexible casing. The multi-rotor considered is assumed to be coupled to its housing through bearings. A clearance is assumed to exist in one of the bearings. The modified analysis procedure is done as follows. The rotor and housing are coupled at their connection points (bearings) except at the bearing with deadband.

The eigen parameters of the coupled system are obtained with the rotor and housing fixed at the location of the deadband. The coupled system is then represented by a truncated set of these modes plus a static constrained mode [18] corresponding to the degrees of freedom at the location of bearing clearance.

The fixed-interface component method as applied here proved to be more accurate for the same total combined number of dynamic and static modes of the system. This is so since the method as modified above allows including more numbers of dynamic coordinates of the case and rotor in the analysis. The modified method becomes more efficient in cases where interaction forces occur at relatively large numbers of locations between the rotor and housing.

The modified approach would allow first coupling the housing and rotor using more numbers of modes than currently being used, then reduce the number of modes of the resulting coupled system.

#### DISCUSSION AND RECOMMENDATIONS

1. Hybrid component representation and numerical incremental procedures for the transient response analysis of complex rotor systems can lead to more efficient methods.
2. The explicit integration methods based on the transition matrices and convolution can be very effective in determining the transient response of large flexible rotor/housing systems such as the SSME turbopumps. The methods are particularly efficient in cases concerning constant spinning rotor speeds and in presence of bearing deadband clearances. More work is, however, still needed to exploit and further develop the methods to their fullest potential.

3. A modified fixed-interference component mode method could be used to construct a reduced size rotor/housing system which is more accurate than that of the original method [18]. The modification concerns the use of smaller number of connection points as the fixed interfaces of the system. Similarly, the hybrid coupling method of McNeal [19] could be extended for application to rotor systems.
4. A numerical harmonic balance method using discrete Fourier Transformation is developed and applied to a modified Jeffcott model including bearing clearances, seal cross coupling forces, a side force and friction due to rubbing. The method can be used to determine all possible steady state solutions for the rotor. The method can be extended to larger rotor systems, taking advantage of the nonlinearities involved being localized. Application of the method will ensure that no potentially damaging periodic nonlinear response of a given rotor will be missed solely depending on numerical integration methods. Arbitrarily selected initial conditions may not necessarily lead to a possible periodic solution using integration techniques.

#### Acknowledgement

This work is being carried out under support of NASA-Marshall Space Flight Center under contract No. NAS8-36182. This support is gratefully acknowledged.

## REFERENCES

1. Childs, D. W., "Transient Rotordynamic Analysis for the Space-Shuttle Main Engine High Pressure Oxygen Turbopump," J. Spacecraft, Vol. 12, No. 1 (1975), pp. 3-4.
2. Childs, D. W. and Moyer, D. S., "Vibration Characteristics of the HPOTP (High Pressure Oxygen Turbopump) of the SSME (Space Shuttle Main Engine), ASME Paper No. 84-GT-31, International Gas Turbine Conference, Amsterdam, Netherlands, June 1984.
3. Childs, D. W., "Two Jeffcott-Based Modal Simulation Models for Flexible Rotating Equipment," ASME J. Engineering for Industry, Vol. 97, No. 3 (1975), pp. 1000-1014.
4. Rouch, K. E. and Kao, J. S., "Dynamic Reduction in Rotor Dynamics by the Finite Element Method, ASME J. of Mechanical Design, Vol. 102, pp. 360-368.
5. Nordmann, R., "Eigenvalues and Resonance Frequency Forms of Turborotors with Sleeve Bearings Crank Excitation, External and Internal Damping," Machine Dynamics Group, Technical University Darmstadt, West Germany, June, 1975.
6. Childs, D. W., "The Space Shuttle Main Engine High-Pressure Fuel Turbopump-Rotordynamic Instability Problem," ASME J. Engineering for Power, Vol. 100, 1978, pp. 48-51.
7. Nelson, H. D., Meacham, W. L., Fleming, D. P. and Kascak, A. F., "Nonlinear Analysis of Rotor Bearing Systems Using Component Mode Synthesis," ASME Paper No. 82-GT-303, 1982.
8. Adams, M. L., "Non-Linear Dynamics of Flexible Multi-Bearing Rotors," J. Sound and Vibration, Vol. 71 (1980), pp. 129-144.
9. Meirovitch, L., computational Methods in Structural Dynamics, Sijthoff and Noordhoff, 1980.
10. Von Pragenau, G. L., "Large Step Integration for Linear Dynamic Systems," Conference Proc. IEEE Southeastcon '81, reprint, April 1981.
11. Kubomura, K., "Transient Loads Analysis by Dynamic Condensation," ASME, J. Applied Mechanics, Vol. 52 (1985), pp. 559-564.
12. Tongue, B. H. and Dowell, E. H., "Component Mode Analysis of Nonlinear, Nonconservative Systems," ASME J. Appl. Mechanics, Vol. 50, 1983, pp. 204-209.



13. Clough, R. W. and Wilson, E. L., "Dynamic Analysis of Large Structural Systems with Local Nonlinearities," Computer Methods in Applied Mechanics and Engineering, Vol. 17/18 (1979), 107-129.
14. Childs, D. W., "Rotordynamics Analysis for the HPOTP of the SSME," Interim Progress Report for NASA Contract NAS8-31233, The University of Louisville/Speed Scientific School, Sept. 1979.
15. Noah, S. T., "Rotordynamic Analysis of the SSME Turbopumps Using Reduced Models," Final Report, NASA Contract NAS8-34505, Texas A&M University, Sept. 1984.
16. Choi, Y.-S. and Noah, S. T., "Nonlinear Steady-State Response of a Rotor-Support System," Submitted to the ASME J. of Vibration, Stress, Acoustics and Reliability in Design, April 1986.
17. Yamauchi, S., "The Nonlinear Vibration of Flexible Rotors, 1st Report Development of a New Analysis Technique," Trans JSME, Vol. 49, No. 446, Series C Oct. 1983, pp. 1862-1868.
18. Glasgow, D. A., and Nelson, H. D., "Stability Analysis of Rotor-Bearing Systems Using Component Mode Synthesis," ASME J. of Mechanical Design, Vol. 102, No. 2, April 1980, pp. 352-359.
19. MacNeal, R. H., "A Hybrid Method of Component Mode Synthesis," Computers and Structures, Vol. 1, 1971, pp. 581-601.

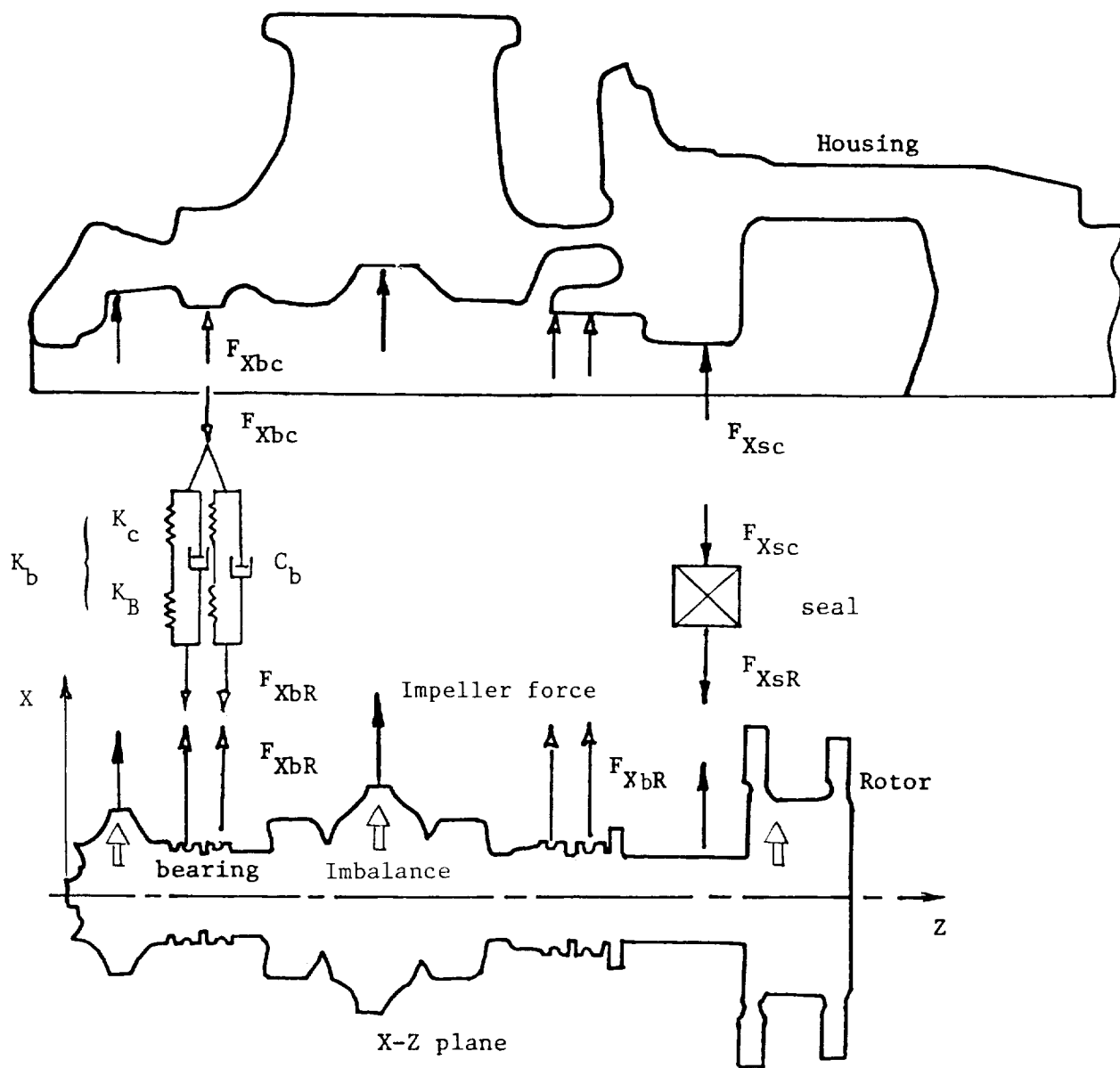


Figure 1. Coupling elements and forces in the HPOTP.

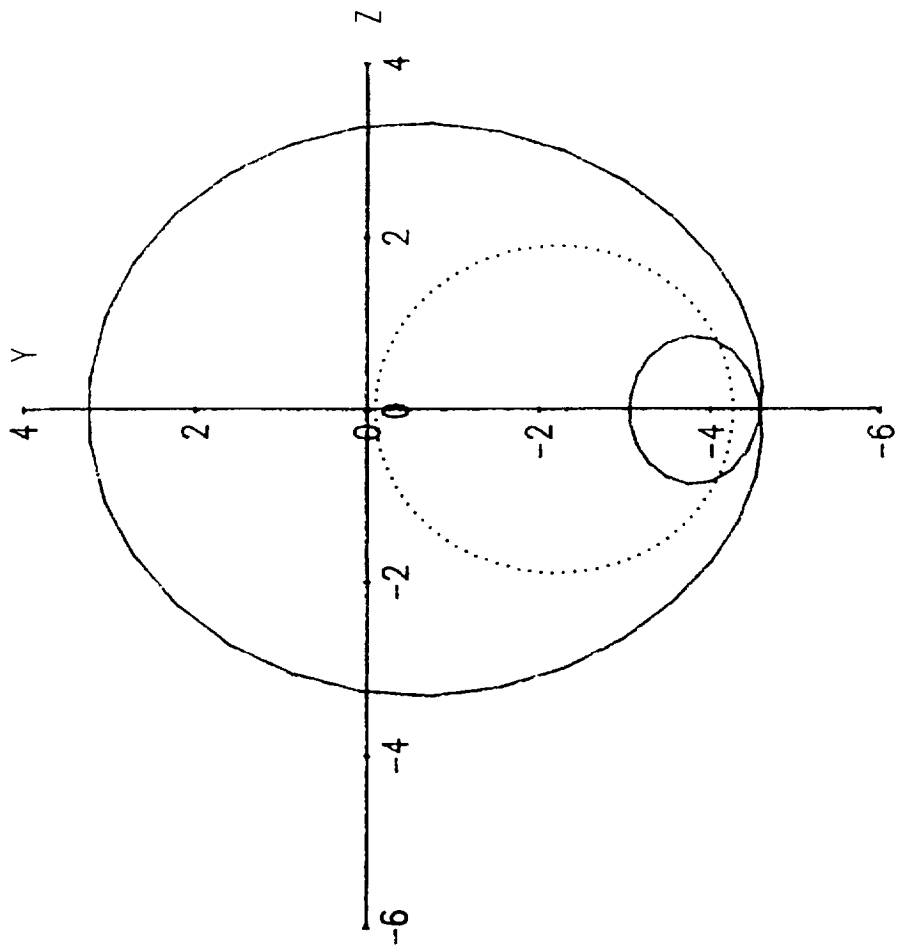


Fig. 2 2nd-Subharmonic and Harmonic Respos

.....: Harmonic Response

—: Subharmonic Response

$\Omega=1.7$

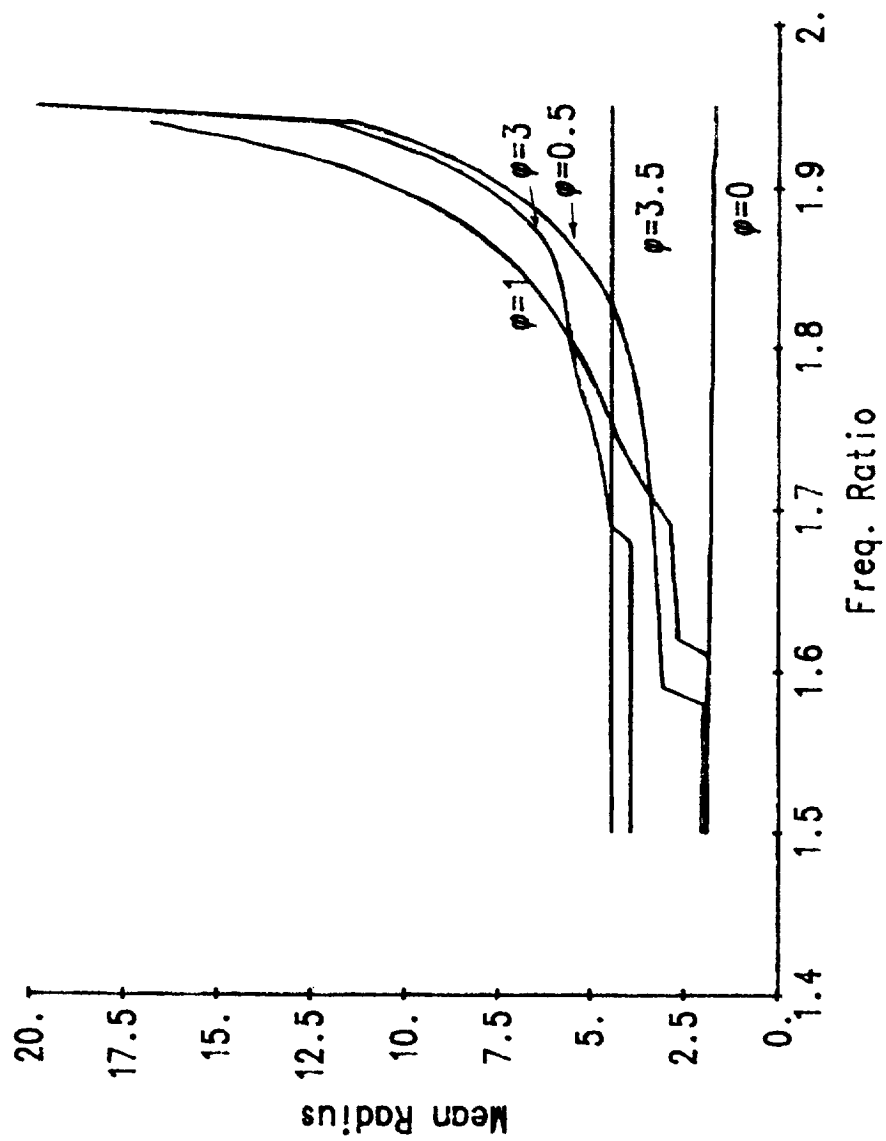


Fig. 3 The effect of the Side Force

Vibrations Induced by  
Nonlinearities in Rotordynamics.

by

William B. Day

Associate Professor of  
Computer Science & Engineering  
Auburn University, AL 36849

This work has been supported by NASA MSFC under Contracts NAS8 - 35992  
and NAS8 - 36475.



ABSTRACT

This paper is an examination of special nonlinearities of the Jeffcott equations in rotordynamics. The immediate application of this analysis is directed toward understanding the excessive vibrations recorded in the LOX pump of the SSME during hot firing ground testing.

Deadband, side force and rubbing are three possible sources of inducing nonlinearity in the Jeffcott equations. The present analysis initially reduces these problems to the same mathematical description. A special frequency, named the nonlinear natural frequency, is defined and used to develop the solutions of the nonlinear Jeffcott equations as singular asymptotic expansions. This nonlinear natural frequency, which is the ratio of the cross-stiffness and the damping, plays a major role in determining response frequencies.

Numerical solutions are included for comparison with the analysis. Also nonlinear frequency-response tables are made for a typical range of values.

## 1. INTRODUCTION

Vibrations are inherent in rotating machinery. Mathematical explanations of vibrations began with Jeffcott's description of the shaft's natural frequency of lateral vibration [6]. Unfortunately, Jeffcott's linear model cannot account for all frequencies that have been observed experimentally. In particular, destructive vibrations have occurred in hot firing ground testing of the LOX pump of the SSME with no clue to these vibrations' origins being offered by the linear model. Specifically, examination of the power spectral density (PSD) plots reveals unaccountable frequencies. Consequently, numerous investigations have been undertaken to study such rotors and to provide descriptions of the solutions of the two, coupled, second-order differential equations which describe the motion of the rotor's center of mass. Following the early work in rotordynamics by Yomamoto [8], one introduces a nonlinearity to the Jeffcott equations by including the effect of bearing clearance or deadband. In the pump, this deadband refers to the load carriers (ball bearings) and physically describes the clearance between the outer race of the bearing and the support housing. The work of Yomamoto did not include cross-stiffness, but a straight-forward derivation with this modification is easily obtained. A more limiting gap in his work is the assumption that the response is simply a perturbation of the forcing function. This is tantamount to assuming that one always has the graph of a circle as the solution. It is shown in this paper that this generally is not the case. Both empirical results by Childs [1, 2] and Gupta et al. [5] and numerical solutions using the fourth order Runge-Kutta algorithm by Control Dynamics Company [3] have been helpful in understanding the rotor's motion for the nonlinear problem. This paper extends the earlier work by using analytic expressions

obtained from singular asymptotic expansions (method of multiple scales) to quantize the solution.

The primary objective of this paper is to describe analytically solutions of the nonlinear Jeffcott equations with deadband (or an equivalent variation such as rubbing). To this end emphasis is placed on determining which frequencies one expects from the nonlinear problem, how these frequencies are related to the parameters of the differential equations, and where the solutions are stable.

Section 2 presents transformations which convert the Jeffcott equations to nondimensional, complex equations. A discussion of physically related problems which are mathematically equivalent to the original equations and corresponding generalizations are included herein.

Section 3 begins with a heuristic explanation of the nonlinear natural frequency. A mathematical derivation of a lower bound for this frequency follows.

Section 4 contains the formal asymptotic expansion of the solution of the Jeffcott equations. A numerical example is discussed vis-a-vis the derived analytic expressions.

Section 5 contains a theorem and related numerical results which show how one can predict whether the solution's geometry is a circle or an annulus.

Section 6 concludes this paper with some remarks on the boundedness and stability of the Jeffcott solutions. Numerical examples illustrate these results.



## 2. NONDIMENSIONALIZATIONS AND GENERALIZATIONS

The linear Jeffcott equations which describe the displacement of the rotor center from its equilibrium position in the inertial, Cartesian coordinate system  $(y,z)$  (each in meters) are these:

$$(1.) \quad m\ddot{y} = -C_s \dot{y} - K_s y - Q_s z + m\omega^2 \cos\omega t$$

$$(2.) \quad m\ddot{z} = -C_s \dot{z} + Q_s y - K_s z + m\omega^2 \sin\omega t$$

where the shaft of the rotor lies along the x-axis and

$m$  = mass (kg.)

$C_s$  = seal damping (kg./s.)

$K_s$  = seal stiffness (kg./s.<sup>2</sup>)

$Q_s$  = cross-coupling stiffness of seal (kg./s.<sup>2</sup>)

$u$  = displacement of the shaft center of mass from the geometric center (m.)

$\omega$  = angular velocity of the shaft (rad./s.)

For the model to include bearing forces which hold the rotor in position, one adds the terms

$$-K_B (y - y\delta / \sqrt{y^2 + z^2}) + \mu K_B (z - z\delta / \sqrt{y^2 + z^2})$$

and

$$-\mu K_B (y - y\delta / \sqrt{y^2 + z^2}) - K_B (z - z\delta / \sqrt{y^2 + z^2}),$$

respectively, to the right-hand sides of equations (1.) and (2.).

Here

$K_B$  = bearing stiffness (kg./s.<sup>2</sup>)

$\delta$  = clearance or deadband between housing and bearing (m.)

$\mu$  = coefficient of friction between housing and bearing (none).

These bearing forces occur only when  $\sqrt{y^2 + z^2} > \delta$ ; otherwise, they are zero.

Since  $\mu$  is nondimensional and typically small, one may regard it as zero without affecting the qualitative results.

Equations (1.) - (2.) then become

$$(3.) \quad \ddot{y} + (C_S/m)\dot{y} + (1/m)[K_S + K_B (1 - \delta/r)] y + (Q_S/m)z = u\omega^2 \cos \omega t$$

$$(4.) \quad \ddot{z} + (C_S/m)\dot{z} - (Q_S/m)y + (1/m)[K_S + K_B (1 - \delta/r)]z = u\omega^2 \sin \omega t$$

when  $r = \sqrt{y^2 + z^2} > \delta$ ; otherwise,  $K_B = 0$ . Equations (3.) - (4.) can be put in nondimensional form using a displacement  $g$  and a frequency  $\sigma$ . One pair of candidates for  $g$  and  $\sigma$  would be  $g = u$ , the deadband size, and  $\sigma^2 = \omega_0^2 = K_S + K_B$ , the natural frequency of the corresponding linear problem ( $\delta = 0$ ). Thus, using  $Y = y/g$ ,  $Z = z/g$ , and  $\tau = \sigma t$ , the dimensionless equations are these:

$$(5.) \quad Y'' + CY' + [A + k(1 - \Delta/R)] Y + BZ = E\phi^2 \cos \phi \tau$$

$$(6.) \quad Z'' + CZ' - BY + [A + k(1 - \Delta/R)] Z = E\phi^2 \sin \phi \tau$$

where prime denotes differentiation with respect to  $\tau$  and  $C = C_S/m/\sigma$ ,  $A = K_S/m/\sigma^2$ ,  $k = K_B/m/\sigma^2$ ,  $B = Q_S/m/\sigma^2$ ,  $\Delta = \delta/g$ ,  $R = r/g$ ,  $E = u/g$ , and  $\phi = \omega/\sigma$ .

Equations (5.) - (6.) can be reduced to the following single equation by defining  $W = Y + iZ$ ;

$$(7.) \quad W'' + CW' + \{A + k(1 - \Delta/|W|) - iB\} W = E\phi^2 \exp(i\phi \tau).$$

A generalization of equation (7.) is

$$(8.) \quad W'' + CW' + AW + K(1 - \Delta/|W|)W = \sum_{n=1}^L F_n(\phi_n) \exp(i\phi_n \tau)$$

where  $C$ ,  $A$ , and  $K$  are complex constants and where the nonlinear left-hand side of equation (8.) is being driven on the right-hand side by multiple forces. The following are special cases of physical interest:

- a. Forcing function is mass imbalance. This is the case derived in equation (7.) and is obtained from equation (8.) with  $N=1$  and  $F_1(\phi_1) = E\phi_1^2$ .

b. Forcing function is side force. This force may be introduced into the Jeffcott equations (1.) - (2.) as a constant replacement for the mass imbalance. In such cases, equation (7.) becomes

$$W'' + CW' + \{A + k(1 - \Delta/|W|)\} W = \text{constant.}$$

Thus, a side force is the special case of equation (8.) with  $N = 1$ ,  $F_1(\phi_1) = \text{constant}$ , and  $\phi_1 = 0$ .

c. Forcing function is rubbing. Contact between a rotor and its housing produces a Coulomb damping force. This force would modify the original Jeffcott equations by the addition of the terms:

$$K_{st}(1 - \delta/r)y - \mu K_{st}(1 - \delta/r)z + K_{st}(1 - \delta/r)G$$

$$\text{and } \mu K_{st}(1 - \delta/r)y + K_{st}(1 - \delta/r)z + \mu K_{st}(1 - \delta/r)G$$

respectively, to the right-hand sides of equations (1.) - (2.).

Here,  $G = \text{constant} = \text{stator offset in the } y - \text{direction}$ ,  $K_{st} = \text{stator stiffness}$  and  $\mu = \text{coefficient of friction}$ , which may not be small. As before these forces would be included only when  $r = (y^2 + z^2)^{\frac{1}{2}} > \delta$ . On replacing  $y - G$  by  $y$ , equation (7.) (and correspondingly its equivalent forms) again occurs but with these modifications:

1.  $i[-B]$  is replaced by  $i[-B + \mu(K_{st}/g^2)(1 - \Delta/R)]$

2. the forcing function  $E\phi^2 \exp(i\phi\tau)$  is replaced by

$$E\phi^2 \exp(i\phi\tau) + (-\omega_0^2 / g^2)(G/\delta).$$

Thus, rubbing is equivalent to having two forcing functions in equation (8.) where  $N = 2$ ,  $F_1(\phi_1) = E\phi_1^2$ ,  $F(\phi_2) = \text{constant}$ , and  $\phi_2 = 0$ .

d. Any combination of mass imbalance, side force, and rubbing.

Initially, attention is restricted to equation (7.); i.e., equation (8.) with  $N = 1$ . It will be seen later that in a first approximation, the more complicated cases of  $N > 1$  can be solved as a superposition of the individual responses which are found using equation (7.).

### 3. NONLINEAR NATURAL FREQUENCY

Consider the dimensional, homogeneous ( $E = 0$ ) equation corresponding to equation (7):

$$(7!) \quad \ddot{w} + (C_s/m)\dot{w} + (1/m) \{[K_s + K_B (1 - \delta/r) - iQ_s]\} w = 0,$$

where  $w = y+iz$ . If this equation were also linear ( $\delta = 0$ ), then exponentially growing or decaying solutions would generally result for a given set of system parameters. In the special case that  $(Q_s/C_s)^2 = K_s + K_B$ , a sinusoidal solution is obtained with frequency  $\beta_0 = Q_s/C_s$ . To see this, consider the characteristic equation for  $w = \exp(pt)$ :

$$\begin{aligned} p^2 + C_s p + [K_s + K_B - iQ_s] &= 0 \\ p &= -C_s/2 \pm \{C_s^2/4 - K_s - K_B + iQ_s\}^{1/2} \\ &= -C_s/2 \pm \{C_s^2/4 - (Q_s/C_s) + iQ_s\}^{1/2} \\ &= -C_s/2 + i\{iC_s/2 - Q_s/C_s\} \\ &= -C_s - iQ_s/C_s, iQ_s/C_s. \end{aligned}$$

In the nonlinear, homogeneous problem,  $K_B$  is replaced by  $K_B(1 - \delta/r)$ ; hence, if  $r$  is a constant, then there is a wide spectrum of  $r$  for which  $(Q_s/C_s)^2$  may be  $K_s + K_B(1 - \delta/r)$ ; i.e., if

$$(9.) \quad K_s < (Q_s/C_s)^2 <= K_s + K_B,$$

then there is a constant value of  $r$  (with  $r > \delta$ ) for which  $(Q_s/C_s)^2 = K_s + K_B(1 - \delta/r)$ . This value of  $r$  is denoted by  $a$  and the corresponding frequency by  $\beta_0 = Q_s/C_s$ . This frequency is labeled the nonlinear natural frequency. Thus, whenever inequality (9.) is satisfied, equations (3.) - (4.) with  $u=0$  have steady-state solutions  $y = a \cos(\beta_0 t)$  and  $z = a \sin(\beta_0 t)$ .

Notice that  $\beta_0 = Q_s/C_s <= (K_s + K_B)^{1/2} = \omega_0$ , the dimensional natural frequency of the linear system. Thus, in considering the general nonhomogeneous problem, it is necessary to be aware of these three

dimensional frequencies:

$\beta_0$  - the nonlinear natural frequency,

$\omega_0$  - the natural frequency,

$\omega$  - the driving frequency.

It will be shown in the next section that the nonlinear frequency  $\beta$  which may appear in a stable solution of the non-homogeneous version of equation (8.) always lies between  $\beta_0$  and  $\omega_0$ .

One final rearrangement of equation (7.) is made here to emphasize the nonlinear natural frequency:

$$(10.) \quad W'' + CW' + \kappa W = \epsilon f(W) + E\phi^2 \exp(i\phi\tau)$$

where  $\kappa = A + k(1 - \Delta/a) - iB$  and  $f(W) = k\Delta [1/|W| - 1/a]W/\epsilon$ .

#### 4. METHOD OF MULTIPLE SCALES.

This section deals with formal, singular asymptotic expansions of the Jeffcott equations as written in equation (10). A straight-forward asymptotic expansion is not general enough for this problem since it always leads to a zero-order approximation of the form:

$$W = M \exp(i\beta_0\tau) + N \exp(i\phi\tau).$$

Typical singular asymptotic expansions suggest that one should replace  $\beta_0\tau$  by  $\beta(\tau)$  and constant  $M$  by function  $M(\tau)$ . In considering a Taylor series expansion of  $\beta(\tau)$ , one can ignore the constant term (or alternatively, assume that it is grouped with the coefficient  $M(\tau)$ ). Then the leading term of the Taylor series should be  $\beta_0\tau$ . This is what one obtains from the straight-forward expansion.

One method, the method of averaging, is appropriate for the Jeffcott equations since it begins with the assumption that

$$W = M(\tau) \exp(i\beta(\tau)) + N \exp(i\phi\tau).$$

Another method, multiple scales, is also appropriate because one can envision the action of the rotor being based on two different time scales. The results are identical for the two methods.

Instead of one time scale  $\tau$ , assume the problem depends on many time scales:

$$T_0 = \tau, T_1 = \epsilon\tau, T_2 = \epsilon^2\tau, \dots$$

Henceforth, only  $T_0$  and  $T_1$  are used. Let  $W(\tau) = W(T_0, T_1) = W_0(T_0, T_1) + \epsilon W_1(T_0, T_1) + \dots$ . Equation (10.) becomes a partial differential equation since

$$d/d\tau = (\partial/\partial T_1)(dT_1/d\tau) + (\partial/\partial T_0)(dT_0/d\tau) = D_0 + \epsilon D_1$$

$$\text{and } (d^2/d\tau^2) = (D_0 + \epsilon D_1)^2.$$

Thus, one finds

$$(11.) \quad (D_0 + \epsilon D_1)^2 (W_0 + \epsilon W_1 + \dots) + C(D_0 + \epsilon D_1) (W_0 + \epsilon W_1 + \dots) \\ + \kappa (W_0 + \epsilon W_1 + \dots) = \epsilon f(W_0 + \epsilon W_1 + \dots) + E\phi^2 \exp(i\phi T_0).$$

Equating like powers of  $\epsilon$  yields

$$(12.) \quad \epsilon^0 : D_0^2 W_0 + CD_0 W_0 + \kappa W_0 = E\phi^2 \exp(i\phi T_0).$$

This is a linear problem with this steady-state solution

$$W_0 = M \exp(i\beta_0 T_0) + N \exp(i\phi T_0)$$

where  $N = E\phi^2 / (-\phi^2 + iC\phi + \kappa)$  and  $M = M(T_1)$ . To determine  $M$  one must examine the  $\epsilon$ -order problem and choose  $M$  to eliminate secular terms; see Nayfeh [7]:

$$\epsilon^1 : D_0^2 W_1 + CW_1 + \kappa W_1 = -2D_0 D_1 W_0 - CD_1 W_0 + f(W_0).$$

With  $V = k\Delta/\epsilon$ , the right-hand side of the last equation becomes

$$-2i\beta_0 M' \exp(i\beta_0 T_0) - CM' \exp(i\beta_0 T_0) \\ + V (1/|W_0| - 1) [M \exp(i\beta_0 T_0) + N \exp(i\phi T_0)]$$

where  $|W_0| = \{|M|^2 + |N|^2 + \overline{MN} \exp[i(\phi - \beta_0) T_0] + M\overline{N} \exp[i(\beta_0 - \phi) T_0]\}^{1/2}$

To avoid secular terms one requires that the collective coefficient of  $\exp(i\beta_0 T_0)$  be zero. Although an analytic solution of the differential equation for  $M(T_1)$  has not been found, one can qualitatively assess  $M$  based on a similar problem (van der Pol's equation) and specific numerical results (presented below).

Since  $M(T_1)$  is complex, it may be written as

$$M(T_1) = \rho(T_1) \exp[i\hat{\beta}(T_1)]. \quad \text{Thus,}$$

$$W_0 = \rho(T_1) \exp[i\beta_0 T_0 + i\hat{\beta}(T_1)] + N \exp(i\phi T_0)$$

or, assuming  $\hat{\beta}(T_1)$  is analytic near  $t=0$ ,  $W_0 = \rho(T_1) \exp[i(\beta_0 + \epsilon\beta_1)\tau + \dots] + N \exp(i\phi\tau)$ . Thus the fundamental frequency of the nonlinear problem is not  $\beta_0$  but  $\beta = \beta_0 + \epsilon\beta_1 + \dots$ ; however,  $\beta$  must reduce to  $\beta_0$  when  $E\phi^2 = 0$ . Consequently, the frequency  $\gamma = \phi - \beta_0$  that appears in the



expression for  $|W_0|$  should be considered as  $\gamma = \phi - \beta$ . Then  $1/|W_0|$  shows all frequencies  $n\gamma$  and  $W_0/|W_0|$  shows all frequencies  $n\gamma \pm \beta$ , for  $n=0, 1, \dots$ . This suggests that  $M$  has a complex Fourier series of the form:

$$\sum_{n=-\infty}^{\infty} s_n \exp(in\gamma T_1).$$

Another factor of  $M$  must also be included since numerical examples show that  $M \neq 0$  if  $E\phi^2$  is greater than some fixed value. This is similar to the behavior of the van der Pol oscillator; see [V]. One possible form of  $M$  would include a factor of the form  $F = 1/[1 + \exp(-\eta T_1)]$  where  $\eta = \eta(E\phi^2)$ . This would imply that  $F \rightarrow 1$  as  $\tau \rightarrow \infty$  when  $\eta > 0$  and  $F \rightarrow 0$  as  $\tau \rightarrow \infty$  when  $\eta < 0$ . Thus,  $M$  looks like:

$$1/[1 + \exp(-\eta T_1)] \sum_{n=-\infty}^{\infty} s_n \exp(in\gamma T_1).$$

PSD plots of  $R$  show the frequencies  $n\gamma$ .

For the case of multiple forcing functions,  $\sum_{i=1}^L F_i(\phi_i) \exp(i\phi_i \tau)$ , one defines  $\gamma_i = \phi_i - \beta$ . Then the zeroth-order asymptotic approximation of the solution of equation (8.) will contain  $L$  terms to account for the  $L$  forcing frequencies,  $\phi_i$ ,  $i = 1, 2, \dots, L$ . Thus, the term  $N \exp(i\phi T_0)$  in  $W_0$  is replaced by  $N_1 \exp(i\phi_1 T_0) + \dots + N_L \exp(i\phi_L T_0)$ . The coefficient  $M$  of the nonlinear frequency  $\beta$  will now contain the Fourier factor

$$\sum_v S_v \exp(i\gamma T_1)$$

where  $\gamma = n_1 \gamma_1 + \dots + n_L \gamma_L$  and the summation is taken over the integer  $v$  from  $-\infty$  to  $+\infty$  with  $v = n_1 + \dots + n_L$ . Typical examples show significant magnitude coefficients,  $S_v$ , only for  $v = 0, +1, -1, +2, -2$ .

Figures 1 and 2 show typical numerical solutions which are obtained using Runge-Kutta fourth order on equations (1.) and (2.). The system constants used are these:  $\mu = 0$ ,  $m = 1 \text{ lb.} - \text{s.}^2/\text{in.}$ ,  $C_s = 240 \text{ lb.} - \text{s.}/\text{in.}$ ,  $K_s = 0.$ ,  $K_b = 1,305,000 \text{ lb.}/\text{in.}$ ,  $Q_s = 200,000 \text{ lb.}/\text{in.}$ ,  $\delta = .0000285 \text{ in.}$ , and  $\omega = 500 \text{ Hertz} = 1000\pi \text{ rad.}/\text{s.}$  Thus,  $\beta_0 = 833.33 \text{ rad.}/\text{s.}$  and  $a = .000060915 \text{ in.}$  The system is made nondimensional using  $a$  for the  $g$ -displacement and  $\beta_0$  for the  $\sigma$ -frequency. With these choices, the constants of this equation

$$W'' + CW' + [k(1 - \Delta/|W|) - iB]W = E\phi^2 \exp(i\phi\tau)$$

have these values:  $C = .288$ ,  $k = 1.8792$ ,  $\Delta = .467865$ ,  $B = .288$ , and  $\phi = 6\pi/5$ .

Figures 1 and 2 show changes in the solution  $Y$  vs.  $Z$  as  $E$  assumes the values  $100n/(1000\pi)^2 a$  for  $n = 0, 1, \dots, 7$ . The graphs are plotted for  $.2 < t \leq .5 \text{ s.}$  The initial circle (for  $E = 0$ ) opens into an annular region, which becomes larger and thicker as  $E$  increases until a (transition) value of  $E$  occurs and the coefficient of  $\exp(i\beta\tau)$  becomes zero. Thus,  $W = N \exp(i\phi\tau)$ , a circle of radius  $|N|$ . As  $E$  increases beyond this transition value, the solution remains a circle (Figure 2.d) with radius  $|N| = |E\phi^2 / (-\phi^2 + iC\phi + k(1 - \Delta/|N|) - iB)|$ .

Figure 3, a typical full PSD plot, is the case  $E = 4/10,000\pi^2 a$ . As shown earlier, one expects frequencies of  $\omega$  and  $\beta$  to appear, as well as harmonics of  $n\gamma \pm \beta$  where  $\gamma = \omega - \beta$  and  $n = 1, 2, \dots$ . Thus, with  $\beta = 150 \text{ Hertz}$ , and  $\omega = 500 \text{ Hertz}$ , one predicts that the PSD plot will exhibit peaks at  $150, 200, 500, 550, 850, 900, \dots \text{ Hertz}$ . Figure 8 confirms these predictions.

## 5. TRANSITION POINTS

In this section a derivation is presented which allows one to calculate in closed-form the precise values at which an annulus replaces a circle as the geometric solution of the Jeffcott equations. This is accomplished by assuming that the solution is a circle and deriving inequalities that must be satisfied. In intervals where the inequalities are not satisfied, a numerical example confirms that the solution is an annulus.

Theorem. The complex Jeffcott equation

$$(7.) \quad W'' + CW' + \{A + k(1 - \Delta/|W|) - iB\}W = E\phi^2 \exp(i\phi\tau).$$

has a solution of the form  $W = N \exp(i\phi\tau + i\phi_0)$ ,  $N \geq \Delta$ ,  $\phi_0 \geq 0$ , if and only if the following conditions are satisfied:

$F \geq 0$  and either

$$k\Delta M + \phi^2(F)^{\frac{1}{2}} \leq E(M^2 + \phi^4)$$

$$\text{and } \frac{\{k\Delta M + \phi^2(F)^{\frac{1}{2}}\} \phi^2}{(M^2 + \phi^4)(B - \phi C)} \geq \Delta$$

or

$$|k\Delta M - \phi^2(F)^{\frac{1}{2}}| \leq E(M^2 + \phi^4)$$

$$\text{and } \frac{\{k\Delta M - \phi^2(F)^{\frac{1}{2}}\} \phi^2}{(M^2 + \phi^4)(B - \phi C)} \geq \Delta$$

where

$$M = \frac{A + k - \phi^2}{B - \phi C} \phi^2 \quad \text{and} \quad F = M^2 E^2 + \phi^4 E^2 - k^2 \Delta^2.$$

The proof of this result will appear in the Final Report of Contract NAS8 - 36475.

Table I is an example which summarizes frequency-response curves for varying ratios of deadband to eccentricity ( $\Delta/E$ ). The transition points between annulus and circle are calculated from the above theorem.

## 6. STABILITY

The stability question is presently under investigation, but pieces of the puzzle are presented here.

First, the solution is bounded when  $(Q_s/C_s)^{\frac{1}{2}} < K_B$  and is unbounded when  $(Q_s/C_s)^{\frac{1}{2}} > K_B + K_S$  for all  $\delta \leq r < \infty$ , as reported in [4]. In a similar derivation one can show that a necessary and sufficient condition for boundedness is that this inequality be satisfied:

$$\operatorname{Re}[\sqrt{(C_s/2)^2 - (K_B + K_S) \pm iQ_s}] < C_s/2.$$

Figure 4 illustrates a broad range of values of  $(K_B + K_S)$  and  $Q_s$  with four different values of  $C_s$ . In each case the curve defines the points where the above inequality becomes an equality. In each case, the region above the curve is bounded and the region below the curve is unbounded. Numerical results with points near the curves verify these bounds.

Conversion of equations (5.) - (6.) to an autonomous system of six, first-order equations is accomplished using

$$u_1 = Y, \quad u_2 = Y', \quad u_3 = Y'',$$

$$u_4 = Z, \quad u_5 = Z', \quad u_6 = Z''$$

$$q = A \text{ if } R < \Delta, \quad q = A + k(1 - \Delta/R) \text{ if } R \geq \Delta$$

$$P = [E^2\phi^4 - (u_3 + Cu_2 + qu_1 + Bu_4)^2]^{\frac{1}{2}}$$

$$L = [E^2\phi^4 - (u_6 + Cu_5 + qu_4 - Bu_1)^2]^{\frac{1}{2}}$$

Then every solution of the Jeffcott equations is a solution of the autonomous system

$$u'_1 = u_2$$

$$u'_2 = u_3$$

$$u'_3 = -Cu_3 - Bu_5 - \phi P - qu_2 - q'u_1$$

$$u'_4 = u_5$$

$$u'_6 = Bu_2 - Cu_6 + \phi L - qu_5 - q'u_4$$

This system can be written in the equivalent form

$$\underline{u}' = f(\underline{u})$$

where  $\underline{u}$  and  $f(\underline{u})$  are column vectors.

Let  $\underline{v}(t)$  be a periodic solution of  $\underline{u} = f(\underline{u})$  with period  $T$ , let

$$a_{ij}(\underline{u}) = \frac{\partial f_i(\underline{u})}{\partial u_j}, \quad b_{ij}(t) = a_{ij}[\underline{v}(t)],$$

$B(t) = \{b_{i,j}(t); i, j = 1, \dots, 6\}$ , let  $X(t)$  be a fundamental matrix solution of

$$\underline{u}' = B(t)\underline{u}, \quad \text{and let } C = [X(0)]^{-1} \cdot X(T).$$

It is known that 0 is an eigenvalue of  $C$ . If the other five eigenvalues of  $C$  have negative real parts, then  $\underline{v}(t)$  is phase asymptotically stable.

The present research deals with locating the critical points analytically and using numerical results for confirmation.

7. REFERENCES:

1. Childs, D. W., "The Space Shuttle Main Engine High-Pressure Fuel Turbopump Rotordynamics Instability Problem", Trans. ASME, Journal of Engineering for Power, Jan. 1978, pp. 48 - 57.
2. Childs, D. W., "Rotordynamic Characteristics of the HPOTP' (High Pressure Oxygen Turbopump) of the SSME (Space Shuttle Main Engine)", NASA MSFC Contract NAS8-34505, Turbomachinery Laboratories Report RD-1-84, 30 January 1984.
3. Control Dynamics Company, "Effects of Bearing Deadbands on Bearing Loads and Rotor Instability", NASA MSFC Contract NAS8-35050, 20 January 1984.
4. Day, W. B., "Nonlinear Rotordynamics Analysis", NASA MSFC Contract NAS8-35992, 15 March 1985.
5. Gupta, P. K., Winn, L. W., and Wilcock, D. F., "Vibrational Characteristics of Ball Bearings", Journal of Lubrication Technology, ASME Trans., Vol 99F, No. 2, 1977, pp. 284 - 289.
6. Jeffcott, H. H., "The Lateral Vibration of Loaded Shafts in the Neighborhood of a Whirling Speed - The Effect of Want of Balance", Philosophical Magazine, Series 6, Vol 37, 1919, p. 304.
7. Nayfeh, A. H., Perturbation Methods, J. Wiley & Sons, 1973.
8. Yamamoto, T. T., "On Critical Speeds of a Shaft", Memories of the Faculty of Engineering, Nagoya (Japan) University, Vol. 6, No. 2, 1954.

ORIGINAL FACE IS  
OF POOR QUALITY

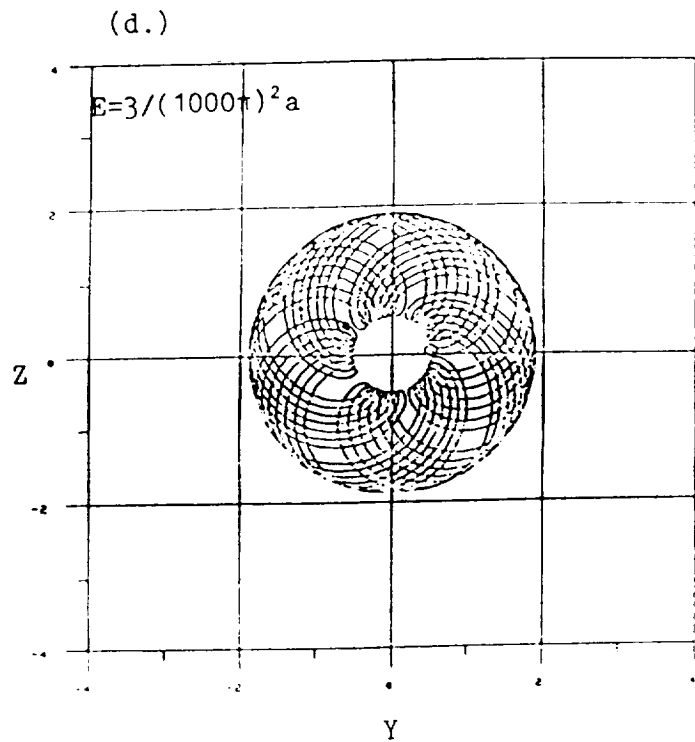
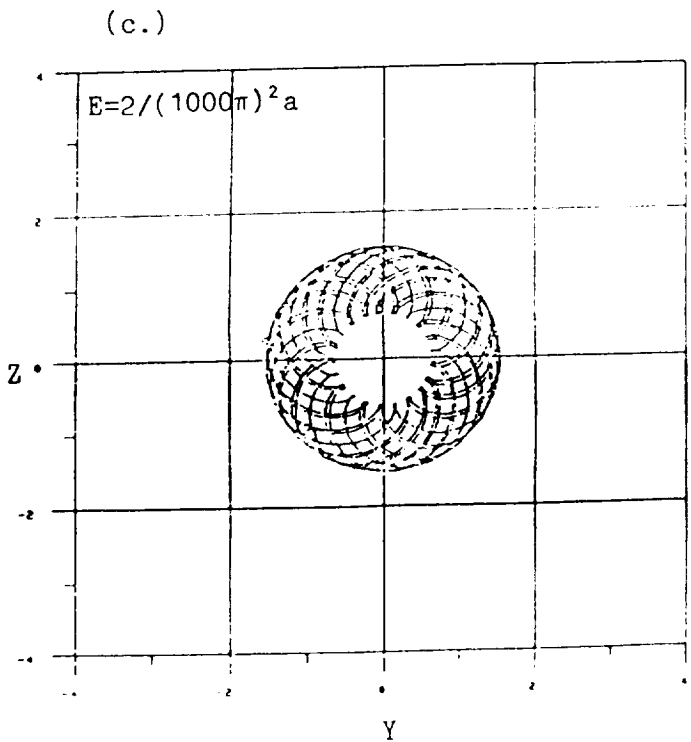
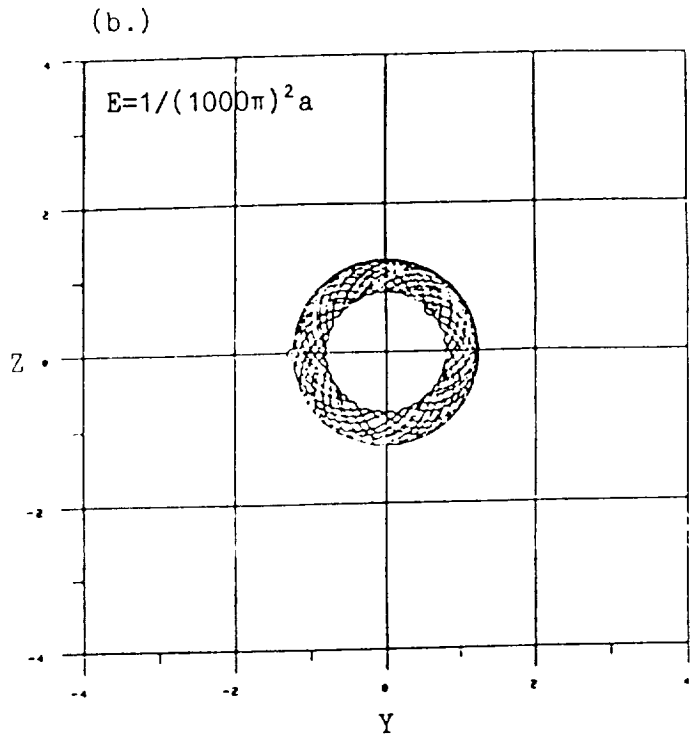
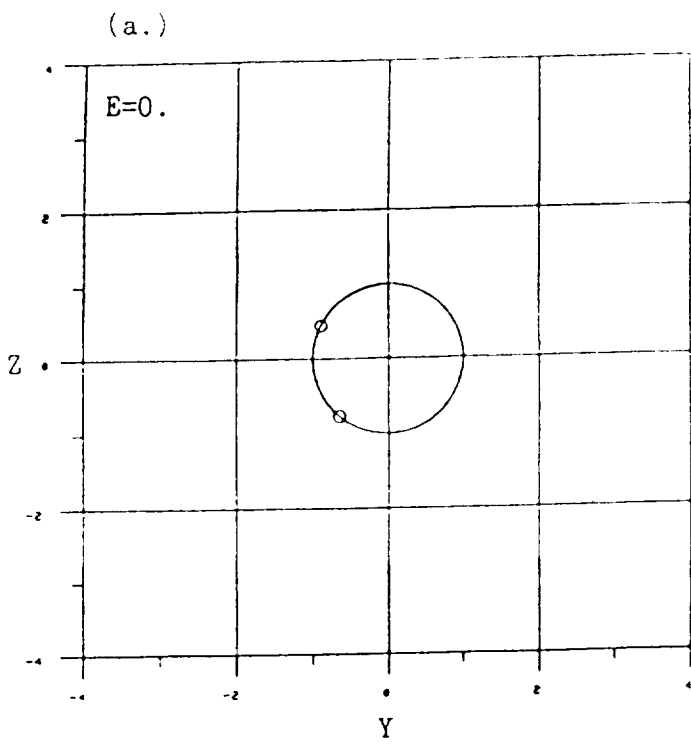


Figure 1

ORIGINAL PAGE IS  
OF POOR QUALITY

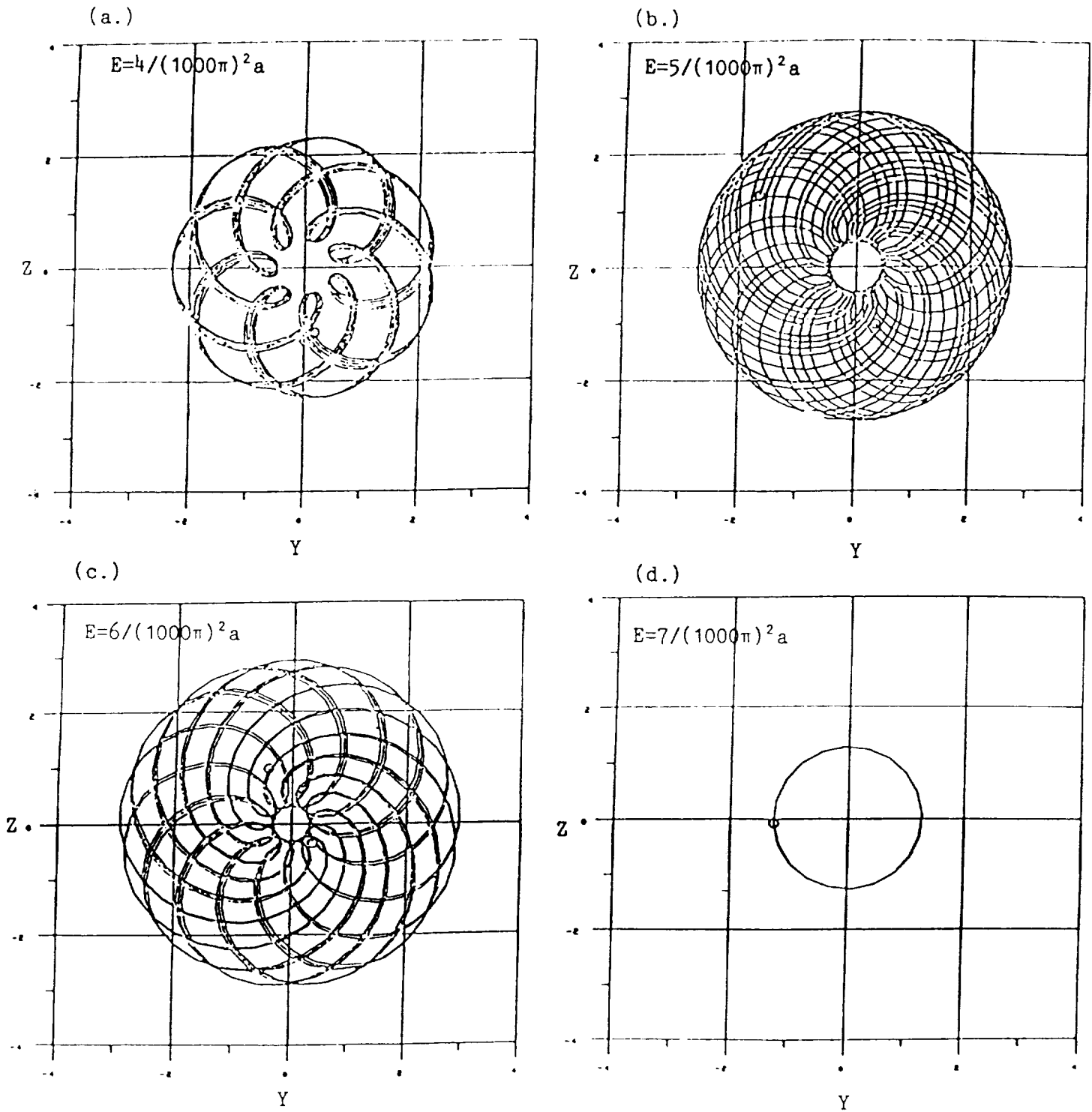


Figure 2



ORIGINAL PAGE IS  
OF POOR QUALITY

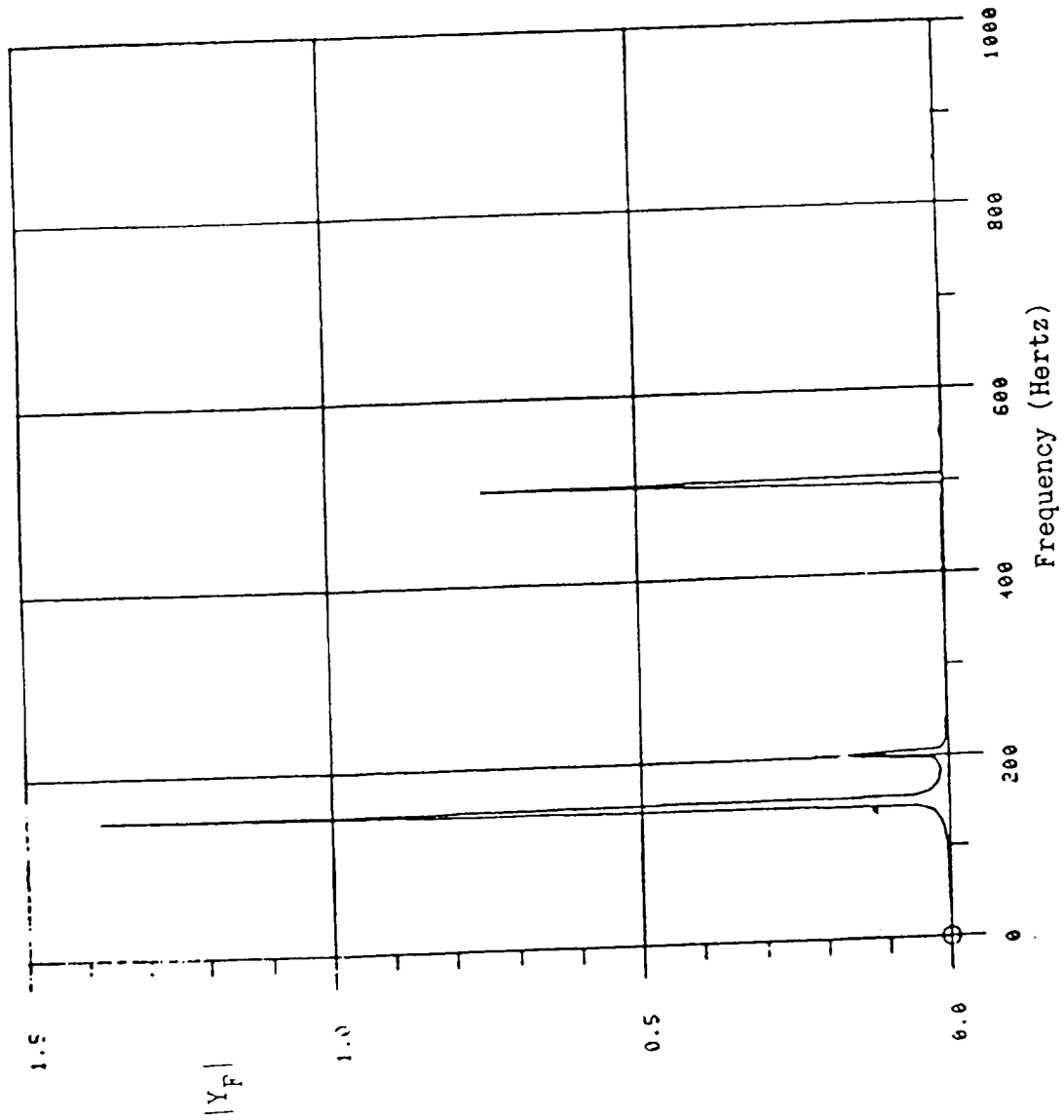


Figure 3

Table I

Absolute coefficient values:

$K_s = 0.0$        $K_b = 1,305,000.0$        $C_s = 240.0$        $Q_s = 200,000.0$   
 eccentricity = 0.0000285      deadband = varied      omega = varied

Non-dimensionalizing parameters:

frequency =  $\sqrt{K_s + K_b}$  = omega - naught =  $\sqrt{1305000.0}$   
 displacement = eccentricity = 0.0000285

Non-dimensionalized coefficient values:

$C = C_s/\text{omega - naught} = \text{ND damping} = 240.0/\sqrt{1305000.0}$   
 $k = K_b/\text{square}(\text{omega - naught}) = \text{ND stiffness} = 1$   
 $B = Q_s/\text{square}(\text{omega = naught}) = \text{ND cross - stiffness} = 200000.0/1$   
 $\phi = \text{omega}/\text{omega - naught} = \text{ND forcing frequency} = \text{varied}$   
 $\delta = \text{deadband}/\text{eccentricity} = \text{ND deadband} = \text{varied}$

deadband/eccentricity	circle/annulus regions
0.1	$\phi = 0.0$ : circle $0.01 \leq \phi \leq 0.11$ : annulus $0.11 \leq \phi \leq 4.00$ : circle
0.5	$\phi = 0.0$ : circle $0.01 \leq \phi \leq 0.23$ : annulus $0.24 \leq \phi \leq 4.00$ : circle
0.9	$\phi = 0.0$ : circle $0.01 \leq \phi \leq 0.29$ : annulus $0.30 \leq \phi \leq 4.00$ : circle
1.0	$\phi = 0.0$ : circle $0.01 \leq \phi \leq 0.31$ : annulus $0.32 \leq \phi \leq 0.99$ : circle $1.00 \leq \phi \leq 4.00$ : annulus
2.0	$\phi = 0.0$ : circle $0.01 \leq \phi \leq 0.40$ : annulus $0.41 \leq \phi \leq 0.95$ : circle $0.96 \leq \phi \leq 4.00$ : annulus
5.0	$\phi = 0.0$ : circle $0.01 \leq \phi \leq 0.53$ : annulus $0.54 \leq \phi \leq 0.88$ : circle $0.89 \leq \phi \leq 4.00$ : annulus
10.0	$\phi = 0.0$ : circle $0.01 \leq \phi \leq 0.61$ : annulus $0.62 \leq \phi \leq 0.83$ : circle $0.84 \leq \phi \leq 4.00$ : annulus

ORIGINAL PAGE IS  
OF POOR QUALITY

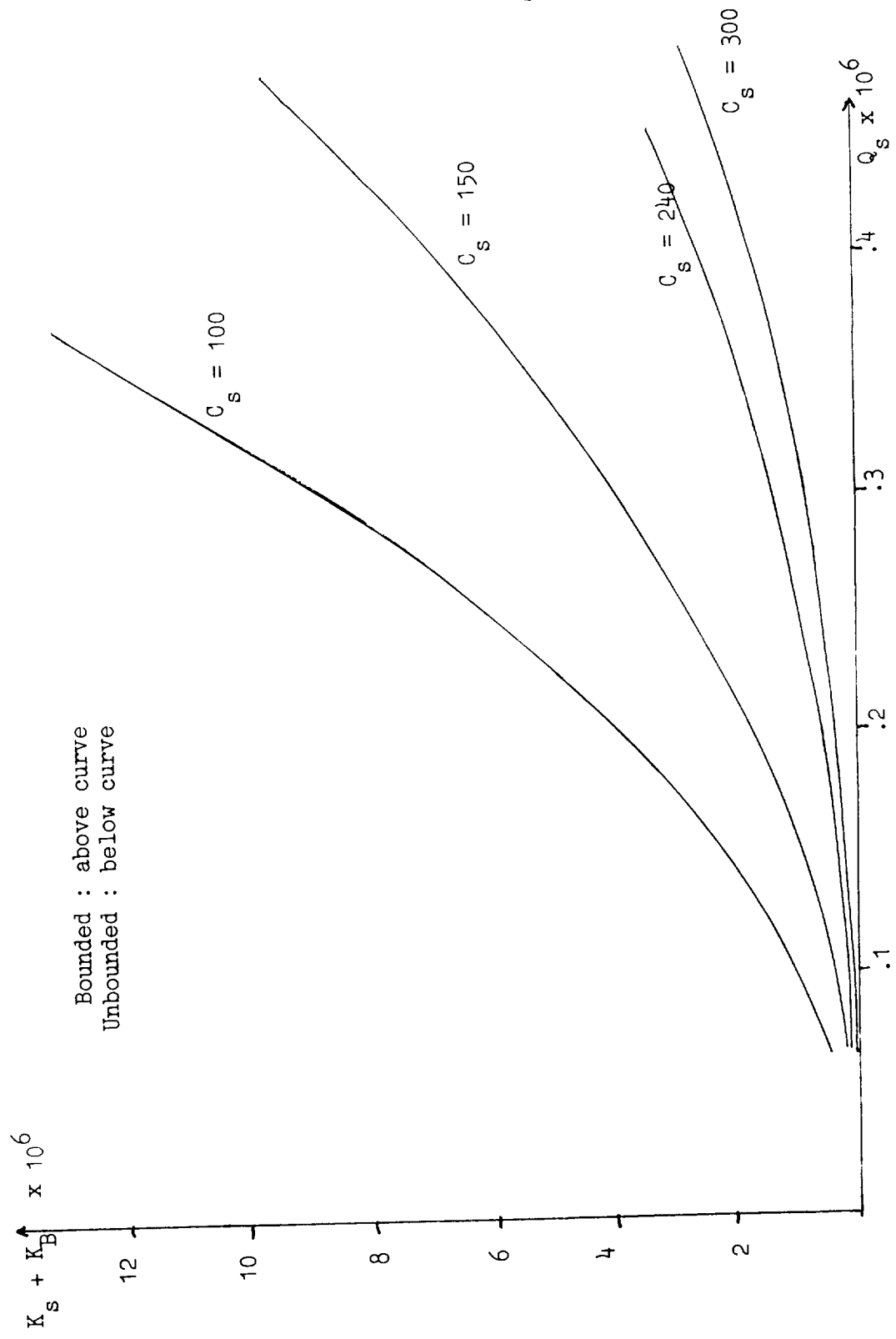


Figure 4

VIII FATIGUE/FRACTURE AND LIFE

## SIMPLIFIED CYCLIC STRUCTURAL ANALYSES OF SSME TURBINE BLADES

A. Kaufman and J.M. Manderscheid  
National Aeronautics and Space Administration  
Lewis Research Center  
Cleveland, Ohio 44135

## SUMMARY

Anisotropic high-temperature alloys are used to meet the safety and durability requirements of turbine blades for high-pressure turbopumps in reusable space propulsion systems. This study assesses the applicability to anisotropic components of a simplified inelastic structural analysis procedure developed at the NASA Lewis Research Center. The procedure uses as input the history of the total strain at the critical crack initiation location computed from elastic finite-element analyses. Cyclic heat transfer and structural analyses were performed for the first stage high-pressure fuel turbopump blade of the space shuttle main engine. The blade alloy is directionally solidified MAR-M 246 (nickel base). The analyses were based on a typical test stand engine cycle. Stress-strain histories for the airfoil critical location were computed using both the MARC nonlinear finite-element computer code and the simplified procedure. Additional cases were analyzed in which the material yield strength was arbitrarily reduced to increase the plastic strains and, therefore, the severity of the problem. Good agreement was shown between the predicted stress-strain solutions from the two methods. The simplified analysis used about 0.01 percent (5 percent with the required elastic finite-element analyses) of the CPU time used by the nonlinear finite element analysis.



## INTRODUCTION

Hot gas-path components of advanced aircraft gas turbine engines and rocket engines for reusable space propulsion systems operate under extreme gas pressure and temperature environments. These operating conditions subject the high-pressure stage turbine nozzles and blades to severe thermal transients that can result in large inelastic strains and rapid crack initiation. To attain the safety and durability requirements for these components frequently necessitates the use of advanced turbine blading alloys. These alloys exhibit mechanical property anisotropy. Assessing or improving the durability of hot section components is contingent on accurate knowledge of the stress-strain history at the critical location for crack initiation.

Nonlinear finite-element analysis techniques have become available in recent years for calculating inelastic structural response under cyclic loading. These methods are based on classical incremental plasticity theory with uncoupled creep constitutive models. Many of the nonlinear finite-element computer codes such as MARC (ref. 1) have the capability of handling materials with anisotropic properties. However, these codes are usually too costly and time consuming to use in the early design stages for aerospace applications. Costs are further increased by the geometrical complexity of high-pressure turbine blades which require three dimensional analyses and sometimes substructuring to obtain accurate solutions. To improve the design of engine hot path components such as turbine blades, simplified and more economical procedures for representing structural response under cyclic loading have been under development (refs. 2 to 4).

The objective of this study was to evaluate the utility of a simplified cyclic structural analysis method in calculating the local stress-strain response of an anisotropic turbine blade airfoil at the critical location for crack initiation. The first high-pressure stage fuel turbine blade (HPFTB) in the liquid hydrogen turbopump of the space shuttle main engine (SSME) was selected for this study. In the past these blades have undergone cracking in the blade shank region and at the airfoil leading edge adjacent to the platform. To achieve

the necessary durability, these blades are currently being cast using directional solidification. Single crystal alloys are also under investigation for future SSME applications. MARC elastic and elastic-plastic finite-element analyses were performed for the blade airfoil. Because of the extensive computation time required for the nonlinear finite-element analyses, neither the blade platform nor shank regions were modeled. The history of the total strain calculated at the critical location from the elastic finite-element analysis was used as input for the simplified procedure. Solutions from the simplified inelastic analyses of these problems for the critical airfoil location were compared to those from the MARC nonlinear analyses.

#### PROBLEM DESCRIPTION

The airfoil of the high pressure stage turbine blade of the SSME fuel turbopump was analyzed because of its history of early crack initiation. This blade is illustrated in figure 1. The uncooled airfoils have a span length of 2.2 cm and a span-to-chord width aspect ratio of approximately unity. The blades are directionally cast from MAR-M 246+Hf alloy. Temperature-dependent properties for this alloy were mainly provided by the Rocketdyne Division of Rockwell International Corporation. Material elastic properties are summarized in table I.

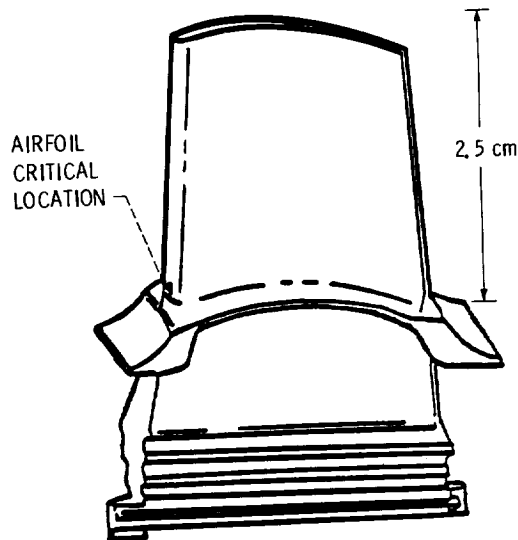


Figure 1. - SSME high-pressure fuel turbopump 1st stage turbine blade.

TABLE I. - DS MAR-M 246 PHYSICAL PROPERTIES

Temperature, C	Modulus of elasticity, GPa		Mean coefficient of Thermal expansion, %/C
	Longitudinal	Transverse	
21	131	183	-----
93	128	179	0.00113
204	125	175	.00130
316	124	173	.00133
427	119	166	.00141
538	114	162	.00148
649	109	156	.00149
760	103	149	.00156
871	97	142	.00160

TABLE II. - DS MAR-M 246 STRESS-STRAIN  
PROPERTIES (LONGITUDINAL)

Plastic strain, %	Stress, MPa		
	21 °C	649 °C	816 °C
0.1	800	808	875
.2	830	855	930
.4	850	895	965
.6	855	930	970
.8	865	945	975
1.0	870	960	980

Mean thermal coefficient of expansion data were converted to instantaneous values for MARC input. Longitudinal stress-strain properties, summarized in table II, were used for the elastic-plastic region; transverse stress-strain properties were not available at the time of this study. A single crystal alloy is also being considered for turbine blades in future SSME applications.

Cracking has occurred during service at the airfoil base near the leading edge and in the blade root shank area. These cracks were apparently initiated during the first few mission cycles due to the severe thermal transients and were propagated by vibratory excitation. Since the primary purpose of this study was to compare nonlinear finite-



element and simplified analytical methods, the blade root and platform were excluded from the analysis to limit the size of the problem and, therefore, reduce the computing time.

The mission used for the analysis is shown in figure 2 in terms of turbine inlet temperature, gas pressure and RPM. This cycle is applicable to a factory test of the engine; it is also reasonably representative of a flight mission except for the foreshortened steady-state operating time. The major factor inducing fatigue cracking is the transient thermal stresses caused by the sharp ignition and shutoff transients.

Transient and steady-state three dimensional heat transfer analyses have been conducted using the MARC code. Film coefficients were obtained from preliminary information supplied by Rocketdyne. The gas temperature was assumed constant around the airfoil surface for each time step. Colder boundary conditions were assumed at the airfoil base to simulate the effects of the cooling of the blade-to-disk attachment region by the liquid hydrogen fuel.

#### ANALYTICAL PROCEDURE

Elastic-plastic analyses have been conducted for the HPFTB airfoil with both a simplified analytical procedure developed at the NASA Lewis Research Center and with the MARC code. The severity of the problem was progressively increased by analyzing a series of cases in which the material yield strength was arbitrarily reduced until plastic strain reversal was obtained in the cycle. Separate MARC analyses were conducted for one case using both orthotropic elastic constants and the Young's modulus and Poisson's coefficient with respect to the longitudinal (spanwise) direction; this was to determine if the longitudinal properties would give a sufficiently accurate elastic-plastic finite-element solution to be used for the simplified analysis. However, the best results were obtained with the simplified procedure by the use of effective elastic moduli based on MARC elastic finite-element analyses with orthotropic material properties. Creep analyses were not conducted because the combination of airfoil temperatures and mission

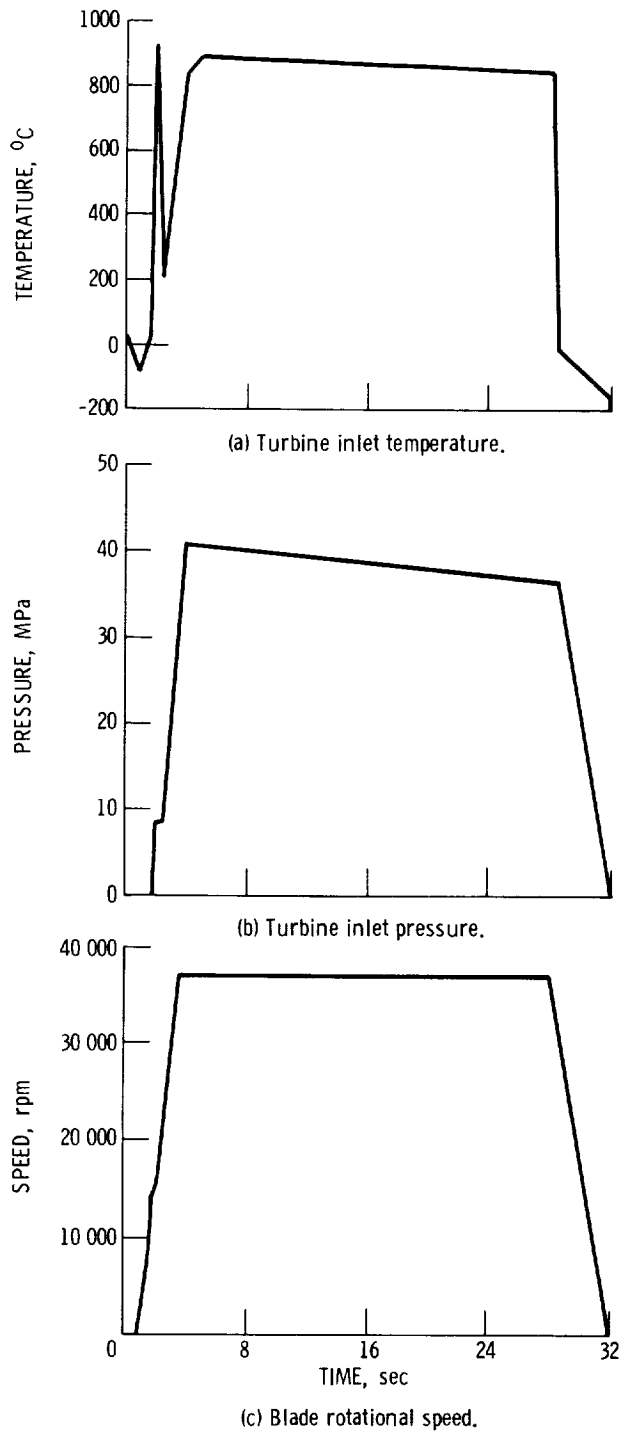


Figure 2 - Mission cycle used for analysis.

dwell times were not severe enough to induce a significant creep problem. Also, there was inadequate knowledge of the creep characteristics of the anisotropic material to perform such analyses even if desired.

## Simplified Analysis

The simplified analytical procedure was developed to economically calculate the stress-strain history at the critical fatigue location of a structure subjected to cyclic thermomechanical loading. This procedure has been exercised on a wide variety of problems including multiaxial loading, nonisothermal conditions, different materials and constitutive models, and dwell times at various points in the cycles. Comparisons of the results of the simplified analyses with MARC inelastic solutions for these problems have shown reasonably good agreement (refs. 2 to 4).

The basic assumption is that the total strain ranges calculated from linear elastic and nonlinear inelastic analyses are approximately equal and, therefore, the material cyclic response can be calculated using as input the total strain history obtained from an elastic analysis. This assumption is essentially true for thermally dominated loading. There is a version of the procedure that uses Neuber-type corrections to account for strain redistribution due to mechanical loading; however, this version was not utilized for this study because of the dominance of the thermal loading during the peak strain parts of the cycle. Classical incremental plasticity methods are used to characterize the yield surface by a yield condition to describe yielding under multiaxial stress states and by a hardening model to establish the location of the yield surface during cycling. This procedure can accommodate itself to any yield criterion or hardening model. The only requirements are that the elastic input data, whether calculated or measured, be in a form consistent with the yield criterion and that the appropriate material properties be used in conjunction with the hardening model.

In these analyses, a bilinear kinematic hardening model was used to represent the effect of cycling on the yield condition. Since the cyclic stress-strain relation is a function of the plastic strain range, it is necessary to iterate between the initially assumed and the calculated maximum plastic strains. This iterative process is usually accomplished within three iterations. However, each iteration

results in some change in the size and shape of the cyclic stress-strain loop. These changes, although generally small, create some difficulty in directly comparing solutions from the simplified procedure against finite-element analysis results because of the differences in the stress-strain curves.

As in most nonlinear computer codes, the von Mises yield criterion has been used in applying stress-strain results from elastic finite-element analyses of multiaxial problems as input for the simplified procedure. To compute cyclic hysteresis loops for life prediction purposes, the input von Mises stresses and strains have to be assigned signs, usually on the basis of the signs of the dominant principal stresses and strains.

The elastic input data are subdivided into a sufficient number of increments to define the stress-strain cycle. As will be discussed later, elastic finite-element solutions for 6 points in the SSME mission cycle proved adequate as the basis to create the total strain history required as input for the simplified analysis of the HPFTB airfoil. These points were at the start and end of the mission and at the maximum and minimum temperature peaks during the preignition and main ignition phases. A total of 120 stress-strain-temperature-time increments were obtained by interpolation from the 6 elastic finite-element solutions for the critical location. These increments are analyzed sequentially to obtain the cumulative plastic and creep strains and to track the yield surface.

An iterative procedure is used to calculate the yield stresses for increments undergoing plastic straining. First, an estimated plastic strain is assumed for calculating an initial yield stress from the stress-strain properties and the simulated hardening model. Then a new plastic strain is calculated as the difference between the total and elastic and creep strain components. The yield stress is then recalculated using the new plastic strain. This iterative procedure is repeated until the new and previous plastic strains agree within a tolerance of 1 percent. Creep computations are performed for increments involving dwell times using the creep characteristics incorporated in the code. Depending on the nature of the problem, the creep

effects are determined on the basis of one of three options to be selected; (1) stress relaxation at constant strain, (2) cumulative creep at constant stress, or (3) a combination of (1) and (2).

A FORTRAN IV computer program (ANSYMP) was created to automatically implement the simplified analytical procedure. A detailed description of the calculational scheme is presented in previous papers (refs. 2 to 4) on the development of this procedure.

### MARC Finite-Element Analysis

A three-dimensional finite-element model of the airfoil (fig. 3) was constructed of eight-node isoparametric elements. The model consisted of 360 elements with 576 nodes and 1661 unsuppressed degrees of freedom. The blade base and most of the platform were omitted for the MARC nonlinear analysis to reduce the computing time and to run the problem in-core on the CRAY computer system at Lewis. Boundary conditions were applied to constrain all nodes at the base of the model to lie on a platform plane. Additional boundary conditions were imposed to prevent rigid body motion in this plane.

The MARC code has been used extensively at NASA Lewis for inelastic analyses of aircraft turbine blades and combustor liners and of space power components. In conducting a cyclic analysis, the loading history is divided into a series of incremental load steps which are sequentially analyzed. The plasticity algorithm is based on a tangent

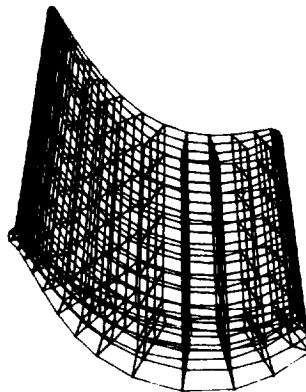


Figure 3. - Airfoil finite element model.

stiffness approach in which the stiffness matrix is reformulated and reassembled for every plastic load increment. The incremental loads are modified by residual load correction vectors to insure that the solution does not drift from a state of equilibrium. Convergence for the iterative plasticity analysis is indicated when the strain energy used in assembling the stiffness matrix approximately equals the energy change resulting from the incremental solution.

The temperature tolerance controls on the MARC transient heat transfer analysis resulted in the automatic subdivision of the mission cycle into 124 time increments. The same increments were used for the elastic-plastic structural analyses. Incremental loading included centrifugal and gas pressure loads and metal temperature distributions as calculated from the heat transfer analysis. Approximately one million words of core storage on a CRAY-1S computer were needed to run the problem. Each cycle of analysis required about 3 hr of central processor unit (CPU) time on the CRAY system. In terms of calendar time, the situation was even more serious because the system was so heavily loaded that such a large block of computing time normally was only available over weekends.

The directionality of the elastic material properties causes anisotropic constraints. Lekhnitskii (ref. 5) has derived the generalized elastic strain equations for an anisotropic body with a transverse plane of isotropy. Matrix inversion of these equations to solve for the stresses results in the relationship

$$\begin{bmatrix} \sigma_x \\ \sigma_y \\ \sigma_z \\ \tau_{yz} \\ \tau_{xz} \\ \tau_{xy} \end{bmatrix} = a \begin{bmatrix} (1 - \nu\nu'^2) & (\nu + \nu\nu'^2) & \nu'(1 + \nu) & 0 & 0 & 0 \\ (\nu + \nu\nu'^2) & (1 - \nu\nu'^2) & \nu'(1 + \nu) & 0 & 0 & 0 \\ \nu'(1 + \nu) & \nu'(1 + \nu) & (1 - \nu^2)/\nu & 0 & 0 & 0 \\ 0 & 0 & 0 & G'/a & 0 & 0 \\ 0 & 0 & 0 & 0 & G'/a & 0 \\ 0 & 0 & 0 & 0 & 0 & G/a \end{bmatrix} \begin{bmatrix} \epsilon_x \\ \epsilon_y \\ \epsilon_z \\ \gamma_{yz} \\ \gamma_{xz} \\ \gamma_{xy} \end{bmatrix}$$

where  $n = E/E'$  and  $a = nE'/((1 + \nu)(1 - \nu - 2n\nu'^2))$ . Here  $E'$ ,  $G'$ , and  $\nu'$  denote the Young's modulus, shear modulus and Poisson's ratio, respectively, for the longitudinal or span direction while  $E$ ,  $G$ , and  $\nu$  denote these constants with respect to any direction in the transverse plane of isotropy. Rocketdyne supplied values of 0.143 and 0.391 were used for  $\nu'$  and  $\nu$ , respectively. This anisotropic stress-strain law was incorporated in the MARC user subroutine, HOOKLW.

Plastic strain calculations were based on incremental plasticity theory using the von Mises yield criterion, the normality flow rule and a kinematic hardening model. The material elastic-plastic behavior was specified by the yield strengths and work hardening properties in the longitudinal direction; transverse properties were not available.

#### DISCUSSION OF RESULTS

Calculated metal temperatures at the leading edge at midspan and at the crack initiation site at the base of the airfoil (critical location) are presented in figure 4 as a function of elapsed time during the cycle. The assumed gas temperature around the airfoil is also indicated. Of particular note is that the leading edge temperature at the airfoil base is cooler than at midspan throughout the cycle. This seems reasonable because of the cooling of the blade-to-disk attachment

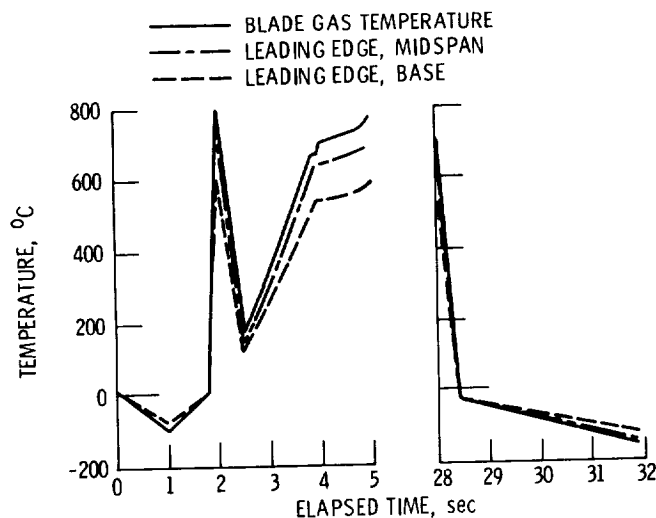


Figure 4. - Airfoil temperature cycle.

region by the liquid hydrogen fuel. The colder airfoil base temperatures induce tensile thermal stresses at the critical leading edge location that are additive to the centrifugal stresses.

The entire discussion of the structural analysis results for the HPFTB airfoil presented herein will be based on the critical location at the leading edge adjacent to the platform as indicated in figure 1, unless otherwise indicated. This location was established from the finite element analysis by determining the Gaussian point which exhibited the largest total strain change during a mission cycle. There was some practical difficulty in determining this location because of the large number of elements, Gaussian integration points and load-time increments involved and the consequent need to survey a vast amount of computer output printout.

A number of cases were analyzed in which the material yield strength was progressively and arbitrarily reduced to increase the severity of the plastic strain until reversed plasticity was induced. Comparisons are made between the stress-strain cycles computed from the simplified and MARC finite-element analyses. The comparisons are limited to the first mission cycle because of the exorbitant computing time required for the nonlinear finite-element analysis. As mentioned previously, creep analyses were not performed because the dwell times were too short for the temperatures involved to have significant creep strains and the creep properties of the material were not adequately defined.

Since the simplified procedure is basically uniaxial, it can not directly account for material anisotropy. The most convenient assumption to have made was that the anisotropic effects could be neglected and the stress-strain history approximated by using only the longitudinal properties. However, the questionableness of this assumption is indicated in figure 5 which shows the difference in the computed stress-strain cycles between finite-element analyses using anisotropic and only longitudinal material properties. The results presented in figure 5 were from MARC elastic-plastic analyses of the HPFTB airfoil in which the material yield strength was deliberately reduced for



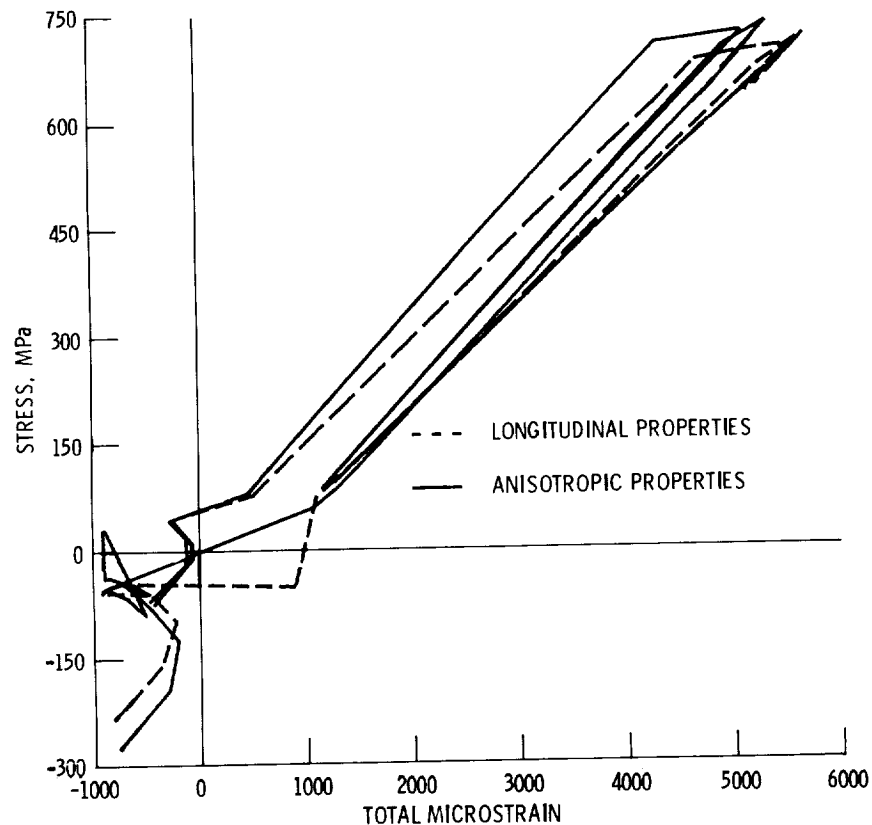


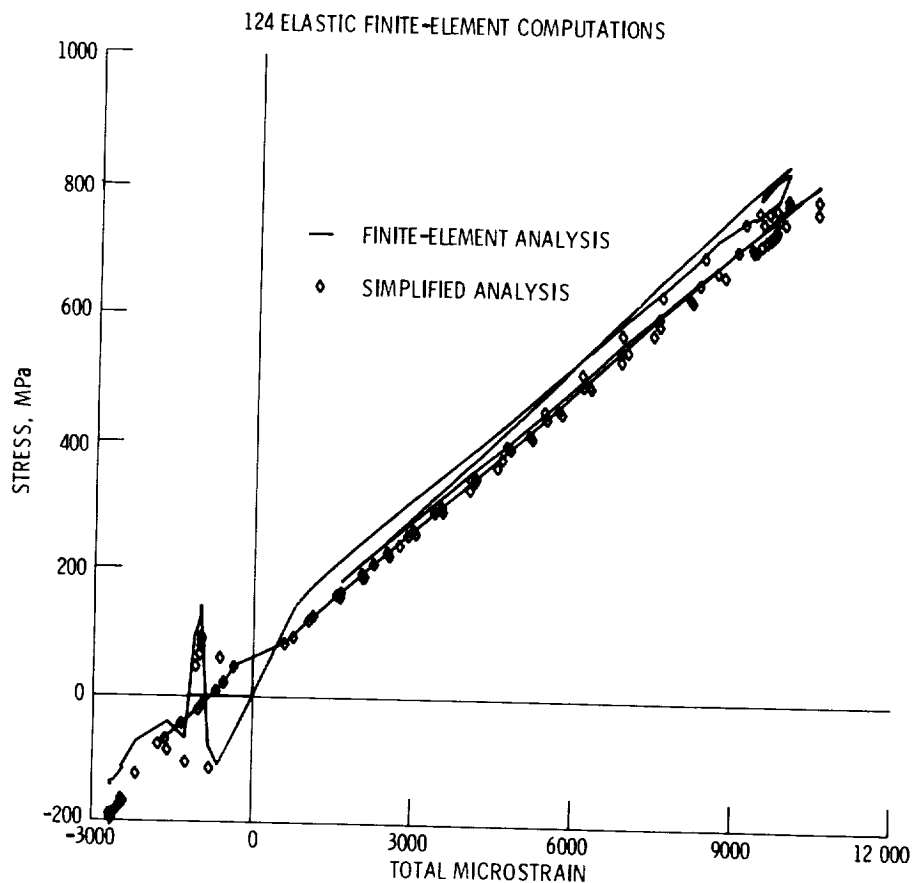
Figure 5. - Comparison of Marc stress-strain cycles for critical location using anisotropic and longitudinal material properties.

analytical purposes to increase the severity of the cycle. The stress-strain hysteresis loops in figure 5 were for a different Gaussian integration point than was subsequently determined as being the critical location based on the maximum cyclical total strain range criterion.

The MARC stress-strain cycle calculated from the orthotropic properties of the directionally solidified MAR-M 246 alloy is shown in figure 6. All of the plastic strain occurred during heatup on the preignition part of the mission. The calculated plastic strain was small (under 300 microstrain) and confined to a local region at the leading edge. Initially, MARC elastic analyses were conducted for all 124 cycle load-time increments used in the elastic-plastic analysis. Effective elastic moduli were obtained throughout the cycle from the computed effective elastic stresses and total strains. The simplified procedure was modified to use these effective elastic moduli to simulate the effects of the material anisotropy. Using this approximation,

very good agreement was obtained between the MARC and simplified analytical cycles as shown in figure 6(a).

The problem was then rerun using only six elastic finite-element solutions as input for the simplified analysis. These solutions were for the start and end points of the mission cycle and for the minimum and maximum temperature points during preignition and ignition. To establish a more complete history of total strain, another 114 load-time increments were obtained by interpolation from the initial elastic solutions. The computed stress-strain cycle from the simplified analysis using the reduced number of elastic solutions also shows reasonably good agreement with the MARC cycle (fig. 6(b)), although not quite as good as when the larger number of elastic finite-element solutions was



(a) 124 Elastic finite-element computations.

Figure 6. - Comparison of simplified and Marc stress-strain cycles at critical location using DS Mar-M246 properties.

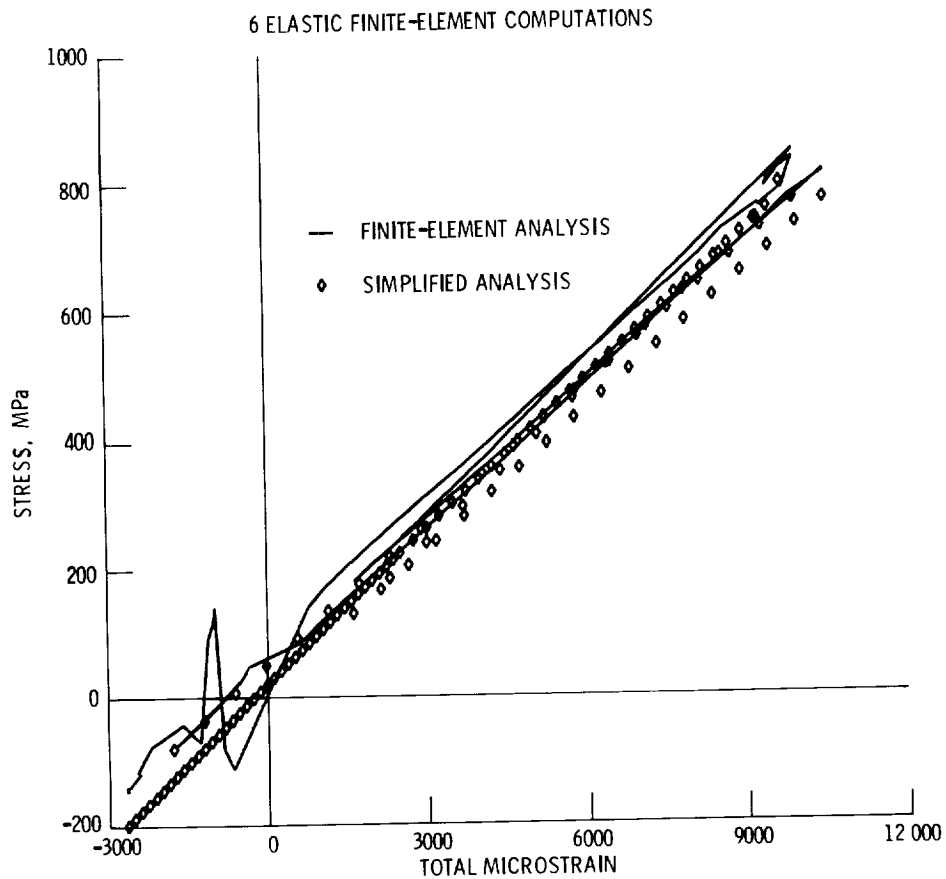


Figure 6. - Concluded.

used as input. A noticeable discrepancy is seen in the compressive strain region where the reduction in elastic analysis points resulted in failure to capture some of the cycle fluctuation due to transient thermal effects during the rapid engine cooldown. The CPU time for the six elastic finite-element analyses amounted to 5 percent of that required for one cycle of the nonlinear finite-element analysis.

To increase the severity of the problem, a series of analytical cases were run in which the material yield strength was arbitrarily and progressively reduced until the occurrence of plastic strain reversal on the unloading part of the cycle. The maximum plastic strain for this case was over 5000 microstrain. Calculated stress-strain cycles from the two analytical methods are compared in figure 7. The same history of total strain as was created previously from the 6 elastic finite-element solutions was used as input for the simplified

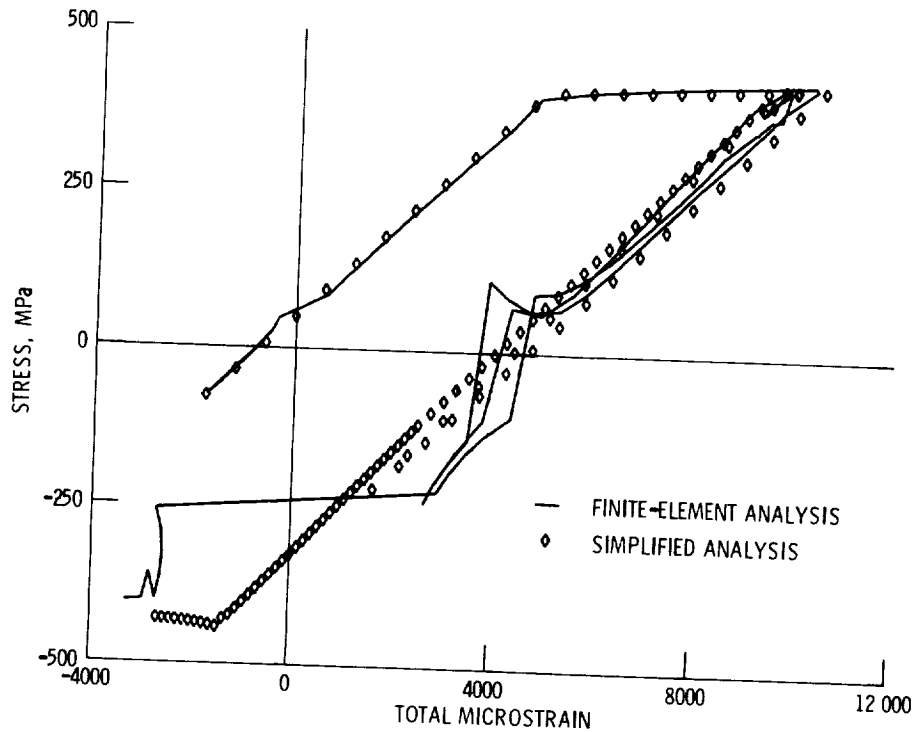


Figure 7. - Comparison of simplified and Marc stress-strain cycles at critical location using reduced yield strength.

analysis for this case. The simplified analysis cycle in figure 7 showed reasonably good agreement with the MARC results. Again the exception was a low stress region during unloading where the severe thermal fluctuations due to cooldown were not fully taken into account with the reduced number of elastic analyses. However, the region of the cycle where this discrepancy occurred was elastic and would not have a significant effect on life prediction based on the calculated stress-strain response. The stress-strain cycle predicted from the simplified method provided the stress/strain ranges and mean stress values normally needed for life prediction purposes to almost the same degree of accuracy as the nonlinear finite-element analysis. The CPU time per cycle for the simplified analysis was less than 0.01 percent of that required for the MARC elastic-plastic analysis.

#### SUMMARY OF RESULTS

A simplified inelastic procedure for calculating the local stress-strain history in a thermomechanically cycled structure was further

developed to handle material anisotropy. This was accomplished by the use of effective elastic moduli that were determined from anisotropic, elastic finite-element analyses for a number of points in the mission cycle. The simplified analysis was exercised on airfoil problems for the first-stage high-pressure fuel turbopump blade of the space shuttle main engine. Predicted stress-strain cycles for the critical airfoil location were compared to stress-strain cycles computed from elastic-plastic finite-element analyses using the MARC code. The following general conclusions were drawn from the evaluation of the improved simplified procedure:

1. The stress-strain response predicted from the simplified analysis was generally in very good agreement with the elastic-plastic finite-element solutions. The predicted stress-strain cycles provided the basic information normally needed for life prediction, such as stress and strain ranges and mean stress, to almost the same degree of accuracy as the finite-element analysis.

2. Limiting the elastic finite-element analyses to several key points in the mission cycle and interpolating between these solutions to create a more complete history of total strain, resulted in some inaccuracy in intermediate parts of the cycle due to the neglect of transient thermal fluctuations during the engine cooldown phase. However, the region where this discrepancy occurred was elastic and would not significantly affect the accuracy of life predictions based on the calculated local stress-strain response.

3. The simplified procedure computed the stress-strain history at the critical location of the structure using about 0.01 percent of the CPU time required for MARC elastic-plastic finite-element analyses. There was an overhead computing cost for conducting elastic finite-element analyses of key points in the mission to define the input total strain history. This additional cost amounted to about 5 percent of the CPU time used in just one cycle of the MARC analyses.

## REFERENCES

1. MARC General Purpose Finite Element Program. Vol. A: User Information Manual; Vol. B: MARC Element Library. MARC Analysis Research Corporation, 1980.
2. Kaufman, A.: A Simplified Method for Elastic-Plastic-Creep Structural Analysis. J. Eng. Gas Turbines Power, vol. 107, no. 1, Jan. 1985, pp. 231-237.
3. Kaufman, A.: Development of a Simplified Procedure for Cyclic Structural Analysis. NASA TP-2243, 1984.
4. Kaufman, A.; and Hwang, S.Y.: Local Strain Redistribution Corrections for a Simplified Inelastic Analysis Procedure Based on an Elastic Finite-Element Analysis. NASA TP-2421, 1985.
5. Lekhnitskii, S.G., and Brandstatter, J.J., eds.: Theory of Elasticity of an Anisotropic Elastic Body. Holden-Day, Inc., 1963., pp. 24-25.

Effects of High Mean Stress on the High-Cycle Fatigue of  
PWA 1480 and DS MAR M 246 + Hf at 1000°F\*

by

S. Majumdar

ARGONNE NATIONAL LABORATORY  
9700 South Cass Avenue  
Argonne, Illinois 60439

Materials Science and Technology Division

April 1986

The submitted manuscript has been authored by a contractor of the U. S. Government under contract No. W-31-109-ENG-38. Accordingly, the U. S. Government retains a nonexclusive, royalty-free license to publish or reproduce the published form of this contribution, or allow others to do so, for U. S. Government purposes.

INVITED PAPER to be presented at the 1986 Conference on Advanced Earth-to-Orbit Propulsion Technology, Marshall Space Flight Center/NASA, Huntsville, Alabama, May 13-16, 1986.

\*Work supported by the NASA Lewis Research Center, Cleveland, OH.

EFFECTS OF HIGH MEAN STRESS ON THE HIGH-CYCLE FATIGUE OF  
PWA 1480 AND DS MAR M 246 + Hf AT 1000°F\*

S. Majumdar  
Materials Science and Technology Division  
Argonne National Laboratory  
Argonne, Illinois 60439

Abstract

The paper summarizes results showing the effects of high mean stress on the high-cycle fatigue lives of single crystal PWA 1480 and DS MAR M 246 + Hf alloys at 1000°F. Selected specimens of PWA 1480 were examined by scanning electron microscopy after the fatigue tests were completed. The results indicate that the high-cycle fatigue resistance of PWA 1480 is less than that of DS MAR M 246 + Hf at low mean stress. However, at high mean stress, PWA 1480 is slightly stronger than MAR M 246 + Hf. The relatively low high-cycle fatigue resistance of PWA 1480 at low mean stress has been traced to the presence of porosities that nucleate fatigue cracks rather early in life. A simplified linear elastic fracture mechanics analysis, which assumes that the cracks are present at the beginning of life, provides reasonable correlation between the present data and the limited crack growth data available for the same material.

Introduction

Single crystal PWA 1480 and directionally solidified (DS) MAR M 246 + Hf are alloys of interest for use in the hot section of NASA space shuttle main engine. As high-pressure turbine blade materials, they will be subjected to vibratory high-cycle fatigue (HCF) loading superimposed on a high mean stress due to centrifugal loading. The present testing program at Argonne National Laboratory was initiated by the NASA Lewis Research Center to study the effects of a high mean stress on the HCF behavior of single-crystal PWA 1480 and DS MAR M 246 + Hf. Since the high mean stress in a turbine blade of the space shuttle main engine occurs near the root region, where temperatures are relatively low, the temperature for testing was restricted to 538°C (1000°F), although some tests were also conducted at 20°C (room temperature). Also, to minimize the effects of oxidation, tests at 1000°F were conducted in a vacuum. Since the principal loading

---

\*Work supported by the NASA Lewis Research Center, Cleveland, OH.



direction of interest is in the [001] direction for the single-crystal PWA 1480 and in the longitudinal direction for the DS MAR M 246 + Hf, only specimens with their axes oriented in these two respective directions were tested for the two alloys.

It is known that microporosities are present in PWA 1480 and that they are often the sites of fatigue crack initiation [1]. The present study was no exception. Although there was a distribution in size, in most cases a fatigue crack was initiated from the largest or a close-to-the-largest micropore present in the gauge section of the specimen. Sometimes a number of pores occur in clusters, resulting in large elastic stress concentration factors. It is likely that cracks initiated from these pores very early in life. Such micropores are not present in DS MAR M 246 + Hf. However, the nature and location of fatigue crack initiation for this alloy was not investigated.

The primary objective of the test program was to conduct tests of single-crystal PWA 1480 and DS MAR M 246 + Hf in order to establish the effects of a high mean stress on the HCF life. Because of the limited scope of the program, the target life was set nominally at one million cycles. A second objective was to conduct metallographic examinations of enough failed specimens of PWA 1480 to establish the effects of microstructure on damage. Such a metallographic study was not undertaken for DS MAR M 246 + Hf.

### Materials

5-mm (0.2 in.)-diameter, 15-cm (6 in.)-long straight gauge smooth specimens (with the specimen axes oriented in the [001] direction for PWA 1480 and in the longitudinal direction for DS MAR M 246 + Hf) were supplied by the NASA Lewis Research Center. The measured elastic modulus, proportional stress limit, 0.2% offset yield stress, and ultimate tensile strength at 20°C (room temperature) and 538°C (1000°F) are given in Table 1. Note that, in contrast to 20°C, significant strain hardening is present in PWA 1480 at 538°C. Thus, although the proportional limit is reduced with increasing temperature, the 0.2% offset yield stress remains relatively constant.

### Test Procedure

In the initial tests, specimens were subjected to axial strain controlled cycles. However, very little cyclic plasticity was observed in these tests. Therefore, all subsequent testing was carried out under load control at a frequency of 20 Hz. Plastic yielding occurred at the tensile end of the first cycle of the high-mean-stress HCF tests. However, the magnitude of the plastic strain is estimated to be only 0.05%, and there was no evidence of plastic strain ratchetting with cycles, shakedown being reached after

Table 1. Mechanical properties of PWA 1480 [001] and DS MAR M 246 + Hf (longitudinal)

Material	Temp., °C	Measured Elastic Modulus, $\times 10^6$ psi	Proportional Stress Limit, ksi	0.2% Offset Yield Stress, ksi	Ultimate Tensile Strength, ksi
PWA 1480					
	20	18.4	146	146	154
	538	16.6	125	144	-
DS MAR M 246 + Hf					
	20	17.0	-	130	155
	538	17.0	-	135	157

the first cycle. In order to minimize oxidation effects, all tests were conducted in a vacuum ( $8 \times 10^{-7}$  torr). The specimens were heated by a Lepel induction heater operating at a frequency of 455 KHz.

#### Test Results

A summary of all the tests conducted is displayed in Fig. 1. A Goodman diagram corresponding to a life of a million cycles estimated from these tests is shown in Fig. 2, which also includes data for DS MAR M 246 + Hf at 840°C (1550°F) obtained from tests conducted at Rockwell International [2]. Fatigue strength of DS MAR M 246 + Hf does not appear to change significantly between 538°C (1000°F) and 840°C (1550°F). The somewhat larger decrease in fatigue strength with increasing mean stress at the higher temperature may be related to creep effects. Note that, although the fatigue strengths of both materials decrease with increasing mean stress, PWA 1480 is more resistant to mean stress effects than DS MAR M 246 + Hf. Thus, although at 538°C (1000°F) DS MAR M 246 + Hf is stronger than PWA 1480 at zero mean stress, at high mean stress the situation is reversed. The higher yield strength of PWA 1480 may be partially responsible for this behavior.

#### Metallographic Observations

Several specimens of PWA 1480 were examined by optical and scanning electron microscopes after fracture. In all cases, crack initiation occurred at micropores. An example is shown in Fig. 3,

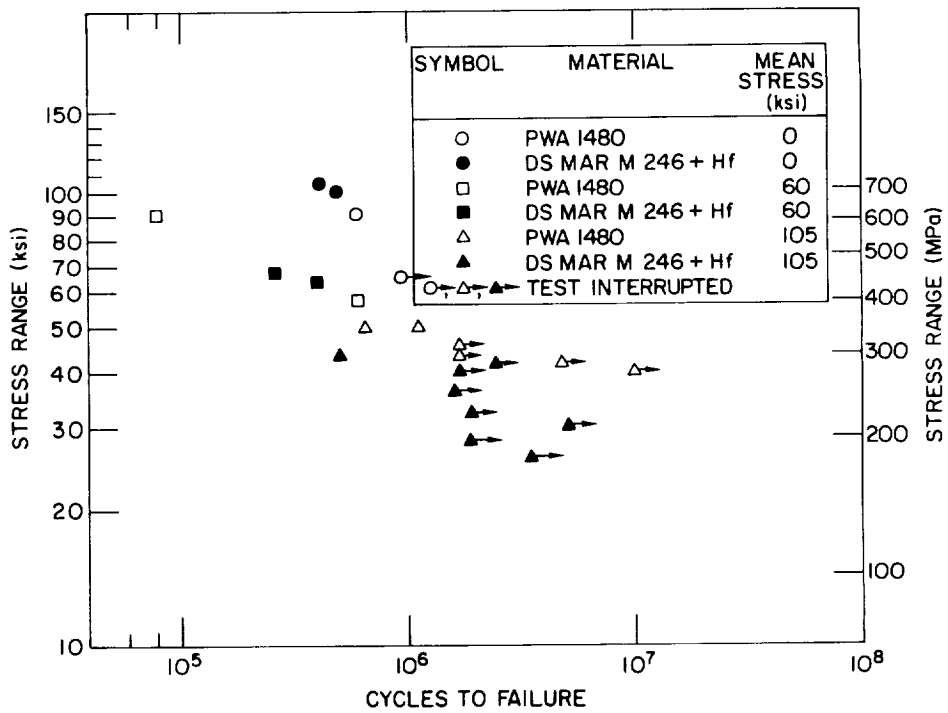


Fig. 1. Summary of HCF tests on PWA 1480 and DS MAR M 246 + Hf at various mean stresses at 1000°F (538°C).

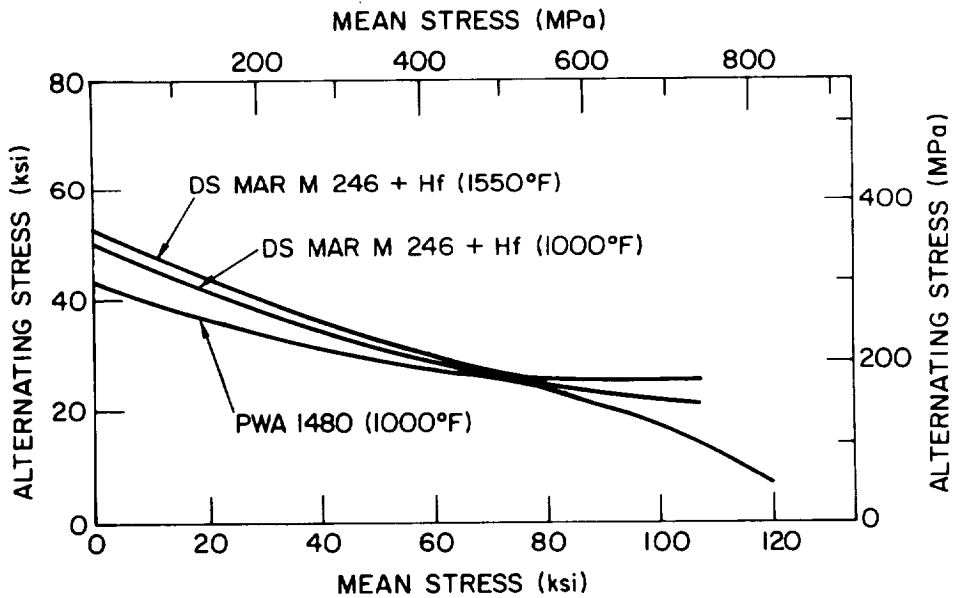


Fig. 2. Goodman diagrams for PWA 1480 at 1000°F (538°C) and for MAR M 246 + Hf at 1000°F and at 1550°F (840°C).

ORIGINAL IMAGE IS  
OF POOR QUALITY

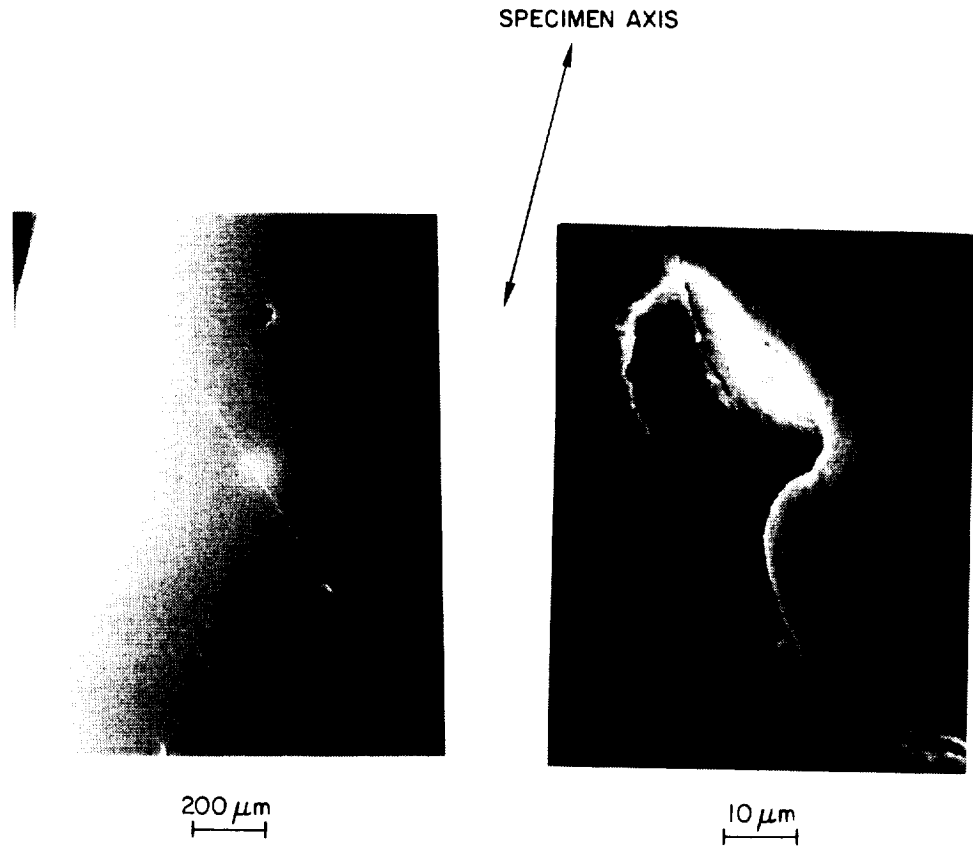


Fig. 3. Scanning electron micrograph showing surface porosity from which a fatigue crack is initiated under HCF loading.

where the crack initiated at a micropore with a major axis of about 40 μm. A more detailed discussion of crack initiation sites in PWA 1480 is given in Ref. [3]. In most cases, crack propagation was crystallographic along [111] type planes. Several slight differences were observed between tests at zero and high mean stress. Specimens at high mean stress tend to have cracks initiated at several sites, whereas those at zero mean stress tend to have a single initiation site. The high-mean-stress test specimens also had a rougher and more textured fracture surface, which may be indicative of a high crack propagation rate.

#### LEFM Analysis

Since fracture in PWA 1480 specimens initiated in all cases from one of the elongated micropores, and since the macroscopic stress strain response for all the tests was essentially linear, linear

elastic fracture mechanics (LEFM) analyses seemed appropriate. However, there are several complications due to anisotropic elastic behavior of the single-crystal material and the crystallographic nature of crack propagation. Several simplifying assumptions were made to carry out the required analysis. Details may be obtained from Ref. [3]. The analysis provided a means of estimating the crack growth behavior of the material from the HCF tests, assuming that the crack growth rate per cycle can be expressed as the following:

$$\frac{da}{dn} = \begin{cases} C[u(R)\Delta K]^n & \text{for } \Delta K > \Delta K_{th} \\ 0 & \text{for } \Delta K < \Delta K_{th} \end{cases} \quad (1)$$

where

$\Delta K$  = Stress-intensity-factor range

$k$  = Ratio between minimum and maximum stress

$u(R)$  = A factor to account for mean stress effects

$\Delta K_{th}$  = Threshold stress-intensity-factor range

$C$  and  $n$  = Material constants

Figure 4 shows a comparison between the derived crack growth rates at both 20°C (room temperature) and 538°C (1000°F) with the limited experimental crack growth data [1] available for this material for  $R = 0.1$  at 427°C (800°F). The excellent agreement may be fortuitous because of the various assumptions made in the analysis. However, the use of these crack growth data (together with reasonable estimates of initial crack length and completely ignoring crack initiation lives) allows one to correlate the observed life data of PWA 1480 generated under the present program within a factor of two [3].

#### Discussions and Conclusions

Tests conducted at 538°C (1000°F) in vacuum have shown that, under a zero-mean-stress condition, HCF strength of DS MAR M 246 + Hf at a life of one million cycles is superior to that of single-crystal PWA 1480. However, the HCF strength of the DS alloy decreases at a faster rate with increasing mean stress than that of the single-crystal alloy, so that at a mean stress of 105 ksi, the HCF strength of PWA 1480 is, in fact, superior to that of DS MAR M 246 + Hf.

Fatigue cracks in PWA 1480 initiate from micropores that are present in the as-received material. Therefore, it is theoretically possible to improve the HCF resistance of this

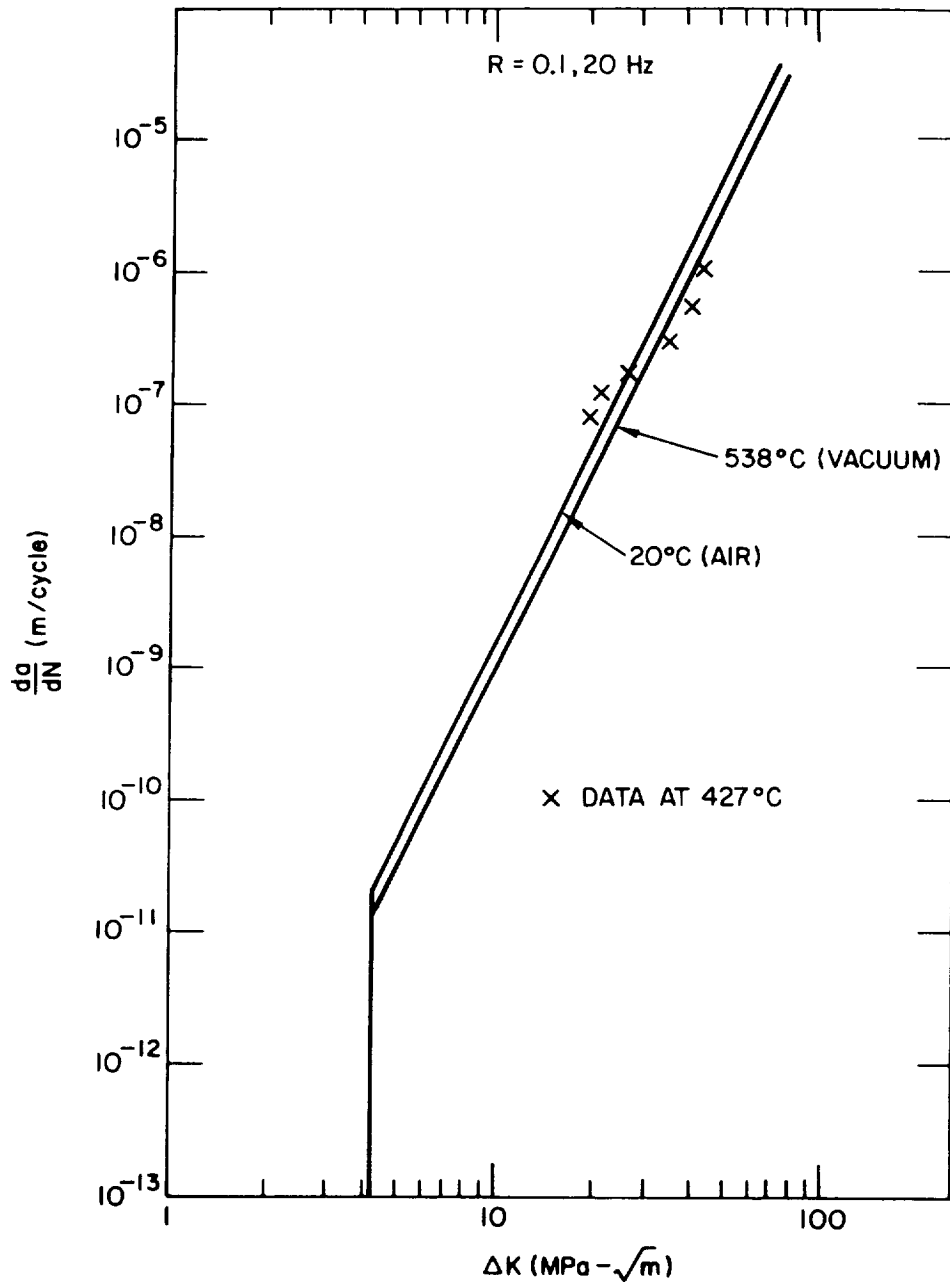


Fig. 4. Comparison of experimental crack growth rate data of PWA 1480 [001] at 427°C (800°F) with derived crack growth rates at 20°C (room temperature) and 538°C (1000°F).

material by limiting the size of the largest micropores. Figure 5 shows the improvement in lives calculated by Eq. (1) as the size of the initiating micropore is reduced from 40  $\mu\text{m}$  to 10  $\mu\text{m}$ . Note that the main benefit from such a reduction in the size of the initiating micropore is achieved at the high cycle end rather than the low cycle end of the fatigue life.

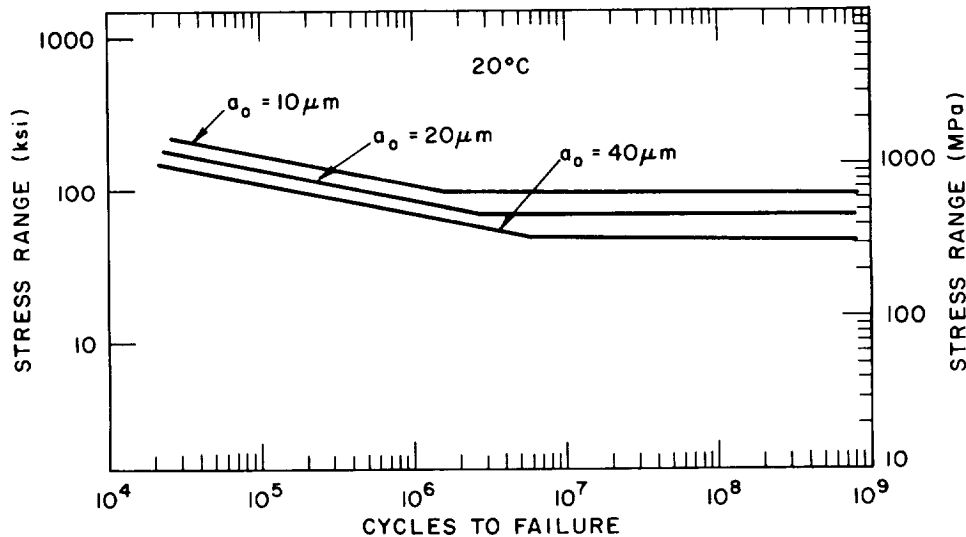


Fig. 5. Possible improvements in the fatiguc properties of PWA 1480 [001] by controlling the size of the initiating micropore at three different values.

#### References

1. D. P. Deluca and B. A. Cowles, Fatigue and Fracture of Advanced Blade Materials, Final Report for Period August 1, 1982 through August 31, 1984, Materials Laboratory, Air Force Wright Aeronautical Laboratories (AFSC) Report ASD-86-0051 (February 1985).
2. J. Lewis, unpublished test results, Rockwell International, Rocketdyne Division (1984).
3. S. Majumdar and R. Kwasny, Effects of a High Mean Stress on the High-Cycle Fatigue Life of PWA 1480 and Correlation of Data by Linear Elastic Fracture Mechanics, Argonne National Laboratory Report ANL-85-74/NASA CR 175057 (1986).

CONSTITUTIVE BEHAVIOR OF SINGLE CRYSTAL PWA 1480  
AND DIRECTIONALLY SOLIDIFIED MAR-M 246 UNDER MONOTONIC  
AND CYCLIC LOADS AT HIGH AND LOW TEMPERATURE

Walter W. Milligan, Eric S. Huron, and  
Stephen D. Antolovich

Fracture and Fatigue Research Laboratory  
School of Materials Engineering  
Georgia Institute of Technology  
Atlanta, Georgia 30332-0245

INTRODUCTION

In recent years, advancements in precision casting have allowed the introduction of directionally solidified and single crystal turbine blades in gas turbine engines and advanced rocket engines. Currently, the turbopump blade in the Space Shuttle Main Engine (SSME) is fabricated from Directionally Solidified Mar-M 246 + Hf. A possible replacement for this alloy is single crystal PWA 1480.

Both alloys result in substantial improvements in creep strength and high temperature fatigue strength over conventionally cast alloys, due to the lack of grain boundaries in the transverse direction. However, their use presents an analytical problem, because of anisotropic elastic and plastic properties. Consequently, the conventional continuum-mechanical approach is frequently inadequate. This has lead designers and analysts to try to understand fundamental metallurgical mechanisms which are active in these alloys, and to attempt to incorporate these mechanisms in their analytical models.

In addition to the complicated anisotropic properties, the microstructures and deformation mechanisms in these alloys are also complex. Deformation mechanisms are very dependent on temperature, strain level, strain rate, and stress state. In the directionally solidified (DS) material, an additional complicating factor is introduced by the longitudinal grain boundaries, and the associated rotational freedom of the grains. Metallurgical analysis is clearly needed in order to fully understand the behavior of these alloys.



The results reported in this paper are intermediate results from a long term project in which the constitutive behavior of the two alloys is being studied. The variables are temperature, strain level, strain rate, orientation, and number of cycles. Additionally, the behavior of the alloys under non-isothermal cyclic loading will be studied. The main focus of the project involves documenting fundamental metallurgical deformation mechanisms, and using this knowledge to develop physically-based constitutive models. To date, interrupted tensile tests have been conducted on PWA 1480, and the associated deformation analysis has been completed. Fully reversed, strain-controlled fatigue tests have been completed on DS Mar-M 246, and tensile tests have also been conducted. The analysis of the deformation behavior has recently begun for this material.

This paper summarizes results obtained to date [1,2]. These references should be consulted for details.

#### MICROSTRUCTURES

The alloys are similar, in that they are based on the two-phase  $\gamma/\gamma'$  structure, and both contain a large volume fraction of  $\gamma'$ . However, there are significant differences in chemistry and microstructure due to the grain boundaries which are present in the DS material. The alloy compositions are given in Table I.

##### PWA 1480

PWA is the simpler of the two, due to the lack of grain boundaries and the subsequent lack of need for grain boundary strengthening phases. The material is single crystalline, with the tensile axis within  $10^\circ$  of  $\langle 001 \rangle$ . The alloy contains a fine dispersion of ordered, cuboidal  $\gamma'$  particles in a disordered  $\gamma$  matrix, Figure 1(a). The  $\gamma'$  size was fairly uniform, ranging from 0.25 to 1.0  $\mu\text{m}$ , with an average  $\gamma'$  size of 0.5  $\mu\text{m}$ . There were isolated areas in the interdendritic regions which contained larger primary  $\gamma'$  particles. The average  $\gamma'$  volume fraction was 55-60%.

As shown in Figure 2(a), the alloy contained a residual dendritic structure with micropores and large interdendritic eutectic pools. The volume fraction of microporosity was 0.15-0.20%, and most pores were less than 50  $\mu\text{m}$  in diameter. The volume fraction of

eutectic was about 5%, with an average diameter of about 150  $\mu\text{m}$ . Due to a low carbon content of 42 ppm, very few carbides were observed. As shown in Figure 1 (a), the initial dislocation density was also very low.

Mar-M 246

The  $\gamma'$  structure of the alloy is shown in Figure 1(b). The volume fraction  $\gamma'$  was 60%, and the average  $\gamma'$  size was also about 0.5  $\mu\text{m}$  in this alloy. In contrast to the low lattice parameter mismatch of 0.28% for PWA 1480, the mismatch between the lattice parameters of the  $\gamma$  and  $\gamma'$  in Mar-M 246 was high, about 0.65%. This high misfit influenced the  $\gamma'$  morphology, as seen by the sharp cube corners of the  $\gamma'$  and the relatively high initial dislocation density in the precipitate/matrix interface. Note that some stacking faults were present in the starting microstructure.

As shown in Figure 2(b), the microstructure consisted of elongated, columnar grains which were parallel to  $\langle 001 \rangle$ . The grain diameters varied, but were on the order of 100  $\mu\text{m}$ . The grain boundaries were serrated and irregular, and some transverse boundaries and tapered grains were observed. Similar to PWA 1480, the  $\gamma'$  was finer near the dendrite cores and larger in the interdendritic regions. MC and  $\text{M}_{23}\text{C}_6$  carbides, as well as eutectic pools were present at grain boundaries and interdendritic boundaries, and the MC carbides exhibited a slight "script" morphology. Some scattered micropores were observed, but the level of porosity was not considered to be significant, as subsequent mechanical testing revealed no initiation or failure due to micropores.

## TENSILE BEHAVIOR

### MECHANICAL PROPERTIES

For PWA 1480, tests were conducted at 20, 705, 760, 815, 871, 982, and 1093 $^{\circ}\text{C}$ . For Mar-M 246, tests were conducted at 20, 704, 927, and 1093 $^{\circ}\text{C}$ . Both alloys were tested at two strain rates, 0.5%/min and 50%/min. The tests on PWA 1480 were interrupted after the yield point, while most the Mar-M 246 tests were conducted to failure.

The behavior of both alloys was similar. As shown in Table II and Figure 3, the yield strength was the same at 20 and 705 $^{\circ}\text{C}$ . Above 760 $^{\circ}\text{C}$ , the strength began to drop off rapidly, and the strain rate began to have

an effect on the strength. The temperature where the strain rate began to have an effect on the strength was a function of strain rate. At the lower strain rate, the strength began to drop off above 760<sup>0</sup>C, while at the higher strain rate, the strength did not begin to fall until above 815<sup>0</sup>C. Such behavior is typical of high volume fraction superalloys.

The stress-strain curves for Mar-M 246 are shown in Figure 4. (Note that the upper endpoints of the curve do not correspond to specimen failure, because the extensometer was removed prior to failure in order to prevent damage to it). The shape of the stress-strain curves indicates a change in strain hardening behavior. At room temperature and 704<sup>0</sup>C at 50%/min, the curves were approximately horizontal after yielding. For all other test conditions, a steeper stress-strain curve was observed. This indicates that the deformation was much more homogeneous at higher temperatures, and this hypothesis was supported by TEM observations which will be discussed later in the paper.

#### YIELD STRENGTH ANALYSIS

As indicated by the strain rate and temperature dependence of the yield strength, yielding at elevated temperatures is a thermally activated process. It is therefore appealing to present the data in the form of an Arrhenius-type relationship. Rate-controlling mechanisms may then be deduced as a function of temperature. Figure 5 is a plot of the modulus-normalized yield strength vs inverse temperature, which represents an equation of the form

$$\sigma / E = A [ \exp(Q'/RT) ] , \dots \dots \dots (1)$$

where  $\sigma$  = Yield strength,  
 $E$  = Elastic modulus at temperature, T,  
 $Q'$  = Apparent activation energy,  
 $A$  = A constant.

As illustrated by Figure 5, there are three distinct temperature regimes when the data are represented in this way:

- a) At low temperatures (below 760<sup>0</sup>C),  $Q'$  was equal to zero, so thermal activation was not a factor in the range of strain rates tested.
- b) At high temperatures (above 927<sup>0</sup>C at 50%/min and above 815<sup>0</sup>C at 0.5%/min),

$Q'$  was a constant equal to 50 kJ/mol, and was independent of strain rate. The true activation energy was calculated to be 500 kJ/mol, which is indicative of a diffusion controlled process [1].

- c) At intermediate temperatures, a transition from the low to the high temperature behavior occurred. It is evident from the shape of the curves that the transition region boundaries and functional forms were a strong function of strain rate.

## DEFORMATION STRUCTURES

Analysis of the deformation substructures at yield resulted in the same three temperature regimes as the Arrhenius analysis for PWA 1480, and the boundaries of the three regimes were the same. As discussed below, low temperature deformation at yield was dominated by  $\gamma'$  shearing, high temperature deformation was dominated by  $\gamma'$  by-pass, and intermediate temperatures exhibited a transition from shearing to by-pass.

### 1. Low Temperatures

Deformation substructures at yield at 20, 705, and 760°C (high strain rate only) were qualitatively similar. The dominant deformation mechanism was shearing of the  $\gamma'$  by pairs of  $a/2\langle 110 \rangle$  dislocations which were confined to octahedral planes. At 20°C, relatively few dislocations were present at yield, and the spacing between dislocations was large. However, the dislocation density at yield was significantly higher than it was in the as heat-treated material. There was also evidence of  $\gamma'$  shearing, including the presence of dislocation pairs and residual loops within the  $\gamma'$ . At 705 and 760°C, the dislocation density at yield was very high, and the structure consisted of intense slip bands which contained closely spaced dislocations, Figure 6. It is possible that this type of structure may have been formed but not observed at 20°C, due to the possibility of extremely localized, non-homogeneous slip.

Through systematic analysis of the dislocation Burgers vectors and line directions, it was determined that the vast majority of dislocations observed after deformation at low temperatures were of the type  $\{111\}a/2\langle 110 \rangle$ . Dislocations travelled through

the  $\gamma'$  as closely-spaced pairs in order to minimize the anti-phase boundary (APB) area created by the  $a/2\langle 110 \rangle$  displacement of the superlattice. This is demonstrated by Figure 7, in which those portions of the dislocations within the precipitate are constricted due to the high APBE, while those portions of the same dislocations which had exited the precipitates are split due to the elastic repulsion.

Dislocation structures observed at failure in Mar-M 246 at low temperatures followed the same trends. At 20 and 705°C, precipitate shearing occurred, and many dislocations were present in the  $\gamma'$  and at the interface (Figure 6 (b)).

## 2. High Temperature

The boundary separating the high and low temperature regimes was a function of strain rate. At 0.5%/min, high temperature behavior was dominant at 815°C and above, while at 50%/min, high temperature behavior did not manifest itself until 927°C and above.

In contrast to the shearing which was observed at low temperatures, deformation during yielding at high temperatures occurred primarily by dislocations moving between and around the precipitates. Figure 8 shows a typical substructure consisting of dislocation loops left in the  $\gamma/\gamma'$  interface and in the  $\gamma$  matrix. Dislocations were only infrequently observed within the  $\gamma'$  after interrupted tests conducted at 0.5%/min above 815°C. Although a few slip bands were observed to have cut the  $\gamma'$  even at 1093°C, the dominant mechanism at low strain levels at 927°C and above was particle bypass at both strain rates. As seen in Figures 8 and 9, this leads to a very homogeneous substructure, which is consistent with the observed high degree of strain hardening.

While dislocations were not observed within the  $\gamma'$  after interrupted tests at the low strain rate, the specimens which were tested to failure at 871 and 982°C contained a high density of dislocations within the  $\gamma'$ , Figure 10. This indicates that the first step in deformation was by-pass of the  $\gamma'$ , which was followed by shearing of the  $\gamma'$  later in the test. Shearing occurred only after large increases in the matrix dislocation density and significant strain hardening had occurred.

At very high temperatures and low strain rates, the  $\gamma'$  coarsened, and the substructure consisted of

interfacial hexagonal networks of dislocations, Figure 11. Under these conditions, the  $\gamma'$  was not sheared, and there was a large amount of dynamic recovery occurring. Consequently, the strain hardening exponent was lower at 1093°C (n=.221) than it was at 927°C (n=.371).

### 3. Intermediate Temperatures

Not surprisingly, a transition from shearing to by-pass was observed at yield in the range from 760 to 927°C (depending on strain rate). Slip bands were only observed at the high strain rate, and the slip band density decreased as the temperature increased.

## DISCUSSION OF TENSILE BEHAVIOR

Both the activation energy analysis and the analysis of the deformation substructures at yield divided the tensile behavior into three regimes. At low temperatures, deformation during yielding occurred by  $\gamma'$  shearing. At high temperatures, deformation during yielding occurred by  $\gamma'$  by-pass. The intermediate temperature regime exhibited transitional behavior. Attempts to model the yielding behavior must therefore be divided into these three regimes. However, the intermediate temperature regime exhibited complex transitional behavior which would be difficult to model with the available data.

As discussed in Reference 1, currently available models of yielding in high volume fraction superalloys are based on the premise that dislocation penetration into the particle is the rate-limiting step. The following type of expression for the Critical Resolved Shear Stress (CRSS) results from such an analysis

$$\tau_c = (\gamma_0/2b) - (T/br_0) + 1/2 (\tau_m + \tau_p) \dots (2)$$

where

- $\tau_c$  = CRSS,
- $\gamma_0$  = Antiphase Boundary Energy,
- $b$  = Dislocation Burgers Vector,
- $T$  = Dislocation Line Tension,
- $r_0$  = Radius of Particles in Slip Plane,
- $\tau_m$  = CRSS of the Precipitates,
- $\tau_p$  = CRSS of the Matrix.

However, the results of this study [1] indicated that penetration was not the rate-limiting step in the yielding process at all temperatures in the shearing regime, so the currently available theories are not completely valid. Further work in this area is

planned.

At high temperatures, deformation during yielding occurred by  $\gamma$ 'by-pass. The rate limiting step in these alloy systems during by-pass is climb of dislocations over the precipitates. As discussed in Reference 1, a model is available for this phenomenon which fits the experimental data very well. The CRSS is given by:

$$\tau_c = \tau_0 + K_1 Q_0 - K_2 T [\ln(k_3 \dot{\epsilon})] \dots \dots \dots (3)$$

where  $\tau_0$  = Threshold Stress  
 $Q_0$  = Activation energy of the rate-limiting diffusion process,  
 $k$ 's = Constants which include microstructural parameters,  
 $T$  = Temperature,  
 $\dot{\epsilon}$  = Strain Rate.

It is observed that the CRSS should be a linearly decreasing function of temperature, and this agrees with the data fairly well.

FATIGUE BEHAVIOR OF DS MAR-M246

LIFE CORRELATION

The LCF test results are summarized in Table 2. The data was first fitted to the well-known Coffin-Manson Law:

$$\Delta \epsilon_p = C (N_f)^\beta \dots \dots \dots (4)$$

where  $\Delta \epsilon$  is the plastic strain range (usually at half-life),  $C^p$  is a constant,  $N_f$  is the number of cycles to failure, and  $\beta$  is the Coffin-Manson exponent. The results are shown in Figure 12 (a). The resulting Coffin-Manson equations developed were:

$$\begin{array}{l} 704^{\circ}\text{C}: \Delta \epsilon_p = .08 N_f^{-.783} \\ 927^{\circ}\text{C}: \Delta \epsilon_p = .11 N_f^{-.676} \dots \dots \dots (5) \\ 1093^{\circ}\text{C}: \Delta \epsilon_p = .80 N_f^{-.762} \end{array}$$

The correlation coefficients were 0.996, 0.986, and 0.999 respectively. Life was also plotted and correlated against stress range (Figure 12 (b)). The effects of strain rate on fatigue life can be noted by comparing Figures 12 (a) and 12 (b). At 704<sup>o</sup>C, the 0.5%/minute strain rate resulted in shorter lives, on the basis of plastic strain range. On the basis of stress range, the lives were approximately equal

between the two strain rates. At 927<sup>0</sup>C and 1093<sup>0</sup>C, oxidation was an important factor in determining life. The slow strain rate lives were longer on the basis of plastic strain range, but when lives were plotted against stress range (Figure 12 (b)), the lives were shorter at the slower strain rates.

It has been shown [3] that LCF life for single crystal 7-14-6 (Ni-6.8Al-13.8Mo-6W) could be correlated well with either ( $\Delta\epsilon_t \times E$ ) or the Neuber parameter ( $\sqrt{\Delta\epsilon_t E \cdot \sigma_{max}}$ ), even for different orientations. The present data for 50%/min were analyzed with these parameters and the correlations were higher than those for  $\sigma_{max}$  or  $\Delta\epsilon_t$  alone. This confirmed that elastic modulus, which is subject to variation in DS materials due to misorientation, is obviously significant in determining fatigue life in the strain-controlled LCF tests, through its effect on stress.

#### CUMULATIVE GLIDE BEHAVIOR

The LCF tests were conducted using total strain control. Representative cumulative glide curves, plotting stress vs. cycle,, are given in Figure 13. At 20<sup>0</sup>C the stress range increased to a maximum, followed by a gradual decrease over the remainder of the test. Similar behavior has been observed in MAR-M200 [4] and Waspaloy [5, 6] and is consistent with precipitate shearing. At 704<sup>0</sup>C, 50%/minute strain rate, the stress range was essentially constant throughout the test. At 927<sup>0</sup>C, 0.5%/minute, and at 1093<sup>0</sup>C, marked softening was observed. Although the softening might at first seem to be due to particle shearing, TEM studies (which are discussed in subsequent paragraphs) revealed that particle coarsening was taking place with relatively little or no shearing.

#### FRACTURE CHARACTER

SEM examination of LCF fracture surfaces revealed marked differences dependent on test condition. At room temperature and 704<sup>0</sup>C, initiation was due to cracking at carbides in the interdendritic regions, and subsequent formation of slip bands (Figure 14 (a)). The slip band spacing was wider at 704<sup>0</sup>C. Fracture surfaces were perpendicular to the stress axis and the fracture was highly crystallographic at 20<sup>0</sup>C, less crystallographic at 704<sup>0</sup>C, 50%/minute (Figure 14 (b)), and only marginally crystallographic at 704<sup>0</sup>C, 0.5%/minute. Optical examination revealed that at both 20<sup>0</sup>C and 704<sup>0</sup>C cracks followed transgranular paths



along interdendritic regions, regions that were expected to be more brittle due to the eutectic and carbides in those regions. Only slight deflection was observed at vertical grain boundaries.

At 927<sup>0</sup>C the fracture character was quite different. The fracture surfaces were still perpendicular to the stress axis, but the initiation region was flat and featureless and not crystallographic (Figure 14 (c)). As expected the surface was heavily oxidized. Optical microscopy (Figure 14 (d)) confirmed the formation of cracks perpendicular to the stress axis (Stage II) due to oxidation of eutectic constituent in interdendritic regions. The oxidation was more severe at the slow strain rate tests, which caused reductions in lives at 927<sup>0</sup>C and 1093<sup>0</sup>C. The initiation region at 1093<sup>0</sup>C was similar to 927<sup>0</sup>C: flat and featureless and resulting from Stage II initiation at oxide spikes. However, behind the flat initiation region, the crack changed direction slightly and deviated from a plane normal to the stress axis.

#### DISLOCATION SUBSTRUCTURES

The dislocation substructures, along with the observations concerning fracture character and cumulative glide behavior, show that the LCF behavior of this material is highly dependent on the precipitate/matrix relationship.

At 20<sup>0</sup>C, there were linear dislocation segments throughout the microstructure with a significant amount of dislocation debris at the precipitate-matrix interface (Figure 15(a)). The overall dislocation density was quite high. The dislocations were found to be of the type  $a/2\langle 110 \rangle \{111\}$ . At 704<sup>0</sup>C, the overall dislocation density was lower. Dislocations were present on the interface and there was evidence of precipitate shearing (Figure 15(b)). Most of the dislocations were of type  $a/2\langle 110 \rangle \{111\}$ . However, some  $a/2\langle 110 \rangle \{110\}$  dislocations were found. These dislocations were pure edge, and near the precipitate/matrix interfaces, where the strong component of the Burger's vector in the direction of the cube face would serve to accommodate the lattice mismatch. Despite the strong strain rate effect on life, there was little qualitative difference between the substructures between the two strain rates with the exception of slightly more "wavy" dislocations in the 0.5%/min strain rate tests, especially along the

interface regions. On the basis of plastic strain range, the lives at 704°C were much shorter than for other test conditions. This corresponds to the minimum in ductility near this temperature, at the maximum  $\gamma'$  strength.

At 927°C, 50%/min, shearing of  $\gamma'$  by  $a/2 \langle 110 \rangle \{111\}$  dislocations was observed, but the density of this type of dislocation within the precipitate was very low (Figure 16 (a)). The significant structural feature observed at 927°C and above was precipitate coarsening, with formation of hexagonal networks of dislocations at the interfaces. Trace analysis showed that the networks were composed of near-edge  $a/2 \langle 110 \rangle$  dislocations on  $\{111\}$  planes with some dislocations were on  $\{110\}$  planes. The interfacial networks were quite well developed at the slow strain rate, and the coarsening was extensive (Figure 16 (b)).

At 1093°C, 0.5%/min, no dislocations were present in the matrix or precipitate interiors (Figure 17). All dislocations were stored in arrays on the precipitate-matrix interfaces, with the same character as observed at 927°C. The  $\gamma'$  coarsened significantly, in an irregular manner, even at 50%/minute strain rate. Similar coarsening was observed at 927°C at 0.5%/minute strain rate, but was absent at the faster strain rate. At 0.5%/minute at 1093°C, the degree of coarsening was severe (Figure 17 (b)). Note that the mean free path between precipitate particles has increased greatly.

Precipitate coarsening is obviously very important in the high temperature deformation of MAR-M246+Hf. In DS Rene 80, coarsening has been shown to be accelerated by stress. To study this effect in MAR-M246+Hf, undeformed samples were held for 49 hours at 927°C and 1093°C. The resulting  $\gamma'$  structure for 1093°C is shown in Figure 17 (c). Some coarsening has occurred. Note that this was without applied stress. The 1093°C, 50%/min. LCF tests coarsened to a greater extent after test times of about 30 minutes, and at 1093°C, 0.5%/min., the structure coarsened even in a tensile test. Thus in MAR-M246+Hf, the high mismatch provides a driving force for coarsening without deformation; however, deformation does increase the rate of coarsening significantly.

## GRAIN BOUNDARY SLIP BEHAVIOR

In the low temperature tests, the slip behavior on the surface could be studied using the SEM. The slip behavior across boundaries varied considerably, and a typical example is given in Figure 18. In Figure 18 (a), the grain at the right showed primary slip with slip traces present on the entire grain surface. The grain on the left contained only short slip traces, adjacent to the grain boundary. In Figure 18 (b), both grains exhibited primary slip. In the grain on the left, secondary slip was observed on two additional slip systems. These effects are similar to the results of bicrystal studies [7 - 12] and indicate that stresses can arise at the boundary due to incompatibility effects. This topic will be considered in more detail in the discussion.

## DISCUSSION OF FATIGUE BEHAVIOR

### 1. Factors Influencing Life

As shown in Figure 12, the effect of strain rate on life for the DS MAR-M246 changed with temperature. The reduction in life at 704°C for the slow strain rate, for a given plastic strain range, could be due to the difference in strain hardening behavior. For a given amount of strain the higher degree of strain hardening at the 0.5%/minute strain rate resulted in a higher stress range. Note that in terms of stress range there is little strain rate effect.

At 927°C and 1093°C, oxidation was an important factor in determining life, and the slow strain rate lives were longer on the basis of plastic strain range. This result was due to the fact that, for a given number of cycles, increased time was available for softening due to precipitate coarsening. This caused a beneficial reduction in stress, although increased time was available for oxidation. However, in terms of stress range (Figure 12 (b)), life was shortened at the slow strain rate. Although beneficial coarsening did occur to a greater extent, more time was available (in a given number of cycles) for detrimental oxidation, so the life was reduced.

Antolovich, Baur, and Liu [13] have presented a model for the effect of oxidation on life. The model assumes parabolic oxidation kinetics and relates the depth of oxide spikes to the time of the test. The relative depth,  $l_i$  of an oxide spike, is given by:

$$l_i = (t/t_0)^{1/2} \dots \dots \dots (6)$$

where  $t$  is the time to failure. For oxide-induced failure, the maximum stress at initiation was proportional to  $t^{1/2}$ , or  $l^{1/4}$ . Figure 19 shows a plot of maximum stress at initiation vs. the relative oxide depth for the present study. Visually, the correlation appears to be best for 1093°C, and the horizontal slope at 704°C implies little or no dependence of failure on oxidation.

#### CUMULATIVE GLIDE BEHAVIOR

The cumulative glide behavior of the MAR-M246 was strongly dependent on temperature due to changes in the deformation mode. At 20°C, the structure was indicative of heterogeneous, planar slip and precipitate shearing, consistent with the surface slip lines, the gradual drop in life over the last portion of the test, and the highly crystallographic fracture behavior. The initial hardening during the test corresponded to hardening in the matrix, which is relatively strong at 20°C. At the point of maximum stress the dislocation density at the precipitate/matrix boundaries and associated stress concentration was sufficiently high to initiate precipitate shearing. It should be noted that the TEM substructure was taken from the failed specimen. A worthwhile experiment would be to run an interrupted test, to a point before the maximum stress is reached, and study the deformation substructure. The completion of the present study will involve a complete matrix of interrupted testing.

At 704°C, at both strain rates, edge dislocations on {110} planes were present after deformation. This is a significant result, because such dislocations in the FCC structure are sessile, would act as strong barriers, and would cause hardening. Note that at 704°C, at both strain rates, the stress range of all tests is stable almost immediately. The stability of the stress range may be due to a balance of precipitate shearing, which would eventually soften the material, and strengthening from the immobile dislocations on {110} planes. Again, completion of interrupted tests will help to clarify these results.

At 927°C, 50%/min., the stress range was also stable. Note that although coarsening and the formation of interfacial networks had begun to occur, some precipitate shearing was still occurring at the

high strain rate (Figure 16 (a)). At 927<sup>0</sup>C, 0.5%/min. and 1093<sup>0</sup>C, a drop in stress over the life of the test was observed, due to coarsening of the  $\gamma'$ . This coarsening, with the resultant interfacial network of dislocations, and the low observed dislocation density in the matrix and precipitate are important in determining fatigue life. First, the low dislocation density is indicative that recovery processes can occur easily. Thus, the damage due to dislocations is probably minimal. The interfacial networks are not actually damage, because they serve to accommodate the mismatch. Also, the interfacial networks themselves can accommodate large strains by serving as sources and sinks for dislocations, and the coarsening increased the mean free path between precipitates. The effects explain the observed increase in fatigue on the basis of plastic strain range at 927<sup>0</sup>C and 1093<sup>0</sup>C. Coarsening has been discussed in studies on Rene 80 [14], and it was shown that at 871 and 982<sup>0</sup>C, life was determined by a balance between beneficial coarsening and detrimental oxidation. Essentially the formation of oxide spikes or regions of higher oxygen content constitute damage to the extent that they nucleate stable cracks. The formation of cracks at these defects depends on the stress level, which is determined by the amount of coarsening. The more coarsening, the lower the stress and the longer the life. As discussed earlier, when the present data (50%/min.) was fitted to the Antolovich model, the correlation was best at 1093<sup>0</sup>C. The lower fit at 927<sup>0</sup>C could be explained by the fact that some shearing (a mechanism not related to oxidation) was occurring at 927<sup>0</sup>C.

#### GRAIN BOUNDARY SLIP BEHAVIOR

The final topic of discussion concerns the grain boundary slip behavior observed at 20<sup>0</sup>C and 704<sup>0</sup>C in the MAR-M246 LCF tests (Figure 18). Studies of bicrystal deformation have provided fundamental information on the role of grain boundaries. As discussed by Hook and Hirth [11, 12], the grain boundary is a source of constraint on deformation, because to remain compatible at the boundary, each grain must contribute to the strains in the grain boundary plane in a like manner. In an ideal DS structure, because of rotational freedom, the grains will possess different compliance matrices relative to a common spatial coordinate system. This leads to elastic incompatibility. In addition, deformation on the operative slip systems will not be geometrically

continous and consequently will cause plastic incompatibility. In an actual DS structure the situation is even more complicated because of a small allowable degree of tilt misorientation. The tilt misorientation will result in changes in modulus (and therefore stress) and changes in Schmid factors for any given slip system.

A detailed analysis of the slip patterns shown in Figure 18 could be made following the methods of Margolin [10]. However, such an analysis would require knowledge of the exact crystallographic orientations of each grain. Because of the grain size, the available X-ray equipment could not be used for these determinations due to the width of the beam. Following the analysis of Prakash [15], the observed slip pattern can be rationalized based on misorientation. The following equation defines an incompatibility parameter, as a function of degree of misorientation,  $\theta$ .

$$\phi = -h/(h_2 + k_2) (1 - \cos \theta - h/k \sin \theta) \dots (7)$$

This equation predicts increasing incompatibility with increasing rotation difference. The misorientations of the grain in Figure 18 were measured by examining the grains structure on transverse planes. The secondary dendrites arms are aligned along  $\langle 001 \rangle$  directions and may be used to measure orientation differences. The misorientation between the grains was  $7^\circ$  in Figure 18 (a) and  $28^\circ$  in Figure 18 (b), correlating well with the observed degree of incompatibility slip. Greater rotational differences lead to greater amounts of slip near the boundary, with cause higher local stresses.

#### CONCLUSIONS

Strain rate, temperature, time, and microstructure had strong effects on the mechanical properties of both alloys, and physical damage mechanisms have been correlated with these effects. This is the first step toward characterizing the constitutive behavior of the alloys from the physical point of view. In the remaining portion of the program, these relationships will be further explored, in hopes of developing constitutive models which will be based on actual microstructural deformation mechanisms in the alloys.

#### ACKNOWLEDGEMENTS

The authors gratefully acknowledge the financial assistance of NASA-Lewis Research Center under Grant NAG3-503, which is monitored by Dr. Robert C. Bill and Dr. Rebecca A. MacKay.

#### REFERENCES

1. W. W. Milligan: NASA CR-175100, 1986.
2. E. S. Huron: NASA CR-175101, 1986.
3. R. P. Dalal, C. R. Thomas, and L. E. Dardi: in Superalloys 1984, M. Gell et. al., eds., AIME, New York, 1984, p. 231.
4. M. Gell and G. R. Leverant: Trans. TMS-AIME, 242, 1968, p. 1869.
5. B. Lerch, N. Jayaraman, and S. D. Antolovich: Mater. Sci. Eng., 66, 1984, p. 151.
6. R. E. Stoltz and A. G. Pineau: Mater. Sci. Eng., 34, 1978, p. 275.
7. K. T. Aust and N. K. Chen: Acta Metall., 2, 1954, p. 632.
8. J. J. Hauser and B. Chalmers: Acta Metall., 9, 1961, p. 802
9. Y. Chuang and H. Margolin: Metall. Trans., 4, 1973, p. 1905.
10. T. K. Lee and H. Margolin: Metall. Trans. A, 8A, 1977, p. 157.
11. R. E. Hook and J. P. Hirth: Acta Metall., 15, 1967, p. 535.
12. R. E. Hook and J. P. Hirth: Acta Metall., 15, 1967, p. 1099.
13. S. D. Antolovich, R. Baur, and S. Liu: in Superalloys 1980, J. K. Tien et. al., eds., ASM, Metals Park, Ohio, 1980, p. 605.

14. S. D. Antolovich, S. Liu, and Baur: Metall. Trans. A, 12A, 1981, p. 473.
15. A. Prakash: Ph.D. Thesis, University of Cincinnati, 1981.



Table I - Alloy Compositions

<u>ELEMENT</u>	<u>PWA 1480</u>	<u>D.S. Mar-M 246</u>
Cr	10	9
Co	5	10
Al	5	6
Ti	1.3	1.5
W		10
Mo		2.5
Ta	12	1.5
Hf		1
C	42 ppm	0.15
B		0.015
Zr		0.05
Ni	Bal.	Bal.

ORIGINAL PAGE IS  
OF POOR QUALITY

Table II(a) - PWA 1480 Tensile Data

Sample #	Temperature (°C)	Strain Rate (%/min)	Degrees From <001>	Elastic Modulus (GPa)	Plastic Strain (%)	Offset Yield Strength (MPa)		
						0.05%	0.1%	0.2%
61-2	20	0.5	6	137	0.14	1010	1015	---
37-2			4	120	0.24	1006	1020	1034
70-1	705	0.5	3	105	0.08	970	---	---
35-2			6	105	0.29	1000	1034	1120
70-2			3	105	0.14	970	1000	---
35-1			6	103	0.35	950	970	1034
60-1	760	0.5	5	100	0.11	844	893	---
44-2			10	103	0.26	908	956	1048
60-2			5	96	0.14	950	1000	---
44-1			10	105	0.35	949	978	1062
1-1	815	0.5	6	94	0.10	675	696	---
83-1			5	94	0.25	640	683	774
1-2			6	98	0.19	942	1006	---
83-2			5	98	0.34	886	957	1083
5-1	871	0.5	4	94	0.09	535	---	---
40-2			8	92	0.24	506	549	612
5-2			4	95	0.15	788	823	---
40-1			8	102	0.32	816	865	932
42-1	927	0.5	4	86	0.09	373	---	---
39-1			6	87	0.24	394	422	457
42-2			4	90	0.18	640	682	---
39-2			6	94	0.35	675	710	767
7-1	982	0.5	6	91	0.10	302	323	---
63-1			5	81	0.25	299	309	351
7-2			6	88	0.19	510	538	---
63-2			5	80	0.34	492	527	583
2-1	1093	0.5	5	71	0.09	168	---	---
37-1			4	71	0.22	172	183	221
2-2			5	72	0.20	274	295	310
61-1			6	77	0.38	302	316	330

Table II(b) - Mar-M 246 Tensile Data

Code	Temp (°C)	Strain Rate %/min	Young's Modulus (GPa)	Yield Strength (MPa)			UTS (MPa)	Red. in Area (%)	Strain Hardening Exponent (n)
				0.05%	0.1%	0.2%			
RTFF1	20	50	119.9	865.3	903.9	915.0	1141.1	7.9	.072
13FH1	704	50	106.2	900.5	907.4	914.6	-	-	.085a.
13SF1	704	0.5	116.5	749.4	831.5	913.6	-	6.4	.226b.
17FF1	927	50	90.3	615.6	675.4	703.6	902.0	8.6	.271
17SF1	927	0.5	82.7	464.4	499.5	562.1	703.6	14.6	.375
20FF1	1093	50	68.4	225.1	242.7	260.3	385.6	35.4	.317
20SF1	1093	0.5	63.6	151.3	161.8	175.9	216.8	37.3	.221

NOTES: a. Interrupted test. b. Test failed outside gage length.

Table III - Mar-M 246 LCF Data

Code	Temp (°C)	Strain Rate (%/min)	Total Strain Range (%)	Plastic Strain Range(a) (%)	Stress Range $\sigma_r/2$ (a) (MPa)	Young's Modulus (GPa)	Cycles to Init.	Cycles to Failure
RTFLF	20	50	1.750	.1517	1028.1	135.1	396	396
13FLF	704	50	1.790	.0968	891.9	106.9	370	386
13FLF2	704	50	1.790	.1290	867.4	100.0	191	191
13FLLF	704	50	1.684	.1064	843.3	104.8	279b	279
13FLLF2	704	50	1.512	.0288	778.7	107.6	1308	1357
13SLF	704	0.5	1.790	.0258	876.0	102.0	380	409
13SLF2	704	0.5	1.790	.0226	869.4	101.4	441	446
17FLF	927	50	1.554	.1742	697.8	94.5	406	417b
17FLF2	927	50	1.554	.1355	635.2	91.0	806	811b
17FLLF	927	50	1.166	.0387	518.6	93.7	3764	3769
17FLLF2	927	50	1.166	.0323	467.6	94.5	6049	6049b
17SLF	927	0.5	1.016	.1740	379.1	94.5	1317	1459
20FLF	1093	50	.756	.2412	175.9	61.4	1954	2050
20FLF2	1093	50	.648	.2000	160.0	65.5	2466	2601
20FLLF	1093	50	.565	.0989	168.8	73.8	c	c
20FLLF2	1093d	50	.565	.0903	141.3	62.7	7231	7425
20SLF2	1093	0.5	.504	.2060	93.5	67.6	6526	8849

NOTES: a. At half-life. b. Outside gage length of extensometer. c. Testing machine shutoff due to error. d. Temperature fell 10°C after half-life.

ORIGINAL PAGE IS  
OF POOR QUALITY

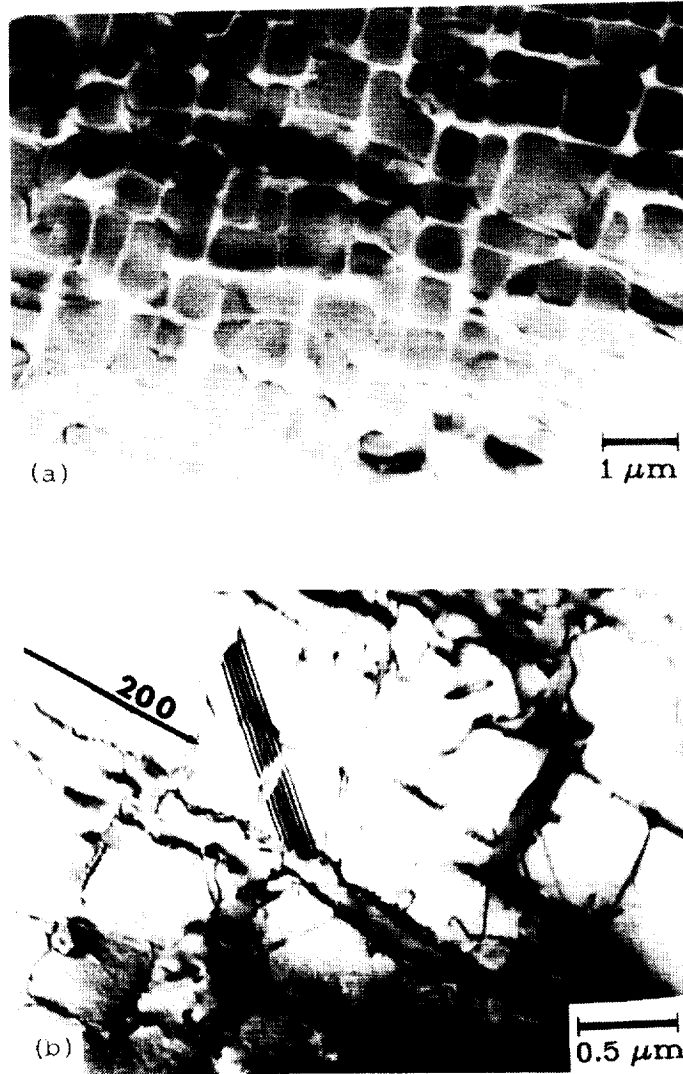


Figure 1. TEM micrographs of the  $\gamma'$  structure,  $g = \langle 200 \rangle$ . (a) PWA 1480. (b) MAR-M 246.

ORIGINAL PAGE IS  
OF POOR QUALITY

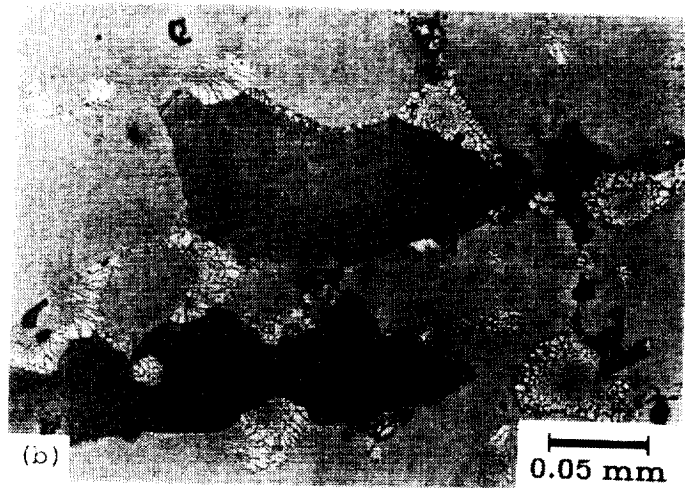
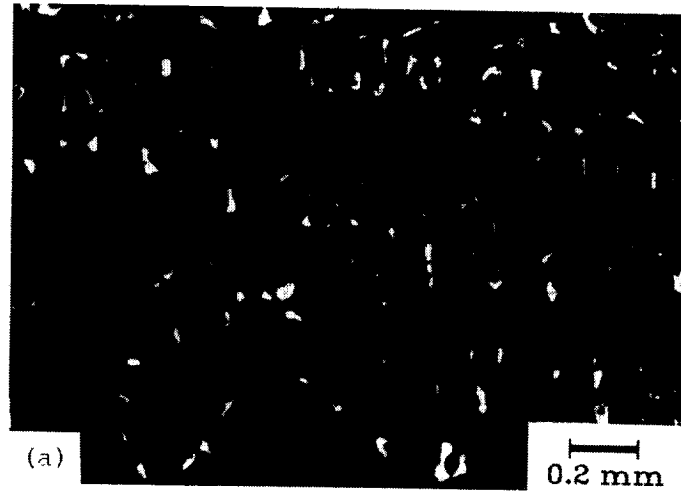
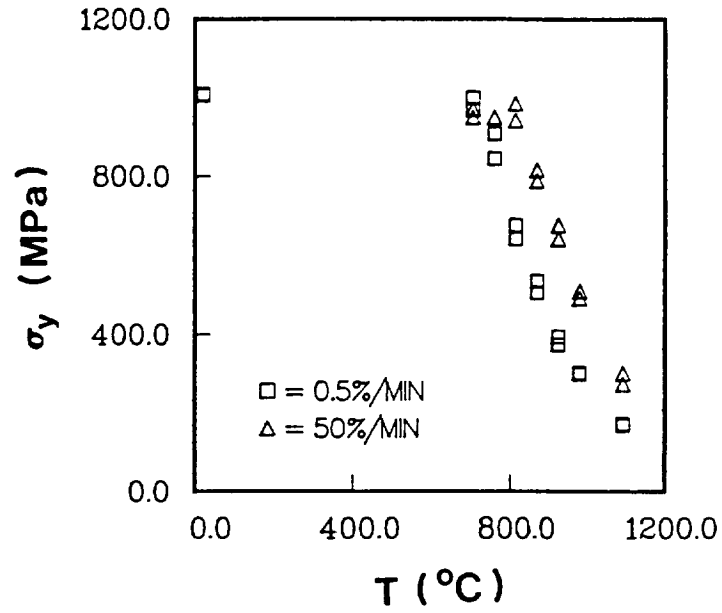
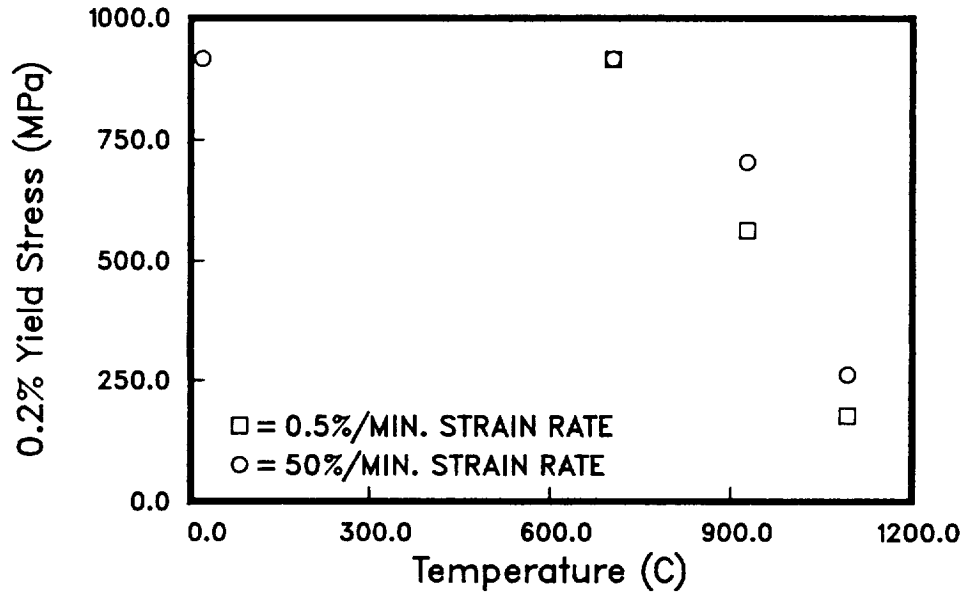


Figure 2. Optical microstructures. (a) PWA 1480. (b) MAR-M 246.



(a)



(b)

Figure 3. Yield strength vs. Temperature. (a) PWA 1480. (b) MAR-M 246.

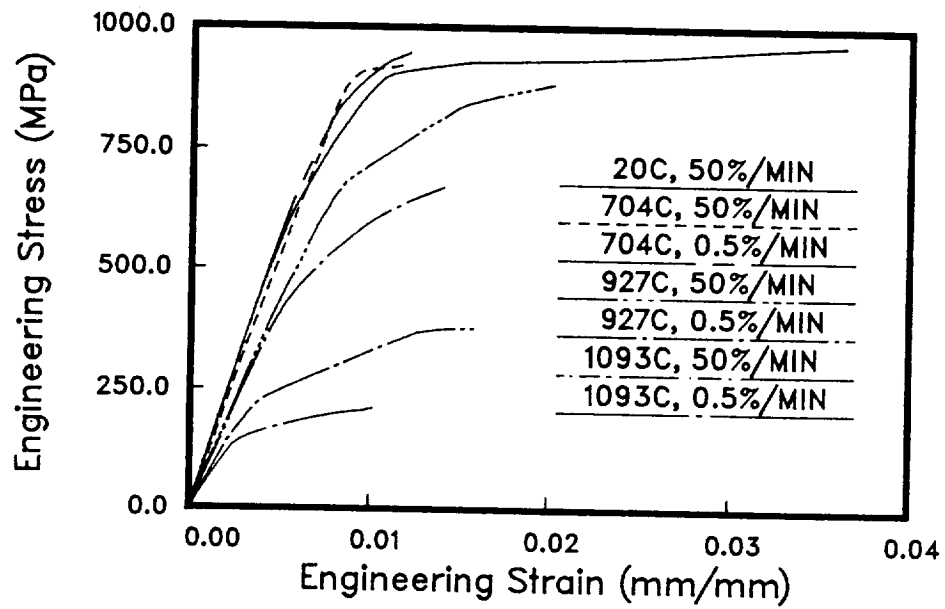


Figure 4. Representative tensile test curves for MAR-M 246.



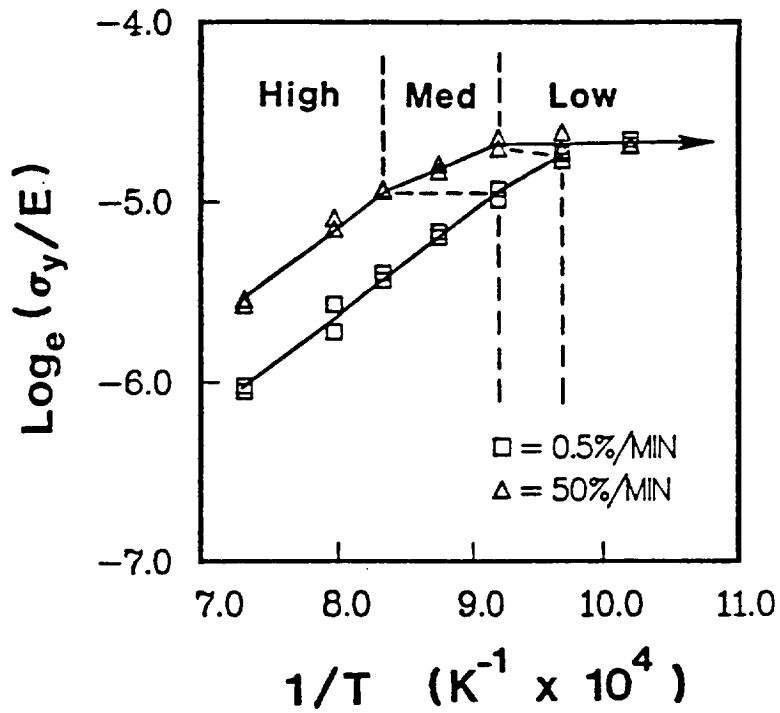


Figure 5. Arrhenius representation of PWA 1480 yielding data

ORIGINAL PAGE IS  
OF POOR QUALITY



Figure 6. Intense shearing of  $\gamma$  at low temperatures in tensile tests. (a) PWA 1480 705<sup>o</sup>C. (b) MAR-M 246, 20<sup>o</sup>C.

ORIGINAL PAGE IS  
OF POOR QUALITY



Figure 7.  $\gamma'$  shearing showing paired dislocations.  
PWA 1480, 705°C, tensile test.

ORIGINAL PAGE IS  
OF POOR QUALITY

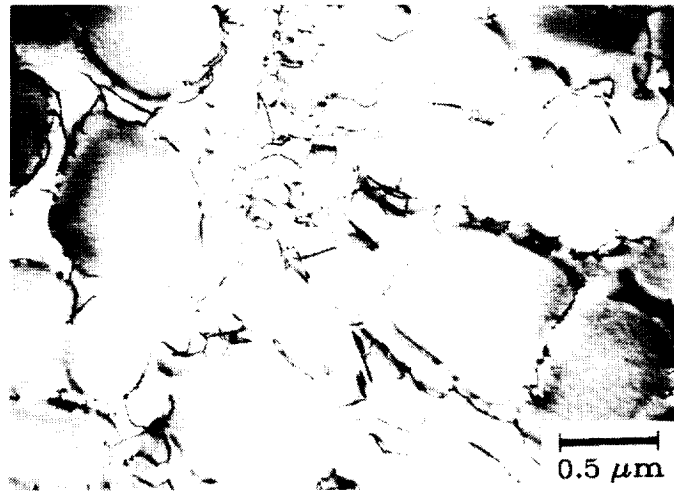


Figure 8.  $\gamma'$  by-pass at yield at high temperature.  
PWA 1480, 982<sup>o</sup>C, 0.3% plastic strain.



Figure 9.  $\gamma'$  by-pass and coarsening after tensile test  
to failure MAR-M 246, 1093<sup>o</sup>C

ORIGINAL PAGE IS  
OF POOR QUALITY

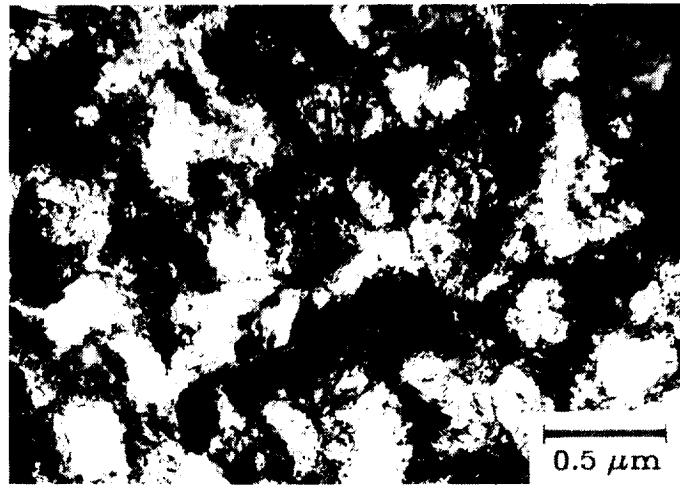


Figure 10.  $\gamma$  shearing during late stages of tensile test in PWA 1480 at 871°C.

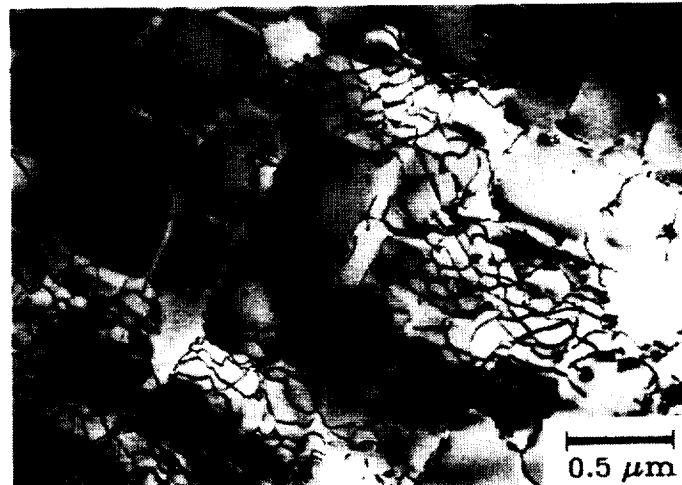
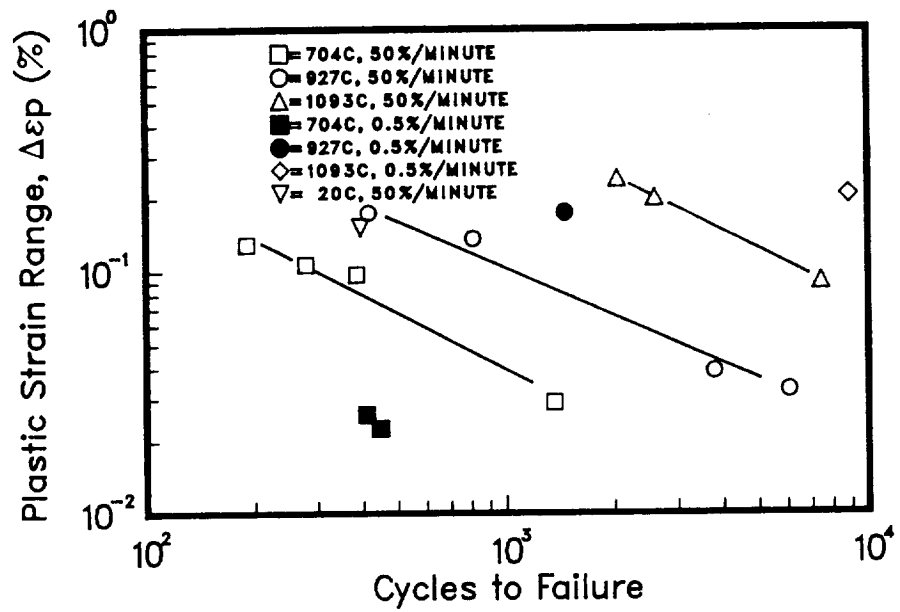
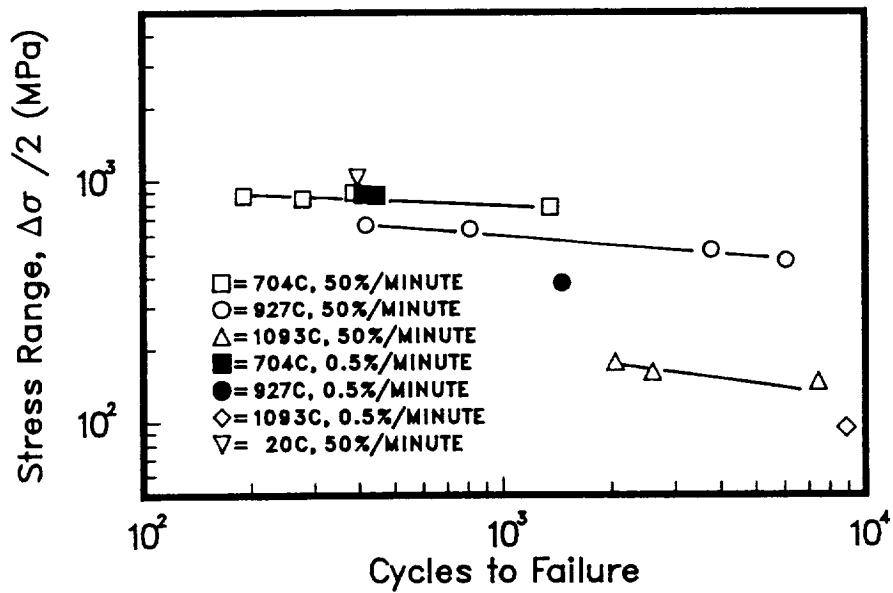


Figure 11. Interfacial networks developed at yield at high temperature. PWA 1480, 1093°C, 0.3% plastic strain



(a)



(b)

Figure 12. Fatigue behavior of MAR-M 246. (a) Coffin-Manson plot. (b)  $\Delta\sigma/N_f$  plot.

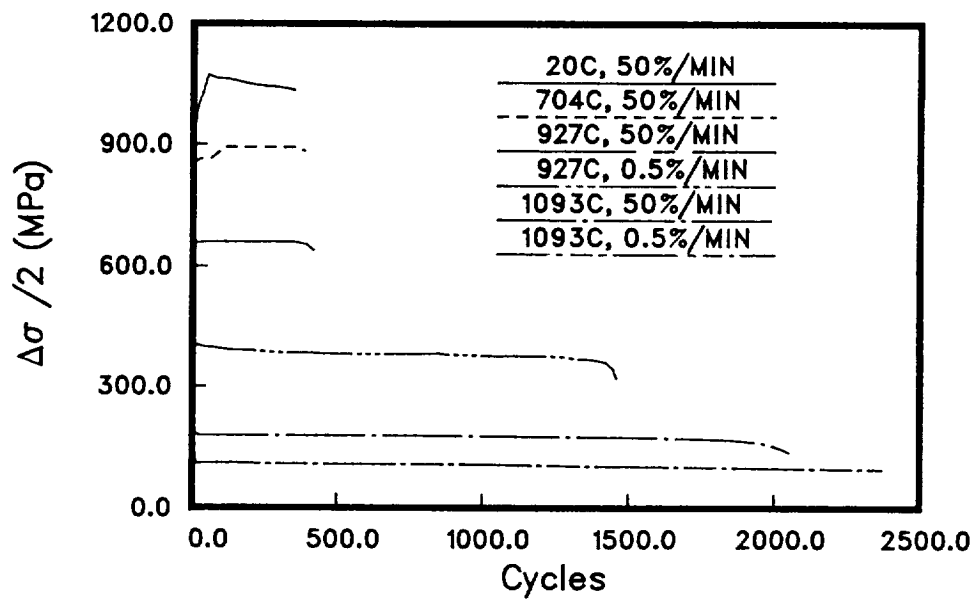


Figure 13. Representative cumulative glide curves for MAR-M 246.

ORIGINAL PAGE IS  
OF POOR QUALITY

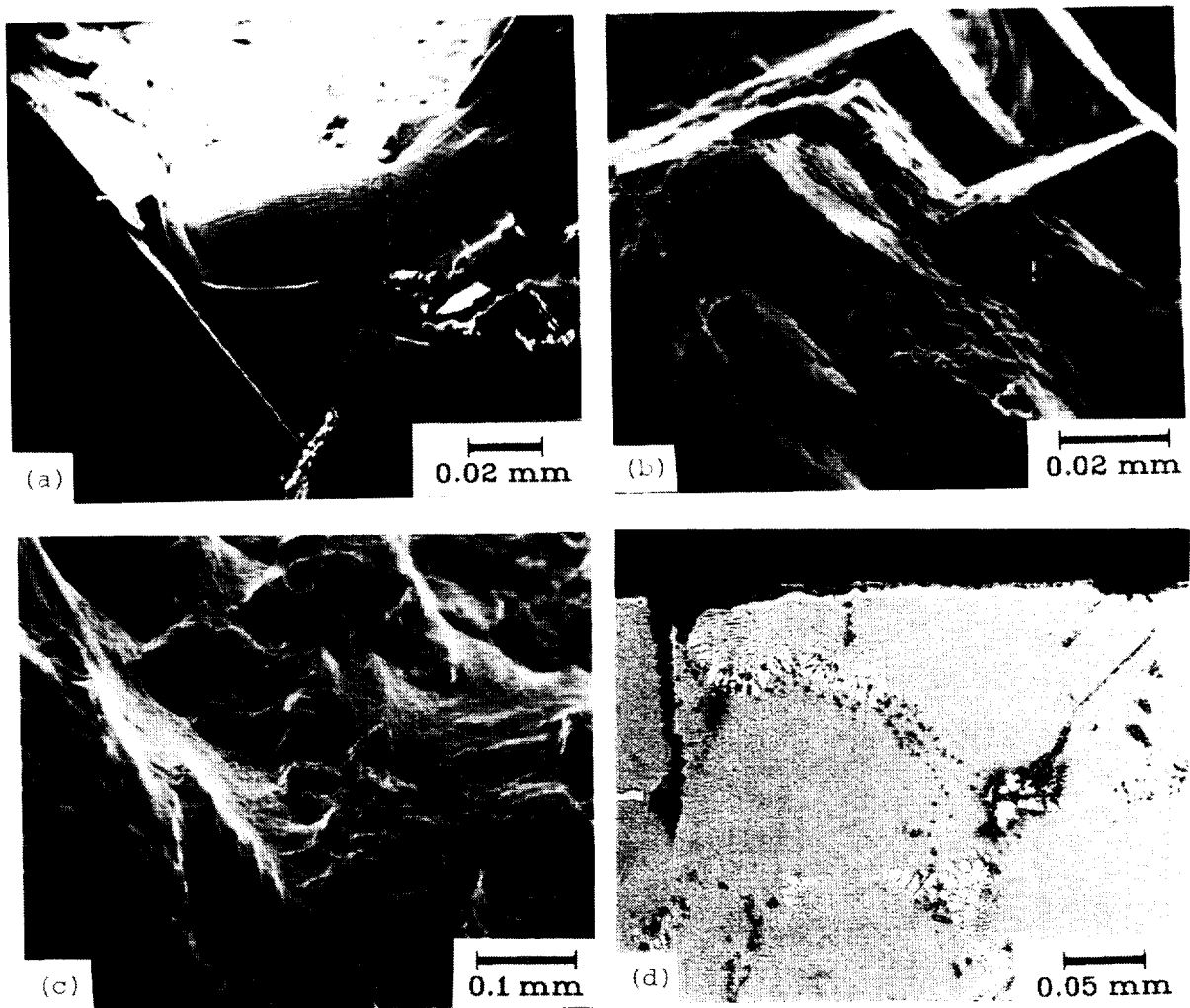


Figure 14. LCF fracture behavior of MAR-M 246. (a) Initiation and crystallographic propagation at 20°C. (b) Less crystallographic fracture at 704°C. (c) Initiation due to oxidation at 927°C. (d) 927°C oxide spikes.



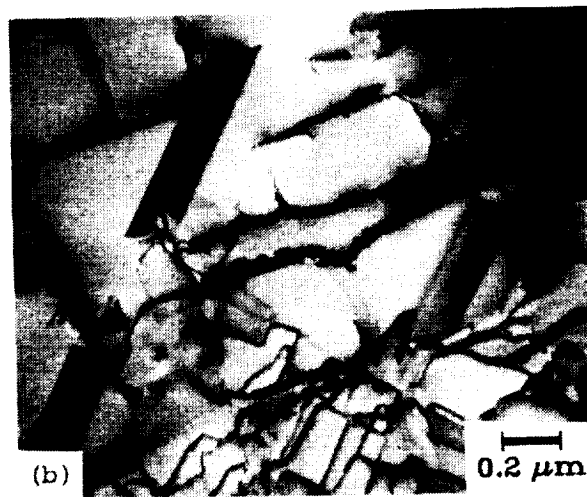
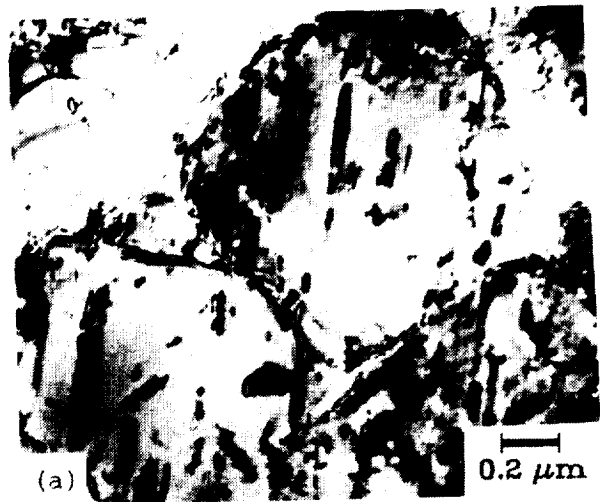


Figure 15. LCF dislocation structures at low temperatures., (a) 20<sup>0</sup>C, 50%/min, showing remnants of  $\gamma$  shearing. (b) 704<sup>0</sup>C, 50%/min Note stacking faults indicative of shearing.

ORIGINAL PAGE IS  
OF POOR QUALITY



Figure 16. LCF dislocation structures at  $927^{\circ}\text{C}$ .  
Interfacial networks have developed and  
coarsening has occurred. (a) 50%/min.  
(b) 0.5%/min.

ORIGINAL PAGE IS  
OF POOR QUALITY

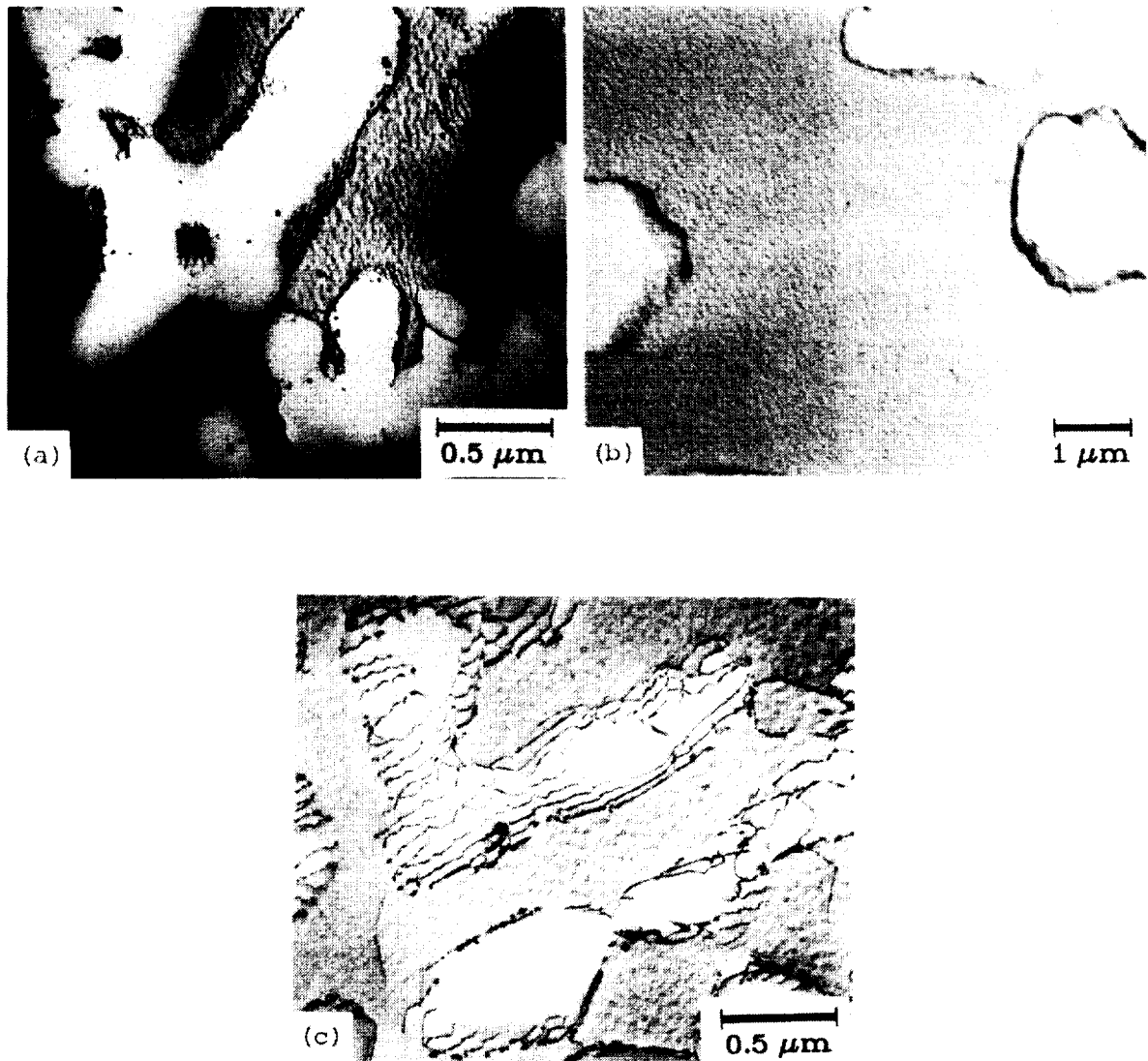


Figure 17. Dislocation structures at 1093<sup>0</sup>C showing interfacial arrays and coarsening. (a) 50%/min LCF. (b) 0.5%/min. LCF, showing greatly coarsened structure. (c) untested, hold at 1093<sup>0</sup>C for 49 hours. Some coarsening has occurred.

ORIGINAL PAGE IS  
OF POOR QUALITY

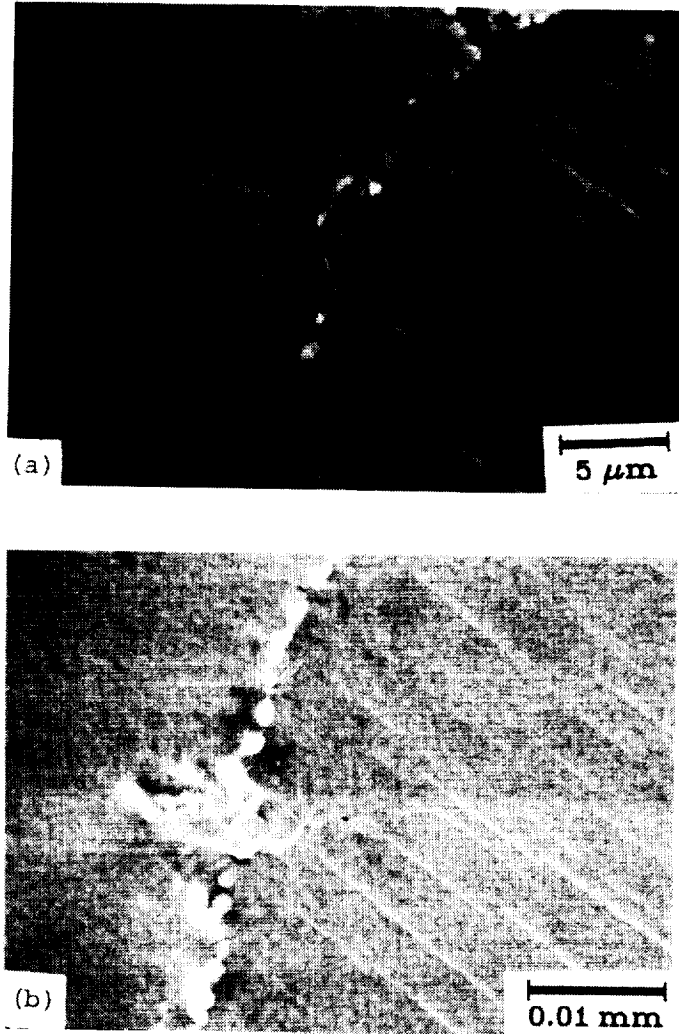


Figure 18. Grain Boundary Slip Behavior in 20<sup>0</sup>C LCF test. (a) Primary slip has occurred in both grains, with secondary slip on two systems in the grain on the left. Misorientation is approximately 28<sup>0</sup>. (b) Primary slip has occurred only in the grain on the right, with some secondary slip in the grain on the left. Misorientation is approximately 7<sup>0</sup>.

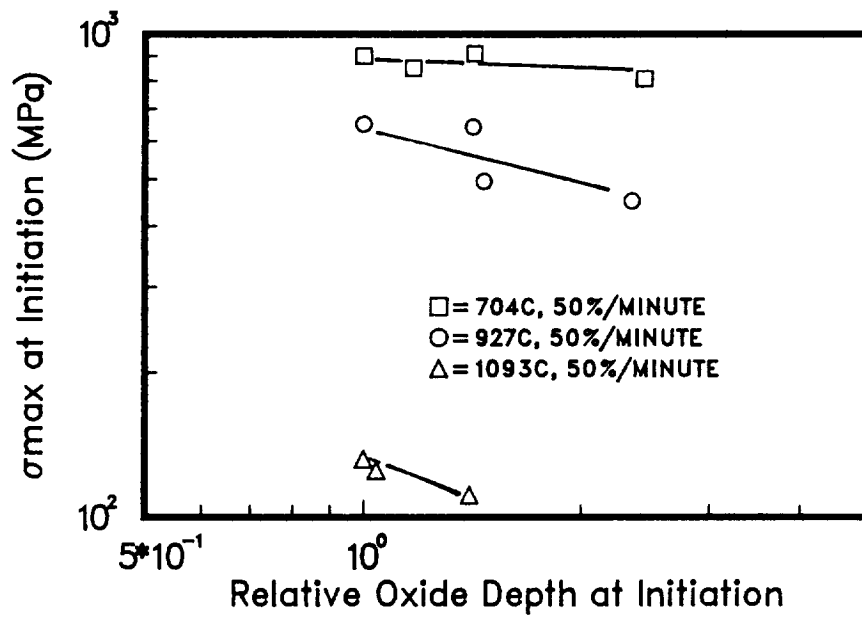


Figure 19. Stress at Initiation vs. Oxide Depth. This plot is based on the model proposed by Antolovich and coworkers [13, 14]. The slopes of the data at 704°C and 927°C are nearly horizontal, indicating little dependence of life on oxidation, while a stronger dependence is noted at 1093°C.

High-Temperature LCF of Ni-201 and 304L S.S.

by

G.R. Halford, Lewis Research Center, NASA

L.R. Johnson, Johnson Space Center, NASA

J.A. Brown, Aerojet Techsystems

ABSTRACT

The high-temperature, low-cycle fatigue characteristics have been investigated for two candidate alloys for use in the nozzle of an advanced design Orbital Maneuverable System (OMS) engine. Strain-controlled, low-cycle, creep-fatigue tests have been performed in air on a commercially pure nickel (Ni201) at 483, 594, and 760 C, and on AISI Type 304L stainless steel at 650, 760, and 870 C. Both continuous strain-cycling tests and compressive-strain, hold-time tests have been used in the evaluation. Direct comparisons are made between the two materials, and recommendations are presented as to which material offers the greatest potential for use.

## INTRODUCTION

### Current OMS Design

The OMS (Orbital Maneuvering System) is the Space Shuttle Orbiter's primary propulsion system for on-orbit operations, such as orbit circulation and orbital transfer. The OMS also provides the thrust necessary to perform orbit insertion, i.e., the final phase of the ascent trajectory after main propulsion system external tank separation from the Orbiter, rendezvous maneuvers, and deorbit. In addition, the OMS is used during Shuttle launch abort operations to provide additional thrust for critical maneuvers to deplete the OMS propellant to an acceptable level (Orbiter propellant mass fraction) for Orbiter flyback and landing. Typical OMS mission duty cycle profiles are shown in fig. 1. On a given flight, the number of OMS maneuvers may vary from a minimum of 3 to approximately 17 and the engine total accumulated operating time may vary from a minimum of approximately 300 seconds to a maximum of 1200 seconds (limited by the amount of propellant onboard). The OMS is housed in two independent pods located one on each side of the Orbiter aft fuselage. Each pod consists of a high-pressure helium propellant pressurization subsystem, fuel and oxidizer propellant tank and distribution subsystem, and the engine subsystem. The pod also contains the aft RCS (Reaction Control System) used for on-orbit attitude control and small differential velocity maneuvers.

The OMS engine (OME) subsystem is a pressure-fed 26,690-N(6,000 lbf) thrust engine that utilizes NTO (nitrogen tetroxide) as its oxidizer and MMH (monomethyl hydrazine) as its fuel propellants. These propellants are hypergolic in nature; therefore, no ignition system is required to initiate combustion. The OME is regeneratively cooled using the fuel propellant as its coolant via circulation through channels in the combustion chamber. After being routed through the cooling jacket, the fuel is then injected into the combustion chamber, where it reacts with the oxidizer. The current OME has the nominal operation characteristics shown in table I.

## Uprated OMS Design

An uprated version of the OMS is currently being investigated by the NASA-JSC (Johnson Space Center) Propulsion and Power Division. The development of an uprated engine for the OMS is an attractive project from several standpoints. An appreciable Shuttle payload gain is achievable with relatively minor Orbiter impacts and a high performance, man-rated storable-propellant engine is available for possible future upper stage applications. The approach to OMS uprating that is currently being pursued is the use of a gas generator cycle pump-fed engine in place of the current pressure-fed engine to increase engine chamber pressure. The pump-fed engine decouples the engine operating pressures from the propellant tank pressures. By this means, the potential of reducing propellant tank pressures is provided and if implemented, an OMS pod structural weight reduction (approximately 499 Kg (1100 lbm) total) is possible. Also, the engine, by operating at a higher chamber pressure, can have a greater nozzle expansion ratio in the same envelope, resulting in increased engine Isp (specific impulse). Higher engine Isp translates into significant benefits to the Orbiter in terms of increased payload capability, increased differential velocity capability, or additional excess propellant for scavenging. For every second of Isp increase over the current OMS engines, the propellant mass requirement is reduced by approximately 34 Kg (75 lbm) or the Orbiter payload capability is increased by this amount. If additional differential velocity were desired instead of reduced propellant mass (increased Orbiter payload capability), each second gained in engine Isp results in an increase in differential velocity capability of 0.91 m/sec (3 ft/sec).

The resulting uprated OME design characteristics also shown in table 1, have been selected primarily with the overall objective in mind of minimizing the impact to the Orbiter. A primary objective is to avoid any structural changes in the OMS pod/Orbiter interface and to have no change in the OME envelope; at the pod/engine interface, any struc-



tural changes required shall be minor enough to avoid requalification of the pod structure and to preclude any impact to the pod thermal requirements. To avoid impacts to the operational characteristics of the Orbiter, it is necessary to maintain the 304.8 m/sec (1000 ft/sec) differential velocity capability and to maintain the current engine redundancy and contingency operations capability.

Significant issues concerning the uprated OME are currently being addressed in the "Uprated OME Component Demonstration Program". This activity is being conducted by Aerojet TechSystems Company under NASA-JSC contract NAS9-17215. The objective of this program is to conduct the trade studies and design efforts necessary to define the preferred uprated OME characteristics, and fabricate and test critical components of the uprated OME to demonstrate feasibility of the performance, life, and operational goals. Issues associated with the Uprated OME and its components include the attainment of the required Isp and combustion stability characteristics at the revised operations, selection of engine chamber pressure and thrust chamber materials that will combine to give acceptable engine life, and demonstration of turbopump and gas generator characteristics compatible with Shuttle program requirements.

Selection of engine chamber pressure 2413 KPa (350 psia) is the most significant issue affecting the uprated engine performance. From the performance standpoint, the higher the pressure the better, since a higher pressure enables a higher nozzle area ratio in the constrained envelope. However, the higher throat heat flux at increased chamber pressure results in combustion chamber wall temperatures that severely impact chamber cycle life as the combustion chamber pressure is increased. The current OME has a predicted chamber life of 137 cycles (engine burns); if the current stainless steel liner were retained, operation at the higher chamber pressure would result in a predicted life in the vicinity of 25 cycles. To attain reasonable life at this higher pressure operating point will require a change in chamber

material; the most likely candidate material at this time is the nickel alloy Ni201.

This material is being considered because it appears to have the best overall properties (low-cycle fatigue, weldability, EF bondability, high thermal conductivity) that are critical to this application. However, mechanical design data, especially LCF (Low-Cycle Fatigue), at elevated temperatures are very limited. As a result, LCF testing was initiated at the NASA LeRC (Lewis Research Center) in the Structures Division's Fatigue and Fracture Branch to evaluate the high-temperature fatigue characteristics of Ni201. Resulting data from this program shall be used to analytically predict the usable design life of the combustion chamber liner. Comparative data for the current bill-of-material alloy, 304L S.S., is also being obtained.

#### EXPERIMENTAL DETAILS

##### Materials

The two alloys for the experimental evaluation were selected because of their known high ductility and suspected resistance to thermal low-cycle fatigue. The 304L stainless steel is the bill-of-material for the current OMS engine, and the Ni201 alloy is being given serious consideration for the upgraded OMS design as a direct replacement for the 304L S.S. Low-cycle fatigue is one of the dominant failure modes to be resisted in the OMS engine because of the severe thermal-strain fatigue cycles imposed during operation. Large cyclic strains result in very low fatigue lives. Fortunately, only a maximum of a few hundred cycles are required for an adequate design. The experimental program has been limited to the life range between 100 and 10,000 cycles to failure.

Both alloys were purchased by Aerojet TechSystems from Harvey Titanium Ltd of Santa Monica, CA.



## Ni201

The commercially pure nickel alloy, Ni201 (ASTM-B-160-81, Heat No. 2170, Teledyne mill) was purchased in the form of annealed (760 C (1400 F)/35 min., air cool) thick-walled pipe (165 mm (6.5") O.D. x 76.2 mm (3.0") I.D.). Chemical composition is listed in table II. The room temperature hardness was Rockwell "B" 47. Yield and ultimate tensile strengths were reported to be 134 MPa (19.5 ksi) and 374 MPa (54.2 ksi), respectively at room temperature. Ductility was reported to be 57.0 percent elongation and 92.1 percent reduction of area.

Uniform gage length fatigue specimens with threaded ends were machined and shipped to the Lewis Research Center for testing in their High Temperature Fatigue and Structures Laboratory. The specimen geometry is shown in fig. 2. This specimen design was used for both the tensile and fatigue tests. No heat treatment was performed after specimen machining

## 304L Stainless Steel

The 304L austenitic stainless steel was purchased in the form of 19.4 mm (0.750 inch) diameter round bar stock (Universal Cyclops Heat No. 1G6074). Bars were mill annealed for 20 minutes at 1052 C (1925 F) and water quenched to a hardness of 140BHN. Chemical composition is given in table II. Room temperature yield and ultimate tensile strengths were reported to be 208 MPa (30.1 ksi) and 546 MPa (79.2 ksi), respectively. The strength is about 50% greater than for the Ni201 alloy. Tensile elongation and reduction of area were 65.0 and 79.5 percent, respectively. Specimens were machined and shipped to the Lewis Research Center for testing. No heat treatment was applied to the specimens prior to testing. The specimen geometry was the same as used for the Ni 201 material.

## Test Equipment

Tensile tests were performed on conventional tensile testing machines in accordance with applicable ASTM standards. A clam-shell, wire-resistance furnace was employed to heat the specimens to the test temperatures.

The isothermal low-cycle fatigue tests were performed on closed-loop, electro-hydraulic, servo-controlled equipment. All tests were strain controlled using a diametral extensometer on the uniform gage length specimens. Heating in ambient air was achieved by passing large alternating current (several hundred amps.) directly through the specimen at low potential drop (1 to 2 volts) across the gage section. Because of the large heat losses through the water cooled grip ends, the temperature profile along the gage length of the specimen was parabolic, being maximum at the center of the gage length. The diametral strain was measured at the maximum temperature location. Maximum temperature was measured by optical pyrometers. At temperatures of 760 and 870 C (1400 and 1600 F), a disappearing-wire pyrometer was used; at lower temperatures of 483, 594, and 760 C (900, 1100, and 1400 F), a two-color, infrared, optical pyrometer was employed. A feedback temperature measurement for control was obtained with a thermocouple spot-welded directly to the specimen surface at a short distance (approximately 10 to 15 mm) from the highest temperature. The thermocouple location was sufficiently removed from the test zone that no fatigue failures initiated from the spot weld.

## Procedures

The programmed cyclic strain waveform was provided by conventional analog function generators. Three types of cyclic waveforms were employed: HRSC, High Rate Strain Cycling using a triangular waveform at a frequency of 0.2Hz; CHSC, Compressive Strain Hold Cycling using a

triangular waveform with a superimposed dwell period of two minutes at the peak compressive strain of each cycle; THSC, Tensile Strain Hold Cycling using a triangular waveform with a superimposed dwell period of two minutes at the peak tensile strain of each cycle. Only a limited number of THSC tests were performed. The waveforms are illustrated in fig. 3. During the dwell period, the stress relaxes from its peak level to a lower value. Future testing calls for five minute CHSC tests to be performed.

After loading the specimen into the low-cycle fatigue machine, the extensometer was attached at the specimen mid-section, and the specimen was heated to the desired temperature and held there for at least one hour prior to testing for thermal stabilization to occur. Load data were recorded continuously on a conventional strip-chart recorder and load and strain were recorded on an XY analog recorder.

Diametral strain results were converted to equivalent axial strain after testing using the following procedure: Diametral inelastic strain range measured from the XY plot was multiplied by two (inverse of the inelastic Poisson's ratio of 0.5 required for constancy of volume) to determine axial inelastic strain range, and axial elastic strain range was calculated by dividing the measured stress range by the modulus of elasticity; the total axial strain range is the sum of the elastic and inelastic axial strain ranges. Using this procedure avoids the necessity for having to know the value of the elastic Poisson's ratio.

Several different measures of cyclic life, in addition to failure into two pieces, were determined from the load versus time trace. The number of cycles was noted for three different levels of drop in cyclic load range; 5, 20, and 50%. In addition, a newly defined measure of life was also adopted. This failure life was defined as the number of cycles for which the ratio of the peak tensile stress to the peak compressive stress dropped from a stabilized value by a fixed

percentage. A value of 10% was used in the present series of tests. The idea behind this measure is to avoid the uncertainty of confusing cyclic strain softening with the drop in load carrying capacity due to specimen cracking. By considering the ratio of the peak stresses, the phenomenon of cyclic softening, which usually affects tensile and compressive load response equally, cancels, and only the loss of load bearing area in tension due to a crack is retained. The load bearing area in compression is largely unaffected by the presence of a crack, since as the crack closes, it can transmit loads across the crack face as if it were not there. In the absence of cyclic softening, the 10% load ratio drop corresponds directly with a 5% load range drop.

## RESULTS AND DISCUSSION

### Tensile Behavior

Tensile test results for both alloys are summarized in table III, and plotted in fig. 4 as a function of temperature. The modulus of elasticity values were determined from the literature. In the case of the Ni201, the modulus values were determined by a pulse-echo technique (ref. 1), hence the results are considered to be representative of the dynamic modulus. The 304L results represent static modulus values (ref. 2). The modulus at 870 C(1800 F) was obtained by extrapolation from lower temperature data.

### Cyclic Stress-Strain Behavior

During the course of generating the LCF data, the cyclic stress-strain response characteristics can be observed and documented. For the present series of tests, the stabilized stress ranges and inelastic strain ranges, as determined from the XY plots, are presented in tabular form along with the LCF results contained in tables IV and V.

Stabilized stress-strain results for both alloys were achieved well before the half-life of the specimens was reached. The influence of temperature in reducing strength is clearly evident from a cursory study of the table. The introduction of a two minute hold period at peak strain further reduces the strength, but only at the highest temperature for each alloy. A comparison of the cyclic stress-strain response under compressive hold period conditions for the two alloys at their only common test temperature, 760 C(1400 F), shows the 304L S.S. to be nearly four times stronger than the Ni201. Such a direct comparison, shown in fig. 5, however, may not be in order with respect to performance in an engine service environment since one would expect lower operating metal temperatures for the Ni201 compared to the 304L S.S. because of the nickel's superior thermal conductivity. Appropriate temperatures for strength comparison would have to be determined from a thermal analysis of a specific OME component(face plate, liner, etc.). The limited cyclic stress-strain response from CHSC tests of the Ni201 at 483 and 594 are also included in fig. 5 to demonstrate that strength differences between the alloys are not significant when lower temperature Ni201 behavior is compared with the higher temperature(760 C) 304L S.S. response. Similar observations hold for the HRSC results.

Not shown in fig. 5 is the transient cyclic hardening and softening response exhibited by the two alloys. Qualitatively, the Ni201 alloy initially hardened a significant amount(by as much as a factor of two or more in stress range), stabilized for approximately half of the life, then proceeded to cyclically soften until failure into two pieces occurred. Greater cyclic hardening was observed at the lowest temperature than at the highest temperature. The 304L S.S. cyclic hardening response was quite similar to the Ni201 in terms of the degree of hardening, i.e., slightly greater than a factor of two at the lowest temperature, down to a factor of 1.5 at the highest temperature. However, the 304L S.S. stabilized sooner in life, and the degree of cyclic softening immediately prior to cracking was less than for the Ni201.

## Low-Cycle, Creep-Fatigue Behavior

Ni201 - Only limited LCF data have been generated to-date for the Ni201 alloy, because of experimental difficulties brought about by the alloy's high thermal conductivity. Several low voltage power transformers have been overheated and ruined as a result of the high current requirements for direct resistance heating of this alloy. Attempts to conduct tests at strain ranges above about two percent met with premature cyclic buckling failures, so the experimental program was conducted at lower strain levels. The low-cycle, creep-fatigue and cyclic stress-strain results obtained are summarized in table IV.

As expected, the HRSC low-cycle fatigue results for this ductile alloy show an excellent resistance to large inelastic cyclic strains. For example, from the Manson-Coffin LCF plots of fig. 6, an inelastic strain range of 1.0% in a HRSC test yields a life of 1000 to 4000 cycles to failure, depending upon temperature. While the temperature dependence on cyclic lifetime is not particularly large, there appears to be a trend for the life to increase at the highest temperature of 760 C(1400 F). This observation is consistent with the fact that the ductility as measured by the reduction of area in the tensile tests showed a modest increase as the test temperature rose.

Only three successful CHSC tests have been completed to failure to date, so we have little information upon which to base preliminary conclusions. Nevertheless, only a small effect on cyclic lifetime of the two minute dwell period has been observed. Again, it appears that the higher the temperature, the greater the cyclic failure life for the CHSC tests. Figure 7 better illustrates the temperature dependence of the LCF curves, with and without hold times. Here the influence of temperature is more apparent. We have refrained from drawing individual curves through these data, and have only shown bounding lines to indicate maximum and minimum behavior. As can be seen, more of the low temperature data fall near the lower bound line while the high temperature results are closest to the upper bound.



Four THSC tests were performed early in the program at 760 C(1400). These, as expected, foreshortened the cyclic lifetime considerably, as seen in fig. 6. Visual inspection of the fracture surfaces indicated severe intergranular cracking compared to specimens failed in HRSC or CHSC tests.

Only the inelastic strain range LCF curves have been discussed above. It is also appropriate to examine the total strain vs. cyclic life response, since the application is one of a thermal strain driven nature in which a fixed mechanical total strain is imposed by the constrained thermal expansion.

The total strain range creep-fatigue behavior of the Ni201 is shown in fig. 8. Again, bounds have been drawn to represent the extremes of the results, with the exception of the THSC results that are clearly different from the HRSC and CHSC behavior. The superior resistance to creep-fatigue at the highest temperature is still observed in the high-strain, low-life regime. However, as the total strain decreases and is more and more dominated by the elastic strain range resistance at longer lives, it is expected that the lower temperature behavior will become superior. This trend is brought about by the significant drop-off in strength (and hence elastic strain) with increasing temperature. Concerns for the OME, however, are in the large strain, short life region of the curve.

Metallography and fractography of fatigued specimens is underway, but has not been completed in time for inclusion herein.

304L S.S. - Considerably more data have been obtained for the 304L S.S. alloy, as shown in table V. As was the case with the Ni201 alloy, tests at strain ranges above about 2 percent resulted in premature cyclic buckling failures. Figure 9 displays the HRSC and CHSC results generated to-date in the form of Manson-Coffin LCF curves.

Cyclic lives for an inelastic strain range of 1.0% are not as high as they are for the Ni201, but are still reasonable, being between 300 and 1000. A compressive hold period of two minutes exerts a negligible affect on cyclic endurance, regardless of the temperature investigated.

Temperature has an opposite effect on cyclic life for the 304L S.S. as compared to the Ni201. As shown in fig. 10, life decreases as the temperature of testing increases; 870 C(1600 F) results fall nearest the lower bound curve, while the 650 C(1200 F) data are closest to the upper bound curve. Although no THSC tests were performed on this alloy, it could be expected that significant life losses would be incurred based upon published literature. Again, this is consistent with the observation from fig. 5 that the tensile ductility also decreases with increasing temperature.

Although no THSC tests were performed on this alloy, published results from the open literature(for example, ref. 3) indicate a substantial life loss through the introduction of tensile hold periods that introduce relaxation type creep strains.

When the 304L S.S. creep-fatigue results are examined on a total strain range basis, fig. 11, the affect of temperature on cyclic life is even more pronounced than when comparison is made on an inelastic strain range basis. Not only does the inelastic strain range vs. life drop with temperature, but so does the strength(and hence elastic strain range). This leads to a modest life reduction in the high-strain, low-life region, and a substantial reduction the low-strain, long-life regime.

Comparison of Ni201 and 304L S.S. - An important objective of the program was to generate comparative creep-fatigue results for the two alloys so that one could be identified as a superior alloy for construction of components in an uprated OMS engine. To this end, the

cyclic stress-strain response has been compared in an earlier section, and it was observed that little strength differences existed if proper temperatures for comparison were considered. A similar observation can be made for the creep-fatigue resistances of the two alloys. Figure 12 compares the total strain range vs. life curves under CHSC conditions for the two alloys at the common temperature of 760 C(1400 F). While a life difference on the order of a factor of two to three would be realized at this temperature for the same imposed total strain range, less of a life difference would be expected if it is realized that the Ni201 alloy would likely run at a lower temperature than the 304L S.S. in the same operating environment. Although results to-date are sparse, the trend is for only a 30% improvement in life of the Ni201 alloy at 483 or 594 C(900 or 1100 F) compared to the 760 C(1400 F) life of the 304L S.S. Similar observations can be made using the HRSC results.

#### SUMMARY AND CONCLUSIONS

The high-temperature, low-cycle, creep-fatigue resistances of Ni201 and 304L S.S. have been investigated under isothermal strain-cycling conditions. Testing included continuous strain-cycling at 0.2Hz and compressive strain hold-time experiments with a two minute dwell period. Results have been presented in terms of inelastic strain range and total strain range vs. life curves. Comparisons between the two alloys shows a greater strength for the 304L S.S., but a lower creep-fatigue resistance. Differences are the greatest when comparisons are made at a single common temperature. However, when high-temperature behavior of the 304L S.S. is compared to lower temperature Ni201 behavior, these differences become less significant.

## FUTURE DIRECTIONS

The preliminary results contained herein are being supplemented by further testing in the Lewis Research Center's High Temperature Fatigue and Structures Laboratory. In addition to filling out the present test matrix, compressive hold-time tests with a five minute dwell period are in progress. A few simulated thermomechanical fatigue experiments are to be conducted to ascertain the sensitivity of the creep-fatigue lives of these alloys to such additional rigors of loading. These results will enable a more realistic assessment of the capabilities of both alloys to resist the engine operating conditions to be found in an updated version of the OME.

## REFERENCES

1. Farraro, R. and McLellan, R.B.: Temperature Dependence of the Young's Modulus and Shear Modulus of Pure Nickel, Platinum, and Molybdenum. Metallurgical Transactions, vol. 8A, October 1977, pp. 1563-1565.
2. Boiler and Pressure Vessel Piping Code Case N-47-22, Section III, Nuclear Components, ASME, New York, NY 1983.
3. Saltsman, J.F. and Halford, G.R.: Application of Strainrange Partitioning to the Prediction of Creep-Fatigue Live of AISI Types 304 and 316 Stainless Steel. Transactions, ASME, Vol. 99, Series J, Journal of Pressure Vessel Technology, No. 2, May 1977, pp. 264-271.

TABLE IV - Low-Cycle, Creep-Fatigue Results for Ni201

<u>900F(483C)</u>								
N03 HRSC	14,805	no data	0.00310	0.00147	0.00457	42.0	290	
N20 HRSC	450	450	0.01812	0.00206	0.02018	59.0	407	
N17 HRSC	416	343	0.02116	0.00198	0.02314	54.6	376	
N18#CHSC	2,517	2,350	0.00640	0.00213	0.00853	52.6	362	
N32 CHSC	3,315+	3,315+	0.00054	0.00125	0.00179	35.8	247	
<u>1100F(594C)</u>								
N21 HRSC	664	616	0.01465	0.00162	0.01627	44.0	303	
N09#HRSC	2,772	2,510	0.00675	0.00150	0.00825	40.7	281	
N38 CHSC	2,656+	2,656+	0.00123	0.00134	0.00257	36.2	250	
<u>1400F(760C)</u>								
N42 HRSC	938	670	0.01470	0.00140	0.01610	34.6	239	
N30 HRSC	1,178	989	0.01470	0.00120	0.01590	29.7	205	
N45 HRSC	1,264	1,155	0.01835	0.00125	0.01950	31.1	214	
N44 HRSC	7,344	7,344	0.00448	0.00085	0.00533	21.1	145	
N43#HRSC	7,772	5,786	0.00456	0.00086	0.00542	21.3	147	
N46 THSC	315	303	0.01496	0.00102	0.01598	25.3	174	
N35 THSC	436	321	0.01480	0.00112	0.01590	27.8	192	
N39 THSC	740	740	0.00426	0.00064	0.00490	15.8	109	
N49#THSC	863	863	0.00434	0.00077	0.00511	19.0	131	
N06 CHSC	358	358	0.03224	0.00118	0.03342	29.3	202	
N52 CHSC	645	645	0.01814	0.00096	0.01910	23.7	163	
N15 CHSC	4,705	4,705	0.00676	0.00090	0.00766	22.2	153	

\* HRSC = High Rate Strain Cycle(0.2Hz)

CHSC = Compressive Strain Hold Cycle(0.2Hz + 120 sec. dwell)

THSC = Tensile Strain Hold Cycle(0.2Hz + 120 sec. dwell)

# Metallographic sample prepared.

+ Specimen did not fail, test discontinued.

TABLE V - Low-Cycle, Creep-Fatigue Results for 304L S.S.

Spec No.	Test* Type	Cycles to		Strain Range			Stress Range	
		Failure Nf	Initiat. Ni	Inelastic cm/cm	Elastic cm/cm	Total cm/cm	ksi	MPa
<u>1200F(650C)</u>								
A39	HRSC	17,952	17,952	0.00187	0.00247	0.00434	51.6	356
A46	HRSC	1,824	1,824	0.00436	0.00320	0.00768	69.4	478
A28#	HRSC	1,824	1,756	0.00660	0.00366	0.01030	76.4	527
A45	HRSC	255	246	0.01770	0.00436	0.02210	91.0	627
A19	CHSC	3,849	3,191	0.00310	0.00264	0.00570	55.1	380
A44#	CHSC	1,103	902	0.00710	0.00320	0.01030	67.0	462
A32	CHSC	216	212	0.01840	0.00450	0.02290	94.5	652
<u>1400F(760C)</u>								
A16	HRSC	138,432+	138,432+	0.00100	0.00180	0.00280	33.5	231
A41	HRSC	6,106	5,962	0.00206	0.00207	0.00413	39.8	274
A02	HRSC	3,420	3,250	0.00324	0.00259	0.00583	49.8	343
A37	HRSC	2,352	2,248	0.00454	0.00296	0.00750	56.9	392
A40#	HRSC	1,601	1,405	0.00660	0.00370	0.01030	70.8	488
A24	HRSC	210	207	0.02160	0.00440	0.02600	84.3	581
A29	HRSC	118@	110	0.02160	0.00540	0.02700	102.7	708
A21	CHSC	4,224	4,224	0.00311	0.00264	0.00575	50.8	350
A42#	CHSC	1,036	1,036	0.00689	0.00342	0.01031	65.8	454
A30	CHSC	119@	117	0.02130	0.00510	0.02640	97.0	669
<u>1600F(870C)</u>								
A43	HRSC	2,339	2,339	0.00240	0.00137	0.00377	23.3	161
A38#	HRSC	834	834	0.00518	0.00170	0.00688	29.9	206
A25	HRSC	285	285	0.01900	0.00287	0.02190	48.7	336
A22	CHSC	1,618	1,618	0.00350	0.00170	0.00520	31.5	217
A31#	CHSC	439	439	0.00746	0.00218	0.00964	37.0	255
A26	CHSC	188	188	0.01920	0.00244	0.02160	41.4	285

- \* HRSC = High Rate Strain Cycle(0.2Hz)  
 CHSC = Compressive Strain Hold Cycle(0.2Hz + 120 sec. dwell)  
 THSC = Tensile Strain Hold Cycle(0.2Hz + 120 sec. dwell)  
 # Metallographic sample prepared.  
 @ Some specimen buckling observed at failure.  
 + Specimen did not fail, test discontinued.

TABLE I - Characteristics of Current and Updated OME.

<u>CHARACTERISTIC</u>	<u>CURRENT OME</u>	<u>UPDATED OME</u>
Thrust, N(lbf)	26,690(6000)	26,690(6000)
Isp, s.	315	315
Chamber Pressure, KPa(psia)	861.8(125)	2,413(350)
Mixture Ratio	1.65	1.90
Exh. Nozzle Expansion Ratio	55:1	154:1
Dry Weight, Kg(lbm)	134.7(297)	146(322)

TABLE II - Chemical Compositions of Alloys.

<u>304L S.S.</u>	<u>Ni201</u>
Cr-18.64	Mn-0.22
Ni- 9.52	Fe-0.10
Mn- 1.49	Si-0.03
Si- 0.72	Cu-0.01
Cu- 0.34	C -0.005
Mo- 0.16	S -0.001
S - 0.025	Ni-Balance
P - 0.024	
C - 0.023	
Fe- Balance	

TABLE III - Tensile Properties

<u>Test</u> <u>Temp</u>	<u>304L S.S.</u>								
	<u>Yield</u> <u>Strength</u>		<u>Ultimate</u> <u>Strength</u>		<u>Red. of</u> <u>Area</u>	<u>Modulus of</u> <u>Elasticity</u>			
	F	C	ksi	MPa	ksi	MPa	%	1000 MPa	1000 ksi
75	24	30.1	208	79.2	546	79.2	195	28.3	
1200	650	23.9	165	45.4	313	93.1	144	20.9	
1400	760	24.1	166	29.9	206	80.6	132	19.2	
1600	870	15.8	109	16.9	117	66.5	117	17.05	
		<u>Ni201</u>							
75	24	19.5	134	54.2	374	92.1	---	----	
900	483	21.3	147	31.7	219	92.5	197	28.6	
1100	594	20.9	144	25.6	177	93.1	187	27.1	
1400	760	12.7	88	17.4	120	94.0	171	24.8	

TABLE I - Characteristics of Current and Up-rated OME.

<u>CHARACTERISTIC</u>	<u>CURRENT OME</u>	<u>UPRATED OME</u>
Thrust, N(lbf)	26,690(6000)	26,690(6000)
Isp, s.	315	315
Chamber Pressure, KPa(psia)	861.8(125)	2,413(350)
Mixture Ratio	1.65	1.90
Exh. Nozzle Expansion Ratio	55:1	154:1
Dry Weight, Kg(lbm)	134.7(297)	146(322)



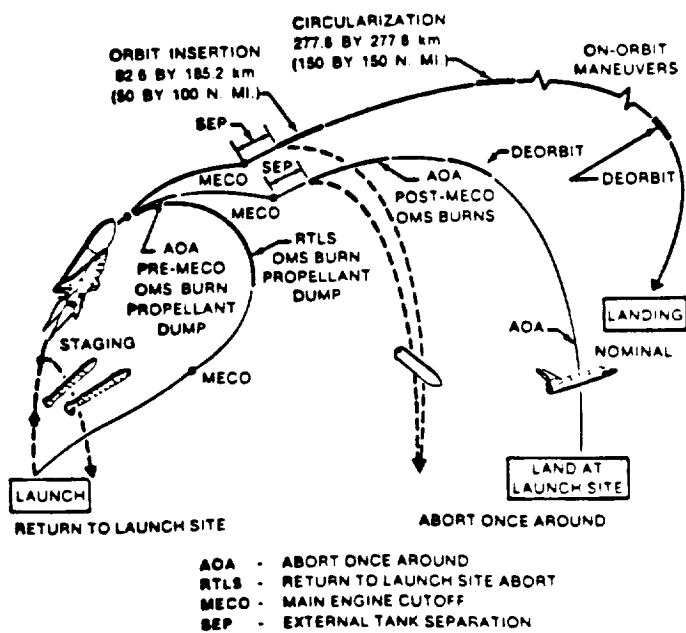
TABLE II - Chemical Compositions of Alloys.

<u>304L S.S.</u>	<u>Ni 201</u>
Cr-18.64	Mn-0.22
Ni- 9.52	Fe-0.10
Mn- 1.49	Si-0.03
Si - 0.72	Cu-0.01
Cu- 0.34	C -0.005
Mo- 0.16	S -0.001
S - 0.025	Ni -Balance
P - 0.024	
C - 0.023	
Fe - Balance	

TABLE III - Tensile Properties

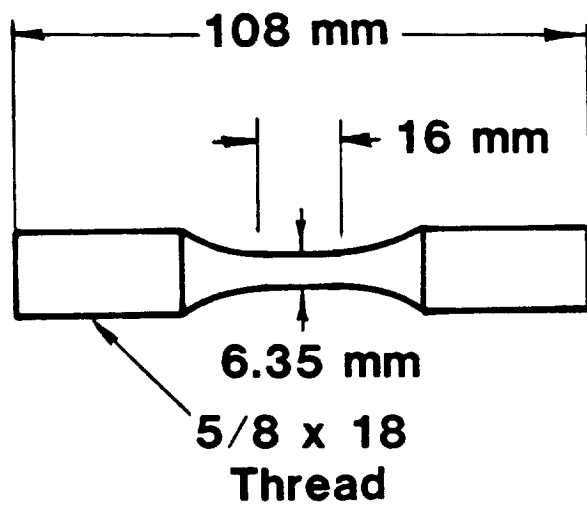
<u>Test</u>		<u>Yield</u>		<u>Ultimate</u>		<u>Red. of</u>	<u>Modulus of</u>		
<u>Temp</u>		<u>Strength</u>		<u>Strength</u>		<u>Area</u>	<u>Elasticity</u>		
F	C	ksi	MPa	ksi	MPa	%	1000 MPa	1000 ksi	
<u>304L S.S.</u>									
75	24	30.1	208	79.2	546	79.2	195	28.3	
1200	650	23.9	165	45.4	313	93.1	144	20.9	
1400	760	24.1	166	29.9	206	80.6	132	19.2	
1600	870	15.8	109	16.9	117	66.5	117	17.05	
<u>Ni201</u>									
75	24	19.5	134	54.2	374	92.1	---	----	
900	483	21.3	147	31.7	219	92.5	197	28.6	
1100	594	20.9	144	25.6	177	93.1	187	27.1	
1400	760	12.7	88	17.4	120	94.0	171	24.8	

ORIGINAL PAGE IS  
OF POOR QUALITY



# COMPONENTS OF TYPICAL OME MISSION DUTY CYCLES

FIGURE 1



**TENSILE AND FATIGUE TEST  
SPECIMEN GEOMETRY**

FIGURE 2

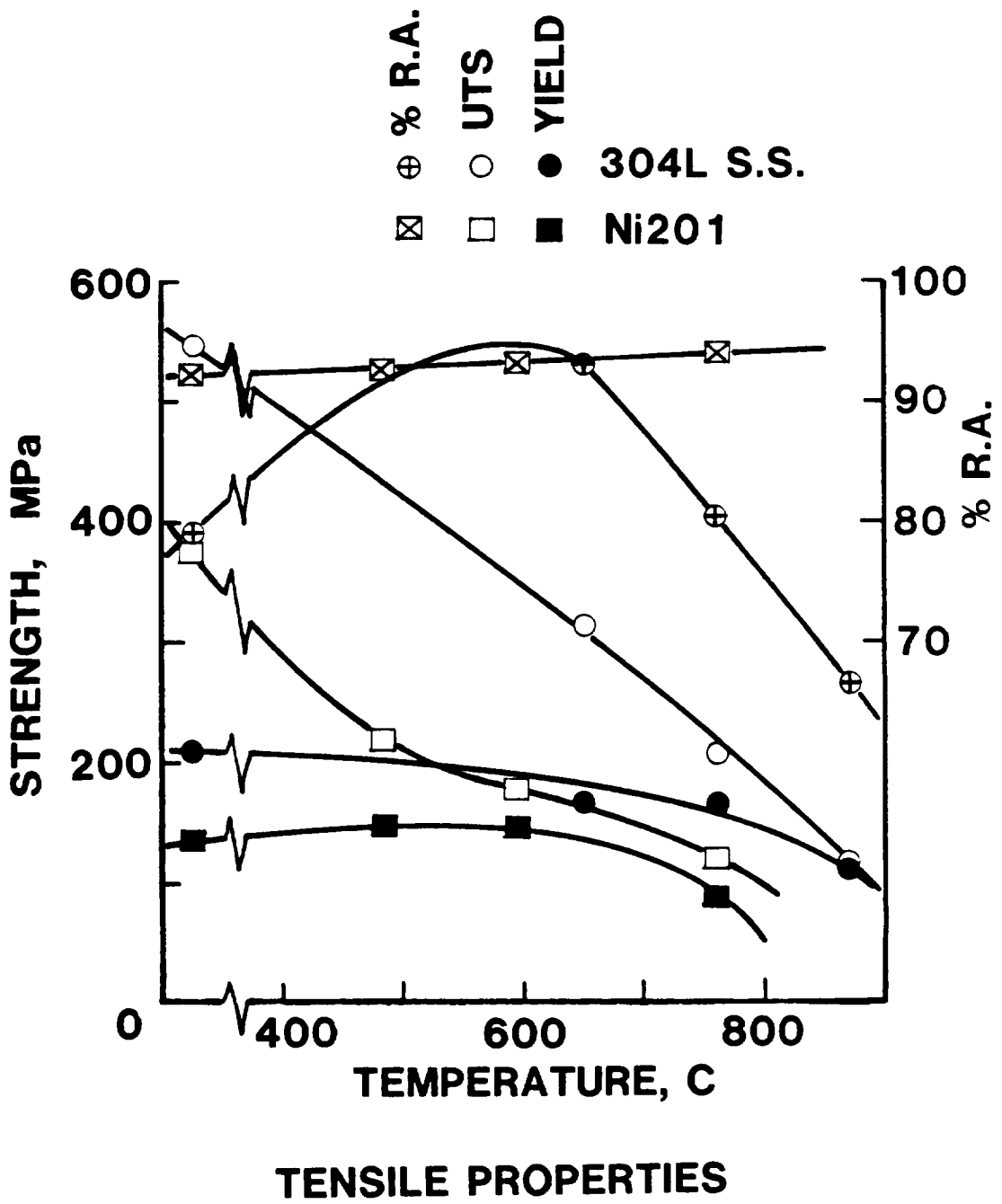


FIGURE 3

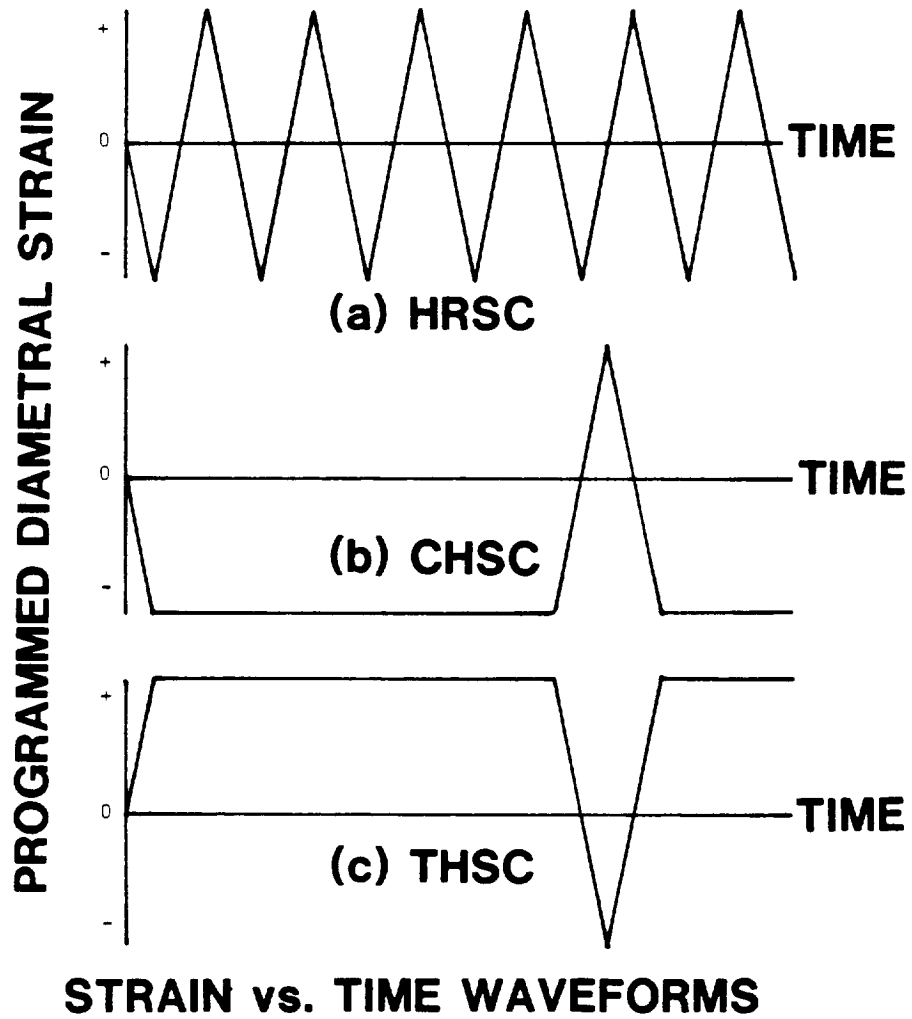
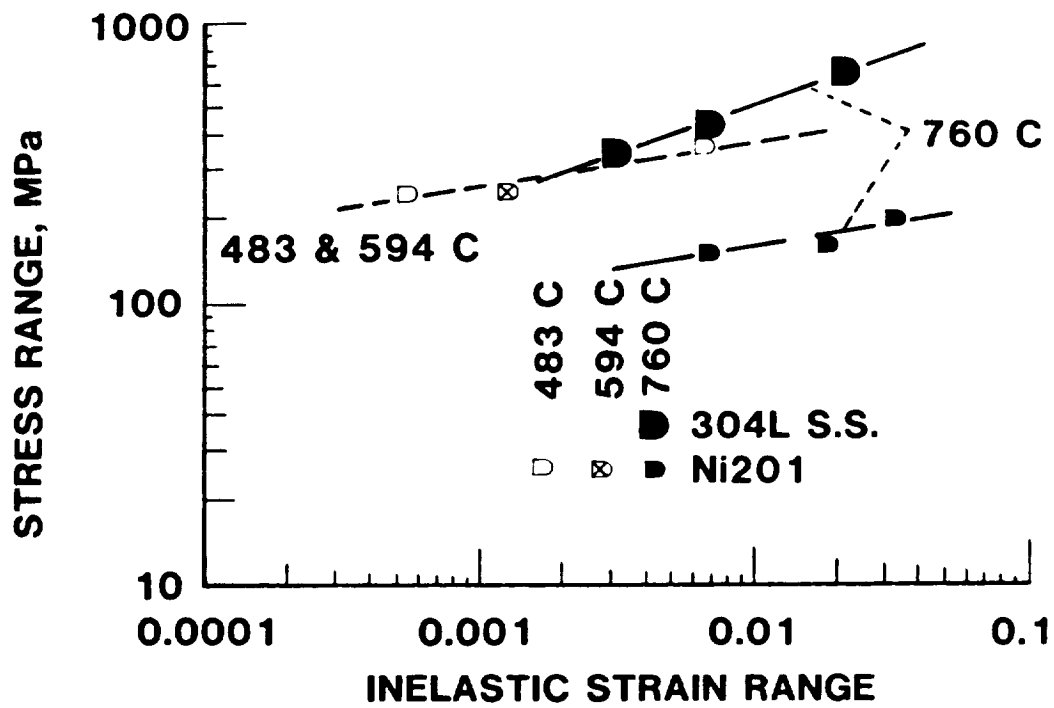
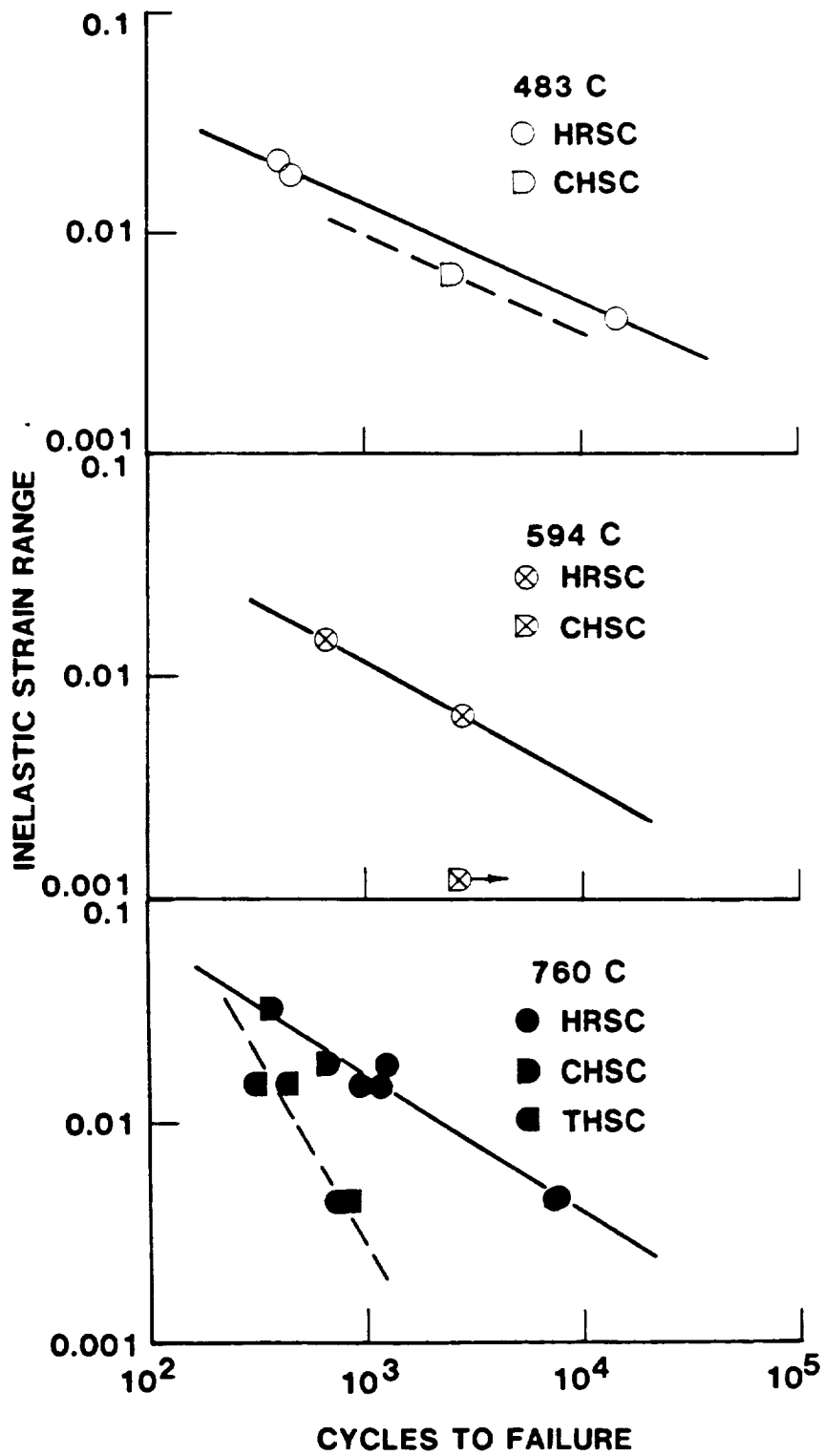


FIGURE 4



COMPARISON OF CYCLIC STRESS STRAIN RESPONSE

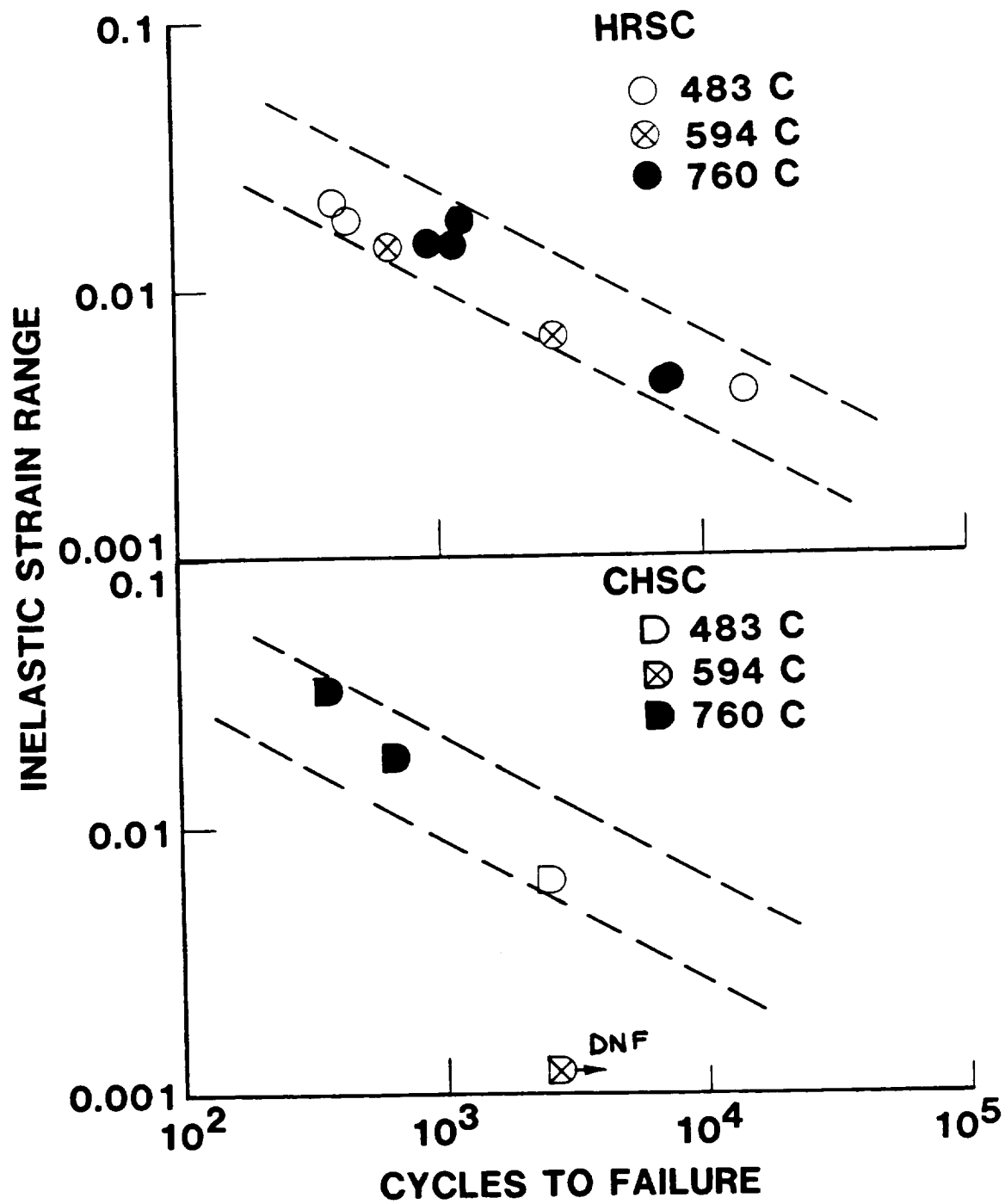
FIGURE 5



MANSON COFFIN CURVES FOR Ni201

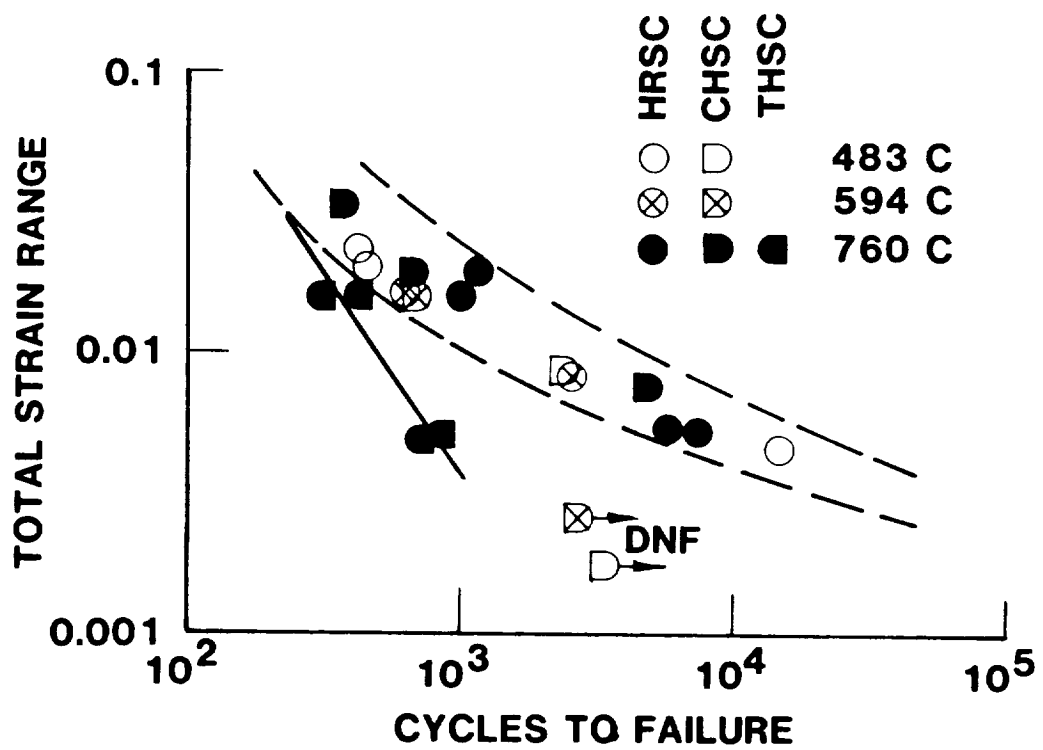
FIGURE 6





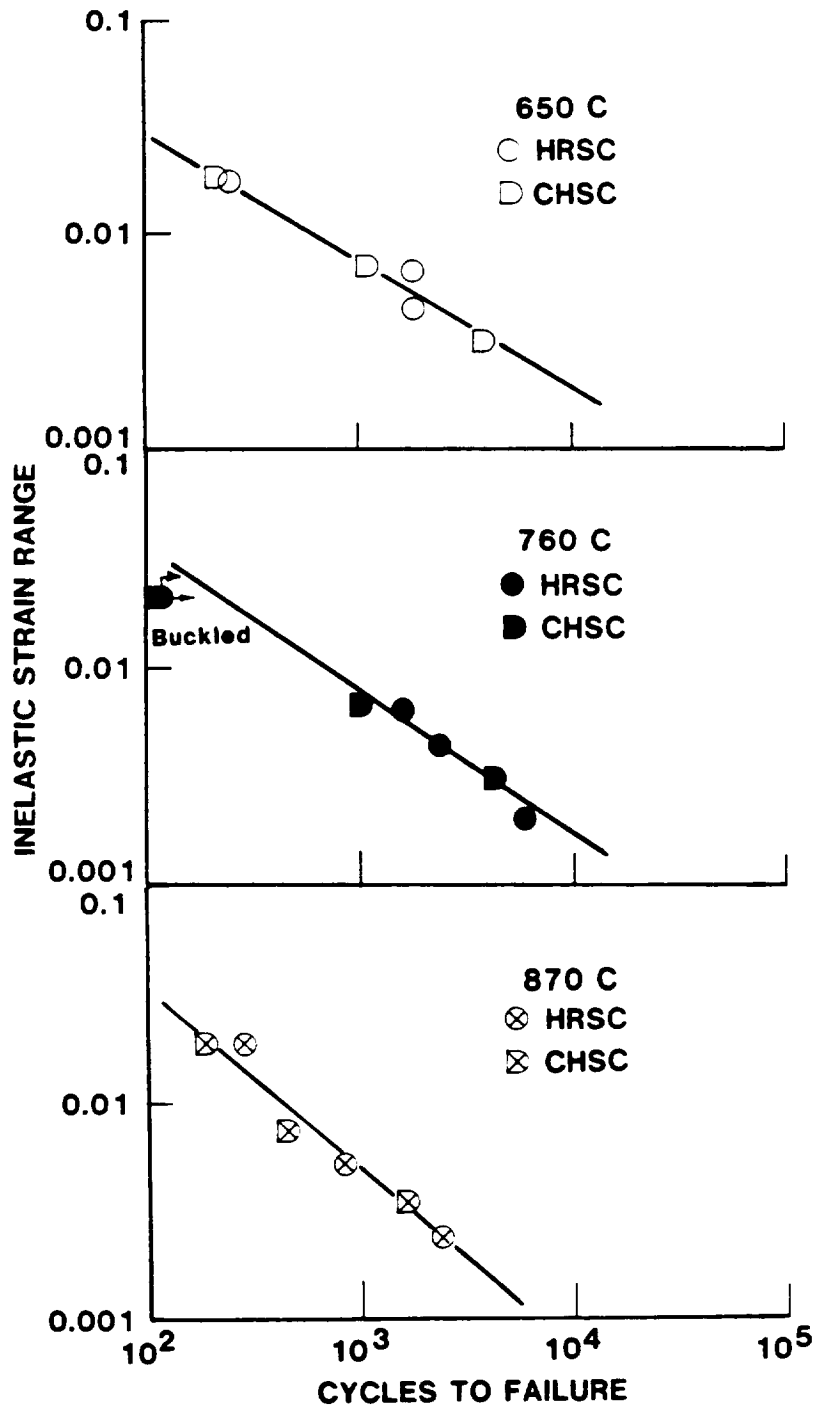
**MANSON COFFIN CURVES OF Ni201  
TEMPERATURE DEPENDENCE**

FIGURE 7



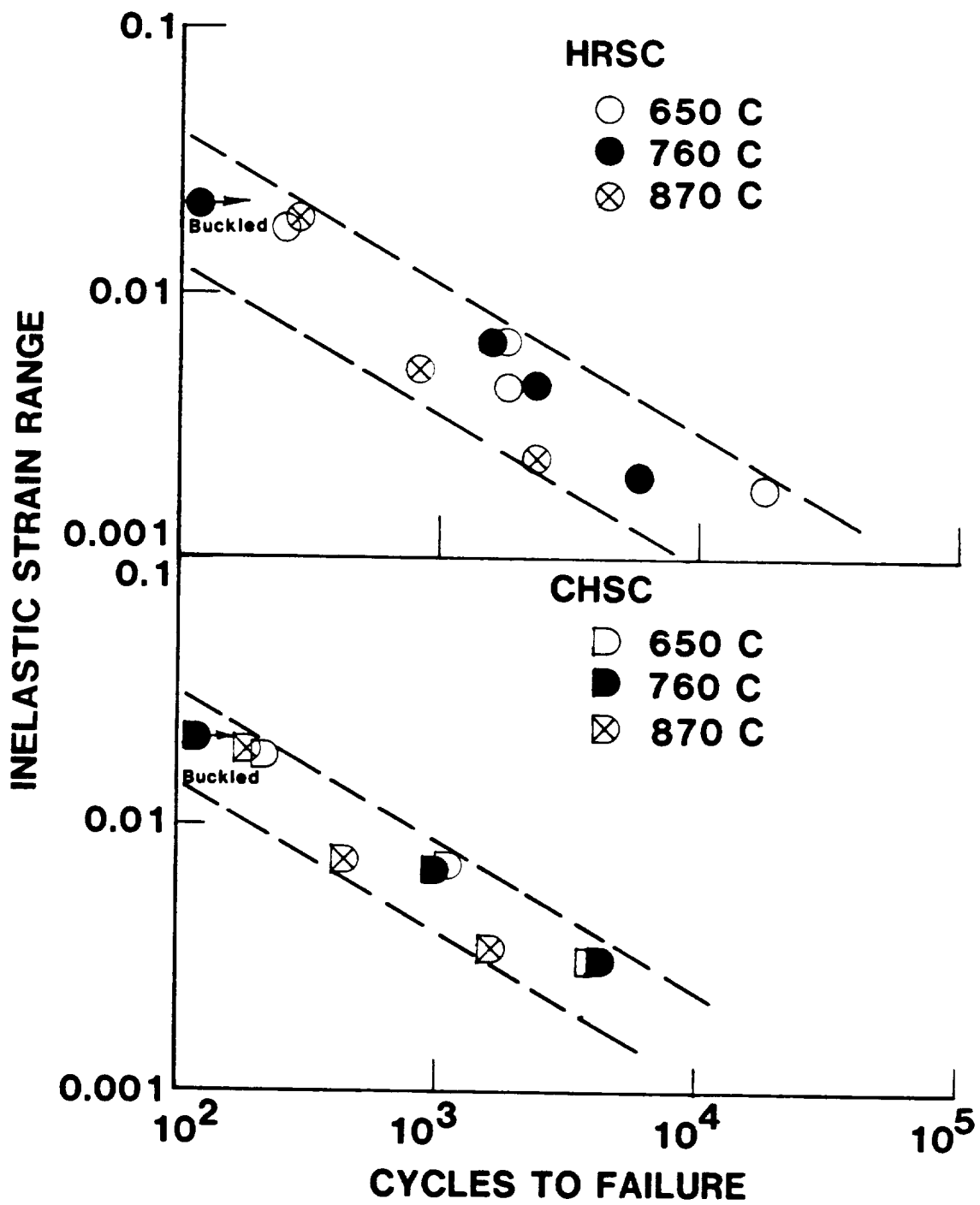
**CREEP FATIGUE BEHAVIOR OF Ni201**

FIGURE 8



MANSON COFFIN CURVES FOR 304L S.S.

FIGURE 9



**MANSON COFFIN CURVES OF 304L S.S.  
TEMPERATURE DEPENDENCE**

FIGURE 10

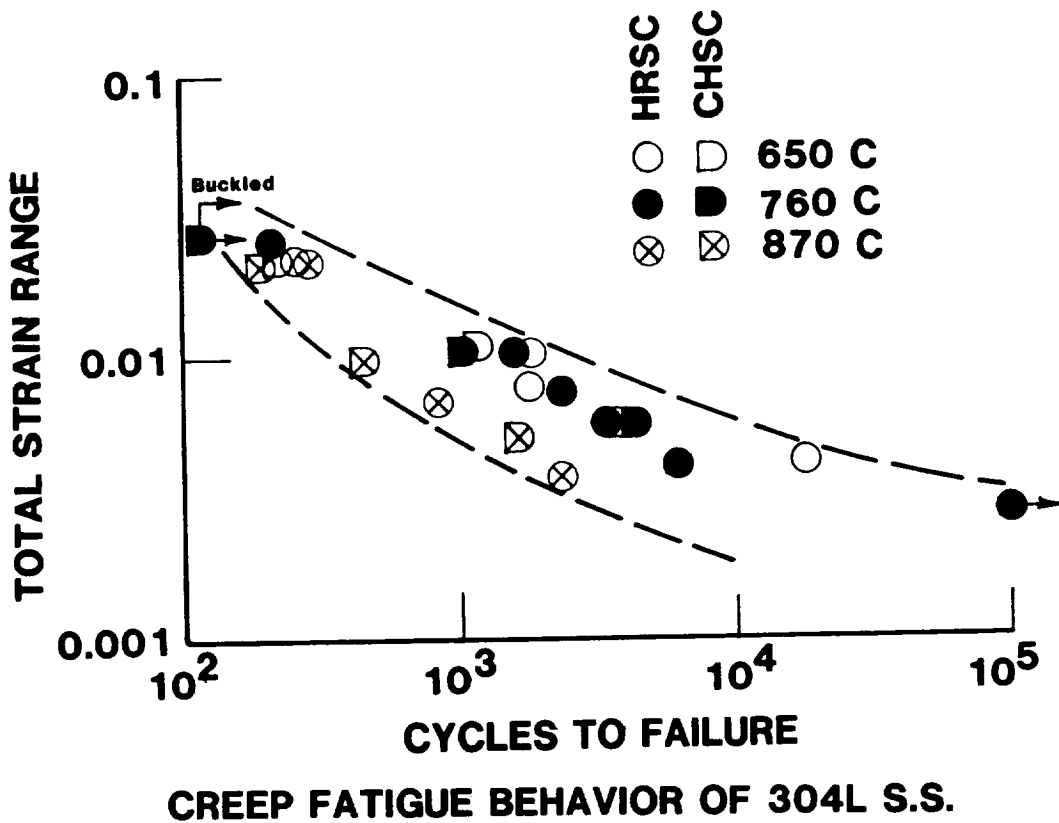
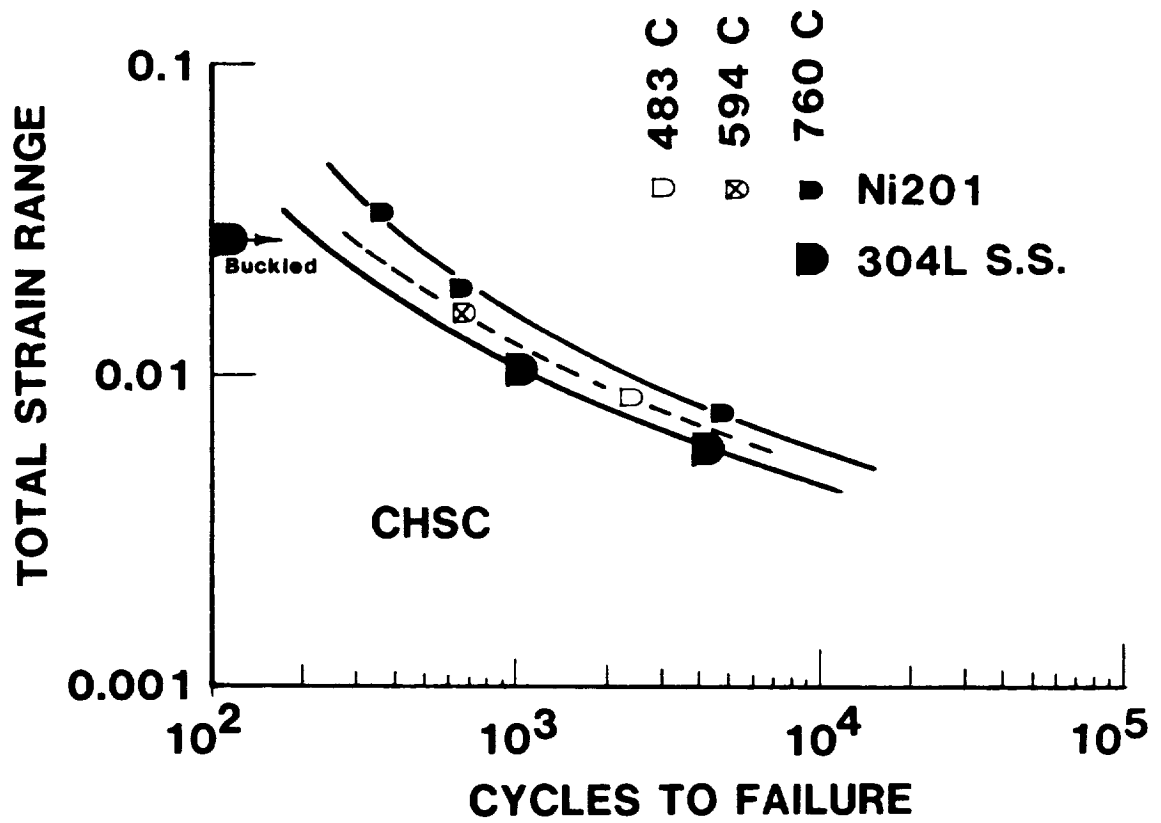


FIGURE 11



**COMPARISON OF CREEP FATIGUE BEHAVIOR  
Ni201 and 304L S.S. at 760 C**

FIGURE 12

FATIGUE CRACK RETARDATION FOLLOWING OVERLOADS IN  
INCONEL 718, Ti-5Al-2.5Sn, AND HAYNES 188

D. E. Matejczyk and R. P. Jewett

Rockwell International/Rocketdyne Division  
Canoga Park, California

D. W. Schmidt and G. C. Hresko III

Materials Research and Testing Division  
Professional Services Group  
Hellertown, Pennsylvania

Abstract

Overload effects on fatigue crack growth have been studied in Inconel 718, Ti-5Al-2.5Sn ELI, and Haynes 188 at several temperatures as a function of load ratio and of overload magnitude. Over the range of materials and experimental conditions studied, a range of overload mechanisms may be operative. Results are compared to a crack tip plastic zone model and a plastic wake closure model. Ti-5Al-2.5Sn ELI results are discussed in terms of crack branching and fracture surface microroughness.

Introduction

Application of a single overload or of block overloads can significantly effect subsequent constant amplitude fatigue crack growth. Any of a number of mechanisms can be responsible for the observed effects, and many models are available for incorporating these effects into life prediction analysis. Several recent publications review current overload models.<sup>1,2</sup> This paper presents results of an ongoing program examining and modeling overload effects in fatigue crack propagation for several alloys used extensively in advanced earth-to-orbit propulsion systems.

Materials

The alloys studied include Inconel 718, a nickel-base superalloy, Haynes 188, a cobalt-base alloy, and Ti-5Al-2.5Sn ELI. Inconel 718 was received as a 1.9-cm (0.75-inch) thick rolled plate. It was subsequently heat treated to the STA-1 condition [1038 C (1900 F) for 30 minutes in argon, cool to room temperature, 760 C (1400 F) for 10 hours in argon, furnace cool to 649 C (1200 F), total age time 20 hours]. Haynes 188 was received as a 2.5-cm (1-inch) thick solution-annealed rolled plate.

Ti-5Al-2.5Sn ELI was obtained as a 15 cm (6 inch) x 15 cm x 15 cm block, which had been forged under conditions producing an equiaxed,

fine-grained microstructure. The forged block was annealed in air at 927 C (1700 F) for 3 hours, then annealed in vacuum at 760 C (1400 F) for 4 hours.

All fatigue crack growth rate testing was carried out on compact tension (CT) specimens having a width of 5.08 cm (2.0 inches). Inconel 718 specimens and Ti-5Al-2.5Sn ELI specimens were 1.3 cm (0.5 inch) thick, and Haynes 188 specimens were 1.3 cm (0.5 inch) thick in some cases and 0.63 cm (0.25 inch) thick on other cases. Both the Inconel 718 and Haynes 188 specimens were machined and tested in the T-L orientation.

Constant amplitude and overload fatigue crack growth rate testing was carried out at room temperature and at a second temperature of interest for each material, as summarized in Table 1. Tests were carried out at load ratios (minimum load/maximum load) of 0.1 and 0.7. Tests of Ti-5Al-2.5Sn ELI were carried out in liquid nitrogen at low temperature and in flowing dry nitrogen at room temperature. Room temperature tests of Inconel 718 and Haynes 188 were carried out in air. All elevated temperature tests were carried out in argon plus 1 percent hydrogen.

Table 1. Fatigue Crack Growth Rate Test Conditions

	Room Temperature	-320 F	1100 F	1350 F
Inconel 718	X		X	
Ti-5Al-2.5Sn ELI	X	X		
Haynes 188	X			X
Note: R = 0.1 and R = 0.7				
Inert environment for all tests except Inconel 718 and Haynes 188 room temperature tests				

This paper will concentrate on the room temperature results from this test matrix.

#### Test Procedure

Tests were carried out on closed-loop servohydraulic test machines with DC electric potential monitoring of crack length. The electric potential drop technique relies on the ability to measure small changes in electrical resistivity associated with a change in crack length. A constant current was passed through the test sample, and the change in resistance associated with crack growth was measured by measuring potential drop between two selected, fixed points. Crack length was related to potential drop using Johnson's equation.<sup>3</sup>

A correction factor was used during data reduction to account for minor discrepancies between visual and electric potential crack measurements arising due to nonuniformity in the current field and due



Test procedures included measuring the difference between potential with the current on and the current off, to eliminate thermally induced voltages. Resolution is further enhanced by sampling hundreds of readings and averaging the results. Sampling and current switching were computer controlled and were synchronized with the loading cycle to minimize effects of crack closure and of stress. The stress intensity solution for the CT specimen was based on the following:<sup>4</sup>

$$K = \frac{P}{BW^{1/2}} \frac{2 + a/w}{(1 - a/w)^{3/2}} [0.866 + 4.64 a/w - 13.32(a/w)^2 + 14.72(a/w)^3 - 5.6(a/w)^4] \quad (1)$$

Monitoring of crack length using compliance techniques could have provided additional valuable data, but these measurements were beyond the scope of the program because a primary goal was to obtain data at low and elevated temperatures.

#### Constant Amplitude Fatigue Crack Growth

Figures 1, 2, and 3 present constant amplitude fatigue crack growth data at room temperature for each of the three materials.

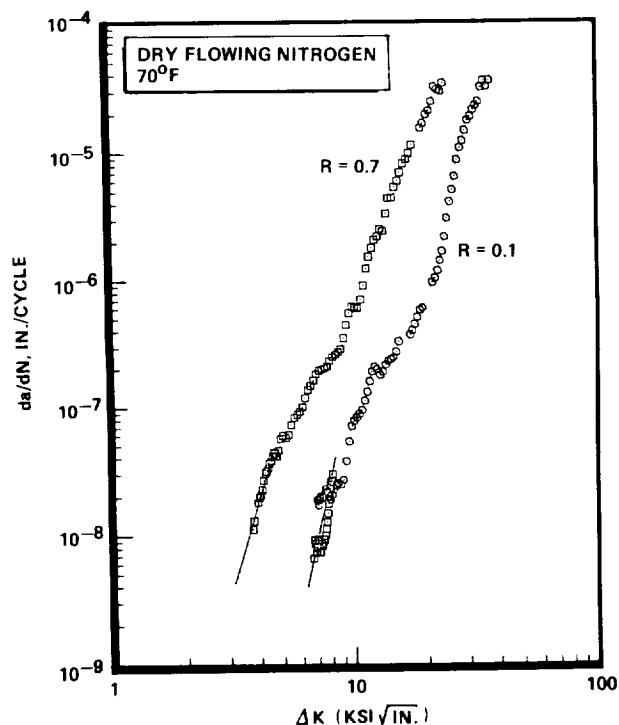


Fig. 1. Ti-5Al-2.5Sn ELI Fatigue Crack Growth Rate vs Stress Intensity Range for R = 0.1 and R = 0.7 at Room Temperature

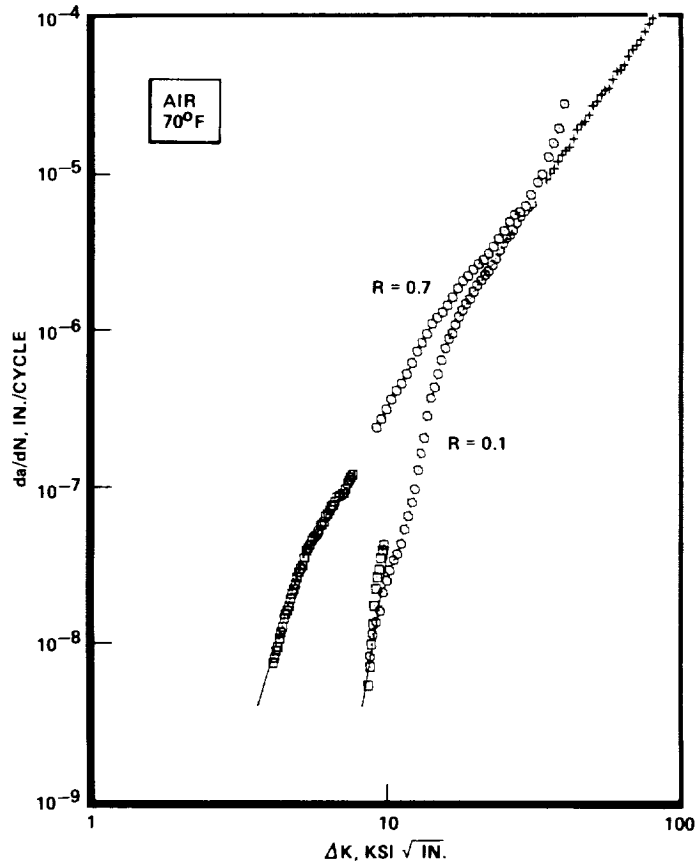


Fig. 2. Inconel 718 Fatigue Crack Growth Rate vs Stress Intensity Range for R = 0.1 and R = 0.7 at Room Temperature

In the constant amplitude tests, stress intensities were controlled and varied using "K gradient" techniques.<sup>5</sup>

The constant amplitude  $da/dN$  data for each material and temperature was represented using the Walker equation (Eq. 2). Table 2 presents Walker equation parameters used below in the application of the Willenborg overload model.

$$\frac{da}{dN} = C \left( \frac{\Delta K}{(1 - R)^{1-m}} \right)^n \quad (2)$$

#### Overload Procedure

To systematically study overload effects, cracks were propagated at chosen baseline stress intensities, a number of single overloads

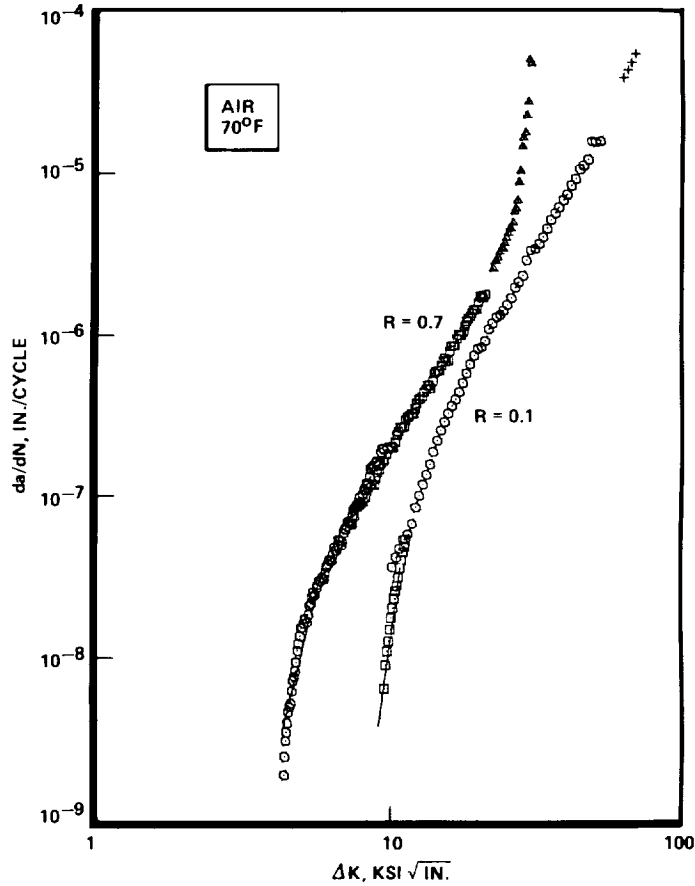


Fig. 3. Haynes 188 Fatigue Crack Growth Rate vs Stress Intensity Range for R = 0.1 and R = 0.7 at Room Temperature

Table 2. Walker Equation Parameters for Constant Amplitude da/dN

Material	Temperature	n	m	C
Inconel 718	21 C	3.0	0.85	1.59E-10

were applied, and crack growth rates were measured following each overload. Overload magnitude was defined as

$$\text{Percent Overload} = \frac{K_{\text{max overload}} - K_{\text{max}}}{K_{\text{max}}}$$

Throughout crack propagation, crack length was continually monitored, and the amplitude of the load applied to each specimen was automatically adjusted to maintain the preselected stress intensity range. The computer-controlled test system stored crack length and cycle number data at programmed intervals, and it provided detailed

point-by-point data on crack length and crack growth rate versus cycle number following each overload.

Figure 4 shows crack length versus cycle number following a 100% overload applied during the propagation of a fatigue crack in Inconel 718 at  $R = 0.1$ ,  $\Delta K = 21.6 \text{ MPa}\sqrt{\text{m}}$  ( $20 \text{ ksi}\sqrt{\text{in.}}$ ), at room temperature. Data summarizing each overload were obtained by fitting a straight line before and after each overload effected region, and then calculating the overload effected crack length ( $a^*$ ), the effective number of delay cycles ( $N^*$ ), and the total number of delay cycles ( $N_t$ ), Fig. 4.

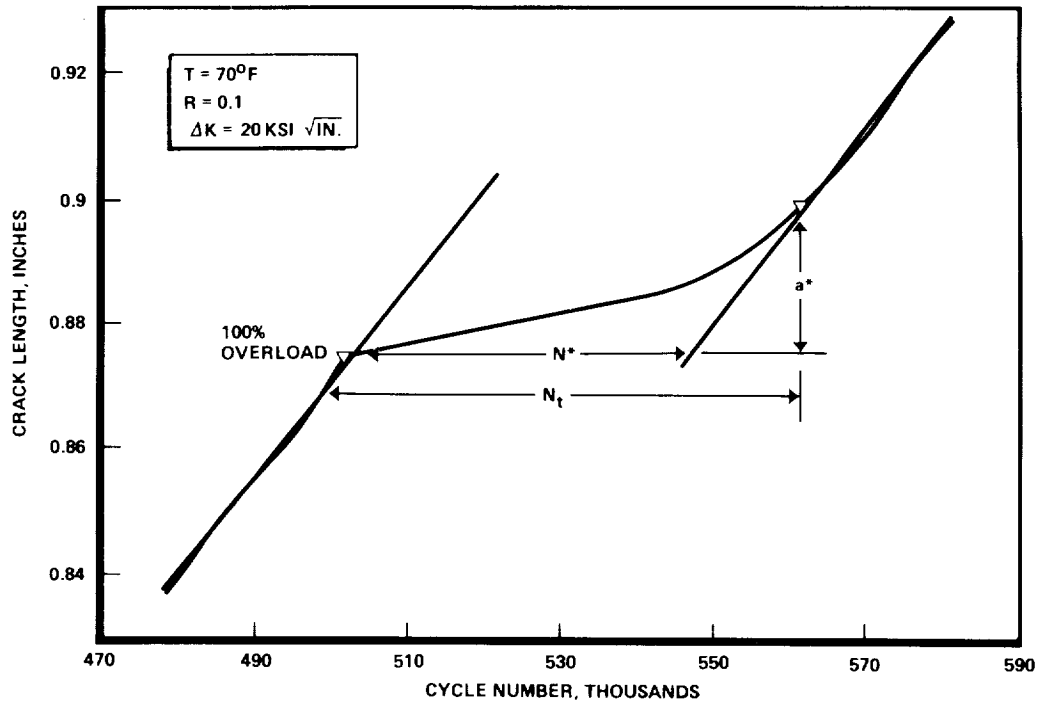


Fig. 4. Crack Length vs Cycle Number Following a 100% Overload During Fatigue Crack Propagation in Inconel 718

#### Fractography

Scanning electron fractography has been carried out on the Inconel 718 room temperature test specimens. Fracture surfaces display ductile striation crack advanced in the intermediate stress intensity region above about  $21.6 \text{ MPa}\sqrt{\text{m}}$  ( $20 \text{ ksi}\sqrt{\text{in.}}$ ), and Stage I crystallographic cracking at lower stress intensities. The crack path did not deviate from the specimen's plane of symmetry.

Preliminary optical examination of the Haynes 188 constant amplitude fracture surfaces suggest similar fractography. Most notably, the fracture surfaces are very flat, with crack propagation on the CT specimen central plane.

The Ti-5Al-2.5Sn ELI constant amplitude fracture surfaces differ significantly from those of Inconel 718 or Haynes 188, showing a pronounced tendency for crack propagation out of the original fracture plane. This results in significantly kinked fatigue cracks.

General Overload Effect Observations

Figure 5A shows a Haynes 188 crack growth specimen [baseline propagation at  $\Delta K = 19.5 \text{ MPa} \sqrt{\text{m}}$  ( $18 \text{ ksi} \sqrt{\text{in.}}$ )] that has received several 60% overload cycles at the indicated locations. Figure 5B shows the corresponding crack growth rate versus crack length. Fatigue crack growth returned to the baseline rate over distances approximately equal to three times the plane strain plastic zone size. Crack growth returned to baseline rates in a consistent, reproducible manner, and crack propagation remained on the original plane. Figure 6 shows overload effected crack length versus calculated plane strain plastic zone size  $(1/3\pi(K/\sigma_y)^2)$  for a variety of overloads applied to Haynes 188.

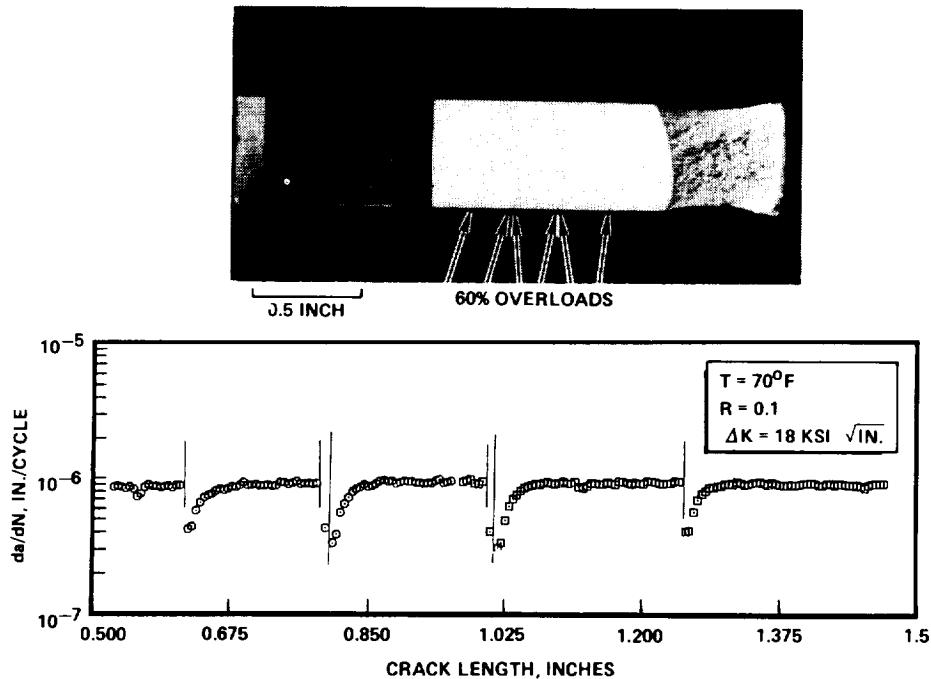


Fig. 5. Haynes 188 Fracture Surface and Corresponding Crack Growth Rate vs Crack Position

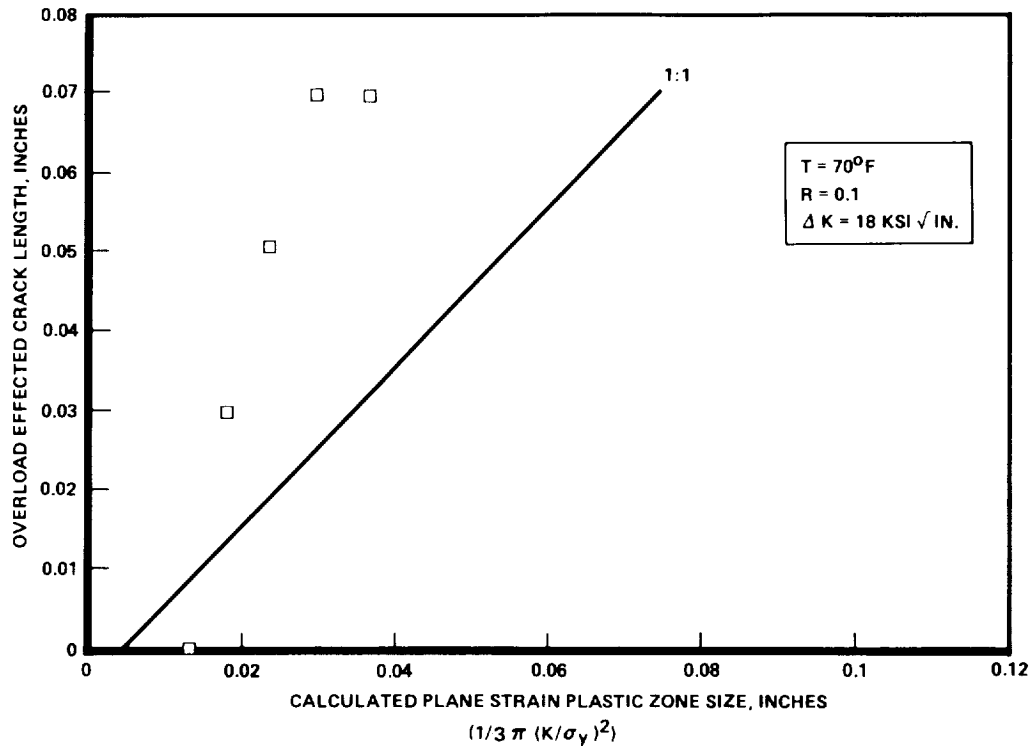


Fig. 6. Haynes 188 Overload Effected Crack Lengths vs Calculated Plane Strain Plastic Zone Sizes

Figure 7 presents overload effected crack length versus calculated plane strain plastic zone size for Inconel 718 at  $R = 0.1$ . Overload effected lengths also are significantly larger than the plane strain plastic zone sizes, and are actually closer to plane stress plastic zone sizes. These results are very similar to results for Inconel 600.<sup>6</sup> In those tests, crack growth rate remained at the minimum value until a crack reached the overload plastic zone boundary, and then the growth rate gradually returned to the preoverload value as the crack closure effect of the interference between the two crack faces gradually diminished.

In some of the Ti-5Al-2.5Sn ELI tests, crack growth acceleration was observed immediately following the overload, as shown in Fig. 8. Damage ahead of the crack tip, either ductile tearing or secondary cracking, is probably responsible for this, and work in progress will detail the nature of this damage. In many of the Ti-5Al-2.5Sn tests, crack growth rates did not return to the preoverload values, as also shown in Fig. 8.

A Ti-5Al-2.5Sn ELI crack growth specimen (baseline propagation at  $\Delta K = 19.5 \text{ MPa} \sqrt{\text{m}}$  ( $18 \text{ ksi} \sqrt{\text{in.}}$ ) that has received several overload cycles at the indicated locations is shown in Fig. 9A. The fracture surface is seen to be very rough, with considerable crack growth

ORIGINAL PAGE IS  
OF POOR QUALITY

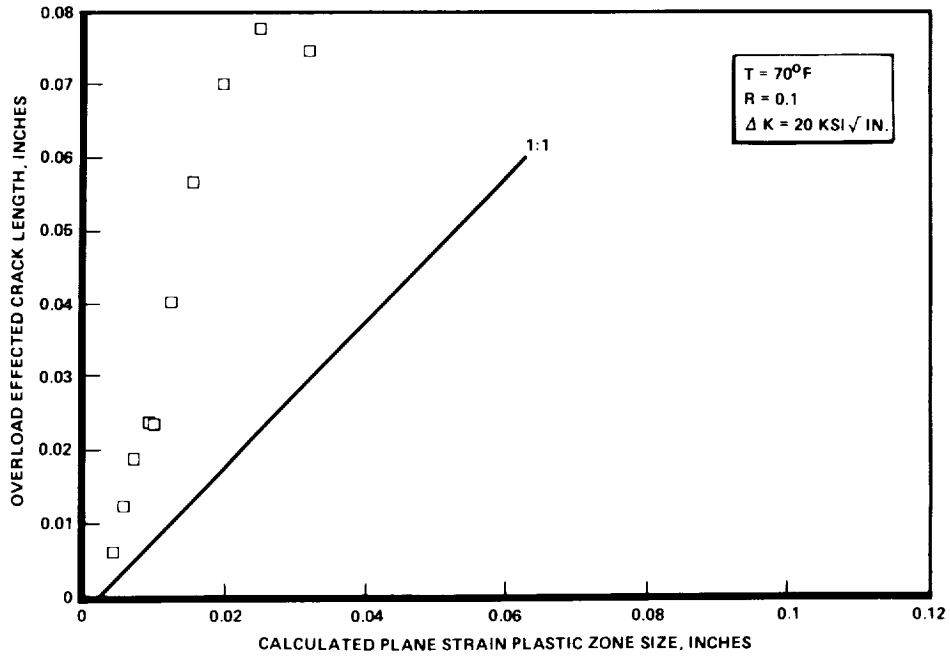


Fig. 7. Inconel 718 Overload Effectuated Crack Lengths vs Calculated Plane Strain Plastic Zone Sizes

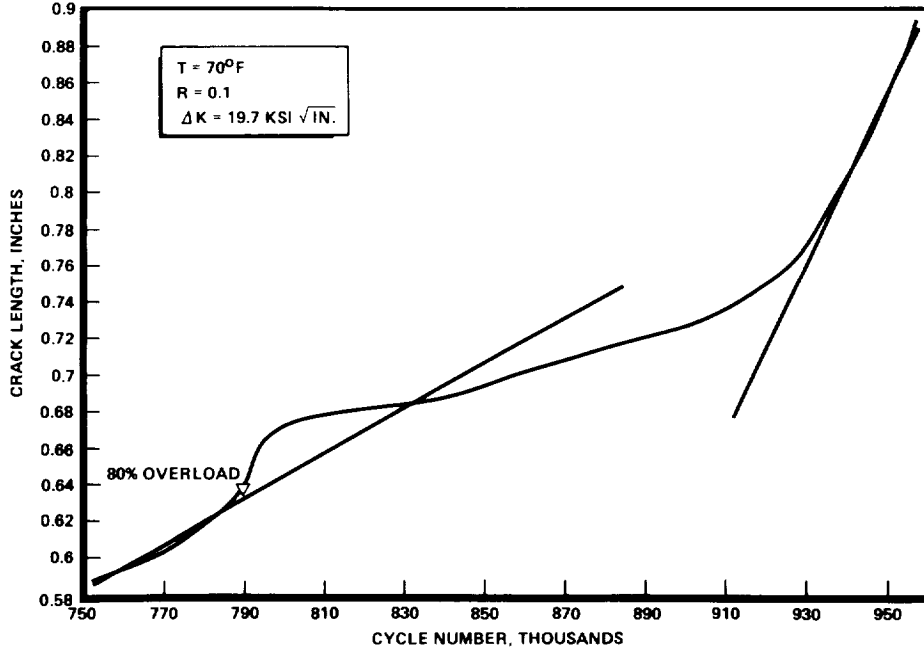


Fig. 8. Ti-5Al-2.5Sn ELI Crack Length vs Cycle Number with an 80% Overload

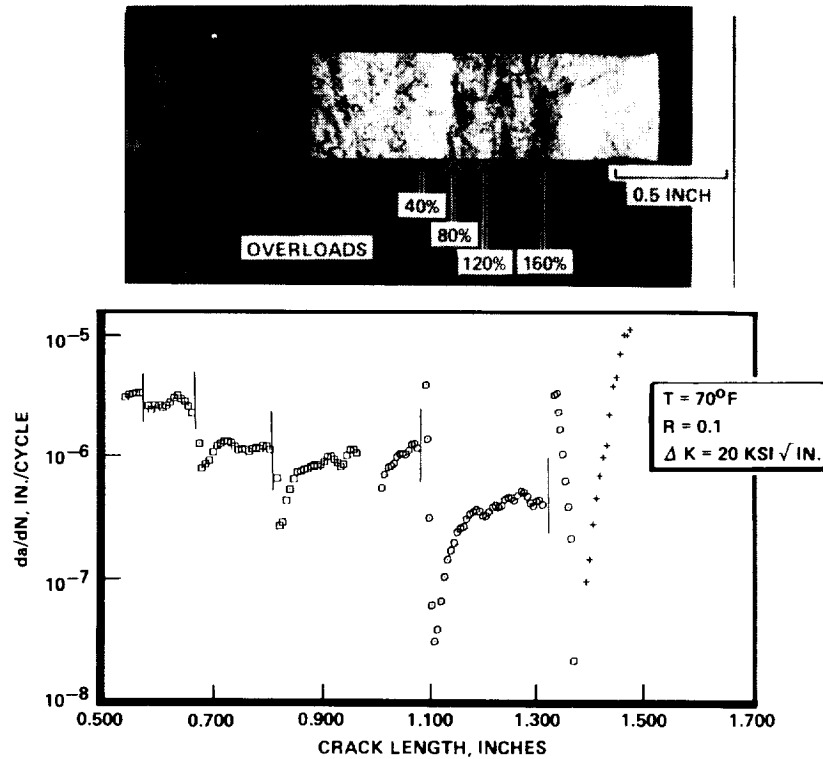


Fig. 9. Ti-5Al-2.5Sn ELI Fracture Surface with Several Overloads and Corresponding Crack Growth Rate vs Crack Position

out of the original crack plane. Figure 9B shows the corresponding crack growth rate versus crack length. Crack growth rates are very scattered and do not return to preoverload values.

Overload effected crack length versus calculated plane strain plastic zone size for Ti-5Al-2.5Sn ELI at  $R = 0.1$  and room temperature is presented in Fig. 10. Overload effected crack lengths are nearly 10 times larger than calculated plane strain plastic zone sizes. Many of the overloads were a large fraction of the plane strain fracture toughness for this material, and the crack branching and the damage ahead of the crack tip at these large overloads may be responsible for these results.

#### Inconel 718 Plastic Wake Effect

The overload effect in Inconel 718 at  $R = 0.1$  seems to extend well beyond the overload plastic zone because of the plastic wedge left behind the advancing crack. One simple way to model this effect is to consider that following an overload, the crack is similar to one wedged open by excess material inserted into the crack mouth. Assuming



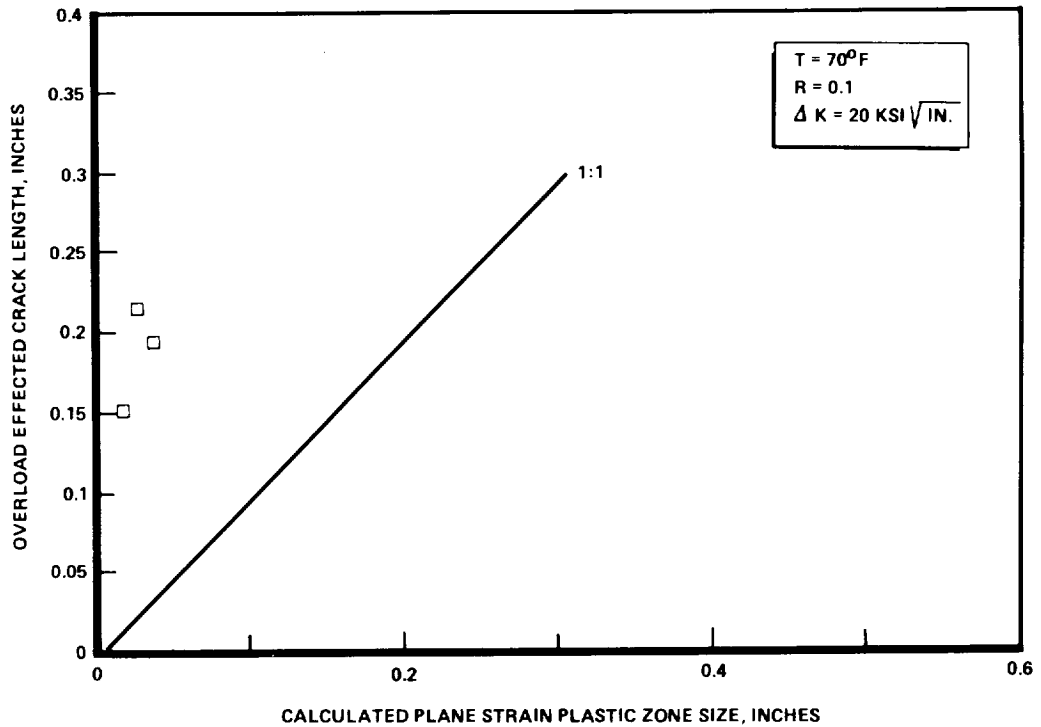


Fig. 10. Ti-5Al-2.5Sn ELI Overload Effected Crack Lengths vs Calculated Plane Strain Plastic Zone Sizes

plastic wake thickness proportional to the stress intensity squared, and referring to the stress intensity solution for the splitting of a body by a semi-infinite wedge, overload effected crack lengths should be related to overload ratios by:

$$a_2/a_1 = (\phi_2/\phi_1)^4$$

where

$a_2$  = effected crack length of overload "2"

$\phi_2$  = overload ratio of overload "2"  
 = percent overload/100 + 1

Figure 11 shows that this function provides a very good fit of the Inconel 718 overload data at room temperature,  $R = 0.1$ , and this demonstrates the role of crack closure arising due to the plastic wake. Further work is in progress to apply plastic wake closure models to these data.

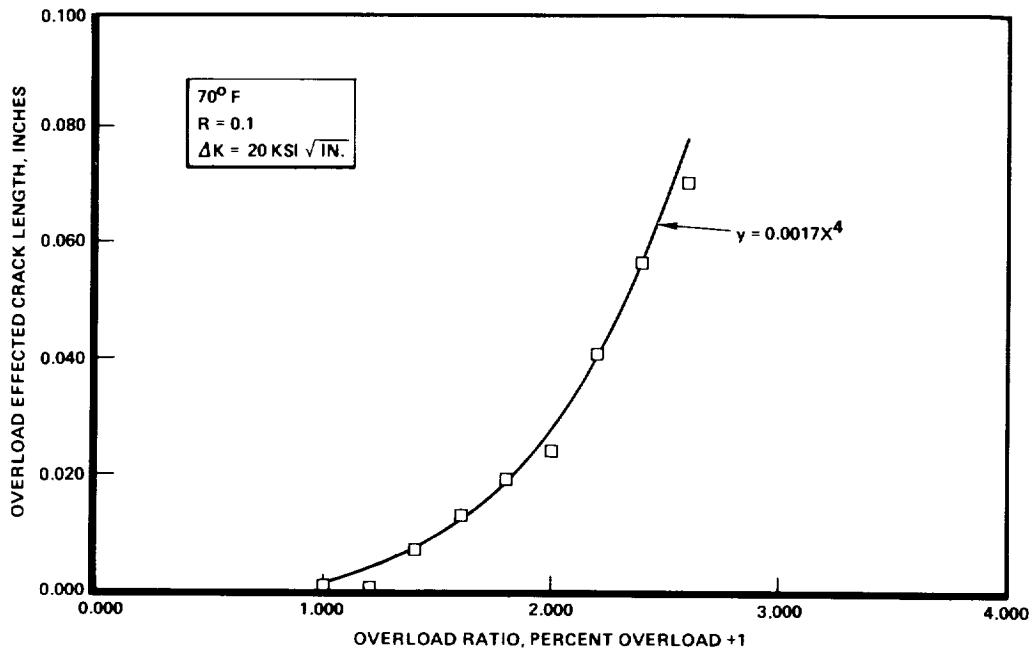


Fig. 11. Overload Effectuated Crack Length vs Overload Ratio for Inconel 718

#### Application of the Generalized Willenborg Model

In the generalized Willenborg model of overload effected fatigue crack growth, the applied stress intensities in a fatigue cycle are each reduced by a factor based on the current crack position within the overload plastic zone.<sup>7</sup> The resulting effective stress intensities are used along with  $da/dN$  data from constant amplitude tests to calculate the instantaneous crack growth rate as the crack grows out of the overload effected region.

Figures 12 and 13 show typical results for the generalized Willenborg model applied to two of the single overloads applied to Inconel 718 at 21 C (70 F). The Willenborg model was applied using (1) the Walker equation data, (2) an overload zone size deduced from the overload effected crack length, and (3) an overload shutoff ratio of 2.2 for the  $R = 0.1$  test and an overload shutoff ratio of 1.5 for the  $R = 0.7$  tests.

#### Ti-5Al-2.5Sn ELI Overload Effects

Models based on plastic zone size or on the plastic wake cannot be applied to the Ti-5Al-2.5 Sn ELI data because of the (1) large variability in crack growth rates after the crack has grown out of the overload effected region, (2) significant overload acceleration

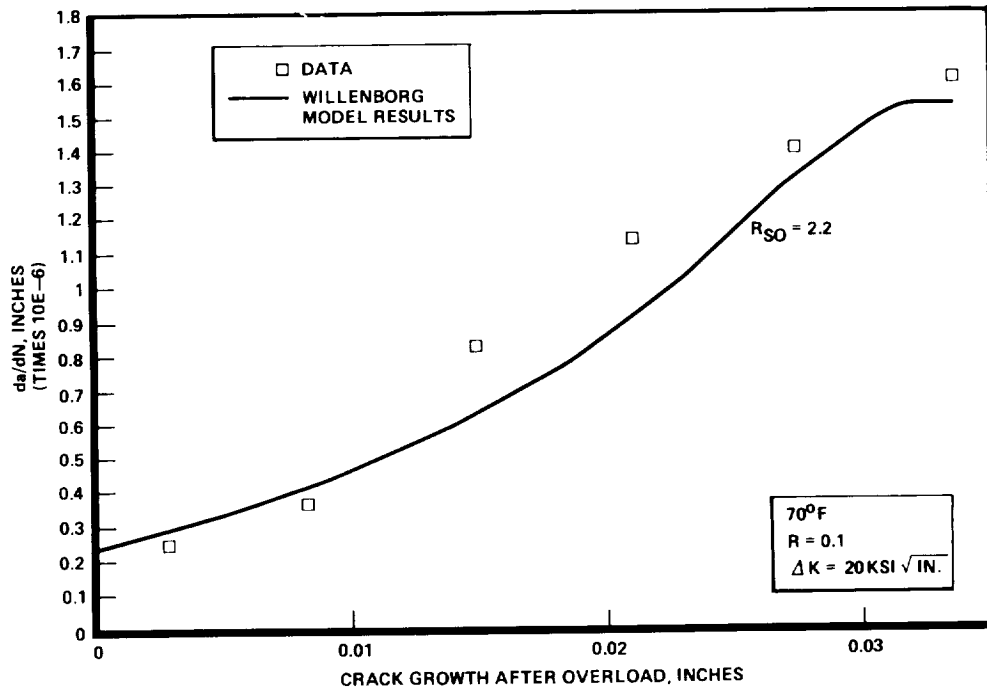


Fig. 12. Willenborg Model Applied to Crack Growth Rate Following a 100% Overload in Inconel 718

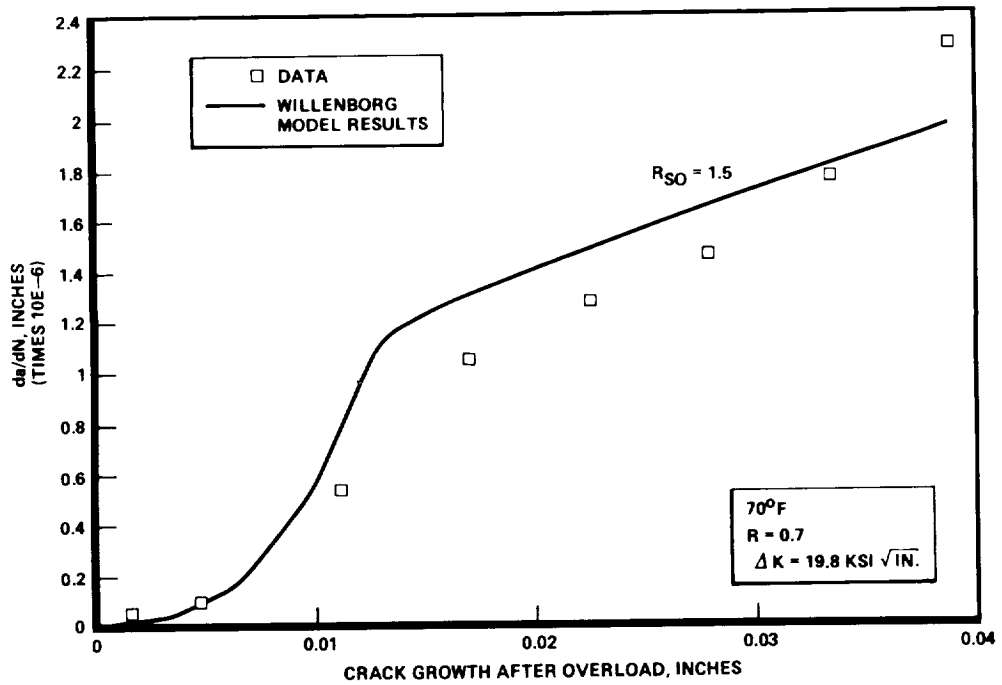


Fig. 13. Willenborg Model Applied to Crack Growth Rate Following a 60% Overload in Inconel 718

following some overloads, and (3) overload retardation considerably beyond the plastic zone. Over large crack growth distances, the crack front remains extensively kinked and is out of the original crack propagation plane. Therefore, it is not possible to apply models that assume the overload effect applies only over a limited overload zone.

In these cases, crack geometry is altered by the overload. The effective stress intensity is controlled by this effect on crack configuration both because of closure and because of the effect of crack kinking on stress intensity.<sup>2</sup> To model these results, specific fracture surface measurements will have to be used along with models that are based on crack kinking and branching.

### Conclusions

A large number of models are available for calculating fatigue crack growth rates following overloads. The experimental data on several structural alloys indicate the variety of possible mechanisms. For Haynes 188 and Inconel 718, models based on overload plastic zones or on plastic-wake-induced closure can model the data fairly well.

For Ti-5Al-2.5Sn ELI, the significant variability in fatigue crack geometry, both for constant amplitude fatigue cycling, and for overload testing, complicates the model effort. Models based on crack kinking and on crack branching may be the only realistic representations for overload effects in this material.

### Acknowledgements

This work is being supported by NASA under contract NAS8-35507, under the direction of Mr. P. M. Munafo.

The authors wish to acknowledge Mr. D. Russell, of Rocketdyne, for helpful guidance and for the derivation of the technique for correlating plastic wake effect.

### References

1. Saff, C. R., "Crack Growth Retardation and Acceleration Models," Damage Tolerance of Metallic Structures: Analysis Methods and Application, ASTM STP 842, J. B. Chang and J. L. Rudd, Eds., American Society for Testing and Materials, pp. 36-49, 1984.
2. Suresh, S., "Micromechanisms of Fatigue Crack Growth Retardation Following Overloads," Engineering Fracture Mechanics, Vol. 18, No. 3, pp. 577-593, 1983.
3. Saxena, R. and S. J. Hudak, Jr., "Review and Extension of Compliance Information for Common Crack Growth Specimens," International Journal of Fracture, Vol. 14, No. 5, pp. 453-468, October 1978.

4. Schwalbe, K. H., and D. Hellmenn, "Application of the Electric Potential Method to Crack Length Measurements Using Johnson's Formula," Journal of Testing and Evaluation, Vol. 9, No. 3, pp. 218-221, May 1981.
5. Saxena, A., S. J. Hudak, Jr., J. K. Donald, and D. W. Schmidt, "Computer-Controlled Decreasing Stress Intensity Technique for Low Rate Fatigue Crack Growth Testing," Journal of Testing and Evaluation, Vol. 6, No. 3, pp. 167-174, May 1978.
6. Brog, T. K., J. W. Jones, and G. S. Was, "Fatigue Crack Growth Retardation Inconel 600," Engineering Fracture Mechanics, Vol. 20, No. 2, pp. 313-320, 1984.
7. Chang, J. B., R. M. Hiyama, and M. Szamossi, Improved Methods for Predicting Spectrum Loading Effects, Volume I - Technical Summary, AFWAL-TR-81-3092, Vol. I, Air Force Flight Dynamics Laboratory, Wright-Patterson Air Force Base, Ohio, 1981.

**IX BEARINGS I**

THERMO-MECHANICAL PERFORMANCE EVALUATION  
OF CRYOGENIC TURBOPUMP BALL BEARINGS

Robert A. Pallini  
SKF Industries, Inc.  
King of Prussia, PA 19406-1352

Abstract

The Space Shuttle Main Engine (SSME) high pressure oxidizer turbopump (HPOTP) presents a severe and demanding operating environment for its rotor-bearing system. The life requirement for the angular contact ball bearings that support the shaft is on the order of 7.5 hours. In actual operation bearing distress has been observed after much shorter times.

A thermo-mechanical analysis of the HPOTP rotor-bearing system was performed with the SHABERTH (SHAft-BEARing-THERmal) computer code. Bearing performance was evaluated as a function of its thermal and mechanical environment. Bearing operating temperatures, heat generation and rolling fatigue life were quantified as functions of operating loads and ball-to-race friction. The latter of these was shown to greatly influence bearing performance. Recommendations for easing the sensitivity of bearing performance to friction levels is addressed.

## Introduction

The rotor/bearing system of the space shuttle main engine cryogenic turbopumps, in particular the high pressure oxidizer turbopump (HPOTP), have been the subject of many research studies aimed at improving their service lives. One component being studied is the shaft support bearings of the HPOTP. Bhat and Dolan [1] have reported heavy spalling and prominent wear of raceways and balls of these bearings after only 2,406 seconds of total running time, with only 1,090 of those seconds at full power level. Other studies [1,2] have revealed heavy wear, smearing, microcracking, and pitting indicative of surface distress associated with inadequate lubrication. The bearings in these studies experienced total operating times of less than 6,000 seconds. In addition, surface oxide films indicative of high ( $>600^{\circ}\text{C}$ ) were observed on the rolling surfaces after only 100 to 4000 seconds total operating time. This latter evidence tends to support the thermal failure scenario presented by Bhat and Dolan [1].

Analytical studies [3,4] performed on these bearings showed that if full-film lubrication conditions exist that predicted bearing life is 100 hours (360,000 seconds) or better. The current life requirement for the HPOTP bearings is 7.5 hours or 27,000 seconds. The present HPOTP bearing lubrication scheme consists of sputtered  $\text{MoS}_2$  films on the rolling surfaces, and a woven-glass-reinforced PTFE cage intended to transfer a lubricating film to the rolling surfaces during operation. Studies of tested bearings have indicated that the  $\text{MoS}_2$  films are short lived and that PTFE film transfer is marginal, resulting in inadequate surface protection. The attendant wear and thermally induced bearing loading have resulted in grossly shortened bearing service life.

This paper highlights an analytical study performed at investigating the thermal failure scenario and identifying the possible driving mechanism. State-of-the-art bearing analysis techniques were employed to parametrically quantify bearing performance as functions of applied loadings and ball-to-race friction levels. The latter of these was found to greatly influence bearing performance.

## HPOTP Rotor Bearing System

The HPOTP (Figure 1) consists of two single-stage centrifugal pumps on a common shaft, directly driven by a



two-stage hot-gas turbine. The shaft is supported by two sets of duplex angular contact ball bearings. The pump rotor is designed to act as a large floating piston, between variable clearance labyrinth seals to balance out, as much as possible, any residual thrust loads on the bearings from the fluid pressures. This requires that the bearing pairs be free to float axially, thereby relieving them of any directly applied thrust load. Preload springs between the bearings in each pair apply thrust preloads of 3.8 to 4.5 kN (850 to 1000 lbf) to prevent skidding. Bearing design data is presented in Table 1.

The rings and balls in the angular contact ball bearings, both pump-end and turbine-end, are made of consumable electrode vacuum melted (CEVM) 440C martensitic stainless steel. The cages are made of a woven glass reinforced polytetrafluoroethylene (PTFE) composite called Armalon, which is intended to provide lubrication for the ball and raceway contacts by PTFE transfer films to the balls from the cage pockets. The cryogenic temperatures and environment preclude the use of any conventional organic oil or grease type lubricant.

Both sets of bearings are cooled by a substantial flow of liquid oxygen. Coolant flow for the pump-end bearings is through the preburner pump impeller hub labyrinth seal, through the bearings, and to the main pump inducer/impeller inlet. The flow rate is approximately 4.5 kg/sec (10 lb/sec). The turbine-end bearings coolant flow is through the preburner impeller bolt, through the hollow shaft, through the bearings, and to the main pump inducer/impeller inlet. The flow rate for the turbine-end bearings is approximately 2 kg/sec (4.5 lb/sec).

The bearings are designed with 52% and 53% ball groove conformities that provide nominal contact angles of 20 to 28 degrees in the unmounted state. The axial freedom, as discussed above is provided by loose fitting of the bearings in their housings. The inner rings are press-fitted on the shaft, which essentially becomes a line-to-line fit during operation, taking into account differential thermal growths and centrifugal effects on both the inner ring and shaft.

#### HPOTP Operating Conditions

The HPOTP loading consists of the combination of a stationary, non-rotating component (primarily weight) and a synchronous rotating component (impeller action) applied to

the impeller shaft. Aside from a transient start-up axial load that ranges from 8.9 kN to 35.6 kN (2000 to 8000 lbf), theoretically, the only axial load present on the bearings is the spring-applied preload. The rotating and non-rotating load components were combined at various rotation angles to provide a range of radial load conditions for use in the analysis. Table 2 provides a matrix of load cases to be used in the analytical studies. Since the objective of the analytical studies was to formulate criteria for material selection, worst case loading conditions were modeled.

The HPOTP shaft speed at rated power level (RPL) is 2969 rad/sec (28,349 rpm), climbing to 3182 rad/sec (30,381 rpm) at full power level (FPL). For the purposes of the analytical studies a shaft speed of 3142 rad/sec (30,000 rpm) was used.

#### Analytical Studies

Analytical studies of the HPOTP rotor/bearing system were undertaken with the primary objective of parametrically quantifying bearing operation to enable the establishment of possible failure scenarios. The bearing system analyses were conducted utilizing SKF computer code SHABERTH (SHAft-BEARing-THERmal) [5]. This approach provides an efficient means of calculating the stress, kinematic, and thermal information required to describe the bearing internal operating environment. Bearing stresses, fatigue lives, heat generation rates, temperatures, rolling and sliding velocities, were calculated. The SHABERTH analysis incorporated the effects of thermal contractions, shaft stiffness, bearing preload, coolant temperature and flow rate, solid lubricant traction coefficients, and material elastic and heat transfer properties.

Two key features of SHABERTH, with respect to the cryogenic turbopump bearing analyses, are the inclusion of a general thermal analysis model and a dry lubrication option. The high bearing heat generation rates due to the use of solid lubrication make consideration of thermal and mechanical interactions very important in analyzing the turbopump bearings. The dry lubrication option makes use of a coulomb friction model to calculate bearing heat generation rates.

The information presented above was used to create detailed thermomechanical models of the HPOTP shaft/bearing/

housing system. All appropriate dimensions were taken from turbopump detailed drawings. Heat transfer mechanisms, including conduction, free and forced convection, and fluid flow are considered in the SHABERTH thermal model. The thermal analysis is coupled with the bearing mechanical analysis enabling consideration of thermomechanical interplay.

In the SHABERTH representation the preloaded bearing pairs are located in their respective positions and connected by a flexible shaft. Radial loads are applied to the shaft. For the HPOTP bearing analysis, the radial shaft loads (as per Table 2) were applied at the centerline of the pump impeller. Resulting bearing loads were calculated considering the elastic deformations of both the shaft and the bearings. Bearing heat generation rates were automatically calculated and fed into the thermal analysis portion of SHABERTH for calculation of bearing, shaft and housing temperatures. This temperature distribution then prompts a revision of the mechanical analysis via thermal dimensional changes of the shaft, bearing and housing components. This in turn alters the bearing load distributions and subsequently the heat generation rates. The SHABERTH program will iterate on this thermomechanical interplay until a steady-state solution is achieved, assuming one exists.

In order to correctly evaluate the thermal aspects of the HPOTP bearing system, proper modelling of the frictional characteristics of the ball/raceway, ball/cage pocket, and cage rail/ring land contacts had to be achieved. SHABERTH normally calculates contact friction forces based on hydrodynamic or elastohydrodynamic (EHD) conditions with conventional oil or grease lubrication, however, the turbopump bearings are lubricated via a transfer film of PTFE (as described in the previous section). In addition to the solid PTFE (Armalon) lubricant, a phosphoric acid bonded MoS<sub>2</sub> lubricant film is burnished onto the raceway surfaces and the balls are sputter coated with MoS<sub>2</sub>. The dry lubrication option in SHABERTH was used to model these HPOTP bearing lubrication conditions. Baseline analyses were performed with a coefficient of sliding friction of 0.2 to represent 440C stainless steel running against itself with dry film lubrication.

Coefficient of friction was one of the bearing operating characteristics that was parameterized. Coefficients varied in the analysis from  $\mu = 0.08$  to  $\mu = 0.5$ . A reported coefficient of friction for 440C on 440C in unlubricated sliding conditions is 0.65 [6]. The precise coefficient of friction

during operation will be influenced by the specific physical/chemical surface condition that is present.

The SHABERTH computer code and model were used to perform a thermomechanical analysis of the aforementioned HPOTP shaft/bearing system.

### Discussion of Results

Bearing fatigue life calculated in SHABERTH is based on classical subsurface initiated failure. Empirically derived multipliers are often applied to this calculated value to reflect observed effects of bearing material quality and lubrication conditions in an adjusted rating life or "expected life". In the current analytical studies a multiplier of 1 was used, i.e., the values indicated are the unadjusted, calculated lives that may be achieved if raceway and rolling element surface integrity is protected against wear and lubrication related distress. Since the development of lubricating films with liquid oxygen is doubtful [7], and quantification of transfer film lubrication effects on life are non-existent, a multiplier of 1 for the purposes of parametric studies is justified. The surface characteristic that was parameterized was coefficient of sliding friction. This permitted characterization of the effect of coefficient of friction on bearing heat generation and the associated thermally induced loading, and the resulting effect of that thermal loading on contact stress levels and fatigue life.

Figure 2 is a plot of bearing fatigue life versus friction coefficient for bearing No. 2 (pump-end) and bearing No. 3. (turbine-end) for two of the radial load conditions analyzed. Under the worst case radial load condition, i.e., 22.2 kN (5000 lbf) total radial shaft load, the life of the in-board turbine bearing (bearing No. 3) decreases from a calculated 9 hours at a coefficient of friction of  $\mu = 0.08$  to a life of less than 1 hour at  $\mu = 0.5$ . When subject to the minimum radial load condition, i.e., 8.5 kN (1915 lbf) total radial shaft load, the calculated life for bearing No. 3 shows a very dramatic decline from 44 hours at  $\mu = 0.08$  to a value of 3 hours at  $\mu = 0.05$ .

This trend in life degradation is severely aggravated by the application of axial load (possibly caused by the failure of outer race/cartridge axial movement). The effect of axial thrust load on life is presented in Figure 3.

Figures 2 and 3 indicate that even if surface initiated failure mechanisms can be ruled out as causes for failure, the HPOTP bearings will have difficulty attaining the design goal fatigue life unless friction can be minimized and the occurrence of transient axial loads can be eliminated.

Figures 4 and 5 illustrate the level of element-to-raceway contact stress as a function of friction coefficient and applied axial load, respectively. Again, a dramatic sensitivity to friction coefficient is noted, with contact stress levels ranging from 2500 MPa to 3500 MPa (362 ksi to 507 ksi). The application of modest axial load can cause contact stress well in excess of 3500 MPa (510 ksi).

These high stress levels and low fatigue lives are a result of thermally induced loading. The radial expansion of the bearing created by the heat generated within the bearing produces thermal radial preloading. Even though the bearings are operating in a cryogenic environment, and coolant flow is present through the bearings, the ball/raceway contacts are still a source of considerable heat generation. Figures 6 and 7 present the calculated heat generation rates for the HPOTP bearings. Heat generation rates of 10 kW to 30 kW are estimated for the normal bearing operating range. The application of small amounts of axial load causes an increase in the heat generation to as high as 70 kW. Table 3 presents the estimated inner ring bulk temperatures for the HPOTP bearings subject to the conditions analyzed.

Figures 6 and 7 show total bearing heat generations, however, it should be noted that 55% to 65% of this generated heat is at the inner race ball/raceway contacts. The computer modeling via SHABERTH assumed that there was no gross sliding or cage slippage. Thus, simple outer race control was governing. Previous analytical studies [7] using a method that more exactly models the situation, indicated that there is no gross slippage. This means that all sliding is due to ball spin and micro-slip (Heathcoat slip) about the ball/raceway point of contact. It is this ball spin at the inner raceway contact (in the presence of a high coefficient of friction) that is the major contributor to the high heat generation rates. Calculated spin-to-roll ratios for the inner race contacts ranged from 0.1 with heavy loads to as high as 0.6 with the light load conditions. A computed spin/roll ratio of 0.3 was typical for nominal operating conditions.

One other bearing design parameter examined was that of inner ring circumferential stress (hoop stress). As previously mentioned, the bearing inner rings are initially press fitted onto the turbopump shaft, however, a line-to-line condition is reached at the operating temperature. The mounted bearing inner ring circumferential tensile stresses were computed to be on the order of 69 MPa to 110 MPa (10 ksi to 16 ksi). However, after chill down to cryogenic temperatures and when operating at 3142 rad/sec (30,000 rpm) the circumferential tensile stress is computed to be 83 MPa (12 ksi). This value represents the maximum circumferential tensile stress at the outer surface (raceway surface) of the inner ring.

### Conclusions of Analytical Study

In summary, the following key conclusions can be made based upon the analytical studies.

1. Due to the rapid depletion of the MoS<sub>2</sub> films on the balls and raceway surfaces, and the reported inability of the PTFE lubricant transfer to be effective in the LOX environment, the HPOTP bearings most likely operate with a coefficient of sliding friction of that similar to dry metal-to-metal contact. That is, a coefficient of friction between 0.4 and 0.6.
2. At these high sliding friction levels and with the heavy radial loads estimated for the HPOTP bearings, the bearing internal heat generation rates reach levels on the order of 20 to 50 kW.
3. The high rate of heat generation creates a situation of inner ring thermal expansion and subsequent loss of internal clearance. This results in high, up to 3447 MPa (500 ksi), ball/raceway contact stress levels and greatly reduced bearing rolling contact fatigue lives.
4. The fatigue lives reported herein are for subsurface initiated rolling contact fatigue. The curves showed that even if this were to be the dominant mode of fatigue, i.e., full film lubrication, the bearing fatigue lives are somewhat less than desired. Based on Conclusion 1, the bearings are operating with little or no low shear strength lubricant film. In this condition and with the high contact traction forces ( $\mu > 0.35$ ) the dominant mode of failure will be surface wear or surface initiated fatigue. The actual bearing life may thus

lower than the lives presented in these results. In addition, studies have shown that for friction coefficients  $\mu > 0.15$  reductions in fatigue life can be expected because of the influence of tangential stress on the subsurface stress field [8,9].

5. The analysis and the above conclusions indicated that if surface fatigue is to be prevented and bearing clearances are to be maintained, a low (less than 0.15) friction coefficient must be supplied and maintained for the ball and raceway surfaces. If this can be accomplished, the analysis indicates that much improved bearing lives may be realized.
6. Inner ring circumferential tensile stresses at bearing operating conditions are less than, or equal to, 83 MPa (12 ksi), and result from centrifugal loading.
7. Any applied thrust load dramatically aggravates the thermal runaway scenario and increases the potential for extremely short bearing fatigue life.

#### Acknowledgement

This work was performed under NASA/MSFC Contract No. NAS8-35341 with SKF Industries, Inc., King of Prussia, PA. The author acknowledges the assistance provided by Gordon Marsh, NASA/MSFC Program Manager, Biliyar N. Bhat, Metallurgy Research Branch, Metallic Material Division and Fred J. Dolan, Chief, Lubrication and Surface Physics Branch, Engineering Physics Division, Materials and Processes Laboratory, MSFC.

#### References

1. Bhat, B. N. and Dolan, F. J., "Past Performance Analysis of HPOTP Bearings," NASA TM-82470, March 1982.
2. Dufrane, K. F. and Kannel, J. W., "Evaluation of Space Shuttle Main Engine Bearings from High Pressure Oxygen Turbopump 9008," Final Report, NASA Marshall Space Flight Center Contract No. NAS8-35576, Task No. 102, July 11, 1980. Submitted by Battelle Columbus Laboratories, Columbus, OH.
3. Broschard, J. L., "Turbopump Bearing Analysis," SKF Report No. AT83X001, March 1983.

4. Sibley, L. B., "Analysis of Turbopump Bearings from Space Shuttle Test Engine No. 5," SKF Report No. AL79T004, January 1979.
5. Crecelius, W. J., "User's Manual for Steady-State and Transient Thermal Analysis of a Shaft Bearing System (SHABERTH)," Contract Report ARBRL-CR-00386, submitted to U.S. Army Ballistics Research Laboratory, Nov. 1982.
6. Spalvins, T., "Coatings for Wear and Lubrication," Thin Solid Films, Vol. 53, pp. 285-300, 1978.
7. Kannel, J. W., Merrimen, T. L., Stockwell, R. D., and Dufrane, K. F., "Evaluation of Outer Race Tilt and Lubrication on Ball Wear and SSME Bearing Life Reductions," Final Report NASA/MSFC Contract NAS8-34908, July 1983 by Battelle Columbus Laboratories, Columbus, OH.
8. Ioannides, E. and Harris, T. A., "A New Fatigue Life Model for Rolling Bearings," ASME Paper No. 84-TRIB-28, Presented at the ASME/ASLE Joint Lubrication Conference, San Diego, CA, October 22-24, 1984.
9. Kannel, J. W. and Tevaarwerk, J. L., "Subsurface Stress Evaluations Under Rolling/Sliding Contacts," ASME Paper No. 83-LUB-18, Presented at the ASME/ASLE Joint Lubrication Conference, Hartford, CT, October 18-20, 1983.



ORIGINAL PAGE IS  
OF POOR QUALITY

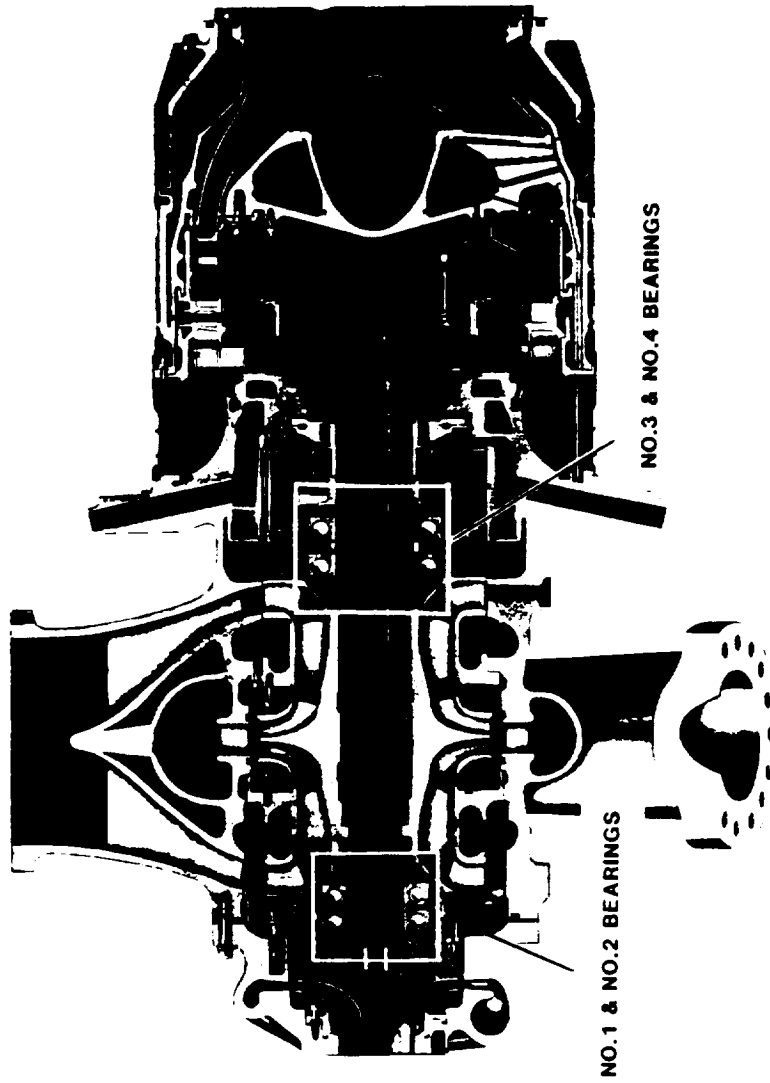


FIGURE 1. SSME HPOTP

TABLE 1

## HPOTP BEARING DESIGN DATA

DESIGN DATA	PUMP END BEARINGS	TURBINE END BEARINGS
BEARING BORE (mm)	45	57.15
BEARING O.D. (mm)	83.9	103.1
BEARING WITDH (mm)	17	18.5
MATERIAL	CEVM 440C	CEVM 440C
PITCH DIAMETER (mm)	65.024	80.518
BALL DIAMETER (mm)	11.113	12.700
NUMBER OF BALLS	13	13
CONTACT ANGLE (deg)	24.34	20.5
RACE CURVATURE %I/%O	53/52	53/53
CAGE MATERIAL	ARMALON	ARMALON
PRELOAD, AXIAL (kN)	3.8	4.5

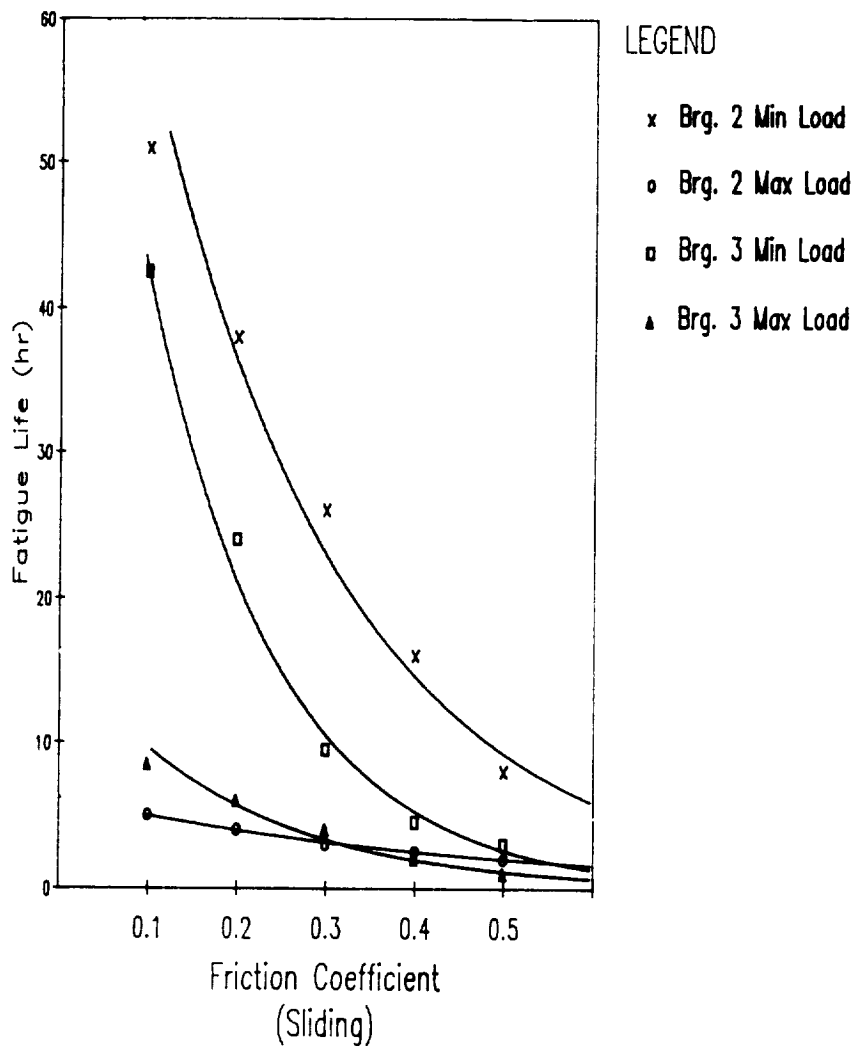
TABLE 2

## HPOTP CONDITIONS USED IN ANALYTICAL STUDIES

LOAD CASE	RADIAL NON-ROTATING LOAD COMPONENT (N)	RADIAL ROTATING LOAD COMPONENT (N)	ORIENTATION OF ROTATING & NON-ROTATING LOAD COMPONENT (DEG)	RESULTANT RADIAL LOAD (N)
1	11120	11120	0	22240
2	11120	11120	45	20550
3	11120	11120	90	15724
4	11120	11120	135	8515
5	11120	11120	180	0

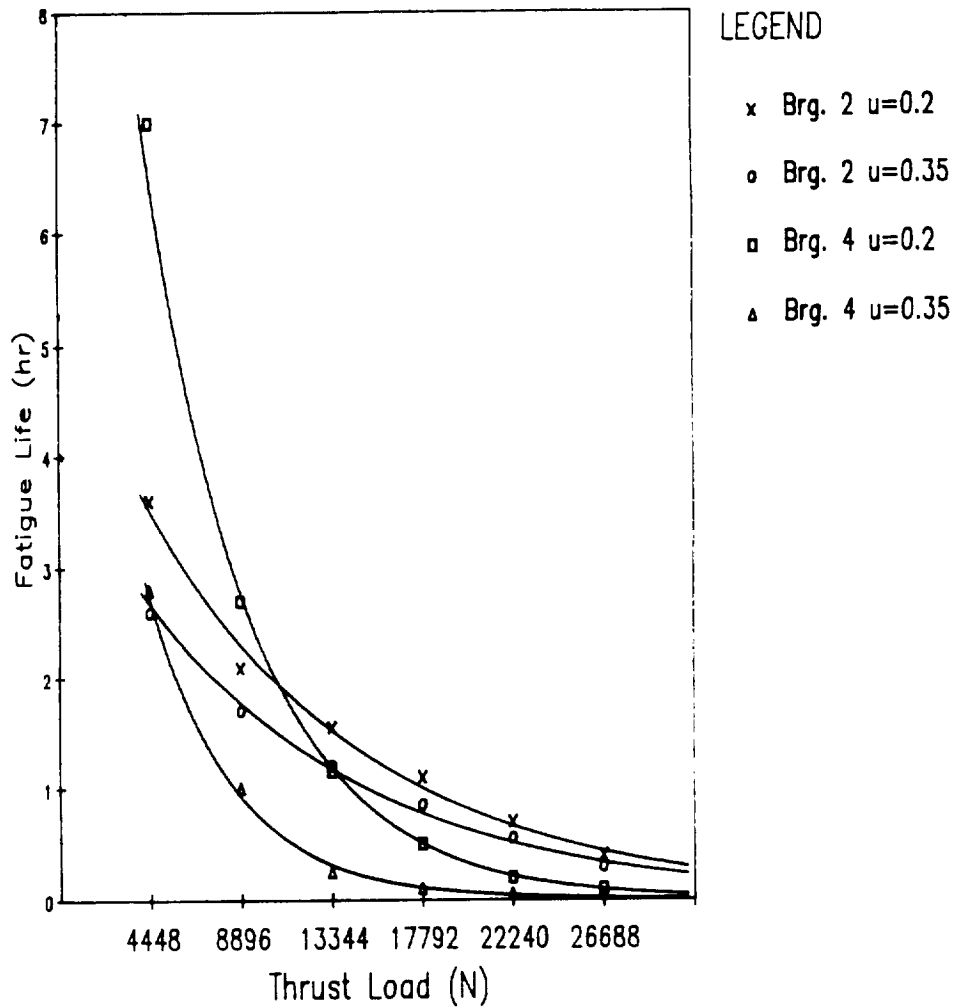
SHAFT SPEED - 30,000 RPM  
 COMBINED STATIC AND ROTATING RADIAL LOAD  
 TRANSIENT AXIAL LOADS - 8,896 TO 35,584 N  
 RANGE OF FRICTION COEFFICIENTS - 0.08 TO 0.5

FIGURE 2  
 SSME HPOTP  
 Fatigue Life vs Friction Coefficient



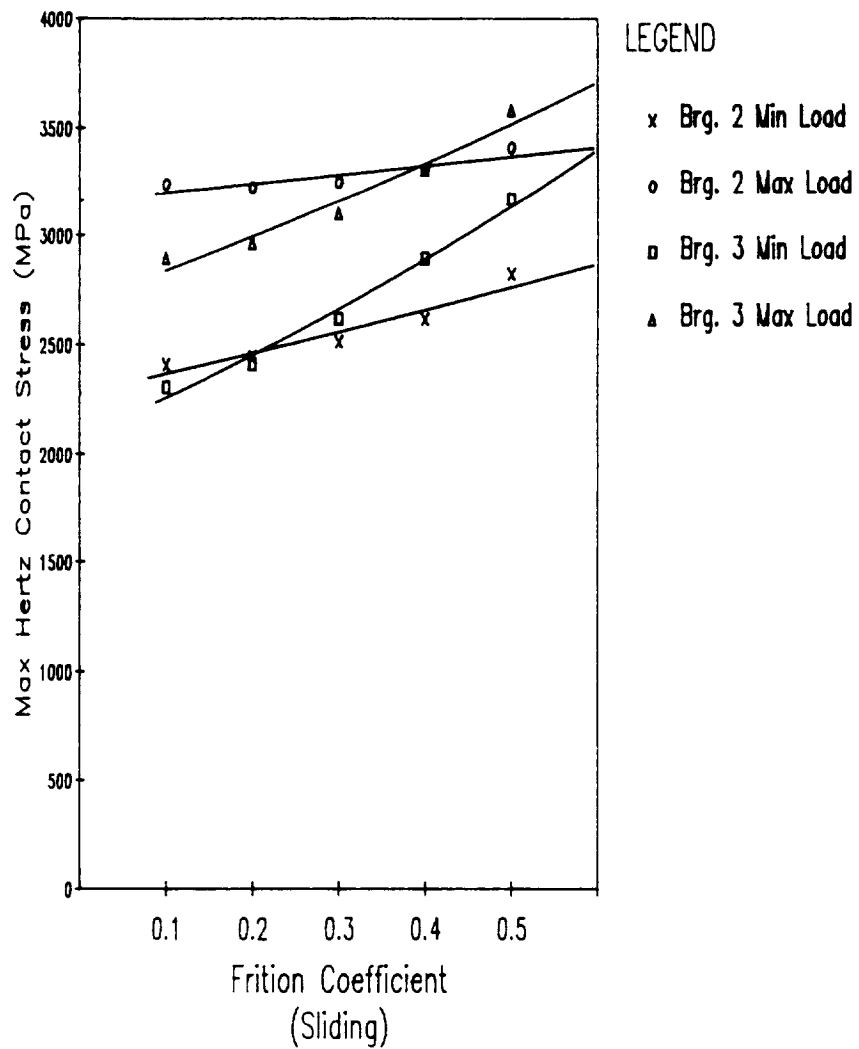
Min=8518 N Max=22240 N

FIGURE 3  
SSME HPOTP  
Fatigue Life vs Thrust Load



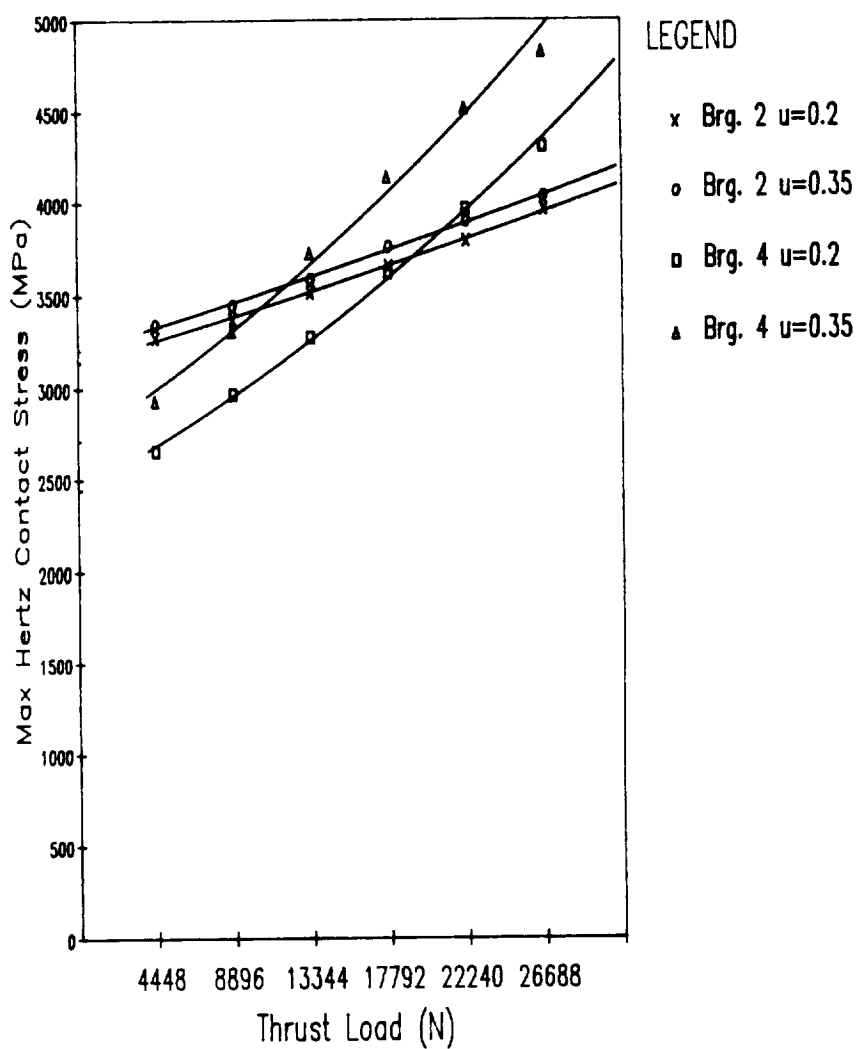
Max Shaft Load=22240 N

FIGURE 4  
 SSME HPOTP  
 Contact Stress vs Friction Coefficient



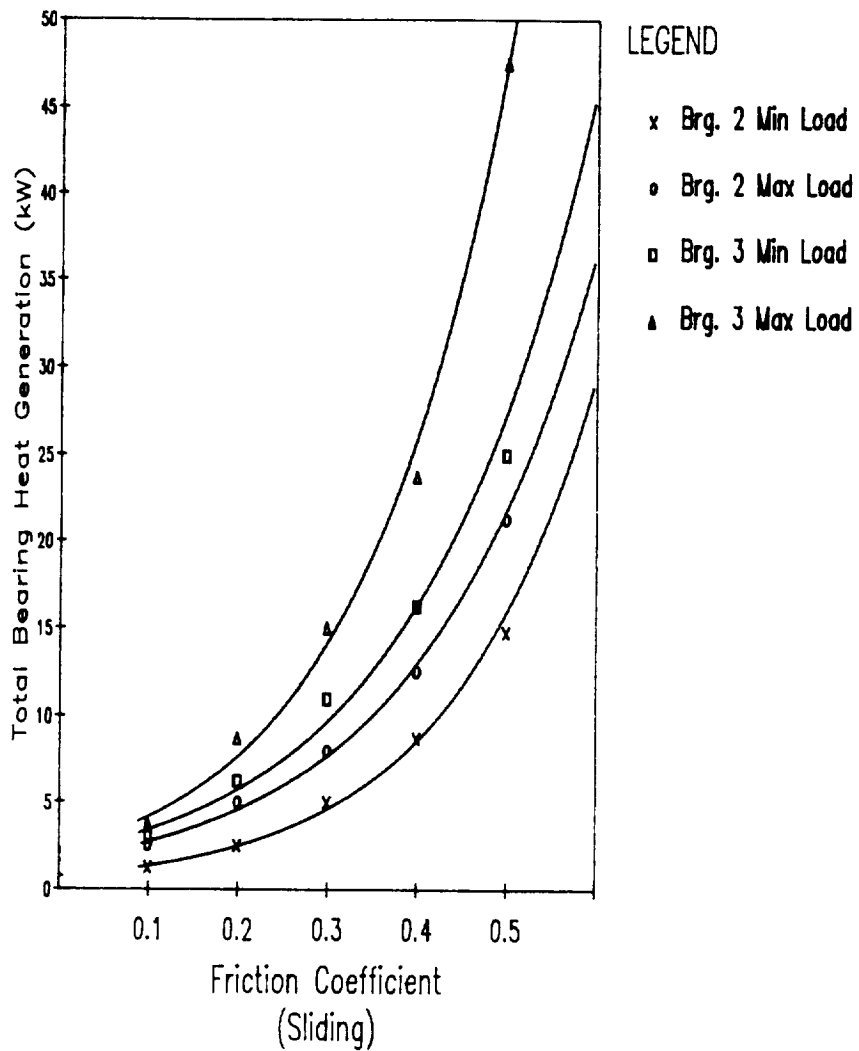
Min=8518 N Max=22240 N

FIGURE 5  
 SSME HPOTP  
 Contact Stress vs Thrust Load



Max Shaft Load=22240 N

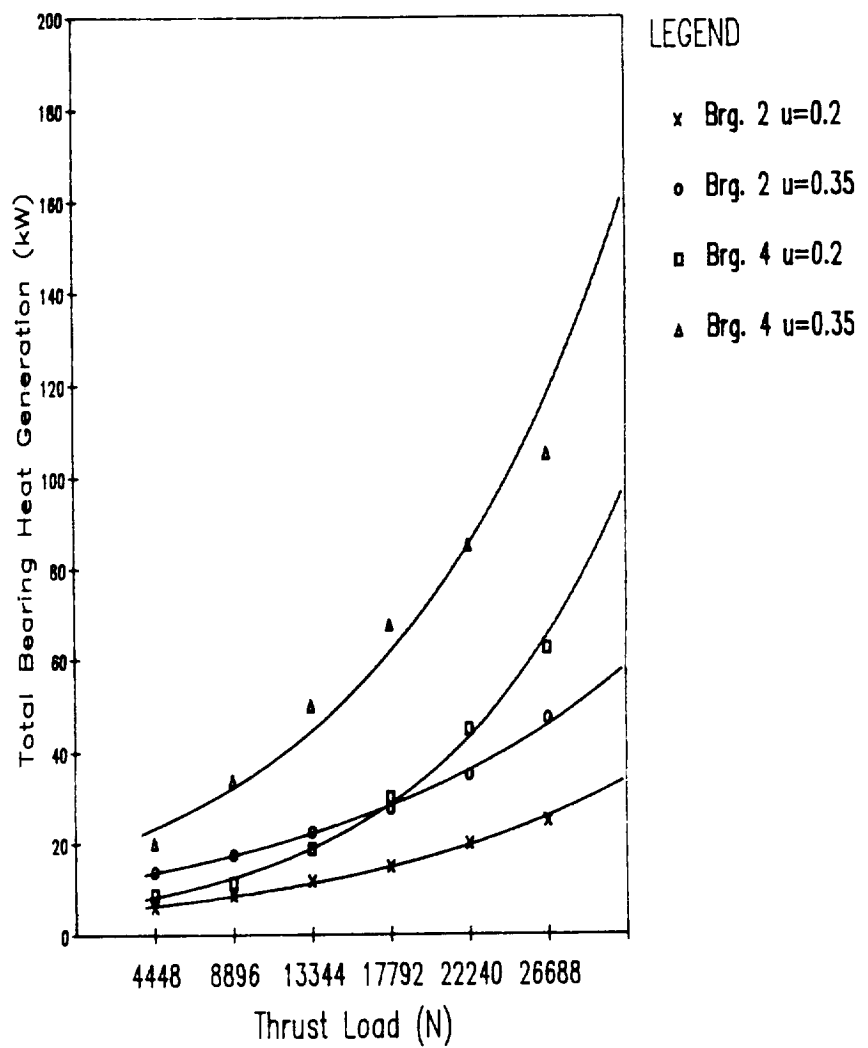
FIGURE 6  
 SSME HPOTP  
 Heat Generation vs Friction Coefficient



Min=8518 N Max=22240 N



FIGURE 7  
 SSME HPOTP  
 Heat Generation vs Thrust Load



Max Shaft Load=22240 N

TABLE 3

HPO7P BEARING INNER RING BULK TEMPERATURES

BEARING NO. 2  
INNER RACE BULK TEMPERATURE  
°C (°F)

	$\mu = 0.15$	$\mu = 0.35$	$\mu = 0.5$
MINIMUM LOAD	-123 (-190)	-83 (-118)	-20 (-4)
MAXIMUM LOAD	-112 (-170)	-48 (-55)	43 (110)

BEARING NO. 3  
INNER RACE BULK TEMPERATURE  
°C (°F)

	$\mu = 0.15$	$\mu = 0.35$	$\mu = 0.5$
MINIMUM LOAD	-84 (-120)	160 (320)	-
MAXIMUM LOAD	-62 (-80)	249 (480)	-


Thermal Analysis of SSME Turbopump Bearings

Joe C. Cody, David Marty and Bruce K. Tiller  
Spectra Research Systems, Inc.

Abstract

A lumped node thermal network model of the pump end bearing of the Space Shuttle Main Engine (SSME) has been developed. The bearing elements, the shaft, isolator, housing, and cryogenic coolant flow characteristics are included. Two phase heat transfer characteristics of the LOX coolant are used in the model. Two computer codes; one thermal, and the other a bearing performance code, have been coupled to provide an overall evaluation of the bearing operating characteristics. Software was developed to allow automatic iteration between the models until a compatible solution was found.

The model was used to develop sensitivity characteristics for the pump end bearing. A broad range of parameters such as contact friction, preload, heat transfer coefficient, coolant flow, subcooling, and outer race misalignments were investigated. In many cases, the solutions of the thermal and performance model would not agree indicating a thermally unstable operating condition which leads to excessive bearing temperatures and possible failure. The results show that bearing component temperatures are very sensitive to contact friction, preloads, and heat transfer coefficients. Although not as sensitive to coolant flow and subcooling, these parameters are very important for marginal conditions. In some cases, thermal instability could be induced by reducing flow or by raising coolant temperature to saturation.



## Introduction

A simulation of the Space Shuttle Main Engine (SSME) Liquid Oxygen (LOX) turbopump shaft/bearing system has been developed. The simulation allows for thermal and mechanical interactions allowing a more representative description of bearing operating characteristics. The model consists of two interacting models; one of the shaft/bearing system modeled on the SHABERTH<sup>1</sup> computer code, and the other a SINDA thermal model representing the pump end bearing pair. The inboard (Number 2) bearing is modeled in detail to allow determination of component temperature profiles and average temperatures. Single and two-phase coolant conditions can be assessed, and heat generation from fluid stirring and bearing friction are included. An executive program controls the iteration between the mechanical and thermal models to arrive at solutions satisfying both models. Solutions that satisfy both models are considered to be realistic and are designated as converged solutions. Conversely, when the solution diverges a realistic operation condition is assumed not to exist.

Parametric analyses were performed on the pump end bearing to investigate the sensitivity of bearing thermal and operating characteristics on contact friction, axial preload, coolant flow rate, coolant inlet temperature, heat transfer coefficients, and outer race misalignment. This effort is directed toward improved analysis and understanding of these important characteristics of bearing systems operating in cryogenics. Continued refinement of the model and correlation of results with the Marshall Space Flight Center (MSFC) Bearing and Seal Materials Tester (BSMT) will significantly enhance the development of a verified analytical tool to aid in the design of high speed bearings operating in cryogenics.

## Model Description

### System Model Description

A system model, representing the Space Shuttle Main Engine (SSME) Liquid Oxygen (LOX) turbopump shaft and bearing configuration, was coded for the SHABERTH bearing/shaft computer program. A detailed nodal representation of the LOX pump pump-end bearing was developed and coded for solution on the SINDA thermal analyzer. Software was developed to allow iteration between the SHABERTH and SINDA models until a compatible solution was obtained.

### SHABERTH Shaft/Bearing Model

The SHABERTH model of the SSME LOX turbopump consists of turbopump shaft, turbine-end and pump-end bearings. The major components of the model are shown in Figure 1. The shaft/bearing system is modeled to allow the effects of bearing radial stiffness and shaft deflection on bearing load sharing to be evaluated. Other parameters such as clearances, outer race tilt, and contact friction can also be investigated. All analyses were conducted using a shaft speed of 30,000 RPM, and the load profile shown for Figure 1. In addition to bearing operating characteristics such as contact angles, clearances, and Hertz stresses the SHABERTH model predicts the reactions for each bearing and the frictional heat generated.

### SINDA Thermal Model

The thermal model is a detailed nodal division of the LOX turbopump Number 2 bearing. The Number 2 bearing was selected for detailed evaluation because it shares a greater percentage of the load than the Number 1 bearing. The model accounts for the heat generated by Bearing Number 1. A nodal representation of Bearing Number 2 is shown in Figure 2. The nodal network is finer in the contact regions where more severe thermal gradients are known to exist. Since the heat transfer coefficient are strong functions of surface temperature, surface nodes are on the order of 5.0 mils thick to provide good representation of the surface temperature. The thermal model solves the conservation equations which include the energy produced by working the fluid, and contact friction in the bearing. Many surface temperatures exceed the saturation temperature of the LOX coolant. Consequently vapor is formed locally at these surfaces requiring the consideration of two phase heat transfer in these regions. Furthermore for some inlet coolant conditions, the coolant can become saturated as it flows through the bearings. The model is capable of accounting for these conditions, and the quality of the coolant at each fluid node can be estimated.

### Model Iteration Process

The shaft/bearing model and thermal model are used in an interactive process which requires iteration between models to determine the operating condition for specific boundary conditions. Failure to find a operating condition satisfying each model results in a diverged solution and the operating point is judged to be thermally unstable. The iteration process is totally automated. The user supplies an initial guess for the bearing component temperatures, and the process iterates until a solution is found or the ball temperature exceeds 2000°F, which indicates a diverged solution.

Figure 3 illustrates the iteration process for a converged case. Here the friction heat from the shaft/bearing model, and the average ball temperature from the thermal model increase to a point of agreement.

Shown in Figure 4 is an example of a diverged case for which no agreement between the shaft/bearing model and the thermal model is found.

## Objectives and Approach

The objectives of the SSME LOX turbopump pump-end bearing analysis were to investigate the sensitivity of bearing operating characteristics to variations in operating parameters. The operating parameters that were considered are listed below with the values investigated.

1. Coolant Flow Rate (lbs/sec)	3.6, 7.0
2. Contact Friction Factor	0.2, 0.3, 0.5
3. Inlet Coolant Temperature to Bearing #1 (°F)	-240, -230, -218
4. Axial Preload (lbs)	350, 480, 850
5. Outer Race Clearance (mils)	2.6, 1.7, 1.0
6. Outer Race Misalignment (min)	0 through 42
7. Heat Transfer Coefficient	Nominal, 2.45 and 3.43 times nominal

The flow rate, friction factor, inlet temperature, and preload were investigated in all combinations while holding the remaining parameters at their initial values. This resulted in 54 initial cases to be simulated. These cases are represented in the parameter data tree of Figure 5. This shows that 42 of the 54 cases were thermally unstable (diverged). It was not necessary to run computer simulations for all the cases to determine thermal instability. For example, if a case with an inlet coolant temperature of  $-218^{\circ}\text{F}$ , flow rate of 7.0 lbs/sec, preload of 850 lbs, and friction factor of 0.2 was unstable, then cases having friction factors of 0.3 or 0.5 with the other parameters the same would obviously not be stable.

The effect of changes in coolant flow rate and inlet coolant temperature were evaluated using the 12 converged cases. However, additional converged cases, over the full range of parameters values, were needed to properly evaluate changes in the remaining operating parameters. Thus, it was decided to increase the boundary heat transfer coefficient to obtain the additional thermally stable cases needed for the sensitivity evaluation.

Changing the boundary heat transfer coefficient introduced the heat transfer coefficient as a parameter into the sensitivity analysis. A second data tree was developed for the heat transfer coefficients and remaining parameters. Figure 6 shows this tree, which provides 18 additional cases.

A nominal case with a flow rate of 7.0 lbs/sec, inlet temperature of  $-230^{\circ}\text{F}$ , friction factor of 0.2, and preload of 480 lbs was used to evaluate these parameters. An increase in heat transfer coefficient to 245% of nominal was needed to converge the case with a 480 lb preload and a friction coefficient of 0.5. An increase in heat transfer coefficient to 343% of nominal was needed to converge the case with an 850 lb preload and a friction coefficient case of 0.5. The variation

of outer race tilt was evaluated separately, holding all other parameters constant.



## Analysis Results

### Mechanical Characteristics

The bearing reactions were first determined for bearings with uniform temperature, and compared with a thermally converged case to assess the influence of the thermal gradient on load sharing. The conditions for the pump-end bearings were: 480 lbs preload, 7 lbs/sec coolant flow, coolant inlet temperatures of  $-230^{\circ}\text{F}$ , and a friction factor of 0.2. Figure 7 shows the results of the comparison. The bracketed values are the reactions considering the thermal gradients in Bearing Number 2. Reactions without brackets are for bearings with uniform temperature. For both cases the inboard bearings support a larger part of the load. This is primarily due to shaft deflection. Bearing 2 receives about 72 percent of the pump-end reaction for the uniform temperature case. This bearing supports about 76 percent of the reaction, when thermal effects are considered. The thermal gradient causes differential thermal growth in the bearing which reduces the internal operating clearances, and increases the radial stiffness. The reduction in internal operating clearances due to thermal effects also increases contact stresses, and reduces the operating contact angle which reduces the capability of the bearing to react to high axial loads.

### Thermal Analysis Results

The thermal model for Bearing Number 2 predicts temperatures for each node point, and then calculates the volume average temperature for each component. The average component temperatures are then used as input to the mechanical model which provides the friction heat generation. These models iterate until they converge or diverge. The boundary heat transfer coefficient is obviously a critical parameter in the evaluation of the bearing component temperatures. Since most of the surface node temperatures exceed the local saturation temperature of the coolant, the two phase heat transfer characteristics must be considered. In this investigation, nominal heat transfer coefficients were estimated as described in Reference 3. Since many conditions of interest would not converge, and the heat transfer coefficient estimates for such a complex flow field are far from exact, the nominal values were increased in two steps to allow convergence and provide sensitivity data for all the parameters of interest.

The results using the nominal heat transfer coefficient are shown in Figure 8. The effects of preload and inlet coolant temperature are shown for a friction factor of 0.2 and flow rates of 3.6 and 7.0 lbs/sec. Stable solutions were not achieved for the 850 lb preload cases, or any cases with friction factors greater than 0.2. This demonstrates the extreme sensitivity of component temperatures to load and contact friction. Although all the temperature data shown is above the coolant saturation temperature, the magnitude of the temperatures

is not severe. The unstable cases would in theory increase in temperature without bound. The implication is that all the 850 lb cases would produce component temperatures beyond the capability of the bearing materials to survive. The changes in component temperature with inlet coolant temperature and flow rate are not as severe. However, for marginal conditions the solution can be made to diverge by reducing flow or increasing inlet coolant temperature.

To provide additional sensitivity data the heat transfer coefficient was increased until the 480 lb preload case with a friction coefficient of 0.5 converged. This required increasing the nominal heat transfer coefficient by a factor of 2.45. Since bearing temperatures were determined to be less sensitive to coolant inlet temperature and flow, the following series of analyses were conducted with a coolant flow of 7 lbs/sec and a coolant inlet temperature of  $-230^{\circ}\text{F}$ . Temperature results for preload and friction factor variations are shown in Figure 9, based on the above coolant characteristics. The high preload and friction case failed to converge. Shown in Figure 10 is a plot of temperatures vs preload and friction which illustrates the dependence of temperature on these parameters.

Convergence for the most severe operating conditions (850 lbs preload and a friction factor of 0.5) required increasing the nominal heat transfer coefficient by a factor of 3.43. To provide added visibility, all preloads and friction factors were evaluated at the increased heat transfer level. The temperature values at these conditions are shown in Figure 11. The most severe loading and friction conditions produced the highest component temperatures among the converged cases even with the highest heat transfer coefficient. These data are graphically presented in Figure 12 which provides a graphical representation of the component temperature sensitivity to loads and friction. Notice the large temperature difference between the maximum track temperature and average temperature. Since heat transfer coefficients and thermal properties are temperature dependent, this should illustrate the importance of defining the temperature profiles throughout the bearing components to arrive at average values rather than assuming a uniform temperature for each component.

Although the increase in heat transfer coefficient was arbitrary to attain convergence for the high load and friction conditions, these increases are not judged to be impractical due to the inexact methods for estimating the boundary heat transfer for the complex two phase flow conditions. Clearly more work is needed to gain a better understanding of this flow field and corresponding heat transfer characteristics. Figure 13 illustrates the sensitivity of bearing temperatures to heat transfer coefficients for the condition noted. More important is the fact that for friction factors greater than .2 and loads greater than 480 lbs the heat transfer coefficients had to be significantly increased to obtain converged solutions.

Angular misalignments of the outer race up to 31.5 minutes were evaluated to determine the effect on bearing operating temperatures. The outer race was tilted toward the heaviest loaded ball, producing the most severe conditions for the radially loaded bearing. Figure 14 shows the effect of misalignment on bearing temperatures for the conditions noted. The maximum outer race tilt that allowed stable operating conditions was 29 minutes. This condition produces the higher stable operating temperatures than any other condition analyzed. The maximum outer race track temperature was estimated to be 1858°F. The misalignment caused the outer race to heat and expand more than the inner race. Thus the bearing is able to maintain a sufficient operating clearance for higher ball temperatures.

The maintenance of an acceptable operating clearance was found to be a criteria for convergence of the system model. Shown in Figure 15 is a plot of ball temperature and internal operating clearance for the conditions noted. Also shown is the approximate internal clearance that separates the converged and diverged solutions. It is emphasized that the set of conditions shown in Figure 15 is not proposed to be general, and only applies to the specific 45 mm bearing operating under the range of parameters and loading conditions analyzed. Even with this qualification, it is interesting to note that a fairly linear relationship exists between the average ball temperature and operating internal clearance; fairly independent of load, heat transfer, and contact friction. As shown the outer race misalignment case deviates from the general trend. This is caused by increased heating of the outer race relative to the ball and inner race, thus maintaining a larger internal clearance for a given ball temperature.

## Conclusions

The 45 mm LOX turbopump bearing temperatures are extremely sensitive to preload, contact friction, and boundary heat transfer. Although bearing temperatures are less sensitive to subcooling and coolant flow, both conditions are important for maintaining thermal stability at severe operating conditions. Alignment of the outer race was found to be critical as bearing temperatures are very sensitive to this parameter. This condition produced the highest temperatures for stable thermal conditions. The maintenance of an acceptable operating internal clearance was found to be a necessary conditions for stable thermal operating conditions. With the exception of outer race misalignment, the conditions of high friction and high heat transfer produced the highest local temperatures for thermally stable cases. It is suggested that hardware exhibiting high local temperatures (discoloration in ball tracks, etc.) without other effects, such as high surface wear, milling etc., is operating under the conditions of higher contact friction and local heat transfer than normally expected.

Since the bearing temperatures are very sensitive to heat transfer, further work should be done to investigate the possible effect of the internal flow fluid characteristics on fluid/boundary

heat transfer. In addition recent tests of the MSFC bearing and seal materials tester showed a higher dependence of bearing temperature on coolant flow than was predicted by this analysis. This inconsistency in the analysis should be investigated and resolved.

#### References

1. SHABERTH Computer Program Operation Manual, Technical Report, AFAPL-TR-76-90, October 1976.
2. SINDA Engineering Program Manual (Contract No. NAS9-10435), June 1971.
3. Advanced Rocket Engine Cryogenic Turbopump Bearing Thermal Model, J. Cody, L. New and B. Tiller, First Advanced High Pressure Oxygen/Hydrogen Propulsion Conference.

FIGURE 1. SSME LOX TURBOPUMP BEARING/SHAFT LOAD CONFIGURATION

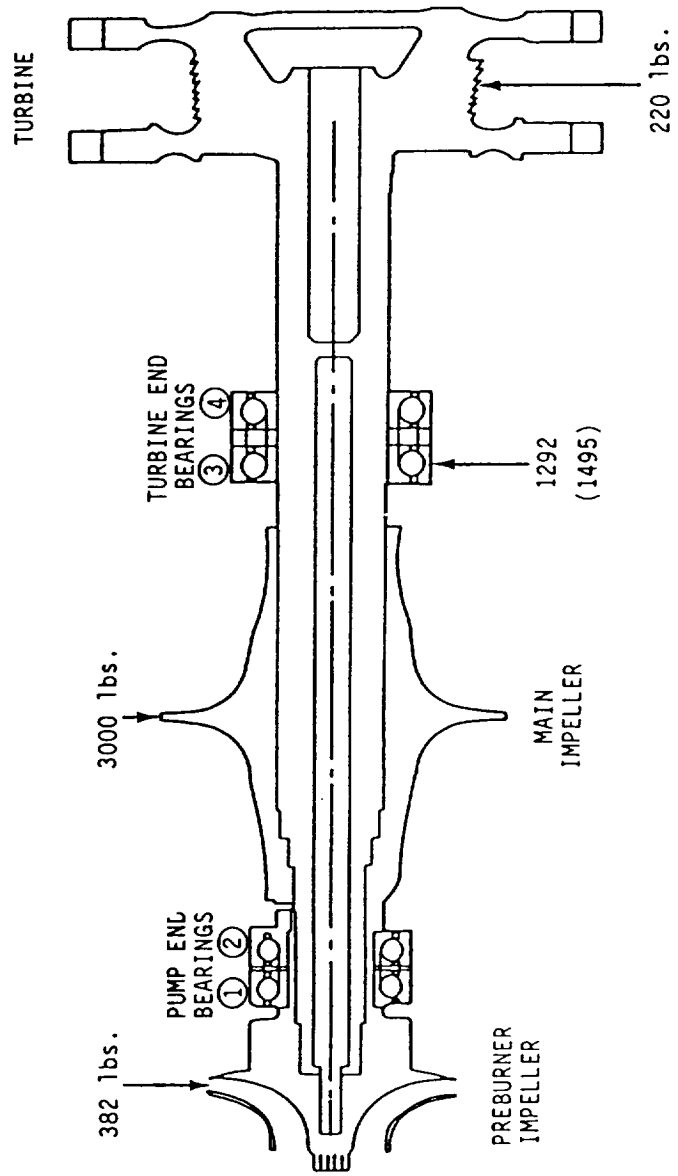


FIGURE 2. NODAL BREAKDOWN OF THE 45mm BEARING THERMAL MODEL

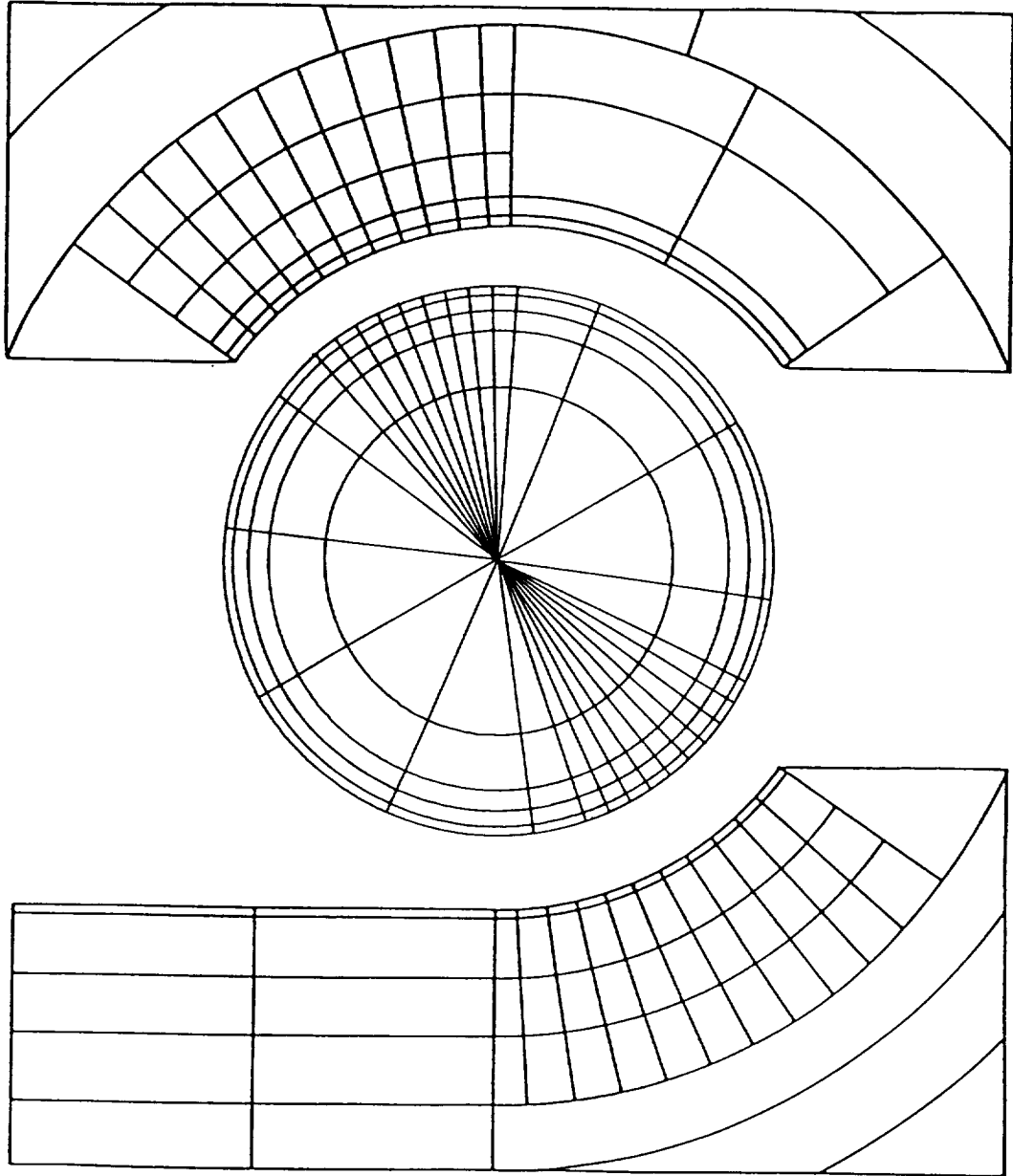


FIGURE 3. ITERATION PROCESS BETWEEN SHABERTH AND SINDA

8501b. AXIAL PRELOAD  
 -230°F INLET TEMP.  
 0.5 FRICTION FACTOR  
 7.0 lbs/sec. COOLANT FLOW  
 343% INCREASED HEAT TRANSFER COEFF.

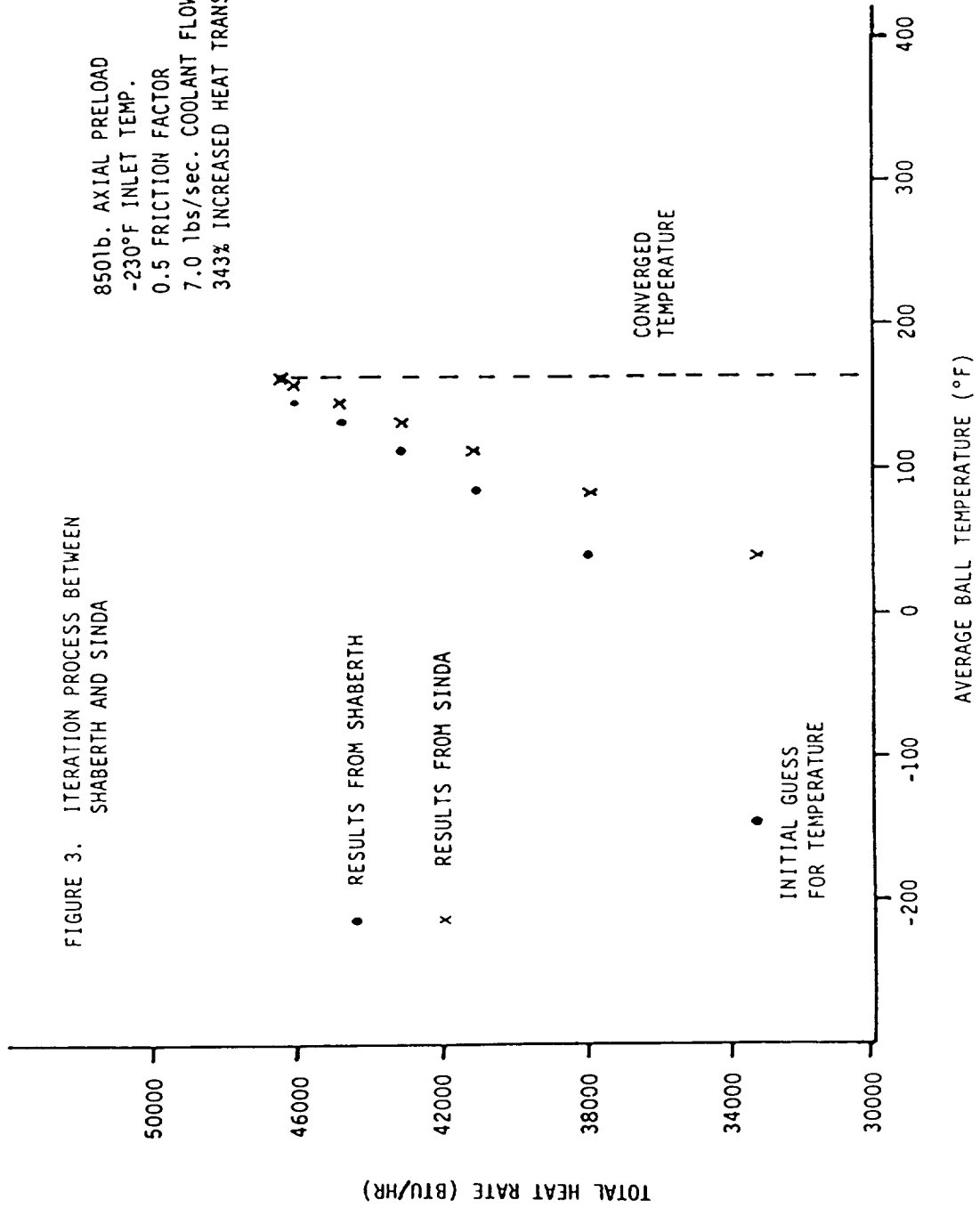
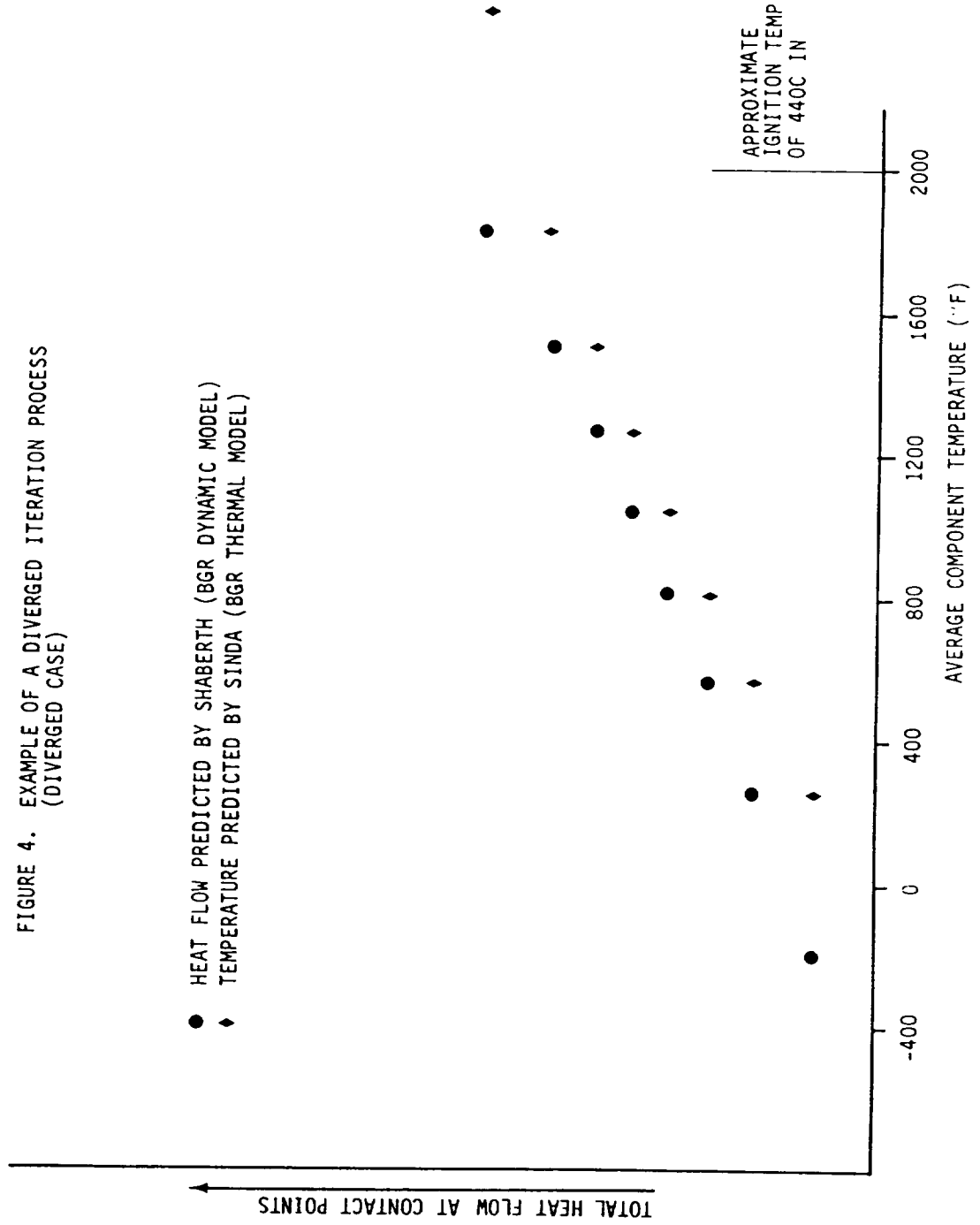


FIGURE 4. EXAMPLE OF A DIVERGED ITERATION PROCESS  
(DIVERGED CASE)





ORIGINAL PAGE IS  
OF POOR QUALITY

FIGURE 5. PARAMETER DATA TREE WITH NOMINAL HEAT TRANSFER COEFFICIENT

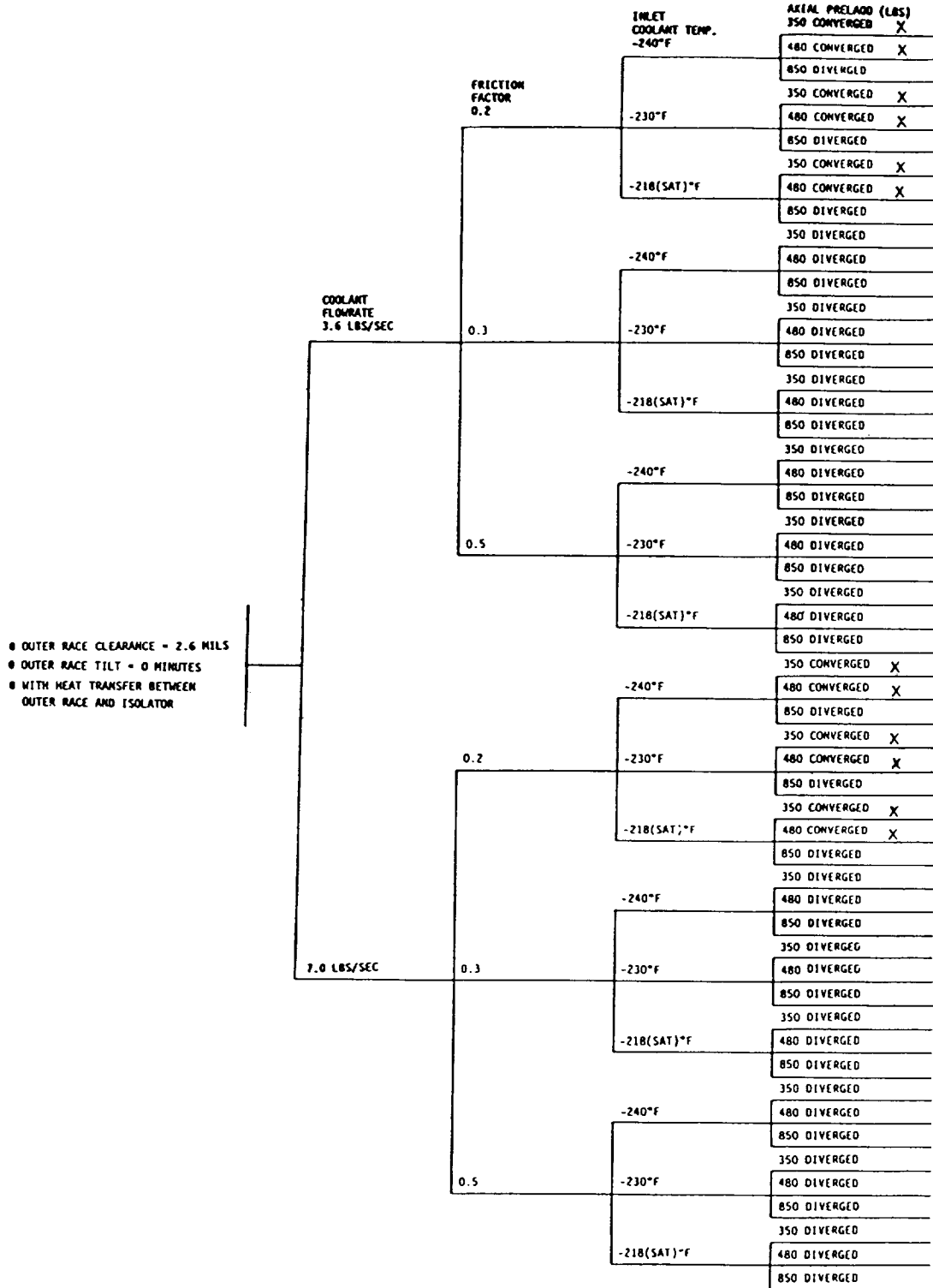


FIGURE 6. PARAMETER DATA TREE WITH INCREASED HEAT TRANSFER COEFFICIENTS

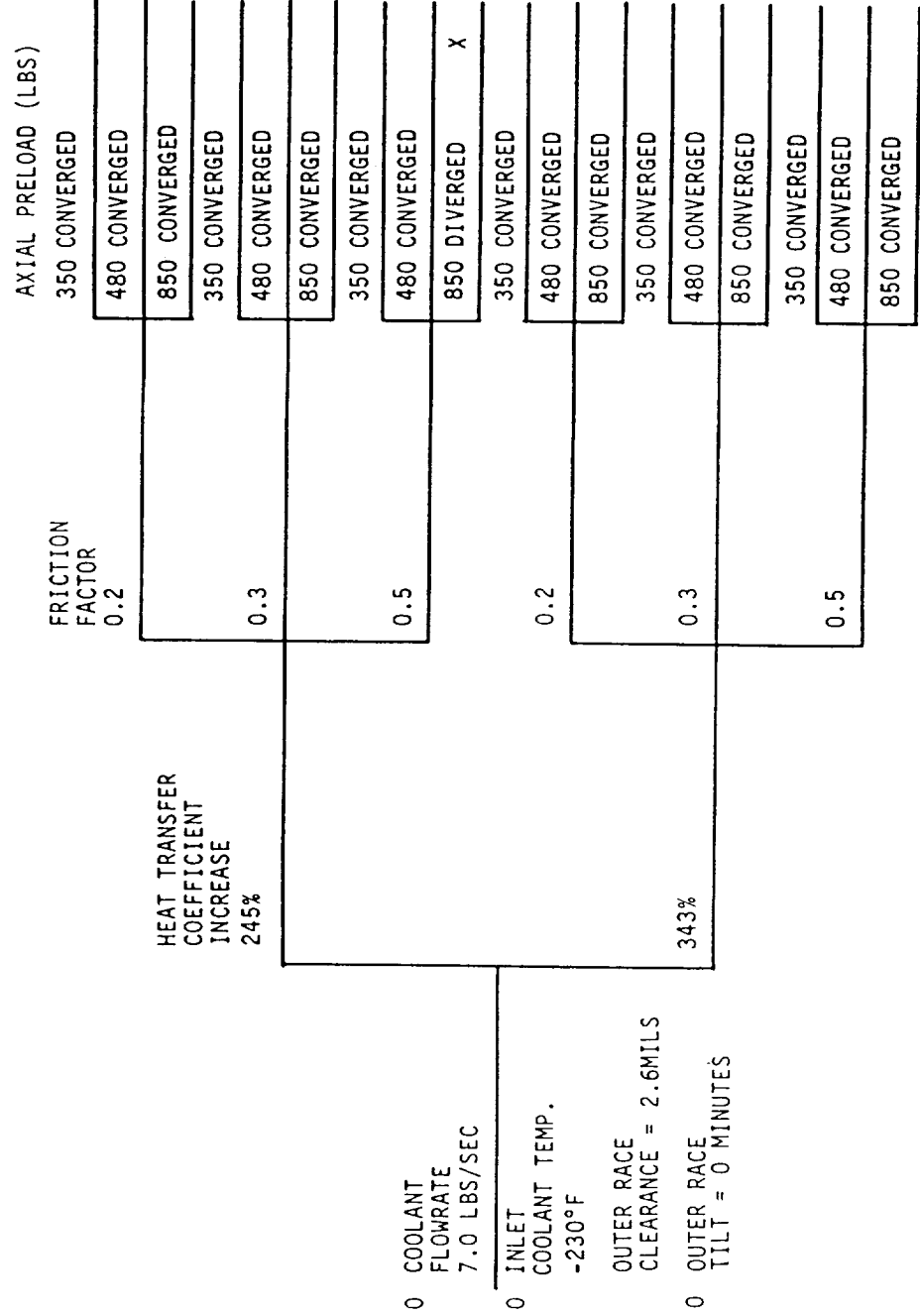
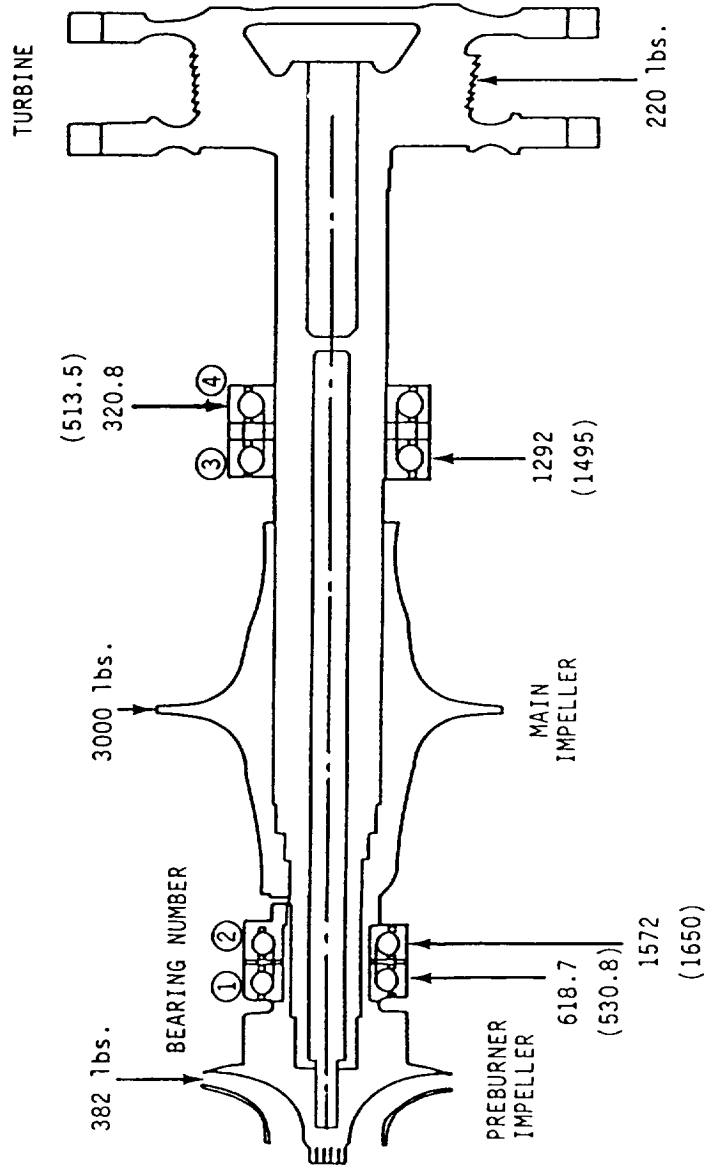


FIGURE 7. SSME LOX TURBOPUMP BEARING/SHAFT LOAD CONFIGURATION  
 UNIFORM TEMPERATURE PROFILE  
 (THERMAL EFFECTS)

480 LB AXIAL PRELOAD  
 6.3 MILS DIAMETRICAL CLEARANCE  
 2.6 MILS OUTER RACE CLEARANCE  
 .2 FRICTION FACTOR



ORIGINAL PAGE IS  
OF POOR QUALITY

FIGURE 8. COMPONENT TEMPERATURES FOR DIFFERENT INLET COOLANT TEMPERATURES

INLET COOLANT TEMPERATURE		BEARING AXIAL PRELOAD (LBS)																	
		350						480						850					
		AVERAGE TEMPERATURE (°F)		MAXIMUM TRACK TEMPERATURE (°F)		AVERAGE TEMPERATURE (°F)		MAXIMUM TRACK TEMPERATURE (°F)		AVERAGE TEMPERATURE (°F)		MAXIMUM TRACK TEMPERATURE (°F)		AVERAGE TEMPERATURE (°F)		MAXIMUM TRACK TEMPERATURE (°F)			
BEARING 1	BEARING 2	INNER RACE	BALL	OUTER RACE	INNER RACE	BALL	OUTER RACE	INNER RACE	BALL	OUTER RACE	INNER RACE	BALL	OUTER RACE	INNER RACE	BALL	OUTER RACE	INNER RACE	BALL	OUTER RACE
-240	-232	-144	-23	-125	65	89	102	-106	47	-101	159	182	172	*	*	*	*	*	*
-230	-223	-125	-1	-113	93	115	120	-95	57	-95	177	195	169	*	*	*	*	*	*
-218	-214	-113	8	-105	106	124	128	-88	63	-88	185	200	176	*	*	*	*	*	*

INLET COOLANT TEMPERATURE		BEARING AXIAL PRELOAD (LBS)																	
		350						480						850					
		AVERAGE TEMPERATURE (°F)		MAXIMUM TRACK TEMPERATURE (°F)		AVERAGE TEMPERATURE (°F)		MAXIMUM TRACK TEMPERATURE (°F)		AVERAGE TEMPERATURE (°F)		MAXIMUM TRACK TEMPERATURE (°F)		AVERAGE TEMPERATURE (°F)		MAXIMUM TRACK TEMPERATURE (°F)			
BEARING 1	BEARING 2	INNER RACE	BALL	OUTER RACE	INNER RACE	BALL	OUTER RACE	INNER RACE	BALL	OUTER RACE	INNER RACE	BALL	OUTER RACE	INNER RACE	BALL	OUTER RACE	INNER RACE	BALL	OUTER RACE
-240	-236	-151	-32	-132	5	79	94	-130	11	-119	118	139	127	*	*	*	*	*	*
-230	-226	-130	-8	-118	85	107	114	-102	49	-101	167	185	162	*	*	*	*	*	*
-218	-214	-113	8	-105	106	124	128	-80	63	-88	185	200	176	*	*	*	*	*	*

COOLANT FLOWRATE = 3.6 LBS/SEC

COOLANT FLOWRATE = 7.0 LBS/SEC

FRICION FACTOR = 0.2  
\* THERMALLY UNSTABLE

FIGURE 9. COMPONENT TEMPERATURES FOR DIFFERENT CONTACT FRICTION FACTORS WITH 245% INCREASE IN HEAT TRANSFER COEFFICIENT

45 MM BEARING

FRICTION FACTOR	BEARING AXIAL PRELOAD (LBS)														
	350				480				850						
	AVERAGE TEMPERATURE (°F)		MAXIMUM TRACK TEMPERATURE (°F)		AVERAGE TEMPERATURE (°F)		MAXIMUM TRACK TEMPERATURE (°F)		AVERAGE TEMPERATURE (°F)		MAXIMUM TRACK TEMPERATURE (°F)				
INNER RACE	OUTER RACE	INNER RACE	OUTER RACE	INNER RACE	OUTER RACE	INNER RACE	OUTER RACE	INNER RACE	OUTER RACE	INNER RACE	OUTER RACE				
0.2	-197	-158	-173	-64	-193	-150	-171	-44	-50	-179	-120	-160	24	8	27
0.3	-176	-110	-139	33	-164	-96	-133	74	59	123	-12	-100	240	205	220
0.5	-98	46	-38	330	-40	157	6	558	503	*	*	*	*	*	*

FLOWRATE = 7.0 LBS/SEC  
 INLET COOLANT TEMPERATURE = -230°F  
 INCREASE IN HEAT TRANSFER COEFFICIENT OF 245%  
 \* THERMALLY UNSTABLE

ORIGINAL PAGE IS  
OF POOR QUALITY

FIGURE 10. 45mm PUMP END BEARING OPERATING TEMPERATURES vs AXIAL PRELOAD

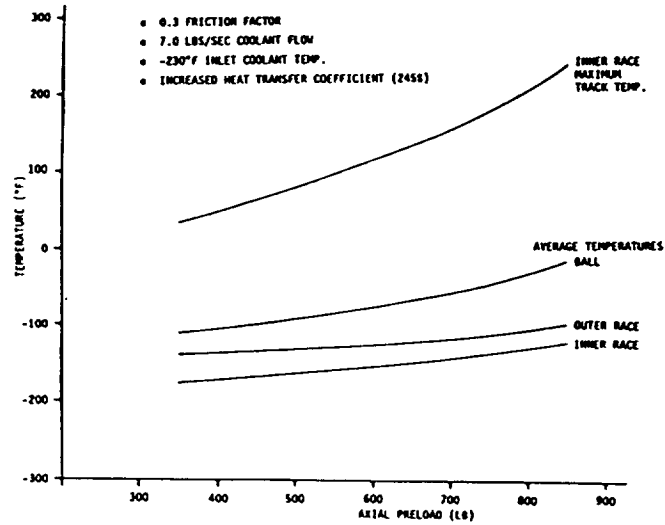
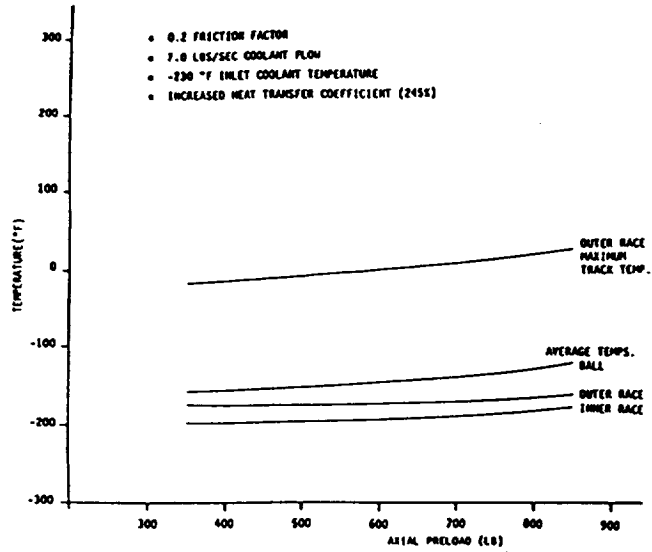


FIGURE 11. COMPONENT TEMPERATURES FOR DIFFERENT CONTACT FRICTION FACTORS WITH 343% INCREASE IN HEAT TRANSFER COEFFICIENT

45 MM BEARING

FRICTION FACTOR	BEARING AXIAL PRELOAD (LBS)																	
	350				480				850									
	AVERAGE TEMPERATURE (°F)			MAXIMUM TRACK TEMPERATURE (°F)	AVERAGE TEMPERATURE (°F)			MAXIMUM TRACK TEMPERATURE (°F)	AVERAGE TEMPERATURE (°F)			MAXIMUM TRACK TEMPERATURE (°F)						
	INNER RACE	BALL	OUTER RACE	INNER RACE	BALL	OUTER RACE	INNER RACE	BALL	OUTER RACE	INNER RACE	BALL	OUTER RACE	INNER RACE	BALL	OUTER RACE			
0.2	-209	-185	-188	-94	-104	-54	-206	-180	-186	-77	-90	-46	-193	-154	-176	-23	-42	-17
0.3	-191	-147	-159	-14	-26	51	-186	-138	-156	14	-4	64	-168	-102	-141	108	73	114
0.5	-149	-62	-92	185	156	292	-132	-32	-81	261	218	328	-28	164	11	719	597	618

FLOWRATE = 7.0 LBS/SEC  
 INLET COOLANT TEMPERATURE = -230 °F  
 INCREASE IN HEAT TRANSFER COEFFICIENT OF 343%

FIGURE 12. 45mm BEARING OPERATING TEMPERATURES vs AXIAL PRELOAD

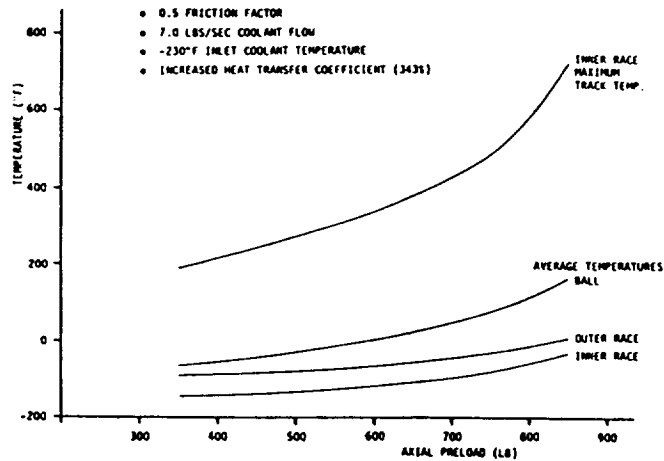
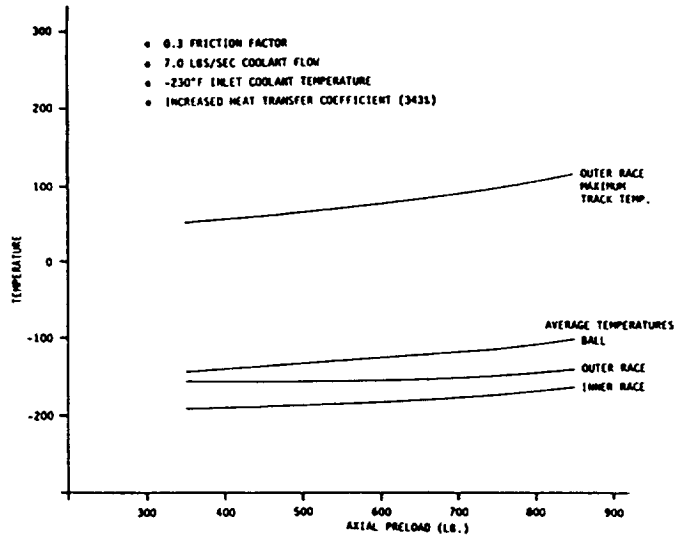
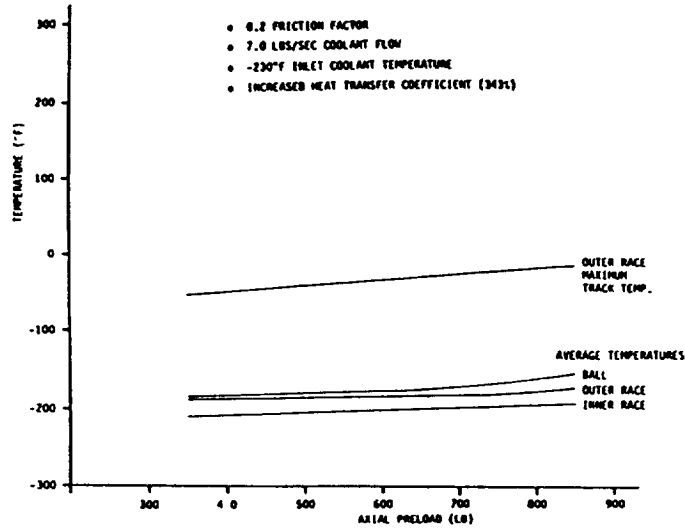
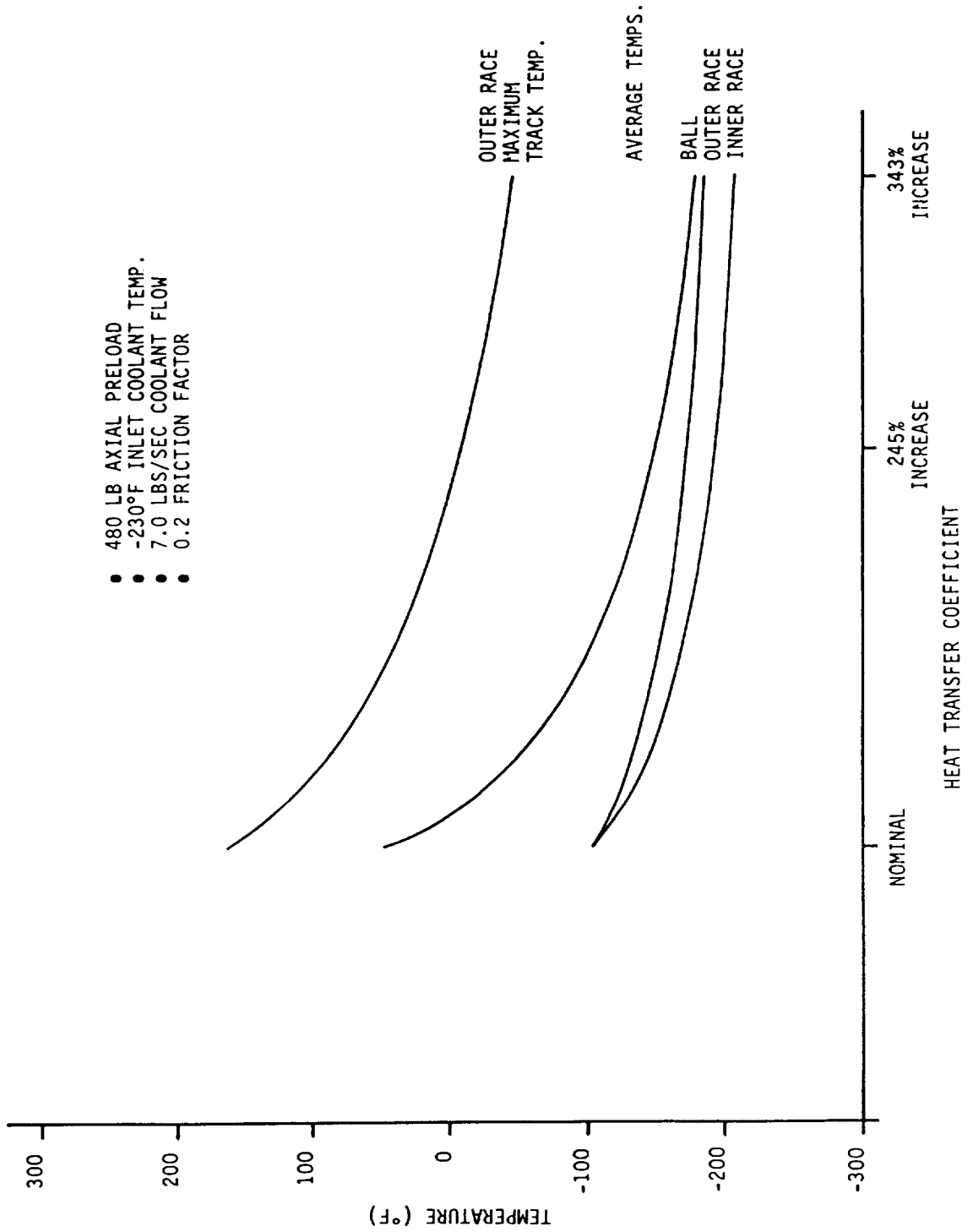




FIGURE 13. 45MM BEARING OPERATING TEMPERATURES VS. HEAT TRANSFER COEFFICIENT



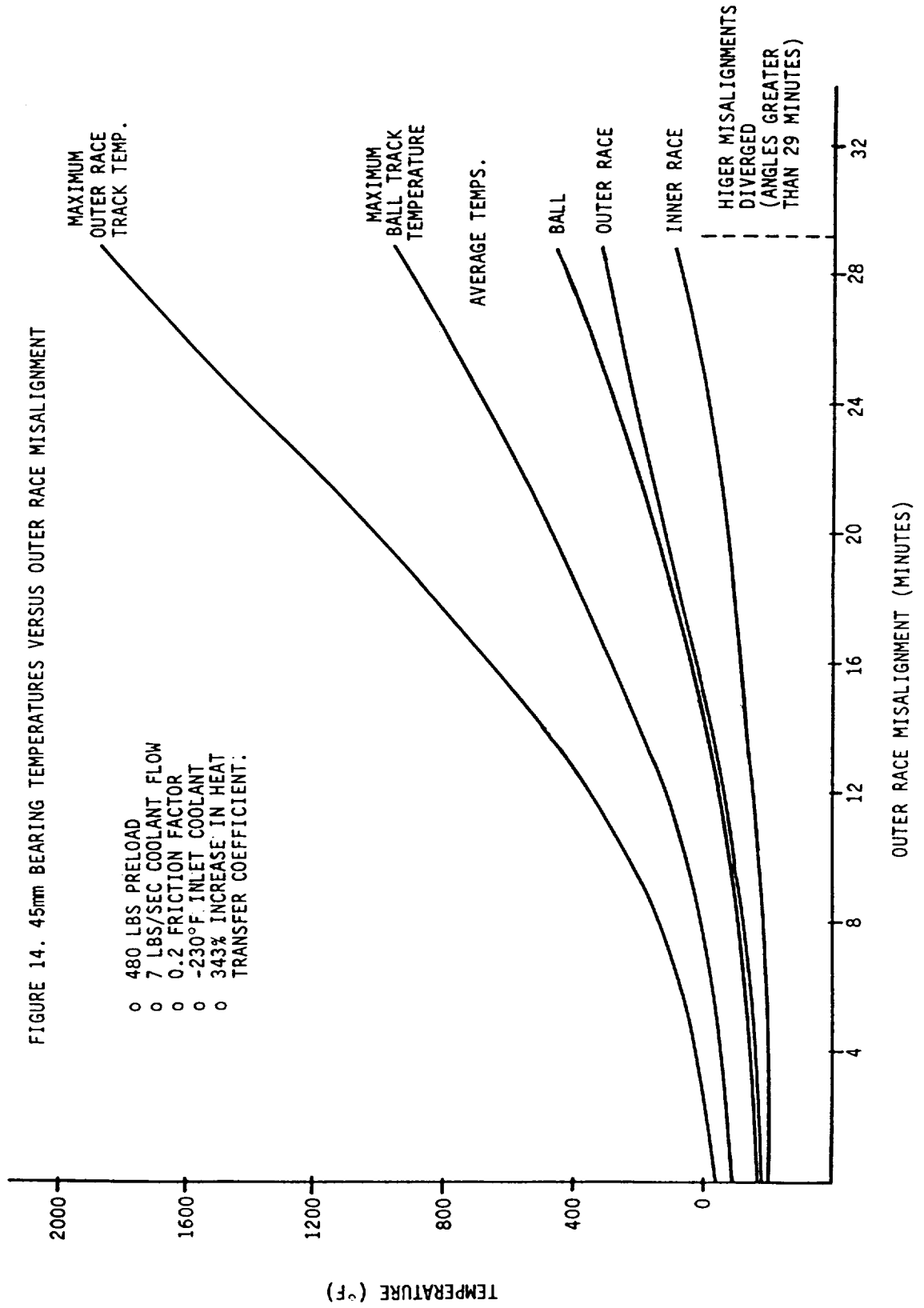
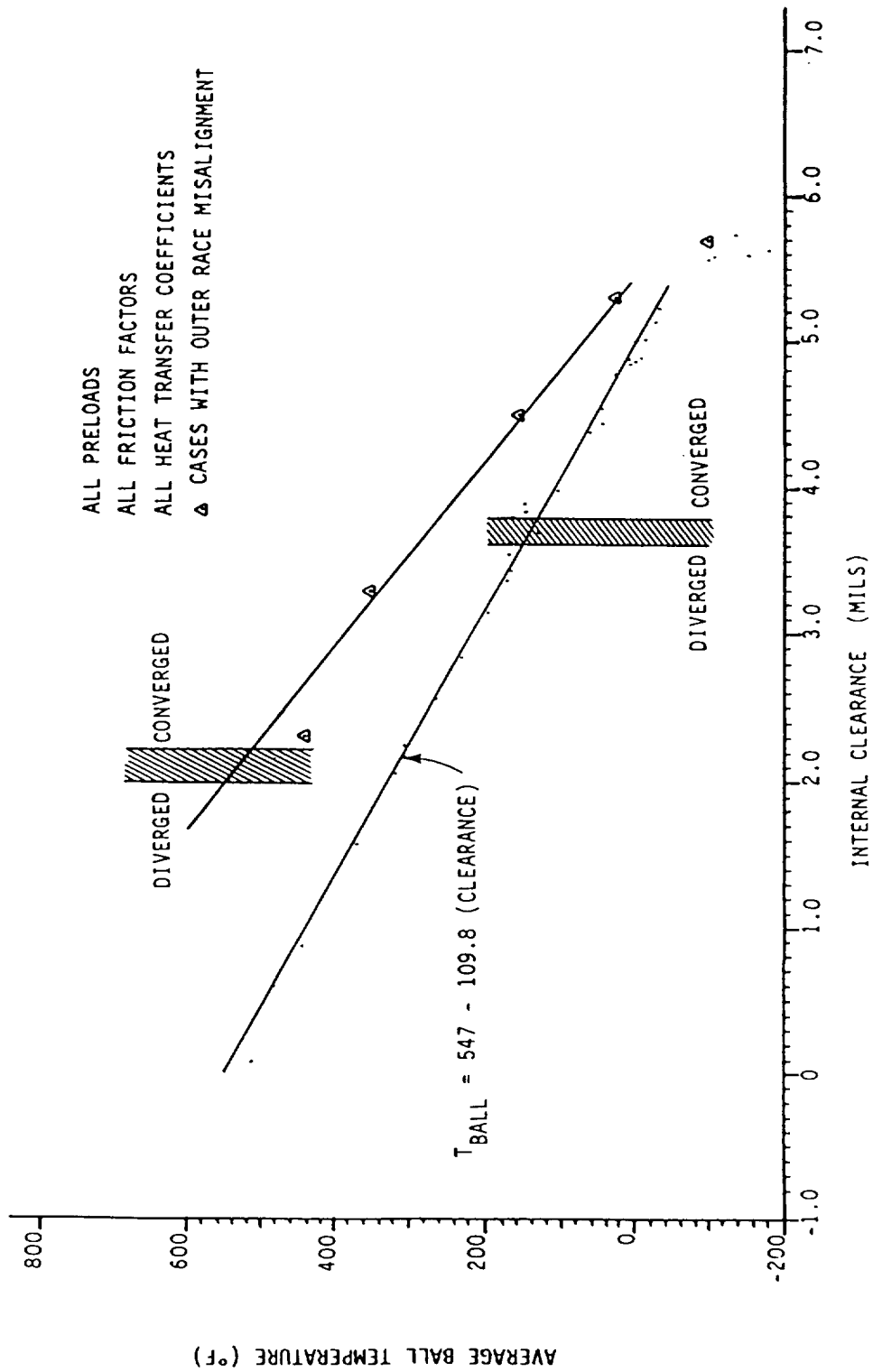


FIGURE 15. AVERAGE BALL TEMPERATURE VS. INTERNAL CLEARANCE



**LUBRICATION EVALUATION OF SSME TURBOPUMP BEARINGS**

by

K. F. Dufrane, J. W. Kannel, and S. A. Barber  
Battelle Columbus Division

**ABSTRACT**

The power density and longevity of the Space Shuttle main engines (SSME) has put enormous demands on the fuel and oxidizer turbopumps. The high pressure oxidizer turbopumps (HPOTP) have required shaft speeds in excess of 30,000 rpm on 57 mm-bore bearings in order to deliver the needed oxygen to the engines. Liquid oxygen is pumped through the bearings to serve as a coolant. With no conventional positive lubrication system, the bearings are lubricated by initial solid films and by possible transfer of polytetrafluoroethylene (PTFE) from the bearing cage to the ball-race interface. Despite the hostile environment, the design goal for the bearings is 27,000 seconds with a high degree of reliability.

The current bearing performance, while still short of the goals, has been adequate for multiple launches. This performance has been achieved through an evolutionary process. The process has involved significant efforts in evaluating and controlling radial and axial loads, coolant flow, bearing dimensions and tolerances, solid film lubrication, and duty cycles. The paper describes some of the rationale for bearing improvements and problems remaining to be solved in order to achieve the optimum life.

## INTRODUCTION

The desired multiple-launch capability of the Space Shuttle requires the SSME turbopumps to operate for 27,000 seconds and 55 starts between overhauls. Besides this extremely long service life (by rocket-engine standards), projected needs for the Shuttle require further increases in SSME power levels through increases in turbopump speed. The projections are:

- 104 percent (current)
- 109 percent (full power level),
- 115 percent (power level growth), and
- 130 percent (ultimate objective).

Since measurements made on the MSFC bearing tester have shown that bearing power consumption increases with nearly the cube of shaft speed, these increases in power level can be expected to cause increases in bearing problems.

Currently the turbopump bearings are capable of multiple launches at the 104 percent power level. This achievement is the result of improved load control, solid lubricant coatings, and bearing design improvements. After a few launches, however, the bearings experience excessive wear and must be replaced. The deterioration apparently is the result of periods of inadequate cooling and/or insufficient lubrication. This paper describes some of the observations made on deteriorated bearings, which helped to guide the improvements to the current levels, and some of the lubrication considerations needed for further life extensions.

## PREVIOUS BEARING SYSTEM IMPROVEMENTS

Numerous improvements were made to the bearing system of the high pressure liquid oxygen turbopumps (HPOTP) after initial testing showed the presence of life-limiting problems. A review of examples of the problems, analyses, and corrections demonstrates the progress and provides the background for the remaining improvements to be made to meet the long-term Shuttle performance goals.

### Initial Bearing Distress

The rotor of the HPOTP is supported by two sets of angular contact ball bearings, Figure 1. The bearings are designed with low contact angles (20 degrees) to provide radial stiffness. An axial preload is provided by spring washers to remove free clearances. The shaft is located axially by bearings 3 and 4 (turbine end), which have a 3800 N (850 lb) preload and are connected to the pump body through a spring cartridge. The cartridge limits the axial travel between positive stops. The dynamic location of the shaft is provided by a balance piston incorporated in the oxygen turbine.

While the early HPOTP tests proved the bearings capable of successful operation for times equivalent to several launches, bearing distress was observed after periods of 2000 to 5000 seconds of operation. Evidence of classic axial overload was apparent, such as the ball contact path extending to the shoulder of the inner race, Figure 2, with a plastically deformed burr replacing the chamfer at the shoulder, Figure 3. Surface spalling was often present, Figure 4, which was associated with a network of subsurface cracks, Figure 5. A few examples of excessive ball-cage loading were also observed, such as shown in Figure 6. Inspection of the inner race ball contact paths on bearings having less overload damage revealed varying path widths and locations, which indicated the presence of synchronous (unbalance) loads on the rotor in addition to the high axial loads.

ORIGINAL PAGE IS  
OF POOR QUALITY

HIGH PRESSURE OXYGEN TURBOPUMP

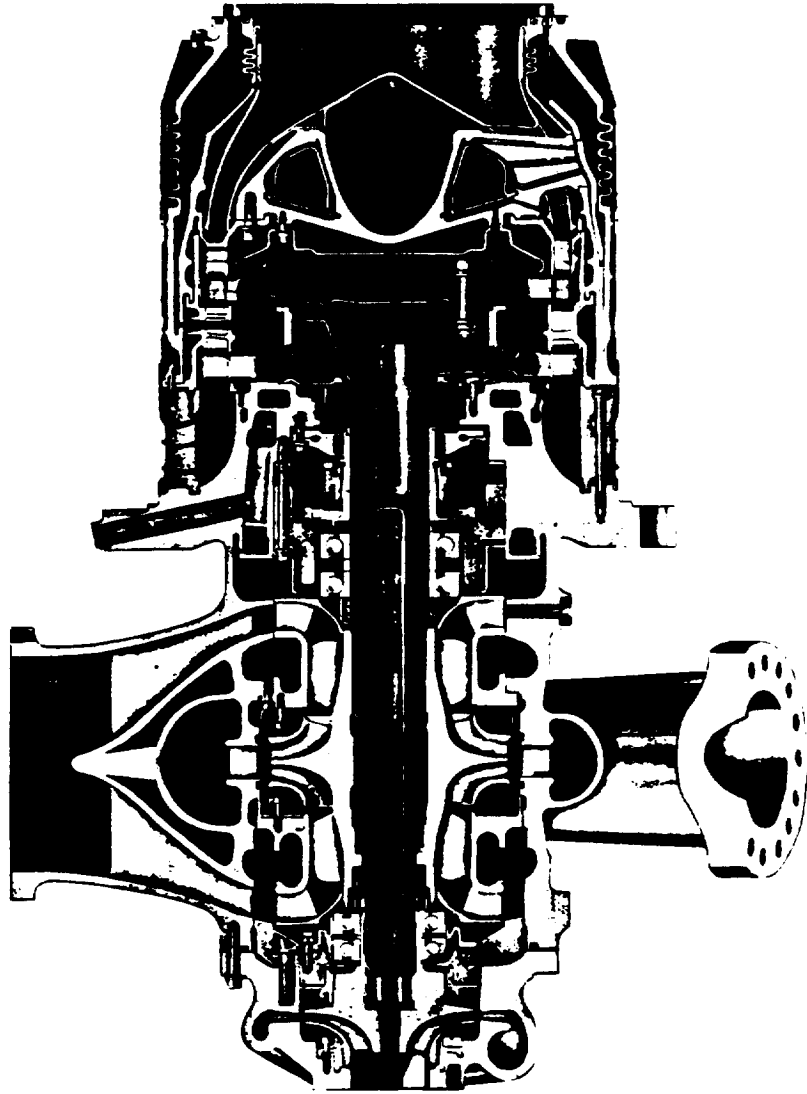
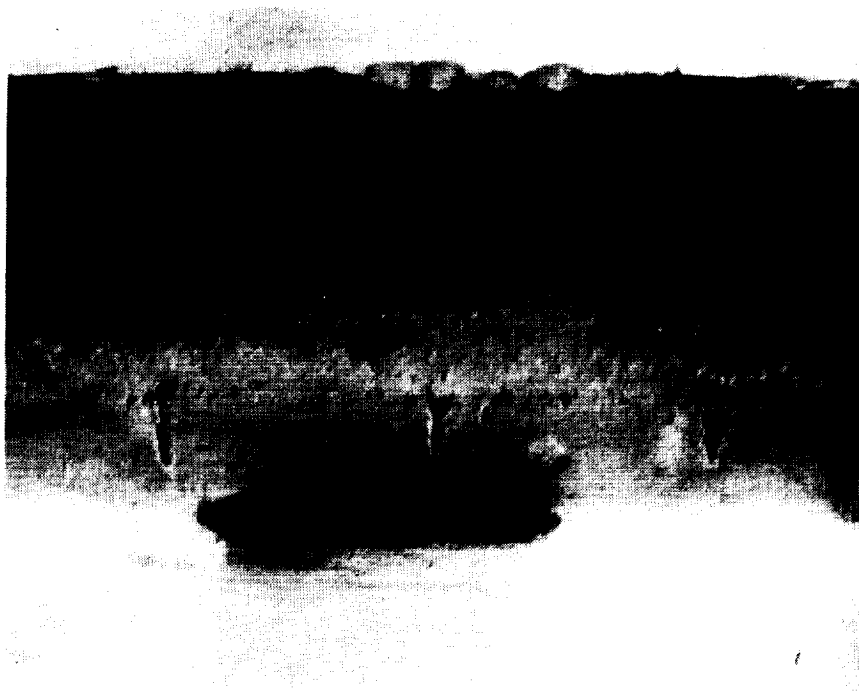


FIGURE 1. BALL BEARINGS SUPPORTING ROTOR OF HPOTP

11

ORIGINAL PAGE IS  
OF POOR QUALITY



8X

OK928

FIGURE 2. BALL-PATH SPALLING AND CHIPPING AT EDGE  
OF RACE CURVATURE ON BEARING NO. 3 FROM  
HPOTP NO. 9008



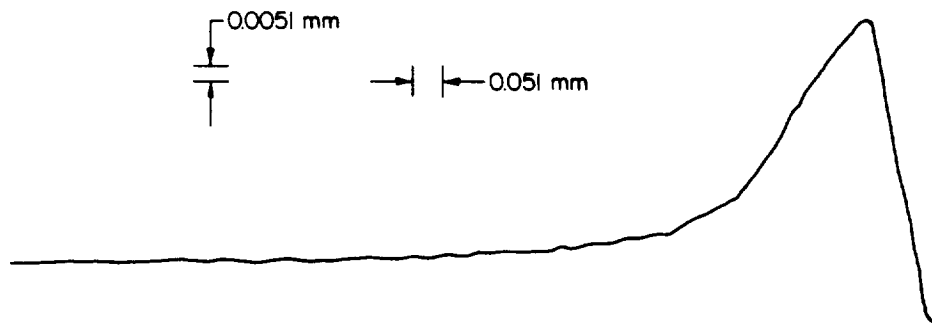
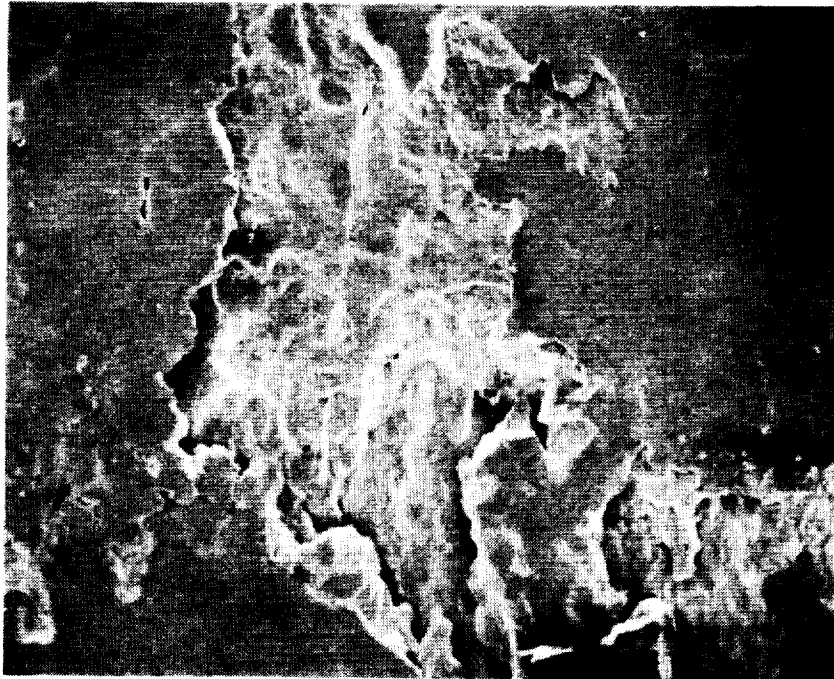


FIGURE 3. PROFILE OF BURR AT EDGE OF RACE CURVATURE ON INNER RACE OF BEARING NO. 3 FROM HPOTP NO. 9008

ORIGINAL PAGE IS  
OF POOR QUALITY



67X

24944A

FIGURE 4. SCANNING ELECTRON MICROGRAPH OF SPALLING ON  
INNER RACE OF BEARING NO. 3 FROM ENGINE  
NO. 9008

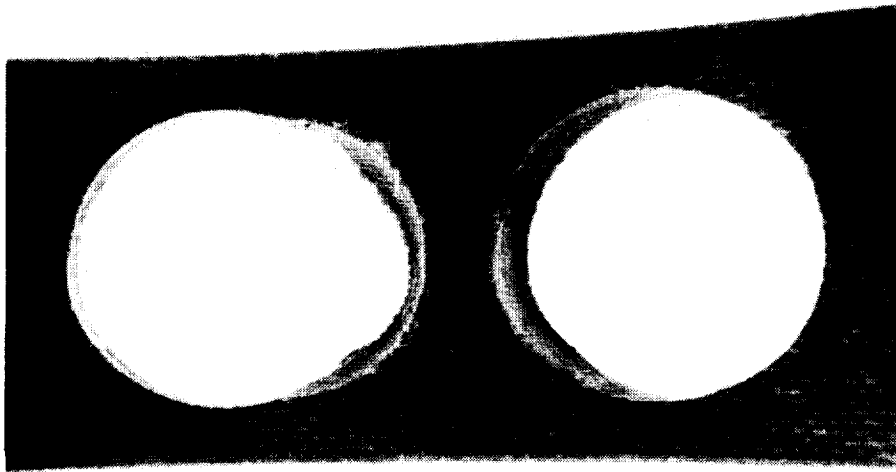


67X

24944A

FIGURE 5. OXIDATION IN SUBSURFACE CRACKS IN OUTER RACE  
OF BEARING NO. 3 FROM ENGINE NO. 9008

ORIGINAL PAGE IS  
OF POOR QUALITY



3X

OK927

FIGURE 6. BALL POCKET ELONGATED BY WEAR IN RETAINER  
OF NO. 3 FROM HPOTP NO. 9008

## Load Determinations

The load computations were performed using the computer program BASDAP\*. BASDAP programs can be used for static and dynamic analyses of bearings of various designs. Ball-race stresses and contact areas, steady-state motions, and contact angles are calculated for normal operation. Also, the dynamic behavior of the retainer is analyzed to determine retainer stability and ball-retainer loads<sup>(1)</sup>. A quasi-dynamic version of the BASDAP computer code was used for the HPOTP bearings. This code calculates ball-race forces (inner and outer), contact pressures, contact dimensions, and contact angles as a function of axial and radial load.

The computation technique involves first computing the load sharing between the balls in the absence of centrifugal forces. This involves a formalized trial and error (nesting type) procedure. Estimates of the axial and radial deflections of the bearing are made. The correct value of these deflections results in the correct radial and axial load. After the ball load sharing has been computed, the effect of centrifugal force on contact angle is computed. Centrifugal force causes the inner and outer race contact angles to be different from each other as well as different from the static contact angles. The method for the deflection and contact angles calculation is modeled after the classic work of A. B. Jones<sup>(2)</sup>.

With the results of the calculations relating contact dimensions and contact angles to axial and radial loads, a comparison was made of the actual ball path dimensions and locations. With the best simultaneous fit of the measured contact widths and locations on both races, an estimate could be made of the actual applied loads experienced by the bearings.

Figure 7 is a cross sectional sketch of a used HPOTP turbine-end bearing that had been subjected to the expected axial loading of 3850 N

---

\*BASDAP is a Battelle-developed bearing dynamic computer model.

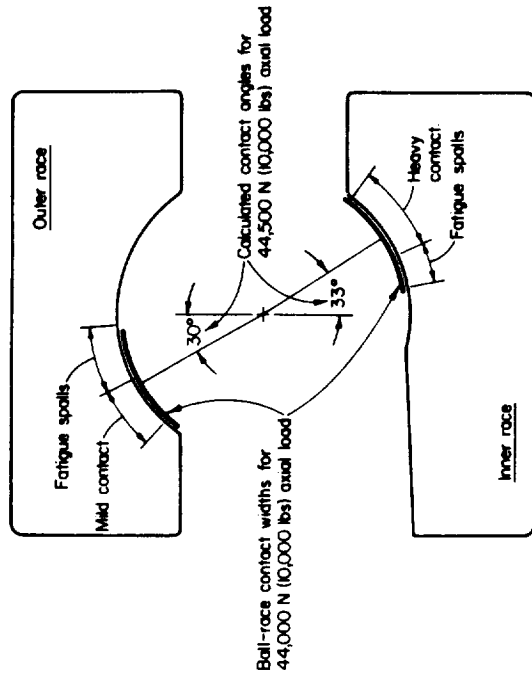


FIGURE 8. LOCATION OF MEASURED BALL CONTACT PATHS ON USED HPTOP TURBINE-END BEARING SUBJECTED TO EXCESSIVE AXIAL LOADING

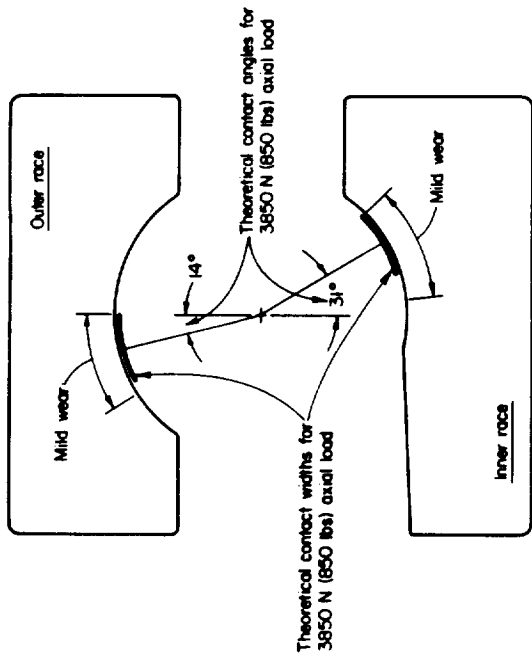


FIGURE 7. COMPARISON OF LOCATION OF ACTUAL BALL CONTACT LOCATIONS WITH THEORETICAL PREDICTIONS ON USED HPTOP TURBINE-END BEARING SUBJECTED TO NORMAL LOADING

(850 lbs). The widths and locations of the actual ball contact paths coincided closely with the BASDAP predictions. Figure 8 shows an example of a second HPOTP turbine-end bearing that had experienced excessive axial loads.

The best simultaneous fit of the contact angles and widths of the ball contact paths indicated an axial load of approximately 44,500 N (10,000 lbs) had been experienced by the bearing. Rows of fatigue spalls also confirmed the high loadings.

Following the load calculations and observations on used bearings, experiments were run on a HPOTP instrumented to measure axial loads during service. These measurements indicated that transitory axial loads to 53,000 N (12,000 lbs) were occurring during portions of the operational cycle.

### Bearing System Improvements

In the course of the SSME program, several design and assembly corrections were made to the HPOTP's. Improved rotor balancing at higher speeds reduced the synchronous radial loads to acceptable levels. Improvements to the balance piston system reduced the axial loads significantly and eliminated the recurring bearing damage from overloading originally observed.

Improvements in the lubrication of the bearings were also made. The bearing components were coated with  $\text{MoS}_2$  to enhance the lubrication intended to be provided by the transfer of PTFE from the ball retainer. Measurable ball and race wear indicated that insufficient PTFE transfer was occurring to lubricate the bearing. The  $\text{MoS}_2$  permitted operation for several launch cycles with minimal ball and race wear.

### CURRENT AND FUTURE BEARING NEEDS

While the initial design, assembly, and lubrication improvements permitted multiple launches at the 104 percent power level, qualification tests at the 109 percent power level have experienced recurring wear problems. After four to five test cycles at the 109 percent level, excessive wear (primarily of the balls) is experienced. Apparently slight degradation of the bearing components and consumption of the solid lubricant films initiates a rapid deterioration process. Ball wear to 0.2 mm (0.008 in.), diametral, has been observed in a single test cycle after five previous successful cycles. Further improvements are clearly needed in the cooling and/or lubrication of the bearings to meet the multiple-launch requirements at 109 percent and greater power levels. The cooling is primarily a design consideration involving the management of the flow of liquid oxygen throughout the HPOTP. Efforts are being pursued by NASA and Rocketdyne to insure adequate bearing cooling. However, improvements in bearing lubrication are needed to extend bearing life and reduce the sensitivity to transient loads or periods of reduced cooling.

## HPOTP LUBRICATION

### Elastohydrodynamic Lubrication

The life of rolling contact bearings is dependent on both the level of contact stresses and on the lubrication at the ball-race interface. Under ideal conditions, a hydrodynamic film of a liquid lubricant is formed between the balls and races, which completely separates the metallic elements. Under full hydrodynamic lubrication ball or race surface distress is eliminated and extremely long bearing life is possible if the loads are controlled. This kind of lubrication, which is known as elastohydrodynamic (EHD) lubrication, occurs in many situations such as the main shaft bearings in a jet engine. In many systems, however, EHD lubrication is not possible and other types of lubrication such as solid films must be used. Solid lubricant films can be formed as a result of a chemical reaction between additives in the liquid lubricant and the balls or races, can be precoated onto the balls and races, or can be transferred from a lubricant source.

### Possibilities of Elastohydrodynamic Lubrication of Turbopump Bearings

In the SSME turbopump bearings the only liquid that is available is the cryogenic fluid (liquid oxygen or hydrogen) that flows through the bearing. These fluids are not considered to be lubricants although they can cause the formation of a hydrodynamic film under low stress conditions<sup>(3)</sup>. EHD films a few tenths of a micrometer in thickness were measured in a twin disk machine simulating ball race contact using liquid nitrogen ( $LN_2$ ) as the "lubricant". The stresses in the experiments were very low ( $\mu 0.3$  GPa) as opposed to SSME turbopump ball-race stress ( $\mu 2$  GPa). When the measured film thickness data were extrapolated to SSME conditions, the predicted films were insufficient to imply separation of the balls and races. In addition, experiments conducted at higher (simulated ball-race) stress levels indicated that the friction



between the surfaces was much higher than would be expected from a hydrodynamic film. It appears to be highly unlikely that the SSME turbopump bearings are or can be hydrodynamically lubricated.

One very positive observation made in the EHD experiments with  $\text{LN}_2$  was the level of surface distress to the disks. After several experiments the disks were still in excellent condition despite the severity of the operating parameters. The lubricant in a conventional high speed bearing actually serves two purposes. One purpose is to separate the surfaces with a replenishable EHD film. The second purpose is to extract the frictional heating from the bearing. The cryogenic fluids serve the second of these purposes and permit the bearings to operate for a useful period. If some non-hydrodynamic layer could be used to separate the balls and races, with the cryogenic fluid providing the cooling, very good SSME life could be achieved. Since the cryogenic fluids are incapable of generating the needed EHD films, solid film coatings appear to be the best possibility to meet the need.

#### Solid Film Pre-Coatings

With the extended life provided by  $\text{MoS}_2$  coatings on the turbopump bearings, laboratory experiments were conducted with  $\text{MoS}_2$  coatings in an  $\text{LN}_2$  environment. The experiments were conducted with a four-ball test device (one ball in sliding contact with three stationary balls), Figure 9. The conditions were selected to simulate stress and slip in an SSME bearing. Table 1 shows wear data for several materials. The friction was very low (0.03) as long as the solid film was present on the balls. Wear of the solid film was relatively low and, of course, there was no wear of the substrate when the film was intact. However, when the solid film was worn off the friction coefficient was high ( $\mu 0.04$ ) and ball wear occurred. The results showed a longer life with thicker coatings and a longer life at ambient temperatures than in  $\text{LN}_2$ . Without lubrication all three ball materials experienced high wear and high friction coefficients.

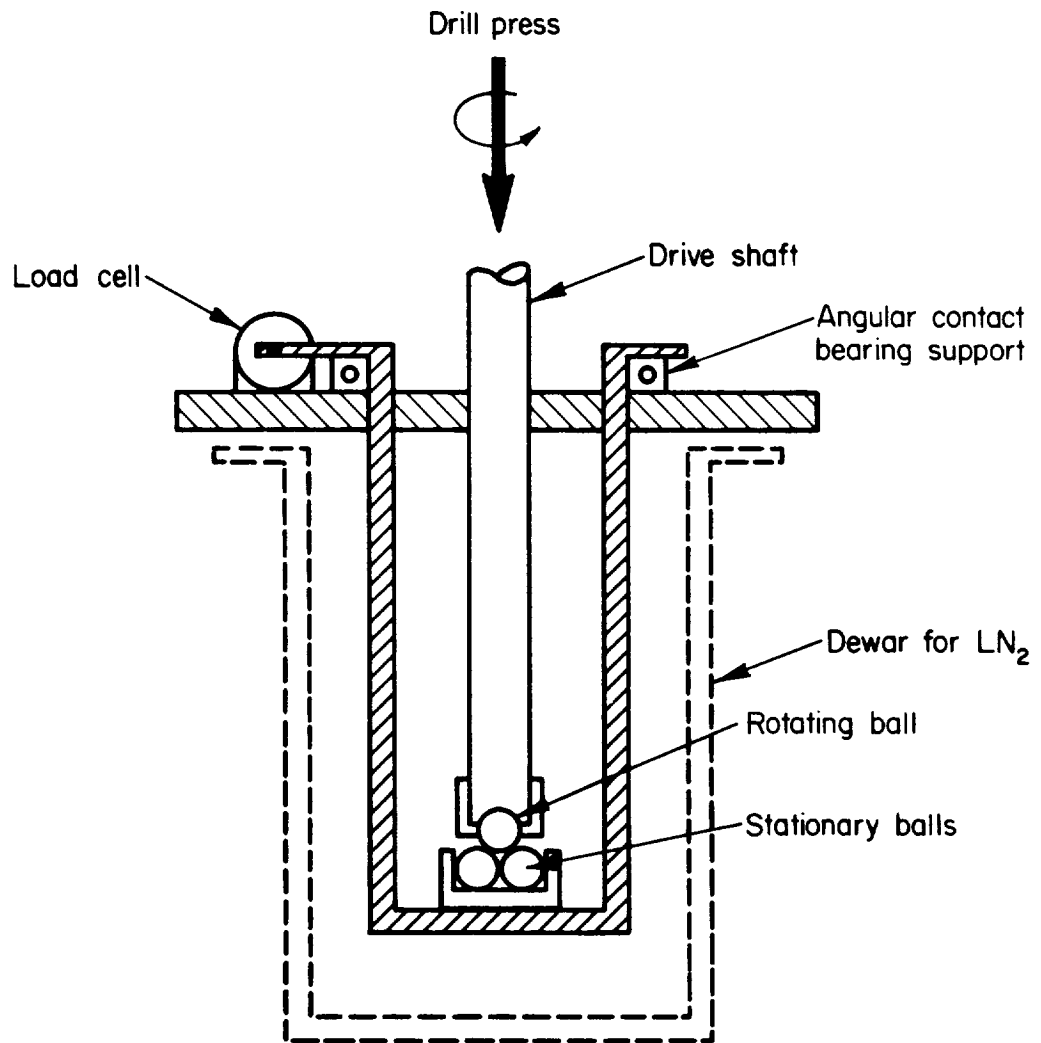


FIGURE 9. SCHEMATIC DRAWING OF FOUR BALL  
FIXTURE FOR WEAR EXPERIMENTS

TABLE 1. SUMMARY OF FOUR BALL WEAR TEST

Material	Coating Thickness $\mu\text{m}$	Coating Duration, min		Wear Scar, mm		Friction Coefficient*	
		Ambient	$\text{LN}_2$	Ambient	$\text{LN}_2$	Ambient	$\text{LN}_2$
440C	none	--	--	2.17	1.68	0.6	0.6
BC42	none	--	--	1.90	1.50	0.4	0.5
StarJ	none	-	--	3.58	2.00	0.4	0.3
440C	$\text{MoS}_2(1.5)$	16.0	1.05	--	--	0.03	0.03
440C	$\text{MoS}_2(0.5)$	9.0	--	--	--	0.03	0.03
BC42	$\text{MoS}_2(1.5)$	45	4.0	--	--	0.03	0.03
BC42	$\text{MoS}_2(0.5)$	6	--	--	--	0.03	0.03
StarJ	$\text{MoS}_2(1.5)$	25	2	--	--	0.03	0.03
StarJ	$\text{MoS}_2(0.5)$	20.5	--	--	--	0.03	0.03

Ball Diameter = 12.7 mm

Speed = 1200 rpm

Load = 165 N

\*Lower limit of detection was 0.03

## Transfer-Film Coatings

### Bearing Experiments

Because of the problems of recoating  $\text{MoS}_2$  on the surfaces, a preferred method for solid-film coating the bearings would be to transfer a solid film from the cage to the balls. Transfer film lubrication can allow for a quantity of solid lubricants to be available to the ball-race interface. The cage in the SSME turbopump bearings is a glass-fiber-reinforced PTFE. Under ideal conditions, the PTFE transfers to the balls and, subsequently, to the races. Low speed full bearing tests were conducted with HPOTP bearing (drawing 7955) to evaluate PTFE lubrication. The apparatus, Figure 10, consisted of a test bearing loaded axially to 60,000 N (13,000 lbs) and driven by variable speed motor. The motor was mounted on a bearing and constrained by a load cell to measure torque. Results of the tests are given in Figure 11.

Bearings preburnished with PTFE or Rulon survived for  $0.27 \times 10^6$  revolutions before a major torque change (indicating loss of film) occurred. Dry bearings lasted for only a few hundred revolutions. The burnished films were thus adequate to lubricate the bearing, but were not replenished by the cage. The cage had been used in previous experiments and apparently the available PTFE had been removed from the cage surface. Figure 12 shows the edge of a cage pocket from a used bearing. The exposed glass fibers protrude from the surface and can be expected to disrupt transfer and cause wear of the balls.

### Ring Experiments

Experiments are currently being conducted to improve the understanding of transfer film lubrication in the SSME turbopump bearings. A block of cage material is loaded against a 440C ring as shown in Figure 13. Several PTFE-rich materials have been evaluated with the apparatus including:

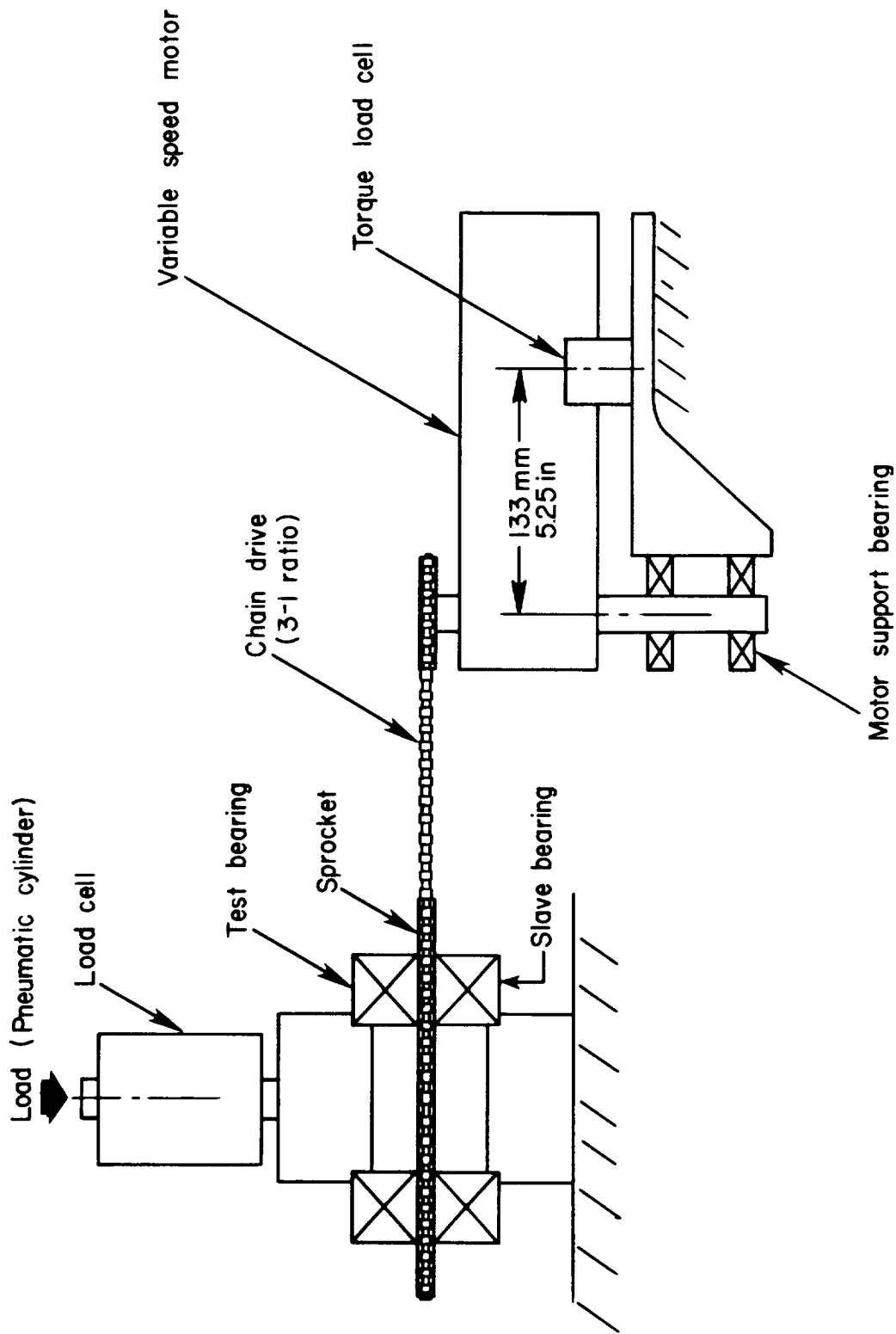


FIGURE 10. SCHEMATIC DIAGRAM OF BEARING TEST APPARATUS

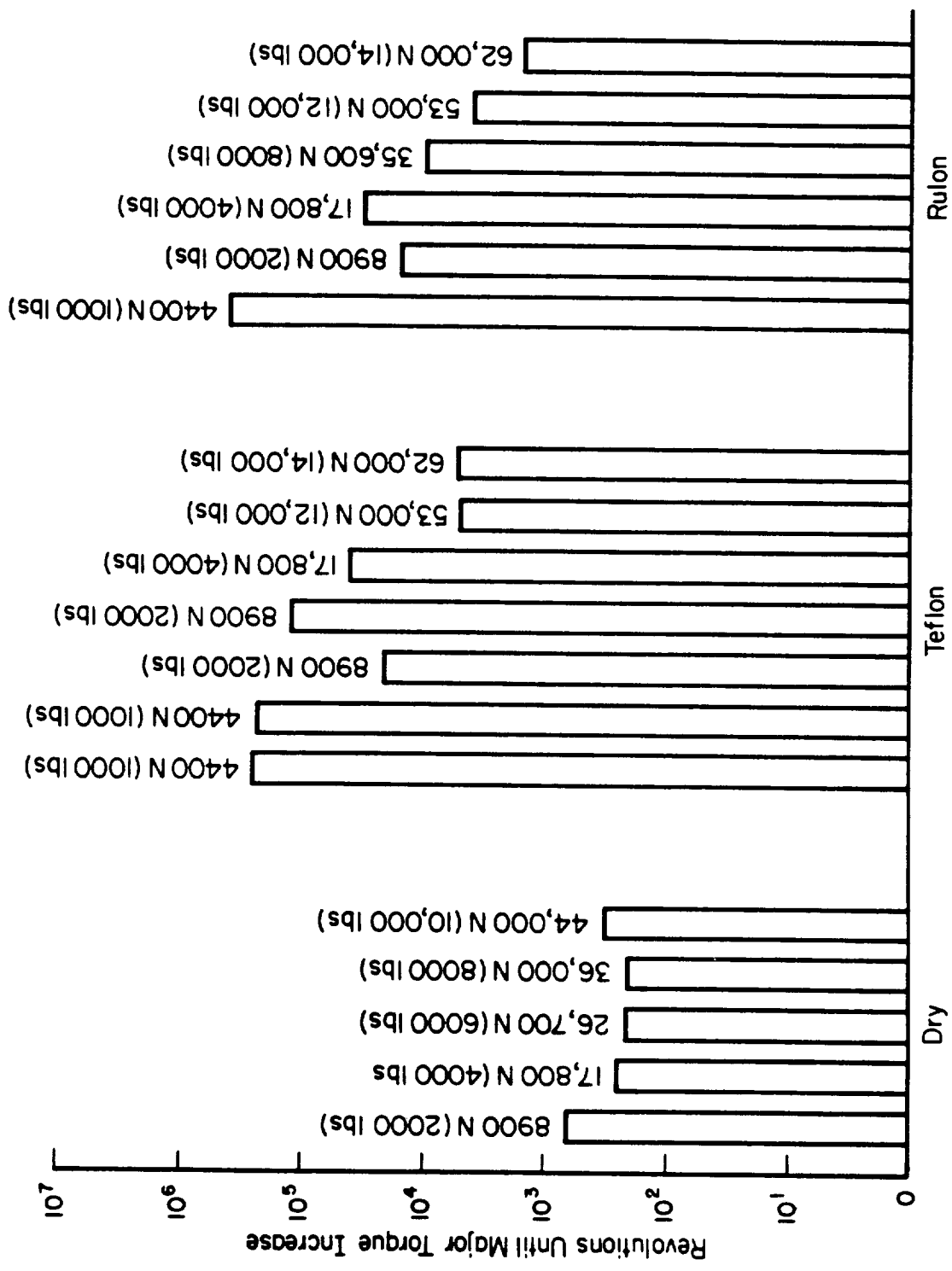
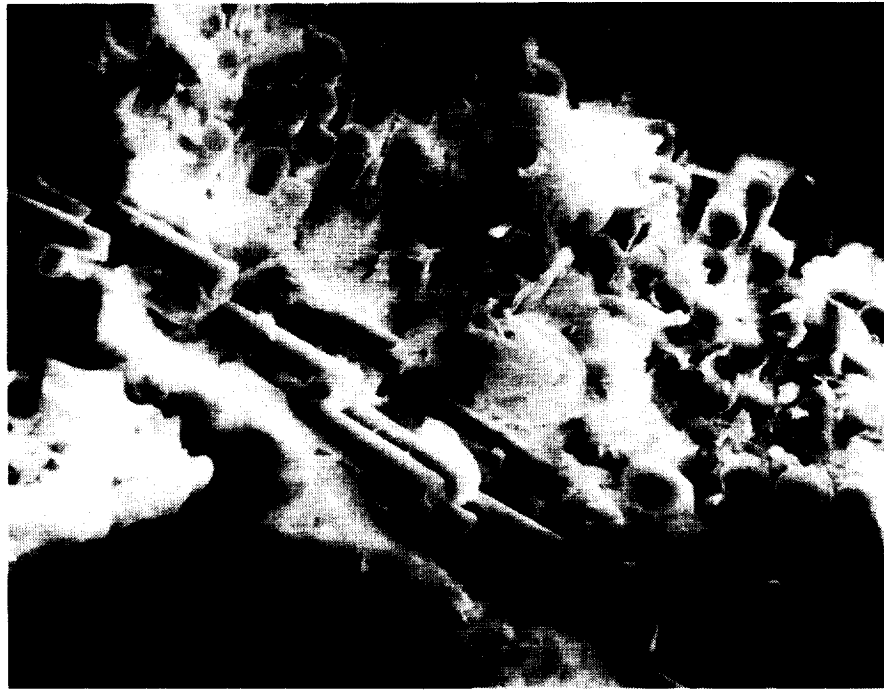


FIGURE 11. SUMMARY OF DURATION OF BURNISHED FILMS

ORIGINAL PAGE IS  
OF POOR QUALITY



21159

1000X

FIGURE 12. ENDS OF GLASS FIBERS IN BALL POCKET  
OF USED HPOTP CAGE

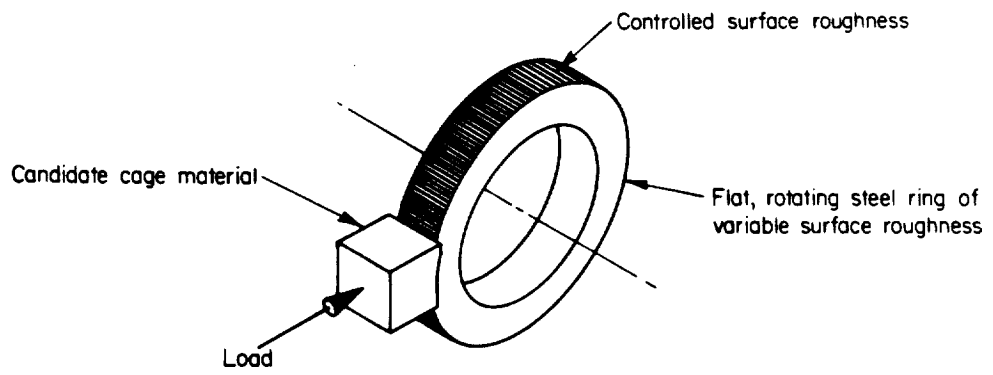


FIGURE 13. GEOMETRY OF APPARATUS USED FOR TRANSFER EXPERIMENTS



- (A) Glass-reinforced PTFE
- (B) 60 percent PTFE - 40 percent bronze
- (C) 55 percent PTFE - 40 percent bronze - 5 percent MoS<sub>2</sub>
- (D) 40 percent PTFE - 60 percent bronze

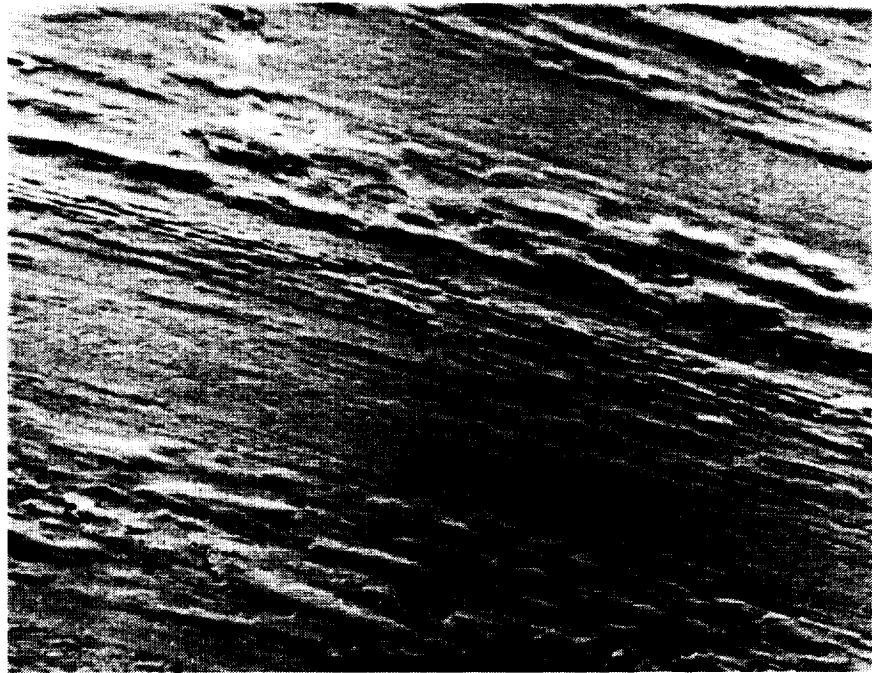
Material A is the current cage material for the SSME, whereas materials B-D are experimental cage-material candidates. Experiments have included tests at room temperature and in LN<sub>2</sub>. Ring surface roughnesses of nominally 0.01, 0.1, and 0.3 micrometers cla (circumferential lay) have been used.

At room temperature, materials (B-D) tend to form a bronze protective coating on the ring surface. A typical photomicrograph is shown in Figure 14. Surface roughness did not seriously alter transfer but as might be expected the highest roughness did increase the wear rate of the candidate cage materials. At a surface roughness of 0.1 micrometer or less the wear rate was, qualitatively, independent of material or roughness. The post-test surface finish of the rings was essentially unchanged for materials B-D but was roughened by material A, Figure 15.

At LN<sub>2</sub> temperatures a transfer layer of PTFE appeared to be present on the rings. Figure 16 shows a typical ring after testing with a "scribe mark" to illustrate the presence of a soft (PTFE) surface layer. All materials produced the apparent PTFE transfer film at LN<sub>2</sub> temperatures. However, when material A was tested surface damage was observed. Initially PTFE was transferred to the 440C ring, but the removal of PTFE from the cage material leaves exposed glass fibers, which abrade the ring.

The next major lubrication improvement in the SSME turbopump bearings is most likely to come from an improved transfer-film lubrication system. This recent research indicates that bronze-filled PTFE can provide transfer films to 440C at LN<sub>2</sub> temperatures. Both bronze films and PTFE films appear to occur and both types of films can offer some level of surface protection to the bearing.

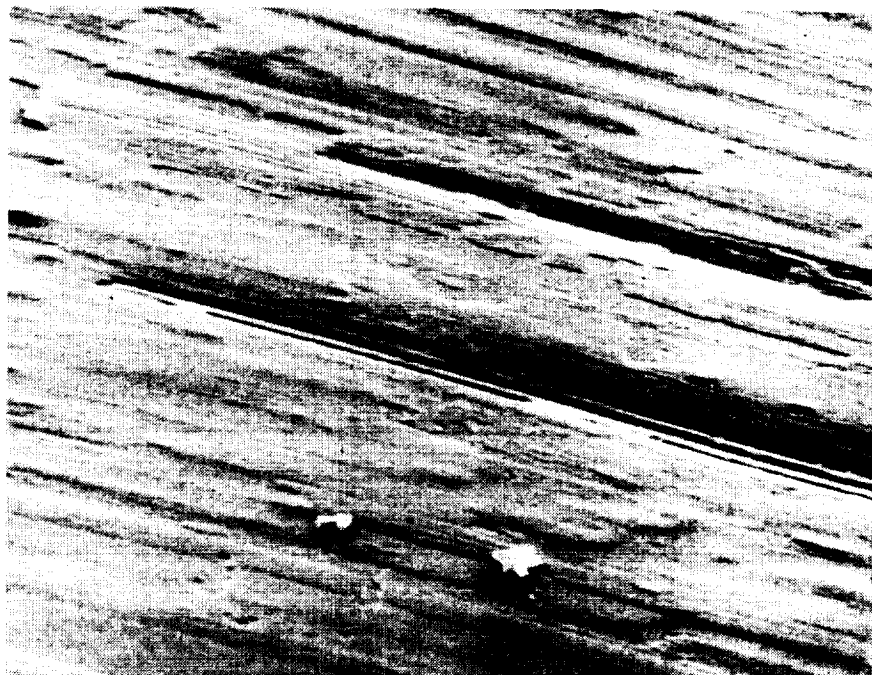
ORIGINAL PAGE IS  
OF POOR QUALITY



500X

FIGURE 14. RING SURFACE AFTER SLIDING CONTACT AGAINST  
60 PERCENT PTFE - 40 PERCENT BRONZE UNDER  
ROOM TEMPERATURE CONDITIONS

ORIGINAL PAGE IS  
OF POOR QUALITY



500X

FIGURE 15. SURFACE OF 440C TEST RING AFTER SLIDING  
CONTACT WITH GLASS REINFORCED PTFE

ORIGINAL PAGE IS  
OF POOR QUALITY

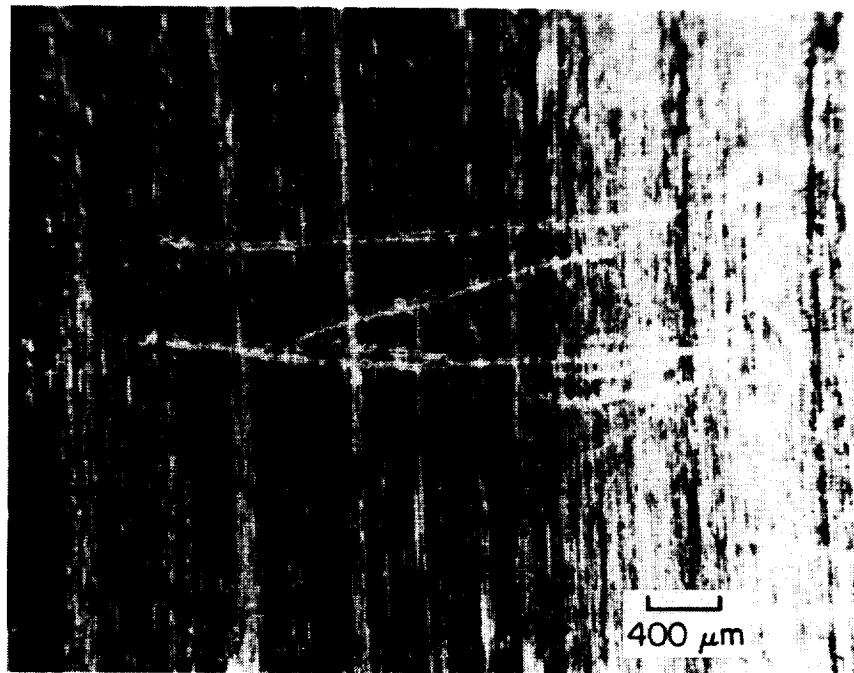


FIGURE 16. RING SURFACE AFTER SLIDING CONTACT IN LN<sub>2</sub>  
CONDITIONS AGAINST GLASS REINFORCED PTFE.  
SURFACE SCRIBED TO SHOW EVIDENCE OF PTFE  
TRANSFER FILM

## CONCLUSIONS

Several bearings operated in SSME turbopumps have been analyzed. In some instances the bearings were found to have incurred very high axial and radial loads. Major improvements in performance life have resulted from reducing loads and applying MoS<sub>2</sub> coatings to the bearing components. Further life extensions will require improved cooling and improved bearing lubrication. The most promising approach for resupplying solid lubricant beyond the MoS<sub>2</sub> precoatings is through films transferred from the cage to the balls. Although the current glass-fiber-reinforced-PTFE cage material is intended to provide transfer films, the glass fibers protrude and abrasively remove the transfer films and abrade the surfaces of the steel balls themselves. Other materials such as bronze filled PTFE appear to offer hope of an improved transfer lubrication scheme.

### REFERENCES

- (1) Kannel, J. W., and Bupara, S. S., "A Simplified Model of Cage Motion in Angular Contact Bearings Operating in the EHD Lubrication Regime", J. of Lub. Tech., Trans. ASME, July 1978, pp. 395-403.
- (2) Jones, A. B., "A General Theory for Elastically Constrained Ball and Roller Bearings Under Auxiliary Load and Speed Conditions", Trans. ASME, J. Basic Eng., Series D., Vol. 82, No. 2, June 1960, pp. 309-320.
- (3) Merriman, T. L., and Kannel, J. W., "Evaluation of EHD Film Thickness for Cryogenic Fluids", ASLE Transactions, Vol. 29, No. 2, pp. 179-184.

**SURFACE CHARACTERISTICS OF LIQUID OXYGEN COOLED  
BALL BEARINGS**

**Myles Butner and Mary Shoemaker**

**Rockwell International/Rocketdyne Division  
Canoga Park, California**

**Abstract**

The bearings used in the Space Shuttle Main Engine operate at high loads and speeds while being cooled by liquid oxygen at temperatures of -250 to -280 F. As a consequence of the lack of lubrication supplied by the coolant, bearing service lives are limited by wear of the balls and races rather than by the classic spalling of subsurface origin expected for more typical operating conditions. Transfer films of Teflon from the cage and dry films of MoS<sub>2</sub> are the only means of lubrication currently available. In assessing the effectiveness of these measures and in searching for more long-lasting lubrication, the as-run surfaces of balls and races have been analyzed for evidence of heating, residual lubricant films, adhesive, and abrasive wear. Techniques used included metallography, optical and SEM (Scanning Electron Microscopy) imaging, AES (Auger Electron Spectroscopy), ellipsometry, and PEE (Photoelectric Emission). The results of these investigations are summarized.

**Introduction**

Wear, rather than rolling contact fatigue, is the most commonly observed life-limiting condition experienced in propellant-cooled bearings in liquid rocket engine turbopumps. These compact, high power units employ ball bearings that run submerged in the pumped propellant to eliminate the complexity inherent in the use of conventional lubricants. The practice of propellant cooling of ball bearings has been successful with many storable and cryogenic fuels and oxidizers because of the ability of ball bearings to start dry, operate with minimal lubrication under conditions of high speed and load, and to tolerate particulate contamination. The bearing service lives realized were entirely satisfactory for the single-flight vehicles used in early space programs. However, with the advent of the Space Shuttle Main Engine (SSME) and other reusable rocket engines, operating conditions are more severe and life requirements have been extended, sometimes exceeding the durability of current bearings. For example, the bearings of the SSME high pressure oxidizer turbopumps (Fig. 1) rotate

---

Work reported herein was sponsored by NASA/Marshall Space Flight Center under Contract NAS8-27980.

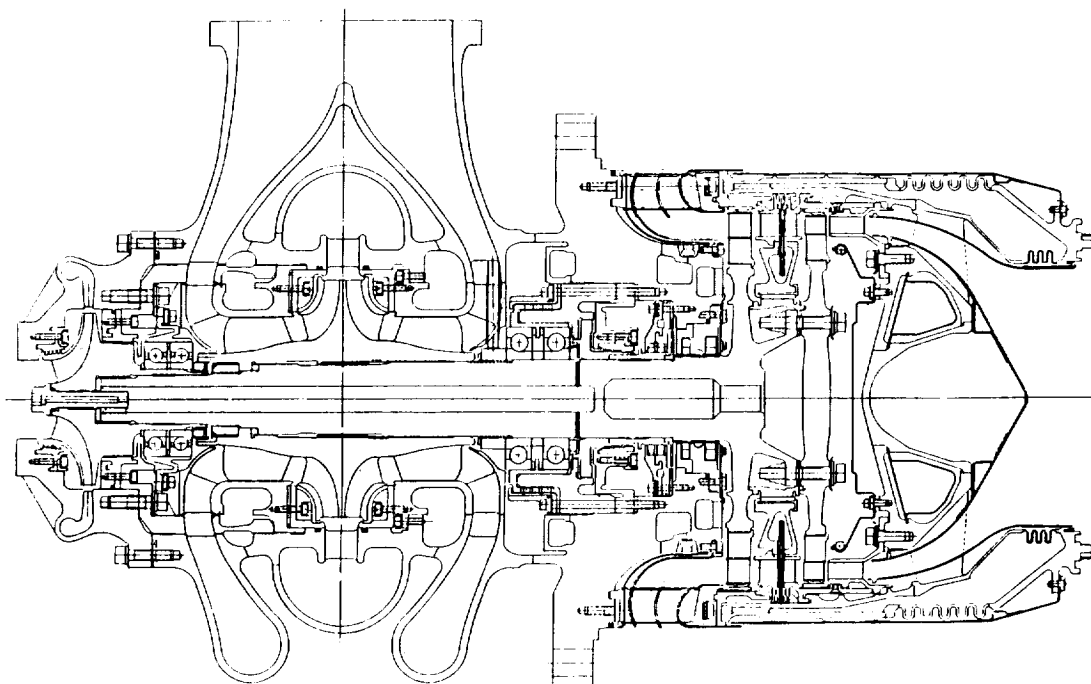


Fig. 1. SSME High Pressure Oxidizer Turbopump

at approximately 30,000 rpm under high radial and transient axial loads, while being cooled by the liquid oxygen. Under these conditions, bearing service life limitations due to wear and surface distress have been encountered. Current hypotheses are that wear is associated with high surface temperature due to sliding under low loads, while high friction at the ball/raceway contact is responsible for surface distress.

As part of an ongoing effort to improve bearing life, an investigation is being made to determine if the bearing contact surfaces have been overheated and whether, in fact, the expected solid lubricant films are present on the contact surfaces of oxidizer turbopump ball bearings. Analysis techniques included metallography, optical and SEM imaging, AES (Auger Electron Spectroscopy), ellipsometry, and photoelectric emission.

#### Surface Temperature and Wear

The dark colors of worn ball and raceway surfaces indicate temperatures in the range of 1200 to 1400 F. To assess the role of surface temperature level in producing wear, the appearance and microstructure of balls worn in service were compared to those of new and artificially heated balls. The results show that temperatures high enough to contribute to the loss of surface material probably exist in cases of wear, but do not penetrate the surface to an appreciable depth nor exist long enough to produce lasting metallurgical transformations.



Temperature Indications

Color. Figure 2 illustrates the appearance of the surface of a ball worn 0.005 inch in diameter during 7117 seconds of operation. It is similar in appearance to other balls that have worn from 0.0005 to 0.008 inch in diameter in that they all are essentially round, with a dark, smooth, dull surface that may be uniform in color or may include lighter and darker areas.

The mating raceway shows similar texture and color (Fig. 3). The relatively smooth surface suggests high sliding velocity with lightly loaded contact distributed evenly over the ball and raceway contact areas.

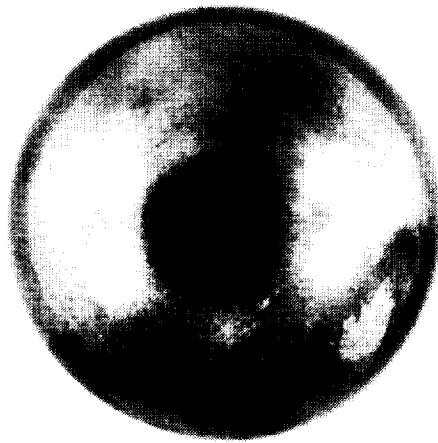


Fig. 2. Worn Ball

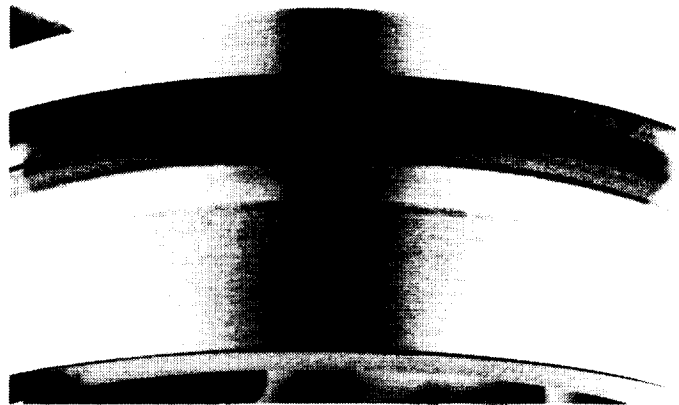


Fig. 3. Worn Inner Raceway

Wycliffe (Ref. 1) investigated the metallurgical aspects of ball wear, using optical and SEM imaging to characterize the near-surface condition of the ball material in Fig. 4 through 10. The 1200 to 1400 F temperatures indicated by the surface colors are expected to produce changes to the microstructure of the 440C ball material. However, etching of worn ball sections showed no evidence of tempering. To resolve this apparent anomaly, a spot-welder was used to produce a high temperature gradient to determine what evidence would be produced in the ball microstructure by intense local heating. In Fig. 4, the effect of high localized heating is illustrated in the shades produced by etching of a section of the specimen. A clearly



Fig. 4. New Ball With High Temperature Gradient

ORIGINAL PAGE IS  
OF POOR QUALITY

discernible gradient exists from the highest temperature, indicated by the light shade representing the austenitized zone around the heat source, through a dark band identifying the surrounding tempered martensite band bordering the cooler unaffected central mass of the ball.

Temper Carbides. A second characteristic found in worn balls was that there were no temper carbides in the vicinity of the surface. This is shown in the replica electron micrograph of a worn ball cross section (Fig. 5). The subject ball had worn 0.0055 inch during 1200 seconds of operation. The light material at the lower left of the micrograph is nickel plating applied to preserve the edge of the specimen. The same result was observed at 5, 500, and 1000 micrometers depth from the worn surface. Figure 6 shows microstructures with no temper carbides present at 5  $\mu\text{m}$  (0.0002 inch) depth.

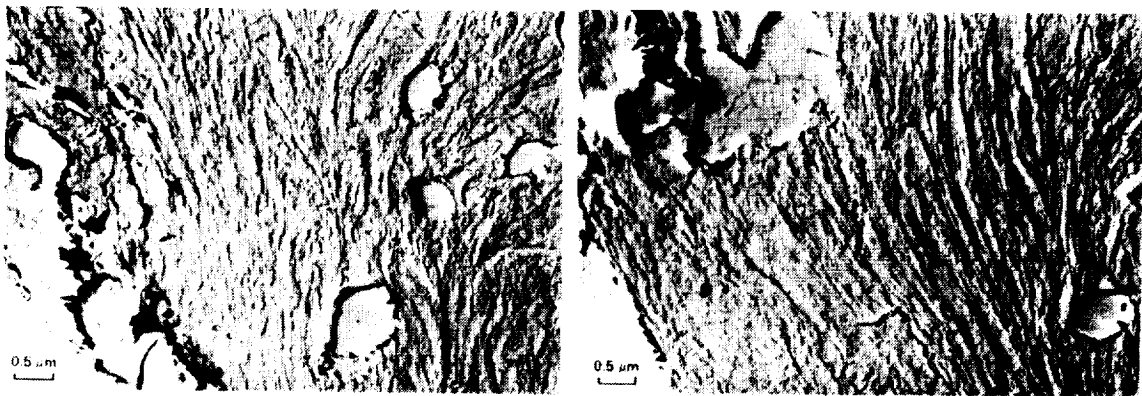


Fig. 5. Replica of Metallographic Section of Nickel-Plated Grossly Worn Ball. Nickel-plated surface is at the bottom left corner of both plates. The material within 5 microns of the surface is plastically deformed.

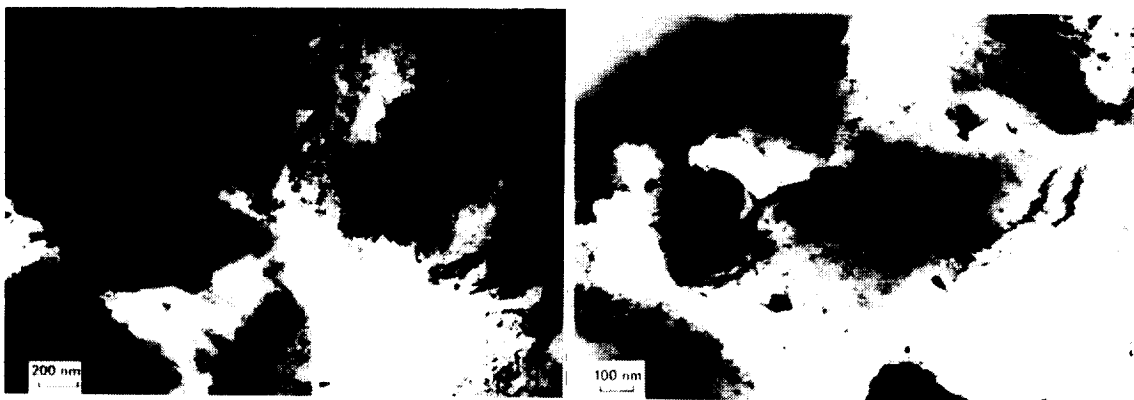


Fig. 6. Section of Worn Ball 5 Microns from Surface. Temper carbides are absent.

ORIGINAL PAGE IS  
OF POOR QUALITY

Experiments showed that temper carbides are developed in the 440C material given sufficient temperature and time exposure. New balls were heated to progressively greater temperatures for 1200 seconds, corresponding to the service time of the worn ball being analyzed. One ball was heated to 1400 F for a shorter time (12 seconds). Temper carbides were not produced after 1200 seconds at 423 C (793 F), but did appear after 1200 seconds at 650 C (1202 F), Fig. 7 and 8. Temper carbides, 50 to 100 nm (2 microinches) were formed within 12 seconds at 780 C (1436 F), Fig. 9.

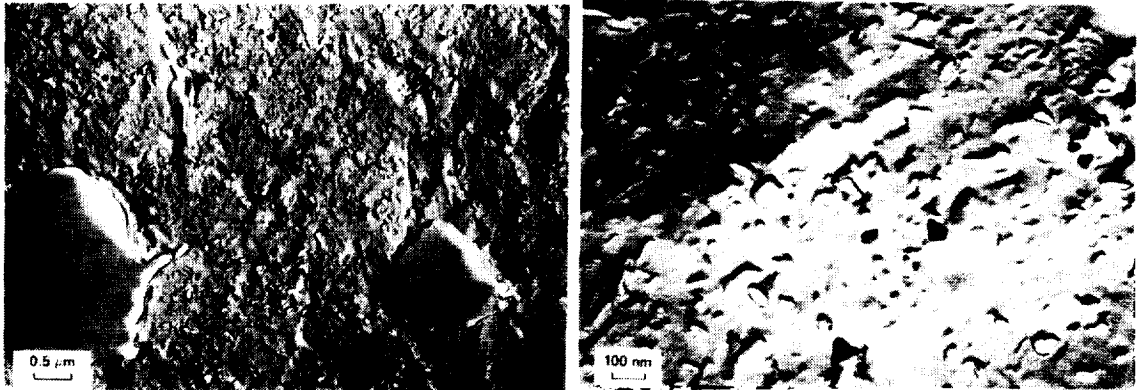


Fig. 7. Replica of Metallographic Section of New Ball Tempered for 20 Minutes at 650 C. Temper carbides 50 to 100 nm diameter are present.

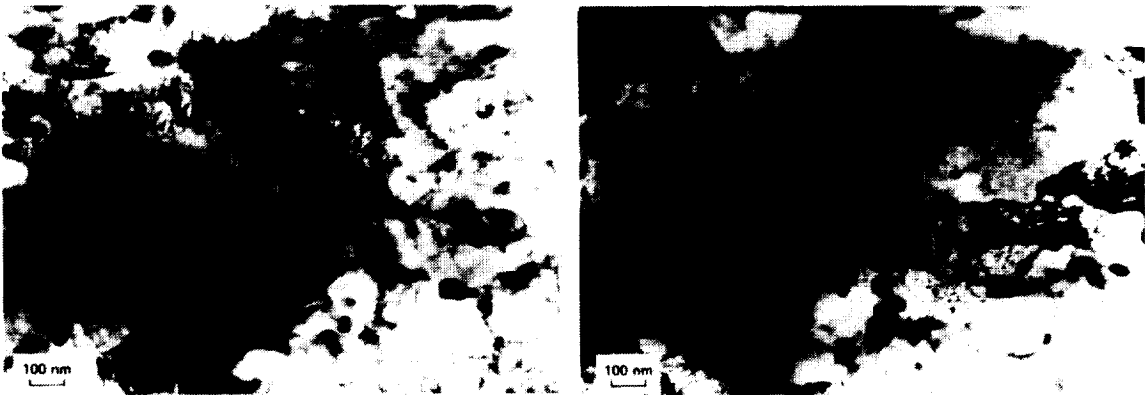


Fig. 8. New Ball Tempered 20 Minutes at 650 C (1200 F). Structure contains temper carbides 50 to 100 nm diameter.

Plastic Deformation

Although there were no temper carbides developed, there were indications of plastic flow of the ball material to a depth of 5 micrometers (0.0002 inch), Fig. 5. The presence of plastic flow would indicate very high loads in fully hard 440C. However, a worn ball cannot

ORIGINAL FACE IS  
OF POOR QUALITY

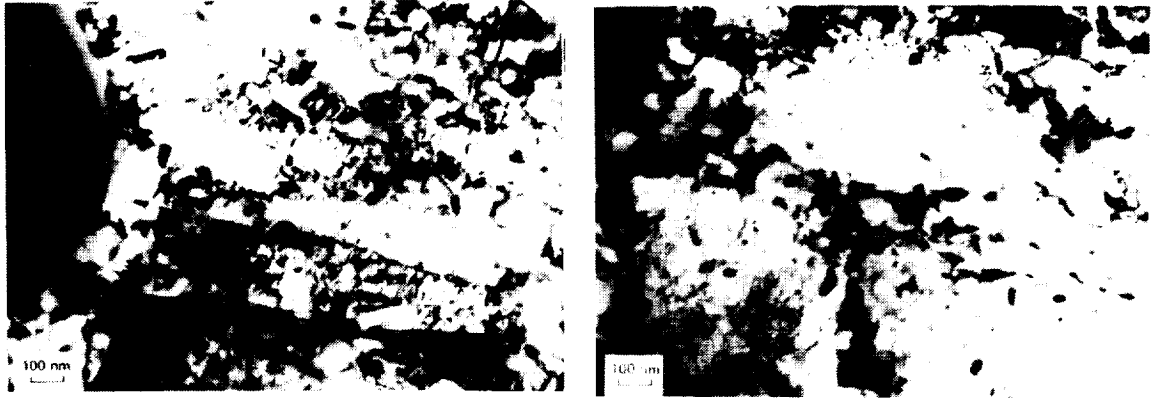


Fig. 9. New Ball Tempered for 12 Seconds at 780 C (1440 F).  
Structure contains temper carbides 50 nm in diameter.

support high loads; when the ball diameter decreases, axial travel of the races is permitted, which will relax the spring preload. At the same time, the opposing bearing of the duplex pair will support radial loads. Rather than high loading, a more probable cause of the plastic deformation is moderate loading combined with high local temperature, which reduces the near-surface yield strength of the material. The time that any one area in contact remains at high temperature is probably not sufficient for metallurgical transformations, which may explain the absence of evidence of tempering by etching and lack of temper carbide formation.

#### Lubrication and Surface Distress

Although liquid oxygen is an effective coolant, provided that it is maintained in a liquid state, it supplies little or no lubrication for bearings. While ball bearings will function unlubricated for some time, rapid deterioration occurs if high friction exists at the ball/race contact zones and at the cage contacts.

#### Ball Contact Lubrication.

Lack of lubrication of the ball/race contact zone is thought to shift the primary life-limiting mechanism from subsurface initiated spalling to surface degradation. The normal load of the ball against the raceway produces compressive stresses that can be calculated by the analytic methods of Hertz, as adapted to bearing design by Jones (Ref. 2) and others to include shear stresses. Given a low friction coefficient  $\mu$  at the rolling element interface, the shear stress at the surface is also low, but increases with depth, attaining a peak value at a particular distance beneath the surface. This model is relevant for oil-lubricated bearings; since  $\mu$  is low, the maximum shear stress occurs at some subsurface point. The normal life-limiting mechanism is fatigue spalling originating at the subsurface level coinciding with the maximum shear stress, although it should be noted that

spalls may also be initiated from other causes such as defects at the surface. A typical fatigue spall is relatively deep, and may be as much as 0.010 inch in depth. The capacity and life relationships used in the bearing industry are based upon tests of conventionally lubricated bearings that incorporate the benefits of low friction achieved through use of lubricants, and to some degree, from elastohydrodynamic (EHD) films.

Conditions are quite different for the ball/race contacts in a propellant-cooled turbopump bearing, since the value of  $\mu$  will be higher and the fluid viscosity is too low to form an EHD film. In addition, high velocity rolling and spinning motions are often present, producing much higher tangential forces at the interface. These shear forces are considered to be the reason for the predominance of surface distress and wear as the primary failure mode for liquid oxygen-cooled bearings.

Fully developed surface distress is the result of a fatigue mechanism arising from inadequate lubrication (Ref. 3). It progresses through three steps: (1) burnishing, or obliteration of the as-manufactured surface finish pattern by compressive yielding of the surface asperities, producing a dull smooth surface, often without directional patterns; (2) shallow cracks form which then combine into (3) microspalls that can cover a wide area without becoming deeper. Spalls associated with surface distress are shallower than fatigue spalls arising from subsurface shear stress, generally being on the order of 0.001 inch deep. The appearance of advanced surface distress is shown in Fig. 10 (ball) and Fig. 11 (raceway). At 50X, the cracks near the edge of the load path are indicative of the surface shear force direction (Fig. 12).

Smith and Liu (Ref. 4) developed methods of including the effects of tangential forces at the contact interface of two cylinders and showed that as friction coefficient increased, the magnitude of the maximum shear stress increased, and occurred progressively nearer to the surface. For friction coefficients of 0.33 or greater, the maximum surface shear stress occurs at the surface and at the center of the contact zone. Figure 13 illustrates the effect of friction coefficient on shear stress magnitude and depth at this central location. If it is assumed that the relations developed for cylinders are representative of ball/race contacts, where tangential forces are caused by ball skidding or spinning, it can be concluded that high surface shear stresses are a consequence of the use of liquid oxygen as the coolant.

Because of the minimal lubrication provided, some degree of surface distress is likely to be present very early in the operating life of all liquid oxygen-cooled bearings. Differences in the contributing factors of loading, friction coefficients, and length of service time account for the range of surface conditions observed, which may vary from burnishing, (Fig. 14) to the advanced state of shallow spalling shown in Fig. 10 and 11.

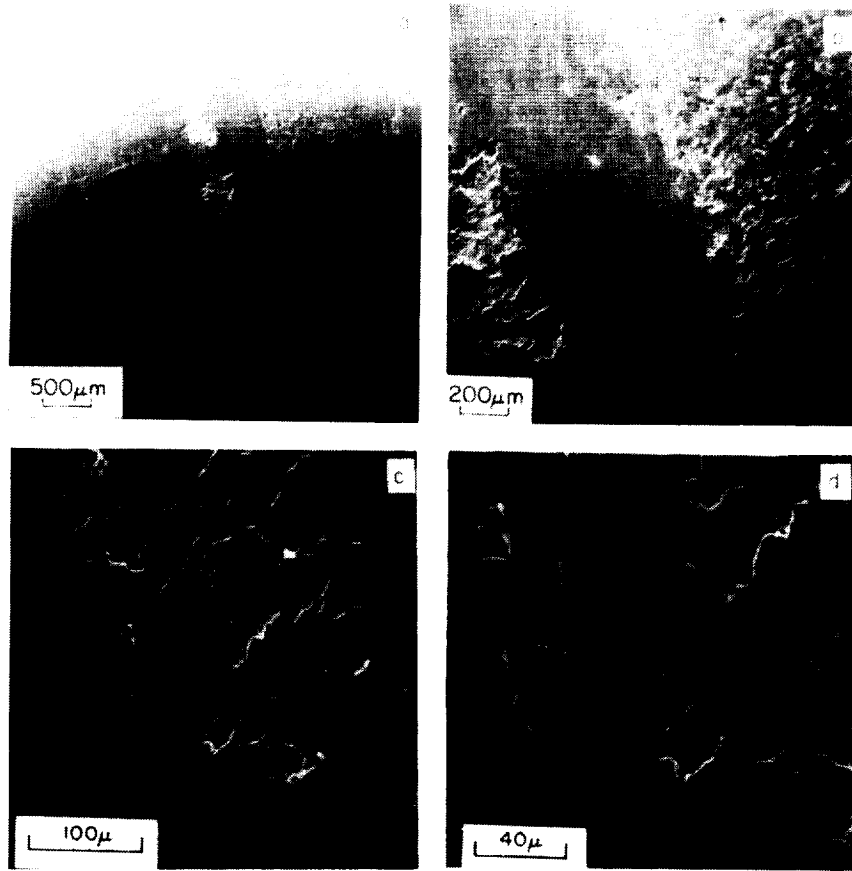


Fig. 10. Surface Distress on Balls

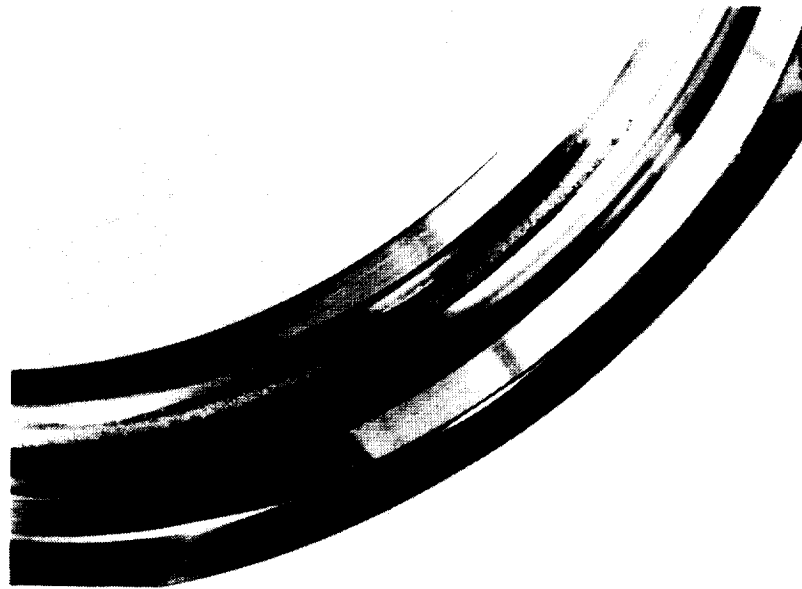


Fig. 11. Raceway with Surface Distress



Fig. 12. Directional Orientation of Surface Distress Cracks on Ball

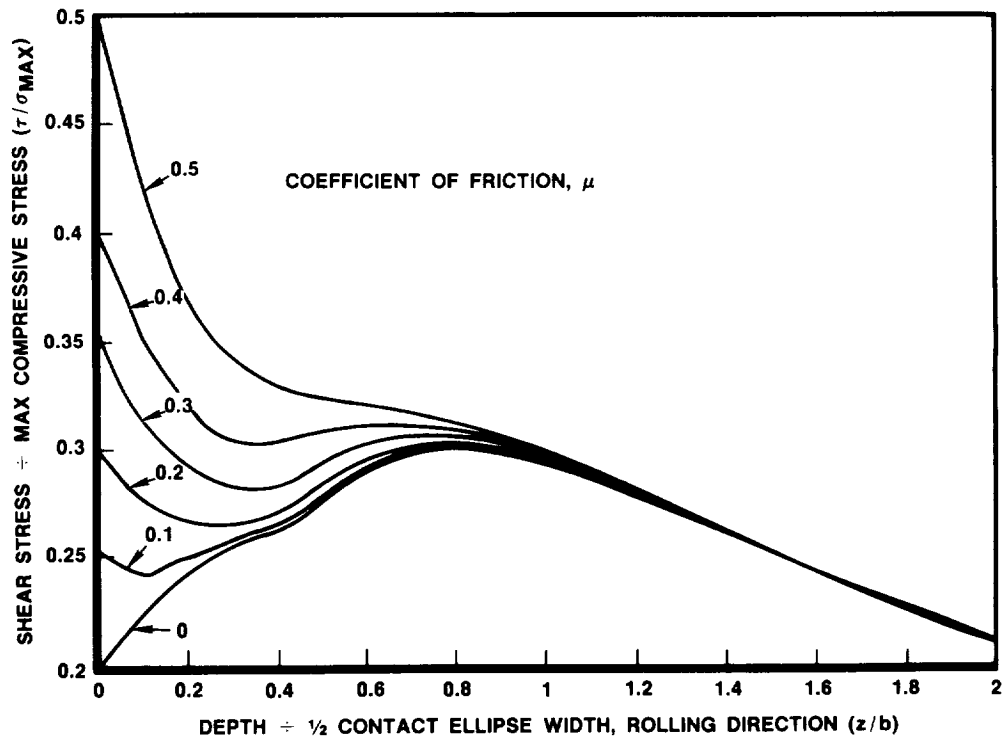


Fig. 13. Effect of Friction Coefficient on Shear Stress Depth

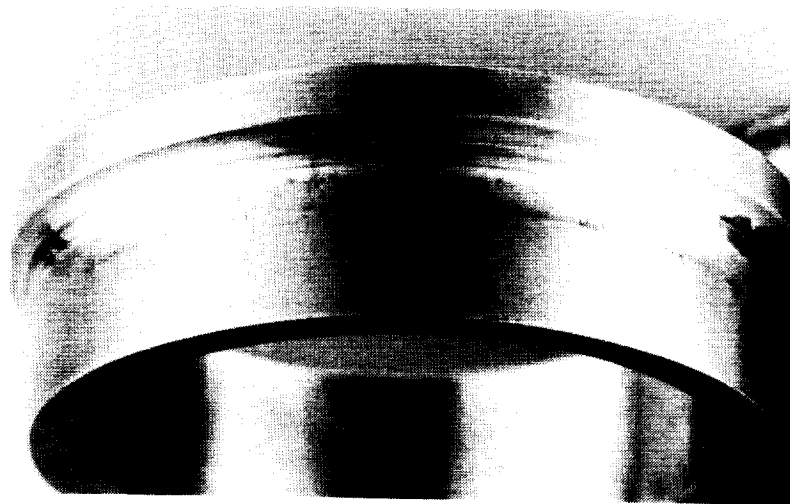


Fig. 14. Burnishing of Raceway

#### Lubrication By Transfer Films

Armalon<sup>®</sup> [glass fabric supported polytetrafluoroethylene (PTFE)] cages are used in all SSME turbopump bearings. As the cage regulates ball speed, normal loads and tangential friction forces are produced at the cage ball pockets and at the cage/race interface. Since cage, ball, and land forces interact and are mutually reinforcing, a high friction coefficient at the cage contacts can lead to unstable cage motion that may cause increased friction torque and heating or cage structural failure. To avoid these circumstances, lubrication of the cage contact areas or the use of cage materials with inherently low friction coefficients are necessary. PTFE-containing cage materials were found to be the most successful for bearings operating in liquid hydrogen (1958) and liquid oxygen (1959), since they impart low friction coefficients and are chemically compatible with liquid oxygen. An additional advantage of these materials is the tendency to transfer some PTFE to the ball and race surfaces.

The mechanism of PTFE transfer had been proposed and quantitatively evaluated by Anderson, Brewster, Scibbe, and Coe at NASA-Lewis Research Center in the 1960s. These studies used a tracing stylus to reproduce profiles of bearing surfaces prior to and at intervals of operation. From the results, it was postulated that PTFE was transferred during initial bearing operation to the balls and then to the raceways but that the available PTFE was soon depleted. Subsequently, the glass fiber ends and particles from the retainer caused abrasive wear of the balls and raceways (Ref. 5 and 6).

In a more recent study of PTFE film transfer to 440C bearing balls and raceways, Kannel, Dufrane, and Zugaro showed that uniform films are not consistently formed, but that lumps and patches of PTFE adhere to the ball surfaces (Ref. 7).



## Surface Analysis

To verify that PTFE is transferred from the cage to the balls and raceways in service, a nondestructive test method was needed to determine the presence and thickness of thin, nonmetallic films. This measurement technique had to be reproducible and accurate when used to analyze films ranging from just a few angstroms ( $\text{\AA}$ ) to several thousand angstroms thick ( $1 \text{ \AA} = 10^{-10} \text{ m}$  or  $3.93 \times 10^{-9}$  inches). Means of identifying the constituents of this film, as well as differentiating between the base metal, surface oxides and wear debris, were needed to complete the surface characterization. With the assistance of Rockwell International Science Center's Surface and Electrochemical Processes staff and facilities, a set of analysis techniques were identified to provide means of determining surface film thickness and composition. Of all the potential methods evaluated, ellipsometry, AES, and PEE appear to have the most potential for accurate, reproducible results. Additionally, the SEM feature of the AES equipment is useful to record the appearance of surface films and wear tracks.

The methods described were used to evaluate surface characteristics of unused bearing components and bearings that had run in liquid oxygen. The analyses conducted by Smith, Lindberg, Stocker, and Kendig of Rockwell Science Center have been used primarily to establish techniques and baselines for more definitive work on used bearing components (Ref. 8). Supporting evidence from these analyses agrees with the earlier findings that PTFE transfer does occur, but in the form of stringers, flakes, and patches of material rather than a uniform thin film. The presence of PTFE in deep wear tracks also suggests that under high contact stresses this transferred film cannot prevent wear.

Ellipsometry. Ellipsometry is a nondestructive method used to measure very thin films (0.01 to 10,000  $\text{\AA}$ ) consisting of transparent or translucent materials. A polarized laser light beam is reflected and refracted through the film as shown schematically in Fig. 15. The deflection angle of the laser beam depends on the materials' index of refraction ( $n$ ), the film thickness ( $d$ ), and the absorption index ( $K$ ). PTFE has an absorption index of  $K_{\text{PTFE}} = 0$  while the absorption index of steel is  $K_{\text{st}} = 1.2$ . The index of refraction for PTFE is  $n_{\text{PTFE}} = 1.35$

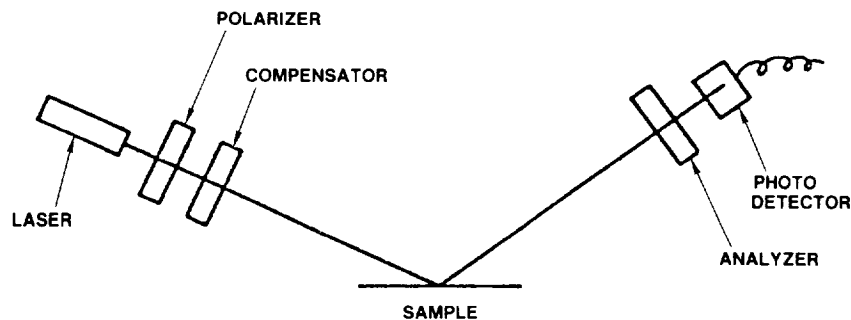


Fig. 15. Ellipsometry Surface Film Thickness Analysis Schematic

while light is not refracted through steel. The great difference between these properties of steel and PTFE allows definitive measurement of film thickness. Film thickness ( $d$ ) is determined from the relationship between the reflected and refracted beams. An example of analysis by ellipsometry is shown in Fig. 16. It appears that a PTFE film is present on both worn and unworn surfaces. Unevenness of film thickness is indicated by the lack of correlation between film thicknesses in worn and unworn regions (Ref. 9).

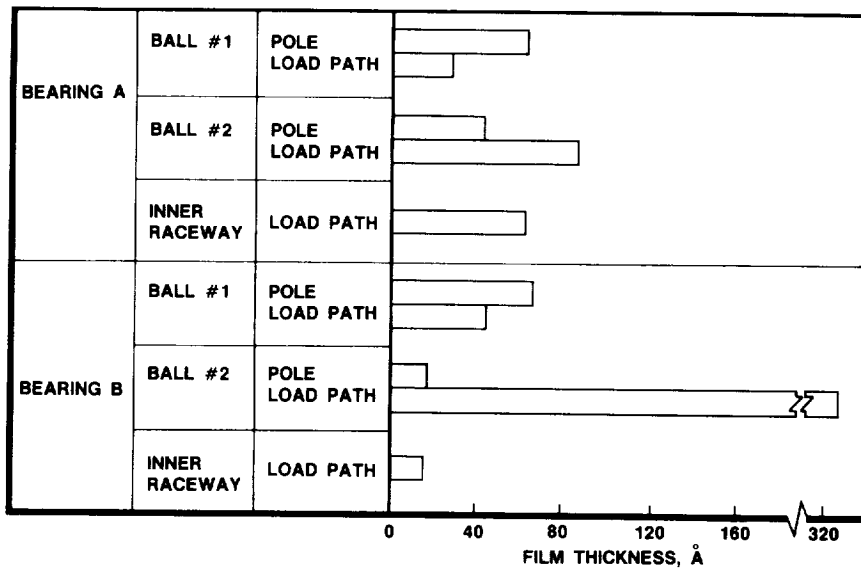


Fig. 16. Surface Film Thickness Measured by Ellipsometry

**AES.** The Auger electron spectroscopy utilizes sputter removal of successive 5 to 10 Å thick film layers to give thickness measurements as well as elemental identification of the material removed. Elements below the atomic number of 3 (lithium) cannot be detected by AES. The results, listed in Table 1, show that the PTFE (as evidenced by the presence of fluorine) is present even in the worn regions of the ball, which is in agreement with the results of ellipsometry. Figure 17 shows the relative quantity of fluorine to oxygen as a function of depth. The presence of fluorine to a greater depth in the worn area suggests that PTFE is physically retained in cavities in the roughened surface (Ref. 9).

**PEE.** In photoelectron emission, ultraviolet (UV) light strikes the surface of a photoemitting substance causing electrons to be emitted. These electrons are collected on a flat plate or probe and analyzed as shown schematically in Fig. 18. The PEE apparatus used for the bearing surface analyses is shown in Fig. 19. Ultraviolet light stimulates electron emission from metal substrates and certain oxide films. Lubricants, oxides, and contaminants, which are transparent to UV light, attenuate the underlying metal's emission and thus the output current giving an indication of the film type and thickness. Emission is also

Table 1. Scanning Auger Microscope Results

Sputter Time, seconds	Area	Elemental Percentage Relative to Amount of Iron Present								
		Fe	O	C	N	S	Cl	F	Ca	Cr
0	Pole	1	3.0	2.0	0.07	0.06	0.53	0.62	0	0
0		1	3.3	1.6	0.06	0.06	0.47	0.67	0	0
300		1	3.1	0.3	0	0.10	0.38	0.27	0	0
600		1	3.0	0.14	0	0.17	0.26	0	0	0.09
1000		1	3.1	0.05	0	0.05	0.28	0	0	0.05
1500		1	2.0	0.06	0	0.06	0.35	0	0	0.05
2000		1	2.7	0.09	0	0.09	0.12	0	0	0.26
2700		1	2.9	0.05	0	0.08	0.11	0	0.05	0.22
0		Wear Ring	1	3.8	1.8	0.07	0.07	0.57	0.63	0
300	1		3.3	0.49	0.05	0.07	0.19	0.59	0.07	0.02
600	1		3.4	0.25	0	0	0.20	0.43	0.10	0
1000	1		2.8	0.16	0	0.18	0.10	0.39	0.10	0.1
1200	1		3.7	0.12	0	0.17	0.08	0.62	0.12	0.12
1500	1		3.5	0.2	0	0	0.15	0.58	0.11	0.11
2000	0		3.8	0.13	0	0.13	0.13	0.56	0.13	0.13
2700	1		3.1	0.14	0	0	0.10	0.46	0.13	0.18
0	Pole		1	2.7	1.45	0.07	0.15	0.20	0.38	0
300		1	3.1	1.04	0.07	0.51	0.20	0.40	0	0
600		1	2.2	0.13	0	0.18	0.07	0.22	0	0.07
1000		1	2.5	0.12	0	0.17	0.09	0	0	0.07
1500		1	2.6	0.04	0	0.12	0.07	0	0	0.12
2000		1	2.1	0.11	0	0.08	0.04	0	0	0.18
0	Wear Ring	1	2.9	1.47	0.09	0.22	0.18	0.95	0	0
300		1	3.0	0.73	0.07	0.55	0.13	0.84	0.07	0.24
600		1	2.2	0.49	0.05	0.38	0.07	0.44	0.09	0.27
1000		1	2.7	0.30	0	0.27	0.10	0.53	0.07	0.17
1200		1	2.3	0.29	0	0.28	0.06	0.40	0.08	0.23
1500		1	2.0	0.21	0	0.17	0.06	0.50	0.05	0.24
2000		1	2.1	0.10	0	0.03	0.02	0.50	0.10	0.28

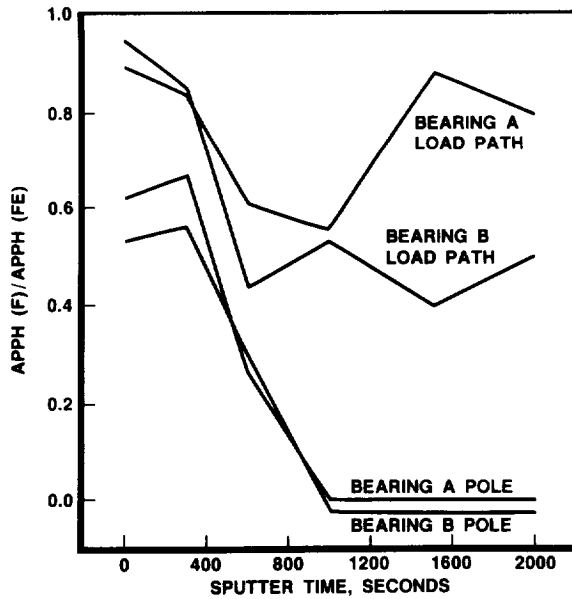


Fig. 17. Percentage Fluorine vs Percentage Iron as a Function of Sputter Time (APPH = atomic percentage peak height)

ORIGINAL PAGE IS  
OF POOR QUALITY

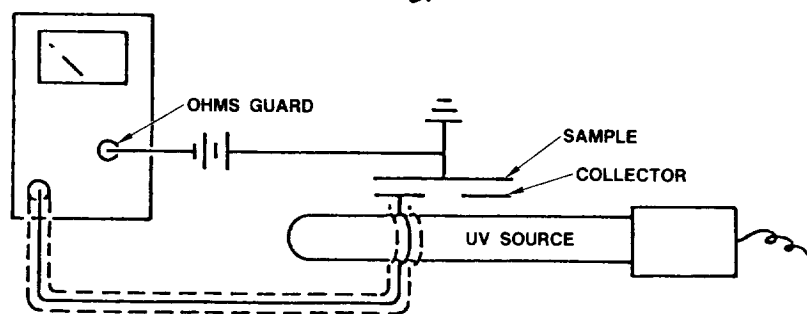


Fig. 18. Photoemission Surface Analysis

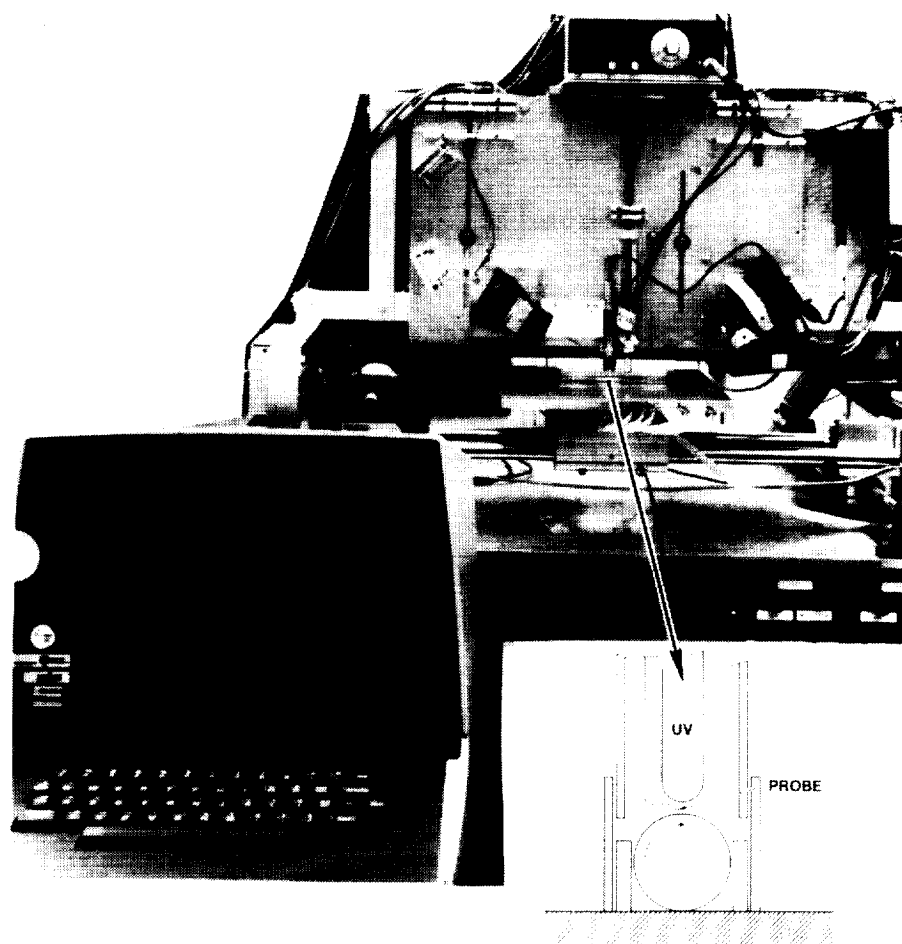


Fig. 19. Photoelectric Emission Apparatus

increased by surface roughness, so a PEE scan of a bearing surface cannot be used to measure film thicknesses in worn regions. It can be used to distinguish worn from unworn regions and to measure film thickness variation on uniformly rough surfaces. A typical example of differences, as measured in picoamperes (pA), between the wear track and smooth regions of bearing balls is shown in Fig. 20 (Ref. 10).

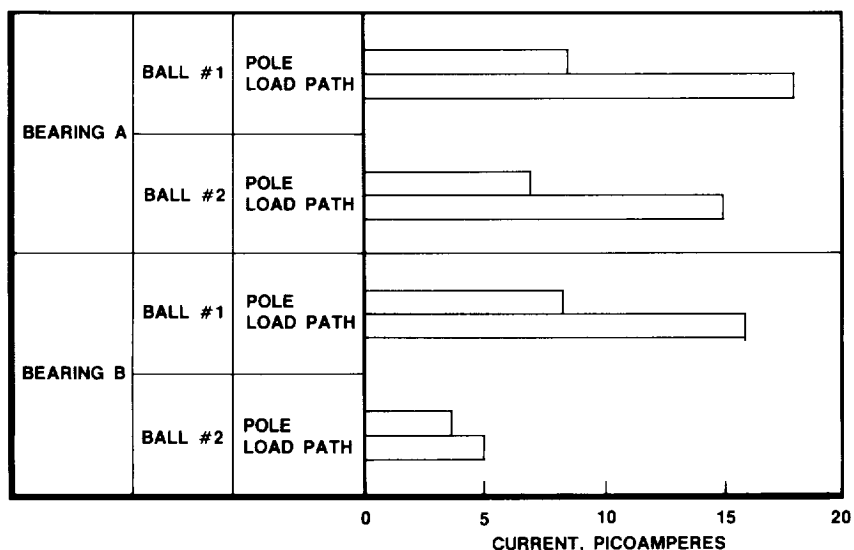


Fig. 20. Surface Indications Photoelectric Emission

Interpretation of Investigation

The metallurgical analyses conducted to date indicate:

1. The bulk material temperature for worn balls was below 800 F.
2. The surface temperature may be as high as 1400 F as evidenced by the ball color. However, the time at temperature may be so short as to preclude formation of temper carbides or transformations detectable by etching.
3. Plastic flow of the surface may be evidence of surface temperature high enough to soften the material immediately at the surface so that it will flow under the conditions of high sliding velocity and low contact loads associated with spinning or sliding contact. The process of material removal may be accelerated by oxidation.

The surface analyses indicate:

1. Unused ball bearings typically have about 20<sup>o</sup>Å of iron-chromium oxides and 50 to 100 Å of nonmetallic contamination on their surfaces.
2. After running for a short time in liquid oxygen, the ball-retainer contact zone heats up causing a thin film of PTFE/metal reaction products about 500 to 1000 Å thick to form over and adjacent to the wear as shown in Fig. 21.

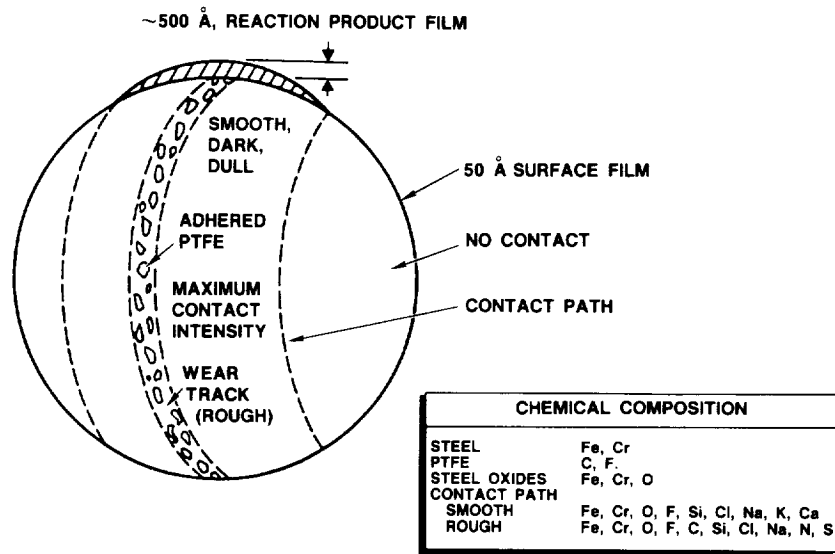


Fig. 21. Schematic Representation of a Liquid Oxygen Cooled Ball Surface

3. This film layer does not prevent wear, as particles are eventually torn from the load path, mixed with the PTFE film, and redistributed in the wear track region on the balls and raceways.
4. Because the ball axis did not shift in the specimen represented in Fig. 21, the surfaces of the balls' polar regions appear similar to those of an unused bearing. Continued operation could be expected to produce crossing, overlapping load paths, distributing any films over the entire ball surface.
5. Of all the surface analysis techniques employed to date, AES provides the most direct indication of lubrication conditions on used bearings.

#### Continuing Investigations

Ongoing efforts to increase the durability of liquid oxygen-cooled bearings are discussed in the following paragraphs.

#### Materials

The wear characteristics of surface treatments for 440C and also alternative ball and race materials are being evaluated for durability in a liquid oxygen environment.

#### Metallurgical Characteristics

The metallography of balls with varying amounts of service time and wear is being characterized using SEM and Energy Dispersive X-Ray

Analysis (EDAX). X-Ray diffraction is being used for determination of residual stresses. Surface analyses are being conducted using AES for identification of surface elements and Electron Spectroscopy for Chemical Analysis (ESCA) for determination of surface compounds.

### Surface Analysis

Initial evaluation of used SSME bearing components has shown that the presence, thickness, and composition of thin, nonmetallic films can be determined by a combination of ellipsometry, AES and PEE instrumental analysis techniques. The next step is to establish quantitative criteria for the bearing component's lubricant films. Current work in this area is focused on (1) developing film thickness standards for oxides and lubricants, (2) improved interpretive techniques for ellipsometry and PEE to increase confidence in the film thickness measurements, and (3) AES identification of the presence of MoS<sub>2</sub> lubricants in the form of sputtered films and spray applied dry film coatings.

Standard 440C specimens (balls and flat plates), unlubricated and with known thicknesses of MoS<sub>2</sub> films, are being characterized by all three instrumental methods. Energy Dispersive X-ray Analyses are being used to augment the elemental composition identification provided by AES. The EDAX method can determine which compounds of the oxides and lubricants are present in the measured films. Surface conditions of bearings operated under known conditions can then be compared with the standards, yielding additional definition of the longevity and effectiveness of the present lubrication techniques. This same method can be adapted to evaluation of candidate new lubricants.

### Recommendation

In view of the influence of friction on rolling bearing life, there is a definite need for quantitative friction coefficient values for bearing material pairs in propellant environments at low sliding velocities. A test program should be conducted to determine these coefficients for 440C vs 440C (and candidate replacements) in a liquid oxygen environment, at sliding rates in the range from 0.1 to 12 ft/sec corresponding to the sliding velocities typical of locations in contact ellipses. The currently available coefficients were taken at much higher velocities (Ref 11). To be usable, the testing must be conducted in the presence of liquid oxygen; otherwise, the chemical interactions will not be simulated, and the results will be inapplicable.

### References

1. Wycliffe, P. A., Ball Bearing Wear Studies, Interim Report, IDWA R-9753, Rockwell International Science Center, January, 1985.

2. Jones, A. B., Analysis of Stresses and Deflections, New Departure Engineering Data, New Departure Division, General Motors Corporation, Bristol, Connecticut, 1946
3. Tallian, T. E., Bails, G. H., Dalal, H., and Gustafsson, O. G., Rolling Bearing Damage Atlas, SKF Industries, Inc., King of Prussia, PA, 1974.
4. Smith, J. O., Liu, C. K., "Stresses Due to Tangential and Normal Loads on an Elastic Solid With Applications to Some Contact Stress Problems," Journal of Applied Mechanics, pp. 157-166, June 1953.
5. Brewe, D. E., Scibbe, H. W., and Anderson, W. J., Film Transfer Studies of Seven Ball Bearing Retainer Materials in 60R (33K) Hydrogen Gas at 0.8 Million DN Value, NASA TN D-3730, 1966.
6. Scibbe, H. W., Brewe, D. E., and Coe, H. H., "Lubrication and Wear of Ball Bearings in Cryogenic Hydrogen," presented at the Bearing Conference at Dartmouth College, Hanover, New Hampshire Sept. 4-6, 1968.
7. Kannel, J. W., Dufrane, K. F., and Zugaro, F. F., Study of Methods for Applying and Enhancing Transfer Film Coatings of Polytetrafluoroethylene (PTFE) to Space Shuttle Main Engine (SSME) High Pressure Oxygen Turbo Pump (HPOTP) Bearings, Final Report, Battelle Institute, Columbus Laboratory, Contract NAS8-33576, Task 107, Nov. 25, 1981.
8. Smith, T., SSME Bearing Lubrication Program, Interim Report, IDWA R-6316, Rockwell International Science Center, June 1981.
9. Smith, T., Surface Properties of Balls and Races from Rocketdyne, Interim Report, IDWA R-6316, Rockwell International Science Center, September 1983.
10. Smith, T., New Techniques for Characterization of Balls from Bearings of the Liquid Oxygen Pumps, Interim Report, IDWA R-9058, Rockwell International Science Center, September 1982.
11. Report No. WADD TR-6-77 (AD259143), Propellant Lubrication Properties Investigation, Wright Air Development, June 1961.



POWDER METALLURGY BEARINGS FOR  
ADVANCED ROCKET ENGINES

B. N. Bhat, T. S. Humphries and R. L. Thom  
Materials and Processes Laboratory  
NASA/MSFC  
Marshall Space Flight Center, Alabama 35812 U.S.A.

G. I. Friedman and V. Moxson  
TRW Aircraft Components Group  
Cleveland, Ohio 44117 U.S.A.

## INTRODUCTION

The Space Shuttle Main Engine (SSME) is a high efficiency rocket engine which uses high pressure liquid hydrogen as fuel and high pressure liquid oxygen as oxidizer. Both liquid hydrogen and liquid oxygen are pumped into the engine by low and high pressure cryogenic turbopumps, operating at high speeds. At present service life of the high pressure oxygen turbopump (HPOTP) appears to be limited by the life of its cryogenic bearings, made from heat treated, corrosion-resistant 440C steel. Detailed analyses of bearing service life have indicated that the service life is limited by fatigue and wear. Bearings removed from the pump often showed discoloration, which indicated oxidation and surface temperatures over 1000°F [1]. This heating is partially due to microwelding and tearing resulting from inadequate lubrication and partially due to the reduced cooling efficiency of the liquid oxygen, some of which vaporizes upon contact with the frictionally heated bearing.

Several approaches to improving bearing service life are being pursued by NASA. One approach is to reduce frictional heating by use of low coefficient of friction coatings [2]. This work is in progress. Another approach is to improve lubrication and cooling, but this approach requires design changes. Yet another approach is to use improved bearing materials. Advanced powder metallurgy (PM) techniques have the potential to develop bearing materials that are resistant to oxidation, wear and rolling contact fatigue, and hence, afford a viable solution to extending the service life of the SSME cryogenic bearings. During powder manufacture, the individual powder particles solidify very rapidly. As a consequence, the primary carbides are very small and uniformly distributed. When properly consolidated this uniform structure is preserved while generating a fully dense product, suitable for bearing applications. Several PM alloys were studied by TRW Inc., as a part of contract NAS8-34763 and the results of this study are reported in a different paper [3]. TRW has identified several promising candidate PM alloys for further evaluation by NASA. The purpose of the evaluation program is to select the top two or three candidate alloys for making bearings which will be tested in the MSFC Bearing Materials Tester and the best candidate material will be recommended for application in the turbopumps. This paper presents the results of the

[REDACTED]

evaluation of the candidate materials in MSFC Materials and Processes Laboratories.

#### TEST PROCEDURE AND RESULTS

Six candidate powder metallurgy materials supplied by TRW were: X-405, MRC-2001, T-440V, 14-4/6V, WD-65, and D-5. The chemistries of the alloys are given in Table 1. Photomicrographs of heat treated alloys are given in Figures 2 through 7. Photomicrograph of 440C is given for comparison (Figure 1). It should be noted that the PM microstructures are finer and devoid of large carbides seen in wrought 440C, and therefore, are expected to have improved rolling contact fatigue (RCF) life.

#### ROLLING CONTACT FATIGUE (RCF) TESTS

The RCF tests in this investigation were run on a ball-rod rolling contact fatigue device (made by Federal-Mogul). A short description of the tester will follow, while a detailed description of the tester can be found in Reference 4. A schematic of the loading part of the tester is shown in Figure 8. The test consists of radially loading three 1.27 cm (0.5 in.) diameter balls against a 0.9525 cm (0.375 in.) diameter test specimen that is rotated at 3600 RPM. The three balls, separated by a bronze retainer, are radially loaded by two tapered bearing cups that are thrust loaded by three calibrated springs. An accelerometer coupled to a shutoff device is used to measure the emergence of a spall on the test specimen; the emergence of a spall is determined when a preset vibration level is exceeded. At that time the motor is automatically stopped and the test is finished. The test specimens were lubricated at a constant drip rate of 6 to 8 drops per minute with MIL-L-7808, a jet turbine engine oil. The tests ran continuously 24 hours a day until a spall occurred or until 200 hours of run time was reached. The specimens used for the tests were 0.9525 cm (0.375 in.) diameter by about 8.25 cm (3.25 in.) long and were ground to a surface finish of between 0.1 to 0.2  $\mu\text{m}$  (4 to 8  $\mu\text{in.}$ ) roughness.

All bearing alloys were tested in the fully heat treated condition. Each sample was subjected to 14 individual rolling contact tests with seven tests being conducted on each end of the rod with a distance of 0.4 cm (0.156 in.) kept between each wear track. The tests were conducted at two stress levels, 5.42 GPa (786 ksi) and 4.04 GPa (586 ksi) maximum Hertzian stress. Each test specimen had seven tests at the higher stress and seven at the lower stress. The test runs of high and low stress were alternated along the length of the test specimens so as to avoid any chance of conflicting results due to the possibility of having any type of a gradient effect.

The results of the RCF tests have been plotted on Weibull graph paper and the  $B_{10}$  lives were calculated for candidate materials (Figures

9, 10, 11, 12). Data for 440C were included for comparison. The  $B_{10}$  lives are an indication of how long the material will last before a spall (failure) occurs and indicates when 10% of the samples will have failed or conversely when 90% of the samples are still running. Some of the Weibull lines were calculated using the Weibayes analysis method due to data that had too few or no failures. These tests were suspended if a failure was not reached after 200 hours ( $102.9 \times 10^6$  cycles). Basically, Weibayes analysis requires that the slope of the line be fixed according to previous test data. This appears to be a good assumption as the slopes of most of the lines with large run times are very similar. A more detailed discussion on Weibull and Weibayes analysis can be found in Reference 5.

RCF data clearly show that the candidate PM alloys have improved fatigue life compared to 440C (Table 2).  $B_{10}$  lives are better than 440C by factors ranging from 1.2 to 5.0. Relative ranking of the candidate materials depends on the maximum Hertzian stress used in the tests. The top three candidates are X-405, MRC-2001 and D-5 at 786 ksi and MRC-2001, T-440V and X-405 at 586 ksi. The final selection will be based on the results of 5-ball tests to be run by TRW, the wear test results (3) and the results of stress corrosion cracking, to be discussed next.

#### STRESS CORROSION CRACKING (SCC) TESTS

SCC tests were run with round tensile specimens hardened and tempered shown in Figure 12. The specimens were placed in small stressing frames and strained a calculated amount using an assumed modulus of  $30 \times 10^6$  psi to give the desired stress (50 or 75 ksi). The frames and ends of the specimens were dipped in a strippable maskant and the reduced portion of the specimens were wiped clean with alcohol. The specimens were placed in a humidity cabinet at 100°F and 100 percent relative humidity.

Results of a series of tests based on 3 months exposure to high humidity are given in Table 3. Results for 440C are included for comparison. All the alloys except T-440V suffered failures at both 50 and 75 ksi. Alloy T-440V failed at 75 ksi, but no failures occurred at 50 ksi. Results for 440C steel are also included for comparison. From Table 3, T-440V has the highest resistance to SCC and the alloy X-405 has the next highest resistance. But even other alloys seem to have at least as much resistance to SCC as 440C. It is emphasized that these results are preliminary and testing is still in progress.

#### SUMMARY AND CONCLUSIONS

Six different powder metallurgy bearing alloys, viz., X-405, MRC-2001, T-440V, 14-4/6V, WD-65, and D-5, were tested for rolling contact fatigue (RCF) life and stress corrosion cracking and the results were compared with standard 440C. The RCF test results clearly showed that

the candidate PM alloys were superior to 440C; B<sub>10</sub> lives were better by factors ranging from 1.2 to 5.0. Stress corrosion cracking resistance of these alloys was as good as or better than that of 440C.

#### REFERENCES

1. B. N. Bhat and F. J. Dolan, "Past Performance Analysis of HPOTP Bearings," NASA-TM-92470, March 1982.
2. R. E. Maurer and R. A. Pallin, "Computer-Aided Selection of Materials for Cryogenic Turbopump Bearings," Proceedings of 40th Annual Meeting of ASLE, Las Vegas, Nevada, May 1985.
3. G. F. Friedman and B. N. Bhat, "Advanced Bearing Materials for Cryogenic Aerospace Engine Turbopump Requirements." To be presented at the AIAA/ASME/SAE/ASEE Joint Propulsion Conference, Huntsville, Alabama, June 16-18, 1986.
4. D. Glover, "A Ball-rod Rolling Contact Fatigue Tester; Rolling Contact Testing of Bearing Steels, ASTM STP 771." J. J. C. 400 Ed., American Society for Testing and Materials, 1982, pp. 107-124.
5. R. B. Abernethy, J. E. Breneman, C. H. Madlin, and G. L. Reinman, "Weibull Analysis Handbook," Government Report No. AFWAL-TR-83-2079.

TABLE 1. CANDIDATE PM BEARING ALLOYS

Alloy	Base	Cr	Mo	Composition (W/O), Typical							Hardness (Rc), Typical
				V	Co	Mn	Si	C	Other		
440C	Fe	17.0	0.75 MX	0.1 Mx	-	1.0 MX	1.0 MX	1.1	-	59	
X-405	Fe	19.0	2.0	1.0	-	-	1.25	1.25	-	61	
MRC-2001	Fe	15.0	6.0	2.0	-	0.5	-	1.20	0.1Cb	62	
T-440V	Fe	17.5	0.5	5.75	-	0.5	0.5	2.20	-	61	
14-4/6V	Fe	14.5	4.5	6.0	-	0.5	0.5	2.0	-	63	
D-5	Fe	12.5	1.5	-	2.75	0.3	0.3	1.25	-	60	
WD-65	Fe	14.0	4.0	2.75	5.75	-	-	1.15	2.5W	62	

TABLE 2.  $B_{10}$  LIFE COMPARISON

Candidate Alloy	<u>Maximum Hertzian Stress</u>			
	<u>786 ksi</u>		<u>586 ksi</u>	
	$B_{10}$ ( $10^6$ cycles)	$\frac{B_{10} \text{ (Alloy)}}{(B_{10})_{440C}}$	$B_{10}$ ( $10^6$ cycles)	$\frac{(B_{10})_{\text{Alloy}}}{(B_{10})_{440C}}$
440C	1.5	1.00	4.4	1.00
X-405	7.5	5.00	10.0	2.27
MRC-2001	5.7	3.80	12.3	2.80
T-440V	2.6	1.73	10.9	2.48
14-4/6V	1.8	1.20	6.2	1.41
D-5	3.5	2.33	7.2	1.64
WD-65	2.7	1.80	7.5	1.70

TABLE 3. SCC TEST RESULTS OF EXPERIMENTAL BEARING ALLOYS AND 440C

<u>Alloy Designation</u>	<u>Applied Stress (ksi)</u>	<u>Failure Ratio</u>	<u>Days to Failure</u>
D-5	50	2/3	17, 42
	75	2/3	4, 7
MRC-2001	50	3/3	36, 36, 37
	75	2/3	4, 7
T-440V	50	0/3	-
	75	2/3	17, 17
WD-65	50	3/3	17, 25, 37
	75	3/3	7, 7, 17
X-405	50	1/3	21
	75	3/3	17, 21, 25
14-4/6V	50	2/3	28, 56
	75	3/3	7, 11, 17
440C (Trans)	50	2/3	3, 36
	75	5/5	1, 1, 6, 14, 21
440C (Long)	50	6/6	1, 1, 2, 6, 14, 21
	75	6/6	1, 1, 1, 2, 2

Results based on 3 months exposure to high humidity (100°F and 100% R.H.)

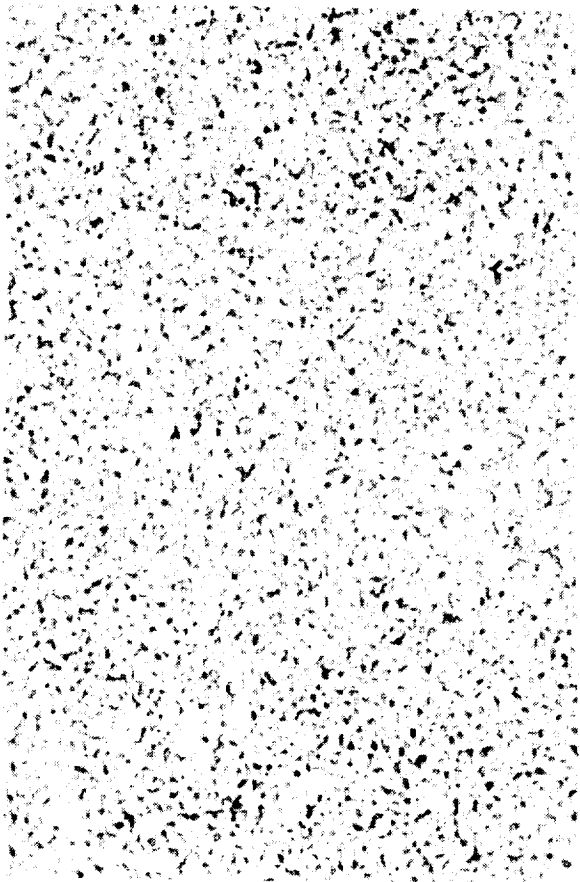


Figure 5. 14-4/6V.



Figure 6. D-5.

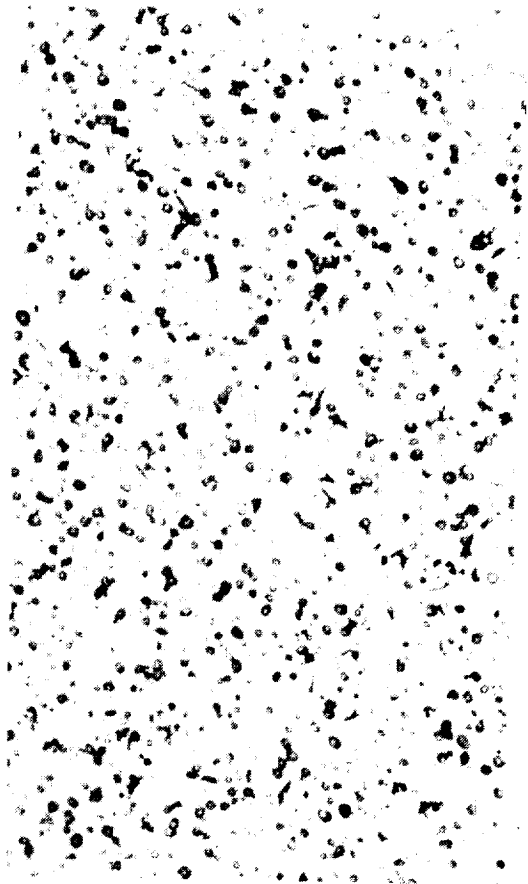


Figure 7. WD-65.

ORIGINAL PAGE IS  
OF POOR QUALITY



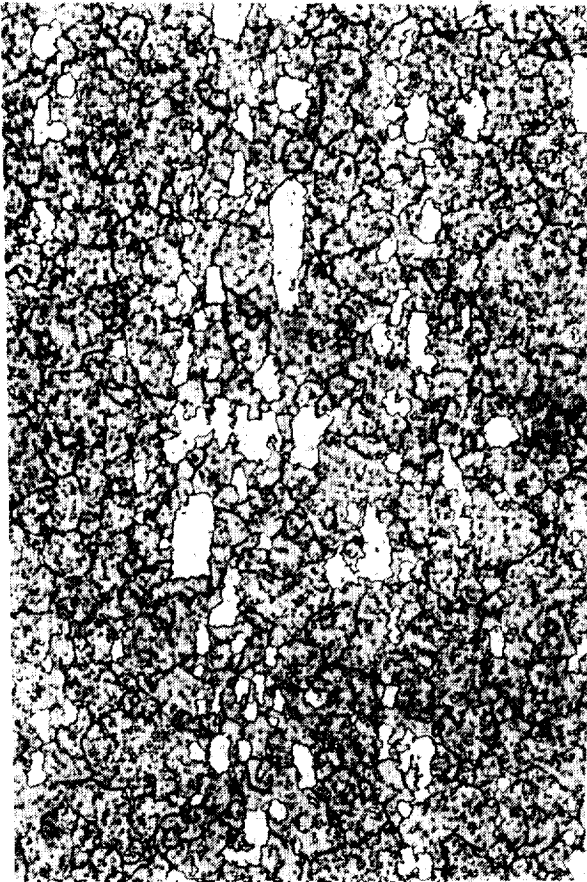


Figure 1. 440C - longitudinal.

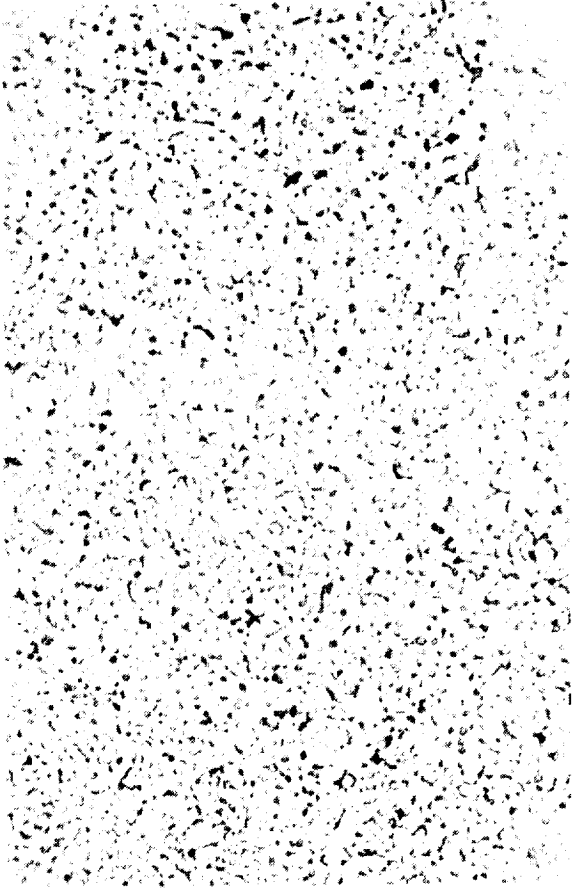


Figure 2. X-405.

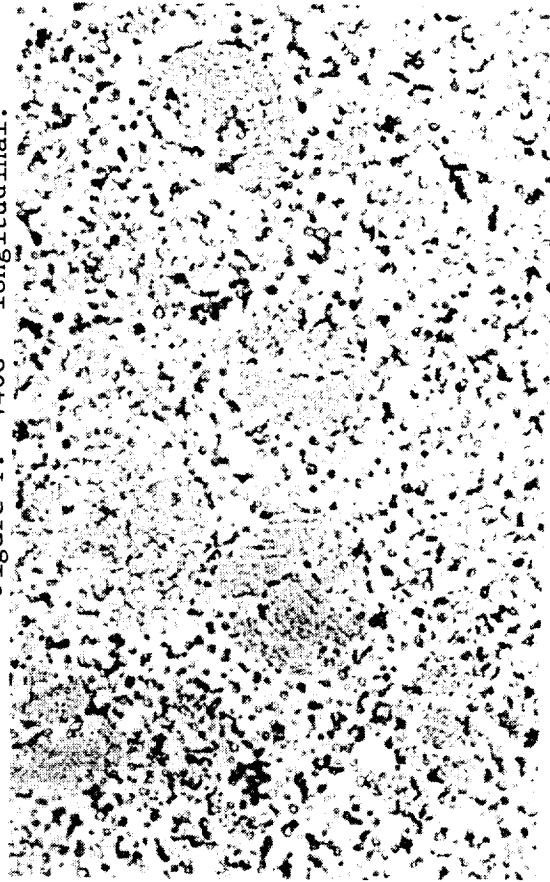


Figure 3. MRC-2001.

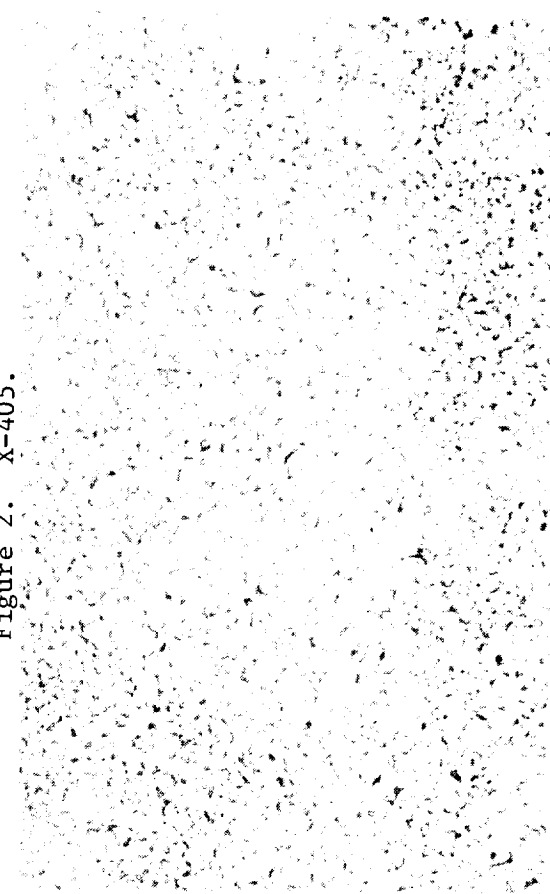


Figure 4. T-440V.

ORIGINAL PAGE IS  
OF POOR QUALITY

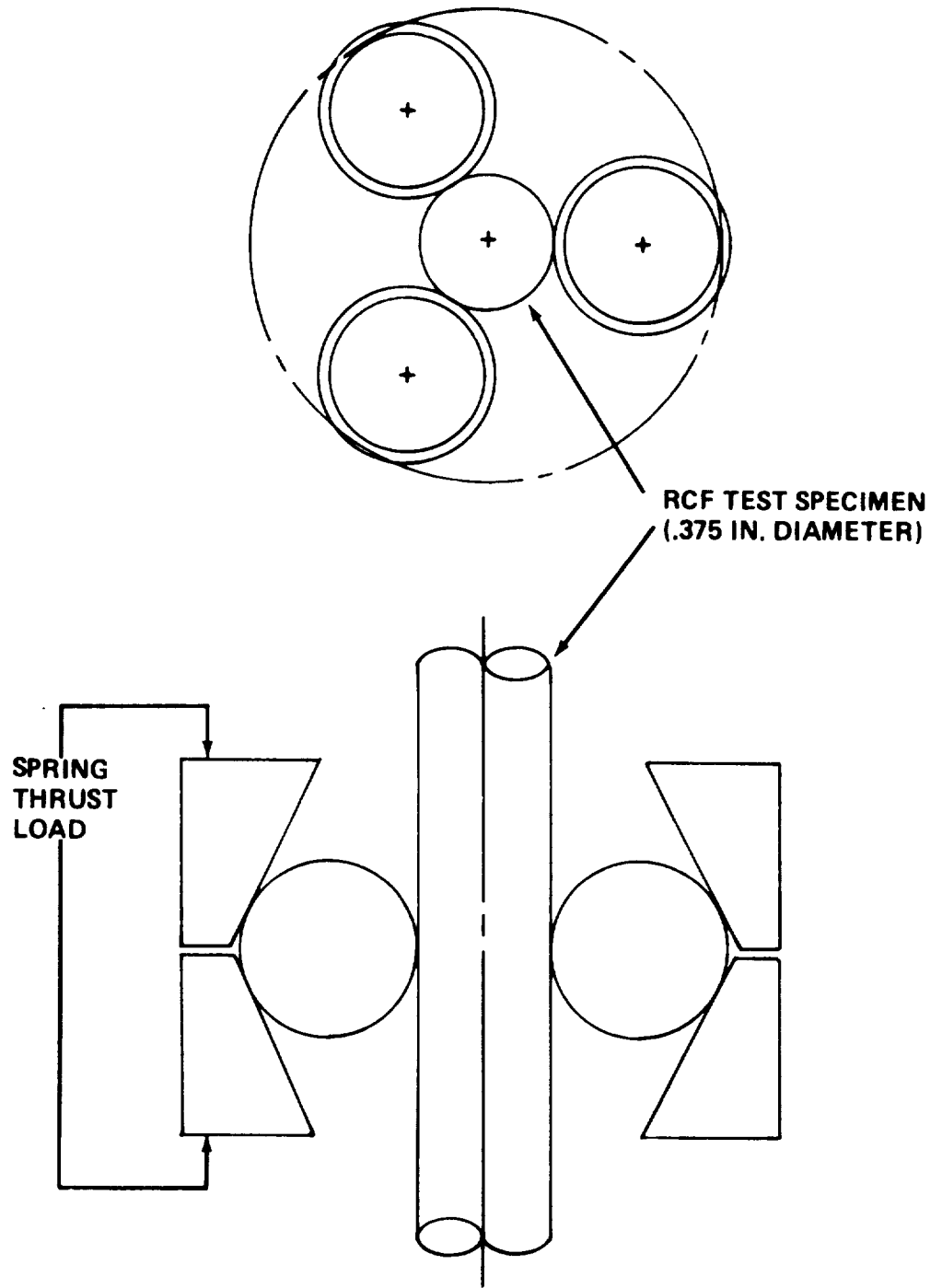


Figure 8. Rolling contact fatigue test arrangement (Federal-Mogul machine).

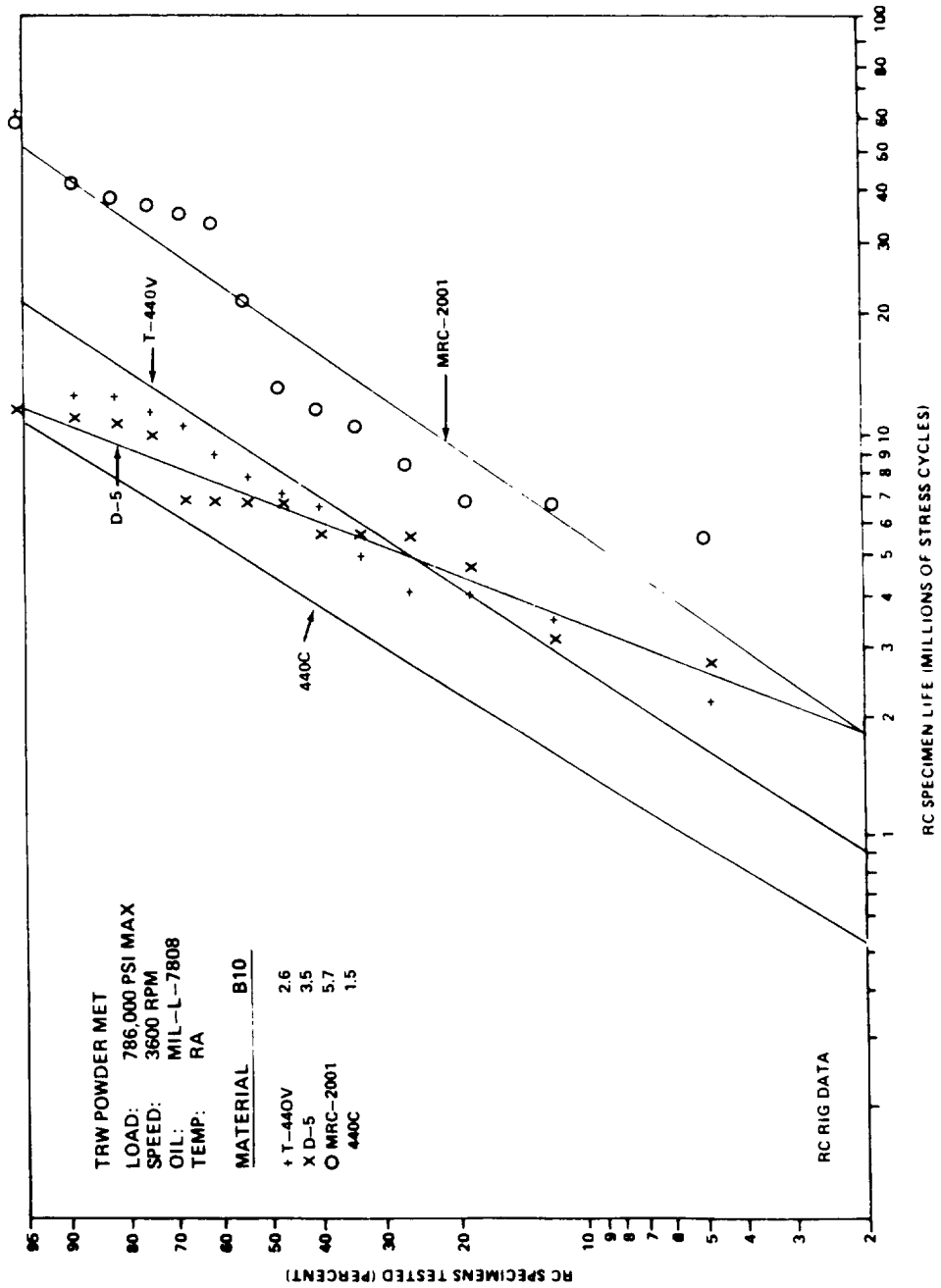


Figure 9. RCF test results for candidate PM bearing alloys.

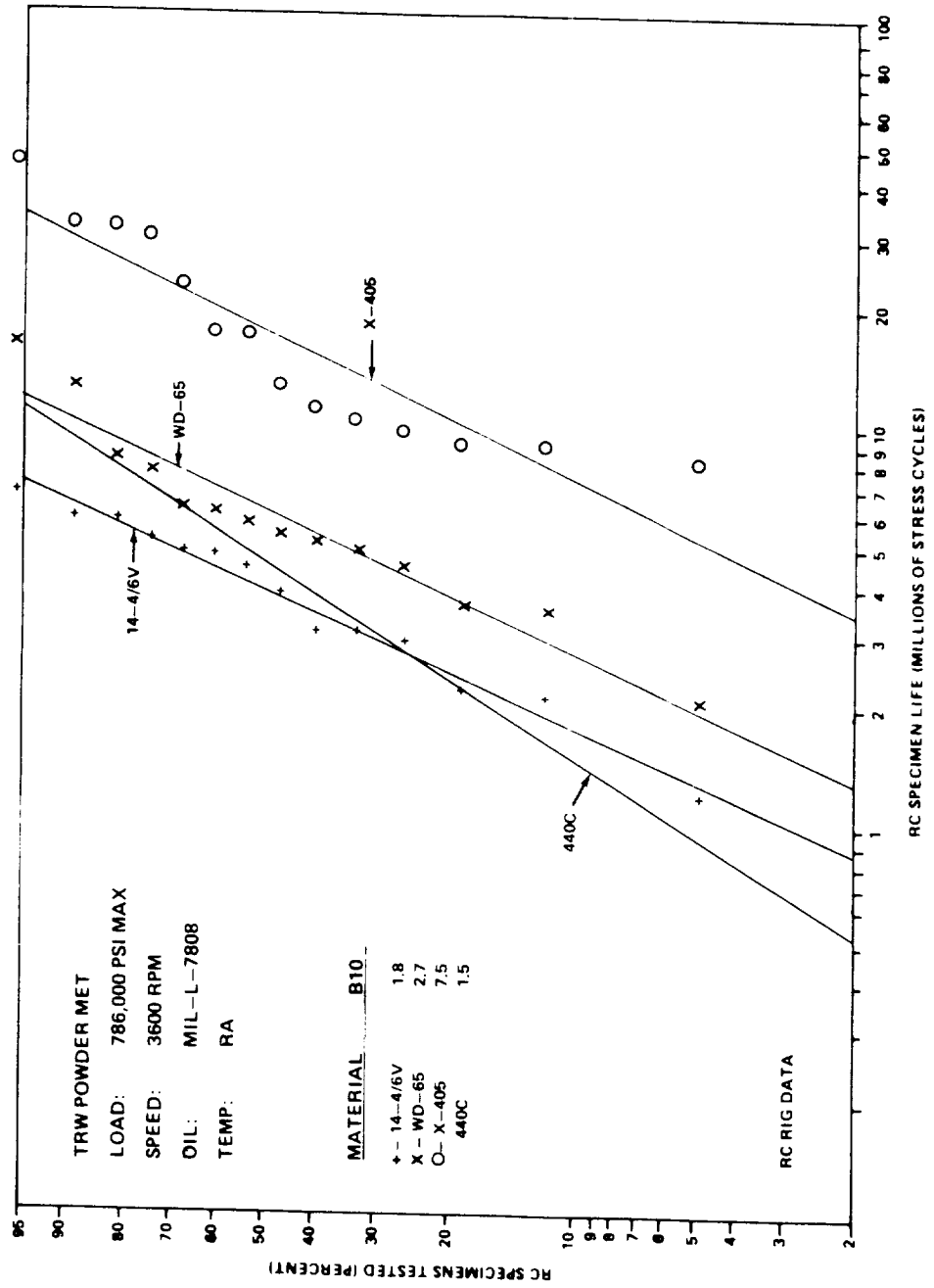


Figure 10. RCF test results for candidate PM bearing alloys.

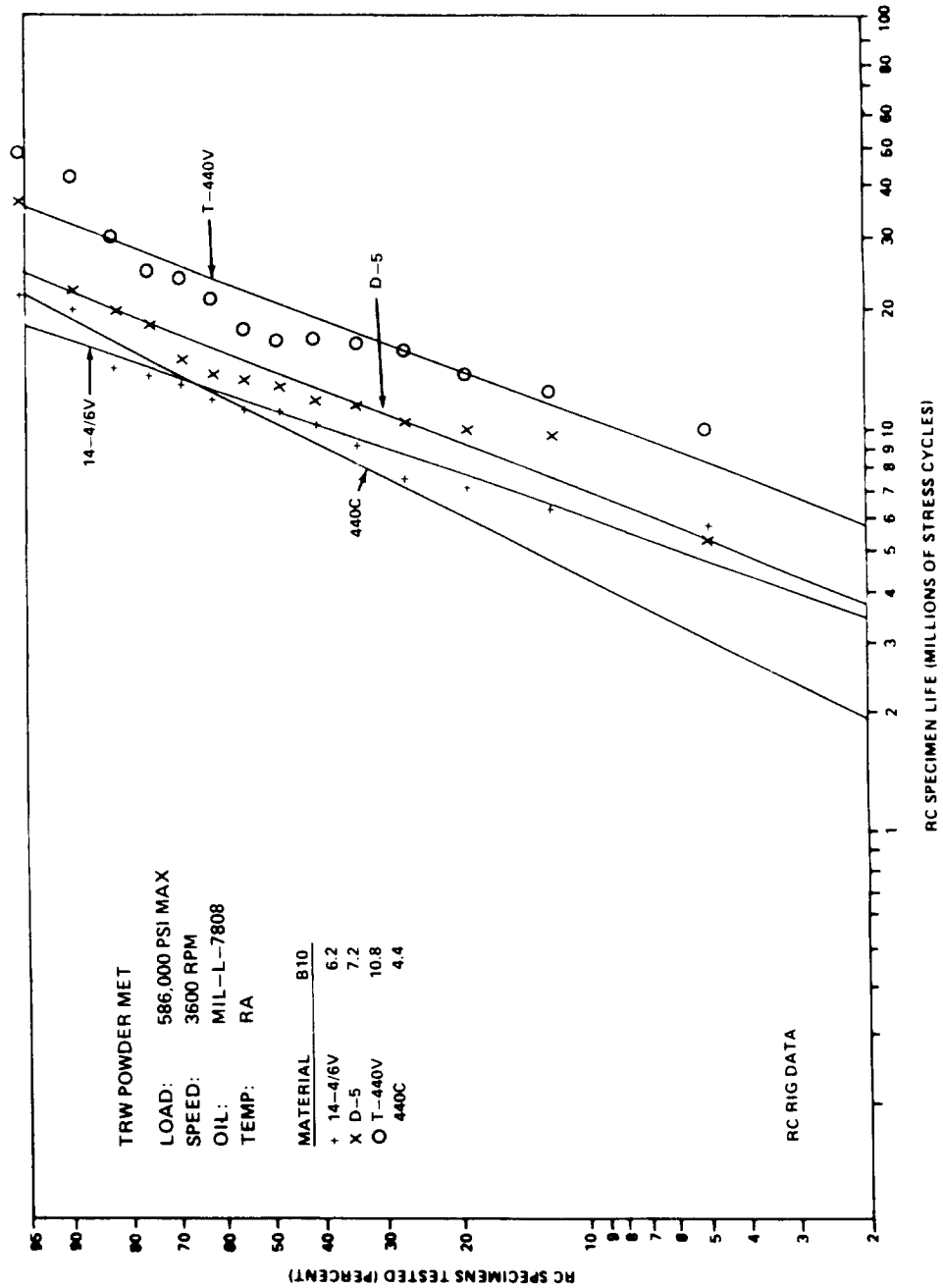


Figure 11. RCF test results for candidate PM bearing alloys.

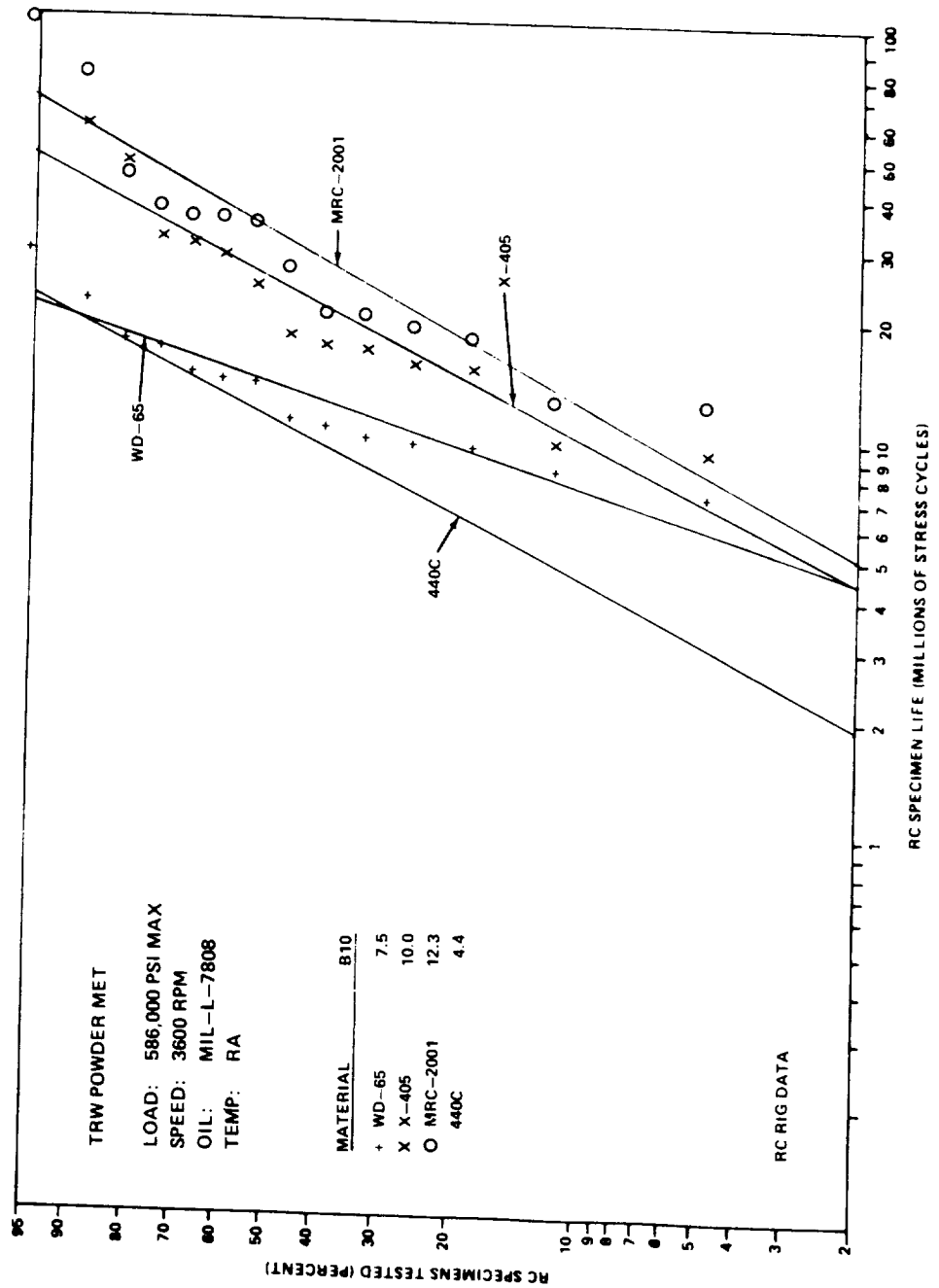
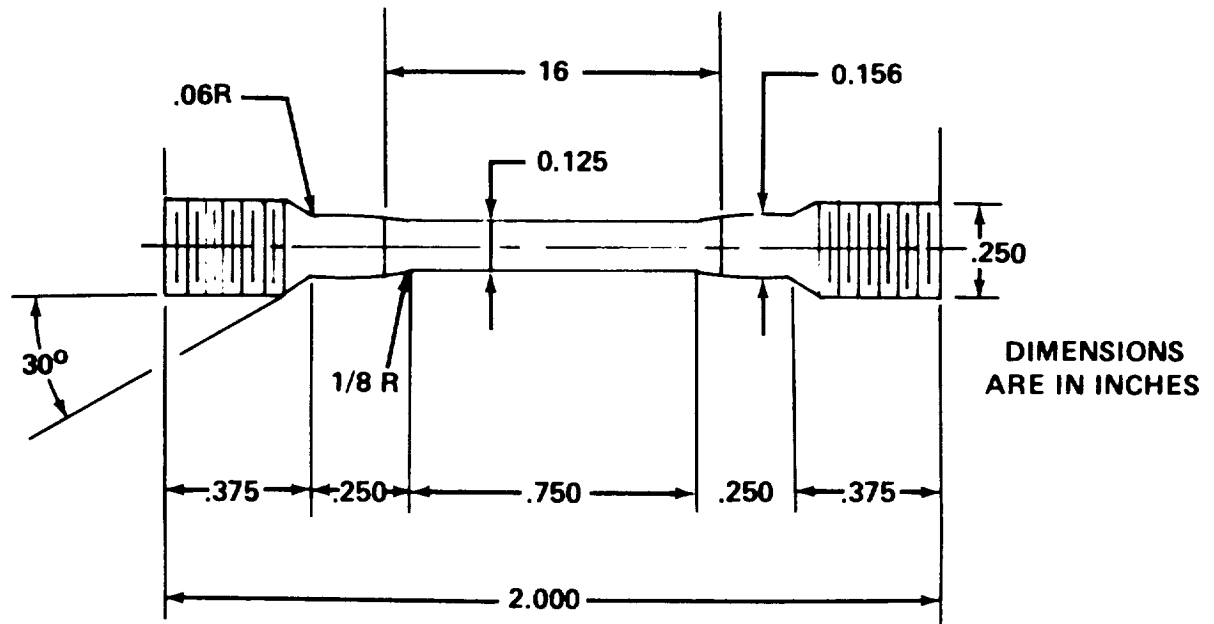
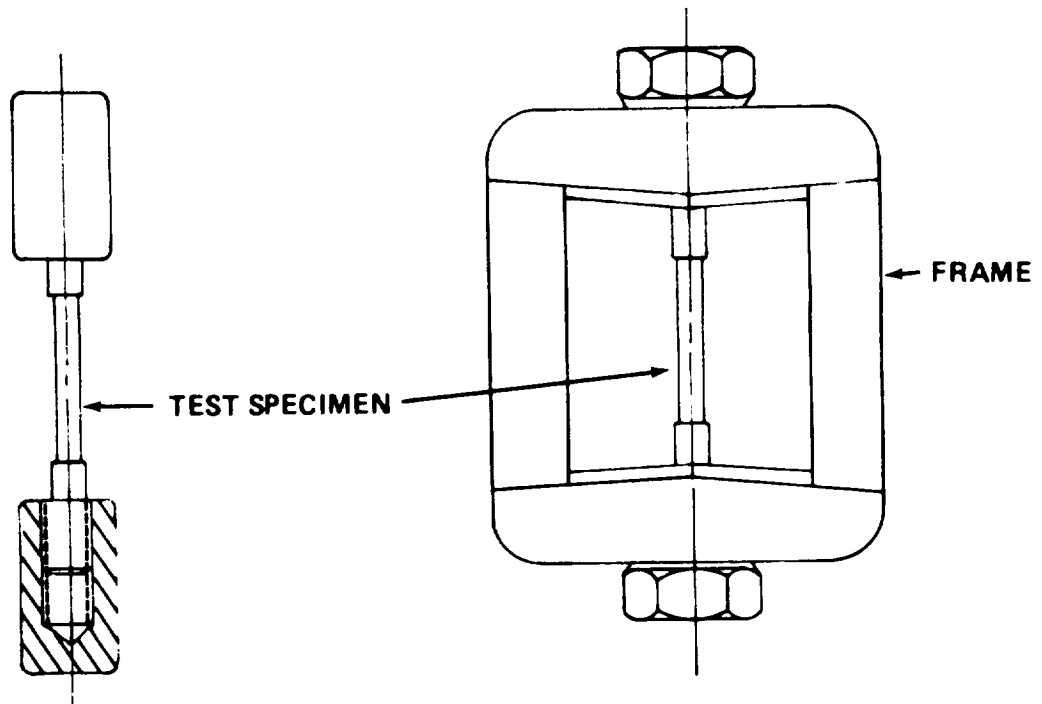


Figure 12. RCF test results for candidate PM bearing alloys.



a. TEST SPECIMEN



b. SPECIMEN FRAME ASSEMBLY

Figure 13. SCC test specimen (a) and specimen frame and assembly (b).

X BEARINGS II



## Rolling Contact Fatigue Life of Zirconium and Molybdenum

## Nitride Sputter Plated AMS 5749 Bearing Steel

Robert L. Thom and Fred J. Dolan  
Materials and Processes Laboratory  
Marshall Space Flight Center, Alabama 35812

Abstract


Hardened AMS 5749 (Latrobes BG42) bearing steel test specimens were reactively sputter plated with zirconium nitride or molybdenum nitride to thicknesses of 0.5  $\mu\text{m}$  and 1.0  $\mu\text{m}$ . The test specimens were evaluated for rolling contact fatigue (RCF) resistance at stresses of both 5.42 GPa (786 ksi) and 4.04 GPa (586 ksi) using a ball on rod test setup. Significant improvements in RCF lives of over 100% were obtained for coated test specimens over the baseline uncoated AMS 5749. These results indicate improvements that can be made to bearings using reactive sputter plating methods.

Introduction

The Space Shuttle Main Engine High Pressure Oxygen Turbopump (HPOTP) has exhibited premature degradation of the shaft support bearings. Bhat and Dolan (1) have reported severe surface distress of the inner and outer raceways and prominent wear of the balls that had undergone 2400 seconds of total run time. They attributed the cause of such a rapid degradation in the bearings to be exacerbated by a thermal runaway type mechanism.

The thermal runaway scenario proposes that during high loading on the bearings the liquid oxygen coolant/lubricant is unable to remove all the heat generated at the rolling element contacts. The bearing then raises in temperature which at a certain point causes the coolant to turn into two phases near the warmest areas. This would tend to speed up the heat buildup process which in turn leads to thermal expansion of the bearing elements. It is proposed that the bearings expand to such a degree that all bearing internal clearance is lost and extremely high stresses internal to the bearing result. This thermal runaway problem can be kept at bay if the liquid oxygen coolant could be kept in its liquid phase as it flows through the bearings.

A study was undertaken in an effort to reduce the coefficient of friction between the bearing rolling elements and thus decrease heat generation and subsequent thermal growth of the inner and outer



raceways and balls. The friction reducing method described in this paper is the application of hard coats to the bearing surface. It is believed that a hard coating will both reduce wear and friction of bearing elements. The newest techniques in vacuum surface coatings were used to apply thin coatings of zirconium nitride (ZrN) and molybdenum nitride (MoN) hard coats to the surface of Latrobe's BG42 (AMS 5749).

### Experimental Procedures

#### A. Material Preparation

The substrate test specimens were prepared from a martensitic stainless steel, Latrobe's BG42 (AMS 5749). The steel was vacuum induction melted (VIM) and vacuum arc remelted (VAR). The test specimens were 0.9525 cm (0.375 in) diameter by 8.25 cm (3.25 in) long. They were ground to a surface finish between 0.1 and 0.2  $\mu\text{m}$  (4-8  $\mu\text{in}$ ) Ra (roughness average). The test specimens were fully hardened to Rockwell C 60 or better prior to film deposition.

#### B. Coating

The test specimens were coated with ZrN and MoN by an outside vendor using a reactive ion sputtering technique. Depending on the coating a zirconium (Zr) or molybdenum (Mo) target was bombarded with ions thus sputtering off the metal atoms. Some of the sputtered atoms become positively ionized and are attracted to the negatively charged substrate. At this time they also become attached to nitrogen creating the desired nitride coating on the substrate surface. The coating operation was performed in a vacuum of approximately 0.3 microns of mercury and the substrate had a negative applied bias of 400 to 500 volts. Prior to coating the test specimens were subjected to a precleaning sputtering operation by creating an argon glow discharge around the substrate.

#### C. Rolling Contact Fatigue Testing

The rolling contact fatigue (RCF) tests in this investigation were conducted on a ball-rod type rolling contact fatigue unit. A short description of the tester follows, however, a more detailed description of this system can be found in reference 2. A schematic diagram of the test unit is shown in figure 1.

The test consisted of radially loading three 1.27 cm (0.5 in) diameter hardened balls against a test specimen being driven at 3600 RPM. The three balls, equally separated by a bronze retainer, are radially loaded by two tapered bearing cups which are loaded axially by three calibrated springs. An accelerometer, coupled to a shutoff

device and magnetically attached to the tester in close proximity to the test specimen, was used to determine the emergence of a spall on the test specimen which was governed by when a preset vibration level was exceeded. At that time the motor was automatically stopped and the test was finished. The test specimens were lubricated at a constant drip rate of 6 to 8 drops per minute with MIL-L-7808, a jet turbine engine oil. The oil is passed through the test system once only. The tests were run continuously 24 hours a day until a spall occurred or until 200 hours of test time was reached.

Each test specimen was subjected to 14 individual rolling contact tests with 7 tests being conducted on each end of the rod. The tests were conducted at two stress levels, 5.42 GPa (786 ksi) and 4.04 GPa (586 ksi) maximum Hertzian stress. Each sample was run with seven tests at the high stress and seven at the lower stress which were alternated along the length of the test specimens to avoid any adverse statistical results due to a gradient effect or variation in the coating along the length of the test specimen.

The balls that were loaded against the test specimens were half-inch diameter AISI 52100 balls, AFBMA Grade 10. The surface finish of the balls was roughened to 0.089  $\mu\text{m}$  (3.5  $\mu\text{in}$ ) roughness average in order to obtain a more severe test of the surface coatings, and to obtain failures before the 200 hour cutoff time.

#### Rolling Contact Fatigue Test Results

The failure of both uncoated baseline and coated test specimens occurred by characteristic pit or spall formation. The size of spalls was smaller for samples tested at lower contact stresses. The results of the rolling contact fatigue (RCF) tests have been plotted on Weibull graph paper and the B10 and B50 lives calculated. A detailed discussion on the Weibull and Weibayes analysis used to calculate the lives can be found in references 3 and 4. The B10 and B50 lives are in general an indication of how long the material being tested will last before a spall (failure) occurs but specifically, they indicate how many stress cycles it requires to obtain failure of 10% and 50% respectively of the test specimens statistical sample.

Figure 3 contains a baseline BG42 plot plus two plots of half micron thick surface coated test specimens tested at 4.04 GPa (586 ksi). The plots clearly show the superior rolling contact fatigue life of the zirconium and molybdenum nitride reactively sputter coated samples with increases in B10 life of 207% and 97% respectively.

Figure 4 contains two plots of one micron thick reactively sputter coated surfaces plus the baseline plot for BG42 tested at 4.04 GPa (586 ksi). The plots show significant increases in rolling contact

fatigue life of 58% and 101% for zirconium and molybdenum nitride coated samples.

Figure 5 is a chart of half micron thick coated test specimens tested at 5.42 GPa (786 ksi). The tests were run between the previous wear tracks of the lower contact stress tests of figure 3. The improvements in B10 life (50% and 10% for zirconium and molybdenum nitride coated samples respectively) are not nearly as dramatic as in the previous charts.

Figure 6 contains the results obtained from tests performed at 5.42 GPa (786 ksi) of one micron thick coated test specimens. These tests were run between the previous wear tracks of the lower contact stress tests of figure 4. The improvements in B10 life (29% and 19% for zirconium and molybdenum nitride respectively) again are not as substantial as in figures 3 and 4.

The confidence levels of the coated test specimens having a B10 life greater than its respective baseline are given in Table 1.

	<u>4.04 GPa (586 ksi)</u>	<u>5.42 GPa (786 ksi)</u>
0.5 $\mu\text{m}$ ZrN	97%	73%
1.0 $\mu\text{m}$ ZrN	75%	67%
0.5 $\mu\text{m}$ MoN	86%	57%
1.0 $\mu\text{m}$ MoN	87%	60%

Table 1. Confidence levels at B10 life.

Figures 7 and 8 are scanning electron microscope (SEM) pictures of Rockwell C hardness indentations into half and one micron molybdenum nitride coated BG42 respectively. The one micron thick coating has flaked off in the vicinity of the indentation whereas the half micron coating appears intact. The micrographs fail to give the visual impression that the BG42 substrate material has bulged up in the area surrounding the indentation. The half micron coating was able to follow the plastically deformed substrate without cracking and flaking off, however, the one micron thick coating did not exhibit the same adherence.

A micrograph of a typical spall is shown in figure 9. Figure 10 is a section of wear track on a one micron thick MoN coated sample. These two micrographs further illustrate the greater adherence of the half versus the one micron thick MoN coatings. There is no evidence of the half micron coating flaking near the spall while in figure 10 the coating was not adherent enough to remain intact. An elemental analysis (EDAX) was performed on the coatings both inside and outside of the wear track. The one micron thick coating showed a strong

molybdenum peak outside the wear track but indicated the absence of molybdenum in the wear track area. For the thinner coating a reduced but definite Mo peak was observed in the wear track area while outside the wear track area strong Mo peak was observed. This indicates that the thinner half micron thick coating did not flake off but underwent wear. The one micron thick coating, however, flaked off leaving no evidence of Mo in the wear track.

Figures 11 and 12 are parallel to figures 7 and 8. In this case the coatings are half and one micron thick, respectively, zirconium nitride. As in the earlier figures the thicker coating has flaked off where plastic deformation "bulging" of the substrate has occurred while the thinner coating exhibits very good adhesion and no flaking off of the coating.

Figure 13 is a typical spall on a half micron thick ZrN coated substrate. This photomicrograph similar to figure 9 also does not display any evidence of the coating breaking up. Elemental analysis indicates an approximately 50% reduced Zr peak in the wear track versus off the wear track. Figure 14 is a photomicrograph on the edge of a wear track showing where the one micron thick coating has flaked off. A Zr peak was not apparent in an elemental analysis of the wear track.

#### Discussion of Results

The parameters considered by most investigators to be critical in rolling contact fatigue are the maximum shear stresses. In these tests the maximum shear stresses are located at depths beneath the surface ranging from 50  $\mu$ m to 150  $\mu$ m for the two contact stresses of 4.04 GPa (586 ksi) and 5.42 GPa (786 ksi), see reference 5. Nahm and Bamberger (6) have noted in RCF tests of M50 that the fatigue spalls were subsurface initiated. This failure mode occurred whether the lubrication regime was boundary, mixed, or fully elastohydrodynamic. Thus, prior to RCF testing of samples coated with thin hard coatings it was believed that no improvements in RCF life would occur, since the coatings are less than 2  $\mu$ m thick yet the maximum shear stresses are located over 50  $\mu$ m below the sample surface.

As the results show, improvements of the RCF life have been obtained even though general belief was that thin coatings would have no effect on the fatigue behavior. The cracks were thought to initiate internally in the bulk of the material. The test results however indicate that the principal mechanism of rolling contact fatigue in this case is initiated at the surface and not subsurface. The zirconium and molybdenum nitride coatings or the treatment the test specimen undergoes while being reactively sputter plated appear to arrest or at least retard the initiation of fatigue microcracks at

the test specimen surface. The thin nitride coatings being so extremely hard and adherent to the substrate could essentially stop the formation of precursor microcrack initiation.

The behavior of thicker coatings flaking off and thinner coatings ( $<0.5 \mu\text{m}$ ) staying intact even under extreme test loads and plastic deformation of the substrate has been documented previously (7). It would be the most beneficial to have a coating thick as possible without cracking and subsequently flaking off. This would allow for the most margin due to wear.

#### References

1. B. N. Bhat and F. J. Dolan, "Past Performance Analysis of HPOTP Bearings," NASA TM-82470, March 1982.
2. D. Glover, "Rolling Contact Fatigue Testing of Bearing Steels," J. J. C. Hoo Ed., ASTM STP #771, 1982, p. 107.
3. R. B. Abernathy, J. E. Breneman, C. H. Medlin, G. L. Reinman, "Weibull Analysis Handbook," Government report #AFWAL-TR-83-2079.
4. L. G. Johnson, "The Statistical Treatment of Fatigue Experiments," Elsevier Publishing Co., 1964.
5. E. N. Bamberger, J. C. Clark, "Rolling Contact Fatigue Testing of Bearing Steels," J. J. C. Hoo Ed., ASTM STP #771, 1982, p. 85.
6. A. N. Nahm, E. N. Bamberger, Trans., ASME (J. Lubr. Technol.), 102 (1980), p. 10.
7. R. F. Hochman, A. Erdemir, F. J. Dolan, and R. L. Thom, J. Vac. Sci. Technol. A 3(6), November/December 1985, p. 2348.

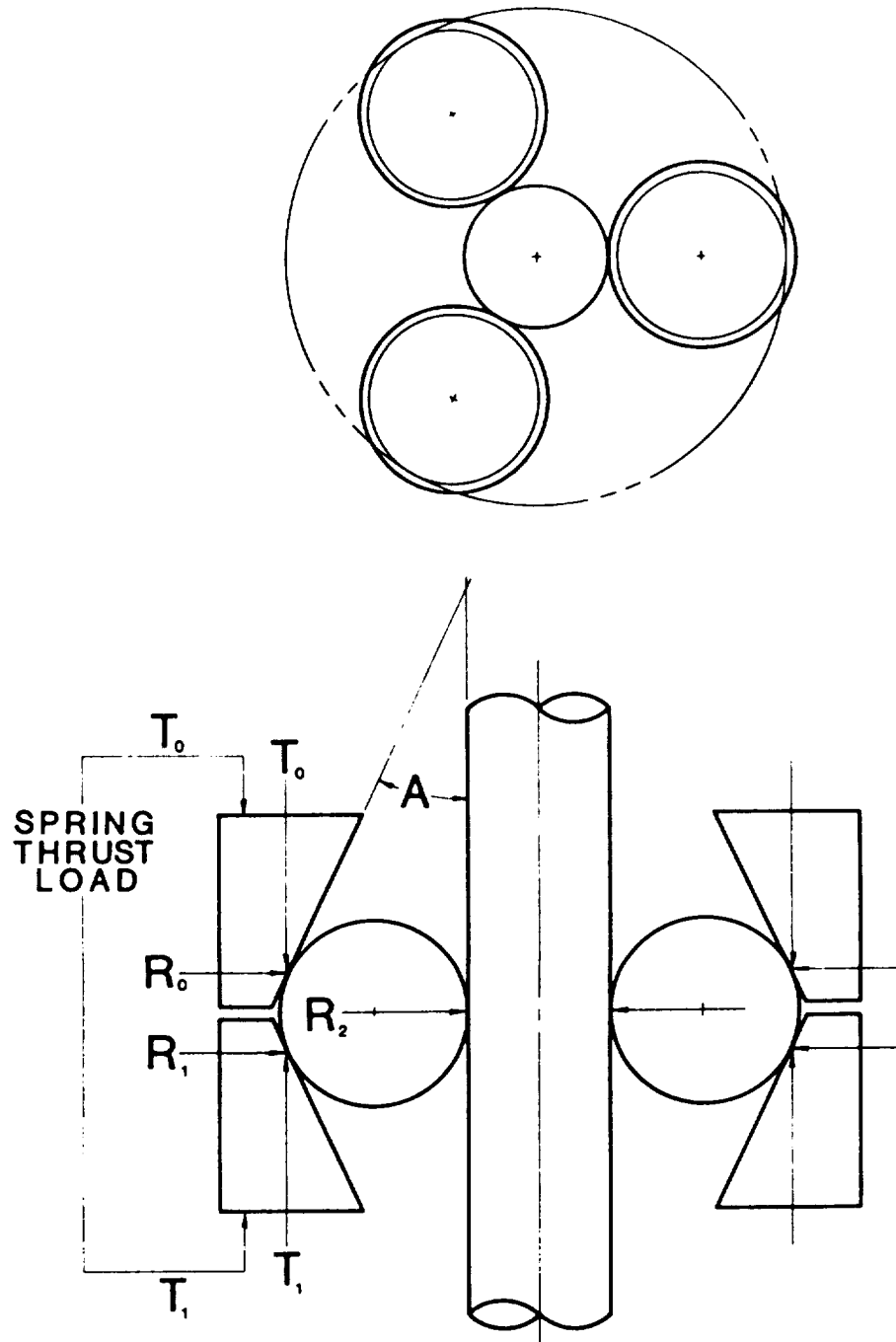


Figure 1: Schematic diagram of RCF tester configuration

ORIGINAL PAGE IS  
OF POOR QUALITY

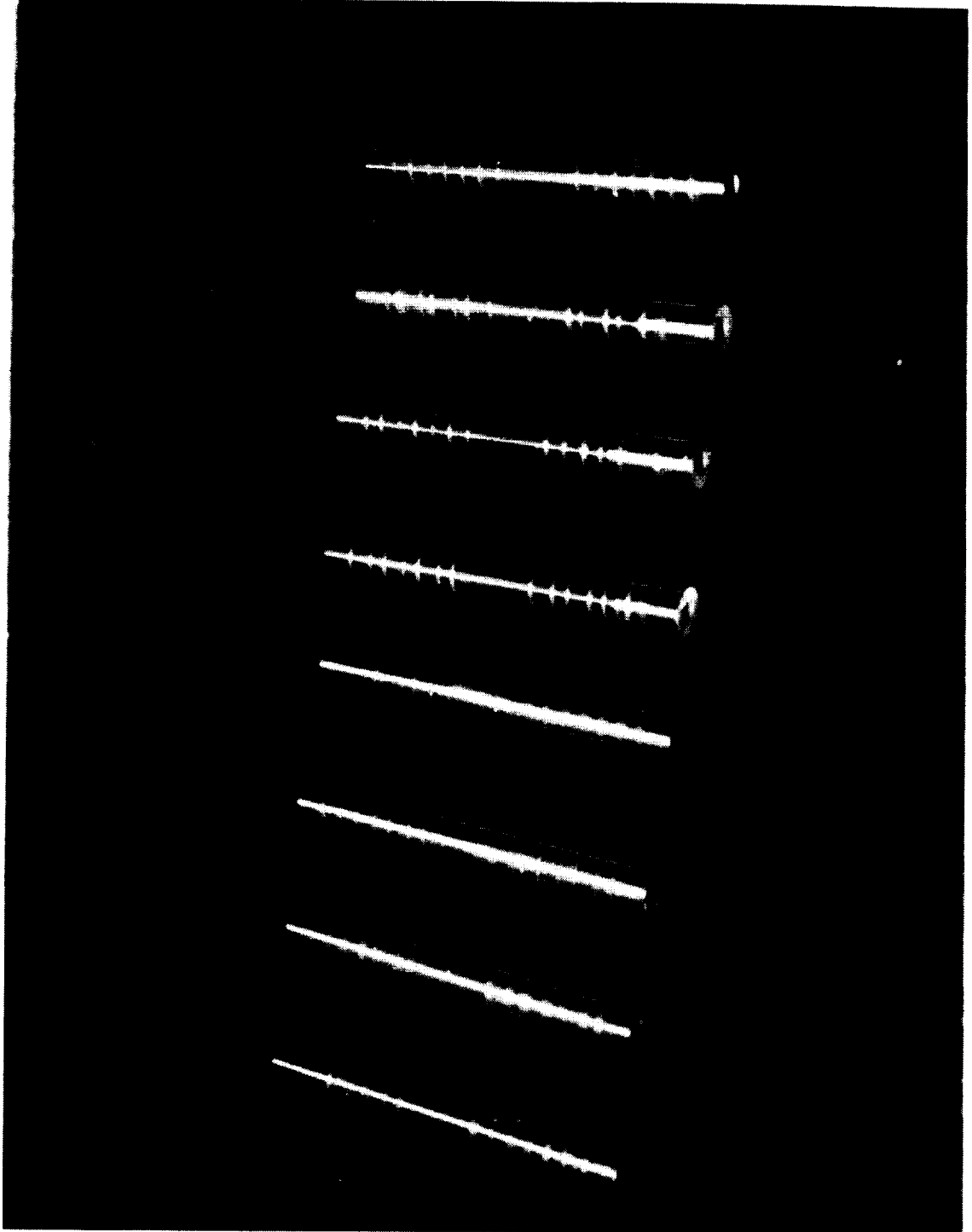


Figure 2: Photograph of eight tested 3 inch long coated RCF test specimens



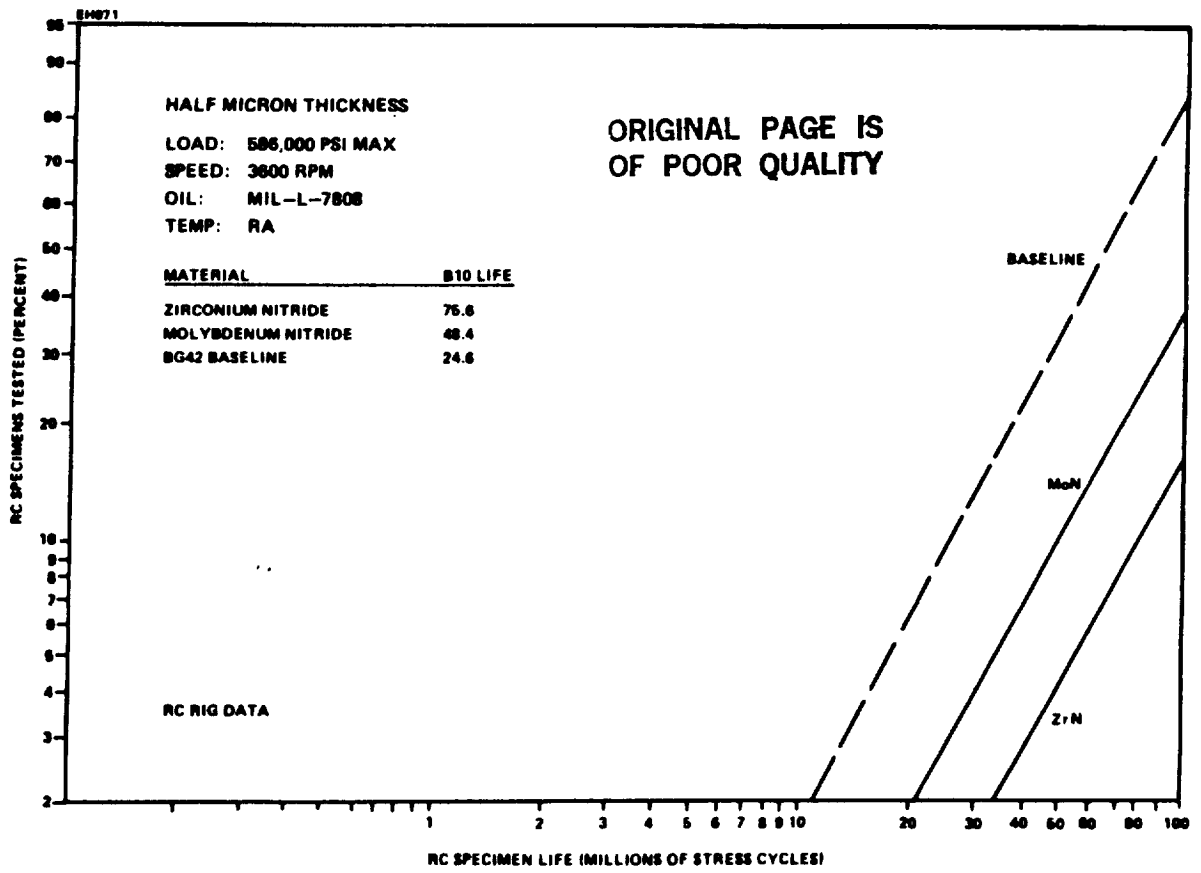


Figure 3: Weibull plot of half micron thick, 586 ksi data

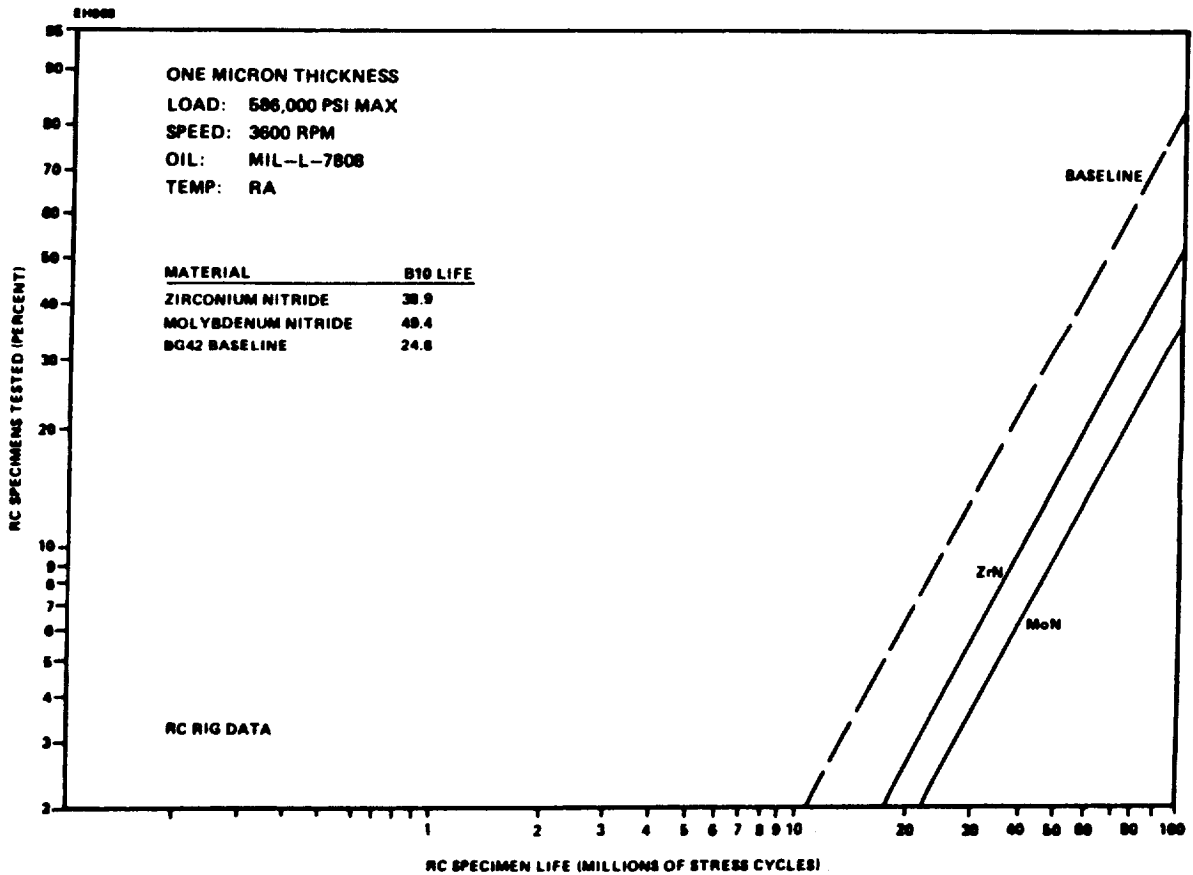


Figure 4: Weibull plot of one micron thick, 586 ksi data

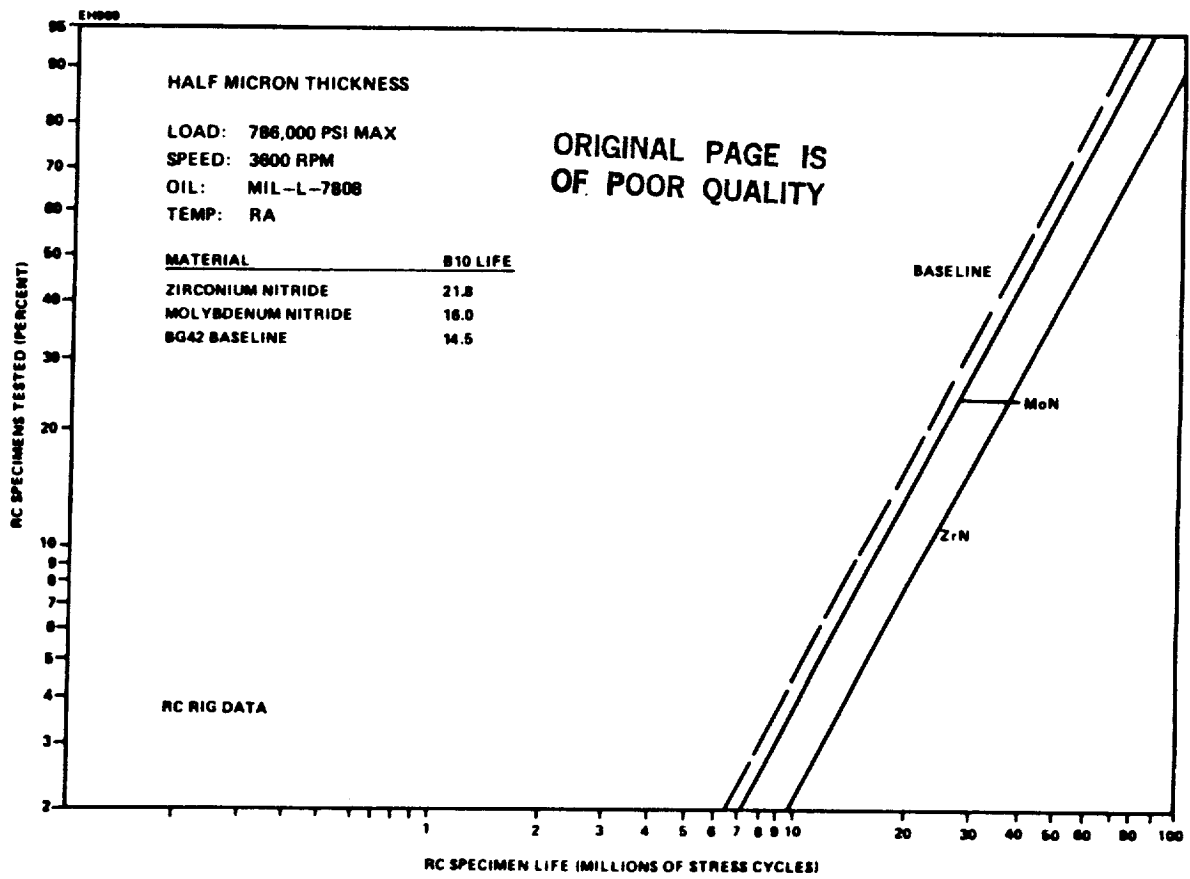


Figure 5: Weibull plot of half micron thick, 786 ksi data

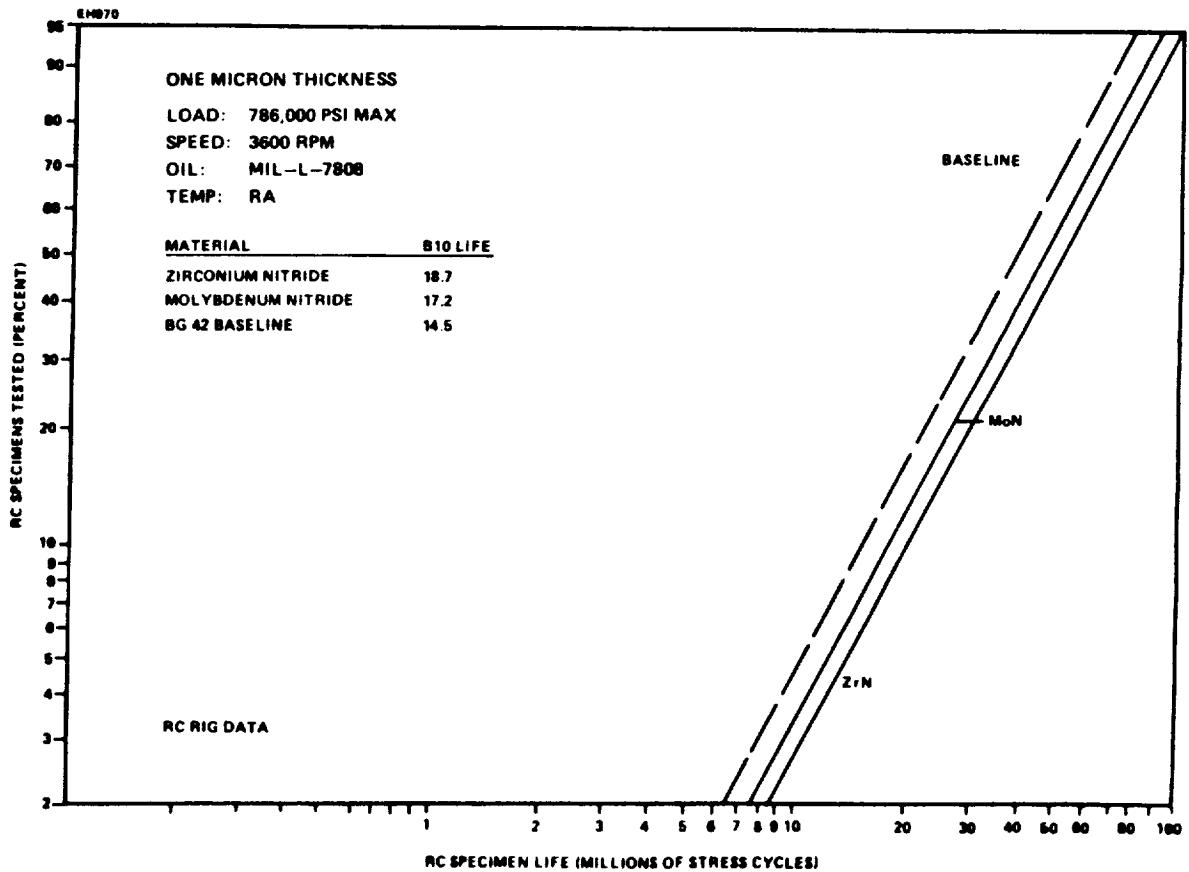


Figure 6: Weibull plot of one micron thick, 786 ksi data

ORIGINAL PAGE IS  
OF POOR QUALITY



Figure 7: Half micron thick molybdenum nitride coating,  
Rockwell "C" hardness indentation



Figure 8: One micron thick molybdenum nitride coating,  
Rockwell "C" hardness indentation

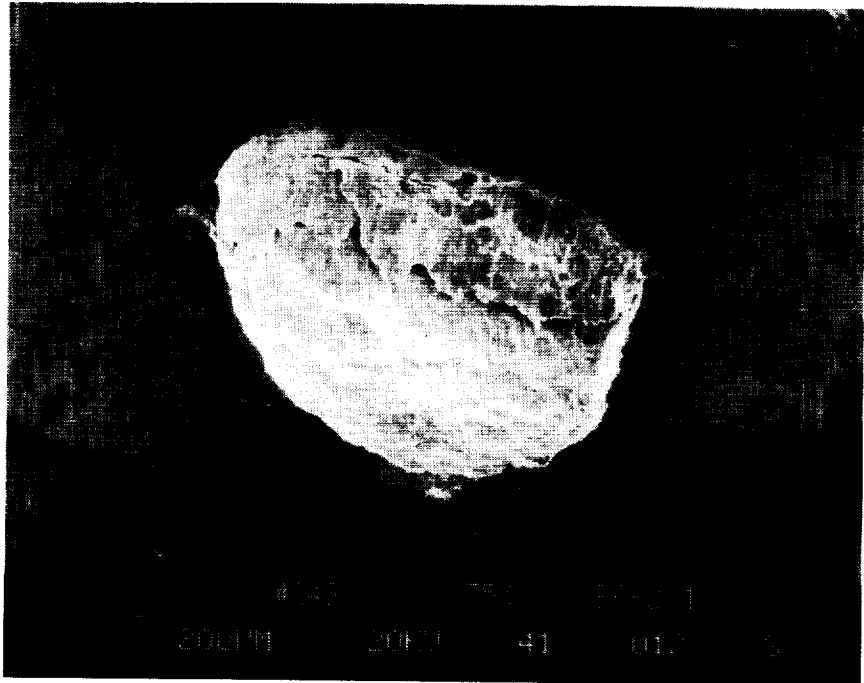


Figure 9: Half micron thick molybdenum,  
typical rolling contact fatigue spall.

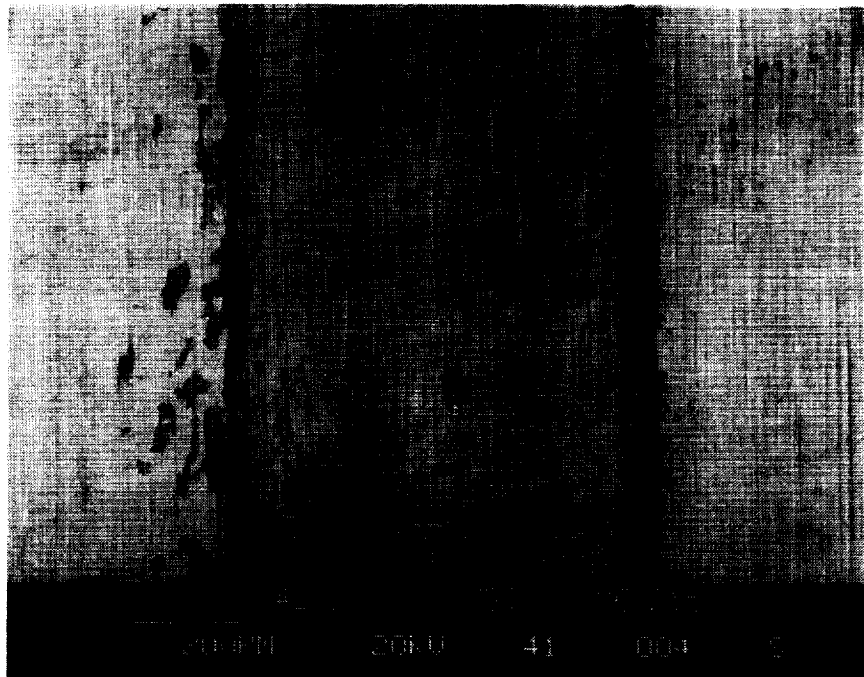


Figure 10: One micron thick molybdenum nitride,  
wear track area

ORIGINAL PAGE IS  
OF POOR QUALITY



Figure 11: Half micron thick zirconium nitride,  
Rockwell "C" hardness indentation



Figure 12: One micron thick zirconium nitride,  
Rockwell "C" hardness indentation

ORIGINAL PAGE IS  
OF POOR QUALITY

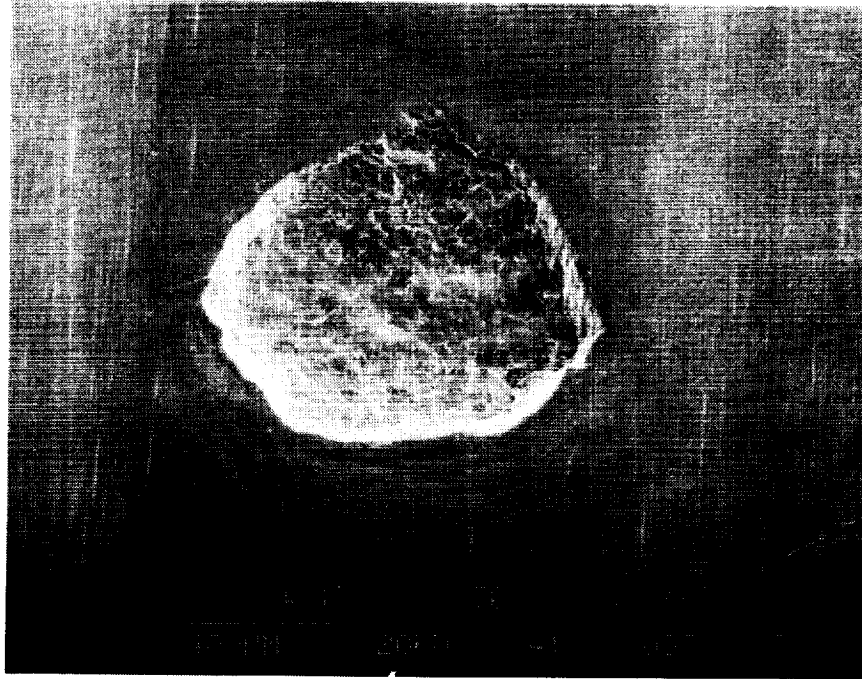


Figure 13: Half micron thick zirconium nitride,  
typical rolling contact fatigue spall

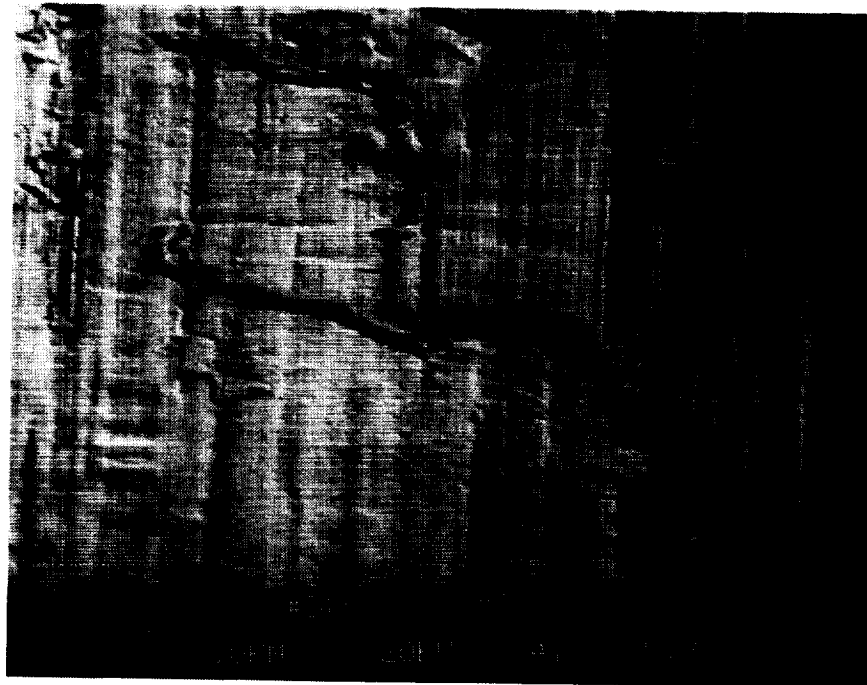


Figure 14: One micron thick zirconium nitride,  
edge of wear track area

MEASUREMENT OF ROTORDYNAMIC COEFFICIENTS  
FOR A HYDROSTATIC RADIAL BEARING

B. T. Murphy and M. N. Wagner

Rockwell International/Rocketdyne Division  
Canoga Park, CaliforniaAbstract

Measurement of rotordynamic coefficients is presented for a hydrostatic radial bearing, including direct and cross-coupled stiffness and damping. Two different hydrostatic configurations were tested: (1) an externally fed bearing 74.9 mm (2.95 inches) in diameter with a nominal direct stiffness of approximately 210 MN/m (1.2 million lb/in.) and (2) an internally fed bearing 54.6 mm (2.15 inches) in diameter with a nominal direct stiffness of approximately 88 MN/m (0.5 million lb/in.). Each bearing had six equally spaced hydrostatic pressure pockets, stationary for the externally fed bearing and rotating for the internally fed bearing. Also, both bearings had extended exit regions to provide additional damping. The top rotational speed was 378 Hz (22,700 rpm) and the maximum axial Reynold's number was 50,000 using a freon derivative (Freon-113) as the working fluid. The test apparatus was a "synchronous rig" as an intentionally eccentric journal was used as the sole source of excitation. The bearing's stator element was flexibly and asymmetrically supported by strain-gage type load cells. While the load cells provided the primary force measurements, eddy current probes were used to measure the elliptic relative motion between stator and journal. Coefficient reduction was done by performing a matrix solution on the data of each tester speed to separate damping from stiffness and inertia. Results show the externally fed bearing to be 20% less stiff than predicted, and to have a significant amount of damping that agrees well with predictions. The internally fed bearing was found to be approximately 60% less stiff than predicted, and to be roughly neutral in terms of damping, as predicted.

Introduction

The ball bearings that support the rotating shafts of the Space Shuttle Main Engine (SSME) high pressure turbopumps have demonstrated their reliability based on numerous hot-fire tests and actual flights of the Space Shuttle. In spite of this, one of the major goals for upgrading the performance of the SSME is to increase the life of the high pressure oxidizer turbopump bearings beyond the current six-mission limit. These bearings operate at extremely high DN values, and also react very large static and dynamic loads. Numerous design

modifications have been made to the high pressure turbopumps to effectively increase the bearing's capacity, and also to reduce loads. As part of the ongoing effort to extend turbopump bearing life, the work reported here describes test results obtained on a high-speed, high-pressure, liquid-fed hydrostatic bearing. The potential application of a hydrostatic bearing to turbopump technology is threefold: (1) it can produce extremely high stiffness, which can be used as a long-life replacement for mechanical element bearings, (2) it can be used as a load-sharing device when used in conjunction with a mechanical bearing, and (3) through proper design, it can be an effective damping device, thereby reducing dynamic bearing loads and increasing rotor stability.

The Rocketdyne hydrostatic bearing test apparatus has been designed, fabricated, and used to measure the rotordynamic stiffness and damping, both direct and cross-coupled, for two kinds of hydrostatic bearings: externally fed and internally fed. A high-density freon derivative was used as a surrogate fluid due to its hydrodynamic similarity to cryogenic turbopump fuels. Forced dynamic motion across the bearing fluid film is generated by mounting the bearing journal eccentrically on the test shaft (Fig. 1). Thus, the test apparatus is operated with a synchronous excitation only. The relative whirl orbits across the fluid film are made to be elliptic with asymmetric stiffness in the test bearing's supporting structure. This elliptic nature is utilized in the data reduction process.

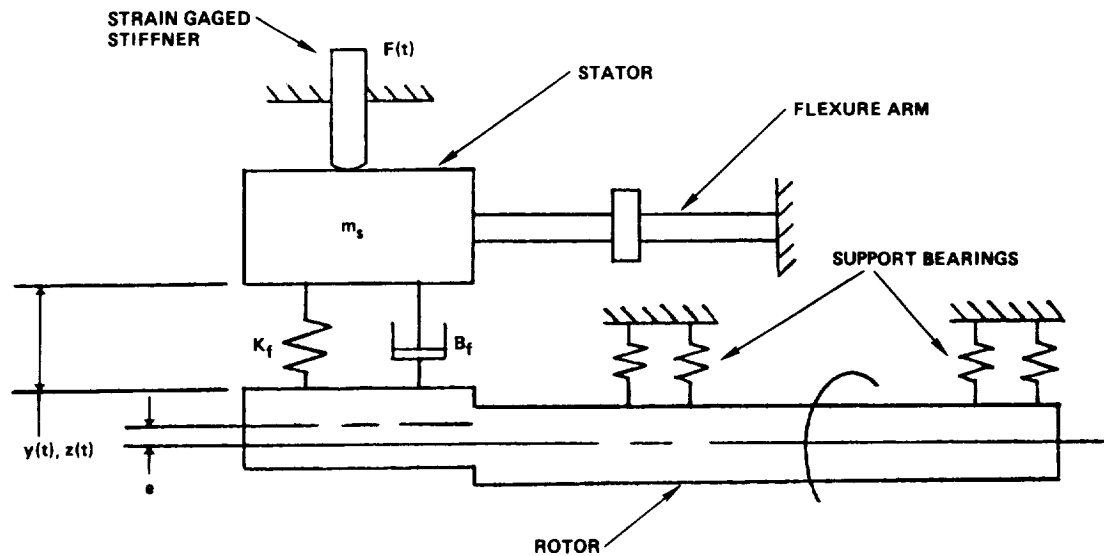


Fig. 1. Measurement technique of hydrostatic bearing tester using an eccentric journal to provide synchronous excitation.



Other test results for a hydrostatic bearing have been reported by Goodwin, et. al.<sup>1</sup> Their experiments were for a combination hydrostatic/hydrodynamic bearing, and do not apply to the types of configurations being tested here. No other test results, particularly direct damping, have been noted in the literature for these types of bearings.

#### Method of Measurement

The test method for determining dynamic coefficients of hydrostatic bearings involves generating a forced dynamic motion across the bearing fluid film and measuring the resulting fluid film displacements and forces. These displacements and forces provide the means for computing the active set of rotordynamic coefficients.

The forced dynamic motion is generated as depicted in Fig. 1. The overhung test bearing is located on the outboard end of a test shaft supported by two duplex pair of ball bearings (Fig. 2). The rotating part of the test bearing has been given an intentional eccentricity (i.e., runout) at the test bearing location. When the shaft rotates, the eccentricity generates an orbital pattern synchronous with shaft speed. This orbital pattern is measured with a pair of eddy current displacement probes mounted directly in the stator of the test bearing (Fig. 3). In this way, with the stator element in motion, the

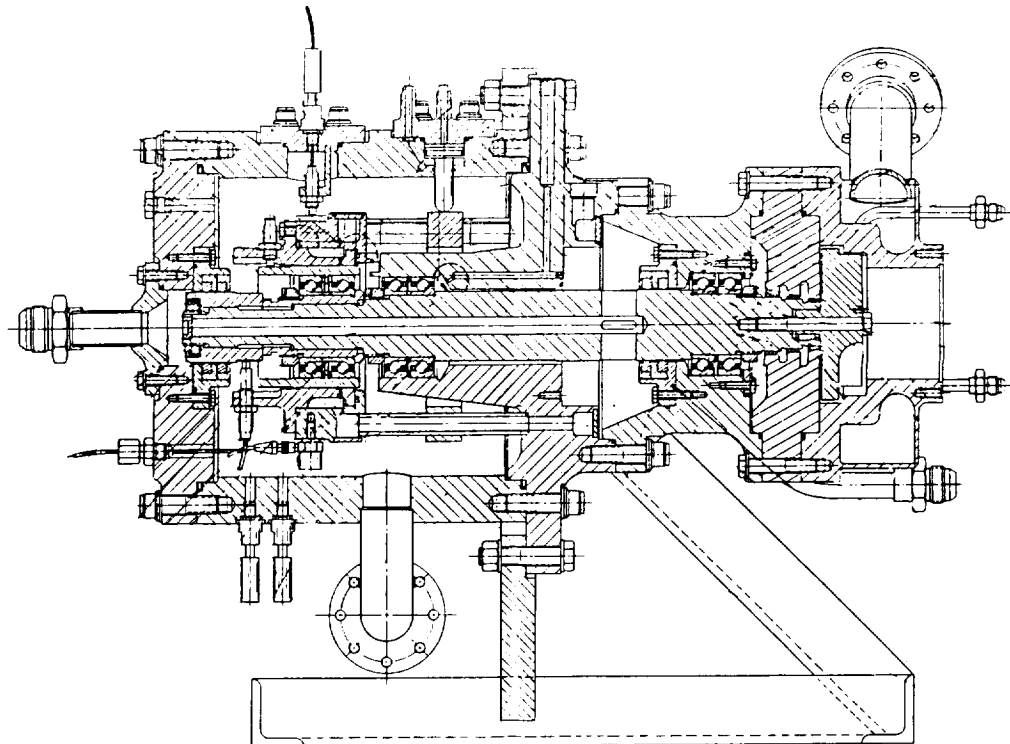


Fig. 2. Cross section of tester. Test element shown is a hybrid bearing with ball and hydrostatic bearings in series (not tested).

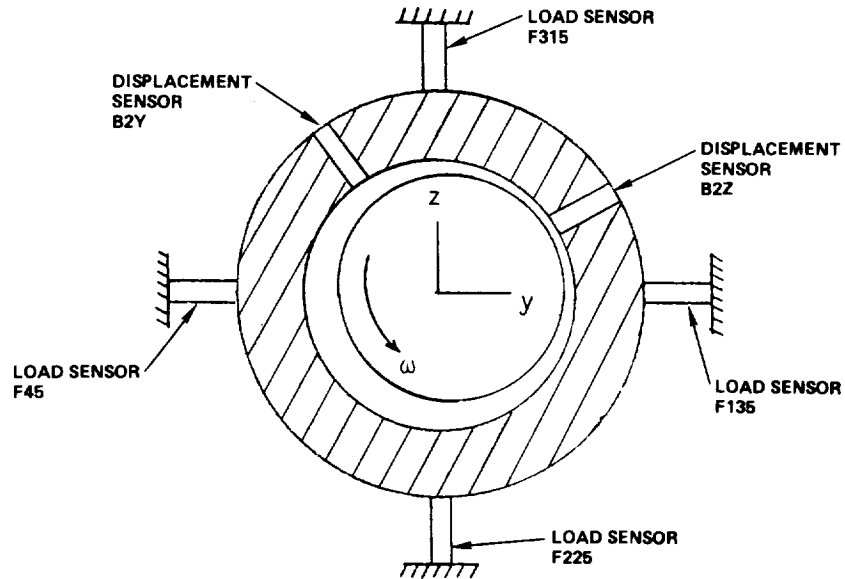


Fig. 3. Arrangement of load and displacement sensing devices. The stator is flexibly supported by four preloaded load sensors.

displacement probes will directly measure the desired relative deflection across the fluid film.

The stator element is supported by eight tubes (flexure arms), one of which is shown in Fig. 1. These tubes supply fluid to the externally fed test bearing. In addition to the stiffness of the flexure arms, the stator element is elastically constrained in the radial direction by two pair of preloaded, strain-gaged load cells (Fig. 1 and 2). The load cells were calibrated for load sensitivity and stiffness by applying known static loads directly to the stator at midplane of the test bearing. Under test conditions, the strain gage readings will then reflect the sum of the fluid film forces and the inertia force of the stator mass. As data reduction to rotordynamic coefficients requires the fluid film force by itself, the stator inertia force must be subtracted from the load cell readings. With the mass of the stator known, this is done as follows:

$$F_y = -\bar{F}_y + m_s (d^2/dt^2) (-\bar{F}_y/K_{sy}) \quad (1)$$

$$F_z = -\bar{F}_z + m_s (d^2/dt^2) (-\bar{F}_z/K_{sz}) \quad (2)$$

where

$\bar{F}_{y,z}$  = components of load cell reaction force acting on stator

$F_{y,z}$  = components of fluid film force acting on stator

$m_s$  = stator mass

$K_{sy, sz}$  = stator support stiffness, can be asymmetric

The technique of using strain gage load data to compute the inertia term was found equally effective to using stator mounted accelerometers, and was employed here since it involves processing fewer data channels.

The most general type of relative fluid film displacement orbits permissible in linear systems are elliptic in nature. Therefore, the goal of the measurement process is to identify the ellipse that describes the relative displacement as a function of time in the following form (relative = rotor - stator):

$$y(t) = a(\cos \omega t) + b(\sin \omega t) \quad (3)$$

$$z(t) = g(\cos \omega t) + h(\sin \omega t) \quad (4)$$

The four coefficients "abgh" are termed Fourier coefficients, and  $\omega$  is the tester speed in radians per second. They are obtained from the synchronous component of a complex frequency spectrum computed for each of the two displacements.

The same procedure is applied to the load data to obtain Fourier coefficients in the following form:

$$\bar{F}_y = \bar{m}(\cos \omega t) + \bar{n}(\sin \omega t) \quad (5)$$

$$\bar{F}_z = \bar{p}(\cos \omega t) + \bar{q}(\sin \omega t) \quad (6)$$

The equations correcting for stator inertia now become:

$$F_y = - [\bar{m}(\cos \omega t) + \bar{n}(\sin \omega t)] + (\bar{m}_s/K_{sy})(\bar{m} \omega^2(\cos \omega t) + \bar{n} \omega^2(\sin \omega t)) \quad (7)$$

$$F_z = - [\bar{p}(\cos \omega t) + \bar{q}(\sin \omega t)] + (\bar{m}_s/K_{sz})(\bar{p} \omega^2(\cos \omega t) + \bar{q} \omega^2(\sin \omega t)) \quad (8)$$

or

$$F_y = m(\cos \omega t) + n(\sin \omega t) \quad (9)$$

$$F_z = p(\cos \omega t) + q(\sin \omega t) \quad (10)$$

where

$$m = \bar{m}(-1 + (m_s \omega^2/K_{sy})), \text{ etc.}$$

mnpq = Fourier coefficients for fluid film force  
(acting on stator)

With the fluid film force and the displacement across the fluid film now specified as functions of time, rotordynamic coefficients can be computed. The generally accepted form for the relationship between these three sets of quantities is:

$$\begin{Bmatrix} F_y \\ F_z \end{Bmatrix} = \begin{bmatrix} K_{yy} & K_{yz} \\ K_{zy} & K_{zz} \end{bmatrix} \begin{Bmatrix} y \\ z \end{Bmatrix} + \begin{bmatrix} B_{yy} & B_{yz} \\ B_{zy} & B_{zz} \end{bmatrix} \begin{Bmatrix} \dot{y} \\ \dot{z} \end{Bmatrix} + \begin{bmatrix} M_{yy} & M_{yz} \\ M_{zy} & M_{zz} \end{bmatrix} \begin{Bmatrix} \ddot{y} \\ \ddot{z} \end{Bmatrix} \quad (11)$$

The displacements and forces were defined above using Fourier coefficients. The velocities and accelerations are obtained by differentiation with respect to time. There are several ways to approach the problem of identifying the 12 unknown rotordynamic coefficients. It should be noted that the measured force and displacement orbits will vary with tester rotational speed, and complete sets of Fourier coefficients can be made available for any rotational speed within the tester's speed range. Thus, one approach for computing the K's, B's and M's would be to rearrange the above matrix equation into the following alternate form (substituting in the Fourier coefficients):

$$\begin{bmatrix} -a\omega^2 & -g\omega^2 & b\omega & h\omega & a g & 0 & 0 & 0 & 0 & 0 & 0 \\ -b\omega^2 & -h\omega^2 & -a\omega & -g\omega & b h & 0 & 0 & 0 & 0 & 0 & 0 \\ 0 & 0 & 0 & 0 & 0 & -a\omega^2 & -g\omega^2 & b\omega & h\omega & a g & 0 \\ 0 & 0 & 0 & 0 & 0 & -b\omega^2 & -h\omega^2 & -a\omega & -g\omega & b h & 0 \end{bmatrix} \begin{Bmatrix} M_{yy} \\ M_{yz} \\ B_{yy} \\ B_{yz} \\ K_{yy} \\ K_{yz} \\ M_{zy} \\ M_{zz} \\ B_{zy} \\ B_{zz} \\ K_{zy} \\ K_{zz} \end{Bmatrix} = \begin{Bmatrix} m \\ n \\ p \\ q \end{Bmatrix} \quad (12)$$

The 12 rotordynamic coefficients are now the unknowns in this matrix equation, and the two equations of the former relation have each been resolved into  $\sin\omega t$  and  $\cos\omega t$  components. Since there are more unknowns than equations, one could use data from multiple values of tester speed, writing four equations for each. Data from three different speeds would yield 12 equations, and Gaussian elimination could be used to find the solution. Or, more than three speed points could be used, along with a least-squares equation solver, to find the

"best fit" coefficient solution. Neither of these approaches will prove successful, however, since the coefficient solution will not be unique. To circumvent this problem, the inertia coefficients must be eliminated from the list of unknowns. This yields the following:

$$\begin{bmatrix} b\omega & h\omega & a & g & 0 & 0 & 0 & 0 \\ -a\omega & -g\omega & b & h & 0 & 0 & 0 & 0 \\ 0 & 0 & 0 & 0 & b\omega & h\omega & a & g \\ 0 & 0 & 0 & 0 & -a\omega & -g\omega & b & h \end{bmatrix} \begin{pmatrix} B_{yy} \\ B_{yz} \\ K_{yy} \\ K_{yz} \\ B_{zy} \\ B_{zz} \\ K_{zy} \\ K_{zz} \end{pmatrix} = \begin{pmatrix} m \\ n \\ p \\ q \end{pmatrix} \quad (13)$$

Since data from multiple speed points must be used, it is necessary that the speeds span as wide a range as possible to give the best definition of the coefficients.

This type of coefficient solution yields one general asymmetric set of constant stiffness and damping coefficients to fit the given data. In practice, however, these coefficients could vary appreciably with speed. Efforts to expand the set of unknown coefficients to include speed dependent terms will once again be unsuccessful due to nonunique solutions. This occurs because a speed dependent set of skew-symmetric coefficients and a set of constant asymmetric coefficients can both be solutions for the same data.

For the type of fluid film element being measured here, the fluid inlet is made circumferentially uniform by using six equally spaced, identical hydrostatic pressure pockets, while the test bearing is centered in its clearance space with no applied static load. These conditions dictate that the rotordynamic coefficients will be skew-symmetric (i.e.,  $K_{yy} = K_{zz}$ ,  $K_{yz} = -K_{zy}$ , and similarly for B and M). This reduces the number of unknowns so that the matrix equation for rotordynamic coefficients becomes:

$$\begin{bmatrix} b & h & a & g \\ -a & -g & b & h \\ h & -b & g & -a \\ -g & a & h & -b \end{bmatrix} \begin{pmatrix} B_{yy} \omega \\ B_{yz} \omega \\ K_{yy} - M_{yy} \omega^2 \\ K_{yz} - M_{yz} \omega^2 \end{pmatrix} = \begin{pmatrix} m \\ n \\ p \\ q \end{pmatrix} \quad (14)$$

where

$\omega$  is the excitation frequency (rad/sec)  
 $\Omega$  is the shaft rotation frequency (rad/sec)  
 for all "synchronous only rigs"  $\omega = \Omega$  always and  
all coefficients are functions of  $\Omega$ .

Define:

$$K'_{yy} = K_{yy} - \Omega^2 M_{yy} \quad (15)$$

$$K'_{yz} = K_{zy} - \Omega^2 M_{yz} \quad (16)$$

Note that the two unknown inertia coefficients have been combined with the stiffness coefficients to form a combined pair of unknowns. This is necessary to ensure a unique solution to the matrix. Since there are now only four unknowns, the matrix solution can be carried out with data from only one speed point. Also, for convenience, the shaft speed has been placed in the unknown column vector instead of in the matrix elements.

The coefficients  $K_{yy}$ ,  $K_{yz}$ ,  $B_{yy}$ ,  $B_{yz}$ ,  $M_{yy}$ , and  $M_{zy}$  will, in general, vary with rotational speed  $\Omega$ , and since only linear model characteristics are desired, they do not vary with excitation frequency  $\omega$ . Tester data can be used with the above matrix to determine how  $K'_{yy}$ ,  $K'_{yz}$ ,  $B_{yy}$ , and  $B_{yz}$  vary with synchronous frequency  $\omega = \Omega$ . Note that the damping terms are completely separated from the stiffness terms without the need to vary tester speed. However, this requires that the fluid film displacement orbit be elliptic. If only circular orbits were possible, the above 4 by 4 matrix would become 2 by 2, and the stiffness and damping terms would need to be combined.

To show how such a separation is possible, and how effective this separation is, consider the displacement orbit shown in Fig. 4. Any displacement ellipse can be transformed into the ellipse of Fig. 4 without any loss in generality, and without altering the coefficient solution (a special result for the skew-symmetric coefficient arrangement). The same transformation is also enacted on the corresponding force ellipse. This transformation (in space and time) results in  $b = g = 0$  for the fluid film displacements, and establishes an easy solution for the unknown coefficients as follows:

$$B_{yy} \omega = -(an + hp)/(a^2 - h^2) \quad (17)$$

$$B_{yz} \omega = (aq - hm)/(a^2 - h^2) \quad (18)$$

$$K'_{yy} = (am - hq)/(a^2 - h^2) \quad (19)$$

$$K'_{yz} = -(ap - hn)/(a^2 - h^2) \quad (20)$$

It is now apparent that for a circular displacement orbit (i.e.,  $a = h$ ) the solution becomes undefined, and for a nearly circular orbit the solution is ill-defined. An adequate solution thus requires a sufficient amount of ellipticity in the displacement orbit.

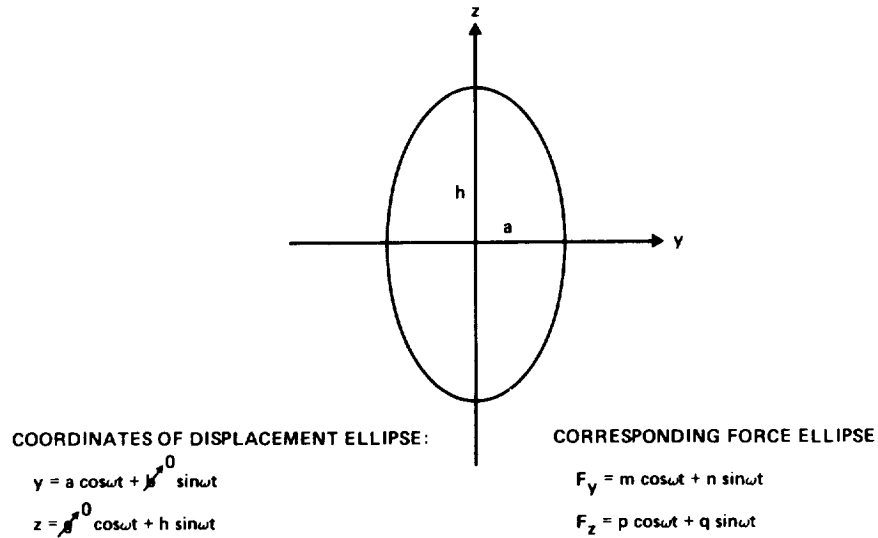


Fig. 4. Any displacement ellipse can be transformed through space and time into the above form without altering the skew-symmetric coefficient solution.

A further understanding of this is gained by rearranging the above solution into a slightly different form:

$$B_{yz} \omega + K'_{yy} = (m + q)/(a + h) \quad (21)$$

$$B_{yz} \omega + K'_{yy} = (m - q)/(a - h) \quad (22)$$

$$B_{yy} \omega + K'_{yz} = (p + n)/(-a + h) \quad (23)$$

$$B_{yy} \omega + K'_{yz} = (p - n)/(a + h) \quad (24)$$

In this "sum and difference form", half of the solution is well defined even for circular orbits, while the other half is not. Synchronous excitation test rigs specifically designed to deliver circular orbits (e.g., see Ref.2) can be used only to measure  $(B_{yz} \omega + K'_{yy})$  and  $(B_{yy} \omega - K'_{yz})$ . The remainder of the solution cannot be identified from circular orbits. The quantity  $(K'_{yy} + B_{yz} \omega)$  is often referred to as the net effective stiffness, and the quantity  $(B_{yy} \omega - K'_{yz})/\omega$  as the net effective damping.

An error analysis has been performed on the coefficient solution to quantify the sensitivity of the computed coefficients to experimental error as a function of the ellipticity ratio defined as follows:

$$\text{ellipticity ratio} = f = h/a \quad (25)$$

Small percentage changes in the data become excessively magnified during solution when  $f$  approaches one (i.e., when the displacement

orbit approaches a circle). As a function of  $f$ , this error magnification is approximated as follows:

$$\text{error magnification} = (f/2)/(1 - f) \quad (26)$$

Figure 5 shows this magnification plotted versus  $f$ . For the work reported here,  $f$  was required to be outside the range  $0.87 < f < 1.175$  so the magnification would be less than 3.5. When  $f$  is outside this range, stiffness and damping constants can be separated and quoted along with the net effective values. When  $f$  is inside this range, only the net effective stiffness and damping values can be obtained. With the test apparatus used here, the stator elastic support was made intentionally asymmetric,  $K_{sy} \neq K_{sz}$ , in order to generate the required ellipticity.

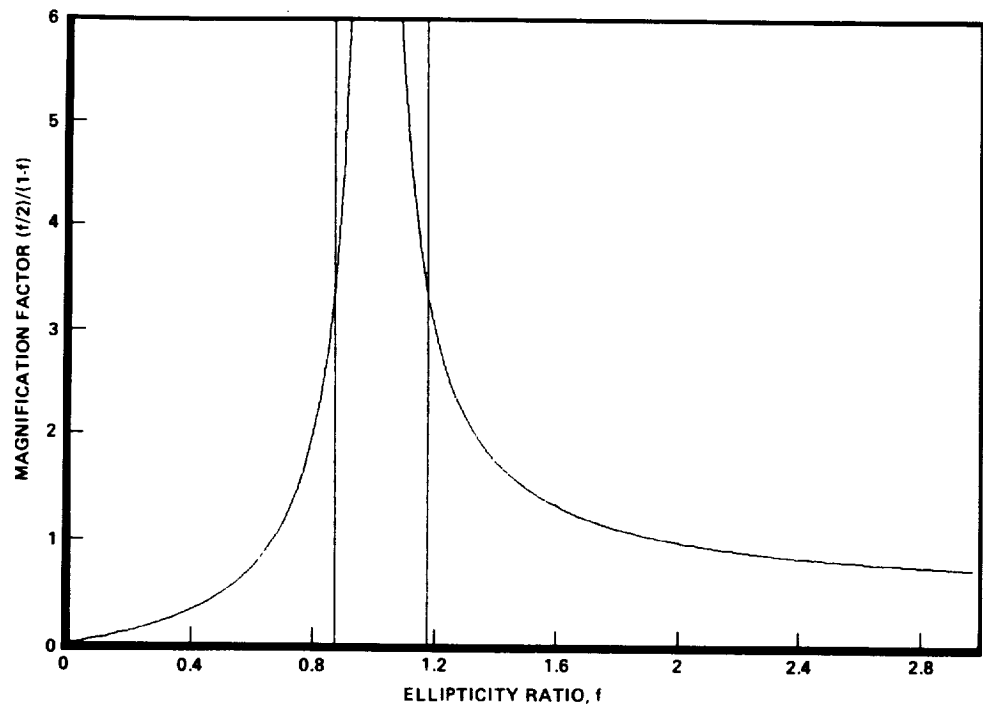


Fig. 5. Measurement error magnification factor for computed rotordynamic coefficients versus the relative displacement ellipticity ratio.

#### Testing Procedure

During data acquisition, the bearing supply pressure was held constant while the rotational speed was slowly ramped across the desired speed range at a rate of 3.3 to 8.3 Hz/sec (200 to 500 rpm/sec). The speed range of the tester operating in Freon was 0 to 378 Hz (22,700 rpm). The duration of any one test was limited to approximately 1 minute by the capacity of the Freon tank.



Analog data was stored on FM tape, and then digitized and downloaded to a minicomputer. Complex frequency spectrums were then computed for each channel to provide the synchronous Fourier coefficients described earlier. The frequency analysis was performed all along the speed ramp, essentially providing a sequence of snapshots at discrete values of tester speed.

After correcting for stator inertia, the data was then ready for use in computing rotordynamic coefficients via the matrix analysis methods previously described. Test results are obtained directly from the output of this program.

### Test Results

Testing was performed using Freon 113 at ambient temperature as the working fluid. Both an externally fed and an internally fed bearing configuration was tested (Fig. 6 and 7). The dimensions of each configuration appear in Table 1.

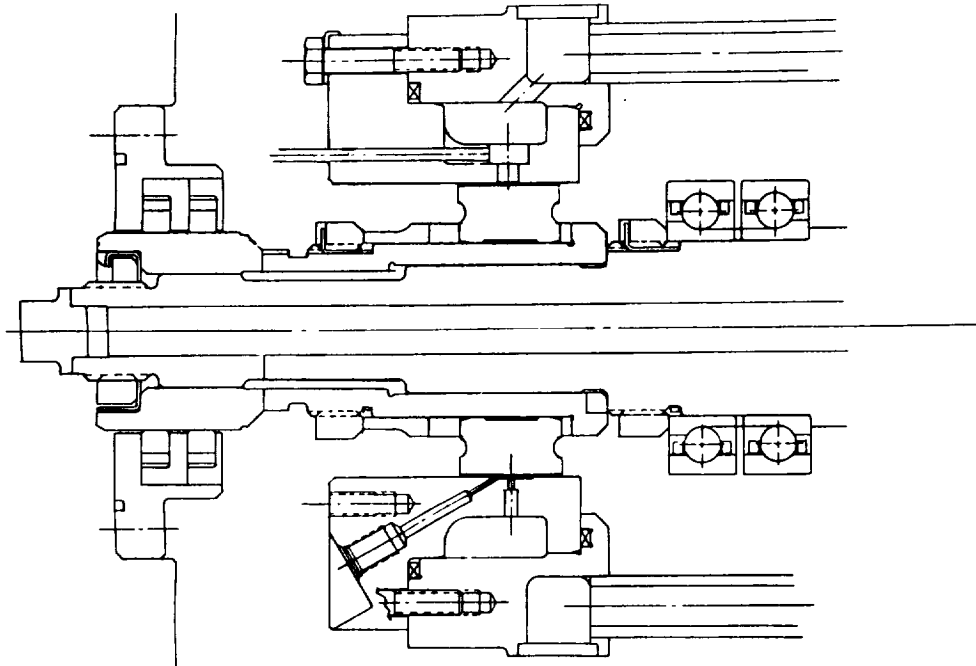


Fig. 6. Cross section of externally fed bearing. Freon flows right to left through flexure arms, and into stationary manifold.

To date, two successful tests have been conducted for both the externally fed and internally fed bearing. The externally fed bearing tests were done with bearing inlet pressures of 3.4 and 10.3 MPa (500 and 1500 psi). The internally fed bearing tests had the same 10.3 MPa (1500 psi) inlet pressure, but the first test produced insufficient

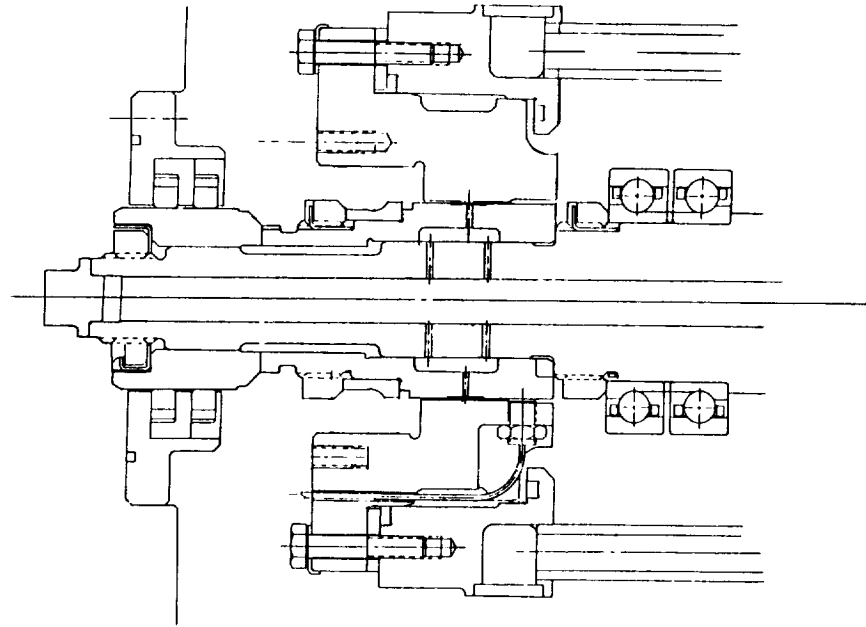


Fig. 7. Cross section of internally fed bearing. Freon flows right to left through hollow shaft, and outward into rotating manifold.

Table 1. Externally and Internally Fed Hydrostatic Bearing Design Description

ITEM		INTERNALLY FED	EXTERNALLY FED
BEARING BORE		54.61 mm	75.04 mm
BEARING LENGTH		25.4	25.4
RADIAL CLEARANCE		.0432	.0670
ORIFICE DIAMETER		1.333	1.270
ORIFICE LENGTH		6.73	1.80
RECESS DESCRIPTION	WIDTH (CIRCUM)	8.18	11.41
	LENGTH (AXIAL)	8.90	8.89
	DEPTH	.2032	.2286
	SURFACE RECESSED	JOURNAL	BEARING
	NUMBER OF RECESSES	6	6
	NUMBER OF ROWS	1	1
	AREA RATIO	.10	.10

ellipticity to permit separation of stiffness from damping via Eq. (14). For this reason, the second test of the internally fed bearing was conducted with two load cells replaced by eddy current displacement probes (F135 and F315 in Fig. 3). The load in that axis was identified by applying the stator displacement measured by the replacement probes to the measured stiffness of the flexure arms (shown in Fig. 1 and 2). This increased the stator support stiffness asymmetry ratio from 1.88 with four load cells to 4.48 with two load cells. The increased support asymmetry resulted in sufficient ellipticity for the latter test of the internally fed bearing.

### Externally Fed Bearing

The ellipticity ratio and the computed set of skew-symmetric rotordynamic coefficients are shown for both upramp and downramp in Fig. 8 through 10 for the externally fed bearing operating with an inlet pressure of 10.3 MPa (1500 psi), see Table 2. Also shown in the figures are the predicted values for these coefficients obtained numerically with the computer program HBEAR described in Ref.3. The ellipticity ratio is seen to satisfy the criteria of being greater than 1.175. Thus, separated stiffness and damping terms can be obtained. All measured coefficients exhibit the same trends versus speed as the predicted coefficients. The measured direct stiffness values

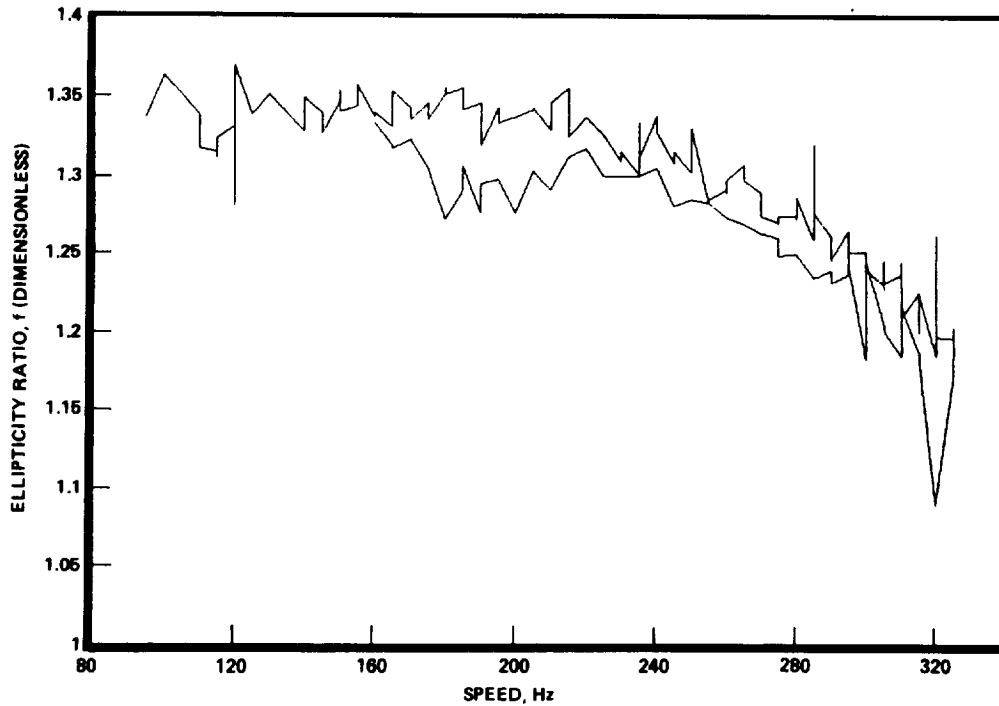


Fig. 8. Displacement orbit ellipticity ratio for the externally fed bearing at 10.3 MPa (test 10).

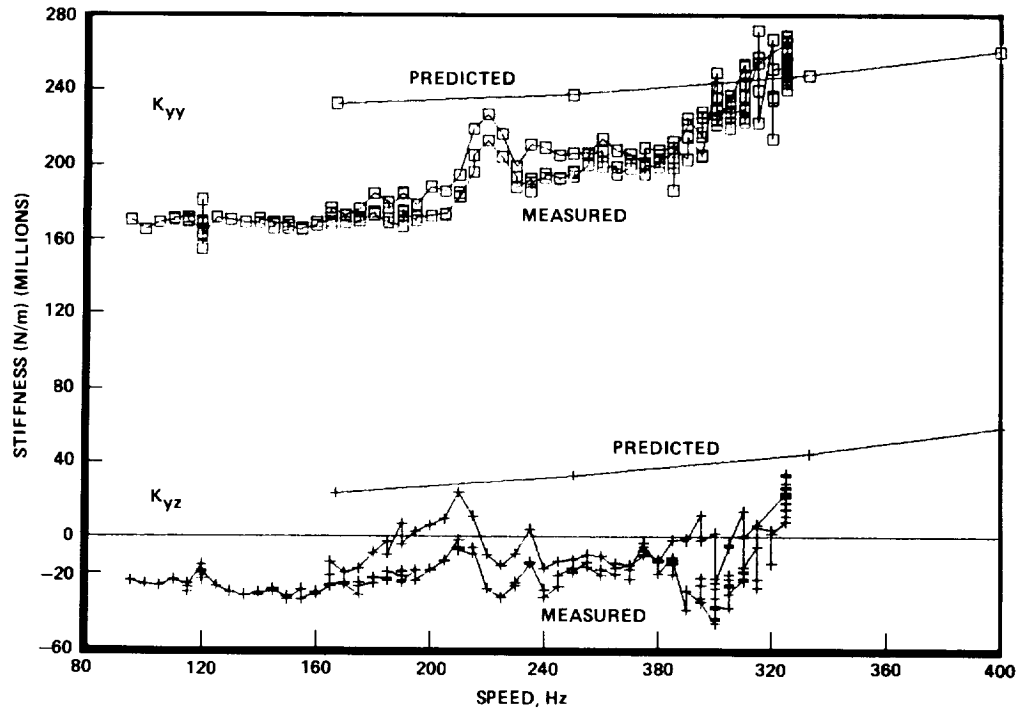


Fig. 9. Measured and predicted direct and cross-coupled stiffness coefficients for the externally fed bearing at 10.3 MPa (test 10).

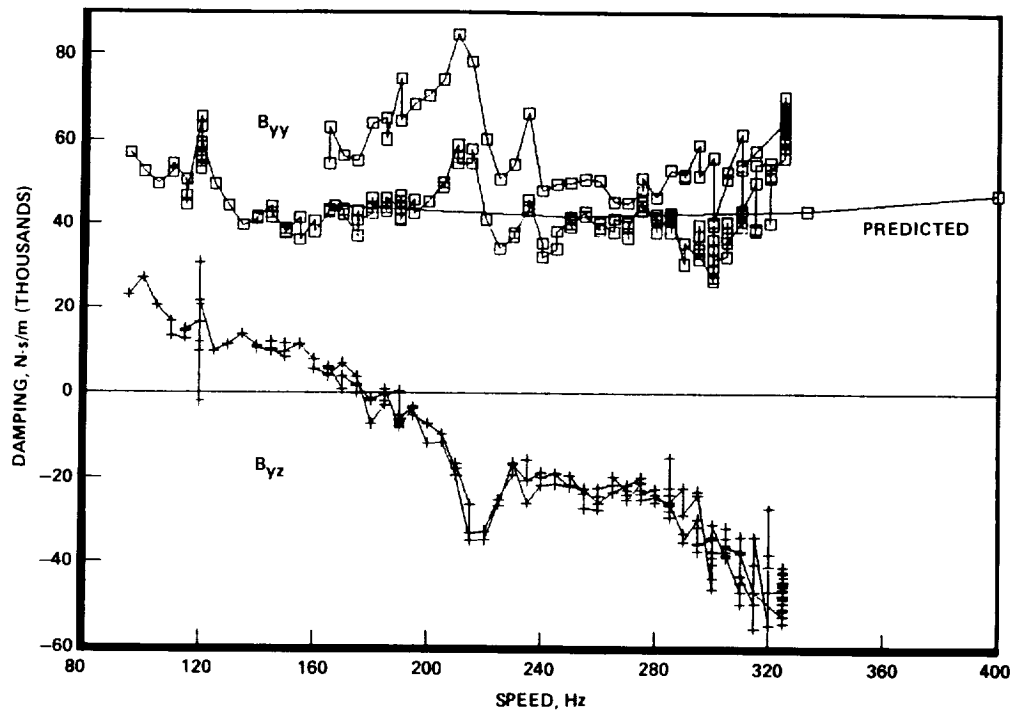


Fig. 10. Measured and Predicted direct and cross-coupled damping coefficients for externally fed bearing at 10.3 MPa (test 10).

Table 2. Hydrostatic Bearing Test Descriptions

TEST NO. ITEM	8	10	28	31
BEARING TYPE	EXTERNAL	EXTERNAL	INTERNAL	INTERNAL
INLET PRESSURE	3.4 MPa	10.3	10.3	10.3
RADIAL CLEARANCE	.0432 mm	.0432	.067	.067
ECCENTRICITY	.0064 mm	.0064	.022	.022
TEMPERATURE	309 K	312	296	295
DENSITY	1540 kg/m <sup>3</sup>	1516	1579	1583
FLOW RATE	.39 kg/s	.61	.48	.47
VISCOSITY	.593 cp	.571	.708	.712
LOAD CELLS USED	4	4	4	2
K <sub>sy</sub> /K <sub>sz</sub>	1.88	1.88	1.88	4.48
f > 1.175	YES	YES	NO	YES

are about 20% less than predicted, and the measured direct damping values are roughly equal to the predicted values. The measured cross-coupled stiffness is less than predicted, and is actually a stabilizing influence at low speed where  $K_{yz} < 0$ .

The analytical code does not predict cross-coupled damping, where as the test measurements show what appears to be a significant amount of cross-coupled damping. It should be noted that one effect of cross-coupled damping is to either add to, or detract from, the apparent amount of asymmetry in the direct stiffness. The coefficient reduction method employed here assumes symmetric direct stiffness. One way asymmetry in the direct stiffness can manifest itself is by the prediction of nonzero cross-coupled damping coefficients. In this particular case, roughly 17.5 MN/m (100,000 lb/in.) of asymmetry could produce the type of cross-coupled damping coefficients shown.

Since neither of the stiffness curves show a strong variation with speed squared, it is concluded that the bearing does not possess a significant inertia effect over this speed range.

Orbit ellipticity makes it possible to separate the stiffness from damping. If the orbits were too nearly circular, only net effective stiffness and damping defined by Eq. (21) and (24) could be determined. Figures 11 and 12 show a comparison of the measured and predicted net effective stiffness and damping values for the bearing of Fig. 8 through 10. For use in analytical rotordynamic models, net effective values will suffice for performing unbalance response studies of symmetrically supported rotors, but they are less than adequate for performing rotordynamic stability studies, or for unbalance studies of asymmetrically supported rotors.

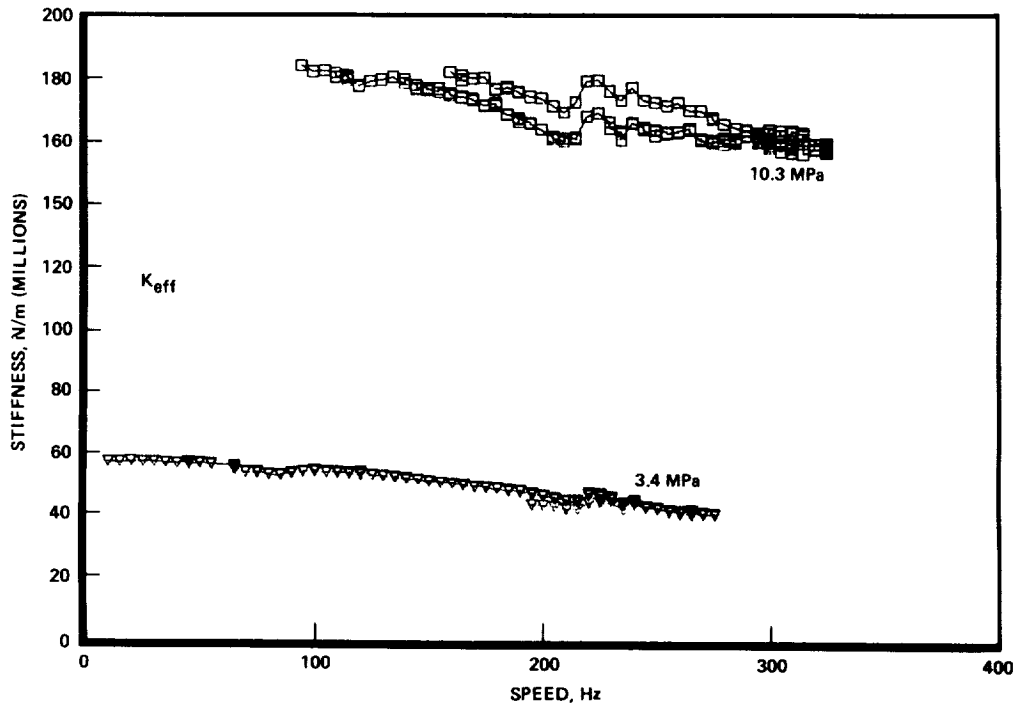


Fig. 11. Comparison of measured net effectiveness stiffness for externally fed bearing with low and high inlet pressure (tests 8 and 10).

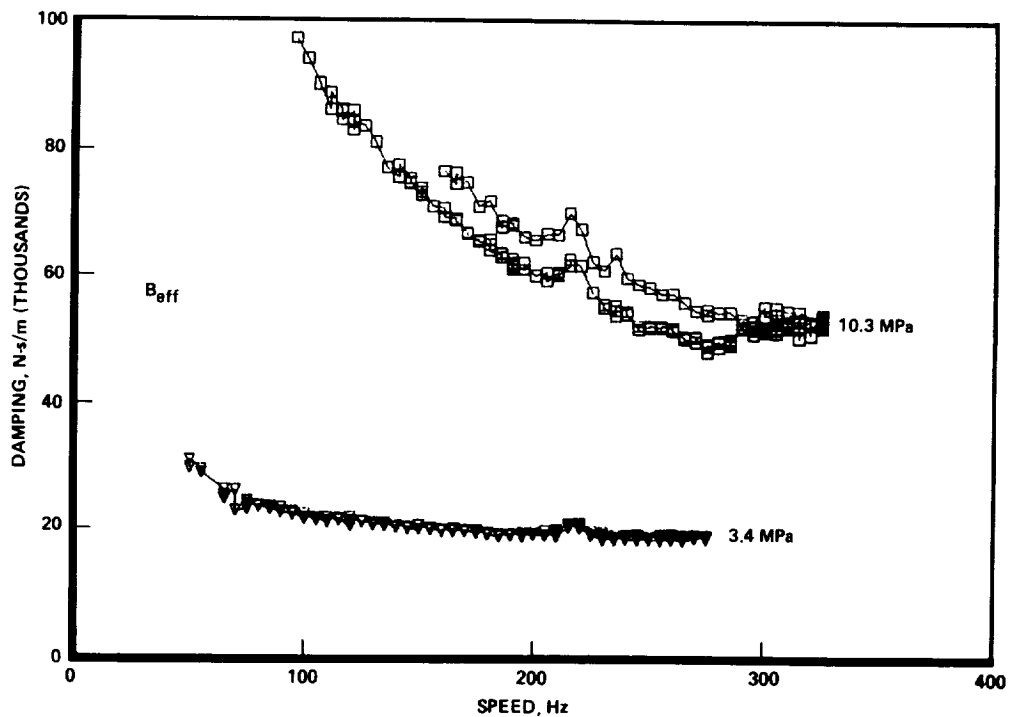


Fig. 12. Comparison of measured net effective damping for externally fed bearing with low and high inlet pressure (tests 8 and 10).

The bearing of Fig. 8 through 12 was tested with a bearing inlet pressure of 10.3 MPa (1500 psi). The same bearing was tested with an inlet pressure of 3.4 MPa (500 psi). Figures 13 through 15 show the ellipticity ratio and comparisons of measured and predicted stiffness and damping. The data are similar to the data for 10.3 MPa except for the correspondingly lower magnitudes due to the lower inlet pressure. Also, agreement with the predictions is not as close as for the higher pressure. Figures 11 and 12 directly compare the net effective values and show them to be very nearly proportional to inlet pressure.

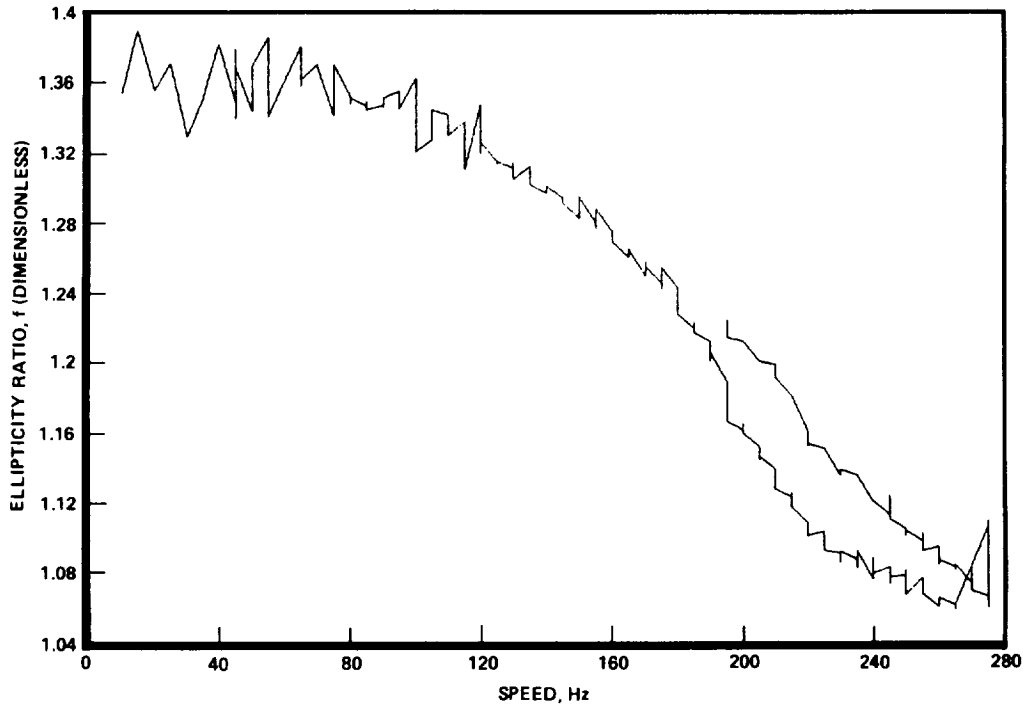


Fig. 13. Displacement orbit ellipticity ratio for externally fed bearing at 3.4 MPa (test 8).

In Fig. 13, note that as tester speed surpasses 200 Hz, the ellipticity ratio falls below the 1.175 criteria for separable data. As this occurs, the curves for the separated coefficients become more erratic (Fig. 14 and 15). Also note that the net effective values of Fig. 11 and 12 should not, and are not, affected by the orbit becoming too circular.

#### Internally Fed Bearing

In the first test of the internally fed bearing the ellipticity ratio was extremely close to 1, and thus only net effective values can be quoted. The cause for small ellipticity is that the internally fed bearing produces a much lower overall stiffness than the externally

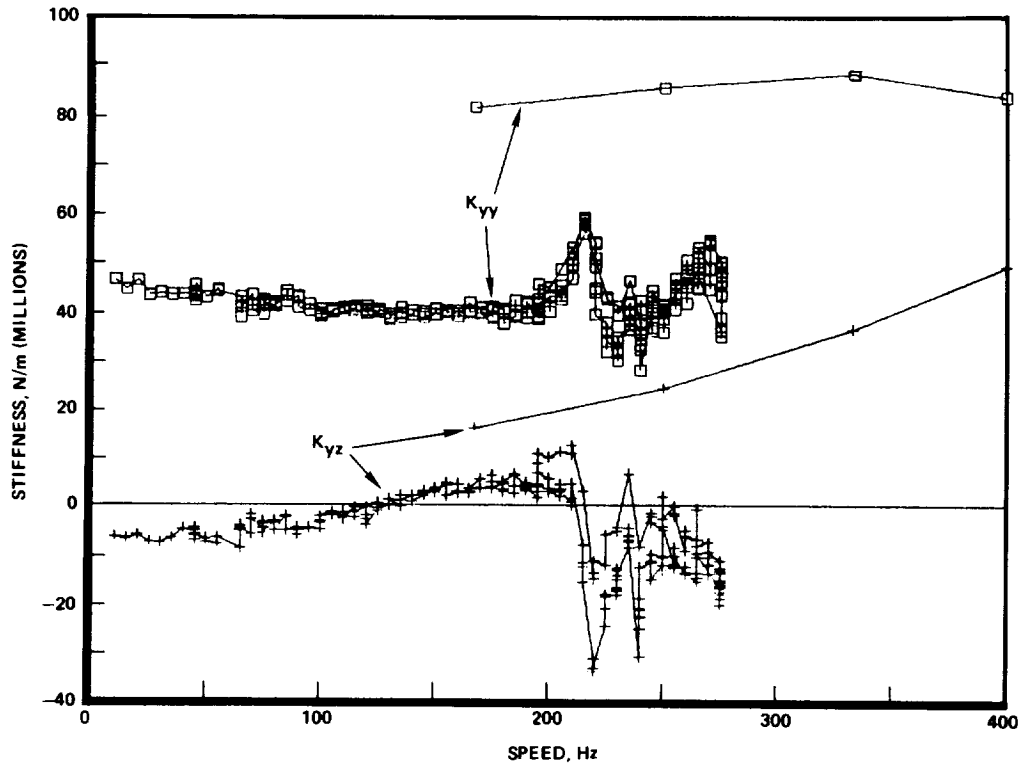


Fig. 14. Measured and predicted direct and cross-coupled stiffness for externally fed bearing at 3.4 MPa (test 8).

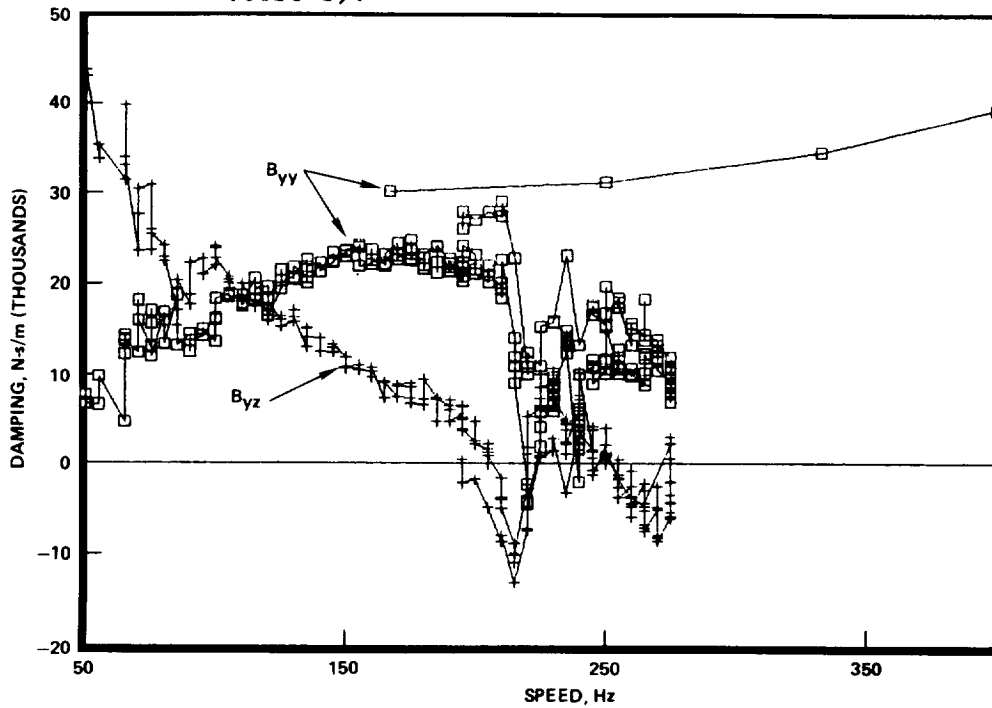


Fig. 15. Measured and predicted direct and cross-coupled damping for externally fed bearing at 3.4 MPa (test 8).



fed bearing, and thus generated less motion of the asymmetrically supported stator. It is forced motion of the stator that causes the relative orbits to be elliptic. Figures 16 through 18 show the ellipticity ratio and the measured and predicted net effective stiffness and damping for this test. The noted differences between predictions and measurements are qualitatively the same as the differences noted for the externally fed bearing. The net effective stiffness was overpredicted by 100 to 150% versus about 20% for the externally fed bearing. The net effective damping was both predicted and measured to be very small, and was underpredicted as it was for the externally fed bearing. Meaningful percentage differences cannot be quoted in this case as the measured and predicted values are of opposite sign.

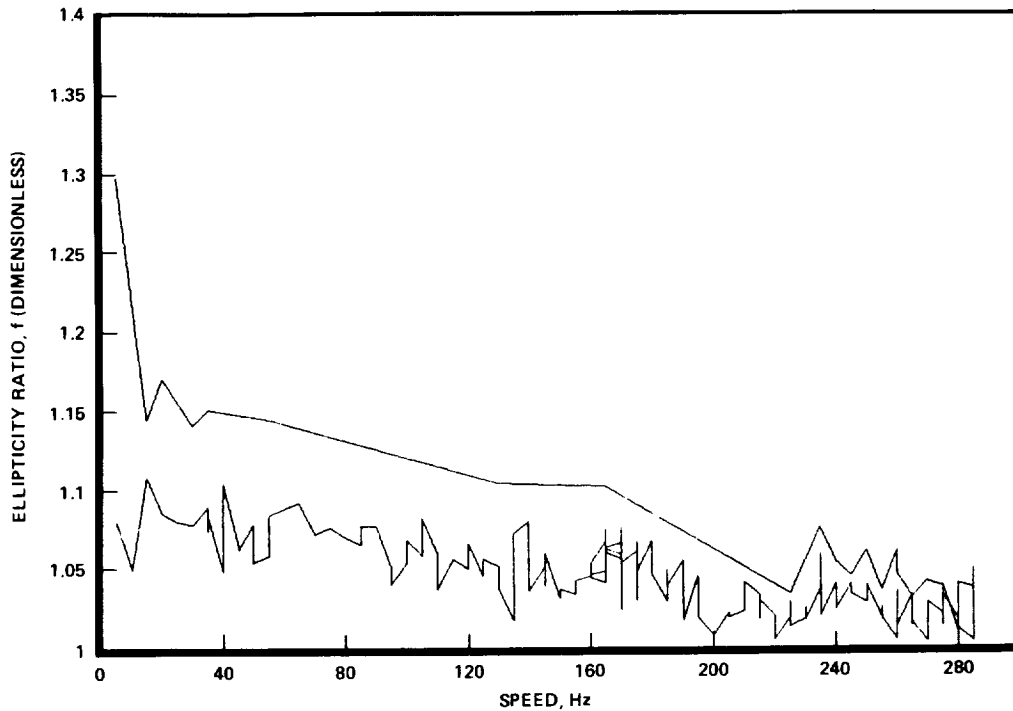


Fig. 16. Displacement orbit ellipticity ratio for internally fed bearing (test 28).

Figures 19 through 21 show the ellipticity ratio and all measured and predicted coefficients for the test of the internally fed bearing with two load cells removed. The separated stiffness and damping coefficients do not exhibit the qualitative agreement with predictions that the externally fed bearing shows. The measured and predicted direct stiffness actually agree quite well in magnitude near 220 Hz (13,200 rpm) shaft speed, but the measurements show a major speed dependency contrary to predictions. The direct damping was measured to be negative at low speed, and it also shows a major speed dependency not predicted.

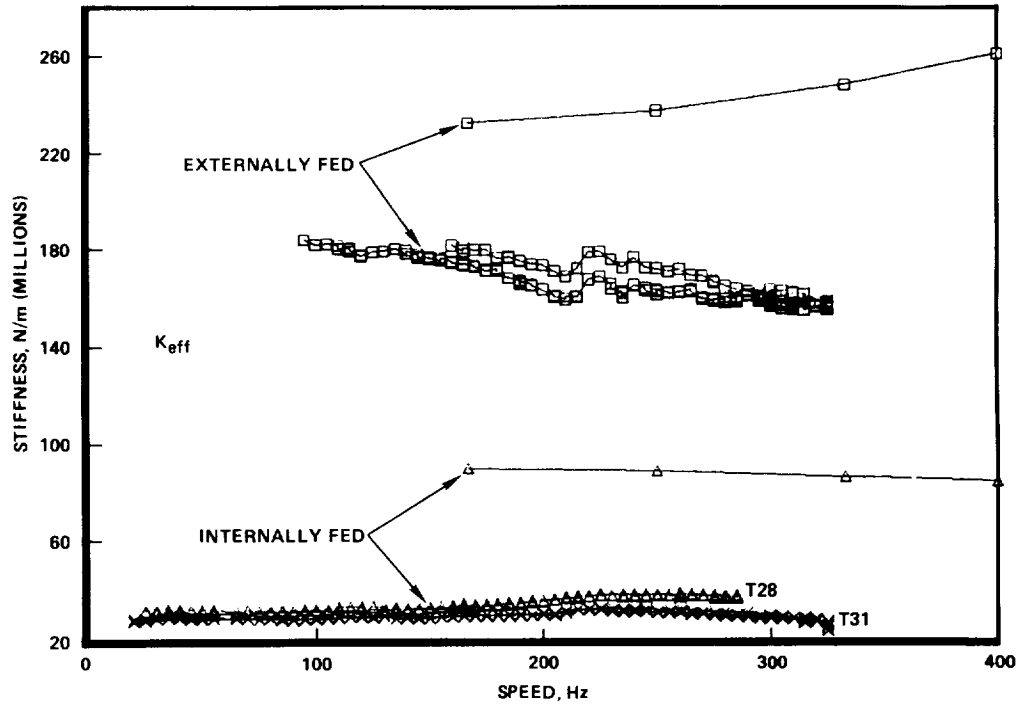


Fig. 17. Comparison of net effective stiffness for externally fed bearing (test 10) and internally fed bearing (tests 28 and 31).

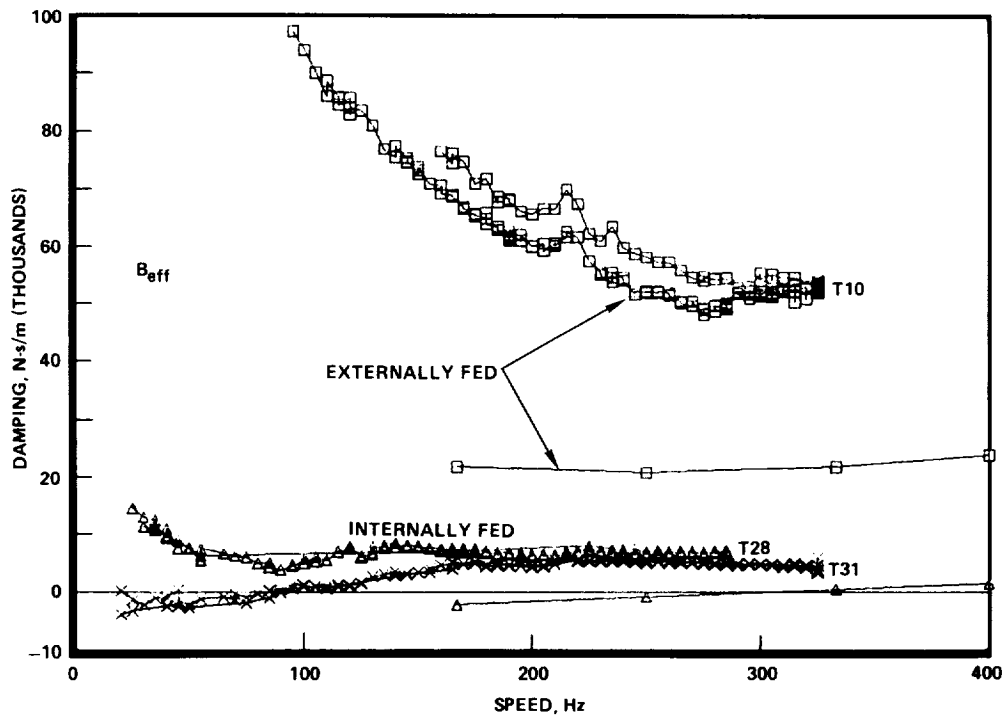


Fig. 18. Comparison of net effective damping for externally fed bearing (test 10) and internally fed bearing (tests 28 and 31).

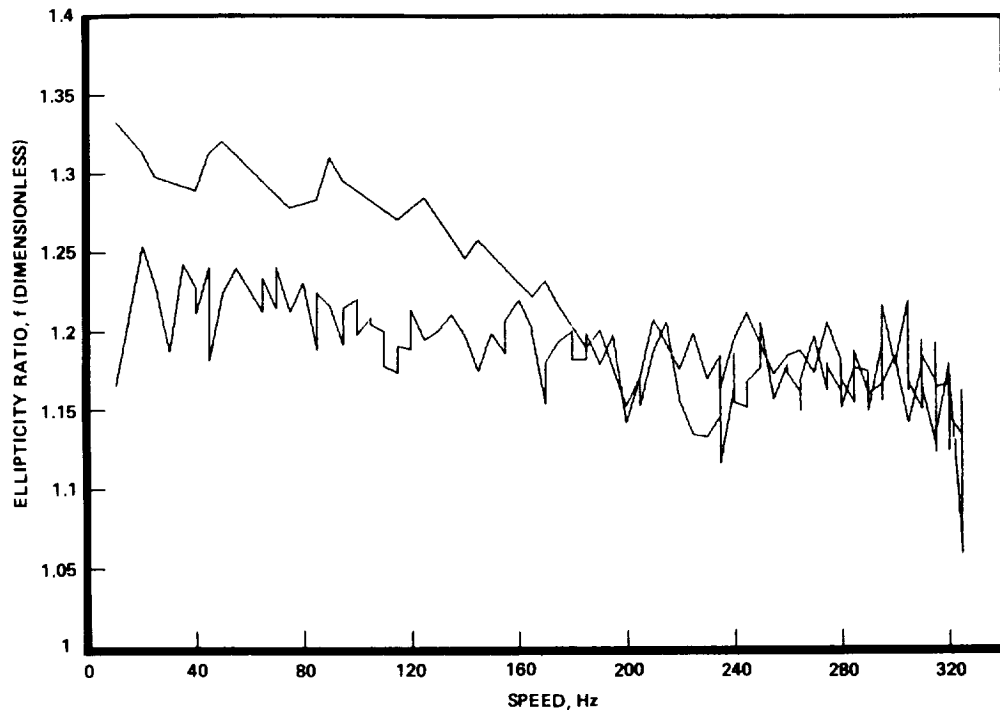


Fig. 19. Displacement orbit ellipticity ratio for internally fed bearing with two load cells (test 31).

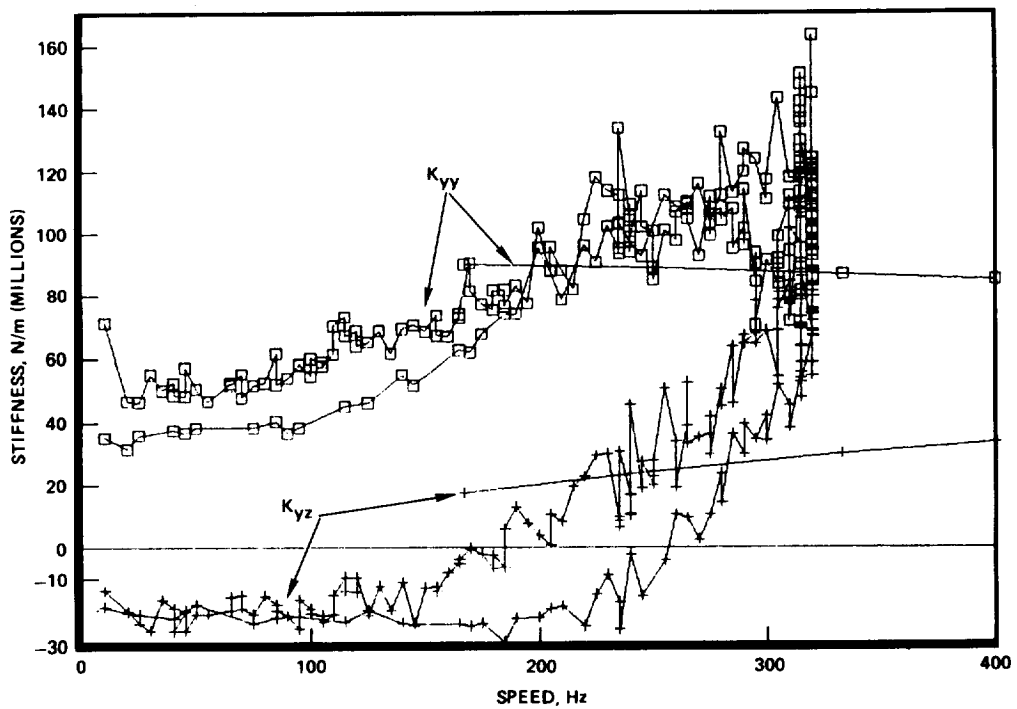


Fig. 20. Measured and predicted direct and cross-coupled stiffness coefficients for internally fed bearing with two load cells (test 31).

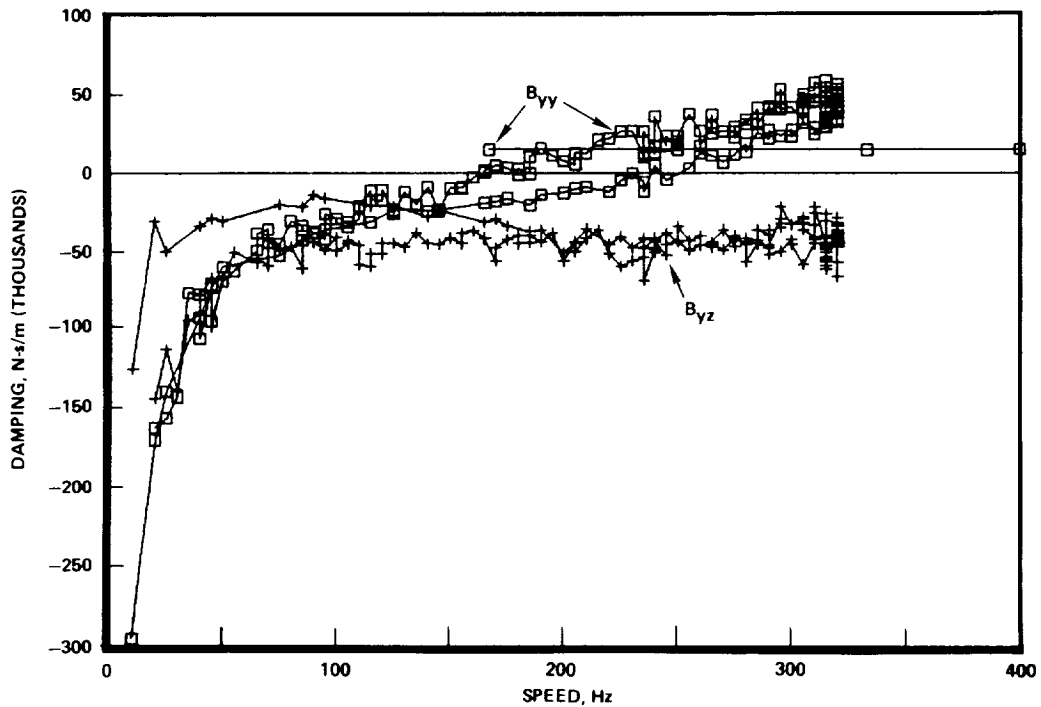


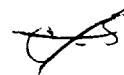
Fig. 21. Measured and predicted direct and cross-coupled damping coefficients for internally fed bearing with two load cells (test 31).

The net effective stiffness and damping values for this test compare favorably to those of the other internally fed bearing test, and had consistent correlation with theory.

Two potential causes exist for the prominent speed dependency exhibited in the skew-symmetric coefficients by the internally fed bearing:

1. The effect of fluid tangential velocity induced by the rotating recesses may have more influence than predicted by the analysis.
2. Although feeler-gage checks of the test bearing clearance indicated that the bearing was centered within 0.0076 mm (0.0003 inch), misalignment of the stator with the shaft centerline will result in speed dependency for the skew-symmetric coefficients.

The data reduction process of Eq. (14) assumes the rotordynamic coefficients to be skew-symmetric. If, in fact, they are not skew-symmetric, this condition can manifest itself in the data reduction process by causing the calculated skew-symmetric coefficients to vary with speed.



### Speed Dependency vs Asymmetry

If the data of the second internally fed bearing test are reduced according to the asymmetric method of Eq. 13, the following set of stiffness and damping values are produced:

$$\begin{bmatrix} K_{yy} & K_{yz} \\ K_{zy} & K_{zz} \end{bmatrix} = \begin{bmatrix} 22.3 & 2.9 \\ -2.9 & 34.6 \end{bmatrix} \text{ MN/m}$$

$$\begin{bmatrix} B_{yy} & B_{yz} \\ B_{zy} & B_{zz} \end{bmatrix} = \begin{bmatrix} -0.96 & 2.13 \\ -0.62 & 13.0 \end{bmatrix} \text{ kN-s/m}$$

These values are dependent on the arbitrary orientation of the yz coordinate system. Stiffness and damping values computed for the yz coordinate system of Fig. 3 have been rotated to make the cross-coupled stiffness values of equal magnitude and opposite sign. In this case the required rotation is 28 degrees counterclockwise. The resulting direct stiffness values are different by a factor of 1.55, and the direct damping values are different by a factor of 13.5, and are of opposite sign.

The same procedure applied to the 10.3 MPa (1500 psi) externally fed bearing test results in:

$$\begin{bmatrix} K_{yy} & K_{yz} \\ K_{zy} & K_{zz} \end{bmatrix} = \begin{bmatrix} 211 & 46 \\ -46 & 174 \end{bmatrix} \text{ MN/m}$$

$$\begin{bmatrix} B_{yy} & B_{yz} \\ B_{zy} & B_{zz} \end{bmatrix} = \begin{bmatrix} 20.5 & 30.4 \\ -0.98 & 32.0 \end{bmatrix} \text{ kN-s/m}$$

Asymmetry in the direct stiffness and damping is much less pronounced in this case with ratios of only 1.2 and 1.6 respectively. Both reduction methods applied to both tests result in stiffness and damping values which produce excellent correlation between the measured forces and displacements. Choosing between the two methods involves choosing between general asymmetry and speed dependency for the rotordynamic coefficients. One set of coefficients contains asymmetry, but is constant versus speed. The other set assumes skew-symmetry, but yields a direct measure of speed dependency. The choice must be dictated by which condition is expected to be most significant.

The predicted coefficients according to Ref. 3 are, in all cases, skew-symmetric and vary with speed. Figures 9 and 10 show that the measured speed dependency parallels the predicted speed dependency for the 10.3 MPa (1500 psi) externally fed bearing. The asymmetric coefficient set for this test also exhibits direct stiffness and damping which are very close in the y and z directions. Figures 20 and 21 for the internally fed bearing, however, show a dramatic difference between measured and predicted speed dependency for skew-symmetric coefficients. Also, the asymmetric coefficient set for this test shows large differences in the direct stiffness and damping.

Thus for the internally fed bearing, either the coefficients are approximately skew-symmetric and the measured speed dependency is real, or the coefficients are in reality asymmetric and the measured speed dependency in the skew-symmetric coefficients is part real and part due to asymmetry.

The only plausible source of significant coefficient asymmetry is static miscentering of the stator about the bearing journal. The feeler-gage checks already mentioned indicated that the bearing was centered within 12% of the clearance. Analysis of generic fluid film components has shown that miscentering must be as much as 40% of the clearance to produce significant asymmetry. Thus, the internally fed hydrostatic bearing may be more sensitive to miscentering than other types of fluid film elements.

### Conclusions

Figures 17 and 18 show the net effective stiffness and damping for the three tests run at a common bearing supply pressure of 10.3 MPa (1500 psi). The internally fed bearing was physically smaller than the externally fed bearing, and also had larger clearance. Both these differences, which tend to lower the stiffness and damping, are accounted for in the predicted values. The most important aspects of a direct comparison of the internally versus externally fed configurations are as follows:

1. Both configurations had measured net effective stiffness values which were lower than predicted, but the externally fed bearing was only 20 to 25% lower whereas the internally fed bearing was 60% lower.
2. Both configurations had net effective damping values which were higher than predicted. The externally fed bearing was predicted, and shown, to have significant direct damping. The internally fed bearing analysis predicted low damping, and the bearing was subsequently shown to have practically neutral net effective damping.

The poor net effective damping qualities of the internally fed bearing are likely due to the fluid swirl condition. This condition results from the fact that the pressure pockets are rotating with the shaft. Fluid enters the bearing through holes in the pressure pocket recesses, and thus immediately has the full tangential velocity of the journal surface. Circumferential flow of this nature is known to have a detrimental effect on net effective damping. The damping performance of the internally fed bearing may be significantly enhanced by providing some type of circumferential flow attenuating device, or by giving the stator increased surface roughness, or both.

#### References

1. Goodwin, M. J., J. E. T. Penny, and C. J. Hooke, "Hydrostatic Supports for Rotating Machinery - Some Aspects of Oil Film Non-Linearity," American Society of Mechanical Engineers, Paper No. 85-DET-123, September 1985.
2. Childs, D. W. and C. H. Kim, "Analysis and Testing for Rotor-dynamic Coefficients of Turbulent Annular Seals with Different, Directionally Homogeneous Surface-Roughness Treatment for Rotor and Stator Elements," NASA Conference Publication 2338, Proceedings of the Workshop on Rotordynamic Instability Problems in High-Performance Turbomachinery, Texas A&M University, 28-30 May 1982.
3. Artiles, A., J. Wallowitz, and W. Shapiro, "Analysis of Hybrid, Fluid Film Journal Bearings with Turbulence and Inertia Effects. Advances in Computer-Aided Bearing Design," Proceedings of ASME-ASLE Lubrication Conference, American Society of Lubrication Engineers, New York, New York, October 1982.

SURFACE MODIFICATION FOR WEAR RESISTANCE IN A  
LIQUID OXYGEN TURBOPUMP ENVIRONMENT

Lillian Ng

Rockwell International/Rocketdyne Division  
Canoga Park, California

Yngve Naerheim

Rockwell International/Science Center  
Thousand Oaks, CaliforniaAbstract

Bearing elements for the Space Shuttle Main Engine oxidizer turbopumps operate in the low viscosity environments of liquid oxygen, which results in an operating condition of poor lubrication. High transient axial loads and high coefficient of friction due to lack of lubricant in the high pressure oxidizer turbopump bearings has resulted in surface wear. Hard coatings have been utilized to lower the coefficient of friction and increase the wear resistance of steels. In this study, three bearing alloys (AMS 5618 (VIM-VAR), AMS 5900, and AMS 6491) were coated with TiN or thin-dense Cr for evaluating the effects of surface modification on wear. Testing was performed in a cone-three-ball tester modified to provide both rolling and sliding friction that simulates operating conditions. Also, a liquid oxygen environment was used to simulate the operating environment. Test results including detailed Scanning Electron Microscopy (SEM), Electron Spectroscopy for Chemical Analysis (ESCA), and optical analysis will be presented.

Introduction

The liquid hydrogen (LH<sub>2</sub>) fuel and liquid oxygen (LO<sub>2</sub>) oxidizer for the Space Shuttle Main Engine (SSME) is provided by low and high pressure turbopumps. The low-viscosity cryogenic liquids that are very poor lubricants flow through the rolling element bearings of the turbopumps. Although solid lubricants in the bearing cage provide some lubrication early in the bearing life, these bearings operate essentially in an unlubricated condition. The High Pressure Oxidizer Turbopump (HPOTP) operates at 30,000 rpm and has a design operational life of 27,000 seconds (7.5 hours) or 50 missions. However, the bearings can begin to wear after operating periods of a few thousand seconds. Advanced turbopump bearings, which will operate at 110,000 rpm, will present an even more rigorous materials challenge.



Since the bearings must have good corrosion resistance, the normally used high-speed bearing materials based on tool steels (i.e., AMS 6444, AMS 6491) cannot be used. Stainless steel bearing alloys such as AMS 5618 (VIM-VAR) and AMS 5749 have inferior wear and fatigue properties when compared to AMS 6491.

The objectives of this study were to (1) design a tester for evaluating HPOTP bearing wear in a cryogenic service environment, (2) determine the necessity for testing in LO<sub>2</sub>, and (3) extend the life of the HPOTP bearings by choosing materials or coatings having better inherent wear resistance than AMS 5618 (VIM-VAR).

The three bearing materials chosen for the study were AMS 5618 (VIM-VAR), AMS 5900, and AMS 6491. AMS 5618 (VIM-VAR) is currently being used in the SSME bearings. It was chosen for its high strength, high hardness (Rc58-62) and corrosion resistance. AMS 5900 is also a stainless steel with compositions almost identical to AMS 6491 except for the amount of chromium (Table 1). AMS 5900 combines the tempering, hot hardness and hardness characteristics of AMS 6491 steel with the corrosion and oxidation resistance of AMS 5618 (VIM-VAR). It can also attain a higher hardness (Rc61-64) than AMS 5618 (VIM-VAR), which indicates higher strength and wear resistance. AMS 6491 is a tool grade steel commonly used for aircraft gas turbine engine bearings. This alloy has proven good wear properties and good fatigue life. However, due to a low chromium content, there is little corrosion resistance.

Table 1. Chemical Composition of Materials (Wt%)

ELEMENT ALLOY	C	Mn	Si	Cr	Mo	V	Ni	Fe
AMS 5618 (VIM-VAR)	0.95-1.20	1.00	1.00	17.00	0.50	—	0.75	BAL.
AMS 5900	1.05-1.15	0.40	0.30	14.00	2.00	1.00	—	BAL.
AMS 6491	0.80-0.85	0.25	0.20	4.10	4.20	1.00	0.08	BAL.

Two hard coatings were evaluated, thin-dense-chromium (TDCr) plating and physical vapor deposited (PVD) titanium nitride. The chromium plating is electrodeposited in a proprietary bath using a high current density resulting in a thin (2 to 2.5 microns), dense, adherent coating. This coating is successfully being used to provide corrosion resistance, low wear, and improved fatigue life in AMS 6444 lubricated bearings. Full-scale bearings were tested in water-based lubricants and without lubricant. All cases exhibited improvements in bearing life over unplated bearings. This coating is also reported not to peel or crack under cryogenic conditions.<sup>1</sup>

Titanium nitride (TiN) hard coatings have been reported to provide improved wear, corrosion resistance, and fatigue life in bearings.<sup>2,3</sup>

Titanium nitride was applied by (1) Radio Frequency (RF) sputtering<sup>4</sup> and (2) Reactive Plasma Ion Bombardment (RPIB).<sup>5</sup> Both titanium nitride coatings were 0.5 micron thick because other investigators have found that thick coatings are likely to crack under high loads.<sup>6</sup>

#### Experimental Procedure

A four-ball lubrication tester was converted to uniquely simulate the operating conditions of the SSME HPOTP bearings. Three 1/2-inch-diameter balls machined to the same size and specification as the SSME HPOTP balls are placed in a test cup. The fourth ball in the tester is replaced by a cone that pyramids upon the three balls in the cup. The configuration is shown in Fig. 1 and 2. The 45-degree cone angle produces a spin/roll ratio of 1.27 (HPOTP turbine bearing has a spin/roll ratio of 0.7). A 45-kg weight applied through a cantilever arm provides a mean Hertz stress of 2.12 GPa (the mean Hertz stress in the HPOTP turbine bearing can be as high as 1.72 GPa). Based on Archard's wear equation, wear is proportional to PV where P is the contact

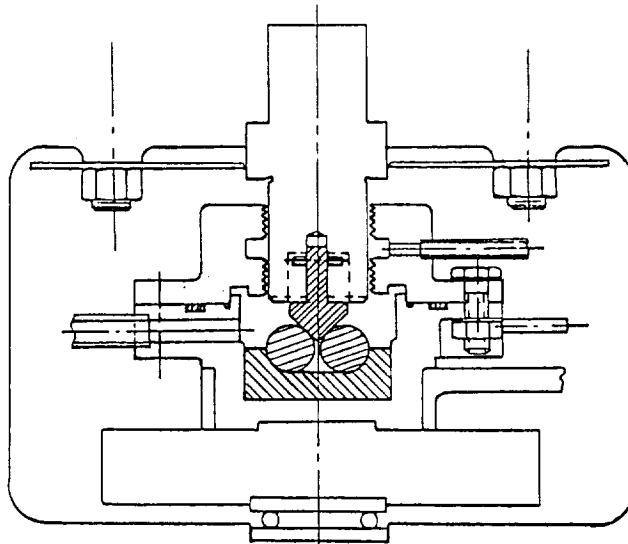


Fig. 1. Schematic of Cone-Three-Ball Tester

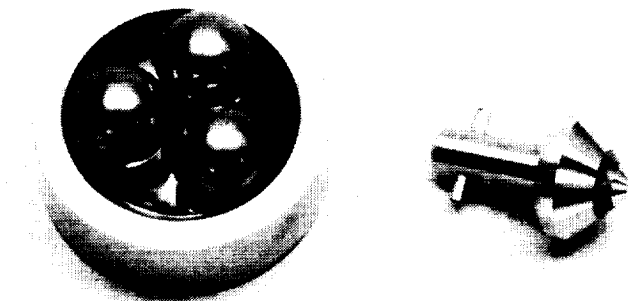


Fig. 2. Picture of Cone-Three-Ball Test Specimens

stress in GPa and  $V$  is the sliding velocity between the contacting surfaces in meters/second.<sup>7</sup> Because the tester runs at 3600 rpm, the maximum achievable PV level is 0.62 GPa x m/s while the SSME PV level is 3.78 GPa x m/s. Therefore, a ratio of rig test time to turbo-pump service time of 6:1 provides similar PV levels. A comparison of HPOTP bearings and cone-three-ball parameters is shown in Fig. 3. The environment is provided by sealing the cone-ball-cup assembly and pumping a constant flow of liquid oxygen or liquid nitrogen through the enclosed chamber. Tests were initially performed in liquid nitrogen for safety reasons to evaluate the tester and to determine the reproducibility of the results.

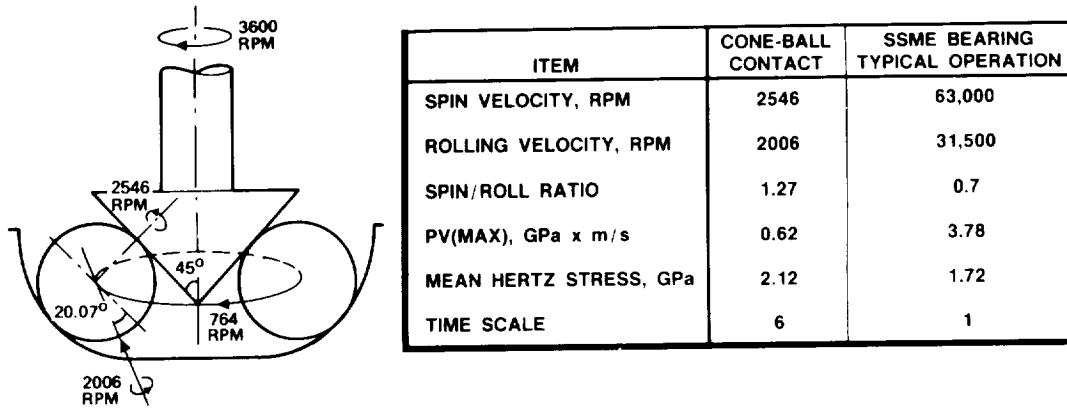


Fig. 3. Comparison of HPOTP Bearing and Cone-Three-Ball Parameters

Subsequent tests were performed in LO<sub>2</sub> for 6 hours to simulate 1 hour of HPOTP turbine bearing service. Tests could be accelerated, if needed, by increasing the cone contact angle, which would increase the ball spin/roll ratio, or by increasing the axial load to induce a higher Hertzian contact stress.

The test matrix is shown in Table 2. All test hardware were rough machined, heat treated to final hardness, final machined, lapped, then coated. In all cases, it was necessary to keep the deposition temperatures below the tempering temperature of the alloys (AMS 5618 (VIM-VAR) = 150 C, AMS 5900 and AMS 6491 = 538 C) to minimize distortion

Table 2. Test Matrix

SURFACE TREATMENT/ALLOY	AMS 5618 (VIM-VAR)	AMS 5900	AMS 6491
RF SPUTTERED TIN	✓	✓	
RPIB TIN	✓	✓	✓
TDCr	✓		
BASELINE	✓	✓	✓

and loss of hardness. The AMS 6491 was coating with RPIB TiN only because the RF sputtered TiN process could not be used to coat the balls. Due to the poor corrosion resistance of AMS 6491, this alloy can only be used in the HPOTP environment if all surfaces were coated. After testing, the wear tracks on the cones were measured with a profilometer and the wear surfaces examined using SEM, Auger, and ESCA.

### Results and Discussion

Initial testing was performed in liquid nitrogen (LN<sub>2</sub>) on baseline AMS 5618 (VIM-VAR) and TDCr plated AMS 5618 (VIM-VAR). As shown in Fig. 4 and Table 3, TDCr-plated AMS 5618 (VIM-VAR) had substantially lower wear resistance than baseline AMS 5618 (VIM-VAR). SEM micrographs in Fig. 5 show that the initial coating had numerous voids and mudcracks; testing caused it to flake off. This coating was also not reproducible. TDCr was therefore eliminated from further testing in the more severe LO<sub>2</sub> environment. However, the tester performed well giving reproducible results on AMS 5618 (VIM-VAR).

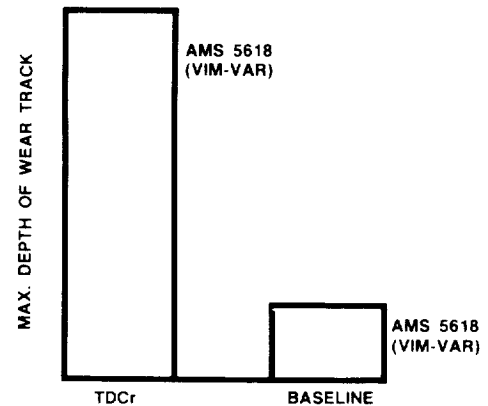


Fig. 4. Comparison of Wear of TDCr Coated and Uncoated AMS 5618 (VIM-VAR)

Testing in LN<sub>2</sub> was followed by testing of AMS 5618 (VIM-VAR) in LO<sub>2</sub> and the wear morphology was compared

Table 3. Cone-Three-Ball Test Results

MATERIAL/SURFACE TREATMENT	MAX. DEPTH OF TRACK (μm)	CROSS SECTION WEAR TRACK (μm <sup>2</sup> )
AMS 5900/RF SPUTTERED TiN	0.2	105
AMS 5618 (VIM-VAR)/RF SPUTTERED TiN	2.0	550
AMS 6491 BASELINE	4.0	1,600
AMS 5618 (VIM-VAR) BASELINE*	9.5	1,698
AMS 5900/RPIB TiN (CONE & BALLS)	10.6	6,200
AMS 5900 BASELINE	12.0	7,650
AMS 5900/RPIB TiN (CONE ONLY)	12.4	6,750
AMS 6491/RPIB TiN	14.4	8,950
AMS 5618 (VIM-VAR)/TDCr*	50.0	50,000
AMS 5618 (VIM-VAR) BASELINE	101.6	196,800
AMS 5618 (VIM-VAR)/RPIB TiN (OVERHEATED)	1092.2	—

\*TESTED IN LN<sub>2</sub>

with the HPOTP bearing wear features to establish how well the cone-three-ball tester simulated the HPOTP bearing wear characteristics. Typical micrographs of HPOTP bearing balls and cone specimens are shown in Fig. 6. The HPOTP bearing had run a total of 3267 seconds and

ORIGINAL SIZE IS  
OF POOR QUALITY

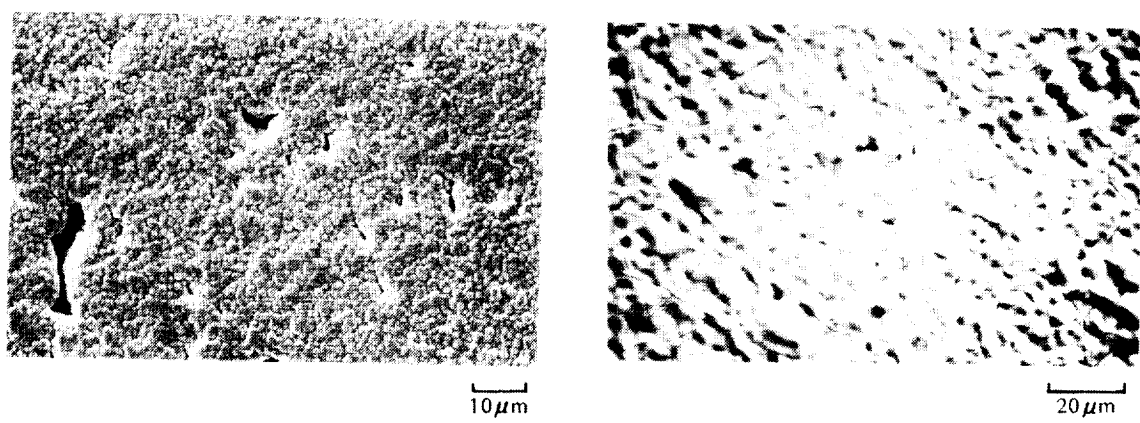
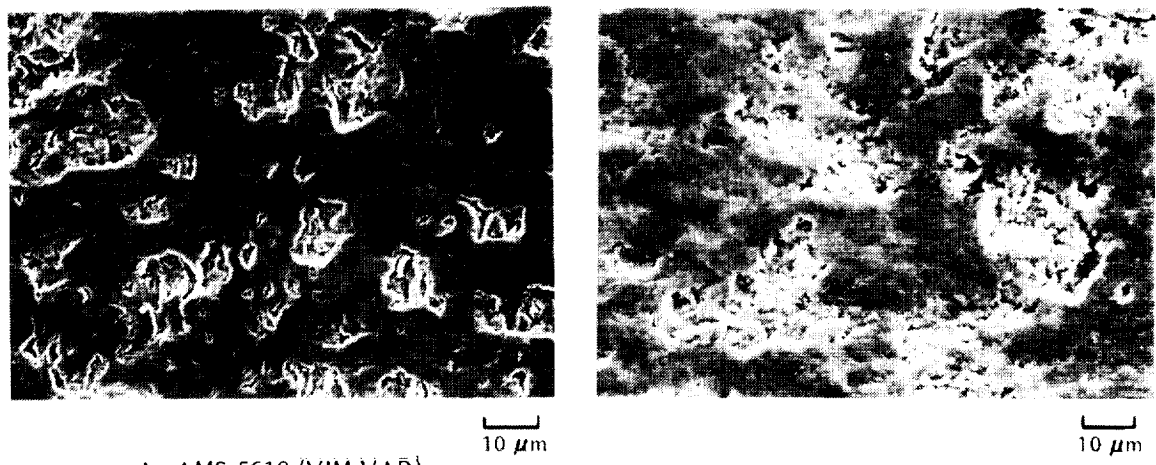
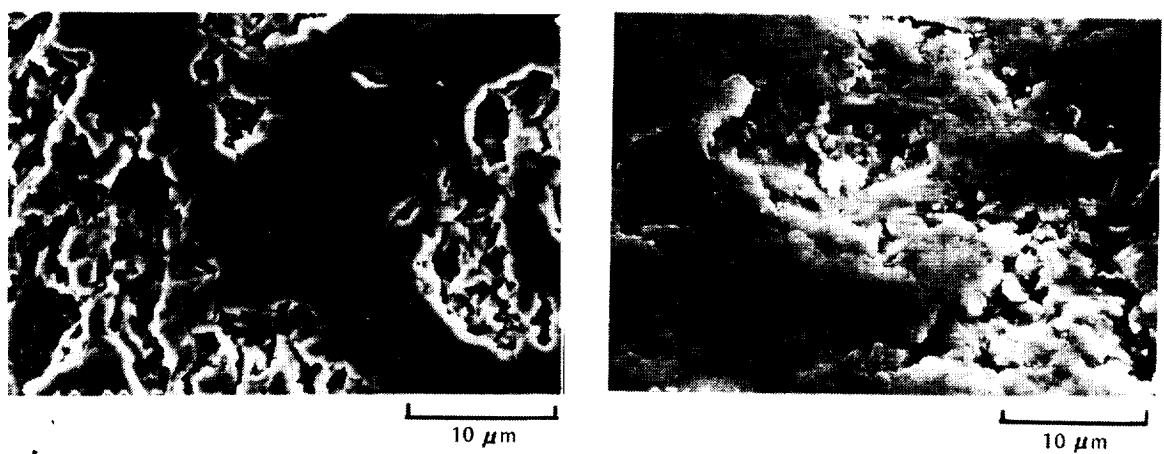


Fig. 5. Typical Morphology of TDCr Coating Before Wear Testing. Note voids and "mudcracks".



A. AMS 5618 (VIM-VAR)  
CONE WEAR TRACK ←→ (6 HOURS LO<sub>2</sub>)

B. HPOTP BALL WEAR (3267 SECONDS)



C. AMS 5618 (VIM-VAR)  
CONE WEAR TRACK ←→ (6 HOURS LO<sub>2</sub>)

D. HPOTP BALL WEAR (3267 SECONDS)

Fig. 6. Typical Morphology of Wear Tracks

the cone for 21,600 seconds, which simulates 3600 seconds of HPOTP operation. The amount of wear in the test specimen (25 to 100 micrometers) is of the same order as the HPOTP ball wear. In both cases, wear occurs by surface delamination as shown in Fig. 7. Material loss occurs by removal of thin, plastically deformed flakes from the surface. Typical ESCA spectra of surface oxides in LO<sub>2</sub> test specimens and HPOTP balls are shown in Fig. 8 and 9 for Fe and Cr, respectively. In both cases, the oxides are Fe<sub>2</sub>O<sub>3</sub> and Cr<sub>2</sub>O<sub>3</sub>. The similar wear mechanisms and surface

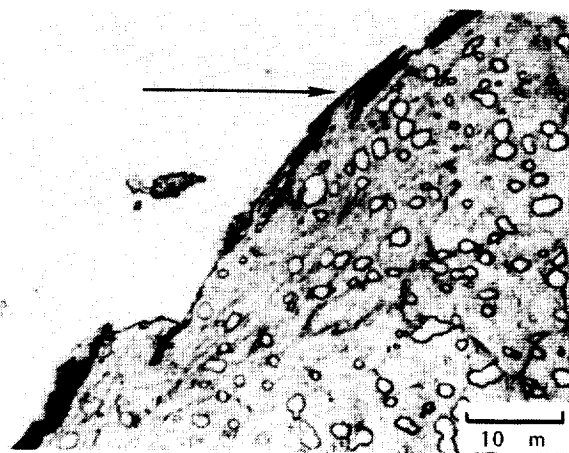


Fig. 7. Cross Section of Wear Track From Fig. 6A Showing Delamination

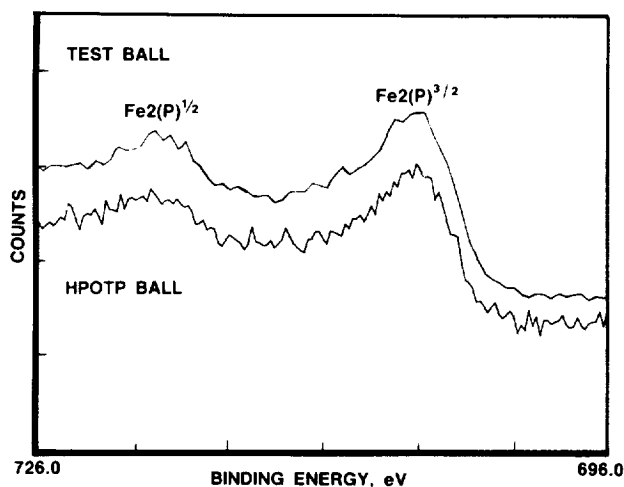


Fig. 8. Typical Fe<sub>2</sub>p ESCA Spectra of HPOTP and Cone-Three-Ball Tester Wear Surfaces

oxides indicate that the tester provides a good simulation of the HPOTP bearing wear. Using such a tester enables more economical evaluation of potential bearing materials without having to build and test complete bearing assemblies.

A comparison of wear of AMS 5618 (VIM-VAR) in LN<sub>2</sub> and LO<sub>2</sub> in Fig. 10 shows that the wear rate in LO<sub>2</sub> is more severe than in LN<sub>2</sub>. Therefore, materials for LO<sub>2</sub> service must be evaluated in LO<sub>2</sub>.

The data given in Table 3 and Fig. 11 show how the different materials and surface treatments perform in LO<sub>2</sub>. AMS 5900 and AMS 6491 were superior to AMS 5618 (VIM-VAR) in the uncoated condition. Although the

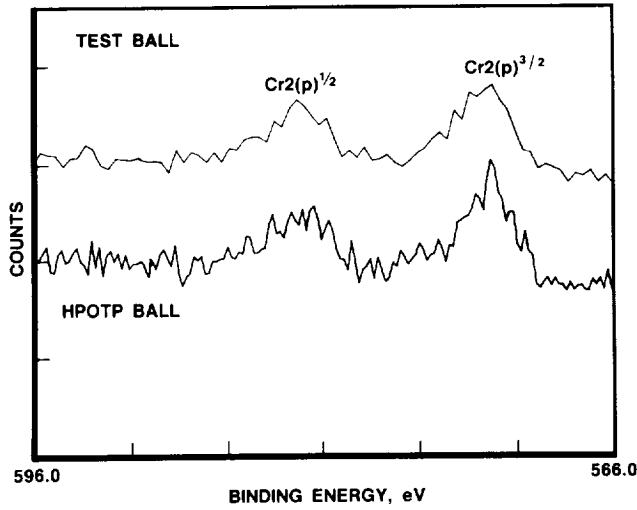


Fig. 9. Typical Cr<sub>2</sub>p ESCA Spectra of HPOTP and Cone-Three-Ball Tester Wear Surfaces

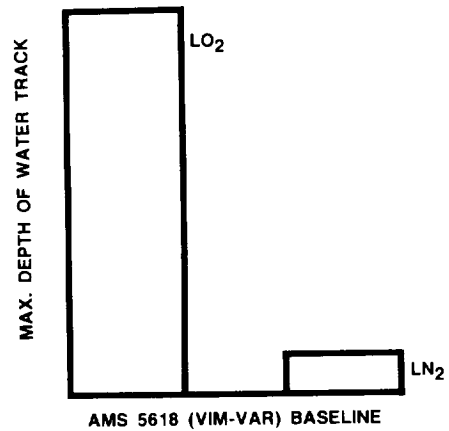


Fig. 10. Comparison of Wear of AMS 5618 (VIM-VAR) in LO<sub>2</sub> and LN<sub>2</sub>

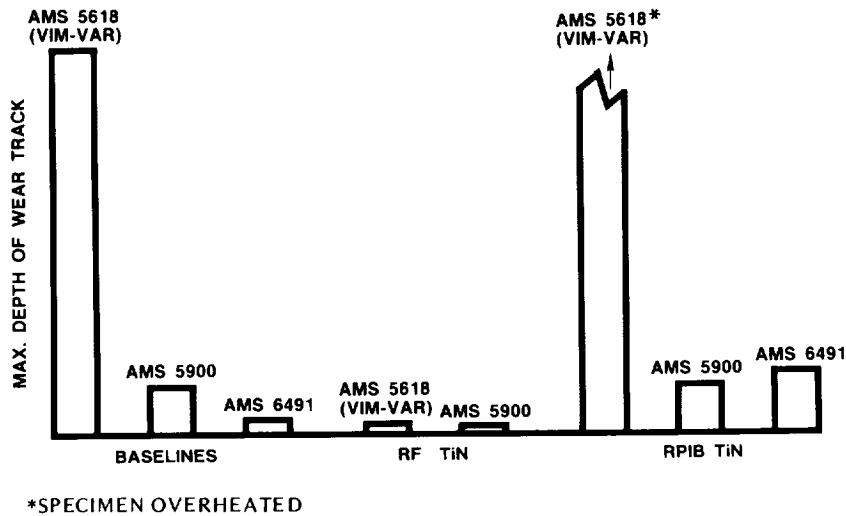
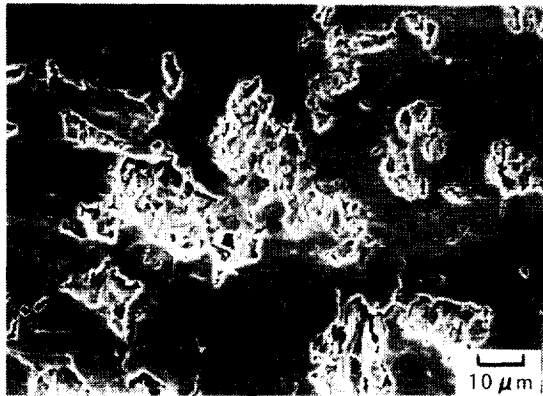


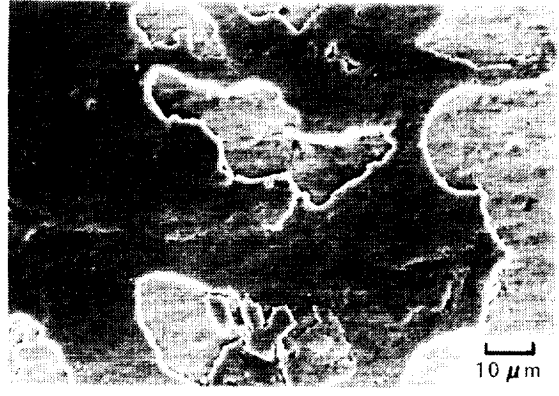
Fig. 11. Cone-Three-Ball Wear of Materials and Surface Treatments Evaluated in this Program

micrographs in Fig. 12A and 12B indicate that the wear mechanisms of the uncoated AMS 5900 and AMS 5618 (VIM-VAR) are similar, the delaminations seem to be thinner for the AMS 5900. Hence, when they flake off, it results in less wear.

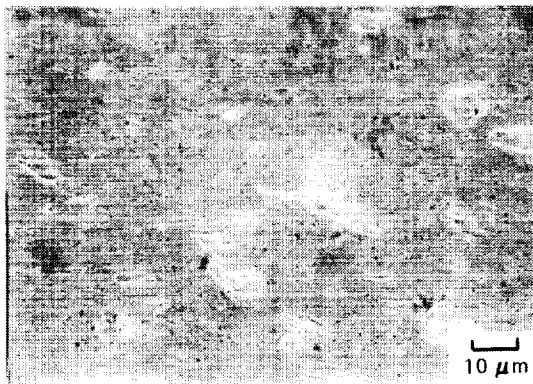
The RPIB TiN coating on AMS 5900 does not significantly affect its wear resistance, whereas it actually increases the wear of AMS 6491. This appears to be related to the poor, inherent corrosion resistance of AMS 6491, which accentuates the wear when the protective coating of RPIB TiN begins to deteriorate.



A. AMS 5618 (VIM-VAR) BASELINE



B. AMS 5900 BASELINE



C. RF TiN ON AMS 5618 (VIM-VAR)



D. RF TiN ON AMS 5900

Fig. 12. Typical Morphology of Wear Surfaces

The RPIB TiN coated AMS 5618 (VIM-VAR) wore even more than the uncoated material. This is due to the substrate being overheated and softened during deposition of the coating. Hence, no final conclusion as to the effectiveness of RPIB TiN on AMS 5618 (VIM-VAR) can be drawn at this time.

Figure 11 shows that an RF TiN coating is very effective in reducing wear of AMS 5618 (VIM-VAR) and AMS 5900. The observed difference in wear of RF TiN coated AMS 5618 (VIM-VAR) and AMS 5900 would not normally be expected since the substrates have very similar hardness and microstructure. However, the temperature of AMS 5900 during RF TiN deposition was higher than for AMS 5618 (VIM-VAR). This could possibly have resulted in a better coating/substrate bond on the AMS 5900 substrate. Some evidence of more flaking of the coating on AMS 5618 (VIM-VAR) compared with the AMS 5900, which indicates a lower bond strength, is evident in Fig. 12C and D.



The data on AMS 5900 in Fig. 11 illustrate how important the coating process and process parameters are for the performance of the coating. Both the RPIB TiN and RF TiN coating had the characteristic gold color. Although, the RF TiN coating was somewhat darker than the RPIB TiN coating, indicating a higher N/Ti ratio of the former, no significant difference in composition could be determined from ESCA analysis.

The better performance of the RF TiN coating could be due to it having a lower coefficient of friction and/or better inherent wear resistance than RPIB TiN. This will be determined by measuring the coefficient of friction in LO<sub>2</sub>.

### Conclusions

The results of this study indicate that it is possible to simulate the condition in cryogenic bearings using a simple cone-three-ball tester. This is exemplified by similar wear morphologies and composition of the surface oxides.

It was also demonstrated that wear in LO<sub>2</sub> is much more severe than wear in LN<sub>2</sub>. Hence, evaluation of HPOTP bearing materials and surface treatments must be performed in LO<sub>2</sub> to be meaningful.

Both RF TiN coated and uncoated AMS 5900 have substantially better wear resistance than the coated and uncoated AMS 5618 (VIM-VAR), respectively. However RF TiN coated AMS 5618 (VIM-VAR) has better wear resistance than uncoated AMS 5900. AMS 6491 also performed better than AMS 5618 (VIM-VAR). Thin-dense chromium coated AMS 5618 (VIM-VAR) wears more than uncoated AMS 5618 (VIM-VAR) possibly due to voids, cracking, and poor adhesion.

The method used and the process parameters for depositing TiN are important for the performance of the coating. In this study, radio-frequency sputtered TiN performed better than the reactive plasma ion bombardment TiN coating.

### Acknowledgement

This work was performed under the Rockwell International Independent Research and Development programs.

### References

1. Waskiewicz, W., "Extending Bearing Life in Off Highway Equipment," Proceeding of SAE Congress and Exposition, Milwaukee, Wisconsin, Paper No. 841124, September 1984.
2. Hinterman, H. E., A. J. Perry, and E. Horvath, "Chemical Vapor Deposition Applied in Tribology," Wear 7, p. 405-415 (1978).

3. Dill, J. F., M. N. Gardos, and H. Hinterman, "Rolling Contact Fatigue Evaluation of Hardcoated Bearing Steels," Proceedings of 3rd International Conference on Solid Lubrication, Denver Colorado, 5-9 August 1984.
4. Pitt, C. W., "The RF Sputtering Process," Proceedings of Conference on Ion Plating and Allied Technology, Edinburgh, Scotland, p. 149-156, June 1977.
5. Bunshah, R. F. and A. C. Raghuram, Journal of Vacuum Science Technology 9, p. 1385 (1972).
6. Ramalingam, S., "Tribological Characteristics of Thin Films and Application of Thin Film Technology for Friction and Wear Reduction," Proceedings of International Conference on Metallurgical Coatings, San Diego, California, p. 335-349, April 1984.
7. Archard, J. F., Journal of Applied Physics 24, p. 981-988 (1953).

SSME BEARING HEALTH MONITORING USING A  
FIBEROPTIC DEFLECTOMETERMichael E. Hampson, J. J. Collins, M. R. Randall,  
and Sarkis BarkhoudarianRockwell International/Rocketdyne Division  
Canoga Park, CaliforniaAbstract

A fiberoptic deflectometer was used to investigate rocket engine turbopump bearing health monitoring. Two Space Shuttle Main Engine (SSME) high pressure oxidizer turbopump turbine-end bearings (16-ball configuration) were operated in a tester under simulated high pressure oxidizer turbopump conditions of speed, axial load, and coolant flowrates: 30,000 rpm, approximately 550 pounds (2448 N), and 30 gpm (114 Lpm) of liquid nitrogen, respectively. The deflectometers measured outer raceway deflection, due to ball passage, in the radial direction. The test data were analyzed and plotted several different ways: deflection at shaft synchronous frequency vs time; synchronous histogram; deflection at second and third cage (2C and 3C), or ball-train, frequencies vs time; 2C and 3C histogram; product of deflections at 3C and synchronous frequencies vs time; histogram of product of 3C and synchronous; ratio of ball pass frequency at outer race to synchronous (BPO/Sync) vs time; histogram of BPO/Sync; and cumulative time that BOP/Sync spent above a threshold level. Accelerometer data from the tests were also analyzed and plotted for comparison. The results determined that bearing health could be successfully monitored using the deflectometer. Several algorithms stood out as the most useful. 2C and 3C vs time consistently showed increases as bearing condition degraded. Indications became obvious approximately 100 seconds before the accelerometers began to register changes. BPO/Sync, and its time spent above threshold, also clearly indicated degrading conditions. This processing provided a measure of the onset and duration of ball slip in the bearing, a strong driver of wear. Indications became obvious approximately 400 seconds before the accelerometers began to register changes.

Introduction

With the progressive development of the reusable rocket engine and vehicle, it has become evident that there is an immediate need for a system to provide information about the health of engine components and a method to predict their remaining useful life. A judiciously

[REDACTED]

developed system of condition monitoring instrumentation to provide such information on a turbopump could allow substantial reductions in cost and turnaround time by reducing or eliminating the requirements for routine scheduled disassembly and inspection, as well as generally premature component replacement. The benefit is twofold in that it reduces scheduled disassembly and inspection procedures and determines replacement of components for cause, thus minimizing the checkout time and cost between operational cycles. The key factors required to develop a Condition Monitoring System (CMS) are the determination of the life-limiting modes present within the turbopumps and the measurement and interpretation of the mode characteristics.

The specific objectives of this program are to design, fabricate, and deliver the components to provide a condition monitoring system for use with Space Shuttle Main Engine (SSME) or similar high pressure turbopumps. The effort is conducted under contract NAS3-23349 with the NASA-Lewis Research Center under the direction of Mr. Robert M. Masters. This paper will describe that portion of the study pertaining to the results of bearing monitoring with the fiberoptic deflectometer.

#### Test Fixture and Instrumentation Description

The bearing monitoring tests were baselined to the SSME High Pressure Oxidizer Turbopump (HPOTP) shown in Fig. 1. The baseline operating conditions were identified as follows:

1. Rotating radial loads up to 2000 lbf
2. Axial loads up to 6000 lbf
3. 30,000 rpm
4. Coolant flowrate to 30 gpm

A bearing tester was used that emulated all of these conditions except the rotating radial loads. Also, liquid nitrogen was used as the coolant instead of liquid oxygen.

The tester is shown in Fig. 2. It incorporates two 16-ball configuration turbine-end bearings, part number RS007787, mounted to a shaft and installed in a housing. Each bearing can be monitored with six deflectometers monitoring radial motion of the outer raceway caused by individual ball passage. The bearing to the left is also monitored upstream and downstream by pressure and temperature probes. Accelerometers are mounted to the housing in three perpendicular planes for real-time test monitors and for correlation to the deflectometer data. Axial loads are provided either by pressurizing a pneumatic piston located to the right of the right-end bearing or by loading the piston with a Belleville spring. Liquid nitrogen flows in from the left and exits from the right.

Monitoring of bearing condition by the fiberoptic deflectometer is accomplished by utilizing reflected light from the bearing outer race

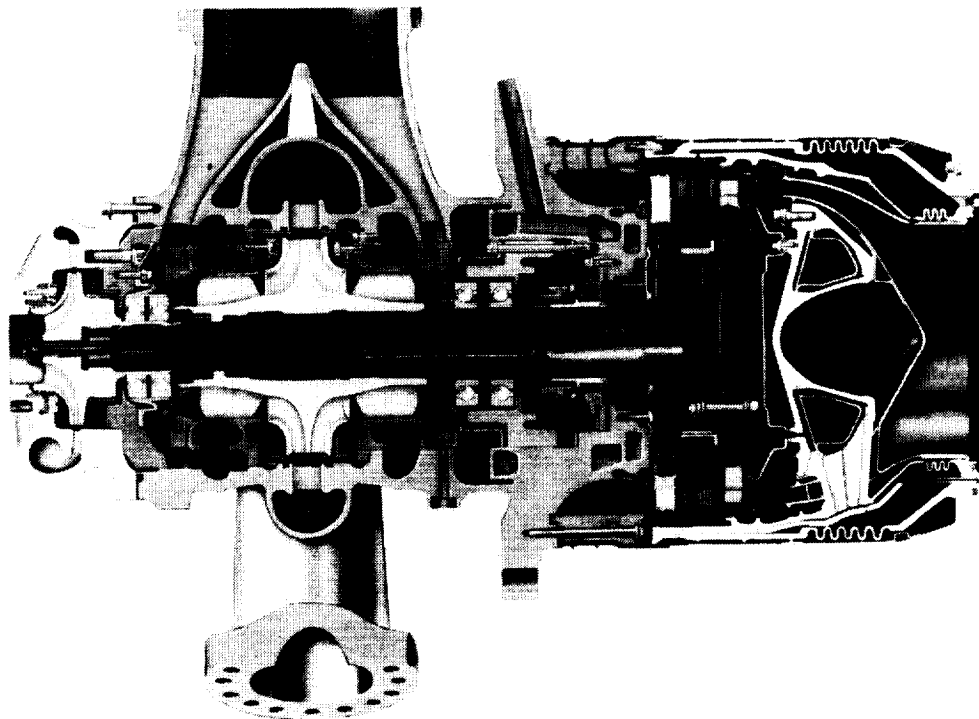


Fig. 1. High Pressure Oxidizer Turbopump

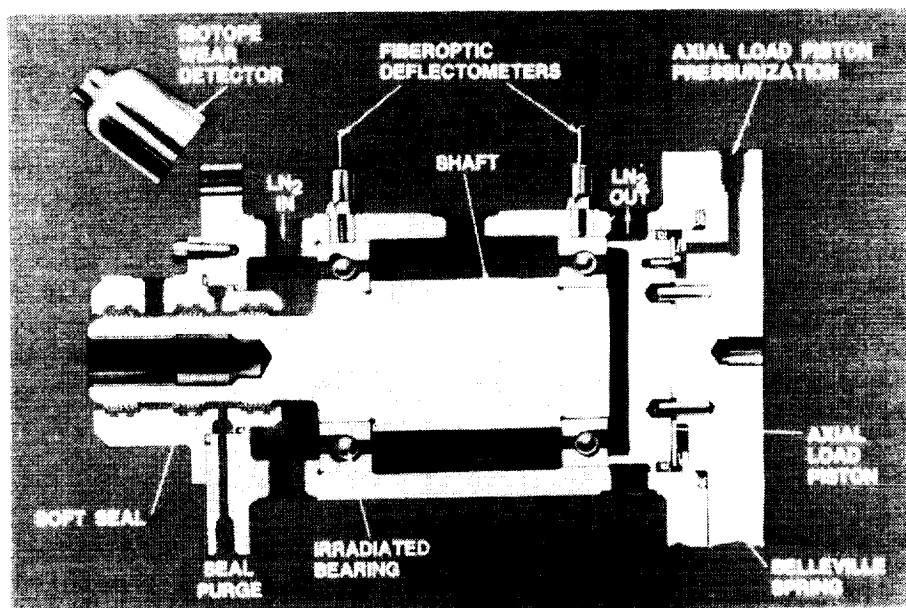


Fig. 2. Bearing Monitoring Tester

surface; Fig. 3 illustrates this principle. Light is transmitted by a portion of the fibers in the probe to the race surface. Some of this light is reflected off the surface and is received by the remainder of the fibers. This light is then processed through a photodetector to

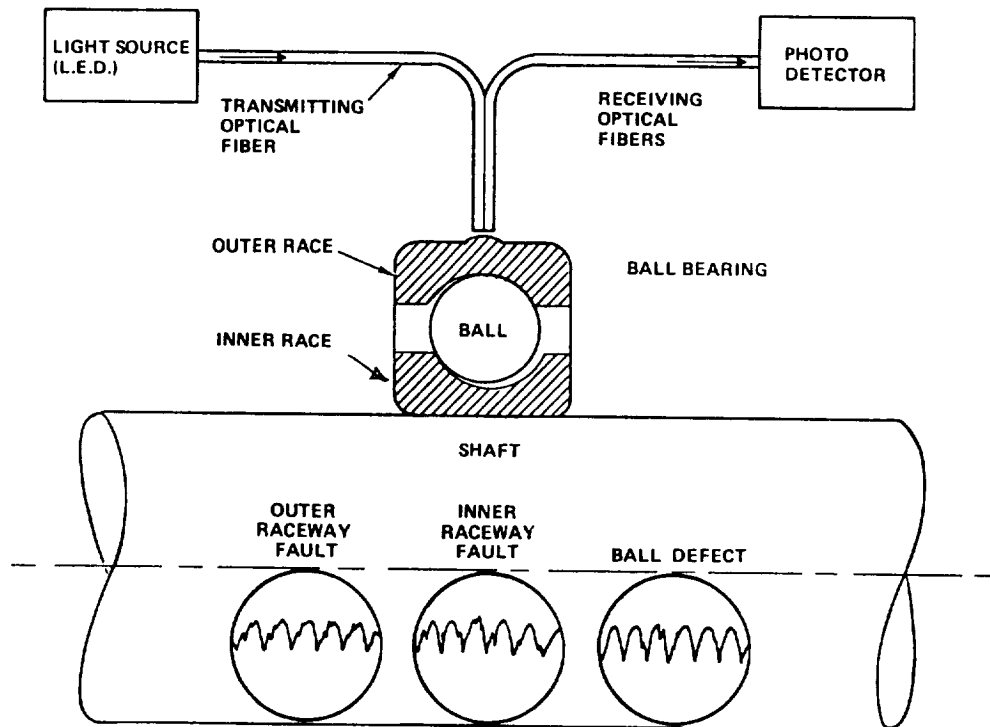


Fig. 3. Fiberoptic Deflectometer

provide an electrical signal proportional to bearing race surface deflection. Frequency and amplitude content analysis of the signal provides information on bearing condition. The probe tip is 0.125 inch in diameter and 3 inches long. The probe is made by MTI, Latham, New York.

Wear of the raceway of the left-end bearing is also monitored using an Isotope Wear Detector (IWD). The ball track in the outer race is irradiated to a low-level and the change in radioactive count-rate is correlated to a wear depth by the IWD. The IWD is made by Spire Corp., Bedford, Massachusetts, which also provides the irradiation service.

#### Analysis of Test Data

The analysis focused on the data from Bearing Monitoring Test No. 3 (BMT3), in which the bearing nearly failed during the third of three tests. It was concluded that this test was the most representative of bearing life in an actual turbopump.

Shown in Fig. 4 is a plot of the shaft synchronous amplitude versus time. Test BMT3.1 began at 0 and ended at 732 seconds. Test BMT3.2 began at 732 and ended at 1454 seconds. The final test, test BMT3.3, began at 1450 and ended at 1917 seconds. "Spikes" in the data of Fig. 4 occurred at the beginning/endpoint of each test during the start/stop

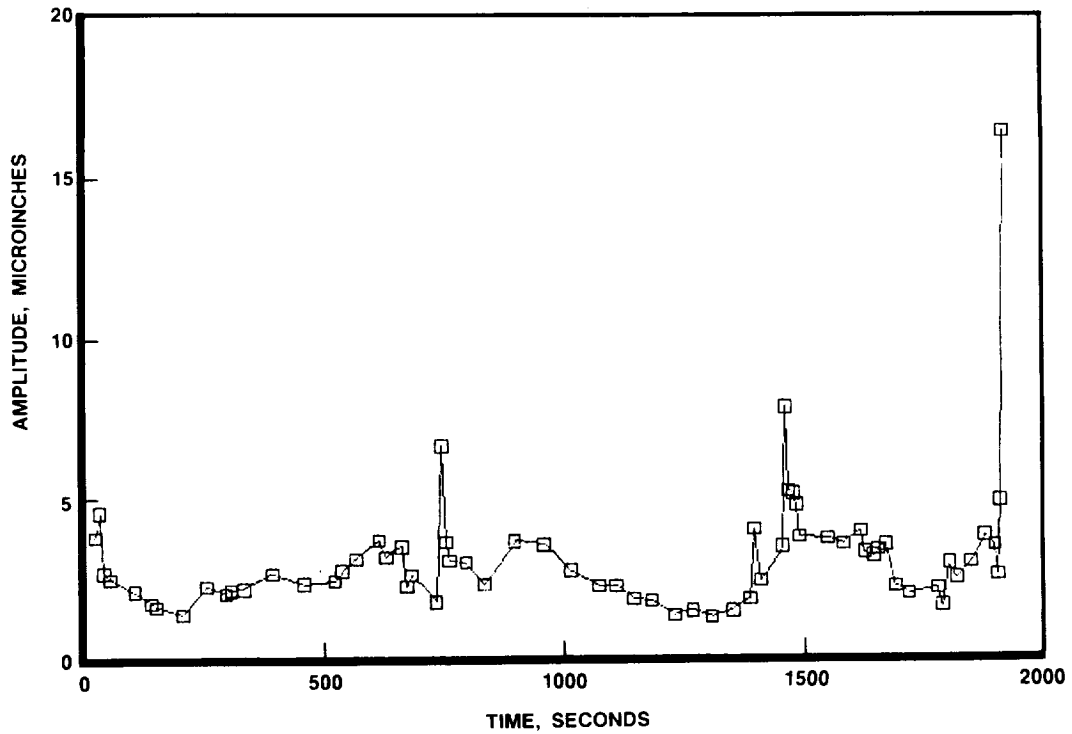


Fig. 4. Synchronous Amplitude vs Time

transient. The data in this figure do not follow any specific trend and were used mainly to verify continuity between tests.

Shown in Fig. 5 is the sync amplitude versus time for test BMT3.3 only. The data show no significant changes prior to the very end of the test.

A histogram of the data from Fig. 4 is shown in Fig. 6. As indicated in the figure, the amplitude at this frequency spent almost all of its time at low levels, mostly below 4.792 microinches (halfway between the midpoint values of 4.343 and 5.241 microinches). It was determined during the course of the data analysis that the best utility of the histogram was in determining redline or cutoff values; once the parameter exceeded the value at which it spent most of its time the test would be cut. This cutoff value would be empirically determined for the application under consideration, e.g., a turbopump. In the case of the tester, use of the histogram in this manner indicates that the test should have been cut around the beginning of test BMT3.3 (see Fig. 5). (The start/stop transient spikes were eliminated from consideration for cutoff indicator due to their short duration and association with the start/stop transient.)

Figure 7 shows the amplitudes of the second and third cage (2C and 3C) harmonics of the fundamental cage rotation frequency versus time.

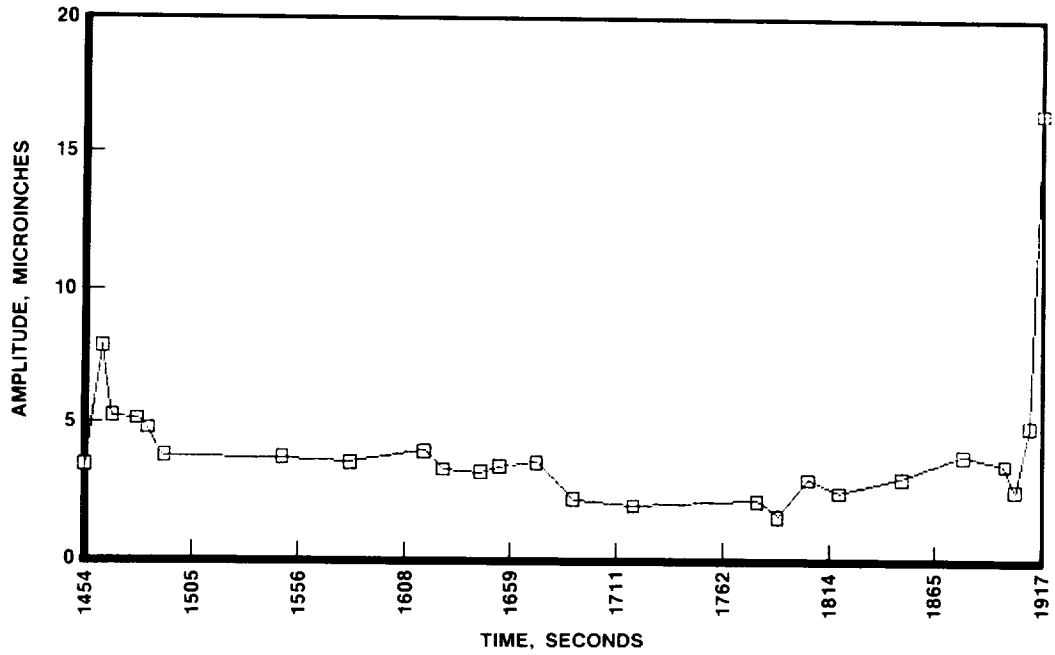


Fig. 5. Synchronous Amplitude vs Time (Test BMT3.3 Only)

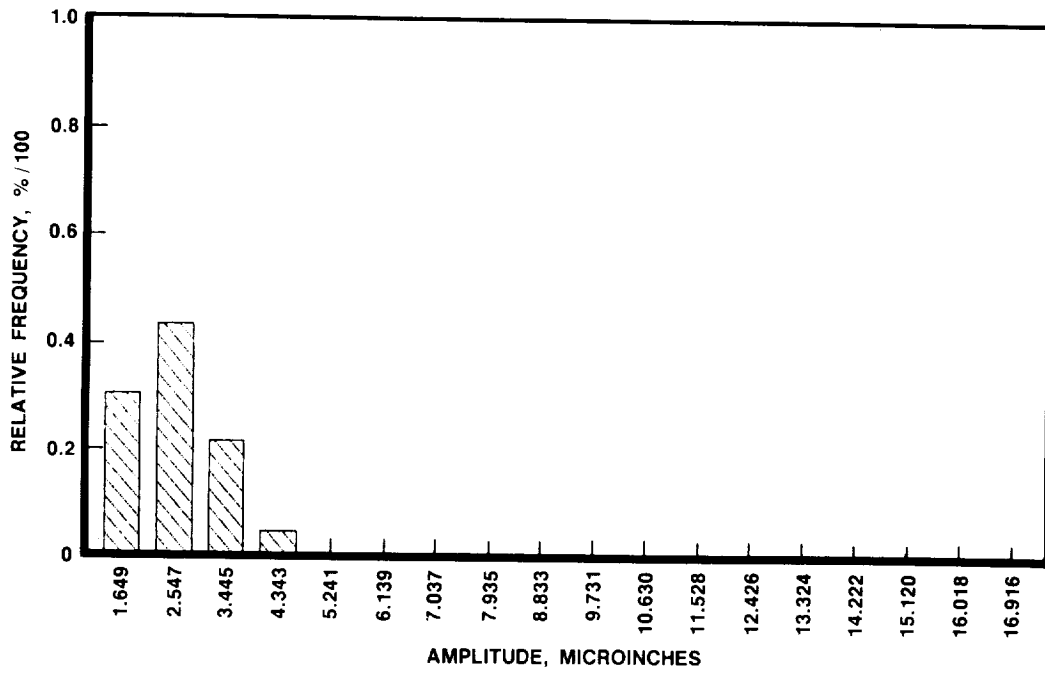


Fig. 6. Synchronous Amplitude Histogram (Entire Test)



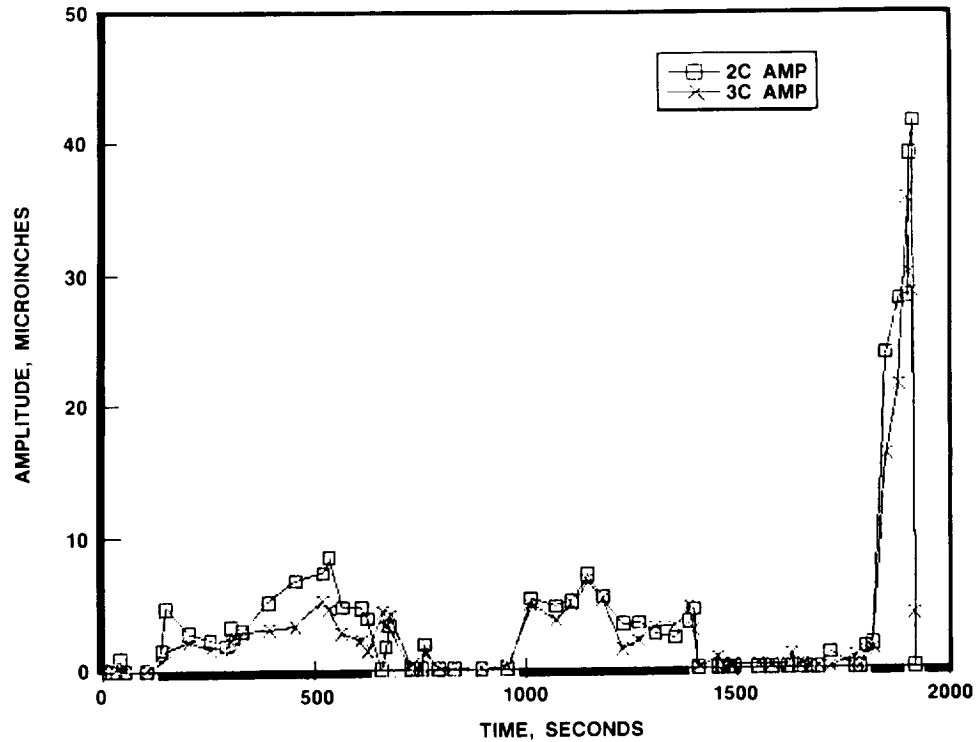


Fig. 7. Second- and Third-Cage Rotation Harmonics vs Time (Entire Test)

These values are actually harmonics of the ball-train rotation frequency. Shown in Fig. 8 are the same data for test BMT3.3 only. Note the large amplitude increases in the data well before the end of the test. These frequencies were monitored real-time during actual testing and provided a cutoff indicator when their amplitudes began to increase significantly.

Shown in Fig. 9 and 10 are histograms for the 2C and 3C data, respectively, for the entire test series. Using the same reasoning used for the sync amplitude histogram, the test should have been cut when 2C exceeded 9.785 microinches, or when 3C exceeded 8.386 microinches (again ignoring the transient spikes). Both exceeded these values at about the same time, around 1840 seconds (Fig. 8). Use of 2C and 3C data for cutoff was preferable to using sync data because the increases that occurred in 2C and 3C were larger in amplitude and duration and consistently appeared during the bearing's final moments, whereas the sync amplitude did not. Also, the sync amplitude histogram indicated that the bearing should have been pulled from service at the beginning of test BMT3.3, whereas 2C and 3C indicated that the bearing's condition was still acceptable at that point. All other data indicated that the bearing was still useful at the beginning of test BMT3.3.

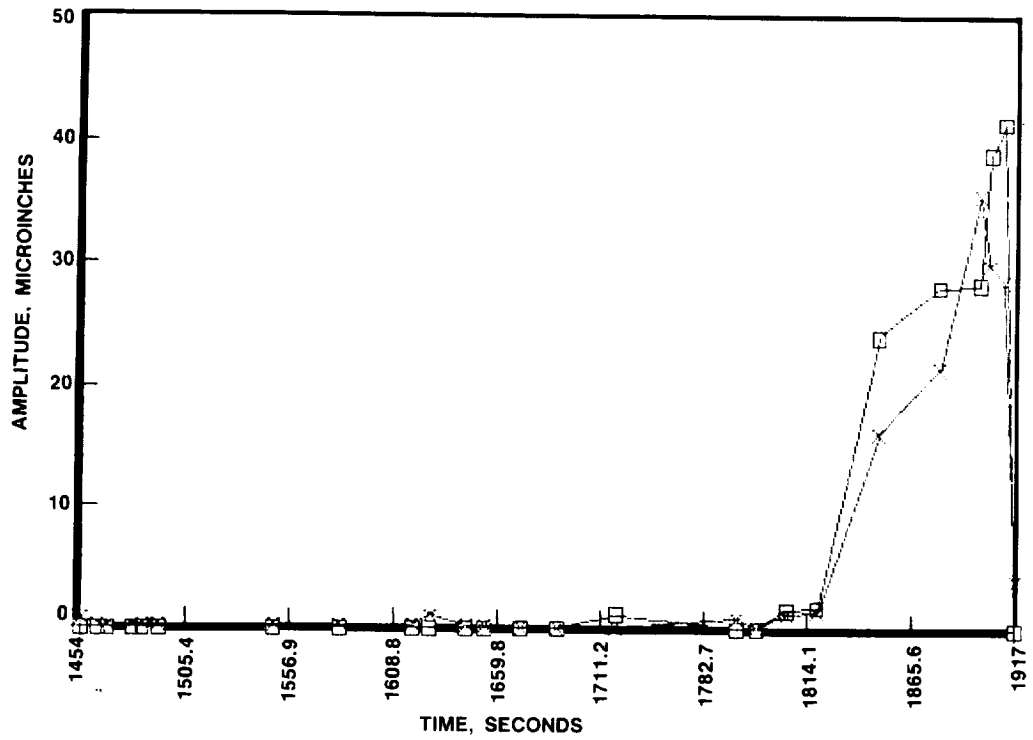


Fig. 8. Second- and Third-Cage Rotation Harmonics vs Time (BMT3.3 Only)

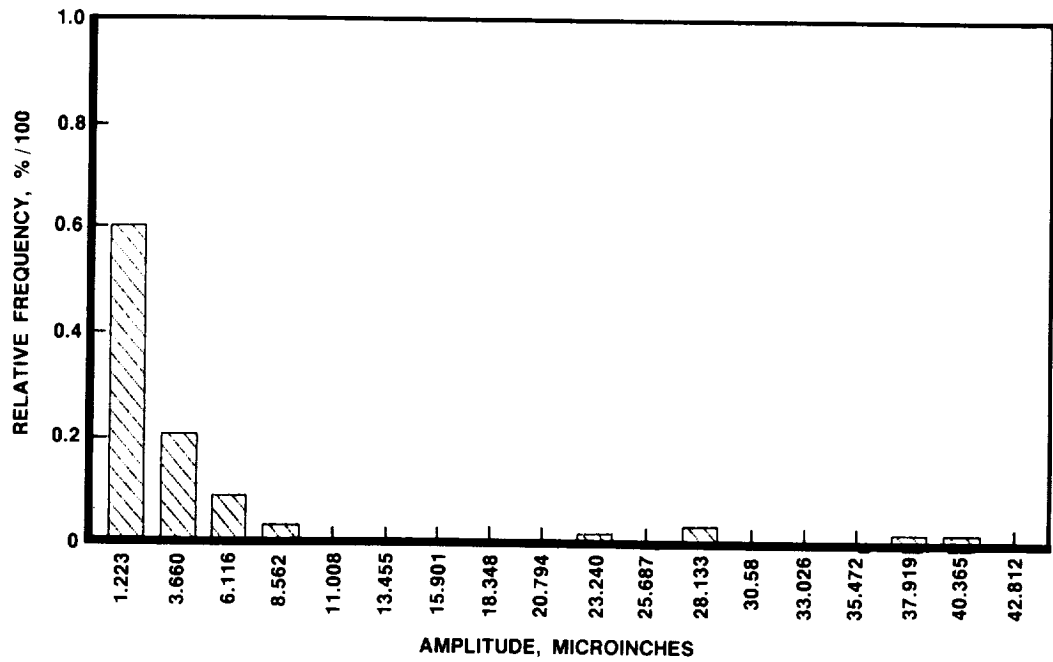


Fig. 9. Second-Cage Histogram (Entire Test)

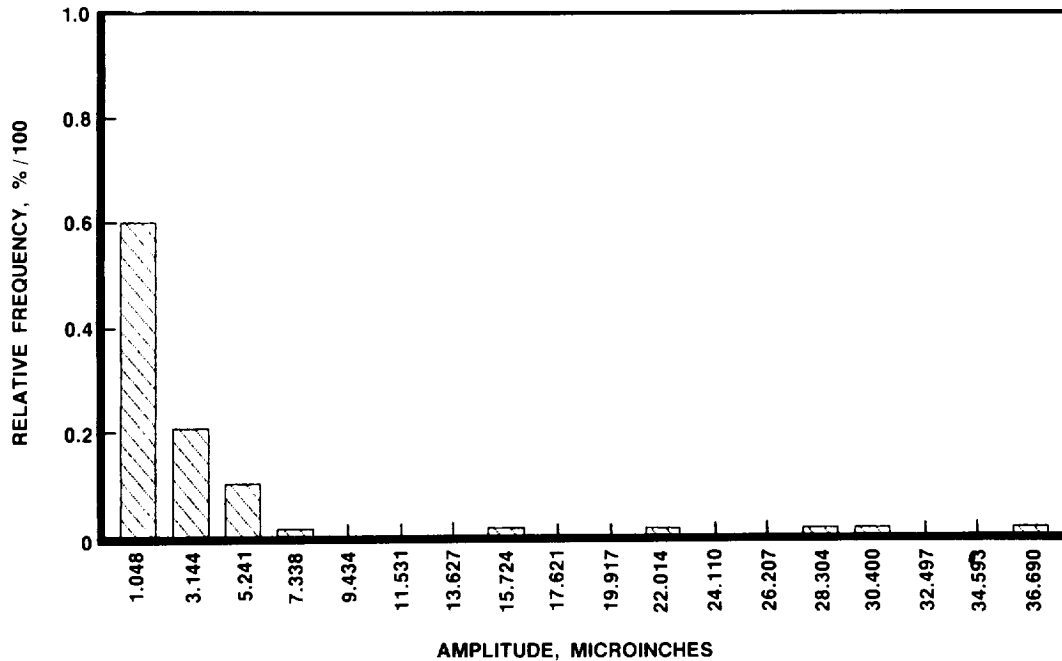


Fig. 10. Third-Cage Histogram (Entire Test)

The product of the sync amp and 3C is shown in Fig. 11. The histogram of this product is shown in Fig. 12. The product provides a stronger signal than either the sync or 3C alone, but also multiplies its error. The data indicate that the bearing should have been pulled from service at the same time that 2C and 3C indicated. No advantage is seen in using this type of processing over 2C or 3C alone.

The ratio of the ball pass frequency at the outer race (BPO) to the sync frequency is shown in Fig. 13. This ratio is a measure of the amount of slip occurring between the balls and the outer race. The actual ratio occurs within the "actual range" shown due to the limited resolution of the processing used to obtain the BPO and sync frequencies. The upper and lower limits of the "ideal range" are determined from histograms of the upper and lower actual range values, respectively; these histograms are shown in Fig. 14 and 15, respectively. Theoretically, the value of the BPO/Sync ratio is somewhat lower than shown by the ideal range, around 6.8. However, this value is dependent on loading, actual geometry of the bearing's components, contact angle, etc., and therefore it is expected that the bearing will not operate exactly where predicted. The histograms of Fig 14 and 15 were used to determine the range of ratios in which the bearing prefers to operate, and these values were then transformed to the ideal range values shown in Fig. 13.

As Fig. 13 shows, slippage occurred at the outer race at the beginning of test BMT3.2 and for the first half of test BMT3.3. These

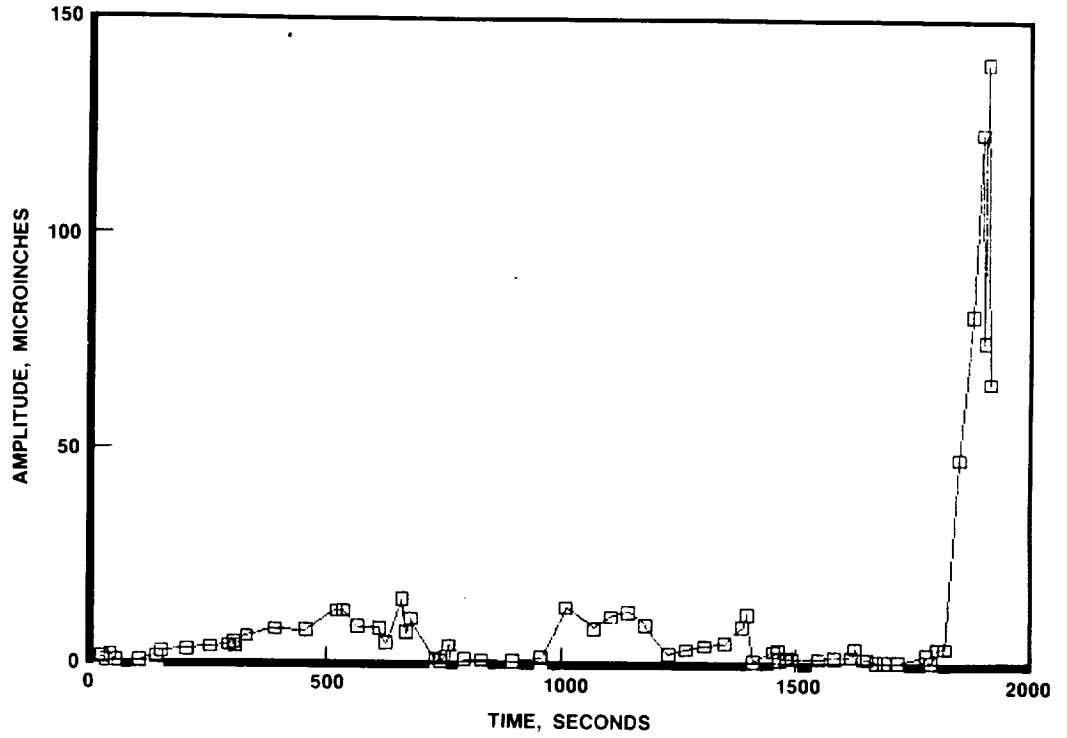


Fig. 11. Product of Third Cage and Synchronous (Entire Test)

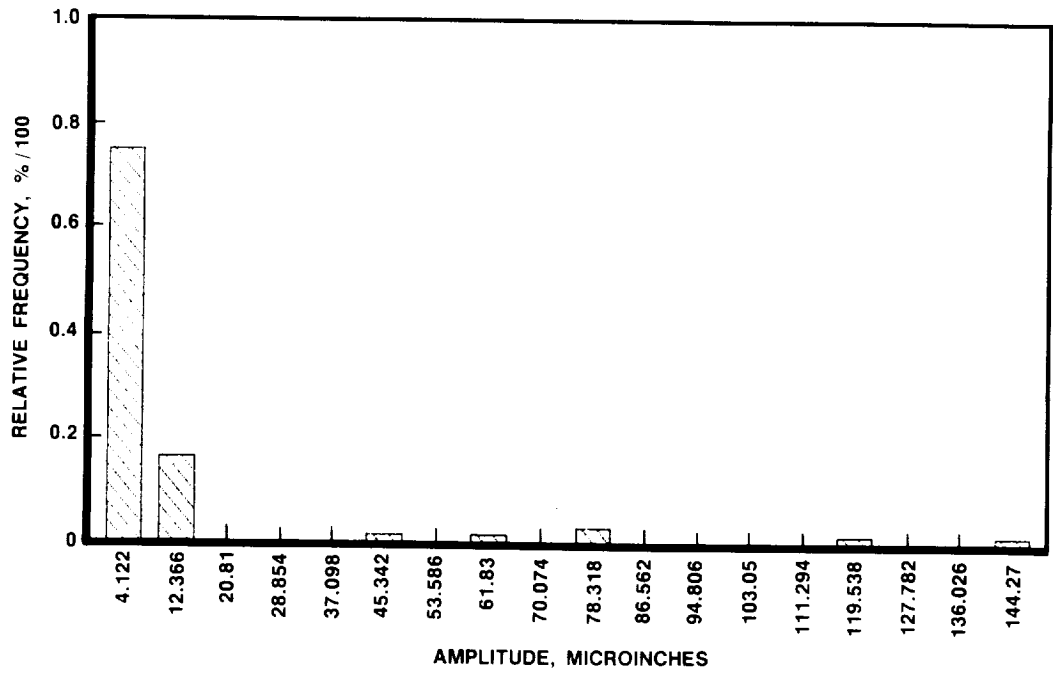


Fig. 12. Histogram of Product of Third Cage and Synchronous (Entire Test)

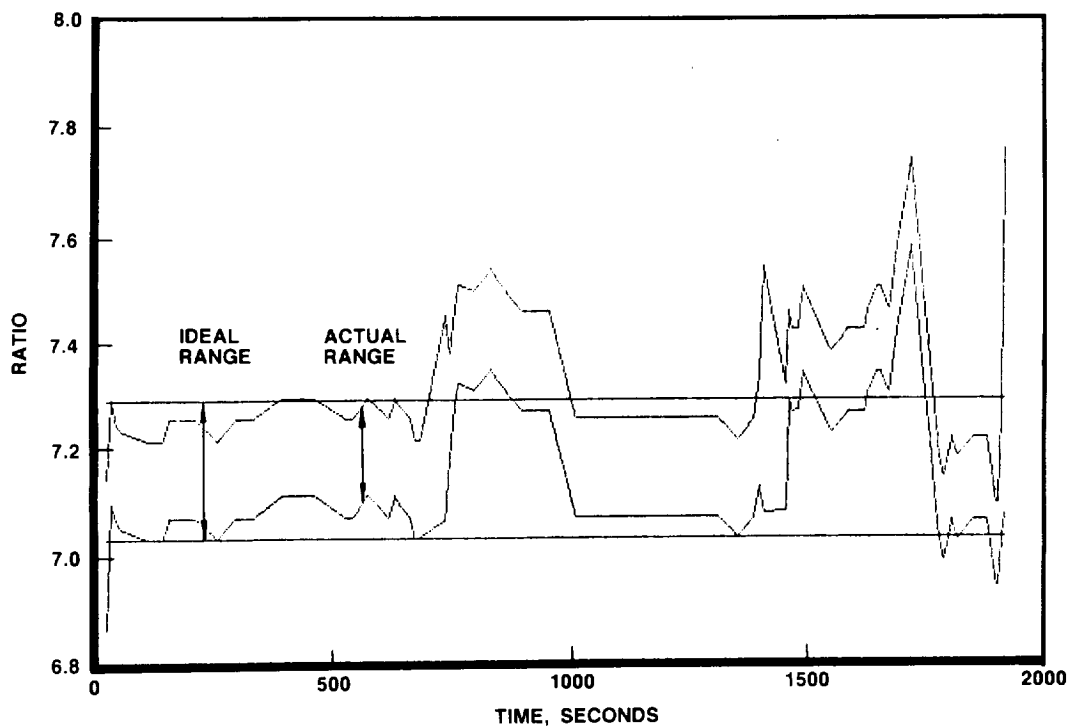


Fig. 13. Ratio of Ball Pass Frequency at Outer Race to Synchronous Frequency (Entire Test)

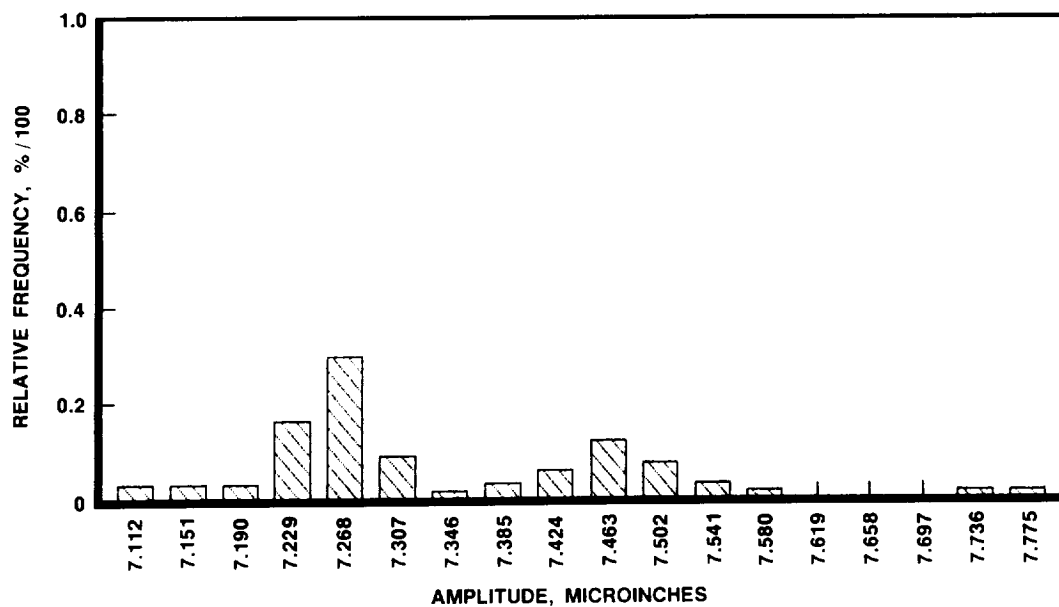


Fig. 14. Histogram of BPO/Sync, Upper Limit (Entire Test)

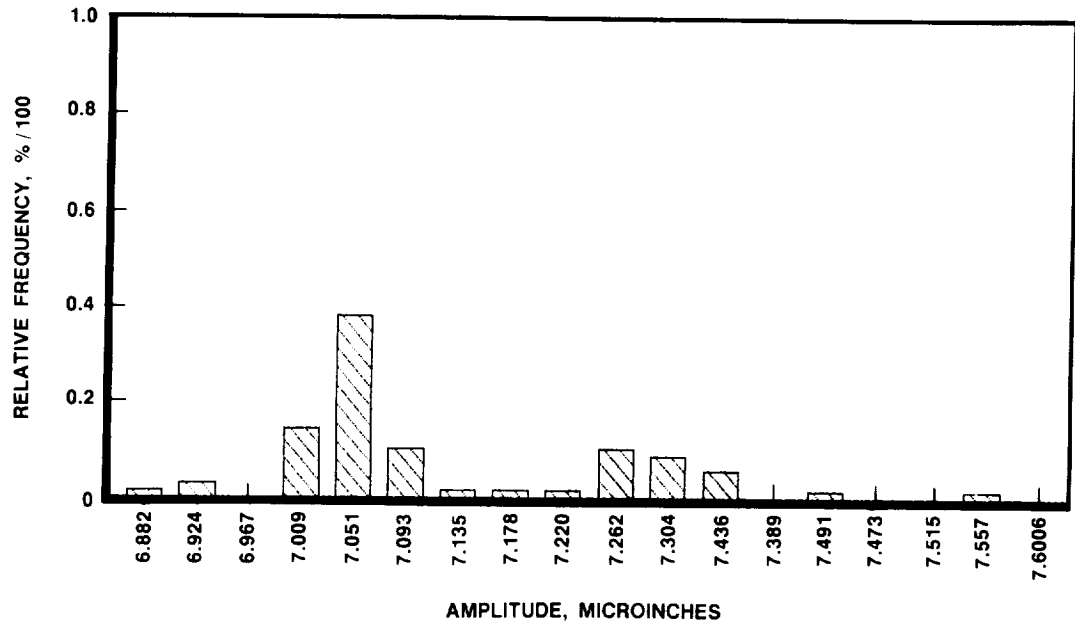


Fig. 15. Histogram of BPO/Sync, Lower Limit (Entire Test)

periods of increased activity correspond to periods of decreased activity in 2C and 3C amplitudes (Fig. 7). One possible explanation of this curious phenomenon is associated with the failure mechanism of the bearings during these tests. Every bearing that failed during the testing was due to a failed, or almost failed, cage in which one or more cage pockets had been severely damaged due to ball contact. Those cage pockets that were severely damaged contained a ball that was smaller by several ten-thousandths of an inch than the rest of the ball train. The smaller ball rolled faster on the inner race than the larger balls and therefore pulled the rest of the ball train around at a faster-than-normal speed. This theory was validated by posttest inspection of the bearing cages which showed that cage pockets with small balls had the front of their pocket (leading side) severely worn and deformed by ball contact, and those pockets with normal sized balls had the back (trailing side) of their pockets worn, indicating that they had been pulled around. The cage from the left-end bearing after test BMT3.3 is shown in Fig. 16. This nonuniform loading caused the BPO/Sync ratio to increase beyond its normal value; the ball train was skidding on the outer race. Energy that would normally have been transmitted to the outer raceway by the balls due to rolling contact was now being dissipated at the ball/cage interfaces due to contact there. The 2C and 3C amplitudes were therefore quieter during periods of slipping.

Aside from this correlation, the BPO/Sync ratio indicates that destructive wear due to ball slip was starting to occur at the beginning of test BMT3.2. Isotope wear detector data at the end of this test did not indicate any significant changes, so it is inferred that

ORIGINAL PAGE IS  
OF POOR QUALITY

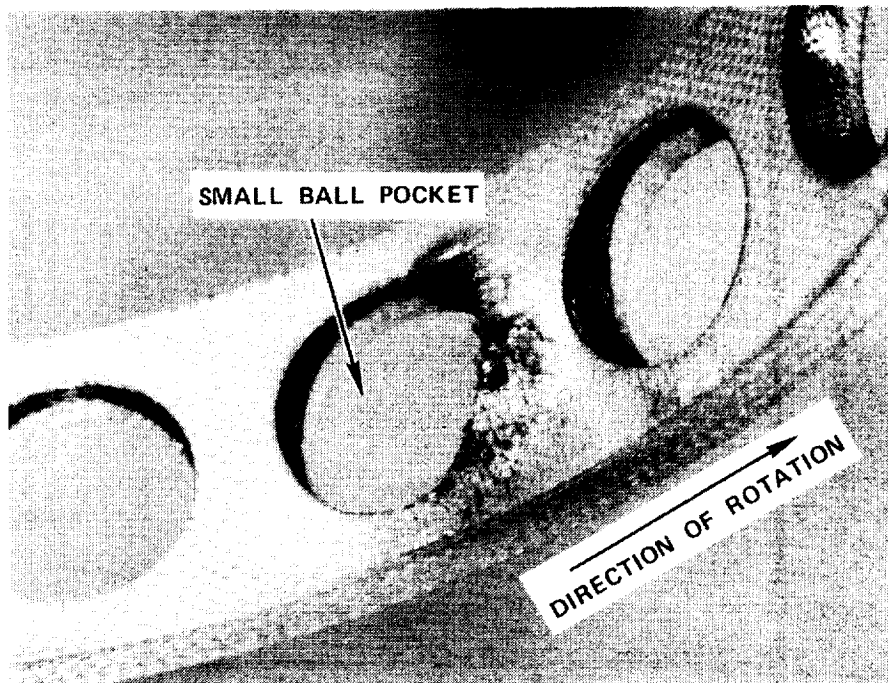


Fig. 16. Bearing Cage After Test BMT3.3

the wear occurring was minimal. The ratio also indicates that significant changes had occurred in the bearing's geometry at the beginning of test BMT3.3, probably the reduction in diameter of one or more of the balls in the ball train, leading to an increase in the ratio (increased slippage). This increase is significant in that it is a relatively large change in the ratio that exists for a long time, making it a good parameter to monitor.

With tighter tolerances on the processing techniques used to determine the BPO and sync frequencies it would be possible to reduce the ranges shown in Fig. 13. This could either be done manually, as was done to establish the data base from which Fig. 13 was developed, or automatically. Automating the procedure would require developing a software package to process the data. Such software development is beyond the scope of the current program, but is not beyond the capabilities of Rocketdyne's Analog Data Processing facility.

Finally, Fig. 17 shows the cumulative difference between the lower limit of the actual range in Fig. 13 and the upper limit of the ideal range versus time. This plot also illustrates when slipping was occurring, but in addition it tells how long the bearing operated with a given amount of slip-induced wear, similar to a "damage fraction" value. It is basically the same information as that in Fig. 13 but is presented in a format in which probable bearing condition is easier to assess. Determining a cutoff value for Fig. 17 would have to be determined empirically for the specific application, but it appears that a

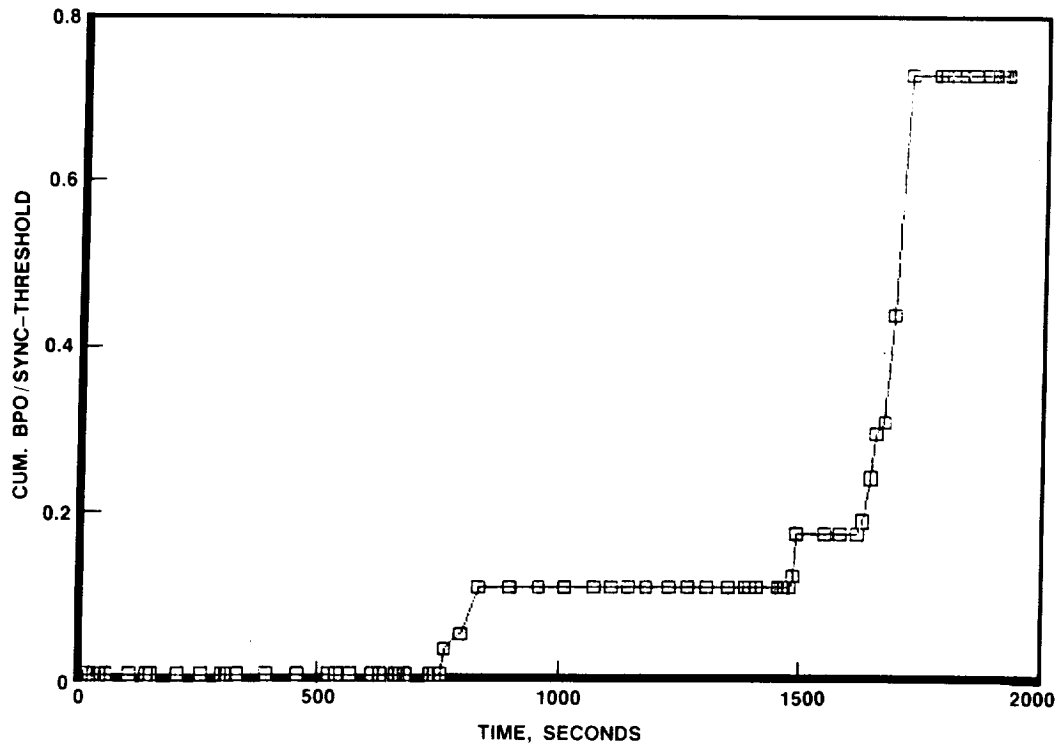


Fig. 17. Time Spent Over Threshold BPO/Sync (Entire Test)

good measure would be the rate of change at which the slippage is occurring. In Fig. 17, the cutoff would probably be between 1650 and 1750 seconds during the period of high slippage. Based on the other data obtained, this cutoff would occur before 2C and 3C began to register large changes, and long before sync began to register changes. The bearing, at this point, was probably at the end of its useful life but was not at the point of severe damage, which would eventually result in damage to the tester.

#### Conclusion

In conclusion, the algorithms deemed most useful for processing deflectometer data are the following:

1. 2C and 3C versus time, using histograms to determine cutoff values (Fig. 7 through 10).
2. BPO/Sync versus time using histograms to determine ideal range (Fig. 13 through 15).
3. BPO/Sync time over threshold versus time (Fig. 17).



Used together it is possible to produce a fairly clear picture of bearing condition with these algorithms. Eventually, through the empirical correlation of data, it may be possible to determine the weighting factors for 2C, 3C, and BPO/Sync versus time and its time over threshold to provide more reliable figures of merit for condition monitoring.

More importantly, though, is that the health of the bearing can be directly detected by installing the deflectometer in the turbopump. It will no longer be necessary to disassemble or borescope the bearings to determine their condition; the deflectometer data will provide this information. Significant reductions in maintenance and turnaround costs can be recognized by implementing the deflectometer into the turbopumps since bearing health will be easily known without disassembly or manual inspection. At the present time, the deflectometer is to be installed on a high pressure oxidizer turbopump for the SSME Technology Test Bed Program.

#### Bibliography

Barkhoudarian, S. and A. T. Zachary, Condition Monitoring for Space-Based Reusable Rocket Engines, presented at the ASME Winter Annual Meeting, New Orleans, Louisiana, December 1984

Hampson, M. E. and S. Barkhoudarian, Reusable Rocket Engine Condition Monitoring, presented at the Advanced High Pressure Oxygen/ Hydrogen Conference, Huntsville, Alabama, June 1984.

Hampson, M. E. and S. Barkhoudarian, Reusable Rocket Engine Condition Monitoring, presented at the SAE Aerospace Congress and Exposition, Long Beach, California, October 1984.

MacGregor, C. A., Reusable Rocket Engine Maintenance Study, Final Report, NASA CR-165569.

XI COMBUSTION AND COOLING PROCESSES I

Aerojet TechSystems Company  
Contribution to LOX/HC Combustion  
and Cooling Technology

S. D. Mercer  
D. C. Rousar  
Aerojet TechSystems Company

I. INTRODUCTION

Developing the capability to economically deliver large payloads to orbit has taken on national priority. This new heavy lift capability will require development of a new oxygen/hydrocarbon (LOX/HC) propellant booster engine. A development program could start as early as 1988-89.

Space Transportation Architecture Studies are underway to define both the vehicle and engine requirements. Engine concept studies are also in place that have as their objective the selection of fuels and engine power cycles; both near and far term concepts will be considered. The final design selections at the engine level will be dominated by technical issues associated with cooling and combustion devices.

Aerojet TechSystems Company (ATC) has been a leader in the field of LOX/HC technology. This paper addresses the LOX/HC combustion and cooling data generated by ATC programs of the past ten years. In addition, ATC is currently conducting LOX/HC combustion technology programs that could have a significant impact on future engine development. The scope and preliminary results from these ongoing programs are presented. Finally, recommendations are made in terms of how future technology programs might be focused in order to have maximum benefit to the engine development program.

II. SUMMARY OF PAST ATC TECHNOLOGY PROGRAMS/RESULTS

Aerojet has over 30 years of experience on oxygen/hydrocarbon propulsion systems. The Titan I program started in 1955. Over 240 engines were fabricated and tested. There were two basic configurations: the 150K lbf first stage engine, (shown during operation in Figure 1), and the 70K lbf second stage engine.

From 1970 to 1985, Aerojet conducted some 20 oxygen/hydrocarbon engine technology programs - about 2/3 of the programs funded during that time by the NASA and the Air Force. These programs can be classified into three technical categories: cooling technology programs, combustion devices programs, and engine system studies. They are summarized in the following paragraphs.

[REDACTED]

## A. COOLING TECHNOLOGY PROGRAMS

There were five cooling technology programs that generated technology potentially applicable to future oxygen/hydrocarbon engines: (1) heated tube tests on propane, (2) heated tube tests on liquid oxygen, (3) a transpiration cooled thrust chamber, (4) a "trans-regen" chamber, and (5) a graphite lined regeneratively cooled thrust chamber. These programs are summarized on Table 1 and in the following paragraphs.

### 1. Propane Heated Tube Tests

Tests on propane flowing in electrically heated tubes were conducted at the range of conditions summarized below. This work was part of the program reported in Reference 1 and is summarized in Reference 2.

Pressure:	450 to 1800 psia,
Temperature:	-250 to 250 F,
Velocity:	50 to 150 ft/sec,
Heat Flux:	up to 12 Btu/in. <sup>2</sup> sec,
Wall Temperature:	up to 1200 F,
Tube Diameter:	1/8 and 3/16 in.

This test program produced the following results relevant to forced convection, critical heat flux, flow oscillations, and coolant side coking.

#### a. Forced Convection Heat Transfer

Data were correlated with the equation shown on Figure 2. This type of correlation is complicated but it works. It is particularly good for matching the observed decrease in heat transfer coefficient at supercritical pressure as the wall temperature is increased. This characteristic is shown in Figure 3.

#### b. Flow Oscillations

Flow oscillations were observed at  $p/p_{cr}$  values  $\leq 1.65$ . They correlated with velocity and wall-to-bulk temperature ratio (Ref. 2).

#### c. Critical Heat Flux

The critical heat flux or burnout heat flux at subcritical pressure was found to be significantly higher than indicated by low velocity data generated during the 1960's. The following correlation was established but should be used with caution at temperatures less than -180 F.

$$\phi_{BO} = 0.5 + 0.000271 V \Delta T_{sub}$$

#### d. Coolant Side Coking

The coking characteristics of propane at 1800 psia were evaluated by conducting long duration tests at fixed heat flux conditions (see Figure 4) with a tube that is chemically compatible with hydrocarbons (Monel K-500). The results, summarized in Figure 5, show (1) that the coking characteristics of propane are about the same as RP-1 and (2) no significant improvement was obtained with high purity propane (natural grade is 95% pure, instrument grade is 99.9% pure).

### 2. Liquid Oxygen Heat Transfer

The heat transfer coefficient of supercritical liquid oxygen was measured at the following range of conditions and the correlation derived from the data is shown on Figure 6 (Ref. 3). This correlation was subsequently verified during  $LO_2$  cooled thrust chamber tests at LeRC (Ref. 4).

Pressure:	2500 to 5000 psia
Bulk Temperature:	173 to 391 R
Wall Temperature:	220 to 1714 R
Heat Flux:	1.2 to 55 Btu/in <sup>2</sup> -sec
Reynold's Number:	$1.5 \times 10^5$ to $3.2 \times 10^6$

### 3. Transpiration Cooled Chamber

A water transpiration cooled chamber fabricated from photo-etched platelets was designed and fabricated for use at the Air Force Rocket Propulsion Lab. as a re-entry nosetip test device (Ref. 5). The  $H_2O$  coolant flow rate was approximately 10% of the hot gas flow rate. The design was based on the ARES thrust chamber, shown on Figure 7. This chamber proved to be extremely durable as it was subsequently fired over 200 times with oxygen/Benzonitrile ( $C_6H_5CN$ ) at a nominal chamber pressure of 3000 psi. A test firing is shown on Figure 8. Carbon deposition occurred in significant amounts but never interfered with the transpiration cooling effectiveness.

### 4. Trans-Regen Chamber

The concept of a regeneratively cooled chamber which has a transpiration cooled throat was

successfully demonstrated during the test program reported in Reference 6. The transpiration coolant was  $\text{GH}_2$ .

#### 5. Graphite-Lined Chamber

A graphite-lined regeneratively cooled chamber was tested with FLOX/methane propellants very successfully in the test program reported in Reference 7. Twenty firings were conducted at 500 psia chamber pressure for a total duration of 540 seconds. The chamber wall operated at a temperature over 4000 F and no wall erosion occurred. A post-test photograph of the chamber is shown in Figure 9.

#### B. COMBUSTION DEVICES PROGRAMS

Aerjet has conducted an extensive list of combustion devices programs - all within the past 10 years. They are summarized on Table 2 and described in the following paragraphs.

##### 1. Carbon Deposition

The generation and deposition of carbon were studied using subscale hardware with LOX/RP-1 propellants. Deposition on a turbine simulator at preburner or gas generator conditions was evaluated at fuel rich mixture ratios of 0.25 to 1.0 and chamber pressures of 750 to 1500 psia. Deposition on the combustion chamber wall was investigated at main chamber mixture ratios of 2.0 to 4.0 and chamber pressures of 1000 to 1500 psia (Ref. 8).

Fuel Rich Preburner Tests - Ignition on all tests was reliable and smooth. The measured combustion efficiencies were consistent with previous test programs and were within about 5% of predictions from a fuel rich combustion model. The carbon content in the exhaust plume varied with mixture ratio as shown in Fig. 10. Pre and post test examination of the turbine simulator showed that significant soot build-up occurred in all but one test, and that the buildup increased at the higher mixture ratios. No deposition was observed during a 100 sec test at 0.25 mixture ratio and 750 psia pressure.

Subsequent follow-on tests have been conducted at fuel rich mixture ratios and are discussed in the next section. Future tests are also planned which will include testing with propane and methane fuels.

Main Combustion Chamber Tests - Ignition on all tests was reliable and smooth. Very high combustion efficiency, >99%, was achieved at the nominal design mixture

ratio of 3.0. Efficiency dropped slightly at both higher and lower mixture ratios but still remained relatively high compared to the 90-93% range of the operational LOX/RP-1 engines developed during the 1955 - 1965 era. No carbon content was ever visible in the exhaust plume during steady state operation.

The approach used to determine carbon deposition for main chamber operating conditions was to measure heat flux versus time. This approach was successfully used previously (Reference 1) for LOX/propane testing at 300 psi chamber pressure.

The measured heat flux did not decrease with firing time as expected for any of the locations in the chamber over the range of operating conditions tested and no significant carbon build-up was noted on the chamber walls during post test inspection. Measured heat fluxes were typical for "clean wall" operating conditions and followed expected "clean wall" trends. This lack of carbon deposition is not consistent with the experience of the industry during previous LOX/RP-1 development programs, Titan I and F-1 for example, and is probably due to the higher pressure and higher combustion efficiency.

## 2. Dual Throat Thermal Model

A program to determine heat flux distributions at critical locations in a dual nozzle chamber with series throats is currently being completed at Aerojet and key results will be published in Reference 9. The dual nozzle concept, heat transfer issues, and the dual throat calorimeter chamber test setup are shown on Figure 11. This engine concept offers a low weight approach to achieving both high thrust - low area ratio operation and low thrust - high area ratio operation.

## 3. Ignition Characteristics

This program defined the ignition characteristics and thruster pulse mode capabilities of the GOX/ethanol propellant combination which was chosen based on a systems analysis of the space shuttle.

Ignition limits were defined in terms of mixture ratio and cold flow pressure using a spark initiated torch igniter. Igniter tests were run over a wide range of cold flow pressure, propellant temperature and mixture ratio (Figure 12). The product of cold flow pressure and igniter chamber diameter was used to correlate mixture ratio regimes of ignition and non-ignition. Engine ignition reliability and pulse mode capability were demonstrated using a 620 lbF

thruster with an integrated torch igniter. The nominal chamber pressure and mixture ratio were 150 psia and 1.8, respectively. Thruster tests were run over a wide range of chamber pressures and mixture ratios. The feasibility of thruster pulse mode operation with the non-hypergolic GOX/ethanol propellant combination was demonstrated with pulse durations and coast times as low as 60 milliseconds. Igniter designs for oxygen/propane and oxygen/methane were also fabricated.

#### 4. Oxygen Compatibility

Oxygen compatibility studies were conducted as part of the Aerojet OTV program. Rubbing and particle impingement tests were performed at White Sands and the results were correlated using a burn factor parameter. Some of the rubbing test results, and a definition for the burn factor are shown on Figure 13.

#### 5. High Pressure Preburner

High-pressure combustion of fuel-rich and oxidizer-rich LOX/RP-1 propellants was experimentally evaluated using 4.0-inch diameter prototype preburner injectors and chambers. Testing covered the pressure range of 1292 to 2540 psia. Fuel-rich mixture ratios ranged from 0.238 to 0.367; oxidizer-rich mixture ratios ranged from 27 to 48.

Performance, gas temperature uniformity, and stability data were measured for two fuel-rich and two oxidizer-rich preburner injectors. One was a conventional like-on-like design, and the other was a platelet design injector.

The performance data are summarized on Figure 14. Measured fuel-rich gas composition and C\* performance are in excellent agreement with kinetic model predictions indicating kinetically-limited combustion. The oxidizer-rich test results indicate equilibrium combustion as predicted.

#### 6. LOX/RP-1 Injector and LOX/Methane Injectors

During these programs, 40K lbf injectors were designed for LOX/RP-1 and LOX/Methane propellants, fabricated, and delivered to MSFC for testing. The LOX/RP-1 injector was subsequently tested at MSFC and the results are summarized in a recent JANNAF paper by Rex Bailey. The LOX/methane injector is scheduled to be tested soon. Photographs of both injectors are shown in Figure 15.

#### 7. High Density Fuel Program



The objective of this program was to determine the combustion and heat transfer characteristics of LOX/RP-1 propellants in the 1000 and 2000 psia chamber pressure range. This was accomplished through the design, fabrication, and testing of injectors with two different patterns. Testing was conducted with both uncooled and cooled "workhorse" chambers and with a calorimeter chamber over a range of pressures and mixture ratios. A LOX/RP-1 torch spark igniter was also designed and demonstrated.

The thrust chamber testing was conducted in 2 parts: an injector test series with water-cooled and graphite "workhorse" chambers and a calorimeter chamber test series. Test durations up to 30 sec with multiple mixture ratio points were included in this series. Other test variables included chamber pressures ranging from 1040 to 1960 psia, fuel temperatures of 50° to 250°F, and chamber lengths of 11 and 15 in.. Hot fire test photographs are shown on Figure 16. Heat flux data are summarized in Figure 17.

The calorimeter chamber data showed that local heat fluxes were below those predicted near the injector and 70% greater than those predicted in the throat. Although the calorimeter chamber was blackened by the testing, the heat transfer data, combined with the very light to nonexistent sooting near the injector, gave no indication of the existence of a soot thermal barrier.

The measured injector performance ranged from 95 to 97.5% ERE (energy release efficiency) depending on the injector pattern and operating conditions. Analysis of the performance data indicated the primary loss mechanism to be low mixing efficiency. The PAT pattern was stable under all operating conditions. However, there were several instances of spontaneous 1-T instability encountered with the TLOL pattern.

#### 8. Combustion Performance and Heat Transfer Program

This program consisted of the three major task areas described below.

##### Task I - Regenerative Cooling Characterization

Forced convection and nucleate boiling heat transfer data and correlations available in the literature for candidate hydrocarbon fuels were reviewed. Those candidates included propane, methane, RP-1, and ammonia. Regenerative chamber cooling analyses were then conducted to compare the

cooling capabilities of each fuel and determine the operating point (thrust and chamber pressure) limits imposed thereby.

#### Tasks II and IV - Subscale Injector Characterization

Tasks II and IV involved the design, fabrication, testing and data analysis of subscale hardware, i.e., nominal thrust of 1000-lbF, to evaluate the combustion performance, stability, and gas-side heat transfer characteristics of liquid oxygen/hydrocarbon propellants. Four injector patterns were tested, including conventional OFO triplets and like-on-like doublets, and platelet injector patterns. Heat sink and water-cooled calorimeter chambers were utilized, and a removable chamber section was used with the former to allow evaluation of chamber length effects. A fuel film coolant ring was used in conjunction with the triplet and platelet injectors. An adjustable acoustic cavity section provided combustion stability. Both propane and ethanol fuels were tested as shown in Figure 18.

#### Task III - Preliminary Engine System Characterization

In Task III numerous engine operating points were analyzed to determine engine performance and weight figures for orbit maneuvering reaction control system thrusters. The work built upon the regenerative cooling studies of Task I and extended to include turbomachinery for pump-fed systems, alternative chamber materials for the orbit maneuvering thruster, and film cooling for the reaction control thrusters. Thruster envelopes were defined by the current engines on the Space Shuttle.

### 9. Photographic Combustion

An experimental and analytical program was conducted to determine if high-speed photography techniques could be utilized to increase the analytical understanding of oxygen/hydrocarbon combustion. The program was conducted in two phases. The objective of Phase I was to demonstrate the advantages and limitations of using high-speed photography to identify potential combustion anomalies (e.g., pops, fuel freezing, reactive stream separation [RSS], carbon formation). The objective of Phase II was to develop combustion evaluation criteria for evaluating promising low-cost propellant combinations and injector elements.

Carbon formation and RSS mechanisms and trends were identified by using high-speed color photography at speeds up to 6000 frames/sec. Single element injectors were tested with LOX/RP-1, LOX/Propane, LOX/Methane and LOX/Ammonia

propellants. Tests were conducted using seven separate injector elements. OFO Triplet; Rectangular Unlike Doublet (RUD); Unlike Doublet (UD); Like-on-Like Doublet (LOL-EDM); Slit Triplet, Transverse Like-on-Like Doublet (TLOL), and the Pre-Atomized Triplet (PAT). All seven injectors were fired at main engine conditions. The RUD and LOL-EDM were also fired at gas generator mixture ratios. Chamber pressure ranged from 125-1500 psia, fuel temperatures ranged from  $-245^{\circ}\text{F}$  to  $158^{\circ}\text{F}$ , and fuel velocities ranged from 48-707 ft/sec. High speed test photographs of the testing are shown on Figure 19.

#### 10. Analysis of Carbon Formation Mixing

This study was an attempt to verify the hypothesis of fuel-vaporization limited carbon formation through analysis of the data from the photographic combustion program.

By applying the Priem-Heidmann Generalized-Length vaporization correlation, the computer model developed predicted the observed spatial variation of propellant vaporization rate, using injector cold-flow results to define the stream tubes. The calculations show that the overall and local propellant vaporization rate and mixture ratio change drastically as the injection element type or the injector operating condition is changed. These results were compared with the regions of carbon formation observed in the photographic combustion testing. The correlation showed that the fuel vaporization rate and the local mixture ratio produced by the injector element have first order effects on the degree of carbon formation. Low fuel vaporization rates significantly increase the degree of carbon formation. Also, fuel rich zones containing vaporizing liquid fuel are sources of carbon formation. For similar injector operating conditions, propane produced less carbon formation than RP-1 because of its higher vaporization rate. Chamber pressure also appeared to have an effect on carbon formation which is observed to decrease with increasing pressure.

#### 11. Dual Throat Cold Flow

The dual throat concept provides a means to obtain a large area ratio adjustment within a single thrust chamber assembly without the need for extendable nozzles. The concept was evaluated with cold flow (nitrogen gas) testing and through analysis for application as a tripropellant engine for single-stage-to-orbit type missions.

Three modes of operation were tested and analyzed: (1) Mode I Series Burn, (2) Mode I Parallel Burn,

and (3) Mode II. Primary emphasis was placed on the Mode II plume attachment aerodynamics and performance.

The conclusions from the test data analysis are as follows: (1) the concept is aerodynamically feasible, (2) the performance loss is as low as 0.5 percent, (3) the loss is minimized by an optimum nozzle spacing corresponding to an AF/ATS ratio of about 1.5 or an  $L_e/R_{tp}$  ratio of 3.0 for the dual throat hardware tested, requiring only 4% bleed flow, (4) the Mode I and Mode II geometry requirements are compatible and pose no significant design problems.

### C. ENGINE SYSTEM STUDIES

The more significant engine system studies which were conducted are summarized in Table 3.

#### 1. Advanced Oxygen/Hydrocarbon Engine Study

This study, completed in 1981, is currently being updated. It consisted of an evaluation of the hydrocarbon engine options based on the technology available at that time.

Parametric engine data were generated over a range of thrust levels from 200K to 1.5M lbF and chamber pressures from 1000 to 5000 psia. Engine coolants included RP-1, refined RP-1,  $CH_4$ ,  $C_3H_8$ ,  $LO_2$ , and  $IH_2$ .

Oxygen/RP-1 G.G. cycles were found to be not acceptable for advanced engines. The highest performing oxygen/RP-1 staged combustion engine cycle identified utilized oxygen as the coolant and incorporated an oxidizer-rich preburner. The highest performing cycle for oxygen/ $CH_4$  and oxygen/ $C_3H_8$  utilized fuel cooling and incorporated both fuel- and oxidizer-rich preburners. Oxygen/HC engine cycles permitting the use of a third fluid (hydrogen) coolant and a hydrogen-rich gas generator provided higher performance at significantly lower pump discharge pressures. The oxygen/HC dual-throat engine, because of its high altitude performance, was found to deliver the highest payload for the vehicle configuration investigated.

#### 2. Dual Fuel, Dual Throat Engine, and Dual Nozzle Aerodynamics and Cooling

In these two programs, the dual nozzle engine idea was explored and identified as a viable SSTD candidate. Two basic dual nozzle configurations were evaluated: series throat, and parallel throat.

### 3. Advanced High Pressure Engine For Dual Mode Applications

In this pioneering study, engines for mixed mode SSTO propulsion systems were evaluated. The mode 1 engine operated with oxygen and a high density fuel. The mode 2 engine propellants were oxygen-hydrogen. Five mode 1 fuels were considered: RP1, RJ5, hydrazine, MMH, methane. Cooling with propellants and auxiliary coolants were considered. Preliminary designs were established for the mode 1 engine and a dual fuel engine.

### III. STATUS OF ONGOING ATC TECHNOLOGY PROGRAMS

ATC is currently under contract for four LOX/HC programs, two engine studies and two combustion technology programs. The two combustion technology programs are 1) Carbon Deposition Model for Oxygen-Hydrocarbon Combustion; NAS8-34715, and 2) Oxygen/Hydrocarbon Injector Characterization; F04611-85-C-0100. The status and some recent results from the two combustion programs are presented in the following paragraphs.

#### A. CARBON DEPOSITION

Testing was resumed on the program in the fall of 1985. The purpose of this testing was to confirm the earlier test results with LOX/RP-1 and investigate the impact of the shutdown transient on test-to-test carbon build-up. The 2.38 inch diameter test rig is shown schematically in Figure 20. Figure 21 shows the test set up. Thirty data points were gathered covering a range of gas generator operating conditions of mixture ratio (.20 to .40) and chamber pressure (750 to 1500 psia).

The data confirmed the earlier results in terms of deposition rates and demonstrated that the test-to-test carbon build-up can be significantly affected by the shutdown transient. The recent data also show that there appears to be a very narrow mixture ratio band where carbon deposition is minimized or perhaps even eliminated. Figure 22 shows the ratio of pressure across the turbine simulator at the beginning and end of the individual tests. As shown, a mixture ratio of 0.28 minimizes the rate of carbon build-up.

A post-test photograph of the turbine simulator is shown in Figure 23. The carbon build-up is significant but of interest is the presence of the small hollow beads lodged between the tubes of the turbine simulator. It is believed that these are the remnants of tube-like formations that have grown around the fuel streams at the injector face. Similar phenomenon have been noted at ATC using metalized propellants.

The program recently has been expanded to include testing of the same hardware using propane and methane fuels. The objective of this testing is to compare the carbon deposition characteristics of these fuels with RP-1. A second objective will be to obtain performance and gas temperature data at gas generator conditions. The latter data does not exist for propane.

#### B. OXYGEN HYDROCARBON INJECTOR CHARACTERIZATION

The Air Force through AFRPL has taken a significant step towards solving the major technical issue associated with LOX/HC propellants; namely, injector performance and combustion stability. This three year program, which represents a significant investment by the Air Force, was undertaken by ATC in October of 1985 and has as its objective the establishment of a generic combustor characterization methodology. This methodology, if successful, could ultimately eliminate the need for TCA level testing and associated facility costs on future engine development programs. The methodology will greatly reduce the risk of encountering combustion stability and performance problems and eliminate the need for full-scale injector design iterations.

Other program objectives include the following: the methodology will consist of only analysis tools and reduced-sized hardware testing; can be used by industry; is applicable to large size engines; and, finally, it must be valid for different fuel types, design and operating conditions. Testing is planned on all the hydrocarbon fuels of interest including RP-1,  $\text{CH}_4$  and  $\text{C}_3\text{H}_8$ , chamber pressures of up to 2000 psia and thrust levels of up to 300,000 lbf.

The program consists of two phases and associated technical objectives as follows: Phase I - Formalize the Methodology, Phase II - Validate the Methodology. The overall program schedule is shown in Figure 24. As shown, the validated methodology will be available for the potential engine development, and we have completed Phase I.

The methodology which we will begin to validate with test data beginning December of this year is described in the following.

The entire injector design process, defined by the methodology, is shown in Figure 25, and considers a large number of requirements and involves several technical disciplines. We have grouped the activities into five elements shown graphically in Figure 25 and defined in Figure 26. The methodology then is really a procedure that prescribes how the five elements will be performed, what analysis tools will be

used, and how the analysis models will be anchored with test data. Figure 26 shows the models that have been selected, the four levels of reduced size testing that have been specified, and the interrelationship between the testing and the analysis models. The testing anchors the specified models which are used to calculate performance and stability and make predictions for the next test level.

The four test levels include uni-element cold flow, multi-element hot fire testing, three-dimensional, reduced size testing and two-dimensional chamber hot fire tests. Uni-element cold flow tests (full size element) provide (a) relative droplet size, (b) an estimate of atomization distance, (c) mixing efficiencies, (d) O/F profiles, and (e) element pressure drop. Multi-element tests are conducted to (a) define energy release efficiency, (b) define the mixing and vaporization characteristics, (c) film or barrier cooling loss trends, and (d) measurements of the combustion profile. The combination of three and two-dimensional testing allows the stability characteristics of the full-scale element to be evaluated over the entire acoustic frequency range of the full-scale engine. The three-dimensional reduced size combustion chamber is sized such that the first tangential mode corresponds to the third tangential mode of the full size engine. Likewise, the two-dimensional chamber is sized such that the first width mode corresponds to the first tangential mode of the full-size engine. Damping devices can also be evaluated as appropriate. In addition to stability data the three-dimensional chamber data confirms the ability to extrapolate performance data with thrust level. As indicated previously, the specified analytical models are anchored with specific data with each test series. The concluding activity then is the projection of the full-scale injector performance, compatibility and stability characteristics.

As discussed, the methodology will be validated with test data on Phase II of our program beginning in December of this year. Approximately 120 tests using RP-1, CH<sub>4</sub> and C<sub>3</sub>H<sub>8</sub> using multi-element, three-dimensional and two-dimensional hardware will be conducted. Triplet (F-O-F), like doublets and coax injection elements, will be included in the validation program as well as acoustic cavities and baffles.

#### IV. FUTURE TECHNOLOGY ISSUES/RECOMMENDATIONS

At this time, it is not clear what the design concept of the next generation booster engine will be or even which hydrocarbon fuel will be selected. It is clear, however, that the design requirements will include long life and minimum maintenance. It is also unfortunate that only a limited investment has been made in IOX/HC propulsion technology due to

other priorities. If the next generation engine is to meet the necessary development and operational goals, then the resources that are available must be focused and key issues addressed. Table 4 presents a list of recommended technologies and the rationale for their selection. Included in the table are technology issues covering the areas of cooling, combustion, turbomachinery and health monitoring. Clearly, this represents a shopping list which must be continuously reviewed as the time available prior to engine development diminishes.

#### References

1. Michel, R. W., "Combustion Performance and Heat Transfer Characterization of LOX/Hydrocarbon Type Propellants," Vol. 1, Final Report, 15958T-1548-MA-129T-003F, Aerojet Liquid Rocket Company, Contract NAS 9-15958, April 1983.
2. D. C. Rousar, R. S. Gross, "Supercritical Convection, Critical Heat Flux, and Coking Characteristics of Propane," AIAA-84-1263, June 1984, Cincinnati, OH.
3. Spencer, R. G., Rousar, D. C., and Price, H. G., "LOX Cooled Thrust Chamber Technology Developments," Journal of Spacecraft and Rockets, Vol. 17, No. 1, Jan.-Feb., 1980.
4. Price, H. G., "Cooling of High Pressure Rocket Thrust Chambers with Liquid Oxygen," Journal of Spacecraft and Rockets, Vol. 18, No. 4, July-August 1981.
5. Hickman, J. E., "ABRES Nostip Thrust Chamber Assembly Tester," AFRPL-1R-76-25, 1976.
6. H. W. Valler, "Performance of A Transpiration-Regenerative Cooled Rocket Thrust Chamber," NASA CR 159742, 1979.
7. V. R. Stubbs, "A Graphite-Lined Regeneratively Cooled Thrust Chamber," NASA CR-120853, NAS 3-13315.
8. M. F. Lausten, D. C. Rousar, "Carbon Deposition With LOX/RP-1 Propellants," AIAA-85-1164, July 1985, Monterey, CA.
9. R. L. Ewen, C. J. O'Brien, "Dual Throat Thruster Test Results," AIAA-86-1518, June 1986, Huntsville, Alabama.
10. B. R. Lawver, D. C. Rousar, "Ignition Characterization of the GOX/Ethanol Propellant Combination," AIAA-84-1467, June 1984, Cincinnati, OH.



11. L. Schoerman, "Selection of Burn Resistant Materials for Oxygen-Driven Turbopumps," AIAA-84-1287, June 1984, Cincinnati, OH.
12. B. R. Lawver, "Test Verification of LOX/RP-1 High Pressure, Fuel/Oxidizer-Rich Preburner Designs," AIAA-82-1153, June 1982, Cleveland, OH.
13. L. Schoerman, R. S. Gross, "Design, Fabrication, Test and Delivery of a High-Pressure Oxygen/RP-1 Injector," NAS 8-33651, Report 33651F, 1979.
14. H. W. Valler, "Design, Fabrication, and Delivery of a High Pressure LOX-Methane Injector," NAS 8-33205, Report 33205F, 1979.
15. R. J. LaBotz, D. C. Rousar, H. W. Valler, "High-Density Fuel Combustion and Cooling Investigation," NASA CR 165167, 1980.
16. D. C. Judd, "Photographic Combustion Characterization of LOX/Hydrocarbon Type Propellants," NAS 9-15724, Report MA-262T, 1980.
17. J. Fang, "LOX/Hydrocarbon Fuel Carbon Formation And Mixing Data Analysis," CR 169006, NAS 3-22823.
18. R. B. Lundgreen, G. R. Nickerson, C. J. O'Brien, "Dual Throat Thruster Cold Flow Analysis," NAS 8-32666, Report 32666F, 1978.
19. C. J. O'Brien, R. L. Ewen, "Advanced Oxygen-Hydrocarbon Rocket Engine Study," Report 33452F, NAS 8-33452, 1981.
20. C. J. O'Brien, "Dual-Fuel, Dual-Throat Engine Preliminary Analysis," Report 32967F, NAS 8-32967, 1979.
21. G. M. Meagher, "Dual Nozzle Aerodynamic and Cooling Study," Report 33553-F, NAS 8-33553, 1981.
22. W. P. Luscher, J. A. Mellish, "Advanced High Pressure Engine Study for Mixed-Mode Vehicle Applications," NASA CR 13514, NAS 3-19727.

Table 1 - LOX/Hydrocarbon Cooling Technology Programs

<u>Program</u>	<u>Coolant</u>	<u>Refer- ence</u>	<u>Date</u>	<u>Scope/results</u>
Combustion performance and heat transfer	$C_3H_8$	1, 2	1980	Heated tube tests Supercritical $H_L$ Subcritical $H_L$ Coking same as RP1
Oxygen heat transfer	$LO_2$	3, 4	1977	Heated tube tests Supercritical $H_L$ LeRC LOX/RP1 tests 20K/2000 psi Leak OK
ANTCAT	$H_2O$	5	1976	Transpiration cooled chamber Re-entry nosetip test device 50K 3000 psi, 200 firings $LOX/C_6H_5$ CN
Trans-regen	$GH_2$	6	1976	Transpiration cooled throat Concept demonstrated
Graphite-lined regeneratively cooled thrust chamber	$CH_4$	7	1972	5000 lbF, 500 psia Chamber - $CH_4$ regen cooled graphite lined No erosion, 540 sec (20 Firings) $T_{wg} > 4000^{\circ}F$

Table 2 - LOX/Hydrocarbon Combustion Devices Programs

<u>Program</u>	<u>Fuel</u>	<u>Refer- ence</u>	<u>Date</u>	<u>Scope/results</u>
Carbon deposition	RP1	8	1986	MC - no deposit, 1000-2000 psia 98% efficiency GG - deposits measured - no test-to-test buildup
Dual throat thermal model	H <sub>2</sub>	9	1986	Q/A measured, mode 1 and mode 2 Data analysis in progress
Ignition characteristics	Ethanol C <sub>3</sub> H <sub>8</sub> CH <sub>4</sub>	10	1984	Ox/ethanol igniter Ox/ethanol thruster Future tests at JSC
O <sub>2</sub> Compatibility (OTV)	-	11	1984	Rubbing, particle impingement test Burn factor correlation Applicable to Ox-rich turbine drive
High pressure preburners	RP1	12	1982 1981	Fuel rich/ox rich preburners Pc = 1300 - 2500 psia Perf/stab/temp
LOX/RP1 injector	RP1	13	1981	40K/3000 psi Recent test, MSFC
LOX/methane injector	CH <sub>4</sub>	14	1979	40K/3000 psi Future test, MSFC
High density fuel	RP1	15	1979	20K/2000 psi Igniter Injector Chamber
Combustion performance and heat transfer	C <sub>3</sub> H <sub>8</sub> C <sub>2</sub> H <sub>5</sub> OH	1	1983	1K/300 psi Injector Chamber

Table 2 - LOX/Hydrocarbon Combustion Devices Programs (cont.)

<u>Program</u>	<u>Fuel</u>	<u>Refer- ence</u>	<u>Date</u>	<u>Scope/results</u>
Photographic combustion	RP1 C <sub>3</sub> H <sub>8</sub> NH <sub>3</sub>	16	1979	Uni-element injector tests  7 element types Photographic study
Analysis of carbon formation and mixing	above	17	1983	Combustion analysis Carbon formation related to fuel vaporization rate
Dual throat cold flow	-	18	1978	Cold flow testing Aerodynamic feasibility

Table 3. LOX/Hydrocarbon Engine System Studies

<u>Programs</u>	<u>Fuel</u>	<u>Refer- ence</u>	<u>Date</u>	<u>Scope/results</u>
Advanced oxygen hydrocarbon Engine	RP-1 CH <sub>4</sub>  C <sub>3</sub> H <sub>8</sub>	19	1981	Evaluation - LOX/HC engine options  Chamber pressure limits Potential performance  Payload Capabilities - 2 stage HLLV Conventional, dual throat nozzles
Dual fuel, dual throat Engine	RP1/H <sub>2</sub>  CH <sub>4</sub> /H <sub>2</sub>	20	1979	Parametric study  Preliminary baseline defined  Viable SSTO candidate
Dual nozzle aerodynamics and cooling analysis	-	21	1979	Dual throat, dual expander concepts feasible
Advanced high pressure engine for Dual Mode Applications	RP-1 RJ-5 CH <sub>4</sub>	22	1977	SSTO mixed mode propulsion 2 sets of engines  Mode 1 - high density Mode 2 - high performance  Series and parallel burn Parametric study Preliminary design - Mode 1 - dual fuel

Table 4  
Technology Issues/Recommendations

Technology Area	Issue	Rationale/Objective
Cooling	Hydrocarbon Fuel Copper Alloy Compatibility	High Pressure LOX/HC Thrust Chambers will be Fabricated from Copper Alloys
	LOX Cooling Demonstration	Existing Data Shows Corrosion of Copper by HC Fuels (Failure in ~ 10 Missions)
	Thrust Chamber Cooling Demonstration	If HC Fuel Cooling is not Acceptable, then LOX Cooling is the Only Alternative to Tripropellant Systems.
	Low Cost/Long Life	Has been Shown to be Technically Feasible  Show Life and Performance Goals can be Achieved with LOX/HC Systems
Combustion	Heavy HC Performance and Compatibility	Heavy Hydrocarbons (RP-1) have Shown Higher than Predicted Thrust Chamber Heat Fluxes Coupled with Low Performance
	Alternative Ignition	Low Maintenance, Reusable Engines will Require a Reliability and Nondamaging Ignition Source
Turbomachinery	Uniform Drive Fluid	Turbine Life Historically Controlled by Drive Fluid Temperature Uniformity and Start and Shut-Down Transients
	Long Life/Low Cost	Long Life Bearings and Seals will be Required  State of the Art Design/Fabrication Processes must be Applied in Order to Reduce Costs
Health Monitoring	Sensor Compatibility with Rocket Engine Environment	Anticipated Operational Requirements will Require Diagnostic Measurements

ORIGINAL PAGE IS  
OF POOR QUALITY

1st Stage - 300K      2nd Stage - 80K

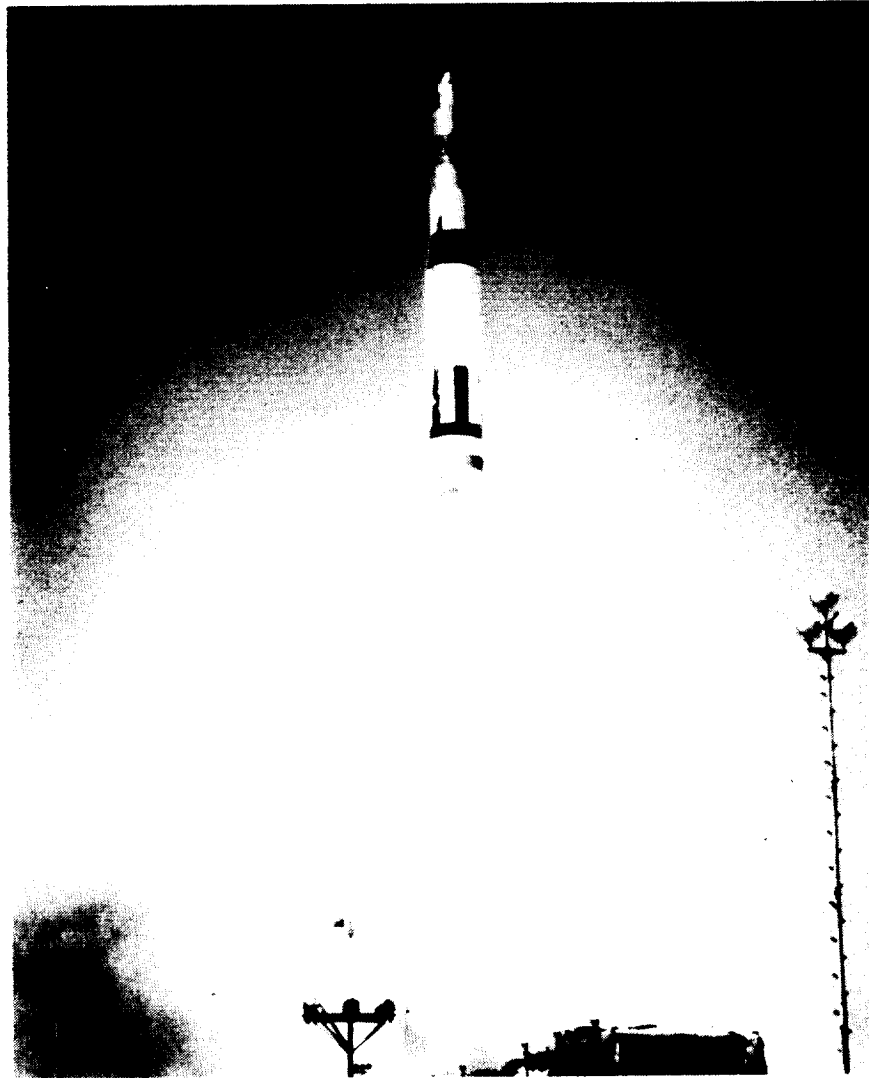
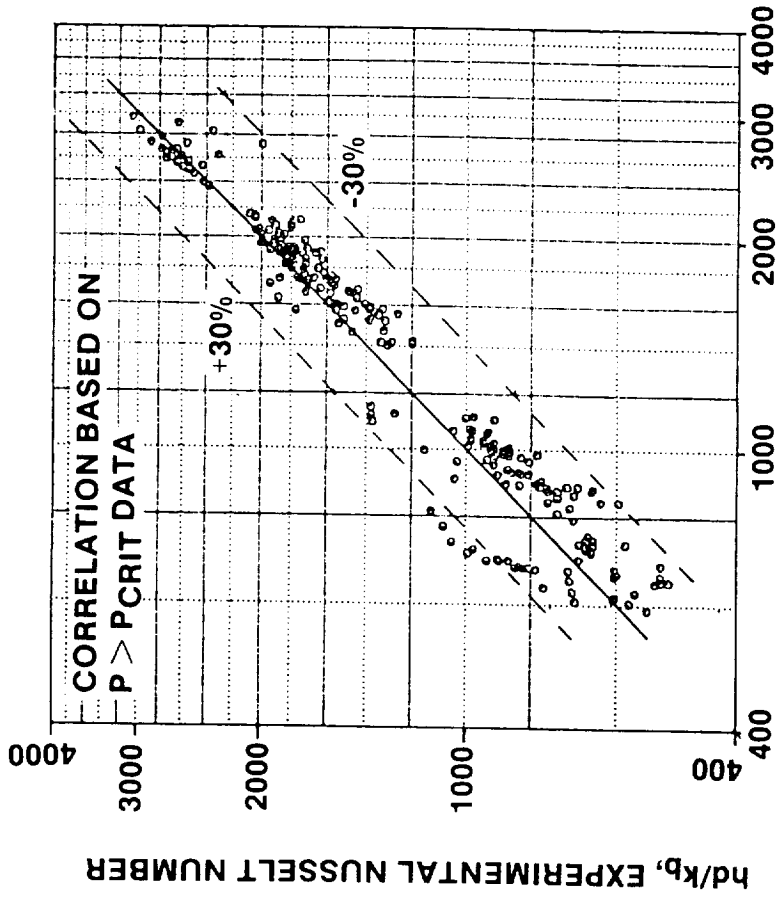


Figure 1. Titan I Launch

ORIGINAL PAGE IS  
OF POOR QUALITY



$$.00569 \text{Re}_b^{.88} \text{Pr}_b^{.4} \left(\frac{\rho_b}{\rho_w}\right)^{.12} \left(\frac{\mu_b}{\mu_w}\right)^{-.13} \left(\frac{k_b}{k_w}\right)^{.83} \left(\frac{C_p}{C_{p,b}}\right)^{-.37} \left(\frac{P}{P_{cr}}\right)^{.25} \left(1 + \frac{2}{L/D}\right)$$

Figure 2. Supercritical Propane Heat Transfer Data



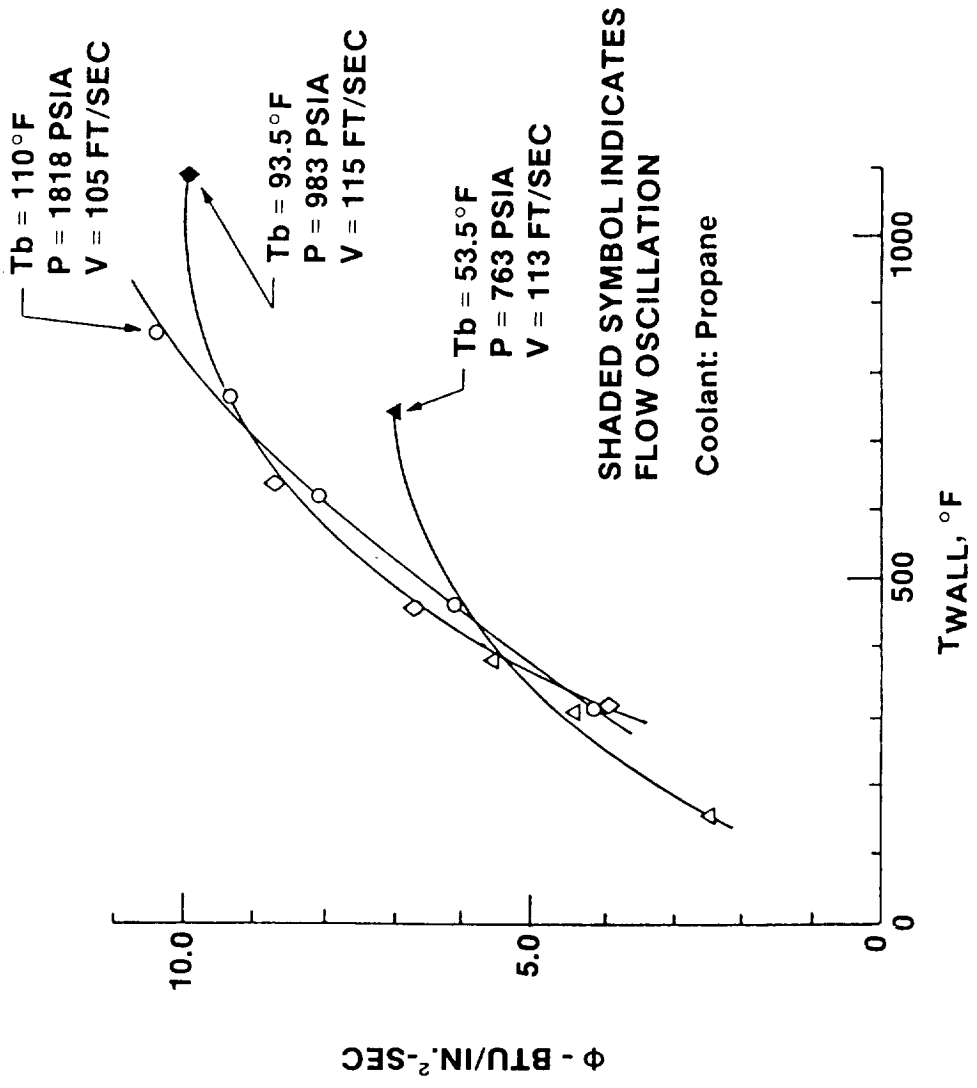


Figure 3. At Supercritical Pressures,  $h_L$  Decreased As  $T_{Wall}$  Increased

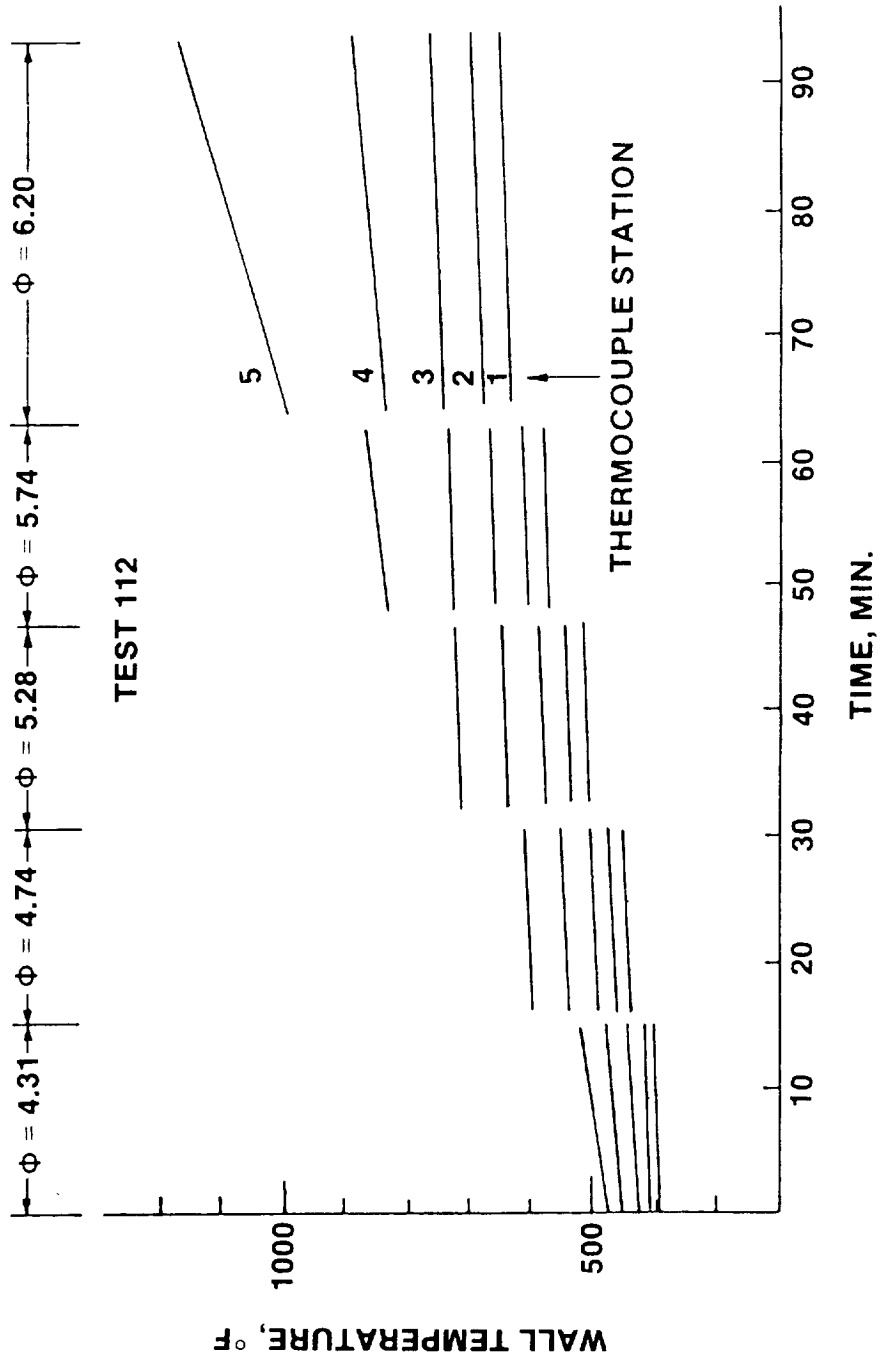


Figure 4. Propane Coking Test Data

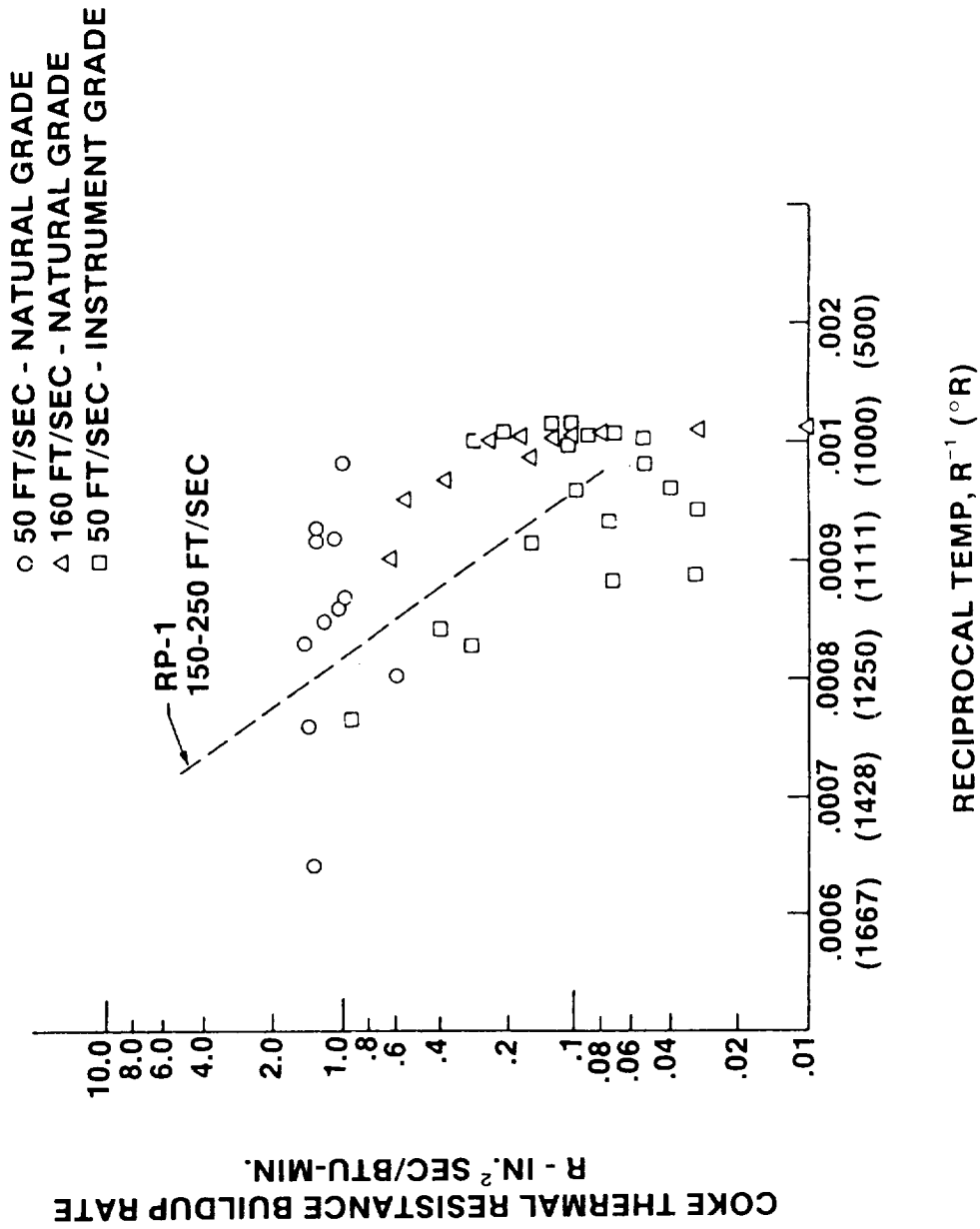
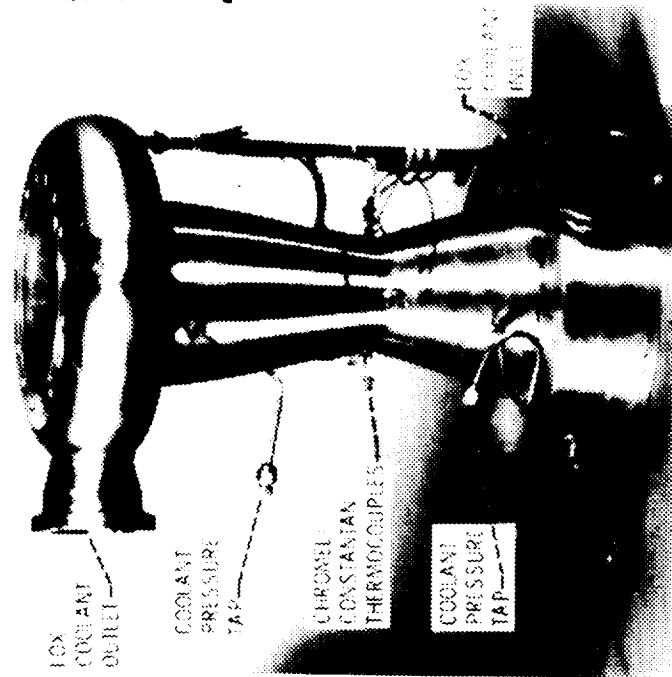
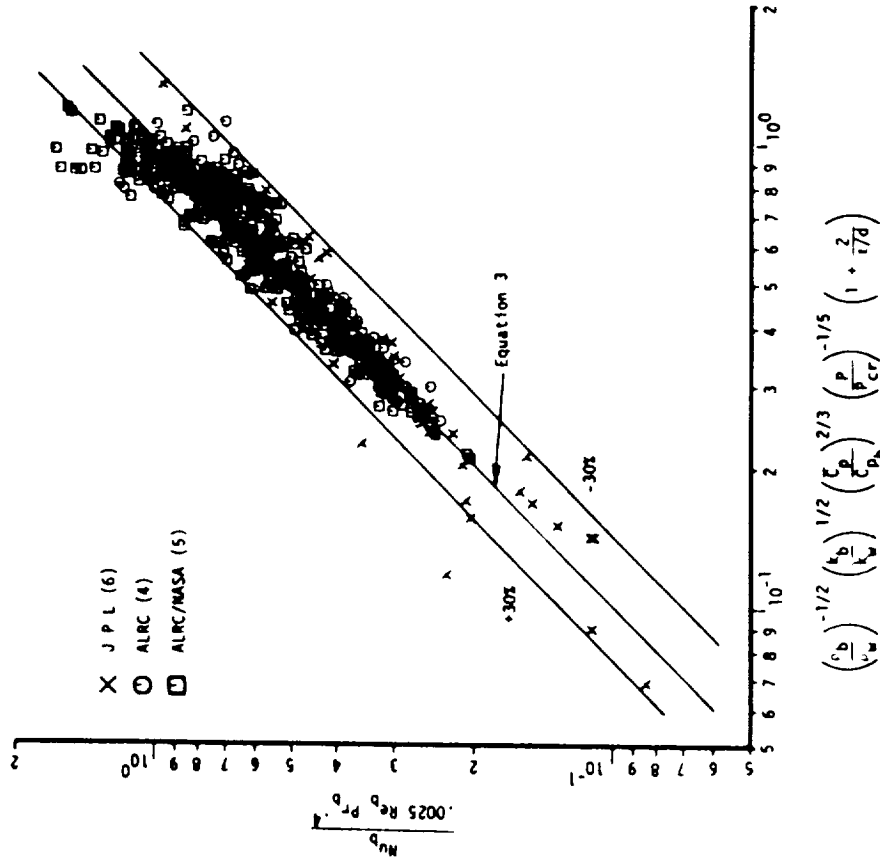


Figure 5. Propane Coking Rates

ORIGINAL PAGE IS  
OF POOR QUALITY



Thrust chamber S/N 2.



Recommended Correlation

Figure 6. The Aerojet LOX Correlation Has Been Test  
Verified At LeRC With LOX/RP-1 At 2000 psia

ORIGINAL PAGE IS  
OF POOR QUALITY

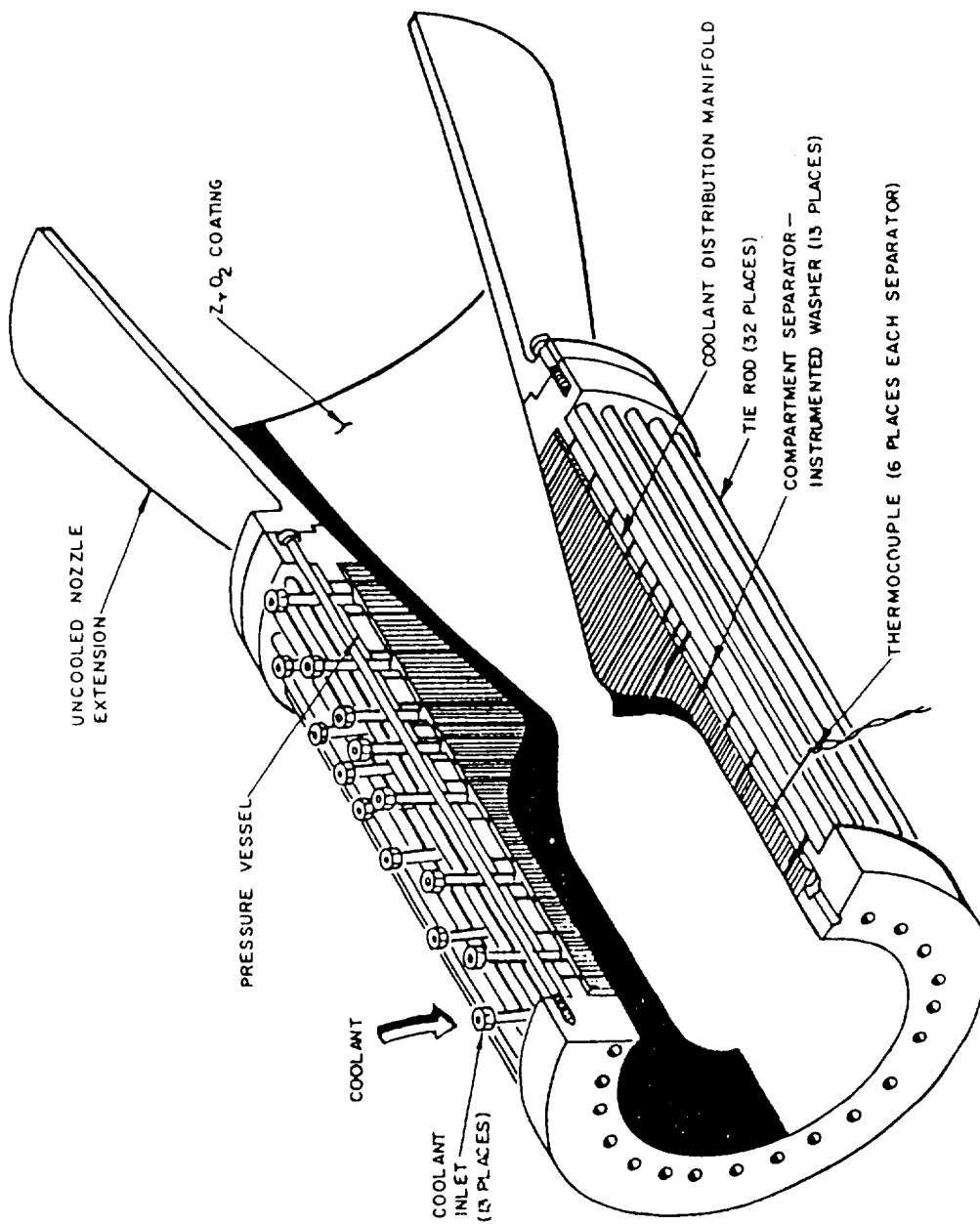


Figure 7. ARES Transpiration-Cooled Combustion Chamber

ORIGINAL PAGE IS  
OF POOR QUALITY

LOX/Benzonitrile, 3000 psia/50 K, H<sub>2</sub>O Transpiration Cooled



Figure 8. Noretip Test Using The ANTCAT Transpiration Cooled Chamber

ORIGINAL PAGE IS  
OF POOR QUALITY

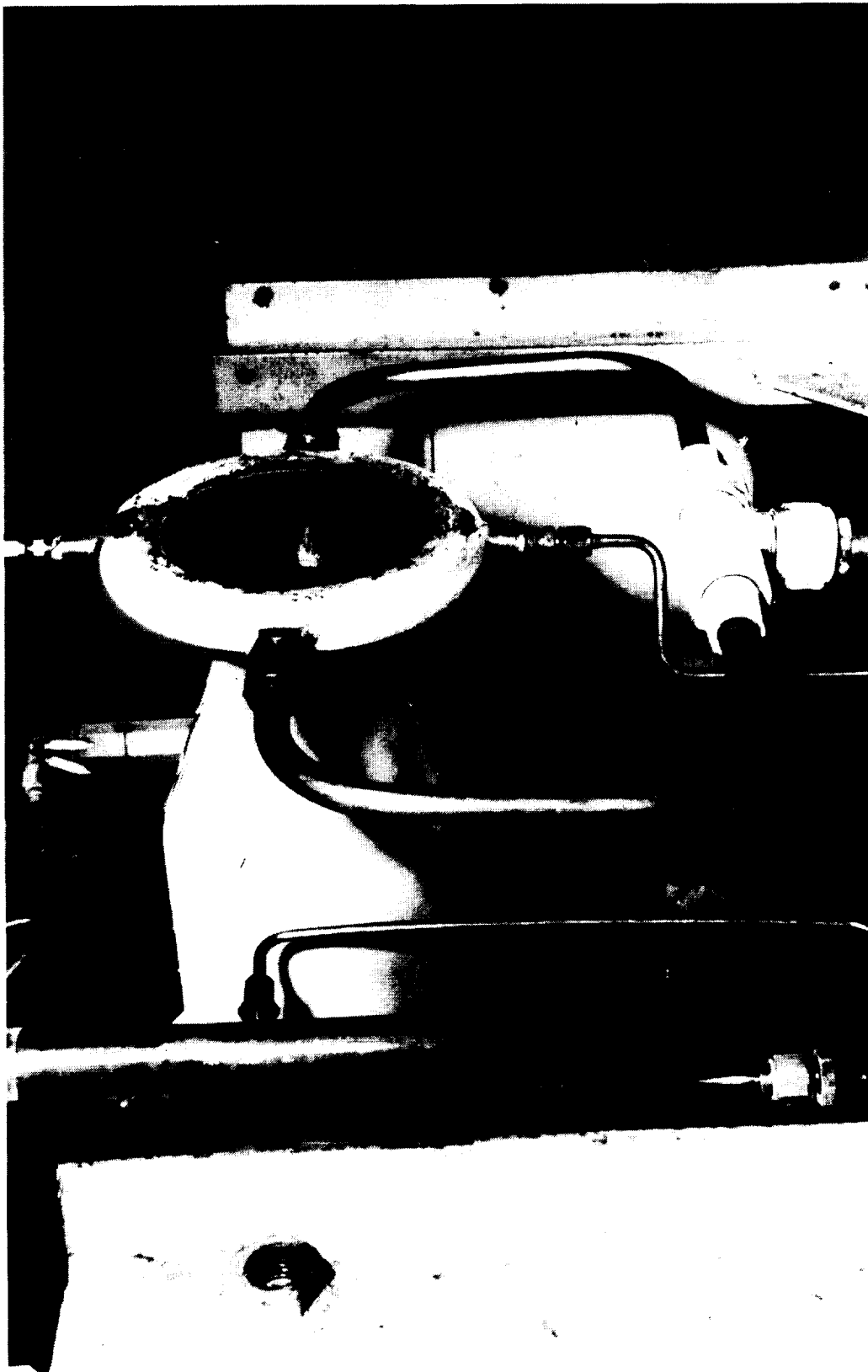


Figure 9. Graphite Lined FLOX/Methane Thrust Chamber (Post-Test)

ORIGINAL PAGE IS  
OF POOR QUALITY

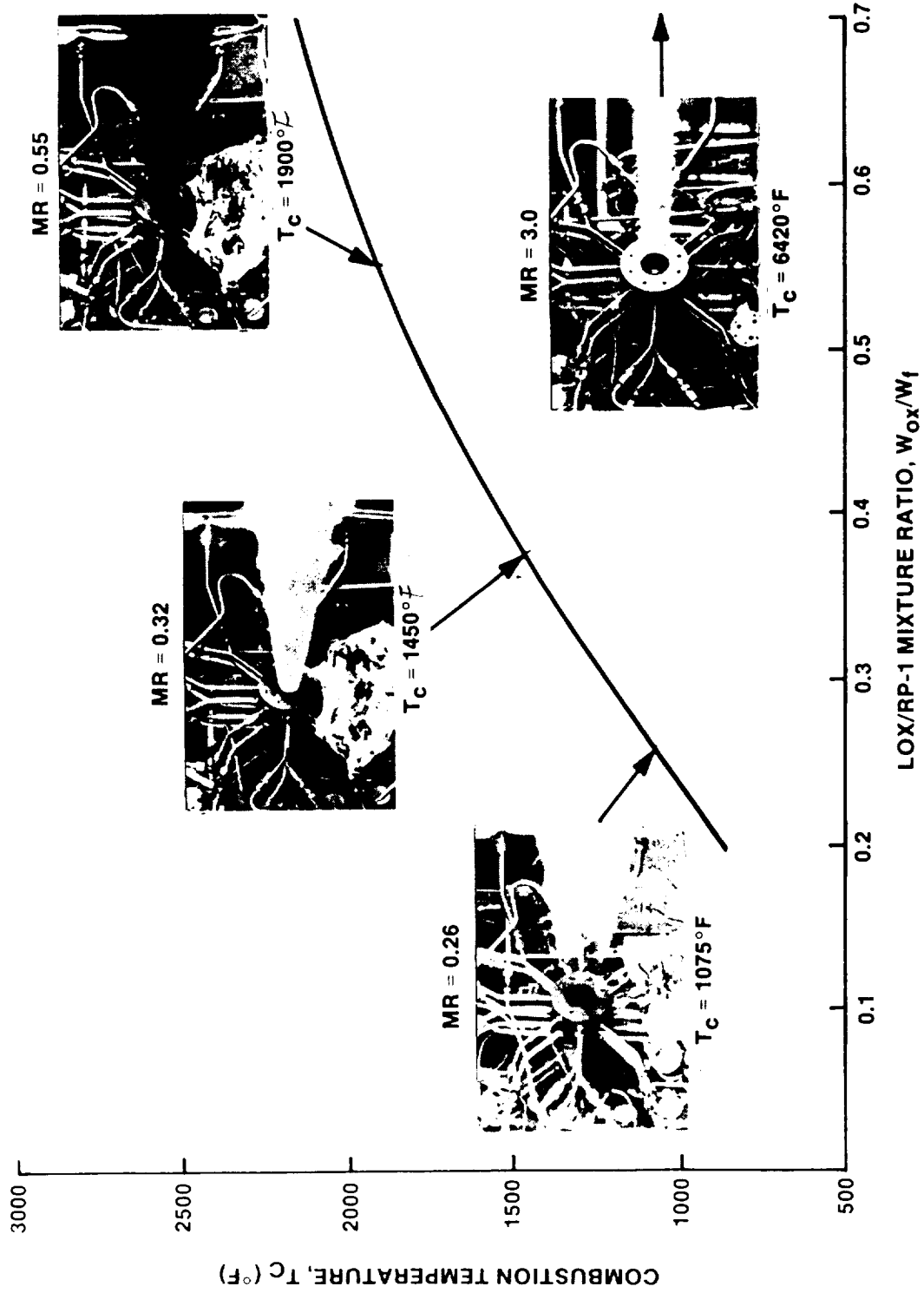
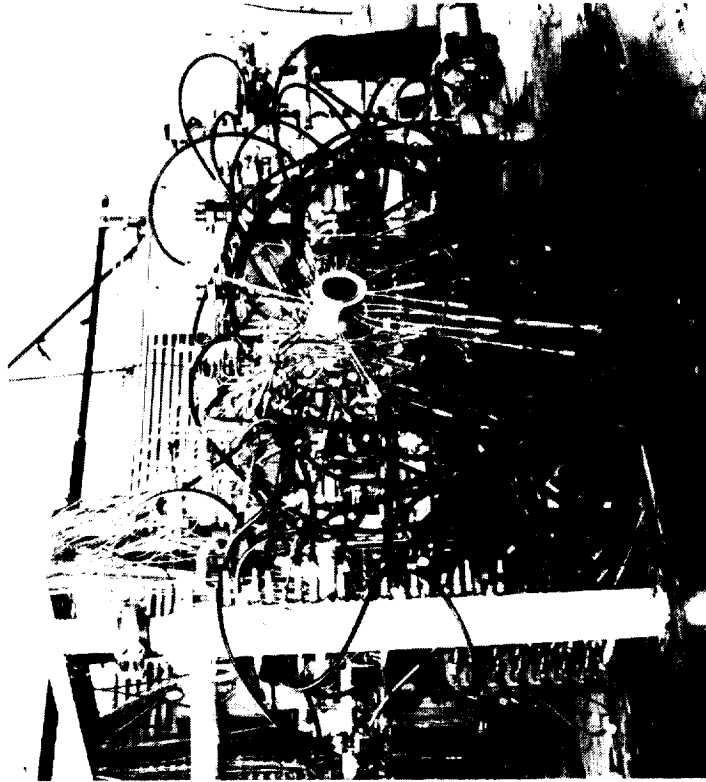
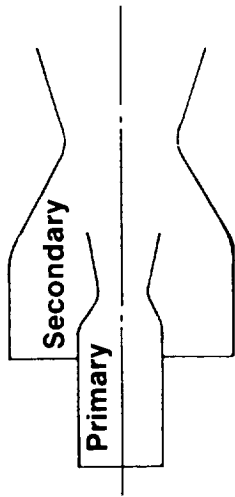


Figure 10. Exhaust Plume Photographs, LOX/RP-1, 1000 psia



- Design
- Operation
  - Mode 1: Primary + secondary
  - Mode 2: Primary only
- Applications
  - SSME
  - SSTO
  - Liquid rocket booster
  - OTV-E
- Benefit
  - Higher payload capability than conventional engine
  - Dual thrust capability
- Heat transfer issues
  - Mode 1: Q/A at tip and in primary nozzle
  - Mode 2: Q/A at re-attachment point



Dual-Throat Calorimeter Chamber

Figure 11. Dual Throat Nozzle Concept

ORIGINAL PAGE IS  
OF POOR QUALITY

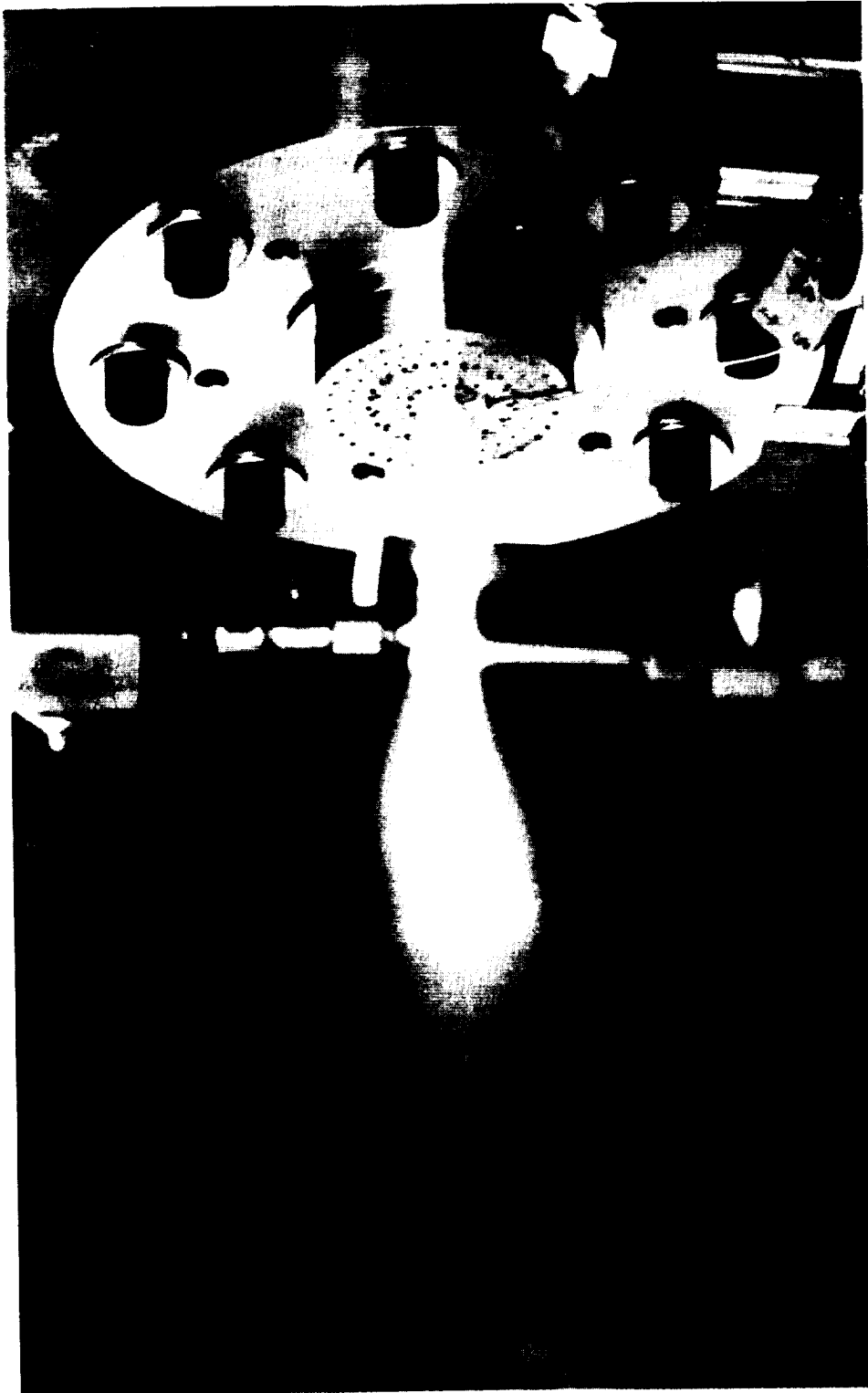
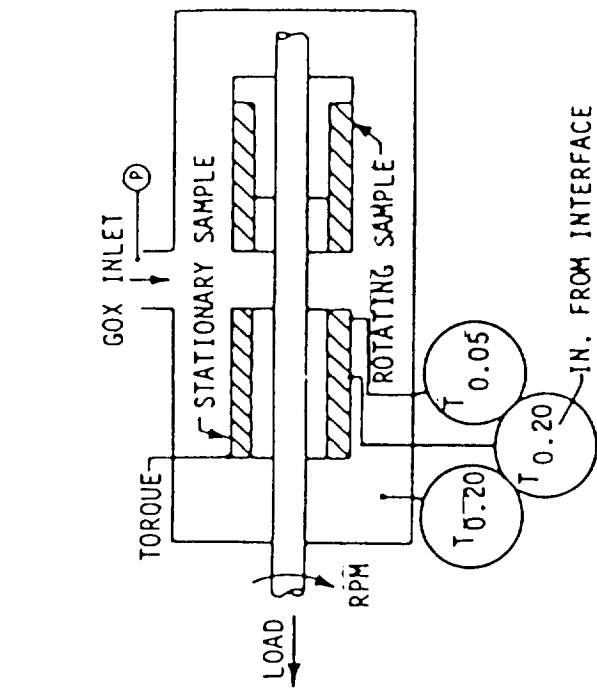
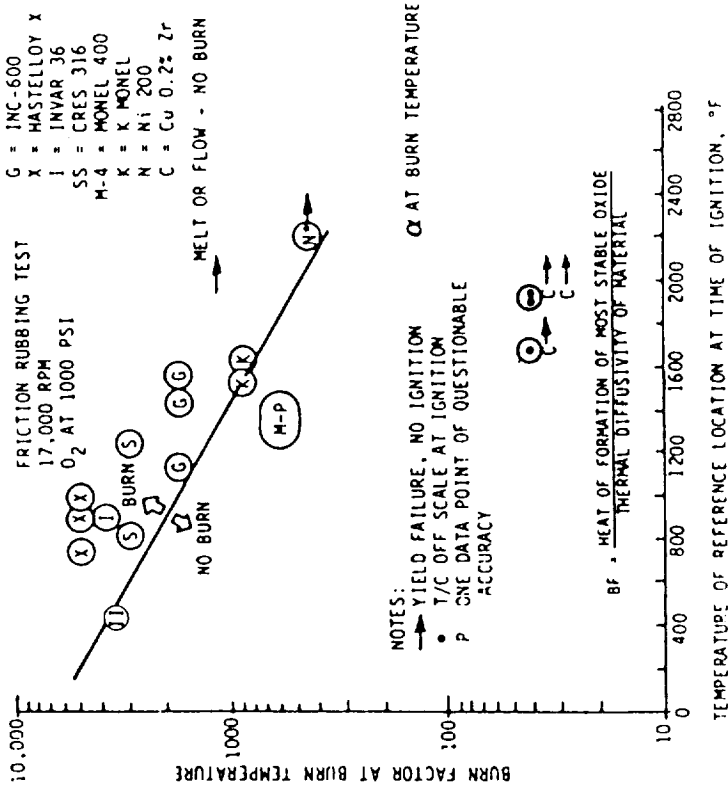


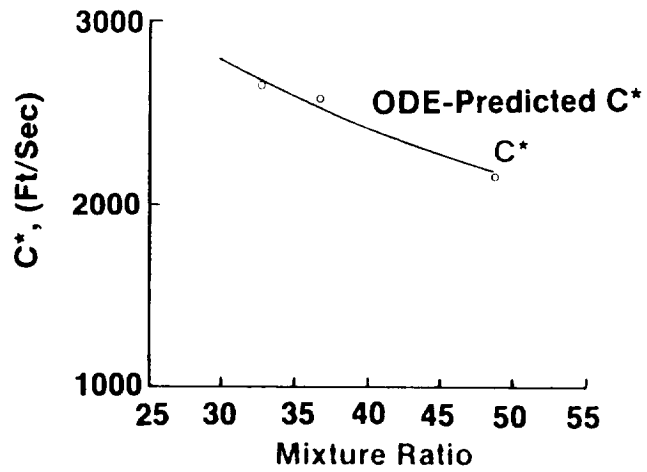
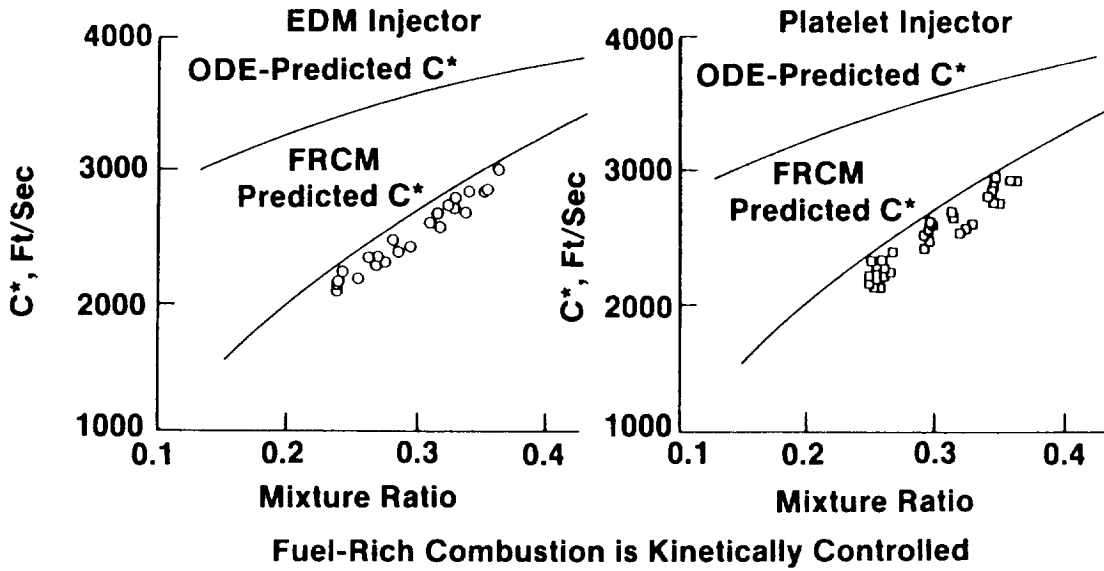
Figure 12. COX/Ethanol Igniter Test Firing



Schematic of Test Chamber of Friction Rubbing Test Apparatus

Burn Factor vs. Ignition Temperature  
in 1000 psi O<sub>2</sub>

Figure 13. Material Compatibility In LOX

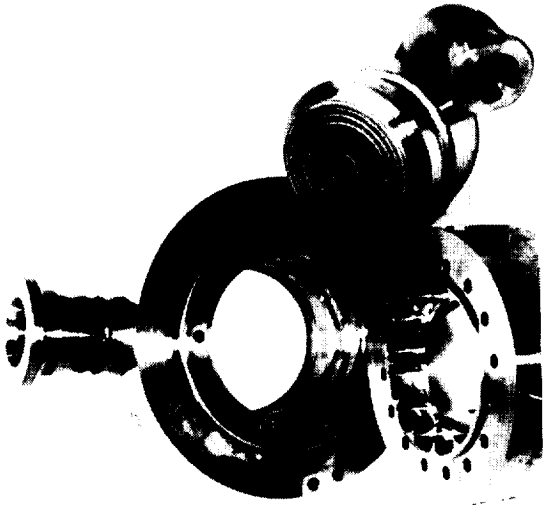


Oxidizer Rich Preburners Exhibit Equilibrium Combustion

Figure 14. Oxygen/RP-1 Preburner Performance

ORIGINAL PAGE IS  
OF POOR QUALITY

### LOX/RP-1 Injector



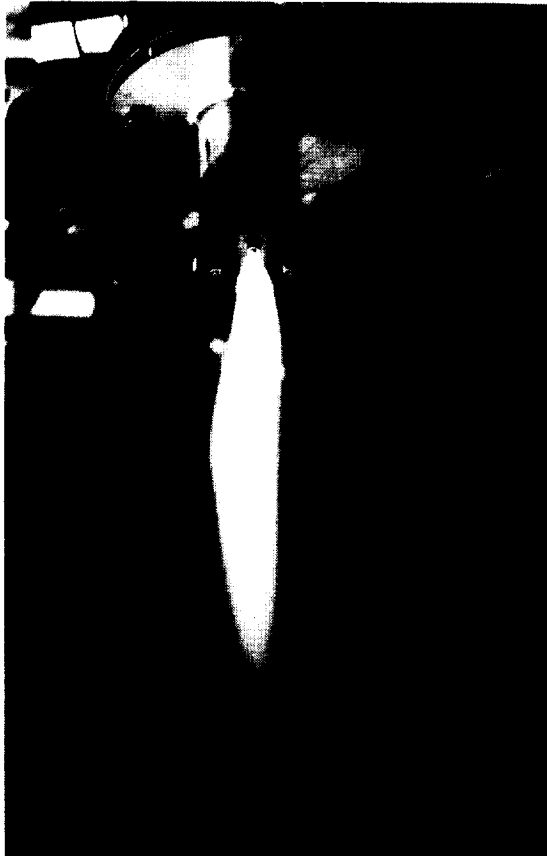
### LOX/CH4 Injector



Figure 15. 3000 psi/40K Injectors

ORIGINAL PAGE IS  
OF POOR QUALITY

**LOX/RP-1 Igniter  
Pc = 250 psia**



**LOX/RP-1 Injector  
NASA Water Cooled Chamber  
Pc = 2000 psia**

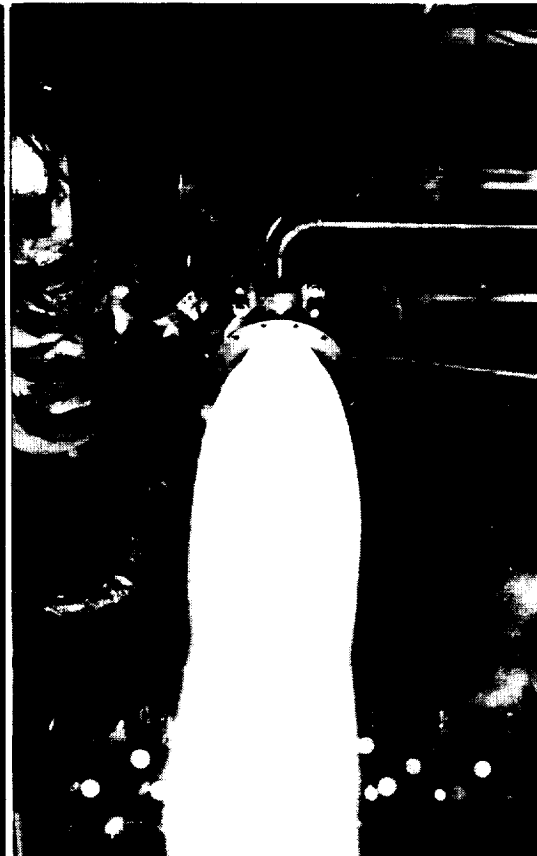


Figure 16. LOX/RP-1 Igniter And Injector Designs Were Demonstrated On The High Density Fuel Program

TEST DATA  
 MR = 1.90 ---  
 MR = 2.58 ---  
 MR = 2.80 ---  
 DESIGN PREDICTION  
 MR = 2.80 ---

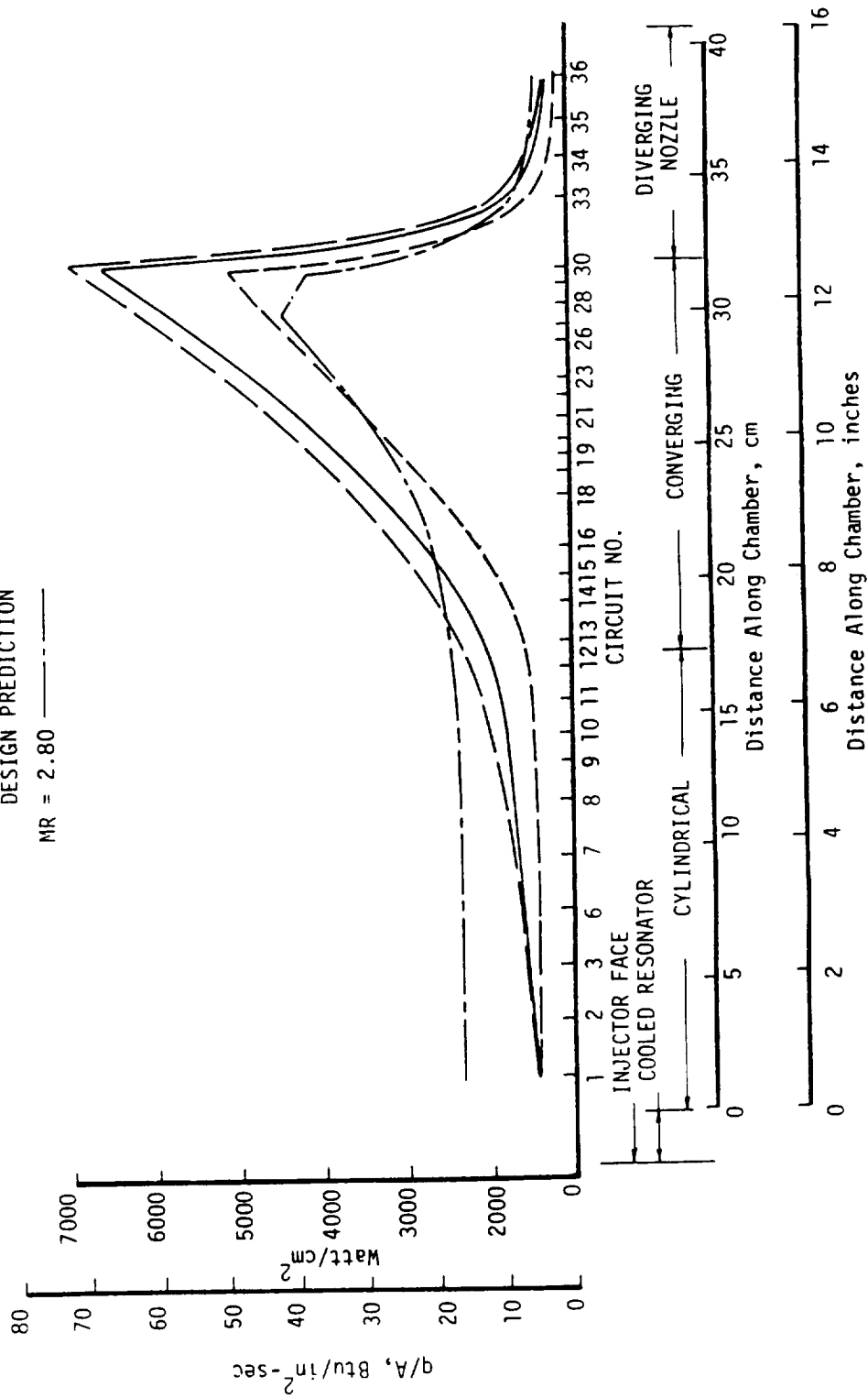
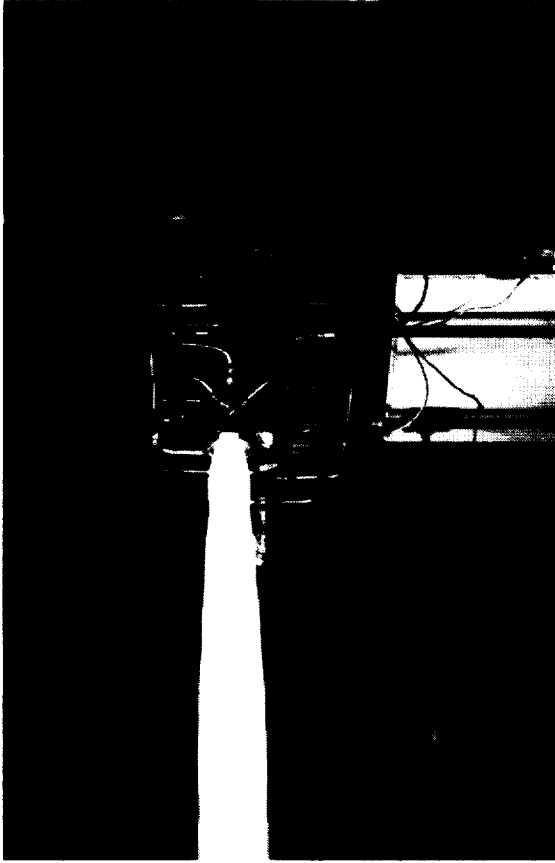


Figure 17. Measured Oxygen/RP-1 Heat Fluxes,  $P_c = 2000 \text{ psia}$

**LOX/C<sub>3</sub>H<sub>8</sub>  
Carbon Deposition Observed**



**LOX/C<sub>2</sub>H<sub>5</sub>OH  
No Carbon Deposition**

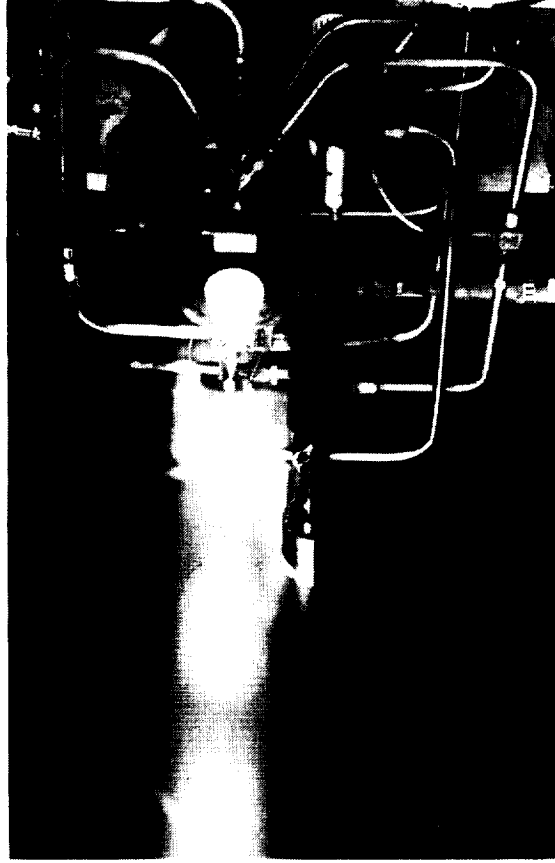


Figure 18. Calorimeter Chamber Testing At 300 psia



ORIGINAL PAGE IS  
OF POOR QUALITY



**EDM L-O-L**



**Transverse L-O-L**



**O-F-O Triplet**



**Pre-Atomized Triplet**

Figure 19. High Speed Photographs Of Unelement Tests

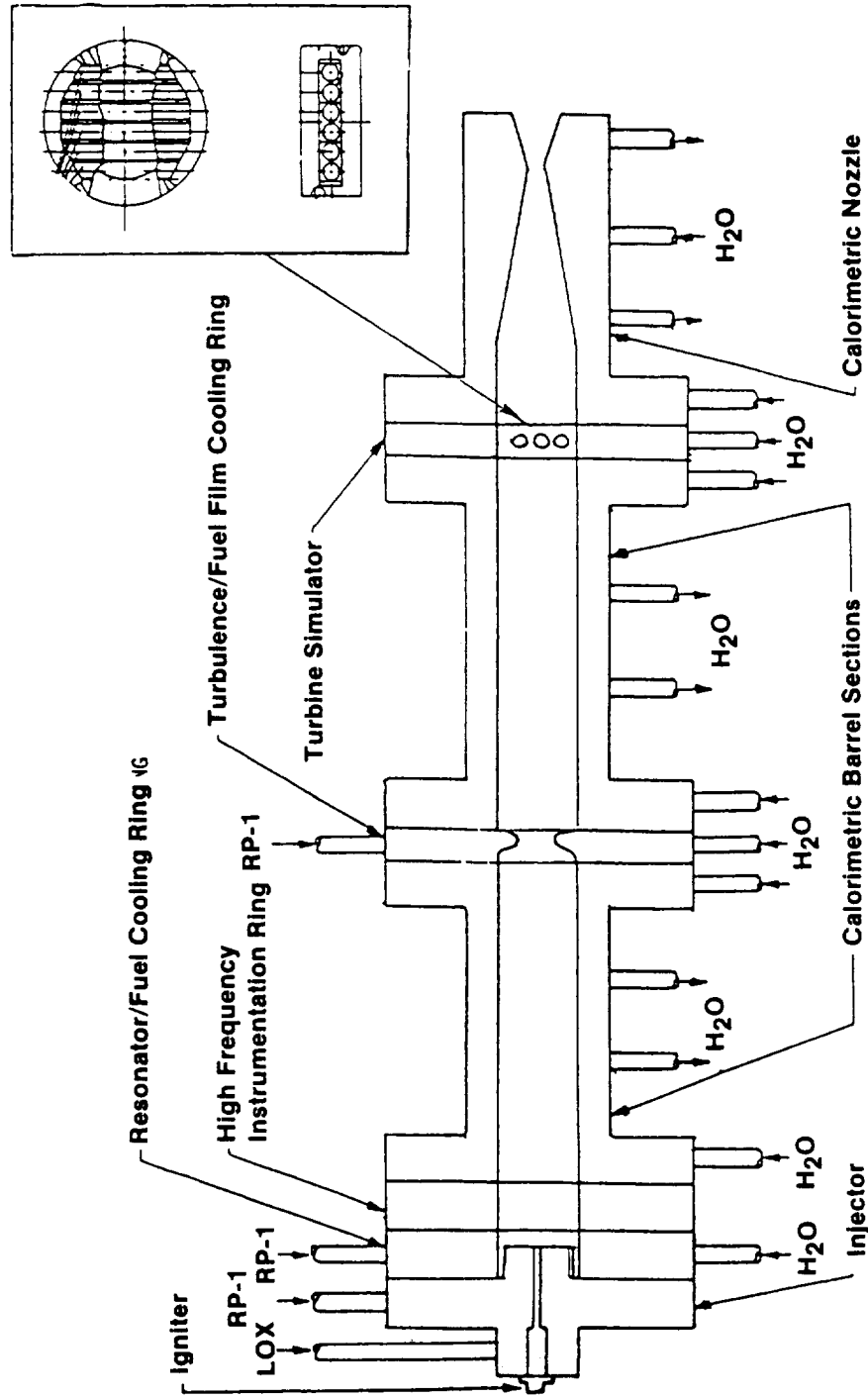


Figure 20. Preburner Assembly Schematic Showing The Water-Cooled Turbine Simulator

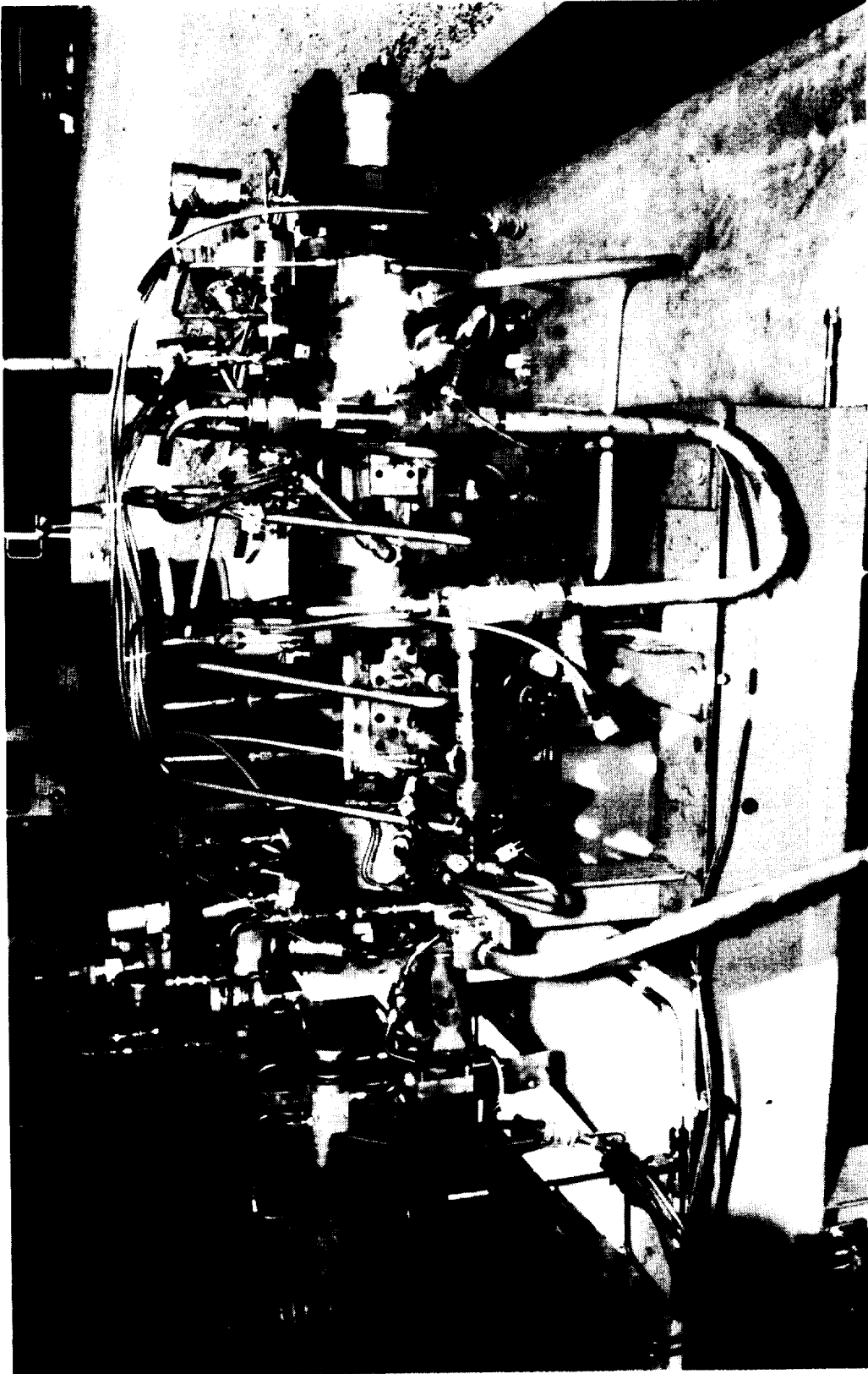


Figure 21. Carbon Deposition Contract  
(MSFC NAS 8-34715) Test Hardware

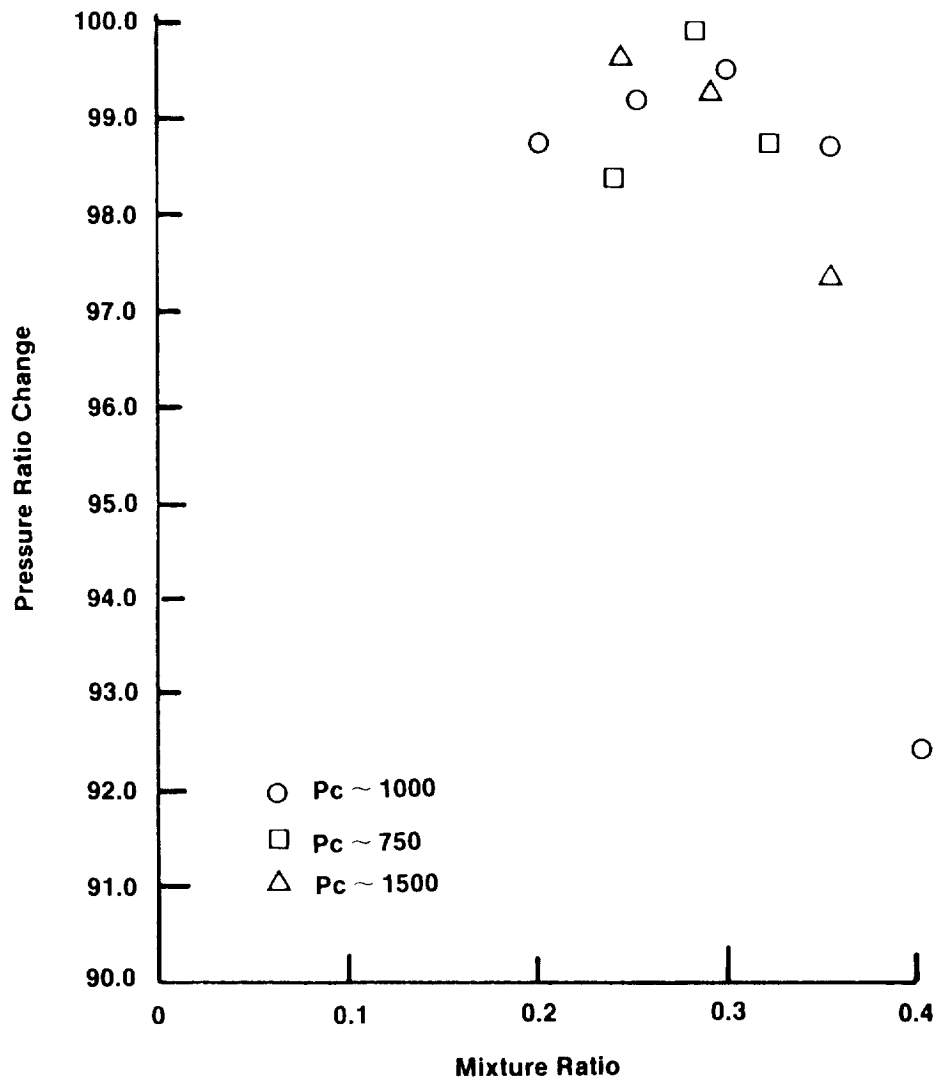


Figure 22. Turbine Simulator Build-Up As Function Of Mixture Ratio And Pressure

ORIGINAL PAGE IS  
OF POOR QUALITY



Figure 23. Turbine Simulator, Post Test Condition

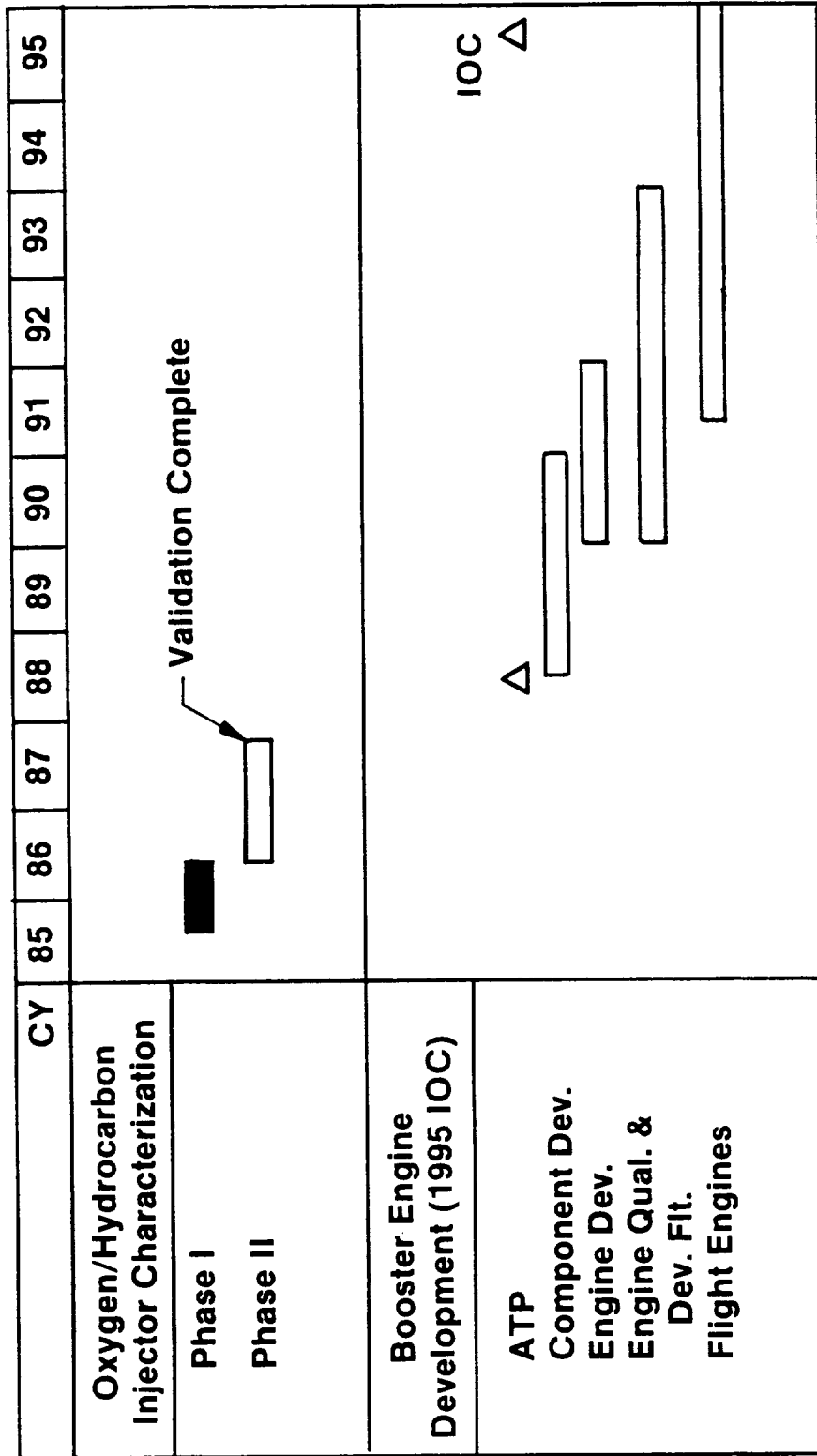


Figure 24 Methodology Will Be Available Prior To Early Engine Development

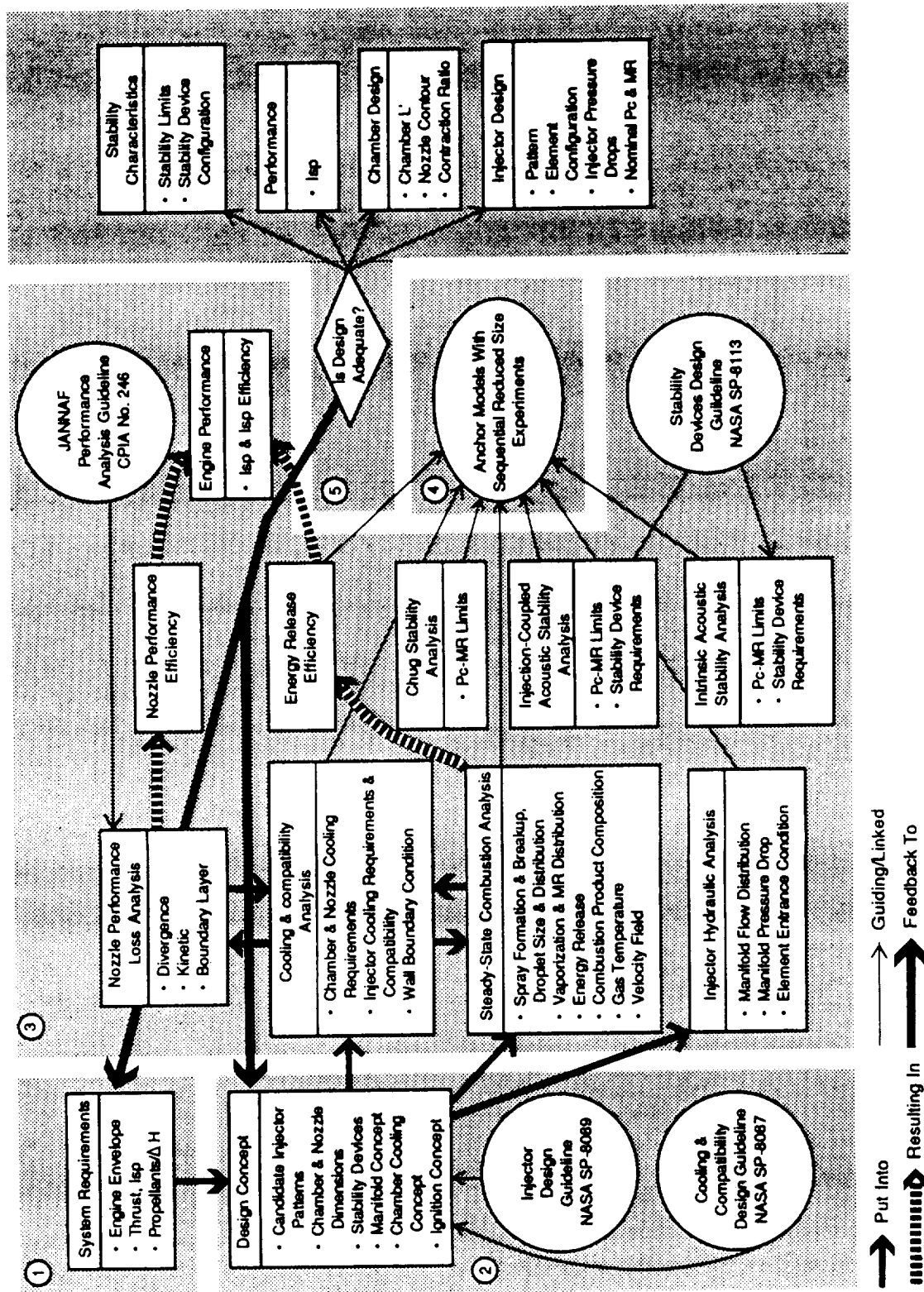


Figure 25. Our 5 Element Injector Characterization Methodology

Analysis Models Have Been Selected	
Chug Stability	LFCS
Intrinsic Acoustic Stability	IFAR
Injection Coupled Stability	ICASE
Steady State Combustion Performance	SDER/CICM
Compatibility	TDK/BLM
	SINDA, HEAT
	HOCOOL

5 Elements of the Methodology	
(1) Define Requirements	
(2) Create Design Concepts	
(3) Perform Analyses	
(4) Anchor Analysis Models	
(5) Feedback and Iterate	

**Analysis Models Are Anchored**

**Reduced Size Testing Provides Confidence**

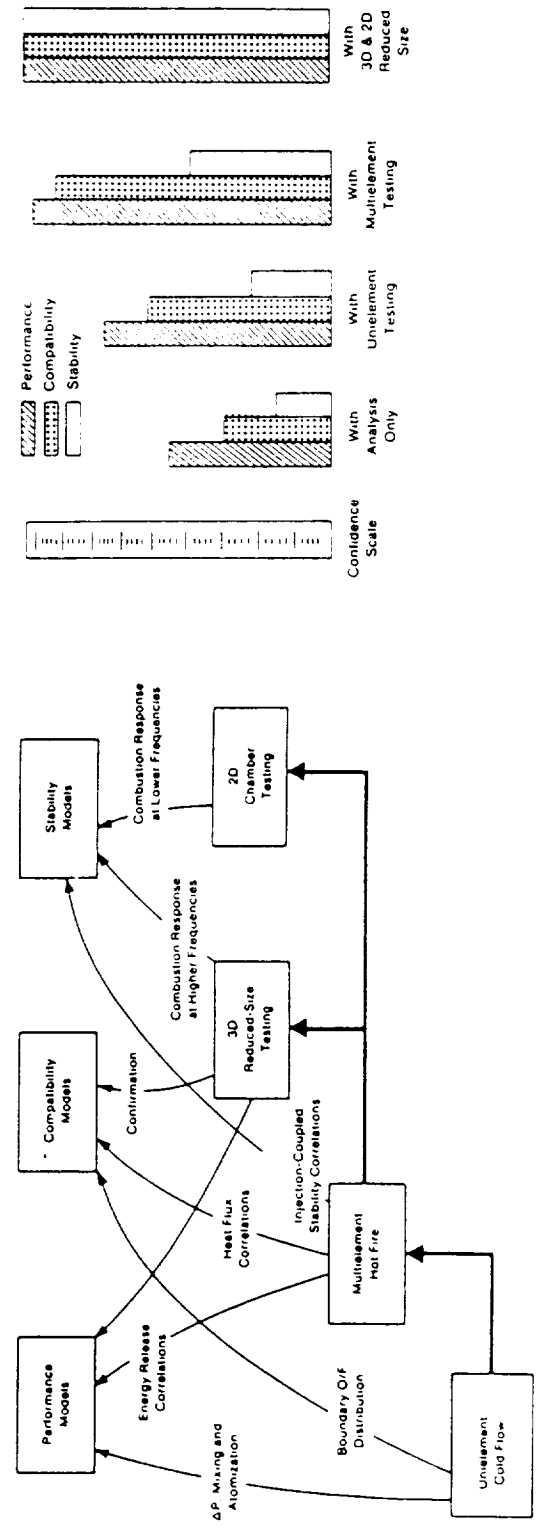


Figure 26. Our New Methodology Is Comprehensive

ORIGINAL PAGE IS OF POOR QUALITY



## SURVEY OF LOX/HYDROCARBON COMBUSTION AND COOLING

A. I. Masters, W. A. Visek & R. G. Carroll  
Pratt & Whitney Aircraft  
United Technologies Corp.

## ABSTRACT

Achieving high chamber pressure in oxygen/hydrocarbon booster engines will require different approaches to regenerative cooling, propellant injection, and combustion stabilization than engines of the past. Comparisons are made with substantiated oxygen/hydrogen combustion technology which has resulted in demonstrated high pressure capability. Means of applying this technology to hydrocarbon booster engines are discussed including: tripropellant cycles with hydrogen cooling, injection techniques for stable efficient combustion and use of acoustic liners as combustion stabilization devices.

## INTRODUCTION

The successful development of the Space Shuttle Main Engine has demonstrated both the feasibility and advantages of rocket engines operating at 3000 psia and higher. The superior cooling characteristics of hydrogen were a key factor in this achievement. Additional vehicle performance gains are possible if high combustion chamber pressure can be achieved using a denser hydrocarbon fuel such as methane, propane or RP-1. This paper reviews some of the new concepts and recent developments which now make a high pressure LOX/hydrocarbon engine practical.

## THRUST CHAMBER COOLING

The earliest rocket developers recognized the advantages of high combustion chamber pressure for minimizing vehicle size and increasing

vehicle payload. High pressure reduces dissociation losses and, more importantly in booster engines, it increases the exhaust nozzle expansion ratio which may be used without flow separation.

Though the need for high chamber pressure was well understood during the intensive rocket development of the 1950's and 60's, the combustion chamber pressure of new oxygen/RP-1 engines increased at a rather modest rate, as shown in Figure 1 (data from Reference 1). This trend is in dramatic contrast to the 10-to-1 increase in pressure for oxygen/hydrogen engines in the 1960's and 70's. The two main reasons for this different trend are the improved thrust chamber cooling achievable with hydrogen, and the new thrust chamber construction techniques which were developed in the late 1960's and early 1970's.

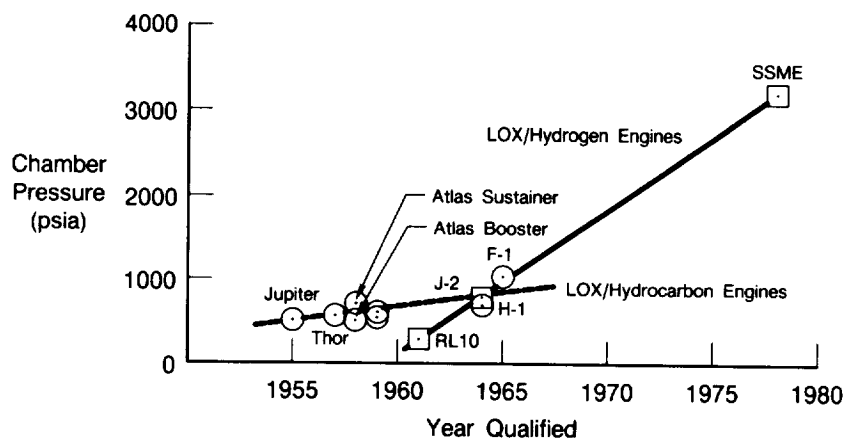


Figure 1. History of Production Engine Chamber Pressure

Hydrogen is an excellent coolant by virtue of its high specific heat, high thermal conductivity and low viscosity. These properties combine to give hydrogen a much higher coolant film coefficient than hydrocarbon fuels such as RP-1 or methane. The high specific heat of hydrogen allows a great deal of heat to be absorbed with only a modest increase in temperature and hydrogen is thermally stable to very high temperatures. In contrast, RP-1 has only one-seventh the heat capacity per unit weight of hydrogen and may begin to decompose and foul cooling passages at fuel temperatures as low as 300 degrees F.

Liquid hydrogen is a deep cryogen with a liquid boiling point of only 37 degrees R. The development of liquid hydrogen production and handling techniques in quantities sufficient for rocket propulsion needs was, in itself, a significant technological accomplishment. The RL 10 (Figure 2) was the first rocket engine developed for use with liquid hydrogen. It is a tribute both to the engine design and the inherent

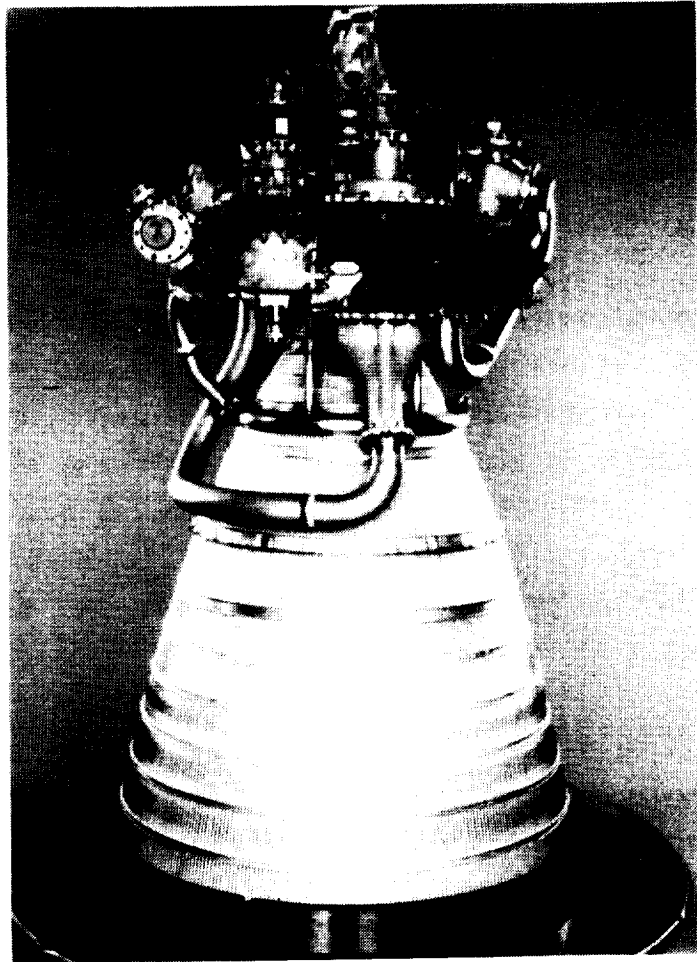


Figure 2. RL 10-A3 Oxygen/Hydrogen Rocket Engine

advantages of hydrogen cooling that the RL 10 is still in use. As of late, 262 engines have been fired in space without a single in-flight failure.

Prior to 1970, most large regeneratively cooled thrust chambers had been fabricated from brazed tube assemblies. In the late 1960's and early 1970's, a number of new construction techniques were investigated which provided much greater flexibility in tailoring cooling passages to provide maximum heat flux capability with minimum coolant pressure drop. P&W and Rocketdyne fabricated forged copper thrust chambers with machined cooling passages that were tested with oxygen/hydrogen propellants at pressures up to 3000 psia. Based upon the success of these tests, copper thrust chambers with machined cooling passages were incorporated in the SSME. Analysis conducted by P&W at that time indicated about a 50% increase in upper limit chamber pressure over conventional tubular chambers with this type of construction.

Transpiration cooling is another method of accommodating very high heat fluxes. It has the advantage of low coolant pressure drop and the adaptability to cool regions where regenerative cooling is difficult. One disadvantage is a potential performance loss, although this loss is incurred primarily with main chamber cooling and does not generally apply to injector faceplate cooling or to most auxiliary component cooling. In some applications, control of coolant flow distribution may be difficult.

Transpiration cooling has been used by P&W in a number of high pressure oxygen/hydrogen engine components. In early development of the XLR-129, an entire thrust chamber assembly was transpiration cooled in 3000 psia tests (Figure 3). Other transpiration cooled components included the mainburner and preburner injector faceplates and preburner ducting. Suitable cooling of all components was accomplished with minimal difficulty.

Satisfactory coolant flow distribution is dependant upon the sensitivity of the coolant flowrate to variations in coolant density. In general, transpiration cooling with hydrogen has worked well. With denser gases, it has been more difficult, and with liquids the problems have generally been severe.

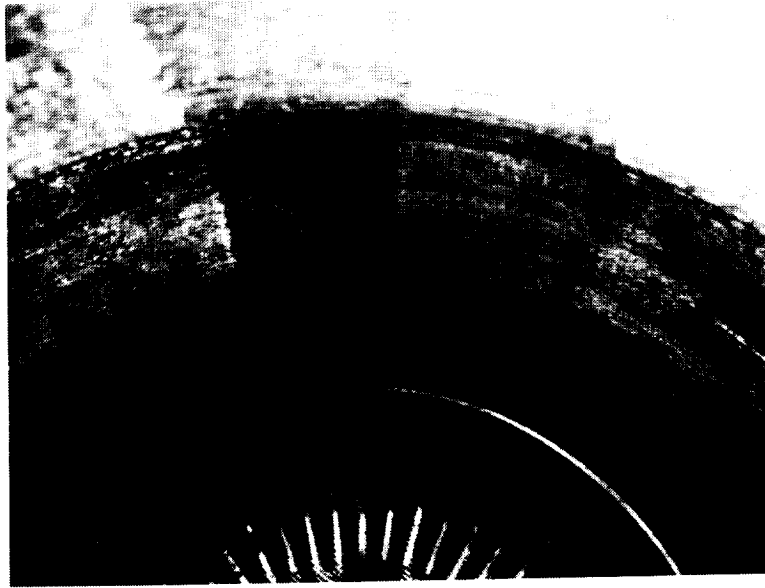


Figure 3. XLR-129 Transpiration Cooled Combustion Chamber

Another factor that has aided cooling of more recent rocket engines has been the trend toward higher engine thrust. High thrust simplifies cooling needs in two ways. First, as shown in Figure 4, for a fixed combustion pressure the peak heat flux in the critical throat region is reduced as the throat diameter (and consequently, the thrust) increases. Secondly, as thrust increases, propellant flow increases proportionately; but the cooled chamber surface upstream of the nozzle throat increases only by the square root of thrust. The result is a substantial increase in available coolant flow per unit area as thrust increases. This increase in coolant flow is only an advantage where allowable coolant temperatures begin to be exceeded, but can be an important consideration in some situations. Using several engines with reduced thrust may enhance reliability by providing engine-out capability, but the offsetting disadvantages of more difficult engine cooling should not be neglected.

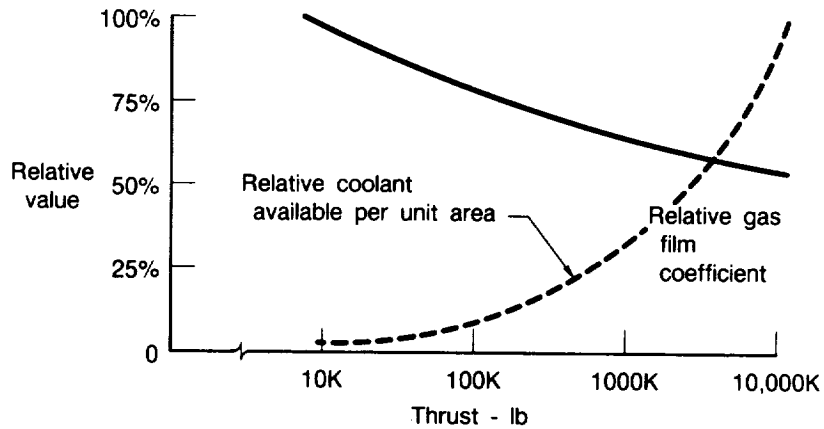


Figure 4. Effect of Thrust on Chamber Pressure Limit

Three hydrocarbon fuels are currently under consideration for the Heavy Lift Launch Vehicle: Methane, propane and RP-1. As shown in Table I, methane is a cryogenic fluid with a relatively high specific impulse and low density. Propane has a slightly higher density than methane and also has a wide liquid range. Subcooling propane to near its melting point, greatly increases its density so that it provides a good density-specific impulse product. RP-1 has, of course, long been the standard hydrocarbon fuel for rocket applications.

Fuel	Melting point (°R)	Boiling point (°R)	Fuel density (lbm/ft <sup>3</sup> )	I <sub>VAC</sub> (theoretical) (lbf/lbm/sec)
CH <sub>4</sub>	163	201	26.5	382.6
C <sub>3</sub> H <sub>8</sub>	154	416	45.0 *	376.7
RP-1	420	882	49.7	371.8

$P_c = 3000$  psia

$\epsilon_e = 77$

\* Subcooled to 155°R

AV310996 860205 0475b

Table I. Hydrocarbon Fuel Comparison

Prediction of rocket heat flux is not the exact science one would desire. Uncertainties exist in both the hot gas side and coolant side film coefficients. Heated tube measurements of coolant side film coefficient have proven to be a useful way of reducing this uncertainty.

Recent experimental programs at Aerojet, Rocketdyne, and United Technology Research Center (Reference 2,3 and 4) have provided valuable heat transfer data at conditions applicable to high pressure engines. Such data have eliminated much of the uncertainty in the coolant film coefficient and will allow a valid assessment of the relative coolant capabilities of the hydrocarbon fuels of interest.

Heated tube testing has also been used to explore the thermal stability of the fuels of interest. Data from Reference 4, shown in Figure 5, indicate the relative stability of methane, propane and RP-1 in terms of the rate of carbon deposition on heated tube walls. As shown, methane was the least susceptible to decomposition while propane was the most susceptible.

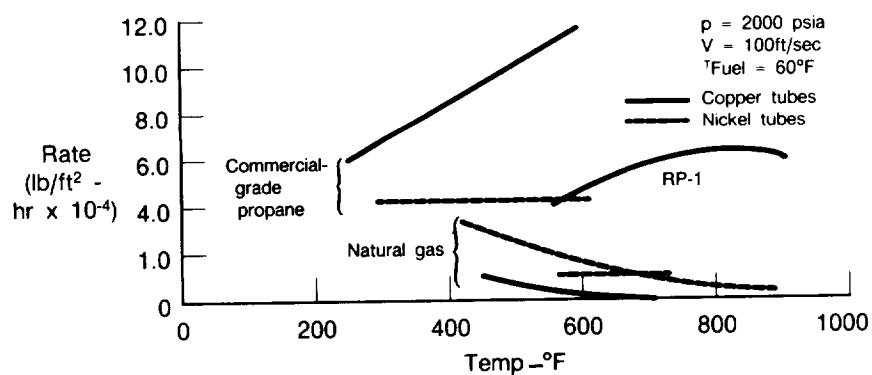


Figure 5. Heated Tube Deposition Data

Copper can catalyze the decomposition rate of many hydrocarbon fuels. Dissolved copper is a known contributor to fuel fouling in aircraft gas turbine engines burning JP-4 and JP-5. This is particularly a problem for the Navy where copper is the material of choice for many shipboard fuel storage components. As shown in Figure 5, copper also has a detrimental effect on the stability of propane and RP-1.

### TRIPROPELLANT ENGINES

The newly available hydrocarbon fuel heat transfer data allow a more reliable quantification of the design limits on combustion chamber pressure for oxygen/hydrocarbon booster engines. These limits are well below those established for oxygen/hydrogen. As shown by the cross hatched bars in Figure 6, for a given thrust, the upper limit chamber pressure with oxygen/RP-1 is about half that of oxygen/hydrogen, and oxygen/methane and oxygen/propane fall somewhere in between.

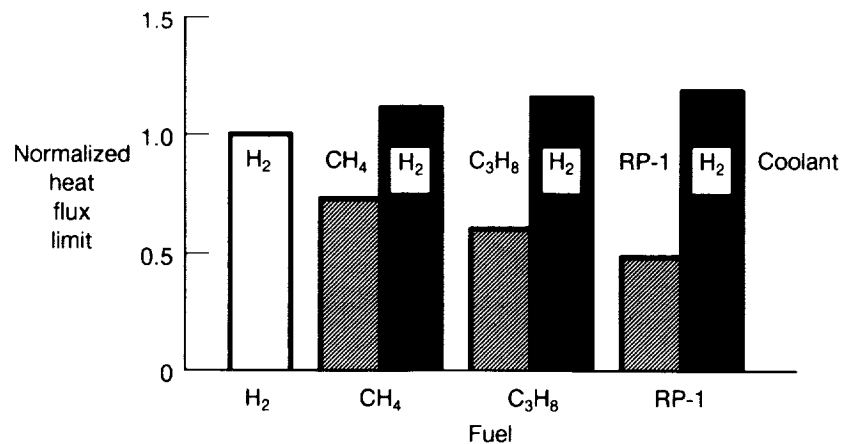


Figure 6. Comparison of Combustion Chamber Pressure Limits



Configuration studies of the Heavy Lift Launch Vehicle are based on the use of oxygen, hydrocarbon and hydrogen propellants to power a number of oxygen/hydrocarbon and oxygen/hydrogen engines. Since both hydrogen and hydrocarbon fuel will be available, it has been suggested that hydrogen be used to cool the oxygen/hydrocarbon engines as well as the oxygen/hydrogen engines (Reference 5). This approach would employ the superior cooling characteristics of hydrogen to allow operation of the oxygen/hydrocarbon engines at much higher chamber pressure. The shaded bars in Figure 6 indicate the relative increase in chamber pressure that can be achieved with hydrogen cooling of the three hydrocarbon fuel combinations. Since the hot gas film coefficient is lower with oxygen/hydrocarbon combustion than with the oxygen/hydrogen combination, higher pressure is possible than with the reference oxygen/hydrogen case. It should be pointed out that in order to keep the hydrogen coolant flow low and, consequently, keep the propellant bulk density high, a high engine thrust is desirable.

Several tripropellant cycles have been suggested; two are shown in Figure 7. In the first, hydrogen is used as the coolant and is then used in the gas generator. The hydrocarbon is used as the fuel in the primary combustor. In the second cycle, hydrogen is used to cool the

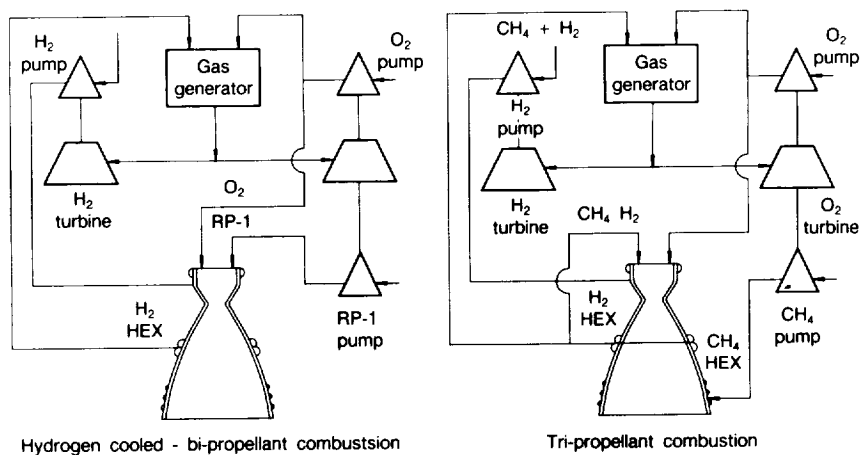


Figure 7. Typical Tripropellant Cycles

main chamber and methane is used to cool the exhaust nozzle. The two are then mixed and injected in both the mainburner and gas generator. Since care must be taken to mix the hydrocarbon with hydrogen at conditions below the hydrocarbon freeze point, this scheme would have limited application to RP-1. The second scheme is a little more complex, but provides enhanced combustion and improved specific impulse from the addition of hydrogen into the main chamber.

There are several advantages to adding hydrogen to the oxygen/hydrocarbon combustion process. Even a small amount of hydrogen can increase the combustion flame speed, reduce ignition lag and expand flammability limits (Figure 8). These improved combustion characteristics would lead to simplified ignition, improved combustion efficiency and inherently more stable combustion. This concept of adding the hydrogen to the main combustion process to stabilize the combustion and improve the efficiency was developed under a company-funded program.

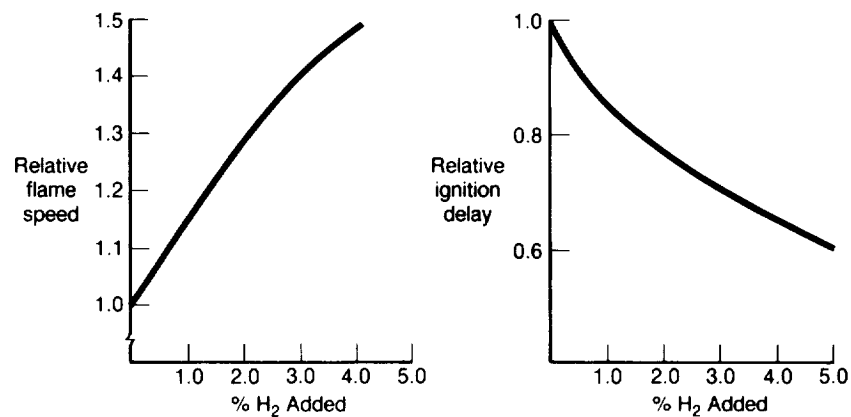


Figure 8. Effect of Hydrogen Addition on Flame Speed and Ignition Delay

One problem with oxygen/RP-1 engines in the past has been the large amount of carbon in the gas generator exhaust. The exhaust smoke has been tolerated, but a portion of the carbon is deposited on the turbine. Deposit rates are so severe that turbine operation is effected. This problem would be magnified by the higher horsepower requirements of a high pressure engine and would become intolerable in a reusable engine. Turbine erosion caused by the carbon particles is also predicted to be severe in a high pressure reusable engine.

As shown in Figure 9, based on theoretical equilibrium calculations, as much as 45% by weight of the exhaust of an oxygen/RP-1 gas generator may be solid carbon. With methane, the theoretical carbon is reduced to about 12% by weight. Solid exhaust concentrations may be somewhat different than equilibrium calculations indicate, but the relative levels are believed to be representative. The inherently lower carbon content in methane combustion products is confirmed by the experimental work of Bailey (Reference 6). Hydrogen addition also reduces exhaust carbon content. As shown in Figure 9, the improvement is dramatic with methane. Below 1900 degrees R, no theoretical carbon is present. Inefficiencies may produce some carbon at these conditions, but probably not enough to affect turbine operation or life.

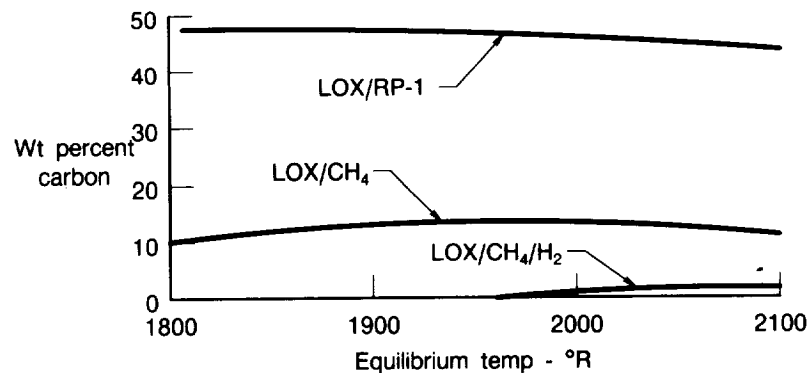


Figure 9. Solid Carbon Concentration in Gas Generator Exhaust (Chemical Equilibrium Assumed)

Table II compares the theoretical vacuum specific impulse and propellant bulk density of the three hydrocarbon fuels with and without hydrogen addition. The performance of oxygen/hydrogen is also included for comparison. The hydrogen percentages shown are appropriate for engines in the 1,000,000 lb. thrust range.

Fuel	Bi-propellants		% H <sub>2</sub>	Tri-propellants	
	I <sub>VAC</sub>	Propellant bulk density (lb/ft <sup>3</sup> )		I <sub>VAC</sub>	Propellant bulk density (lb/ft <sup>3</sup> )
CH <sub>4</sub>	382.6	52.0	7.0	392.0	45.5
C <sub>3</sub> H <sub>8</sub> *	376.7	62.9	7.0	388.5	52.3
RP-1	371.8	64.5	7.0	384.6	52.8
H <sub>2</sub>	465.1	22.6			

P<sub>c</sub>= 3000 psia

ε<sub>e</sub>= 77

\* Subcooled to 155°R

AV314551 060205 0475b

Table II. Tripropellant Performance Comparison

Since methane can be readily combined with hydrogen and the resulting combination makes a good gas generator fuel as well as a mainburner fuel, the oxygen/methane/hydrogen tripropellant cycle with mixed methane/hydrogen fuel appears quite feasible. Fuel-hydrogen mixing is more difficult with RP-1 and RP-1 presents a problem as a gas generator fuel in reusable engines. The bipropellant cycle with hydrogen cooling is, therefore, more applicable with RP-1.

#### COMBUSTION EFFICIENCY AND STABILITY

Achievement of stable combustion has been one of the most difficult oxygen/RP-1 engine development problems. The inherent difficulty in achieving stable combustion increases at high thrust. Baffles have been used to stabilize combustion with success at low thrust; but at high thrust, it has been necessary to compromise combustion efficiency to increase the combustion time lag even when baffles have been used. As

shown in Table 3, several oxygen/hydrocarbon engines have demonstrated characteristic velocity efficiencies above 97%, but the efficiency of the F-1 was below 94% (data from Reference 2). The reduced efficiency was primarily due to design changes to improve combustion stability through increased combustion time lag and to provide baffle cooling. Higher chamber pressure may also have been a contributing factor.

	F (1000 lbf)	$\eta_c$ *
Jupiter	150	94.7
Thor, MB-3	170	95.7
Atlas booster	165	95.5
Atlas sustainer	57	96.4
Titan I booster	180	97.8
Titan I sustainer	80	98.9
H-1	204	97.3
F-1	1550	93.8

Table III. Oxygen/RP-1 Production Engine Efficiencies

Many approaches to combustion efficiency estimation predict that increased pressure will accelerate droplet burning rates and thereby increase efficiency. Spaulding (Reference 7) and Rosner (Reference 8) have shown how these theories break down at pressures above the reactant critical pressure. Figure 10 indicates the trend in combustion efficiency versus chamber pressure based on constant propellant atomization (droplet size). The curve indicates the increased difficulty of achieving efficient combustion at supercritical pressures and the need for more efficient droplet atomization at these conditions.

ORIGINAL PAGE IS  
OF POOR QUALITY

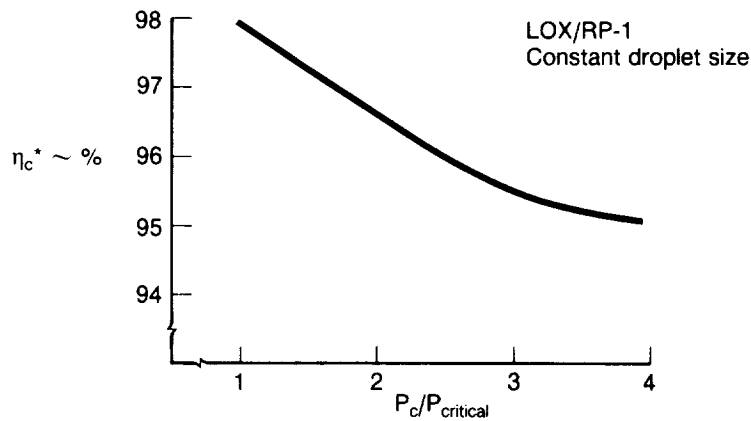


Figure 10. Effect of Supercritical Pressure on Combustion Efficiency

Where they are applicable, coaxial injectors have been shown to provide inherently stable efficient combustion. The RL 10 (Figure 11) was the first production rocket engine to employ coaxial injection. The concept has proven especially attractive for gas-liquid injection. While many design arrangements are possible, the only production engine coaxial injector applications in this country have been limited to liquid oxygen/gaseous hydrogen with transpiration cooled faceplates.

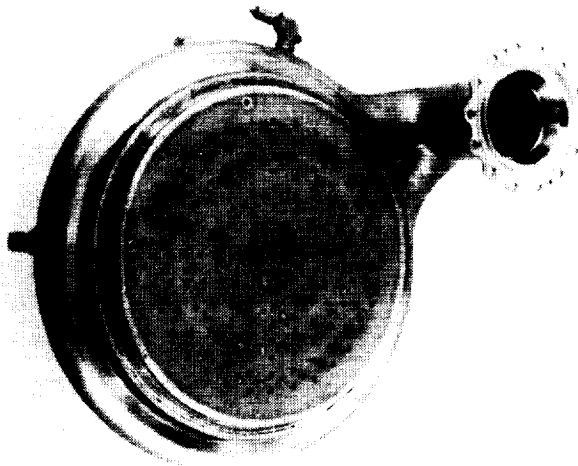


Figure 11. RL 10 Coaxial Injector

The most severe limitation on the use of coaxial injectors stems from the use of fuel transpiration cooling of the faceplate and geometric limitations on the fuel annulus. A low density gaseous fuel is highly desirable to meet these limitations. The fuel flow area is set by the oxidizer spud diameter and the fuel annulus height. A favorable combination of low oxidizer-to-fuel ratio and low fuel density is necessary to maintain an adequate annulus height. Otherwise, dimensional tolerance limitations will lead to severe fuel maldistribution. Reversing the fuel and oxidizer to overcome these geometric limitations was done by Herch at NASA Lewis Research Center (Reference 9). The results, with regard to combustion, were entirely satisfactory, but faceplate cooling with oxygen would be very difficult at high pressure.

A great deal of work has been done to define the limits of stability with coaxial injection. Figure 12 shows the results of one early investigation (Reference 10). This study, as most of the work done in this area, tied stability to hydrogen injection temperature and several other injection and combustor design parameters. High injection momentum ratio and high contraction ratio are shown to be stabilizing. Other studies have used hydrogen velocity, fuel-to-oxidizer flow area and hydrogen density as correlating parameters (References 10 & 11). In virtually all cases, coaxial injection with oxygen/hydrogen has been stable at hydrogen injection temperatures above about 100 degrees R.

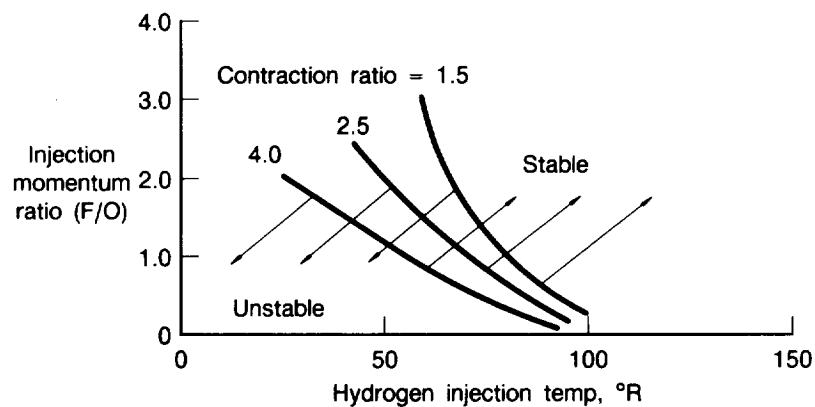


Figure 12. Coaxial Injector Stability Limits

The trends established by the low pressure test results presented in Figure 12 have also been found to apply at high pressure where hydrogen density is much higher. High pressure tests at P&W have consisted of low oxygen- to-hydrogen ratio preburner tests and oxygen burned with the preburner exhaust in mainburner tests. All high pressure tests at both 50,000 and 250,000 lb. thrust demonstrated stable combustion. The injector used in the 250,000 lb. thrust tests is shown in Figure 13.

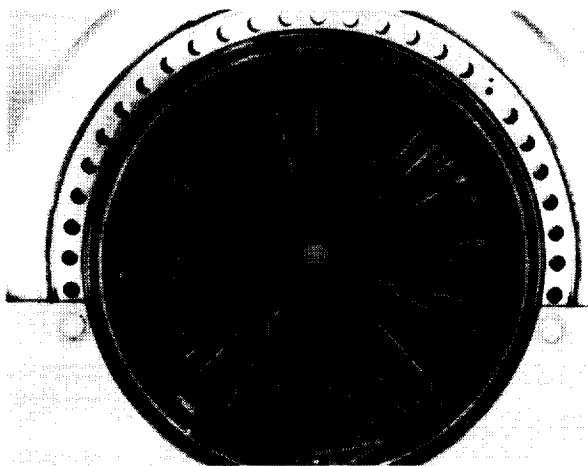


Figure 13. XLR-129 Injector

Light hydrocarbon fuels including methane and propane have also been tested using coaxial injectors with both oxygen and oxygen/fluorine mixtures at pressures up to 500 psia (References 12,13 & 14). All tests with coaxial injectors were dynamically stable. Tests at similar conditions with impinging injectors were unstable. These limited data provide one strong indication that the inherent stability of coaxial injectors applies to fuels other than hydrogen.

Even using such advantageous design techniques as coaxial injection, light hydrocarbon fuels and hydrogen addition does not provide complete confidence that stable oxygen/hydrocarbon combustion can be achieved without the use of an additional stabilizing device. Baffles have been used on most previous oxygen/hydrocarbon booster



engines. Baffles have been generally successful, but they are difficult to cool and typically result in reduced combustion efficiency due to fewer injection elements and non-uniform propellant distribution.

In the 1960's, Garrison and Russell pioneered the development of acoustic liners for suppression of combustion instability (References 15 through 24). Acoustic liners are perforated surfaces that absorb a portion of a reflected pressure wave, thereby damping the intensity of the reflected wave and decoupling the wave from the combustion process (Figure 14). The fraction of the incident energy absorbed is termed the absorption coefficient. For successful combustion stabilization, the liners must be tuned to provide adequate absorption at the frequency or frequency range of concern.

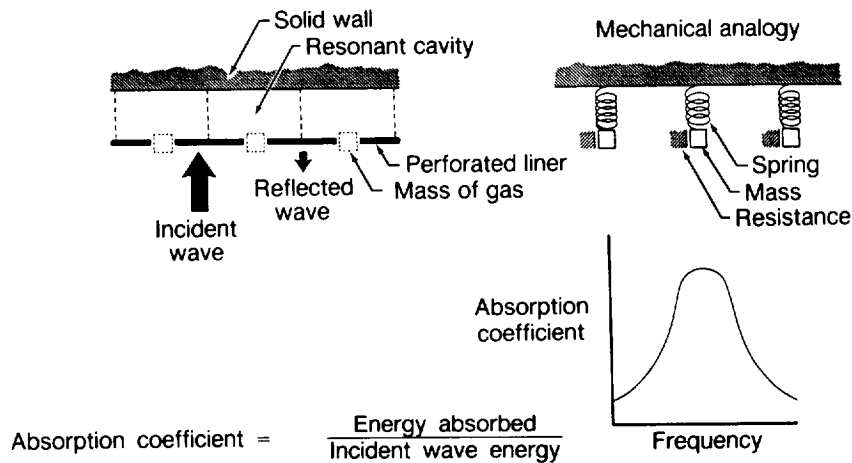
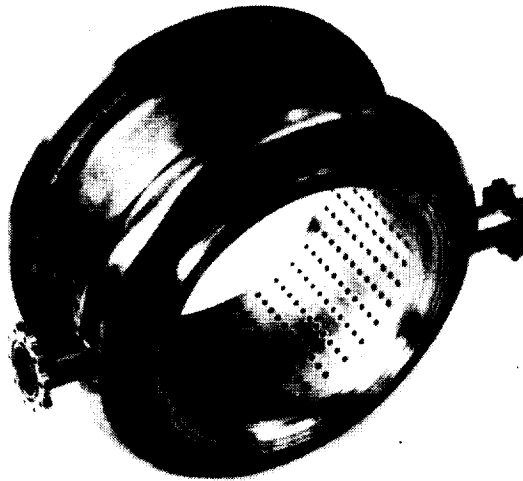


Figure 14. Acoustic Liner Principles

Except for acoustic cavity type designs mounted on or near the injector, acoustic liners have not been used in production rocket engines. They have, however, been successfully employed in many experimental evaluations. They have been used successfully with all of the propellants listed in Figure 15. Uncooled, regeneratively cooled and ablation cooled liners have been tested with equal success.



- LOX/H<sub>2</sub> (low fuel temp)
- N<sub>2</sub> O<sub>4</sub>/aerozine
- FLOX/butene
- LOX/RP-1 (F-1 vernier)
- Uncooled, regeneratively cooled & ablation cooled

Figure 15. Acoustic Liner Rocket Applications

Most rocket acoustic liner testing has been done at relatively low thrust. Some concern has been expressed that acoustic liners might not be adequate for stabilization of large diameter thrust chambers because of lower surface-to-volume ratios and the increased difficulty in stabilizing the lower frequencies inherent in these devices. These concerns should be allayed by the total success of acoustic liners in stabilizing combustion in jet engine afterburners. Every afterburning engine produced by P&W used an acoustic liner for combustion stabilization (Figure 16). Every afterburner in use has been dynamically stable. Most afterburners tested without an acoustic liner have been unstable. (The unstable data are limited because liners are now so routinely used.) The same theory is applied to the design of both rockets and afterburners, and the acoustic frequencies encountered in afterburners are typical of large rocket engines.

ORIGINAL PAGE IS  
OF POOR QUALITY

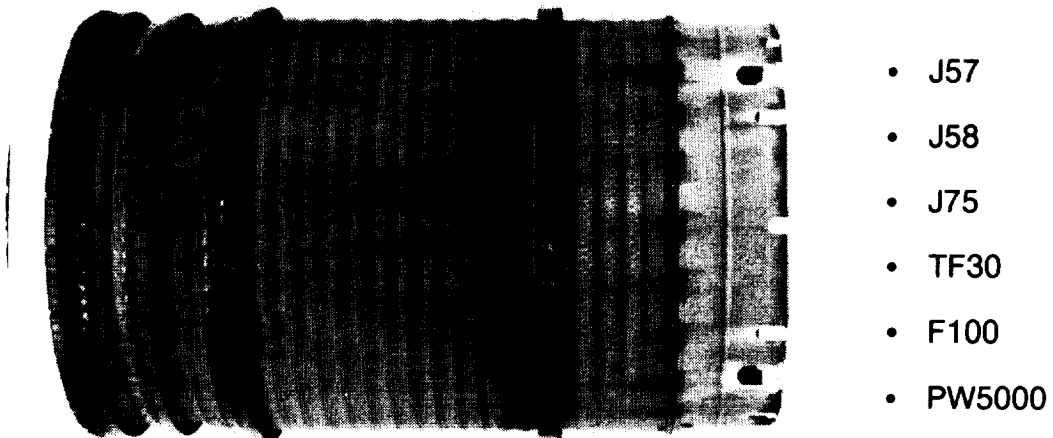


Figure 16. Acoustic Liner Turbojet Experience

#### SUMMARY

Significant increases in oxygen/hydrocarbon engine combustion pressure are possible through the use of advanced thrust chamber cooling techniques. Even higher pressure is possible by using hydrogen as the main chamber coolant in a tripropellant cycle.

If hydrogen is used as the primary coolant, it offers additional advantages if introduced into the combustion process. Easier ignition, higher combustion efficiency and more inherently stable combustion are predicted. Other design features which are predicted to enhance combustion stability include use of coaxial injectors, acoustic liners and injection of gaseous light hydrocarbon fuels rather than liquid fuels. Turbine fouling downstream of the gas generator can be eliminated by use of methane, hydrogen or a hydrogen-methane mixture as the gas generator fuel.

## REFERENCES

1. "Liquid Rocket Engine Injectors", NASA SP-8089, March 1976.
2. Michel, R.W., "Combustion Performance and Heat Transfer Characterization of LOX/Hydrocarbon Type Propellants," Report 1548-MA-129T-003F, Aerojet Liquid Rocket Company, April 1983.
3. Morinishi, R. and Cook, R.T., "Methane Heat Transfer Investigation," Final Report, Contract NAS8-34977.
4. Geovanetti, A.J., Spadaccini, J.H., and Szetela, E.J., "Deposit Formation and Heat Transfer in Hydrocarbon Rocket Fuels, NASA CR 168277, United Technologies Research Center, October 1983.
5. Martin, James A., "Effects of Tripropellant Engines on Earth-To-Orbit Vehicles," Journal of Spacecraft and Rockets, Vol. 22, No. 6, Nov.-Dec. 1985.
6. Bailey, C.R., "High Pressure LOX/Natural Gas Staged Combustion Technology," 1984 JANAF Propulsion Meeting, 2/8/84.
7. Spaulding, D.B., "Theory of Particle Combustion at High Pressure," ARS Journal, November 1959.
8. Rosner, D.E., "On Liquid Droplet Combustion at High Pressures," AIAA Journal, Vol. 5, No. 1, January 1967.
9. Hersch, Martin, "Effect of Interchanging Propellants on Rocket Combustor Performance with Coaxial Injection," NASA TN D-2169, February 1964.
10. Harrje, D.T., et al, "Liquid Propellant Rocket Combustion Instability," NASA SP-194, 1972.
11. Wanhainen, J.P., Parish, C.H., and Conrad, E.W., "Effect on Propellant Injection Velocity on Screech in 20,000 Pound Hydrogen-Oxygen Rocket Engine," NASA TN D-3373, April 1966.
12. Masters, A.I., "Investigation of Light Hydrocarbon Fuels with Flox Mixtures as Liquid Rocket Propellants - Final Report," PWA FR-1443, Contract NAS3-4195, NASA CR-54445, 9/1/65.

13. Masters, A.I., "Investigation of Light Hydrocarbon Fuels with Fluorine-Oxygen Mixtures as Liquid Rocket Propellants - Final Report," PWA FR-2227, Contract NAS3-6296, NASA CR-72147, 9/15/67.
14. Masters, A.I., "Investigation of Light Hydrocarbon Fuels with Fluorine-Oxygen Mixtures as Liquid Rocket Propellants - Final Report," PWA FR-2872, Contract NAS3-10294, NASA CR-72425 11/15/68.
15. Garrison, G.D., "Acoustic Liners for Storable Propellant Rocket Chambers - Phase I Final Report," Pratt & Whitney Report, AFRPL-TR-67-205, July 1967.
16. Garrison, G.D., "Acoustic Liners for Storable Propellant Rocket Chambers - Phase II Final Report," Pratt & Whitney Report PWA FR-2812, (AFRPL-TR-68-118), August 1968.
17. Garrison, G.D., "Absorbing Liners for Rocket Combustion Chambers Theory and Design Techniques," Pratt & Whitney AFRPL-TR-66-234, August 1966.
18. Russell, P.L., Garrison, G.D., et al, "Absorbing Liners for Storable Propellant Rocket Engines, Part 1 - Uncooled Liner Tests," Pratt & Whitney FR-2554 (no date).
19. Russell, P.L., Garrison, G.D., et al, "A Study of the Suppression of Combustion Oscillations with Mechanical Damping Devices," Pratt & Whitney FR-2596, 11/20/67.
20. Garrison, G.D., Russell, P.L., et al, "Acoustic Liners for Storable Propellant Rocket Chambers - Phase II," Pratt & Whitney AFRPL-TR-68-118, August 1968.
21. Garrison, G.D., Russell, P.L., et al, "Suppression of Combustion Oscillations with Mechanical Damping Devices," Pratt & Whitney FR-3299, 8/8/69.
22. Garrison, G.D., Russell, P.L., et al, "Acoustic Liner Design and Demonstration - Final Report," Pratt & Whitney AFRPL-TR-71-75, 8/28/71.
23. Garrison, G.D., Russell, P.L., et al, "Investigation of Damping Methods for Augmentor Combustion Instability," Pratt & Whitney AFAPL-TR-72-84, 8/30/72.

24. Garrison, G.D., Russell, P.L., et al, "Suppression of Combustion Oscillations with Mechanical Damping Devices," Pratt & Whitney FR-4993, 6/12/72.

## LOX/HYDROCARBON COMBUSTION AND COOLING SURVEY

R. T. Cook and F. M. Kirby

Rockwell International/Rocketdyne Division  
Canoga Park, CaliforniaAbstract

Liquid oxygen (LOX) and hydrocarbon fuels (methane, propane, and RP-1) are very attractive for booster rocket engine applications because of their high bulk density and respectful performance. Vehicle payload capability is dependent on the attainable engine chamber pressure and the combustion efficiency of the selected propellant combination. The chamber pressure is limited by the cooling capability of the main combustor. Therefore, the aspects of (1) combustion as related to combustion stability and efficiency and (2) cooling as related to cooling effectivity and combustor materials compatibility are key factors in selecting a hydrocarbon fuel and engine cycle for maximum payload. This survey of LOX/hydrocarbon combustion and cooling presents the results of pertinent company-sponsored activities and NASA/MSFC and LeRC contracts conducted by Rocketdyne.

Combustor design approaches are presented to attain maximum cooling, stability, combustion efficiency, and reusable life. Experimental combustion efficiency and hot-gas heat-transfer rates are discussed as related to combustor contour, thrust level scaling, and injector characteristics including mixture ratio biasing and film cooling. These experimental data are compared to theory, and empirical relationships are derived. Convective cooling relationships and coking limits are presented for potential hydrocarbon fuels as derived from high heat flux and high pressure electrically heated tube experiments. Experimental results of combustor coolant liner materials compatibility with hydrocarbon fuels are discussed. The application of the results of these studies to future LOX/hydrocarbon engines are delineated.

Introduction

LOX/hydrocarbon propellants are attractive for booster engines because of their high propellant bulk density and moderate performance. LOX/RP-1 was utilized for booster engine propulsion systems during the Apollo and Saturn programs. The chamber pressure and performance levels of these engines were relatively low compared to today's technology standards. The next generation LOX/hydrocarbon booster engine is trended toward a reusable, high-performance, high

chamber pressure engine similar to the LOX/hydrogen Space Shuttle Main Engine (SSME).

The performance level of the next generation booster engine will be dictated by the attainable combustion efficiency and the cooling limits of the main combustion chamber. The selection of a hydrocarbon fuel and engine cycle will depend greatly on the cooling capability and attainable combustion efficiency.

### Propellant Considerations

Desirable requisites are high performance and high bulk density. The propellant bulk density and performance is shown in Fig. 1 for the considered hydrocarbon propellants and compared to LOX/hydrogen for various mixture ratios. The performance presented in Fig. 1 represents a fixed chamber pressure at a fixed nozzle area ratio, and accordingly, a fixed nozzle exit pressure. The delivered vacuum specific impulse represents a staged combustion engine cycle with far-term technology. The performance of a gas generator cycle for a similar engine would be approximately 10 seconds lower. The performance and bulk density of the hydrocarbon propellant combinations are presented at their maximum thrust chamber specific impulse. Similarly, a mixture ratio of 6.0 represents the maximum specific impulse for the LOX/hydrogen propellant combination. The benefits of a hydrocarbon engine over a high mixture ratio (high bulk density) LOX/hydrogen engine is readily observable.

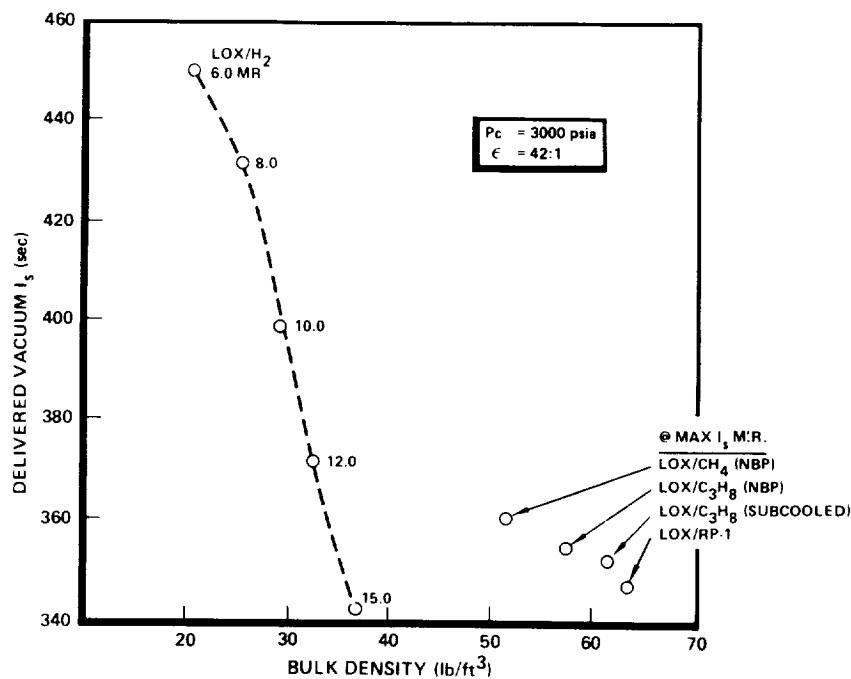


Fig. 1. Propellant Bulk Density and Performance Comparison



Numerous vehicle studies have shown payload and gross liftoff weight to be extremely sensitive to performance. In fact, some studies have shown LOX/hydrogen at its peak performance to be competitive. Therefore, there appears to be an imaginary band intersecting the hydrocarbon propellants and LOX/hydrogen at their maximum specific impulse mixture ratio that results in a near-equal trade between performance and propellant bulk density. This makes it very difficult to select a hydrocarbon propellant combination. Therefore, the hydrocarbon propellant combination to be selected for the next generation booster engine will probably depend on the logistics of propellant handling, combustion stability, combustion efficiency, heat transfer characteristics, and main combustion chamber materials compatibility with the selected fuel.

The selection of a hydrocarbon propellant combination is further complicated by the fact that the lower density propellant, being more akin to LOX/hydrogen, is most favorable for combustion stability, combustion efficiency, and cooling capability. Methane is most favorable for providing the desirable combustion and cooling characteristics and provides the minimum development risk. RP-1 is the most characterized, but at low performance values, and may be a high risk for high performance and with questionable cooling capability. Subcooled propane looks attractive because of its high bulk density, but the logistics of propellant handling and thermal management may be very costly. The combustion and cooling characteristics of propane are the least defined for high pressure booster engines.

#### Thrust Chamber Cooling Limits

Vehicle payload capability is dependent on the attainable engine chamber pressure and the combustion efficiency of the selected propellant combination. The chamber pressure is limited by the cooling capability of the main combustor for a specified turbopump technology level (turbine gas temperature and turbine tip speed). The cooling requirements of the thrust chamber nozzle is insignificant since it can be cooled with about 10 percent of the coolant pressure drop required to cool the main combustor. The regenerative cooling capability of all potential coolants are depicted in Fig. 2 for a 600,000 pound thrust engine with LOX/hydrocarbon combustion. This is applicable for any LOX/hydrocarbon propellant combination and reflects theoretical heat transfer rates equivalent to 70 percent of LOX/hydrogen, baselined to the SSME without film cooling or mixture ratio biasing. These coolant delta-P requirements are for a reusable life of 100 missions and realistically assumes no carbon deposit on the combustor hot gas wall. The coolant wall temperatures are below the coolant surface coking limits specified later.

The maximum attainable chamber pressure for RP-1 is approximately 2200 psia and requires a high pump discharge pressure even for a gas generator cycle. The chamber pressure limits of the other hydrocarbon

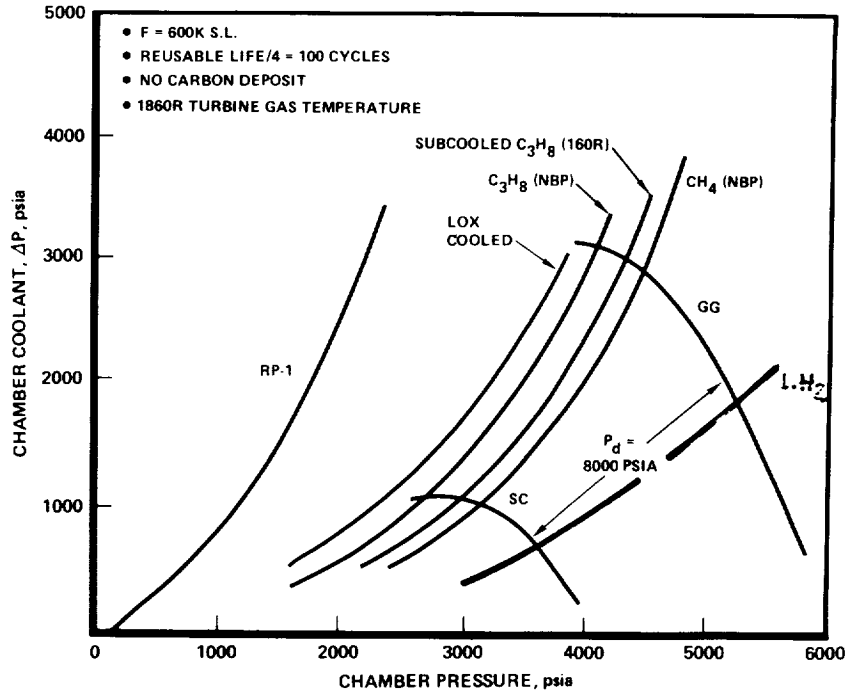


Fig. 2. Thrust Chamber Cooling Technology

fuels and for liquid oxygen are in the 3000 to 4000 psia chamber pressure range. Hydrogen cooling is most attractive but requires an auxiliary propellant to be carried aboard the vehicle. Gas generator cycle and staged combustion cycle chamber pressure cooling limits are noted for a current technology pump discharge pressure of 8000 psia.

Although the gas generator cycle can achieve a higher chamber pressure for a specified pump discharge pressure, the maximum specific impulse occurs at a considerably lower chamber pressure, approximately the same chamber pressure as the staged combustion cycle engine, as discussed below.

#### Engine Cycle Performance

The engine cycle selection will depend on the performance benefits to be gained, the propellant combination, and the complexity of the engine system. These benefits and trades are depicted in Fig. 3 as related to specific impulse gains available as a function of chamber pressure. The optimum chamber pressure is the chamber pressure where the maximum specific impulse is obtained for a specified level of turbopump technology. This occurs at approximately two-thirds of the cooling limit for the gas generator cycle because the combustor coolant  $\Delta P$  noted in Fig. 2 increases significantly with chamber pressure and requires a larger percentage of propellant to drive the turbine. Although the nozzle area ratio is increasing as associated

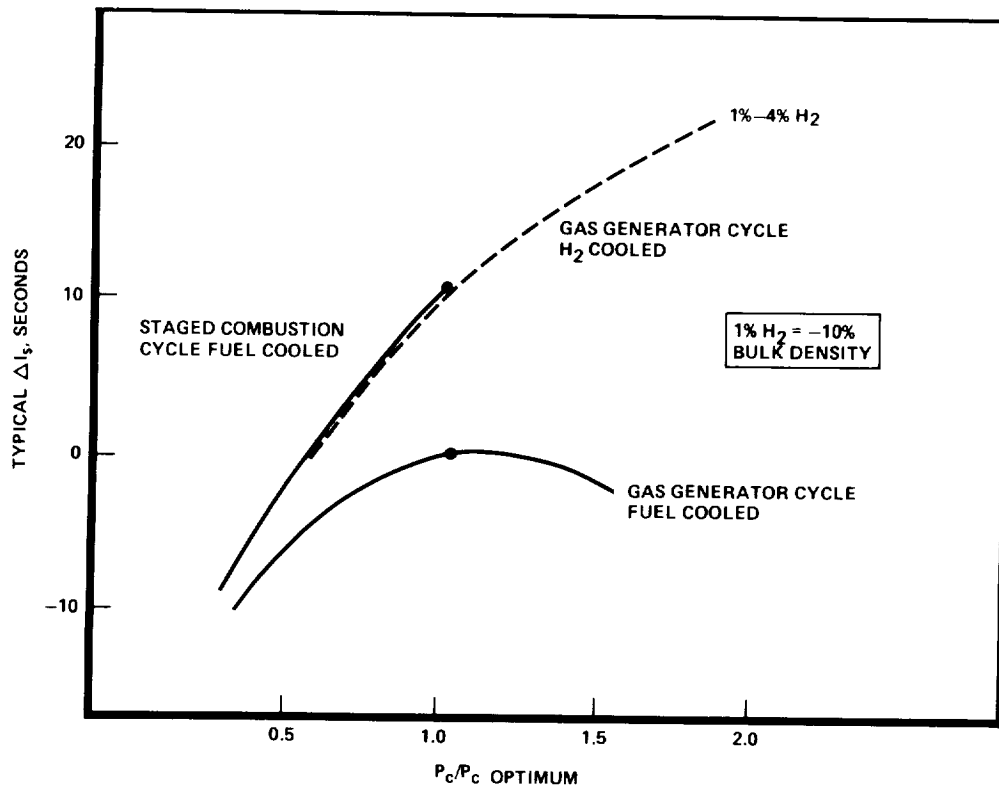


Fig. 3. Hydrocarbon Engine Cycle Performance

with a fixed nozzle exit pressure, the larger percentage of gas generator turbine drive gases being dumped into the nozzle overcomes the specific impulse gain of the larger nozzle area ratio. In the staged combustion cycle, the turbine drive gases are introduced into the main combustor and there are no secondary flow losses. Therefore, the optimum chamber pressure for the staged combustion cycle occurs at the cooling limit established for a specified turbopump technology level. The optimum (maximum) chamber pressure for the staged combustion engine is approximately the same as the optimum chamber pressure for the gas generator cycle engine. The tradeoff is a considerably lower pump discharge pressure for the gas generator cycle at a sacrifice of approximately 3 percent in specific impulse.

A high performance engine cycle is provided by the use of LOX/hydrogen turbine drive gases. High chamber pressures are afforded by the high cooling capability of hydrogen. A minimum hydrogen flowrate is desirable to maintain a high propellant bulk density. The required hydrogen flowrate is dictated by the turbopump power requirements and the combustor/nozzle cooling requirements. The minimum hydrogen flowrate required to cool the combustor/nozzle varies between 1 and 2 percent of the total propellant flowrate, depending on the chamber pressure level. The hydrogen flowrate dictated by turbopump requirements varies between 1 and 4 percent, depending on chamber pressure level and propellant combination. The effectiveness of this cycle favors the

LOX/RP-1 propellant combination for the minimum bulk density degradation. One percent hydrogen flow relates to approximately 10 percent decrease in propellant bulk density.

#### Combustion Performance Goals

The combustion performance goals and chamber pressure levels for near-term and far-term hydrocarbon engines are considerably higher than the LOX/RP-1 engines of the 1960s, as shown in Fig. 4. The combustion efficiency goals of the various on-going hydrocarbon studies are a function of propellant combination and near/far term capability. The lower performance is associated with RP-1 and the higher performance is associated with methane, which reflect the confidence of achieving high performance with hydrocarbon combustion. The chamber pressure levels achievable with the various coolant media are noted in Fig. 4. An RP-1 cooled combustor is limited to approximately 2000 psia chamber pressure and a methane cooled combustor can approach 3500 psia chamber pressure for similar turbopump technology.

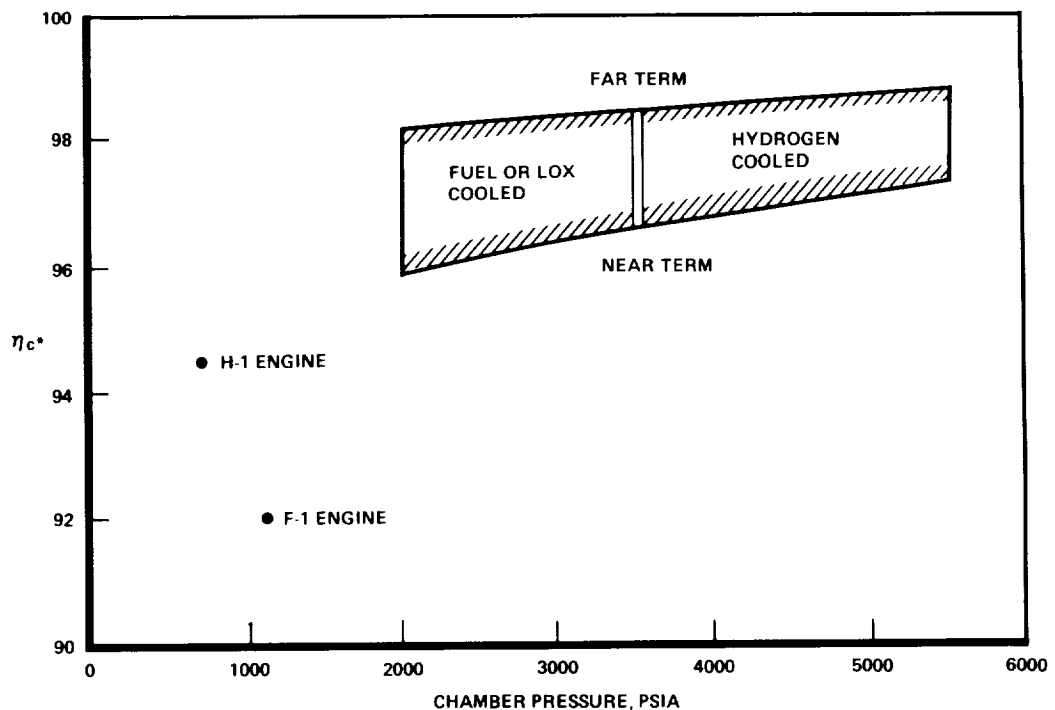


Fig. 4. Hydrocarbon Performance Goals

The LOX/RP-1 engines of the 1960s were operated at relatively low performance and low chamber pressure. Stability aids were utilized that also reduced the performance levels. Injector end fuel film cooling was employed and resulted in low thrust chamber heat transfer rates because of the extensive carbon deposition on the hot gas wall.

### Cooling Requirements

The heat transfer level of the LOX/RP-1 engines of the 1960s were very low as associated with low chamber pressure and low combustion efficiency, which provided a carbon thermal barrier on the thrust chamber hot gas wall. Future high performance hydrocarbon engines will not be afforded this thermal barrier and as a result will require combustion chamber designs similar to the high performance LOX/hydrogen SSME. The theoretical heat transfer rate of high performance LOX/hydrocarbon combustors is 70 percent of LOX/hydrogen combustors and do not possess a carbon thermal barrier.

The throat heat flux and chamber pressure levels of the next generation hydrocarbon engines are compared to the past generation engines in Fig. 5. The throat heat flux of past engines was about one-tenth of future hydrocarbon engines. Therefore, it is obvious why tubular steel constructed thrust chambers sufficed for the 1960s but future combustors will need to be fabricated of a channel-configured copper-base alloy.

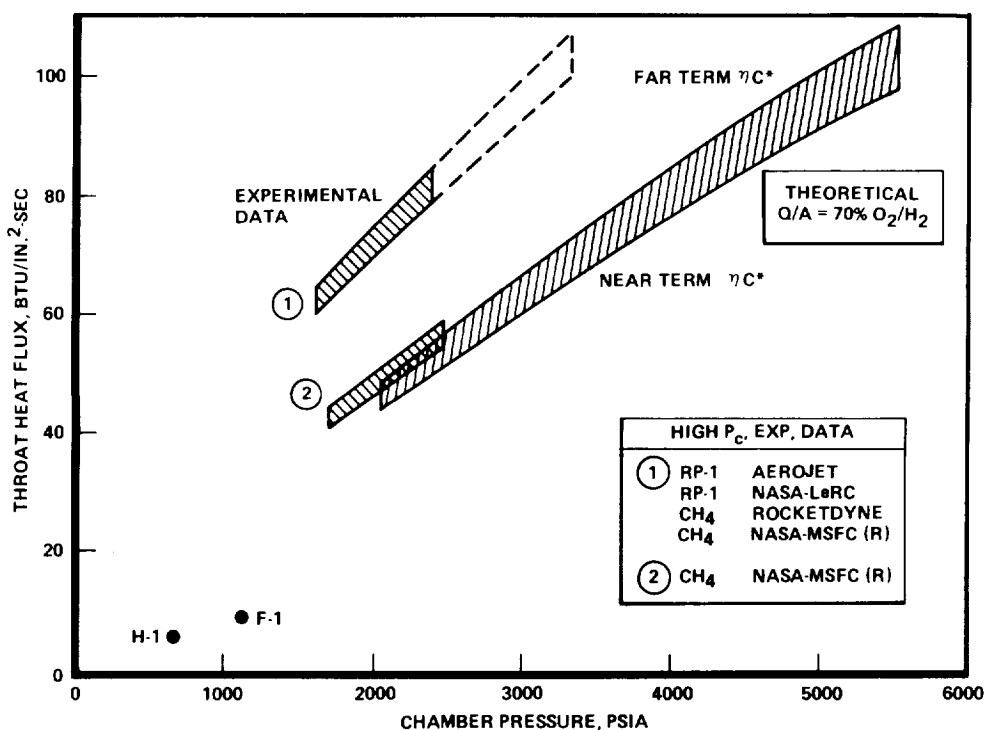


Fig. 5. Hydrocarbon Cooling Requirements

The cooling assessment presented in Fig. 2 is based on the theoretical hot gas heat transfer rates noted in Fig. 5. These theoretical heat transfer conditions are 70 percent of those derived from subscale and full-scale SSME experimental data without film cooling or mixture ratio biasing.

A number of high performance, high chamber pressure, LOX/hydrocarbon subscale injectors have been fabricated and tested over the past 6 years. These consisted of several 20,000-pound thrust LOX/RP-1 injectors fabricated by Aerojet and NASA/LeRC, and several 40,000-pound thrust LOX/CH<sub>4</sub> injectors fabricated by Rocketdyne. All of these injectors, with the exception of the last LOX/CH<sub>4</sub> injector, displayed heat transfer rates 40 percent higher than theoretical, equivalent to the high performance LOX/hydrogen SSME without film cooling or mixture ratio biasing. This anomaly is not fully understood. These high heat flux injectors displayed combustion efficiencies slightly lower than anticipated. Only recently was a high performance (98 to 99 percent  $\eta_{c^*}$ ) LOX/CH<sub>4</sub> injector tested that displayed theoretical heat transfer rates without film cooling or mixture ratio biasing. This coaxial element injector was designed by Rocketdyne for LOX/CH<sub>4</sub> operation at 3000 psia chamber pressure. It was tested between 1700 and 2400 psia chamber pressure at MSFC and displayed heat transfer characteristics 70 percent of the SSME throughout the combustor length.

The previous two LOX/CH<sub>4</sub> injectors were SSME 40,000-pound thrust injectors with modifications to accommodate the higher density methane fuel. One each was tested at Rocketdyne and NASA/MSFC. Both displayed the heat transfer characteristics of LOX/hydrogen, similar to the previous tested LOX/RP-1 injectors by Aerojet and NASA/LeRC. The combustion performance was lower than the latter LOX/CH<sub>4</sub> injector. Both injectors were successfully modified to reduce their heat flux level to the theoretical value. The MSFC-tested injector utilized mixture ratio biasing of the injector elements adjacent to the combustor wall and the Rocketdyne-tested injector utilized injector end film cooling. Both modifications resulted in a slight performance degradation.

The high heat transfer rates experienced with high performance hydrocarbon injectors cannot be theoretically quantified nor can the large suppression of the heat transfer rate by film cooling or mixture ratio biasing. The chamber pressure cooling limit for the higher heat transfer rates would be 50 percent of the theoretical value as can be seen in Fig. 5 by comparing chamber pressure level for the equivalent theoretical heat flux. This is definitely an area of concern and is probably influenced both by injector design and propellant combination.

The methodology utilized for defining the hot gas heat transfer rate of a combustor for scaling from lower calorimetric chamber pressures and subscale hardware is depicted in Fig. 6 and discussed below. The methodology is identical to that used and verified during the SSME development. Local heat transfer rates were determined using a 40,000-pound thrust calorimeter combustor at chamber pressure levels between 1500 and 2000 psia chamber pressure. Chamber pressure scaling, or more correctly  $\rho V$  scaling, adhered to  $(\rho V)^{0.8}$ . The 40,000-pound thrust regenerative combustor heat load was verified at the calorimeter chamber pressure level and  $(\rho V)^{0.8}$  scaling verified up to 3000 psia chamber pressure. The full-scale SSME combustor heat load and local thermal characteristics were projected by scaling local  $(\rho V)^{0.8}$ .

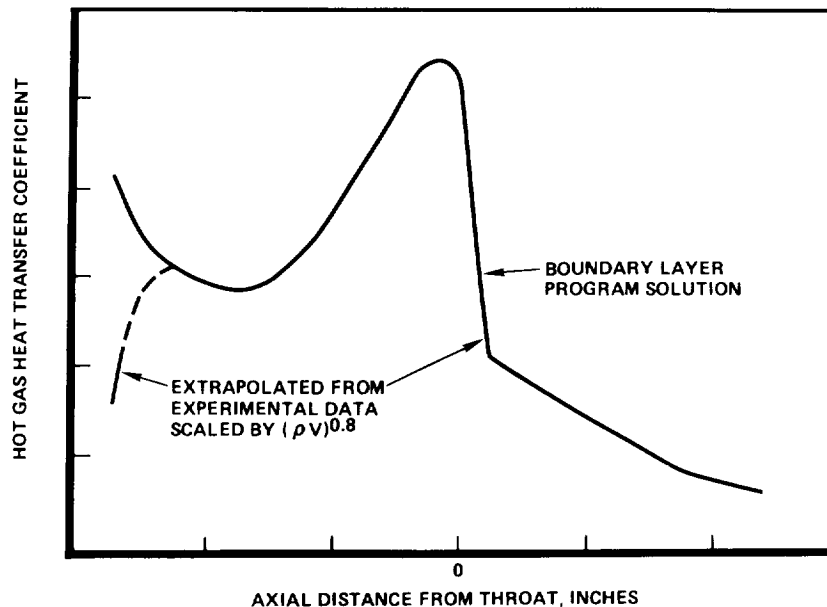


Fig. 6. Hot Gas Heat Transfer Coefficient Profile

This approach was confirmed on full-scale combustor testing. An alternate approach is the Nusselt pipe flow relationship that applies a diameter correction of  $(1/D)^{0.2}$ . However, this approach would have resulted in a 30-percent reduction in the hot gas heat transfer coefficient for the full-size SSME combustor, representing nearly 400 F lower hot gas wall temperatures. The SSME combustor scaling test results negate the use of a diameter correction.

#### Combustor Design Considerations

Combustion chamber geometry (liner hot gas wall contour) affects the weight, performance, heat transfer, and life. Influencing parameters are length, contraction area ratio, and wall contour. The optimum combustion chamber design is one with minimum engine weight, minimum hot gas wall temperature (maximum life), and maximum performance. In addition, engine constraints are imposed on the chamber design as related to coolant pressure drop and flowrate requirements established for an engine with minimum oxidizer and fuel pump discharge pressures. The optimum coolant passage geometry for maximum life normally approaches the minimum wall thickness and minimum channel and land widths which are dictated by manufacturing limits.

The selection of combustor length and contraction area ratio is primarily dictated by heat transfer, system weight, and combustion performance. The combustion chamber coolant pressure drop is primarily a function of the chamber length and contraction area ratio.

Typical designs use a cylindrical section at the injector end and a large radius to convergence that provides injector-to-combustor wall

compatibility. A generous upstream convergence radius joining the cylindrical combustion chamber section with the throat entrance ramp provides a smooth transition to avoid flow separation at the turn or impingement at the initial portion of the chamber convergence ramp on the hot gas wall. It also prevents degradation of the coolant film coefficient due to reverse curvature effects.

Steep throat entrance angles result in late boundary layer attachment and consequent high throat heat flux; whereas, shallow entrance angles result in continuous boundary layer growth with minimum throat heat flux. Shallow entrance angles do, however, impose a slightly greater integrated heat load due to a lower average contraction area ratio. A 25- to 30-degree convergence angle is typical, favoring a lower throat heat flux for maximum life.

The radius of curvature relative to the throat radius ( $r_c/r_t$ ) entering the throat transonic region affects both the distortion and location of the sonic line and the distribution of the transonic flow field in the throat region. A desirable throat radius ratio varies between 0.5 and 1.0.

Typical combustor contours used for high pressure, high performance hydrocarbon engine studies are shown in Fig. 7. These contours are identical to the SSME combustor. Slight variations in combustor contraction ratio (2.6 to 3.0) may be traded for combustor cylindrical length and throat radius for the same  $\Delta P/P_c$  cooling relationship. Common hydrocarbon engine study guidelines are noted in Table 1.

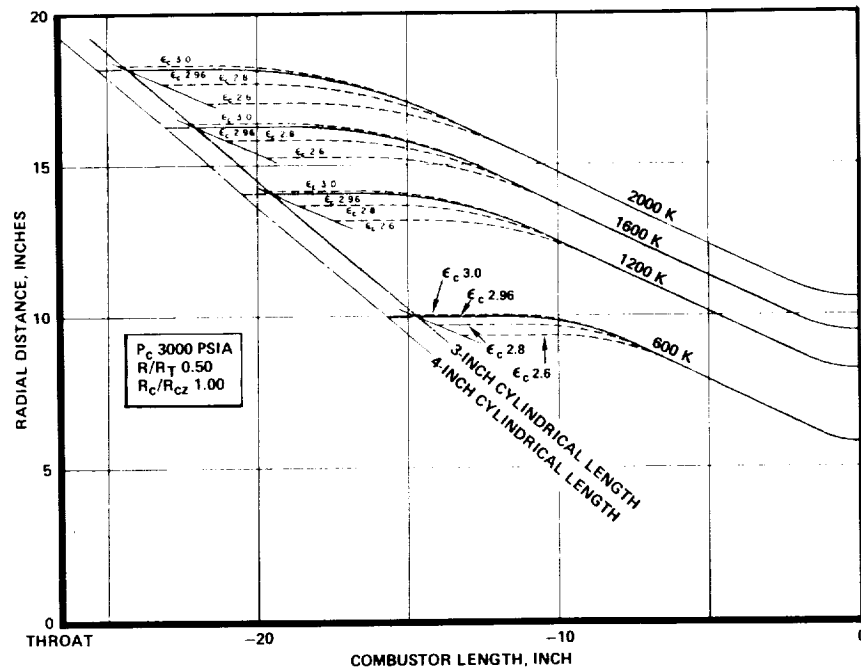


Fig. 7. LOX/Hydrocarbon Main Combustion Chamber



CRITICAL POINTS  
OF POOR QUALITY

Table 1. Hydrocarbon Engine Study Guidelines

Parameter	Guidelines
Propellants	<ul style="list-style-type: none"> <li>● LOX/RP-1 at <math>(MR)_{TC} = 2.8</math></li> <li>● LOX/CH<sub>4</sub> at <math>(MR)_{TC} = 3.5</math></li> <li>● LOX/C<sub>3</sub>H<sub>8</sub> at <math>(MR)_{TC} = 3.1</math></li> </ul>
Engine Size	<ul style="list-style-type: none"> <li>● 200K to 2000K pound thrust level</li> <li>● Nozzle <math>\epsilon</math> for 6 psia exit pressure</li> </ul>
Performance	<ul style="list-style-type: none"> <li>● Baseline <math>\eta_{c*} = 98\%</math> (heat transfer parametrics corrected for other <math>\eta_{c*}</math> as noted)</li> </ul>
Thrust Chamber Geometry	<ul style="list-style-type: none"> <li>● Tubular nozzle</li> <li>● Channel combustor               <ul style="list-style-type: none"> <li>● Minimum channel width 0.030 inch</li> <li>● Minimum land width 0.030 inch</li> <li>● Maximum channel height/channel width = 5:1</li> </ul> </li> </ul>
Combustion Chamber Liner	<ul style="list-style-type: none"> <li>● NARloy-Z with electrodeposited nickel closeout</li> </ul>
Coolant Wall Coking Limits	<ul style="list-style-type: none"> <li>● RP-1 1060 to 1200 R (function of mass velocity)</li> <li>● C<sub>3</sub>H<sub>8</sub> 1320 R</li> <li>● CH<sub>4</sub> 1760 R</li> </ul>
Hot Gas Heat Transfer	<ul style="list-style-type: none"> <li>● No carbon deposition</li> <li>● Empirical relationships</li> </ul>
Coolant Heat Transfer	<ul style="list-style-type: none"> <li>● <math>\Delta P/P_c</math> relationships based on latest coolant correlations</li> <li>● Coolants evaluated               <ul style="list-style-type: none"> <li>● Fuels (RP-1, C<sub>3</sub>H<sub>8</sub>, CH<sub>4</sub>)</li> <li>● Oxygen</li> <li>● Hydrogen auxiliary cooling</li> </ul> </li> <li>● Surface roughness               <ul style="list-style-type: none"> <li>● 20 microinches for main combustion chamber</li> <li>● 40 microinches for nozzle</li> </ul> </li> <li>● Coolant inlet temperatures, R               <ul style="list-style-type: none"> <li>● RP-1 530</li> <li>● C<sub>3</sub>H<sub>8</sub> (SC) 160</li> <li>● (NBP) 420</li> <li>● CH<sub>4</sub> 210</li> <li>● Hydrogen 100</li> <li>● Oxygen 165</li> </ul> </li> <li>● Coolant flow split               <ul style="list-style-type: none"> <li>● Approximately 50/50 (main combustion chamber/nozzle)</li> </ul> </li> </ul>
Reusable Life	<ul style="list-style-type: none"> <li>● 100 missions               <ul style="list-style-type: none"> <li>● <math>N_f/4 = 100</math> cycles</li> <li>● <math>t/4 = 8</math> hours</li> </ul> </li> </ul>

Experimental High Pressure Cooling Data

Convective cooling heat transfer relationships and coking limits of hydrocarbon fuels are typically determined with an electrically heated tube apparatus as shown in Fig. 8. The cooling medium is passed through the tube while the tube is heated by electrical power. Local heat transfer measurements define the cooling capability of the fluid over a wide range of thermal and fluid conditions representing the combustor thermal operating levels. A summary of the high pressure (5000 psia) hydrocarbon fuel experimental data is presented in Table 2.

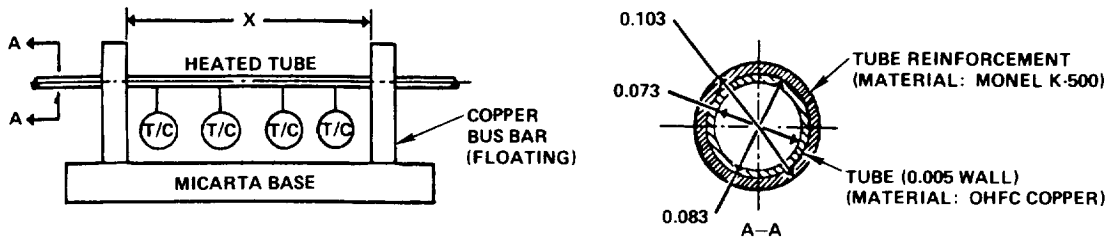


Fig. 8. Experimental High Pressure Cooling Data  
(Electrically Heated Tubes)

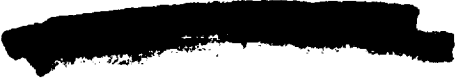
Table 2. Experimental High Pressure Cooling Data

Evaluator	Tube Material	Fuels	Maximum Q/A, Btu/in. <sup>2</sup> -sec
Rocketdyne	Stainless Steel	CH <sub>4</sub> , C <sub>3</sub> H <sub>8</sub> , RP-1	35
Rocketdyne (NASA/MSFC)	K-Monel/Copper	CH <sub>4</sub>	85
UTRC	K-Monel/Copper	CH <sub>4</sub> , C <sub>3</sub> H <sub>8</sub> , RP-1	8

Rocketdyne developed convective cooling relationships and thermal decomposition (coking) limits for the three hydrocarbon fuels under a company-sponsored effort approximately 6 years ago. These experimental data were obtained from electrically heated stainless steel tubes with a heat flux limit of 35 Btu/in.<sup>2</sup>-sec. These data were used for the parametric cooling studies shown in Fig. 2, with the coking limits noted in Table 1.

United Technology Research Center (UTRC), under a NASA/LeRC contract, conducted experiments using a bimetallic tube configuration (noted in Fig. 8), which exposed the coolant medium to a heated copper surface typical of high chamber pressure combustors. Although the experimental data were at low heat flux levels, they did report the observance of coking, particularly for RP-1 and propane. However, more importantly was the indication of a chemical incompatibility between the hydrocarbon fuels and the copper surface.

This effort was followed by a Rocketdyne study, under a NASA/MSFC contract, evaluating methane in a similar bimetallic tube configuration but at heat transfer rates to be experienced in high performance, high chamber pressure combustors. The advantages of the bimetallic tube configuration can be readily seen in the attainable heat transfer level. The convective cooling correlation was typical of that obtained from the previous stainless steel tube experiments. Again, coking was not detected even at the elevated heat flux. However, severe erosion/corrosion of the copper surface was experienced. This phenomenon appeared to be a function of heat flux, surface temperature, and coolant mass velocity. This phenomenon generally started at operating conditions typical of a combustor operating level of approximately 30 Btu/in.<sup>2</sup>-sec. The erosion process progressed rapidly at elevated thermal conditions where up to 0.003 inch of the copper surface was



eroded away in a period of several minutes. This experiment was verified to be a materials compatibility problem with the methane by conducting similar heat transfer tests with hydrogen that produced no surface deterioration. However, it is not known at this time whether this phenomenon is only associated with the electrical heating of a copper surface in the presence of a flowing hydrocarbon fuel.

#### Conclusions

Hydrocarbon engine studies conducted over the past 8 years by the NASA, Air Force, and rocket propulsion contractors have identified the next generation hydrocarbon engine to be more akin to the SSME than to past generation LOX/RP-1 engines, such as the H-1 and F-1. The overwhelming attractiveness for high performance and reusability demands a sophisticated main injector with a main combustor design typical of the high performance Space Shuttle Main Engine.

Experimental investigations have identified two areas of concern. These are the predominantly high heat transfer rates of the main combustor and the potential hydrocarbon fuel incompatibility with a copper-base main combustor liner.

LIQUID OXYGEN COOLING OF  
HIGH PRESSURE LOX/HYDROCARBON  
ROCKET THRUST CHAMBERS

H. G. Price  
Lewis Research Center  
Cleveland, OH 44135

ABSTRACT

An experimental program using liquid oxygen (LOX) and RP-1 as the propellants and supercritical LOX as the coolant was conducted at 4.14, 8.274 and 13.79 MN/m<sup>2</sup> (600, 1200 and 2000 psia) chamber pressure. The objectives of this program were to evaluate the cooling characteristics of LOX with the LOX/RP-1 propellants, the buildup of soot on the hot-gas-side chamber wall and the effect of an internal LOX leak on the structural integrity of the combustor.

Five thrust chambers with throat diameters of 6.6cm (2.6 in.) were tested successfully. The first three were tested at 4.14 MN/m<sup>2</sup> (600 psia) chamber pressure over a mixture ratio range of 2.25 to 2.92. One of these three was tested for over 22 cyclic tests after the first through crack from the coolant channel to the combustion zone was observed with no apparent metal burning or distress. The fourth chamber was tested at 8.274 MN/m<sup>2</sup> (1200 psia) chamber pressure over a mixture range of 1.93 to 2.98. The fourth and fifth chambers were tested at 13.79 MN/m<sup>2</sup> (2000 psia) chamber pressure over a mixture ratio range of 1.79 to 2.68.

## Liquid Oxygen Cooling of High Pressure LOX/Hydrocarbon Rocket Thrust Chambers

### Introduction

Preliminary design studies by NASA and its contractors (references 1, 2, 3, 4) for vehicles such as the mixed-mode, single-stage-to-orbit (SSTO) and the heavy lift launch vehicle (HLLV), have shown a requirement for a new high pressure ( $27.58\text{MN/m}^2$  - 4000 psia chamber pressure) booster engine using a hydrocarbon fuel and oxygen for propellants. Furthermore, ongoing studies are evaluating hydrocarbon fueled propulsion systems applicable to operations for a quick response, highly maneuverable launch vehicle. These systems would ultimately lead to a truly economical means of accomplishing many of the space missions envisioned in the 1990 time period and beyond. The candidate hydrocarbon fuels for these assumed systems appear to be RP-1, propane and methane. One specific hydrocarbon fuel or propulsion system has not been selected at this time.

One characteristic of LOX/RP-1 and LOX/propane combustion over the mixture range (O/F) of interest is the formation of soot and the buildup of a carbon layer along the hot thrust chamber wall. This carbon layer acts as an insulator reducing the heat transfer into the combustor walls. The carbon layer thickness will vary with different axial locations and may be affected by chamber pressure level and by the start and shutdown sequences of the test firings. A reasonable assumption, supported by experimental evidence, relating to hot gas deposits is that an equilibrium is reached between the depositing layer and that which is being eroded away. There is evidence that chemical reaction plays a significant role in determining the equilibrium when molecular and/or atomic oxygen is present in the hot gas stream. However, some deposit would likely flake off the wall by the erosion effect of the gas moving over the deposit surface resulting in hot spots.

The requirements for a very high chamber pressure, (very high heat flux) hydrocarbon fueled rocket engine has necessitated that the engine designer consider evaluating the cooling capability of both the fuel and the oxidizer. An inherent disadvantage of RP-1 and even the lighter paraffinic hydrocarbon propane, is the tendency for these hydrocarbons to undergo decomposition (coking) in the coolant passages. They form barrier coatings from the decomposition (coking), thereby greatly reducing their cooling capability. A further complication with hydrocarbon propellant cooling recently identified in reference 5 is the corrosion of copper by chemical attack caused by trace metallic impurities in the fuel.

Because of the coking cooling limitation and chemical attack problems associated with using a hydrocarbon as the regenerative coolant, it is necessary to consider the oxidant (oxygen) as a possible coolant option for the advanced LOX-hydrocarbon engine. Supercritical liquid oxygen is a desirable heat transfer candidate due to its generally favorable thermodynamic and transport properties. However, a concern

with the use of oxygen as a coolant is what would happen if a through-crack formed in the wall allowing oxygen to enter the combustor. One hypothesis offered is that the oxygen upon entering the combustion chamber through the crack could potentially oxidize the carbon layer or react with the fuel rich combustor products which in turn could heat the thrust chamber wall to its ignition temperature and cause a catastrophic failure. Another scenario offered is that the LOX entering through the crack would film-cool the carbon layer with no oxidation of either the carbon layer or the metal wall.

The purposes of the present program were to evaluate the cooling characteristics of liquid oxygen with LOX/RP-1 propellants, determine the buildup of soot on the hot-gas-side chamber wall, and observe the effect of an internal LOX leak on the structural integrity of the combustor.

This program focused on LOX/RP-1 propellant combustion and achieved test results at a chamber pressure approximately half the chamber pressure of an advanced system. The effort concentrated on the design and test of small thrust chambers (22,241 to 75,619N-5,000 to 17,000 lbs. force thrust) and involved developing procedures for smooth starts and shutdowns and the design of resonator hardware for combustion stability as well as injectors to assess combustion efficiency comparisons.

A series of experimental tests in which soot deposit on the wall was determined were conducted at 4.14, 8.27, and 13.79 MN/m<sup>2</sup> (600, 1200 and 2000 psia) chamber pressure with LOX/RP-1 as the propellants and using LOX as the coolant. The 4.14 MN/m<sup>2</sup> (600 psia) chamber pressure tests covered an O/F range of 2.2 to 2.9, the 8.274MN/m<sup>2</sup> (1200 psia) chamber pressure tests covered an O/F range of 1.9 to 3.0 and the 13.79 MN/m<sup>2</sup> (2000 psia) chamber pressure tests covered an O/F range of 1.8 to 2.7. To evaluate the effect of a LOX leak on structural integrity, a cyclic hot fire test series at 4.14 MN/m<sup>2</sup> (600 psia) chamber pressure was conducted until a crack developed in the hot gas wall.

### Heat Transfer Correlation

Heat transfer to supercritical oxygen has been investigated (Ref. 6) with a series of heated tubes at high pressures ranging from 17 to 34.5 MN/m<sup>2</sup> (2000 to 5000 psia) and bulk temperature of 96 to 217K (173° to 391°R). From this test data and previously existing data (Ref. 7 & 8), a multiple regression analysis was conducted as part of the work done in Ref. 6 which led to the following design correlation for calculating supercritical oxygen heat transfer coefficients:

$$Nu_b = 0.0025 Re_b Pr^{0.4} \left( \frac{\rho_b}{\rho_w} \right)^{-1/2} \left( \frac{K_b}{K_w} \right)^{1/2} \left( \frac{C_p}{C_{pb}} \right)^{2/3} \left( \frac{P_b}{P_{cr}} \right)^{-1/5} \left( 1 + \frac{2}{L/D} \right)$$

where:

$C_p$  constant pressure specific heat

$\overline{C_p}$  integrated average specific heat from  $T_w$  to  $T_b$

D inside tube diameter  
h heat transfer coefficient  
K thermal conductivity  
L heated tube length  
Nu Nusselt number,  $hD/K$   
P pressure (local static)  
Pr Prandtl number,  $C_p \mu / K$   
Re Reynolds number,  $\rho DV / \mu$   
T temperature  
V fluid velocity  
 $\mu$  viscosity  
 $\rho$  density

Subscripts:

b evaluated at bulk temperature  
cr critical state  
w evaluated at wall temperature

The thrust chambers used in this investigation were designed and fabricated using this cooling side heat transfer correlation. Refer to Ref. 9 for design details. This correlation was validated by the work of reference 10, where the measured wall temperatures agreed with the analytically predicted wall temperature.

### Apparatus and Procedures

#### Injectors

A typical injector used in this program (Ref. 11) at 4.14 MN/m<sup>2</sup> (600 psia) chamber pressure is shown in figure 1. This injector is a 37 element oxidizer-fuel-oxidizer triplet injector with an impingement half angle of the oxidizer onto the fuel of 30°. The triplet element pattern was arranged to provide mutually perpendicular LOX fans.

To obtain a more uniform flow distribution behind the injector face

for the higher chamber pressures, a 61 element injector as shown in Figure 2 was used for the  $8.274 \text{ MN/m}^2$  (1200 psia) chamber pressure testing. This injector was originally fabricated with the 61 elements as triplets arranged in a pattern to provide LOX tangential fans. However, this injector pattern resulted in a high temperature of the hot-gas wall. As a result, the injector was modified in the outer ring of elements by welding closed all the holes and then redrilling the fuel holes and inner LOX holes as showerheads. The outer zone then consisted of 24 fuel holes and 24 oxidant holes. This pattern provided 25% of the total fuel flow and 13% of the oxygen flow in the outer zone. At an overall O/F of 2, there was an O/F of 1.03 in the outer zone and an O/F of 2.32 in the core.

Figure 3 shows a 61 element injector used for the  $13.79 \text{ MN/m}^2$  2000 psia chamber pressure testing. This injector was modified in the outer ring of elements as the  $8.274 \text{ MN/m}^2$  (1200 psia) chamber pressure injector was. The outer ring of elements were welded closed and the fuel holes and inner LOX holes redrilled as showerheads. This pattern provided 30% fuel flow in the outer zone and 18% oxygen in the outer zone. At an overall O/F of 2, there was an O/F of 1.18 in the outer zone and an O/F of 2.35 in the core. The hole sizes, areas, and pressure drops for the three injectors are shown in Table I.

#### Combustion Chambers

The thrust chamber hot gas liners were fabricated of an oxygen-free, high-conductivity (OFHC) copper and contained 100 axial milled slots for the coolant passages. The passages were closed out with electroformed nickel. The details of the coolant channel dimensions are given in Ref. 9.

Because of the higher heat releases at  $8.274 \text{ MN/m}^2$  (1200 psia) and  $13.79 \text{ MN/m}^2$  (2000 psia) chamber pressure, a shorter combustion chamber was used at these chamber pressures than at  $4.14 \text{ MN/m}^2$  (600 psia) chamber pressure. The dimensions of the thrust chambers are shown in Figure 4 and Table II.

Five thrust chambers were used during this program. A photograph of a chamber in the test stand being fired vertically downward is shown in Figure 5. A photograph of a chamber, resonator, and injector is shown in Fig. 6. The thrust chambers were instrumented with Chromel/Constantan thermocouples imbedded in the rib between coolant channels approximately 1.27 mm (.05 in.) from the hot gas wall as described in Ref. 12. All of the chambers had 16 thermocouples evenly spaced circumferentially in four axial positions, two upstream of the throat, one at the throat, and one downstream of the throat. In the shorter chambers, the two planes upstream of the throat were at 16.5cm and 26.0cm (6.5 and 10.25 in.), the throat was 29.2cm (11.5 in.), and the downstream plane was 31.8cm (12.5 in.) from the injector face. In the longer chambers the two planes upstream of the throat were at 26.0cm and 36.2cm (10.25 and 14.25 in.), the throat was 39.4cm (15.5 in.), and the downstream plane was 41.9cm



(16.5 in.) from the injector face. These positions provide temperature instrumentation in the cylindrical, convergent, throat, and divergent portions of the thrust chamber. The instrumentation can be seen in the thrust chamber portion of Fig. 6.

### Resonators

A water-cooled resonator, as shown in the middle portion of Fig. 6, was used in this investigation to provide stable combustion. It was composed of sixteen cavities arranged evenly around its inside surface. The resonator was coaxial with, and placed between, the chamber and the injector. The cavities were in line with the thrust chamber at its edge and were 3.63cm (1.43 inch) long. The injector formed the inner wall of the cavities which were 2.54 cm (1 inch) long (see Fig.4). This corresponded to a quarter wave tube to dampen the 2nd tangential frequency of 9700 cycles/sec which was the expected frequency of the combustion oscillations causing the instability. The same type of resonator had been used in the work described in Ref. 13.

### Igniter

Propellant ignition was accomplished with a hydrogen/oxygen spark torch igniter inserted through the resonator wall just downstream of the cavities. This igniter was started just prior to the main propellant flow and supplied the energy necessary to start the LOX/RP-1 combustion. After LOX/RP-1 combustion was initiated the torch flows were turned off and a small inert purge gas flow started to prevent hot combustion gas from backing up into the igniter.

### Test Facility and Procedures

This program was conducted in a 222 410 N (50,000 lbf) thrust, sea-level rocket test stand equipped with an exhaust-gas muffler and scrubber. The facility used pressurized propellant storage tanks to supply the propellants to the combustion chamber. The propellants were liquid oxygen (LOX) and ambient-temperature RP-1. A separate source of LOX was used as the coolant. Installation of the thrust chamber on the facility thrust stand can be seen in Fig. 7.

Two types of tests, cyclic and steady state, were performed during this program. In the cyclic tests, the chamber was brought up to the desired pressure and maintained at that pressure for .5 second and then the propellant valves were closed for a duration of 2 seconds. The fuel valve was closed first to avoid fuel contamination of the LOX portion of the injector when cyclic tests were performed. This was followed immediately by a second cycle to the same operating condition. As many as 25 consecutive cycles at a time were performed in this manner. The LOX coolant flow continued during both firing and non-firing portions of the cycle. This type of test was used to first produce a crack into the combustion chamber and then to investigate the effect of a LOX leak through the crack on thrust chamber wall integrity with the chamber still firing.

In the steady-state tests, the pressure was brought up in the chamber and maintained at the desired level for a duration from 1.3 to 10 seconds. The heat transfer information was obtained from this type of test. The thermocouples imbedded in the channel ribs reached steady values in approximately 1 second and remained constant while the data were recorded.

Test cycles were programmed into a solid-state timer that was accurate and repeatable to within  $\pm 0.001$  second. Fuel and oxidizer flows were controlled by fixed-position valves and propellant tank pressure. Coolant inlet pressure was controlled by coolant tank pressure. Coolant exit pressure was kept constant by a closed-loop controller modulating a back pressure valve. With this arrangement, the coolant flow rate started high and decreased to the desired value as the final combustion conditions were reached. The coolant was vented after use.

Control room operation of the test included monitoring of the test hardware by means of three closed-circuit television cameras. The output of one television camera was recorded on magnetic tape for later playback.

Data was recorded every 0.02 second, averaged over five recordings, and the average reported every 0.10 second.

### Test Results

#### Test Conditions

Five thrust chambers were tested during this program. The conditions for these tests are shown in Table II. Chambers S/N 1, 2, and 3 were operated at  $4.14 \text{ MN/m}^2$  (600 psia) chamber pressure. Chamber S/N 4 was operated at  $8.274 \text{ MN/m}^2$  (1200 psia) chamber pressure and chamber S/N 4 and 5 were operated at  $13.79 \text{ MN/m}^2$  (2000 psia) chamber pressure. One of these thrust chambers (S/N 3) was cyclically tested until a crack through the cooling channel to the combustion chamber was observed. The crack developed sometime between the 42nd and 71st cycle. It was further tested until 93 cycles had been accumulated. At this time testing was stopped, but further tests could have been run. Chamber S/N 1 was tested 9 times, chamber S/N 2 - 13 times, chamber S/N 4 - 31 times, and chamber S/N 5 - 1 time. Only chamber S/N 3 developed a crack. Thus, successful cooling with LOX was demonstrated with no catastrophic failures.

#### Injector Performance

Figure 8 is a plot of the  $C^*$  efficiency which was determined from chamber pressure versus the mixture ratio tested. The measured performance of three different injectors are plotted on this graph. The differences in these injectors were explained in the Injector section.

Except for some data scatter, it can be seen that the  $4.14 \text{ MN/m}^2$  (600 psia) injector developed over 99% efficiency, the  $8.274 \text{ MN/m}^2$

(1200 psia) injector 95% efficiency, and the 13.79 MN/m<sup>2</sup> (2000 psia) injector 96% efficiency. The lower efficiency for the two higher chamber pressures resulted from the injector modifications to reduce the wall temperatures and the shorter chamber lengths. Ref. 14 gives a further explanation of why zone cooling of a rocket thrust chamber can reduce the injector efficiency.

### Soot Thickness Analysis

Because of uncertainty of effects of startup and shutdown on soot deposition, an analytical approach was utilized to determine the deposit thickness. A calculation was performed to predict the temperature distribution in the thrust chamber walls at the four axial locations where the instrumentation was located. This was done with a modified SINDA (a two-dimensional, finite difference, relaxation heat transfer) computer code for a slotted copper liner configuration with an electroformed nickel close-out as the thrust chambers used in this program were fabricated. The predictions were performed at the chamber pressure and mixture ratio operating conditions that were experimentally run. A value of .00125 cal/cm.sec<sup>o</sup>c ( $7 \times 10^{-6}$  BTU/in. sec.<sup>o</sup>F) was used for the thermal conductivity of soot. The axial locations were in the cylindrical section, the converging section, the throat, and the diverging section. A soot coating of various (1, 2, and 3 mils i.e., .001, .002, and .003 inches) thickness was assumed on the hot gas wall. From these calculations, figures 9 (a, b, c, d and e) for the cylindrical section, figures 10 (a, b, c, d, and e) for the converging section, figures 11 (a, b, c, d, and e) for the throat, and figures 12 (a, b, c, d, and e) for the diverging section were constructed showing the predicted wall temperature at the location of the rib thermocouples for various soot deposit thicknesses. Then the plot was entered with the experimentally measured rib temperature and the soot thickness determined.

Figure 13 (a, b, c, d, and e) is a plot of the soot thickness at the various chamber axial locations for the chamber pressure and mixture ratio range experimentally covered in this investigation.

Figure 14 (a, b, c, and d) shows the soot thickness over the chamber pressure range covered at an O/F of nominally 2.8. Figure 14a shows the soot thickness in the cylindrical portion of the chamber to be uniform at 4 mils thick. Figure 14b shows that in the convergent section, the soot thickness decreases from 2 mils at 4.14 MN/m<sup>2</sup> (600 psia) chamber pressure down to 0 thickness at 13.79 MN/m<sup>2</sup> (2000 psia) chamber pressure. Figure 14c shows the same conditions at the throat over the pressure range, and Figure 14d indicates that the soot thickness decreases from around 4 mils at 4.14 MN/m<sup>2</sup> (600 psia) down to 1 mil at 13.79 MN/m<sup>2</sup> (2000 psia) chamber pressure in the divergent section.

Figure 15 (a, b, c, and d) shows the soot thickness over the mixture ratio range covered at a nominal chamber pressure of 8.274 MN/m<sup>2</sup> (1200 psia). Figure 15a shows the soot thickness in the cylindrical portion of the chamber to decrease from 6.5 mils thick at an O/F of nominally 2 down

to a thickness of 4 mils at an O/F of nominally 3. Figure 15b shows that in the convergent section, the soot thickness decreases from just over 2 mils at an O/F of nominally 2 down to a thickness of 1 mil at an O/F of nominally 3. Figure 15c shows that at the throat the thickness varies from a thickness of 1.5 at an O/F of nominally 2 down to a thickness of just over .5 mil at an O/F of nominally 3. Finally, in the diverging section Figure 15d shows that the thickness varies from a thickness of 3 mils at an O/F of nominally 2 down to a thickness of 1.5 mils at an O/F of nominally 3.

#### Effects of LOX Leaks on the Thrust Chamber Integrity

Cyclic test operation was performed to determine what effect a crack in the combustion chamber wall would have if it allowed oxygen to enter the combustion zone. It was postulated that there would be no effect if the metal wall were maintained below its ignition temperature. From Table II it can be seen that one of the chambers was operated until cracks developed. These cracks were in the throat region. Leakage through these cracks was very evident by observing the large amounts of vapors leaving the chamber between cycles and at the beginning of the tests. This was particularly true from cycle 71 to cycle 93 after the cracks had been visually identified. The chamber showed no signs of apparent metal burning or distress. In fact, upon post inspection the lack of discoloration revealed that the area around the crack was overcooled by the leaking oxygen. This was also observed in thrust chamber tests with cracks in which hydrogen was used as the coolant, and thrust chamber tests with cracks in which LOX was used to cool hydrogen/oxygen propellants (Ref. 10). There was no catastrophic failure.

#### Concluding Remarks

The present phase of the LOX cooling program has demonstrated that supercritical LOX is capable of cooling thrust chambers using LOX/RP-1 as the combustion propellants. These propellants were thought to perhaps present a more severe operating environment if a small crack developed in the chamber wall because of the presence of a soot layer. The concern was that the leaking coolant, LOX, entering the combustion chamber through the crack, could oxidize the soot film which could in turn heat the chamber wall to its ignition temperature. From the soot analysis at the  $4.14 \text{ MN/m}^2$  (600 psia) chamber pressure, a soot layer was indeed present in the area where the cracks developed (the throat), however, this did not aggravate the situation. The metal wall was maintained below its ignition temperature and no catastrophic failure resulted.

## Summary of Results

Five thrust chambers with identical coolant passage geometries were tested with LOX/RP-1 as the propellants and LOX as the coolant. Three of these thrust chambers were tested at  $4.14 \text{ MN/m}^2$  (600 psia) chamber pressure and over a mixture ratio range of 2.25 to 2.92. One thrust chamber was tested at  $8.274 \text{ MN/m}^2$  (1200 psia) chamber pressure over a mixture range of 1.93 to 2.98. Two of the thrust chambers were tested at  $13.79 \text{ MN/m}^2$  (2000 psia) chamber pressure over a mixture ratio range of 1.79 to 2.68. The results of these tests were as follows:

1. Successful cooling with LOX was demonstrated.
2. One chamber was cyclically tested 93 times. During this testing, cracks appeared in the hot-gas wall that permitted oxygen to flow into the combustion region with no catastrophic failures. With this chamber, more than 22 cyclic tests were made after the first through-crack was observed with no apparent metal ignition or distress.
3. The LOX passing through the crack in the hot-gas wall did not react with the carbon layer at the throat on the combustion wall, thereby, raising the metal wall temperature to its ignition temperature and causing a catastrophic failure. It also did not react directly with the metal wall.
4. The thrust chamber wall cracks that formed as a result of the cyclic testing with LOX as the coolant, appeared to have similar characteristics as those from a previous program where liquid hydrogen was the coolant.
5. The LOX cooling of LOX/RP-1 propellants was very similar to the LOX cooling of hydrogen/oxygen propellants.
6. At a nominal O/F of 2.8, soot thickness decreases as chamber pressure increases, except in the cylindrical portion of the thruster where it remained a constant thickness.
7. Soot deposition was the least in the throat region at all chamber pressures and mixture ratios.
8. Soot thickness decreased at a given thrust chamber axial location as mixture ratio increased in the range from 2 to 3.

### References

1. Luscher, W. P., and Mellish, J. A., "Advanced High Pressure Engine Study for Mixed-Mode Vehicle Applications," Aerojet Liquid Rocket Company, Sacramento, CA, January 1977. (NASA CR-135141)
2. Haefeli, R. C., Littler, E. G., Hurley, S. B., and Winter, M. G., "Technology Requirements for Advanced Earth-Orbital Transportation Systems," Martin Marietta Corp., Denver, CO, June 1977. (NASA CR-2866)
3. Hepler, A. K. and Bangsund, E. L., "Technology Requirements for Advanced Earth Orbital Transportation Systems," Boeing Aerospace Co., Seattle, WA, July 1978. (NASA CR-2878)
4. Caluori, V. A., Conrad, R. T., and Jenkins, J. C., "Technology Requirements for Future Earth-to-Geosynchronous Orbit Transportation Systems," Boeing Aerospace Co., Seattle, WA, April 1980. (NASA CR-3265)
5. Giovantetti, Anthony J., Spadacinni, Louis J., and Szetela, Eugene J., "Deposit Formation and Heat Transfer in Hydrocarbon Rocket Fuels," United Technologies Research Center, East Hartford, CT, October 1983. (NASA CR-168277)
6. Spencer, R. G., and Rousar, D. C., "Supercritical Oxygen Heat Transfer," Aerojet Liquid Rocket Company, Sacramento, CA, November 1977. (NASA CR-135339)
7. Rousar, D. C., and Miller, E., "Cooling with Supercritical Oxygen," AIAA Paper 75-1248, September 1975.
8. Powell, W. B., "Heat Transfer to Fluids in the Region of the Critical Temperature," Jet Propulsion Laboratory, Pasadena, CA, Progress Report No. 20-285, 1956.
9. Spencer, R. G., Rousar, D. C., and Price, H. G., "LOX-Cooled Thrust Chamber Technology Developments," AIAA Paper 78-1035, July 1978.
10. Price, H.G., "Cooling of High Pressure Rocket Thrust Chambers with Liquid Oxygen," NASA TM 81503, 1980.
11. Pavli, A. J., "Design and Evaluation of High Performance Rocket Engine Injectors for Use with Hydrocarbon Fuels," NASA TM79319, 1979.

12. Hannum, N. P., Kasper, H. J., and Pavli, A. J., "Experimental and Theoretical Investigation of Fatigue Life in Reusable Rocket Thrust Chambers," NASA TMX-73413, 1976.
13. LaBotz, R. J., Rousar, D. C., & Valler, H. W., "High Density Fuel Combustion and Cooling Investigation," Aerojet Liquid Rocket Company, Sacramento, CA, September 1980. (NASA CR-165177)
14. Winter, Jerry M., Pavli, Albert J., and Shinn, Jr., Arthur M., "Design and Evaluation of an Oxidant-Fuel-Ratio-Zoned Rocket Injector for High Performance and Ablative Engine Compatibility," NASA TN D-6918, 1972.

TABLE 1. INJECTOR HOLES SIZES, AREAS, AND PRESSURE DROPS.

Injector No.	No. of Elements	Pattern	Fuel Hole Size			Fuel Area			LOX Hole Size			LOX Area			$\Delta P$ at O/F = 2.8	
			mm (in.)	mm <sup>2</sup> (in. <sup>2</sup> )	mm (in.)	mm <sup>2</sup> (in. <sup>2</sup> )	mm (in.)	mm <sup>2</sup> (in. <sup>2</sup> )	mm (in.)	mm <sup>2</sup> (in. <sup>2</sup> )	mm <sup>2</sup> (in. <sup>2</sup> ) (psid)	mm <sup>2</sup> (in. <sup>2</sup> ) (psid)				
1	37	Triplet O-F-O LOX fans Mutually Perpen- dicular	1.702 (.067)			84.129 (.1304)			1.489 (.059)			130.5 (.2023)			.414 (60)	1.311 (190)
			Zone Hole Sizes			Zone Hole Areas			Zone Hole Sizes			Zone Hole Areas				
2	61	Triplet O-F-O Tangential LOX Fans	24	36	1	Outer	Core	Center	24	72	3	Outer	Core	Center	1.932 (280)	4.071 (590)
			Outer Holes	Core Holes	Center Hole	Outer	Core	Center	Outer Holes	Core Holes	Center Holes	Outer	Core	Center		
3	61	Triplet O-F-O Tangential LOX Fans	24	36	1	Outer	Core	Center	24	72	3	Outer	Core	Center	2.346 (340)	4.485 (650)
			Outer Holes	Core Holes	Center Hole	Outer	Core	Center	Outer Holes	Core Holes	Center Holes	Outer	Core	Center		

ORIGINAL PAGE IS  
OF POOR QUALITY



TABLE II - TEST CONDITIONS AND HISTORY

Chamber S/N	Chamber Length Injector to Throat cm (inch)	Nominal Chamber Pressure MN/m <sup>2</sup> (psia)	Nominal Mixture Ratio Range	Number of Cycles Thrust Chamber tested	Nominal Coolant Flow Rate, Kg/Sec. (lb/Sec)	Nominal Coolant Inlet Pressure MN/m <sup>2</sup> (psia)	Nominal Coolant Outlet Pressure MN/m <sup>2</sup> (psia)
1	39.4 (15.5)	4.14 (600)	2.25 to 2.92	9	7.3 (16)	16.20 (2350)	12.07 (1750)
2	39.4 (15.5)			13			
3	39.4 (15.5)			93			
				(cracked between 42-71)			
4	29.2 (11.5)	8.274 (1200)	1.93 to 2.98	26	11 (25)	24.13 (3500)	17.93 (2600)
4	29.2 (11.5)	13.79 (2000)	1.79 to 2.68	5	18 (39)	20.68 (3000)	5.86 (850)
5	29.2 (11.5)			1			

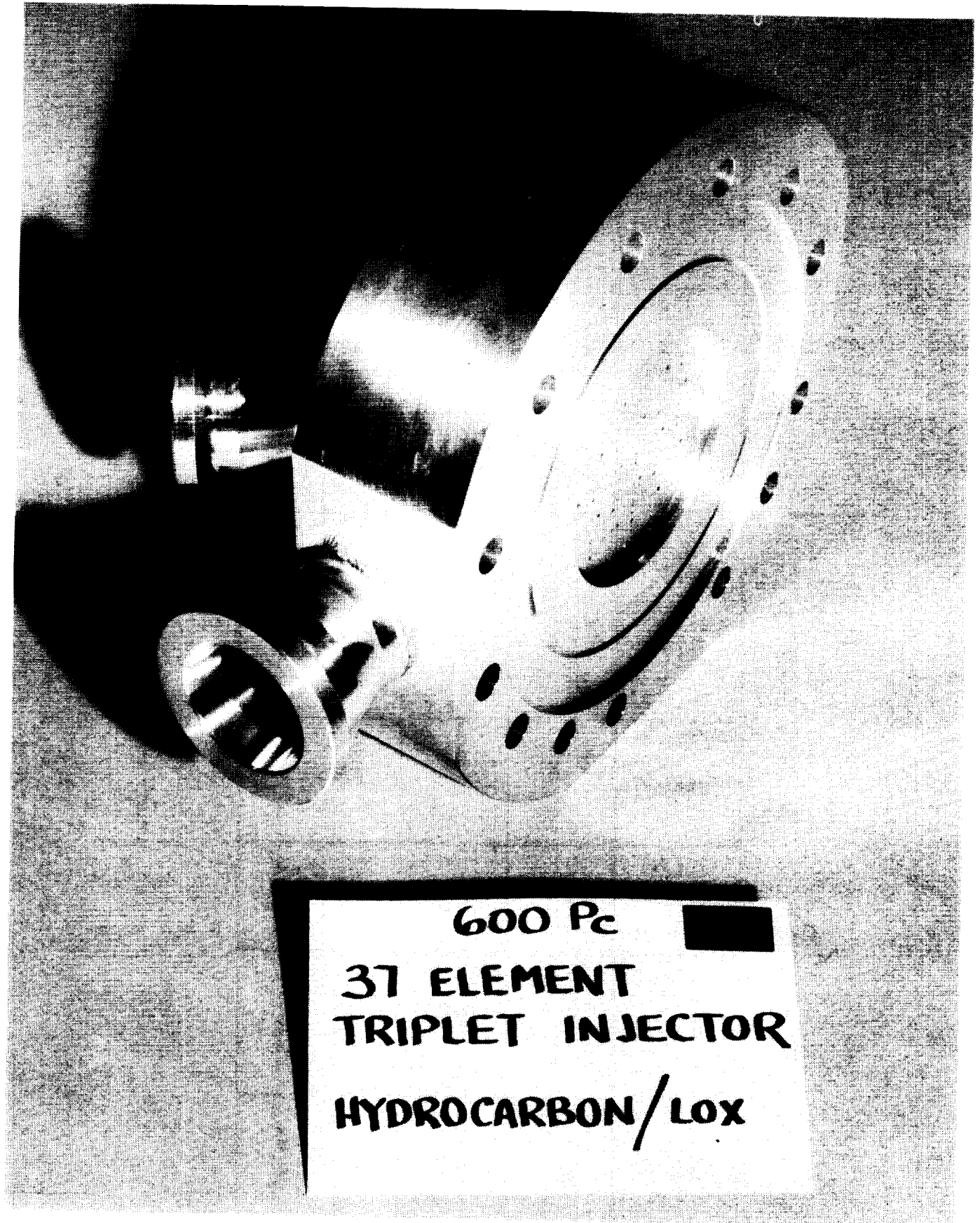


Figure 1. - Typical  $4.14\text{MN/m}^2$  (600 psia) chamber pressure injector.

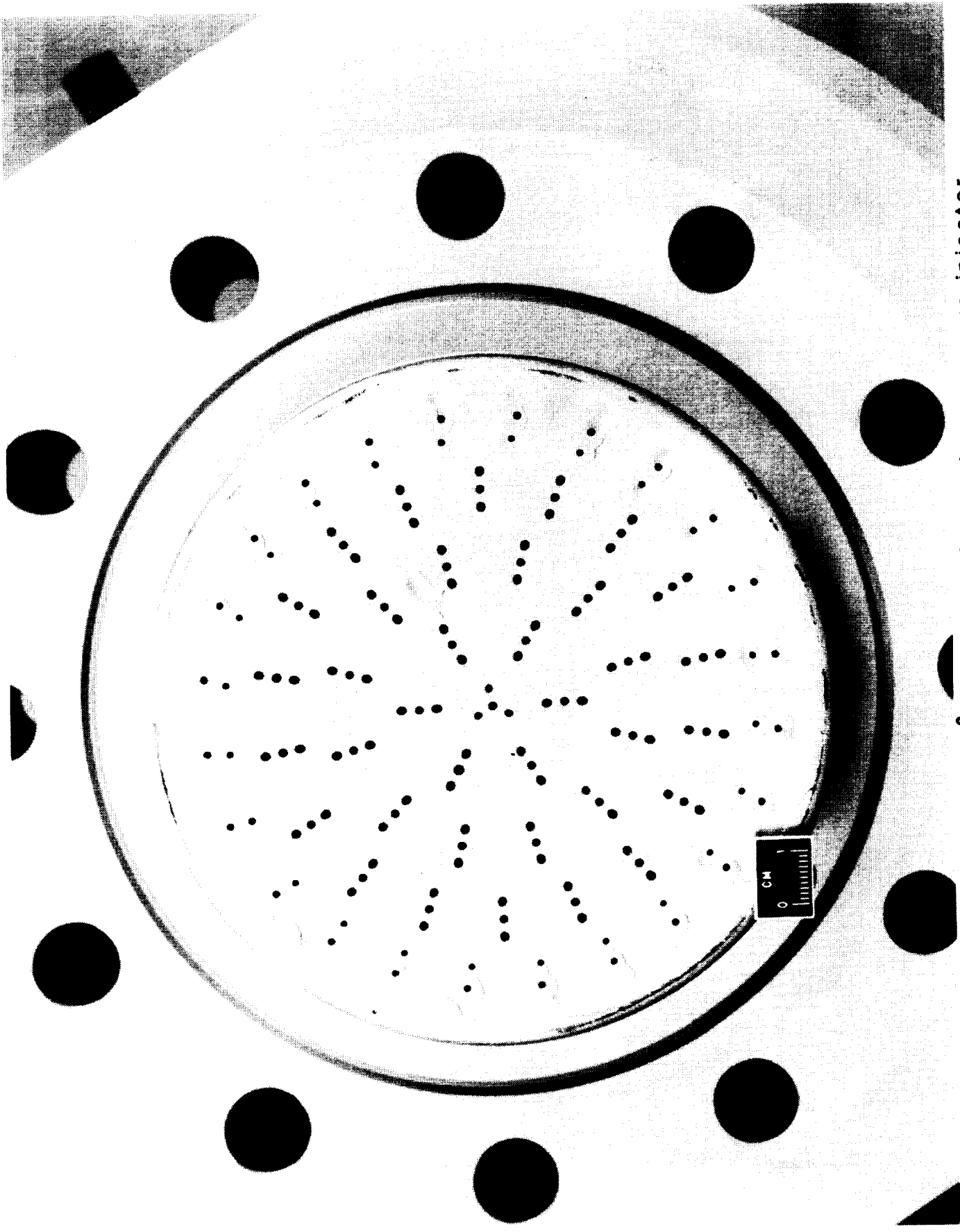


Figure 2. - Typical 8.274 MN/m<sup>2</sup> (1200 psia) chamber pressure injector.

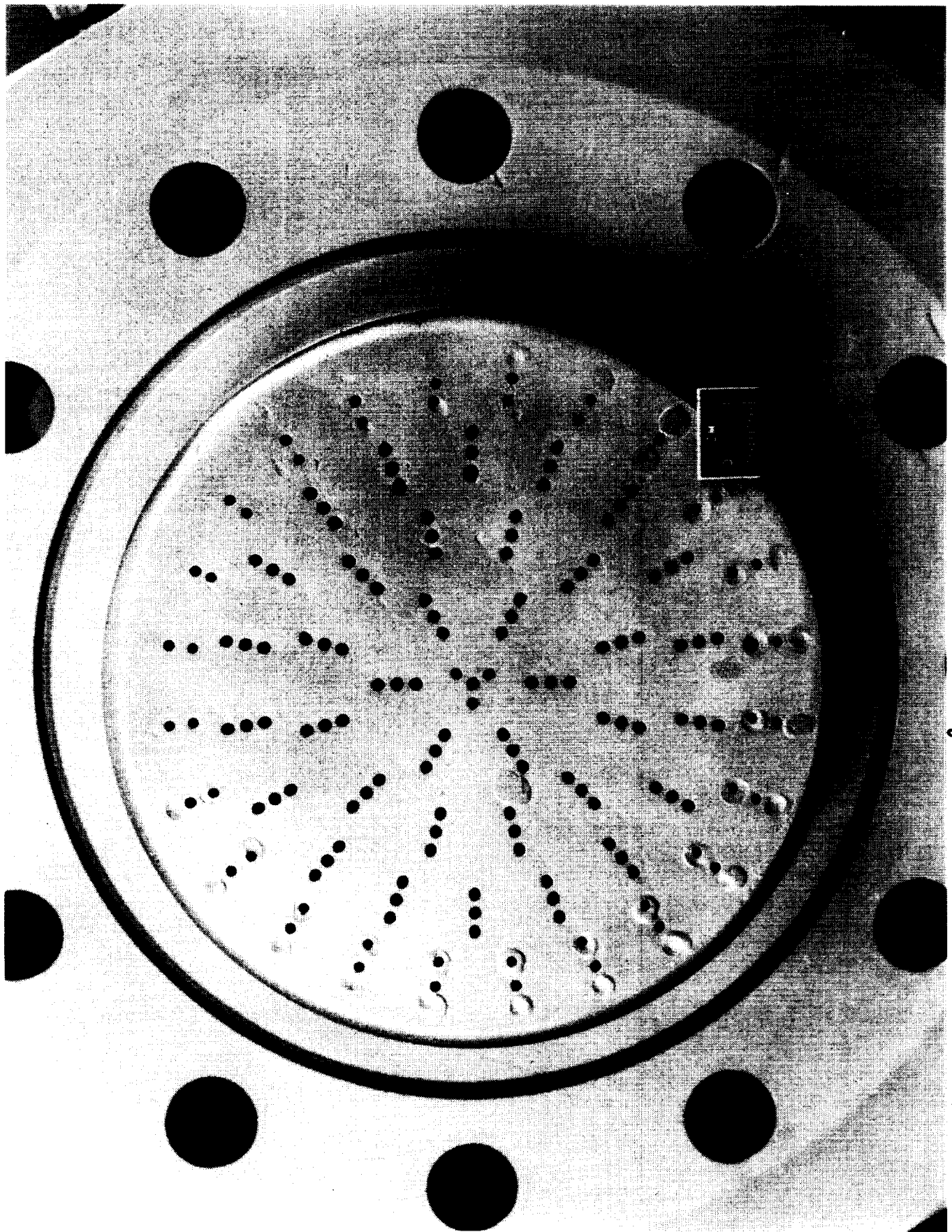


Figure 3. - Typical 13.79 MN/m<sup>2</sup> (2000 psia) chamber pressure injector.

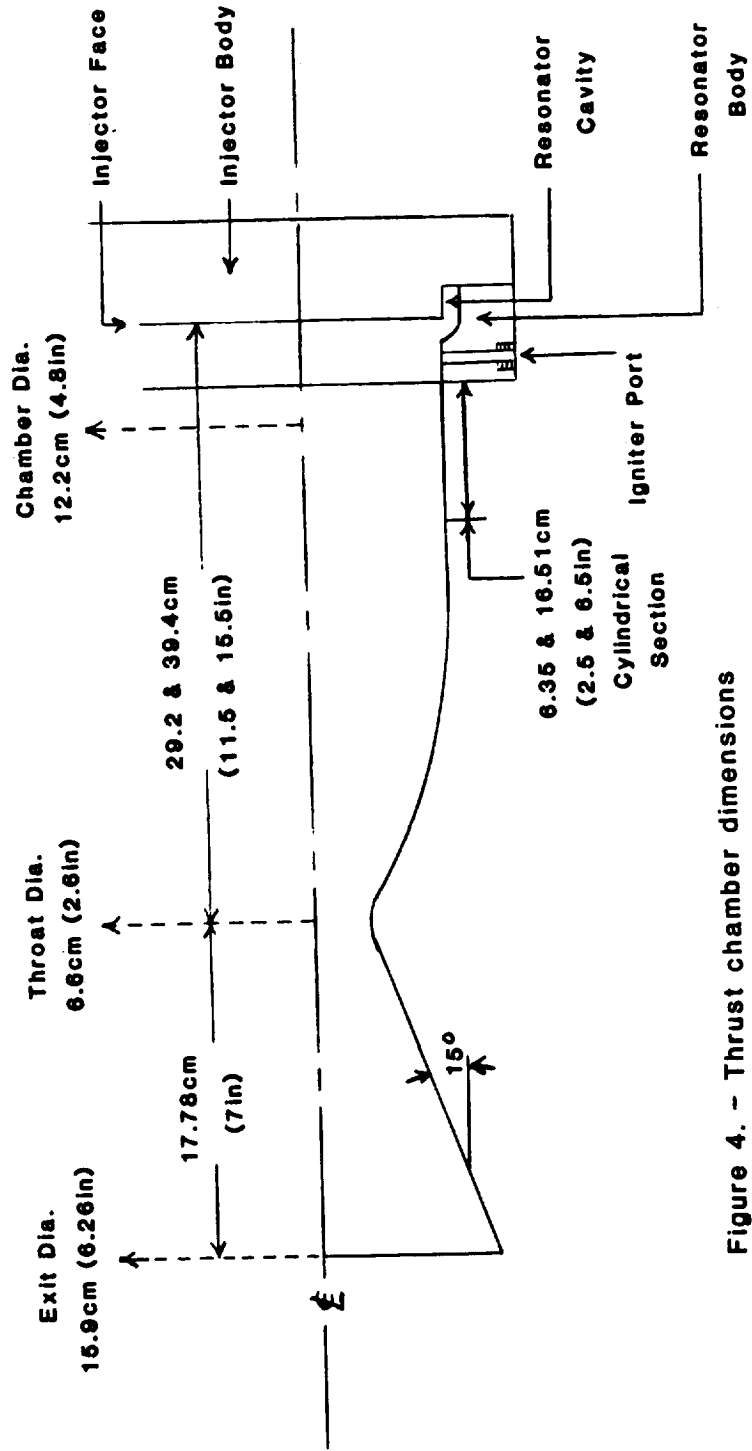


Figure 4. - Thrust chamber dimensions

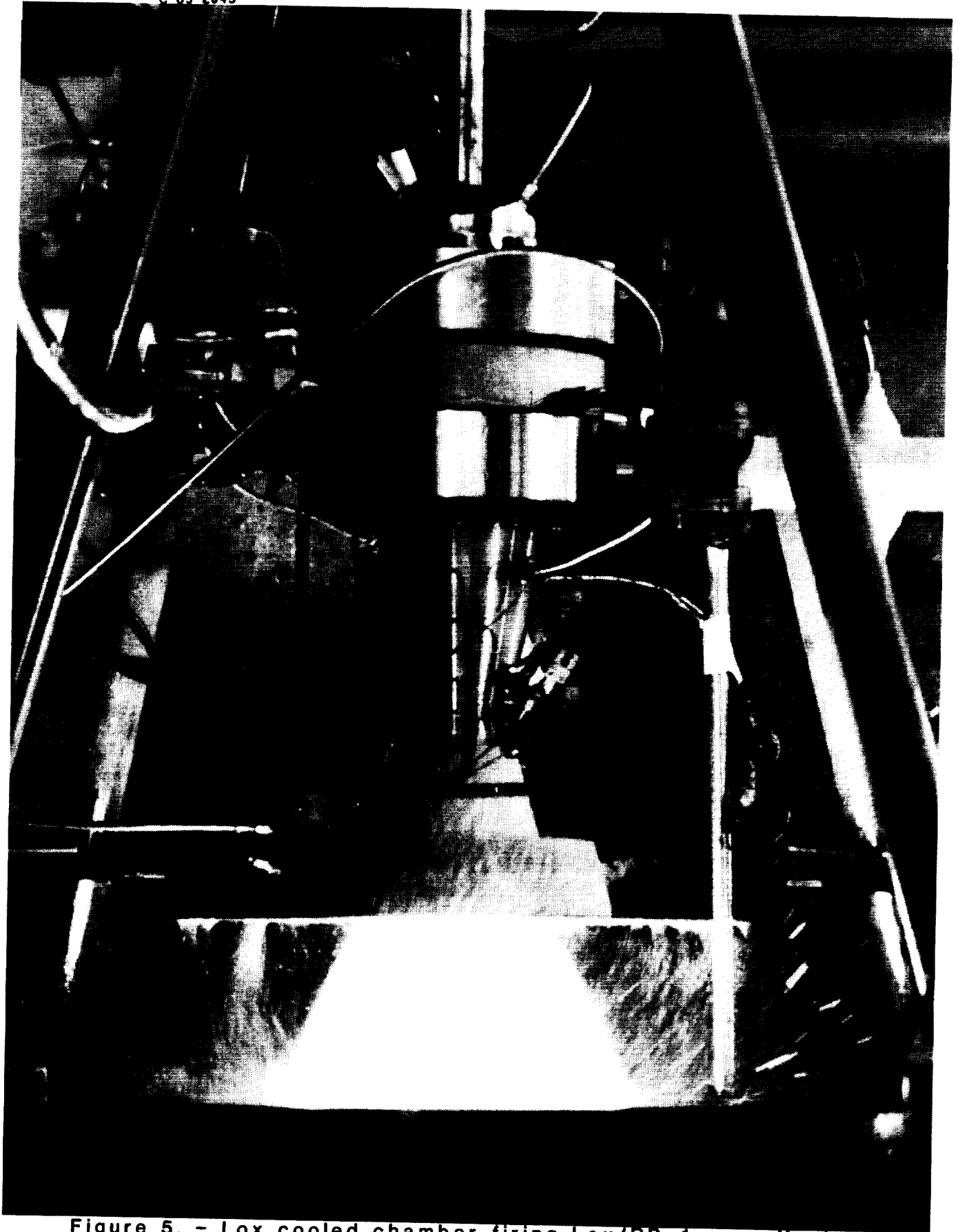


Figure 5. - Lox cooled chamber firing Lox/RP-1 propellants at  
8.274 MN/m<sup>2</sup> (1200 psia) chamber pressure.

ORIGINAL PAGE IS  
OF POOR QUALITY

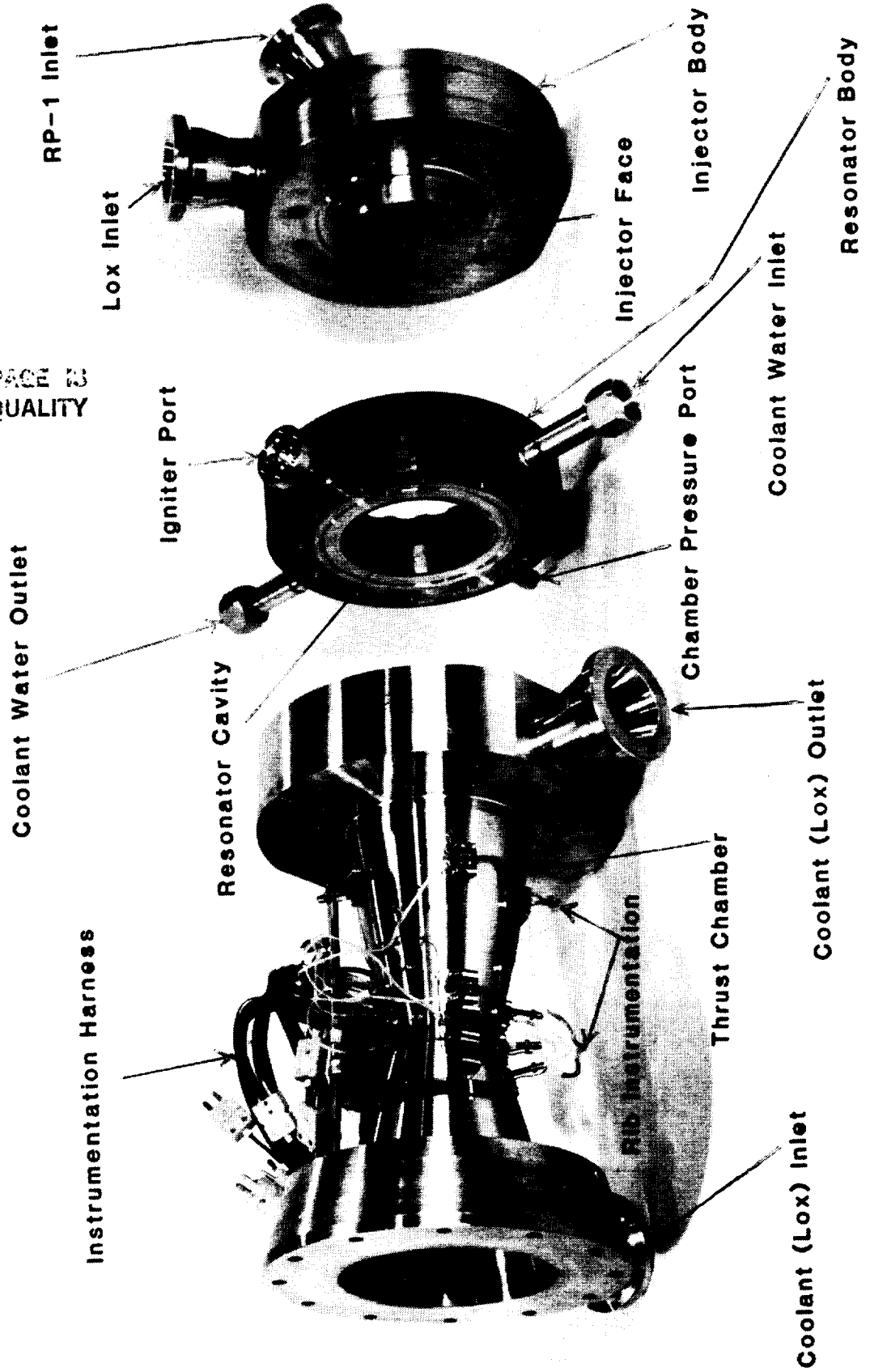


Figure 6. - Thrust chamber, resonator, and injector.

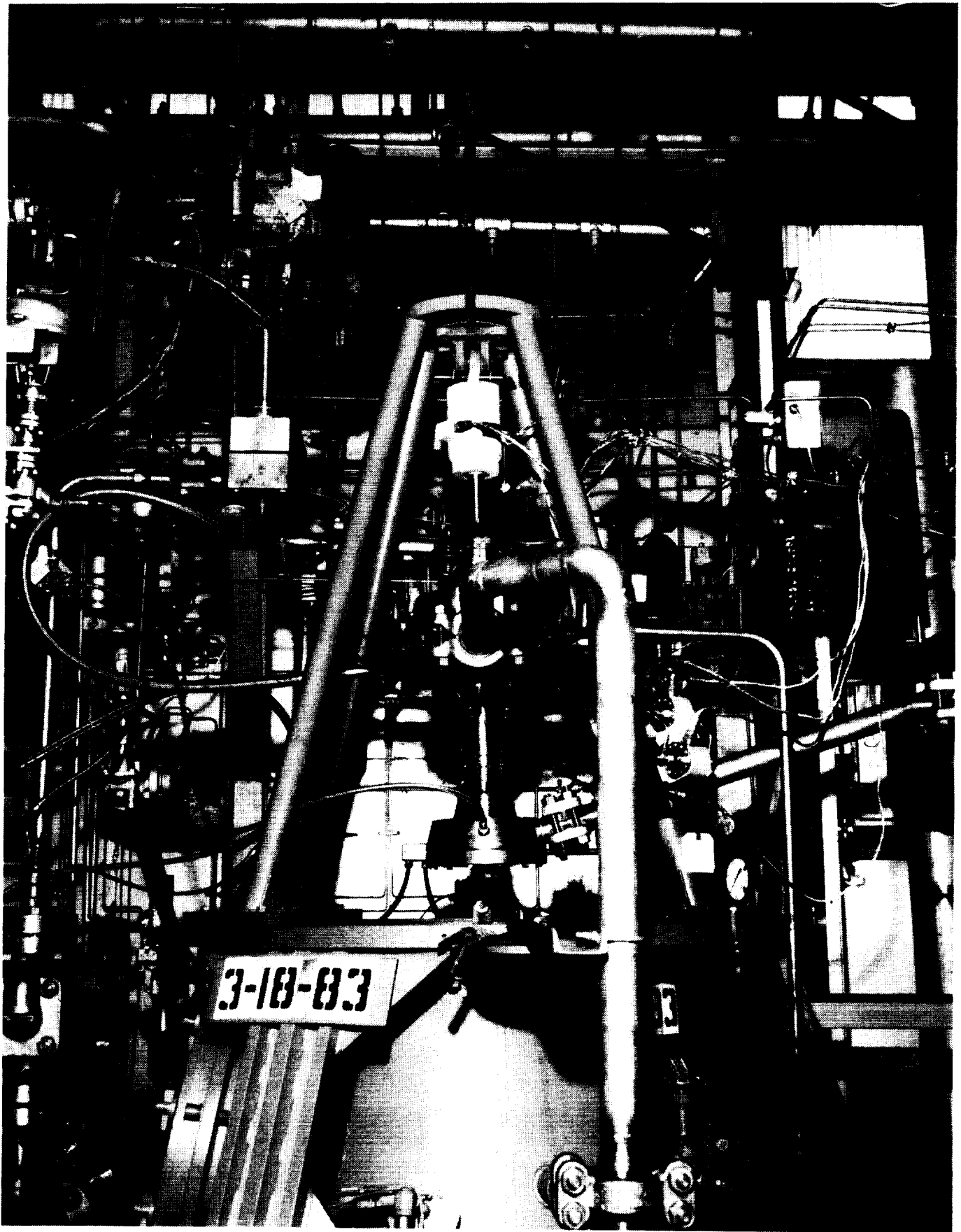


Figure 7. - Thrust chamber mounted in test facility.



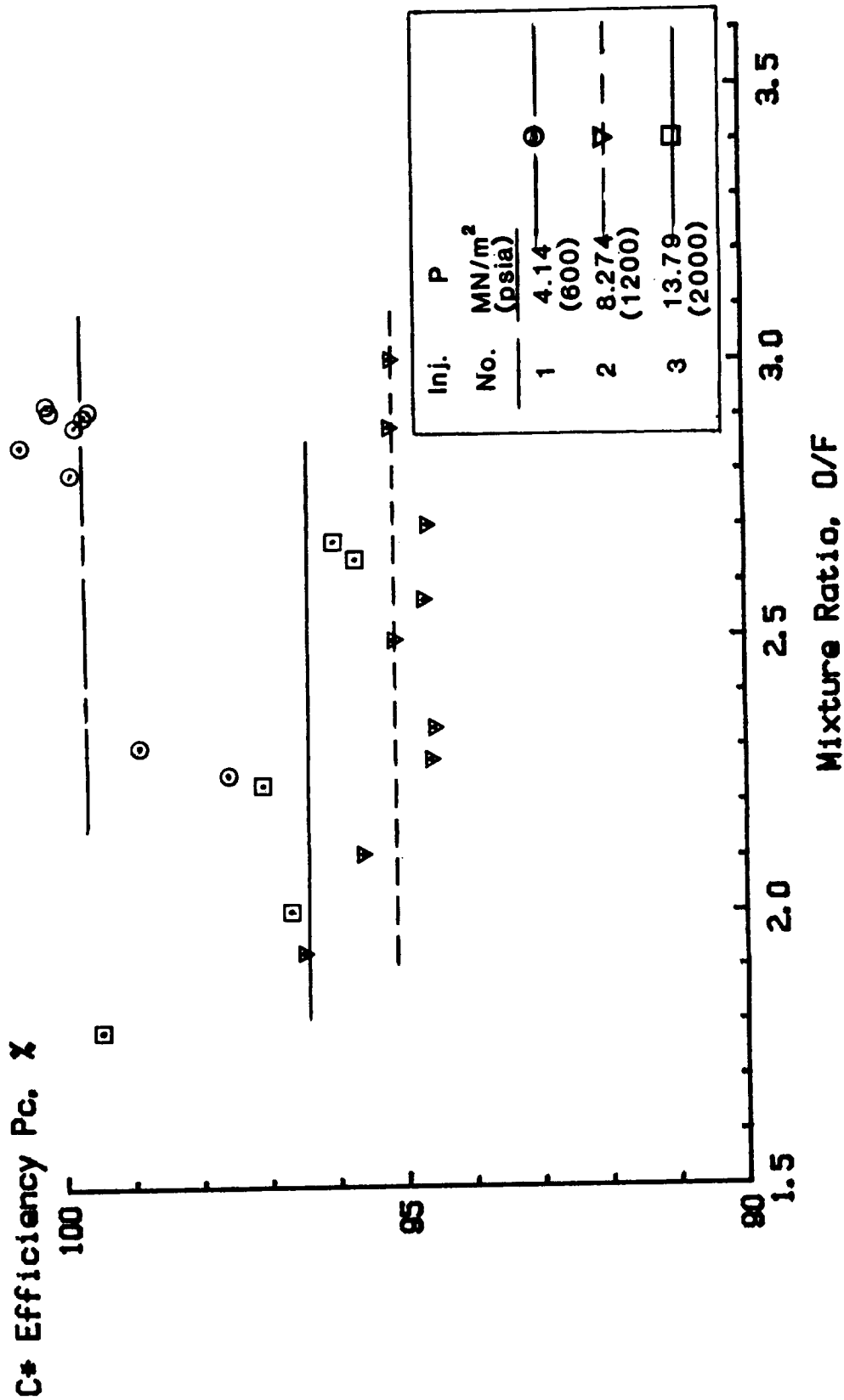


Figure 8. - Injector Performance.

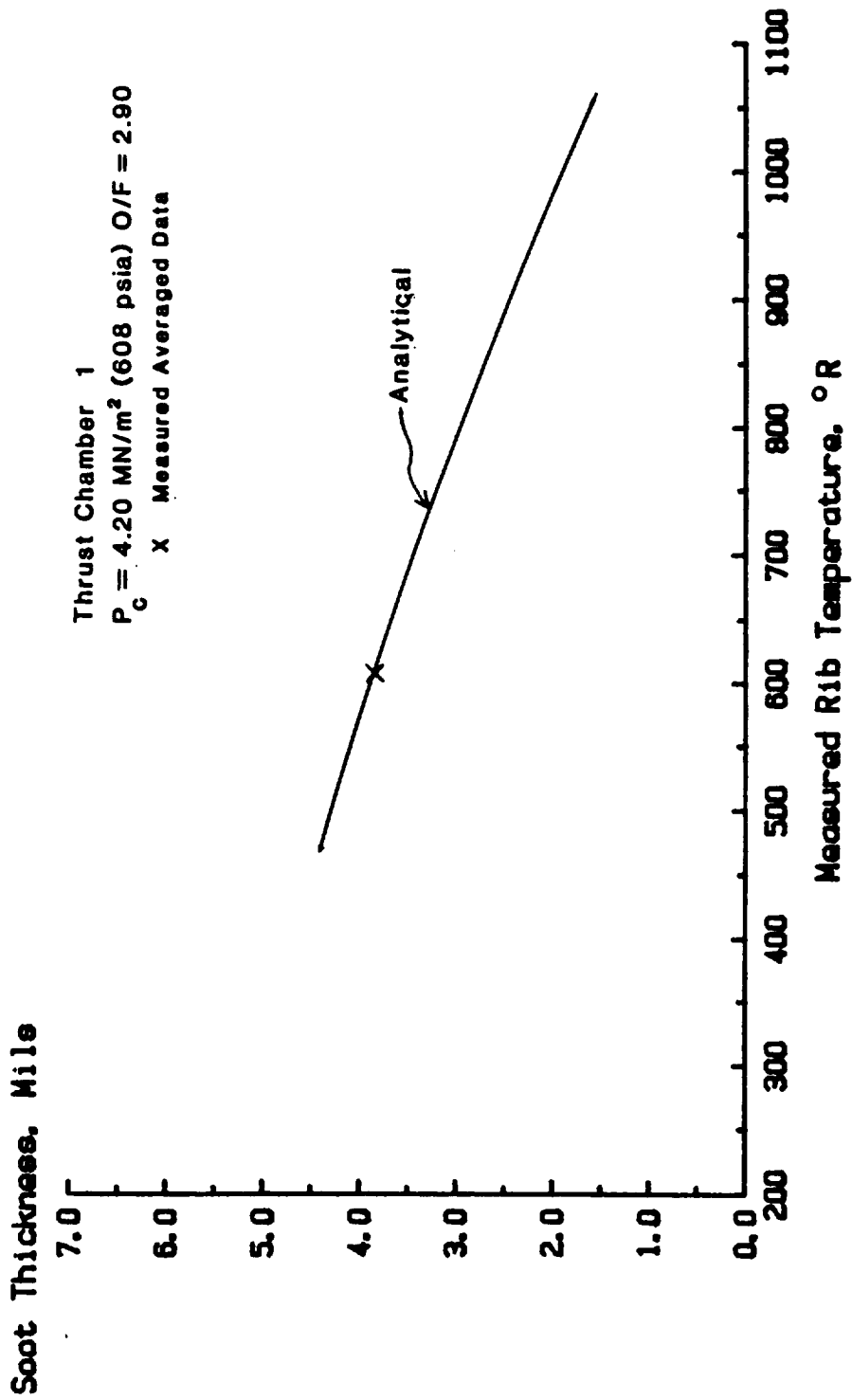


Figure 9a. - Soot thickness 26 cm (10.25 inches) from injector face.

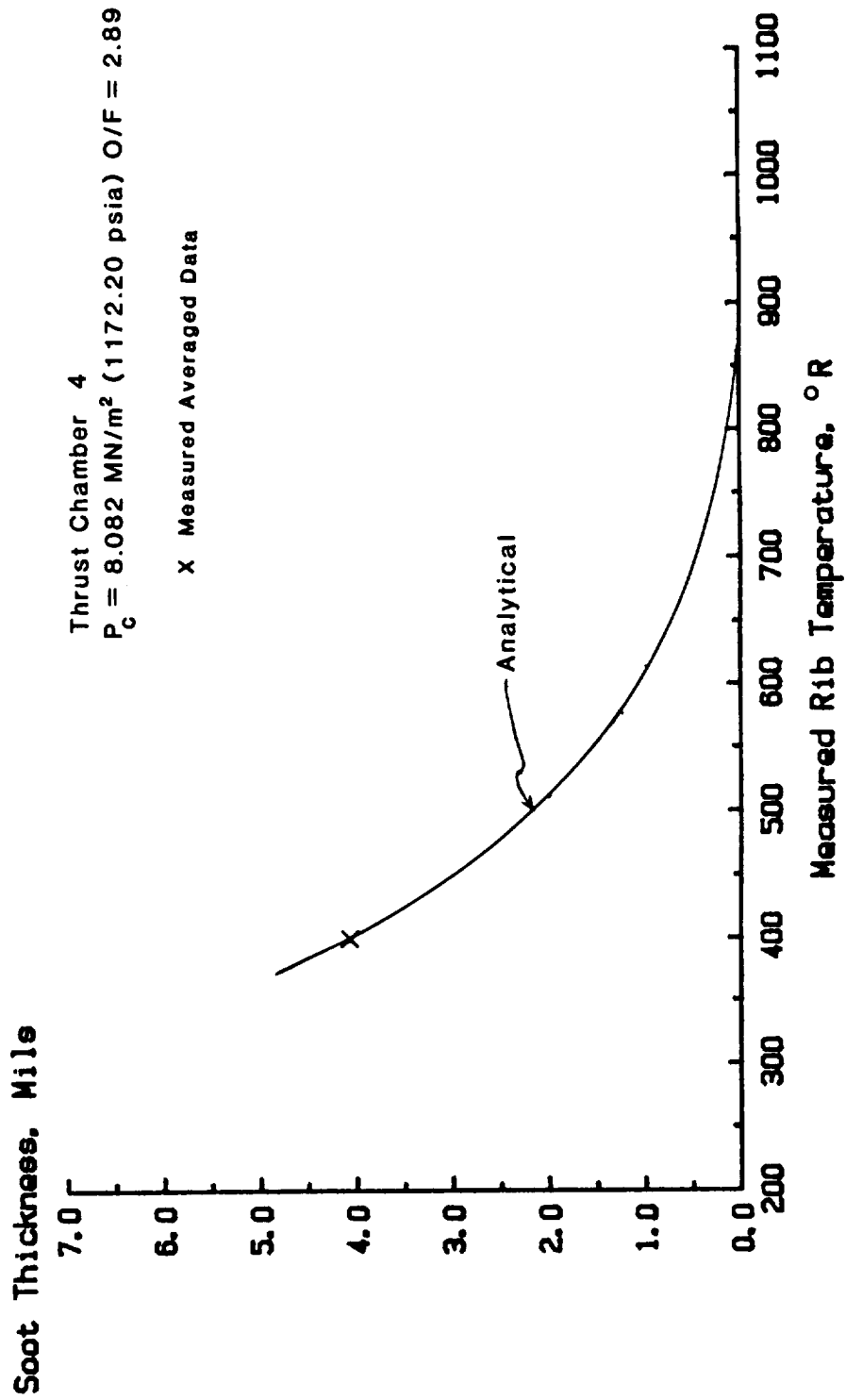


Figure 9b. - Spot thickness 16.5 cm (6.5 inches) from injector face.

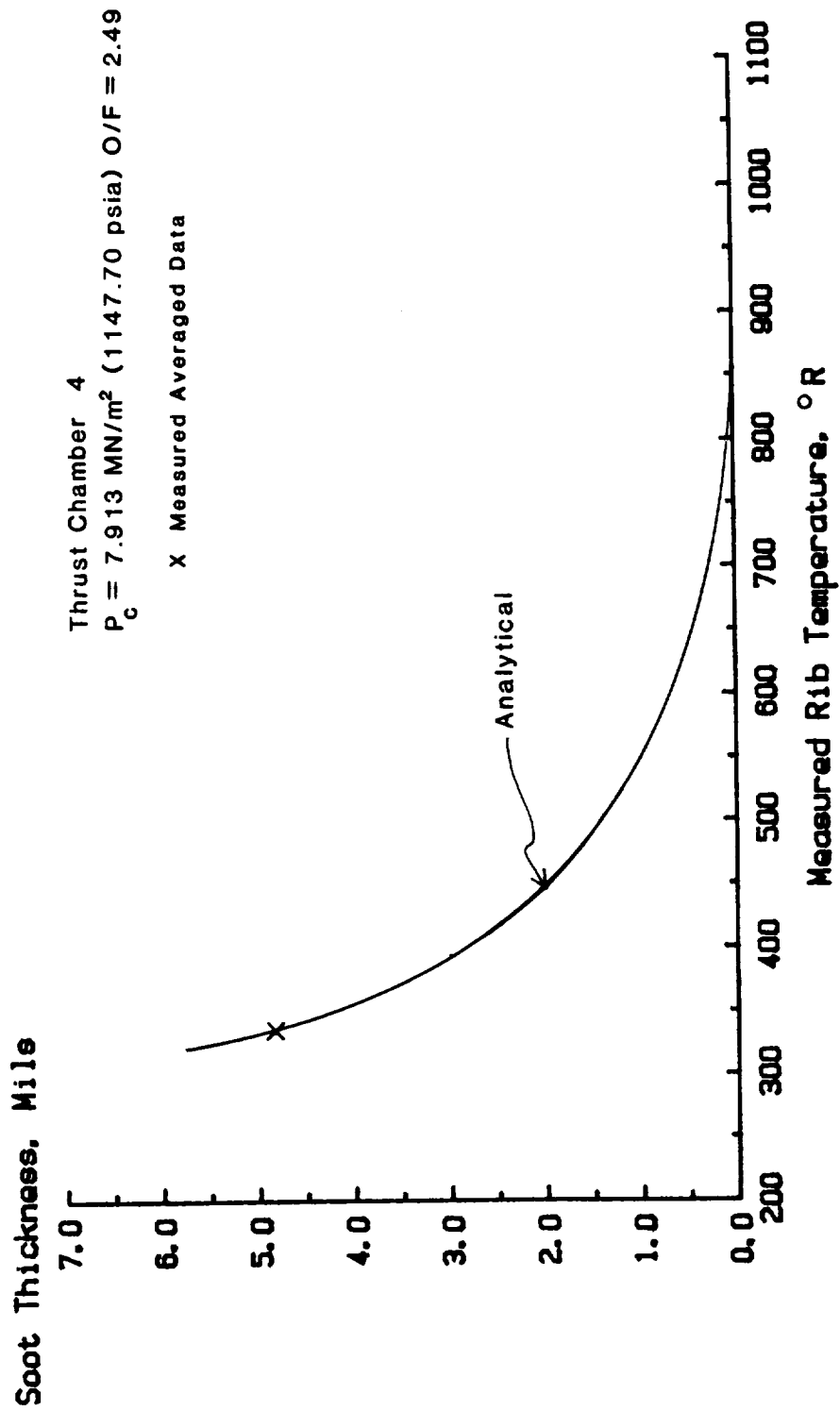


Figure 9c. - Soot thickness 16.5 cm (6.5 inches) from injector face.

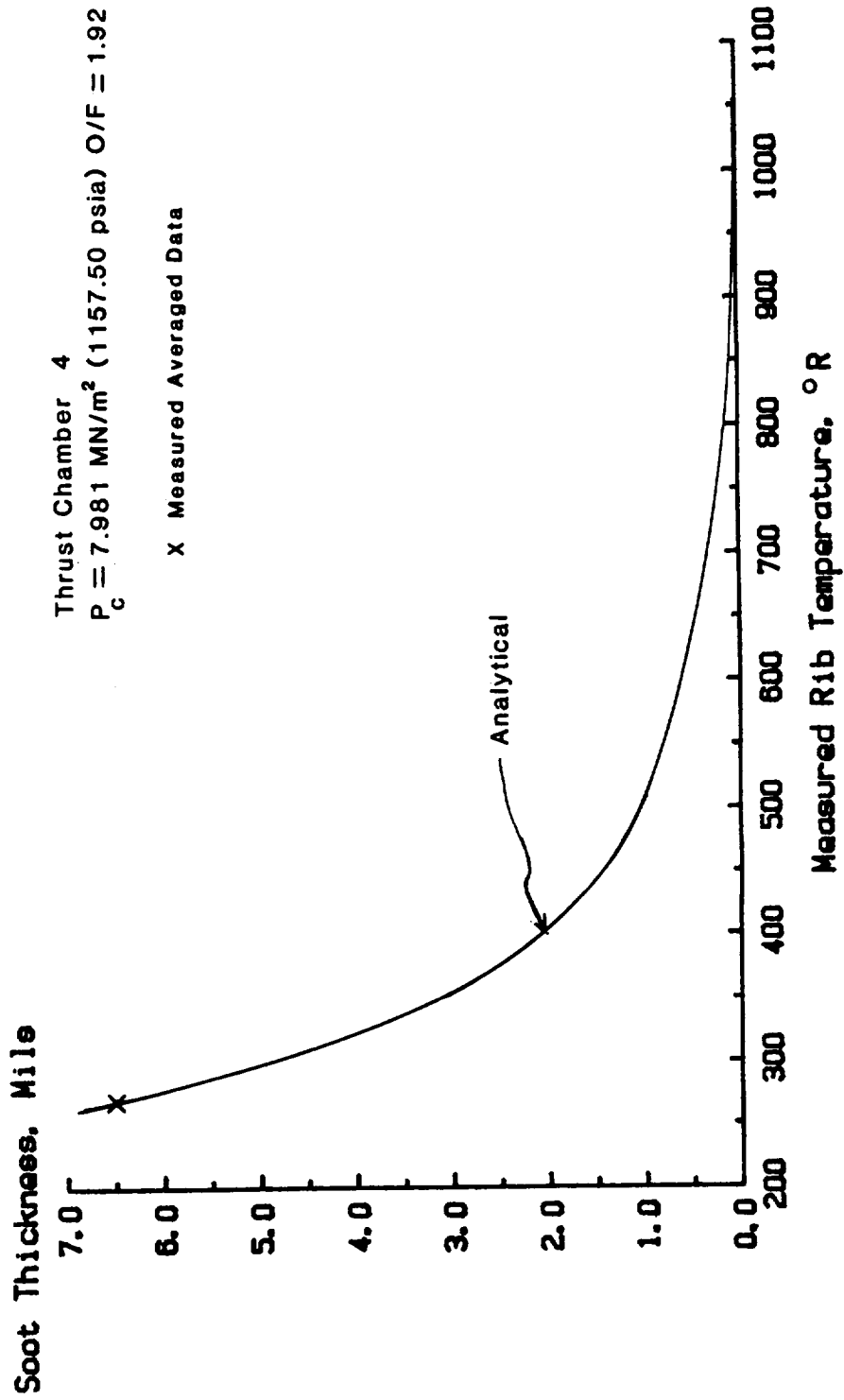


Figure 9d. - Soot thickness 16.5 cm (6.5 inches) from injector face.

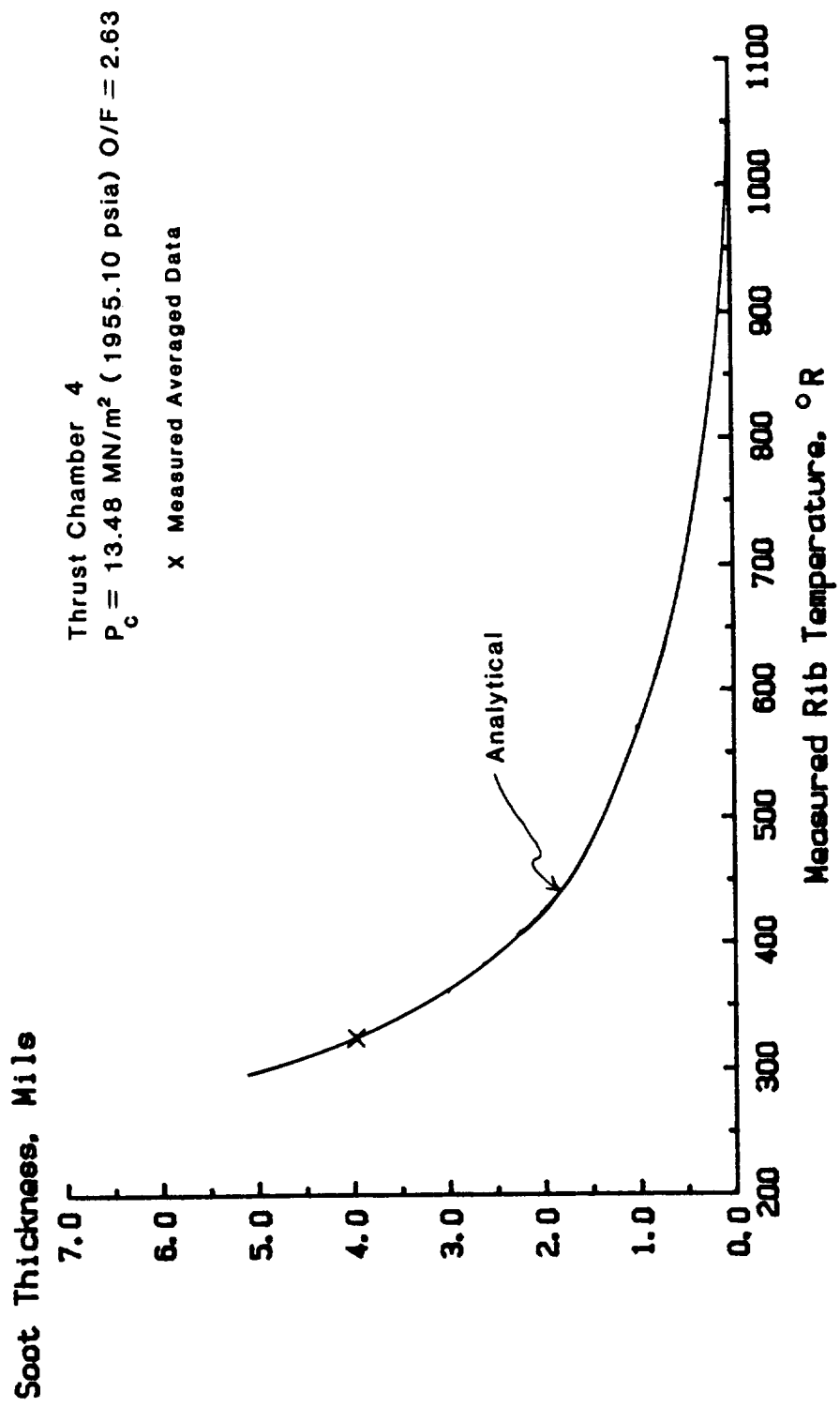


Figure 9e. - Soot thickness 16.5 cm (6.5 inches) from injector face.

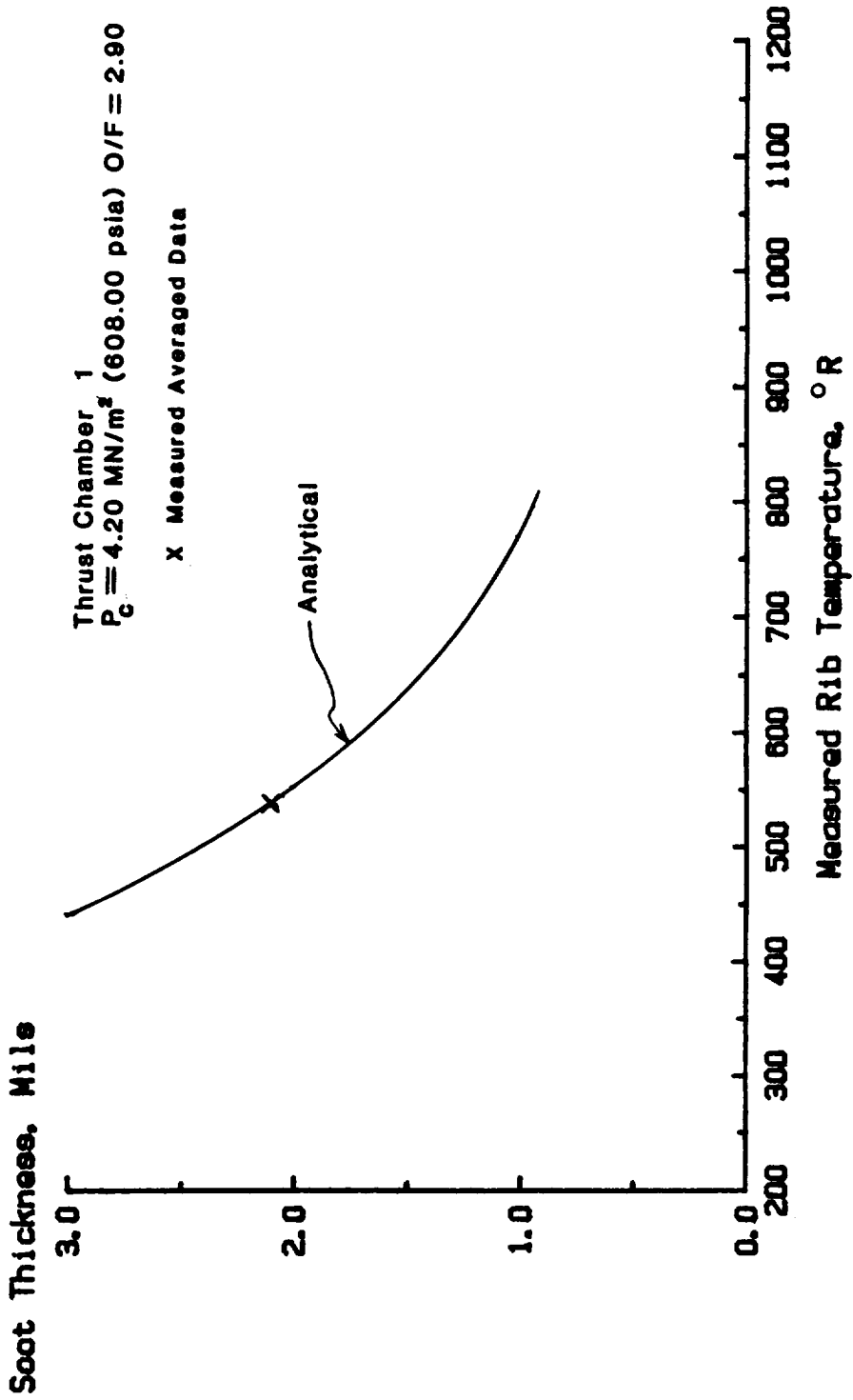


Figure 10a. - Soot thickness 36.2 cm (14.25 inches) from injector face.

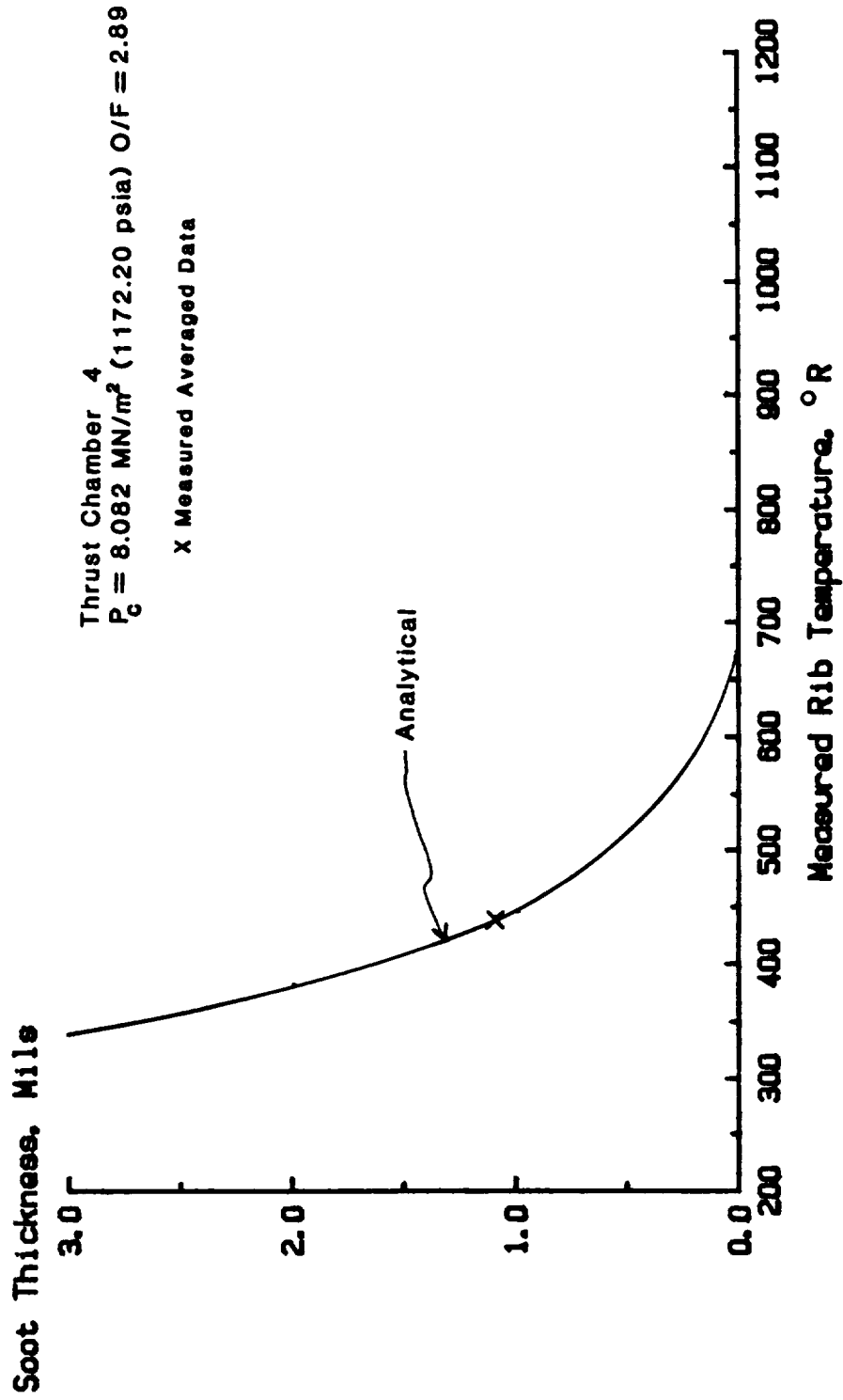


Figure 10b. - Soot thickness 26 cm (10.25 inches) from injector face.



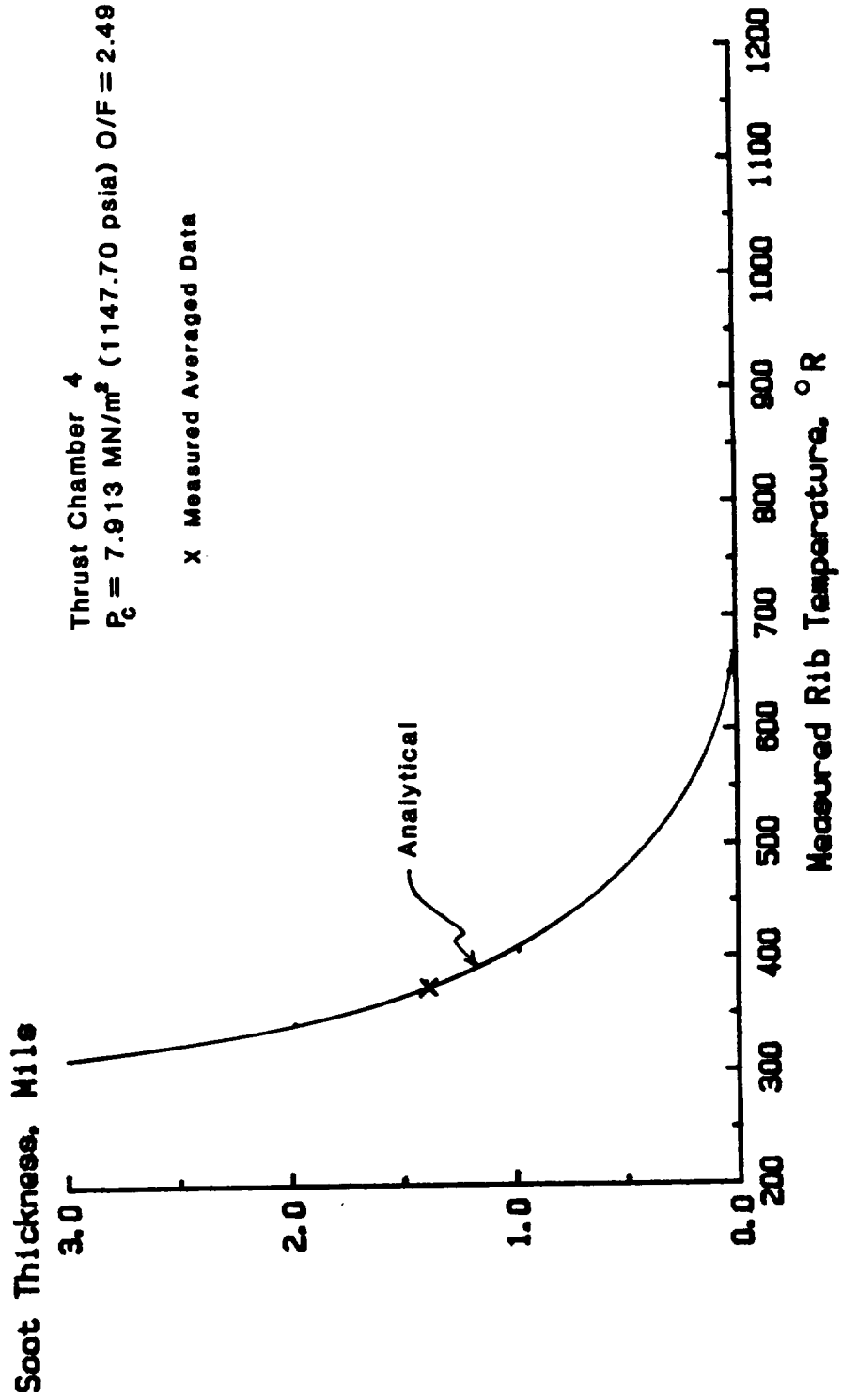


Figure 10c. - Soot thickness 26 cm (10.25 inches) from injector face.

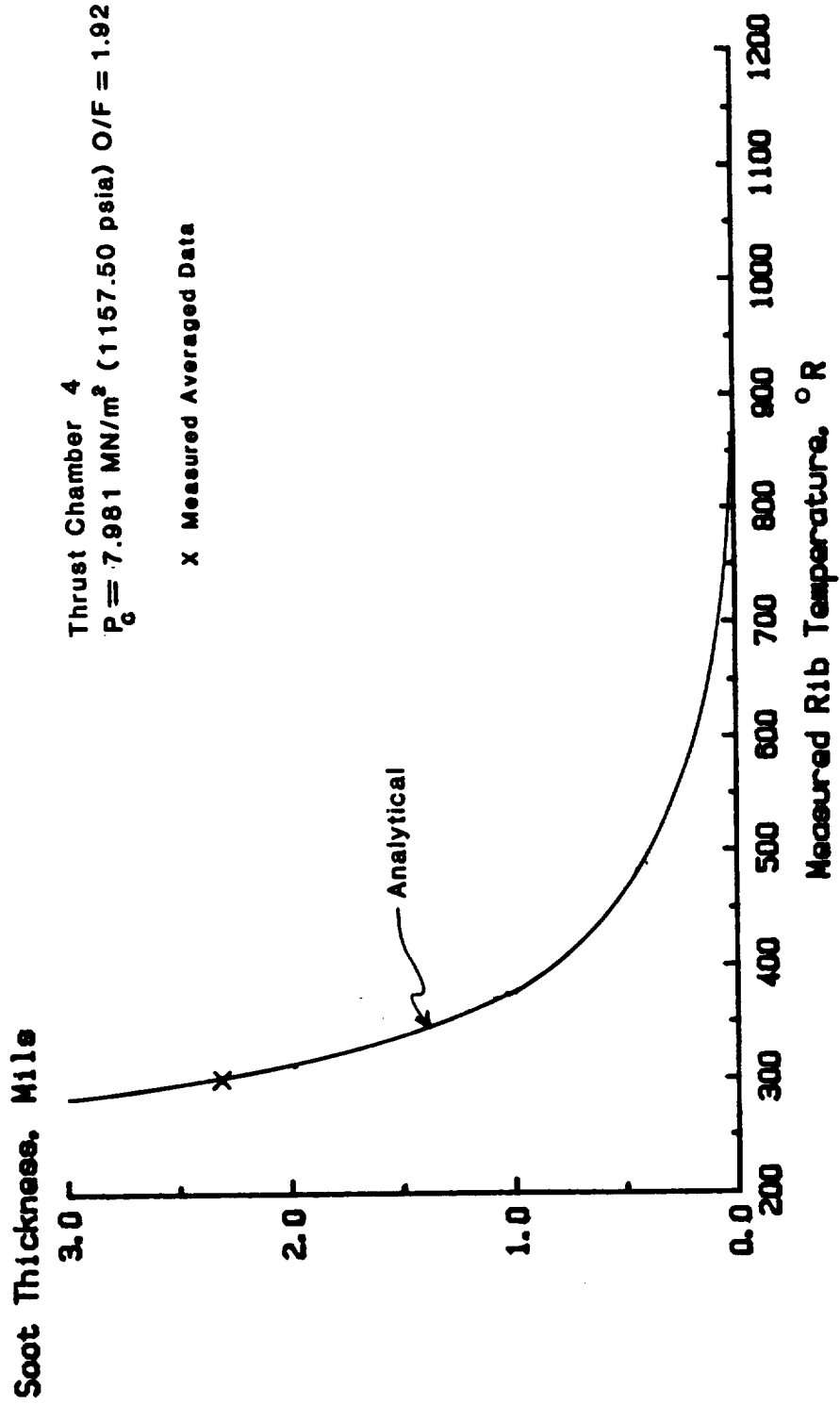


Figure 10d. - Soot thickness 26 cm (10.25 inches) from injector face.

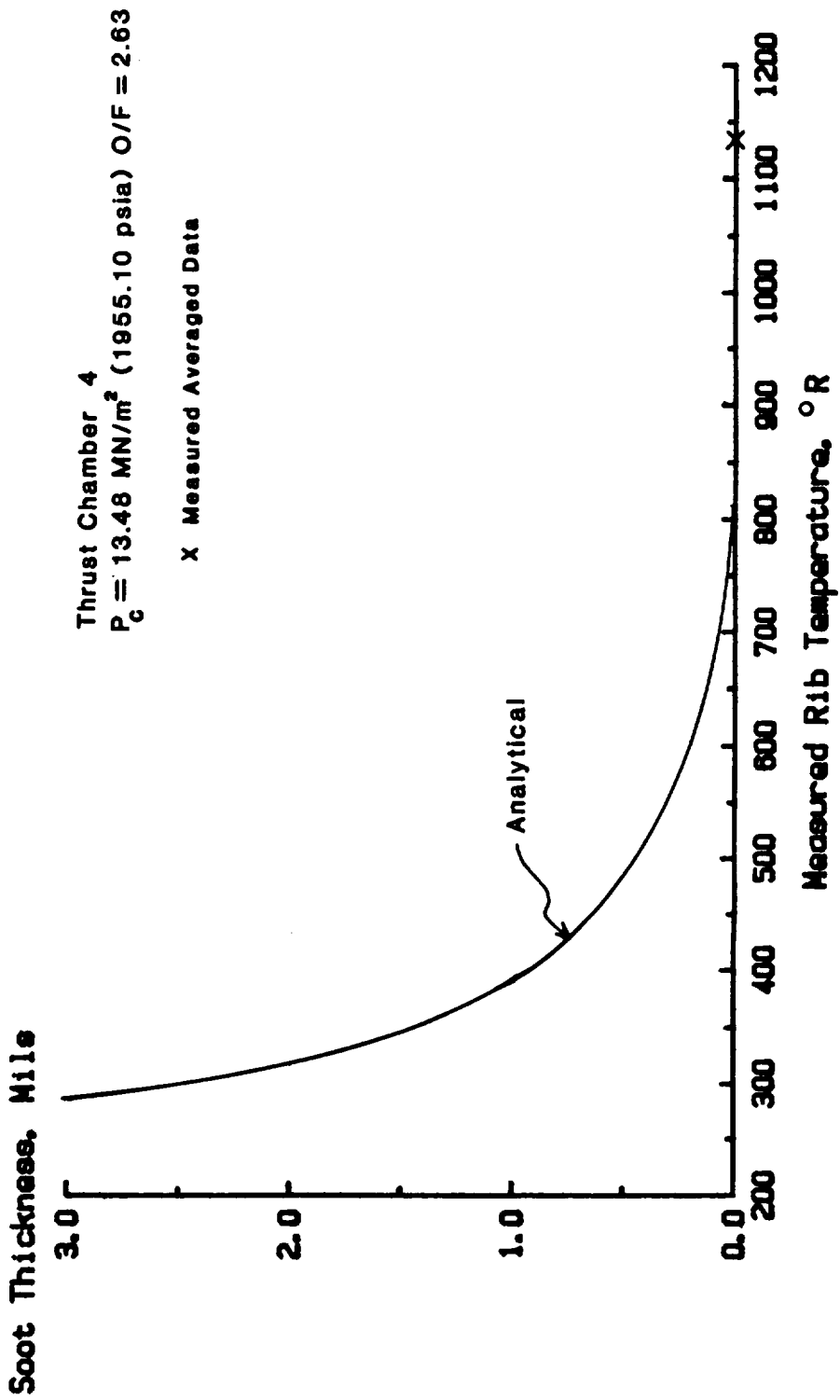


Figure 10e. - Soot thickness 26 cm (inches) from injector face.

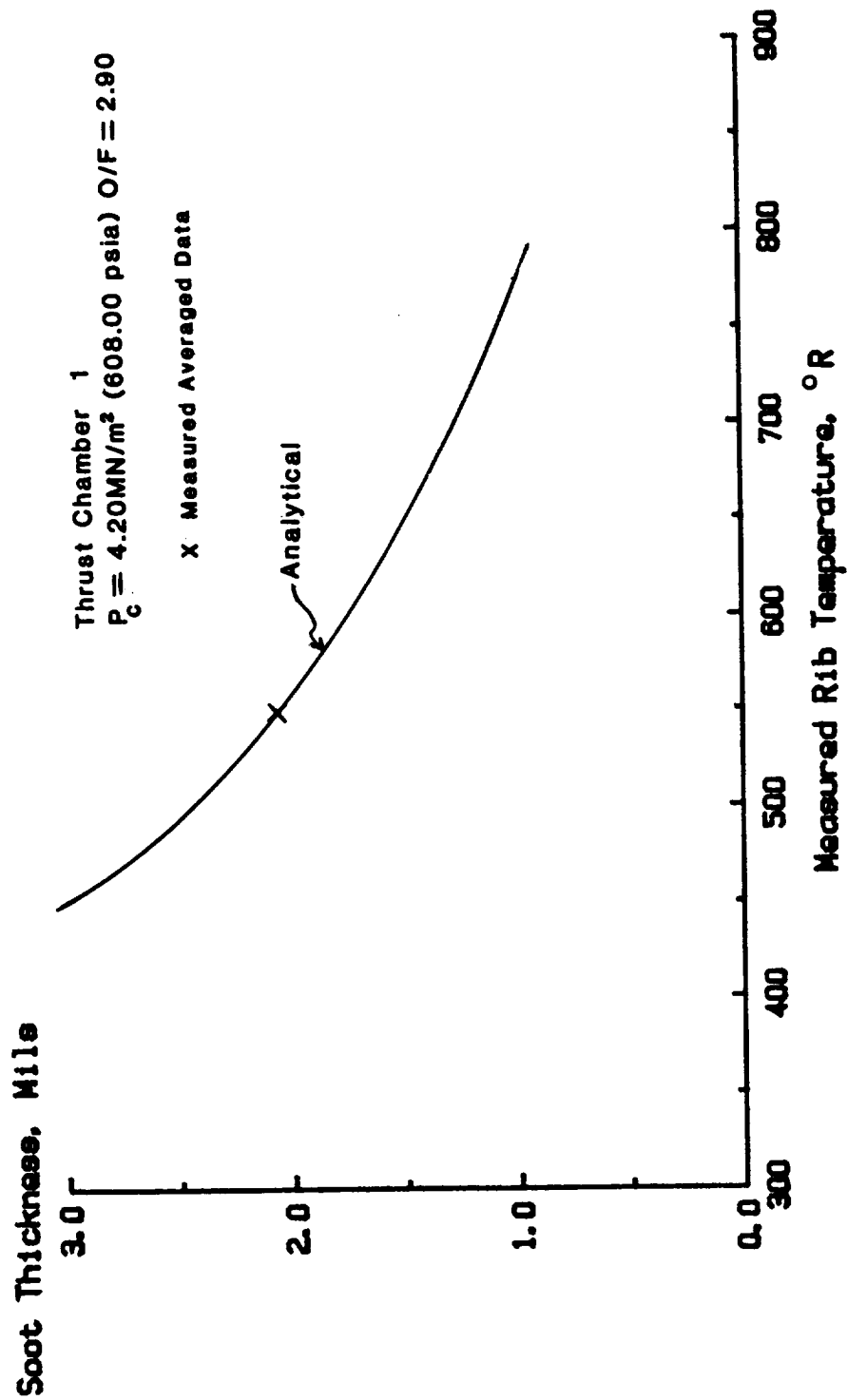


Figure 11a. - Soot thickness at throat 39.4 cm (15.5 inches) from injector face.

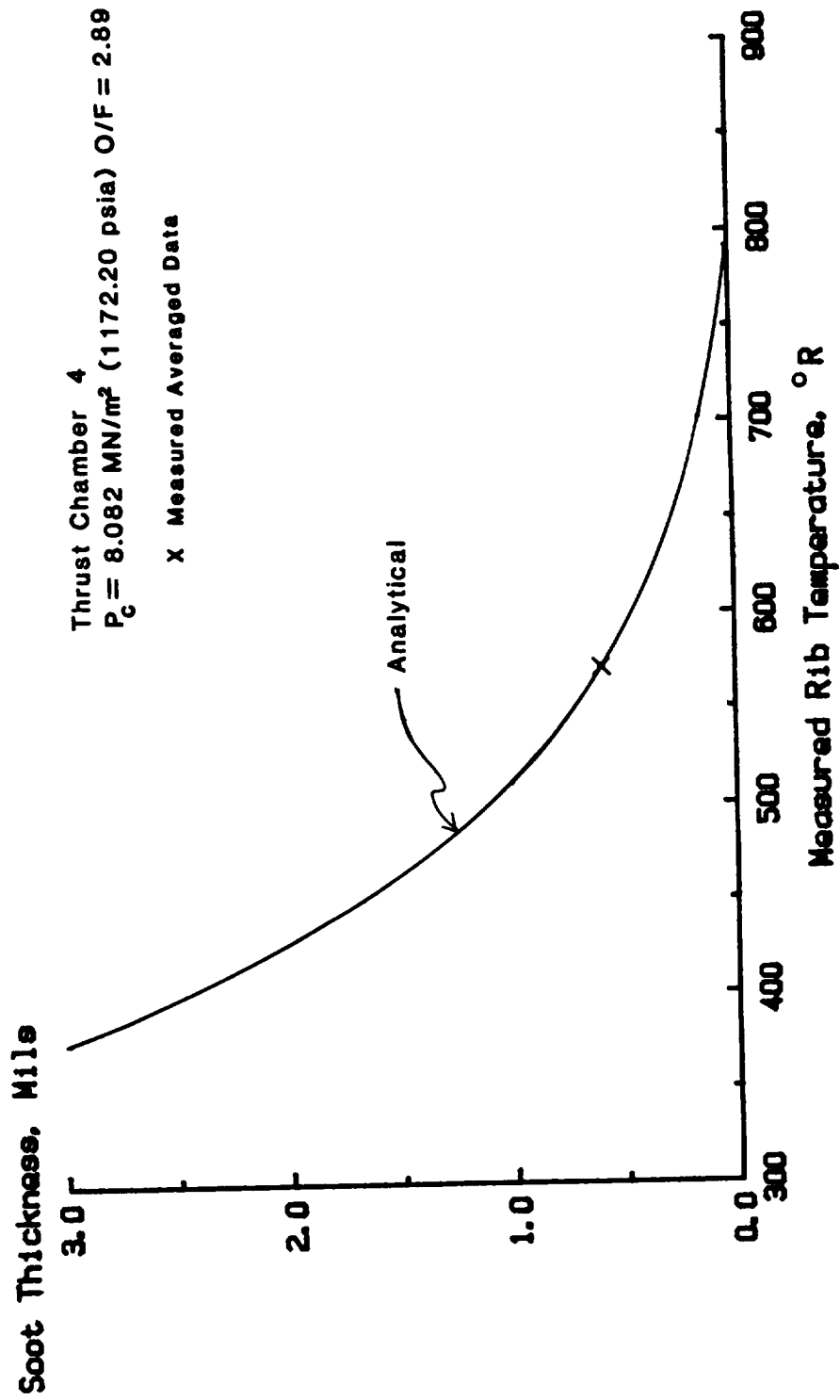


Figure 11b. - Soot thickness at throat 29.2 cm (11.5 inches) from injector face.

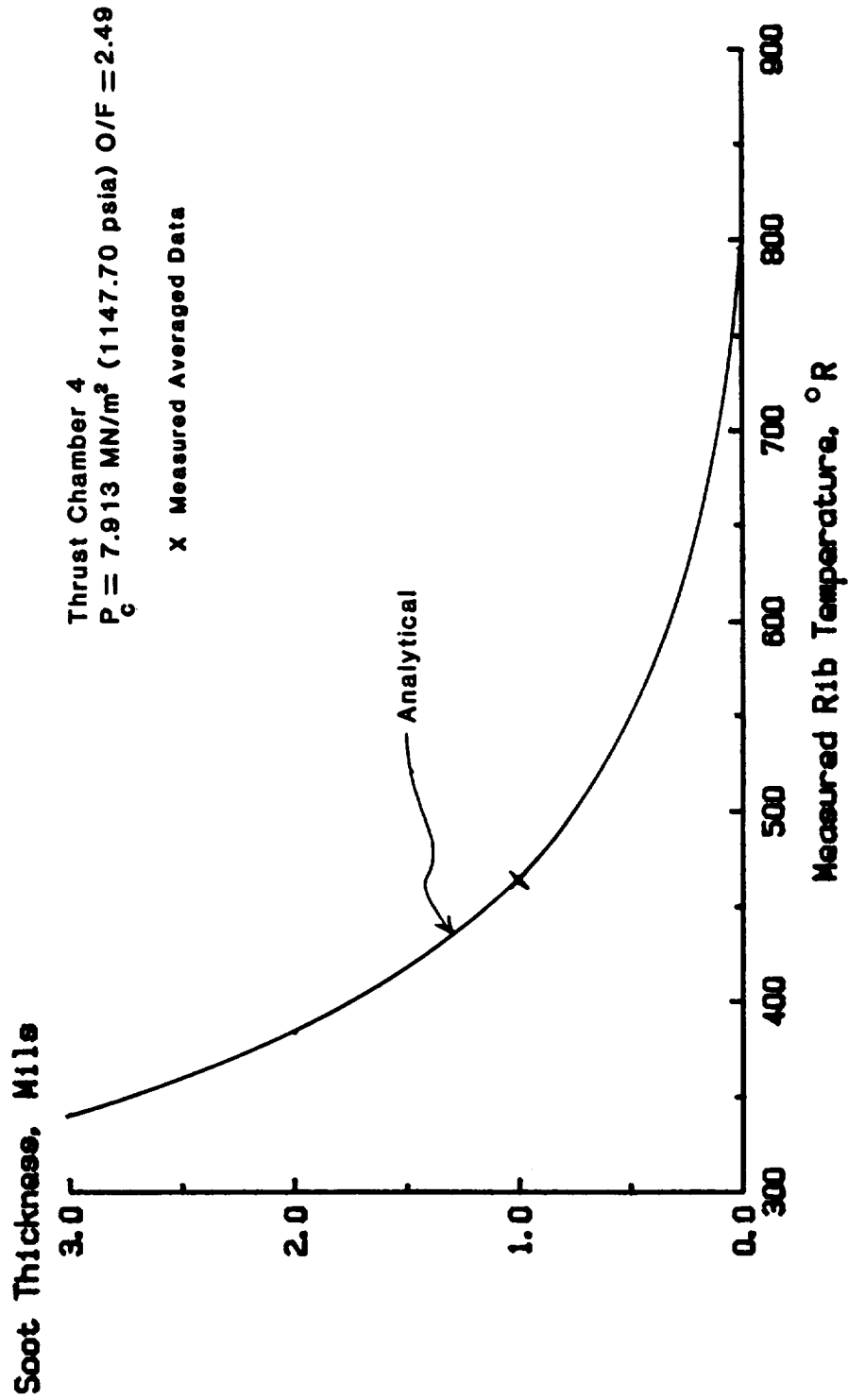


Figure 11c. - Soot thickness at throat 29.2 cm (11.5 inches) from injector face.

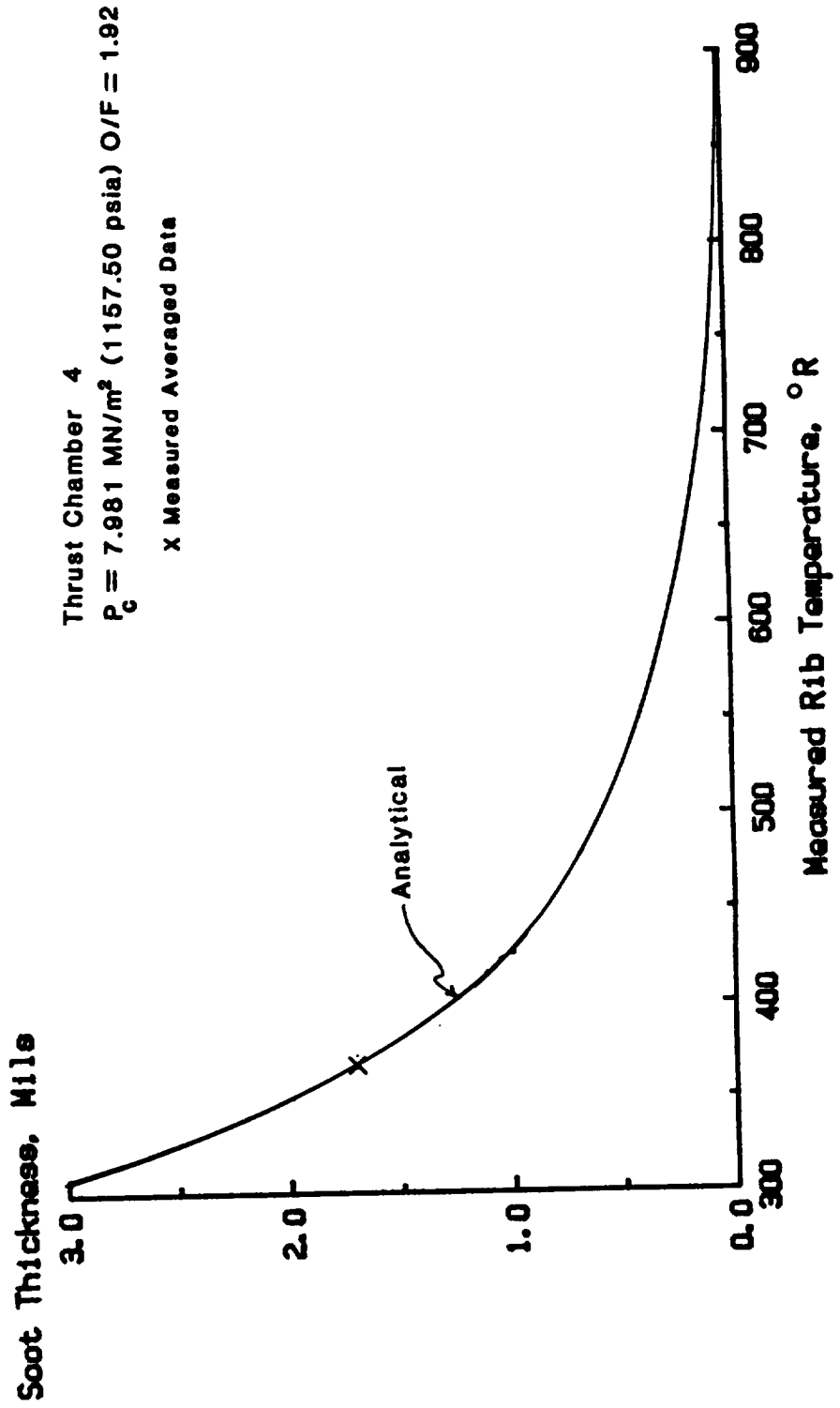


Figure 11d. - Soot thickness at throat 29.2 cm (11.5 inches) from injector face.

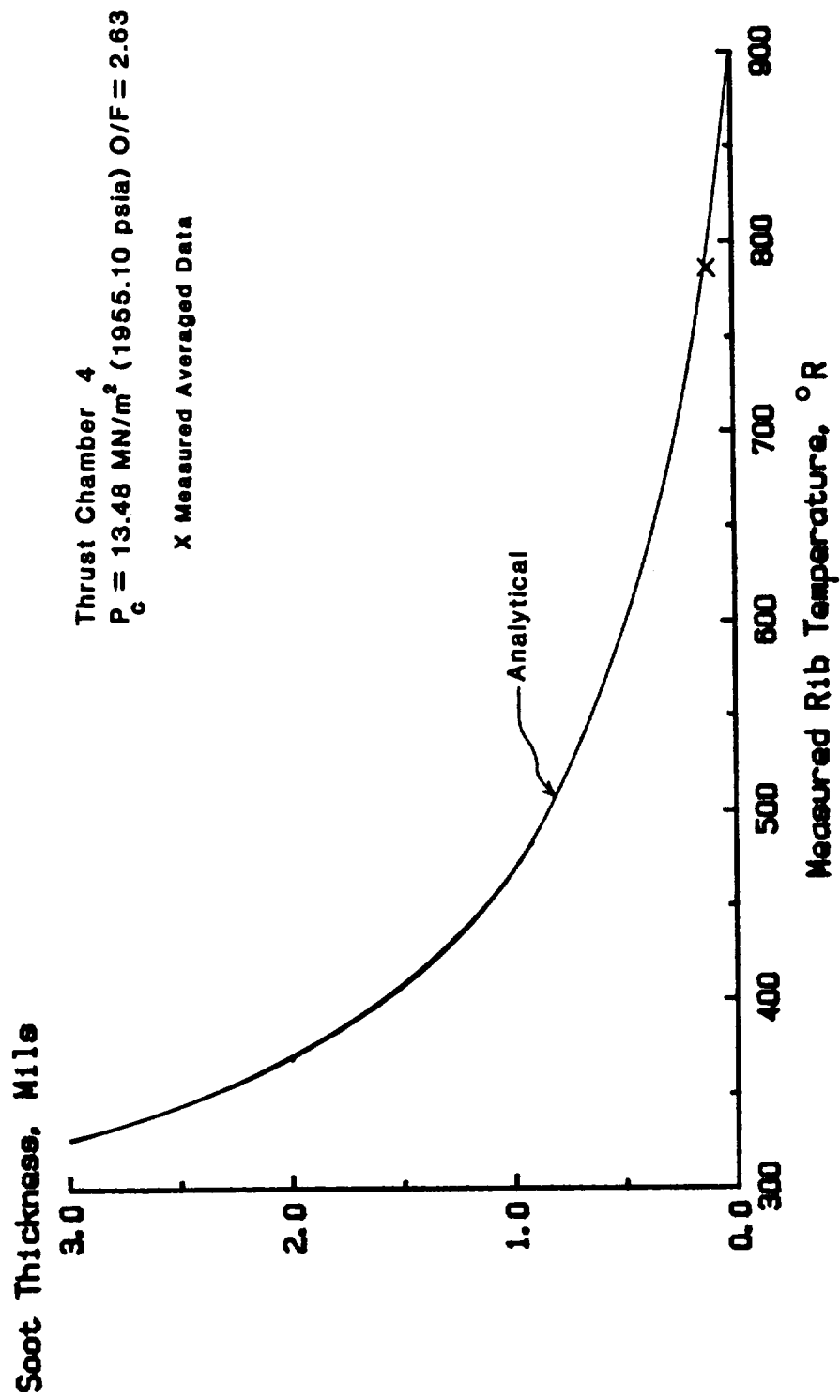


Figure 11e. - Soot thickness at throat 29.2 cm (11.5 inches) from injector face.



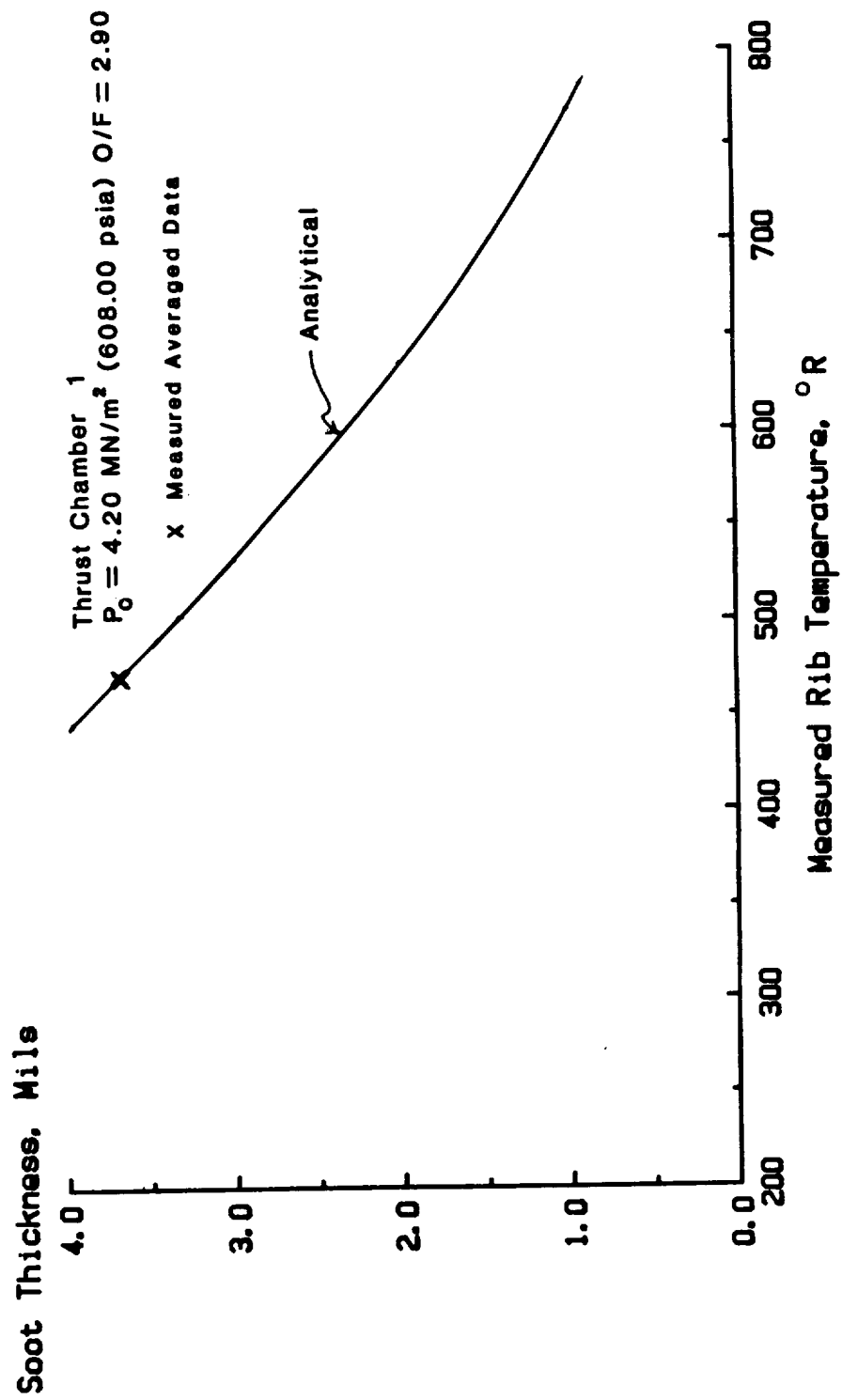


Figure 12a. - Soot thickness 41.9 cm (16.5 inches) from injector face.

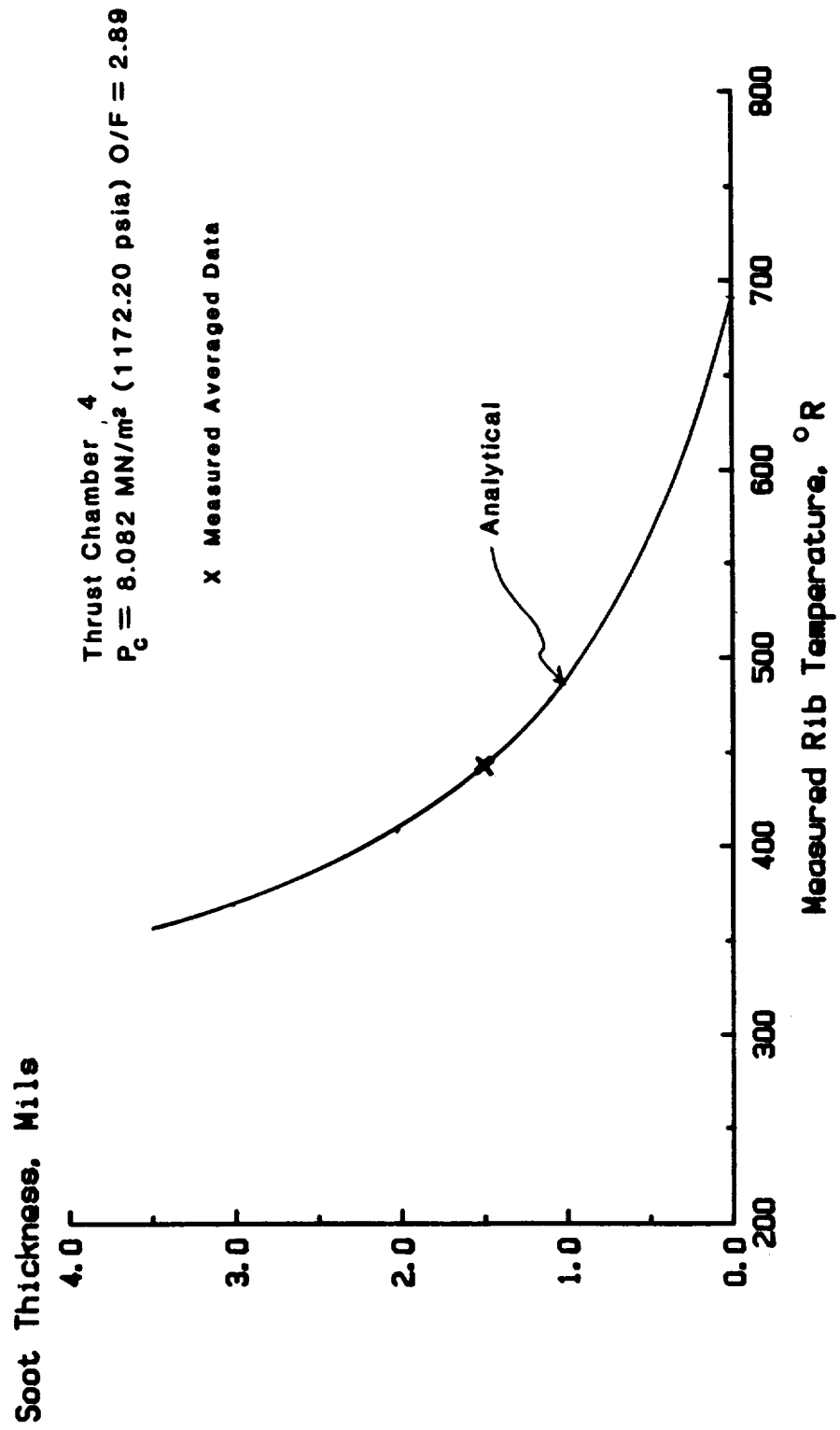


Figure 12b. - Soot thickness 31.8 cm (12.5 inches) from injector face.

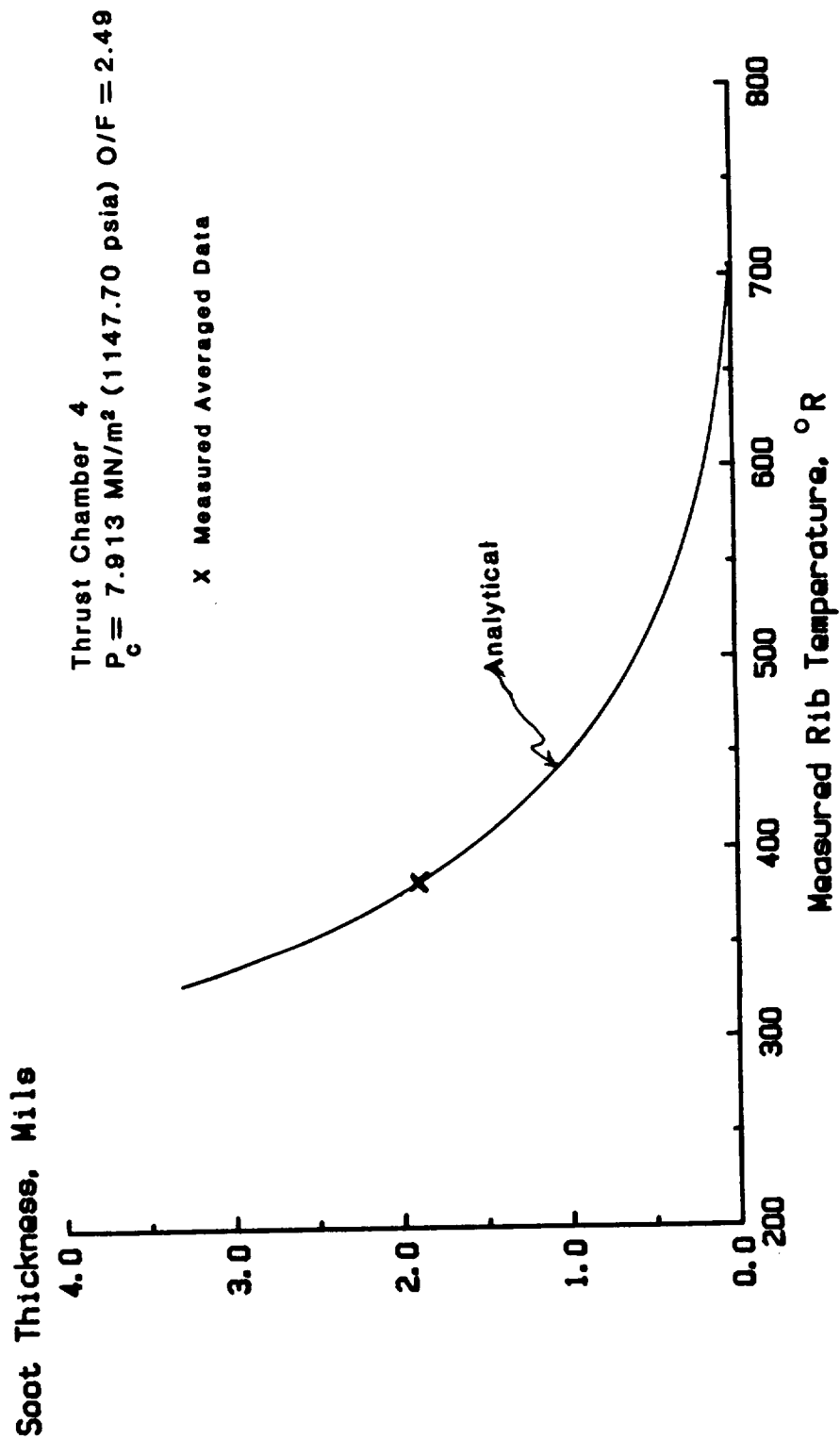


Figure 12c. - Soot thickness 31.8 cm (12.5 inches) from injector face.

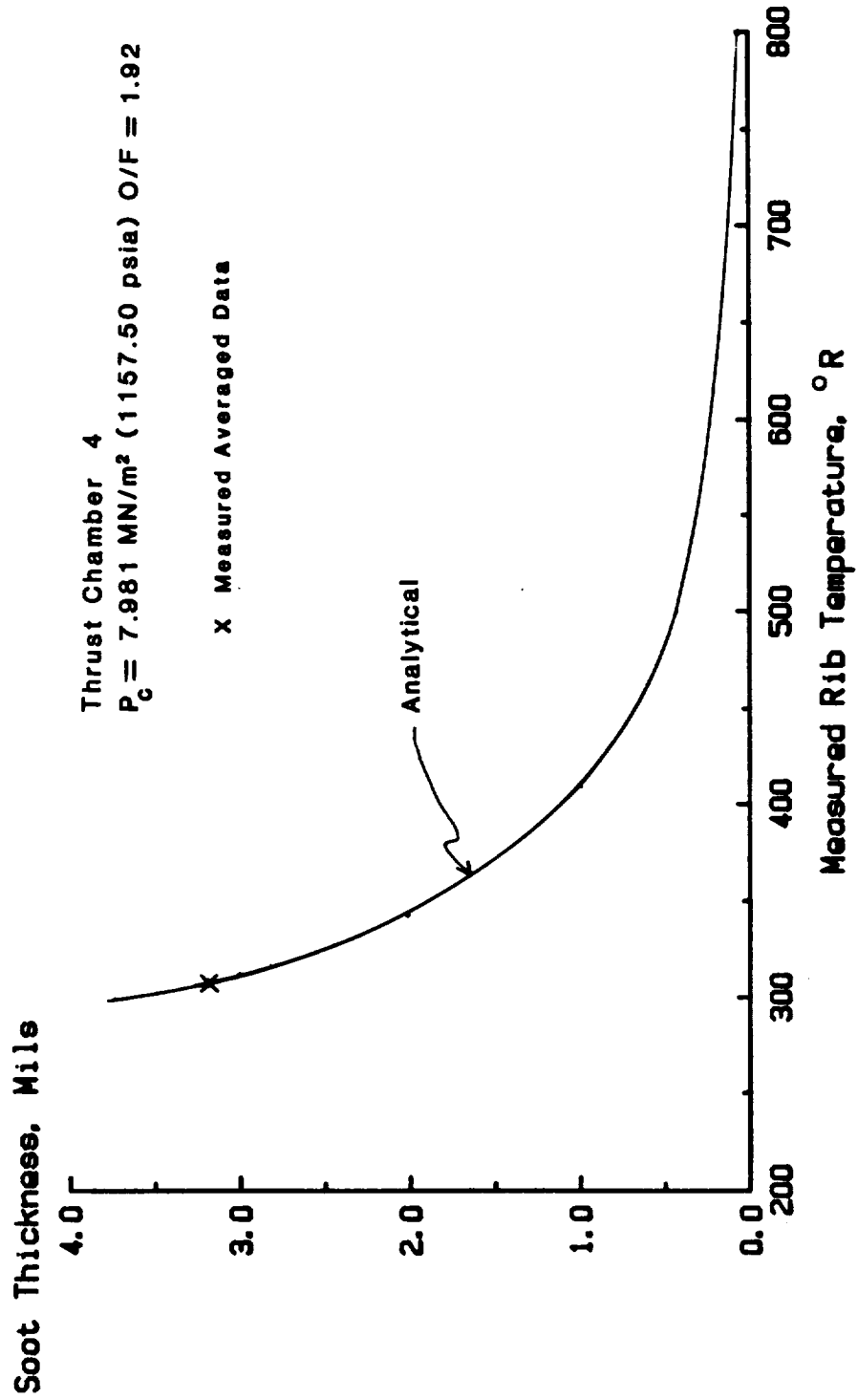


Figure 12d. - Soot thickness 31.8 cm (12.5 inches) from injector face.

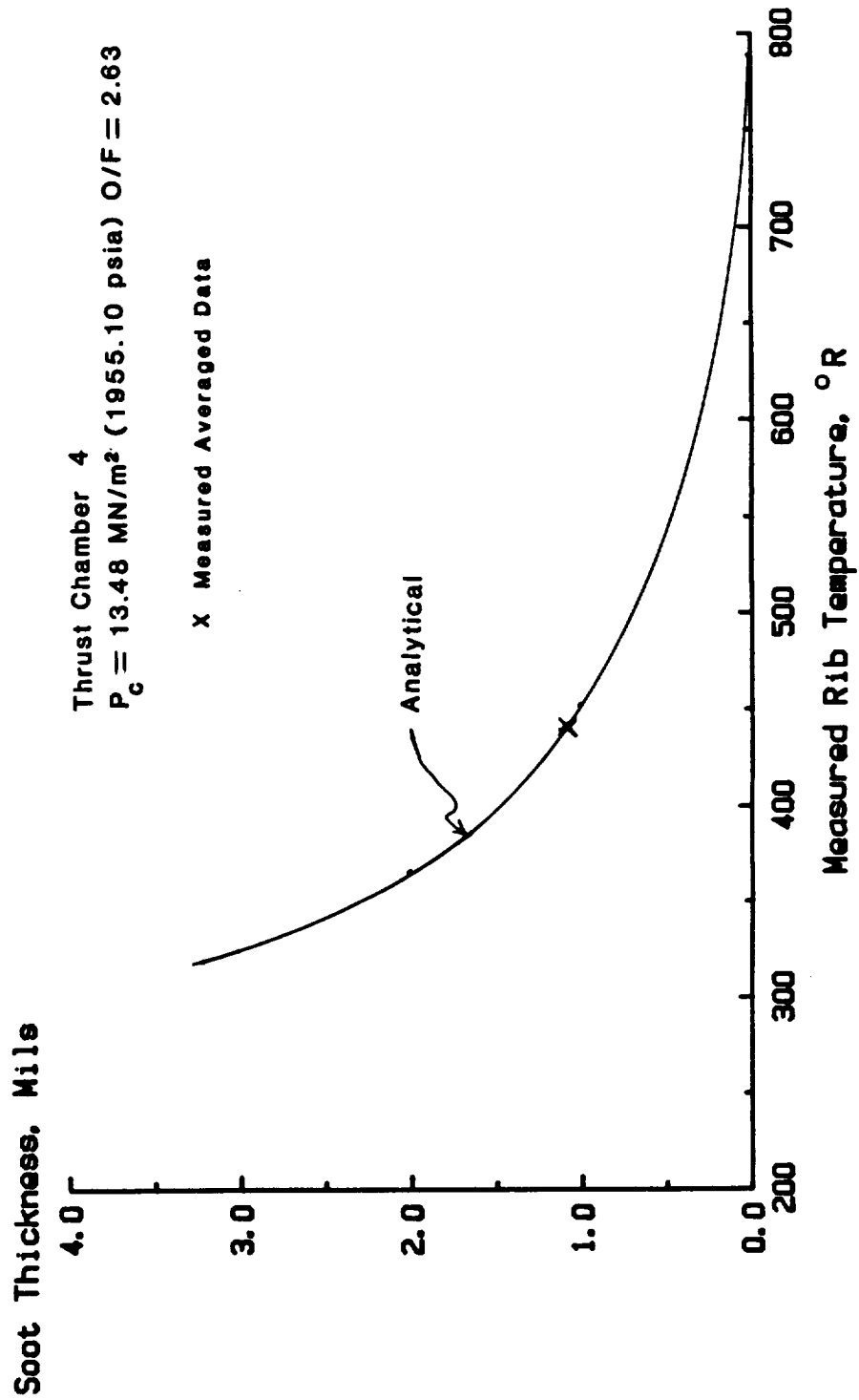


Figure 12e. - Soot thickness 31.8 cm (12.5 inches) from injector face.

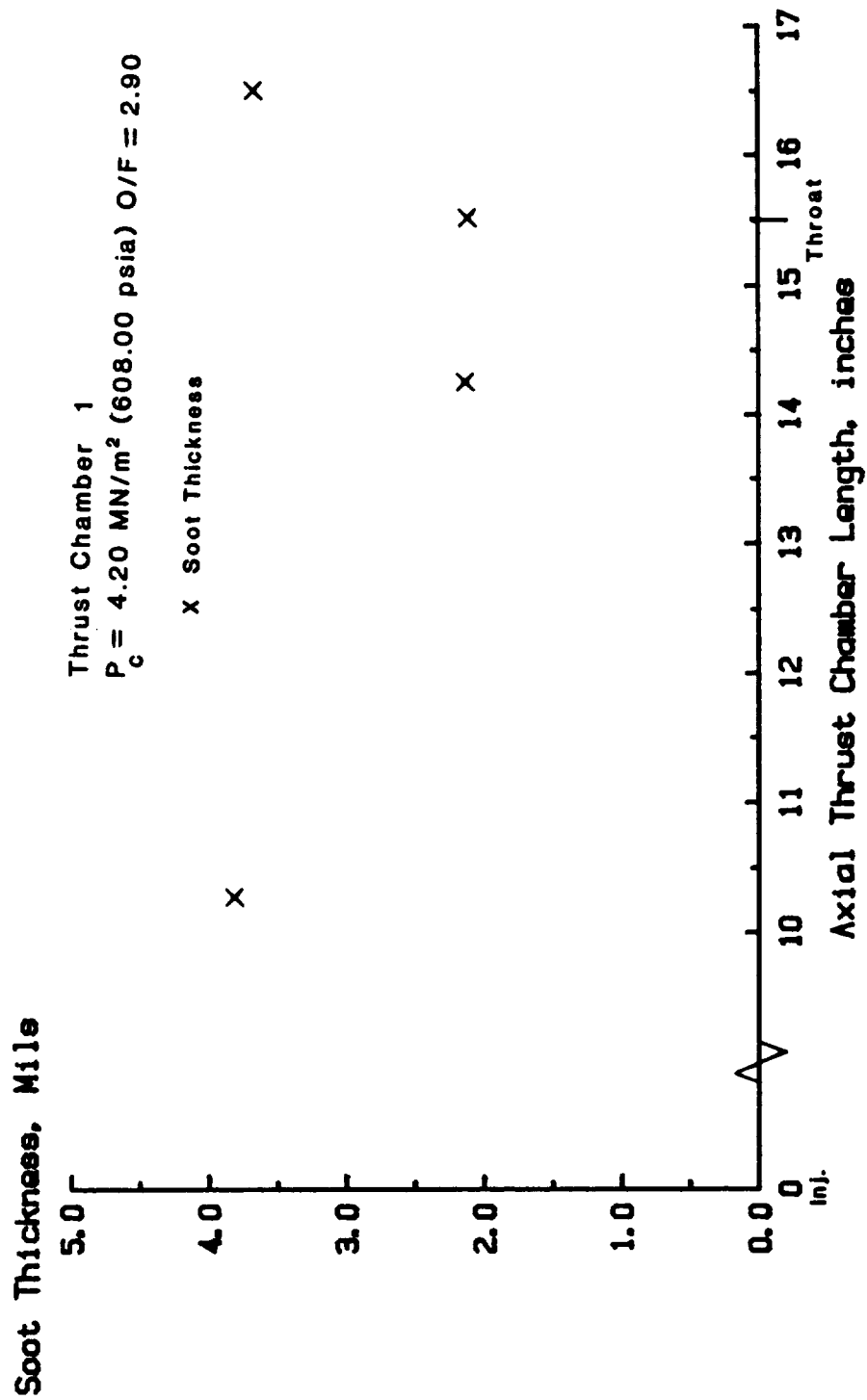


Figure 13a. - Axial soot build up on hot gas wall surface of rocket thrust chamber.

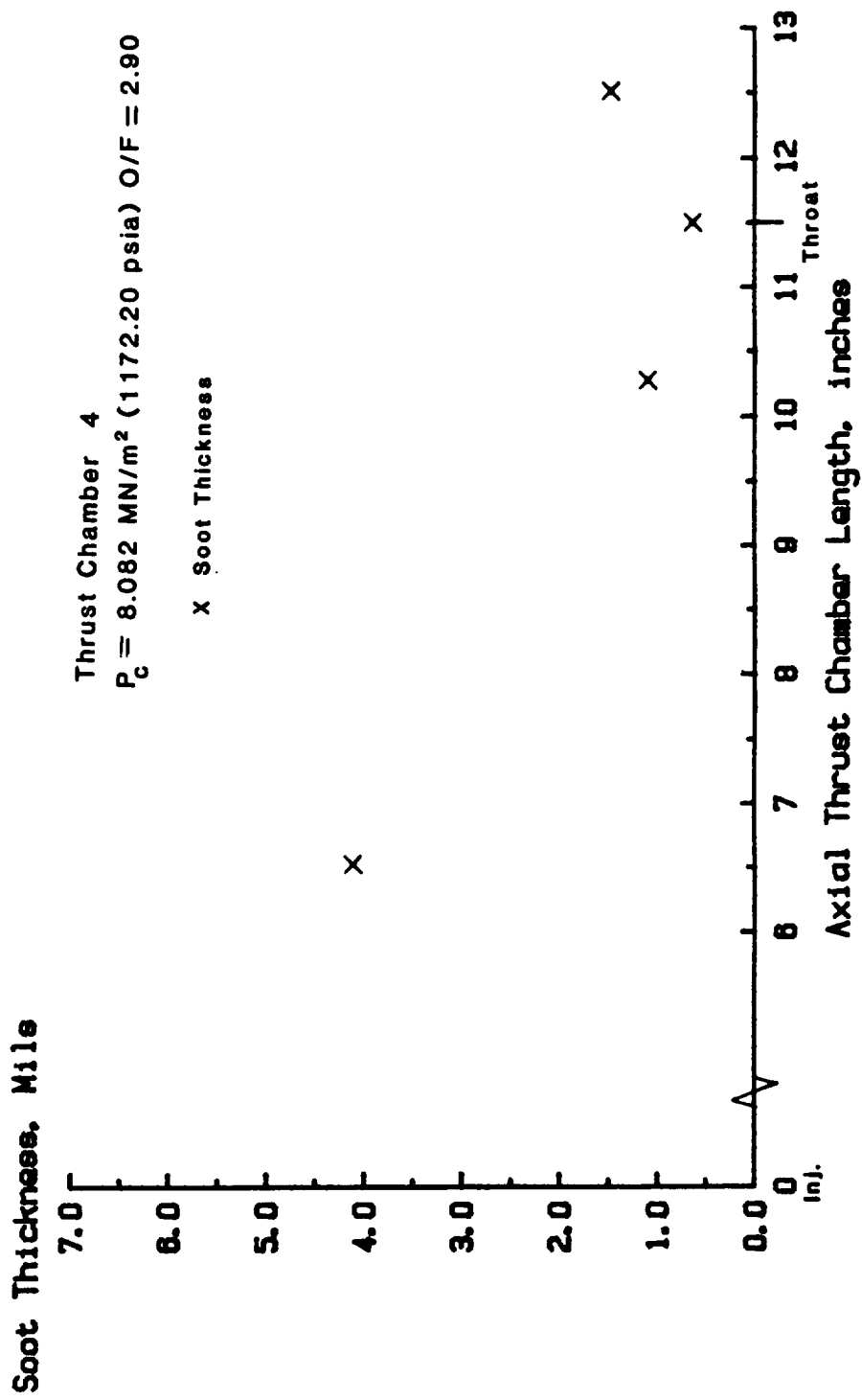


Figure 13b. - Axial soot build up on hot gas wall surface of rocket thrust chamber.

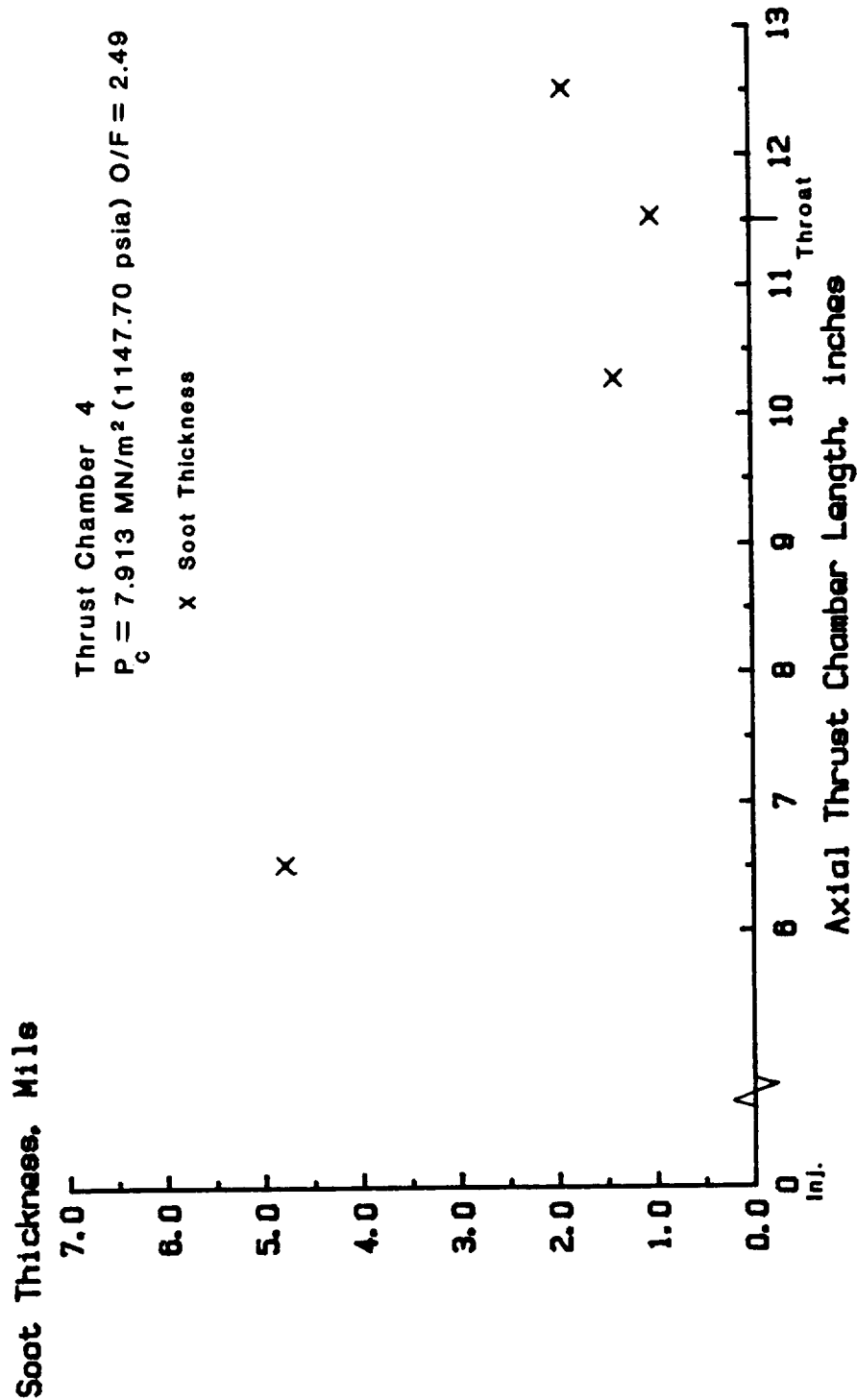


Figure 13c. - Axial soot build up on hot gas wall surface of rocket thrust chamber.



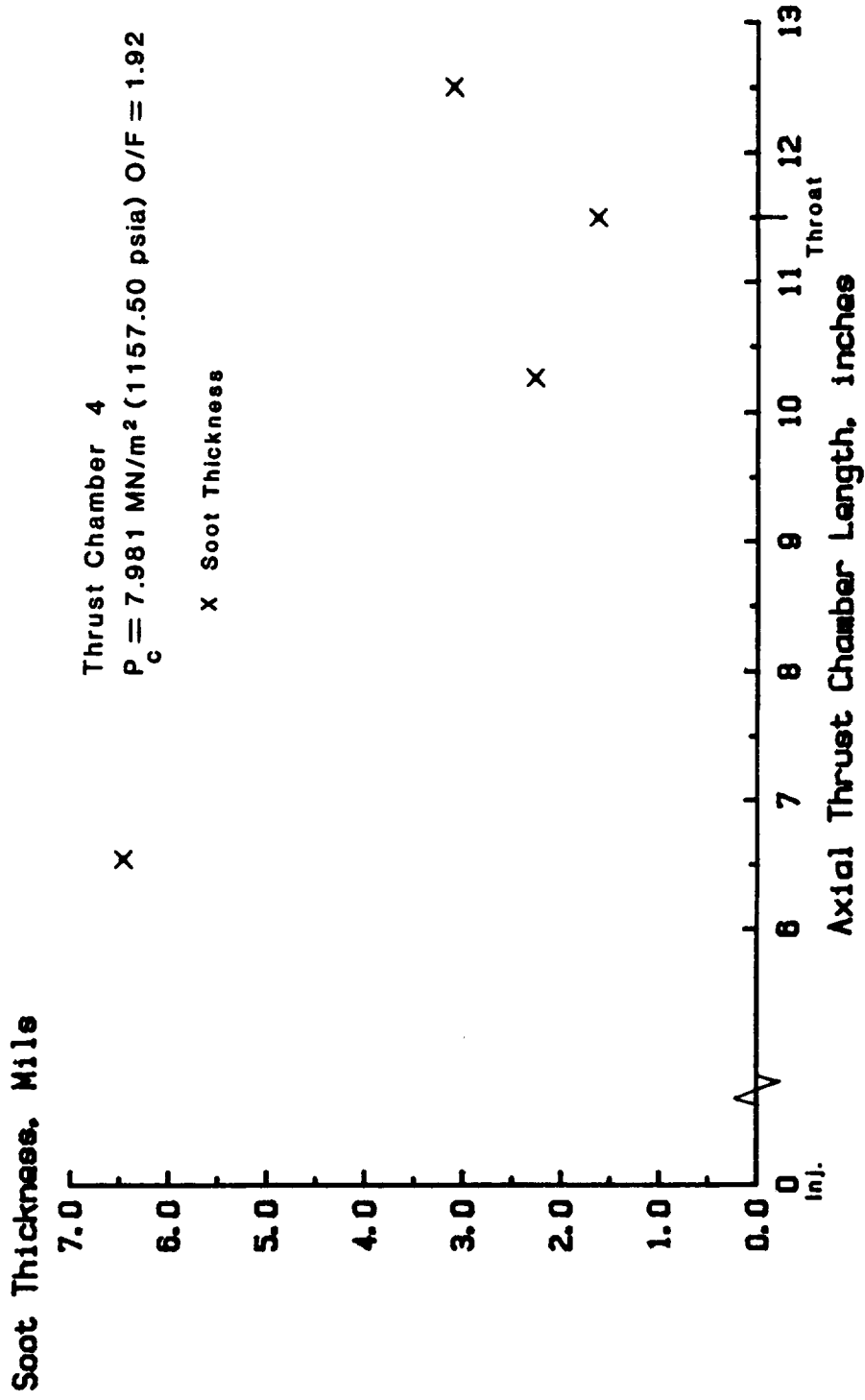


Figure 13d. - Axial soot build up on hot gas wall surface of rocket thrust chamber.

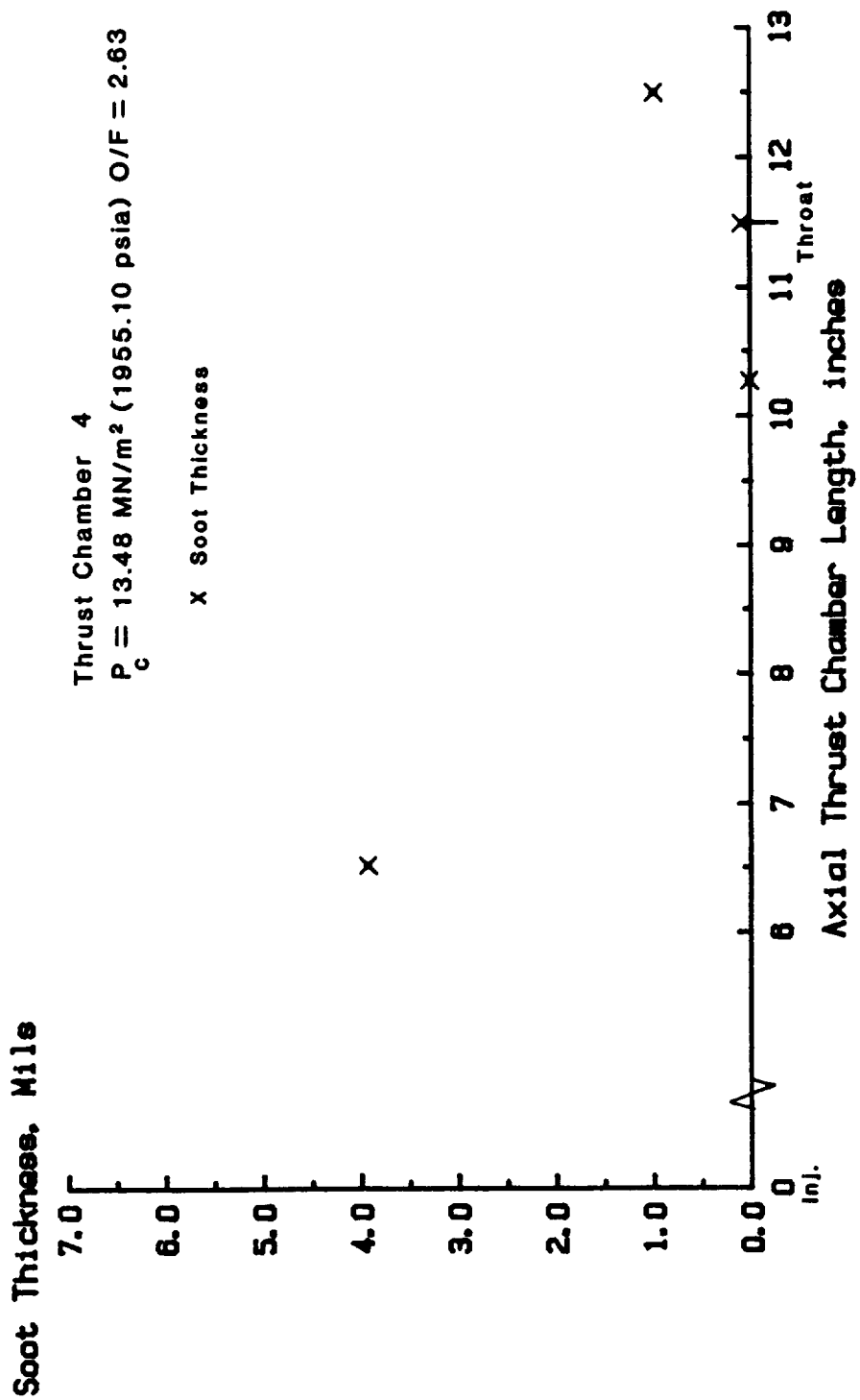


Figure 13e. - Axial soot build up on hot gas wall surface of rocket thrust chamber.

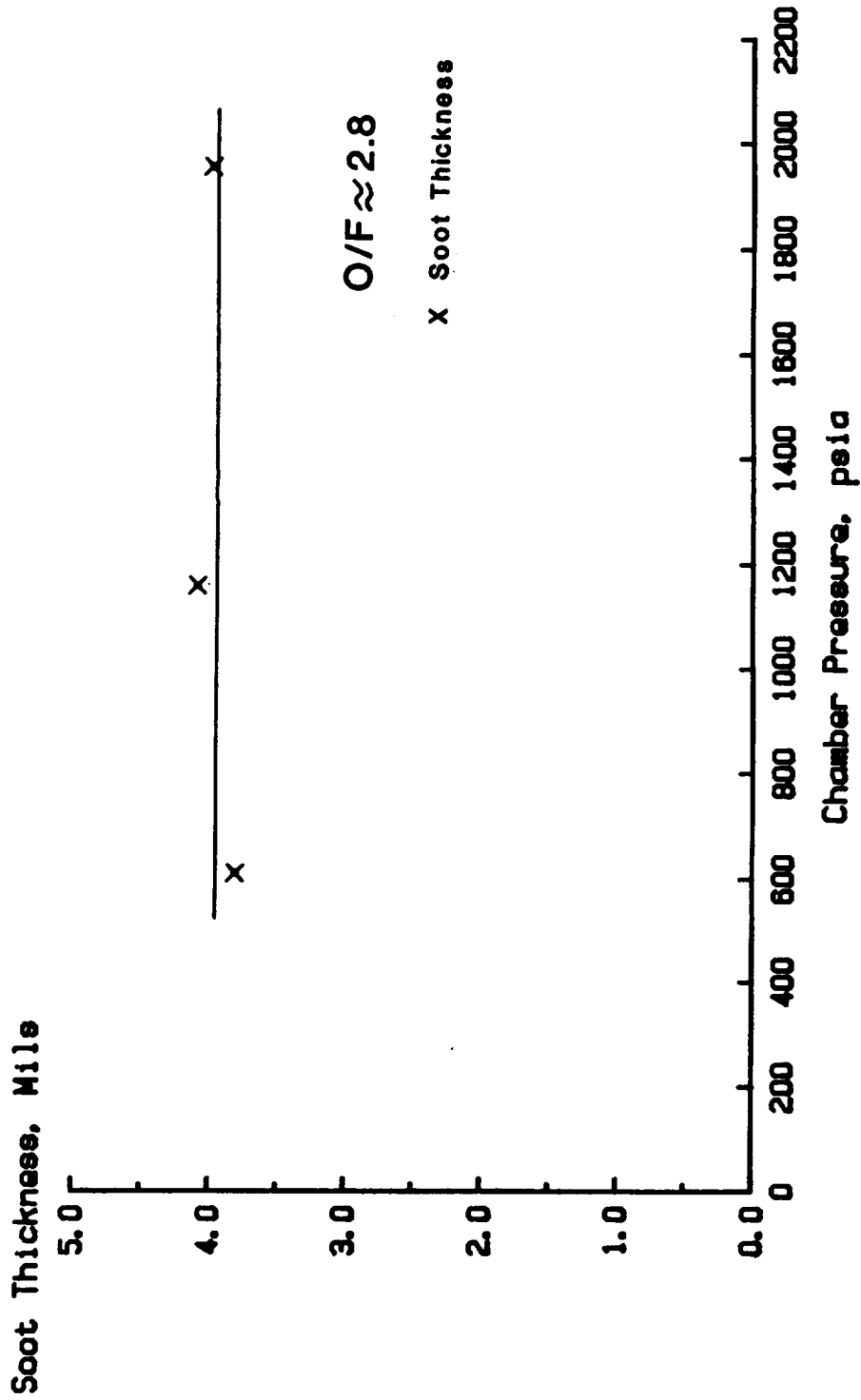


Figure 14a. - Soot thickness on the hot gas wall in the cylindrical section vs. chamber pressure.

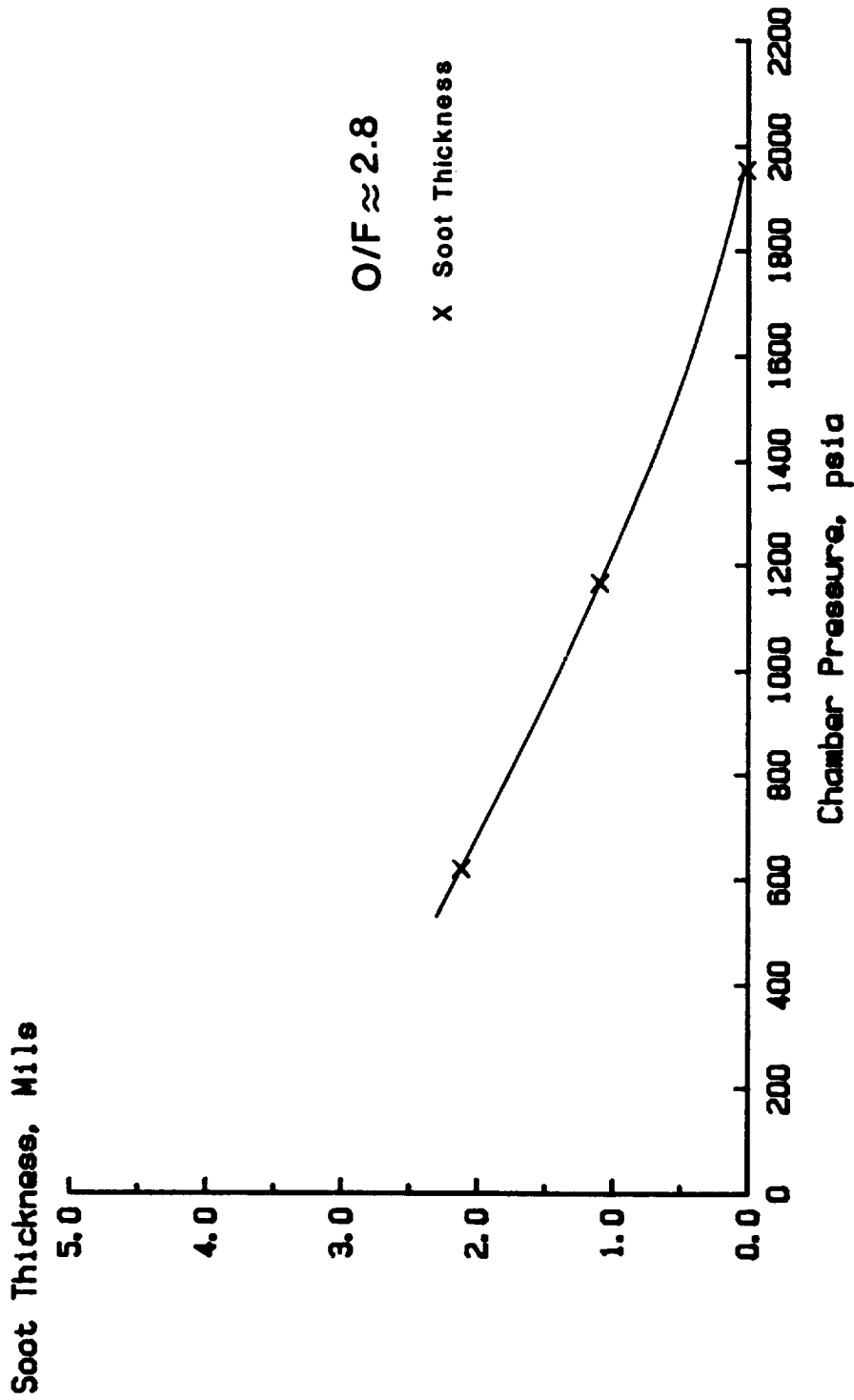


Figure 14b. - Soot thickness on the hot gas wall in the converging section vs. chamber pressure.

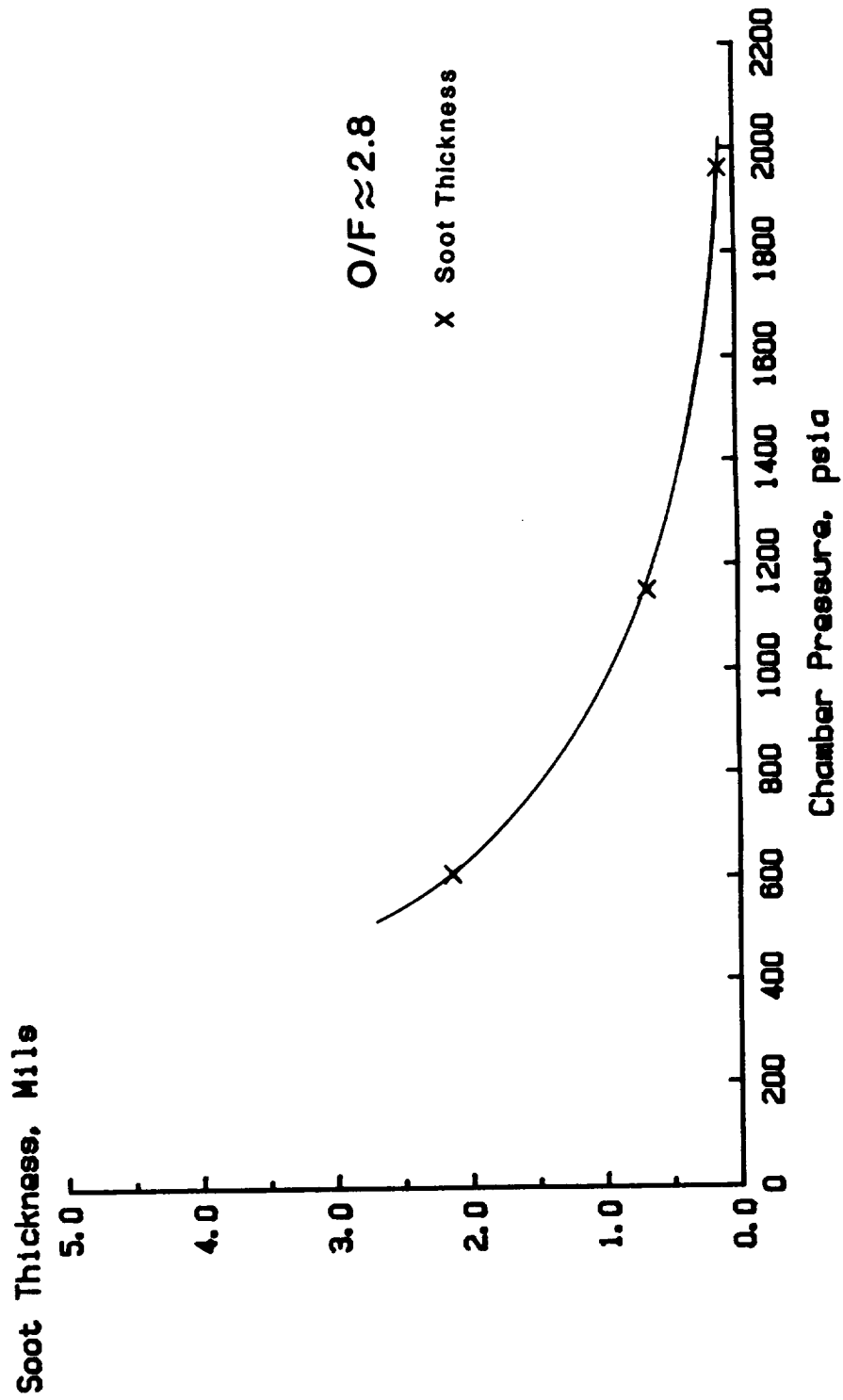


Figure 14c. - Soot thickness on the hot gas wall at the throat vs. chamber pressure.

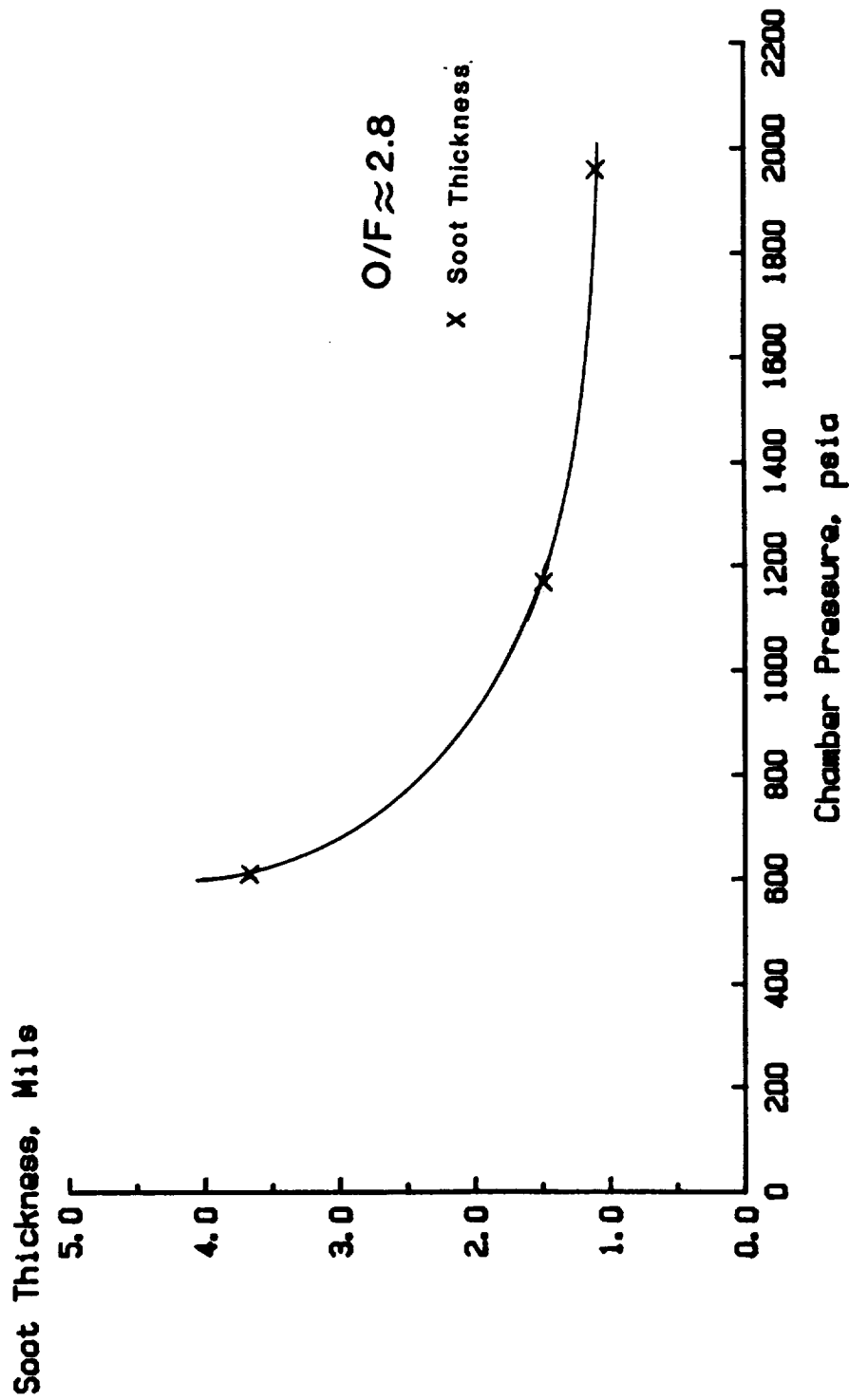


Figure 14d. - Soot thickness on the hot gas wall in the diverging section vs. chamber pressure.

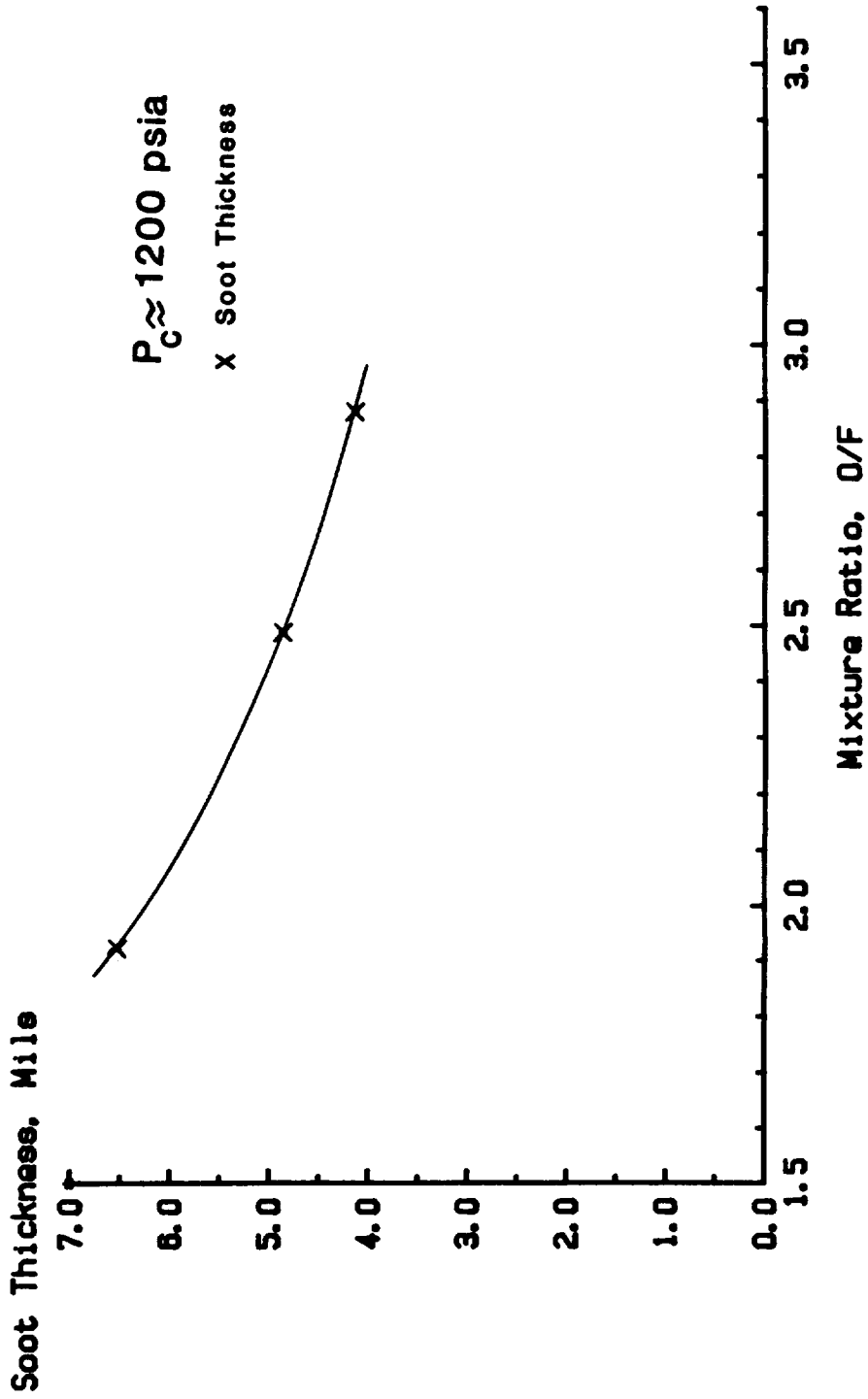


Figure 15a. - Soot thickness on the hot gas wall  
in the cylindrical section vs. mixture ratio.

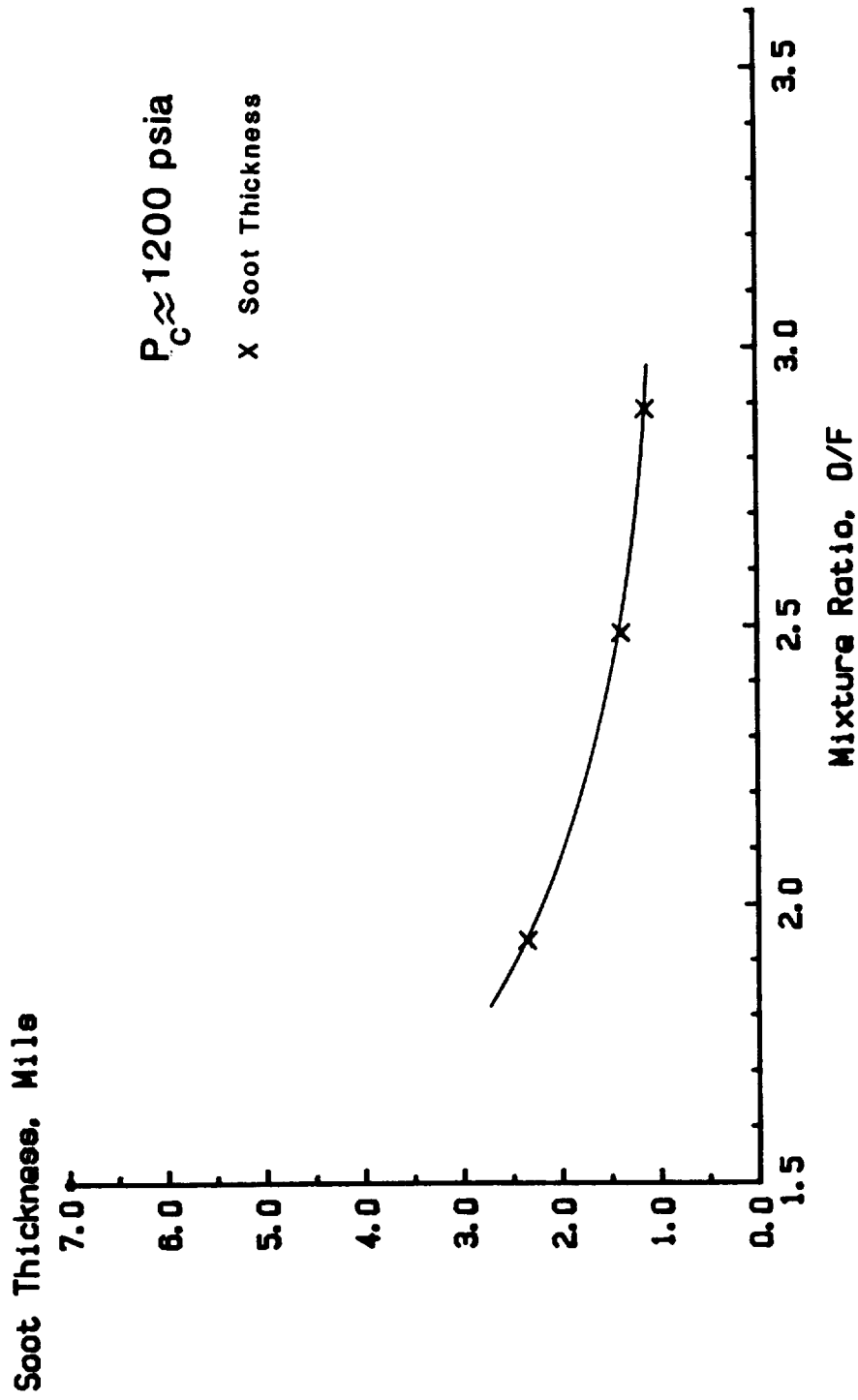


Figure 15b. - Soot thickness on the hot gas wall in the converging section vs. mixture ratio,



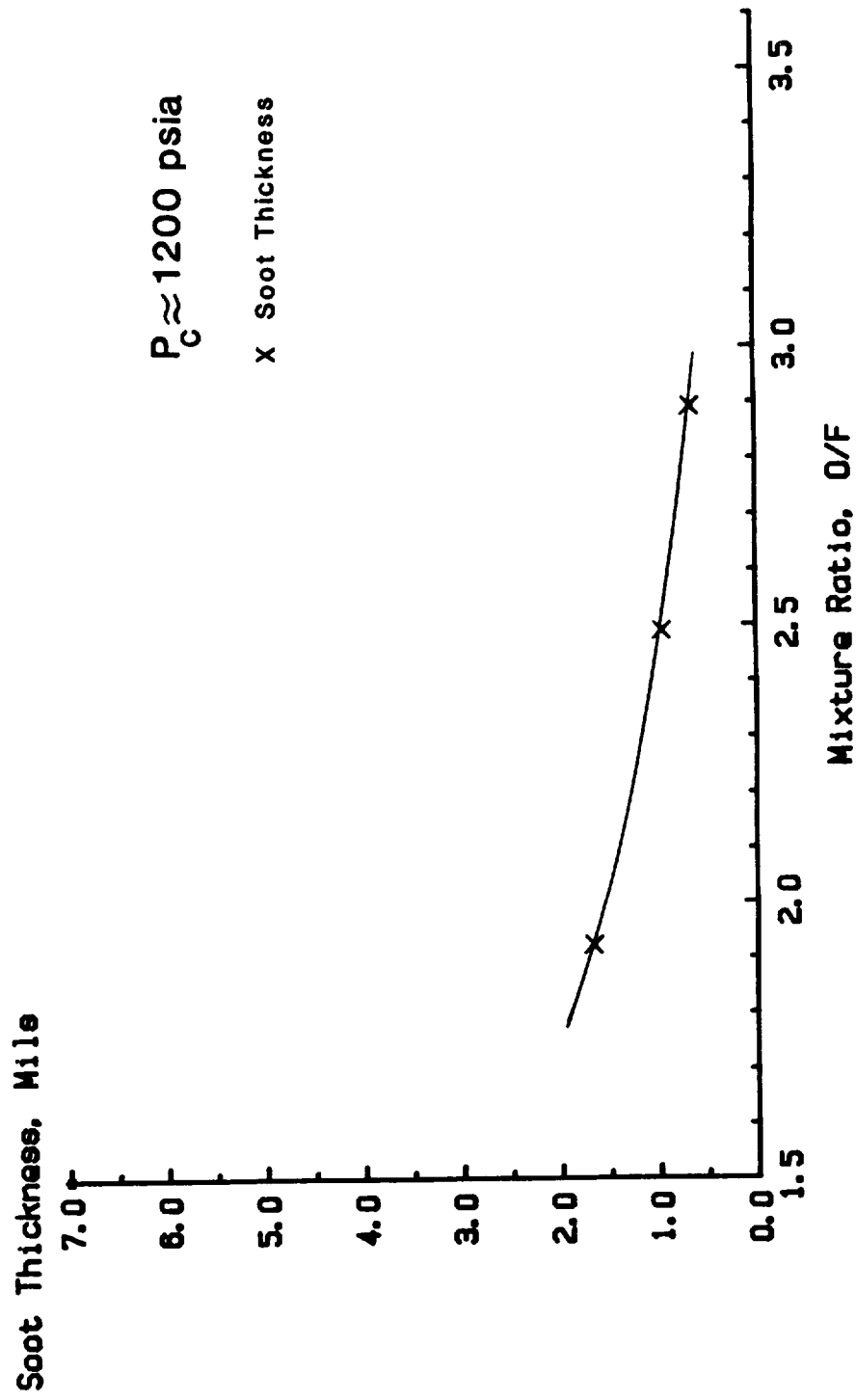


Figure 15c. - Soot thickness on the hot gas wall at the throat vs. mixture ratio.

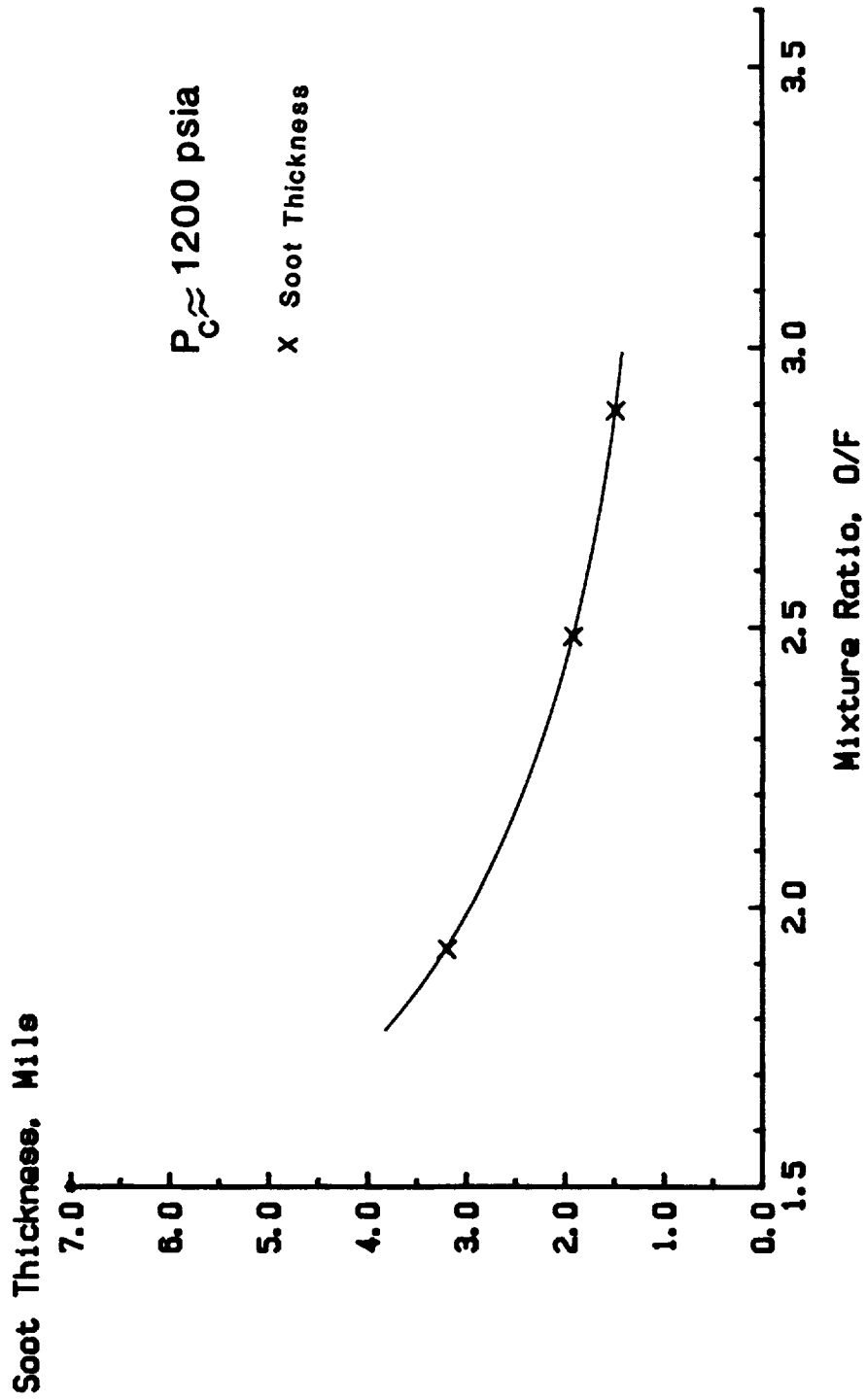


Figure 15d. - Soot thickness on the hot gas wall in the diverging section vs. mixture ratio.

## RP-1 AND METHANE COMBUSTION AND COOLING EXPERIMENTS

C. R. Bailey

National Aeronautics and Space Administration  
George C. Marshall Space Flight Center, Alabama

## ABSTRACT

A program was conducted to investigate ignition, combustion and heat transfer characteristics of liquid oxygen and either RP-1 or methane fuel applicable to advanced booster engines. Experimental data for both staged combustion and gas generator cycles were obtained for methane. Testing using RP-1 was conducted in support of the gas generator cycle. A pressure-fed combustion system rated at 40,000 pounds thrust was used for all testing. Preburner and gas generator combustion data for both propellant combinations were obtained at pressures ranging from 1500 to 3100 psia and temperatures from 1600 to 2000 degrees Rankine. Main injector evaluations were accomplished primarily with test firings using a water-cooled calorimeter main combustion chamber. With this chamber, heat flux profiles and combustion performance were obtained at pressures to approximately 2200 psia. Several tests were conducted using a methane-cooled combustion chamber.

## INTRODUCTION

During the past several years, interest has increased in the potential use of hydrocarbon fuels in combination with liquid oxygen for advanced launch vehicle booster engines. Several fuels have been considered including RP-1 and methane. Although neither of these generate a specific impulse as high as hydrogen, the greater densities and reduced tankage weights associated with the hydrocarbon fuels offer the potential of payload increases.

The Marshall Space Flight Center (MSFC) has underway a long-range effort to provide a combustion devices technology base adequate to initiate an advanced Lox-hydrocarbon engine development program. The data base is intended to include methane fuel for either gas generator or staged combustion engine cycles and RP-1 fuel for the gas generator engine cycle. These engines are expected to operate at main combustion chamber pressures at least 2000 psia. The goal of this program has been to provide supporting data primarily applicable to ignition, combustion performance and heat transfer.

## BACKGROUND AND APPROACH

The program was structured to make maximum use of a residual sub-scale space shuttle main engine (SSME) combustion system used several years ago to investigate low cycle fatigue characteristics of the main combustion chamber liner. Model SSME components used included preburner chambers and nozzles and a water-cooled calorimeter main combustion

chamber used for main injector evaluation. The injectors were either procured by competitive contract or designed and fabricated at MSFC.

The basic preburner assembly used for all preburner and gas generator testing is shown in Figure 1. The combustion chamber is 11 in. long with a 3.5 in. I.D. and is drilled at six places in the downstream flange for thermocouples to be inserted into the gas stream. A 4 in. chamber extension was available to provide longer combustor lengths if needed. A chlorine trifluoride torch igniter is mounted in the upstream flange. Several different sized nozzles were available to allow chamber pressure to be varied independent of propellant flow rate. Accommodations for flush-mounted high frequency pressure transducers for stability measurements are provided in the combustion chamber and both fuel and oxidizer manifolds.

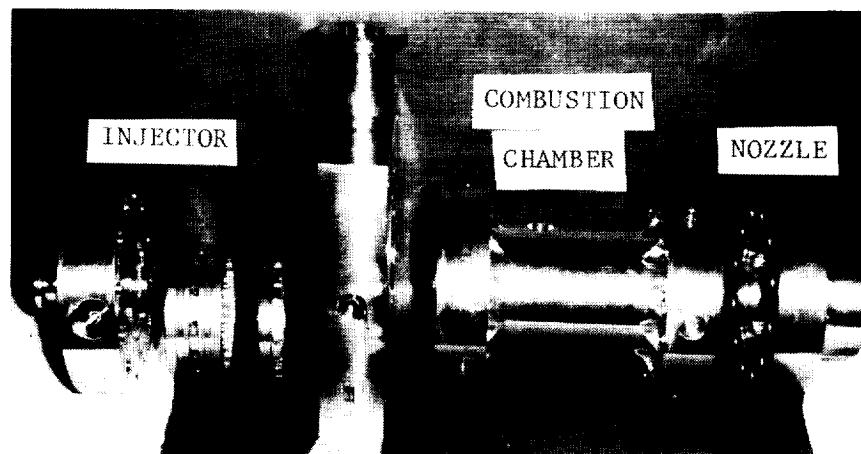


Figure 1. Preburner Components

The calorimeter main combustion chamber used for main injector evaluation is shown in Figure 2. The chamber has a copper alloy inner liner with 116 milled circumferential cooling water channels. The channels are manifolded into groups of two, providing 58 individual coolant circuits for heat transfer measurement along the length of the chamber. The length from the injector to the throat is 14 in. and the throat diameter is 3.31 in.

All testing was conducted at Test Position 116, Marshall Space Flight Center, AL. This is a high pressure facility used primarily for acoustics and combustion devices testing. Liquid propellant tank working pressures are 5000 psi, and natural gas which was used as a substitute for methane was supplied from 10,000 psi storage bottles. The selection of natural gas instead of methane was made primarily because of the availability of high methane content liquified natural gas (LNG) at low cost. Methane content of the purchased LNG ranged from 95 to 97 mol percent with the remainder being ethane and propane.

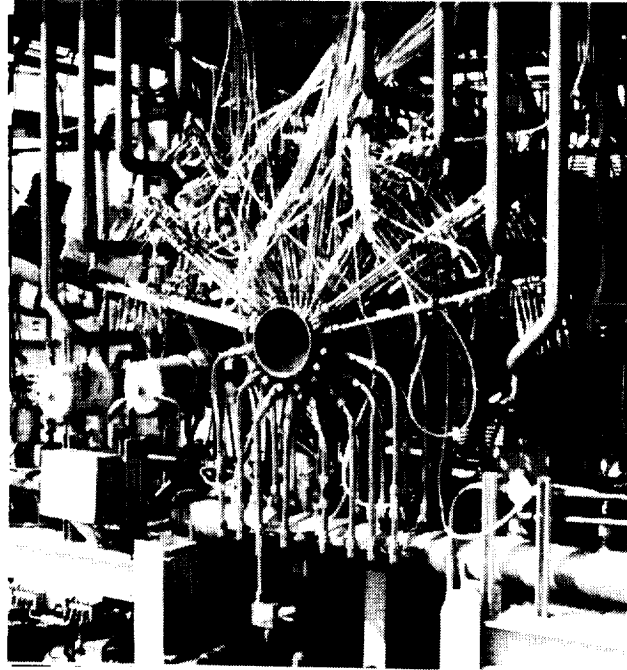


Figure 2. Calorimeter Combustion Chamber Installation

LOX-METHANE STAGED COMBUSTION

Preburner Performance

The preburner injector was obtained by contract (Reference 1) and is pictured in Figure 3. The design has 49 shear coaxial elements. The I.D. of each oxygen tube at the point of injection is 0.088 in. The tube O.D. is 0.1355 in. and the fuel port diameter is 0.1730 in.



Figure 3. LOX-Methane Preburner Injector

Initial attempts to ignite the propellants at planned steady-state mixture ratio were unsuccessful. It was concluded that propellant ignition with this injector could be accomplished only by using a higher mixture ratio during the start transient and shifting to the planned mixture ratio only after propellant burning was fully established. It was determined that a mixture ratio equivalent to a combustion temperature of approximately 2000°F was required for reliable ignition. Combustion chamber pressure and temperature traces for a typical test are shown in Figure 4. Comparison of characteristic velocity and combustion temperature tests data to ODE theoretical predictions is presented in Figures 5 and 6. Combustion performance was generally as expected, and the goal of combustion temperature uniformity within  $\pm 50^\circ\text{F}$  across the chamber was achieved in five of the eight tests. Combustion pressure oscillations expressed as a percentage of chamber pressure ranged from 1.3 to 4.2 percent as compared to a program goal of 5.0 percent maximum.

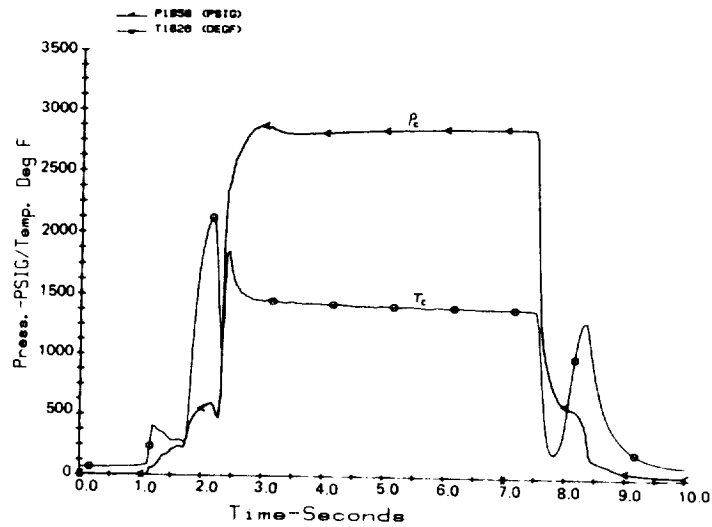


Figure 4. LOX-Methane Preburner Test Data

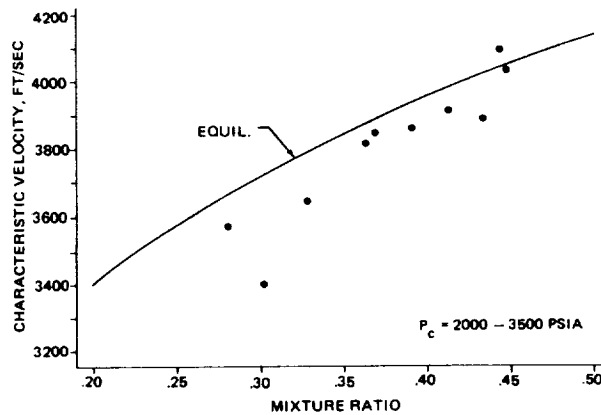


Figure 5. Comparison of Test Data to Theoretical Characteristic Velocity

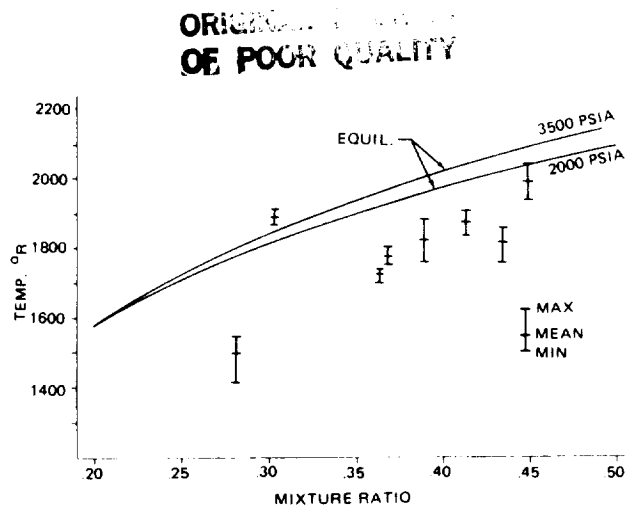


Figure 6. Comparison of Test Data to Theoretical Combustion Temperature

### Staged Combustion Performance

The main injector used for staged combustion testing was a slightly modified version of the subscale SSME main injector which used full size SSME coaxial elements. The only significant modification was a reduction in fuel sleeve I.D. to compensate for the difference in density between methane and hydrogen. A photograph of the injector is shown in Figure 7. The assembly consists of 61 coaxial elements plus a coaxial igniter element located in the center of the face. Primary fuel is the fuel-rich preburner exhaust gas. In addition, ambient temperature methane is supplied to a cavity between two porous metal mesh faceplates and serves as the transpiration coolant for the faceplates plus the fuel supply for the igniter. Liquid oxygen flow control for each of the 61 oxygen posts is provided by a metering orifice at the entrance to the post. At the injection plane, Lox post I.D. is 0.188 in. and the O.D. is 0.230 in. The fuel sleeve I.D. which serves as the fuel injection annulus initially had an I.D. of 0.310 in. for all elements.

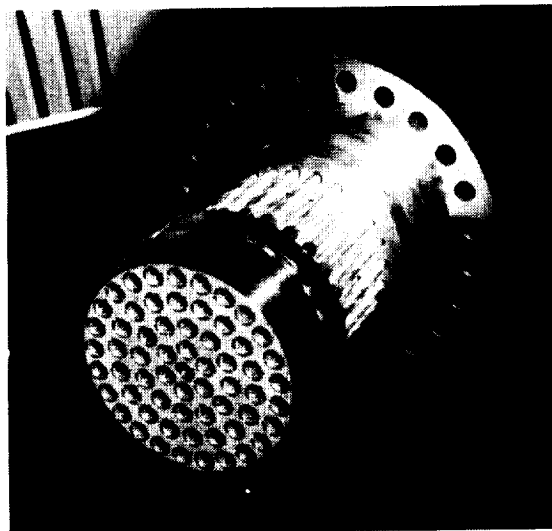


Figure 7. LOX-Methane Staged Combustion Main Injector

Nine staged combustion tests were conducted using the calorimeter combustion chamber which provided both combustion performance and heat transfer data. Chamber pressures ranged from 1400 to 2135 psia and mixture ratios varied from 2.38 to 3.52. The first five tests were conducted with the baseline uniform mixture ratio (UMR) injector. Characteristic velocity ( $C^*$ ) efficiency exceeded 98 percent for each test but showed a trend of decreasing efficiency with increasing chamber pressure. Heating rate in the throat region was approximately 18 percent higher than had been predicted. The predicted heat transfer profile was calculated using standard Nusselt Number scaling from oxygen-hydrogen data previously obtained with the same combustion chamber. Both the predicted and measured heating rate profiles, scaled to 3000 psia, are shown in Figure 8. In addition, Figure 9 shows both predicted and measured nozzle throat heating rates expressed as a fraction of the equivalent rates using oxygen-hydrogen at a mixture ratio of 6.0. This was a convenient way to non-dimensionalize the information for comparative purposes.

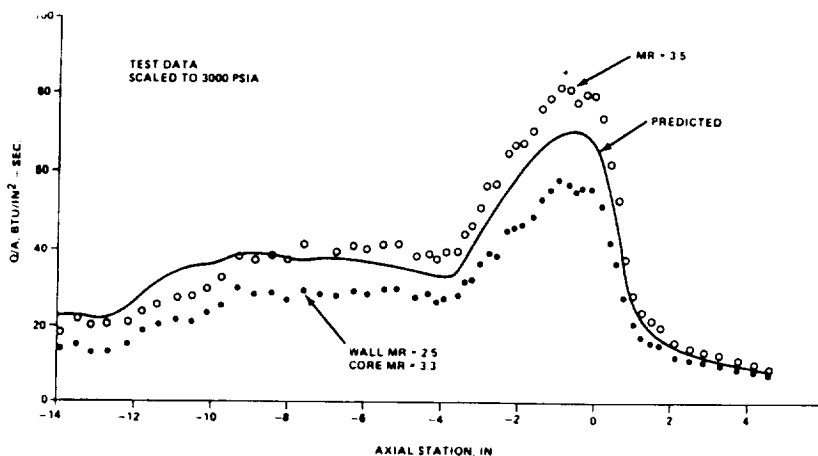


Figure 8. Heat Flux Profiles, LOX-Methane Staged Combustion

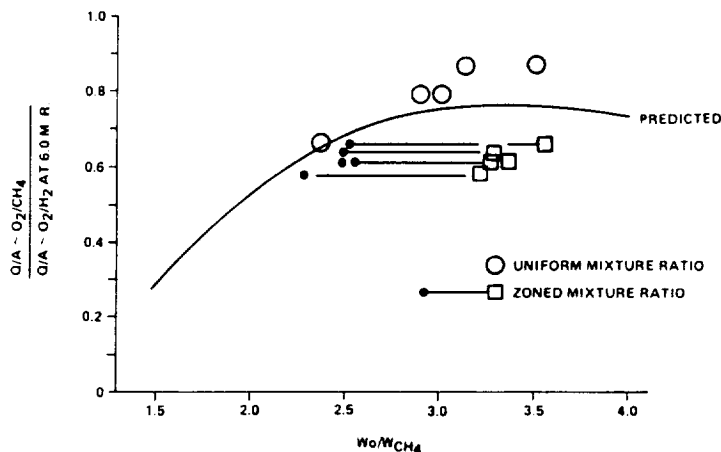


Figure 9. Nozzle Throat Heating Rates



Note in Figure 9 the agreement between prediction and UMR data at low mixture ratio, and the divergence between the two as mixture ratio increases. It was decided to bias the outer injector element ring fuel rich in an attempt to reduce heating rate, provided the expected reduction in specific impulse performance was not excessive. The results of this analysis are shown in Figure 10. For a 600,000 lb thrust engine having a nozzle area ratio of 42, specific impulse peaks at a mixture of 3.5. If all of the injector outer ring elements were biased to a mixture ratio of 2.5 and the overall mixture ratio remained at 3.5, the remainder of the injector elements would have to operate at a mixture ratio of approximately 3.7. Figure 10 shows graphically the effect of this modification on specific impulse assuming no mixing between the two stream tubes. Engine vacuum specific impulse would be reduced 3.8 seconds. This reduction in performance could be minimized by operating the core of the injector at the peak performance mixture ratio of 3.5 and allowing the overall mixture ratio to drop to approximately 3.3. For this condition, the compromise in performance is only about 2.0 sec. Performance losses within this range were considered to be tentatively acceptable, and the injector was modified to provide an outer zone mixture ratio of 2.5. The results of the zoned mixture ratio tests are shown in Figures 8 and 9. They indicate that outer zone mixture ratio biasing is effective in controlling heating rate.

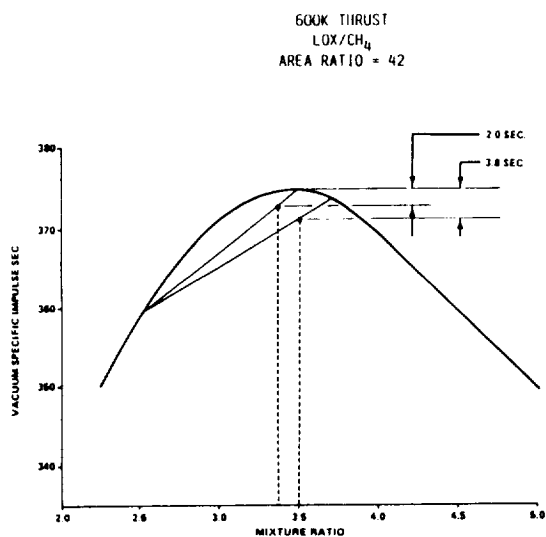


Figure 10. Performance Loss Using Zoned Combustion

Four tests were conducted using a single up-pass liquid methane cooled combustion chamber. The test objective was to operate at chamber pressures greater than the approximate 2200 psi limit of the calorimeter chamber. These tests were characterized by a sharp reduction in combustion efficiency as propellant flowrates were increased. The decrease in efficiency as a function of oxidizer flowrate is shown in Figure 11. During the final firing, localized wall overheating

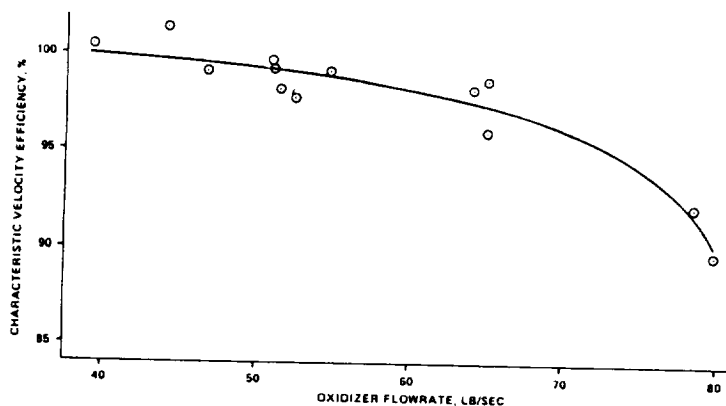


Figure 11. LOX-Methane Staged Combustion Main Injector Performance

occurred in the nozzle throat and testing was terminated. It was believed that the low combustion efficiencies were caused by the reduced fuel injection velocities associated with using methane instead of hydrogen, and that the resulting delays in oxygen vaporization and mixing disrupted the boundary layer and increased the throat heating rate.

Neither of the main combustion chambers was designed for use with pressure transducers capable of monitoring acoustic mode instability. However, the absence of pressure oscillations as measured by the pre-burner high frequency transducer is at least a qualitative indication that main chamber combustion was stable.

#### LOX-METHANE GAS GENERATOR CYCLE

##### Main Injector Performance

Two main injectors applicable to the gas generator cycle were obtained by the contracts listed in References 2 and 3. Test preparations to evaluate the Reference 3 injector are now underway. This report describes the test results of the Reference 2 injector which is pictured in Figure 12. The injector was designed and fabricated by Rocketdyne Division of Rockwell International. The design has 82 shear coaxial injector elements: this is a significantly finer pattern than was used in the staged combustion main injector. The igniter is a chlorine trifluoride/methane torch located in the center of the injector.

Eight test firings using this injector and the calorimeter combustion chamber were conducted over a chamber pressure range of 1200 to 2100 psia and a mixture ratio range of 2.5 to 3.6. The performance goal of 97 percent minimum C\* efficiency was exceeded in all tests, and the combustion chamber heat flux profiles were essentially as predicted. Characteristic velocity efficiency is shown in Figure 13 as a function of mixture ratio and in Figure 14 as a function of fuel injection velocity minus oxidizer injection velocity. Efficiency was not strongly affected by either of these variables. Nozzle throat heating rates

ORIGINAL DOCUMENT  
OF POOR QUALITY

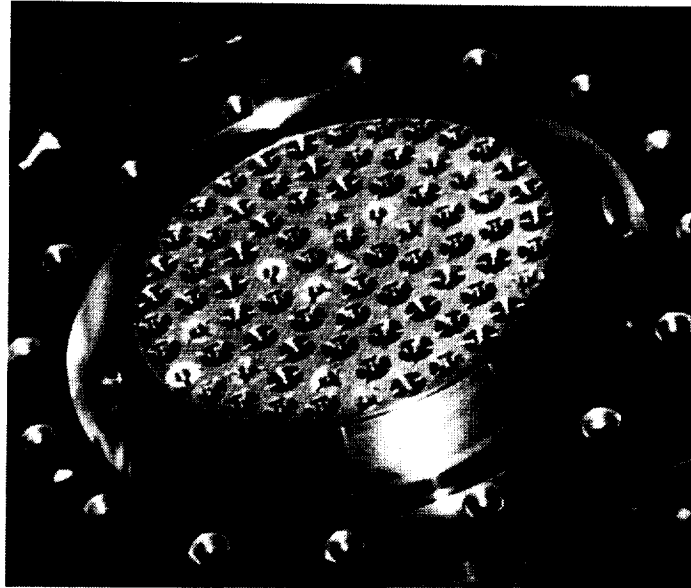


Figure 12. LOX-Methane Main Injector for Gas Generator Cycle

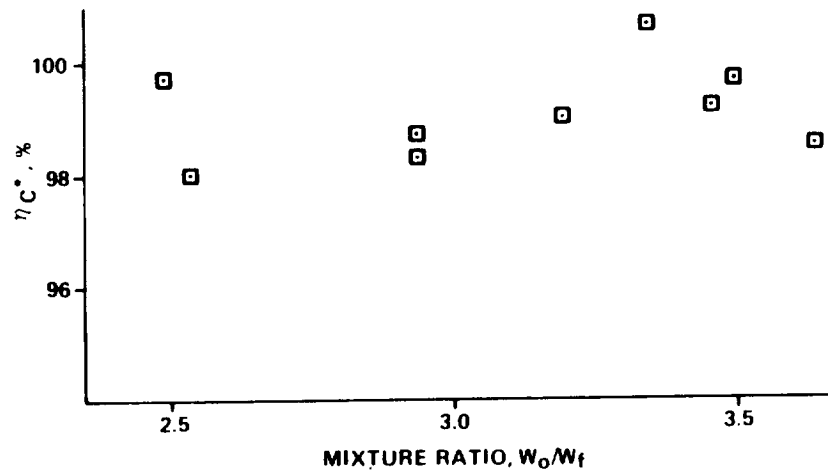


Figure 13. Main Injector Performance as a Function of Mixture Ratio

expressed as a fraction of the equivalent rate with oxygen-hydrogen is shown in Figure 15. Measured heating rates were slightly lower than predicted at all test conditions. There was no acoustic mode combustion instability during any of the tests, but oxidizer feed system oscillations were evident during some of the firings at lower chamber pressures. Pressure amplitudes ranged from 250 to 500 psi peak-to-peak. Relatively minor erosion at the outer edge of the faceplate occurred during several of these periods of instability.

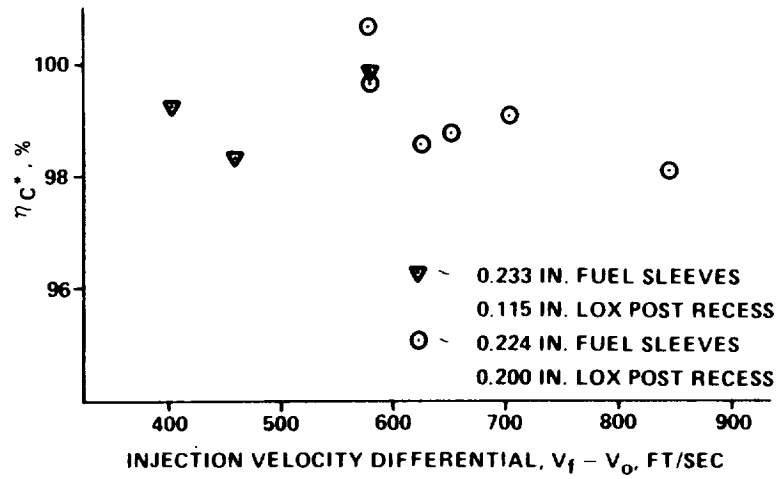


Figure 14. Main Injector Performance as a Function of Injection Velocity Differential

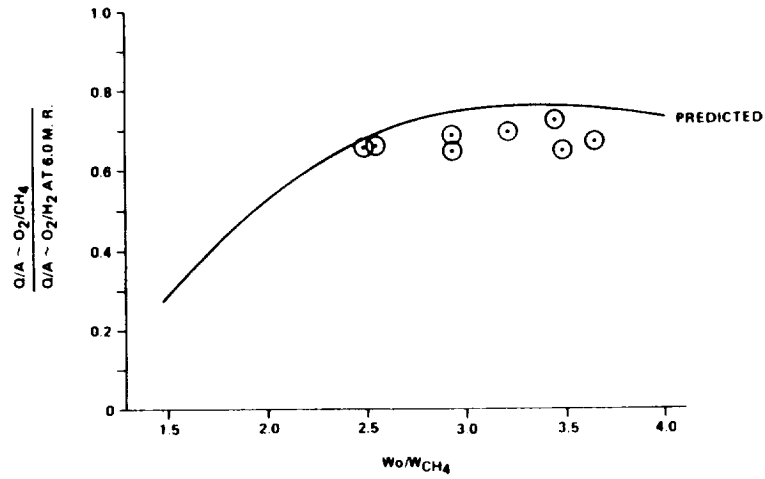


Figure 15. Throat Heating Rates Using Shear Coaxial Injector

One test was conducted using a liquid methane cooled combustion chamber at a chamber pressure of 2380 and a mixture ratio of 3.3. Significant chamber erosion occurred along a cooling passage which had a low cycle fatigue crack resulting from a previous test series. The cause of this damage is still being investigated.

## LOX/RP-1 GAS GENERATOR CYCLE

### Gas Generator Performance

The program objectives were to demonstrate C\* combustion efficiencies and gas temperature profiles adequate for engine operation at chamber pressures ranging from 2000 to 3000 psi with stable combustion. Specific program goals included gas temperature uniformity across the combustion chamber within  $\pm 50^\circ\text{F}$  and combustion pressure oscillations not to exceed  $\pm 5$  percent of chamber pressure.

Two gas generator injectors were evaluated in this task. The first injector, shown in Figure 16, has 39 fuel doublets and 37 oxidizer shower head elements and was designed and fabricated at Marshall Space Flight Center. A total of 28 tests were conducted using this injector. The first nine tests were igniter system demonstrations and attempts to use a low-flow bypass system for main propellant ignition. This system proved to be neither successful nor needed. Reliable ignition was achieved by ramping the main propellant valves open using a 40 millisecond fuel lead after igniter operation was verified. Neither pressure nor temperature spikes was a problem. A comparison of characteristic velocity and combustion temperature data to both theoretical one-dimensional equilibrium and nonequilibrium predictions is presented in Figures 17 and 18. The nonequilibrium method resulted from work

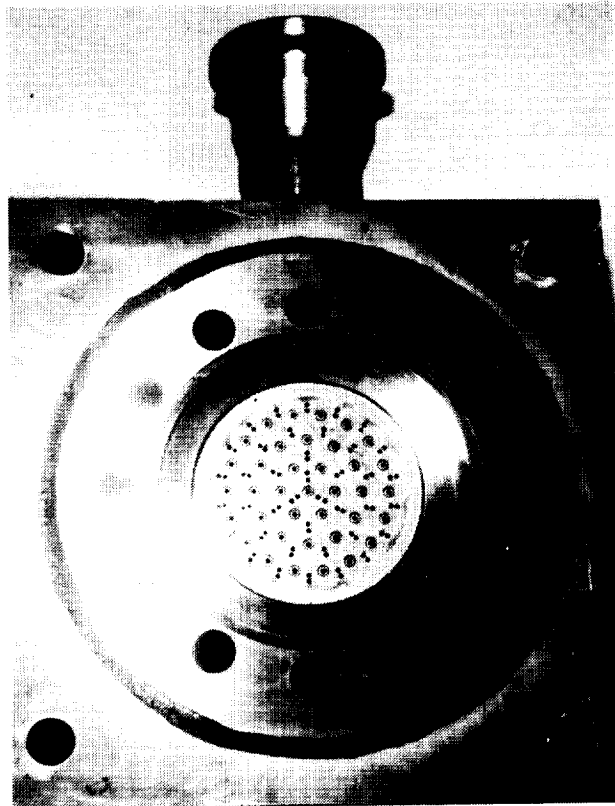


Figure 16. Fuel Doublet LOX/RP-1 Gas Generator Injector

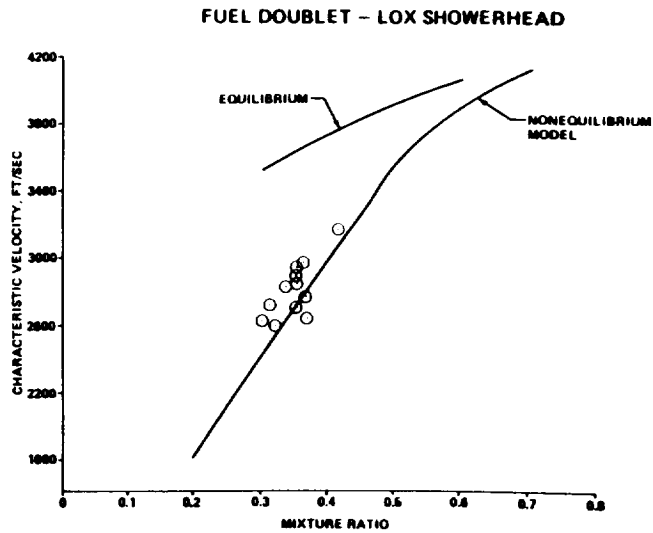


Figure 17. Characteristic Velocity Performance

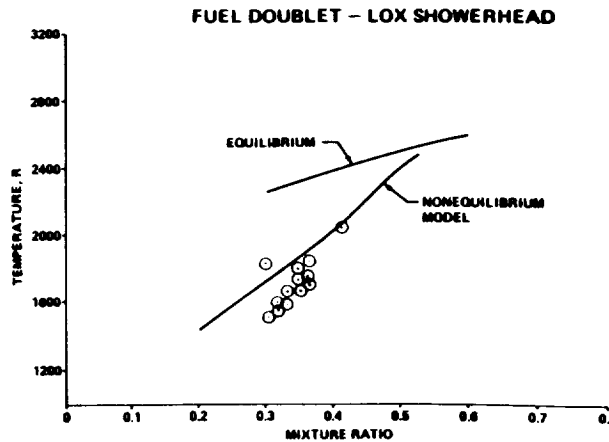


Figure 18. Combustion Gas Mean Temperature

reported in Reference 1. Gas temperature uniformity and combustion stability were both strong functions of fuel injection pressure drop. The gas temperature nonuniformity as measured by a six-thermocouple rake 10 in. downstream of the injector face is presented in Figure 19. The two design modifications noted on this figure represent plugged injection ports to increase differential pressure. Low frequency stability characteristics are shown in Figure 20, and indicate a chug threshold for the doublet injector at a fuel pressure drop to chamber pressure ratio of approximately 12 percent. The program goals from both gas temperature uniformity and combustion stability standpoints were achieved during the three final firings using the Mod. 2 injector. No attempt was made to measure carbon deposition on the chamber walls or nozzle. It was generally observed that the amount of carbon deposited did not vary with chamber pressure.

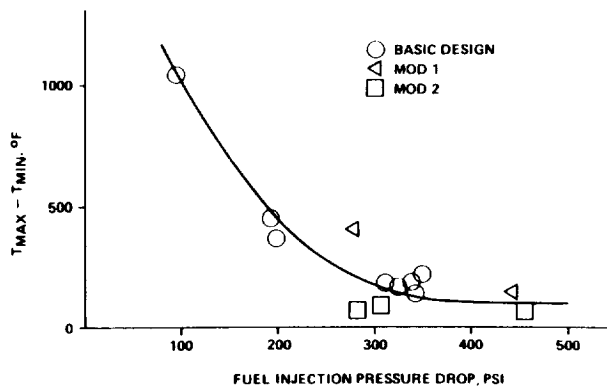


Figure 19. Doublet Injector Gas Temperature Nonuniformity

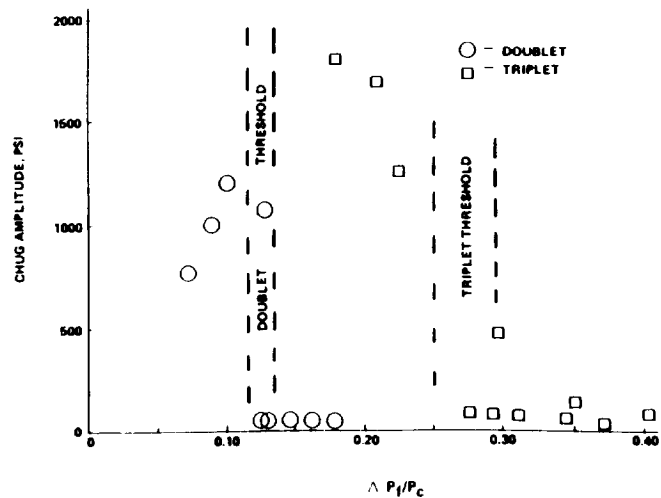


Figure 20. Low Frequency Stability Characteristics

The second injector design had triplet injection elements and was obtained through the Reference 1 contract. A photograph of the injector face is shown in Figure 21. A total of 66 F-O-F elements was used. Fuel port diameter was 0.0560 in. and oxidizer port diameter was 0.456 in. Ten mainstage data firings were conducted. This injector exhibited a strong tendency to generate chugging unless an abnormally high fuel injection pressure drop was maintained. Attempts were made to minimize the problem by adding resistance in the fuel feed system to decouple the resonance. First, an orifice was installed in the inlet flange to the fuel manifold to add approximately 200 psi pressure drop. The change had no effect on the instability. Next, the single orifice was removed and individual orifices were installed in each of the twelve radial fuel feed passages in the injector body. Again, the increase in pressure drop was approximately 200 psi. Any changes in chugging characteristics were insignificant, and it was concluded that the design

ORIGINAL DESIGN  
OF POOR QUALITY

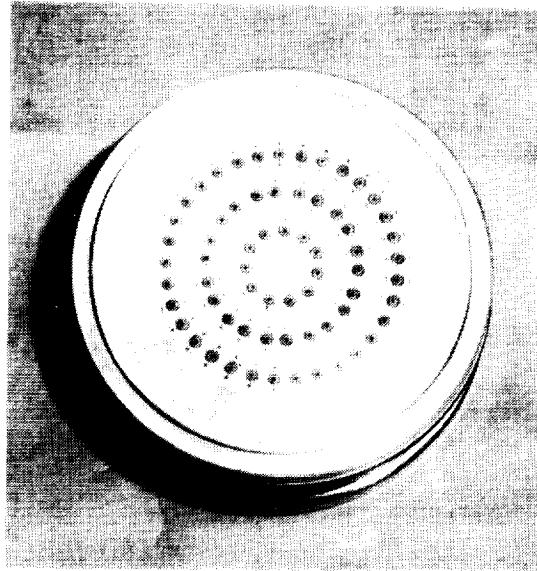


Figure 21. Triplet LOX/RP-1 Gas Generator Injector

is inherently deficient in this respect. The problem could possibly be minimized by an injector redesign to reduce fuel manifold volume, but it was not attempted in this program. Stability threshold for the injector is shown in Figure 20.

Characteristic velocity and combustion temperature data are compared to theoretical predictions in Figures 22 and 23. The data agreed reasonably well with the nonequilibrium model predictions, although the mean gas temperature shows more scatter at the higher mixture ratios than desired. This is probably due in part to a reduction in venturi

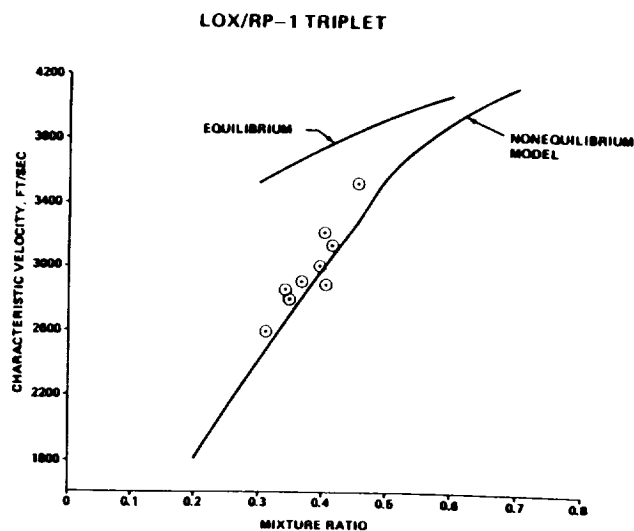


Figure 22. Comparison of Test Data to Theoretical Characteristic Velocity



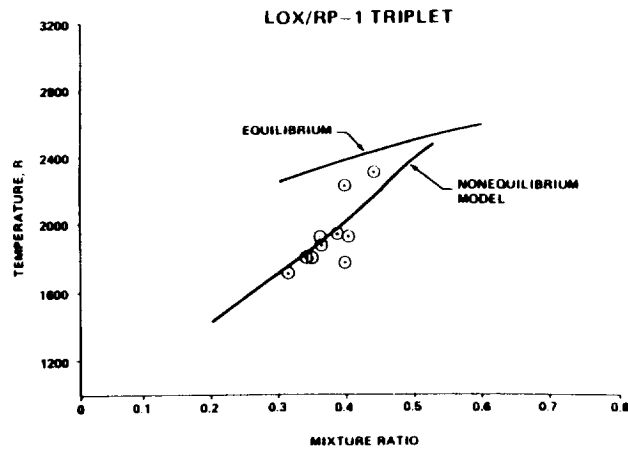


Figure 23. Comparison of Test Data to Theoretical Combustion Temperature

flow control and measurement accuracy during chugging. Seven of the ten tests satisfied the gas temperature uniformity goal of  $\pm 50^{\circ}\text{F}$  and three tests did not. In general, the gas temperature was more uniform at lower mixture ratios and was not affected by a 4-in. increase in chamber length. Carbon deposition to the chamber and nozzle was comparable to that previously observed with the doublet injector.

#### Main Injector Performance

The LOX/RP-1 main injector was obtained through the contract listed in Reference 4 and was designed and fabricated by the Aerojet Liquid Rocket Company. The design used preatomized triplet (PAT) elements which consisted of two fuel fans impinging on one liquid oxygen fan. This type of injector element had been tested previously (Reference 5) using lox and RP-1 at 2000 psia chamber pressure, and had produced stable combustion with moderately high efficiencies. However, a very serious deficiency discovered during the program was the generation of nozzle throat heating rates approximately 50 percent greater than predicted. The injector mixing efficiency was also discovered to be low (73 percent), and was attributed to reactive stream separation (RSS) whereby the effects of initial combustion force the propellant streams apart and reduce mixing. A major goal of the subject program was to experimentally determine the effects of injector design changes made to minimize the nozzle heating rate problem and to improve propellant mixing.

A sketch of the injector and resonator installation is shown in Figure 24, and a photograph of the injector and resonator are shown in Figure 25. The injector face was fabricated using a stack of thin, photo-etched nickel plates bonded and electron-beam welded to a stainless steel body. Eighty percent of the propellant flow is injected through 72 PAT elements. The remaining 20 percent of the flow is injected through unlike preatomized doublet elements which are supplied from

ORIGINAL PAGE IS  
OF POOR QUALITY

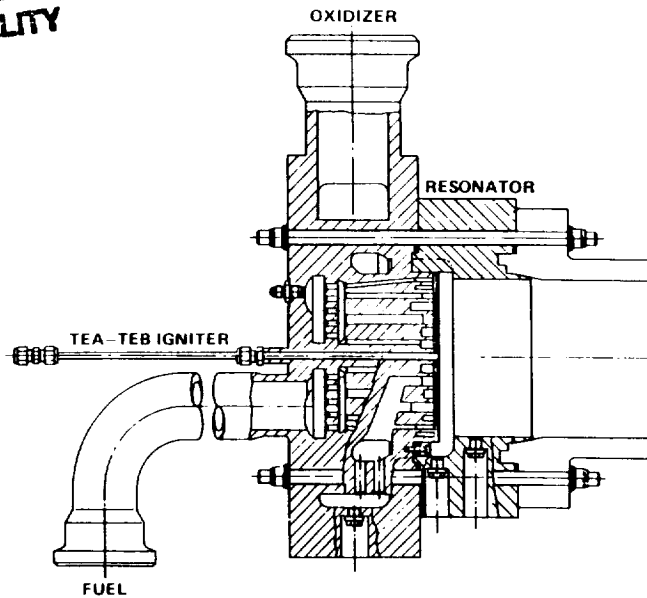


Figure 24. LOX/RP-1 Main Injector and Resonator Installation

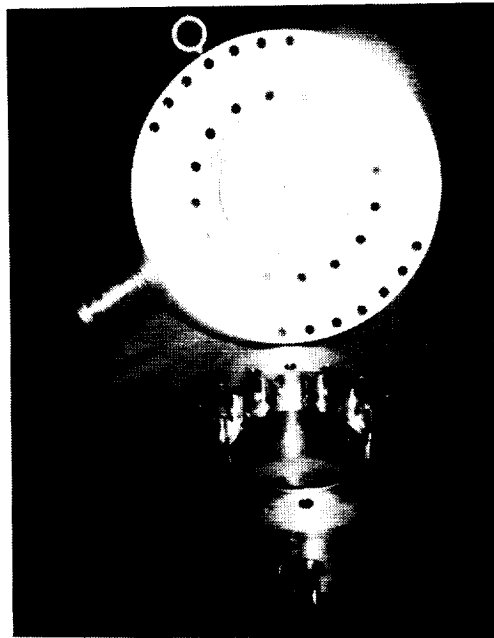


Figure 25. Injector and Resonator

the two outer propellant rings. The doublets were known to be low performance elements but were incorporated into the design to serve as compatibility elements and reduce nozzle heating rates. Since the percentage of total propellant flowrate to the compatibility elements would be significantly reduced in a large booster engine, the predicted one-half percent compromise in specific impulse efficiency was considered acceptable. Two PAT element design modifications were made

relative to the Reference 5 configurations. The fuel impingement angle was increased from 60 degrees to 90 degrees total included angle to improve intra-element mixing, and the element angle relative to the wall was changed to improve inter-element mixing.

Three firings which provided meaningful mainstage data were conducted using the PAT injector and calorimeter chamber. Chamber pressure ranged from 1726 to 2263 psia, and mixture ratios varied from 2.0 to 2.8. The test series was prematurely terminated when the uncooled resonator body overheated and failed. Test results are characterized by a sharp reduction in nozzle throat heating rates compared to those previously measured using this type of injection element. This was a primary program goal; however, the heating rate reductions were achieved at the expense of characteristic velocity efficiencies which were significantly lower than expected. Predicted  $C^*$  efficiencies were approximately 98 percent for the PAT core elements and approximately 95 percent for the doublet barrier elements. Had these element efficiencies been achieved, an overall efficiency of approximately 97 percent would have resulted. The actual overall efficiencies ranged from 91 percent to 94 percent. It was concluded that the performance of both the core and barrier elements was lower than predicted.

The chamber heating rate data shown in Figure 26 was obtained from Reference 5 and illustrates the extreme rates in the throat region which the subject program attempted to minimize. The same throat data are presented in Figure 27 as a function of mixture ratio. Note that the heating rates with the subject injector were greatly reduced from those previously obtained.

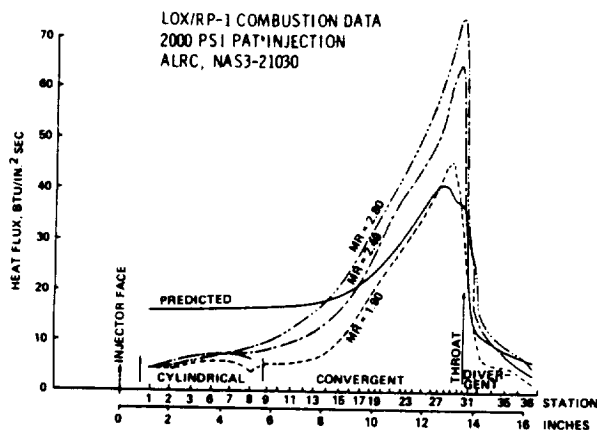


Figure 26. Chamber Heating Rates

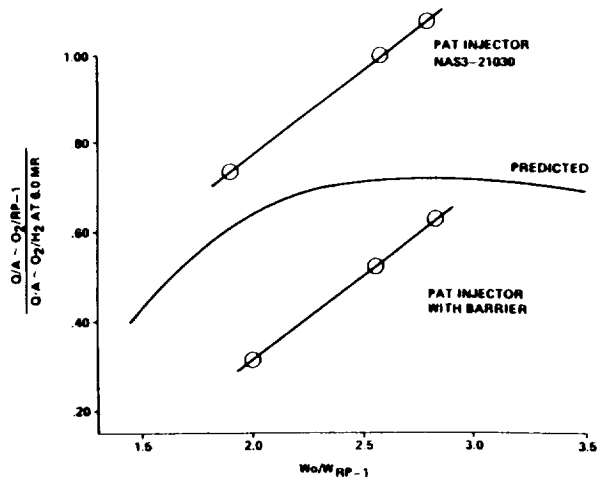


Figure 27. Nozzle Throat Heating Rates

## RESULTS AND CONCLUSIONS

### LOX-Methane Propellants

Preburner or gas generator performance data met or approximated program goals from the standpoints of gas temperature uniformity and combustion performance at chamber pressures to 3100 psia. Carbon accumulation was minor. Additional work will probably be required to minimize the high temperature excursions required for ignition.

A reduction in element size for shear coaxial main injector elements is required for LOX-methane as compared to LOX-hydrogen propellants. The smaller elements yielded characteristic velocity efficiencies ranging from 98 to 100 percent at chamber pressures to approximately 2400 psia. Theoretical combustion chamber heating rates were experimentally verified using the high performance injector. A lower performing injector generated throat heating rates approximately 18 percent higher than predicted. Biasing the outer ring of injection elements to a lower mixture ratio proved to be an effective method of reducing heating rates.

### LOX/RP-1 Propellants

Two gas generator injector designs were tested to chamber pressures of 3100 psia and both produced C\* efficiencies and mean gas temperatures as predicted by a nonequilibrium combustion model. Both injectors were marginally acceptable from the standpoint of gas temperature uniformity particularly at high mixture ratios. Low frequency stability was a problem with one of the injectors unless abnormally high injection pressure drops were used. The technology base for lox/RP-1 high pressure gas generators is considered adequate to support an engine development program. No problems surfaced during this effort which are

considered unique to high pressure operation or which would not be considered readily solvable during a normal development program.

The main injector testing did not achieve the program performance goal. Measured C\* efficiencies ranged from 91 to 94 percent as compared to a goal of 97 percent. Nozzle throat heating rate goals were achieved. The desired combination of stable, high efficiency combustion with moderate nozzle heating rates using high pressure lox/RP-1 main injection has not yet been demonstrated. Until this is accomplished, advanced vehicle planning using RP-1 as the fuel should limit efficiencies to levels demonstrated by developed engines.

## REFERENCES

1. Huebner, A. W., "High Pressure LOX/Hydrocarbon Preburners and Gas Generators," Final Report, Contract NAS8-33243, Rockwell International, Rocketdyne Div., April 1981.
2. Wheeler, D. B. and Kirby, F. M., "High Pressure LOX/CH<sub>4</sub> Injector Program," Final Report, Contract NAS8-33206, Report No. RI/RD79-278, Rockwell International, Rocketdyne Div., Sept. 1979.
3. Valler, H. W., "Design, Fabrication and Delivery of a High Pressure LOX-Methane Injector," Final Report, Contract NAS8-33205, Report 33205F, Aerojet Liquid Rocket Company, November, 1979.
4. Schoenman, L., Gross, R. S., "Design, Fabrication, Test and Delivery of a High-Pressure Oxygen/RP-1 Injector," Final Report, Contract NAS8-33651, Report 33651F, Aerojet Liquid Rocket Company, September 1981.
5. LaBotz, R. J., Rousar, D. C., Valler, H. W., "High Density Fuel Combustion and Cooling Investigation," Final Report, Contract NAS3-21030, NASA CR-165177, Aerojet Liquid Rocket Company, September 1980.



XII COMBUSTION AND COOLING PROCESSES II

A handwritten mark or signature consisting of a horizontal line with a vertical line intersecting it from below, and a diagonal line extending upwards and to the right.

## RESULTS OF COAXIAL INJECTOR ELEMENT TESTING

S. C. Fisher

Rockwell International/Rocketdyne Division  
Canoga Park, California

## ABSTRACT

The Turbine Drive Combustor Ignition and Durability Technology Program (NAS8-34928) was created to develop new technology that can be utilized to support the design and/or modification of reliable and durable future generation high performance oxygen/hydrogen rocket engine turbine drive combustors. The general objective was broken down into the two specific tasks of developing a new analytical code for liquid rocket engine combustion systems and gathering part of the data required to anchor/verify this code and future codes. Hot fire tests were conducted to gain insight into the low mixture ratio ignition and combustion characteristics of coaxial elements as well as to collect data to support the code work. This paper discusses a portion of the recent hot fire testing conducted on this program.

After conducting over 115 low pressure oxygen/hydrogen ignition tests, it became obvious that the flame-holding characteristics of coaxial injector elements operating with gaseous propellants play a very important role in the ignition and combustion processes of these types of injectors. As a result, a new hot fire test series to study the flame-holding characteristics of coaxial elements was structured and conducted. A total of 51 low pressure (100 to 200 psia) hot fire tests were run on a single Space Shuttle Main Engine oxidizer preburner element injector. The results of these tests are the main topic of this paper.

Two high speed optical diagnostic systems were utilized to observe and gather data on the processes within the actual combustion zone of an experimental hot fire test chamber fitted with large fused-silica windows. A high speed (up to 11,000 frames per second) laser Schlieren cinematography system was utilized to observe the fluid motions, flame propagation, and varying temperature zones during the ignition and "steady-state" combustion. In addition, a high speed ultraviolet (up to 4000 frames/sec) cinematography system was employed to locate and observe the zones in which the combustion reactions were actually occurring.



By combining the results from the two diagnostic visualization techniques, it was possible to observe the motion of the fluids, flame propagation, and combustion zones. These observations have lead to new information on the ignition, flame propagation, flame holding, and sustained combustion characteristics and mechanisms of the coaxial injector elements with gaseous oxygen and hydrogen propellants. These new insights are presented and discussed.

### Introduction and Background

The present start requirements of the Space Shuttle Main Engine (SSME) dictate that the preburners, utilized to power the high pressure turbopumps, ignite at overall mixture ratios as low as 0.3 (oxidizer/fuel), which is substantially below the well mixed flammability limit for the oxygen/hydrogen propellant combination (Fig. 1). The preburner coaxial elements have regularly accomplished ignition under these conditions, however, repeatability is sensitive to small engine flow control variations and some delayed ignitions have occurred. The physical mechanisms that allow ignition and sustained combustion of the propellant flows from a coaxial element ignition at very low mixture ratios, and subsequently contribute to this sensitivity, were not well understood.

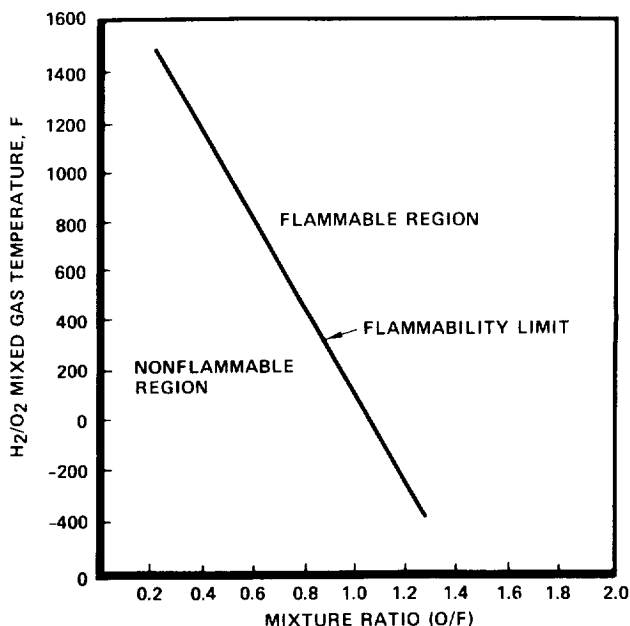


Fig. 1. Flammability Limits for Mixed Oxygen/Hydrogen

Technology advancements are required, which will increase the understanding of the physical mechanisms that influence low mixture

ratio coaxial element operation, leading to analysis and design techniques that will improve the ignition characteristics of turbine drive combustors for current and future liquid rocket engine systems.

The Turbine Drive Combustor Ignition and Durability Technology Program includes a combination of computer modeling analysis and hot fire testing that will lead to a better understanding of the physical mechanisms affecting turbine drive combustor ignition. This paper discusses a portion of the hot fire testing performed to study the ignition and flame-holding characteristics of coaxial elements and the laser Schlieren and ultraviolet diagnostic setup utilized to gather the visualization data, which has led to some new insights on the operation of these elements. The low pressure testing was conducted at Rockwell International's Thermodynamics Laboratory at the North American Aircraft Operations Division. All of the testing utilized a 4-inch diameter solid wall combustor with 4-inch diameter fused-silica windows on opposite sides of the combustion chamber. The ignition and combustion process was viewed through the windows and recorded on high speed motion picture film utilizing both a laser Schlieren and an ultraviolet camera system.

A total of 51 ambient oxygen/ambient hydrogen low pressure ignition/flame-holding hot fire tests were conducted. All of the tests were conducted with a single SSME Oxidizer Preburner (OPB) coaxial element injector. The targeted chamber pressure for all of the tests was 100 psia, the mixture ratio was targeted between 0.3 and 1.5 (oxidizer/fuel), and the total flowrate was targeted for either 0.01 or 0.02 lb/sec.

#### Hardware Description

The combustor assembly used for the test series is shown in Fig. 2 and 3. An injector utilizing a single SSME OPB element injector was used for all of the flame-holding tests. The coaxial design of the SSME OPB element is shown in the cutaway view of Fig. 4. During main-stage operation on the SSME, high velocity hydrogen gas flows through the fuel annulus surrounding the liquid oxygen (LOX) post. The LOX flowing through this center tube is then atomized by the stripping action of the high velocity fuel shroud. The coaxial element design has proven to be one of the most successful injector element configurations for LOX/hydrogen combustors. However, during the initial phase of the start sequence on the SSME, gaseous oxygen flows through the LOX post. It is this gas/gas ignition phase that the flame-holding test series is based on.

The solid-wall, uncooled combustion chamber has two unique fused-silica window assemblies through which the combustion process can be viewed optically. Two instrumentation ports are located 90 degrees to both of the windows. These ports were used for special instrumentation

ORIGINAL PAGE IS  
OF POOR QUALITY

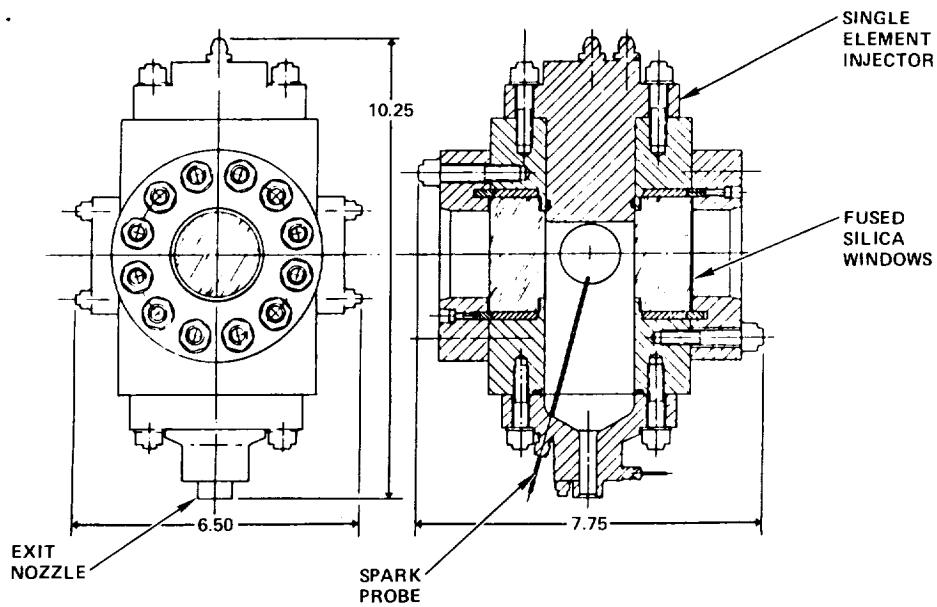


Fig. 2. Turbine Drive Combustor Technology Test Chamber

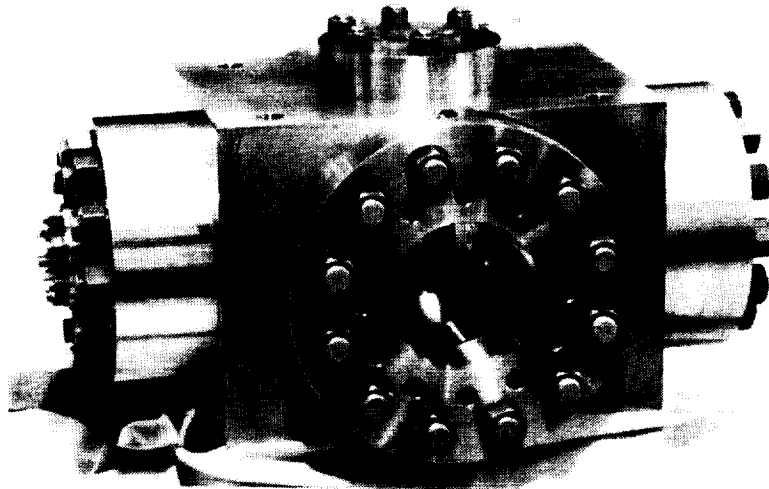


Fig. 3. Combustion Chamber Assembly

requirements. Separate fittings were designed to accept pressure transducers, ignition probes, thermocouples, and thermocouple rake assemblies.

The chamber pressure was controlled by the back-pressure nozzle diameter. The nozzle is a nickel insert, which is sealed to the exit housing by serrations machined into the housing and exit flange. Several nozzles of different diameters were fabricated for the various targeted mixture ratios and flowrates. All of the inlet flows were controlled externally by the facility, utilizing calibrated critical venturis and regulated upstream pressures.

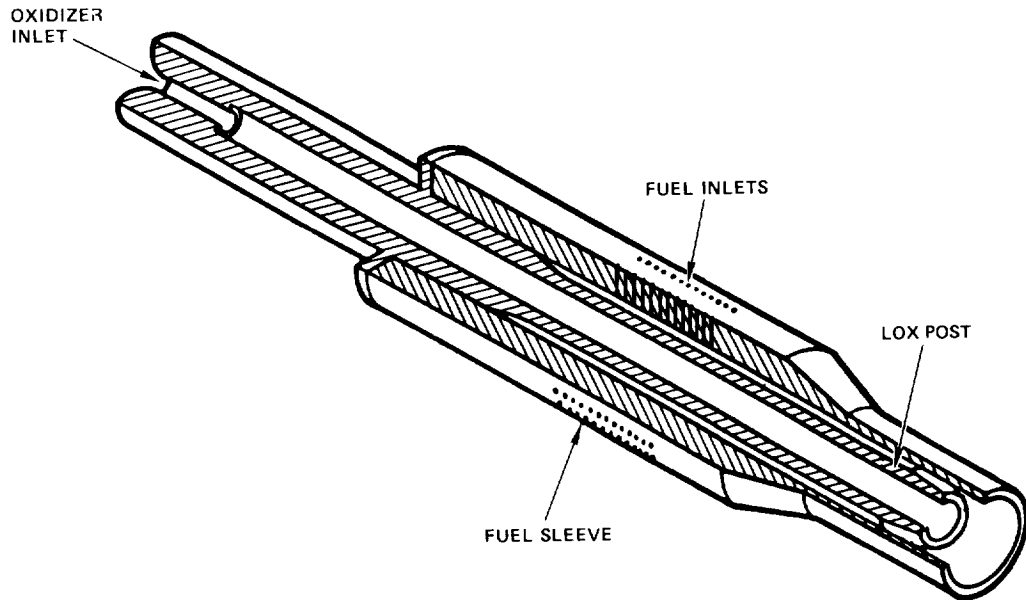


Fig. 4. SSME Preburner Injector Element

All of the combustor assembly details were designed to permit the test configuration to be easily changed. The facility mounting holes in the chamber body allow any detail to be removed and replaced without removing the assembly from the test stand.

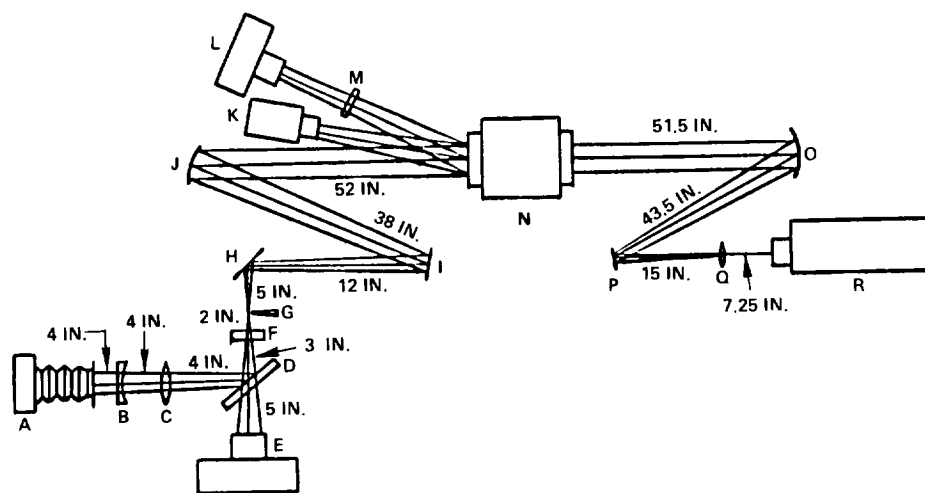
#### Diagnostic System Description

The high speed cinematography diagnostic system is shown in Fig. 5. The diagnostic system was made up of 4 separate subsystems:

1. High Speed Ultraviolet Cinematography System
2. High Speed Laser Schlieren Cinematography System
3. Polaroid Laser Schlieren System
4. Vidicon TV Monitor System

#### Speed Ultraviolet Cinematography System

The high speed ultraviolet cinematography system was used to view the OH specie concentrations in the combusting flow. The ability to view only the OH concentration is very useful in studying the oxygen/hydrogen combustion process. The OH radical is very short lived, kinetic (at the test conditions), and exists mainly as a part of the overall chain of kinetic reactions in the combustion process. Therefore, the OH concentrations are a direct indicator of the locations where the actual combustion reactions are taking place. At the low mixture ratios (temperatures) typically run, OH concentrations are insignificant in the equilibrium combustion products.



- |                           |                                |                                  |
|---------------------------|--------------------------------|----------------------------------|
| A) 4 x 5 WITNESS CAMERA   | H) FLAT TURNING MIRROR         | N) COMBUSTION CHAMBER            |
| B) IMAGING LENS           | I) FLAT TURNING MIRROR         | FUSED-SILICA WINDOWS             |
| C) IMAGING LENS           | J) 60-IN. FL. SPHERICAL MIRROR | O) 60-IN. FL. SPHERICAL MIRROR   |
| D) VARIABLE BEAMSSPLITTER | K) TV MONITOR                  | P) FLAT TURNING MIRROR           |
| E) HYCAM CAMERA           | L) FASTAX CAMERA QUARTZ        | Q) 10 x MICROSCOPE OBJECTIVE AND |
| F) SCHLIEREN FILTER       | LENS AND SAPPHIRE PRISM        | 25-MICRON PINHOLE ASSEMBLY       |
| G) SCHLIEREN OBSTRUCTION  | M) FASTAX FILTER               | R) ARGON ION LASER               |

Fig. 5. Diagnostic System Setup

In a typical oxygen/hydrogen combustion process, the reactions are in part characterized by various species that emit radiation between 0.2 and 1.2 micron wavelengths. As can be seen in Fig. 6, OH is a predominate contributor to the radiation emitted from the combustion process.

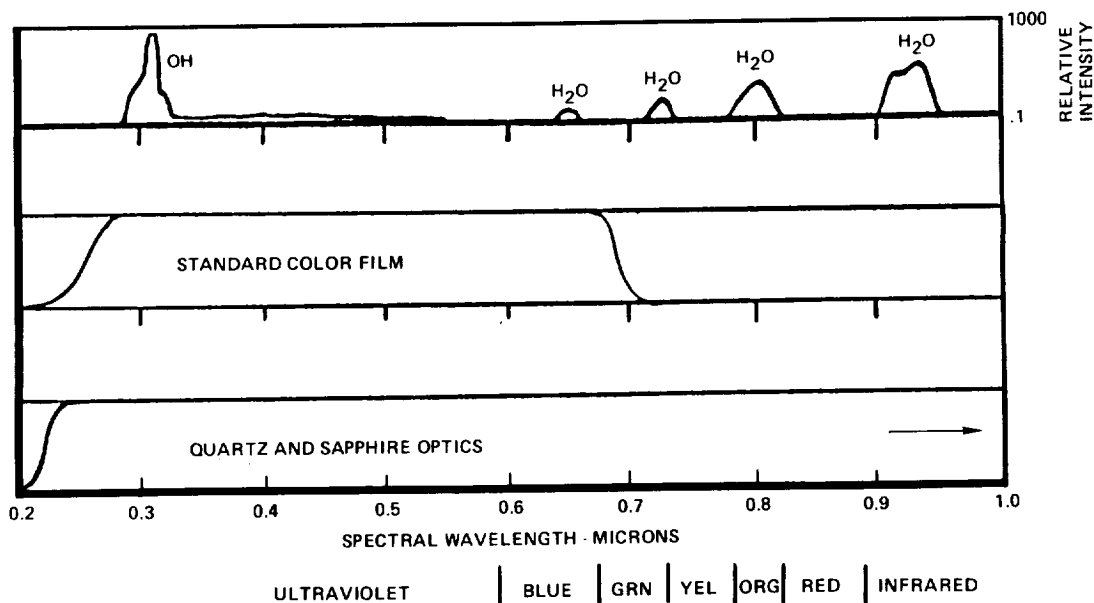


Fig. 6. Typical Spectral Transmission Response, and Optical Spectrum for Oxygen/Hydrogen Combustion System

The OH species emits at a wavelength of approximately 0.31 micron, which is in the ultraviolet range and can be detected with standard color film. However, standard "glass" type optics typically will not transmit below a wavelength of 0.38 to 0.4 micron. Because of this, all of the optical components in the ultraviolet diagnostic system were either quartz, fused silica, or sapphire.

On some of the previous ignition tests conducted on the same program, a special ultraviolet filter (0.25 to 0.35 micron) was used. On later tests, because of exposure problems and the fact that the filter only transmitted 60 to 70% of the light in its narrow band, the filter was not used. Since the OH intensity is much higher than the H<sub>2</sub>O intensities (Fig. 5), the high framing rates effectively filtered all but the OH radiation. This was verified by comparing films of identical conditions with and without the filter. Because of the previous success with the filter removed, it was not used during most of the tests in this series.

A Milikan camera fitted with a special quartz lens was used to record the ultraviolet data. Very good results were obtained even on the lower mixture ratio tests with 400 ASA film and a camera speed of approximately 400 frames per second.

#### High Speed Laser Schlieren Cinematography System

The high speed laser Schlieren cinematography system has proven to be a very useful diagnostic for studying the oxygen/hydrogen combustion process. Run at very high framing rates (9,000 to 11,000 frames/sec), the system was able to record flow patterns, spark heated gas "puffs," spark ignition, propagation of the ignition process, flame-outs, and steady-state combustion/flow patterns.

The Schlieren system utilized a 0.5-watt argon-ion laser, standard Schlieren/laser optics, and a Hycam camera with 400 ASA film. Figures 7 and 8 show the actual diagnostic setup. The use of a laser light source for the Schlieren work was advantageous for two reasons. First, the intensity of the laser made it possible to record Schlieren data at high framing rates on standard film. Second, it was possible to filter out the illumination created by the combustion process and view only the narrow band wavelengths of the laser/Schlieren system flow field data. An additional side benefit was that the laser system was easier to work with optically.

Most of the tests were conducted with a camera speed of 9,000 frames/sec and gave very good results. A few tests were conducted with framing rates of 11,000 frames per second, but camera problems precluded running at these rates on a regular basis. However, it would be possible to record at much higher framing rates with the proper camera equipment.

ORIGINAL PAGE IS  
OF POOR QUALITY

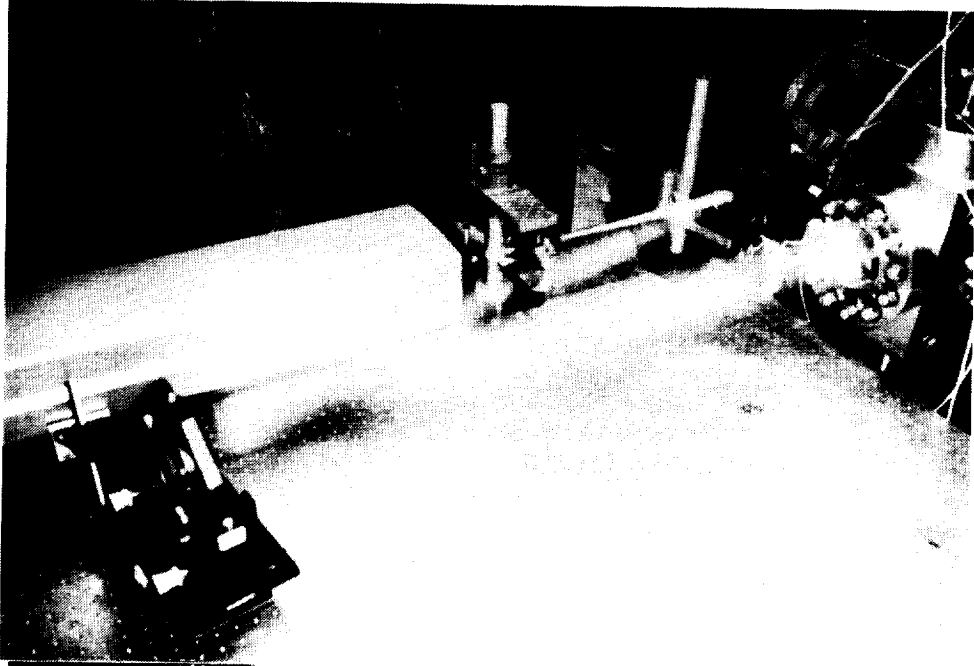


Fig. 7. Laser Schlieren Source Setup

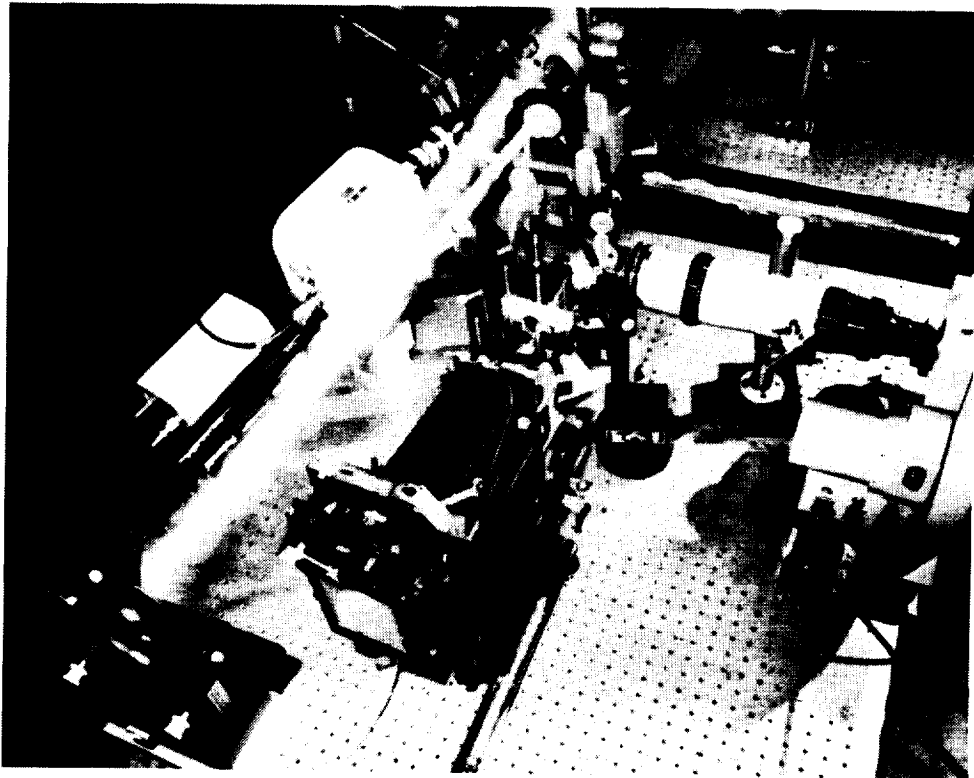


Fig. 8. Laser Schlieren Recording System

### Polaroid Laser Schlieren System

To determine and correct setup or test problems without waiting for processed film from the Hycam camera to be returned and viewed, a parallel Polaroid camera system was used to witness the Schlieren tests. The Polaroid system was set up such that the exposure requirements were similar to those for the Hycam system. Following a test, the Polaroid film was reviewed to determine if the test should be rerun with different adjustments.

### Vidicon Monitor System

A real-time TV monitor and recording system was set up to remotely monitor the hot fire tests from the control room. No direct view of the test cell was available from the control room. The monitor was observed for real-time discrepancies during the tests. The tape was played back and studied following test stand securing. The monitor was very useful in discovering spark probe problems just prior to test, during tests, and post test, and for detection of ignitions and flameouts.

### Description of the Flame-Holding Tests Conducted

The basic objective of the flame-holding test series was to gather high speed laser Schlieren and ultraviolet data on the flame-holding mechanism of coaxial elements operating with gaseous propellants. The testing was directed at gaining a better understanding of the flame-holding phenomena observed during the previous ignition test series. A total of 51 ambient oxygen/hydrogen low pressure ( $P_c$  approximately 100 psia) tests were conducted on the single SSME element coaxial injector. Both fuel lead (Fig. 9) and oxidizer lead (Fig. 10) sequences were run. A summary of the flame-holding test series is presented in Table 1.

For these tests, the optics were adjusted to "zoom" in on the flame-holding area near the tip of the LOX post in an effort to visualize the flame-holding phenomena. The view of the diagnostic systems is shown in Fig. 11.

All of the tests utilized the "point" ignition probe developed earlier in the program during ignition test series. The 1/8-inch diameter probe was located 0.385 inch from the injector face and 0.25 inch from the chamber centerline (Fig. 11).

The first series of flame-holding tests were targeted for conditions that had repeatedly produced ignitions during the previous testing. All of the tests had total flowrates targeted for either 0.01 or 0.02 lb/sec and a chamber pressure of 100 psia. Laser Schlieren and ultraviolet film data was collected to determine the actual location of the flame holding mechanism.



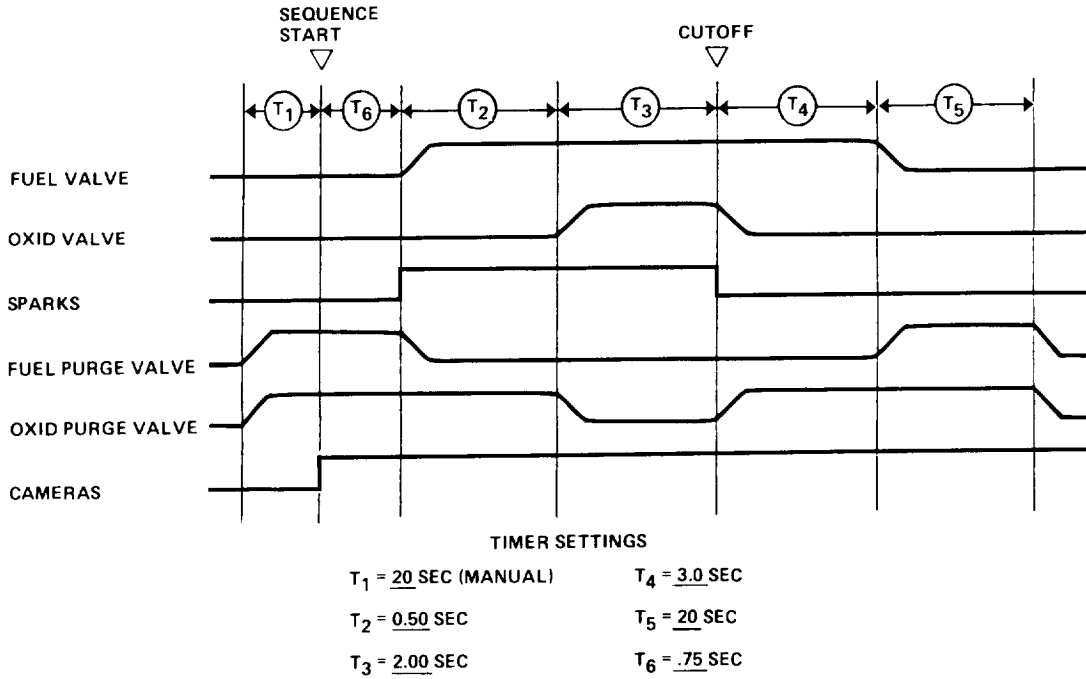


Fig. 9. Fuel Lead Sequence

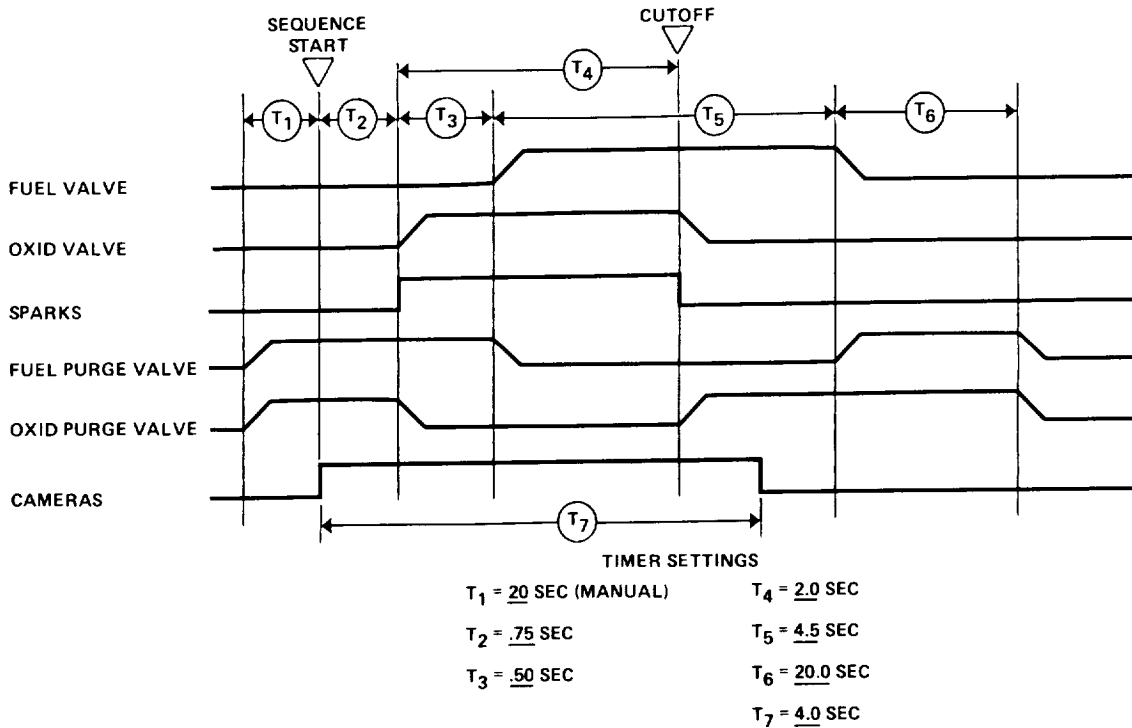


Fig. 10. Oxidizer Lead Sequence

Table 1. Summary of Flame-Holding Tests

Test No.	Target Conditions		Sequence	Objectives	Number of Tests
	MR (o/f)	W, lb/sec			
2.1-2.4	0.5	0.02	OX LD	Checkout tests	4
3.1-3.2	0.5	0.02	OX LD	Checkout Tests	2
4.1-4.3	0.3	0.02	OX LD	Flame-holding data	3
4.4	1.5	0.02	FL LD	Flame-holding data	1
5.1-5.2	1.5	0.02	FL LD	Flame-holding data	2
6.1	1.5	0.02	FL LD	Flame-holding data	1
6.2	1.3	0.02	FL LD	Flame-holding data	1
6.3	1.5	0.02	FL LD	flame holding data	1
7.1	1.5	0.02	FL LD	Flame-holding data	1
8.1-8.2	1.5	0.01	FL LD	Flame-holding data	2
8.3-8.4	1.3	0.01	FL LD	Flame-holding data	2
9.1	1.3	0.01	FL LD	Flame-holding data	1
10.1-10.5	0.5	0.01	OX LD	Flame-holding data	5
11.1-11.3	0.5	0.01	OX LD, Reduce MR	Flame-holding data	3
12.1	0.5	0.01	OX LD	Flame-holding data	1
12.2	0.4	0.01	OX LD	Flame-holding data	1
12.2-12.3	0.5	0.01	OX LD, Reduce MR	Flame-holding data	2
13.1	0.5	0.01	FL LD	Flame-holding data	1
14.1-14.2	1.5	0.02	FL LD	Flame-holding data	2
15.1-15.3	0.5	0.02	OX LD, Reduce MR	Flame-holding data	3
16.1	0.5	0.02	OX LD	Flame-holding data	1
17.1-17.3	0.5	0.02	OX LD	Flame-holding data	3
17.4-17.5	0.3	0.2	OX LD	Flame-holding data	2
18.1-18.2	0.5	0.2	OX LD	LOX Post Extension	2
18.3	0.3	0.018	OX LD	LOX Post Extension	1
18.4	0.5	0.02	OX LD	LOX Post Extension	1
18.5	0.3	0.02	OX LD	LOX Post Extension	1
18.6	0.64	0.17	OX LD, Reduce MR	LOX Post Extension	1

NOTE: OX LD = Oxidizer Lead  
FL LD = Fuel Lead

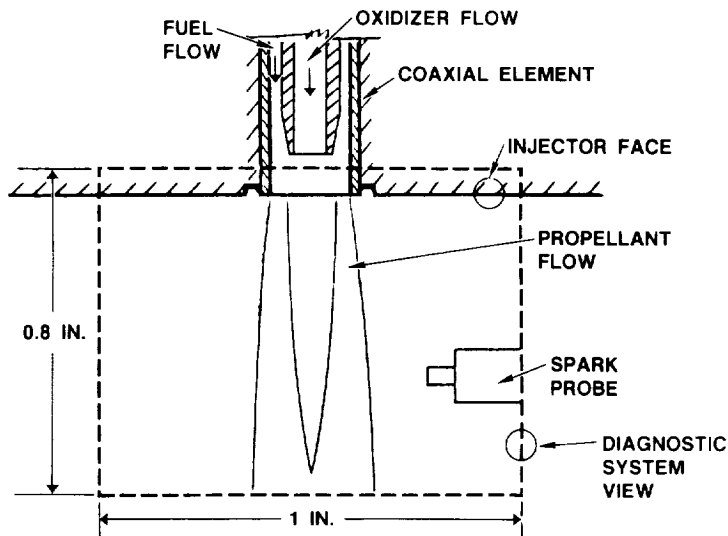


Fig. 11. View of Diagnostic System

ORIGINAL PAGE IS  
OF POOR QUALITY

Next, in an effort to determine the sensitivity of the flame-holding mechanism to reduced mixture ratios, a series of mixture ratio reduction tests was run. In these tests, following ignition at an ignitable mixture ratio, the mixture ratio was reduced by bypassing a portion of the oxygen flow away from the injector with a bleed valve. The mixture ratio was effectively ramped down from the start of the test through cutoff.

On all of the tests, the flame zone appeared to extend up inside the coaxial element recess. The standard SSME preburner element has a recessed tip, which is hidden from the view of the diagnostic system by the injector face (Fig. 11). As a result, the actual start of the flame zone and the flame-holding mechanism was not visible to the diagnostic systems. Because of this, the last six tests conducted utilized a special LOX post tip extension that was bonded to the tip of the SSME element, shown in Fig. 12. By adding the special tip extension, which extended the end of the LOX post approximately 0.040 inch beyond the injector face, the relation of the flame-holding zone and the LOX post could be directly viewed with the diagnostic systems.

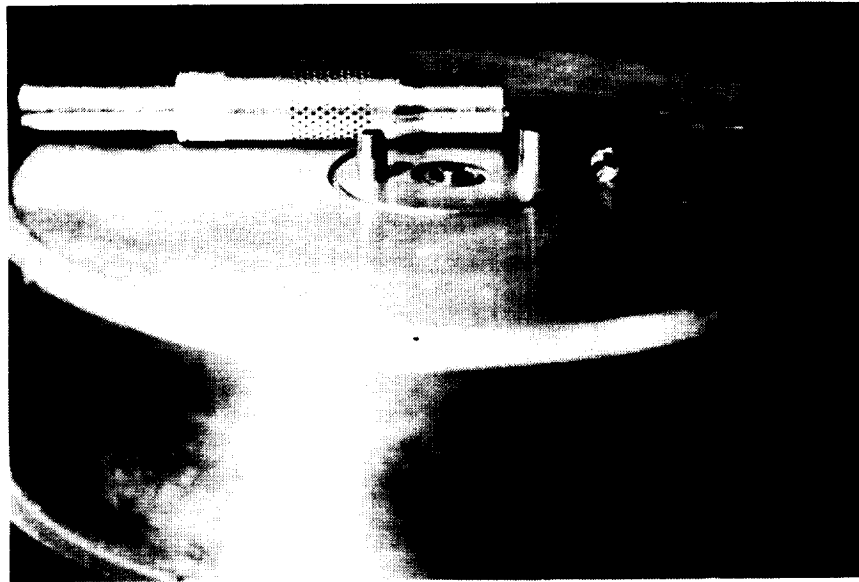


Fig. 12. LOX Post Tip Extension

Results and Conclusions

The data from the high speed laser Schlieren and ultraviolet diagnostic systems has lead to a much better understanding of the ignition and steady-state combustion process of gas/gas coaxial injector elements operating at low mixture ratios.

### Flame-Holding Mechanism of Gas/Gas Coaxial Elements

During the earlier ignition tests, the combustion zone was observed to extend up to the face of the injector. Because of the graininess of the 400 ASA film, the faint intensity and the small diameter of the combustion zone, it was impossible to determine much detail about the flame-holding mechanism. The actual flame-holding mechanism was not known but was hypothesized to be either the recirculation zone at the outer edge of the fuel sleeve and the injector face or the recirculation zone at the tip of the LOX post.

The flame-holding tests which "zoomed" in on the area near the end of the coaxial element shed some additional light on the flame-holding zone but did not answer all of the questions. Figure 13 is a typical frame of the ultraviolet film showing the combustion zone extending up into the cup recess area. It was clear that the flame-holding mechanism was somewhere up inside the recessed cup and that the combustion zone was the diameter of the LOX post.

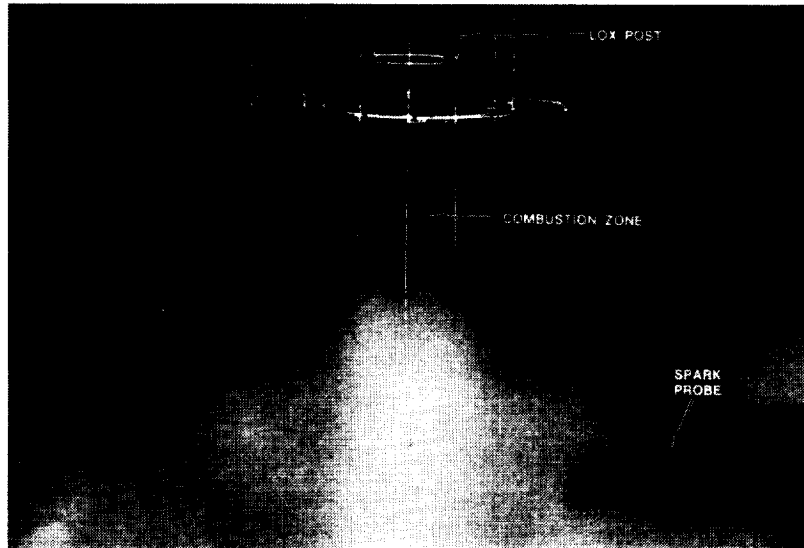


Fig. 13. Combustion Zone in Cup Recess

On some of the tests, a reddish glow was observed and appeared to be coming from a zone up inside the cup as shown in Fig. 14. It was theorized that this glow might be coming from the LOX post tip, which might be heated by the combustion process. As a result, the injector was removed from the test stand and carefully inspected. As suspected, the LOX post tip was discolored and showed signs of over heating. This seemed to support the theory that the wake or recirculation created at the tip of the LOX post was providing the flame-holding mechanism.

ORIGINAL PAGE IS  
OF POOR QUALITY

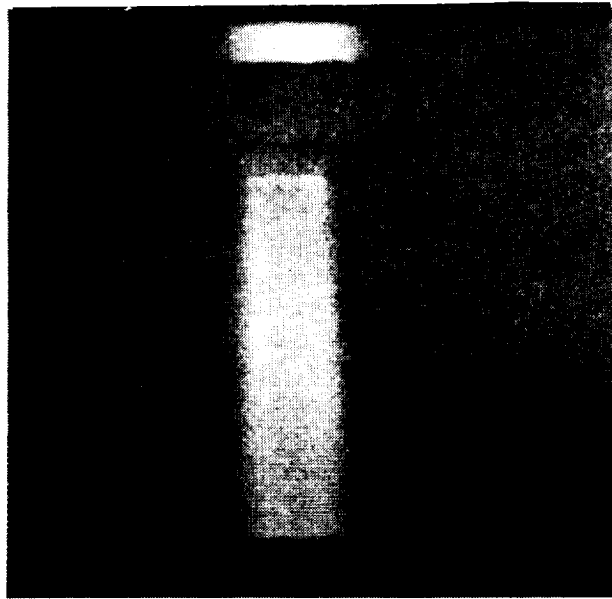


Fig. 14. Glow in Cup Region

Finally, the extended LOX post tip tests provided additional evidence that the flame-holding mechanism was actually the recirculation zone at the tip LOX post. Figure 15 clearly shows the combustion zone "hanging" from the tip of the LOX post. However, the overheating or reddish glow observed on the recessed tip test was not present in any of the six extended tip tests.

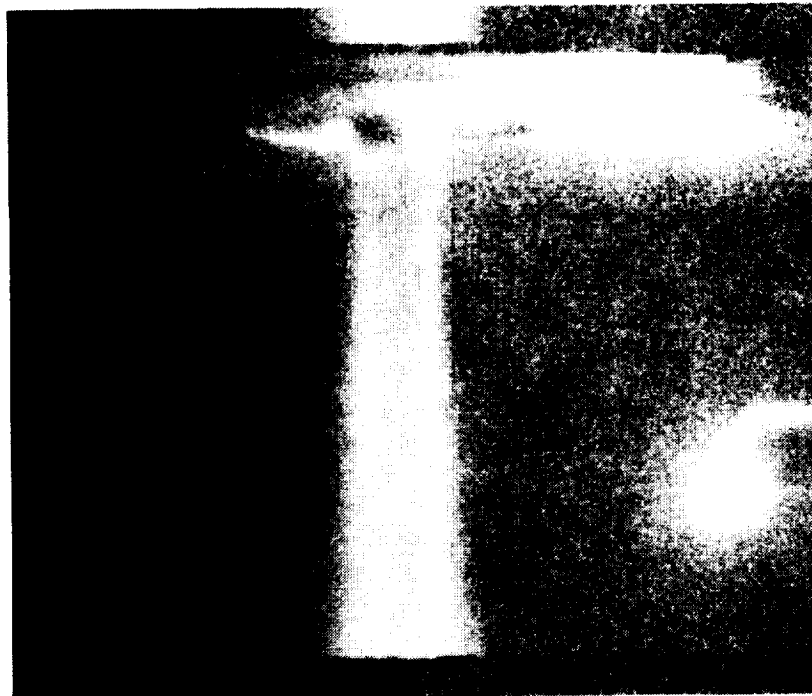


Fig. 15. Combustion Zone with Extended LOX Post

After reviewing the data from over 200 gas/gas low pressure tests (from previous ignition tests, the flame-holding tests, and more recent testing) it appears that once the flame-holding zone at the end of the LOX post tip is ignited, it will remain ignited and the combustion process will sustain itself even at extremely low mixture ratios. On the tests during which the mixture ratio was reduced, the combustion process was sustained at mixture ratios less than 0.01 (oxidizer/fuel) which is an order of magnitude less than the well mixed flammability limit (see Fig. 1). The flame zone on the mixture ratio reduction tests gradually shrank shorter and shorter until they disappeared up inside the cup or the intensity of the OH zone was not visible on the film. There was no evidence of flameout or blowoff of the flame-holding zone.

#### Ignition of Gas/Gas Coaxial Elements

The conclusions described in this section are drawn from the over 200 low pressure tests conducted to date, which includes the 51 flame-holding tests. The flame-holding mechanism described previously plays a very important function in the ignition process for gas/gas coaxial elements. The ignition process is not complete until the flame-holding zone is ignited and able to sustain the steady-state combustion. The terms successful ignition used in this discussion in reference to the ignition of the coaxial propellant flow will mean the successful completion of the ignition process including the sustained combustion required for steady-state operation.

To have a successful ignition of the gas/gas coaxial element system, the flame-holding zone must be ignited. The ignition of this zone with gaseous propellants at low overall mixture ratios (less than 1.5 oxygen/hydrogen) is not easily accomplished. Without an ignition source at the tip of each coaxial injector element, the recirculation of the propellants and combustion products outside of the coaxial jet flow must provide the propagation of the flame from the ignition source to the flame-holding zone.

If the recirculating gases, which are relatively well mixed, do not have a mixture ratio much greater than 1.0 (oxygen/hydrogen), the combustion will not propagate from the ignition source through the recirculating gases (see Fig. 1). This was well documented on the previous fuel lead sequence ignition tests. If the mixture ratio was lower than 1.0, the spark probe was unable to even ignite the slow moving recirculating gases. It should be noted, that on the fuel lead tests, the initial mixture ratio of the recirculating gases is 0.0 and once the oxygen is flowing it gradually increases until it matches the mixture ratio flowing through the injector. There were no successful ignitions on fuel lead tests with injector mixture ratios less than 1.0.

Once the recirculating gases are ignited, the combustion must propagate through the recirculating gases, through the high velocity fuel jet at the tip of the coaxial element, and then ignite the combustible gases in the flame-holding zone at the tip of the LOX post. Once this is accomplished, the combustion process will then sustain itself. The real problem comes in the penetration of the high velocity (1000 to 2000 ft/sec) gases at the tip of the element to ignite the flame-holding zone.

The flame propagation speeds for mixtures of oxygen and hydrogen are in the range of 100 to 600 ft/sec. Therefore, the combustion zone is not likely to propagate upstream through the mixing zone of the element jet flow to the tip of the LOX post. There was no noted indication that the flame was able to propagate up the jet flow to the LOX post tip on any of the tests conducted to date. Several tests were conducted in the earlier ignition series with the spark probe located directly below the injector element to determine if the combustion process could propagate upstream in the jet flow. The film data showed that the combustion zone ignited in the high mixture ratio jet flow was blown downstream away from the injector each time.

The only observed mechanism that allowed for successful ignition of the flame holding zone of the coaxial injector elements, and resulting steady-state combustion, was a pressure surge.

This mechanism was observed on both the fuel lead and oxidizer lead tests. The pressure surge, created by the combustion of the mixed gases in the recirculation zone slowed down the jet flow (and actually reversed it on several tests) and allowed the combusting gases to ignite the flame-holding zone at the LOX post tip. On the fuel lead tests the mixture ratio had to be 1.4 or higher to generate a fast enough pressure rise. If the pressure rise was too slow, the combustion zone propagated through out the mixed recirculating gases without igniting the flame-holding zone. This phenomena is shown in the sequence of frames from the laser Schlieren film of a fuel lead test in Fig. 16. This was a typical fuel lead test with a fairly high mixture ratio (1.1 oxidizer/fuel). After all of the recirculating gases were combusted, the combustion went out without igniting the flame-holding zone. The extinguishment of the combustion process was confirmed by reviewing the ultraviolet data on the same test.

This sequence of photos (only 15 frames out of a 400-foot roll) also gives a representation of the type of information available from the laser Schlieren films. Every fifth frame of the actual sequence was printed. The sequence goes from left to right. The actual framing rate was near 9000 frames per second. The reproduction of the film for this paper unfortunately does not portray the quality and the information available from these films.

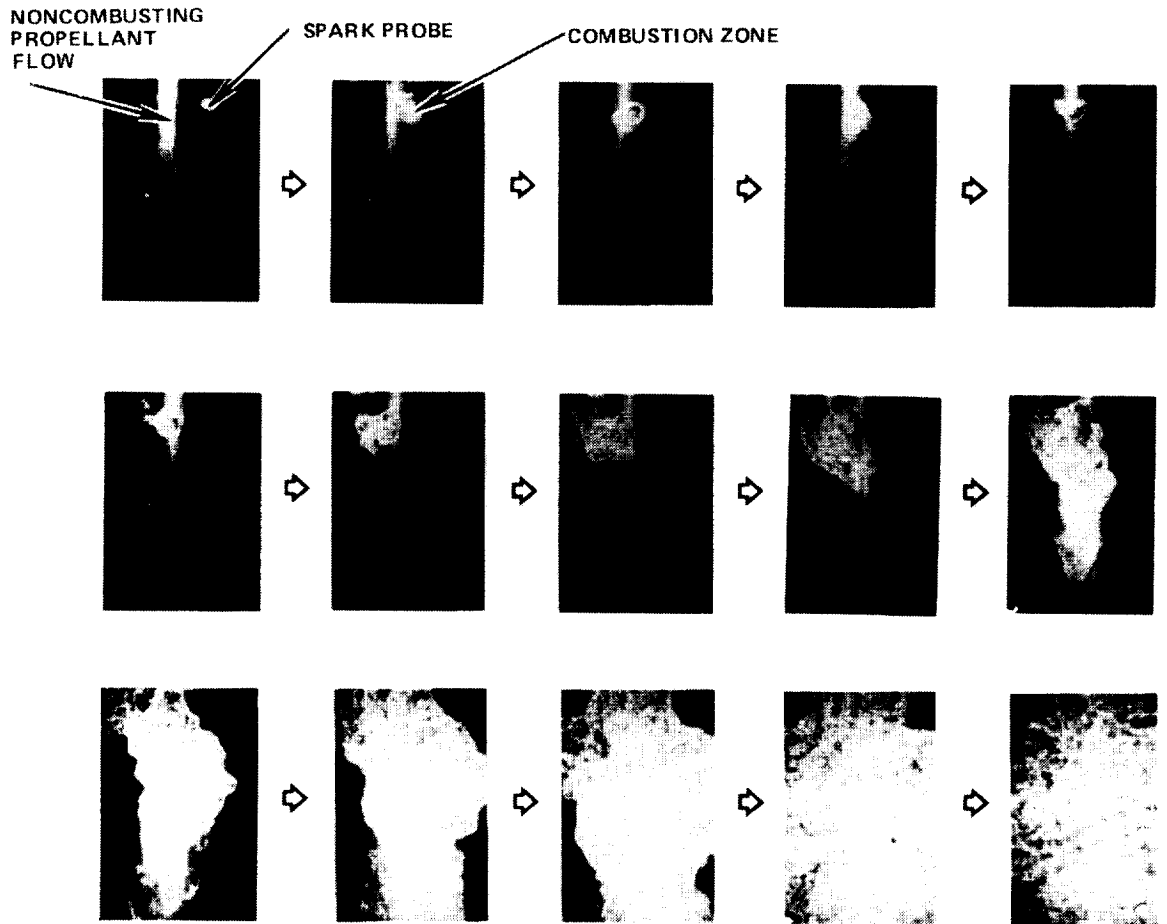


Fig. 16. Fuel Lead Schlieren Sequence

On the fuel lead tests, which had successful ignition, the injector mixture ratio was in range of 1.4 or higher. The combustion of the higher mixture ratio jet along with the recirculating gases produced a sufficient pressure surge to slow the jet flow enough to allow ignition of the flame-holding region.

Figure 17 is a collection of photographs made from the high speed ultraviolet film from a typical oxidizer lead test with a targeted mixture ratio of 0.5 (oxidizer/fuel). It should be noted that in an oxidizer lead test, the mixture ratio of the recirculating gases goes from infinity and gradually reduces when the fuel flow starts until it reaches the mixture ratio of the element flow. As a result, the high mixture ratio of the recirculating gases is easily ignited even on tests with fairly low steady-state injector mixture ratios. The high mixture ratio also creates a strong pressure surge during ignition and slows or reverses the element jet flow.

ORIGINAL PAGE  
OF POOR QUALITY



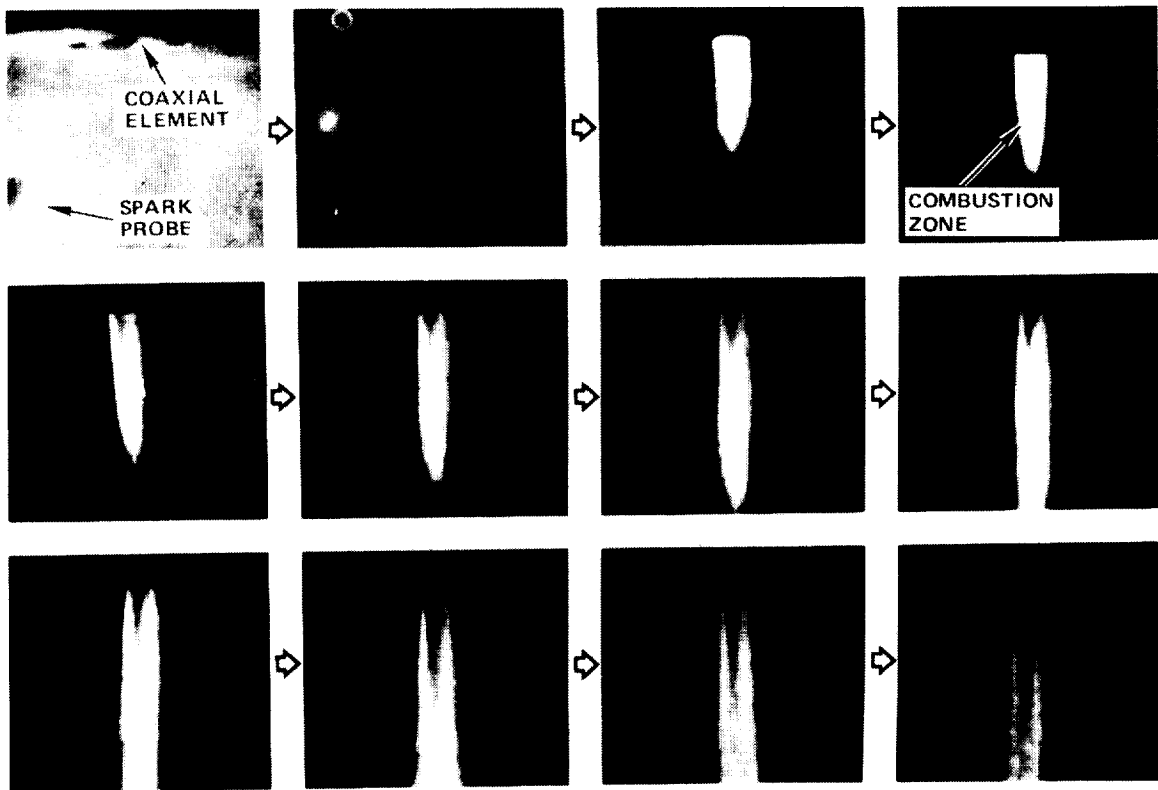


Fig. 17. Oxidizer Lead Ultraviolet Sequence

The flow reversal phenomena is clearly seen in Fig. 17. The sequence goes from left to right and the framing speed is near 400 frames/sec. The series starts out just after the recirculating high mixture ratio gases have been ignited by a previous spark. The spark in the first frame (after the initial spark that ignited the gases) has illuminated the chamber and the single coaxial element is clearly visible. In the first two frames, the element flow has actually been reversed, pushed back up in the element, by the pressure surge created during the ignition of the high mixture ratio recirculating gases. In the third frame, the element flow is observed starting to flow back out of the cup area and is already ignited. The flow continues to build up through the rest of the sequence.

Again, this sequence is a series of only 9 frames out of a 100-foot roll of film and is presented to give a representation of the type of information available from the ultraviolet films. Again, the reproduction of the film for this paper unfortunately does not portray well the quality and the information available from these films. To study any of the phenomena described, the actual test films must be reviewed.

This pressure surge or "pop" may also account for some of the late ignitions observed on the SSME oxidizer preburner. The pops experienced during the start sequence and the change in chamber pressure before and after the pop seems to fit the observed phenomena in the Turbine Drive Combustor Ignition and Durability Technology testing. The following scenario is offered as a possible description of the sequence of events in the late ignition or pops of the SSME oxidizer preburner.

The SSME start sequence requires the OPB mixture ratios to be very low during the ignition phase. Because of the low mixture ratios in the OPB during the start phase, not all of the elements may have their corresponding flame-holding zones ignited. As the sequence proceeds and the unburned propellants accumulate, they are finally ignited by either the augmented spark igniter or the combustion products from the other ignited elements. The rapid combustion of the unburned propellants then creates a pop or pressure surge which in turn slows down or reverses the element flow and allows the remaining element flame-holding zones to be ignited.

#### Summary of Observations from Flame-Holding Tests

The following is a list of the most important observations and conclusions from the coaxial gas/gas flame holding and ignition testing completed to date on the Turbine Drive Combustor Ignition and Durability Technology Program.

1. There is a flame-holding zone located in the recirculation or wake area at the tip of the LOX post.
2. This flame-holding zone is required to sustain steady-state combustion at mixture ratios less than 1.0 (oxidizer/fuel) with gaseous propellants.
3. Once this flame-holding zone is ignited, the mixture ratio of the element flow can be lowered to values well below the mixed flammability limit.
4. If the ignition system relies on combustion propagation through the recirculating gases or the jet flow for ignition of this flame-holding zone, the element jet flow must be temporarily slowed down to allow for ignition of the zone at the end of the LOX post.

#### Future Plans

Because of the successful application of these techniques and the large amount of insight gained, additional refined studies into low mixture ratio oxygen/hydrogen ignition and combustion are planned

which should be very productive in helping to further understand the mechanisms involved in the ignition and combustion processes of coaxial injectors. The additional planned effort will include testing with different LOX post geometries to try and establish the sensitivity of flame-holding zone to the width of the LOX post tip. Also, testing of new variable geometry fuel sleeves, smaller element sizes, and higher pressures tests with LOX are planned. These efforts are scheduled to be conducted over the next 18 months.

## COMBUSTION MODELING: PROGRESS AND PROJECTIONS

P. Y. Liang

Rockwell International/Rocketdyne Division  
Canoga Park, CaliforniaAbstract

In 1985 Rocketdyne's ARICC combustion code entered operational phase from developmental phase with a successful engineering analysis of the SSME preburner injector element flows. The cases studied correspond to two design geometries and two engine operation conditions. Based on this experience, a much better understanding of the unique challenges of combustion modeling for multiphase flows and of the weakest links in the physical model is obtained. This presentation will discuss the nature of combustion model development and highlight the results of the injector study, especially the qualitative features of the problem that pertains to the choice of the numerical methodology. Numerical issues encountered that are peculiar to the simulation of combustion flows will be briefly discussed. Finally, the plan for future refinement of ARICC and its subcomponents into a reliable combustion model, as conceived at Rocketdyne, will be outlined.

Introduction

The complex flowpaths of the Space Shuttle Main Engine (SSME) contain many sections in which significant chemical processes take place within the fluid medium. These are the sections for which combustion modeling, and not just fluid dynamic simulation, must be employed. To name a few, the fuel and oxidizer preburners, the Augmented Spark Igniters (ASI) and individual injector elements contained therein, the Main Combustion Chamber (MCC), and possibly the main nozzle boundary layers are all flow regions that fall under this category (Fig. 1). To model and analyze these components adequately, a number of physical processes must be incorporated into the computational fluid dynamics scheme. The interactions between these physical submodels and the basic approach for solution of the fluid dynamic governing equations must be a subject of careful study, for herein lies the art of the computational fluid dynamicist turned combustion modeler.

It may be instructive to review the true nature of the distinction between the so-called basic governing equations and the physical submodels. The former supposedly are derived from the "fundamental" principles, such as Newton's laws of mechanics or the laws of thermodynamics. The latter are intended to represent physical processes whose detailed mechanisms are still too obscure to be rigorously

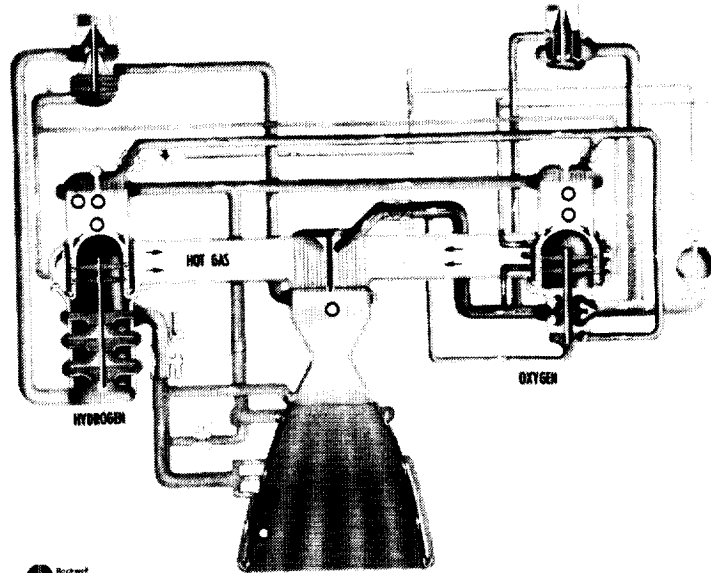


Fig. 1. Some SSME Flow Components that Require Combustion Modeling (White Dots)

described, but the net effect of their presence are at least partially known. Such are the processes of atomization, evaporation, and chemical kinetics. Some processes, such as turbulence, may be described rigorously in principle but the resulting equations would be too expensive to solve on a practical scale. Thus, semiempirical models are employed to simulate the effect of these processes on the flow.

The simplest method of incorporating these models into the overall solution is to treat them as perturbations to the computed flow field in the form of distributed source terms (Fig. 2A), essentially neglecting the dependence of the model on the type of flows that it is perturbing except for local parameters. The physical models are thus nothing more than point transfer functions. When exothermic chemical reactions are modeled as distributed heat sources, such is the approach adopted. Sometimes, however, the details of the physical mechanisms are partially resolved by the finite differencing scheme and hence the basic CFD solution provides insight as to how the semiempirical model should be constructed to broaden its general applicability and enhance its realism (Fig. 2B). If the droplets are treated as discrete particles, the transport process taking place across the drop/ambient interface is by definition not resolved by the finite difference grid. Yet whether the evaporation rate should be expressed as primarily being concentration driven, or heat transfer driven, or drop breakup driven can be determined with the help of the CFD scheme itself through some parametric calculations. The resultant, more-sophisticated model is then reincorporated into the "global" model to cover a broader range of phenomena. This iteration process can be repeated many times between the "CFD" and the "empirical" sides of the

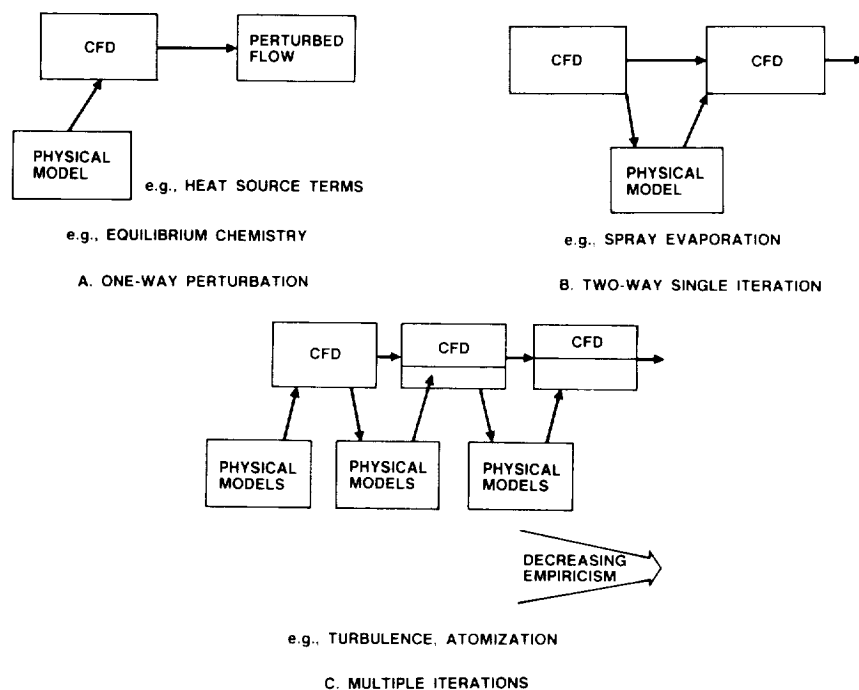


Fig. 2. Three Modes of Interaction Between Basic Governing Equations and Physical Submodels

model (Fig. 2C), the former being characterized by partial differential equations and the latter by tables, algebraic expressions, or ordinary differential equations. As the iteration progresses more and more, the empirical models become amenable to a "rigorous" field description from fundamental principles, which can then be solved finite-difference fashion as additional governing equations rather than merely as uncoupled source terms. The net result is decreased empiricism. This relationship between the two parts is analogous to that between hypothetization and experimentation (to verify or disprove it) in development of scientific theories. The CFD is the instrument for numerical experimentation, guided by physical understanding. The experimental results in turn enrich the theory (the physical model). The iteration skillfully employed greatly accelerates the rate of progress. The present author has found this to be precisely the path followed in the continuing evolution of the atomization model in the Advanced Rocket Injector Combustor Code (ARICC) described below.

Initially treated as mere injection species source terms as in most combustion models, the ARICC atomization model then developed into more-refined local transfer functions with various empirical constants. When the liquid-gas multiple free surface capability became available in ARICC, atomization was then treated as a spatially distributed process. Flow field inside the liquid jet is actually

resolved, although the drop formation criteria and initial drop characteristics are still determined empirically. As more physical understanding of the drop formation mechanism is acquired through two-fluid simulations by ARICC, the entire atomization process will then be modeled rigorously, occurring as a natural result of solving the set of governing equations.

From the modeling point of view, combustion modeling places many additional requirements on the task of the modeler. These are summarized in Table 1, and fall into three major areas that call for concerted research efforts.

Table 1. Special Requirements of Combustion Modeling

<u>Physical Requirements</u>
<ul style="list-style-type: none"> <li>● Physical Properties               <ul style="list-style-type: none"> <li>● Multicomponents</li> <li>● Supercritical</li> </ul> </li> <li>● Drop Dynamics</li> <li>● Chemical Kinetics/Turbulent Diffusion</li> </ul>
<u>Numerical Requirements</u>
<ul style="list-style-type: none"> <li>● Stiffness</li> <li>● Real-Time Accuracy</li> <li>● Multiphase Treatment</li> </ul>
<u>Data Base and Diagnostic Requirements</u>
<ul style="list-style-type: none"> <li>● Concentration and Temperature Data for Anchoring</li> <li>● Controlled Experiments of Drop Dynamics Processes</li> </ul>

Physically, since chemical reactions inevitably involve more than one chemically active species, physical properties for a mixture of multiple species must be somehow estimated and supplied to the code. Determining the effective viscosity of a gaseous mixture, for instance, can be far from a trivial task. Although rigorous estimates can be obtained through molecular kinetic theory, that path is usually too tumultuous and the computational load too large to warrant the trouble on a point-to-point basis. Simple interpolation "mixing" laws are instead employed. On the other hand, for the case of high pressure liquid rocket engines, supercritical spray properties are necessary and are generally not available from standard handbooks. Closely related to this is the modeling of droplet dynamics, including the processes of drop formation, drop transient heatup and evaporation, and secondary drop breakups. The presence of a droplet phase and possibly a liquid phase adds a whole new dimension to the complexity of the finite difference codes.

Another important physical requirement in combustion modeling is the description of the chemical reactions themselves. Strictly speaking, all reactions should be formulated as finite rate kinetic equations with temperature- and pressure-dependent coefficients. In practice, the choices of which reactions to include, how many to include,

the expressions for the rate constants, and the best available estimates of the values of the coefficients are always difficult tasks unique to each modeling situation. Chemical kinetics are also closely tied to the correctness of the turbulent diffusion calculations, for which very little understanding is still available when combustion is present.

Numerically, the additional challenges can be categorized into the areas of stiffness, accuracy in real time, and the ability to handle multiphase flows. Finally, as in all complex modeling work, a vast body of well documented and reliable data is required for code anchoring purposes, which points to the need for extensive development of modern nonintrusive diagnostic capabilities. In particular, species concentration and temperature data are necessary for proper assessment of a certain numerically predicted flow field, in addition to the standard point velocity measurements done for nonreactive flows. When the hot fire environment extends into extremely high pressure regimes, as in the case of liquid rocket engines, the test hardware requirements are often overwhelming. Many physical submodels used in a combustion code and expressed as empirical correlations are themselves also in need of anchoring. Most notable among them is the need for better-controlled experiments on the drop dynamic processes such as atomization and breakup.

The impact of all these different sources of complication, as contrasted with a "simple" hydrodynamic situation, can be understood from the perspective of the governing equations. In Fig. 3, a "generalized" Navier-Stokes equation for an arbitrary field variable has been written. Each of the terms on the right-hand side of the equal sign represents the major physical processes of convection, diffusion, and production (or consumption) of that particular quantity, respectively. From the above discussion, it may be pointed out then that numerical stiffness and/or stability is affected when many different coupled physical processes are incorporated into the model described by many different but coupled partial differential equations. The presence of multiple phases primarily change the convection terms, since a means to determine how much of one phase is convected across a cell boundary

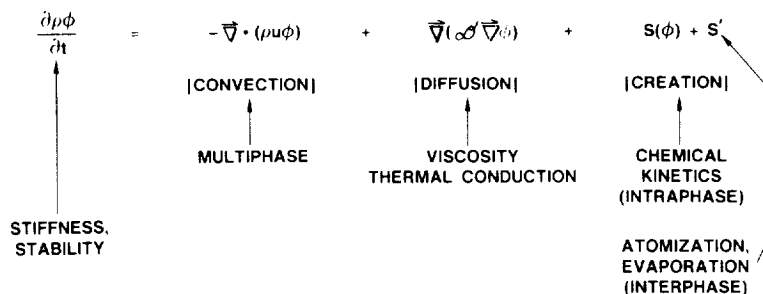


Fig. 3. Impact of Physical Submodels on the Generalized Navier-Stokes



versus another phase must now be formulated. Turbulence modeling affects momentum, heat, and species diffusion. Furthermore, chemical kinetics leads to the appearance of certain "intrapphase" source terms. Their values are usually a function of the concentration of the species themselves. Finally, certain creation processes take place across phase boundaries, such as liquid jet atomization or droplet evaporation. An interphase source term may not even be a direct function of the local values of the variable under consideration. Thus, in other words, the additional challenges of combustion modeling enter into play through all aspects of the fluid flow represented by different terms of the governing equations.

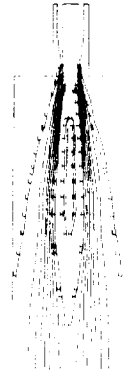
### The ARICC Combustion Code Development Experience

A first-hand experience of most of the abovementioned challenges was obtained in the course of Rocketdyne's development of the NASA/MSFC ARICC,<sup>1</sup> which may be considered to typify a first-generation computational capability of its kind in multiphase combustion modeling. The objective of the effort is to achieve a multiphase, multispecies, transient-reacting flow modeling capability with physical submodels to represent all major physical processes in liquid rocket engine components. Table 2 summarizes the existing features of the basic version of ARICC as well as some advanced features that are recommended for incorporation in future code development activities. They reflect the needs of the liquid rocket engine designers. The major advancement over previously available CFD models lies in the ability to simulate atomizing liquid jets and a dense, supercritical spray.

Table 2. Summary of ARICC Development Status

Operational Features	Features to Add
<ul style="list-style-type: none"> <li>● Injector Flow Configuration               <ul style="list-style-type: none"> <li>● Auto Grid Generation</li> </ul> </li> <li>● 2-Phase ARICC               <ul style="list-style-type: none"> <li>● Liquid-Gas Properties</li> <li>● Finite Size Drops</li> </ul> </li> <li>● 3-Phase ARICC               <ul style="list-style-type: none"> <li>● VOF Liquid Jet</li> </ul> </li> <li>● Dense/Supercritical Spray Refinements               <ul style="list-style-type: none"> <li>● Variable Drop Densities</li> <li>● Drop Coagulation</li> </ul> </li> </ul>	<ul style="list-style-type: none"> <li>● Surface Tension               <ul style="list-style-type: none"> <li>● High Accuracy Scheme</li> <li>● Improved Drop Breakup Models</li> </ul> </li> <li>● Nonreflective Boundary Condition Options</li> <li>● Adaptive Gridding</li> <li>● Vectorization</li> </ul>

A demonstration of the intricate relationship among the different combustion processes can be obtained from the results of a recent study<sup>2</sup> conducted using ARICC on the reactive flow field of an SSME preburner injector element (Fig. 4 through 6). One objective of the study was to determine the overall mixing efficiency of the coaxial injector element in hot fire. A "body-fitting" curvilinear grid depicting a center post with tapered tip inside an annular "sleeve" with cup recess is generated. Low velocity liquid oxygen (LOX) is injected



$T_H = 3780$  K  
 $T_L = 546$  K

Fig. 4. Isotherm Plots of SSME Ejector Flow Field

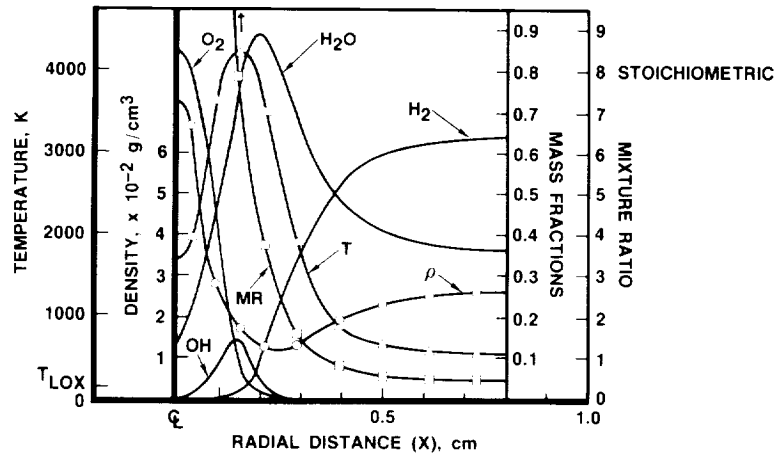


Fig. 5. Cross-Sectional Profiles of Gaseous Temperature, Density, Species Mass Fractions, and Mixture

through the center post while high velocity gaseous hydrogen is injected through the annulus. The large shearing forces break up the liquid stream rapidly into a dense spray, which then vaporizes within 0.75 inch corresponding to the size of the combustion zone. The isotherms in Fig. 4 reveal these details never before obtainable in hot fire measurements, and lead to the conclusion that the flame is of an external group combustion type. In Fig. 5, cross-sectional profiles of various thermodynamic variables and species concentrations across the widest portion of the flame display clearly turbulent diffusion flame characteristics. Figure 6 shows the  $H_2O$  mass fraction contours. A careful analysis<sup>2,3</sup> of the numerical results indicated that droplet evaporation is a key rate-controlling step in determining characteristics of the flame. Furthermore, a feedback type of coupling exists

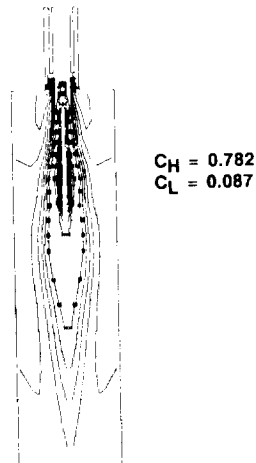
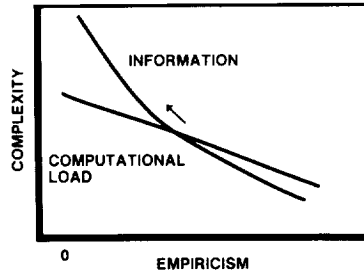


Fig. 6. Contour Map of  $H_2O$  Mass Fractions in SSME Ejector Flow Field

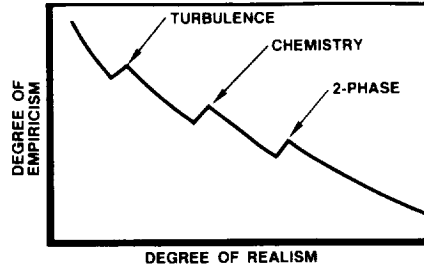
among the processes of atomization, evaporation, and combustion. Large shear velocities enhance atomization as well as evaporation especially through the process of secondary droplet breakup, which in turn increases the local combustion rate. The highly exothermic reaction inputs energy into the flow, which in turn accelerates the local gas velocity. Thus, a positive feedback loop is established, and such intermittent outbursts of rapid activity could in some case contribute to combustion instability.

In summary, the experience in developing ARICC and applying it to the SSME injector element flow may be stated as follows:

1. Atomization and droplet breakup are processes that are important and poorly understood. While including them in a combustion model significantly increases the computational load, the improvement in the model's realism and versatility is definitely necessary (Fig. 7A). A vast amount of detailed information is generated and their interrelationships came to light in the SSME case cited. However, although the increase in the degree of realism and the overall decrease in the degree of empiricism go hand in hand, the latter changes in stages rather than continuously (Fig. 7B). Whenever a new physical submodel is first included, the amount of empirical data required initially increases. They may be problem-specific coefficients in a turbulence model, rate constants in a chemistry package, or atomization rate constants in a two-phase model. As these models are refined through usage, their sophistication level increases and constants give way to expressions making the models applicable to a wider range of conditions. Eventually, the algebraic expressions will be replaced with ordinary differential equations and then perhaps partial differential equations. By then, description for the phenomenon passes from the realm of physical modeling to that of the "basic" governing equations. Hence, in light of this, it is found that a most profitable means of



A. COMPLEXITY OF GOVERNING EQUATIONS GOES UP ARITHMETICALLY BUT AMOUNT OF INFORMATION GENERATED GOES UP GEOMETRICALLY



B. NUMBER OF EMPIRICAL PARAMETERS ALSO INCREASES LINEARLY WHEN NEW PROCESSES ARE ADDED

Fig. 7. Relationship Among the Computation Load, Degree of Empiricism, and Degree of Realism in a Combustion Model

using such codes is in a "dual-use" mode, both as a "global model" to simulate entire hardware components and also as an apparatus for numerical experimentation to improve the physical submodels. Such is the path that would be pursued in future refinement of the atomization model in ARICC.

2. Positive feedback mechanisms exist in liquid injection rocket engines that can be the cause of combustion instabilities. To adequately simulate such phenomena, however, further improvements in real-time accuracy and computational efficiency may be necessary. This is the motivation for some of the recommended refinements listed in Table 2.

3. In a complex situation such as multiphase combustion flow, intricate interactions take place between the numerics and physics of the model. This important topic is the subject of another paper<sup>3</sup> to be published. Here, it suffices to say that the modeler must have a full appreciation of not only the different physical phenomena and of the numerical algorithm, but how they affect each other. In other words, the effects of physics and of the choice of certain numerical schemes are not separable. The relationship between numerical diffusion and physical diffusion is exemplary of this statement. Much still remains to be learned.

### Future Challenges

In conclusion, it may be profitable to point out what the present author believes to be some of the most-pressing needs in the different elements that make up the whole combustion model, or the most-desirable objectives in the near term. They may guide the directions for research in the near future. They are:

1. Numerical verification of classical combustion theories
2. Reduction of the degree of empiricism of critical processes, e.g., atomization
3. Conquering of numerical stiffness issues

Some promising approaches to tackling the last objective are the development of adaptive gridding methods, the use of "smart" algorithms that are "mission-configured" according to the stiffness characteristics of the local flow situation, and the incorporation of improved boundary conditions including the use of nonreflective "acoustic" boundaries to facilitate convergence to steady state. All these areas, within the domain of the art of computational fluid dynamics models, are ready for significant advances and should be vigorously pursued.

### Acknowledgment

The author would like to thank Mr. D. Pryor and Dr. McCay of MSFC for their guidance in original development of the ARICC.

### References

1. Liang, P. Y., S. Fisher, and Y. M. Chang, "Comprehensive Modeling of a Liquid Rocket Combustion Chamber," J. Prop. and Power, Vol. 2, No. 2, Mar/Apr (1986).
2. Liang, P. Y., R. J. Jensen, and Y. M. Chang, "Numerical Analysis of SSME Preburner Injector Atomization and Combustion Processes," AIAA-86-0454, Jan (1986).
3. Liang, P. Y., "Analysis of Coaxial Spray Combustion Flames and Related Numerical Issues," AIAA-86-1511, Jun (1986).

Effects of Oxygen/Hydrogen Combustion Chamber  
Environment on Copper Alloys

M. Murphy  
R. E. Anderson  
D. C. Rousar  
J. A. Van Kleeck

Aerojet TechSystems Company

I. INTRODUCTION

Main chamber liner deterioration in SSME engines frequently is sufficient to cause local chamber wall failures in the form of cracks through the copper alloy chamber wall. This deterioration has been termed "blanching" and is characterized by an increase in local wall roughness and a bright, shiny, "new penny" type appearance. Test experience has shown that the increase in surface roughness leads to increased heat transfer rates, consequently postfire SSME operations include inspection of the main chamber liners and hand-polishing of the blanching areas. Sketches of the blanching and main chamber wall damage found on three SSME's after a recent shuttle flight are shown on Figure 1.

One of the objectives of the Main Chamber Combustion and Cooling Technology Study, Contract NAS 8-36167, is to develop an understanding of the blanching phenomenon. The specific scope of this program has included:

1. Thermochemical analysis of the copper-oxygen-hydrogen system,
2. Thermogravimetric analysis (TGA) oxidation tests of NARloy-Z copper samples,
3. Metallurgical analyses of samples from 40K and full-scale SSME chamber liners, and
4. TGA surface study tests under oxidation-reduction conditions with NARloy-Z, NARloy-A, OFHC, and zirconium copper alloys.<sup>1</sup>

The results of the above activities and a discussion of the impact of the test results on the design of main chamber assemblies for advanced, high pressure oxygen-hydrogen engines are presented in the following sections of this paper.

---

<sup>1</sup>Nominal compositions listed at the end of this paper.

## II. BACKGROUND

Main chamber blanching has been found in 40K and full scale SSME chambers and it appears to be a major life limiting factor for copper alloy main chamber liners in high pressure oxygen/hydrogen rocket engines. Previously it was postulated that blanching is caused by oxidation-reduction reactions, but no systematic evaluation of that hypothesis was conducted (Ref. 1). Similar surface roughening, termed "orange peeling", has been observed during research programs at the NASA Lewis Research Center that have tended to focus on thermal ratcheting or "dog-housing", another major life limiting factor for copper chamber liners (Ref. 2).

Testing experience has shown that a blanching threshold exists for the SSME. Many firings at 90% power level produce no blanching, then severe blanching occurs at higher thrust levels even though the calculated wall temperature increase is only 50<sup>o</sup>F. During the recent Space Shuttle Engine Study at Aerojet, it was found that blanching and cracking appear to correlate with the position of the hot gas manifold inlets and is, therefore, possibly related to local mixture ratio (MR) maldistributions produced by the manifold (Figure 2). A nickel plated SSME main chamber liner has been tested with mixed results: after a series of test firings the chamber showed no evidence of blanching, but 200-300 holes developed in the chamber wall and many transverse subsurface cracks were found to have formed within the wall.

## III. METALLURGICAL ANALYSIS

### A. EFFECTS OF TEMPERATURE AND GAS COMPOSITION ON NARloy-Z

Chemical thermodynamic analyses and phase behavior studies of the copper-hydrogen-oxygen system provided an approach for predicting which copper species or phases should be stable at various temperatures in atmospheres containing H<sub>2</sub>O, H<sub>2</sub>, and O<sub>2</sub>. The results of the analyses performed are shown on Figures 3 and 4 and 5<sup>1</sup>. The reliability of these predictions, particularly as applied to NARloy-Z, was then subjected to laboratory verification testing using a sophisticated thermogravimetric analysis (TGA) apparatus. Using this device, small NARloy-Z samples (approximately 100 mg each) were exposed to tightly controlled conditions of

---

<sup>1</sup>Note: Equivalent MR (MR eq) is defined as the equivalent hot gas oxygen-hydrogen mixture ratio at 3000 psia, excluding high temperature dissociation effects.

temperature and composition of the surrounding atmosphere while sample weights were monitored continuously with high precision. The NARloy-Z samples were taken from a scrapped SSME main chamber which had not been test fired. The total pressure for all tests was nominally 15 psia.

The first series of TGA tests were conducted in five different atmospheres ranging from inert to reducing to oxidizing gases and included: (1) ultra-pure helium, (2) hydrogen, (3)  $H_2/H_2O$  (36:1 by volume), (4) water vapor, and (5)  $H_2O/O_2$  (10:1 by volume). In these tests, the specimens were heated from approximately 25 to 950°C at a rate of 10°C/min. in each of the slowly flowing test atmospheres while the sample temperatures and weights were electronically recorded. The resulting data were processed and plotted using a mini-computer system to yield data plots such as that shown in Figure 6 for the  $H_2O/O_2$  (10:1 by volume) test gas.

The pertinent data from this first series of TGA tests are summarized on Figure 7. The significant facts to observe from this plot are: (1) only the atmosphere containing  $H_2O/O_2$  caused NARloy-Z to gain any appreciable weight and is indicative of an oxidation reaction, (2) the hydrogen atmosphere caused a very small weight loss which suggests the reduction of a trace of initial surface oxide on the specimen, and (3)  $H_2/H_2O$  and  $H_2O$  atmospheres had vitually no effect. These facts are in very good agreement with the theoretical stability predictions given by Figures 3 and 4. For example, the upper curve in Figure 7 for  $H_2O/O_2$  represents an atmosphere containing oxygen at a partial pressure of about  $3 \times 10^{-3}$  atm. and Figure 4 predicts  $CuO(s)$  is the stable phase at temperatures up to about 840°C and  $Cu_2O(s)$  is the stable phase from about 840-1220°C at that oxygen partial pressure. Thus, copper surfaces exposed to the  $H_2O/O_2$  test gas should oxidize and cause specimen weight gain. Similarly, the two lower curves in Figure 7 for  $H_2$  and  $H_2/H_2O$  represent atmospheres having  $H_2O/H_2$  volume or pressure ratios of zero and  $2.8 \times 10^{-2}$ , respectively. Although those values are off Figure 3 on the left-hand side, they clearly are in the region where  $Cu(s)$  is the stable phase up to its melting point. Thus, fresh copper surfaces should remain unchanged and oxide surface layers should be reduced and cause the specimens' weights to remain constant or decrease slightly. The curve for  $H_2O$  in Figure 7 actually represents water vapor containing a trace of



contaminating oxygen ( $O_2$  partial pressure of less than  $4 \times 10^{-5}$  atm.). The stability diagram in Figure 4 indicates  $CuO(s)$  is the stable phase at that oxygen partial pressure and up to a temperature of about  $700^\circ C$  but at higher temperatures tends to convert to  $Cu_2O(s)$ . Therefore, copper surfaces exposed to the slightly  $O_2$ -contaminated  $H_2O$  vapor would be expected to surface oxidize to  $CuO$  and gain a slight amount of weight up to a temperature in the vicinity of  $700^\circ C$  then lose some of that weight gain as the surface  $CuO$  decomposed to  $Cu_2O$  with the loss of oxygen. The curve for  $H_2O$  in Figure 7 shows just such behavior but it may be only a fortuitous indication since the weight changes are extremely small and difficult to measure.

SEM and visual examination of the TGA samples showed a distinct difference in surface morphology between the samples exposed to an oxidizing environment vs. a reducing environment. This is shown in Figure 8.

The first series of TGA tests generally verified the validity of the stability diagrams (Figures 3 and 4) and showed that copper is attacked only when free oxygen is present in the test gas. Subsequently, a second series of TGA tests was conducted to determine the effects of temperature and oxygen concentration on the initial surface oxidation rate of NARloy-Z. These oxidation rate tests involved heating NARloy-Z specimens rapidly ( $100^\circ C/min$ ) to a specified temperature in ultra-pure helium then switching to a specified oxygen-containing test gas while maintaining a constant temperature for an extended period of time (about 1 hour). The test gases contained oxygen at partial pressures of 0.003, 0.20, or 0.95 atm. and water vapor at a partial pressure of .027 atm. along with some helium or nitrogen to give a total pressure of slightly more than 1 atm. Test temperatures varied from about  $300-1000^\circ C$  (about  $600-1800^\circ F$ ). A typical test data plot is shown in Figure 9.

The pertinent data from the oxidation rate tests are summarized in terms of surface reaction rate versus temperature in Figure 10. The significant facts to observe from Figure 10 are: (1) reaction rates increase more or less logarithmically with temperature, although not in the classical Arrhenius fashion and (2) contrary to expectations, oxygen partial pressure did not affect the reaction rate in any simple analytical fashion. Perhaps, these results partially reflect the limitations of a TGA apparatus for obtaining readily interpretable surface kinetics data and the inherent difficulty of elucidating applicable rate equations. The surface reaction

rates depicted by Figure 10 probably cannot be directly applied to a rocket chamber liner environment because they do not include the effects of high heat flux and shear stress produced by the hot gas stream. They do, however, clearly show that oxidation rate is a strong function of temperature. For example, between 1000°F and 1700°F, the rate increases by an order of magnitude.

B. CHAMBER SPECIMEN ANALYSES

1. 40K SSME Chamber

Visual Description

An entire segment of the 40K SSME chamber, residual from the program reported in Reference 3, was provided by MSFC for analysis, Figure 11. The specimen had one obvious area of blanching on the cylinder wall. The unblanched area was dull black-brown in color, indicative of cupric oxide, and exhibited alternating smooth and rough streaks corresponding to areas over channels and lands respectively. The blanched area was considerably rougher than the over-land areas, and had a dull copper sheen. This chamber specimen dates back to 1976, and has been exposed to the atmosphere since then.

Roughness Measurements

The surface roughness measurements obtained for the 40K chamber are summarized below. The values shown are center line averages and expressed in micro-inches.

	<u>Longitudinal Direction</u>	<u>Circumferential Direction</u>
Blanched Area	250-320	360-400
Unblanched Area	90	180-220

Scanning Electron Microscopy (SEM)

Samples were removed from blanched and unblanched areas for SEM examination. A typical example of the blanched surface morphology is shown in Figure 12. The severe interconnected porosity appears to be the primary characteristic of blanching. This figure also shows streaks of solid copper overlaying portions of the porosity. This solid layer is interpreted as evidence of melted copper on the porous layer. The streaking is evidence of flow of the molten metal induced by the combustion gas stream. The area shown in Figure 13 is of a visually unblanched area considerably removed from the blanched area and includes both over-channel and over-land areas. The smooth surfaces corresponding to over cooling

channels show no obvious damage. The rough surfaces correspond to areas over lands and exhibit surface features similar to the areas considered to be blanched except that the rough surface is more granular in appearance than the blanched area and the solid metal streaking is missing. The areas over the lands between channels appear to have been subjected to an environment similar to that which causes blanching but the maximum wall temperature would seem to be considerably less. The abrupt boundary between smooth and rough surfaces suggest that some geometrical effect may effect the roughening mechanism. Currently the most plausible theory is that the over-land areas are subject to high compressive stresses during exposure to a blanching environment. Therefore, it would seem that blanching involves high wall temperatures, high compressive stresses, and an environment which induces the surface porosity.

#### Optical Microscopy

Cross sections of blanched and unblanched areas were examined to determine the depth of the blanching effect and the corresponding metallurgical changes to the substrate. Figure 14 shows a cross section of blanching from the center of a land to the center of a channel. The surface porosity can be seen to extend to a depth of approximately .0015 inches over the land and to a negligible depth over the channel. Figure 15 shows the characteristic "dog house" deformation previously reported (Reference 2). It can be seen that the gas side surface of this sample shows a larger grain size than the bulk of the alloy and that there is an absence of precipitates at the surface. Since the solution temperature of the  $(\text{CuAg})_3\text{Zr}$  intermetallic precipitate occurs at approximately 1700 F, this establishes the lower limit wall temperature at this location within the 40K chamber.

## 2. SSME Main Combustion Chamber

#### Visual Description

Ten sections of an SSME chamber which had been tested extensively were supplied for analysis.<sup>2</sup> Five of the specimens contained major longitudinal cracks, however, the gas-side surface of these specimens had been polished (abraded)

---

<sup>2</sup>Unit No. 0007: 96 starts and 21,705 sec of main stage operation (5538 sec at 100% RPL, 6700 sec at 104%, and 4695 sec at 109%).

per routine post-test chamber inspection procedures which removed direct surface indications of blanching. The remaining unblanched specimens showed faint indications of the over-land patterns observed on the 40K chamber.

#### Scanning Electron Microscopy

The unblanched samples from the SSME chamber do not show any of the worm holes or surface roughening observed in the 40K specimen, Figure 16. The surfaces show scratches running parallel to the chamber axis and may represent erosion from the combustion gas stream. The surface of a polished blanching area, Figure 17, shows an undulating morphology suggestive of general deformation. Several defects are present which may correspond to grain boundary cracks. Photomicrographs of a large longitudinal crack shows that the interior surface of the crack contains some of the characteristics of blanching "worm holes" (porosity), Figure 18. Significant surface damage was also observed in samples not identified as being blanching, Figure 19. Pitting or cratering has occurred which appears roughened with a suggestion of worm-holing.

#### Optical Metallography

Because of the post-test polishing, cross sections of reportedly blanching areas of the MCC specimens fail to reveal the porous layer noted in the 40K samples as expected. However, these samples show an enlarged surface grain and evidence of precipitate resolution in the vicinity of longitudinal cracks in blanching samples, Figure 20. Samples from the throat area specimens show "dog house" deformation with adjacent intergranular subsurface cracks, Figure 21. The subsurface cracks run parallel to the gas wall surface, and occur near the top of the coolant channels. They do not appear to be directly related to the amount of channel deformation but rather to be localized to several adjacent channels in the samples. Three of the four throat specimens supplied showed these subsurface intergranular cracks. Subsurface cracks were not observed in any other areas (cylinder, convergent, or nozzle), including blanching specimens. Several areas of crack coalescence were observed with associated surface craters or pits extending from the gas-side surface to the coalesced cracks, Figure 22. These craters seem to correspond to the crater/pits observed in the SEM photomicrographs, Figure 19.

#### C. TGA SURFACE STUDIES TESTS

##### Oxidizing - Reducing Conditions

A series of TGA tests were run by sequentially oxidizing with air and reducing NARloy-Z samples at various

temperatures. The oxidizing gas was air saturated with water at room temperature, and the reducing gas was hydrogen. The duration of the oxidizing atmosphere exposure was controlled by the specimen weight gain, typically a few tenths of a percent. Typical test data are shown on Figure 23. Subsequent SEM examination revealed several pertinent facts: (1) certain specimens oxidized to form a relatively thick coherent oxide scale, and subsequently reduction formed a continuous skin of copper over a partially reduced oxide subscale, (Figure 24), (2) specimens oxidized under less severe conditions, and then reduced, formed a porous surface (Figure 25). The porosity of these latter specimens was very similar to the blanching chamber specimens except for the size of the "worm holes". This porosity phenomenon was observed for several conditions as shown on Figure 26. The scale of the porosity was not always repeatable. Multiple oxidation/reduction cycles at conditions shown to produce the porous surface effect did not have the anticipated coarsening effect, Figure 27. Oxidation/reduction of OFHC copper, NARloy-A copper, and zirconium copper produced similar results, as shown in Figure 28.

The thin layer of metallic copper which formed on top of the oxide layer during the reduction cycle in certain of these tests would probably not form on a main chamber wall because of the high heat flux and wall shear conditions which exist in a rocket engine. Thus the tests in which a porous layer formed are considered more typical of actual main chamber surface conditions.

#### D. WALL DETERIORATION MECHANISMS

The two types of damage observed in the NARloy-Z 40K and full scale SSME chamber walls are: (1) longitudinal through-wall cracking associated with blanching, and (2) gas side surface pits and craters associated with subsurface cracks. Both forms of damage appear to be related to excessive wall temperatures, however, they are representative of different mechanisms and different conditions.

##### 1. Blanching And Cracking

The correlation between longitudinal cracking and blanching has been reasonably well established by the SSME MCC wall damage maps, Figure 1. Inspections of the cracked coolant channels have revealed the characteristic deformation referred to as "dog housing". Finite element stress analyses have demonstrated that this type of deformation is thermal ratcheting and is due to cyclic exposure to high wall temperatures and heat fluxes.

NARloy-Z, OFHC, zirconium copper, and NARloy-A specimens exposed to oxidizing, reducing, and

oxidizing/reducing environments show that the characteristic porosity of blached surfaces is due to exposure to oxidizing then reducing conditions, (Figure 28). Since the porosity formed in the TGA tests approximates the morphology of the blached surface, but not the severity, the exact mechanism of porosity formation is not known.

Copper exposed to oxygen will normally form cupric oxide,  $\text{CuO}$ . Cuprous oxide,  $\text{Cu}_2\text{O}$ , forms only at high temperature, Figure 5. A mixture of these two oxides can form either as a subscale below a continuous  $\text{CuO}$  layer, or if the combustion gas is highly turbulent and near stoichiometric so that the local wall mixture ratio oscillates. If these mixed oxides are exposed to hydrogen, for instance if the  $\text{CuO}$  scale spalls during fuel rich shutdown or if the mixture ratio at the wall fluctuates between fuel rich and oxidizer-rich values, then the different reduction kinetics of the two oxides, and/or the differential volume contraction of the two oxides during reduction could form the characteristic worm holes.

The inability of the TGA tests to reproduce the severity of the worm holing suggests that a rapidly fluctuating local gas mixture ratio is possibly the cause of the worm holes.

The metallographic analysis performed on the blached surface of the 40K subscale chamber has provided some indication that the temperatures at the blached walls are at least 1700 F, as indicated by the resolutioning of  $(\text{CuAg})_3\text{Zr}$  precipitates, Figure 15, and possibly greater than the melting point of copper (1981 F), as indicated by the unusual surface features, Figure 17. The severe porosity of the blached surfaces correspond to a very high roughness indicating that these surfaces probably have a higher heat transfer coefficient than smoother surfaces. NASA-LeRC test experience has shown that an increase in surface roughness to 300 microinches can increase the heat transfer coefficient by 24% (Ref. 2). Wall temperatures calculated by accounting for the effect of roughness on heat transfer coefficient fall short of the estimated temperatures of blached areas, Figure 29, but the effect of porosity was not accounted for in these calculations and it would tend to increase wall temperature even further.

Therefore, it appears that blanching roughness in itself does not cause longitudinal cracking but it does appear to produce locally high wall temperatures which lead to premature failure of copper chambers.

## 2. Pitting, Cratering, And Subsurface Cracks

The secondary form of damage observed in the SSME MCC is the pitting/cratering observed primarily in the SSME throat region. The surface pits appear to result from local melting of the surface over areas where subsurface intergranular cracks have coalesced to form a thermal barrier, Figure 21. Metallographic evaluation of the areas of subsurface cracking do not reveal the extreme temperatures (>1700 F) associated with blanching as evidenced by the lack of precipitate resolution observed in the blanched substrates. However, there does appear to be a correlation between wall temperature and stress, and subsurface cracking. Finite element stress model predictions indicate that the region of cracking corresponds to areas where the local stress exceeds the yield strength of the alloy.

The grain boundaries themselves do not appear embrittled, as witnessed by the bluntness of the cracks. The mechanism of subsurface crack formation is unknown. These cracks have not been reported associated with blanching, and therefore are not directly related solely to high stress and temperature. This type of damage may be some form of gradual hydrogen degradation of the alloy, but the effect has not been reported in the literature. While it is certainly secondary to blanching and longitudinal cracking, it represents a damage mechanism which may become more evident and life limiting if the blanching mechanism can be eliminated.

Similar but much more extensive subsurface cracks were observed to have developed in the nickel-plated SSME main chamber after it had been subjected to a series of test firings. In this chamber, the cratering was severe enough that 200-300 hydrogen leaks developed in the cooling channels (Ref. 1).

### E. METALLURGICAL CONCLUSIONS

The following conclusions can be made regarding the two types of copper chamber liner damage observed in the 40K subscale chamber and the SSME MCC.

#### Blanching/Longitudinal Cracking-

1. Blanching can be superficially described on the microscopic scale as severe interconnected porosity, with a surface roughness of approximately 400 microinch CIA.

2. Copper and copper alloys will oxidize at temperatures as low as 600 F, if free oxygen is available. The oxidation rates are exponential with temperature.

3. Blanching of copper and copper alloys is caused by an oxidation reduction reaction and is possibly associated with local fluctuations in the combustion gas composition which represent alternating oxidizing and reducing conditions.

4. Blanched areas are indicative of surface temperatures greater than 1981 F, and substrate temperatures greater than 1700 F.

5. Longitudinal cracking is caused by the high wall temperatures and increased heat transfer coefficient associated with blanching.

#### Subsurface Intergranular Cracking-

1. Subsurface intergranular cracks can coalesce sufficiently to reduce regenerative cooling efficiency locally which results in small burn through pits or craters.

2. Subsurface cracking is not associated with the extreme temperatures connected with blanching.

3. Cracked grain boundaries are not embrittled.

4. Subsurface crack coalescence appears to proceed very slowly.

5. Finite element modeling shows that wall temperatures of 1400 F result in operational stresses greater than yield in zones which correlate to areas of intergranular cracking.

#### IV. DESIGN CONSIDERATIONS

Avoidance of blanching is an important design consideration for high pressure oxygen/hydrogen engines, since blanching degrades chamber life significantly. Blanching results in porosity at the hot gas surface and a surface roughness of 300-400 microinches, compared to a nominal of 30-40 microinches. The porosity reduces wall conductance and the roughness increases the gas-side heat transfer coefficient. The result is higher wall temperature and a corresponding order of magnitude decrease in life. The actual life of the SSME chamber is 2-10 cycles. The previously predicted design life, excluding blanching effects, is 80-100 cycles at full power level (Ref. 4). Recent analyses at Aerojet yield non-blanching life predictions of 46 to 56 cycles (Ref. 5).

The results of our TGA tests and chamber sample analyses indicate blanching is caused by an oxidation-reduction



reaction. It will occur in copper and copper alloy chambers whenever free oxygen is present in the combustion gas adjacent to the wall and the wall is subsequently exposed to a fuel rich gas. To prevent blanching it is necessary to either eliminate the possibility of free oxygen at the wall or provide a means of protecting the wall from the oxygen.

At the range of temperatures a copper chamber wall can withstand, free oxygen does not exist in  $O_2/H_2$  combustion gas until the stoichiometric mixture ratio of 7.94 is exceeded. Due to high temperature dissociation effects, free oxygen and hydroxyl radicals are present in the SSME free stream combustion gas at mixture ratios as low as 6 as shown in Figure 30. During nominal SSME operation the chamber operates at an overall MR = 6, with MR = 4.5 at the wall due to peripheral film coolant and local mixture ratio adjustments. If the engine were operating as designed we would not expect blanching unless the free stream was so turbulent that it penetrated the boundary layer and impacted the wall before the rapid re-association reactions could occur.

Since the engine does blanch, this gives us evidence that free oxygen is present at the wall and that the wall mixture ratio is at least  $\geq 6$  and possibly  $>7.94$  depending on the extent of re-association. It is possible that local flow nonuniformities in the injector and upstream manifold exist that manifest themselves in locally high mixture ratios at the wall. It is considered unlikely that the injector element would produce the asymmetric blanching pattern noted in the chamber, although it is possible that local element to element fabrication tolerances could produce some mixture ratio variations. If the problem were inherent to the injector element type we would expect more uniform chamber blanching. Since the pattern is asymmetric (Figure 2) it is most likely produced by maldistributed flow generated in the upstream manifold where evidence of extreme turbulence currently exists, Reference 6.

In the design of future engines, both manifold and injector should be scrutinized carefully in light of the blanching phenomena. To avoid chamber blanching either the suspected cause of maldistributions must be eliminated or the chamber wall must be protected from the ox-rich gases, or both. The history of liquid rocket engine development shows it is difficult to produce a high performance injector which produces a perfectly uniform mixture ratio combustion gas. Consequently, both mixture ratio control and oxidation resistant coatings are recommended to eliminate blanching.

The gas mixture ratio at the wall can be controlled in a variety of ways: element type, element mixture ratio, film

coolant and manifold changes are typical. A benign, controllable injector element should be chosen at least at the injector periphery. This will help avoid oxidizer impingement on the wall. Fuel film cooling will help though may not be sufficient in avoiding the problem especially if it is manifold related. Significant amounts of film cooling will, of course, degrade performance. In conjunction with careful injector design the manifold should be given special attention to avoid nonuniformities and excessive velocities especially at the periphery. Analyses performed during Aerojet's Space Shuttle Engine Study indicate that, due to high cross flow gas velocities, the mixture ratio at the wall would be  $>7$  if film coolant were not injected. Flow straighteners and/or screens should be incorporated to ensure flow uniformity.

If the injector/manifold cannot be designed to inherently eliminate copper blanching then the chamber must be crutched to withstand it. Since test results indicate that oxidation-reduction surface damage will probably occur at temperatures  $\geq 600^{\circ}\text{F}$ , lowering the design wall temperature will probably not eliminate blanching, though it will raise the expected LCF and plastic instability life, and probably decrease the blanching rate. Smaller channels, and thermal coatings are desirable from this standpoint. The best single chamber design feature to minimize blanching effects would be the addition of an oxidation resistant treatment to the gas-side surface. Considerable development may be required to develop and minimize the risk of using oxidation resistant coatings. Past experience with the Nickel plated SSME indicates the potential for other unrelated problems to occur when coatings are applied.

#### V. RECOMMENDATIONS

1. A series of subscale tests to evaluate the interrelationship between element design, element mixture ratio, and blanching is recommended so that the conditions which preclude blanching can be identified and used to establish main injector design criteria.

2. The development of oxidation resistant coatings or surface treatments for copper alloy combustion chambers is recommended as a means to protect chamber walls from local non-uniformities which are difficult to completely avoid in a liquid rocket engine.

### Nominal Alloy Compositions

<u>Alloy</u>	<u>Cu</u>	<u>Ag</u>	<u>Zr</u>
NARloy-Z	96 min.	2.75 - 3.25	.30 - .55
NARloy-A	96.5 min.	3.25 - 3.75	-
Zirconium-Copper	99.8 min.	-	.13 - .20
OFHC	99.99 min.	-	-

### Acknowledgements

This work was performed on Contract NAS 8-36167 for the George C. Marshall Space Flight Center. The NASA program manager is Dick Counts. The materials testing and SEM work were accomplished through the efforts of Kent Schaplowsky, Jackie Cabeal, and Guy Sheble. Significant contributions were made by Dwayne McCay, Don Pryor, and Brian McPherson of MSFC.

### References

1. Personal Communication With Dick Counts, George C. Marshall Space Flight Center, July 1983 to April 1986.
2. Some Effects of Thermal-Cycle-Induced Deformation In Rocket Thrust Chambers, Ned P. Hannum and Harold G. Price, Jr., NASA Lewis Research Center, Tech. Paper 1834, 1981.
3. Failure Analysis of 40K Subscale Chamber Liner Cracks, NASA George C. Marshall Space Flight Center Memo by R. A. Pan, 8 Nov. 1976.
4. SSME Main Combustion Chamber Life Prediction, NASA CR-168215, NAS 3-23256, May 1983.
5. Monthly Status Report M-7, Contract NAS 8-36167, Aerojet TechSystems Company, Feb. 1986.
6. Duct Flow Nonuniformities Study Final Report (Draft), 10 June 1983, RI/RD83-160.

ORIGINAL PAGE IS  
OF POOR QUALITY

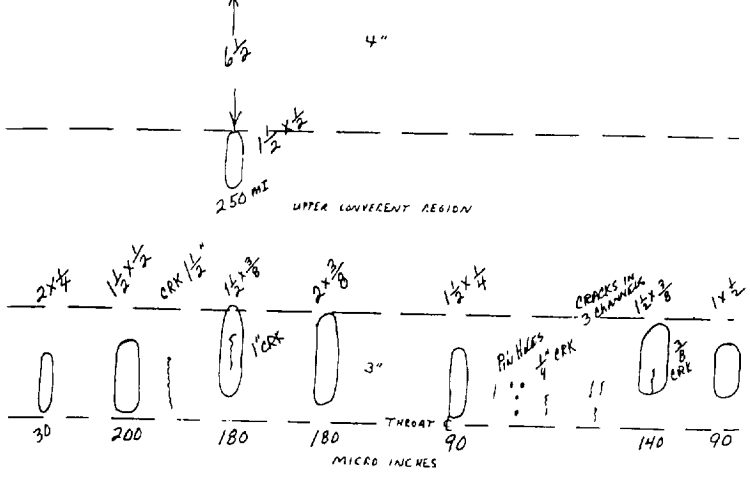
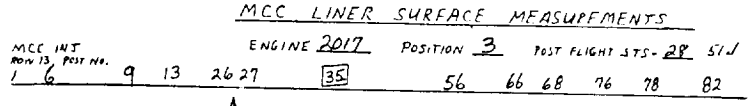
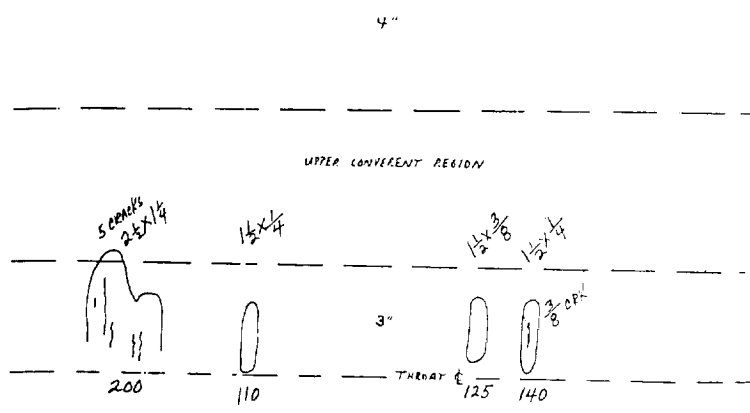
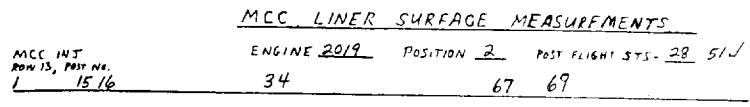
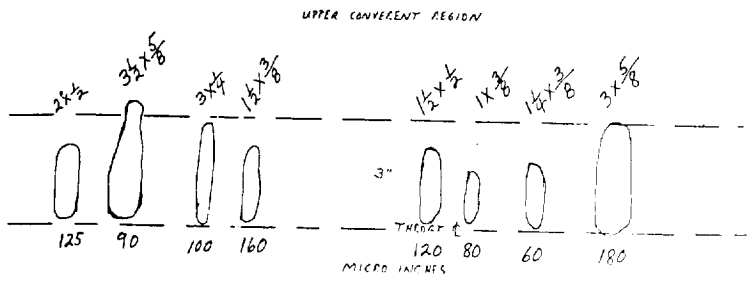
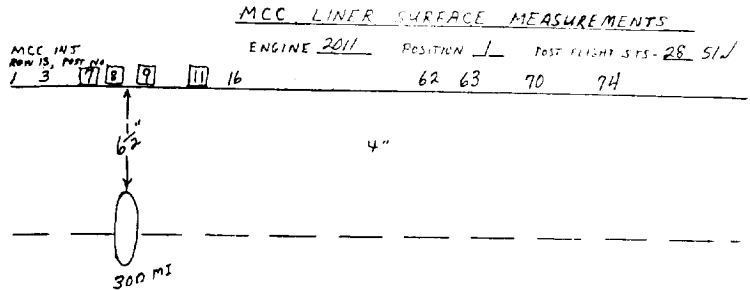


Figure 1

ORIGINAL DESIGN  
OF POOR QUALITY

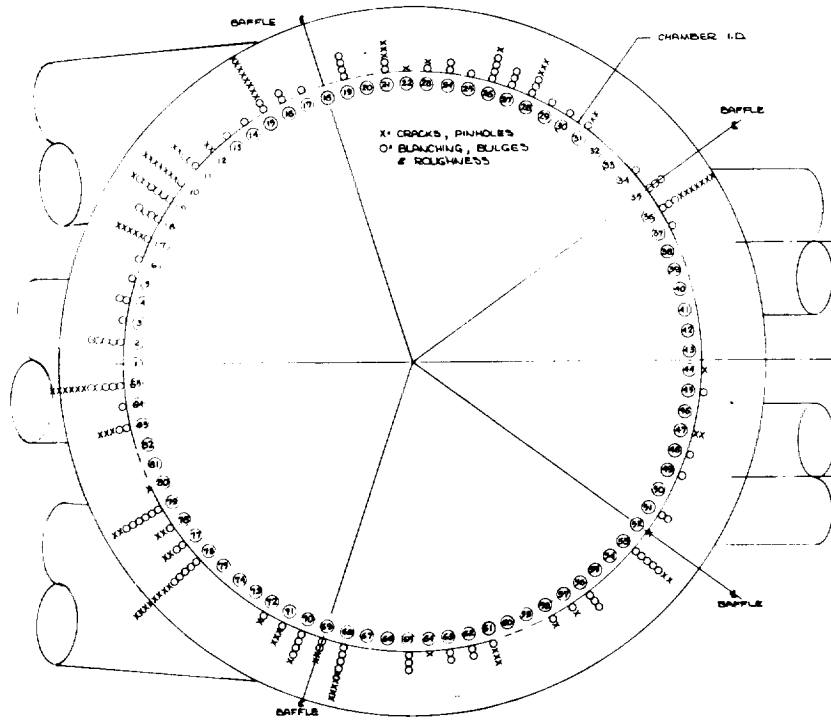


Figure 2

SSME Chamber Blanching and Crack Locations, 1979-1984

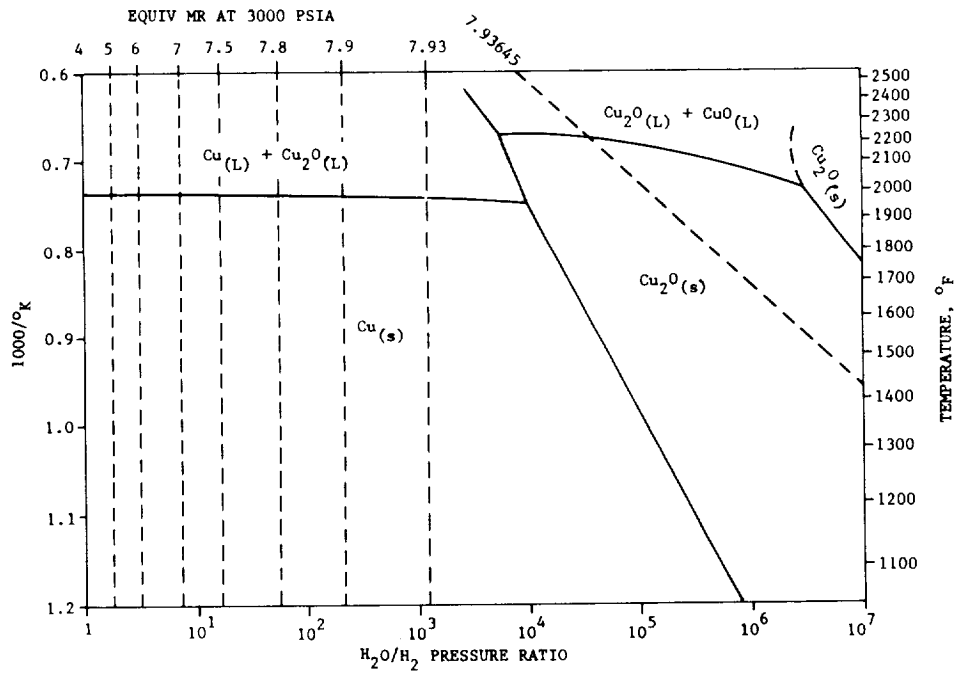


Figure 3

Stability Diagram For Copper in the Presence of  
 $H_2O/H_2$  Containing Atmospheres

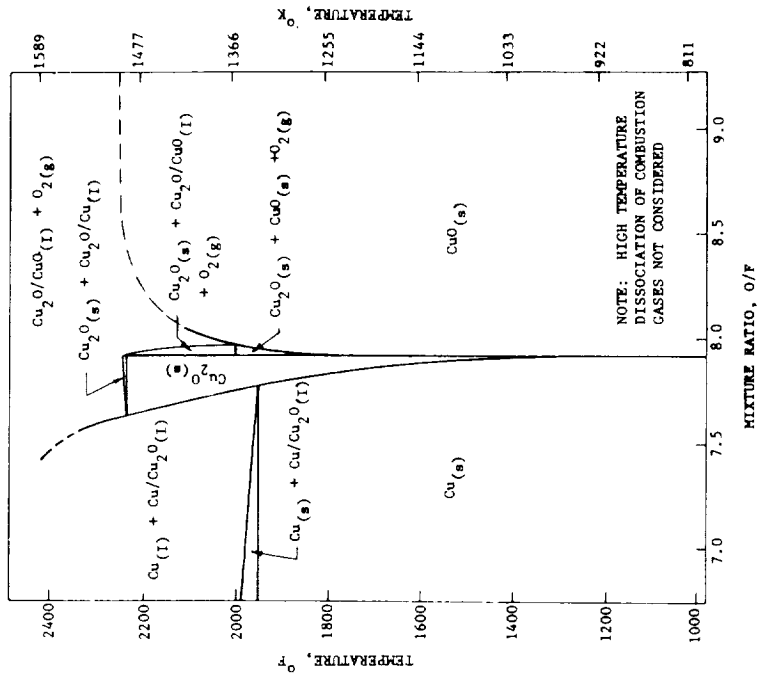


Figure 5

Predictions of the Stable Cu-O Phases in the Presence of  $O_2/H_2$  Combustion Products at 3000 psia

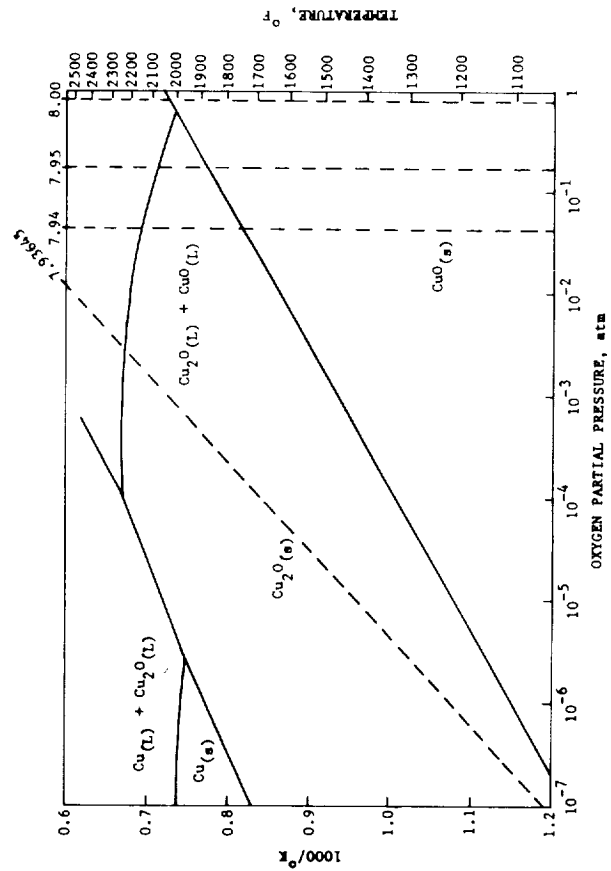


Figure 4

Stability Diagram For Copper in the Presence of Oxygen Containing Atmospheres

CONFIDENTIAL  
 OF HIGH QUALITY

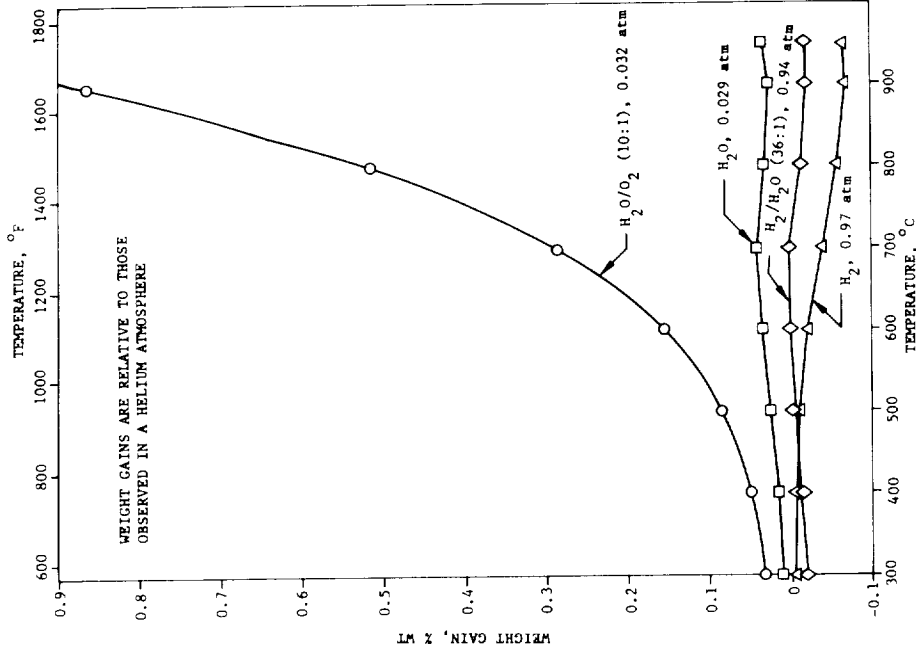


Figure 7

Effects of Temperature and Gas Composition  
 on NARloy-Z

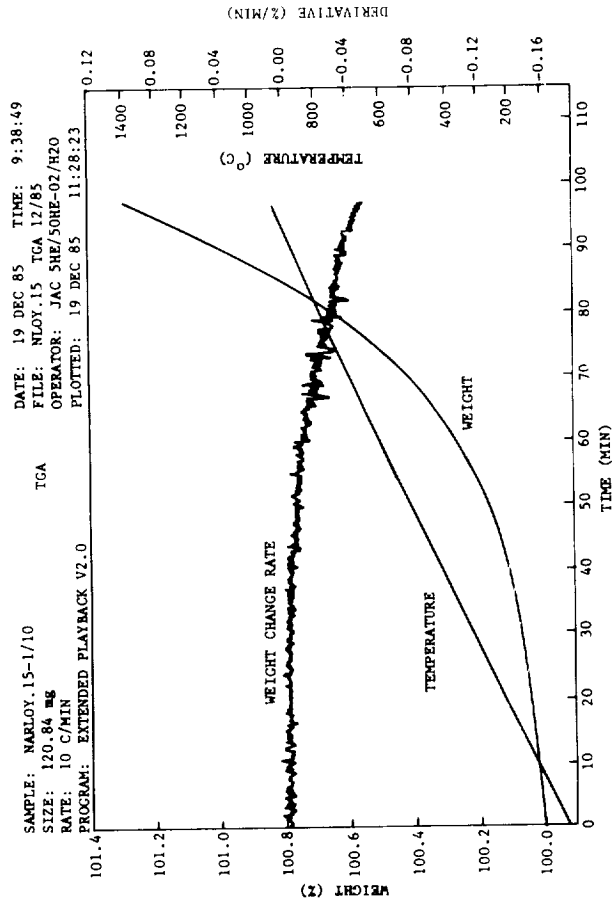


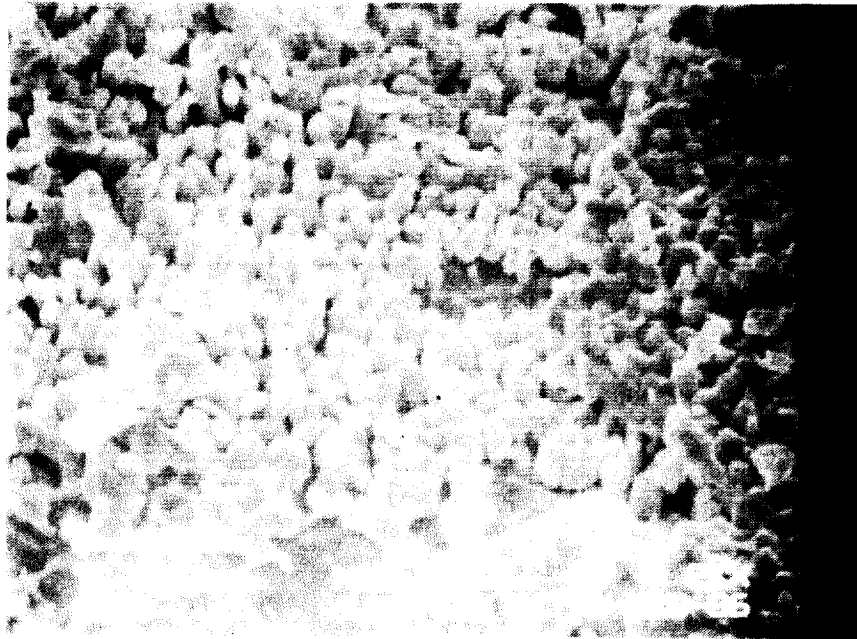
Figure 6

TGA Test Data, Ramped Temperature Tests

OF POOR QUALITY



MAG 2000X



MAG 2000X

Figure 8

The TGA Specimen Exposed to Just a Reducing Environment Shows a Reasonably Smooth, Undulating Surface (Top), While an Oxidized Specimen Shows a Granular Surface (Bottom).



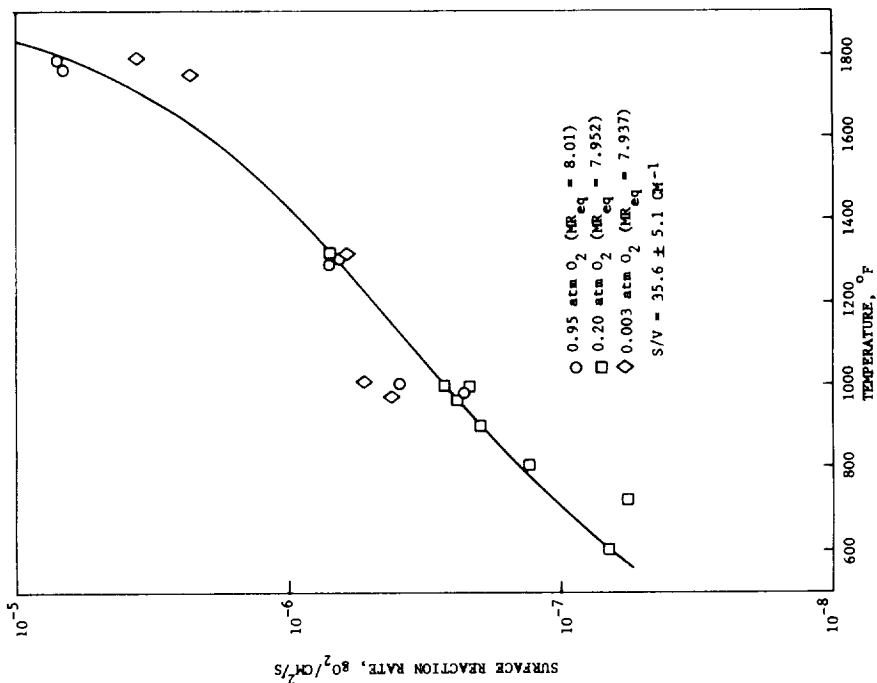


Figure 10  
NARLOY-Z Oxidation Rates

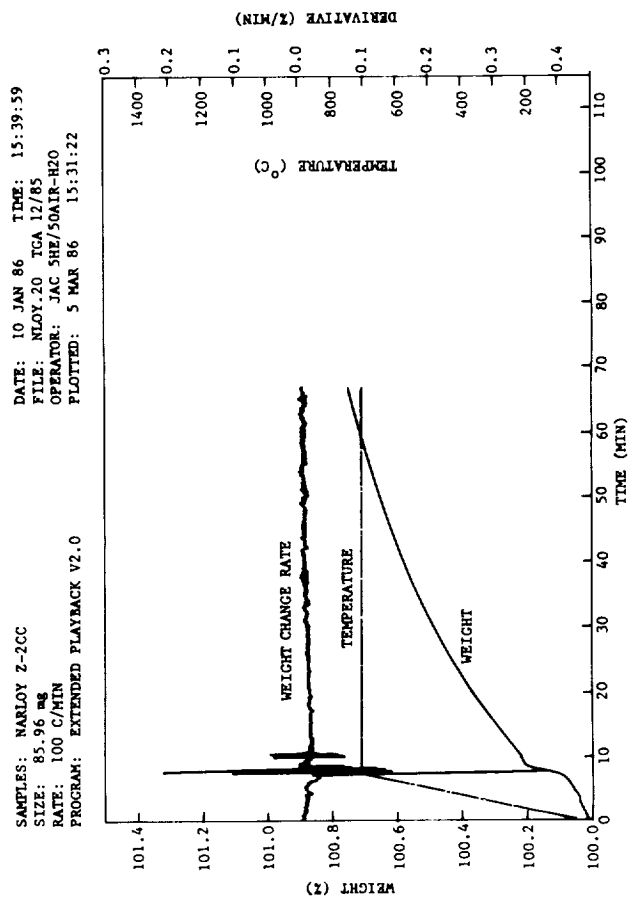
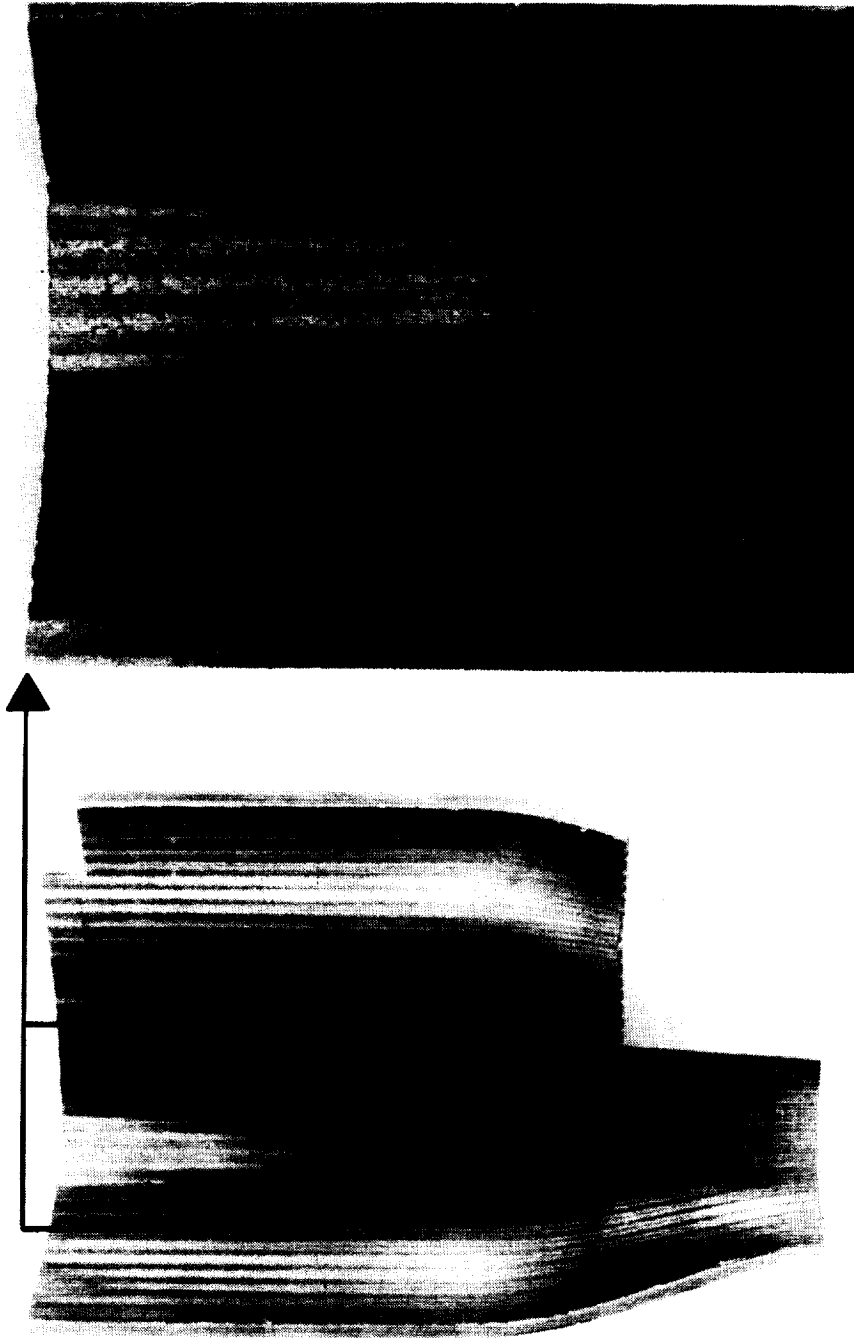


Figure 9  
TGA Test Data, Oxidation Rate Test



MAG 1.5X

MAG 0.6X

Figure 11

An Intact Segment of the 40K Subscale Was Supplied by NASA For Analysis (Left Photo). The  
Blanching Area (Right Photo) is a portion of the Area Analyzed by NASA (Ref 3). Parallel  
Vertical Lines Are Rough Areas Over Lands, Alternating With Smooth Areas Over Channels.

ORIGINAL PHOTO IS  
OF POOR QUALITY

SEM IMAGES CHARACTERIZING SURFACE MORPHOLOGY OF CU/AG/ZR ALLOY SECTIONS FROM  
A 40K SUB-SCALE CHAMBER - AREA #10

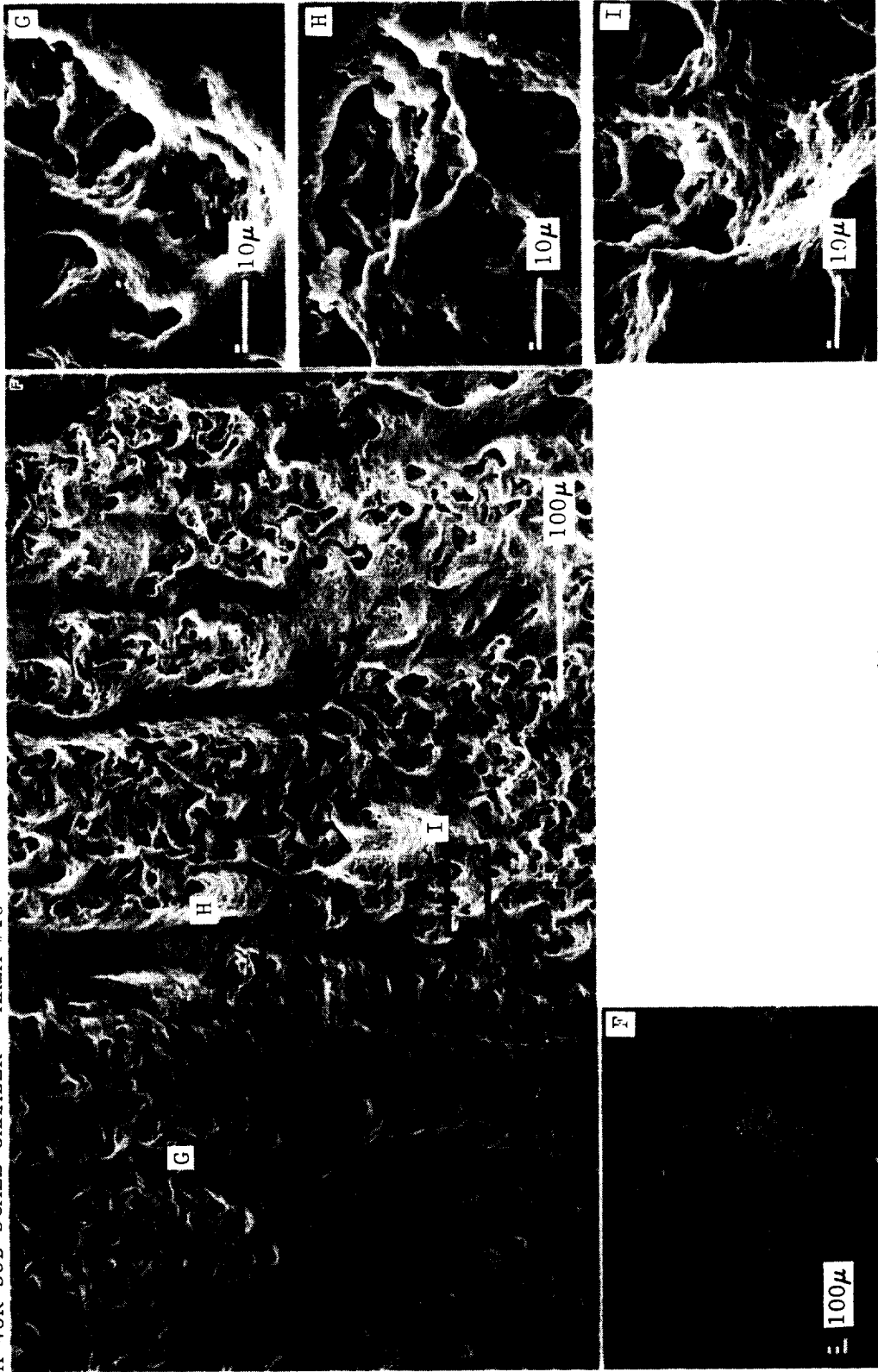


Figure 12

A Typical Blanched Area on the 40K Chamber Specimen is Characteristically a Network of Interconnected Porosity, Overlaid by Streaks of Solid Material Which Appears to Have Been Molten.

SEM IMAGES CHARACTERIZING SURFACE MORPHOLOGY OF CU/AG/AR ALLOY SECTIONS FROM  
A 40K SUB-SCALE CHAMBER - AREA #9

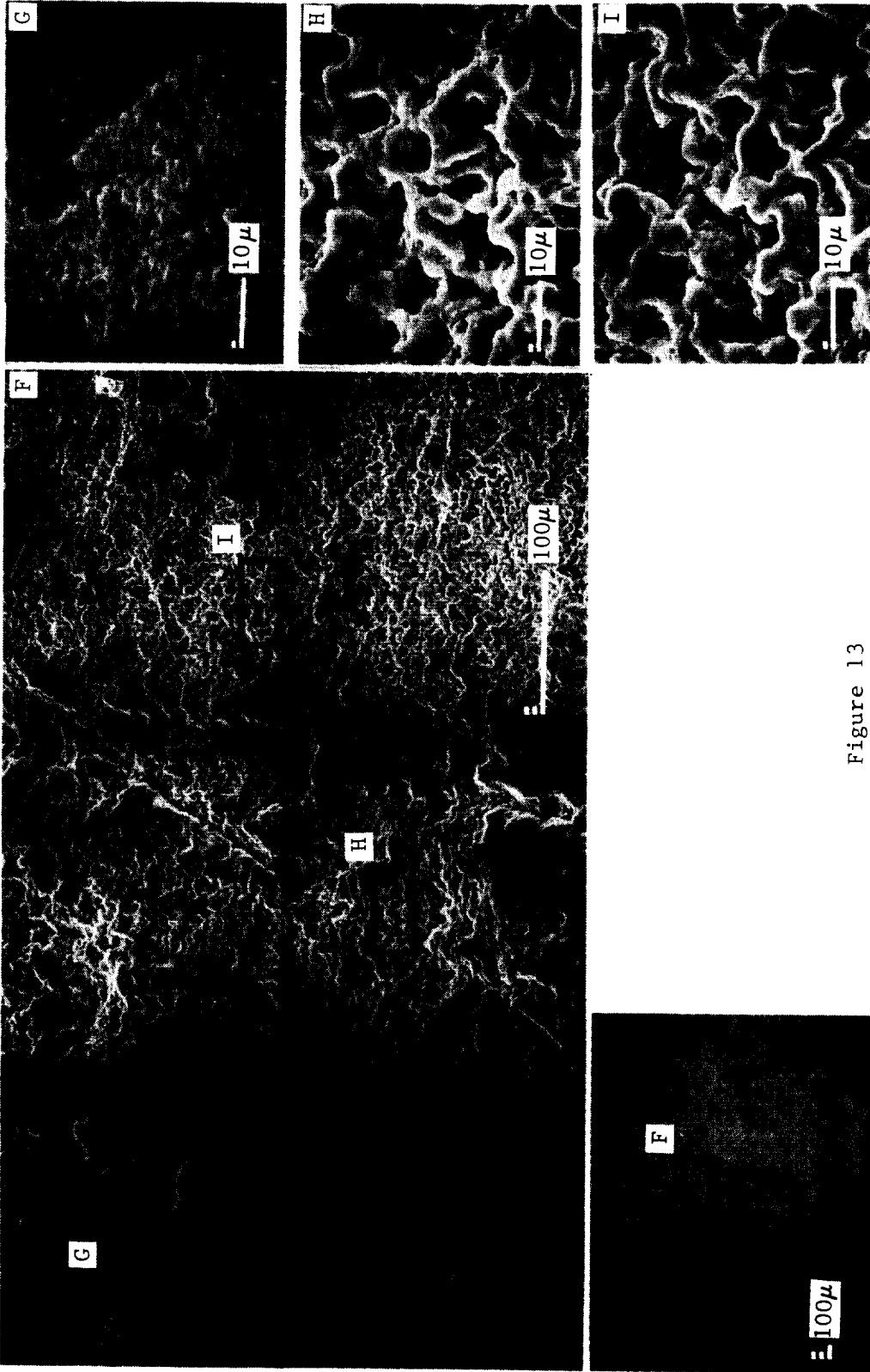


Figure 13

Typical Unblanched Regions on the 40K Chamber Show Smooth Surfaces Over Channels, and Rough Surfaces Over Lands. The Rough Surface Morphology Appears Similar to Blanching, But is Much More Sharply Delineated.

ORIGINAL PAGE IS  
OF POOR QUALITY

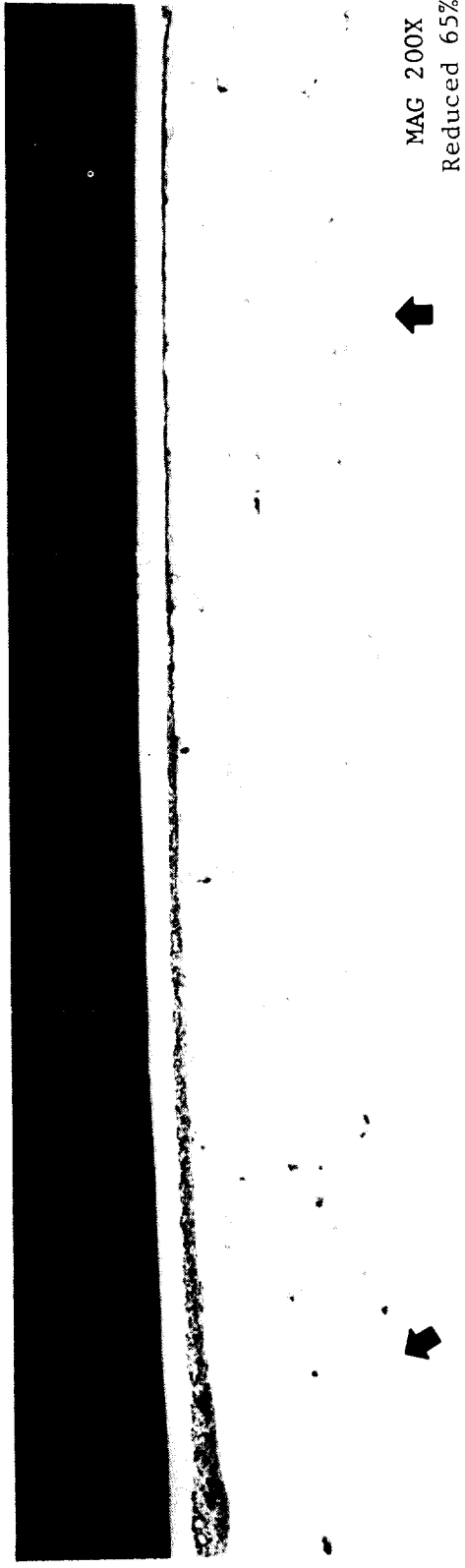
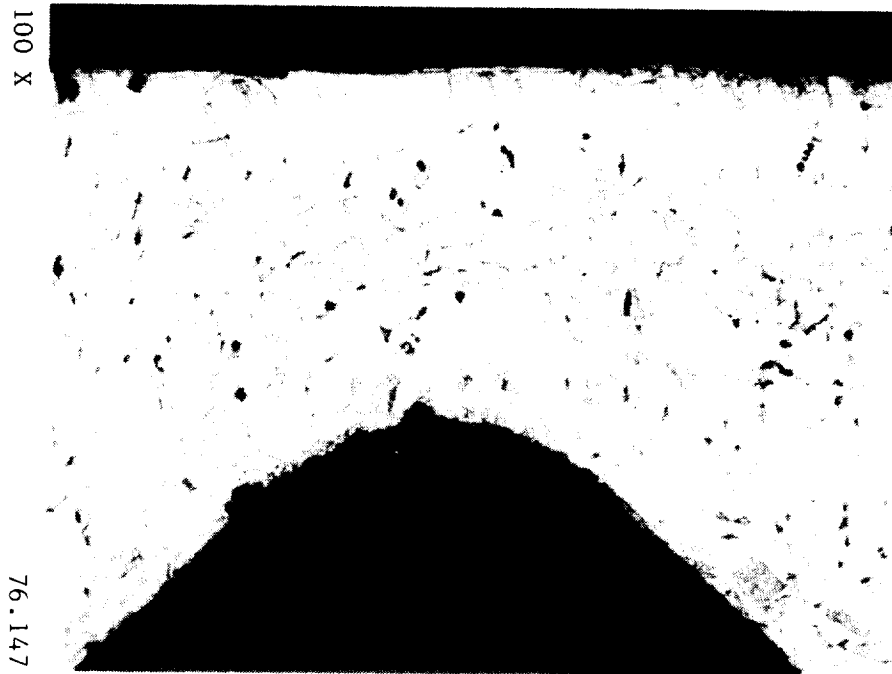


Figure 14

A Cross Section Through the Blanched Area of the 40K Specimen Shows the Maximum Depth of the Porous Layer (0.0015") and the Tapering Thickness From the Center of the Land (Left Arrow) to the Center of the Adjacent Channel (Right Arrow). The White Layer Overlaying the Porosity is Electroless Nickel Deposited For Edge Retention During Preparation.

ORIGINAL PAGE IS  
OF POOR QUALITY



100 X

76.147

Figure 15

The Original Square Bottom Channels of the 40K Specimen Have Been Severely Deformed in the Blanched Region to Form the Characteristic Pointed "Dog House" Deformation. The Large Grain Size and Lack of Precipitates at the Gas-Side Wall Surface Indicate Metal Temperatures Greater Than 1700<sup>o</sup>F, the Solution Temperature of NARloy-Z.

ORIGINAL PAGE IS  
OF POOR QUALITY

SEM IMAGES CHARACTERIZING SURFACE MORPHOLOGY OF CU/AG/ZR ALLOY SECTIONS  
FROM THE SHUTTLE MAIN ENGINE - #1

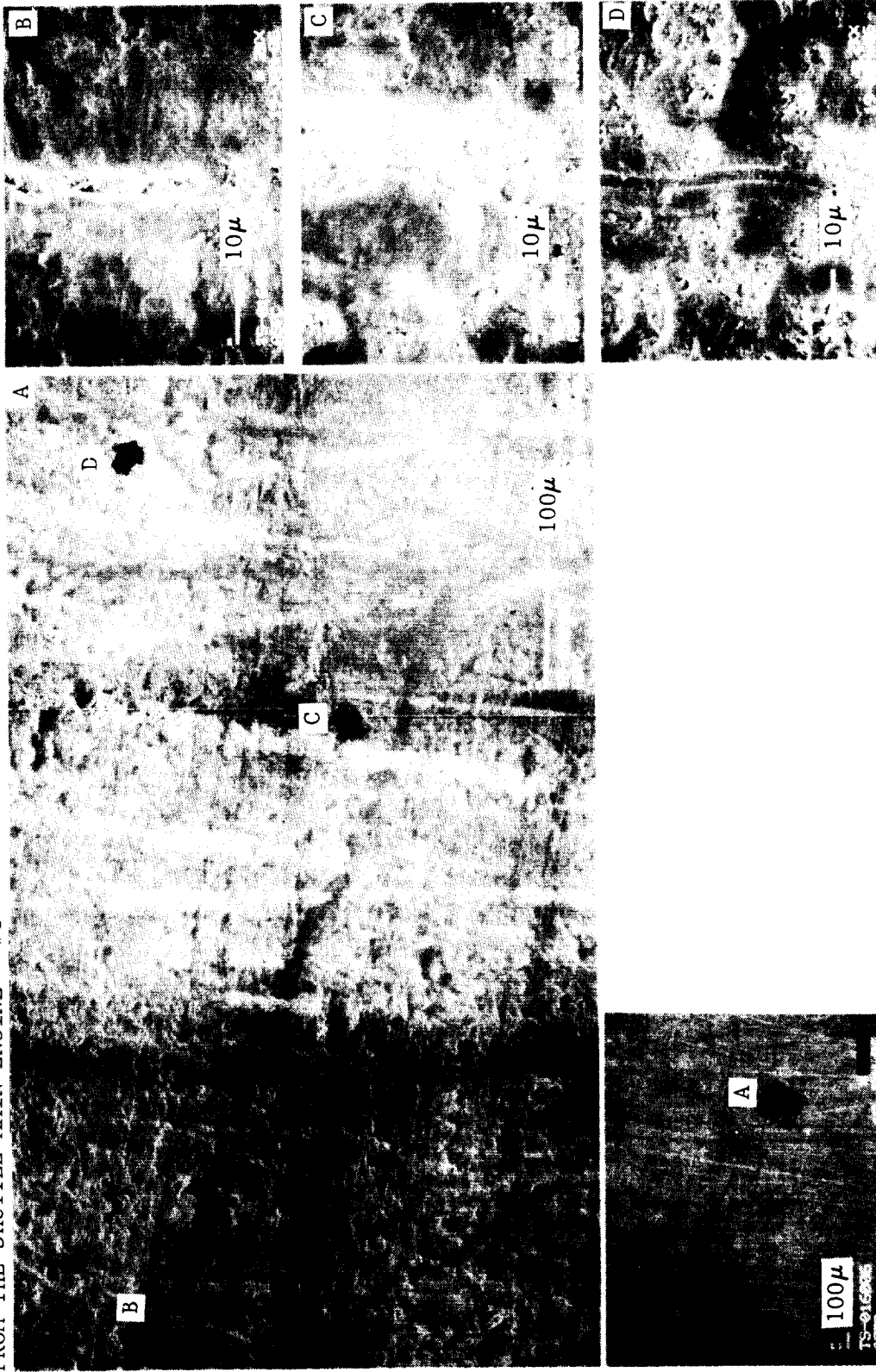


Figure 16

The Surface of an Unblanched, Unpolished Area From the Cylindrical Section of the SSME MCC Shows Vertical (Longitudinal) Lines From Gas Erosion. The Slight Surface Roughening Does Not Appear Significant.

SEM IMAGES CHARACTERIZING THE SURFACE MORPHOLOGY OF CU/AG/ZR ALLOY SECTIONS FROM THE SHUTTLE MAIN ENGINE - #3

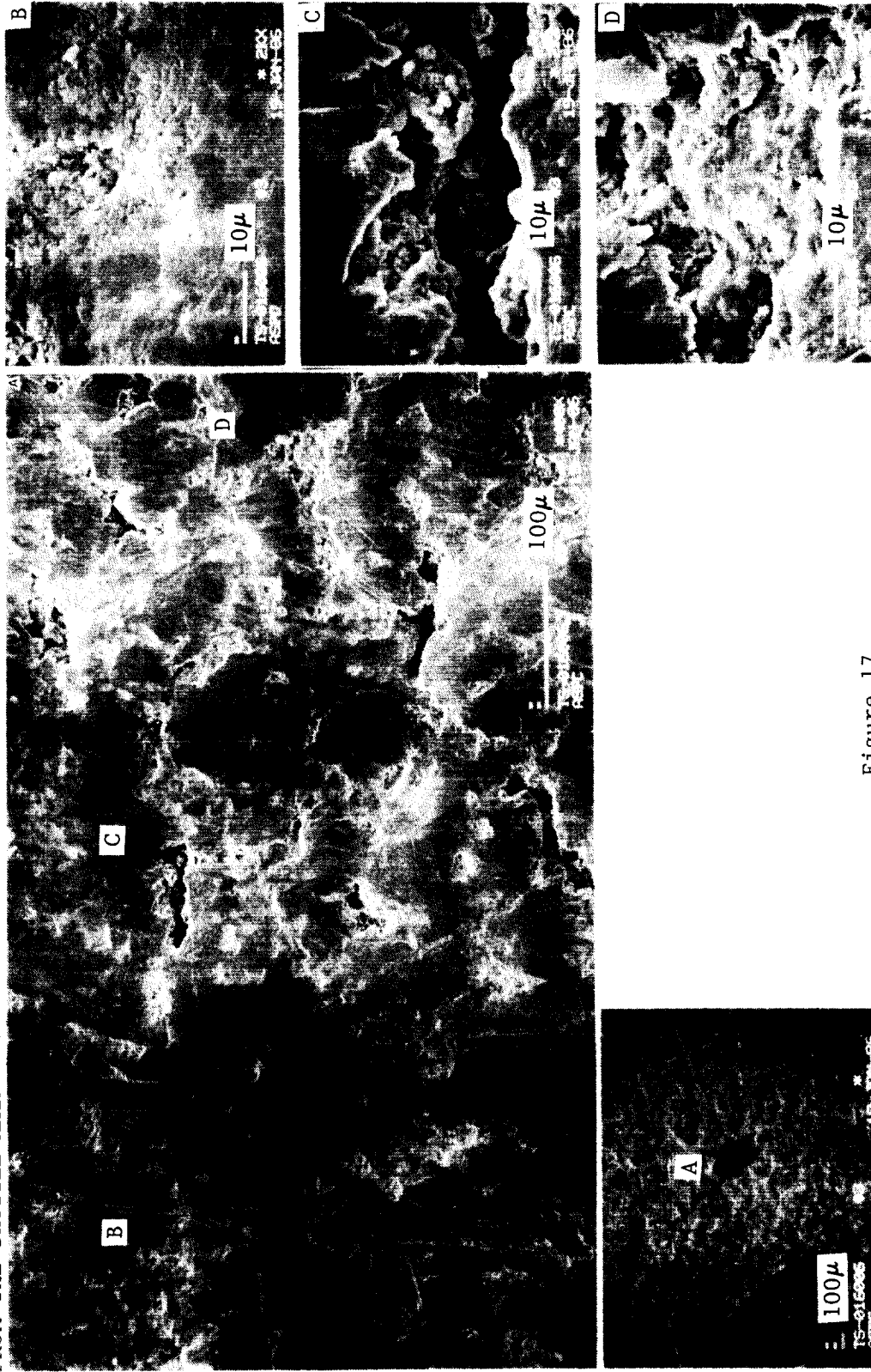


Figure 17

Post-Fire Polishing has Removed Most Indications of Blanching From This Convergent Section Specimen. Most of This Surface Represents Material Removal and Some Metal Smearing. The Transverse Defects Appear to be Shallow Surface Intergranular Cracks.



SEM IMAGES CHARACTERIZING THE SURFACE MORPHOLOGY OF CU/AG/ZR ALLOY SECTIONS  
FROM THE SHUTTLE MAIN ENGINE - #5A

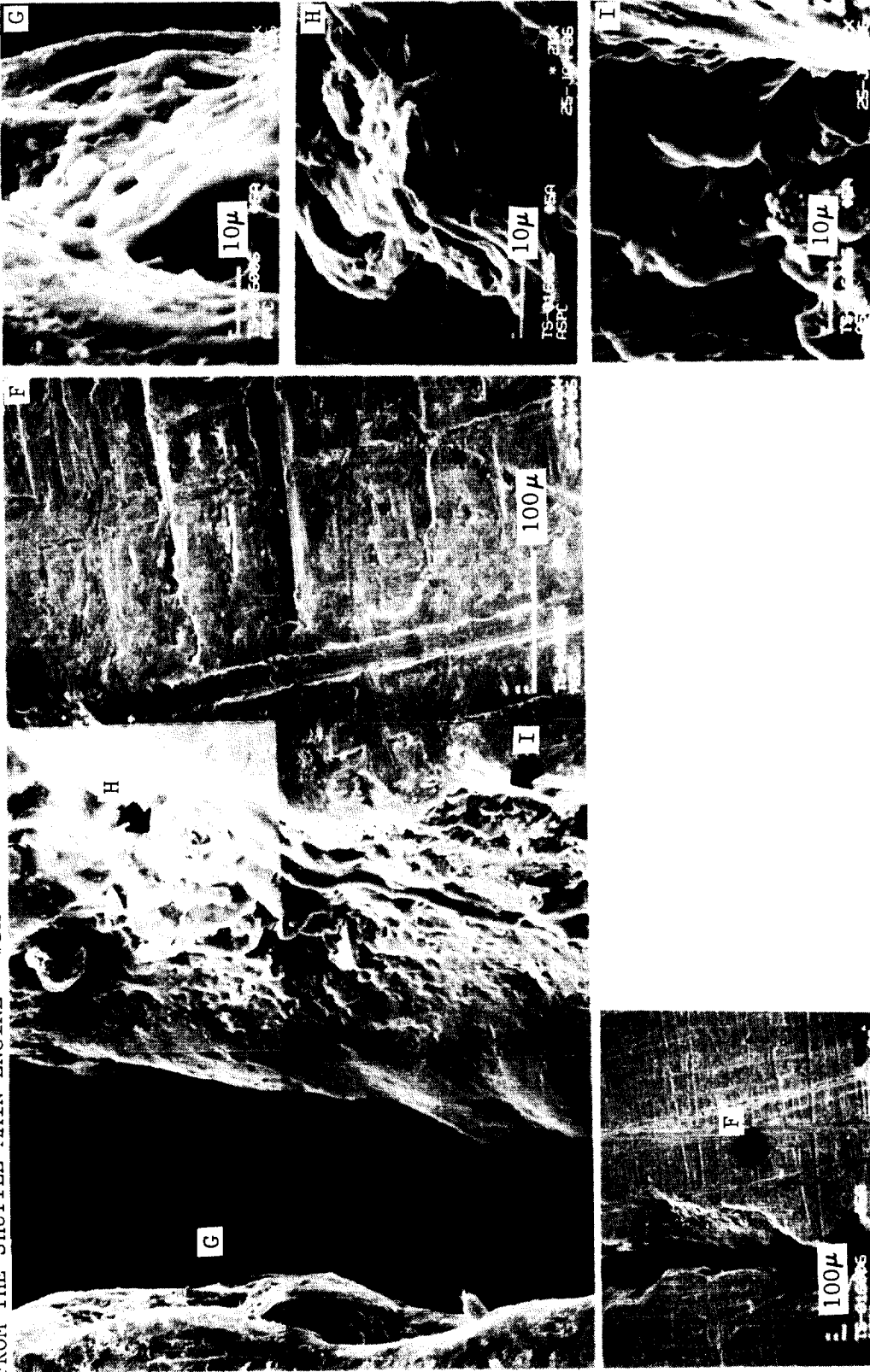


Figure 18

The Interior Surface of a Large Longitudinal Crack Shows Some of the Features of Blanching (Area "I").

SEM IMAGES CHARACTERIZING THE SURFACE MORPHOLOGY OF CU/AG/ZR ALLOY SECTIONS FROM THE SHUTTLE MAIN ENGINE - #9

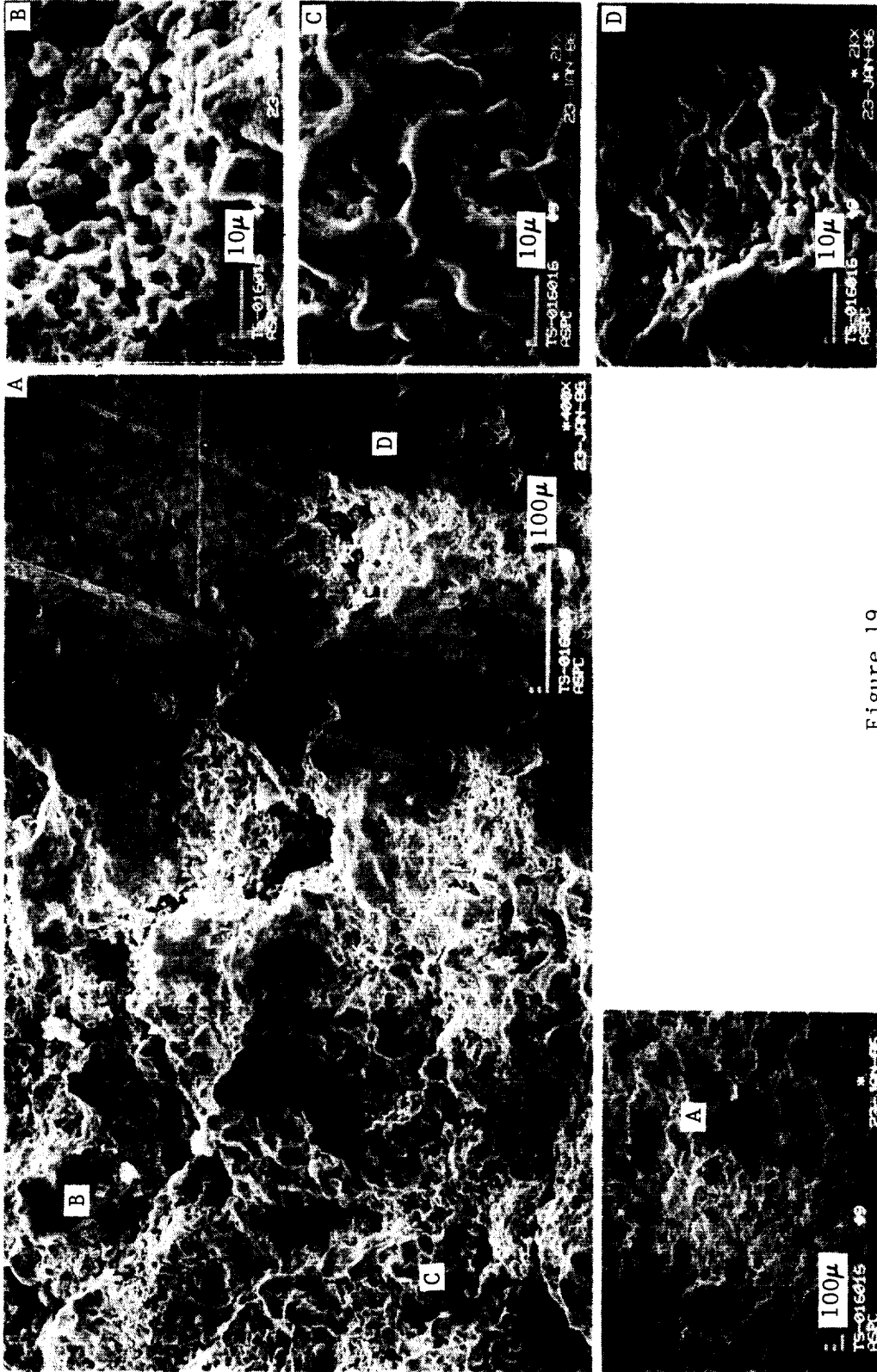


Figure 19

This Throat Region Specimen was Identified as Being From an Unblanched Area. The Roughness is Characteristic of Blanching, but the Localized Depth of the Defects Appears to be a Typical.



MAG 100X

Figure 21

A Throat Region Specimen from the SSME MCC Identified as Unblanched showed "Dog House" Deformation and Subsurface Intergranular Cracks. Grain Size and Alloy Precipitates Suggest that the Gas-Side Wall Temperature did not Reach 1700°F.



MAG 100X

Figure 20

A Cross Section of a Longitudinal Crack in a Convergent Region Specimen from the SSME MCC shows Grain Growth and Precipitate Resolution (Solid Arrow). The White Surface Layer is Electroless Nickel as in Figure D14.



MAG 100X

Figure 22

In Some Throat Areas the Intergranular Cracks have Grown and Coalesced to the Point where Regenerative Cooling Efficiency Dropped and Craters were Burned through to the Crack Depth (Arrow). The White Material in the Crater is Electroless Nickel.

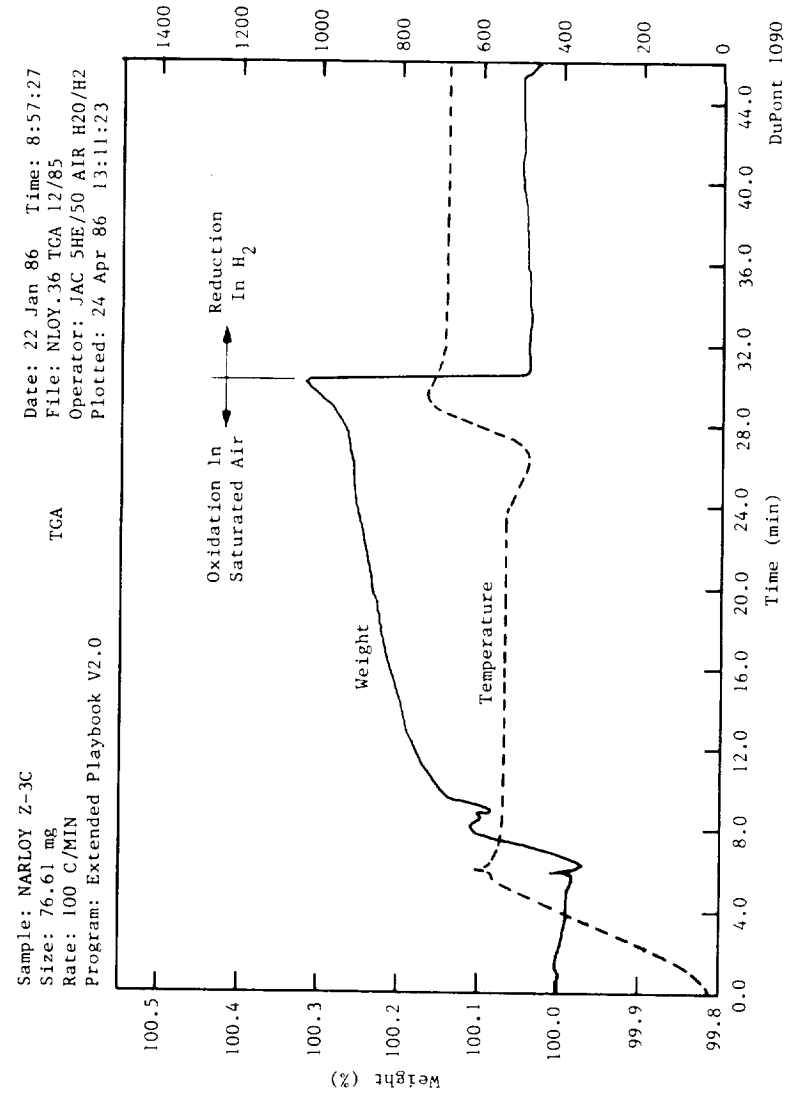
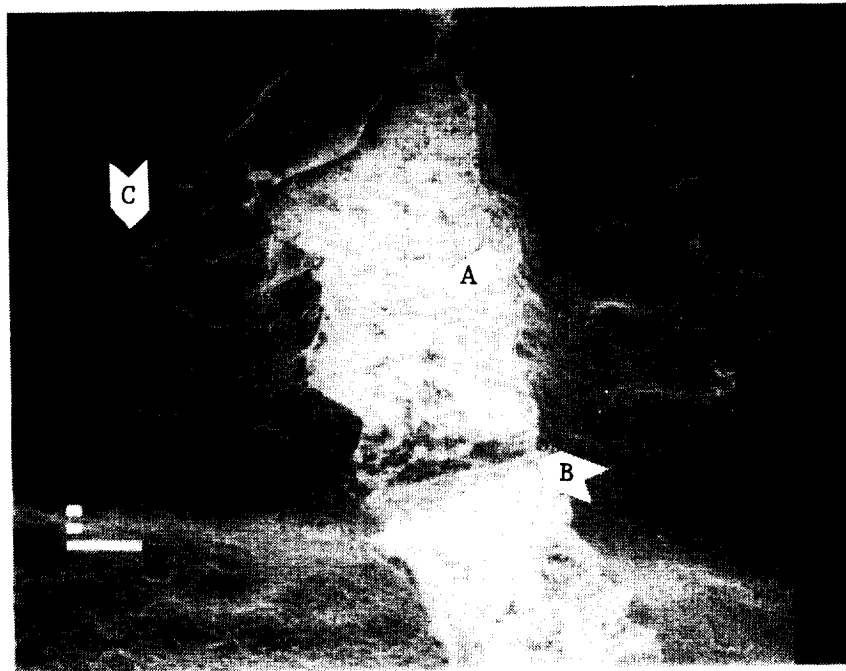


Figure 23  
 TGA Test Data, Oxidation-Reduction Test

ORIGINAL PHOTOGRAPH  
OF POOR QUALITY



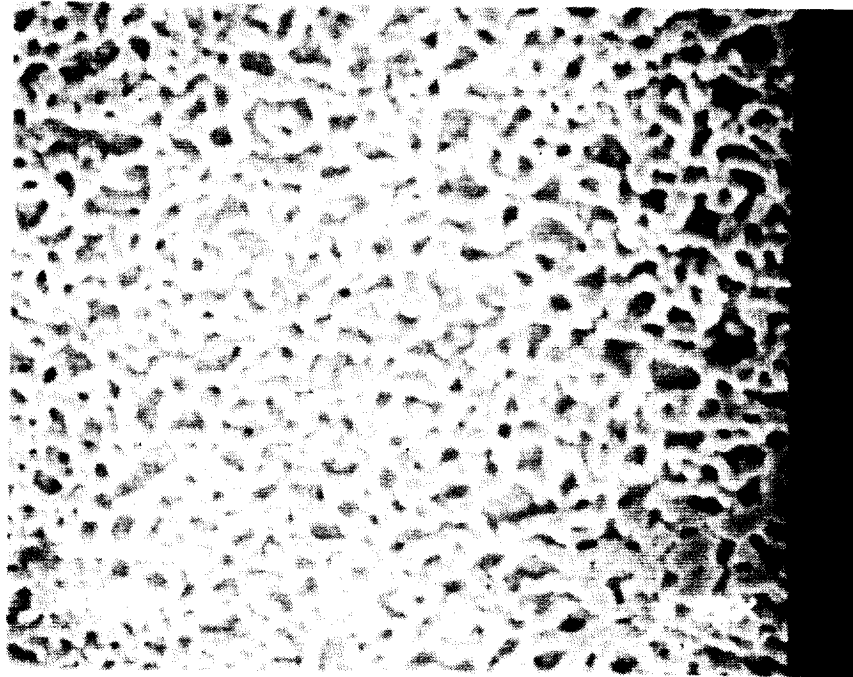
MAG 100X

Figure 24

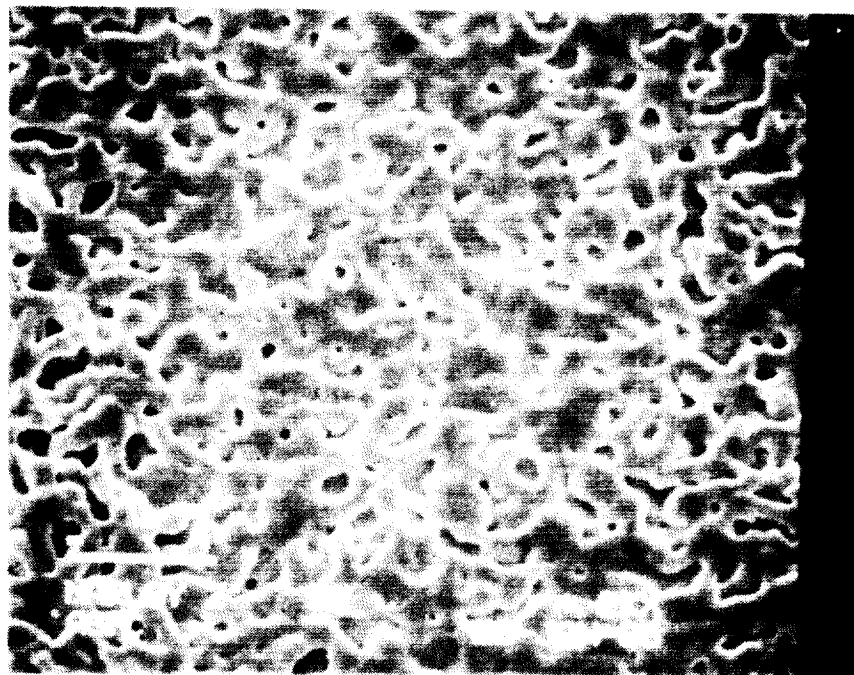
A TGA Specimen Oxidized at  $1000^{\circ}\text{F}$  and Reduced at  $1600^{\circ}\text{F}$  Shows a Granular Oxide Layer (A) Below a Continuous Copper Skin (C).

The Copper Skin Has Been Locally Peeled Back (B) to Reveal the Subscale.

ORIGINAL COPY  
OF POOR QUALITY



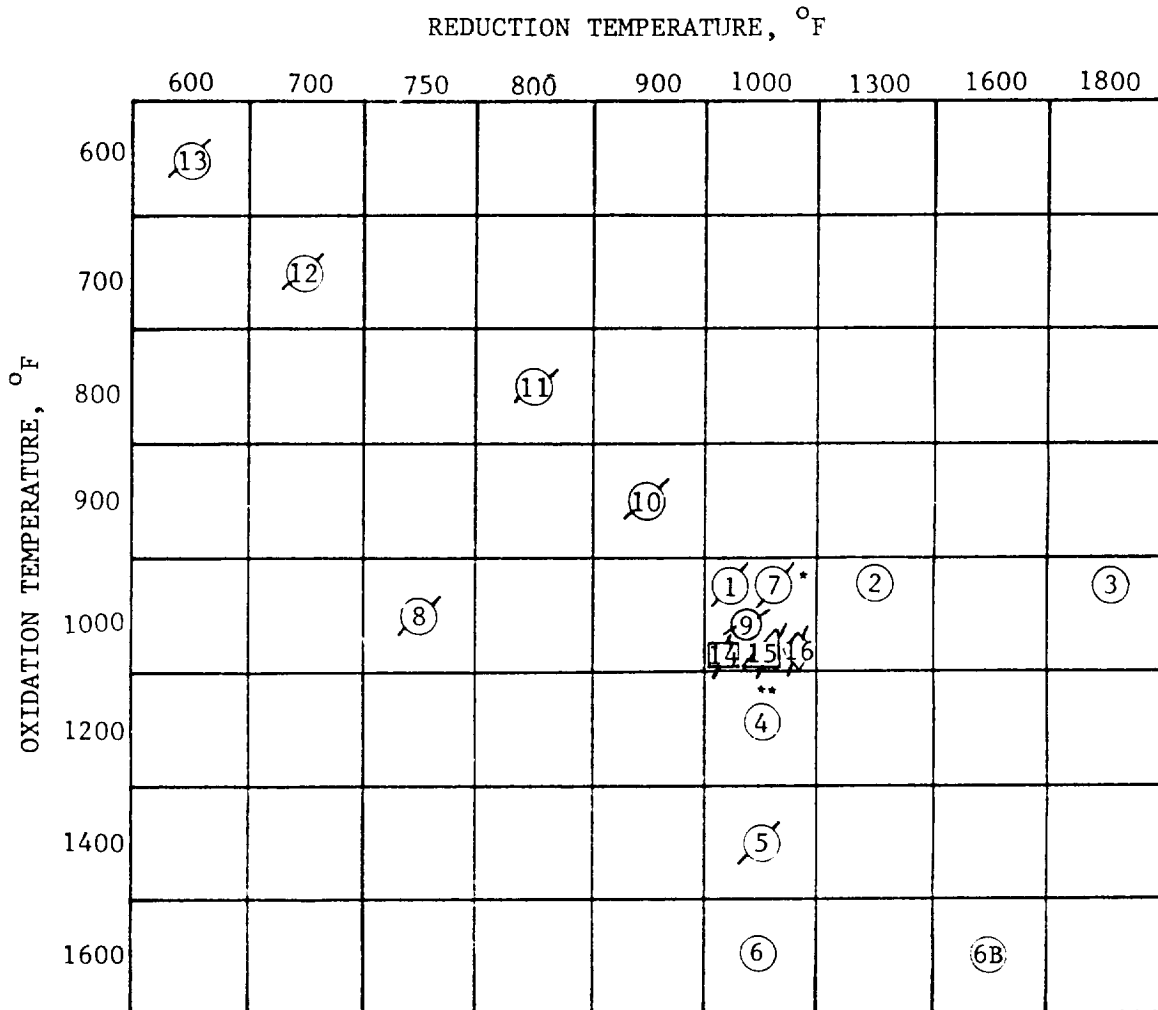
MAG 2000X



MAG 2000X

Figure 25

TGA Specimens Oxidized at 1000°F and 1400°F, and Then Subsequently Reduced at 1000°F (Top and Bottom Respectively) Show a Fine Network of Interconnected Porosity Very Similar in Appearance to Blanching.



\*\* SMOOTH LAYER ON TOP OF POROUS LAYER

\* FINER GRAIN THAN 1

NO. OF CYCLES : 7 - 5 CYCLES

ALL OTHERS - 1 CYCLE

Ø INDICATES SURFACE DAMAGE, POST-TEST

SYMBOL - ○ □ ▽ ◇

MH - NARloy-2 OFHC ZrCu NARloy-A

Figure 26

TGA Oxidation-Reduction Test Matrix

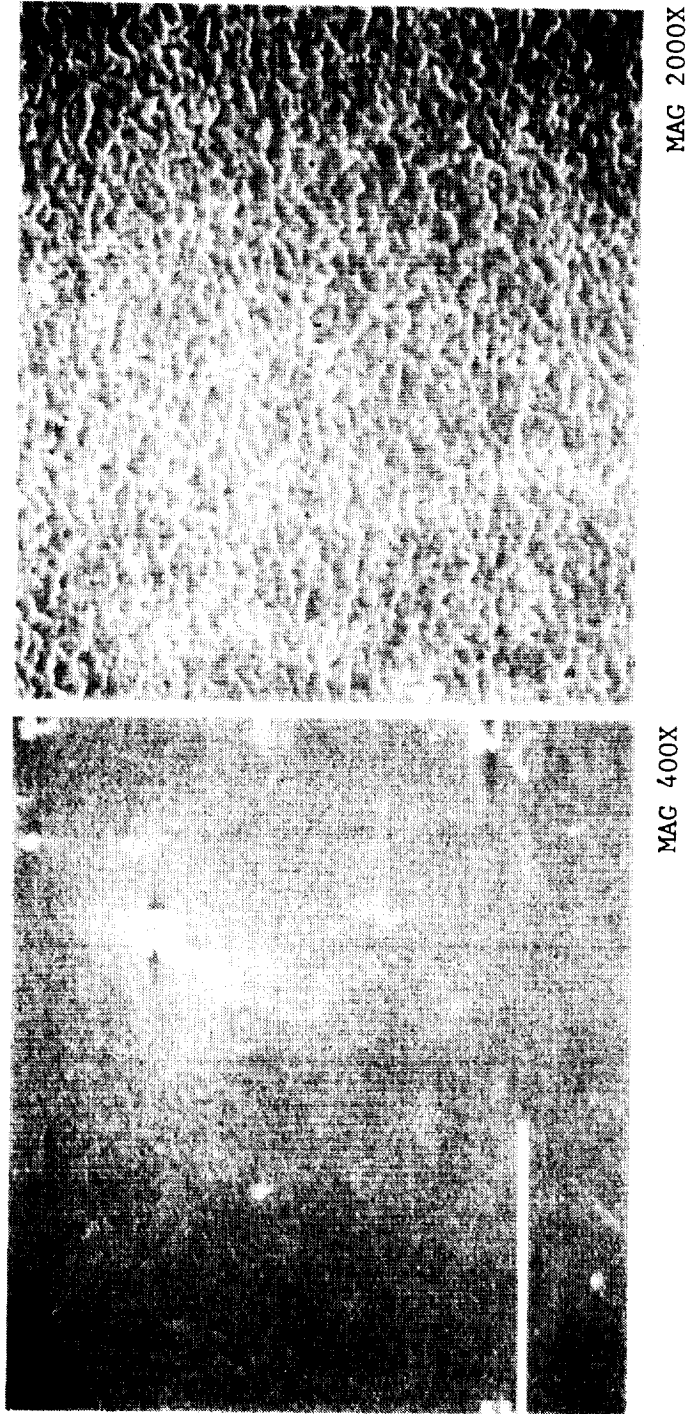
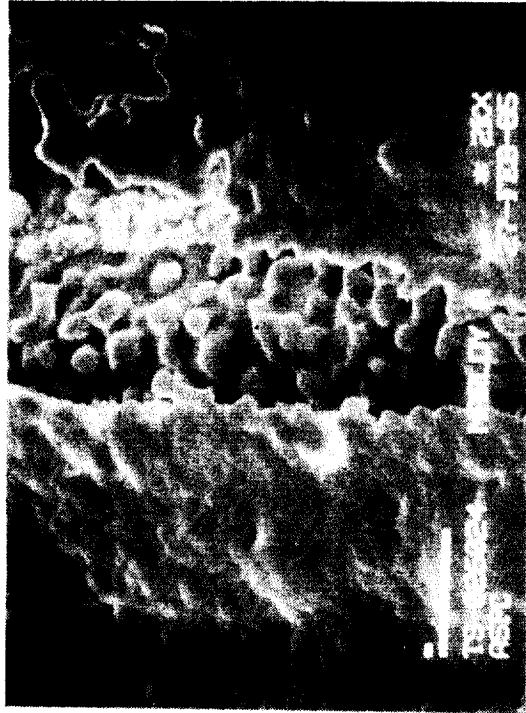


Figure 27

A TGA Specimen Oxidized and Reduced at 1000°F Five Times Does Not Show an Increase in the Severity of Porosity. The Surface Morphology is Somewhat Different From a Single Oxidation/Reduction Cycle at 1000°F (See Figure Q25), and May Represent a Copper Skin Surface.



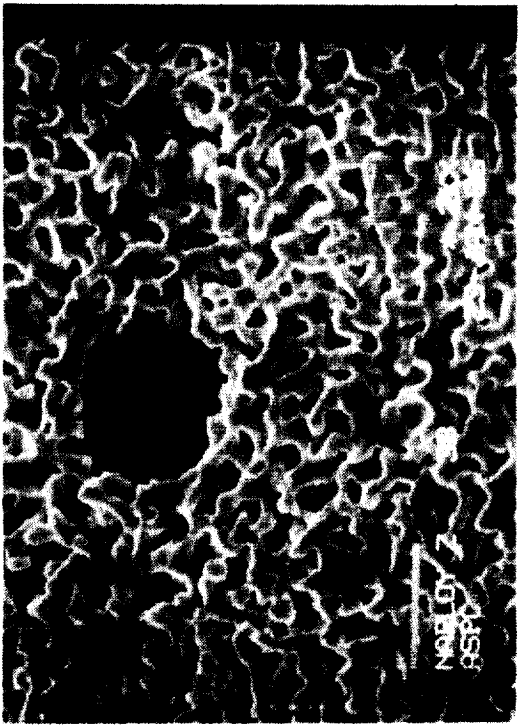
CRITICAL POINT  
OF POOR QUALITY



NARLOY A  
MAG 2000X



ZrCu  
MAG 2000X



NARLOY Z  
MAG 2000X



OFHC Cu  
MAG 2000X

Figure 28  
NARloy Z, NARloy A, OFHC Copper, and Zirconium Copper Oxidized and Reduced at 1000°F All Show  
Some Indications of Surface Features Similar to Blanching (83% Reduction)

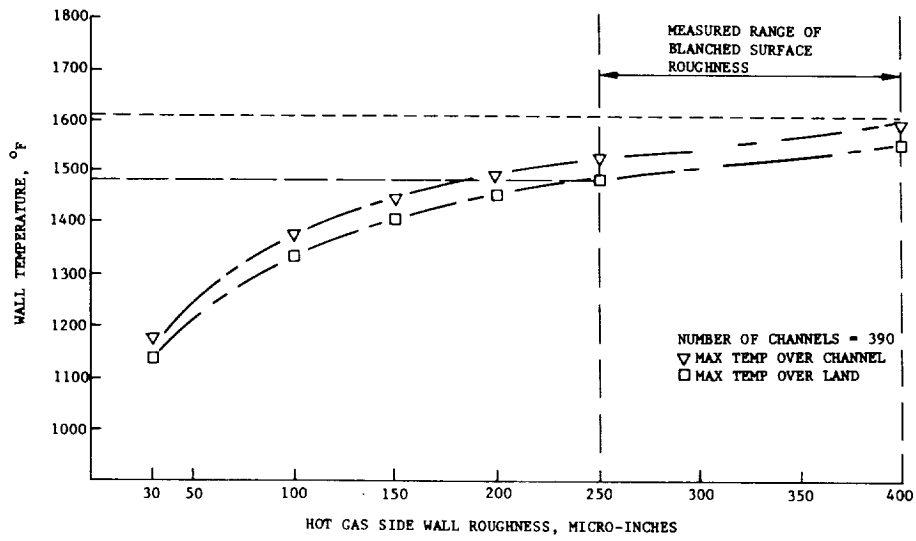


Figure 29

Gas Side Wall Temperature vs Hot Gas Wall Roughness Predictions

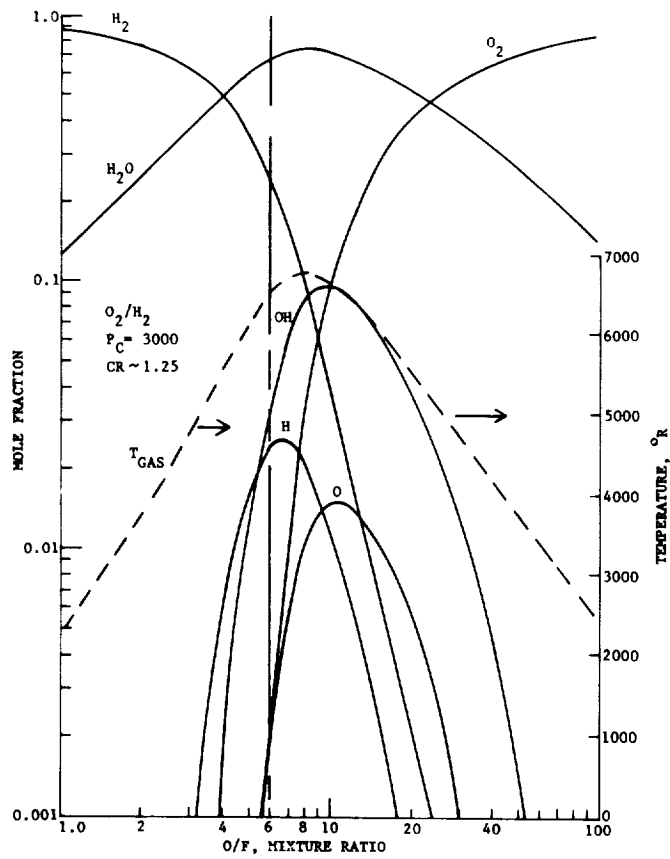



Figure 30

Chemical Composition of  $O_2/H_2$  Combustion Gases (High Temperature Dissociation Effects Included)



HYDROGEN ENVIRONMENT EMBRITTLEMENT IN ADVANCED  
PROPULSION SYSTEMS WORKSHOP

HYDROGEN-ENVIRONMENT EMBRITTLEMENT AND ITS CONTROL IN  
HIGH PRESSURE HYDROGEN/OXYGEN ROCKET ENGINES

W. T. Chandler

Rockwell International/Rocketdyne Division  
Canoga Park, CaliforniaAbstract

The workshop on hydrogen environment embrittlement was organized to examine in some detail the effects on metallic materials of the hydrogen environments encountered in high pressure hydrogen/oxygen rocket engines and to discuss methods of preventing hydrogen environment induced failures under such exposure conditions. The Space Shuttle Main Engine (SSME) is the most advanced high pressure hydrogen/oxygen rocket engine currently in service. To serve as a basis for the discussions to follow, the conditions under which materials are exposed to hydrogen environments in the SSME will be outlined and methods used in the design of the SSME to prevent hydrogen environment induced failures will be described. Data generated at Rocketdyne on the effects of high pressure hydrogen on properties of metallic materials will be presented.

Introduction

The workshop on Hydrogen-Environment Embrittlement (HEE) was organized to provide a forum for the discussion of HEE as it applies under conditions that occur in high pressure hydrogen/oxygen rocket engines. To serve as a basis for these discussions, the conditions under which materials are exposed to hydrogen environments in the SSME, the most advanced high pressure hydrogen/oxygen rocket engine currently in service, will be reviewed.

A flow schematic for the SSME is presented in Fig. 1. Liquid hydrogen is pumped first through a low pressure turbopump and then through a high pressure turbopump to a pressure above  $41.4 \text{ MN/m}^2$  (6000 psi). The high pressure hydrogen is used to cool various structures such as the nozzle and combustion chamber and the hot gas manifold and to drive the low pressure hydrogen pump turbine. The high pressure hydrogen is reacted with a limited quantity of oxygen in the preburners to produce a very hydrogen-rich steam that is used to drive both the high pressure hydrogen and oxygen turbopump turbines. The  $\text{H}_2$ :  $\text{H}_2\text{O}$  ratio is 7:1 for the hydrogen-rich steam that drives the high pressure fuel (hydrogen) turbopump (HPFTP). The hydrogen-rich steam exhaust from the HPFTP and the high pressure oxidizer turbopump (HPOTP) is combusted with additional oxygen in the combustion chamber

# ORIGIN OF OF POOR QUALITY

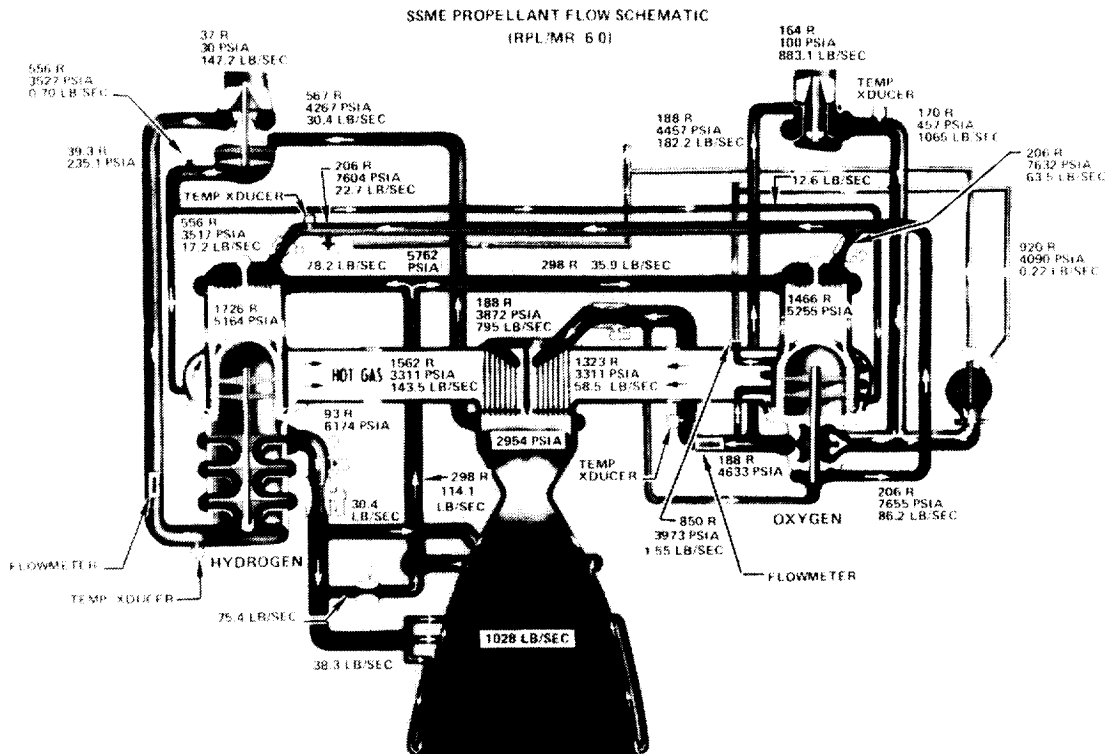


Fig. 1. SSME Propellant Flow Schematic

to produce the gas exhausted out the rocket nozzle to provide the thrust. Thus, in the SSME, metals are in contact with hydrogen environments at pressures from  $0.21 \text{ MN/m}^2$  (30 psi) to over  $41.4 \text{ MN/m}^2$  (6000 psi) and at temperatures from  $-253 \text{ C}$  ( $-423 \text{ F}$ ) to over  $649 \text{ C}$  ( $1200 \text{ F}$ ). An SSME operates for approximately 520 seconds during a Space Shuttle flight and the design life goal is 55 engine firings for a total design life goal of 28,600 seconds (approximately 7.9 hours). Engine startup and shutdown occur very rapidly so that in some components there is a very rapid application of load and rise in temperature on startup and a very rapid decrease of load and temperature on shutdown. With these conditions in mind, let us review the characteristics of HEE.

### Characteristics of HEE

The term hydrogen-environment embrittlement (HEE) is used to denote the degradation of mechanical properties that occurs while the metal is exposed to a hydrogen environment as compared to air or an inert environment. Susceptible metals exhibit the following behavior when exposed to hydrogen environments: (1) the tensile ductility of the metal is lower in hydrogen than in other environments, (2) tensile

plastic deformation in hydrogen results in surface cracking, (3) sub-critical crack growth occurs in hydrogen, and (4) cyclic and sustained load crack growth rates are faster in hydrogen than in air or inert environments.<sup>1</sup>

For all practical purposes, the elastic properties and tensile yield strengths of metals are the same in hydrogen as in air or inert environments. The most significant effects of hydrogen environments are on tensile ductility, notch tensile strength, and crack behavior. The hydrogen environment embrittles the surface or a thin surface layer of the metal. When a susceptible metal is stressed in tension in hydrogen, at some critical amount of surface plastic deformation the surface fractures, that is, a surface crack forms. Thus, we refer to a strain-to-crack initiation.

A tensile test in hydrogen is no longer a "normal" tensile test after surface cracking begins, but is a rather complex test of a crack specimen. The crack is extending as the load on the specimen is continuing to be increased. The strength and ductility values obtained are very sensitive to loading rates. Thus, care must be used in assessing the meaning and usefulness of strength and ductility data obtained from these tests.

HEE is an environmental effect and no hold time in the hydrogen environment is required to establish the embrittlement. However, HEE is very sensitive to strain rate or crack propagation rate. At high strain or crack propagation rates, the effect of the hydrogen environment will be reduced or even eliminated. This is evidenced by the fact that the final failure in a tensile specimen tested in hydrogen is a ductile, overload failure that is unaffected by the hydrogen environment. The effect of test rate is related to the processes by which hydrogen moves from the environment onto or into the metal. Thus, environmental parameters are of great importance.

For example, HEE increases with increasing hydrogen pressure as is shown in Fig. 2 for electrodeposited nickel (EDNi). It should be noted that significant effects of hydrogen environments on properties of some metals can occur at pressures of 1 atmosphere or lower. The interest in the HEE of EDNi is because the regeneratively cooled SSME combustion chamber is constructed of a high-conductivity copper alloy liner into which slots are machined and closed out with EDNi to form the channels for the hydrogen coolant.

HEE occurs over a wide range of temperatures from cryogenic<sup>2</sup> to at least 871 C (1600 F)<sup>3</sup> but is most severe in the vicinity of room temperature. The variation in HEE with temperature may be quite rapid near room temperature as is shown in Fig. 3 for EDNi.

At higher temperatures, one must be alert to the potential for hydrogen reaction embrittlement or for the absorption of sufficient

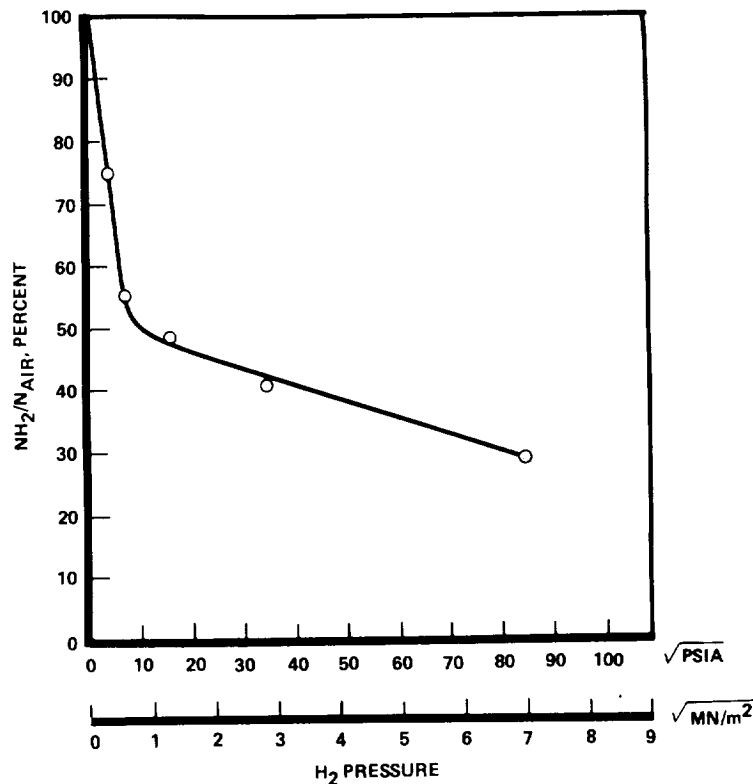


Fig. 2. HEE of EDNi (As-Deposited) vs Hydrogen Pressure  
 $N_{H_2}$  and  $N_{Air}$  are the Tensile Strengths of  
 Notched Specimens in  $H_2$  and Air, Respectively

hydrogen to result in internal hydrogen embrittlement. These types of embrittlement can add to or synergistically interact with HEE.

The purity of the hydrogen environment is important. For example, even small amounts of oxygen in hydrogen inhibits HEE, as shown in Fig. 4.<sup>4</sup> The embrittlement inhibiting effect of oxygen in 10.1 MN/m<sup>2</sup> (1500 psi) hydrogen becomes noticeable above 0.1 ppm oxygen. A few tensile tests performed at Rocketdyne on notched specimens of Inconel 718 in 48.3 MN/m<sup>2</sup> (7000 psi) hydrogen at room temperature showed no inhibition of HEE by the addition of 1 torr air (approximately 0.5 ppm oxygen) to the hydrogen and complete inhibition by the addition of 1 atmosphere air (approximately 400 ppm oxygen).

The concentration of hydrogen that metals and alloys can absorb from hydrogen at pressures prevailing in the SSME and at temperatures near room temperature where HEE is most severe are not large enough to cause HEE. The hydrogen must be concentrated by some mechanism to produce at fracture initiation sites the critical concentration necessary

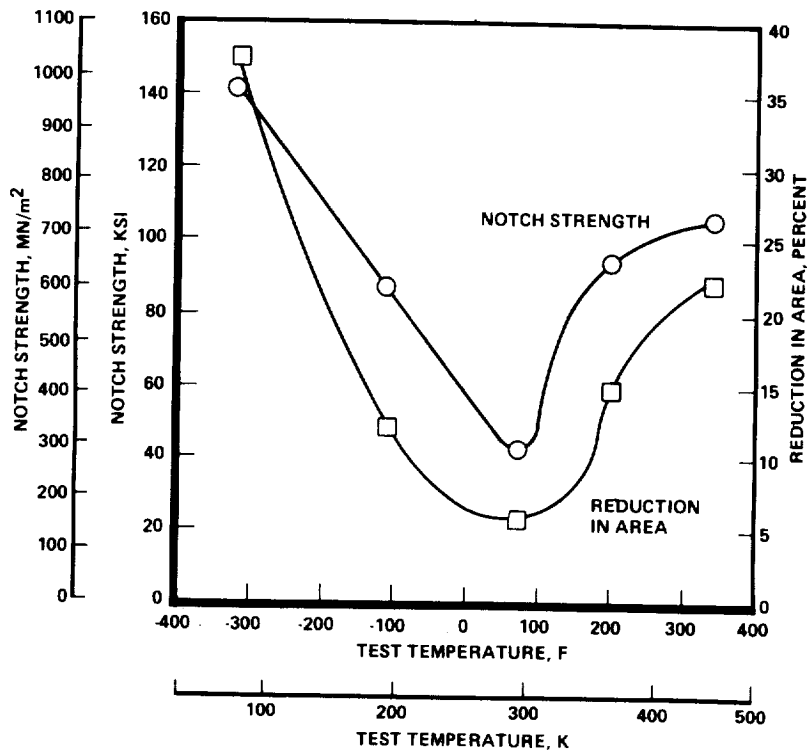


Fig. 3. Effect of Temperature on the Strength of Notched Specimens and the Reduction of Area of Unnotched Specimens for EDNi (As-Deposited) in 8.3 MN/m<sup>2</sup> (1200 psi) Hydrogen

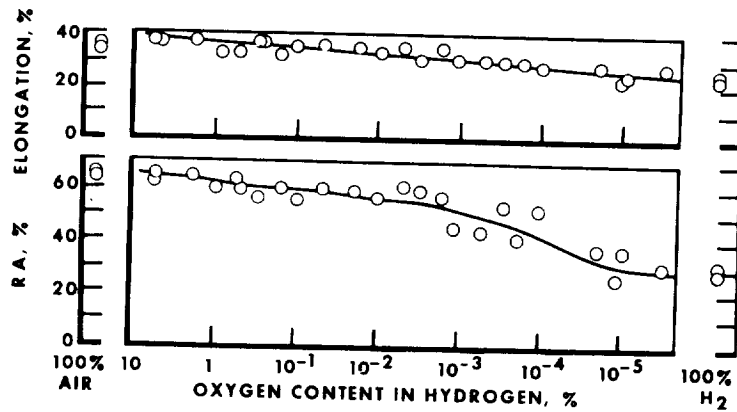


Fig. 4. Effect of Oxygen Content in 10.1 MN/m<sup>2</sup> (1500 psi) Hydrogen on the Ductility of a Plain Carbon (0.20% C) Steel

for hydrogen embrittlement. Two hydrogen concentration mechanisms have been identified:

1. Hydrogen diffusion to regions of lattice dilation<sup>5</sup>
2. Dislocation transport of hydrogen<sup>6,7</sup>



Triaxial tensile stresses cause lattice dilation and thus promote the first mechanism while the second mechanism requires shear stresses for dislocation motion. Some metals will be more sensitive to the first mechanism of hydrogen concentration while others will be more sensitive to the second. Thus, as has been discussed,<sup>8</sup> it is important to assess the stress state of the metal under the hydrogen service conditions and to ensure that any tests used to qualify materials for that service adequately evaluates the potential for hydrogen embrittlement.

Since an SSME operates for only approximately 520 seconds during a Space Shuttle flight, the time for hydrogen absorption and diffusion from the surface into the metal is short. Thus, at least at temperatures near room temperature, any hydrogen concentration due to hydrogen diffusion to regions of lattice dilation is probably small and the dislocation transport of hydrogen will be dominant. In such a case, the tensile test serves as an effective screening test for HEE since the maximum shear stress is larger than is usually encountered with the multiaxial loading conditions typical of service exposures. Of course, in some cases tensile tests may be too conservative, indicating more severe HEE than would be encountered in service.

#### HEE of Various Metals

A variety of metals and alloys have been tensile tested in high-pressure hydrogen at Rocketdyne. Particularly sensitive to hydrogen environments are the ultimate strength of notched specimens and the reduction of area of unnotched specimens. The effect of high pressure hydrogen on these properties is shown in Table 1 for various metals and alloys. Those used in high pressure hydrogen in the SSME are highlighted.

The condition of a metal can have a profound effect on the degree of HEE. For example, data are included in Table 1 for Inconel 718 and EDNi, each in two different conditions that suffer significantly different degrees of HEE. In each case, only the less embrittled condition is used in the SSME. Table 2 presents the results of an investigation<sup>9</sup> of the HEE of Inconel 718 in three forms and three heat treatments.

The heat treatments with the low [1214 K (1750 F)] solution annealing temperatures resulted in both the least HEE with the plate that was fine grained and remained fine grained through the heat treatment and the greatest HEE for the rolled bar or forging that were coarse grained. The STAl heat treatment used in the SSME resulted in the highest notch strengths in both hydrogen and helium and a moderate but consistent ratio of notch strength in hydrogen to notch strength in helium.

Table 1. Effect of High Pressure Hydrogen on Tensile Properties at Room Temperature for Various Metals

Material	Hydrogen Pressure ksi	Notched Specimen				Unnotched Specimen		
		Strength, ksi				Reduction of Area, %		
		K <sub>t</sub>	He	H <sub>2</sub>	Ratio H <sub>2</sub> /He	He	H <sub>2</sub>	Ratio H <sub>2</sub> /He
18Ni-250 MAR Steel	10	8.4	423	50	0.12	55	2.5	0.05
H-11 Steel	10	8.4	252	63	0.25	30	0	0
440C SS	10	8.4	149	74	0.50	3.2	0	0
17-7 PH SS	10	8.4	302	70	0.23	45	2.5	0.06
Inconel X-750	7	6.3	222	57	0.26	24	4	0.17
Fe-9Ni-4Co-0.20C	10	8.4	367	89	0.24	67	15	0.22
Inconel 718-STA2	10	8.4	274	126	0.46	26	1	0.04
AISI 4140 Q&T	10	8.4	313	125	0.40	48	9	0.19
MAR-M246(HF)(DS)	7	6.3	176	43	0.24	12	4	0.33
Rene 41	10	8.4	280	77	0.27	29	11	0.38
EDNi-As Deposited	1.2	8.4	148	64	0.43	90	38	0.42
ASTM A-372 Class IV	10	8.4	200	148	0.74	53	18	0.34
Inconel 625	7	6.3	155	121	0.78	63	23	0.37
AISI 1042-Normalized	10	8.4	153	115	0.75	59	27	0.46
Inconel 718-STA1	5	8.4	339	258	0.76	34	16	0.47
Waspaloy TMP	7	6.3	278	221	0.79	34	15	0.44
ASTM A-212-61T-Norm.	10	8.4	111	75	0.68	57	34	0.60
Nickel 270	10	8.4	77	54	0.70	89	67	0.75
Armco Iron-Annealed	10	8.4	121	105	0.87	83	50	0.60
Haynes 188	7	6.3	164	151	0.92	63	40	0.63
HY-100	10	8.4	224	164	0.73	76	63	0.83
EDNi-482C (900F) Anneal	1.2	8.4	96	80	65	0.81		
AISI 1020 Hot Rolled	10	8.4	105	90	0.86	40	32	0.80
Ti-5Al-2.5Sn ELI	10	8.4	201	162	0.81	45	39	0.87
Ti-6Al-4V STA	10	8.4	243	183	0.75	48	48	1.0
304L SS	10	8.4	102	89	0.87	78	71	0.91
310 SS	10	8.4	116	108	0.93	64	63	0.98
Nitronic 40-Cast-CW	7	6.3	234	229	0.98	32	30	0.94
Be-Cu Alloy 25	10	8.4	195	181	0.93	72	71	0.99
7075-T73	10	8.4	116	114	0.98	37	35	0.95
A-286	10	8.4	233	227	0.97	44	43	0.98
OFHC Cu	10	8.4	87	86	0.99	94	94	1.00
NARloy Z-Cu Alloy	5.8	8.4	53	56	1.06	70	69	0.99
316 SS	10	8.4	161	161	1.00	72	75	1.04
Incoloy 903	7	6.3	208	201	0.97	41	47	1.15
6061-T6	10	8.4	72	78	1.08	61	66	1.08

Effect of High Pressure Hydrogen Environments on Properties of Inconel 718

The use of metals in hydrogen systems must be based on properties determined in the hydrogen environment under test conditions pertinent to the service conditions. In many cases, properties other than tensile properties must be considered in designing components of hydrogen systems.

Inconel 718, which we have seen is susceptible to HEE, is used extensively in the SSME, including components of the high pressure hydrogen system. Thus, a very extensive test program has been conducted at Rocketdyne on the effect of high pressure hydrogen on the properties of Inconel 718. In this section, then, we will use Inconel 718 as an example to present data on the effect of hydrogen environments on properties most sensitive to those environments.

ORIGINAL PAGE IS  
OF POOR QUALITY

Table 2. Effect of 34.5 MN/m<sup>2</sup> (5000 psi) Hydrogen at Room Temperature on the Properties of Notched ( $K_t = 8.4$ ) Specimens of Inconel 718 in Various Conditions

HEAT TREATMENT	MATERIAL	ENVIRONMENT	NOTCHED PROPERTIES		
			STRENGTH, MN/m <sup>2</sup>	NH <sub>2</sub> /NHe	RA, PERCENT
1214, 991-894 K (1725, 1325-1150 F) STA 2 ↓	ROLLED BAR	HELIUM	1950	--	2.9
		HYDROGEN	1050	0.54	0.9
	FORGING	HELIUM	2000	--	3.0
		HYDROGEN	1170	0.59	1.1
	PLATE	HELIUM	1980	--	3.0
		HYDROGEN	1700	0.86	2.0
1214, 1089-922 K (1725, 1500-1200 F) ↓	ROLLED BAR	HELIUM	1650	--	2.9
		HYDROGEN	1160	0.70	1.8
	FORGING	HELIUM	1740	--	2.2
		HYDROGEN	990	0.57	1.2
	PLATE	HELIUM	1730	--	2.7
		HYDROGEN	1500	0.86	2.1
1325, 1033-922 K (1925, 1400-1200 F) STA 1 ↓	ROLLED BAR	HELIUM	2220	--	5.0
		HYDROGEN	1590	0.71	1.7
	FORGING	HELIUM	2340	--	4.6
		HYDROGEN	1780	0.76	1.8
	PLATE	HELIUM	2210	--	3.7
		HYDROGEN	1700	0.77	2.3

The most severe property degradation in high pressure hydrogen of specimens that do not initially contain cracks occurs in tests involving plastic strain. Thus, considerable effect of hydrogen environments on low-cycle fatigue (strain cycling) life can be expected and is shown in Fig. 5 for Inconel 718.

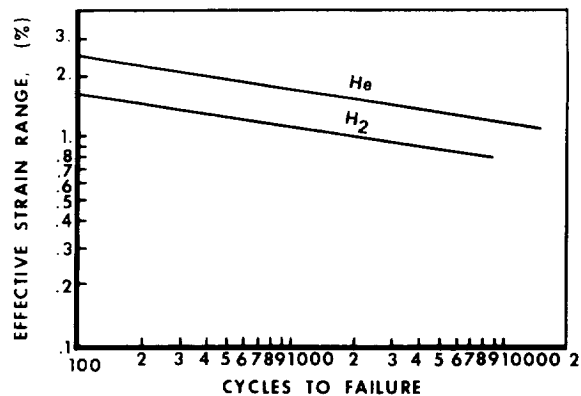


Fig. 5. Effect of 41.4 MN/m<sup>2</sup> (6000 psi) H<sub>2</sub> at RT on the Low Cycle Fatigue Life of Inconel 718

The most significant effect of hydrogen environments on metals is on crack initiation and propagation. Therefore, fracture mechanics is

a valuable approach to be applied, where feasible, to life verification of components of hydrogen systems. Such an analysis requires data on threshold stress intensities for crack growth and crack growth rates.

The effect of a hydrogen environment on the threshold stress intensity ( $K_{TH}$ ) for sustained load crack growth in Inconel 718 is shown in Table 3.<sup>10</sup>  $K_{TH}$  is much lower for the STA2 heat treatment than for the STA1 heat treatment used in the SSME. For Inconel 718 STA1 at 144 K (-200 F),  $K_{TH}$  in hydrogen is the same as  $K_{Ic}$  in helium indicating no significant hydrogen effect.

Table 3. Threshold Stress Intensities ( $K_{TH}$ ) for Sustained-Load Crack Growth in Inconel 718 Exposed to  $34.5 \text{ MN/m}^2$  (5000 psi) Hydrogen and Helium Environments at Ambient and Cryogenic Temperatures

HEAT TREATMENT	ENVIRONMENT	TEMPERATURE		$K_{TH}^*$		$K_{Ic}^*$	
		K	F	$\text{MN/m}^{3/2}$	$\text{ksi} \sqrt{\text{in.}}$	$\text{MN/m}^{3/2}$	$\text{ksi} \sqrt{\text{in.}}$
STA 2	HELIUM	295	70	58	53	78	71
	HYDROGEN	295	70	14	13	---	---
STA 2	HELIUM	144	-200	81	74	98	89
	HYDROGEN	144	-200	72	66	---	---
STA 1	HELIUM	295	70	112	102	119**	108**
	HYDROGEN	295	70	42	38	---	---
STA 1	HELIUM	200	-100	160**	146**	149**	146**
	HYDROGEN	200	-100	<47	<43	---	---
STA 1	HELIUM	144	-200	139	126	122	111
	HYDROGEN	144	-200	123	112	---	---

\*AVERAGE OF 2 TESTS IN HELIUM AND 3 TESTS IN HYDROGEN.  
 \*\*NOT VALID PLANE STRAIN FRACTURE TOUGHNESS ACCORDING TO ASTM 399.

Table 4<sup>10</sup> contains data on sustained-load crack growth rates ( $da/dt$ ) in hydrogen for Inconel 718 in both the STA1 and STA2 heat treatment conditions.  $da/dt$  in Inconel 718 with the STA2 heat treatment was much faster than in the Inconel 718 with STA1 heat treatment.

The effect of hydrogen at room temperature on cyclic-load crack growth rates ( $da/dN$ ) in Inconel 718 in the STA2 heat treatment condition was determined for various hydrogen pressures and for two cycling frequencies.<sup>10</sup> The results are summarized in Fig. 6.  $da/dN$  increased with increasing hydrogen pressure and with decreasing cyclic frequency. The hydrogen environment caused a significant increase of  $da/dN$  even at a pressure of  $0.069 \text{ MN/m}^2$  (10 psi).

Under the SSME program,  $da/dN$  tests are conducted in support of fracture life verification analyses. It is evident from Fig. 6 that cyclic frequency has a significant effect on  $da/dN$ . Thus,  $da/dN$  tests

Table 4. Sustained-Load Crack Growth Rate in Inconel 718 Exposed to 34.5 MN/m<sup>2</sup> (5000 psi) Hydrogen at Room Temperature

HEAT TREATMENT	STRESS INTENSITY		CRACK GROWTH RATE	
	MN/m <sup>3/2</sup>	ksi √ in.	m/sec	in./hr
STA2	27	25	4.66 x 10 <sup>-6</sup>	0.65
STA2	36	32	3.17 x 10 <sup>-5</sup>	4.5
STA1	44	40	1.76 x 10 <sup>-8</sup>	0.0025

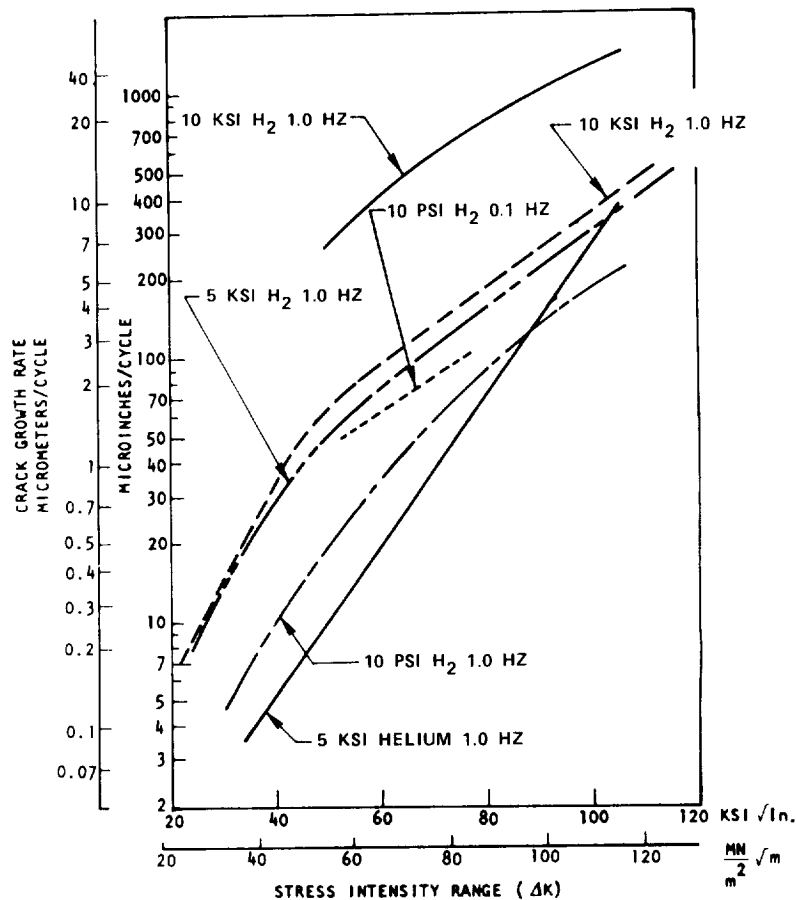


Fig. 6. Cyclic-Load Crack Growth Rate (da/dN) as a Function of Stress Intensity Range for Inconel 718 in the STA1 Heat Treatment Condition Exposed to H<sub>2</sub> and He at Various Pressures at Ambient Temperatures (R = 0.1)

are being performed utilizing a cycle nearly 9 minutes long that simulates the SSME operating cycle. The load-time profile is shown in Fig. 7. The long cycle time required to simulate the SSME engine cycle results in very long test times.

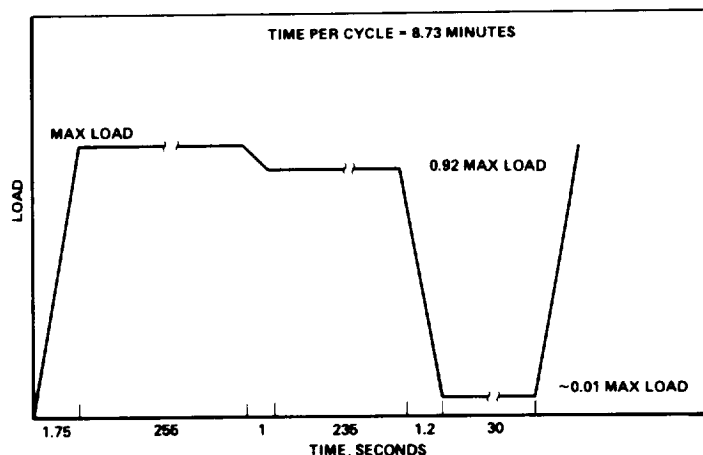


Fig. 7. Simulated SSME Load--Time Cycle

The effect of hydrogen environments on  $da/dN$  in Inconel 718 using the simulated SSME cycle has been determined for forged, cast, and welded material.  $da/dN$  was determined for cracks in the weld metal and in the heat-affected zone (HAZ) for both as-weld and heat-treated welds. Some of these results are presented in Fig. 8.<sup>11</sup> The weld and HAZ results are for heat-treated welds. In all cases, the STAl heat treatment has been used. The large effect of hydrogen on  $da/dN$  in Inconel 718 is evident. Somewhat unexpectedly,  $da/dN$  in hydrogen was slower in the weld metal and HAZ than in the forged base metal.

#### Designing for Service in High Pressure Hydrogen

The preceding summary of the characteristics of HEE and of some of the property effects suggests a number of approaches that can be employed in the design of high pressure hydrogen systems. A simplified logic diagram for designing for high pressure hydrogen service is presented in Fig. 9. In the following, examples from the SSME relating to each of the blocks in Fig. 9. will be presented.

First, of course, the service conditions should be carefully reviewed (considering all transient conditions) to determine if HEE is a potential problem. If the temperature of the metal part in operation is well below room temperature, there may be no embrittlement caused by the hydrogen environment. An example, is a fuel bleed assembly bellows that is made of Inconel 718 STAl. Before the Inconel 718 in the bellows is stressed in operation, the temperature has been reduced to below  $-129\text{ C}$  ( $-200\text{ F}$ ) at which temperature, as shown in Table 3, there is negligible effect of high pressure hydrogen. Also, the hydrogen pressure in the bellows is only  $2.07\text{ MN/m}^2$  (300 psi).

If it is established that the conditions of hydrogen exposure are conducive to HEE, then, obviously, the first approach is to select a metal not susceptible to HEE. The turbine of the low pressure fuel

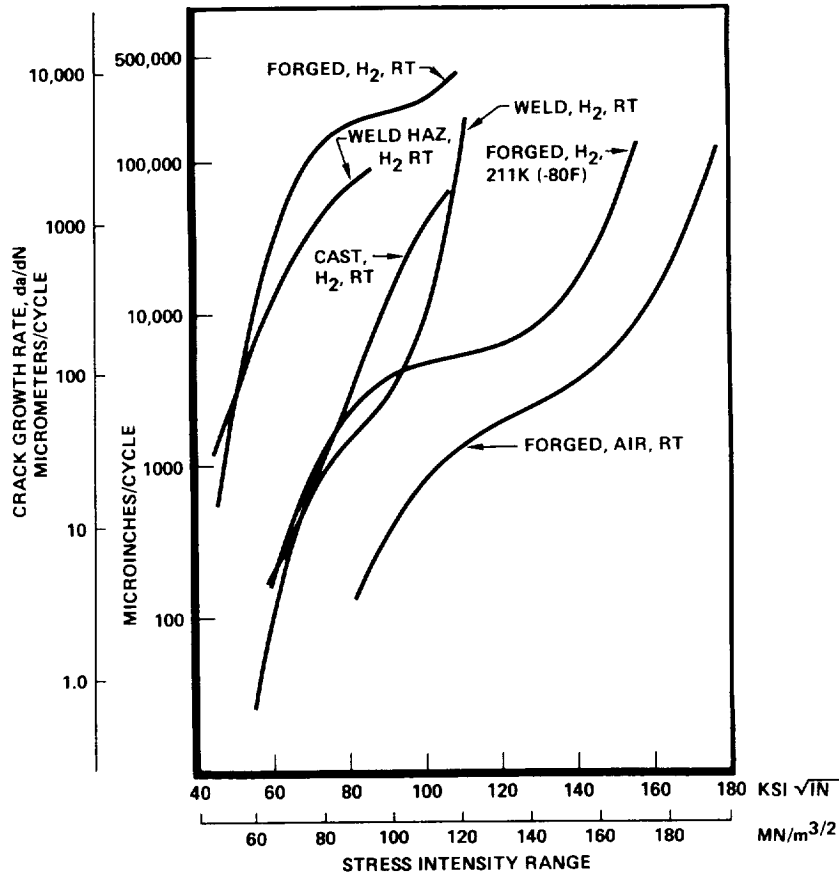


Fig. 8. Effect of  $34.5 \text{ MN/m}^2$  (5000 psi) Hydrogen at Room Temperature on  $da/dN$  in Inconel 718 Using Simulated SSME Cycle

turbopump in the SSME is driven by hydrogen at a pressure of  $29.4 \text{ MN/m}^2$  (4267 psi) pressure and a temperature of  $42 \text{ C}$  ( $107 \text{ F}$ ), see Fig. 1. The turbine disk with integral blades is made of A-286, which is not susceptible to HEE at temperatures near room temperature.

It can be seen from Table 1 that the range of properties available from the alloys not susceptible to HEE are quite limited. Therefore, in many instances to meet other requirements, metals susceptible to some degree to HEE will have to be used under conditions conducive to HEE. In such case, the selected metals should be used in the condition least embrittled by the hydrogen environment. Two examples from the SSME have already been noted, that is, EDNi for which annealing significantly reduces susceptibility to HEE and Inconel 718 for which the degree of HEE is much less with the STA1 heat treatment than the STA2 heat treatment.

In some instances, when design permits, a susceptible metal may be designed into a hydrogen system by utilizing a "brittle material"

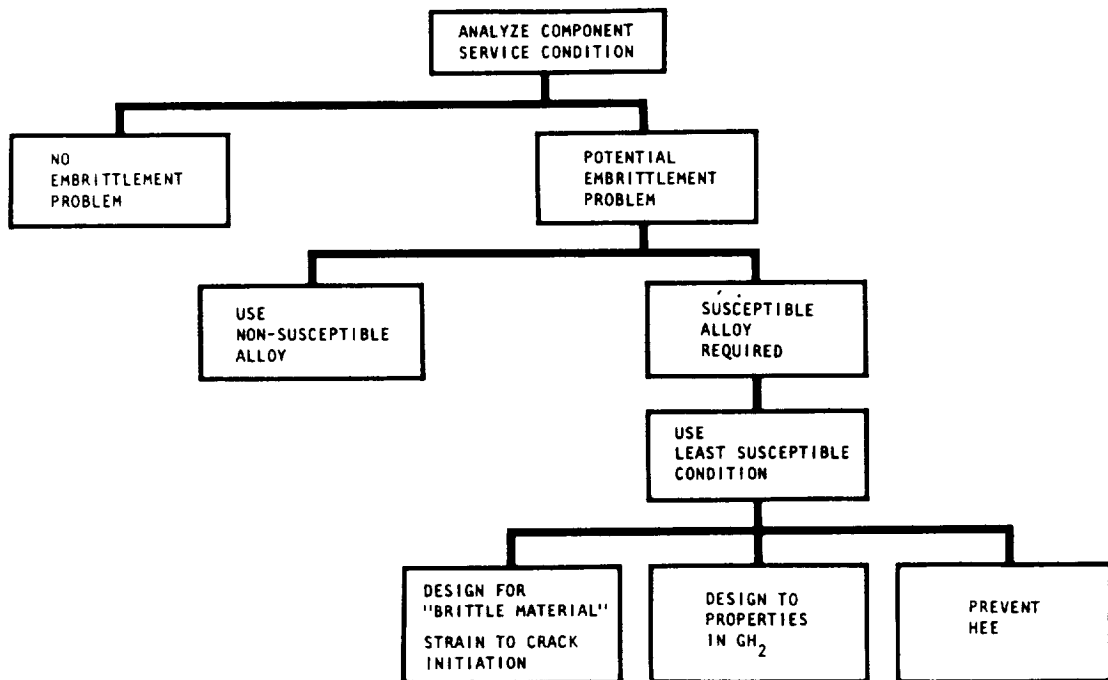


Fig. 9. Designing for Service in High Pressure Hydrogen

design approach. The following characteristics are essential for such an approach. The structure must not contain sharp notches and the finish and accessibility to inspection of the surface in contact with hydrogen must be such that the absence of surface cracks can be ensured. The stresses and strains must be predictable with a high degree of confidence based on accurately known loads and configuration simplicity. Most importantly, the peak or localized strains must be less than the "available" strain for the material in hydrogen, that is, the strain at which cracks initiate in hydrogen under the service conditions. This approach has been used in the SSME hot-gas manifold, which is made of Inconel 718 STA1. The Inconel 718 is exposed to approximately  $20.7 \text{ MN/m}^2$  (3000 psi) hydrogen at room temperature. The section thickness of the Inconel 718 was increased so that the strains are limited to 0.5 percent (essentially elastic). Considerable testing has shown the strain-to-crack initiation in Inconel 718 STA1 to be in excess of 3 percent.

When metals that are susceptible to HEE are to be used in hydrogen environments, the design may be based on the appropriate properties of the metal determined in the hydrogen environment under conditions that adequately simulate service conditions.

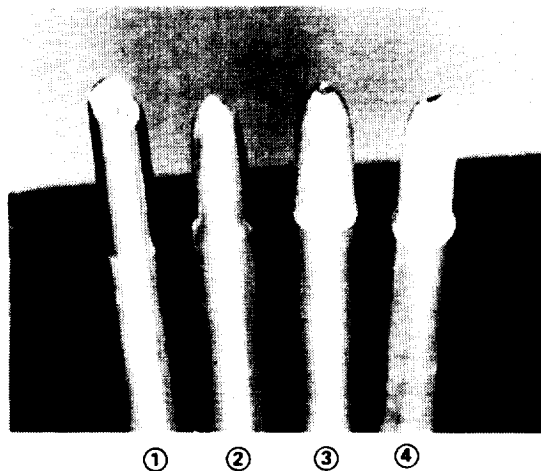
The main injector interpropellant plate of the SSME is exposed to approximately  $22 \text{ MN/m}^2$  (3200 psi) hydrogen and the surface temperature



reaches approximately 538 C (1000 F) and the life-limiting property is low-cycle fatigue. Inconel 718 STA1 is used for this part based on its low-cycle fatigue properties determined in high pressure hydrogen.

Situations may arise in designing hydrogen systems in which a metal has such an attractive combination of properties for a certain application as to dictate its use, but it is susceptible to HEE and the degree of embrittlement under the service conditions is unacceptable. The most effective approach may then be to use that metal and prevent its embrittlement.

Extensive investigations have been conducted at Rocketdyne on the use of coatings to prevent HEE. Since HEE occurs when a metal is plastically deformed in hydrogen, any coating for the prevention of HEE must be effective during plastic deformation of the metal to be protected. Copper and gold coatings were found to be effective in preventing embrittlement of susceptible metals by high pressure hydrogen as shown in Fig. 10 for as-deposited EDNi. The uncoated EDNi specimen tensile tested in hydrogen has a very brittle appearing fracture while the specimens coated with copper or gold have the same very ductile appearance as the uncoated specimen tested in helium. Because EDNi is susceptible to HEE, in the SSME, the EDNi (annealed) closeout of the combustion chamber coolant passages is protected by a layer of electrodeposited copper (EDCu). To confirm the effectiveness of EDCu to protect EDNi, a series of burst, sustained, and cyclic pressure tests were performed on slotted specimens designed to simulate the combustion chamber coolant passages.<sup>12</sup>



1. AS DEPOSITED, TESTED IN  $8.3 \text{ MN/m}^2$  (1200 PSI) HYDROGEN AT AMBIENT TEMPERATURE
2. AS DEPOSITED, TESTED IN  $8.3 \text{ MN/m}^2$  (1200 PSI) HELIUM AT AMBIENT TEMPERATURE
3. COPPER PLATED, AS DEPOSITED, TESTED IN  $8.3 \text{ MN/m}^2$  (1200 PSI) HYDROGEN AT AMBIENT TEMPERATURE
4. GOLD PLATED, AS DEPOSITED, TESTED IN  $8.3 \text{ MN/m}^2$  (1200 PSI) HYDROGEN AT AMBIENT TEMPERATURE

Fig. 10. Macrographs of EDNi Specimens After Tensile Testing

In certain locations in the SSME, Inconel 718 is protected from the hydrogen environment by EDCu. Tensile tests on unnotched specimens showed that the copper-coated Inconel 718 specimens had the same ductility in hydrogen as in helium provided that the copper was at least 38  $\mu$ m (0.0015 inch) thick for specimens given the STAl heat treatment after copper plating or at least 76  $\mu$ m (0.003 inch) thick for specimens heat treated before plating.

However, the protection afforded Inconel 718 in low-cycle fatigue tests was found to depend on the strain range as shown in Fig. 11. The copper coating improves low-cycle fatigue life only for strain ranges above 1 percent. This is because the copper basically has poorer low-cycle fatigue properties than Inconel 718 at the lower strain ranges. That is, the copper fails first because of low-cycle fatigue, thus exposing the Inconel 718 to hydrogen. Fortunately, copper does provide protection at the strain ranges above 1 percent, which are the strain ranges for which protection is required in the SSME. The cycle life requirement of the SSME is 60 cycles, and to provide a factor of safety, it is designed to a cyclic life of 240 cycles. But again, these results show the importance of conducting tests in hydrogen, which simulate service conditions

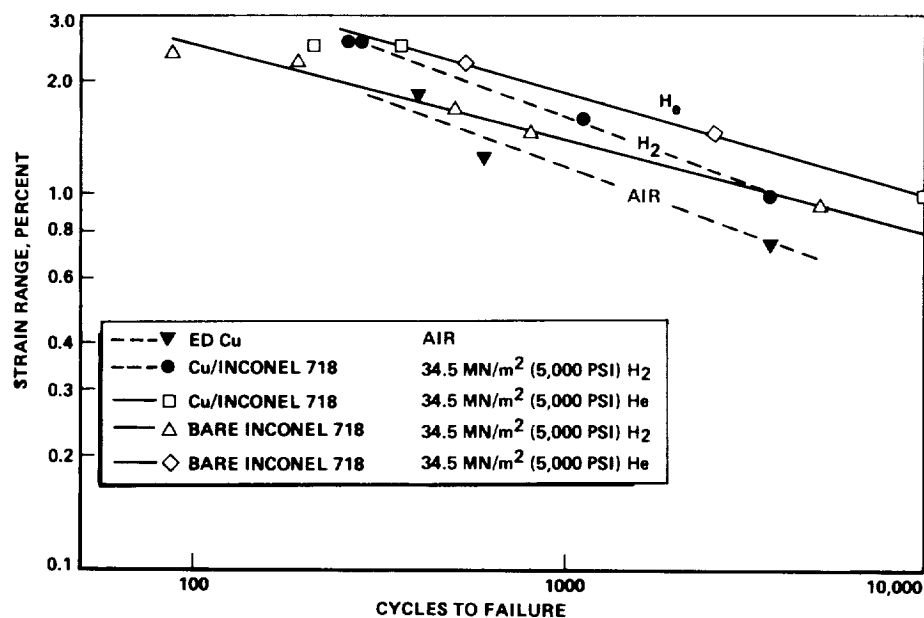


Fig. 11. Effect of Hydrogen Environment on the Low-Cycle Fatigue at Room Temperature of Uncoated and Copper Plated Inconel 718 ( $R = -1$ ,  $f = 0.5$ )

Areas in the SSME where EDCu is used to protect Inconel 718 STAl from hydrogen include the main combustion chamber outlet, which is exposed to approximately 38.6  $\text{MN}/\text{m}^2$  (5600 psi) hydrogen at room temperature and the main turbine housings of both the HPFTP and HPOTP,

which are exposed to approximately 34.5 MN/m<sup>2</sup> (5000 psi) hydrogen at temperatures from room temperature to 260 C (500 F).

#### Summary

To summarize, in designing components of high pressure hydrogen systems, including those on rocket engines, the conditions of hydrogen exposure are analyzed to determine if HEE is a potential problem. If it is, then, if possible, metals not susceptible to HEE are used. If susceptible metals must be used, good design and production processes are especially important. Notches and stress concentrations are reduced and, if possible, eliminated and surface finishes are controlled. The least susceptible condition of the metal is used. Where possible, parts are designed so that susceptible metals are not plastically deformed in hydrogen. Properties used in design are based on tests (e.g., tensile, fatigue, and fracture mechanics) performed in hydrogen under conditions simulating service conditions. As required, coatings are used to protect susceptible metals from the hydrogen environment.

#### Acknowledgements

The following personnel (listed alphabetically) made major contributions to the HEE programs conducted at Rocketdyne: D. A. Bowman, G. E. Dyer, R. P. Jewett, A. F. Konigsfeld, M. C. Metcalf, A. R. Murphy, R. M. Parker, D. A. Pearson, R. F. Rothring, and R. J. Walter.

The work performed at Rocketdyne reported herein was sponsored by NASA/MSFC under Contract NAS8-27980 (SSME Program) and other contracts.

#### References

1. Jewett, R. P., R. J. Walter, W. T. Chandler, and R. P. Frohberg, Hydrogen-Environment Embrittlement of Metals, A NASA Technology Survey, NASA CR-2163, March 1973.
2. Walter, R. J. and W. T. Chandler, Influence of Gaseous Hydrogen on Metals - Final Report, Rockwell International/Rocketdyne Division, Canoga Park, CA, NASA CR-124410, October 1973.
3. Harris, J. A., Jr. and M. C. Van Wanderham, Properties of Materials in High-Pressure Hydrogen at Cryogenic, Room, and Elevated Temperatures, Final Report, NASA Contract NAS8-26191, Pratt & Whitney Aircraft Florida Research and Development Center, West Palm Beach, Florida, Report No. FR-5768, 31 July 1973.
4. Hofmann, W. and W. Rauls, "Ductility of Steel Under the Influence of External High-Pressure Hydrogen," Welding Journal, Vol. 44, pp. 225s-230s, 1965.

5. Troiano, A. R., "The Role of Hydrogen and Other Interstitials in the Mechanical Behavior of Metals," Trans. ASM, Vol. 52, pp. 54-80, 1960.
6. Louthan, M. R., Jr., G. R. Caskey, Jr., J. A. Donovan, and D. E. Rawl, Jr., "Hydrogen Embrittlement of Metals," Mater. Sci. Eng., Vol. 10, pp. 357-368, 1972.
7. Nair, S. V., R. R. Jensen, and J. K. Tien, "Kinetic Enrichment of Hydrogen at Interfaces and Voids by Dislocation Sweep-in of Hydrogen," Met. Trans. A, Vol. 14A, pp. 385-393, 1983.
8. Louthan, M. R., Jr., R. P. McNitt, and R. D. Sisson, "Importance of Stress State on Hydrogen Embrittlement," Advanced Techniques for Characterizing Hydrogen in Metals, edited by N. F. Fiore and B. J. Berkowitz, The Metallurgical Society of AIME, pp. 25-41, 1982.
9. Walter, F. J. and W. T. Chandler, "Influence of Gaseous Hydrogen on Inconel 718," Hydrogen in Metals, edited by I. M. Bernstein and Anthony W. Thompson, American Society of Metals, Metals Park, Ohio, pp. 515-525, 1973.
10. Walter, R. J. and W. T. Chandler, "Influence of Hydrogen Environments on Crack Growth in Inconel 718," Environmental Degradation of Engineering Materials, edited by M. R. Louthan, Jr., and R. P. McNitt, Virginia Polytechnic Institute, Blacksburg, Virginia, pp. 513-522, 1977.
11. Chandler, W. T., "Hydrogen Embrittlement and Its Control in Hydrogen-Fueled Engine Systems," Recent Advances in Structures for Hypersonic Flight, NASA Conference Publication 2065, Part I, pp. 195-249, 1978.
12. Chandler, W. T., R. J. Walter, C. E. Moeller, and H. W. Carpenter, "Effect of High-Pressure Hydrogen on Electrodeposited Nickel," Plating and Surface Finishing, Vol. 65, No. 5, pp. 63-70, May 1978.

**MULTISPECIMEN TEST FACILITY FOR HIGH-PRESSURE  
HYDROGEN CREEP STUDIES**

by

S. K. Verma\*

**ABSTRACT**


The paper describes IITRI-developed equipment for creep rupture evaluation of materials in hydrogen at up to 20.7 MPa and 925°C. This facility can test six specimens simultaneously within a single vessel with continuous measurement of specimen extension within the vessel. A double-wall vessel design concept with balanced pressure across the inner wall has been adopted successfully. All temperature and strain measurements are transmitted to a data logger for storage and analysis. Typical rupture life, minimum creep rate, and time to 1% strain for selective alloys are presented, as well as analysis using Orowan-Sherby-Dorn temperature-compensated technique to estimate 3500 h rupture life and stress to obtain 1% strain in 3500 h.

**INTRODUCTION**

The adverse effect of hydrogen on mechanical properties of engineering materials has been known for years, but the existing mechanistic models are not adequate to predict the mechanical properties in hydrogen at elevated temperature.<sup>1-13</sup> The only available method for assessing the material behavior in hydrogen is to actually test specific alloys in a simulated environment. In simulation, the accurate control of various variables is indeed important; for example, alloy composition and microstructure, system hydrogen pressure, load levels and strain rates, and temperature of application have been found important in various studies. This paper describes the unique creep facility at IIT Research Institute (IITRI) in which many variables can be controlled for materials development for technologies such as the space shuttle main engine (SSME),<sup>5</sup> Stirling engine, and hydrogen-powered spacecraft for 12-15 Mach hypersonic speeds.<sup>6</sup>

---

\*S. K. Verma is Director of the Surface Engineering Center at IIT Research Institute, Chicago, Illinois, 60616.



The high temperature-high pressure creep facility was designed by IITRI and was funded by NASA-Lewis to support materials development and testing for the Stirling engine in automotive application.<sup>9-13</sup> The Stirling engine development undertaken by the U.S. Department of Energy and NASA-Lewis has advantages of high fuel efficiency, multiple fuel capability, low pollution, and low noise.<sup>1-4</sup> Information on materials behavior in hydrogen, however, was not available for Stirling engine applications. IITRI designed and fabricated the unique facility to provide the necessary information on creep behavior of a number of alloys over the temperature range 650°-950°C in 15 MPa H<sub>2</sub>.<sup>9-13</sup> In this study, the long-term effects of high-pressure hydrogen on the creep properties of materials were determined for components such as heater heads, cylinders, turbines, and regenerator housings. Tests were done on iron-base alloys and one cobalt-base alloy in hydrogen and in air for direct evaluation of the effect of hydrogen. Details of these studies can be found elsewhere.<sup>10</sup> This paper describes equipment details, typical test results, and methods implemented to adopt these test results for engineering design purposes. Finally, the versatility of the creep facility for other applications is considered.

### **HIGH-PRESSURE HYDROGEN TEST EQUIPMENT AND TEST PROCEDURE<sup>9-13</sup>**

#### **Apparatus Features**

A schematic diagram of the equipment is shown in Figure 1. The significant features of the equipment are as follows:

- Six specimens can be tested simultaneously within the single high-pressure vessel.
- Continuous direct measurement of creep extension is possible within the vessel
- External specimen loading is by deadweight through a 10:1 level arm.
- All specimens are mounted on a central support column, which is assembled outside the vessel.
- All temperature and elongation data are continuously recorded for computer analysis.
- The double-wall vessel design is adopted, with balanced pressure across the hot inner wall.
- A double-studded vessel is used, avoiding all welding.
- The vessel is trunnion-mounted on a vibration-dampening frame for easy operation.

## Testing Details and Procedure

Six specimens can be loaded to their initial stress levels stepwise. The initial stress levels are adjusted for both internal pressure effect and friction between the Teflon seal and the stainless steel pull wire. The overall accuracy of the initial stress is better than 1% at stress levels exceeding 100 MPa and between 1 and 2% at stresses less than 100 MPa. Each specimen temperature along the gage length is monitored continuously with two Chromel-Alumel thermocouples mounted just outside the gage length. Temperatures can be controlled within  $\pm 2^\circ\text{C}$  on each specimen and between the specimens.

The specimens are uniformly heated by resistance-wound, 4 kW capacity elements controlled by a Barber-Colman Model 560 temperature controller. The two halves of the furnace elements can be controlled separately, and the element temperatures are monitored and controlled.

Capacitance-type transducers with a sensitivity of  $0.25\ \mu\text{m}$  (10  $\mu\text{in.}$ ), connected to specially designed concentric tube extensometers, are loaded in the upper cooler region ( $150^\circ\text{C}$  max) of the vessel, and creep extension signals are recorded at any desired intervals. During loading, signals are generally recorded at 3-s intervals, which are later increased to 10-min intervals and are further changed to 4-h or longer intervals for long-term tests.

Automatic timers record test durations. A mercury cut-off switch is mounted on the loading arm which indicates rupture time when the arm drops from the horizontal position upon rupture. Hydrogen pressure inside the inner test vessel is balanced against nitrogen pressure outside it using a differential pressure gage. When the pressure between the inner and outer chambers exceeds  $\pm 70\ \text{kPa}$ , automatic demand-operated solenoid valves allow the entry of the desired gas (either hydrogen to inside or nitrogen to outside) to keep the pressure balanced across the hot wall of the inner vessel.

Before starting the test, the vessel interior is flushed with nitrogen (obtained from liquid nitrogen), which is pressurized to 3.5 MPa and cycled to ambient pressure three times (<1 ppm oxygen pressure and cycled twice to ambient pressure. Finally, the test hydrogen is introduced at a pressure lower than the final test pressure of 15 MPa. The vessel is heated, and in about 4 h the desired temperature ( $900^\circ\text{C}$ ) level can be obtained and stabilized; the hydrogen pressure can be adjusted to the desired level, e.g., 15 MPa. To ensure environment purity, periodic gas analysis must be conducted in all cases. The oxygen level in this testing was 1 ppm or less, and traces of ammonia and methane were noted with levels reaching a few hundred ppm in a 1000-h test.

Before each test, specimen dimensions are measured to  $\pm 25.4\ \mu\text{m}$  and the cross-sectional areas are calculated to three significant digits.

Extensometers are attached to the specimen shoulders in the test assembly. The fractured specimens are fitted, and the extensometer position marks are remeasured to obtain the total extension. To calculate elongation (as percent), the divisor is taken as the adjusted length of the reduced section, as defined in ASTM E-139.

Incremental loading has been used, and extension on loading is noted during extension. Extensometer readings on full loading are used as the zero base for all subsequent extension measurements as a function of time taken from the conclusion of full load application.

In several tests in previous studies, when one or more specimens did not rupture before the tests were discontinued, other valuable information on minimum creep rate and time to 1% creep strain was documented and used in the analysis even if no endpoint rupture life data were obtained from such tests.

The internal transducers have generally given excellent results. However, when one or two transducers malfunction, externally mounted dial gages (or LVDTs) reading to the nearest 25  $\mu\text{m}$  (0.001 in.) attached to the horizontal loading arms provide valuable creep data.

#### **ALLOYS AND HEAT TREATMENT OF ALLOYS<sup>10-13</sup>**

Composition and heat treatments of the iron-base alloys and the cobalt-base alloy are given in Tables 1 and 2. Of these ten alloys, HS-31, SA-F11, CRM-6D, and XF-818 are casting alloys, and the other six are sheet alloys in the thickness range of 0.79 to 0.99 mm (0.031 to 0.039 in.)--comparable to the wall thickness of the tubes used in the Stirling engine. Five of the sheet alloys--A-286, INCOLOY Alloy 800H (or 800H), N-155, 19-9DL, and CG-27--were purchased from U.S. commercial suppliers; 12RN72, a Sandvik alloy, is specially rolled into sheet form for United Stirling AB, Sweden (US/AB), the supplier who provided the material.

The CRM-6D and XF-818 investment cast specimens were obtained from two sources: Climax Molybdenum Co., Research Laboratory, Ann Arbor, Michigan, USA, and United Stirling AB, Sweden. The HS-31 and SA-F11 investment cast specimens were obtained from United Stirling AB, Sweden. The investment cast NASAUT (developed by United Technologies and designated 4G-A1) was received from NASA-Lewis.

The alloys were both sheet and cylindrical samples. Their dimensions are shown in Appendix Figure A-1.

#### **RESULTS AND ANALYSIS**

Altogether, 22 tests have been completed with a total test duration exceeding 12,000 h. A complete set of high-pressure hydrogen creep-rupture data is given in Appendix Table A-1. The corresponding air creep data can be found in NASA CR-168071.<sup>10</sup>



## Creep Curves

The creep data were directly plotted from recordings made in the computer. To illustrate the sensitivity of the internal transducer measurements and techniques of obtaining the minimum creep rate and time to 1% creep elongation data, a typical initial loading extension-time curve, the creep extension in the early primary stages, and a complete creep-time curve for an experimental NASA alloy are shown in Figures 2a, b, and c, respectively. Figure 2a shows that in about 150 s the total loading was completed in six steps, each loading step consisting of a rapid rise in strain followed by a leveling off, all occurring within 20 to 30 s.

Figure 2b shows the smooth, almost parabolic primary creep stage under full load. The very high initial creep rate in the first 30 s decreased by a factor of about 20 in the first half-hour. On similar curves, a horizontal line is drawn at the appropriate creep extension level (in this case at the 1% level), and its intersection with the creep curve determines the time taken to obtain the desired creep extension. From plots similar to Figure 2c, the slope in the secondary steady-state stage determines the minimum creep rate and the rupture life is indicated from both the elapsed time clock and the creep curve termination.

## Data Analysis

The data given in Appendix Table A-1 can be analyzed in many different ways combining stress and temperature. Temperature-compensated analysis, called the Orowan-Sherby-Dorn (O-S-D) method, has been often used in the past.<sup>15-20</sup> The O-S-D relationship is given by:

$$\ln Y = \ln k + n \ln \sigma + Q/RT \quad (1)$$

where  $Y = t_r, t_{0.01},$  or  $\dot{\epsilon}_m$

$Q =$  the apparent activation energy, kJ/mol

$\sigma =$  the initial stress, MPa

$T =$  the test temperature, K

$R =$  the universal gas constant, 8.313 kJ/mol

$n =$  the stress exponent

$K =$  a constant.

A linear regression analysis of Equation 1 determines the apparent activation energy ( $Q$ ) and the slope of the fitted line ( $n$ ), which is the stress exponent based on the power-law relationship. Equation 1 can be rearranged in the following manner:

$$(\ln Y - Q/RT) = \ln k + n \ln \sigma \quad (2)$$

The rupture life, minimum creep rate, and time to 1% creep strain data given in Appendix Table A-1, were analyzed using Equation 2. The results of these analyses are given in Tables 3, 4, and 5.

Finally, based on this analysis, 3500-h rupture life stresses in 15 MPa hydrogen have been estimated and compared with the design criteria stresses for the automotive Stirling engine in Table 6.

**Rupture Life, Minimum Creep Rate, and Time for 1% Creep Strain.**

The temperature-compensated rupture life vs stress for the alloys is shown in Table 3. The NASAUT alloy has the maximum stress component and apparent activation energy which makes it more susceptible to variations in stress as well as temperature than the others. The CRM-6D (aged) alloy has similar values as that of NASAUT alloy. As expected, the heat treatment of the alloys affects the creep properties significantly as shown in Table 3.

The minimum creep rate or time to 1% creep strain analysis shown in Tables 4 and 5 show a similar tendency for NASAUT alloy, i.e., higher sensitivity to the temperature and stress compared to other alloys.

**Predicted Stresses for Rupture and 1% Creep in 3500 Hours.** Based on the temperature-compensated analytical data given in Tables 4, 5, and 6, mean stresses for 3500 h rupture life and 1% creep in 3500 h for various alloys can be estimated and are summarized in Table 6. Although the NASAUT alloy had shown maximum sensitivity to the test temperature and stress, the 3500-h rupture life did not show improvement over other alloys. Considering the design criterion of 119 MPa at 775°C and the lower (90%) confidence limits for the alloys, NASAUT, XF-818 as-cast, and CRM-6D braze-cycled fail to meet the 119 MPa criterion at 775°C.

**Analysis of Elongation and Reduction-in-Area Data**

Elongation and reduction in area for various alloys are presented in Appendix Table A-2. In the data shown below HS-31 had the maximum total elongation before rupture. Casting defects prior to testing may have affected NASAUT alloy; the precise effect on data is not available.

Alloy	Temp., °C	Max. Total Elong., %
HS-31 <sup>a</sup>	760	28.1
CRM-6D <sup>a</sup>	760	21.1
XF-818 <sup>a</sup>	760	14.7
NASAUT <sup>b</sup> 4G-Al	775	13.6
XF-818 <sup>c</sup>	760	10.7
CRM-6D <sup>c</sup>	760	7.4
SA-F11 <sup>a</sup>	760	6.3

<sup>a</sup>Braze-cycled.

<sup>b</sup>Heat-treated.

<sup>c</sup>XF-818 (as-cast), CRM-6D (aged).

### Comparison of Hydrogen Creep Data with Air Creep Data<sup>9,13</sup>

The effect of hydrogen on creep properties is not straightforward because both the exponent "n" and activation energy "Q" are affected in a complex manner, as shown in Tables 3-6. Similar data on creep in air reveals that hydrogen effects on the alloys tested at IITRI were minimum in the condition tested. The ductility is severely affected in most of the alloys. Some comparisons of data in air and hydrogen are provided here using alloy CRM-6D only, but analogy can be extended to other alloys.

For alloy CRM-6D, the rupture life stress exponent (n) became significantly negative in hydrogen environment compared to that observed in air as shown in Appendix Table A-3. Also, a large increase in activation energy (Q) has taken place in the H<sub>2</sub> environment. These two trends oppose each other. A more negative exponent implies a greater sensitivity to small stress fluctuations. For example, with all other variables in Equation 1 remaining constant, an increase in stress by 10% will affect rupture life in CRM-6D by the following factors:

$$\begin{aligned}\text{Air: } (1.10)^{-9.12} &= 0.42 \\ 15 \text{ MPa H}_2: (1.10)^{-13.3} &= 0.28\end{aligned}$$

In other words, the estimated rupture life in hydrogen will become two-thirds that in air under a moderate stress fluctuation.

On the other hand, the higher Q for hydrogen environment affects rupture life differently with a change in temperature. For example, if temperature (T) is decreased by 10%--say, from 1100 K (827°C) to 990 K (717°C)--in both air and hydrogen environments, then the Q/RT term in Equation 1 will change to Q/0.9 RT, i.e., an increase of 11% from the energy term to the rupture life; and a larger (more positive) Q for rupture life in hydrogen (720 kJ/mol, over a 461 kJ/mol) will mean a more significant increase in rupture life.

The overall environment effect due to changes in (n) and (Q) on rupture life will, however, depend on the relative amounts of these changes, and the predicted 3500-h rupture stress values for both 15 MPa hydrogen and air, given later, indicate this combined effect.

The available data for minimum creep rate suggest that creep rate is less sensitive than rupture life to environment effects. The data for CRM-6D are shown in Figures 3 and 4. The predicted stress for 3500 h rupture life was not significantly affected, but the rupture elongation data were affected by as much as 60% for some alloys such as 19-9DL at 815°C. The difference between air and hydrogen ductility data for a few alloys has been shown in Appendix Table A-3. A significant amount of fractography has been conducted to assist in the understanding of the microstructural dependence of creep properties. Typical photographs of fractured wrought and cast alloys along with the micrographs on

intergranular fracture are shown in Figures 5 and 6.<sup>7</sup> The presence of hydrogen increased the relative brittle fracture area on the overall fracture front.<sup>9-13</sup>

#### SUMMARY AND CONCLUSIONS

- (1) The creep facility for high temperature-high pressure hydrogen is a versatile one that can be used to assess the materials behavior of engineering alloys for diversified applications.
- (2) Several alloys have been found to meet the design criteria of components of Stirling engines; some of the alloys identified as suitable are CG-27, N-155, and 19-9DL, while for heater head and regenerator housing, cast alloy CRM-6D, SA-F11, and HS-31 are adequate.
- (3) Rupture ductility in hydrogen is lower than that in air in all tube and cast alloys studied at IITRI.

#### ACKNOWLEDGMENTS

The study was sponsored under Contracts DEN3-217 and DEN3-303 by NASA-Lewis Research Center, Cleveland, Ohio, for the United States Department of Energy, Office of Transportation Programs. Contributions by J. R. Stephens and R. H. Titran of NASA-Lewis were significant in this study, and support of the programs is appreciated. The work was conducted by S. Bhattacharyya, C. Hales, C. J. Moore, and W. Peterman.

## REFERENCES

1. J. A. Misencik, "Evaluation of Candidate Stirling Engine Heater Tube Alloys for 1000 Hours at 760°C," NASA TM-81578, U.S. Dept. of Energy, Washington, D.C., November 1980.
2. J. R. Stephens, "Stirling Engine Materials Research," presented at the Automotive Technology Department Contractor Coordination Meeting, Dearborn, Mich., November 11-13, 1980.
3. J. R. Stephens, "Hostile Environmental Conditions Facing Candidate Alloys for the Automotive Stirling Engine," Conference Proceedings on Environment Degradation of Engineering Materials in Hydrogen, Virginia Polytechnic Institute, Blacksburg, Va., September 21-23, 1981, pp. 123-132.
4. J. R. Stephens, "Characterization of Stirling Engine Materials," presented at the Automotive Technology Development Contractor Coordination Meeting, Dearborn, Mich., October 25-28, 1982.
5. S. K. Verma, "Applications of Advanced Coating Techniques to Rocket Engine Components," Final Report IITRI-M06130-7 on Contract NAS8-35661 to NASA-Marshall, 31 March 1985.
6. R. Scarborough, "DARPA Eyes Family of Planes," Defense Week, April 14, 1986.
7. S. Bhattacharyya, E. J. Vesely, Jr., and V. L. Hill, "High Pressure/High Temperature Hydrogen Permeability in Candidate Stirling Engine Alloys," J. Mater. Energy Syst. (Trans. ASM), **3**(4) 12 (1982).
8. S. Bhattacharyya, E. J. Vesely, Jr., and V. L. Hill, "Determination of Hydrogen Permeability in Uncoated and Coated Superalloys," Interim Report, NASA CR-165209, U.S. Dept. of Energy, Office of Transportation Programs, Washington, D.C., January 1981.
9. S. Bhattacharyya, "Creep-Rupture Behavior of Six Candidate Stirling Engine Superalloys Tested in Air," J. Eng. Mater. Technol. (Trans. ASME), **106**, 50 (1984).
10. S. Bhattacharyya, "Creep-Rupture Behavior of Six Candidate Stirling Engine Iron-Base Superalloys in High Pressure Hydrogen, Vol. I: Air Creep-Rupture Behavior," NASA CR-168071, NASA-Lewis Research Center, Cleveland, Ohio, December 1982.
11. S. Bhattacharyya, "Creep-Rupture and Fractographic Analysis of Candidate Stirling Engine Superalloys Tested in Air," J. Mater. Energy Syst. (Trans. ASM), **5**(4), 188 (1984).

12. S. Bhattacharyya, W. Peterman, and C. Hales, "Creep-Rupture Behavior of Candidate Stirling Engine Iron Superalloys in High-Pressure Hydrogen, Vol. II: Hydrogen Creep-Rupture Behavior," NASA CR-174701, NASA-Lewis Research Center, Cleveland, Ohio, June 1984.
13. S. Bhattacharyya and W. Peterman, "Creep-Rupture Behavior of Iron Superalloys in High-Pressure Hydrogen," NASA CR-175027, NASA-Lewis Research Center, Cleveland, Ohio, December 1985.
14. W. R. Witzke and J. R. Stephens, "Creep-Rupture Behavior of Seven Iron-Base Alloys After Long-Term Aging at 760°C in Low Pressure Hydrogen," NASA TM-81534, NASA-Lewis Research Center, Cleveland, Ohio, August 1980.
15. F. R. Larson and J. Miller, Trans. ASME, **74**, 765 (1952).
16. S. S. Manson and A. M. Haferd, "A Linear Time-Temperature Relation for Extrapolation and Creep and Stress-Rupture Data," NACA Technical Note 2890, March 1952.
17. S. S. Manson and W. R. Broan, Proc. ASTM, **53**, 693 (1953).
18. O. D. Sherby, "Factors Affecting the High Temperature Strength of Polycrystalline Solids," Acta Metall., **10**(2), 135-147 (1962).
19. J. E. Dorn, "The Spectrum of Activation Energies for Creep," in Creep and Recovery, American Society for Metals, Metals Park, Ohio, 1957, pp. 255-283.
20. R. M. Goldhoff, "The Evaluation of Elevated Temperature Creep and Rupture Strength Data: An Historical Perspective," in Characterization of Materials for Service at Elevated Temperatures, G. V. Smith (Ed.), Publ. No. MPC-7, ASME, New York, 1978, pp. 247-265.

TABLE 1. NOMINAL COMPOSITION OF SUPERALLOYS TESTED

Alloys	Nominal Composition, %													Others
	C	Mn	Si	Cr	Ni	Co	Mo	W	Nb	Ti	Al	B	Fe	
A-286 <sup>a</sup>	0.05	1.40	0.40	15	26	-	1.25	-	-	2.15	0.2	0.003	Bal	0.03 V
INCOLOY Alloy 800H <sup>a,b</sup>	0.08	0.8	0.5	21	32.5	-	-	-	-	0.4	0.4	-	Bal	0.4 Cu
N-155 <sup>a</sup>	0.12	1.5	0.5	21	20	20	3.0	2.5	1.0 <sup>c</sup>	-	-	-	Bal	0.15 N, 0.5 Cu max
19-90L <sup>a</sup>	0.30	1.10	0.60	19	9.0	-	1.25	1.20	0.40	0.30	-	-	Bal	-
12RN72 <sup>d</sup>	0.1	1.8	0.4	19	25	-	1.4	-	-	0.5	-	0.006	Bal	0.030 P, 0.015 S max
CG-27 <sup>a</sup>	0.05	0.1	0.1	13	38	-	5.5	-	0.6	2.5	1.5	0.01	Bal	-
HS-31 <sup>e</sup>	0.5	0.75	0.75	25.5	10.5	Bal	-	7.5	-	-	-	-	-	-
SA-F11 <sup>f</sup>	0.63	0.5	0.6	23.0	16.0	-	-	12.0	-	-	-	0.4	Bal	-
CRM-60 <sup>a</sup>	1.05	5.00	0.50	22	5.0	-	1.0	1.0	1.0	-	-	0.003	Bal	-
XF-818 <sup>g</sup>	0.21	0.29	0.34	18.3	18.0	-	7.32	-	0.43	-	-	0.75	Bal	0.106 N, 0.007 P, 0.010 S
NASAUT	1.5	15.0	1.0	15.5	-	-	20	-	-	-	-	-	64.5	1.0 Cb+Ta

<sup>a</sup> 1983 Materials & Processing Databook, Metal Progress, Vol. 124, No. 1, p. 64.

<sup>b</sup> INCOLOY Alloy 800H is a registered trademark of Huntington Alloys, Inc. In all subsequent tables, figures, and in the text, the alloy is identified either fully or as 800H.

<sup>c</sup> Includes tantalum.

<sup>d</sup> Sandvik Lecture No. 56-10E, Paper presented at the MI Con 78 Symposium, Houston, Texas, April 1978, Steel Research Center, Sandvik, Sandviken, Sweden.

<sup>e</sup> ASM Metals Handbook, Vol. 3, 9th Ed., p. 268.

<sup>f</sup> Composition supplied by NASA-Lewis Research Laboratory, Cleveland, Ohio.

<sup>g</sup> Climax Molybdenum Co., Research Laboratory, Ann Arbor, Michigan.

TABLE 2. HEAT TREATMENT, HARDNESS, AND GRAIN SIZE OF TESTED ALLOYS

Alloy	Heat Treatment	Average Hardness, HRA (HV) <sup>a</sup>	Average Grain Dia., $\mu\text{m}$
A-286	Solution annealed at 1149°C. <sup>b,c</sup> aged at 718°C for 16 h and air cooled.	51.9 (163)	108
800H	Solution annealed at 1149°C <sup>b,c</sup>	40.0 (108)	64
N-155	Solution annealed at 1177°C <sup>b,c</sup>	51.5 (161)	42
19-9DL	Solution annealed at 1204°C-10 min <sup>c</sup>	50.5 (156)	33
12RN72	Solution annealed at 1150°C-15 min <sup>c</sup>	39.7 (107)	56
CG-27	Solution annealed at 1150°C in vacuum for 10 min, furnace-cooled to room temperature, aged at 790°C in vacuum for 16 h, cooled to 650°C, held for 4 h, and furnace cooled.	69.7 (378)	194
HS-31 <sup>d</sup>	Simulative brazing cycle heat treatment, 1 h at 1150°C in 10 <sup>-6</sup> mm vacuum followed by furnace cooling	61.0 (243)	-
SA-F11 <sup>d</sup>		62.1 (256)	-
XF-818 <sup>d</sup>		61.6 (249)	-
XF-818 <sup>d</sup>		52.1 (164)	-
CRM-6D <sup>e</sup>	Aged at 650°C-100 h	62.4 (260)	-
XF-818 <sup>e</sup>	As-cast	50.5 (156)	-
NASAUT	790°C-20 h, 1065°C-15 min, 760°C-16 h, 650°C-16 h (furnace-cooled to room temperature in each cycle)		

<sup>a</sup>Vicker's hardness number (HV) converted from Rockwell hardness A scale (HRA).

<sup>b</sup>Solution annealing time 142 s/mm (1 h/in.) thickness minimum.

<sup>c</sup>Rapidly cooled from solution temperature.

<sup>d</sup>Cast by United Stirling AB, Sweden. The molten alloy was fed in the mold from one end. Simulative braze cycle heat treatment by NASA-LeRC, Cleveland, Ohio.

<sup>e</sup>Cast by Climax Molybdenum Co., Ann Arbor, Michigan. The molten alloy was fed in the mold from the side.



**TABLE 3. RUPTURE LIFE STRESS EXPONENT AND APPARENT ACTIVATION ENERGY OF VARIOUS CAST ALLOYS TESTED IN 15 MPa HYDROGEN**

Alloy	Condition	No. of Data	R <sup>2</sup>	Stress Exponent (n)	Apparent Activation Energy (Q), kJ/mol
NASAUT 4G-Al	Heat treated	8	0.962	-22.4	1201
XF-818	As-cast	10	0.894	-7.93	436
XF-818	Braze-cycled	6	0.993	-8.43	591
CRM-6D	Aged	8	0.962	-13.3	720
CRM-6D	Braze-cycled	6	0.998	-6.94	273
SA-F11	Braze-cycled	6	0.972	-6.85	508
HS-31	Braze-cycled	6	0.769	-10.2	551

**TABLE 4. MINIMUM CREEP RATE STRESS EXPONENT AND APPARENT ACTIVATION ENERGY OF VARIOUS CAST ALLOYS TESTED IN 15 MPa HYDROGEN**

Alloy	Condition	No. of Data	R <sup>2</sup>	Stress Exponent (n)	Apparent Activation Energy (Q), kJ/mol
NASAUT 4G-Al	Heat-treated	8	0.739	20.0	-923
XF-818	As-cast	10	0.825	7.55	-450
XF-818	Braze-cycled	6	0.991	9.74	-708
CRM-6D	Aged	9	0.948	11.8	-551
CRM-6D	Braze-cycled	6	0.987	6.76	-239
SA-F11	Braze-cycled	6	0.949	6.58	-505
HS-31	Braze-cycled	6	0.793	12.6	-600

**TABLE 5. TIME TO 1 PERCENT CREEP STRAIN STRESS EXPONENT AND APPARENT ACTIVATION ENERGY OF VARIOUS CAST ALLOYS TESTED IN 15 MPa HYDROGEN**

Alloy	Condition	No. of Data	R <sup>2</sup>	Stress Exponent (n)	Apparent Activation Energy (Q), kJ/mol
NASAUT 4G-A1	Heat-treated	8	0.804	-19.2	814
XF-818	As-cast	9	0.833	-8.70	512
XF-818	Braze-cycled	6	0.919	-7.76	603
CRM-6D	Aged	9	0.938	-11.1	512
CRM-6D	Braze-cycled	6	0.968	-6.90	309
SA-F11	Braze-cycled	6	0.942	-7.06	510
HS-31	Braze-cycled	6	0.710	-4.54	256

**TABLE 6. A COMPARISON OF PREDICTED STRESSES FOR VARIOUS CAST ALLOYS TESTED AT 775°C (1427°F) IN 15 MPa HYDROGEN<sup>a</sup>**

Alloy	Condition	Estimated Stress, MPa (ksi)			
		Mean	90% Conf. Limits		
			Low	High	
<u>3500-h Rupture Life</u>					
NASAUT 4G-A1	Heat-treated	140	(20.3)	94.3	186
XF-818	As-cast	126	(18.3)	110	144
XF-818	Braze-cycled	125	(18.1)	122	128
CRM-6D	Aged	164	(23.8)	154	174
CRM-6D	Braze-cycled	87.7	(12.7)	84.7	90.9
SA-F11	Braze-cycled	160	(23.2)	154	167
HS-31	Braze-cycled	169	(24.5)	156	183
<u>1% Creep Strain in 3500 h</u>					
NASAUT 4G-A1	Heat-treated	57.8	(8.38)	b	126
XF-818	As-cast	105	(15.2)	88.9	123
XF-818	Braze-cycled	90.0	(13.1)	82.5	98.1
CRM-6D	Aged	130	(18.9)	118	143
CRM-6D	Braze-cycled	615	(8.92)	53.0	71.3
SA-F11	Braze-cycled	126	(18.3)	119	134
HS-31	Braze-cycled	46.2	(6.70)	42.0	50.7

<sup>a</sup>Design criterion = 119 MPa at 775°C.

<sup>a</sup>Because of large standard deviation, the lower value becomes negative.

ORIGINAL PAGE IS  
OF POOR QUALITY

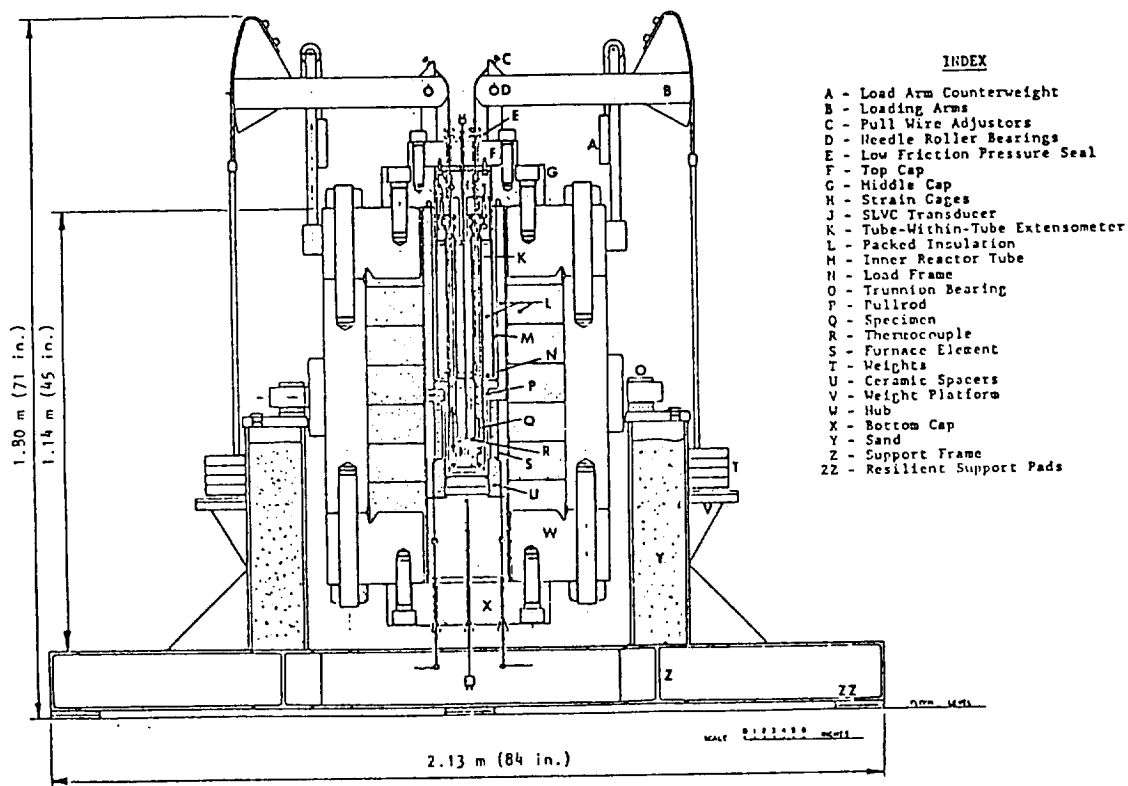


Figure 1. High-pressure multispecimen test facility for creep-rupture evaluation of materials in controlled environments.

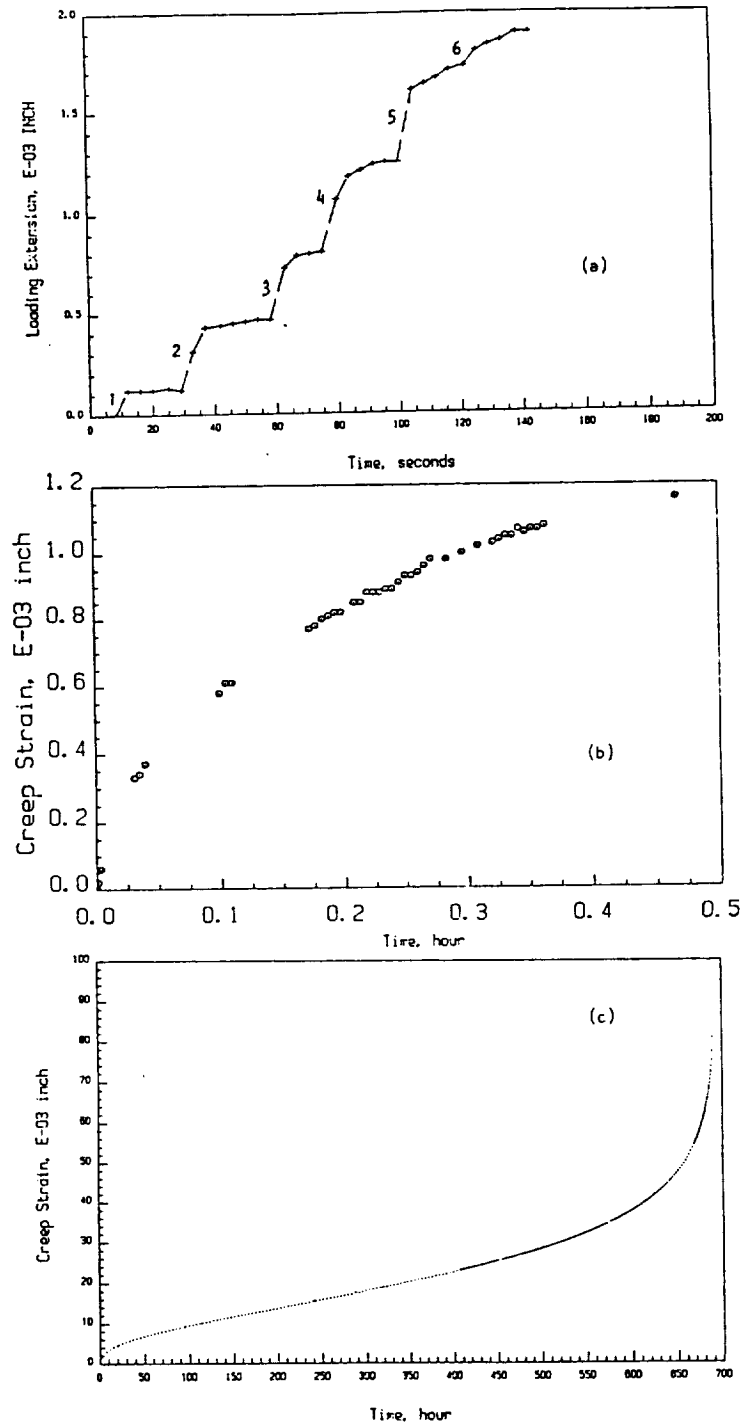


Figure 2. Computer-plotted, continuously recorded creep-time curves for a NASA experimental alloy at 775°C in 15 MPa H<sub>2</sub>. (a) Typical 6-step deadweight loading extension-time response; (b) details of extension during the early primary creep stage; (c) the complete creep curve.

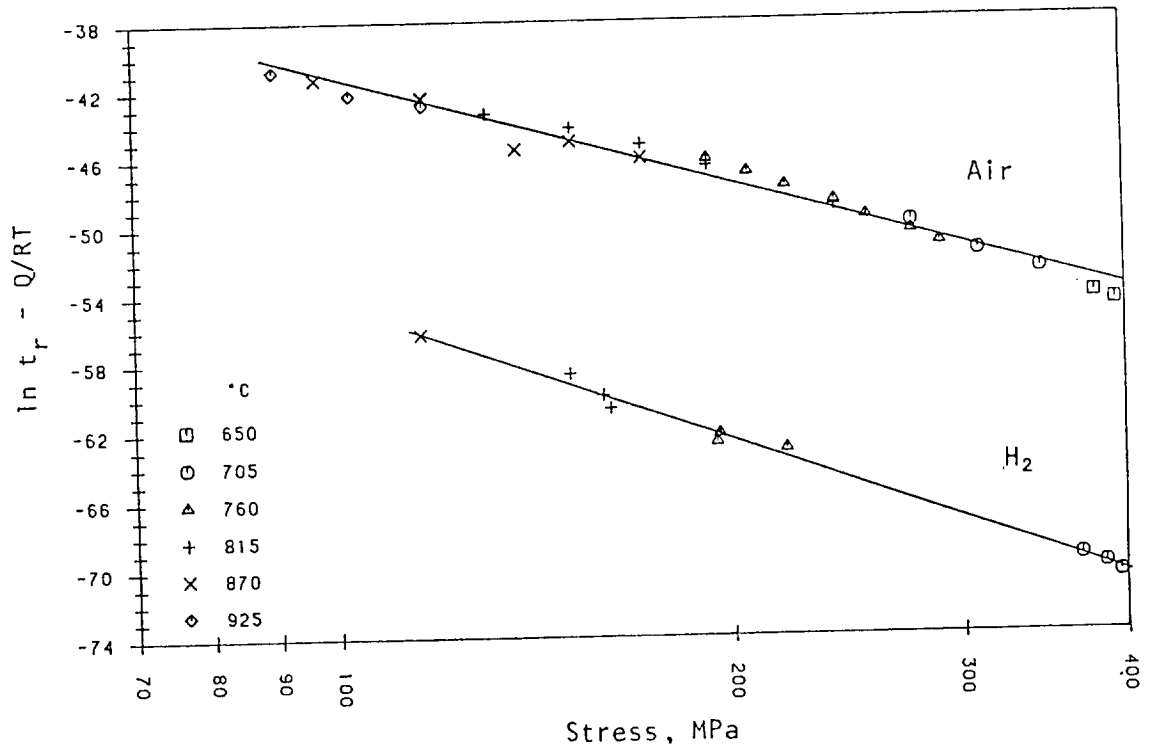


Figure 3. Effect of environment on temperature-compensated rupture life for CRM-6D (aged).

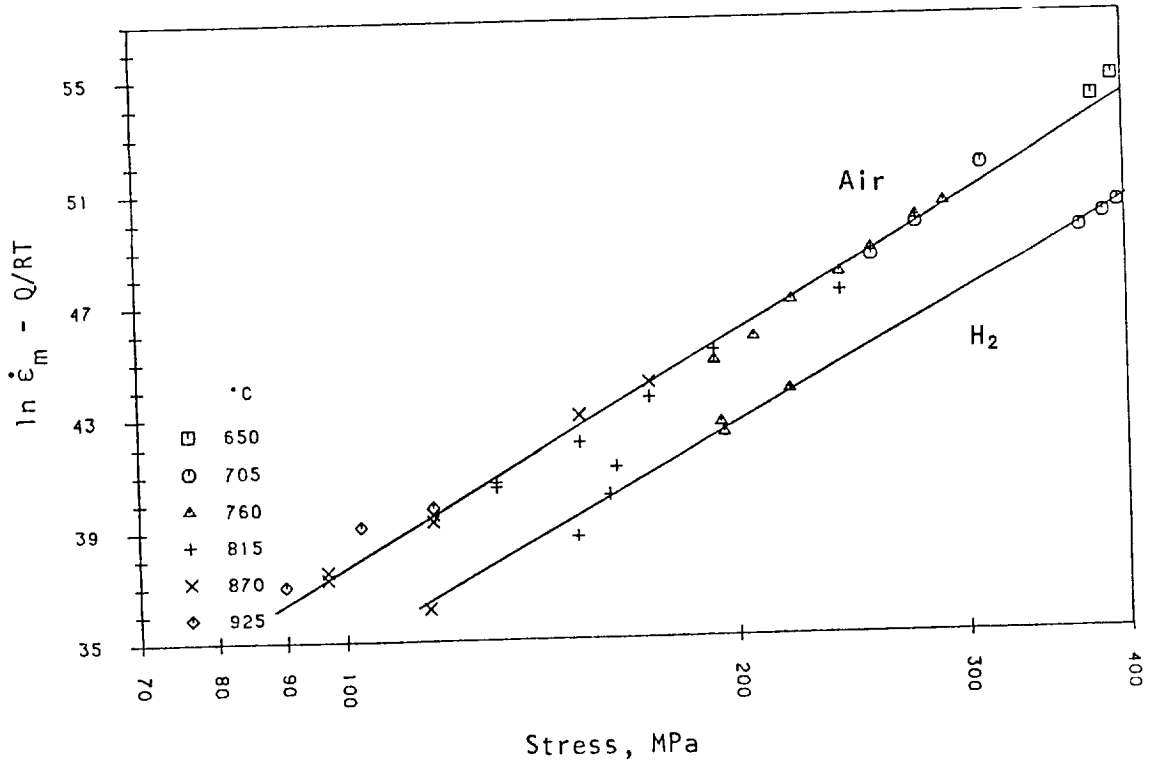
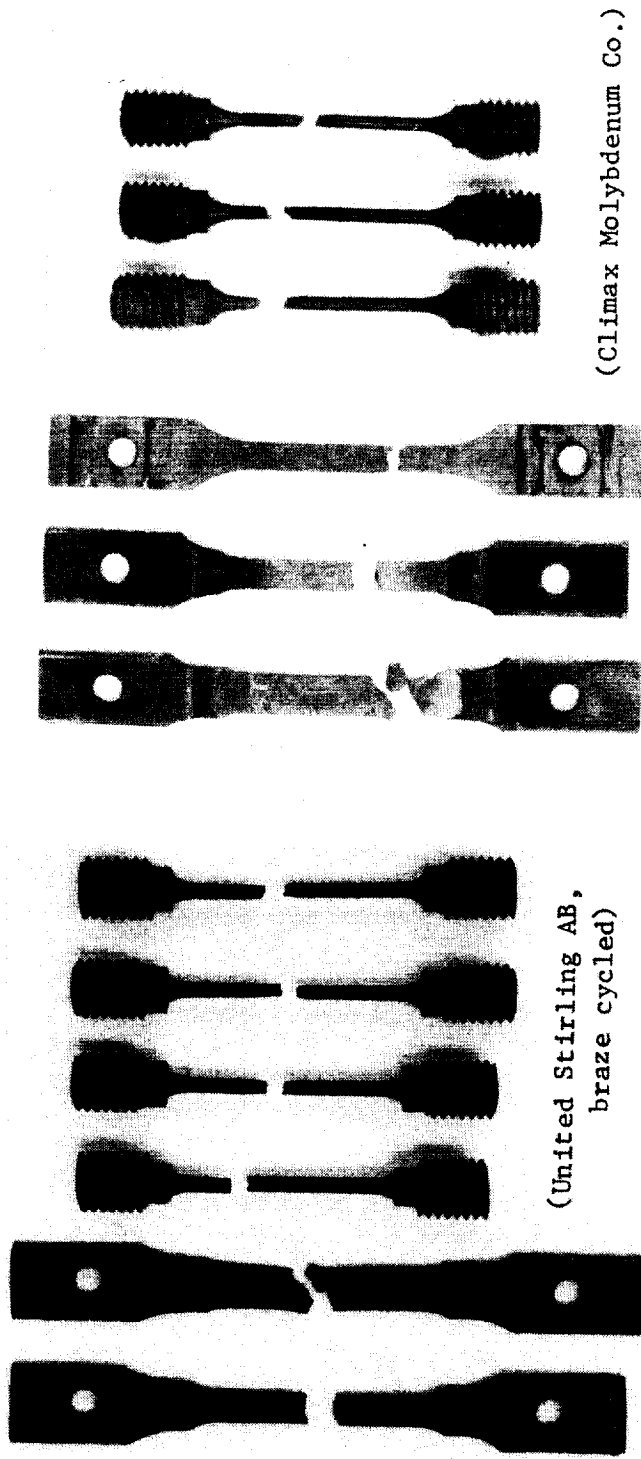


Figure 4. Effect of environment on temperature-compensated minimum creep rate for CRM-6D (aged).



(United Stirling AB,  
braze cycled)

(Climax Molybdenum Co.)

Alloy	CG-27	12RN72	SA-F11	HS-31	CRM-6D	XF-818	12RN72	CG-27	800H	CRM-6D	XF-818	XF-818
Elong., %	6.5	20.9	6.3	30.6	39.2	33.3	15.4	2.6	13.8	22.6	10.7	8.5
Stress, MPa	140	50.0	145	157	87.0	106	85.0	275	95.0	220	195	210

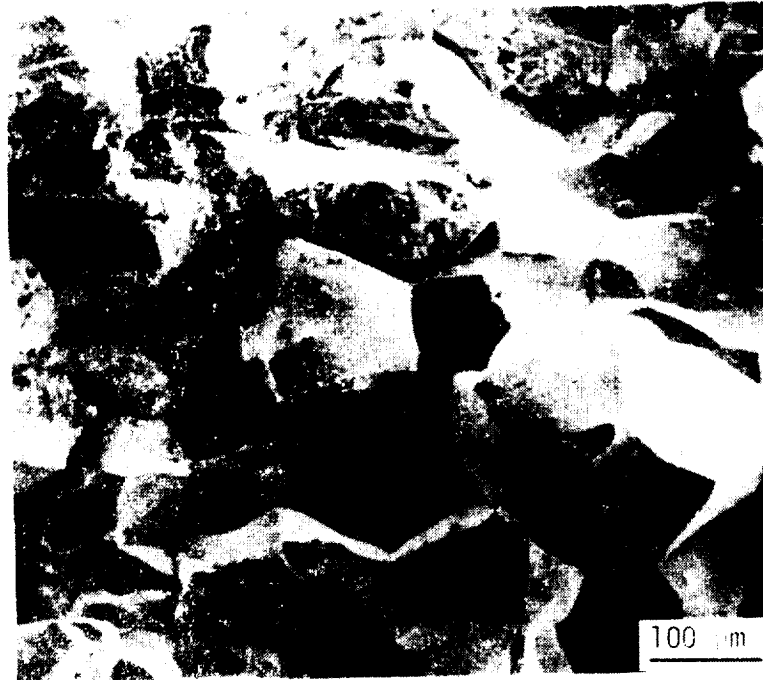
25 mm

25 mm

Neg. No. 55698

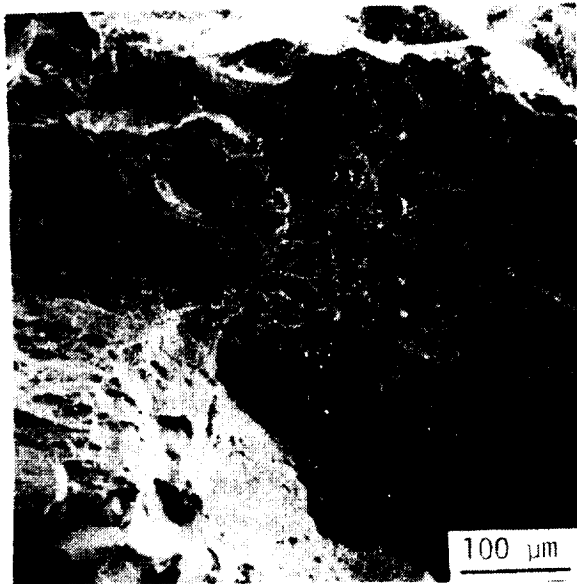
Neg. No. 55515

Figure 5. Appearance of fractured wrought and cast alloy specimens tested in 15 MPa hydrogen.  
(a) 815°C, (b) 760°C.



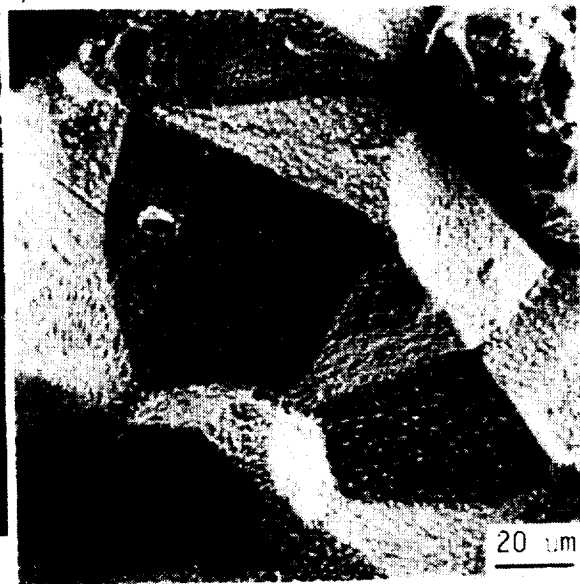
SEM No. 8375A

(a)



SEM No. 8377B

(b)



SEM No. 8375B

(c)

Figure 6. SEM microfractographs of A-286 tested in 15 MPa H<sub>2</sub> at 750°C. (a) Intergranular fracture; (b) ductile dimple fracture near the surface; (c) intergranular fracture with second phases on grain surfaces.

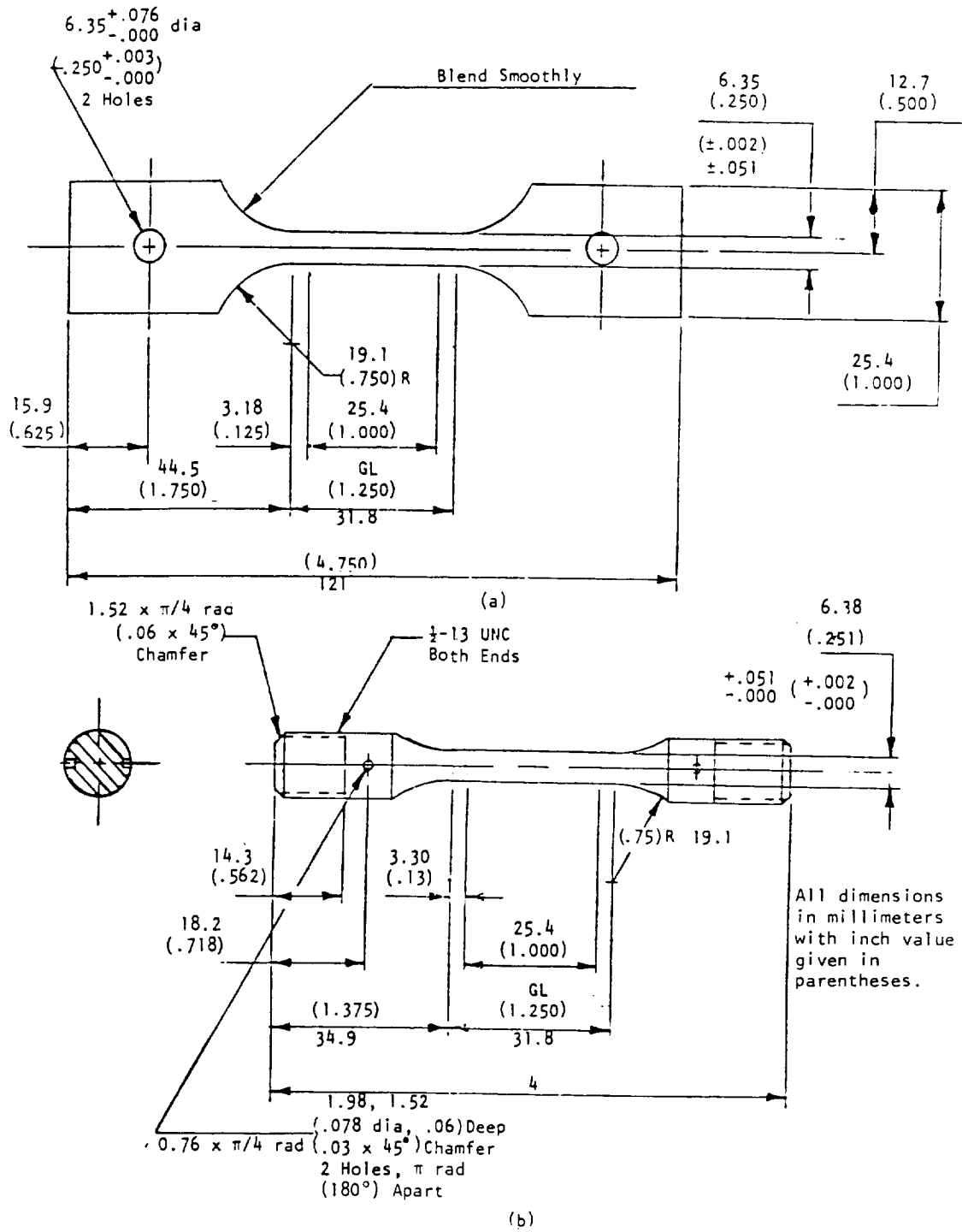


Figure A-1. Creep-rupture specimen design. (a) Wrought (sheet), (b) cast.



**TABLE A-1. HIGH-PRESSURE (15 MPa) HYDROGEN CREEP-RUPTURE DATA ON MOST OF THE ALLOYS TESTED AT IITR<sup>12,13</sup>**

(1) Test No.	(2) Env.	(3) Alloy <sup>a</sup>	(4) Temp., °C	(5) Stress, MPa	(6) $t_r$ , h	(7) Min. Creep Rate, s <sup>-1</sup>	(8) $t_{0.01}$ , h	(9) $t_{ter}$ , h	(10) El., %	(11) R.A., %
H03	HYD	CRM	705	395	9.0	7.11E-07	1.0	5.0	5.6	19.6
H04	HYD	CRM	705	385	15.7	4.86E-07	0.9	8.0	6.0	12.2
H05	HYD	CRM	705	369	25.8	3.03E-07	4.0		7.8	17.6
H19	HYD	CRM	760	220	306	3.18E-08	17.2	233	7.0	22.6
H06	HYD	CRM	760	195	470+	1.04E-08	65.0	350	3.1+	2.1+
H08	HYD	CRM	760	198	749	7.16E-09	99.0	579	7.4	37.2
H07	HYD	CRM	815	162	111	5.21E-08	16.5	70.0	8.1	58.3
H20	HYD	CRM	815	160	238	1.94E-08	61.9	150	8.5	45.0
H10	HYD	CRM	815	151	842	4.40E-09	131	500	7.0	21.5
H09	HYD	CRM	870	116	383+	5.90E-09	7.5		1.6+	
H13	HYD	CRM	760	252	3.7	5.21E-08	0.4	1.0	20.1	35.0
H14	HYD	CRM	760	130	357	6.54E-08	27.0	150	14.8	43.3
H18	HYD	CRM	760	117	742	3.35E-08	75.0	300	21.1	55.6
H15	HYD	CRM	815	105	273	9.56E-08	12.5	140	27.3	50.4
H16	HYD	CRM	815	100	504	3.77E-08	43.5	140	20.8	39.3
H17	HYD	CRM	815	87	1210	1.34E-08	125	330	24.7	39.2
H05	HYD	XF8	705	396	6.4	7.46E-07	1.2	2.2	5.0	11.9
H03	HYD	XF8	705	395	15.0				6.0	6.2
H06	HYD	XF8	760	216	182	5.44E-08	27.5	47.0	10.4	36.6
H19	HYD	XF8	760	210	167	7.86E-08	23.5	80.0	8.5	24.7
H19	HYD	XF8	760	195	424	2.98E-08	44.4	150	10.7	23.9
H08	HYD	XF8	760	166	1492+	5.99E-09	108	750	6.6+	11.4+
H01	HYD	XF8	815	176	56.7	1.17E-07	7.8	41.0	10.3	30.6
H07	HYD	XF8	815	133	275	4.00E-08	41.8	75.0	14.2	57.3
H12	HYD	XF8	815	131	200	5.51E-08	14.0	80.0	10.1	47.3
H20	HYD	XF8	815	125	387	3.94E-08		200	11.0	47.8
H10	HYD	XF8	815	118	1091	8.78E-09	200	200	16.2	21.1
H09	HYD	XF8	870	93.6	221	5.90E-08	38.0		15.4	47.2
H13	HYD	XF8	760	192	258	6.32E-08	35.0	55.0	11.6	20.7
H14	HYD	XF8	760	185	325	5.72E-08	36.0	100	14.7	21.1
H18	HYD	XF8	760	158	1303	1.07E-08	90.6	620	12.9	22.6
H15	HYD	XF8	815	135	141	1.59E-07	10.2	47.0	19.7	40.6
H16	HYD	XF8	815	120	460	4.41E-08	25.0	147	19.0	34.7
H17	HYD	XF8	815	106	1082	1.46E-08	105	375	15.6	33.3
H13	HYD	HS3	760	242	193	2.04E-07	3.0	125	23.2	42.6
H14	HYD	HS3	760	235	245	1.73E-07	2.6	165	28.1	51.0
H18	HYD	HS3	760	220	895	3.02E-08	5.4	556	20.7	48.0
H15	HYD	HS3	815	180	209	1.13E-07	2.6	107	18.3	40.3
H16	HYD	HS3	815	165	551	3.71E-08	3.9	292	17.9	43.9
H17	HYD	HS3	815	157	500	3.87E-08	4.0	280	13.5	30.6
H13	HYD	SAF	760	257	336	2.33E-08	62.0	150	6.1	8.4
H14	HYD	SAF	760	230	605	1.11E-08	113	210	5.0	6.3
H18	HYD	SAF	760	220	1023	7.57E-09	158	324	6.3	7.7
H15	HYD	SAF	815	180	198	3.63E-08	35.0	76.0	8.6	8.3
H16	HYD	SAF	815	160	364	2.50E-08	61.0	127	7.0	12.0
H17	HYD	SAF	815	145	886	9.12E-09	190	300	7.1	6.3
H04	HYD	A28	705	446	0.5	1.50E-05			14.0	
H03	HYD	A28	705	365	15.0+	7.76E-08	2.5		2.0+	
H05	HYD	A28	705	359	26.4	1.32E-07	6.9	17.0	7.0	
H02	HYD	A28	760	254	45.5	1.31E-08	36.2	21.0	4.7	
H06	HYD	A28	760	160	437	4.60E-10	270	80.0	9.8	
H08	HYD	A28	760	131	1202	7.25E-10	570	130	8.1	
H01	HYD	A28	815	138	27.7	1.12E-09	17.0	12.5	7.9	
H07	HYD	A28	815	70.2	571+	9.17E-09	195	50.0	2.7+	
H20	HYD	A28	815	70.0	533	1.46E-10	163	20.0	8.1	
H10	HYD	A28	815	55.8	1331+	1.95E-09	25.0	1100	4.8+	
H09	HYD	A28	870	24.7	383+	1.17E-07	3.5		21.0+	
H04	HYD	IN8	705	230	3.8	8.00E-06	0.1	2.0	30.0	
H03	HYD	IN8	705	193	14.3	3.40E-06	0.2	9.4	32.0	
H02	HYD	IN8	760	124	24.8	1.76E-06	0.3	17.0	26.3	
H19	HYD	IN8	760	95.0	96.7	2.04E-07	9.5	57.5	13.8	
H06	HYD	IN8	760	78.0	470+	6.04E-08	23.0	100	13.8+	
H08	HYD	IN8	760	74.9	1391	2.82E-08	54.0	752	29.1	
H01	HYD	IN8	815	107	2.7	1.22E-07	0.2	1.0	19.2	

TABLE A-1 (Continued)

(1) Test No.	(2) Env.	(3) Alloy <sup>a</sup>	(4) Temp., °C	(5) Stress, MPa	(6) $t_r$ , h	(7) Min. Creep Rate, s <sup>-1</sup>	(8) $t_{0.01}$ , h	(9) $t_{ter}$ , h	(10) El., %	(11) R.A., %
H07	HYD	IN8	815	82.5	107	3.92E-07	0.5		21.4	
H12	HYD	IN8	815	80.7	240	1.27E-07	9.7	175	16.4	
H10	HYD	IN8	815	54.8	1331+	2.31E-08	11.0	1000	16.3+	
H09	HYD	IN8	870	41.0	383+	1.32E-07	10.0		22.8+	
H04	HYD	N15	705	319	11.2	1.19E-06	0.3	8.0	17.0	
H05	HYD	N15	705	283	39.0	5.24E-07	0.7	17.0	24.0	
H02	HYD	N15	760	193	30.4	9.28E-07	0.7	15.0	35.0	
H06	HYD	N15	760	138	460		210		30.0	
H08	HYD	N15	760	118	1193	1.18E-08	41.0	550	25.8	
H01	HYD	N15	815	124	46.2+	8.81E-07	1.4	29.0	24.0+	
H12	HYD	N15	815	107	146	2.09E-07	4.7	30.0	35.3	
H07	HYD	N15	815	97.0	349	8.15E-08	19.0	100	33.9	
H12	HYD	N15	815	89.1	573	3.15E-08	25.0	175	24.6	
H10	HYD	N15	815	80.0	1331+	5.50E-09	300	500	6.1+	
H04	HYD	199	705	306	1.7	1.68E-06			8.0	
H05	HYD	199	705	237	28.4	2.40E-07	4.7	8.0	15.0	
H02	HYD	199	760	163	20.7	4.53E-07	1.6	2.0	28.5	
H06	HYD	199	760	109	304	4.07E-08	29.4	125	9.3	
H08	HYD	199	760	88.5	1195	4.71E-09	85.0	579	7.9	
H01	HYD	199	815	93.4	32.1	2.09E-07	7.8	12.5	9.4	
H07	HYD	199	815	72.7	342	3.13E-08	31.1	200	9.3	
H12	HYD	199	815	71.3	508	1.86E-08	50.0	240	9.0	
H20	HYD	199	815	68.0	439	2.64E-08	92.5	229	11.7	
H10	HYD	199	815	57.8	1331+	1.10E-09	1000	1080	2.9+	
H13	HYD	12R	760	97	450+		7.0	350	3.8+	
H14	HYD	12R	760	90	247	1.14E-07	32.5	195	18.4	
H19	HYD	12R	760	85	456+	2.64E-08	71.7	81.7	15.4+	
H18	HYD	12R	760	75	891	1.75E-08	131	200	21.1	
H15	HYD	12R	815	60	350+	5.26E-08	33.5	129	7.8+	
H16	HYD	12R	815	57	650	2.03E-08	104	67.6	24.7	
H17	HYD	12R	815	50	1323	8.02E-09	225	80.0	20.9	
H19	HYD	CG2	760	275	277	3.96E-09	275	85.5	2.6	
H18	HYD	CG2	760	250	599			135		
H13	HYD	CG2	760	198	450+		5.0		4.4+	
H15	HYD	CG2	815	190	189	2.59E-08	62.5	62.0	5.77	
H16	HYD	CG2	815	165	313	2.23E-08	80.0	104	7.25	
H20	HYD	CG2	815	145	499	1.36E-08	71.6	475	3.8	
H17	HYD	CG2	815	140	819	8.64E-09	280	420	6.46	
H21	HYD	4GA	775	162	126.5	7.14E-08	25.7	567	6.5	22.2
H21	HYD	4GA	775	159	209.0	3.72E-08	49.7	98	6.0	13.2
H21	HYD	4GA	775	155	435.7	1.50E-08	25.0	333	6.7	7.4
H21	HYD	4GA	775	152	215.5	2.85E-08	55.2	120	4.2	15.4
H21	HYD	4GA	775	150	689.4	9.30E-09	178	475	9.9	33.1
H21	HYD	4GA	775	150	893.2	1.03E-08	127	522	13.6	32.4
H22	HYD	4GA	825	116	580.9	3.11E-09	343	162	7.5	28.3
H22	HYD	4GA	825	113	757.1	4.54E-09	450	333	3.6	18.2
H22	HYD	4GA	825	113	778.4	1.14E-08	194	511	6.8	15.7
H22	HYD	4GA	825	110	312.7	5.97E-09	299	247	1.1	1.1
H22	HYD	4GA	825	110	375.1	5.93E-09	331	270	1.3	1.9
H22	HYD	4GA	825	105	359.0	8.01E-09	216	184	2.6	3.5

<sup>a</sup>Alloy code: CRM = CRM-6D castings  
 XF8 = XF-818 castings  
 HS3 = HS-31 castings  
 SAF = SA-F11 castings  
 A28 = A-286  
 IN8 = INCOLOY Alloy 800H  
 N15 = N-155  
 199 = 19-9DL  
 12R = 12RN72  
 CG2 = CG-27  
 NGA = NASAUT 4G-A1

<sup>b</sup>Aged (Climax Molybdenum Co.).

<sup>c</sup>Braze-cycled (United Stirling AB, Sweden).

<sup>d</sup>As-cast (Climax Molybdenum Co.).

ORIGINAL PAGE IS  
 OF POOR QUALITY

**TABLE A-2. STATISTICAL DATA ON TEMPERATURE-COMPENSATED ANALYSIS  
OF CAST ALLOYS CRM-6D AND XF-818 IN AIR AND 15 MPa H<sub>2</sub>**

Alloy <sup>a</sup>	Environment	No. of Data	R <sup>2</sup>	ln k	n	Q, kJ/mol
<u>Rupture Life (t<sub>r</sub>)</u>						
CRM-6D	Air	26	0.843	0.829	-9.12	461
	15 MPa H <sub>2</sub>	8	0.962	-6.35	-13.3	720
XF-818	Air	14	0.991	-13.2	-7.52	505
	15 MPa H <sub>2</sub>	10	0.894	-3.51	-7.93	435
<u>Time to Reach 1% Creep Strain (t<sub>0.01</sub>)</u>						
CRM-6D	Air	29	0.973	5.59	-10.6	468
	15 MPa H <sub>2</sub>	9	0.938	3.48	11.1	512
XF-818	Air	14	0.988	-20.8	-6.86	522
	15 MPa H <sub>2</sub>	9	0.833	-10.1	-8.70	512
<u>Minimum Creep Rate (ε̇<sub>m</sub>)</u>						
CRM-6D	Air	28	0.947	-16.9	11.8	-551
	15 MPa H <sub>2</sub>	9	0.948	-14.2	11.8	-574
XF-818	Air	14	0.990	6.85	7.47	-545
	15 MPa H <sub>2</sub>	10	0.825	-4.51	7.55	-450

<sup>a</sup>Alloys cast by Climax Molybdenum Co., Ann Arbor, Michigan. CRM-6D and XF-818 were tested in aged and as-cast conditions, respectively.

**TABLE A-3. ELONGATION DATA<sup>12</sup>**

Environment	Temp., °C	Stress Range, MPa	Elongation Range, %
<u>Alloy A-286</u>			
Air	650	441, 483	8.4, 11.4
Air	705	179-379	3.4-21.0
15 MPa H <sub>2</sub>	705	359, 446	7.0, 14.0
Air	760	124-345	8.7-26.3
15 MPa H <sub>2</sub>	760	131-254	4.7-9.8
Air	815	55-138	10.7-44.6
15 MPa H <sub>2</sub>	815	70, 138	12.5, 20.0
Air	870	21-55	29.8-87.2
15 MPa H <sub>2</sub>	870	24.7	21.0 <sup>a</sup>
Air	925	17-28	38.7-58.4
<u>INCOLOY Alloy 800H</u>			
Air	650	207-276	15.0-32.3
Air	705	110-186	19.6-36.8
15 MPa H <sub>2</sub>	705	193-230	2.0-9.4
Air	760	70-152	28.1-53.0
15 MPa H <sub>2</sub>	870	74.9-124	13.8-29.1
Air	815	45-110	18.1-59.6
15 MPa H <sub>2</sub>	815	54.8-62.5	16.3 <sup>a</sup> -21.4
Air	870	26-76	15.9-32.2
15 MPa H <sub>2</sub>	870	41.0	22.8 <sup>a</sup>
Air	925	31-48	19.7-24.0
<u>N-155</u>			
Air	650	276-414	19.9-26.2
Air	705	159-276	28.3-46.0
15 MPa H <sub>2</sub>	705	283, 319	17.0, 24.0
Air	760	97-241	18.0-51.5
15 MPa H <sub>2</sub>	760	118-193	25.8-35.0
Air	815	63-165	12.1-58.3
15 MPa H <sub>2</sub>	815	80-124	6.1 <sup>a</sup> -35.3
Air	870	4-110	26.3-65.0
Air	925	41-69	27.7-43.4
<u>19-9DL</u>			
Air	650	276-414	10.1-18.8
Air	705	131-276	12.1-24.2
15 MPa H <sub>2</sub>	705	237, 306	8.0, 15.0
Air	760	86-193	12.1-37.4
15 MPa H <sub>2</sub>	760	88.5-163	7.9-28.5
Air	815	59-138	10.1-44.8
15 MPa H <sub>2</sub>	815	68-93.4	9.0-11.7
Air	870	33-103	20.8-61.6
	925	35-69	27.5-47.6
<u>12RN72</u>			
15 MPa H <sub>2</sub>	760	75, 90	18.4, 21.1
15 MPa H <sub>2</sub>	815	50, 57	20.9, 24.7

**TABLE A-3 (continued)**

Environment	Temp., °C	Stress Range, MPa	Elongation Range, %
<u>CG-27</u>			
15 MPa H <sub>2</sub>	760	275	2.6
15 MPa H <sub>2</sub> <sup>2</sup>	815	140-190	6.5-7.3
<u>CRM-6D<sup>b</sup></u>			
Air 650	379, 393	4.2, 5.6	
Air 705	276-345	7.8-8.4	
15 MPa H <sub>2</sub>	705	369-395	5.6-7.8
Air 760	193-290	7.7-10.7	
15 MPa H <sub>2</sub>	760	196, 220	7.0, 7.4
Air 815	131-241	4.6-13.9	
15 MPa H <sub>2</sub>	815	151-162	7.0-8.5
Air 870	97-172	2.8-21.7	
15 MPa H <sub>2</sub>	870	116	1.6 <sup>a</sup>
Air 925	90-117	5.5-12.5	
<u>CRM-6D<sup>c</sup></u>			
15 MPa H <sub>2</sub>	760	117-252	14.8-21.1
15 MPa H <sub>2</sub> <sup>2</sup>	815	87-105	20..8-27.3
<u>XF-818<sup>b</sup></u>			
Air 650	393, 414	7.5, 8.0	
Air 705	283-414	6.7-10.1	
15 MPa H <sub>2</sub>	705	395, 396	5.0, 6.0
Air 760	207-331	8.2-13.6	
15 MPa H <sub>2</sub>	760	195-216	8.5-10.7
Air 815	103-241	14.1-23.8	
15 MPa H <sub>2</sub>	815	118-176	10.1-16.2
Air 870	63-172	12.9-20.6	
15 MPa H <sub>2</sub>	870	93.6	15.4
Air 925	55-103	18.4-25.2	
<u>XF-818<sup>c</sup></u>			
15 MPa H <sub>2</sub>	760	158-192	11.6-14.7
15 MPa H <sub>2</sub> <sup>2</sup>	815	106-135	15.6-19.7
<u>HS-31<sup>c</sup></u>			
15 MPa H <sub>2</sub>	760	220-242	20.7-28.1
15 MPa H <sub>2</sub> <sup>2</sup>	815	157-180	13.5-18.3
<u>SA-F11<sup>c</sup></u>			
15 MPa H <sub>2</sub>	760	220-257	5.0-6.3
15 MPa H <sub>2</sub> <sup>2</sup>	815	145-180	7.0-8.6

<sup>a</sup>Tests discontinued without failure.

<sup>b</sup>Climax Molybdenum Co.; castings, CRM-6D (aged), XF-818 (as-cast).

<sup>c</sup>United Stirling AB, Sweden; castings, braze-cycle treated.

## PRATT & WHITNEY'S HYDROGEN TEST FACILITIES

R. L. Fowler, Jr.  
Pratt & Whitney  
Engineering Division South  
P. O. Box 2691  
West Palm Beach, Florida 33402

Described in this paper are the high pressure hydrogen test facilities at Pratt & Whitney, Engineering Division South. Included in this system are test vessels and test stands capable of conducting tensile, creep-rupture, low-cycle fatigue and crack growth rate tests at pressures up to 34.5 MPa (5000 psig) and temperatures up to 871°C (1600°F). Currently under development are facilities for testing up to 55.2 MPa (8000 psig) and 1093°C (2000°F).

MANUSCRIPT NOT AVAILABLE

**A HIGH PRESSURE, HIGH TEMPERATURE HYDROGEN ENVIRONMENT  
FOR METALS PROPERTIES TESTING SYSTEM**

**Michael J. Rother  
MTS Systems Corporation**

The use of materials in an adverse environment has always been a concern of design engineers. The additional constraints of today's aerodynamic requirements, especially high strength-to-weight ratios for engineering components, have increased the necessity for detailed information of the environmental effects on material properties. MTS Systems designed and is in the process of manufacturing a test system for NASA-MSFC to evaluate the effects of high pressure, high temperature hydrogen gas on the material properties of metals. The design process for the system is discussed below with a presentation of the system's final configuration.

Material Properties

The design of any engineering component requires knowledge of the static properties of stiffness and ultimate strength, and the dynamic properties of fatigue and crack growth resistance. The minimum complement of material tests required for the target test system and the relevant ASTM specifications are :

- Tensile and Notched Tensile [ ASTM E8 ]
- Low Cycle Fatigue [ ASTM E606 ]
- High Cycle Fatigue [ ASTM E466 ]
- Fatigue Crack Growth [ ASTM E647 ]
- Plane Strain Fracture Toughness [ ASTM E399 ]

Test Environment

The test environmental conditions were selected to yield information on the degradation of material properties as a function of the test gas temperature and pressure. The requested temperature range for the test specimen is room temperature to +2000 ° F ( +1090 ° C ). The gaseous environment consists of either hydrogen, helium, or argon at pressures up to 10,000 psig. (69 MN / m<sup>2</sup> ).

Design Constraints

The combined material testing and environmental requirements place many constraints on the design of the test system. Increasing the versatility of any test system will generally complicate the design because of the often contradictory nature of different test and environmental requirements. For example, placing the load cell directly in the drive train of the loading subsystem results in conflicting problems regarding heat transfer and load frame lateral stiffness and alignment. Increasing the length of the pull rod between the specimen and load cell (which has a limited maximum operating temperature) will decrease the heat flow down the pull rod by increasing thermal resistance of the element. On the other hand, the increased length of the pull rod will have negative effect on the lateral stiffness and alignment of the loading system causing a problem in fatigue tests with compressive loads. Therefore, the system designer has to consider the combination of the myriad of trade-offs to obtain an optimal solution. Some of the design considerations which have to be evaluated are :

- Strain Measurement Technique
- Load Measurement Inside The Pressure Vessel
- Frame Stiffness And Alignment
- Dynamic Loading Requirements
- Component Force Capacities
- Thermal Distribution Inside The Pressure Vessel
- High Pressure Gas Effects
- System Control.

Additional design constraints, further defining the starting point of the project, are obtained from other external factors such as past experience with similar systems. The predominant area of these additional constraints for the target test system is in the pressure vessel design. The vessel approach is to incorporate a single, cold walled, monolithic dome design. This vessel design approach is selected for the following reasons :

- the pressure vessel dome experiences only pressure loads (i.e. no mechanical system loads).
- the number of vessel penetrations and sealing locations is minimized.
- the cold walled approach places the furnace assembly inside the vessel , hence decreasing the strength requirements of the vessel material at maximum specimen temperature.

The starting point for the design of the pressure vessel assembly with the external load frame is shown in figure 1.

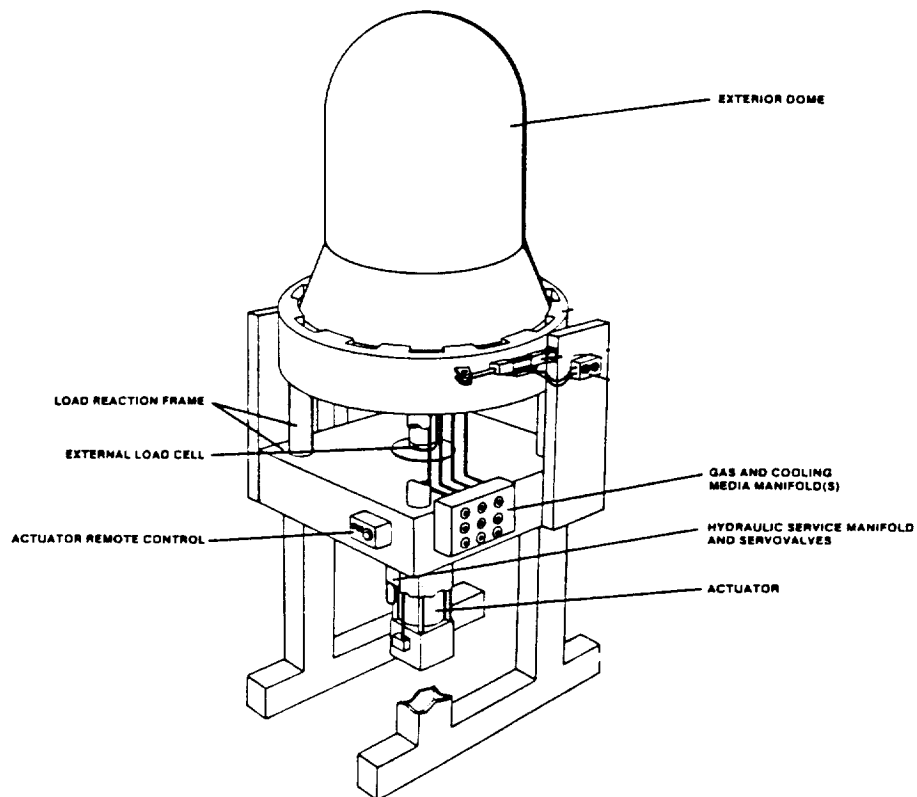


Figure 1. Pressure Vessel And External Load Frame



### Alternative Design Approaches

The combination of the above constraints led to the proposal of three alternative approaches to design. These are differentiated primarily by the techniques of strain measurement. The selection of the strain measurement approach affected the design of the furnace, grips, internal load frame, internal load cell, and pressure vessel. The three approaches are named:

- The Rod -in-Tube Approach
- The Feed Rod Approach
- The Center Rod Approach.

The basic considerations in the selection of a design of a subsystem for specimen strain measurement are:

- the selection of the strain sensing element along with the associated environmental operation constraints such as temperature and pressure.
- the travel and frequency requirements of the extensometer assembly.
- the effect of extensometer design approach on other system elements such as grips and furnaces.
- the accuracy and sensitivity of the extensometer assembly.
- the analysis of the sources of errors.
- the risk involved in application of the extensometer approach to the system.

The following sections discuss each approach along with the attributes which led to their consideration.

### Rod-In-Tube Approach

The Rod-In-Tube approach was developed many years ago for strain measurement in elevated temperature tests and is widely used in industry. The main basis of the approach is to locate the sensing devices below the test specimen in a location which has proven to be cooler. The basics of the Rod-In-Tube approach are shown in figure 2 for the fatigue and tensile test specimens. The test specimen is mechanically clamped at two points, effectively defining the gage length for strain measurement. The top clamp is connected via swivel joints to two small diameter solid rods on opposite sides of the specimen. Similarly, the lower clamp is connected via two swivel joints to two tubes. The rods are run down through the tubes to two sensing elements, typically linear variable displacement transducers (LVDT's). The two sensing output signals are averaged to obtain the specimen gage length changes during the test.

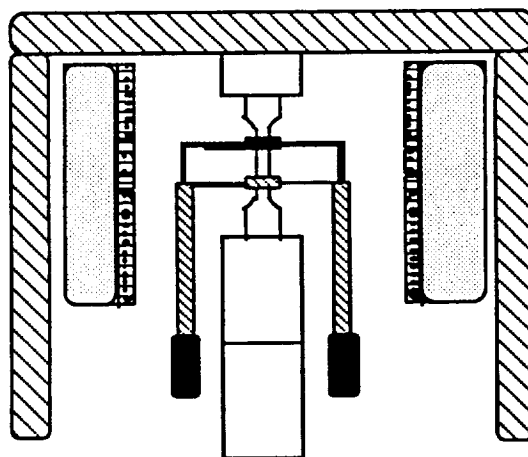


Figure 2. Rod-In-Tube Approach

The application of this approach to the target testing system is complicated by the additional constraints of the hanging rod-in-tube assemblies interfering with the grip and furnace design. The mechanical clamping assemblies and strain measurement rods and tubes are located in the hot zone of the furnace and present potential thermal expansion errors.

Positive attributes of the approach are :

- it's easy to use
- the specimen gage length doesn't affect the approach
- sensing elements in the lower region of the pressure vessel are at lower temperatures
- it is a proven strain measurement concept.

Deficiencies of the approach are :

- causes additional constraints on furnace and grip designs
- the mechanical clamping on specimen can cause extraneous stresses
- the mechanical clamping is in the furnace hot zone
- a high moving mass of extensometry
- frequency performance is limited.

#### Feed Rod Approach

The Feed Rod Approach is shown in figure 3. The strain measurement technique utilizes resistance type, foil strain gages bonded to a metallic element to form a Wheatstone bridge. Because of the high strength and low thermal expansion requirements, the feed rods are made from high purity alumina. The feed rods transmit specimen deflection to the metallic element causing bending and, hence, straining the bonded gages. Matching extensometer / feed rod sets are applied to both sides of the specimen, thereby balancing lateral forces on the specimen.

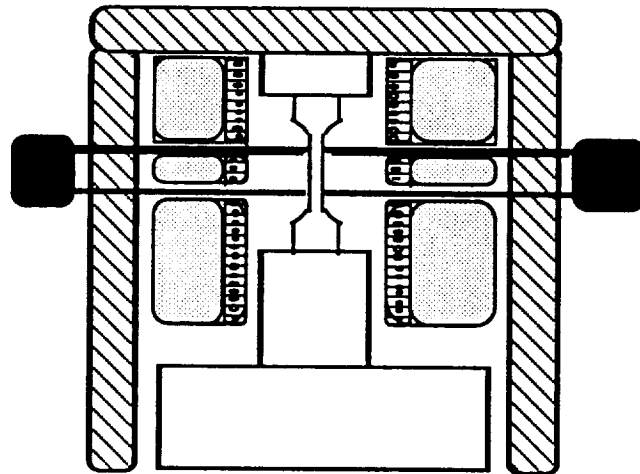


Figure 3. Feed Rod Approach

Application of the feed rod approach to the system also constrained its design. Although the furnace elements can be located physically closer to the specimen, slots for the feed rods must be incorporated into the design. The sensing elements are located at a position radial from the hot zone, requiring additional heat transfer studies to establish the temperature at the sensing elements locations. This approach would call for modifications of the current cross flexure assembly, thereby complicating the design and decreasing frequency performance relative to standard units.

Positive attributes of the approach are :

- it minimizes constraints in grip and furnace designs
- the high expansion materials are in cooler regions of the pressure vessel
- it's easy to use
- the specimen interface is only a tip contact
- the low moving mass of extensometry

Deficiencies of the approach are :

- it requires low radial temperature distribution.
- it requires design of additional cross flexure assembly.
- the limited feed rod length constrains overall system size.

#### Center Rod Approach

The final approach to be considered is called the Center Rod Approach; the approach initially proposed for the target test system. The principal advantage leading to the consideration of this approach is removal of all strain measurement components from the system hot zone. A representation of the approach is shown in figure 4. The specimen is contacted by precision-ground rods of alumina at the base of the specimen, inside the grips. The rods are connected to reaction beams to transmit specimen deflection to the strain sensing elements. The reaction beams and struts are integrated into the internal load frame and are made from stiff, low thermal expansion materials to minimize errors. The strain sensors are located in an area of proven cooler temperatures. The output of the two sensors are averaged to obtain specimen strain. Furnace and grip design are practically independent of the strain sensing components, resulting in a much simpler configuration .

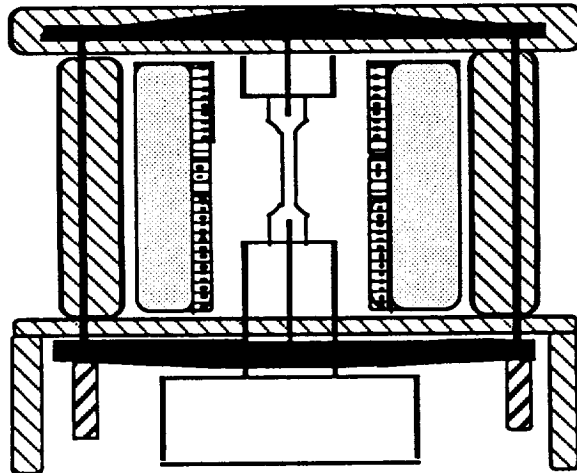


Figure 4. Center Rod Approach

The center rod approach added many constraints into the design of the internal load frame and strain sensing elements. Furthermore, the approach is a considerable extension of any current strain sensing techniques raising the uncertainty of the dynamic performance. The specimen strain is measured from two locations outside the gage length and requires a calibration curve of measured travel to specimen strain.

Positive attributes of the approach are :

- all of the strain sensing components are outside the hot zone of the furnace
- it has minimal interface with grip and furnace design
- the specimen interface is outside the hot zone
- different gage lengths do not affect approach
- the sensing elements are located in a region of proven lower temperatures.

Deficiencies of the approach are :

- it does not directly measure changes in specimen gage length.
- the high moving mass of extensometry.
- it has unproven frequency performance.
- it is difficult to use.

### **SYSTEM DESIGN**

MTS Systems and NASA-MSFC personnel discussed the alternatives and decided to utilize the feed rod design approach, provided the radial mode of heat transfer could be controlled. The initial stage of the system design consisted of performing modeling of the conduction, convection, and radiant modes of heat transfer in the direction radial from the specimen. The models indicated the radial modes of heat loss could be minimized and the natural convection loops could be used to cool the sensing elements. Extending the analysis of the heat transfer to the linear direction provided information on the operating temperature of the load cell. After the thermal models were established, design iterations modifying component dimensions were performed. The resulting system is shown in figure 5. The discussion of the final system design that follows proceeds from the specimen toward the vessel and finally to the external loading system.

### **Grips Designs**

The grip designs are quite simple due to the operating environment. The objective was to permit testing up to +2000 ° F while minimizing the highly stressed mechanical couplings used in conventional grips. In order to decrease the specimen temperature gradient, the grips are required to experience the same conditions as the test specimen. Additional constraints were to minimize the grip size, which allowed a smaller diameter hot zone, and increase insulation in the furnace assemblies. The grips for the tensile and fatigue specimens consisted of threaded tubes of high strength superalloys.

The major challenge of the grips turned out to be finding a way to minimize heat flow to the load cell. The design constraints for the lower grip assembly are:

- The portion of the grip tubes in the furnace hot zone is at +2000 ° F .
- The lower portion of the grip tubes mates up to the top of the load cell.
- The maximum operating temperature of the load cell is +350 ° F .
- The temperature gradient across the load cell strain gages should be minimized.
- The grip tube length should be minimized to increase lateral stiffness.

The final design approach is shown in figure 6. The lower portion of the tube is hollowed out to permit the insertion of a "cold-finger" assembly. The cold-finger element is rigidly fixed to the pull rod passing through the pressure vessel base. The design must take into account that any contact between the cold-finger and load cell or grip rod will cause erroneous load readings. The "cold-finger" component is made from a metal with high thermal conductivity and has direct internal water cooling from the pull rod. The approach takes advantage of the high thermal conductivity of hydrogen and helium gas. The comparison of the temperature profile with and without the cold-finger assembly is shown in figure 7. The thermal analysis also showed that testing with argon would be limited to +1600 ° F because of the decreased thermal conductivity (figure 8).

1. Pressure Vessel
2. Grip Tubes
3. Internal Load Frame
4. Furnace
5. Extensometers and Load Cells
6. External Load Frame

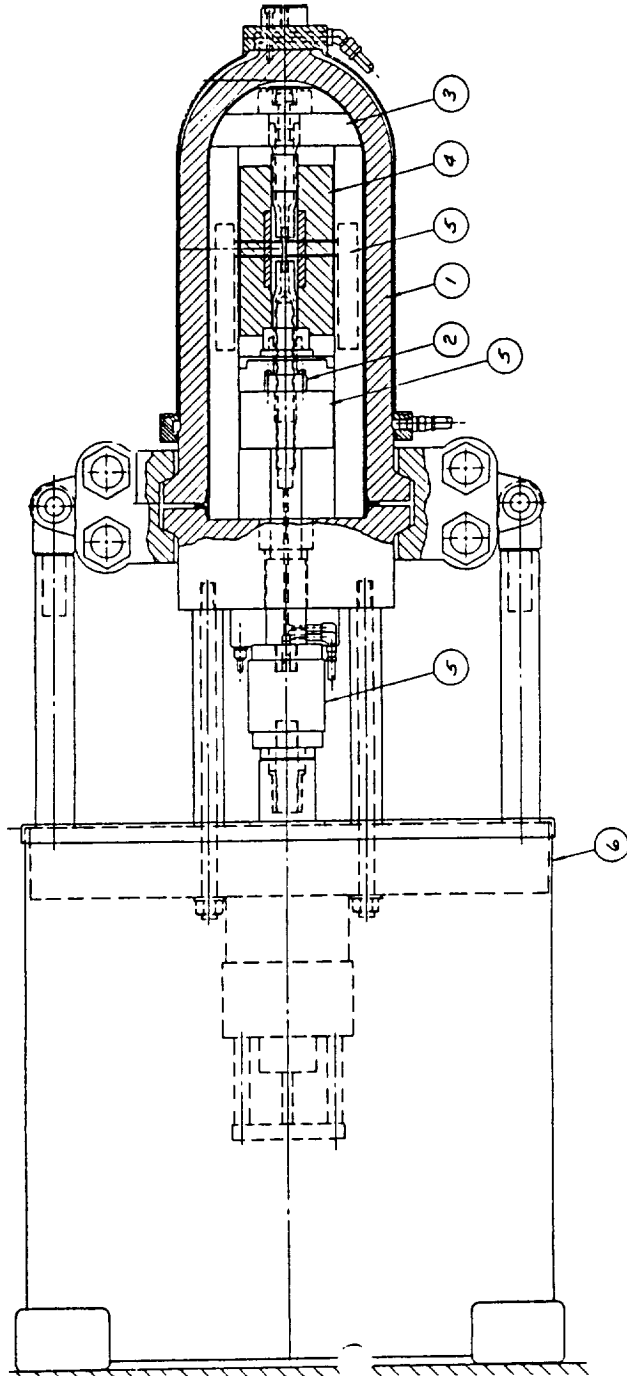


Figure 5. System Assembly

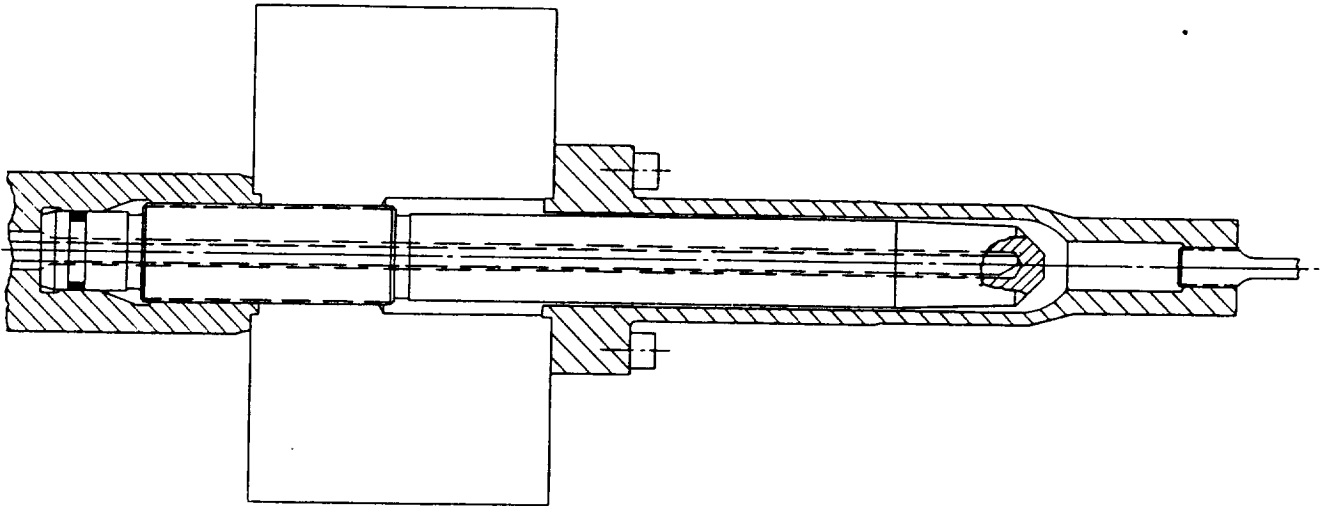


Figure 6. Cold Finger Assembly

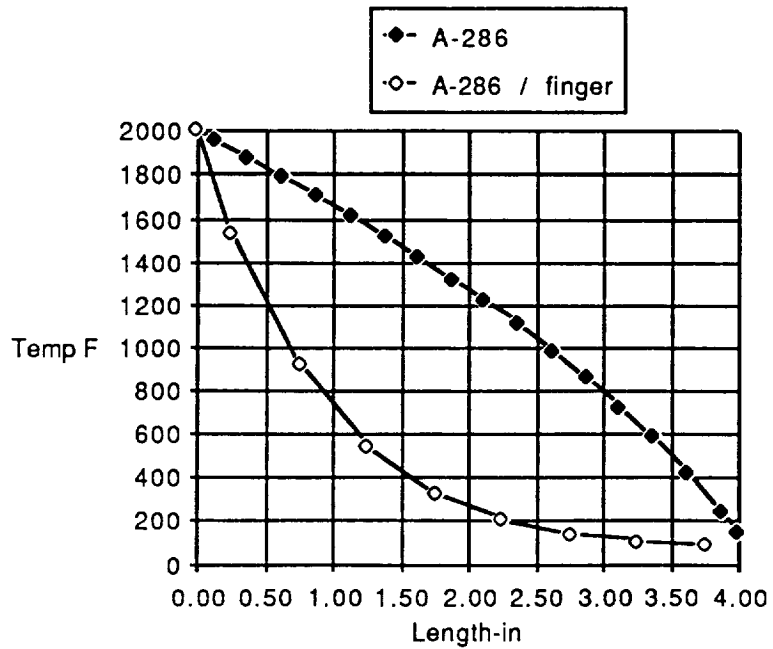


Figure 7. Temperature Profile Of GripTube With And Without Cold-Finger Assembly

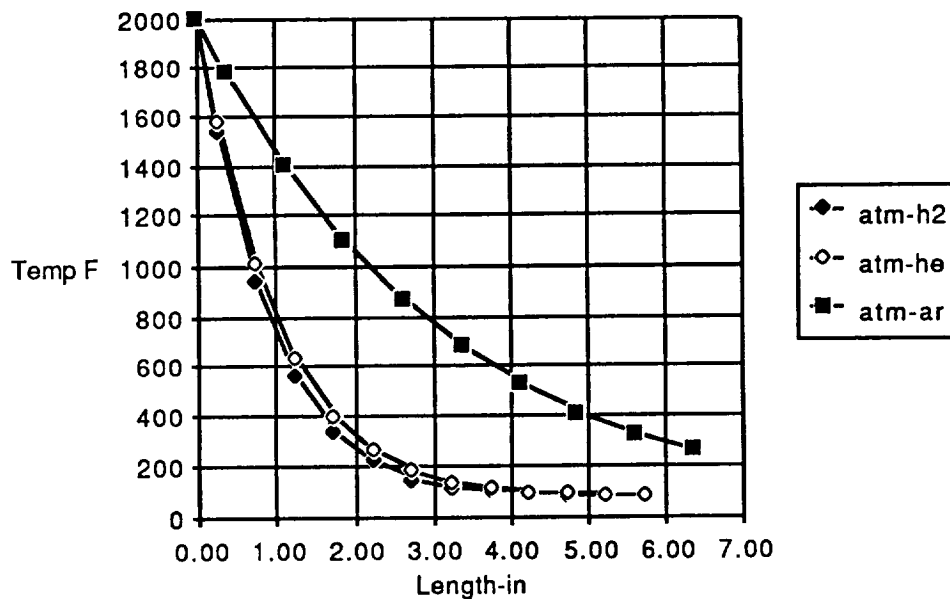


Figure 8. Gas Environment Effects On The Grip Tube Temperature Profiles

#### Furnace Design

The furnace design had to account for heating the specimen and grip assemblies to +2000 ° F in hydrogen and helium, permit the slots for the feed rods extended to include test travel, and have sufficient insulation to hold radial heat losses to an acceptable level. The thermal analysis information was used to determine the amount of power required from the furnaces. The selection of the element material and furnace insulation was further complicated by the hydrogen gas environment. The materials selected were molybdenum wire for the elements and alumina for the insulation. The target system required two separate furnaces, one for tensile and fatigue specimens and the other for fracture mechanics specimens. Each furnace had two separate control zones in order to achieve the specified specimen gradient.

#### Internal Load Cell

The internal load cell shown in the system assembly drawing is a new design. The system requirements leading to its development were :

- The use of highly stressed mechanical components should be avoided in the test environment.
- The load train has two possible pivot points; the specimen and internal load cell. The design should have a high over-turning moment and column load cells should be avoided.
- The vertical height of the load cell should be minimized in order to increase the lateral stiffness for fatigue tests.
- The maximum temperature of the strain gages is +350.° F. A technique is required to keep the load cell below this temperature.

The load cell developed utilizes a one piece construction to avoid the problems of mechanical couplings. The design measures load in a shear mode resulting in high sensitivity and lateral stiffness. The load cell design permits a direct path up the center for cooling with the "cold-finger" or alternative techniques. A patent is pending on this design.

ORIGINAL PAGE IS  
OF POOR QUALITY

Extensometer Design

After the decision was made to further investigate the Feed Rod approach to extensometry, the thermal analysis performed yielded information about the operating temperatures of the various extensometer components. The temperature at the location of the sensing unit was close enough to the maximum temperature of the bonded gages (+350 ° F) to require a modification in the approach. The design implemented is shown in figure 9. The modification consists of a dual cross flexure assembly. The upper cross flexure is a one piece construction made from a superalloy resistant to hydrogen embrittlement. The lower cross flexure is a patented design similar to those utilized in standard MTS extensometers. The specimen deflection is transmitted through the upper cross flexure to the strain gages on the lower cross flexure. Specially designed spring assemblies, mounted to the internal load frame, supply the force required to hold the extensometer rods against the specimen.

Internal Load Frame Design

The actual design constraints for the internal load frame are minimal. The complication of the internal load frame design is to integrate all of the other internal vessel assemblies. In addition to reacting the applied load, the internal load frame is used for :

- the frame provides mounting positions for extensometer hold down springs.
- the frame provides mounting location for furnaces.
- the frame provides thermal shielding of the extensometer assemblies.
- the frame provides cooling for internal components via close tolerances to the pressure vessel inside diameter.
- the capability of upper grip rod attachment and alignment.

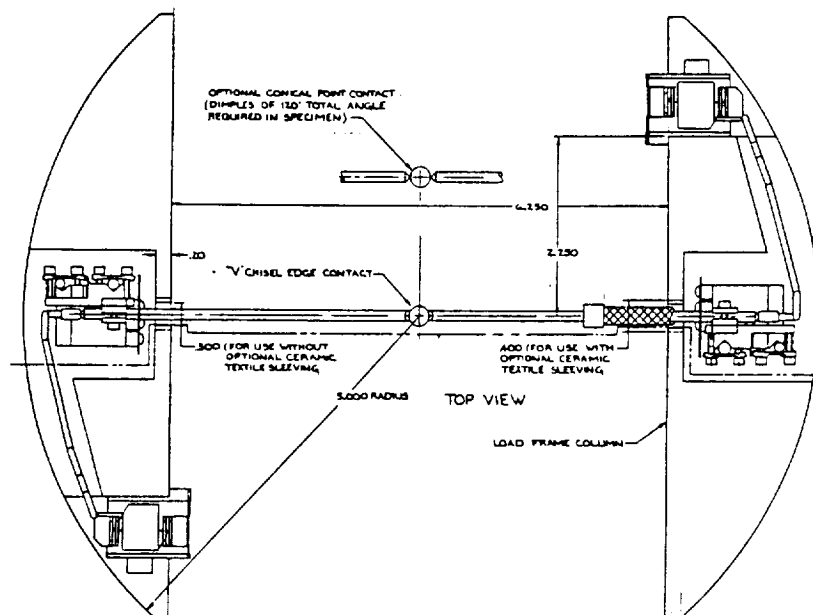
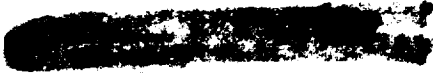


Figure 9. Extensometer Assembly For Tensile And Fatigue Test Specimens





### Pressure Vessel Design

As discussed in previous sections, the pressure vessel approach was predetermined to consist of a single, cold walled, monolithic dome design. The interior surface of the pressure vessel has a finish of 32  $\mu$ -inch to minimize surface flaw sites and is chemically etched to facilitate die penetrant testing. The closure method chosen was a GRAYLOC. The material selected for the vessel was A-286, a specialty stainless steel, because of its resistance to hydrogen embrittlement and superior strength. The external surface of the dome section is fitted with a stainless steel jacket for water cooling. The cooling mode is via direct contact between the water and vessel exterior surface. The base of the vessel had considerably more design constraints. The dynamic seal assembly had a maximum leak rate of less than 100 psi/hour while testing at 10,000 psi and cycling the actuator at 30 hertz and .010 inch double amplitude displacement. A seal evaluation rig was constructed during the early stages of the project in order to obtain a design to meet the specification. All of the instrumentation feed thru's for the load cell, extensometers, furnaces power, and thermocouples sensors are also passed through the vessel's base. Because of the close tolerances between the pressure vessel and the internal load frame and to increase the ease of use, a guidance system for raising and lowering the vessel between tests was designed.

### System Status

The majority of the equipment for the testing system has been received at MTS Systems and assembly has begun. The testing of the pressure and temperature capabilities will begin during the month of June. Installation of the test system at NASA-MSFC is scheduled for the September 1986.

DEVELOPMENT OF A COMPUTER-CONTROLLED TECHNIQUE TO DETERMINE  
CRACK GROWTH RATE PROPERTIES IN CONTROLLED ENVIRONMENTS  
USING CRACK OPENING DISPLACEMENT

By D. Moore, D. Drinan, and J. Hodo  
Marshall Space Flight Center/NASA

ABSTRACT

A computer-controlled testing technique has been developed that utilizes crack opening displacement to predict crack lengths for compact tension specimens in crack growth rate ( $da/dN$  versus  $\Delta K$ ) determinations. The crack growth rate data generated by the developed technique was compared statistically to data results of a highly reliable optical method. No significant difference could be determined between the data generated by either method. The computer-controlled method did prove, however, to be a reliable and cost effective method of determining crack growth rate data and can be incorporated in controlled environment crack growth rate determinations.

## INTRODUCTION

Accurate crack length measurements of compact tension test specimens are critical for determination of material crack growth rate properties. To date, the most widely used method of determining these crack lengths has been some type of optical measurement. Optical methods usually prove to be very time consuming, labor intensive approaches that provide surface crack analyses which must be adjusted for subsurface crack curvature (tunnelling). It has been shown, however, that crack opening displacement (COD) methods can be employed as a reliable alternative to optical measurements [1-4,6].

Saxena and Hudak [3] have developed elastic compliance expressions (see Appendix I) to predict crack lengths of compact tension specimens. These equations, however, do not account for non-ideal conditions of plane strain and plane stress. This study has taken the Saxena-Hudak equations and, in accordance with ASTM E647-83 guidelines, has developed a modified technique of crack length prediction by using an effective modulus for each specimen. A computer-controlled testing sequence was developed to minimize measurement and calculation errors, improve testing speed and control, and completely eliminate the need for any optical crack length measurements. The program, written in MTS BASIC, and a summary of the testing sequence are listed in Appendix III (Fig. 10).

By the use of this modified COD technique and this computer program (or a similar program) crack growth rate data ( $da/dN$  versus  $\Delta K$ ) can be generated in an accurate and cost effective manner, even in harsh environments that inhibit optical methods (e.g., high temperature atmospheres, cryogenic liquids, high pressure  $\text{GH}_2$ , etc.).

## TEST PROCEDURE

### Specimen Geometry and Material Selection

Fatigue crack growth rate tests were conducted on Titanium 10V-2Fe-3Al alloy. Table 1 shows the nominal dimensions that were used in accordance with ASTM E647-83 specifications:

Table 1. Nominal Specimen Geometry  
(For specimen drawing see Fig. 1)

<u>Material</u>	<u>B</u>	<u>W</u>
Ti 10V-2Fe-3Al	0.300	2.000

### Test Equipment

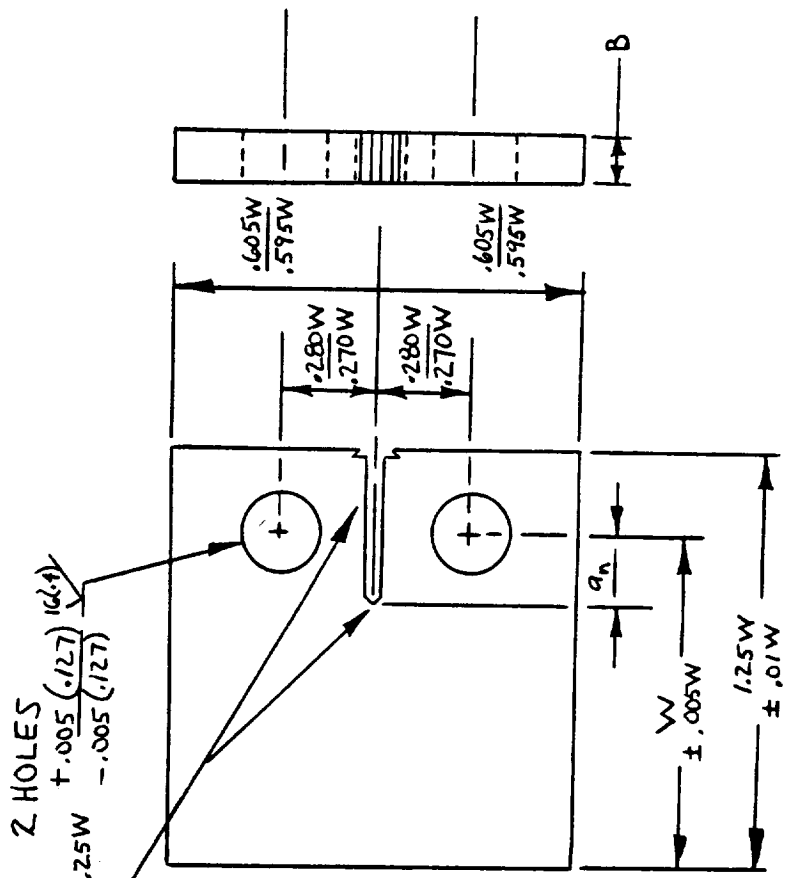
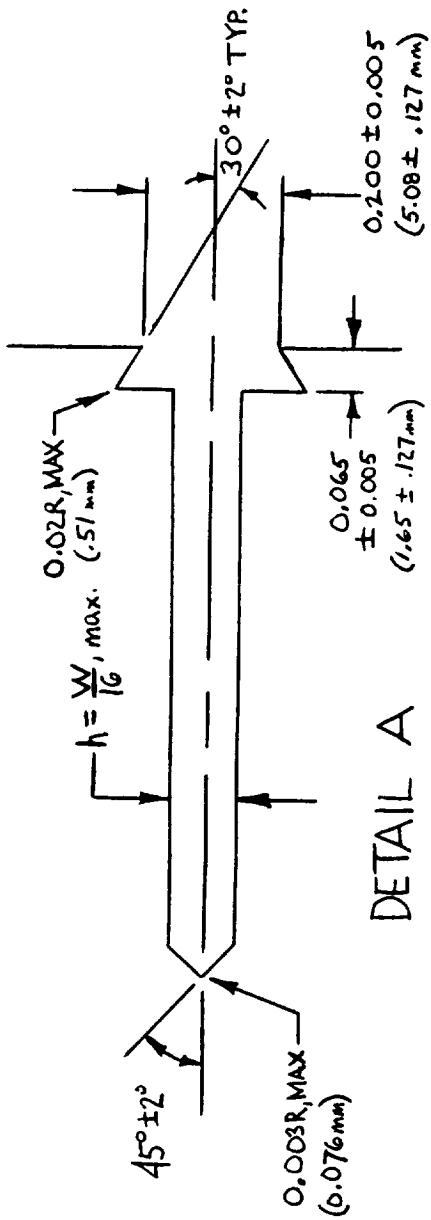
All specimen tests were conducted on a 5000 pound MTS closed loop, servo-hydraulic controlled test machine. All optical measurements were made using a 1-70X microscope on a traversing vernier scale (Fig. 2). Measurement repeatability was verified to be within  $\pm 0.0005$  in., well within ASTM E647-83 specification of  $\pm 0.002$  W. A  $\pm 5^\circ$  deviation from horizontal on crack propagation was monitored by marking  $\pm 5^\circ$  lines on each specimen with a marking pen (Fig. 3).

Measurements were made on both sides of specimens in order to compare one-sided versus two-sided measurements. According to ASTM E647-83-8.6.3, one-sided measurements are considered valid for specimens with  $B/W \leq 0.15$ . After preliminary analyses confirmed no significant difference between one-sided and two-sided measurements, one-sided measurements were continued for the remainder of the optical versus COD comparisons.

### Computer-Controlled Testing Sequence

Unique to these tests was the development of a computer program (Appendix III) to monitor and record all raw data (number of cycles, COD, load) and calculate crack lengths during test cycling (nominal values - used to monitor trends and approximate crack length intervals) and during a controlled measurement routine (actual data point values).

A computer operator needed only to input specimen dimensions (B, W, notch length) and loading conditions to conduct a test. For specimens in this report, maximum running loads of 3000, 1700, and 1300 pounds were used with  $R = 0.05$ .



- NOTES:**
- ①  $\sqrt[3]{(R)}$  FINISH ALL SURFACES EXCEPT AS NOTED
  - ② ALL DIMENSIONS IN INCHES (MILLIMETRES)
  - ③  $a_n = 0.20W$
  - ④ MINIMUM  $W = 1.0$  (25)
  - ⑤ RECOMMENDED THICKNESS:  $\frac{W}{20} \leq B \leq \frac{W}{4}$

Figure 1. Specimen Drawing.

ORIGINAL PAGE IS  
OF POOR QUALITY



Figure 2. Microscope on Traversing Vernier Scale.

ORIGINAL PAGE IS  
OF POOR QUALITY

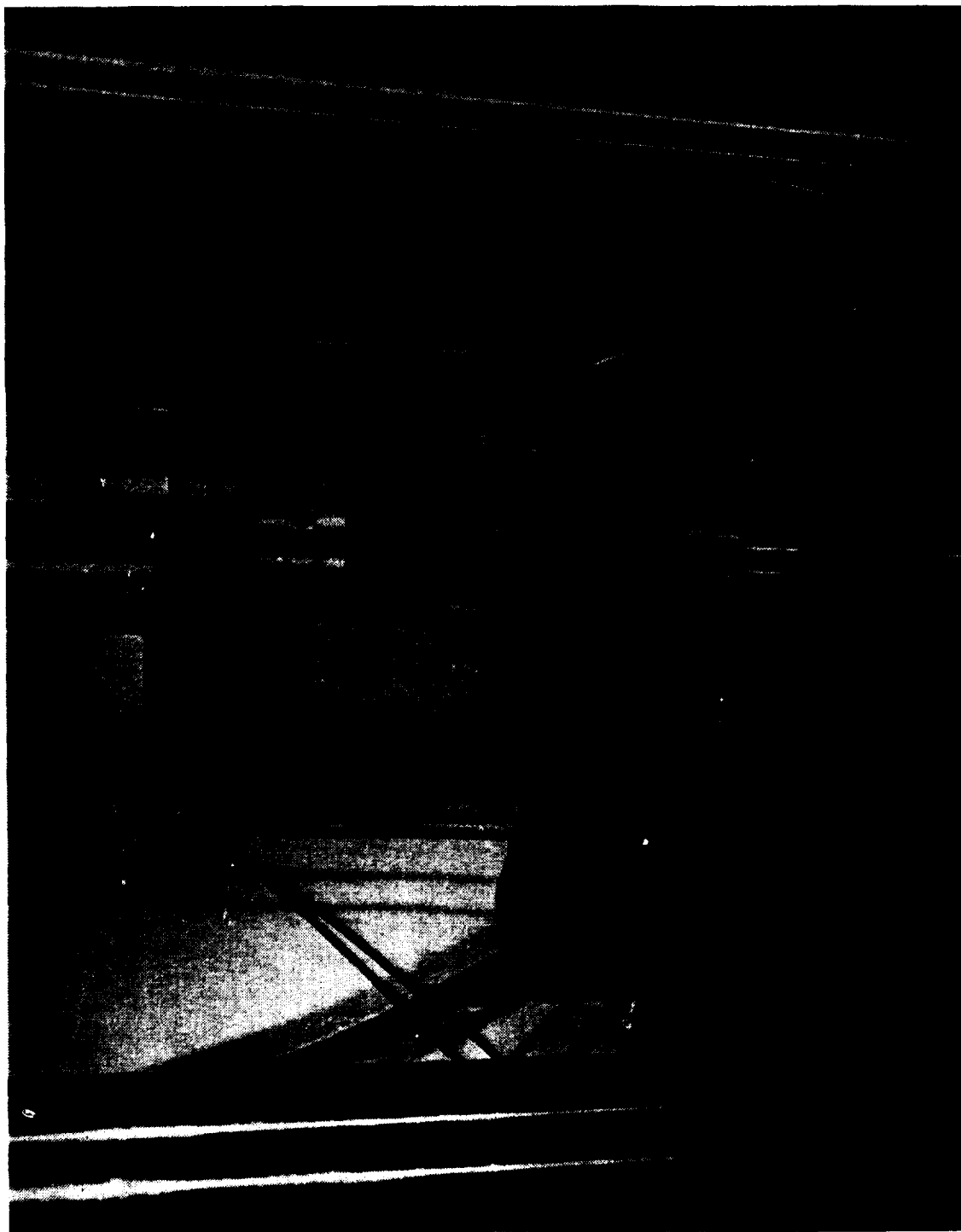


Figure 3. Mounted Specimen.

## DISCUSSION AND RESULTS

Some typical results comparing the COD method of determining crack lengths to the optical method are listed in Table 2. The  $da/dN$  versus  $\Delta K$  results comparing the two methods in this example are tabulated in Table 3 and illustrated in Figure 4. The rest of the  $da/dN$  versus  $\Delta K$  results that were part of this study are included in Appendix II. Visually, there appears to be no significant difference between the  $da/dN$  versus  $\Delta K$  curves generated by either of the two methods.

To reinforce this observation, a statistical analysis of covariance was performed on data generated for each specimen to test for a difference between the two methods. At a level of significance of 0.05, the statistical analysis did not show any significant difference between the two methods.

During evaluation of the COD method the COD technique, which utilizes a computer program, was revised several times. Initially, an effective modulus was determined after completion of a test. The specimen would be broken after the test and the final crack length would be determined. An effective modulus was calculated based on the final crack length. All preceding crack lengths of the test were predicted using the effective modulus and the COD relationship (see Appendix I). After a few tests, it was realized that the original machined notch of an uncracked specimen could be used to establish the effective modulus. By determining the effective modulus both ways several times, it was concluded that using the machined notch to calculate the effective modulus was as accurate as using the last crack length. Therefore, the technique and computer program were revised to use only the original machined notch in establishing an effective modulus. Another revision that was made to the original technique consisted of the way the crack was measured during the test. Previously, the crack length was predicted by reading peak voltage outputs of load and COD for the duration of the test. The test would not be stopped until the crack had reached sufficient length to end the test. It was discovered that this technique was not nearly as accurate as



Table 2. Typical Results Comparing the COD Method to the Optical Method

<u>Cycles</u>	<u>COD (<math>\text{m}\times 10^{-3}</math>) (in.)</u>	<u>Optical A-SIDE Crack Length (<math>\text{m}\times 10^{-3}</math>) (in.)</u>	<u>Optical B-SIDE Crack Length (<math>\text{m}\times 10^{-3}</math>) (in.)</u>	<u>Optical Avg. Crack Length + Tunneling (<math>\text{m}\times 10^{-3}</math>) (in.)</u>	<u>Crack Length by COD (<math>\text{m}\times 10^{-3}</math>) (in.)</u>
0	0.1575 (0.0062)	13.38 (0.5269)	13.70 (0.5394)	14.29 (0.5627)	14.36 (0.5652)
5000	0.1676 (0.0066)	14.24 (0.5607)	14.62 (0.5757)	15.18 (0.5977)	15.25 (0.6004)
10000	0.1829 (0.0072)	15.37 (0.6051)	15.58 (0.6135)	16.23 (0.6388)	16.48 (0.6487)
15000	0.1981 (0.0078)	16.64 (0.6552)	16.94 (0.6668)	17.54 (0.6905)	17.58 (0.6923)
20000	0.2235 (0.0088)	18.12 (0.7135)	18.28 (0.7198)	18.95 (0.7462)	19.22 (0.7565)
24500	0.2515 (0.0099)	19.67 (0.7744)	19.96 (0.7859)	20.57 (0.8097)	20.76 (0.8174)
26500	0.2642 (0.0104)	20.46 (0.8055)	20.68 (0.8143)	21.32 (0.8394)	21.29 (0.8423)
28000	0.2794 (0.0110)	21.09 (0.8304)	21.48 (0.8458)	22.04 (0.8676)	22.10 (0.8702)
29300	0.2946 (0.0116)	21.67 (0.8533)	22.0 (0.8660)	22.59 (0.8892)	22.76 (0.8962)
30400	0.3048 (0.0120)	22.12 (0.8709)	22.48 (0.8852)	23.05 (0.9076)	23.18 (0.9126)
31500	0.3200 (0.0126)	22.75 (0.8958)	23.05 (0.9075)	23.65 (0.9312)	23.77 (0.9359)
32500	0.3353 (0.0132)	23.36 (0.9198)	23.60 (0.9292)	24.23 (0.9540)	24.33 (0.9578)
33400	0.3480 (0.0137)	24.02 (0.9458)	24.23 (0.9541)	24.88 (0.9795)	24.77 (0.9750)
34200	0.3708 (0.0146)	24.50 (0.9647)	24.88 (0.9797)	25.44 (1.0017)	25.50 (1.0040)
35000	0.3886 (0.0153)	25.26 (0.9943)	25.61 (1.0081)	26.18 (1.0307)	26.03 (1.0249)
35700	0.4089 (0.0161)	25.82 (1.0165)	25.98 (1.0227)	26.65 (1.0491)	26.60 (1.0473)
36400	0.4242 (0.0167)	26.36 (1.0378)	26.79 (1.0548)	27.33 (1.0758)	27.00 (1.0630)
37000	0.4496 (0.0177)	26.82 (1.0558)	27.44 (1.0802)	27.88 (1.0975)	27.63 (1.0877)
37550	0.4750 (0.0187)	27.49 (1.0821)	28.02 (1.1032)	28.50 (1.1222)	28.21 (1.1105)
38050	0.5131 (0.0202)	28.24 (1.1120)	28.95 (1.1398)	29.35 (1.1554)	29.00 (1.1416)
38400	0.5486 (0.0216)	28.74 (1.1316)	29.46 (1.1599)	29.85 (1.1753)	29.66 (1.1678)
38700	0.5893 (0.0232)	29.36 (1.1561)	30.13 (1.1861)	30.50 (1.2006)	30.35 (1.1950)
38900	0.6274 (0.0247)	29.81 (1.1738)	30.56 (1.2033)	30.94 (1.2181)	30.94 (1.2181)

Table 3. Typical Results of da/dN and ΔK Comparing the COD Method to the Optical Method

$\frac{da/dN}{\text{cycle}} \text{ (Optical)}$ $(\text{in.} \times 10^{-6}/\text{cycle})$	$\frac{\Delta K \text{ (Optical)}}{(\text{MPa} \sqrt{\text{m}})}$ $(\text{KSI} \sqrt{\text{in.}})$	$\frac{da/dN \text{ (COD)}}{(\text{in.} \times 10^{-7}/\text{cycle})}$	$\frac{\Delta K \text{ (COD)}}{(\text{MPa} \sqrt{\text{m}})}$ $(\text{KSI} \sqrt{\text{in.}})$	
1.78	(7.00)	17.42 (15.85)	1.79 (7.04)	17.48 (15.85)
2.09	(8.22)	18.30 (16.65)	2.45 (9.66)	18.45 (16.65)
2.63	(10.34)	19.43 (17.68)	2.21 (8.72)	19.57 (17.68)
2.88	(11.14)	20.80 (18.93)	3.26 (12.84)	20.97 (18.93)
3.58	(14.11)	22.47 (20.45)	3.44 (13.53)	22.75 (20.45)
3.77	(14.85)	23.90 (21.75)	3.16 (12.45)	24.08 (21.75)
4.78	(18.80)	24.86 (22.62)	4.72 (18.60)	24.94 (22.62)
4.22	(16.62)	25.71 (23.40)	5.08 (20.00)	25.89 (23.40)
4.25	(16.73)	26.44 (24.06)	3.79 (14.91)	26.66 (24.06)
5.45	(21.45)	27.23 (24.78)	5.38 (21.18)	27.43 (24.78)
5.79	(22.80)	28.16 (25.63)	5.56 (21.90)	28.34 (25.63)
7.20	(28.33)	29.18 (26.55)	4.85 (19.11)	29.16 (26.55)
7.05	(27.75)	30.24 (27.52)	9.21 (36.25)	30.19 (27.52)
9.21	(36.25)	31.46 (28.63)	6.64 (26.13)	31.37 (28.63)
6.68	(26.29)	32.66 (29.72)	8.13 (32.00)	32.46 (29.72)
9.69	(38.14)	33.88 (30.83)	5.70 (22.43)	33.47 (30.83)
9.19	(36.17)	35.26 (32.09)	10.46 (41.17)	34.60 (32.09)
11.41	(44.91)	36.70 (33.40)	10.53 (41.45)	36.02 (33.40)
16.87	(66.40)	38.63 (35.15)	15.8 (62.20)	37.76 (35.15)
14.44	(56.86)	40.55 (36.90)	19.01 (74.86)	39.76 (36.90)
21.42	(84.33)	42.32 (38.51)	23.03 (90.67)	41.79 (38.51)
22.23	(87.50)	44.12 (40.15)	29.34 (115.50)	43.88 (40.15)

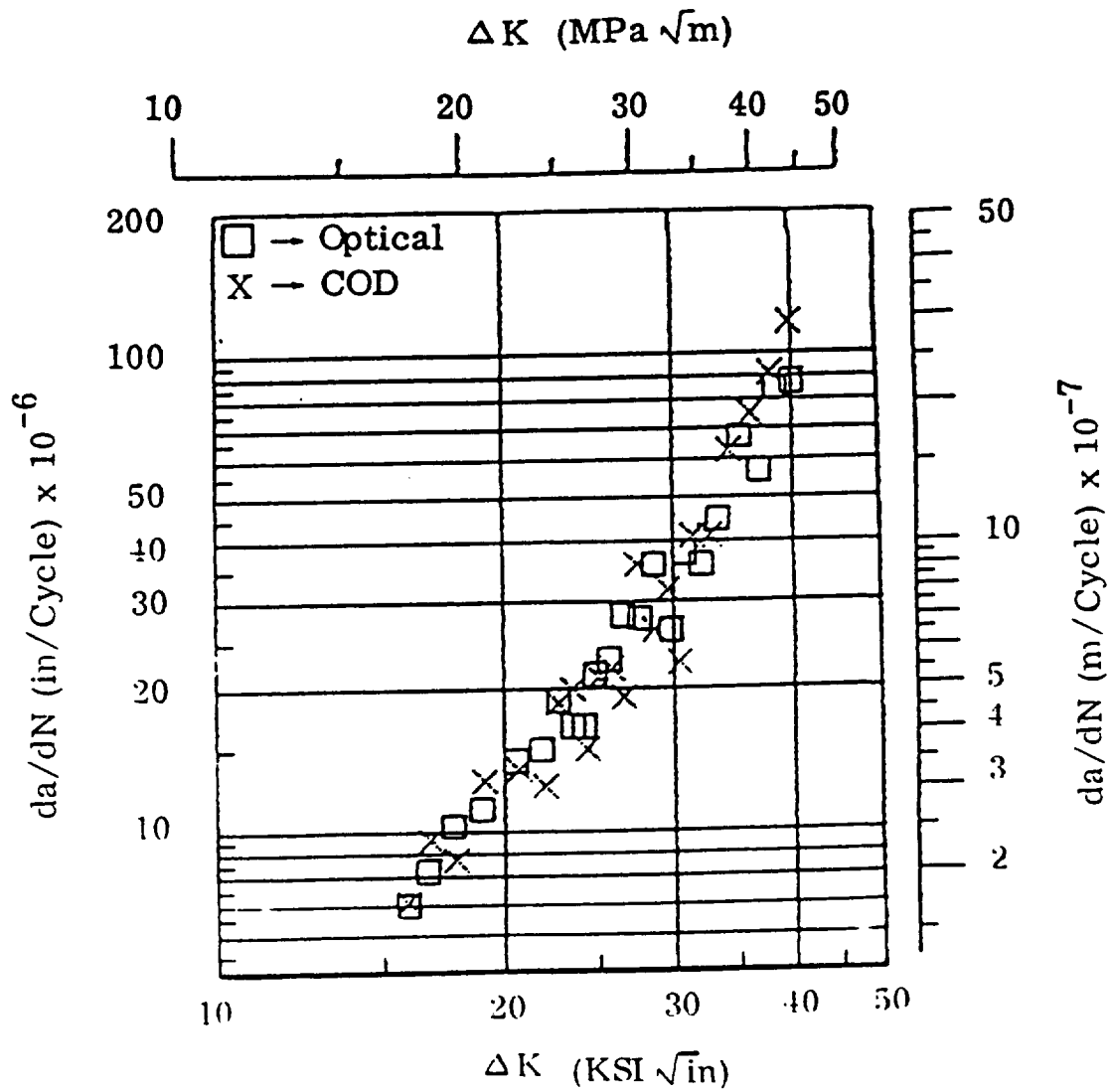


Figure 4. COD versus Optical ( $da/dN$  versus  $\Delta K$ )  
 Ti 10-2-3, 1300 lbs at R = 0.05

what would be required for predicting crack lengths. The technique was then revised to incorporate a  $\Delta$  load and  $\Delta$  COD as suggested by ASTM STP 738 [4]. Using the predicted crack lengths, estimated by the peak voltages as before, a test was continued until the predicted crack was long enough to make an accurate crack measurement. The test would then be stopped, the load would be ramped to 0.475 times the maximum running load, and one hundred measurements of load and COD would be recorded and averaged. The load would then be ramped to 0.95 times the maximum running load for another average of one hundred measurements of load and COD. The two differences between these averages ( $\Delta$  COD and  $\Delta$  load) were used in the compliance equation (Appendix I) to determine the crack length. The load cycling would then be continued until the predicted crack was long enough to make another accurate crack measurement. The entire method of measuring the crack length took approximately 35 seconds for one measurement. The method proved to be very effective in accurately determining crack lengths. It must be recognized here, however, that even just a 35 second delay in cycling could be critical and produce some invalid results in some cases where environmental effects are critically time dependent. A continuously cycling test, using a slower frequency during the measurement routine, is a possible alternative for such tests.

A listing of the finally revised computer program developed through this study is in Appendix III.

### CONCLUSIONS AND RECOMMENDATIONS

Analysis of these test results, on both a statistical and an engineering basis, clearly shows that no significant difference exists between crack growth rate data generated optically or by this crack opening displacement (COD) method. This computer-controlled technique drastically reduces time and expertise required to generate accurate crack growth rate behavior ( $Da/DN$  versus  $\Delta K$ ) data.

Environmental constraints that inhibit accurate optical measurement methods are now limited only by accurate electronic displacement measurement of the specimen (the clip-on gauge used for these tests,

for example, is also capable of providing accurate displacement data in cryogenic and in high pressure hydrogen environments).

The cost effectiveness and reliability of this method greatly increases the potential for crack growth rate study and will help generate data that, until now, has not been available.

## APPENDIX I

Compliance Crack Opening Displacement (COD)  
Equations Used for Crack Length and  
Stress Intensity Factor ( $\Delta K$ ) Calculations [3,5]

Saxena and Hudak [3] have developed a relationship for  $a/w$  as a function of BEV/P (compliance):

$$a/w = C_0 + C_1 (U_x) + C_2 (U_x)^2 + C_3 (U_x)^3 + C_4 (U_x)^4 + C_5 (U_x)^5$$

where

$$U_x = f \left( \frac{\text{BEV}_x}{P} \right)$$

and  $C_0, C_1, \dots, C_5$  are regression coefficients. For COD measurements at front face of our specimens the equation is:

$$a/w = 1.0010 - 4.6695 (U_x) + 18.460 (U_x)^2 - 236.82 (U_x)^3 + 1214.9 (U_x)^4 - 2143.6 (U_x)^5$$

Multiplying both sides by  $W$  gives us our crack length equation:

$$a = [1.0010 - 4.6695 (U_x) + 18.460 (U_x)^2 - 236.82 (U_x)^3 + 1214.9 (U_x)^4 - 2143.6 (U_x)^5] W$$

ASTM E647-83 gives an equation for stress intensity factor ( $\Delta K$ ):

$$\Delta K = \frac{\Delta P}{B\sqrt{W}} \frac{(2 + \alpha)}{(1 - \alpha)^{3/2}} (0.886 + 4.64 \alpha - 13.32 \alpha^2 + 14.72 \alpha^3 - 5.6 \alpha^4)$$

$$\text{where } \alpha = \frac{a}{W}$$

APPENDIX II

Da/DN versus  $\Delta K$  Curves Comparing COD  
Method to Optical Method



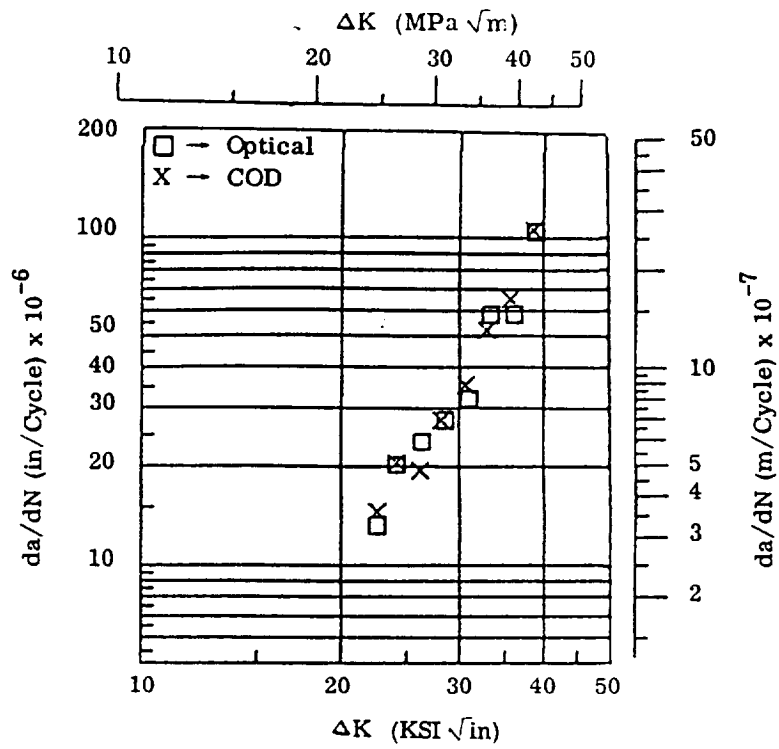


Figure 5. COD versus Optical (da/dN versus ΔK)  
Ti 10-2-3, 1700 lbs at R = 0.05

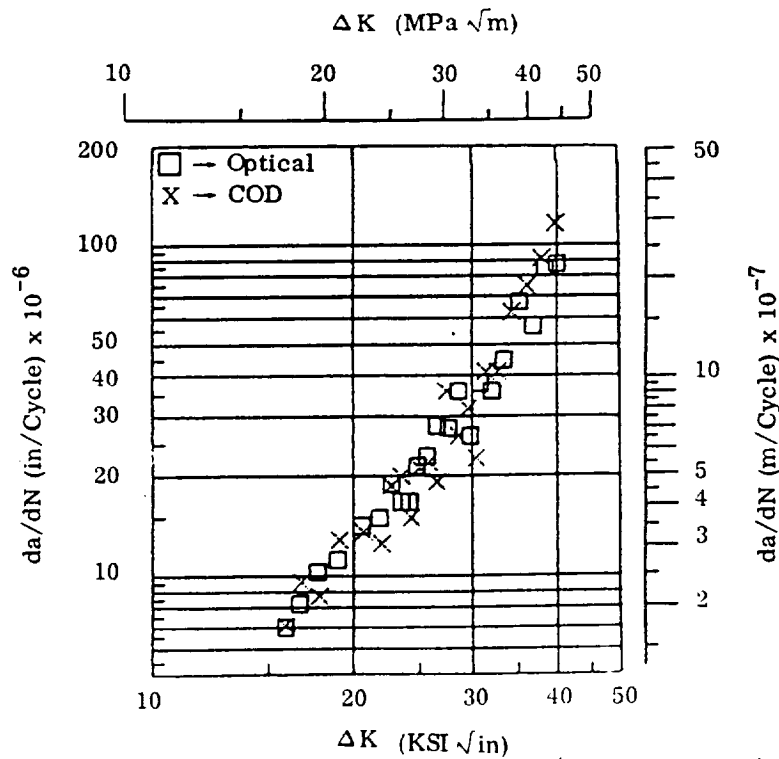


Figure 6. COD versus Optical (da/dN versus ΔK)  
Ti 10-2-3, 1300 lbs at R = 0.05

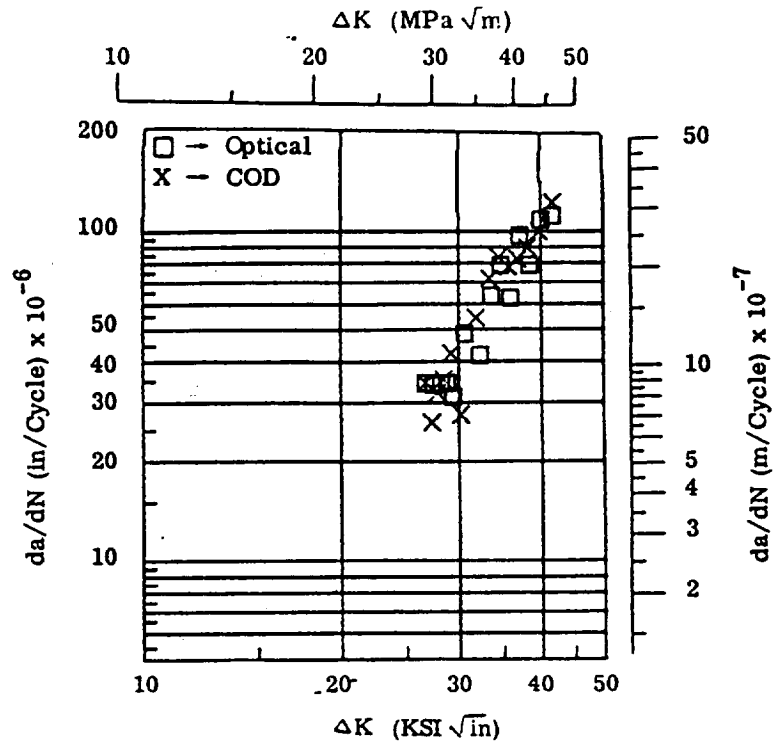


Figure 7. COD versus Optical (da/dN versus ΔK)  
Ti 10-2-3, 2000 lbs at R = 0.05

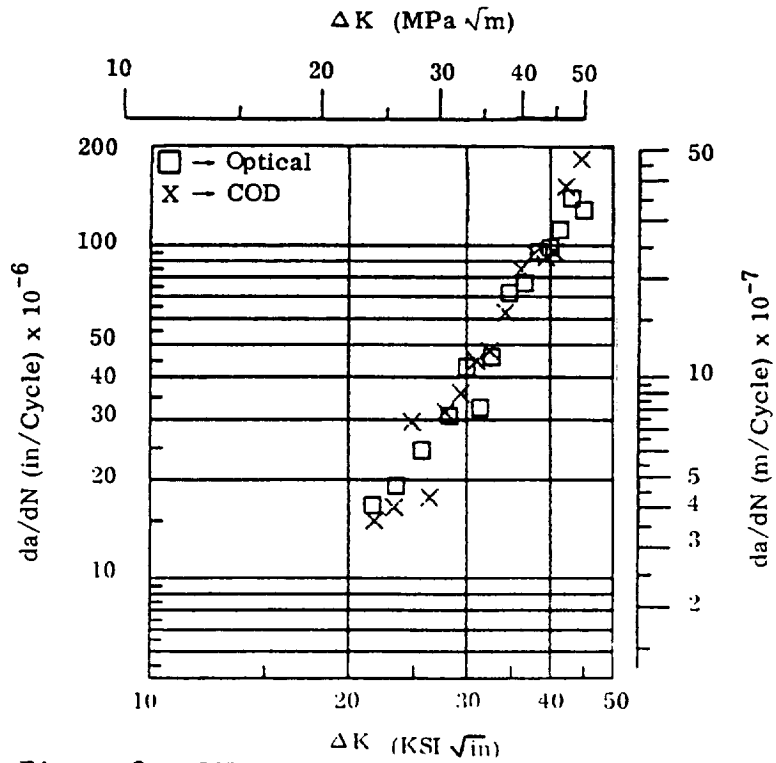


Figure 8. COD versus Optical (da/dN versus ΔK)  
Ti 10-2-3, 1700 lbs at R = 0.05

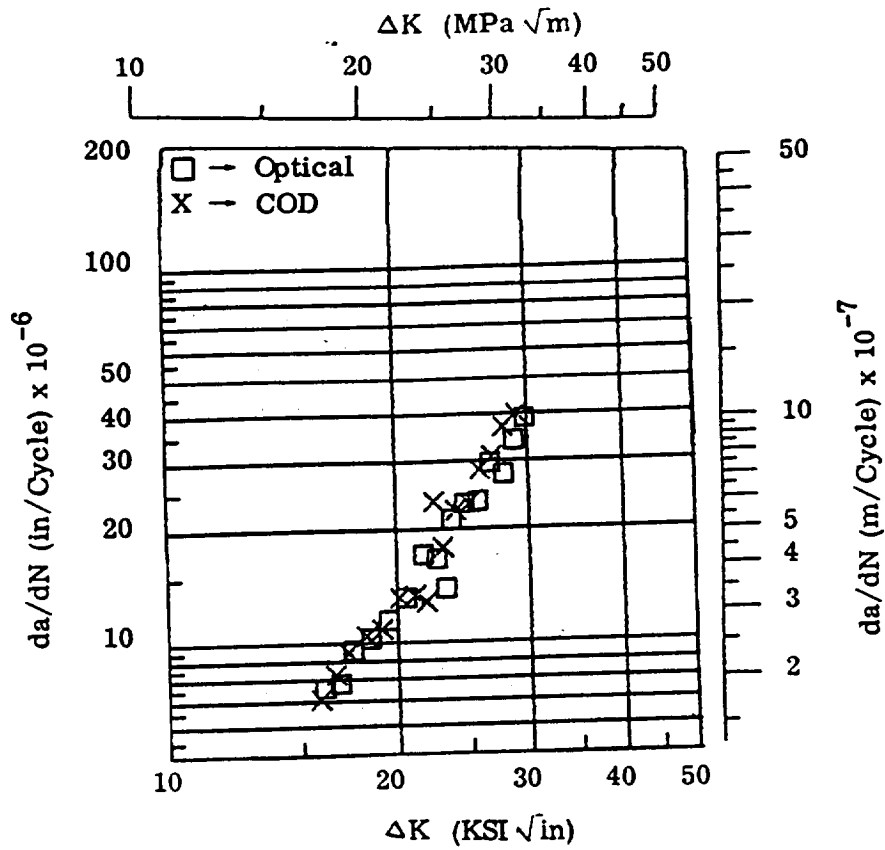
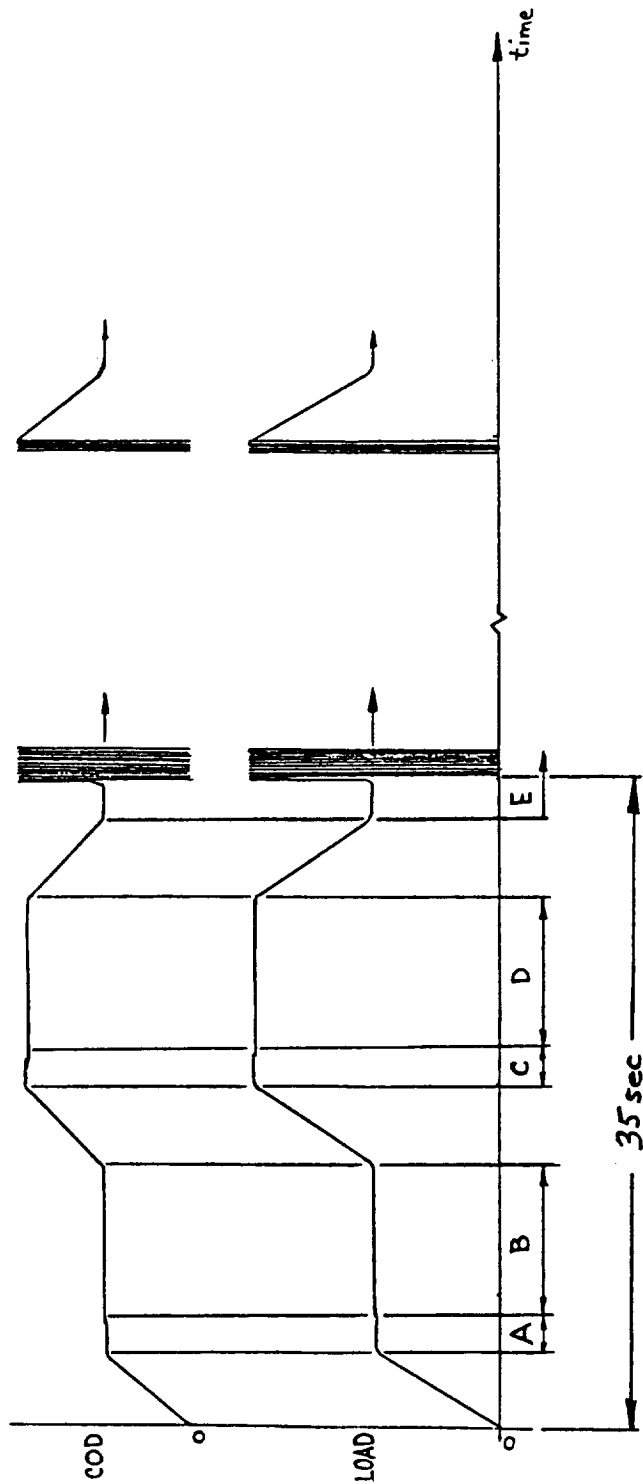


Figure 9. COD versus Optical ( $da/dN$  versus  $\Delta K$ )  
 Ti 10-2-3, 1300 lbs at  $R = 0.05$

APPENDIX III

Computer Program for and Summary of COD Test Sequence



**SUMMARY OF TESTING SEQUENCE**

Load ramps to A where a tolerance condition is satisfied by computer comparison and adjustment of input load command to output reading. After tolerance condition is satisfied, 100 measurements are made in B section and average load and displacement values are calculated. Load then ramps to C where tolerance condition is again satisfied. Another 100 measurements of load and displacement are averaged in D and now, with accurate  $\Delta P$  and  $\Delta COD$  values, an "effective" modulus ( $E'$ ) is calculated based on measured notch length. From this point the computer ramps the load down to a midrange value and begins cycling (E). Real time calculations are made of peak displacement measurements to determine when a specified crack length interval has been reached, at which point the measurement routine is repeated. All measurements made from this point on use the "effective" modulus to determine new crack lengths based on new  $\Delta COD$  values.

Figure 10. Summary of Testing Sequence.

ORIGINAL PAGE IS  
OF POOR QUALITY

```
10 FGSTOP \ ADSTOP \ FGSTEP(1,0) \ IF D5=1 THEN CLOSE 49
20 DIM M1(1,2),M2(1,2),W(1,1),X(1,1),B(2,1)
30 DIM B$(500,2),A$(500)
40 KBINT('S',, LINE 980 ) \ KBENB
50 DIM D$(250,4)
60 DEF FNA(U8)=(1.001-4.6695*U8+18.46*U8^2-236.82*U8^3+1214.9*U8^4-2143.6*U8^5)*W
70 DEF FNB(V3)=(INT(V3*100+.5)/100)
80 K=1 \ W2=0
90 K7=0
100 GO TO 2830
110 PRINT #9;K;TAB(15);D$(K,1);TAB(30);D$(K,2);TAB(45);D$(K,3);TAB(60);D$(K,4)
120 PRINT #;TAB(15);D$(K,1);TAB(30);D$(K,2);TAB(45);D$(K,3);TAB(60);D$(K,4) \ RETURN
130 CKTIME(1,5.00000E-03)
140 ADMAX(1,X,1) \ ADRHIN(3,N,1)
150 FGARB(1,'RAMP', TIME 210,1)
160 RETURN
170 CKTIME(1,1.30000E-05)
180 ADMAX(1,M1,M1,1,200,2) \ ADMIN(1,M2,M2,1,200,2)
190 ADBUFEND(1,4, LINE 920 )
200 FGARB(1,'S', FREQ BINVAR F, BINARRAY B,2, VAR Q9)
210 FGRUFEND(1,2, LINE 970 )
220 RETURN
230 C8=F5 \ V=ELEVEL(M1(1,2))
240 IF V<=0 THEN 330
250 K7=1 \ F7=F7+F8
260 V=(INT(V*10000)/1000)
270 V3=40*(V/10)
280 V3=V3/1000
290 U8=1/((B1*10^6/P*E*V3)^.5+1)
300 A3=FNA(U8)
310 A3=(INT(A3*100+.5)/100)
320 K=D(0,0)+1 \ D(1,K)=V3 \ D(2,K)=C8 \ D(0,0)=K
330 RETURN
340 Q9=0
350 F4=.475*(L2/L)
360 A=0 \ A2=0 \ A3=0 \ A4=0
370 F6=.95*(L2/L)
380 ETIME(S2)
390 ETIME(S3) \ IF S3-S2<5 THEN 390
400 FGINMED(1,'RAMP', TIME 2,F4)
410 ETIME(S2)
420 ETIME(S3) \ IF S3-S2<5 THEN 420
430 ETIME(S2)
440 ADIMMED(1,S) \ IF ABS(F4-S)>3.00000E-03 THEN FGSTEP(1,F4+(F4-S))
450 ETIME(S3) \ IF S3-S2<5 THEN 440
460 FOR I=1 TO 100
470 ADIMMED(1,S) \ ADIMMED(2,H) \ A=A+S \ A2=A2+H
480 NEXT I
490 FGINMED(1,'RAMP', TIME 2,F6)
500 ETIME(S2)
510 ETIME(S3) \ IF S3-S2<5 THEN 510
520 ADIMMED(1,S) \ IF ABS(F6-S)>3.00000E-03 THEN FGSTEP(1,F6+(F6-S))
530 ETIME(S2) \ IF S2-S3<5 THEN 520
540 FOR I=1 TO 100
550 ADIMMED(1,S) \ ADIMMED(2,H) \ A3=A3+S \ A4=A4+H
560 NEXT I
570 A=A/100 \ A2=A2/100 \ A3=A3/100 \ A4=A4/100
580 P=A3-A \ V=A4-A2
590 P=P*L \ P=ABS(P)
600 P=INT(P*10+.5)/10
610 V3=40*V \ V3=INT(V3*100+.5)/100 \ V3=V3/1000 \ V3=ABS(V3)
620 U8=1/((B1*10^6/P*E*V3)^.5+1)
```

ORIGINAL PAGE IS  
OF POOR QUALITY

```
630 A3=FNA(U8)
640 A3=(INT(A3*10000+.5)/10000)
650 FGINMED(1,'RAMP', TIME 1,F4)
660 ETIME(S2)
670 ETIME(S3) \ IF S3-S2<2 THEN 670
680 Q9=32000
690 RETURN
700 F4=.475*(L2/L) \ F6=.95*(L2/L)
710 FGINMED(1,'RAMP', TIME 1,F4)
720 A=0 \ A2=0 \ A3=0 \ A4=0
730 ETIME(S2)
740 ETIME(S3) \ IF S3-S2<5 THEN 740
750 ADIMMED(1,S) \ IF S<F4-3.00000E-03 THEN 750
760 FOR I=1 TO 100
770 ADIMMED(1,S) \ ADIMMED(2,M) \ A=A+S \ A2=A2+H
780 NEXT I
790 FGINMED(1,'RAMP', TIME 1,F6)
800 ETIME(S2)
810 ADIMMED(1,S) \ IF S<F6-3.00000E-03 THEN 810
820 ETIME(S3) \ IF S3-S2<5 THEN 810
830 FOR I=1 TO 100
840 ADIMMED(1,S) \ ADIMMED(2,M) \ A3=A3+S \ A4=A4+H
850 NEXT I
860 A=A/100 \ A2=A2/100 \ A3=A3/100 \ A4=A4/100
870 P=A3-A \ V=A4-A2
880 U3=40*V \ U3=U3/1000
890 P=P*L
900 FGINMED(1,'RAMP', TIME 1,.475*L3/L)
910 RETURN
920 IF ABS(M1(1,1)-U3)<=250 THEN IF ABS(M2(1,1)-U4)<=10 THEN RETURN
930 Z7=B(1,0)+INT((U3-M1(1,1))/1.5) \ IF Z7>32752 THEN PRINT '*** OUT OF UPPER LIMIT ***' \ B(1,0)=U1 \ RETURN
940 B(1,0)=Z7
950 B(2,0)=B(2,0)+INT((U4-M2(1,1))/1.5)
960 RETURN
970 H=1 \ RETURN
980 P9=1 \ RETURN
990 PRINT \ PRINT 'ENTER SAMPLE (FILE NAME) [4 CHR. MAX] ' ; \ INPUT F$
1000 PRINT \ PRINT 'NEW SAMPLE OR OLD (O) OR (N) ' ; \ INPUT H$
1010 GOSUB 2930
1020 K$=K1$+' '+F$
1030 IF H$='N' THEN GO TO 1090
1040 (OPEN K$ AS FILE VF1$(10)=(24), FILESIZE 10, ERROR J9
1050 X$=VF1(0)
1060 CLOSE VF1
1070 K2=VAL(X$)
1080 RETURN
1090 OPEN K$ FOR OUTPUT AS FILE VF1$(10)=(24), FILESIZE 10, ERROR J9
1100 VF1(0)='0'
1110 CLOSE VF1
1120 D$(0,0)='0'
1130 K2=0
1140 GO TO 1080
1150 F=FGBINFREQ(F0)
1160 U1=L3/L \ U2=(L2/L*.05)
1170 U1=INT(U1*32752) \ U2=INT(U2*32752)
1180 U5=INT((L2/L)*32752)
1190 U3=U1 \ U4=U2
1200 U1=U1-U2
1210 B(1,0)=U1 \ B(2,0)=U2
1220 Q9=32000
1230 H=0
1240 P9=0
```

```

1250 RETURN
1260 PRINT \ PRINT
1270 PRINT , 'ENTER FILE NAME ' ; \ INPUT F$
1280 GOSUB 2930
1290 K$=K1$+' '+F$
1300 OPEN K$ AS FILE VF1$(10)=(24), FILESIZE 10, ERROR J9
1310 X$=VF1(0)
1320 K=VAL(X$)
1330 B$='/'
1340 FOR I=1 TO K
1350 A$(I)=VF1(I)
1360 NEXT I
1370 CLOSE VF1
1380 FOR I=1 TO K
1390 L6=POS(A$(I),B$,1) \ D$(I,1)=SEG$(A$(I),1,L6-1)
1400 L7=POS(A$(I),B$,L6+1) \ D$(I,2)=SEG$(A$(I),L6+1,L7-1)
1410 L6=POS(A$(I),B$,L7+1) \ D$(I,3)=SEG$(A$(I),L7+1,L6-1)
1420 D$(I,4)=SEG$(A$(I),L6+1,(LEN(A$(I))))
1430 NEXT I
1440 PRINT \ PRINT
1450 OPEN "LP:" FOR OUTPUT AS FILE #9 \ OS=1
1460 PRINT #9: \ PRINT #9:
1470 PRINT #9:TAB(35);F$
1480 PRINT #9: \ PRINT #9: \ PRINT #9:
1490 I=K
1500 FOR K=1 TO I
1510 GOSUB 110
1520 NEXT K
1530 CLOSE #9 \ OS=0
1540 RETURN
1550 FOR I=1 TO 6 \ PRINT \ NEXT I
1560 GOSUB 990
1570 P9=0
1580 PRINT \ PRINT ,, 'ENTER NOTCH LENGTH ' ; \ INPUT I8
1590 PRINT \ PRINT ,, 'ENTER PRECRACK LOAD IN LBS. ' ; \ INPUT L3
1600 PRINT \ PRINT ,, 'ENTER CYCLE LOAD IN LBS. ' ; \ INPUT L2
1610 PRINT \ PRINT ,, 'ENTER LONGEST ALLOWABLE CRACK '
1620 PRINT ,, 'MEASUREMENT' ; \ INPUT W5
1630 PRINT \ PRINT \ PRINT
1640 PRINT ,, 'ENTER LOAD RANGE ' ; \ INPUT L
1650 PRINT \ PRINT
1660 PRINT ,, 'ENTER PRE-CRACK FREQUENCY ' ; \ INPUT F0
1670 PRINT ,, 'ENTER INITIAL TEST FREQUENCY ' ; \ INPUT W0
1680 PRINT \ PRINT \ PRINT
1690 PRINT 'LOAD RANGE', 'PRE-LOAD', 'CYCLE LOAD', 'MIN LOAD', 'FREQ.'
1700 P=INT(L2*.05+.5)
1710 P1=(L2/(L/10)) \ P2=(P/(L/10))
1720 P4=(L3/(L/10))
1730 PRINT L,L3,L2,P,F0
1740 PRINT ,P4; ' VOLTS',P1; ' VOLTS',P2; ' VOLTS'
1750 PRINT \ PRINT 'DATA O.K. N=NO <CR>=YES'; \ INPUT J$
1760 IF J$='N' THEN 1630
1770 GOSUB 2780
1780 FGSTEP(1,0)
1790 GOSUB 1150
1800 FOR I=1 TO 5 \ PRINT \ NEXT I
1810 PRINT '***** MOUNT SAMPLE *****'
1820 PRINT '*****ZERO LOAD *****'
1830 PRINT \ PRINT \ PRINT
1840 PRINT 'PRESS RETURN TO START TEST'; \ INPUT J$
1850 OPEN "LP:" FOR OUTPUT AS FILE #9 \ OS=1
1860 GOSUB 700

```

ORIGINAL PAGE IS  
OF POOR QUALITY



ORIGINAL PAGE IS  
OF POOR QUALITY

```

1870 Z5=I8/W
1880 Y2=1+Z5 \ Y3=1-Z5 \ Y4=Y2/Y3 \ Y5=Y4^2
1890 X2=Z5^2 \ X3=Z5^3 \ X4=Z5^4 \ X5=Z5^5
1900 E2=(P/(B1*V3))*(1+.25/Z5)*Y5*(1.6137+12.678*Z5-14.231*X2-16.61*X3+35.05*X4-14.49*X5)
1910 E=E2/10^6
1920 PRINT \ PRINT \ PRINT , 'MODULUS = ' ; E , 'COD LOAD = ' ; P
1930 PRINT #9: \ PRINT #9: \ PRINT #9: TAB(35); F#
1940 PRINT #9: \ PRINT #9: \ PRINT #9: TAB(35); 'E' = ' ; E
1950 PRINT #9: \ PRINT #9:
1960 PRINT #9: TAB(35); 'COD LOAD = ' ; P
1970 PRINT #9: \ PRINT #9: \ PRINT #9: TAB(15); 'CYCLES'; TAB(30); 'C O D KILS'; TAB(45); 'CRACK LENGTH'; TAB(60); 'COD-LOAD'
1980 PRINT #9: \ PRINT #9:
1990 GOSUB 170
2000 ADGO \ ADINIT
2010 FGGO
2020 GOSUB 3030
2030 H=1
2040 C=0 \ T0=0
2050 IF Q9<15 THEN Q9=32000
2060 IF P9=1 THEN 2620
2070 FGCYCLES(1,F5) \ V=ELEVEL(H1(1,2))
2080 P=ELEVEL(H1(1,1))*L
2090 IF V<=0 THEN 2050
2100 V=(INT(V*10000)/10000) \ V3=40*V
2110 V3=V3/1000
2120 U8=1/((B1*10^6/P*E*V3)^.5+1)
2130 B3=(1.001-4.6695*U8+18.46*U8^2-236.82*U8^3+1214.9*U8^4-2143.6*U8^5)*W
2140 B3=(INT(B3*10000+.5)/10000)
2150 PRINT 'CRACK = ' ; B3 ; ' (1)'
2160 IF H=1 THEN I8=B3 \ H=0
2170 IF T0=0 THEN IF (B3-I8)<.015 THEN 2050
2180 IF T0=0 THEN PRINT , , '.015 MARK' \ W1=0 \ GOSUB 2970 \ W1=1
2190 IF T0=1 THEN GO TO 2210
2200 GOSUB 3030 \ GOSUB 3030 \ GOSUB 3030 \ T0=1
2210 IF B3<.255*W THEN 2050
2220 FGHOLD \ FGINMED(1,'RAMP', TIME 1,.5*L2/L) \ FGSTOP \ ADSTOP \ GOSUB 350
2230 A6=B3
2240 D$(K,1)='0' \ D$(K,2)=STR$(V3*1000) \ D$(K,3)=STR$(A3) \ D$(K,4)=STR$(P)
2250 GOSUB 110
2260 K=K+1
2270 A8=A3
2280 FGCYCLES(1)
2290 IF A3>.375*W THEN F0=10 \ GOSUB 2970 \ GO TO 2470
2300 IF W2=0 THEN GOSUB 2970 \ W2=1 \ GO TO 2310
2310 IF Q9<15 THEN Q9=32000
2320 IF P9=1 THEN 2620
2330 FGCYCLES(1,F5) \ V=ELEVEL(H1(1,2))
2340 P=ELEVEL(H1(1,1))*L
2350 V=(INT(V*10000)/10000) \ V3=40*V
2360 V3=V3/1000 \ P=ABS(P) \ V3=ABS(V3)
2370 U8=1/((B1*10^6/P*E*V3)^.5+1)
2380 B3=(1.001-4.6695*U8+18.46*U8^2-236.82*U8^3+1214.9*U8^4-2143.6*U8^5)*W
2390 B3=(INT(B3*10000+.5)/10000)
2400 PRINT 'CRACK = ' ; B3 ; ' (2)'
2410 IF B3-A6>.0225*W THEN FGHOLD \ FGINMED(1,'RAMP', TIME 1,.5*L2/L) \ FGSTOP \ ADSTOP \ GOSUB 350 \ GO TO 2430
2420 GO TO 2310
2430 D$(K,1)=STR$(F5) \ D$(K,2)=STR$(V3*1000) \ D$(K,3)=STR$(A3) \ D$(K,4)=STR$(P)
2440 A8=A3 \ A6=B3 \ GOSUB 110 \ K=K+1
2450 IF A3<.375*W THEN GOSUB 170 \ ADGO \ ADINIT \ FGGO \ GO TO 2310
2460 W1=0 \ F0=10 \ GOSUB 2970
2470 IF Q9<15 THEN Q9=32000
2480 IF P9=1 THEN 2620

```

```

2490 FGCYCLES(1,F5)\ V=ELEVEL(M1(1,2))
2500 P=ELEVEL(M1(1,1))\L
2510 V=(INT(V*10000)/10000) \ V3=40*V
2520 V3=V3/1000 \ P=ABS(P) \ V3=ABS(V3)
2530 U8=1/((B1*10^6/P*E*V3)^.5+1)
2540 B3=(1.001-4.6695*U8+18.46*U8^2-236.82*U8^3+1214.9*U8^4-2143.6*U8^5)*W
2550 B3=(INT(B3*10000+.5)/10000)
2560 PRINT 'CRACK = ';B3;' (3)'
2570 IF B3-A6>.0125*W THEN ADSTOP \ FGIMMED(1,'RAMP', TIME 1,.5*L2/L) \ GOSUB 350 \ GO TO 2590
2580 GO TO 2470
2590 D$(K,1)=STR$(F5)\ D$(K,2)=STR$(V3*1000) \ D$(K,3)=STR$(A3) \ D$(K,4)=STR$(P)
2600 A8=A3 \ A6=B3 \ GOSUB 110 \ K=K+1
2610 IF A3<W5 THEN GOSUB 170 \ ADGO \ ADINIT \ FGGO \ GO TO 2470
2620 FGSTOP \ ADSTOP
2630 FGIMMED(1,'RAMP', TIME 1,0)
2640 CLOSE #9 \ O5=0
2650 GOSUB 2670
2660 RETURN
2670 OPEN K# AS FILE VF1$(10)=(24), FILESIZE (10), ERROR J9
2680 K=K-1
2690 FOR I=K2+1 TO K+K2
2700 A# =D$(I,1)+'/'+D$(I,2)+'/'+D$(I,3)+'/'+D$(I,4)
2710 VF1(I)=A#
2720 A#=""
2730 NEXT I
2740 K2=K2+K
2750 VF1(0)=STR$(K2)
2760 CLOSE VF1
2770 RETURN
2780 PRINT \ PRINT
2790 PRINT 'ENTER SAMPLE THICKNESS '; \ INPUT B1
2900 PRINT 'ENTER SAMPLE (W) '; \ INPUT W
2910 P=L2
2820 RETURN
2830 FOR I=1 TO 12 \ PRINT \ NEXT I
2840 PRINT '# CYCLES = ';F5 \ PRINT \ PRINT
2850 PRINT '1---NEW SAMPLE'
2860 PRINT '2---PRINT FILE TO PRINTER'
2870 PRINT \ PRINT \ PRINT
2880 PRINT 'ENTER NUMBER'; \ INPUT J
2890 IF J<0 THEN 2830
2900 IF J>8 THEN 2830
2910 ON J GOSUB 1550,1260
2920 GO TO 10
2930 PRINT \ PRINT
2940 PRINT 'ENTER (DY0) OR (DY1) FOR DISK I.D. '; \ INPUT K1#
2950 PRINT \ PRINT
2960 RETURN
2970 FGSTOP \ ADSTOP \ FGIMMED(1,'RAMP', TIME 1,.5*L2/L)
2980 IF W1>0 THEN F0=W0
2990 F=FGBINFREQ(F0) \ U1=L2/L \ U2=U1*.05 \ U1=INT(U1*32752) \ U2=INT(U2*32752)
3000 U3=U1 \ U4=U2 \ U1=U1-U2 \ B(1,0)=U1 \ B(2,0)=U2 \ Q9=32000
3010 GOSUB 170
3020 ADGO \ ADINIT \ FGGO \ RETURN
3030 ETIME(S2)
3040 ETIME(S3) \ IF ABS(S3-S2)<2 THEN 3040
3050 RETURN

```

ORIGINAL PAGE IS  
OF POOR QUALITY



## REFERENCES

1. Sullivan, A. M., "Crack Length Determination of Compact Tension Specimen Using a Crack Opening Displacement Calibration," Naval Research Lab Report 7888, June 24, 1975.
2. Newman, J. C., "Crack Opening Displacements in Center Crack, Compact and Crack Line Wedge Loaded Specimens," NASA-TN-D-8268, Washington, D.C. (July 1976).
3. Saxena, Ashok and Hudak, S. J., Jr., "Review and Extension of Compliance Information for Common Crack Growth Specimens," International Journal of Fracture, Vol. 14, No. 5, October 1978, pp. 453-468.
4. Yoder, G. R., Codey, L. A., and Crooker, T. W., "Procedures for Precision Measurements of Fatigue Crack Growth Rate Using Crack-Opening Displacement Techniques," Fatigue Crack Growth Measurement and Data Analysis, ASTM STP 738, S. N. Hudak, Jr., and R. J. Bucci, Eds., American Society for Testing and Materials, 1981, pp. 85-102.
5. "Standard Test Method for Constant-Load-Amplitude Fatigue Crack Growth Rates Above  $10^{-8}$  m/Cycle," E647-83, American Society for Testing and Materials, 1983.
6. Maxwell, D. C., Gallagher, J. P., and Ashbaugh, N. E., "Evaluation of COD Compliance Determined Crack Growth Rates," University of Dayton Research Institute for Materials Laboratory, Air Force Wright Aeronautics Laboratories.

Hydrogen Effects on the Fatigue and Tensile Behavior of  
CMSX-2 Nickel Base Superalloy Single Crystals

I.M. Bernstein, S. Walston, M. Dollar, A. Domnanovich, and W. Kromp

Carnegie-Mellon University

Pittsburgh, PA 15212

### Introduction

A number of studies have suggested that specific nickel-based superalloy single crystal materials can be susceptible to varying degrees of hydrogen embrittlement under a variety of testing conditions in gaseous high pressure hydrogen (1), an important environment, for example, for space shuttle main engine turbo pumps. A particular alloy, CMSX-2, has shown a varying sensitivity to hydrogen depending on the heat treatment (2). For example, a heat treatment reported to improve the high temperature creep resistance of this alloy (3), also reduced the susceptibility to hydrogen embrittlement, when tested in both smooth and notched tensile configurations (1,2). We have been extending these studies to investigate the room temperature tensile and fatigue behavior, as a function of the mode of hydrogen introduction, of the amount and distribution of dissolved hydrogen and of heat treatment. A particular focus has been to correlate observed hydrogen effects with the role of microstructural heterogeneities as trapping centers for hydrogen.

### Previous Results

[001] oriented CMSX-2 single crystals of composition given in Table I were supplied from the vendor in the as-solutionized state of 3 hours at 1315°C. Standard tensile specimens, sub-size tensiles and solid and hollow fatigue specimens were prepared, as previously described (4). These samples were encapsulated in argon and heat treated in one of two ways; either a 1050°C/16h/air cool + 850°C/48h/air cool or 980°C 5h/air cool + 850°C/48h/air cool heat treating schedule. The latter has been designated as a standard treatment and the former was developed by the French laboratory, ONERA, (3) primarily to improve creep resistance. The resultant macrostructure consisted of significant non-uniform grown-in porosity at

variable levels between 0.1 to 0.3 volume percent. While the average size is 10-20 microns in diameter, some larger pores (as large as 70 microns in length) were found and significant clustering was often observed.

A strong dendritic structure, following both heat treatments persisted, with the following average size dimensions: Core diameter  $\sim$  100 microns; arm length 500-600 microns; and spacing  $\sim$  150 microns. Quantitative microprobe analysis revealed the presence of significant segregation (5). In particular the dendrite core is enriched in W and Cr and depleted in Ta and to lesser extent Al.

The microstructure consisted of about a 70% volume fraction of 0.5 micron cuboidal  $\gamma'$  in a  $\gamma$  matrix. The ONERA heat treatment led to slightly larger, more aligned and more cuboidal  $\gamma'$ .

The most effective way found to introduce hydrogen was by cathodic potentiostatic charging on polished samples primarily in a mixture of molten salts of 57% sodium bisulfate and 43% potassium bisulfate at 150°C. All charging was performed at  $150 \pm 5^\circ\text{C}$  for 5 hours.

The introduction of hydrogen in this manner significantly reduced the tensile elongation of bulk and small specimens (4),(6). The changes varied from about a 20% reduction in elongation in bulk specimens to more than 80% in small tensiles, for both heat treatments, standard and ONERA. This behavior has been explained on the basis of the relative volume of hydrogen containing material, which scales with specimen size, and on the important and deleterious role played by sub-surface voids (5),(7).

A similar degradation was observed due to hydrogen on the low cycle fatigue behavior of both bulk and hollow specimens tested at room temperature for  $R=-1$  and under constant plastic strain range control ranging from 0.1 to 0.4%. The most striking behavior, following molten salt charging, was a significant reduction in the number of cycles to failure, in some cases almost an order of magnitude reduction (4). The ratio of the cycles to failure between uncharged and charged specimens appeared to correlate with the magnitude of the hydrogenated volume. For example, the

ratio in bulk samples was about a factor of 2-1/2 smaller than that of the hollow samples, comparable to the ratio of the hydrogen containing versus the unaffected volume.

In both tensile and fatigue behavior hydrogen degradation was associated with a change in fracture mode from predominantly shear to a normal fracture, seemingly related to either cleavage along cube planes or along the  $\gamma - \gamma'$  interface. Significant surface cracking was also observed.

The purpose of this paper is to describe followup studies to clarify and extend the above results. Specifically, the following three areas will be stressed:

1. Extension of the low cycle fatigue tests to a lower plastic strain range and to hydrogen conditions produced by high pressure thermal charging .
2. A more detailed fractographic study to ascertain the hydrogen induced fracture plane.
3. An enhanced solutionizing treatment to break up the dendritic macrostructure and an evaluation of how this thermal processing change affects hydrogen compatibility.

#### **Fatigue Behavior of CMSX-2 at Low Plastic Strain Ranges**

In addition to the samples charged in molten salt, as described above, both bulk and hollow samples were exposed to hydrogen charging under a gas pressure of hydrogen of 5000 psi, temperature 950°F for a period of 24 hours, followed by a 6 hour cool down. This work was carried out at the Rocketdyne Test Facility. As discussed, the hollow and solid samples were compared to investigate the influence of increasing the volume of hydrogen containing material as well as the role of the surface on the fatigue behavior. The hydrogen gas phase charging was expected to increase the depth of hydrogen dissolution and thus to increase the volume to surface ratio of the material exposed to hydrogen, again allowing us to compare these two parameters.

As previously reported (4) the accumulated plastic strain to fracture in the hydrogen charged samples is lower than in the uncharged, often significantly so, Table II. No significant difference in the fatigue behavior

was observed between the specimens charged in molten salt and those under hydrogen pressure, comparing separately either the bulk or hollow samples, although the numbers of cycles to failure was significantly shorter for the latter case. The similar behavior of the molten salt and gas phase charged samples in both specimen types suggests that, in addition to the total hydrogen concentration, the surface area to volume ratio plays a critical role in determining the fatigue life, presumably through enhanced surface initiated crack initiation. It would appear that the earlier observation of a correlation with the ratio of the hydrogen to non-hydrogen containing volume may be better explained as due to differences in concentration.

The hydrogen degradation persisted even at the smallest plastic strain range although a marked difference was observed in cyclic behavior between large (0.4 to 0.1%) and small (0.02%) strain ranges. While the amplitudes between 0.4 to 0.1% showed a symmetric hysteresis loop, the smaller amplitude of 0.02% occasionally exhibited load drops during both the tension and the compression portion of the cycle. Such load drops were shown to be associated with highly localized plastic strain peaks manifested by shear band formation. Figure 1 shows the magnitude of such localized plastic strain peaks (associated with each load drop) as a function of the accumulated plastic strain for both uncharged and charged samples. The frequency of occurrence of the load drops is clearly lower in the hydrogen charged samples. Note that the localized strain values were calculated over the entire specimen gage length and not with respect to the locally deformed region, which is difficult to determine experimentally. As such, they are average values which while relatively correct underestimate the localized strain.

Figure 2 shows the dependence of the localized plastic strain versus the accumulated strain for both uncharged and charged samples. While the total amount of localized plastic strain in both samples seems comparable, it occurs by smaller but more frequent load drops in the uncharged sample in contrast to larger, but less frequent ones in the charged material. Interestingly, load drops do not occur in the hollow samples suggesting that the periodic buildup of the dislocation structure and associated stress

field maybe of the order of or larger than the wall thickness of the hollow sample. Further, the number of load drops in tension or compression correlates closely to the number of shear bands observed on the specimen surface, Figure 3, where the shear bands in the hydrogen charged material are fewer but have a larger step size. Qualitatively, this agrees with the general coarsening (strain localization) of the deformation morphology frequently observed in hydrogen charged materials (8). It suggests that fatigue fracture is controlled by the need to accumulate a given amount of localized strain. While the magnitude appears similar in both charged and uncharged samples, enhanced localization permits it to be attained earlier in the former case. These results are both intriguing and somewhat surprising, particularly since the failure mode is not the same for both conditions, and geometries, as discussed in the next section. Studies to clarify this aspect are continuing.

#### Hydrogen Induced Fracture Path

From observations on both tensile and fatigue specimens it was clear that hydrogen caused a major change in fracture mode, as well as promoting a much more significant role of grown in porosity in the fracture process (4). Uncharged samples fractured predominantly along planes parallel to multiple crystallographic {111} slip systems, with evidence for matrix tearing and  $\gamma/\gamma'$  delamination. Hydrogen containing samples, on the other hand, were clearly embrittled, with a more planar surface of an orientation normal to the loading axis, and with evidence of decohesion along the  $\gamma/\gamma'$  interface (4,5).

The most striking way to illustrate these differences is by way of Figure 4. Hydrogen induces cracking in the Luders band of a small tensile sample and on a plane not parallel to any operating or possible slip plane. In contrast, in the absence of hydrogen, failure occurred parallel to the Luders band. Figure 5 shows extensive cracking on two faces of the tensile sample, and subsequent surface trace analysis conclusively showed that such cracks are parallel to {100} planes. It yet remains to be established whether this results from "cleavage" in the fcc  $\gamma$  or to preferential decohesion along the  $\gamma/\gamma'$  interface. The latter possibility may be more likely, particularly if the interface contains coherency strains which could then enhance the local hydrogen concentration.



Similar changes were observed in fractured fatigue samples; Figure 6 shows surface markings for both the uncharged and charged conditions for tests run at a plastic strain range of 0.1%. Slip markings are clearly seen in the former case, and the hydrogen-induced surface cracks are not parallel to these or to any slip plane. If this mode change persists, as expected, to lower plastic strain ranges, the observed correlation that the accumulated localized plastic strain prior to fracture is similar with and without hydrogen (Figure 2), implies a role of strain exhaustion in both cases.

### The Role of Solutionizing Treatments

The presence of a strong, persistent dendritic macrostructure with its associated concentration gradients made it difficult to assess hydrogen effects in a homogeneous  $\gamma/\gamma'$  microstructure. Extended solutionizing treatments, limited to the same temperature because of the closeness to the liquidus solvus, were carried out to determine if the dendrite structure could be broken down and, if so, to see if a change in mechanical properties ensued. Figure 7 traces the changes in macrostructure from a 3 hour solutionizing at  $1315^{\circ}\text{C}$  (a standard treatment), to 12, 52 and 72 hours. Deep etching reveals that the last two times are effective in reducing or eliminating the well defined dendrites, although the persistence of uneven shading suggests residual segregation effects. Microprobe analysis is underway to quantify these observations.

Small tensile samples solutionized at  $1315^{\circ}\text{C}$  for 3 and 52 hours and given the ONERA heat treatment, were compared to investigate the effect of homogenization on subsequent room temperature mechanical properties. The results are summarized in Table III for both the uncharged and molten salt charged condition. Also included for comparison are results from an earlier study (5). A number of observations can be made: The higher strength values observed in the previous study (5), are believed to result from chemical and orientation variations from bar to bar (4). Solutionizing for longer times does not affect mechanical properties for the uncharged condition, and the alloy's high sensitivity to embrittlement, as monitored by a change in the uniform elongation, persists. There does appear to be a significant reduction in the yield and ultimate tensile stress due to hydrogen after the homogenization treatment, which is not found after a

standard solutionizing treatment. Homogenization also leads to differences in hydrogen cracking behavior, even though the relative elongation loss is comparable for both conditions. This is obvious from a comparison of Figure 5 and Figure 8. Much less severe and less planar cracks are observed in the homogenized case, although the crack plane continues to be parallel to {100}. Both the observed changes in strength and in crack nature, associated with homogenization require further, more careful study.

#### REFERENCES

1. W.S. Alter, R.A. Parr, M.H. Johnston, J.P. Strizak, NASA TM Report No. 86464, August 1984.
2. W.T. Chandler, Contract NAS 3-23536 Report, November, 1983.
3. T. Khan, P. Caron, Fourth RISO International Symposium on "Metallurgy and Material Science", Roskilde (Denmark), September 5-9, 1983.
4. 1985 Renewal Proposal "Hydrogen Effects on Tensile and Fatigue Behavior of [001] Oriented CMSX-2 Single Crystals", NAG 3-463 NASA Lewis, Carnegie-Mellon University.
5. J. Chene, C.L. Baker, I.M. Bernstein and J.C. Williams, Proceedings of "High Temperature Alloys for Gas Turbines and Other Applications", Liege, Belgium 1986.
6. C.L. Baker, J. Chene, W. Kromp, H. Pinczolit, I.M. Bernstein, and J.C. Williams, in "Structural Integrity and Durability of Reusable Space Propulsion Systems", NASA Conference Publication No. 2381, NASA Lewis Research Center, Cleveland, Ohio, 1985.
7. C.L. Baker, J. Chene, I.M. Bernstein, and J.C. Williams, submitted to Met Trans.
8. O.A. Onyewuenyi and J.P. Hirth, Met. Trans, 13A 1982, p. 2209.

Table 1

CMSX-2 Composition (weight percent)

Al	5.6
Ti	1.07
Cr	8.0
Ni	balance
Co	4.6
Ta	6.0
W	8.0
Mo	0.6
Fe	0.08
Si	0.015

C	: 15	} ppm wt.
S	: 10	
N	: 4	
O	: 2	

Table II

Fatigue Behavior as a Function of Plastic Strain Range  
and Charging Conditions

Specimen Type	$\Delta\epsilon_p$ (%)	Charging Conditions	Cycles to Failure		$n_u/n_c$
			uncharged	charged	
Bulk	0.4	5h at 150°C (molten salt)	57	16	3.6
	0.2		131	57	2.3
	0.1		214	80	2.7
	0.02	24h at 950°F 5000 psi	3348	1260	2.7
	0.4		57	39	1.5
	0.1		370	71	5.2
Hollow	0.4	5h at 150°C (molten salt)	67	9	7.4
	0.1		184	27	6.8
	0.02		557	110	5.1
	0.1	24h at 950°F 5000 psi	164	27	6.1

Heat Treatment: 1315°C - 3h + ONERA

R = -1, Room Temperature Testing

Table III

Room Temperature Tensile Behavior\* of Small Tensile Samples

$$\dot{\epsilon} = 5 \times 10^{-3} \text{ s}^{-1}$$

<u>Heat Treatment</u>	<u>Charging Conditions</u>	<u>YS (MPa)</u>	<u>UTS (MPa)</u>	<u>Uniform Elongation</u>
1315°C - 3h + ONERA	uncharged	711	1029	12.3
1315°C - 52h + ONERA	uncharged	692	944	12.5
1315°C - 52h + ONERA	charged 5h at 150°C	539	907	3.6
1315°C - 3h** + ONERA	uncharged	874	901	18.5
1315°C - 3h** + ONERA	charged 5h at 150°C	879	847	6.2

\*mean value of two tests.

\*\*data from previous study (5).

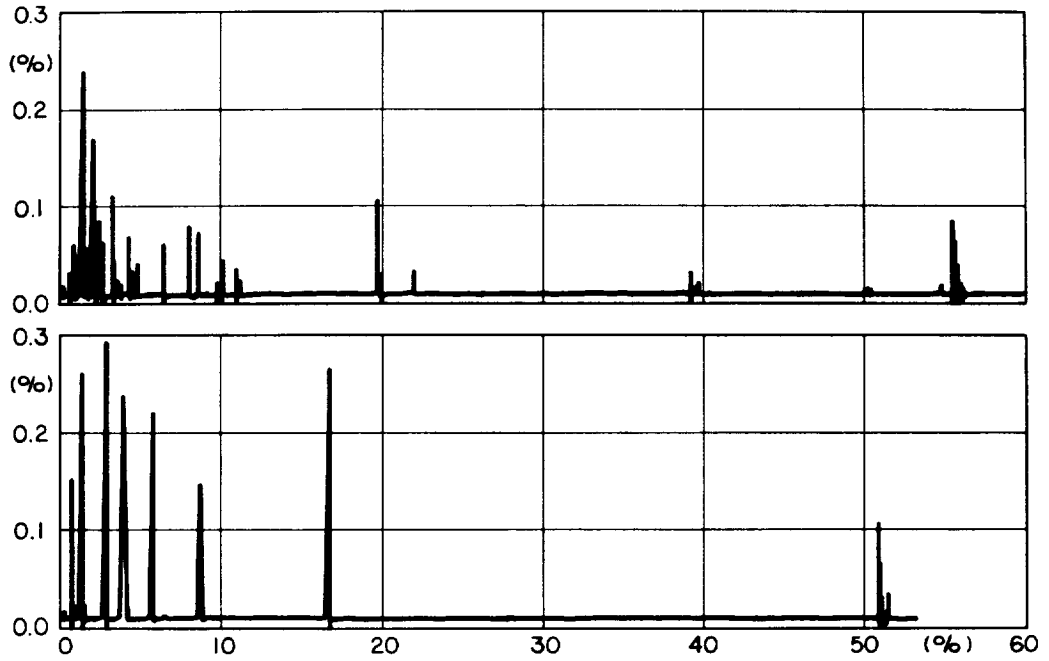


FIGURE 1: LOCALIZED PLASTIC STRAIN ASSOCIATED WITH PEAKS DURING TENSION AND COMPRESSION CYCLES FOR BOTH HYDROGEN FREE (UPPER) AND CHARGED (LOWER) SAMPLES.  $\Delta\epsilon_p=0.02\%$ .

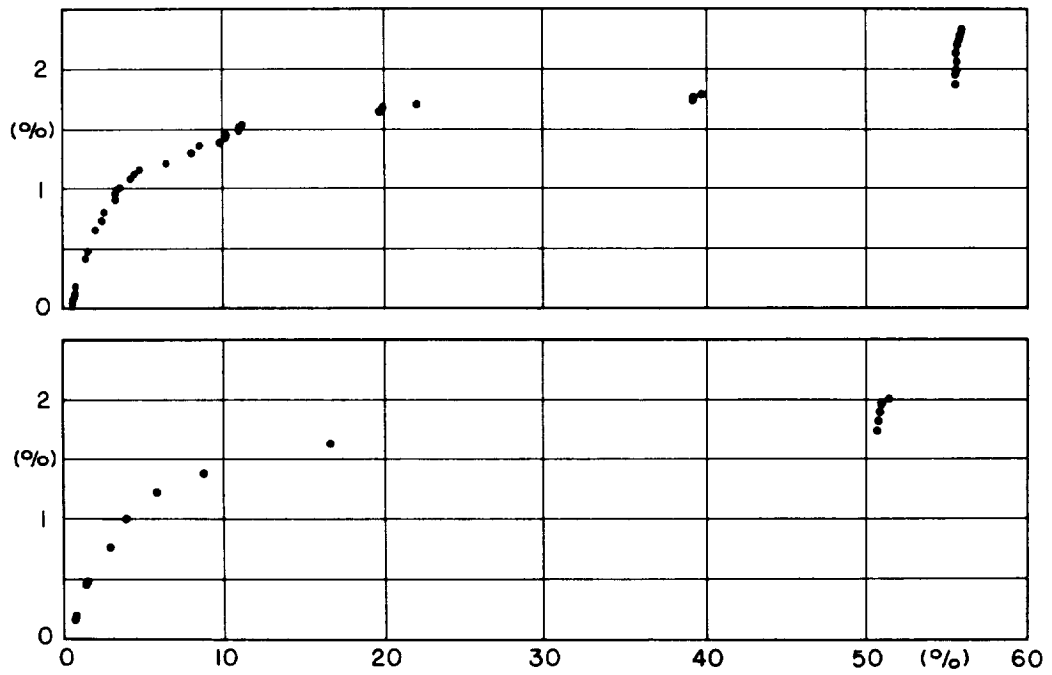


FIGURE 2: ACCUMULATED LOCALIZED PLASTIC STRAIN AS A FUNCTION OF ACCUMULATED PLASTIC STRAIN FOR BOTH HYDROGEN FREE (UPPER) AND CHARGED (LOWER) SAMPLES, AS IN FIGURE 1.

ORIGINAL SIZE IS  
OF POOR QUALITY

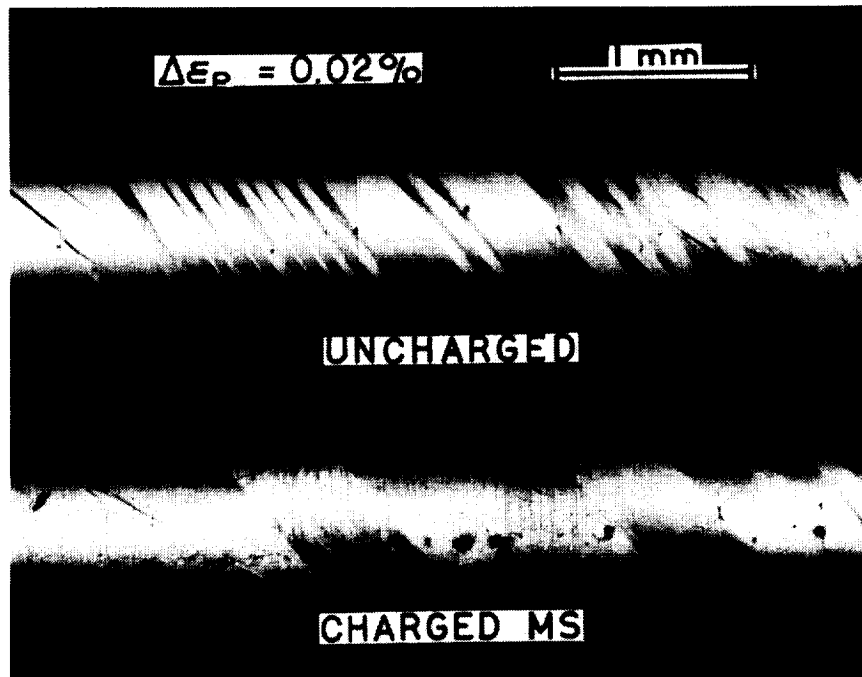


FIGURE 3: OPTICAL MICROGRAPHS OF LOCALIZED SHEAR BANDS IN HYDROGEN CHARGED AND UNCHARGED FRACTURED FATIGUE SAMPLES.

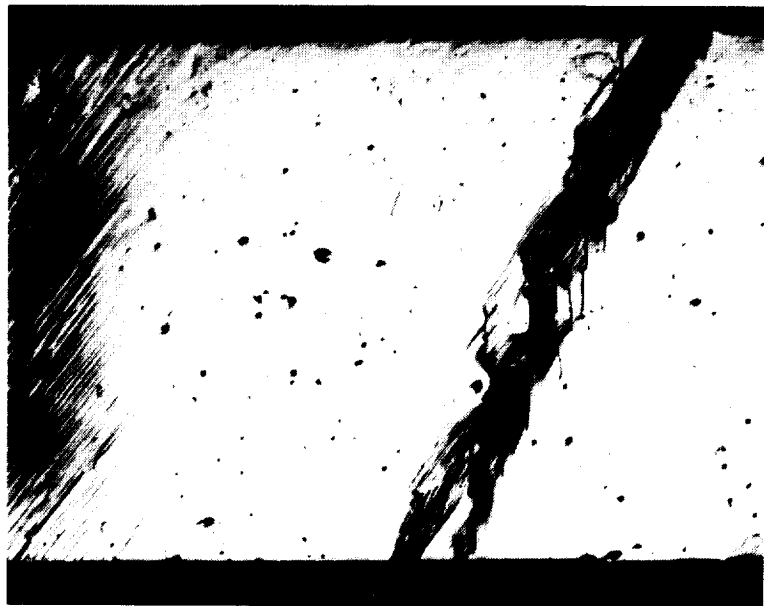


FIGURE 4: LUDERS BAND CRACKING IN A MOLTEN SALT HYDROGEN CHARGED TENSILE SAMPLE.



ORIGINAL PAGE IS  
OF POOR QUALITY

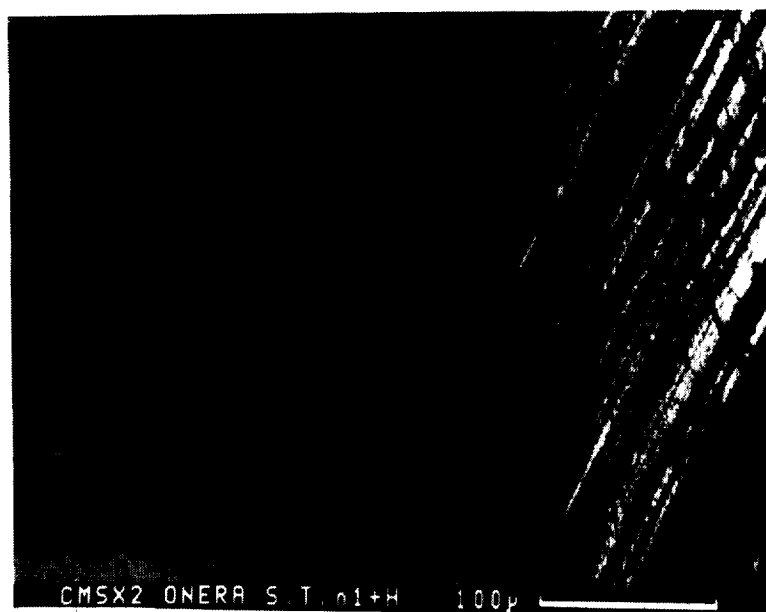
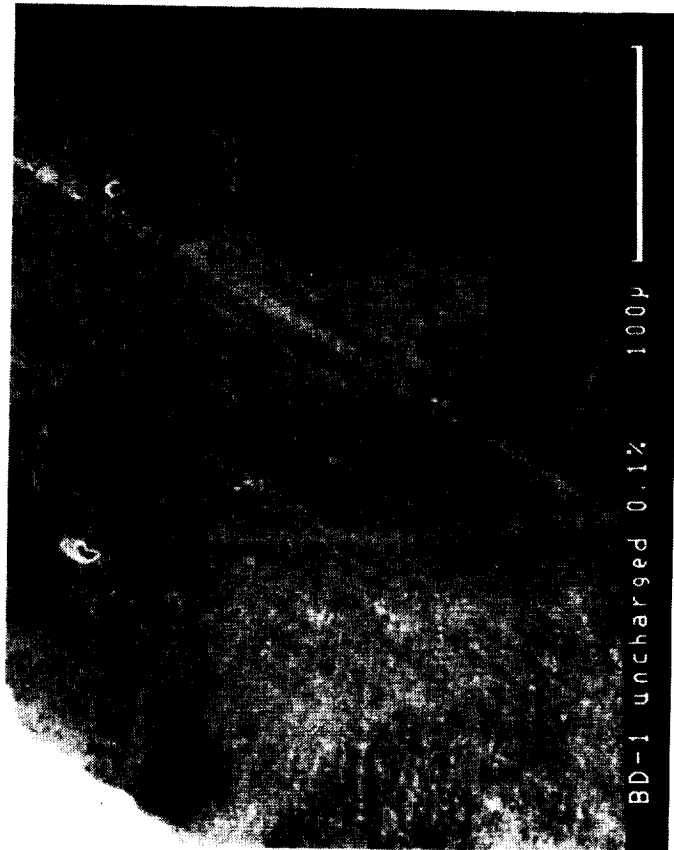


FIGURE 5: CRACKS ON TWO NON-PARALLEL SURFACES, AS IN FIGURE 4.

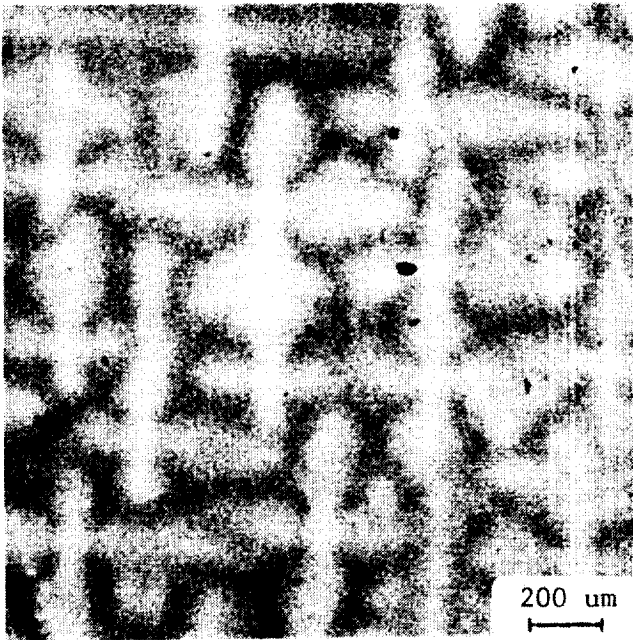


BD-1 uncharged 0.1% 100 $\mu$

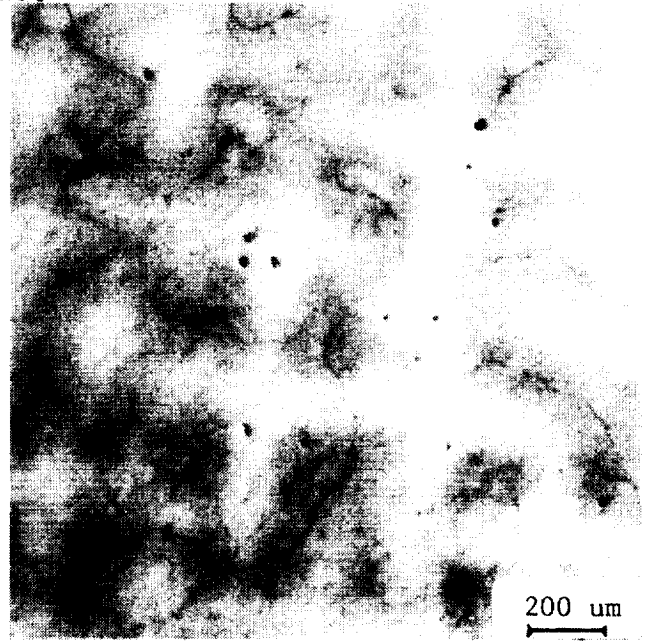


Charged Fatigue 0.1% 100 $\mu$

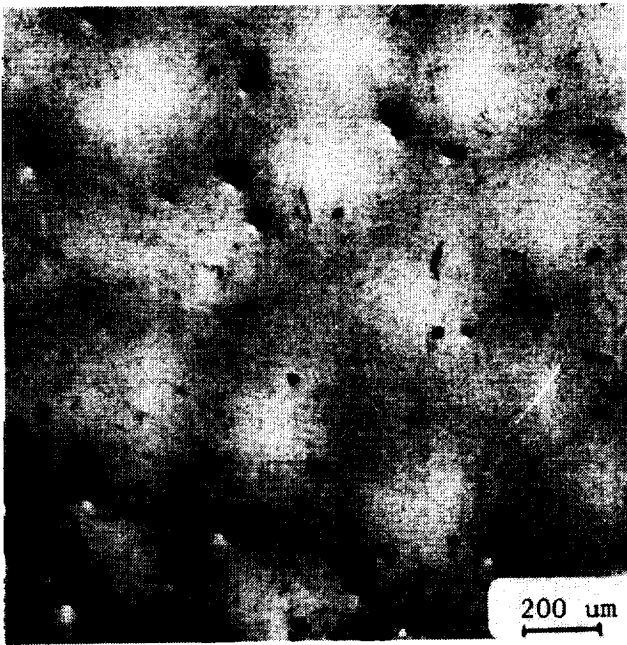
FIGURE 6: SLIP TRACES AND SURFACE CRACKING IN A MOLTEN SALT HYDROGEN CHARGED FATIGUE SAMPLE,  $\Delta\epsilon_p=0.1\%$ .



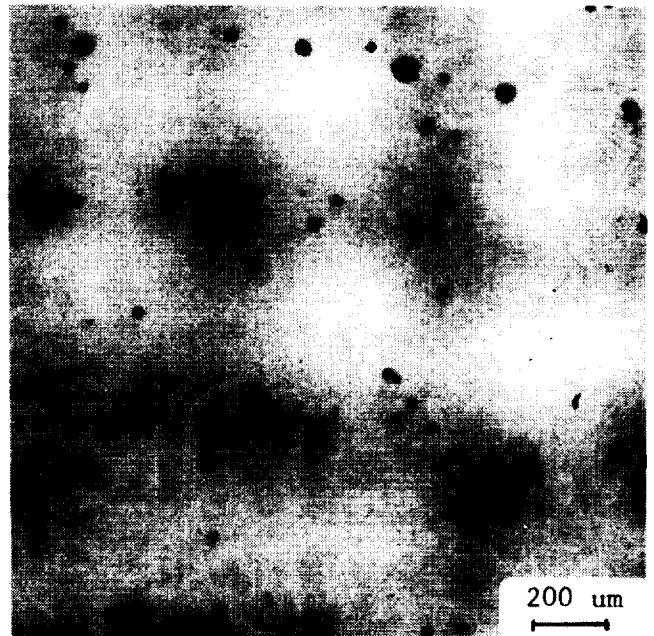
3 hrs



12 hrs



51 hrs



72 hrs

FIGURE 7: EFFECT OF SOLUTIONIZING TIME AT 1315°C ON THE DENDRITIC MACROSTRUCTURE.

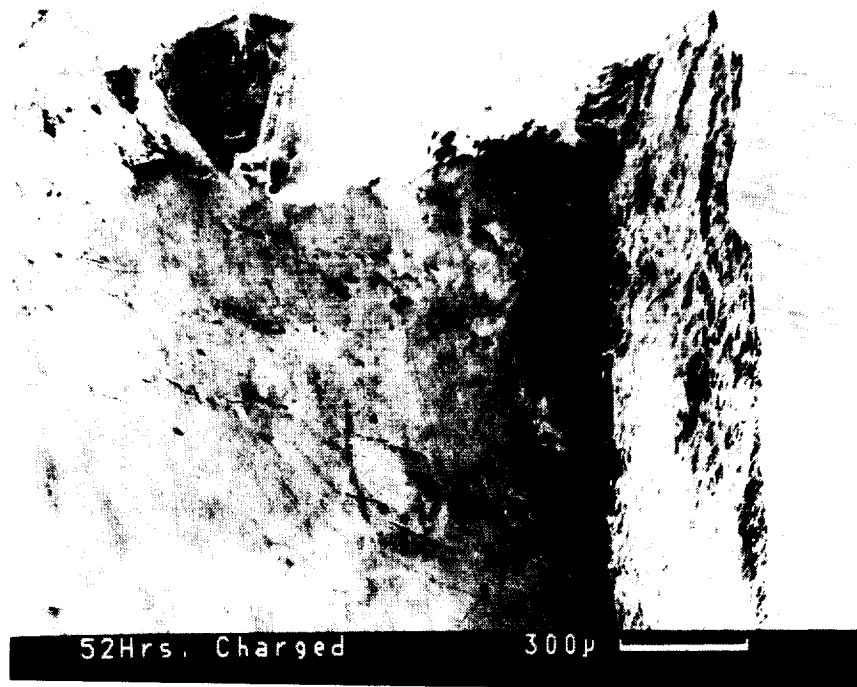


FIGURE 8: CRACKS ON TWO NON-PARALLEL SURFACES OF A MOLTEN SALT HYDROGEN CHARGED HOMOGENIZED TENSILE SAMPLE. COMPARE WITH FIGURE 5.

The Determination of Mobile Hydrogen  
in Aerospace Engine Alloys

Merlin D. Danford  
Corrosion Research Branch  
Materials & Processes Laboratory  
NASA/MSFC  
Marshall Space Flight Center  
Alabama 35812

ABSTRACT

Hydrogen desorption data (coulombs desorbed vs. time) have been obtained for Waspaloy and Rene' 41 using electrochemical methods. A more general method of analysis, using diffusion theory, has been developed and applied. The method may assume an initial hydrogen distribution which conforms to that predicted by diffusion theory or a uniform initial distribution. The data are interpreted in terms of either of these initial distributions or a combination thereof. It was found that the initial hydrogen distributions for Waspaloy and Rene' 41, after both electrolytic charging and charging at 5000 psi hydrogen pressure, conformed closely to those predicted by diffusion theory. The hydrogen desorption is completely explained by the nature of the initial hydrogen distribution in the metal, which has previously been assumed to be uniform, and the "fast" hydrogen is not due to surface and subsurface hydride formation, as we previously proposed. Finally, the hydrogen solubilities in the metals, for electrolytically charged samples, depend strongly on the charging rate and are about the same for Rene' 41 and Waspaloy.

The Determination of Mobile Hydrogen  
in Aerospace Engine Alloys

I. Introduction

The importance of hydrogen induced failure of materials has been widely recognized. Catastrophic failure of high strength steel parts, such as aircraft landing gear, can often be attributed to hydrogen embrittlement. The source of hydrogen which causes failure in the presence of stress can be a corrosion reaction, but can also be a pretreatment process such as pickling, welding or a plating process.

To properly understand hydrogen embrittlement, two kinds of hydrogen and their relative roles must be studied, these being the mobile or diffusible hydrogen and the trapped hydrogen. The present technique is electrochemical in nature, and deals exclusively with the diffusible hydrogen. It has been developed to be used in conjunction with other methods which will allow determination of both the diffusible and non-diffusible components.

II. Background

A basis for measurement of hydrogen concentration,  $C_0$ , is an electrochemical permeation method which was first described by Devanathan and Stachurski [1,2]. In this method, hydrogen is produced on one side of a metal foil, either as the result of a corrosion reaction in acidic media, or by the application of a cathodic current. On the other side of the foil, hydrogen which has diffused through the metal is removed by application of an anodic constant potential which leads to the oxidation of hydrogen to water. The measurement is carried out in an alkaline solution. Under the assumption that semi-infinite diffusion occurs in a sample of finite thickness, the solution of the diffusion equations:

$$I = -ZFD \left( \frac{\partial C}{\partial X} \right)_{X=0} \quad (1)$$

$$\frac{\partial^2 C}{\partial X^2} - \frac{1}{D} \left( \frac{\partial C}{\partial t} \right) = 0 \quad (2)$$

leads to the well known Cottrell equation for the permeation current  $I_p$ :

$$I_p = ZFC_0 \left( \frac{D}{\pi} \right)^{1/2} \quad (3)$$

Here,  $Z$  is the number of electrons involved in the reaction (one),  $F$  is the Faraday constant,  $D$  is the diffusivity of hydrogen through the

metal, and  $I_p$  is the current density at time  $t$ . The use of equation (3) requires an a priori knowledge of the diffusion coefficient. It requires only a short time for data collection, e.g. 30 minutes, and requires that a blank run be made for a non-hydrogen containing sample so that the current due to hydrogen only can be obtained by subtraction. Equation (3) has been used successfully by Deluccia, Berman, et al. [3,4] and by Mansfeld, et al. [5] for evaluating hydrogen concentrations with a device termed the "barnacle electrode". A shortcoming of the Cottrell equation is that the assumption is made that the initial hydrogen distribution in the metal is uniform in nature, a condition which is probably seldom realized. The same is true for the method proposed by Zakroczymski [6], which will be briefly described next.

The method proposed by Zakroczymski [6] is based on the electrochemical measurement of hydrogen desorption rate. The amount of hydrogen desorbed at time  $t$  for a finite slab is given by:

$$Q_H = Q_H^\infty \left\{ 1 - \frac{8}{\pi^2} \sum_{m=1}^{\infty} \frac{1}{(2m-1)^2} \exp(-t/\tau) \right\} \quad (4)$$

where:  $\tau = L^2/\pi^2 D$ ,  $D$  = hydrogen diffusion coefficient,  $t$  = time and  $L$  = sample thickness. In the above equation, the initial hydrogen concentration  $C_0$  is constant throughout the specimen and is given by:

$$C_0 = Q_H^\infty/L \quad (5)$$

The remainder of the details of the method are similar to those for the present method, which will be described in the next section. The assumption of a uniform initial distribution in this case led to the postulation of the formation of hydrides which are unstable at room temperature and decompose rapidly. This mechanism was proposed to explain the fast rate of hydrogen desorption, which was faster than that which would be predicted by a uniform initial distribution.

### III. The Present Method

The basic difference between the present method and that of Zakroczymski is that a uniform initial hydrogen distribution need not be assumed, and the data analysis is of a more general nature. All of the diffusion equations employed in this work have been described by Barrer [7]. For the case of hydrogen absorption, the hydrogen absorption after charging time  $t$  is give by:

$$C(x,t) = S + \frac{2S}{\pi} \sum_{m=1}^{\infty} \frac{(\cos m\pi - 1)}{m} \frac{\sin m\pi x}{L} \exp \left[ \frac{-Dm^2 \pi^2 t}{L^2} \right] \quad (6)$$

where  $S$  is the solubility of hydrogen in the metal under a given set of conditions and  $x$  is the depth in the sample. The mean concentration is given by:

$$\bar{C} = \frac{1}{L} \int_0^L C(x,t) dx \quad (7)$$

The solubility  $S$  in equation (6) is obtained by dividing the observed concentration by that obtained using equations (6) and (7) where unit values have been assumed for  $S$  in equation (6). A typical case for the initial hydrogen distribution in a flat sample of Waspaloy, where the distribution conforms to that predicted by equation (6), is shown in Figure 1. The general equation for hydrogen desorption is:

$$C(x,t) = \frac{2}{L} \sum_{m=1}^{\infty} \frac{\sin \frac{m\pi x}{L}}{L} \exp \left[ \frac{-Dm^2 \pi^2 t}{L^2} \right] \int_0^L f(x') \sin \frac{m\pi x'}{L} dx' \quad (8)$$

Here, it is assumed that the concentration of hydrogen at the sample surfaces is zero for all time. The values of  $f(x')$  are those calculated by equation (6) for a given charge time. In the case of uniform initial distribution, equation (8) reduces to:

$$C(x,t) = \frac{4C_0}{\pi} \sum_{m=0}^{\infty} \frac{1}{(2m+1)} \frac{\sin(2m+1)\pi x}{L} \exp \left[ \frac{-D(2m+1)^2 \pi^2 t}{L^2} \right] \quad (9)$$

Typical cases for hydrogen desorption are illustrated in Figures 2 and 3. Figure 2 shows the desorption from a Waspaloy sample where the initial distribution is that given by equation (6), which is referred to as a non-uniform distribution. As shown in Figure 2, the peak in the hydrogen distribution curve decreases in amplitude and moves inward with increasing desorption time. Figure 3 shows the desorption curves assuming a uniform initial distribution. Desorption with the non-uniform distribution is much more rapid than that for a uniform initial distribution. The amount of hydrogen desorbed after a time  $t$  is given by:

$$Q(t) = Q_{HM}^{\infty} - 0.0957341d \int_0^L C(x,t) dx \quad (10)$$

Here,  $d$  is the metal density, and the conversion factor is that necessary to convert from ppm-cm to coulombs/cm<sup>2</sup>.  $Q_{HM}^{\infty}$ , the total H<sub>2</sub>, is an experimentally measured quantity. Equation (10) allows direct comparison of calculated desorption curves with those obtained through electrochemical means. Finally, it should be mentioned that a computer program, PDEONE [8], is available, which can calculate all of the necessary quantities for the present analysis numerically with only a few modifications.



WASPALOY  
 CHARGED 1 HOUR AT 5,000 PSI  
 THEORETICAL (NON-UNIFORM) DISTRIBUTION  
 L = .202 cm

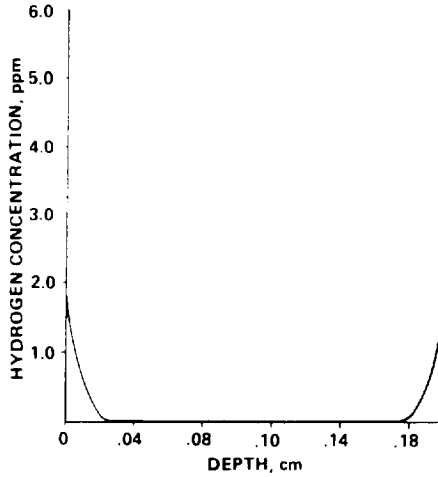


Fig. 1 Theoretical Hydrogen Distribution in Waspaloy after Charging at 5,000 psi

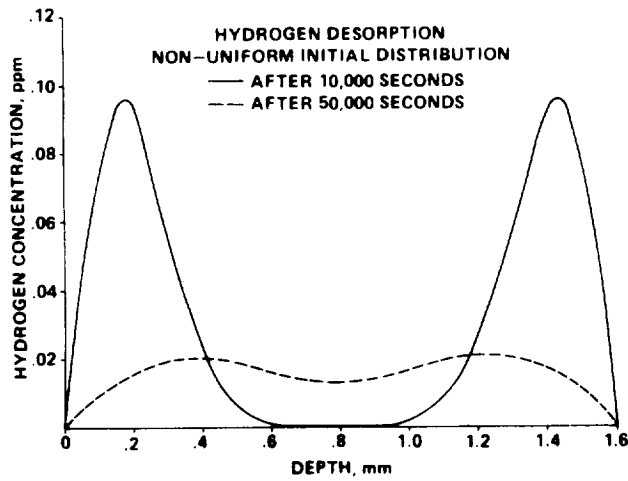


Fig. 2 The Variation of Hydrogen Distribution in Waspaloy with Time of Discharge, Non-Uniform Initial Distribution

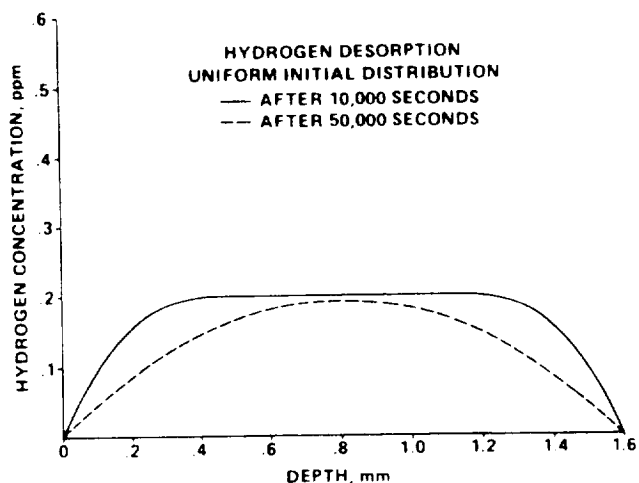


Fig. 3 The Variation of Hydrogen Distribution in Waspaloy with Time of Discharge, Uniform Initial Distribution

#### IV. Experimental

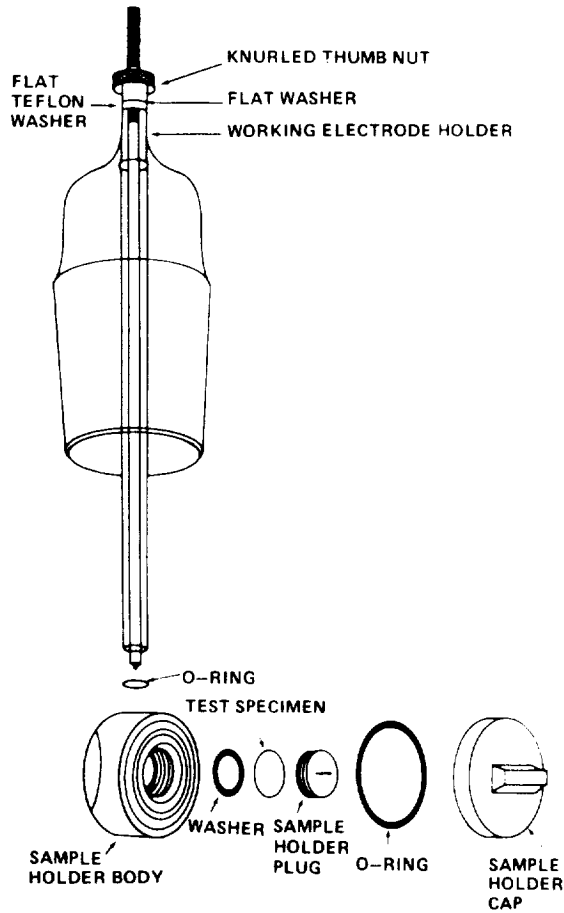
The EG&G-PARC Model 350A corrosion measurement console was employed for all measurements in this work. The sample holder employed is shown in Figure 4. It presents a sample area of  $1.0\text{cm}^2$  in contact with the solution in the electrolytic cell, in this case  $0.1\text{N NaOH}$ . Samples of Waspaloy and Rene' 41 were subjected to measurement. Samples of Rene' 41 were used as obtained (annealed) without heat treatment. All samples were  $1.59\text{ cm}$  ( $5/8\text{ in.}$ ) in diameter, with an average thickness of  $0.2\text{ cm}$ .

The samples were prepared by wet sanding with 150C and 220A grit silicon carbide paper and degreasing in boiling trichloroethylene. Sample blanks were run at a constant potential of  $+0.25\text{V}$  (NHE) in a  $0.1\text{N NaOH}$  solution at  $25^\circ\text{C}$ . The period of measurement was  $150,000$  seconds for each sample, with the current being measured at  $500$  second intervals.

Samples of both materials were electrolytically charged at  $25^\circ\text{C}$  with hydrogen in  $0.1\text{N H}_2\text{SO}_4$  at two different charge rates,  $60\text{ ma/cm}^2$  and  $1\text{ ma/cm}^2$ . In addition, a sample of Waspaloy was charged electrolytically at  $150^\circ\text{C}$  in a eutectic mixture of molten  $\text{NaHSO}_4 \cdot \text{H}_2\text{O}$  and  $\text{KHSO}_4$ . Data for the hydrogen-containing samples were collected in the same manner as those for the blanks, with the currents due to hydrogen being obtained by subtraction.

After each run, the current versus time data was read to a computer and saved. After data from both the hydrogen containing sample and its corresponding blank were obtained, the experimental curve,  $Q(t)$  versus time, was obtained by integration of the current-time curves corresponding to the current due to hydrogen only. Values of  $Q_H$ ,  $Q_{HM}$ , the observed concentration ( $C_0$ ) and the diffusion

coefficient for  $H_2$  (D) were obtained according to the method developed by Zakroczymski [6].



#### SAMPLE HOLDER – EXPLODED VIEW

Fig. 4 Exploded View of the Sample Holder

### V. Results and Discussion

The solubilities of hydrogen in Waspaloy and Rene' 41 for given sets of charging conditions are shown in Table 1. As seen from the table, the solubility depends on the charge rate for electrolytic charging, being lower for lower charge rates. The solubility for a sample of Waspaloy charged for 1 hour at 5,000 psi is about the same as that for a sample charged electrolytically at  $60 \text{ mA/cm}^2$ . The solubilities for Rene' 41 are about the same as those for Waspaloy.

TABLE 1. OBSERVED SOLUBILITIES FOR NICKEL BASE ALLOYS

<u>MATERIAL</u>	<u>METHOD</u>	<u>CHARGE RATE</u>	<u>SOLUBILITY (ppm)</u>
WASPALOY	ELECTROLYTIC	FAST <sup>a</sup> (25°C)	1.28
	ELECTROLYTIC	SLOW <sup>b</sup> (25°C)	0.75
	ELECTROLYTIC	FAST (150°C)	3.64
	5000 PSI	-	1.28
RENE' 41	ELECTROLYTIC	FAST (25°C)	1.17
	ELECTROLYTIC	SLOW (25°C)	0.29

(a) 60 MA/CM<sup>2</sup>(b) 1 MA/CM<sup>2</sup>Desorption by Waspaloy

The desorption curves for electrolytically charged Waspaloy at 25°C for charge rates of 1 mA/cm<sup>2</sup> and 60 mA/cm<sup>2</sup> are shown in Figures 5 and 6. As shown in these figures, the desorption curves are very well described by the theoretical curves (non-uniform distributions) calculated by equation (6). The theoretical curve shown in Figure 5, for a sample charged for 1 hour at 60 mA/cm<sup>2</sup>, is best described by a hybrid curve corresponding to a 10.2 percent uniform distribution. The desorption curve for a sample charged electrolytically at 150°C in a eutectic mixture of molten NaHSO<sub>4</sub>·H<sub>2</sub>O and KHSO<sub>4</sub> is shown in Figure 7. The hydrogen distribution was 77.4% uniform in nature, which would be predicted by the temperature variation of the diffusion coefficient. Similar curves for Waspaloy charged for 1 hour (25°C) at 5,000 psi are shown in Figure 8. The experimental curve was best fit with a theoretical curve corresponding to an 18.6% uniform distribution. All initial hydrogen distributions for Waspaloy, therefore are essentially those which would be predicted by diffusion theory.

Desorption by Rene' 41

Desorption curves for electrolytically charged Rene' 41 are shown in Figures 9 and 10. As shown by these figures, the desorption is completely explained by 100 percent non-uniform distributions for both fast and slow charging rates. The results are, therefore, very similar to those obtained for Waspaloy

Summary

The desorption curves for both Waspaloy and Rene' 41 are all consistent with non-uniform initial distributions after charging, either at high pressure or by electrolysis. The desorption curves are completely explained by the nature of the initial hydrogen distributions in the metals after charging, which have previously been

assumed to be uniform in theoretical calculations. The "fast" hydrogen is therefore not due to the formation of surface and sub-surface hydride formation, as has been previously proposed. Also, the hydrogen solubilities in the metals, for electrolytically charged samples, depend strongly on the charging rate, and are about the same for Rene' 41 and Waspaloy. Although this work has been concerned entirely with the mobile hydrogen aspect, future work will also include studies of trapped hydrogen content as well, and hopefully, will lead to a clearer understanding of the hydrogen embrittlement problem in general.

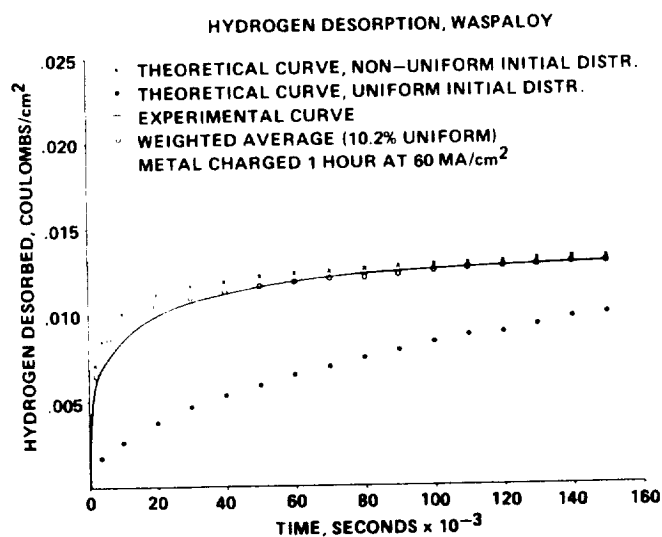


Fig. 5 Theoretical and Experimental Desorption Curves for Waspaloy, Fast Charge

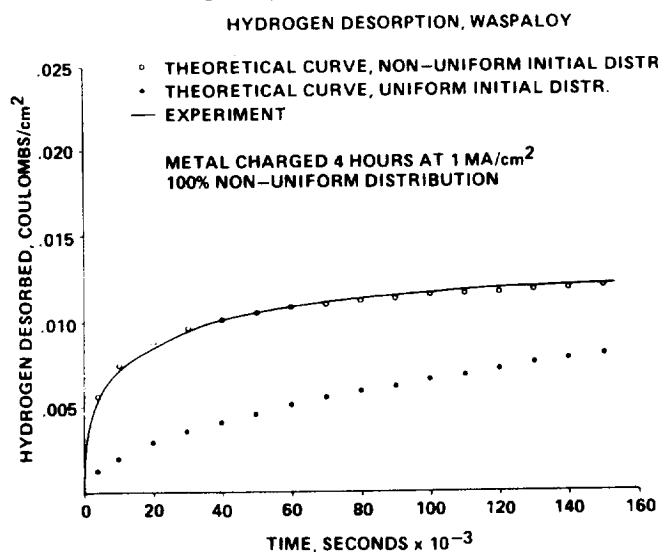


Fig. 6 Theoretical and Experimental Desorption Curves for Waspaloy, Slow Charge

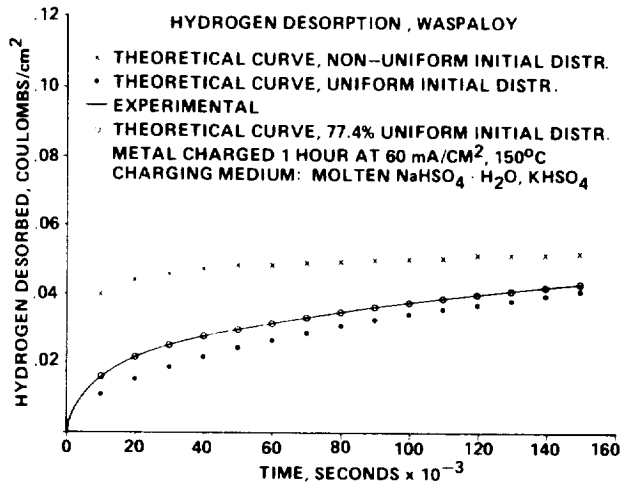


Fig. 7 Theoretical and Experimental Desorption Curves for Waspaloy, Fast Charge at 150°C

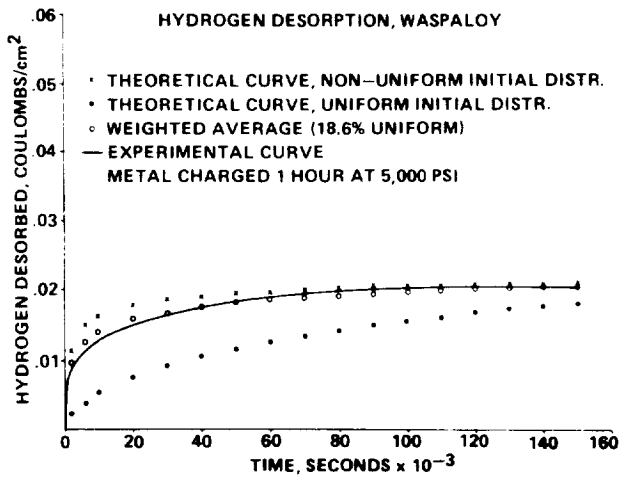


Fig. 8 Theoretical and Experimental Desorption Curves for Waspaloy, Charged at 5,000 psi

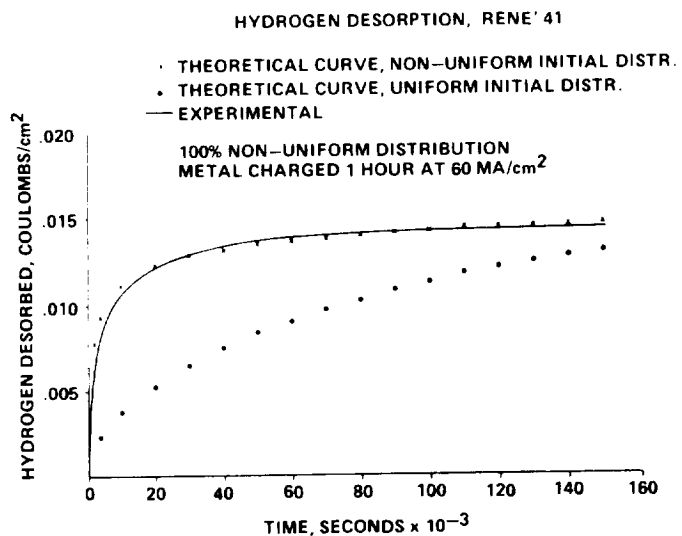


Fig. 9 Theoretical and Experimental Desorption Curves for Rene' 41, Fast Charge

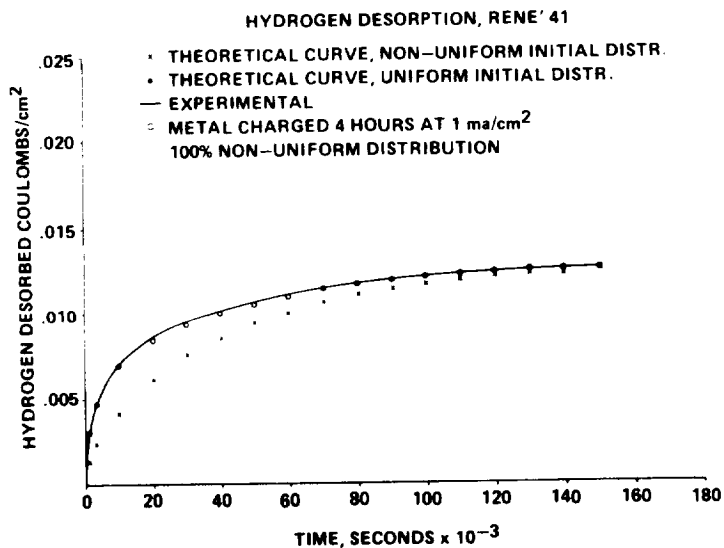


Fig. 10 Theoretical and Experimental Desorption Curves for Rene' 41, Slow Charge

### References

1. Devanathan, M.A.V. and Stachurski, Z.: Proc. Roy. Soc., Vol. A 270, 1962, p. 90.
2. Devanathan, M.A.V. and Stachurski, Z., and Beck, W.J.: Electrochem. Soc., Vol. 110, 1963, p. 886.
3. Berman, D.A., Beck, W., and Deluccia, J.J.: Hydrogen in Metals, I.M. Bernstein and W.W. Thompson (editors), ASM, 1984, p. 595.
4. Berman, D.A.: Indexing the Degree of Hydrogen Embrittlement of 4340 Steel Using the Bernacle Electrode. Naval Air Development Center, Report No. NADC-76359-30, November 1976.
5. Mansfeld, F., Jeanjaquet, S., and Roe, D.K.: Materials Performance, 1982, p. 35.
6. Zakroczymski, T.: An Electrochemical Method for Hydrogen Determination in Steel. Corrosion, Vol. 38, 1982, p. 218.
7. Barrer, R.M.: Diffusion in and Through Solids, Cambridge, 1941.
8. Sincovec, R.F. and Madsen, N.K.: Software for Nonlinear Partial Differential Equations. ACM Trans. Math. Software, Vol. 1, No. 3, 1985, p. 232-260.
9. Groeneveld, T.P., Fletcher, E.E., and Elsa, A.R.: A Study of Hydrogen Embrittlement of Various Alloys. Battelle Memorial Institute, Report No. DCN 1-7-54-20107 S1 (1F), January, 1969.



LCF AND CRACK GROWTH RATE OF TURBINE BLADE ALLOYS  
IN HYDROGEN AND HYDROGEN/STEAM ENVIRONMENTS

BY B. A. COWLES, D. P. DELUCA, J. R. WARREN AND F. K. HAAKE

PRATT & WHITNEY  
ENGINEERING DIVISION SOUTH  
P.O. BOX 2691  
WEST PALM BEACH, FLORIDA 33402

ABSTRACT

This paper describes the LCF and fatigue crack growth testing of MAR-M246+Hf and PWA 1480 in high pressure hydrogen and hydrogen enriched steam at elevated temperatures. The PWA 1480 single crystal exhibited the best properties overall, compared to both single crystal and directionally solidified MAR-M246+Hf. Addition of water vapor to the hydrogen atmosphere caused more pronounced reduction in the properties of the directionally solidified material than in the single crystal.

## INTRODUCTION

The nickel based superalloy MAR-M246 in directionally solidified form is currently used as a turbopump airfoil material in the Space Shuttle Main Engine (SSME). The extremely severe operating cycle, combined with the pure or partial high-pressure hydrogen environment, has resulted in evaluation of alternative materials and processing to increase airfoil service life.

Several programs (References 1, 2, 3) have been sponsored by the NASA Marshall Space Flight Center under the direction of W. B. McPherson, to evaluate MAR-M246+Hf in both directionally solidified (DS) and single crystal (SC) forms, as well as the single crystal alloy PWA 1480.

Under these programs, tensile, creep-rupture, smooth low cycle fatigue, and crack growth properties were evaluated for the alloys in high pressure hydrogen and hydrogen-enriched steam environments at temperatures up to 870°C (1600°F).

This paper summarizes results of the low cycle fatigue and crack growth tests performed in hydrogen and hydrogen-steam environments.

## MATERIALS

The alloys evaluated were MAR-M246 + Hf in both cast single crystal and directionally solidified form, and cast single crystal PWA 1480. Both alloys are high strength, gamma prime strengthened nickel base superalloys for high temperature use in turbine blades and vanes. Chemical compositions of the alloys are presented in Table 1. MAR-M246 + Hf in the directionally solidified form is the current SSME turbine blade material. PWA 1480 is an advanced alloy developed for use in single crystal form (Ref. 4), which is currently in use in commercial and military gas turbine engines.

All test material was furnished by the NASA Marshall Space Flight Center (MSFC). The DS MAR-M246+Hf material was supplied in the as-cast condition in the form of rectangular castings, 1.25 cm X 3.8 cm X 14.0 cm (0.5 X 1.5 X 5.5 inches) with solidification axis, nominally (001) crystallographically, in the 14 cm direction. The SC MAR-M246+Hf material, also as-cast, was supplied as rectangular blocks, 1.25 cm X 3.8 cm X 10.2 cm (0.5 X 1.5 X 4 inches) with the primary crystal axis in the 10.2 cm direction. The single crystal PWA 1480 material was provided in a fully heat treated condition in both rectangular cast bars of similar thickness to the MAR-M246 and round bars 1.25 cm diameter and 8 cm length (0.5 X 3.125 inches).

The PWA 1480 and the DS and SC MAR-M246+Hf material underwent metallographic examination in order to determine alloy thermal history and document microstructure as received. The MAR-M246+Hf required solution and precipitation heat treatment. The MAR-M246 material which was needed for transverse property test specimens required TLP<sup>®</sup> bonding to obtain material of sufficient length for specimen fabrication. The TLP bond cycle was then followed by the standard MAR-M246 heat treatment cycle.

The PWA 1480 material was supplied in the fully heat-treated condition although the cooling rate appeared to have been slower than optimum. Microstructural examination and tensile test results indicated that the material required re-heat treatment. The PWA 1480 heat treatment was then performed.

Details of the TLP bond cycle and heat treatment are presented in Table 2.

## EXPERIMENTAL PROGRAM

### TEST SPECIMENS

Test specimens were fabricated in both the transverse and longitudinal directions relative to the solidification direction of the castings. The solidification direction corresponds to the columnar grain growth direction in the DS castings, and to the (001) crystallographic direction ( $+10^{\circ}$ ) for the single crystal bars. Crystallographic orientation of the single crystal material was determined by the Laue back reflection technique. Transverse direction single crystal specimen orientations could vary from the (010) to the (110) direction. Since the (010) direction is a primary cubic crystal axis direction, properties of transverse-oriented test specimens with axes along the (010) direction were expected to be very similar to those of longitudinal specimens (oriented along the (001) direction). Consequently, where sufficient test material was available, cast bars with orientations near the (110) direction were preferentially selected for transverse property testing.

Since standard tensile, creep, and LCF test specimens are longer than 3.8 cm (1.5 in.), additional material had to be bonded to each side of the cast MAR-M246+Hf blocks for fabrication of these transverse test specimens. Bonding of additional material to the test blocks was accomplished using the transient-liquid-phase (TLP<sup>®</sup>) diffusion bonding process. (TLP is a registered trademark for the transient liquid phase bonding process patented by Pratt & Whitney Aircraft Group). Bonding of extensions to the test material is illustrated schematically in Figure 1. Crack growth specimens were obtained without the need for TLP bonding as shown in Figure 2. The transverse-oriented PWA 1480 tensile, creep, and LCF specimens were machined from 7.6 cm (1.25 in.) square cast blocks and did not require TLP bonding of additional material.

Smooth tensile, creep-rupture, smooth LCF, and compact tension crack growth specimens were machined from the cast bars for test. Typical specimens are shown in Figure 3.

#### TEST PLAN

An extensive mechanical property test program including smooth tensile, creep, smooth LCF, and crack growth was carried out under three separate NASA contracts (References 1, 2, 3). The LCF and crack growth results from the three contracts are discussed in this paper.

The majority of the tests were conducted at 870°C (1600°F) and 760°C (1400°F). LCF tests were run to define total and inelastic strain vs. life curves for each material, mostly for specimen loading orientations transverse to the casting solidification direction. PWA 1480 was also tested with specimen loading axis parallel to the solidification (001) direction.

Crack growth tests were also run at 870°C and 760°C, but each cycle incorporated a 480 second dwell at maximum load. These specimens were loaded along the solidification direction, producing crack growth normal to the solidification direction. Directionally solidified MAR-M246 was also tested with the loading axis transverse to the solidification direction.

#### TEST GASES

Test environments for all tests described in this paper consisted of hydrogen or hydrogen plus water vapor at 34.5 MPa (5000 psig). Nitrogen was used as a preliminary purge gas. Propellant grade hydrogen was provided under Military Specification P-27201, which requires the gas to have an oxygen content of less than 1 part per million. Periodic analysis verified the gas to be of this purity. The hydrogen and water vapor environment was obtained by utilizing triple distilled water and a retort system so the water was vaporized by furnace heat while maintaining the specified pressure. The hydrogen-water vapor atmosphere was 50% water-vapor and 50% hydrogen by weight.

Gas handling systems supplying the test vessels were equipped to enable sampling before and after specimen tests. The hydrogen was sampled extensively, both dry and saturated with water vapor (wet hydrogen was dried prior to analysis). Samples were analyzed with a gas chromatograph with accuracy in the parts per billion range.

Analysis verified that the gas was of the required purity (1 ppm O<sub>2</sub>). Hydrogen environment pressure was maintained at 34.5 MPa (5000 psig) during testing.

## TEST PROCEDURES

High-pressure environmental tests were conducted on closed-loop type, hydraulically actuated test machines. Each test machine is located in an isolated test cell with all controls and instrumentation located in an adjacent blockhouse. P&WA designed pressure vessels, mounted on the upper platen of the test machine, incorporate Grayloc type high-pressure flanges for sealing and ease of assembly. The test machine compensates through the servosystem for the load in the specimen due to pressure acting over differential specimen/adaptor areas. A pressure transducer is used to provide a feedback signal, proportional to chamber pressure, to the servocontroller. This signal was used in controlling a mean load applied to the linkage so zero strain was maintained in the specimen gage when the vessel assembly was pressurized. This same load was then superimposed on the cyclic load during testing.

Both internal (to the pressure vessel) and external load cells were used to obtain cyclic load to account for friction at the load rod seals. Electrical connections to the load cell, extensometer system, furnace (for elevated temperature tests), and thermocouples were made through the vessel wall via high-pressure bulkhead connectors. Setups of the pressure vessel showing the extensometer system and furnace arrangement are shown in Figure 4.

Smooth, round, solid specimens were used for the axial strain-controlled LCF tests. The specimen configuration incorporates integral machined extensometer collars. A calibration procedure has been established to relate the maximum strain to collar deflection during both the elastic and plastic portion of the strain cycle. The specimen design and calibration procedure were verified both experimentally and analytically.

Specimen axial strain was measured and controlled by means of a proximity probe extensometer. Split extensometer heads were attached to the specimen by mating the grooves in the heads with the integral collars on the specimen and bolting the assembly together. Collar deflection was measured and controlled via proximity probes attached to the open ends of the extensometer tubes so that the extensometer rod ends moved relative to the probes as the specimen collars deflected. The LCF strain cycle was fully reversed, and performed at a frequency of 0.067 Hz.

The specimen used for crack growth testing was the standard compact specimen (with  $w = 1.0$  inch). This specimen incorporated a chevron-type crack-starter notch and integrally machined knife edges for Crack Opening Displacement (COD) extensometry attachment as recommended by ASTM E399-74, "Plane-Strain Fracture Toughness of metallic materials". Specimen thickness was chosen to conform to supplied raw material dimensions, and to the high pressure test vessel retort size.

To accommodate testing in the high pressure vessels, a compliance calibration was conducted to relate the COD measured by the test extensometry to the test specimen crack length. The compliance between the measured COD and the handbook prediction (Reference 5) was compared at various crack length, load, and temperature conditions. The measured COD agreed with the handbook predictions, and the handbook relationship was used for all environmental testing. Stress intensity was then estimated using the standard ASTM solution for the specimen, calculated for an isotropic material.

Crack growth tests were conducted in the load controlled mode. The test consisted of cyclic loading of the specimen between the minimum load and the maximum load until complete fracture occurred. The loading cycle was all tensile with a 480-second hold time at the maximum load. All specimens were tested at a stress ratio (minimum load/maximum load) of 0.1. The test loading cycle is shown in Figure 5.

Crack growth data for this program was analyzed using the hyperbolic sine based "SINH" model, an interpolative model developed for the analysis of elevated temperature fatigue crack propagation data (References 6, 7). The model has been successfully used to describe the parametric effects of three fundamental influences on crack propagation: frequency ( $\nu$ ), stress ratio (R), and temperature (T).

This interpolative model is based on the hyperbolic sine equation,

$$\log (da/dn) = C_1 \sinh (C_2 (\log (\Delta K) + C_3)) + C_4$$

where the coefficients are simple empirical functions of test frequency, stress ratio, and temperature. This model presents a flexible alternative to the familiar Paris equation and has gained acceptance in the aerospace industry. In several cases for this data a Paris fit would have worked as well, but in most cases SINH was used because it is the standard model for P&WA Engineering.

## RESULTS

### LOW CYCLE FATIGUE

All of the MAR-M246+Hf LCF specimens were oriented in the transverse direction as required by the NASA contracts. For the directionally solidified material, this produced fractures parallel to the columnar grain growth direction. For the single crystal material, the loading axis corresponded to a near (110) crystallographic direction. The PWA 1480 single crystal alloy was tested in both the longitudinal (001) and the transverse (110) orientations.

Results of the transverse oriented MAR-M246 LCF at 870°C are shown in Figure 6. The single crystal form showed substantially higher life than the DS material, with the difference much more pronounced at strain ranges below 1.0%. Addition of steam to the environment produced no difference in the single crystal alloy, but appeared to reduce the life of the directionally solidified material by more than half.

The PWA 1480 LCF results at 870°C are shown in Figure 7. The significant effect of crystallographic orientation is clearly evident, as expected from the significant elastic modulus difference between (001) and (110) orientations (References 8, 9). As with the SC MAR-M246, the addition of steam to the hydrogen environment caused no apparent reduction in LCF life.

Data for both of the alloys at 870°C is presented in Figure 8 for comparison. At the low life/high strain ranges representative of severe rocket engine service conditions, the PWA 1480 longitudinal data is clearly superior. However, at high strain ranges the transverse oriented materials all appeared similar, including the DS MAR-M246. At low strain ranges, the SC MAR-M246 appeared best in the transverse orientation.

A similar summary of data for all three materials tested at 760°C is presented in Figure 9. Here the DS MAR-M246 had clearly lower LCF capability than the single crystal materials, and, as expected, the transverse oriented single crystals exhibited lower LCF life than the longitudinal orientation. As at 870°C, the PWA 1480 longitudinal data showed the highest LCF life at high strain ranges.

#### FATIGUE CRACK GROWTH

The compact specimens were oriented to produce crack growth normal to the solidification direction as required by the NASA contracts. This corresponded to an (001) loading axis for the specimens. The exception was for the DS MAR-M246, which was tested in both transverse and longitudinal orientations. The test loads were selected to produce very short lives, typically hundreds of cycles, compared to normal elastic crack growth rate tests. The data are presented for comparison in terms of stress intensity vs. crack growth rate. Isotropic Mode I stress and strain intensity solutions for directionally solidified and orthotropic single crystal materials have been used in other studies (References 8, 9, 10) and appear acceptable for cases where crack growth is both planar and normal to the loading axis - that is, Mode I growth in a non-crystallographic manner. Recent work by Chen (Reference 11) indicates that crystallographic fracture, along (111) crystal planes, is controlled entirely by the shear stress intensity factor,  $K_{II}$ . Some of these tests resulted in crystallographic fracture during the low

temperature, high frequency precracking, and the specimens had to be discarded. However, fracture paths during actual testing were generally in plane and non-crystallographic, so the data are presented as  $\Delta K_I$  vs. growth rate.

It should be noted, however, that use of this data for purposes other than direct comparison with similar tests is not recommended because of the high net section stresses, the extended tensile dwell period each cycle, and the anisotropy of the materials.

Crack growth rate for the SC MAR-M246 is shown in Figure 10. There was no significant difference between 870°C and 760°C in the pure hydrogen environment. As for the LCF tests, addition of steam to the hydrogen produced no apparent effect on crack growth rate at 870°C. Although the regression curve for the hydrogen/steam tests shows apparently slower growth rate at low stress intensity, the pure hydrogen environment data scatter encompasses the hydrogen/steam data and no clear cut effect due to the steam addition is apparent.

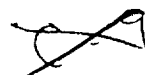
The PWA 1480 SC tests produced similar results, with no differences noted due to changing temperature from 870°C to 760°C, or with addition of steam to the hydrogen atmosphere. Results are shown in Figure 11.

In contrast, however, are the results for DS MAR-M246 loaded transverse to the solidification direction. As shown in Figure 12, the addition of steam to the hydrogen produced a significantly faster crack growth rate at the 870°C test temperature. This result is again consistent with the LCF data. Results for DS MAR-M246 loaded longitudinal to the solidification direction were highly scattered and are not presented.

The 870°C data in pure hydrogen are combined for comparison in Figure 13. Surprisingly, there appears to be little or no difference between the transversely loaded DS MAR-M246, and the single crystal form of the alloy. The PWA 1480 SC material does, however, look significantly better in crack growth rate than either form of MAR-M246. A similar comparison at 870°C with steam added to the hydrogen is presented in Figure 14. Here, however, the DS MAR-M246 loaded transversely to the solidification direction, exhibited much faster crack growth than either single crystal alloy. The PWA 1480 SC looked slightly better than the SC MAR-M246, based on limited data.

#### CONCLUSIONS AND SUMMARY

The LCF and crack growth behavior of MAR-M246+Hf in single crystal and directionally solidified form, and the single crystal alloy PWA 1480, were evaluated in high pressure hydrogen and hydrogen enriched steam environments at elevated temperatures.





The single crystal alloys were superior to the directionally solidified material in both LCF and crack growth. The differences were pronounced, and for worst case conditions order of magnitude or greater life differences were observed.

Addition of steam to the hydrogen environment had little or no effect on the single crystal materials, but showed potentially large detrimental effects on both LCF and crack growth rate of the directionally solidified material. LCF life was reduced by 50% or more; and an order of magnitude increase in crack growth rate was observed with the addition of steam for transversely loaded DS MAR-M246 (favorable orientation for intergranular crack propagation).

PWA 1480 exhibited the best properties overall, in both LCF and crack growth. The differences in LCF were most pronounced at the high strain range/low life condition of interest to severe rocket engine applications.

#### REFERENCES

1. "Mechanical Properties of Several Nickel Alloys in Hydrogen at Elevated Temperatures," NASA-MSFC contract NAS8-30744, Exhibit D. Contractor final report, Pratt & Whitney Aircraft Group report FR-8971, September 1977.
2. "Low Cycle Fatigue Properties of MAR-M246 Hf in Hydrogen", NASA-MSFC contract NAS8-33109. Contract final report, Pratt & Whitney Aircraft Group report FR-11852, June 1979.
3. "Mechanical Properties of Turbine Blade Alloys in Hydrogen at Elevated Temperatures," NASA-MSFC contract NAS8-33561. Contract final report, Pratt & Whitney Aircraft-Government Products Division report FR-14844, July 1981.
4. Gell, M., D. N. Duhl and A. F. Giamei, "The Development of Single Crystal Superalloy Turbine Blades," Superalloys 1980, Proceedings of the Fourth International Symposium on Superalloys, American Society for Metals, Metals Park, Ohio, pp. 205-214, 1980.
5. Tada, H., P. C. Paris, and G. R. Irwin, "The Stress Analysis of Crack Handbook," Del Research Corporation, Hellertown, Pennsylvania, 1973.
6. Annis, C. G., R. M. Wallace, and D. L. Sims, "An Interpolative Model for Elevated Temperature Fatigue Crack Propagation," AFWAL contract F33615-75-C-5097 Contractor Final Report No. AFML-TR-76-176, November 1976.

REFERENCES cont.

7. Schwartz, B. J., and D. T. Hunter, "A Completely Integrated System for the Treatment of Crack Growth Test Data," *Experimental Techniques*, Vol. 10, No. 3, March, 1986.
8. Deluca, D. P., and B. A. Cowles, "Fatigue and Fracture of Advanced Blade Materials," Air Force Wright Aeronautical Laboratories Contractor Final Report, Contract F33615-82-C-5109, AFWAL-TR-84-4167, (P&W/ED/FR-18518), February, 1985.
9. Wright, P. K., H. Jang, and H. G. Popp, "Fatigue and Fracture of Advanced Blade Materials," Air Force Wright Aeronautical Laboratories, Contractor Final Report contract F33615-82-C-5031, AFWAL-TR-84-4166, February, 1985.
10. Gemma, A. E., B. S. Langer, and G. R. Leverant, "Thermomechanical Fatigue Crack Propagation in an Anisotropic (Directionally Solidified) Nickel Base Superalloy", Thermal Fatigue of Materials and Components, ASTM STP 612, American Society for Testing and Materials, 1976, pp. 199-213.
11. Chen, O. Y., "Crystallographic Fatigue Crack Propagation in Single Crystal Nickel-Base Superalloy", Ph.D. Dissertation, University of Connecticut, 1985.

*Table 1 Chemical Composition of Turbine Blade Alloys Used for Mechanical Properties Investigation*

<i>Material</i>	<i>Form</i>	<i>Heat No.</i>	<i>C</i>	<i>Si</i>	<i>Mn</i>	<i>P</i>	<i>S</i>	<i>Cr</i>	<i>Ni</i>	<i>Mo</i>	<i>Al</i>	<i>Ti</i>
MAR-M-246 (Hf Modified)	Directionally Solidified and Single Crystal	DE-008	0.14	0.06	<0.10		6 ppm	8.85	Bal	2.70	5.50	1.55
PWA 1480	Single Crystal	P.O. 298577 298578 298579	40 ppm	0.03	0.01	0.005	0.004	10.18	Bal		5.12	1.38

<i>Material</i>	<i>Form</i>	<i>Heat No.</i>	<i>Cu</i>	<i>Fe</i>	<i>Mg</i>	<i>Ta</i>	<i>Co</i>	<i>W</i>	<i>Zr</i>	<i>B</i>	<i>Hf</i>
MAR-M-246 (Hf Modified)	Directionally Solidified and Single Crystal	DE-008	<0.10	0.19	6 ppm	1.51	10.20	10.10	0.04	0.014	1.85
PWA 1480	Single Crystal	P.O. 298577 298578 298579	0.01	0.05		12.07	4.78	3.94	70 ppm	10 ppm	50 ppm

*Table 2 Turbine Blade Alloys Evaluated for Mechanical Properties in High Pressure Hydrogen Environments*

<i>Material</i>	<i>Form</i>	<i>Vendor</i>	<i>Heat No.</i>	<i>As-Tested Condition (Heat Treatment)</i>
MAR-M-246 (Hf Modified)	Directionally Solidified	Howmet	DE-008	TLP Bond Cycle*: 1196°C/22 hr in vacuum/Heat to 1221°C  Solution HT: 1221°C/2 hr in vacuum/Cool to room temp  Precipitation HT: 871°C/24 hr in vacuum/Cool to room temp
MAR-M-246 (Hf Modified)	Single Crystal	Howmet	DE-008	TLP Bond Cycle*: 1196°C/22 hr in heat to 1221°C  Solution HT: 1221°C/2 hr in vacuum/Cool to room temp  Precipitation HT: 871°C/24 hr in vacuum/Cool to room temp
PW 1480	Single Crystal	Howmet	P.O.'s 298577, 298578, 298759	Solution HT: 1288°C/4 hr in protective atmos/Cool at 139°C/min to 871°C/AC  Coating HT: 1079°C/4 hr in protective atmos/Cool at 33°C/min to 871°C/AC  Precipitation HT: 871°C/32 hr in air/AC

\*Only transverse oriented LCF, Creep, and Tensile specimen material received this TLP Bond cycle to obtain sufficient length of raw material in transverse direction to fabricate specimens.

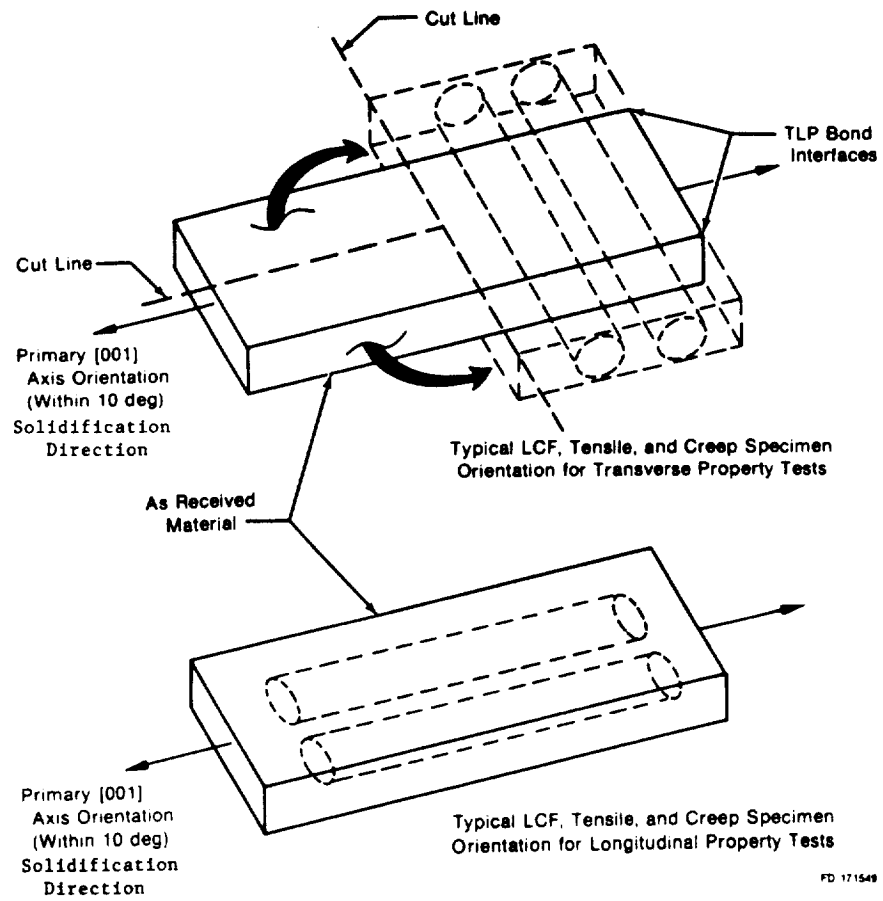


FIGURE 1 - TYPICAL SPECIMEN TEST BLANK FABRICATION AND BONDING SCHEMATIC

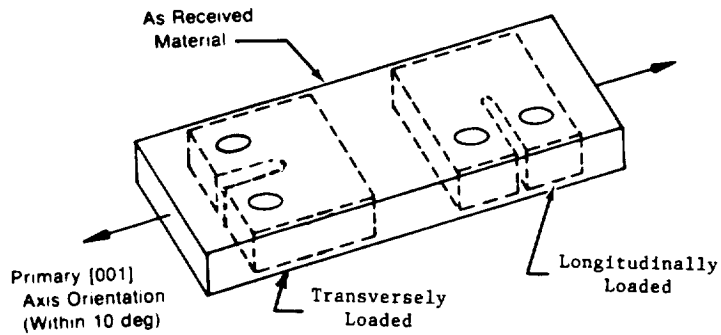


FIGURE 2 - TYPICAL CRACK GROWTH SPECIMEN BLANK ORIENTATIONS

ORIGINAL PAGE IS  
OF POOR QUALITY

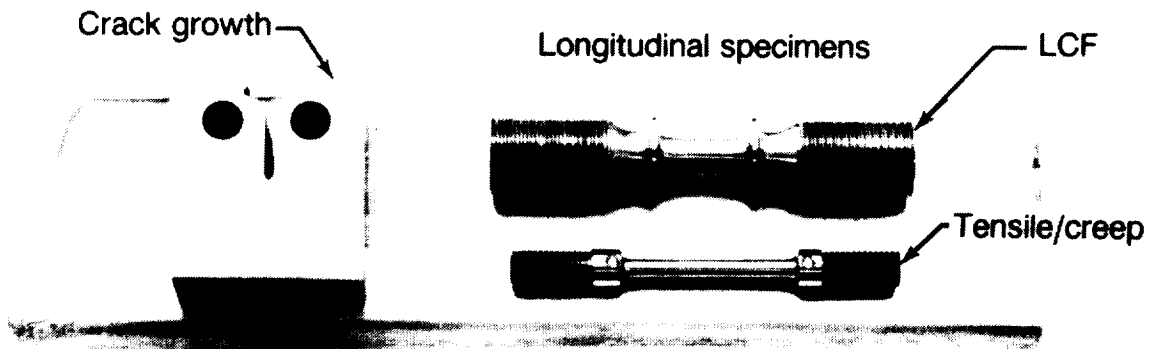
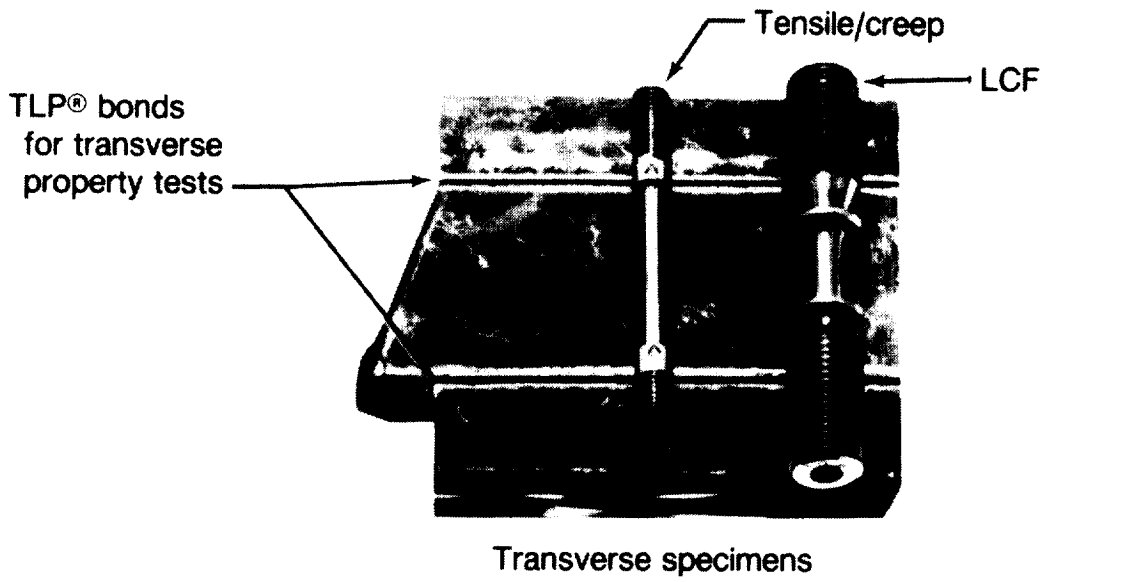
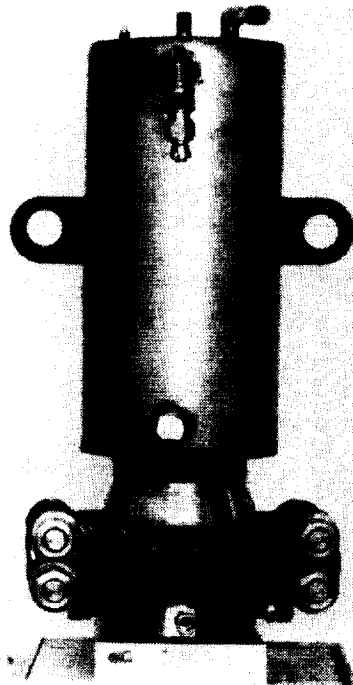


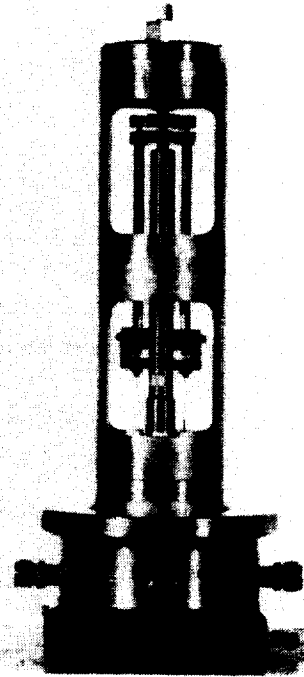
FIGURE 3 - TEST SPECIMENS AND TYPICAL ORIENTATION IN CAST BARS

ORIGINAL PAGE IS  
OF POOR QUALITY



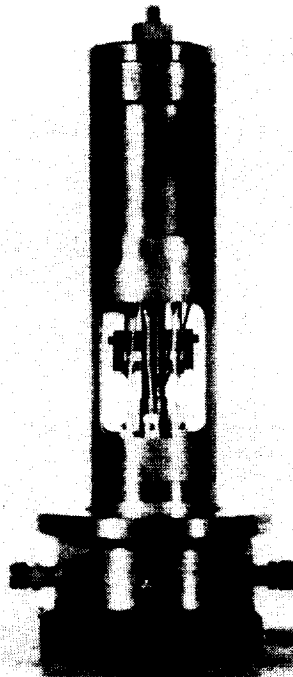
FAE 146129

a) Test Vessel Closed



FAE 146121

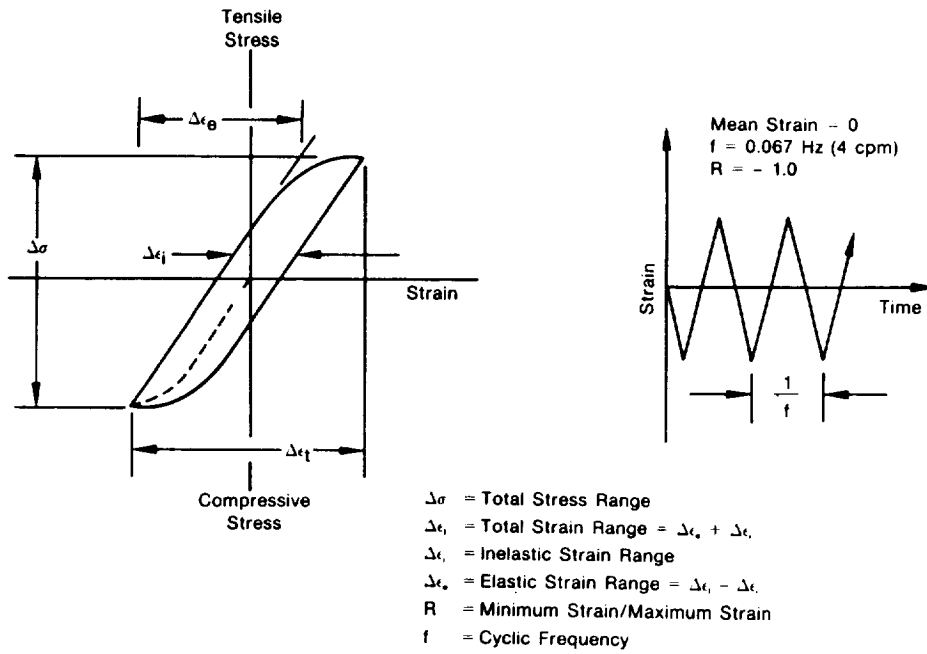
b) Test Vessel Open Showing  
Extensometer System



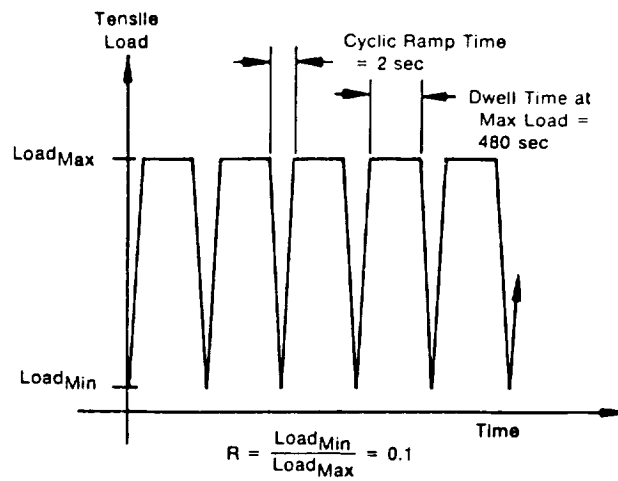
FAE 146122

c) Test Vessel Open Showing Furnace  
In Place

FIGURE 4 - LOW CYCLE FATIGUE HIGH PRESSURE ENVIRONMENTAL  
TEST VESSEL (CRACK GROWTH VESSEL SIMILAR)



Typical LCF Cycle



Typical Crack Growth Cycle

FIGURE 5 - TYPICAL STRAIN CONTROLLED LCF CYCLE (TOP) AND LOAD CONTROLLED CRACK GROWTH CYCLE (BOTTOM)

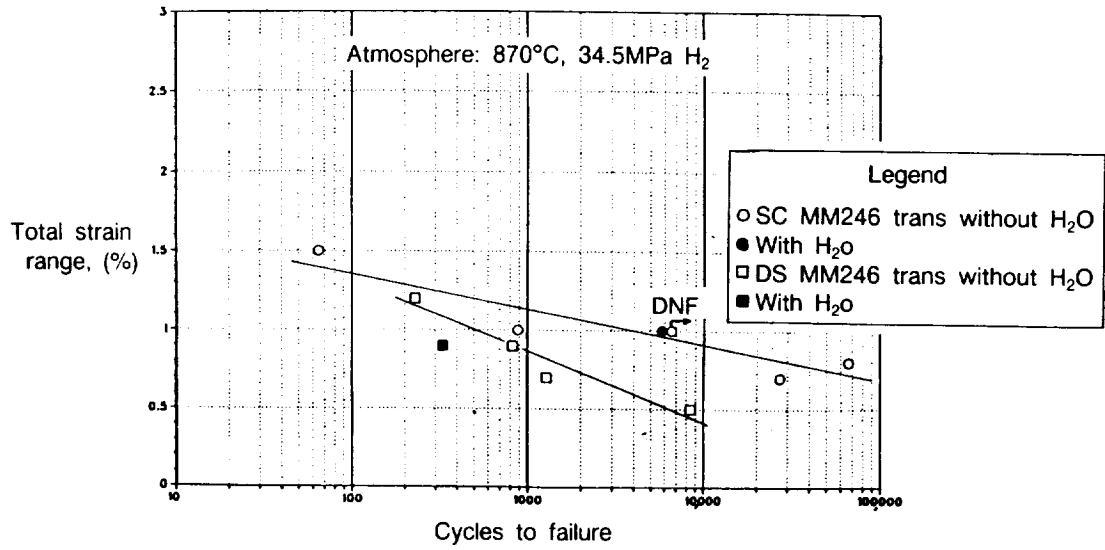


FIGURE 6 - TRANSVERSE MAR-M246 LCF IN HYDROGEN AND HYDROGEN/STEAM

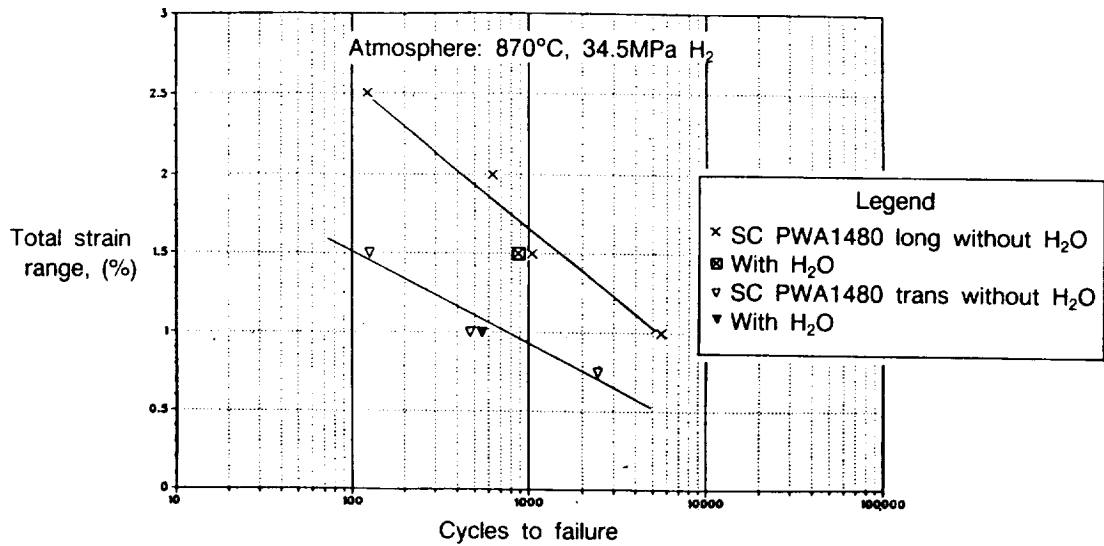


FIGURE 7 - PWA 1480 LCF IN HYDROGEN AND HYDROGEN/STEAM



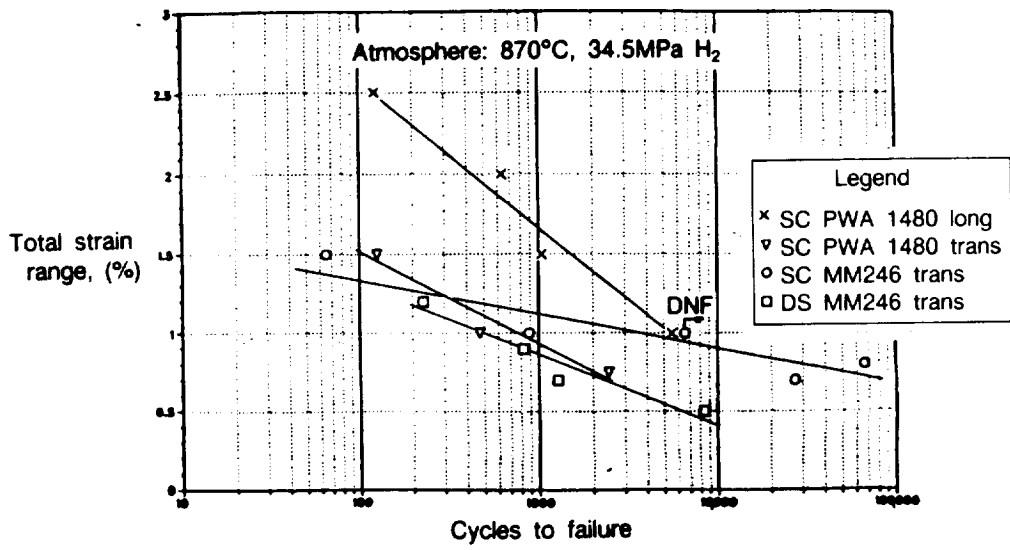
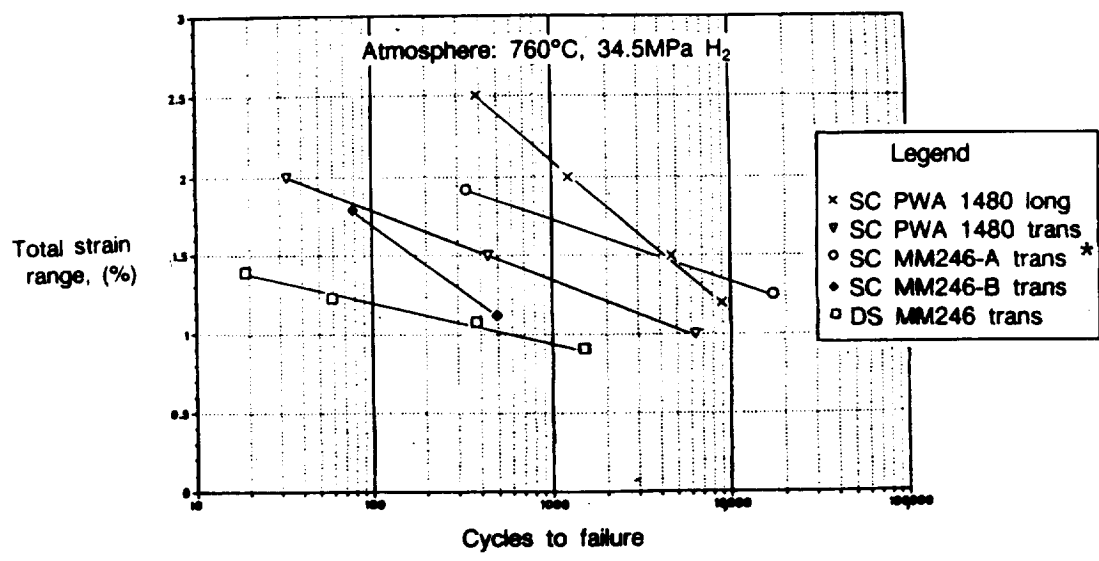


FIGURE 8 - PWA 1480 AND MAR-M246 LCF IN HYDROGEN AT 870°C



\*NOTE SC MM 246-A ORIENTATION NEAR (010)-SHOULD BE TREATED LIKE LONGITUDINAL (001)

FIGURE 9 - PWA 1480 AND MAR-M246 LCF IN HYDROGEN AT 760°C

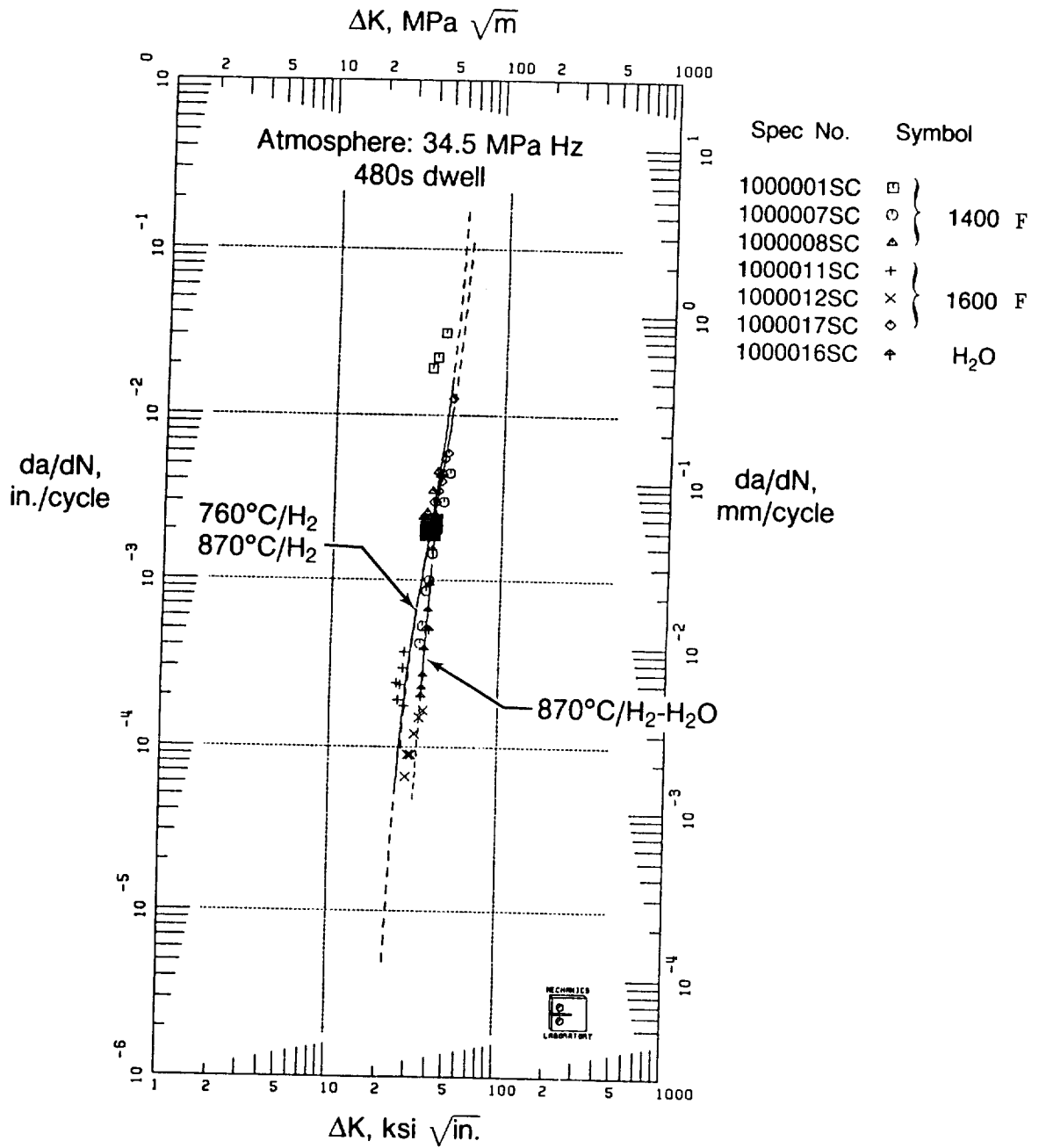


FIGURE 10 - SINGLE CRYSTAL MAR-M246 CRACK GROWTH IN HYDROGEN AND HYDROGEN/STEAM

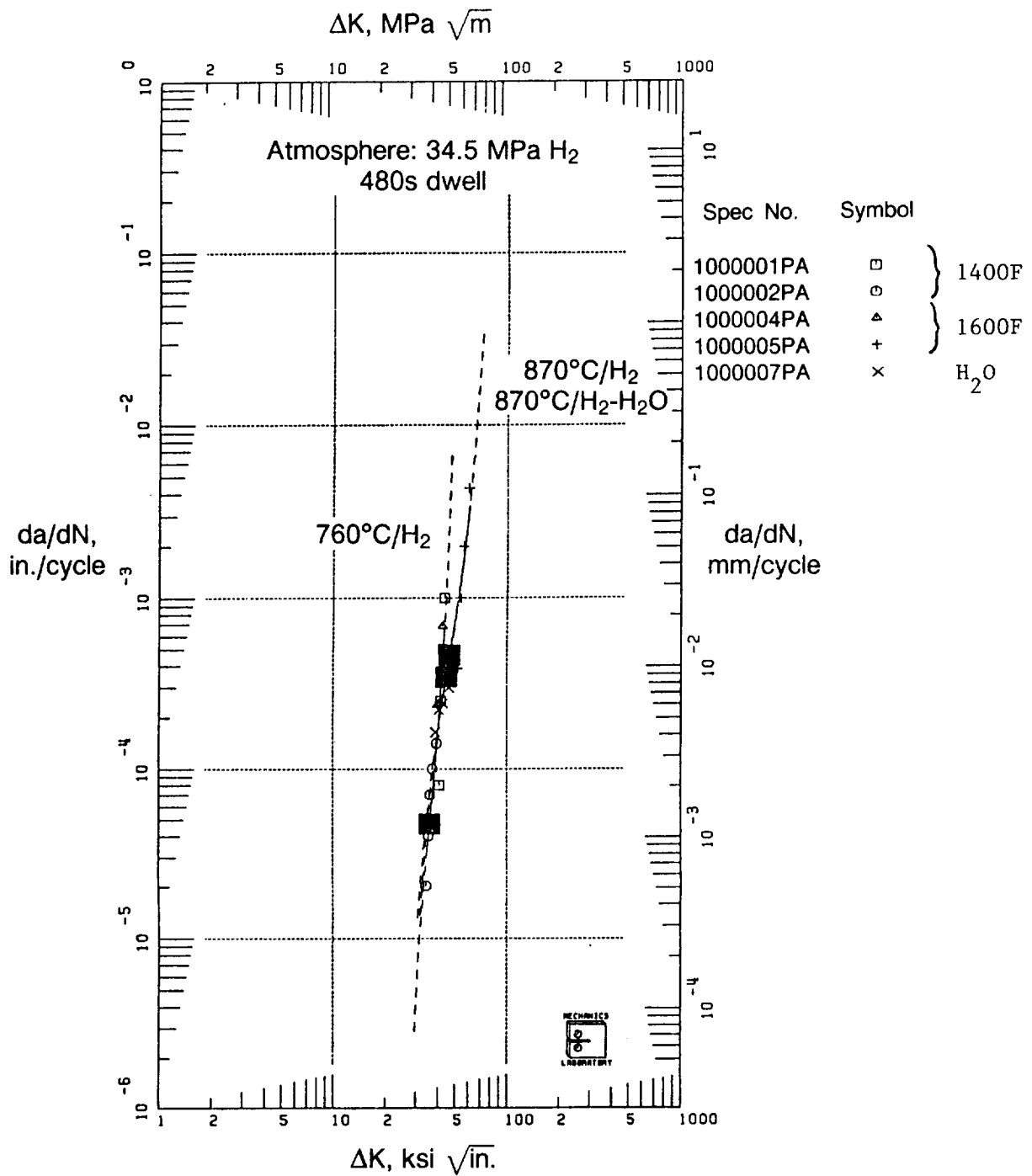


FIGURE 11 - PWA 1480 CRACK GROWTH IN HYDROGEN AND HYDROGEN/STEAM

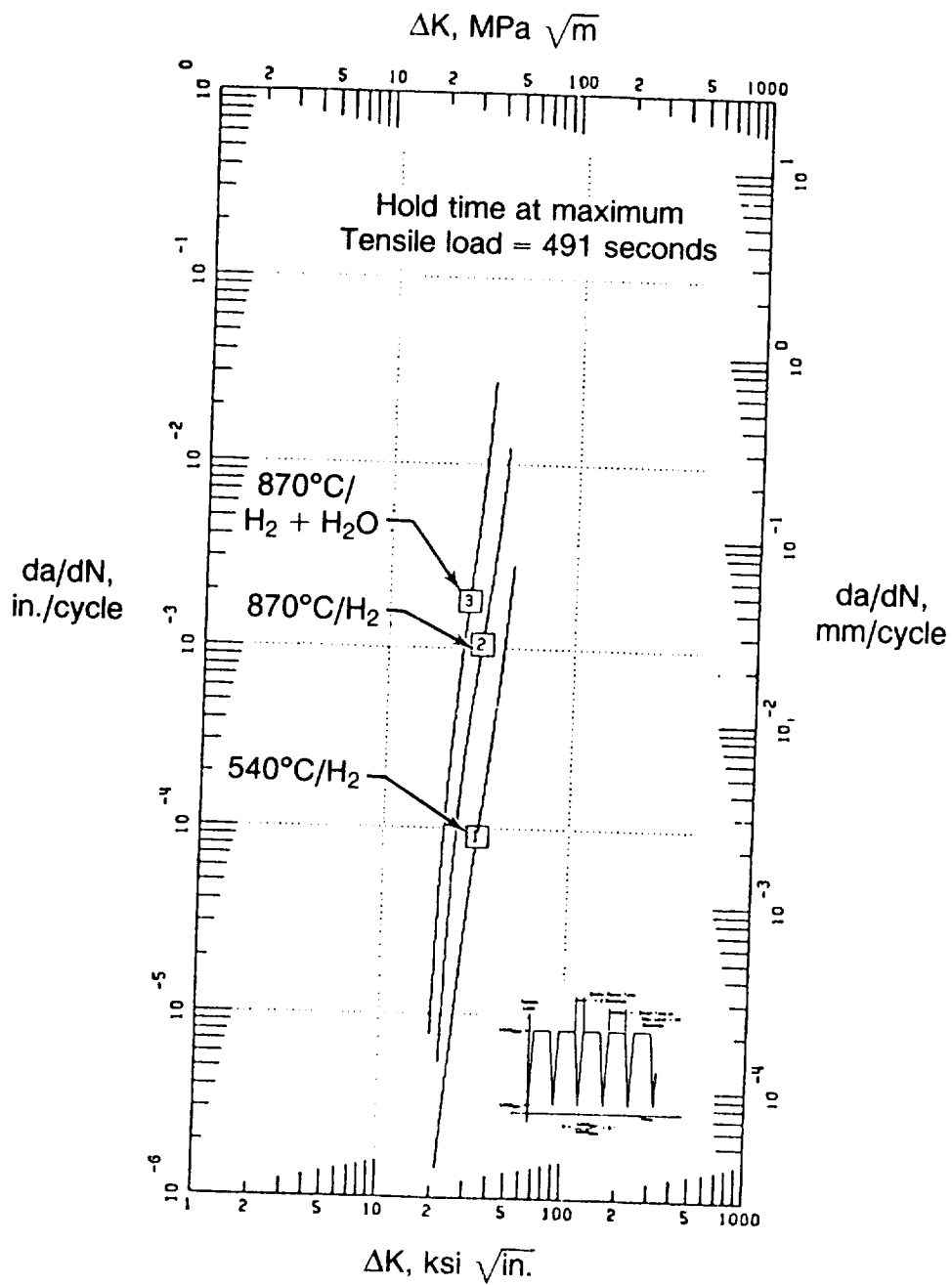


FIGURE 12 - TRANSVERSELY LOADED DS MAR-M246 CRACK GROWTH IN HYDROGEN AND HYDROGEN/STEAM

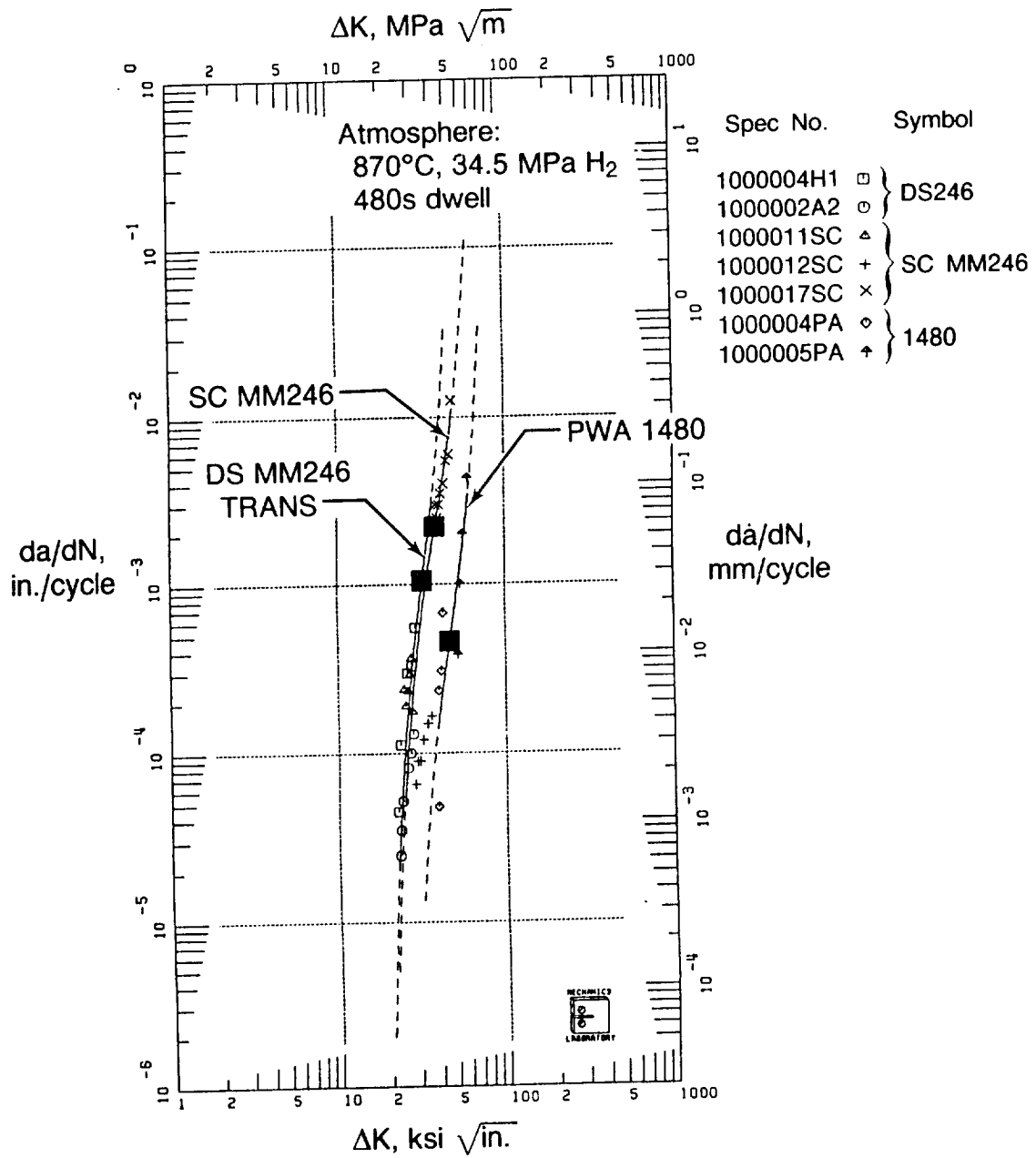


FIGURE 13 - PWA 1480 AND MAR-M246 CRACK GROWTH IN HYDROGEN AT 870°C

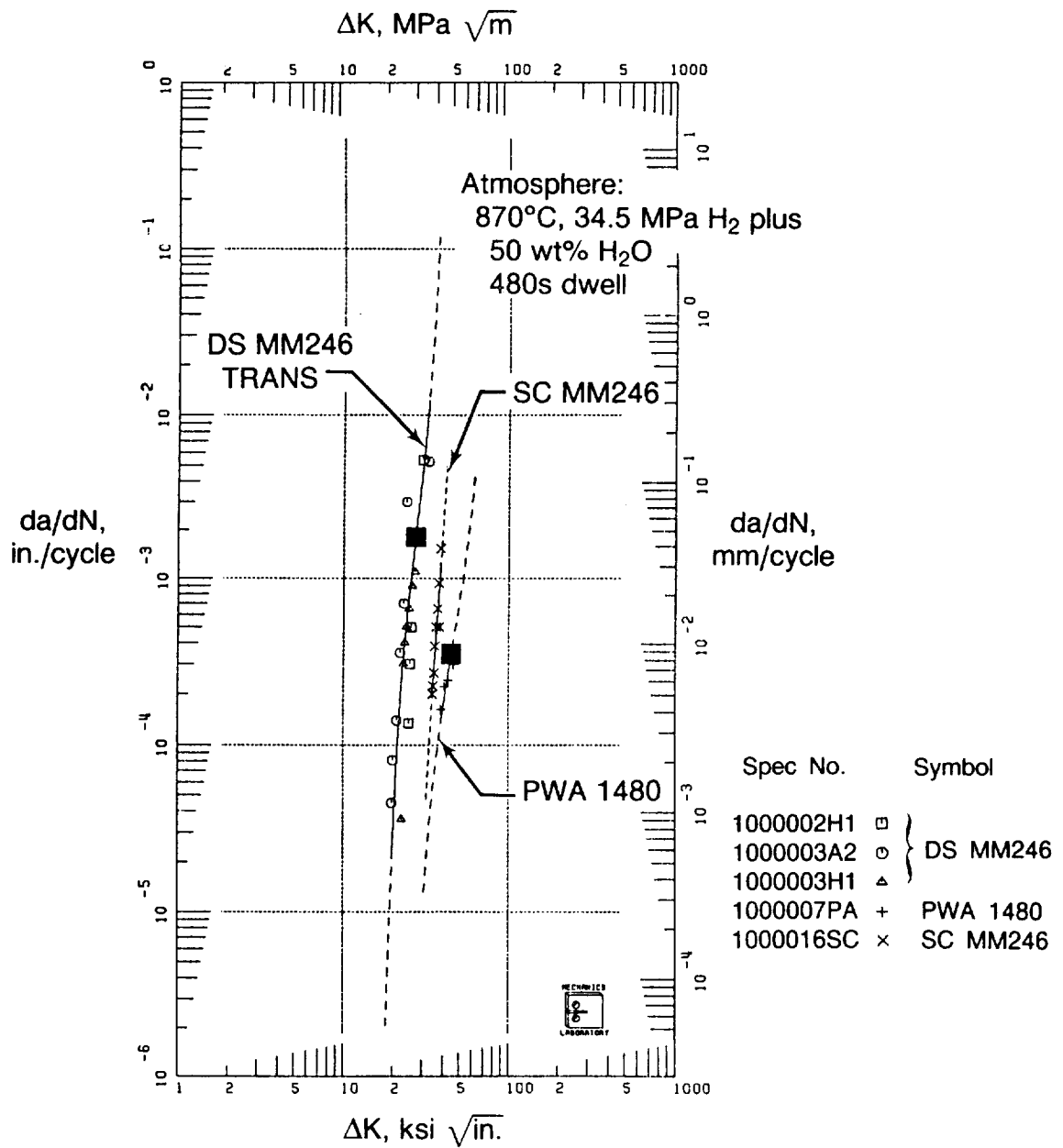


FIGURE 14 - PWA 1480 AND MAR-M246 CRACK GROWTH IN HYDROGEN/STEAM AT 870°C

PROGRESS REPORT ON THE DEVELOPMENT  
OF A HYDROGEN RESISTANT ALLOY

W. B. McPherson  
National Aeronautics and Space Administration  
Marshall Space Flight Center, Alabama 35812

Abstract

In the continuous search for hydrogen tolerant alloys, this paper describes the latest evaluation of various compositions of the Fe-Ni-Co-Cr system with elemental additions of Cb, Ti and Al. After processing, notched tensile specimens were tested in 34.5 MPa (5000 psi) hydrogen at room temperature as the main screening test. The H<sub>2</sub>/Air ratio was used as the selection/rejection criteria. Several Compositions approach the objective strength, 1241MPa (180 ksi) ultimate and 1103MPa (160 ksi) yield, with little or no degradation in hydrogen.

Introduction

Nickel base alloys are used extensively in rocket engines because of their high strength and corrosion/oxidation resistance. Most of these alloys perform well at cryogenic and elevated temperature. However, most nickel alloys are severely degraded by gaseous hydrogen (H<sub>2</sub>). The austenitic stainless steels are generally acceptable for H<sub>2</sub> service with the stable 316 showing no degradation at room temperature, but, the low yield strength of these alloys, 241 MPa (35 ksi), limits their usefulness in a weight restricted engine. Nitronic 40 (21-6-9) has a slightly higher yield, 414 MPa (60 ksi). A-286, the highest strength alloy of the austenitic steel group, 621MPa (90 ksi) yield, has limited weldability in thick sections. An iron-nickel (Fe-Ni) alloy, Incoloy 903, with strength almost equal to Inconel 718, is not subject to any strength or ductility degradation in H<sub>2</sub> and is being used in some Space Shuttle Main Engine (SSME) parts exposed to H<sub>2</sub>.

In a staged-combustion engine, such as the SSME, there is a second potentially pernicious environment, hydrogen rich steam (H<sub>2</sub>/H<sub>2</sub>O). In low-cycle fatigue (LCF) tests in which H<sub>2</sub> and helium (He) tests had the same

value, Figure 1, LCF tests of 903 in H<sub>2</sub>/H<sub>2</sub>O at 760°C (1400°F) had a life 20 times shorter than in pure H<sub>2</sub>.<sup>1</sup>

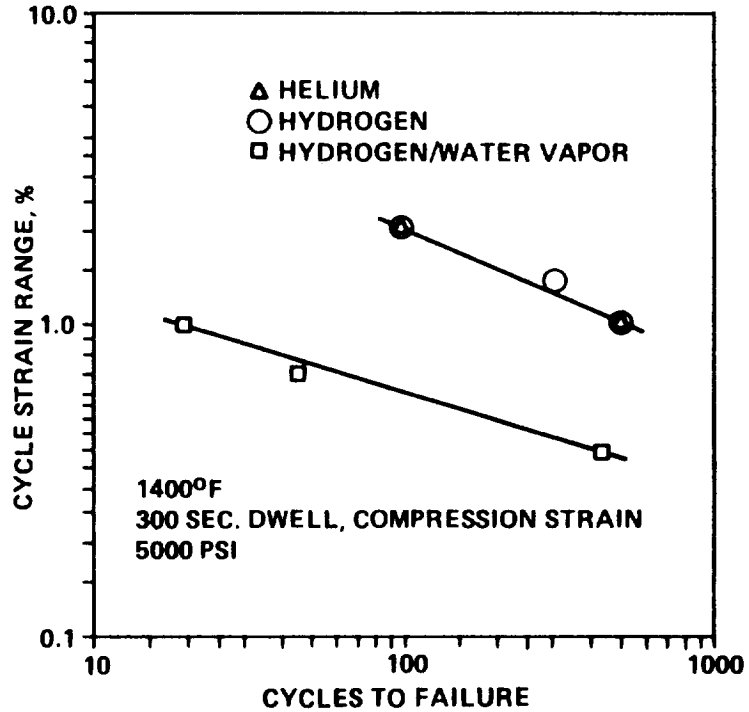
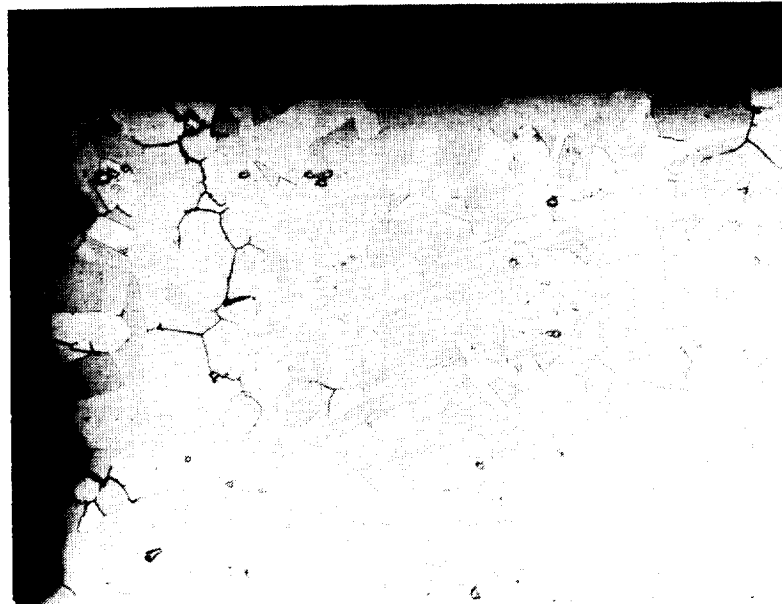


Figure 1 Low-Cycle Fatigue Results Of Incoloy 903 In Various Environments At 760°C (1400°F)

Metallographic examination of one of the LCF specimens, Figure 2, indicated an oxidized surface with intergranular cracks<sup>2</sup> and the overall appearance of stress-corrosion cracking. A similar deterioration was reported by Smith et al<sup>3,4</sup> and Bricknell and Woodford<sup>5</sup>, who referred to the phenomenon



ORIGINAL PAGE IS  
OF POOR QUALITY



Glyceric acid etch

100X

Figure 2 Incoloy 903 Low-Cycle Fatigue Specimen  
Tested In  $H_2/H_2O$  At  $760^\circ C$  ( $1400^\circ F$ )

as "stress accelerated grain boundary oxidation." Earlier, Nelson<sup>6</sup> had reported that 903 was not susceptible to stress corrosion cracking but, after six months in the salt spray and alternate immersion, pitting was evident.

It seemed that an  $H_2$  resistant alloy was needed that had high strength, 1103 MPa (160 ksi) yield and 1241 MPa (180 ksi) ultimate, corrosion/oxidation resistance and was weldable.

#### Approach

Upon reviewing all the alloys that had been evaluated in  $H_2$ , the Fe-Ni alloys, of which 903 is an example, seemed the best to pursue. It also seemed prudent to maintain the Ni plus cobalt (Co) to Fe ratio at 1.26, the same as 903, with Co at 15%. Chromium (Cr) was selected for corrosion oxidation resistance. Basically, the alloy would be an Fe-Ni alloy with Co and Cr and hardeners such as columbium (Cb), titanium (Ti) and aluminum (Al).

## Experimental Procedure

### Alloy Processing

Three and six-tenths kilogram (8 lbs.) charges were made of electrolytic Fe, Co and Cr, Ni pellets, scrap Cb (99.9%), Ti sponge (compacted), Al shot (99.9%) and, when required, graphite. The charge was melted in a calcia-stablized zirconia crucible in a vacuum-induction furnace. The melt was cast in a magnesia "throw-away" crucible, cooled and grit blasted. The ingots, 63.5 mm diameter by 152.4 mm long (2.5 dia. by 6 inches), were homogenized 20-24 hours at 1093°C (2000°F) and hot rolled at 1093-982°C (2000-1800°F) with two to four intermediate hot soaks. After the ingots were squared, they were cross-rolled to 76.2 mm (3 in.) wide then final hot rolled to 15.9 mm (5/8 in.) thick and air cooled. The plates were solution treated at 954°C (1750°F) for 1 hour and water quenched. They were then aged at 718°C (1325°F) for 8 hours, water quenched then on the second day aged at 621°C (1150°F) for 10 hours and air cooled. All tensile specimens were cut in the transverse direction.

### Testing and Evaluation

Smooth tensile specimens were tested in air to establish the alloy's strength. Notch tensile specimens with a stress concentration of 8 ( $K_t=8$ ) were tested in air at ambient pressure and 34.5 MPa (5000 psi)  $H_2$ . The notched test results were then used as the  $H_2$ /air ratio to give the relative resistance to  $H_2$ .

## Results and Discussion

Above 10% Cr, the  $H_2$ /air notch ratio dropped below 0.90. So the Cr was set at 10% with the Co maintained at 15%. Since the yield strength of the alloys was 344.7 MPa (50 ksi) below the objective strength, the next experiments concentrated on improving strength.

With Ti from 1 to 3% and Al 0.1 to 1.0%, several alloys had high strength and most had good properties in  $H_2$ , particularly, 0.5% Al and 2-3% Ti. The complete results are illustrated in the Figure 3 matrix.

The microstructures of two of the alloys are illustrated in Figures 4 and 5. Both structures are duplex, fine grains with scattered larger elongated grains in Alloy A and fine grains with very large, partially elongated grains in Alloy B. Alloy B contains an intergranular phase where as Alloy A contains the intergranular phase and an intragranular phase with Widmanstätten form and platelets with almost a pearlitic appearance. Unexplainably, Alloy A contained 2% more Ti than planned and is probably the main difference between the two alloys. The strength, ductility and  $H_2$  resistance of Alloy A

was lower than B.

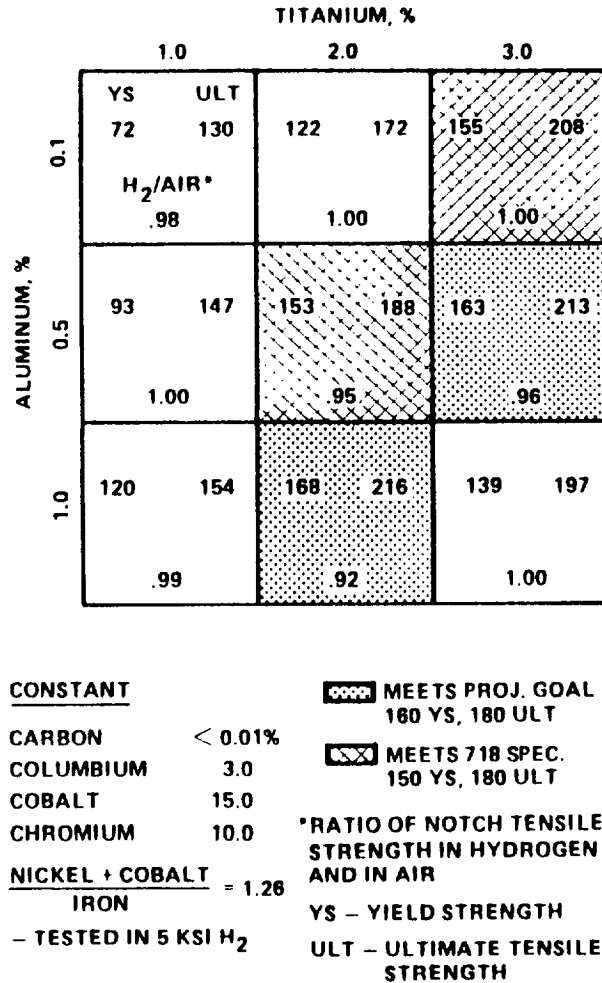
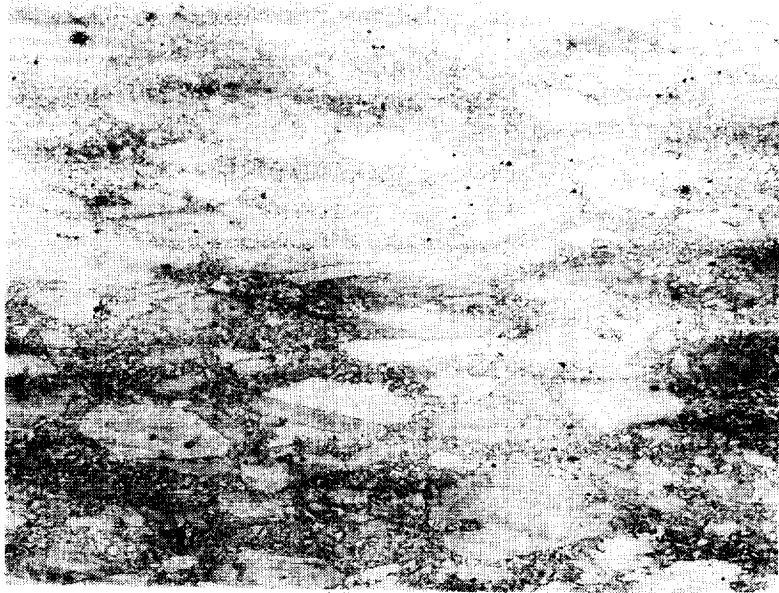


Figure 3 Experimental Matrix With Various Aluminum And Titanium Contents

The Fe-Ni alloys with Co, Cb, Ti and Al usually contain an austenitic matrix,  $\delta'$  and sometimes two platelet phases:  $Ni_3Cb$  ( $\delta$ ) and  $Ni_3Ti$  ( $\eta$ ) with some scattered MC carbides.<sup>7</sup> The  $\delta$  and  $\eta$  phases are probably the dominate phases in these alloys. In the Fe-Ni alloys, Ti promotes and Al tends to inhibit the formation of the  $\eta$  phases.<sup>8</sup> So the composition should probably be 2 to 3% Ti and 0.5 to 1% Al.

No carbon had been added to the alloys but was averaging slightly less than 0.01%. Carbon was added to three basic compositions and the analyses was 0.01, 0.016 and 0.035%. There was little difference in these alloys. The ultimate strength was 1310 MPa (190 ksi) but the yields were 172 MPa



100X

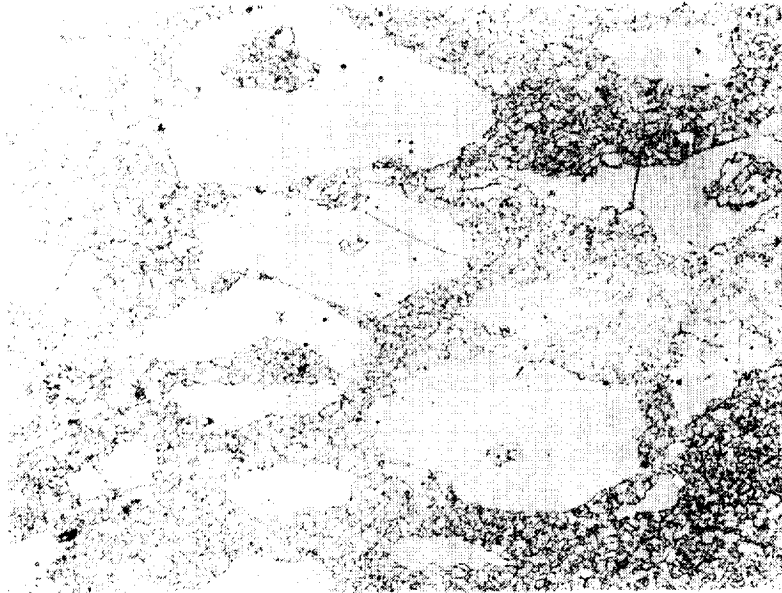


1000X

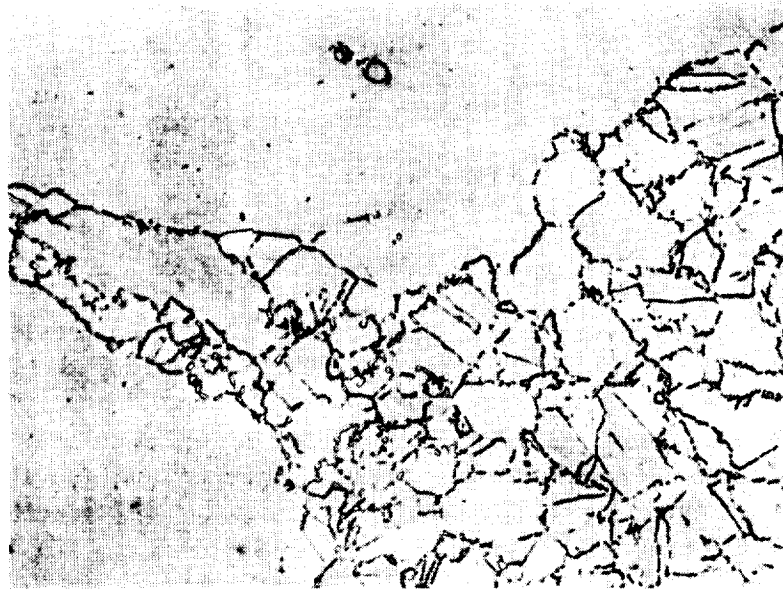
Figure 4 Alloy A With 3.93% Ti And 0.84% Al  
(Glyceria etch)

ORIGINAL PAGE IS  
OF POOR QUALITY

ORIGINAL PAGE IS  
OF POOR QUALITY



100X



1000X

Figure 5 Alloy B With 2.83% Ti and 0.69% Al  
(Glycerregia etch)

(25 ksi) too low. The  $H_2$ /air notch ratio ranged from 0.96 to 0.98.

While molybdenum (Mo) is a solid-solution strengthener in Fe-Ni alloys, it may be effective in suppressing the  $\gamma$  phases.<sup>9</sup> Two melts were made of the basic composition with Mo addition of 0.5 and 1.0%. As depicted in Figure 5, the plates cracked during hot rolling and no specimens could be salvaged. Since no explanation for cracking was evident, Mo additions will be attempted again.



Figure 6 Plates Containing Molybdenum, 0% (top), 0.5% (middle) and 1.0% (bottom)

#### Summary

It seems from some of the experiments that Al should be increased to possibly retard the  $\gamma$  formation. Also, the Mo additions should be attempted again for the same purpose. Although some of the alloys had very good strength and indicated good  $H_2$  resistance, the microstructure may not produce satisfactory fatigue or creep-rupture properties or even weldability, so more effort must be directed toward investigating different heat treat cycles. The most promising alloy composition is: 37% Fe, 32% Ni, 15% Co, 10% Cr, 3% Cb, 2-3% Ti and 0.5-1% A. The carbon should not exceed 0.04%. The Fe and Ni would be adjusted depending on the Ti, Al and Mo additions.

### References

1. J. A. Harris and M. C. Van Wanderham, "Influence of Gaseous Hydrogen on the Mechanical Properties of Incoloy 903," PWA Report FR-7175, September 1975.
2. R. A. Parr, "Failure Analyses of Wrought (STA 2) Incoloy 903 Low Cycle Fatigue Specimens," MSFC, M&FA Report EH22 (77-62), April 11, 1977.
3. D. F. Smith, E. F. Clatworthy, D. G. Tipton and W. L. Mankins, "Improving the Notch-Rupture Strength of Low-Expansion Superalloys," Superalloys 1980, September 1980; p. 521.
4. D. F. Smith and E. F. Clatworthy, "The Development of High Strength, Low Expansion Alloys," Metal Progress, vol. 124, No. 3, March 1981, p. 32.
5. R. H. Bricknell and D. A. Woodford, "Grain Boundary Embrittlement of the Iron-Base Superalloy IN 903 A," Metallurgical Transactions, vol. 12A, September 1981, p. 1673.
6. E. E. Nelson, "Resistance of Incoloy 903 to Stress Corrosion and General Corrosion in Several Environments," MSFC, EH24 (74-19), September 6, 1974.
7. D. R. Muzyka, C. R. Whitney and D. K. Schlosser, "Physical Metallurgy and Properties of a New Controlled-Expansion Superalloy," Journal of Metals, July 1975, p. 11.
8. C. P. Sullivan and M. J. Donachie, Jr., "Microstructures and Mechanical Properties of Iron-Base (-Containing) Superalloys," Metals Engineering Quarterly, November 1971, p. 1.
9. Donald R. Muzyka, "The Metallurgy of Nickel-Iron Alloys," The Superalloys, ed. Chester T. Sims and William C. Hagel, John Wiley and Sons, New York, 1972, p. 113.

HYDROGEN EFFECTS ON THE CRACK GROWTH  
RESISTANCE OF AN IRON BASED SUPERALLOY

N. R. Moody, M. W. Perra and R. E. Staltz  
Sandia National Laboratories  
P. O. Box 969  
Livermore, CA 94550

Fracture toughness and slow crack growth thresholds were determined in the Fe-Ni-Co superalloy IN903 as a function of hydrogen concentration and grain size. Fracture toughness measured with precharged samples was independent of grain size and decreased from 90 to 50 MPa-m<sup>1/2</sup> as hydrogen concentration increased from zero to 5000 appm. Slow crack growth thresholds determined in a gaseous environment decreased to 30 MPa-m<sup>1/2</sup> at a pressure of 207 MPa (equilibrium surface concentration of 5000 appm H). These values increased with increased grain size. The effect of hydrogen on fracture toughness and slow crack growth thresholds will be explained by the relationship between the microstructure and fracture modes.

This work supported by U. S. DOE contract number DE-AC04-460P00789.

MANUSCRIPT NOT AVAILABLE



## PARTICIPANTS

Alan Adams  
J. T. Akin  
David W. Allen  
Steve L. Allums  
Robert Ammon  
Olof Anderson  
W. J. Armstrong  
Joseph J. Attinello  
Clarence B. Auchter  
S. Don Bai  
Sarkis Barkhoudarian  
Donald A. Barnes  
Gary Bartee  
Lt. Angela B. Bartholomew  
John C. Bennett  
James T. Berling  
Mel Bernstein  
Ronald Bledsoe  
Wayne Bordelon, Jr.  
Kim Bowen  
James W. Bransford  
Mel Bryant  
O. Hal Burnside  
Miles S. Butner  
Tom Byrd  
W. E. Campbell  
James Cannon  
Charles E. Cataldo  
William V. Chambers  
W. T. Chandler  
Muwon Chang  
Shoei-Sheng Chen  
Lynn C. Chou  
Dr. A. Choudry  
Henry Cialone  
Harry Cikanek  
Joe C. Cody  
Thomas Coffin  
Anton Coles  
Dr. N. C. Costes  
Wilford H. Couts, Jr.  
B. A. Cowles,  
Preston S. Craig  
John M. Crapuchettes  
Robert J. Cronin  
Jeremy P. B. Cuffe  
Leslie A. Curtis  
Youssef M. Dakhoul  
Dan David  
Rory R. Davis  
William B. Day  
William J. Dickinson  
Thomas Dollman  
Robert Dominic  
Robert E. Doyle  
Robert Dreshfield  
Dan Drinan  
Robert Dring  
Thomas DuBell  
Roger Dugas  
Dr. Michale G. Dunn  
Matthew C. Ek  
T. C. Evatt  
Charles Finnegan  
Lorraine Finnegan  
Jeff A. Fisher  
Steven C. Fisher  
Anthony Fortini  
Robert L. Fowler  
D. B. Franklin  
Alonzo Frost  
Donald L. Fulton  
Gordon H. Gainer, Jr.  
Fred S. Garcia  
Thomas Garosshen  
Ashoke Ghosh  
Harold M. Gibson  
Lou Ann Gibson  
John Giordano  
John R. Glease  
R. Glover  
O. K. Goetz  
Sol Gorland  
Lynnon F. Grant  
Stanley Gray  
Willard Green  
Klaus Gross  
Gary Gustafson  
Jack Halbrooks  
Dr. Gary R. Halford  
Richard L. Hall  
James D. Hankins  
Dr. Gary Harloff  
Harland Harman  
Robert D. Harris  
B. B. Henson

Rosemary Hernandez  
Philip Hess  
Richard R. Holmes  
Dale A. Hopkins  
Vance Houston  
J. E. Hughes  
Edwin P. Jacobs  
Richard Jentgen  
Belgacem Jery  
James A. Johnston  
Jen-Yi Jong  
Albert Kaufman  
James E. Kingsbury  
Kenneth G. Kirk  
Zach Kirkland  
John M. Knadler, III  
Arthur Kobayashi  
Dr. Richard D. Kramer  
Dr. Robert E. Kurth  
Paul H. Kutschenreuter  
T. Cleon Lacefield  
Debra Leath  
Brenda L. Lindley-Anderson  
O. Leon Lindsey  
Stuart H. Loewenthal  
Thomas L. Lopez  
Carl H. Lund  
Charles Lundquist  
Stuart G. MacDonald  
A. K. Majumdar  
Saurin Majumdar  
Arthur I. Master  
Dan Matejczyk  
Glen Malone  
Robert G. Mapes  
S. J. Marsik  
David E. Marty  
Mason D. Marvin  
Ronald A. Mayville  
Patrick E. McBurnett  
Michael A. McGraw  
Timothy McHechnie  
Melvin C. McIlwain  
Eugene McKannou  
Joseph A. McKenzie  
Bryan McPherson  
Jay Medley  
Daniel Mellon  
Stephen Mercer  
Donald V. Merrifield  
Dr. S. Midturi  
Kathrine Mims  
Dr. N. R. Moody

Dennis Moore  
Lance Moore  
S. F. Morea  
George S. Morefield  
Stanley A. Mosier  
Dr. Tonmoy Mukerjee  
B. T. Murphy  
Mike Murphy  
James A. Nesbitt  
William Nieberding  
Sherif T. Noah  
Richard Norman  
Arthur C. Nunes, Jr.  
Gordon S. Oakley  
Charles J. O'Brien  
Richard A. Parr  
Robert A. Pallini  
Arvind C. Patel  
Dr. Neil E. Paton  
Donald Paulus  
Mark L. Pearson  
Dennis G. Pelaccio  
Roy Pelmas  
Arlen Petersen  
Donald W. Petrusek  
Alan Philips  
Jerry Pieper  
William E. Poole  
S. Porowski  
Dr. Louis A. Povinelli  
William T. Powers  
Harlan Pratt  
Harold G. Price  
Robert J. Prozen  
A. J. Przekwas  
Richard Quentmeyer  
Thomas A. Rackley, III  
Dr. G. V. R. Rao  
J. R. Redus  
Chris Rhemer  
James S. Richards  
Robert J. Richmond  
Curtis L. Robinson  
Dr. Robert P. Roger  
Dr. Sanders Rosenberg  
Michael Rother  
Don C. Rousar  
Robert Rowe  
Paul Royall  
Richard Ryan  
Jeffery W. Salmon  
Douglas S. Sandridge  
Carla Schindler

Leonard Schoenman  
Fredrick T. Schuller  
David C. Seymour  
Lalit K. Sharma  
Dr. John A. Shirley  
J. D. Siegwarth  
Ashok Kumar Singhal  
Richard L. Smith  
William Soong  
Louis J. Spadaccini  
Paul Spica  
Roderick Stallworth  
Frank W. Stephenson, Jr.  
Henry P. Stinson  
Sally L. Stohler  
Albert Storace  
Don Stouffer  
Wayne L. Swanson  
Marion S. Swint  
Luen Tong Tam  
John K. Tein  
Linnis G. Thomas  
Jerry Thomson  
Anthony W. Thompson  
Dr. Robert G. Thompson  
Bruce K. Tiller  
Alan E. Tischer  
Isaias Torres  
Philip L. Tygielski  
David A. Utah  
M. C. Vanwanderham  
Alex Vary  
H. G. Vick  
George L. Von Pragenau  
Richard E. Walker  
Scott Walston  
Martin W. Wambsganss  
J. Peter Wanhainen  
K. Kevin Ward  
W. B. Watkins  
W. B. White  
Michael R. Whitley  
Clyde Wiley  
Glenn E. Wilmer, Jr.  
A. L. Worlund  
S. T. Wu  
Jim L. Yuen  
Robert Zera  
Joe E. Zimmerman

APPENDIX

VOLUME ONE

TABLE OF CONTENTS

FOREWORD . . . . . ii

WELCOME ADDRESS  
James E. Kingsbury . . . . . 1

PROGRAM OVERVIEW  
Frank W. Stephenson, Jr. . . . . 2

OXYGEN/HYDROGEN TECHNOLOGY TEST BED  
A. L. Worlund . . . . . 13

I STRUCTURAL DYNAMICS

Statistical Techniques for Detecting Bearing Defects  
Richard Smith and Jack Frarey . . . . . 20

Diagnostic Assessment of Turbomachinery by the Hyper-Coherence Method  
Jen-Yi Jong and Thomas Coffin . . . . . 45

Probabilistic Structural Analysis Methods: SSME Propulsion Components  
D. A. Hopkins and C. C. Chamis . . . . . 65

Fatigue Life Predictions from Measured Strains  
Robert A. Sire . . . . . 88

II INSTRUMENTATION

Fiber Optic Raman Thermometer for Space Shuttle Main Engine Preburner Profiling  
John A. Shirley . . . . . 107

An Advanced Solid State Pressure Transducer for High Reliability SSME Applications  
G. E. Gustafson and J. J. Shea . . . . . 124


Vortex Shedding Flowmeter for Fluids at High Flow Velocities  
James D. Siegwarth . . . . . 139

Non-Intrusive Shaft Speed Sensor  
L. Wyett and S. Barkhoudarian . . . . . 154

SSME Failure Characteristics with Regard to Failure Detection  
T. C. Evatt, L. R. Iwanicki, M. H. Taniguchi, and H. A. Cikanek, III . . . . . 159

Heat Flux Sensor Calibration A. Dybbs and M. Krane . . . . .	165
Development of An Acoustic Monitor to Detect Incipient Bearing Failure William D. Jolly, W. R. Van der Veer and John M. Knadler . . . .	178
Laser Anemometry Systems Design for Velocity Measurements in the SSME L. K. Sharma, T. V. Ferguson, J. C. Craddock, and D. G. Pelaccio . . . . .	197
III DYNAMIC CHARACTERISTICS OF TURBOMACHINERY	
A Facility to Study Turbine Rotor and Seal Clearance Forces B. Jery, Y. Qiu, M. Martinez-Sanchez, and E. M. Greitzer. . . .	233
Impeller Fluid Forces C. E. Brennen, A. J. Acosta, and T. K. Caughey . . . . .	270
Force and Moment Rotordynamic Coefficients for Pump- Impeller Shroud Surfaces Dara W. Childs . . . . .	296
Experimental Rotordynamic Coefficient Results for Teeth- On-Rotor and Teeth-On-Stator Labyrinth Gas Seals Dara W. Childs and Joseph K. Scharrer . . . . .	327
Test Results for Sawtooth-Pattern Damper Seals: Leakage and Rotordynamic Coefficients D. Childs and Frank Garcia . . . . .	346
IV MATERIAL TECHNOLOGY	
Ignition Characteristics of Selected SSME Alloys James W. Bransford, Phillip A. Billiard, James A. Hurley and Isaura Vazquez . . . . .	366
Tailored Single Crystal Airfoil Development K. Bowen and P. Nagy . . . . .	387
Evaluation of Turbine Disk PM Alloys in Hydrogen W. H. Coutts, Jr. . . . .	413
Application of Advanced Coating Techniques to Rocket Engine Components S. K. Verma . . . . .	422
Evaluation of Fiber-Reinforced Superalloy Composites for SSME Turbine Blade Applications J. L. Yuen . . . . .	451

New Developments in Electroformed Nickel Based Structural Alloys Glenn A. Malone . . . . .	480
V FLUID AND GAS DYNAMICS I	
Water Flow Test of the Space Shuttle Main Engine Hot Gas Manifold Bruce M. Wiegmann . . . . .	498
Viscous Flow Computations for the HGM II <sup>+</sup> Version of the SSME/HGM R. P. Roger and S. J. Robertson . . . . .	518
Flow Induced Vibrations in the SSME Injector G. V. R. Rao . . . . .	559
Highlights of the Space Shuttle Main Engine (SSME) Computational Fluid Dynamics (CFD) Fourth Working Group Meeting H. V. McConnaughey . . . . .	571
Numerical Simulation of Multiple Jet Interaction S. D. Bai, S. T. Wu and C. Warren Campbell . . . . .	576
SSME Aerothermodynamics Load Definition L. A. Povinelli . . . . .	595
VI FLUID AND GAS DYNAMICS II	
Assessment of a Parabolic Analysis for Axisymmetric Internal Flows in Rocket and Turbomachinery Ducts G. D. Power and O. L. Anderson . . . . .	597
Analysis of Multistage Turbomachinery Flows J. J. Adamczyk . . . . .	613
Experimental Measurements of Heat-Flux Distributions in a Turbine Stage with Upstream Disturbances M. G. Dunn . . . . .	614
Computational and Experimental Study of Flow-Induced Vibration of the SSME Main Injector Post S. S. Chen, J. A. Jendrzejczyk, and M. W. Wambsganss . . . . .	637
Real Gas Properties and Space Shuttle Main Engine Fuel Turbine Performance Evaluation G. J. Harloff . . . . .	663
PARTICIPANTS . . . . .	688
APPENDIX	
Table of Contents of Volume Two . . . . .	691

1. REPORT NO. NASA CP-2437		2. GOVERNMENT ACCESSION NO.		3. RECIPIENT'S CATALOG NO.	
4. TITLE AND SUBTITLE Advanced Earth-to-Orbit Propulsion Technology - 1986 Volume II			5. REPORT DATE October 1986		
			6. PERFORMING ORGANIZATION CODE		
7. AUTHOR(S) R.J. Richmond and S.T. Wu, Editors			8. PERFORMING ORGANIZATION REPORT #		
9. PERFORMING ORGANIZATION NAME AND ADDRESS George C. Marshall Space Flight Center Marshall Space Flight Center, Alabama 35812			10. WORK UNIT NO. M-541		
			11. CONTRACT OR GRANT NO.		
12. SPONSORING AGENCY NAME AND ADDRESS National Aeronautics and Space Administration Washington, DC 20546			13. TYPE OF REPORT & PERIOD COVERED Conference Publication		
			14. SPONSORING AGENCY CODE		
15. SUPPLEMENTARY NOTES R.J. Richmond - George C. Marshall Space Flight Center, Huntsville, Alabama S.T. Wu - The University of Alabama in Huntsville, Huntsville, Alabama Proceedings of a conference held at the George C. Marshall Space Flight Center					
16. ABSTRACT The 1986 conference on Advanced Earth-to-Orbit Propulsion Technology was held on May 13-15, 1986 at the George C. Marshall Space Flight Center. The purpose of the conference was to disseminate to the industry, government and university propulsion community the results emerging from NASA's Advanced Earth-to-Orbit Propulsion Technology Program.  The technical information presented was organized into twelve sessions and one workshop dealing with rocket engine structural dynamics, instrumentation, turbomachinery rotor-dynamics, materials, fluid and gas dynamics, fatigue and fracture mechanics, bearings, combustion and cooling, and hydrogen embrittlement.  A total of 75 papers was presented and approximately 250 rocket engine technologists and developers from industry, government, and universities attended. The proceedings of this conference are published in two volumes. This publication is Volume 2 and contains the manuscripts from the remaining six sessions and the workshop.					
17. KEY WORDS Liquid rocket engines Propulsion technology O <sub>2</sub> /H <sub>2</sub> technology O <sub>2</sub> /Hydrocarbon technology			18. DISTRIBUTION STATEMENT  Until September 1988  Subject Category 20		
19. SECURITY CLASSIF. (of this report) Unclassified		20. SECURITY CLASSIF. (of this page) Unclassified		21. NO. OF PAGES 773	22. PRICE A99